Effects of RADIATION *on* MATERIALS

19th International Symposium

Margaret L. Hamilton
Arvind S. Kumar
Stan T. Rosinski
Martin L. Grossbeck
Editors

ASTM STP 1366

STP 1366

Effects of Radiation on Materials: 19th International Symposium

Margaret L. Hamilton, Arvind S. Kumar, Stan T. Rosinski, and Martin L. Grossbeck, editors

ASTM Stock Number: STP1366

ASTM
100 Barr Harbor Drive
West Conshohocken, PA 19428-2959

Printed in the U.S.A.

ISBN: 0-8031-2852-5
ISSN: 1050-7515

Copyright © 2000 AMERICAN SOCIETY FOR TESTING AND MATERIALS, West Conshohocken, PA. All rights reserved. This material may not be reproduced or copied, in whole or in part, in any printed, mechanical, electronic, film, or other distribution and storage media, without the written consent of the publisher.

Photocopy Rights

Authorization to photocopy items for internal, personal, or educational classroom use, or the internal, personal, or educational classroom use of specific clients, is granted by the American Society for Testing and Materials (ASTM) provided that the appropriate fee is paid to the Copyright Clearance Center, 222 Rosewood Drive, Danvers, MA 01923; Tel: 508-750-8400; online: http://www.copyright.com/.

Peer Review Policy

Each paper published in this volume was evaluated by two peer reviewers and at least one editor. The authors addressed all of the reviewers' comments to the satisfaction of both the technical editor(s) and the ASTM Committee on Publications.

To make technical information available as quickly as possible, the peer-reviewed papers in this publication were prepared "camera-ready" as submitted by the authors.

The quality of the papers in this publication reflects not only the obvious efforts of the authors and the technical editor(s), but also the work of the peer reviewers. In keeping with long-standing publication practices, ASTM maintains the anonymity of the peer reviewers. The ASTM Committee on Publications acknowledges with appreciation their dedication and contribution of time and effort on behalf of ASTM.

Printed in Philadelphia, PA
March 2000

Foreword

This publication, *Effects of Radiation on Materials: 19th International Symposium,* contains papers presented at the symposium of the same name held in Seattle, Washington on 16–18 June 1998. The symposium was sponsored by ASTM Committee E10 on Nuclear Technology and Applications. The symposium chairman was Margaret L. Hamilton, Pacific Northwest Laboratory. Arvind S. Kumar, University of Missouri-Rolla, Stan T. Rosinski, Electric Power Research Institute, and Martin L. Grossbeck, Oak Ridge National Laboratory, served as co-chairmen.

Of the various nuclear-oriented symposia, this series is the oldest and most comprehensive. The first symposium with the current name was held in 1960 but grew out of an earlier series that was initiated in 1956 by Committee E10, then called the Committee on Radioisotopes and Radiation Effects.

This 19th international symposium continues the tradition of earlier symposia in that there is a large contribution from the international nuclear community, with a significant increase from countries of the former Soviet Union. As is typical of this series, the largest segment of papers is devoted to pressure vessel embrittlement and its mitigation. Smaller segments address issues of continuing interest in light water reactors, fusion reactors, and to a lesser extent, breeder reactors. These issues are presented in separate sections devoted to classes of materials.

Several emerging issues are addressed in some papers, for example, reduced activation, welding of irradiated materials, and damage resulting from high-energy proton beams in accelerator-driven nuclear systems. It is the expectation of the leaders of this symposium that this publication will continue to reflect the emerging concerns of the nuclear materials community as we proceed into the twenty-first century.

Contents

PRESSURE VESSEL STEELS—MECHANICAL PROPERTIES

A Comparison of East/West Steels for Pressurized Water Reactors— M. DAVIES, A. KRYUKOV, C. ENGLISH, Y. NIKOLAEV, AND W. L. SERVER 3

Exploratory Test of 288°C Radiation Resistance of Two USSR-Produced Reactor Pressure Vessel Steels—J. R. HAWTHORNE, M. A. SOKOLOV, AND W. L. SERVER 16

Analysis of Irradiation Data for A302B and A533B Correlation Monitor Materials—J. A. WANG 33

Comparison of Static and Dynamic Transition Temperature Shifts in VVER Reactor Pressure Vessel Steels—M. BRUMOVSKY, M. FALCNIK, M. KYTKA, J. MALEK, AND P. NOVOSAD 56

Effect of Radiation on Material Used for 600MW Chinese Nuclear Power Plant Reactor Pressure Vessel—X. JIA, Y. XU, W. YANG, AND C. ZHANG 69

Comparison of Fracture Toughness of Irradiated Reactor Vessel Welds—Predicted by ASTM E 900 and Measured—K. K. YOON AND W. A. PAVINICH 76

Neutron Spectrum Effect and Damage Analysis on Pressure Vessel Steel Irradiation Behaviour—C. PICHON, C. BRILLAUD, D. DEYDIER, A. ALBERMAN, AND P. SOULAT 87

Characterization of the Decommissioned Novovoronesh-1 Pressure Vessel Wall Materials by Through-Wall Trepans—M. J. VALO, A. D. AMAEV, R. AHLSTRAND, D. A. CHISTIAKOV, E. KRASIKOV, A. KRYUKOV, A. M. MOROSOV, V. A. NIKOLAEV, P. PLATONOV, R. RINTAMAA, V. V. RYBIN, Y. SHTROMBAKH, AND K. WALLIN 98

The Effects of Flux on Radiation Embrittlement of Low-Copper Pressure Vessel Steels—Y. XU, X. JIA, C. ZHANG, G. NING, AND Q. YU 118

Technical Basis for Application of the Master Curve Approach to Reactor Pressure Vessel Integrity Assessment—W. L SERVER AND S. T. ROSINSKI 127

Bias and Precision of T_o Values Determined Using ASTM Standard E 1921-97 for Nuclear Reactor Pressure Vessel Steels—M. KIRK, R. LOTT, W. L. SERVER, R. HARDIES, AND S. ROSINSKI 143

Fracture Toughness of the Ni-Modified A302-B Plate of the BR3 Reactor Pressure Vessel—R. CHAOUADI, A. FABRY, E. VAN WALLE, AND J. VAN DE VELDE 162

Application of Master Curve Technology to Biaxial and Shallow Crack Fracture Data For A533B Steels—J. A. JOYCE, R. L. TREGONING, AND X. J. ZHANG 177

Effect of Irradiation on Fracture Toughness in the Transition Range of RPV Steels—K. ONIZAWA, T. TOBITA, AND M. SUZUKI 204

Supplementary Surveillance Program for Reactor Pressure Vessels of VVER-440/V-213C Type Reactors in NPP Dukovany—M. BRUMOVSKY, O. ERBEN, AND P. NOVOSAD 220

PRESSURE VESSEL WELDS—MECHANICAL PROPERTIES

Irradiation Behavior of Submerged Arc Welding Materials with Different Copper Content—R. LANGER, R. BARTSCH, AND G. NAGEL 235

Effects of Irradiation on Crack-Arrest Toughness of a Low Upper-Shelf Energy, High-Copper Weld—S. K. ISKANDER, R. K. NANSTAD, D. E. MCCABE, AND R. L. SWAIN 245

Effect of Location of V-Notch on Neutron Irradiation-Induced Shift in DBTT of HAZ of Welded Pressure Vessel Steel—T. SUZUKI, K. ITOH, Y. NARUSE, H. MATSUI, AND A. KIMURA 266

Fracture Toughness Test Results of Precracked Charpy Specimens of Irradiated 73W Weld Material—R. CHAOUADI, E. VAN WALLE, A. FABRY, M. SCIBETTA, AND J. VAN DE VELDE 279

Fracture Toughness of Submerged-Arc Weld Samples from a Decommissioned Magnox Reactor Pressure Vessel: Initial Results—P. J. E. BISCHLER, M. R. WOOTTON, AND C. J. BOLTON 295

Effects of Irradiation and Thermal Annealing on Fracture Toughness of the Midland Reactor Weld WF-70—D. E. MCCABE, R. K. NANSTAD, AND M. A. SOKOLOV 306

PRESSURE VESSEL STEELS—SEGREGATION AND MICROSTRUCTURE

Irradiation Damage Structure in VVER-440 Steels after Irradiation at Different Temperatures and Post-Irradiation Annealing—M. GROSSE AND J. BÖHMERT 323

Grain Boundary Phosphorus Segregation under Neutron Irradiation and Aging in 2.25Cr1Mo Steel—S. SONG, R. G. FAULKNER, P. E. J. FLEWITT, P. MARMY, AND M. VICTORIA 343

Microstructure of the Neutron Irradiated VVER-type Reactor Pressure Vessel Steels—J. KOČÍK, E. KEILOVÁ, I. PROCHÁZKA, AND J. ČÍŽEK 354

Influence of Thermal Neutrons on the Hardening and Embrittlement of Plate Steels—R. B. JONES, D. J. EDENS, AND M. R. WOOTTON 366

Radiation-Induced Grain Boundary Segregation of Phosphorus in ASME SA533B Ferritic Pressure Vessel Steel—D. MEADE, R. G. FAULKNER, AND D. ELLIS 383

Comparison of Observed and Predicted Data on Radiation Induced Grain Boundary Phosphorus Segregation in VVER Type Steels—A. V. NIKOLAEVA, Y. R. KEVORKYAN, AND Y. A. NIKOLAEV 399

FERRITIC AND FERRITIC/MARTENSITIC STEELS—ANNEALING AND REIRRADIATION BEHAVIOR

Irradiation, Annealing, and Reirradiation Effects on American and Russian Reactor Pressure Vessel Steels—M. A. SOKOLOV, A. A. CHERNOBAEVA, R. K. NANSTAD, Y. A. NIKOLAEV, AND Y. N. KOROLEV 415

Annealing of a Low Copper Steel: Hardness, SANS, Atom Probe and Thermoelectric Power Investigations—P. PAREIGE, P. AUGER, S. WELZEL, J.-C. VAN DUYSEN, AND S. MILOUDI 435

Two-Step Recovery Process of Irradiation Hardening in 1%Ni Doped 9%Cr-2% W Martensitic Steel—R. KASADA, T. MORIMURA, H. MATSUI, M. NARUI, AND A. KIMURA 448

Application of the Floating Curve Model for Estimation of Re-Irradiation Embrittlement of VVER-440 RPV Steels—Y. NIKOLAEV AND A. V. NIKOLAEVA 460

IRRADIATION-INDUCED BEHAVIOR OF IRON, MODEL ALLOYS, AND FERRITIC/MARTENSITIC ALLOYS

Embrittlement, Hardening, and Grain Boundary Composition in an Fe-P-C Alloy after Irradiation or Thermal Aging—R. B. JONES, J. R. COWAN, R. C. CORCORAN, AND J. C. WALMSLEY 473

Microstructure and Hardening in Thermally Aged and Neutron-Irradiated Fe-Cu Model Alloy—H. KAWANISHI AND M. SUZUKI 492

Neutron Irradiation Rate Dependence of Damage Structures in Fe-Cu Model Alloys—S. YANAGITA, Q. XU, T. YOSHIIE, AND H. INO 516

Gamma-Radiation Annealing to Mitigate Neutron-Induced Degradation of Both Model and Structural Reactor Materials—V. I. KARPUKHIN, Y. A. KRASIKOV, V. A. NIKOLAENKO, AND Y. I. SHTROMBAKH 525

Analysis of Stress-Induced Burgers Vector Anisotropy in Pressurized Tube Specimens of Irradiated Ferritic-Martensitic Steels: JFMS and JLF-1—D. S. GELLES, A. KIMURA, AND T. SHIBAYAMA 535

An Evaluation of Neutron Energy Spectrum Effects in Iron Based on Molecular Dynamics Displacement Cascade Simulations—R. E. STOLLER AND L. R. GREENWOOD 548

Effects of Neutron Irradiation on Fe-Cu Model Alloys and RPV Steels Probed by Positron Annihilation and Hardness Measurements—A. HEMPEL, M. SANEYASU, Z. TANG, M. HASEGAWA, G. BRAUER, F. PLAZAOLA, S. YAMAGUCHI, F. KANO, AND A. KAWAI 560

Irradiation Behavior of Ferritic-Martensitic 9-12% Cr Steels—M. G. HORSTEN, E. V. VAN OSCH, D. S. GELLES, AND M. L. HAMILTON 579

LOW ACTIVATION FERRITIC/MARTENSITIC ALLOYS

Mechanical Properties and Microstructure of HFR-Irradiated Ferritic/Martensitic Low-Activation Alloys—E. I. MATERNA-MORRIS, M. RIETH, AND K. EHRLICH 597

Mechanical Properties of Four 7-9%Cr Reduced Activation Martensitic Steels after 2.5 dpa, 300°C Irradiation—E. VAN OSCH, M. HORSTEN, G. E. LUCAS, AND G. R. ODETTE 612

Evaluation of Ductile-Brittle Transition Behavior of Helium-implanted Reduced Activation 9Cr-2W Martensitic Steel by Small Punch Tests—A. KIMURA, T. MORIMURA, R. KASADA, H. MATSUI, A. HASEGAWA, AND K. ABE 626

Irradiation Creep and the Creep-Swelling Relationship

Irradiation Creep of Austenitic Steels Irradiated Up to High Damage Dose— V. S. NEUSTROEV AND V. K. SHAMARDIN 645

Reanalysis of Swelling and Irradiation Creep Data on 316 Type Stainless Steels Irradiated in the FFTF and Phénix Fast Reactors— M. B. TOLOCZKO AND F. A. GARNER 655

The Relationship Between Swelling and Irradiation Creep in 20% Cold-Worked 316 Stainless Steel—F. A. GARNER, M. B. TOLOCZKO, AND R. J. PUIGH 667

Irradiation Creep and Stress-Affected Swelling in Austenitic Stainless Steel 16Cr-15Ni-3Mo-Nb-B Irradiated in the BN-350 Reactor—S. I. POROLLO, A. N. VOROBJEV, Y. V. KONOBEEV, N. I. BUDYLKIN, E. G. MIRONOVA, AND F. A. GARNER 679

Effects of Impurity on Radiation Creep Rate of the Interstitial Solid Solutions—A. D. LOPUGA AND Y. S. PYATILETOV 688

On the Role of Internal Stresses in Void Denuded Zone Formation Under HVEM-Irradiation of Metals and Alloys Preconditioned by Reactor Exposure—Y. V. KONOBEEV, V. A. PECHENKIN, AND F. A. GARNER 699

Creep-Fatigue Response of 20% CW 316 SS Under Irradiation at 60°C— Y. MURASE, J. NAGAKAWA, N. YAMAMOTO, AND Y. FUKUZAWA 713

In-Reactor Creep Regularities of Copper—E. S. AITKHOZHIN, Y. S. PYATILETOV, AND E. V. CHUMAKOV 725

Austenitic Alloys—Irradiation-Induced Swelling, Segregation and Microstructure

The Correlation Between Swelling and Radiation-Induced Segregation in Iron-Chromium-Nickel Alloys—T. R. ALLEN, J. T. BUSBY, J. GAN, E. A. KENIK, AND G. S. WAS 739

Effect of IVa and Va Elements on Void Formation in Neutron-Irradiated 316 Stainless Steels—S. OHNUKI, S. YAMASHITA, H. TAKAHASHI, AND T. KATO 756

The Question of Saturation of Void Swelling in Fe-Cr-Ni Austenitic Alloys— F. A. GARNER AND C. A. BLACK 767

Influence of Minor Alloying Elements and Stress on Microstructural Evolution and Void Swelling of Austenitic Steels Under Neutron Irradiation— R. HÜBNER AND K. EHRLICH 778

Temperature-Shift of Void Swelling Observed in Annealed Fe-18Cr-10Ni-Ti Stainless Steel Irradiated in the Reflector Region of BOR-60—V. S. NEUSTROEV, V. K. SHAMARDIN, Z. E. OSTROVSKY, A. M. PECHERIN, AND F. A. GARNER 792

The Effect of Molybdenum on the Grain Boundary Segregation of Chromium Exhibited by Austenitic Stainless Steels after Neutron Irradiation in a BWR—C. C. GOODWIN, R. G. FAULKNER, J. C. WALMSLEY, AND P. SPELLWARD 801

Microstructure Modeling of a 316L Stainless Steel Irradiated with Electrons—J. HENRY, A. BARBU, AND A. HARDOUIN-DUPARC 816

Effects of Damage Rate on Formation of Voids and Dislocation Loops in Metals—Q. XU, T. YOSHIIE, AND M. ISEKI 836

Stress-Affected Dislocation Development of Stainless Steel During Neutron Irradiation—S. I. POROLLO, Y. V. KONOBEEV, A. S. KRUGLOV, Y. M. PEVCHIKH, AND F. A. GARNER 850

Influence of Silicon or Titanium on the Microstructural Evolution of Fe-Cr-35Ni Alloys Irradiated with Neutrons or Self-Ions—H. WATANABE AND F. A. GARNER 859

Void-Induced Swelling and Embrittlement in the Russian EI-847 Stainless Steel at PWR-Relevant End-of-Life Conditions—F. A. GARNER, S. I. POROLLO, A. N. VOROBJEV, Y. V. KONOBEEV, A. M. DVORIASHIN, V. M. KRIGAN, N. I. BUDYLKIN, AND E. G. MIRONOVA 874

Interaction of Void-Induced Phase Instability and Subsequent Void Growth in AISI 304 Stainless Steel—D. L. PORTER, F. A. GARNER, AND G. M. BOND 884

On the Formation of α-Ferrite in Stainless Steel Alloys—W. SCHÜLE 894

A Composite Model for Segregation and Microstructural Evolution Under Electron Irradiation—S. WATANABE, N. SAKAGUCHI, H. TAKAHASHI, AND S. OHNUKI 919

IRRADIATED STRUCTURAL ALLOYS—WELDING

Stress-Modified Welding of Neutron Irradiated Steels—C. A. WANG, H. C. WIKLE, III, M. L. GROSSBECK, AND B. A. CHIN 935

Thick Plate Welding of Irradiated Stainless Steel—K. ASANO, R. KATSURA, S. KAWANO, AND M. KOSHIISHI 944

Cracks in TIG Welded, Neutron-Irradiated 304 Stainless Steel—A. KOHYAMA, T. HIROSE, T. SUZUKI, M. NARUI, AND Y. KATOH 959

Modeling of Helium Bubble Formation During Welding of Irradiated Stainless Steels—T. HASHIMOTO AND M. MOCHIZUKI 973

Effect of Neutron Irradiation on Mechanical Properties of Cu-Alloy/SS316 Joints—K. TSUCHIYA, M. NAKAMICHI, AND H. KAWAMURA 988

EXPERIMENTAL TECHNIQUES AND FACILITIES

Neutron-Induced Evolution of Mechanical Properties of 20% Cold-Worked 316 Stainless Steel as Observed in Both Miniature Tensile and TEM Shear Punch Specimens—M. L. HAMILTON, F. A. GARNER, G. L. HANKIN, R. G. FAULKNER, AND M. B. TOLOCZKO 1003

An Investigation into the Origin and Nature of the Slope and x-axis Intercept of the Shear Punch-Tensile Yield Strength Correlation using Finite Element Analysis—G. L. HANKIN, M. B. TOLOCZKO, K. I. JOHNSON, M. A. KHALEEL, M. L. HAMILTON, F. A. GARNER, R. W. DAVIES, AND R. G. FAULKNER 1018

Thermoelectric Power: A Nondestructive Method for Monitoring Irradiation Effects in Ferritic Steels—S. MILOUDI, S. JUMEL, P. PAREIGE, J. F. COSTE, AND J. C. VAN DUYSEN 1029

Design of a Dedicated Electron Beam Facility for Material Treatment—J. MITTENDORFER 1043

BERYLLIUM AND CERAMICS

Microstructural Examination of Irradiated Beryllium Pebbles—D. S. GELLES, M. DALLE DONNE, H. KAWAMURA, S. OHNUKI, AND F. SCAFFIDI-ARGENTINA 1051

Measurement and Calculation of Helium Generation in Beryllium Pebbles Irradiated in EBR-II—L. R. GREENWOOD, B. M. OLIVER, D. S. GELLES, D. L. BALDWIN, M. DALLE DONNE, H. KAWAMURA, AND F. SCAFFIDI-ARGENTINA 1062

In-situ Electrical Resistivity Measurement of $MgO \cdot Al_2O_3$ Coating under Neutron Irradiation—M. NAKAMICHI AND H. KAWAMURA 1075

Effect of Ionizing and Displacive Components of Irradiation on the Structural Transformations in Pyrolitic Boron Nitride Ceramics—V. A. STEPANOV, P. A. STEPANOV, V. M. CHERNOV, A. V. GOLOVINOV, AND L. M. KRYUKOVA 1084

OTHER MATERIALS

Effect of Irradiation on Structural Materials in Fusion Reactors—F. TAVASSOLI, H. BURLET, A. LIND, B. N. SINGH, S. TÄHTINEN, AND E. VAN OSCH 1093

Helium/Hydrogen Measurements in High-Energy Proton-Irradiated Tungsten—B. M. OLIVER, M. L. HAMILTON, F. A. GARNER, W. F. SOMMER, S. A. MALOY, AND P. D. FERGUSON 1109

Amorphization of Solids Irradiated by Fast Neutrons—V. D. PARKHOMENKO, S. F. DUBININ, S. G. TEPLOUKHOV, AND B. N. GOSHCHITSKII 1122

Effects of Fast Neutron Irradiation at 80K on Titanium Nickelide—S. F. DUBININ, V. D. PARKHOMENKO, AND S. G. TEPLOUKHOV 1131

Irradiation Aging of Aluminum Alloys—F. GILLEMOT, L. GILLEMOT, AND G. URI 1137

Effect of Ion-Irradiation on Phase Transformation in TiNi Shape Memory Alloys—Y. MATSUKAWA, Y. SUMITA, S. OHNUKI, S. WATANABE, C. NAMBA, AND H. TAKAHASHI 1147

Irradiation Growth of Zirconium Alloys at High Neutron Fluences—V. K. SHAMARDIN, G. P. KOBYLYANSKY, AND V. M. KOSENKOV 1159

Neutron Irradiation Test of Optical Components for Fusion Reactor—E. ISHITSUKA, H. SAGAWA, A. NAGASHIMA, T. SUGIE, T. NISHITANI, S. YAMAMOTO, AND H. KAWAMURA 1176

Correlation of Hardening and Microstructure of Tantalum Irradiated with Heavy Ions—T. MUROGA, K. YASUNAGA, Y. KATOH, H. WATANABE, N. YOSHIDA, AND N. NODA 1186

Improvement of Post Irradiation Ductility of V-Ti-Cr-Si Type Alloys Neutron Irradiated Around 400°C—M. SATOU, T. CHUTO, A. HASEGAWA, AND K. ABE 1197

The Influence of Transmutation and Initial Composition on the Microstructural Evolution of Vanadium and V-Cr-Ti Alloys Irradiated in HFIR—S. OHNUKI, H. TAKAHASHI, AND F. A. GARNER 1212

Neutron Irradiation Induced High Temperature Embrittlement of Pure Copper and High Strength Copper Alloys—S. A. FABRITSIEV, A. S. POKROVSKY, S. J. ZINKLE, AND D. J. EDWARDS 1226

Effect of Neutron Irradiation on Tensile and Fracture Toughness Properties of Copper Alloys and Their Joints with Stainless Steel—S. J. TÄHTINEN, M. T. PYYKKÖNEN, B. N. SINGH, AND P. TOFT 1243

Indexes 1261

Pressure Vessel Steels—Mechanical Properties

Myrddin Davies,[1] Alexandr Kryukov,[2] Colin English,[3] Yuri Nikolaev,[2] and William L. Server[4]

A Comparison of East/West Steels for Pressurized Water Reactors

Reference: Davies, M., Kryukov, A., English, C., Nikolaev, Y., and Server, W. L., **"A Comparison of East/West Steels for Pressurized Water Reactors,"** *Effects of Radiation on Materials: 19th International Symposium, ASTM STP 1366*, M. L. Hamilton, A. S. Kumar, S. T. Rosinski, and M. L. Grossbeck, Eds., American Society for Testing and Materials, West Conshohocken, PA, 2000.

Abstract: Recent studies have shown that for the older East and West water reactor pressure vessel steels there is a similar degradation in mechanical properties during equivalent neutron irradiation. In both cases with the identification of and a reduction in the deleterious element concentration the sensitivity of the steels to neutron irradiation was reduced. The deleterious elements which have been identified in the national databases as being responsible for the sensitivity are different. In the 'Western' case copper and nickel are identified and used in the current version of the USNRC Regulatory Guide while phosphorus and copper are identified in the Russian Codes. For the comparison neutron fluence is harmonized and the end-of-life fluence differences are considered. Annealing is a mitigating action for reducing the effect of irradiation on these steels and another coincidence in the similarity of the response of these steels is seen. The paper reviews the current understanding on the mechanisms of irradiation embrittlement of these steels and also the role of compositional variations in their irradiation sensitivity. Phosphorus concentration is seen as the key difference between East and West steels. When the phosphorus concentration is greater than about 0.012 wt%, then its effect is a dominating one with regard to irradiation effects.

Keywords: PWR, WWER, reactor pressure vessels, Western steels, Eastern steels, Russian, copper, embrittlement, phosphorus, nickel, neutrons, annealing.

A recent European study concluded [*1*] that for earlier 'Eastern' and 'Western' Pressure vessel steels having deleterious element concentrations above certain levels there was, coincidentally, a similar degradation in mechanical properties for equivalent neutron irradiation using the same neutron energy threshold. With the identification of and reduction in the concentration of the sensitizing elements, then the irradiation sensitivity was reduced and the shift in mechanical properties upon irradiation was also reduced.

[1]Consultant, LMD Consultancy, 176 Cumnor Hill, Oxford, UK.
[2]Deputy Head of Laboratory, Senior Researcher, respectively, Kurchatov Research Centre, Moscow, Russia.
[3] Research Manager, AEA Technology, Harwell, Oxon, UK.
[4] President, ATI Consulting, 3860 Blackhawk Road, Danville, CA.

Copyright© 2000 by ASTM International www.astm.org

[Figure 1].

While the key features of this comparison are described below it will be noted that in Figure 1 the neutron fluence has been normalized to E>1MeV and the extent of the fluence scale reflects the end-of-life peak fluences for the Eastern and Western steel pressure vessels. The curves are based on the compositions of 'real' steels used in practice; the predictions are from the use of the Russian Codes [*2*] for the Eastern steels and from the USNRC Regulatory Guide 1.99 Rev 2 [*3*] for the Western steels.

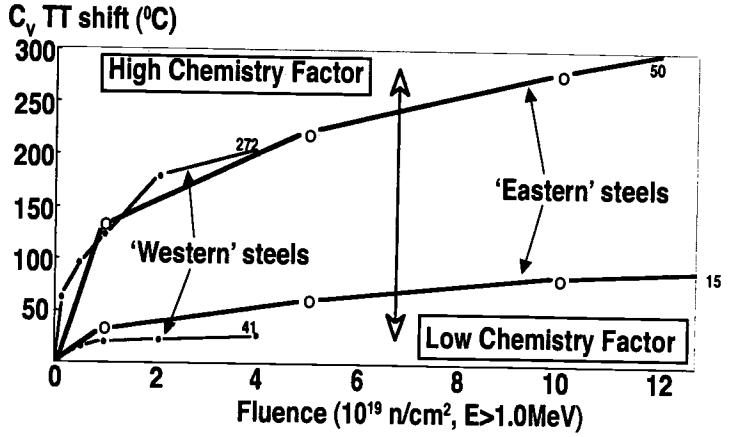


Figure 1-*Predicted shift in the transition temperature versus neutron fluence (E>1MeV) for an appropriate range of Chemistry Factors encompassing the compositions of 'real' Eastern and Western steels. Note that the curves for Western steels are truncated at a fluence which is the limit of the database underpinning the USNRC Regulatory Guide 1.99 Rev 2. The results for the Eastern steels are plotted up to the end-of-life peak weld fluence for the WWER-440 reactors.*

Regulatory Codes and Guides

The US Nuclear Regulatory Commission Regulatory Guide 1.99 Rev 2 [3] to describe irradiation effects in pressure vessel steels states that:

$$\mathbf{RT_{NDT} = RT_{NDT}\ initial + \Delta RT_{NDT} + Margin} \qquad (1)$$

Where:

$\mathbf{RT_{NDT}}$ is the reference temperature for unirradiated material

$\mathbf{\Delta RT_{NDT}}$ is the increase in this temperature due to irradiation

Margin is the quantity to be added to address conservatively uncertainties in the initial and transition temperature shift transition.

The value of ΔRT_{NDT} should be calculated by means of the following equation:

$$\mathbf{\Delta RT_{NDT} = (CF)f^{(0.28-0.010\ log\ f)} = (CF)\ (FF)}$$

where:

f is the fluence in units of 10^{19}n/cm^2 (E>1MeV)
FF is the fluence factor
CF is the Chemistry Factor from the copper and nickel content and can be derived from the measured surveillance results or from tables in the Guide. In the US CF is in ^{0}F. For the purpose of comparison CF is in ^{0}C in this report.

Using this approach and the appropriate values from published data for the composition of US welds allows the shift in transition temperature to be calculated up to a fluence of 4 x 10^{23} n/m^2 (E>1MeV). The fluence for use in applying the guide is limited by the availability of high fluence data underpinning the Guide and the end-of-life fluence of the pressure vessels. The results are shown in Table 1 and Figure 2 below:

Table 1- *Shift, in ^{0}C, in transition temperature for selected US RPV welds.*

				FLUENCE (10^{23}nm^{-2}, E>1MeV)				
	Cu	**Ni**	**CF(^{0}F)**	**1.0**	**2.0**	**3.0**	**4.0**	**5.0**
CE Hi Cu, Hi Ni	0.35	1.0	272	151	180	195	205	212
B&W Hi Cu Linde 80	0.35	0.6	212	118	140	152	160	165
B&W Int Cu Linde 80	0.20	0.6	160	89	106	115	121	125
HiCu LoNi	0.30	0.1	139	77	92	99	104	108
LoCu HiNi	0.03	1.0	41	23	27	29	31	32
B&W LoCu Linde 80	0.03	0.6	41	23	27	29	31	32

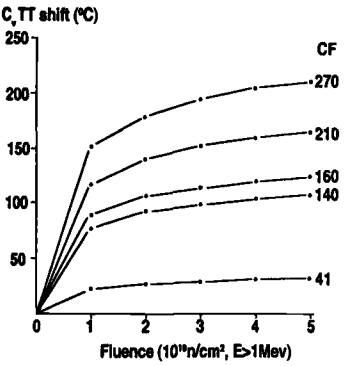


Figure 2- *Shift in transition temperature of US welds encompassing a range of Chemistry Factors for 'real' welds and using USNRC Reg Guide 1.99 Rev 2.*

The Russian Code prediction for weld metal irradiated at 270^{0}C is as follows:

$$\Delta T = 800\,(P+0.07Cu).(f)^{0.33} \qquad (2)$$

The copper and phosphorus values for the critical welds in WWER welds have been published [4] and this allows the Chemistry Factor for Eastern steels to be calculated as in Table 2 and plotted in Figure 3 below.

Table 2 - *Chemistry Factors for WWER 440 weld 4 in pressure vessels of reactor plants.*

PLANT	Copper	Phosphorus	800(P+0.07Cu)
Kola 1	0.15	0.033	34.8
Kola 2	0.15	0.04	40.4
Armenia 1	0.16	0.03	33.0
Armenia 2	No values given		
Novovoronezh 3	0.15	0.031	33.2
Novovoronezh 4	0.17	0.03	33.5
Kozloduy 1	0.12	0.052	48.3
Kosloduy 2	0.18	0.038	40.5
Kosloduy 3	0.20	0.036	40.0
Kosloduy 4	0.04	0.021	19.0
Bohunice 1	0.10	0.043	40.2
Bohunice 2	0.11	0.026	27.0
Greifswald 1	0.10	0.043	40.2
Greifswald 2	0.15	0.036	37.2
Greifswald 3	0.12	0.035	34.7
Greifswald 4	0.16	0.035	37.0

[Of course some of these values for deleterious element contents could be modified in the light of additional analysis, but the values given above suffice for the purpose of this paper]

This Chemistry Factor allows the transition temperature shift to be calculated as in Table 3 for different neutron fluences. It is usual for the fluence to be calculated for neutron energies of E>0.5 MeV. This fluence can be approximately converted to a neutron energy spectrum of E>1.0 MeV by using the following relationship deriving from [5]:

$$F(E_n>0.5MeV)/F(E_n>1MeV)\ \alpha\ 1.78 \qquad (3)$$

These two sets of predictions in Tables 1 and 3 and shown in Figures 2 and 3 using the USNRC Regulatory Guide and the Russian Code and the extreme cases of the worst and best steels in these tables and figures are compared in Figure 1. Two features are immediately evident. First, the irradiation behavior of the Eastern and Western steels are the same. The older steels show the greatest degradation. The more modern steels, with a

reduced concentration of deleterious elements show the expected improvement in sensitivity to irradiation. The second feature is that the end-of-life fluence of the WWER welds are significantly higher than the PWRs because of the higher neutron flux incident on the pressure vessel wall in the WWER 440.

Table 3.-*Shift in transition temperature for WWER 440 welds covering the range of Chemistry Factors in Table 2 for two different neutron energy spectra.*

CHEMISTRY	FLUENCE						
FACTOR	F>1.0MeV	0.1	0.5	1.0	5.0	10	15	20
	F>0.5MeV	0.18	0.89	1.78	8.92	17.8	26.8	35.7
15		18	31	39	67	84	97	106
20		24	41	52	89	113	129	142
30		36	62	78	134	169	193	213
40		49	83	104	179	225	258	284
50		61	104	131	223	282	322	355

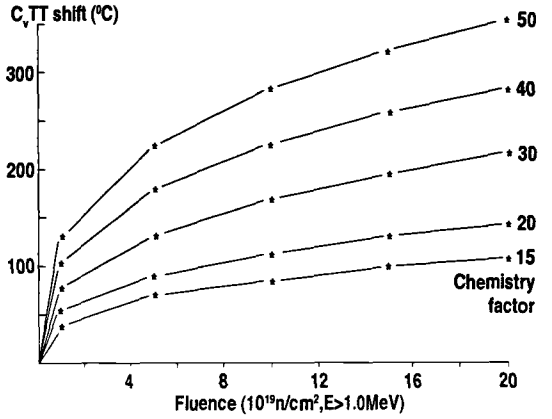


Figure 3-*Predicted shift in transition temperature for WWER Number 4 welds for the range of Chemistry Factors of interest in 'real' materials plotted as a function of neutron fluence with E>1MeV.*

It is emphasized that the Western steels, as confirmed by the USNRC Regulatory Guide 1.99 Rev 2, show a marked sensitivity to copper and nickel content (as shown in Equation 1 above). Little sensitivity to phosphorus concentration is observed. On the other hand the Eastern steels are sensitive to phosphorus content and show a significantly lower sensitivity to copper content as shown in the Russian Code (and illustrated in Equation 2 above). Yet the degradation upon irradiation is the same. This is the first example of a remarkable and unexpected coincidence when comparing these materials. It will be remembered that the database for the two Guides/Codes has been generated in

different countries and there are differences in the mathematical/statistical treatment. However, the developments in the production of these steels with regard to improving their irradiation resistance on reducing the deleterious elements has been effective.

However, it is an inescapable conclusion that *copper and nickel* confer an irradiation sensitivity to the older Western steels while *phosphorus and copper* confer a sensitivity to the older Eastern steels. The role of phosphorus and nickel in irradiation embrittlement are then of greater significance in trying to understand the integrity of reactor pressure vessel. However, it is stressed here that an unequivocal quantitative description of the embrittlement role of phosphorus is necessary for empirical predictive purposes because it can apparently act in both a hardening and non-hardening way.

Irradiation Damage Effects

It is assumed that any difference in the irradiation shift predicted by the different trend equations is more of a reflection of the differences in the predictive equations and their particular unique databases than on any other fundamental differences. The many common factors which are used to describe the cause of change in mechanical properties can be simply shown in the following way for the components of matrix hardening (ΔRT_{matrix}), precipitate hardening (ΔRT_{ppt}) and segregation effects (ΔRT_{seg}) causing the change in mechanical properties.

$$\Delta RT_{NDT} = \Delta RT_{matrix} + \Delta RT_{ppt} + \Delta RT_{seg} \qquad (4)$$

-point defects -microvoids -dislocation loops or clusters (stabilized by nitrogen) -carbon -fluence dependence -nitrogen effects (low dose, low temp.) -fluence rate effects -etc	-dissolved copper -Cu+Ni,Mn -phosphorus as phosphides -etc -irr enhanced saturation. -saturation effects. -fluence rate effects	-phosphorus -etc

Pavinich et al [7] have described the factors causing the degradation of mechanical properties on neutron irradiation as being caused by:

- defect production from displacement cascades (vacancies, interstitials, dislocation loops, vacancy clusters, vacancy-interstitial pairs)
- formation of ultrafine copper rich precipitates
- ultrafine phosphide formation
- ultrafine carbide formation
- temper embrittlement.

They considered that the first two processes were the most important for irradiation embrittlement. It is appreciated that their statements were for Western steels. But, the suggestion here is that phosphorus at levels higher than ~0.012 wt% and also nickel, particularly at the higher concentrations should also be included in the description of degradation in real materials when including both Eastern and Western steels. English and Phythian [*9*] and Odette [*10*] have also described the micromechanisms causing changes in mechanical properties on irradiation as matrix damage due to irradiation produced defect clusters and dislocation loops, irradiation induced/enhanced grain boundary segregation of embrittling elements such as phosphorus.

It is also important to note that Russian workers [*11*] [*12*] concluded that for WWER vessels irradiated at temperatures of 250-270^{0}C the most likely effect of irradiation is the interaction of phosphorus directly with radiation defects and dislocations. Gurovich et al [*13*] had a slightly different explanation in that they ascribed the mechanical property changes to matrix radiation hardening, grain boundary segregation of impurities and the segregation of impurities to precipitate interfaces. They saw that an essential part of radiation embrittlement could be attributed to phosphorus segregation to interfaces produced by irradiation. They also found that grain boundary phosphorus in irradiated steels was responsible, in their cases, for an insignificant portion of the DBTT shift (not exceeding 10-20%). It is interesting to note that Kuleshova [*14*] observed that increased phosphorus levels in Eastern and Western steels induces the appearance of the brittle intergranular component on the fracture surfaces of Charpy specimens but in Russian weld metal the brittle intergranular component can be observed only in fractures of sub-size Charpy specimens but never in full size specimens.

To encompass these explanations the shift in ductile-brittle transition temperature can be described as follows:

$$\Delta T40J_{total} = \Delta T40J_{CU,P} + \Delta T40J_{matrix} + \Delta T40J_{gb} \qquad (5)$$

It becomes important to realize that phosphorus can behave in an analagous way to copper but can also segregate to grain boundaries. Remember that the segregation of phosphorus to grain boundaries can lead to a reduction of fracture stress but not to the yield stress. It is important to measure yield stress in these steels as well as the fracture properties. It is also important to realize that the hardening and embrittlement is probably associated with a particular concentration of phosphorus. For the general composition of Western steels this may be sufficiently low and at a narrow range of concentration level for the effect of phosphorus to be not as significant as in the Eastern steels.

Discussion of the role of nickel in irradiation embrittlement, in a comparative exercise such as this, is difficult because of a shortage of surveillance data and comparative irradiations. There are MTR data, see [*1*], which shows that above a certain nickel concentration there is a marked sensitization. Steels with low copper, low phosphorus but with high nickel (1.5-1.9 wt%) were developed for the WWER 1000 reactor pressure vessels. For the role of nickel in irradiation effects see Figure 4 [*8*]. Unfortunately there has been little published data from WWER 1000 surveillance specimens, because of difficulties in fluence estimation. However, from the limited data available there is a marked irradiation sensitivity within the operational lifetime fluence when the nickel content is very high (~2.4 wt%). So, four possible component parts of the trend equation

to empirically describe irradiation effects include the copper, phosphorus, nickel content and neutron fluence. Neither the USNRC Regulatory Guide or the Russian Code include all three compositional elements.

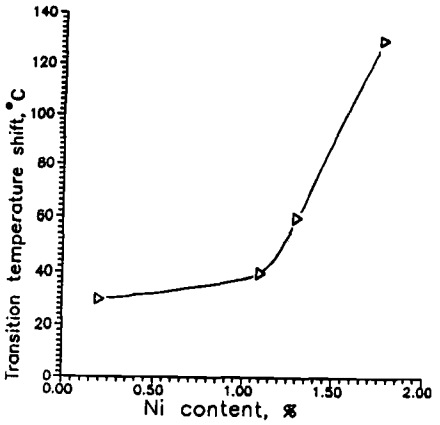


Figure 4-*Transition temperature shift with different nickel contents but with 0.05 wt% copper and 0.010 wt% phosphorus irradiated to 1 x 10^{20}n.cm^2 (E>0.5 MeV), irradiation temperature 270^{0}C. After Kryukov [8].*

Annealing Irradiation Damage

Annealing has been extensively studied and reviewed [*6*]. The recovery changes primarily relate to the transition temperature. The recovery of upper shelf properties occurs at temperatures lower than that required for the recovery of the transition temperatures. Over-recovery in upper shelf Charpy energies have been seen and reported in many US materials [*18*].

Of direct technological significance is the observation that substantial recovery (>75%) of the unirradiated properties occurs under similar conditions of temperature and time (450-500^{0}C for about a week). The second remarkable coincidence is that these annealing conditions prevail for both Eastern and Western steels. Comparison of Figures 5 and 6 [*8,15*] show this similarity. There has been a tendency for the US data to be generated at lower temperatures than the Russian/Eastern data.

The primary reason for the difference in the annealing temperatures used in the US is in meeting the concerns of the ASME Code criteria (as stated in the relevant ASME Code Case N-557) which are related to high thermal stresses and the potential for permanent offset due to to the beginning of creep effects. The development of the ASME Code criteria also considered the possibility of temper embrittlement at higher temperatures. Due to convential time-temperature relationships, the higher temperature can lead to a decrease in the annealing time.

Fifteen operating WWER vessels have now been annealed and the conditions have been supported by much experimental work. Besides establishing the annealing conditions it has been found [*12*] that the residual embrittlement after annealing

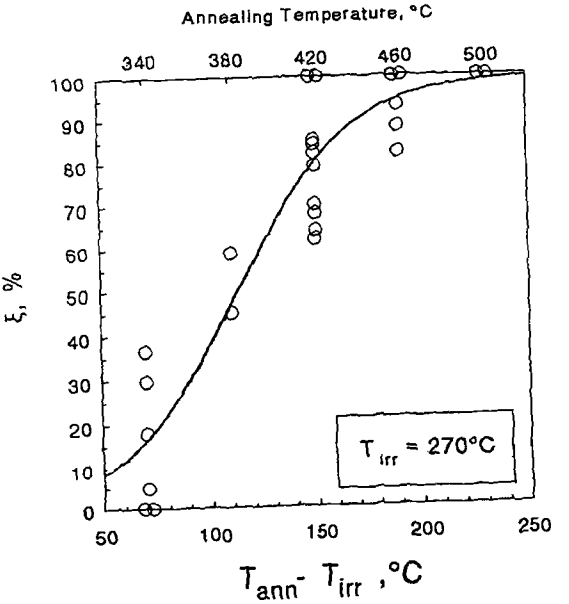


Figure 5-*Annealing effectiveness as a function of annealing temperature for WWER steels.*

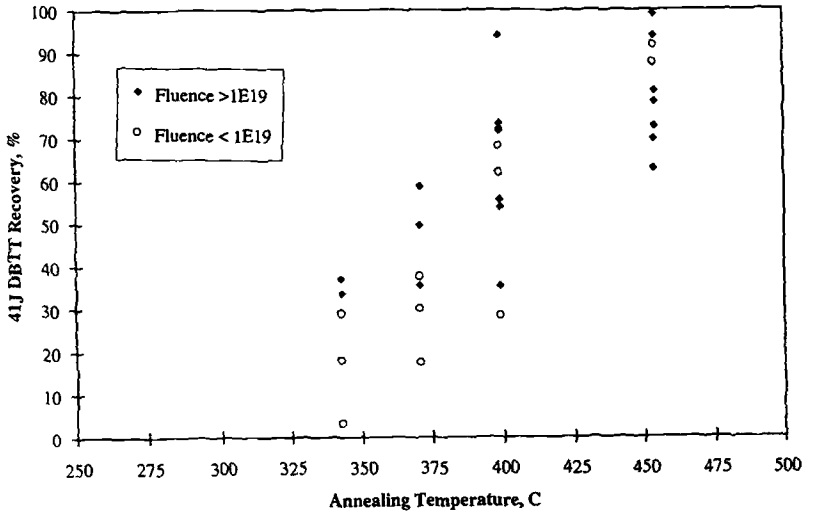


Figure 6-*Recovery on annealing at a variety of temperatures on US materials. After Mager [15]. In this report it is assumed that the annealing recovery is the same for MTR irradiated materials as for surveillance materials.*

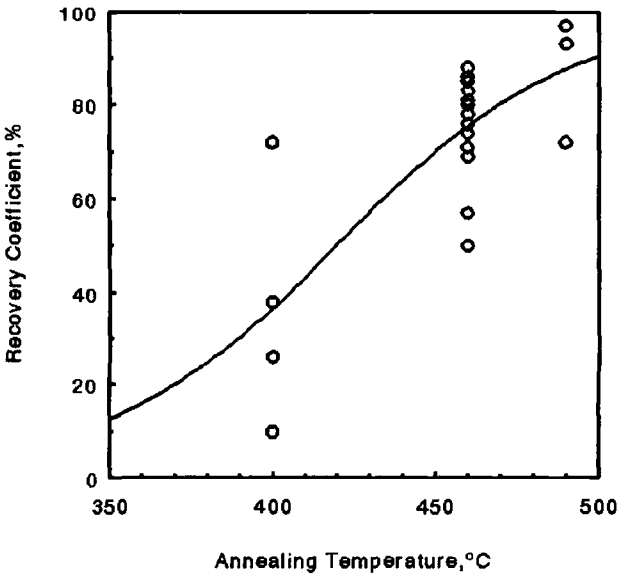
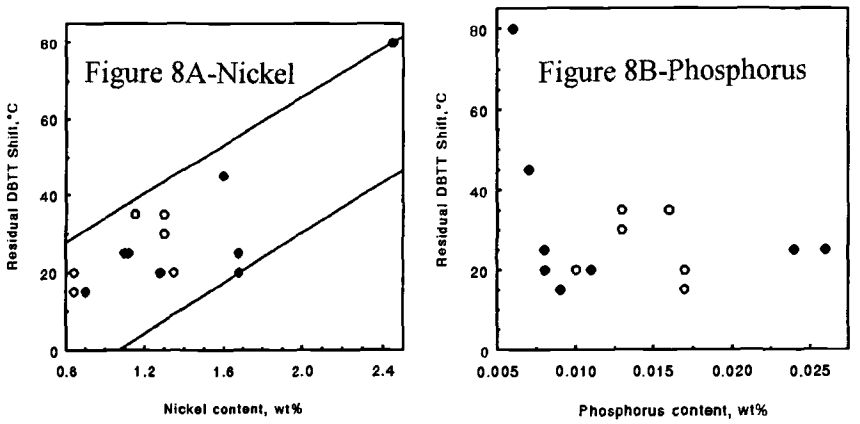


Figure 7. *Annealing effectiveness of WWER-1000 high nickel (2.45 wt%) weld. After Y.Nikolaev [16].*



Figures 8A and 8B. *Residual shift of WWER-1000 materials. Annealed as a function of both nickel and phosphorus content. After Nikolaev [16]. The nickel content seems to dominate the residual shift and one of the samples contained 2.45 wt% nickel.Nikolaev commented that the phosphorus seems to be constant except for the specimens with very low nickel-but samples with very low phosphorus content had high nickel contents so the variation with low and high concentrations could not be readily distinguished.*

is defined by the phosphorus content of the steel and not on the neutron fluence . Recovery on annealing 2.45 wt% nickel steels show incomplete recovery at an annealing temperature of 490^{0}C, see Figure 7. However, in the high nickel content WWER 1000 steels the nickel concentration dominates the residual shift (see Figures 8A and 8b). In these particular steels the specimens with very high (~2.45 wt%) nickel had a low phosphorus but a high sensitivity to neutron irradiation. Because of this variation the causal effect could not be readily distinguished.

All this leads to the conclusion that the conditions for annealing are roughly the same for Eastern and Western steels which would tend to indicate that the rate of recovery might be controlled by the same mechanism in the two cases. Server and Rosinski [*17*] have shown a computer model/database for annealing re-embrittlement projections that allows a projection to be made that can be related to a mechanistic basis. However, there seems to be a need for more underlying work on mechanisms to understand more fully what is happening during annealing.

As part of preparing for the possible need for annealing the US PWR pressure vessels a trial demonstration anneal has been carried out on the Marble Hill NPP [*17*]. This was an unirradiated plant. The trial was successful and used an indirect gas-fired heating method. An alternative furnace using electrical resistance heating (similar to that used for annealing the WWER vessels) was also successfully developed for a trial in the Midland NPP but the project was terminated after the furnace had been constructed. [*An essential difference between the Western and Eastern vessels is that many of the earlier PWR vessels were made from plates and, as a result, contain axial welds. In addition the active core length is greater. This requires a greater axial height to be annealed. This higher axial length leads to a higher strain than the WWER case where only the material in the narrow 'weld 4' region which requires annealing.*] It is unlikely that there will be a need to anneal PWR vessels in the near future.

Conclusions

Irradiation degrades the mechanical properties of PWR and WWER steels. Because of crucial differences in the deleterious element concentration the steels cannot be directly compared. However, the Russian Code and the USNRC Regulatory Guide have been developed for each of these two categories of pressure vessel materials. Predictions can therefore be based on these approaches. But the arguments are circular in the sense that predictions are only possible by the interpolation of the database upon which the Code and Guide are based.

For the earlier steels there is a coincidentally similar degradation in mechanical properties. Later steels have been improved by reducing the concentration of deleterious elements identified in the Code and Guide. The exception to this statement is the enhanced irradiation sensitive behavior of WWER 1000steels where phosphorus and copper were reduced but the nickel was increased to obtain desirable unirradiated start-of-life properties.

The peak neutron fluence in WWER pressure vessels is significantly higher than for the Western PWRs. The problems of irradiation embrittlement were therefore seen earlier in 'life' than in PWRs.

The most significant mechanistic feature of the comparison of Eastern and Westrn steels is the behavior of phosphorus. In the Eastern steels it seems to be behaving in the

same way as copper in Western steels. This feature has been explained in terms of concentration levels where phosphorus becomes the dominant sensitizing element above about 0.012 wt%. The phosphorus levels in Western steels tend to be lower than this level, which explains the lack of sensitivity in Western steels, but the phosphorus levels tend to be higher in Eastern steels (up to ~0.05 wt%), hence their sensitivity. When the phosphorus is <0.012 wt% then copper is the dominant sensitizing element for irradiation embrittlement.

Annealing under the same conditions of temperature and time to remove irradiation degradation produces similar beneficial effects in both Eastern and Western steels. This has provided the 'technological fix' to the irradiation problems of the early WWER pressure vessels.

References

[1] Davies, L. M., " A comparison of Eastern and Western Steels" Published by the European Commission, AMES Report No. 10, Eur 17327EN, JRC IAM, PB2, NL-1755, ZG Petten, Netherlands.

[2] "Strength Analysis Standards for Equipment and Piping at Nuclear Power Plants", Russian Code PNAE G-7-002-86, Moscow.

[3] USNRC Guide 1.99 Rev 2, Washington DC, May 1988.

[4] IAEA Report WWER-RD-72,Table iii, Weld 4, IAEA, Vienna, 1994

[5] Zaritsky, S. M., and Osmera, B., "Review of theoretical and experimental investigations of WWER PV irradiation damage in engineering benchmarks", Proc. Int Conf. on dosimetry, Tel Aviv, Jan 1994, pp 757-765.

[6] Pelli, R., Torronen, K., "State of the art review on thermal annealing", Published by the European Commission, AMES Report no 2, Eur 16278 EN, JRC IAM, PB2, NL-1755, ZG Petten, Netherlands

[7] Pavinich, W.A., Griesbach, T.J., and Server, W.L., "An overview of radiation embrittlement modelling for reactor vessel steels", ASTM STP 1170, 1993, pp 99-118.

[8] Kryukov, A. M., "The state of the art of WWER type RPV irradiation embrittlement and mitigation", Proc.of IAEA Specialist Meeting held in Vladimir, Russia 15-19 September, 1997, published by IAEA, Vienna, 1997

[9] English, C., and Phythian, W., J. Nuc. Matls, 205, 162, 1993.

[10] Odette, R., J. Nuc Matls, 212-215, 45, 1994

[11] Amaev, A D., Kryukov, A. M., Levit, V. I., Sokolov, M. A., "Radiation Stability of WWER-440 Materials", ASTM STP 1170,1973, pp 9-29

[12] Nikolaev, V.A., et al, "On the role of impurities in irradiation embrittlement of low alloyed steels", Atomnaja, Energia, Vol 47, 1, 1979, pp 21-25.

[13] Gurovich, B. A., Kuleshova, E. A., Nikolaev, Yu. A., Shtrombach,Yu.I., J. Nuc. Matls, 246, 91-120, 1994.

[14] Kuleshova, E. A., Gurovich, B. A., "Reflection of the changes in properties of PV metal due to annealing and re-irradiation in relation to fractures obtained in Charpy testing", Proc of IAEA Specialist meeting held in Vladimir, Russia, 1997, published by IAEA, Vienna, 1997.

[15] Mager, T., 9.22, Proc. DoE/SNL/EPRI Workshop on annealing RPVs, Sandia report SAND94-1515/1.UC-523, 1994.

[16] Nikolaev, Y., Paper presented at the 4th International Conference on Material issues in Design, Manufacturing and Operation of NPP, Published by CRISM-PROMETEY, St Petersburg, Russia, 1996
[17] Server, W., and Rosinski, S., EPRI Conference on RPV thermal annealing demonstration, Santa Fe, USA, March 1998.
[18] Eason, E., Wright, J., Odette, R., Mader, E., "Models for annealing recovery due to annealing of RPV steels", Report NUREG/CR-6327, 1995.

J. R. Hawthorne,[1] M. A. Sokolov,[2] and W. L. Server[3]

Exploratory Test of 288°C Radiation Resistance of Two USSR-Produced Reactor Pressure Vessel Steels

Reference: Hawthorne, J. R., Sokolov, M. A., and Server, W. L., **"Exploratory Test of 288°C Radiation Resistance of Two USSR-Produced Reactor Pressure Vessel Steels,"** *Effects of Radiation on Materials: 19th International Symposium, ASTM STP 1366,* M. L. Hamilton, A. S. Kumar, S. T. Rosinski, and M. L. Grossbeck, Eds., American Society for Testing and Materials, West Conshohocken, PA, 2000.

Abstract: The effects of 288°C (550°F) irradiation to 1.0×10^{19} n/cm^2, E > 1 MeV, on the Charpy V-notch ductilities of two USSR-produced forging materials were determined experimentally. The materials were provided by the Kurchatov Institute under the umbrella of a joint USA-USSR agreement and represent the Cr-Mo-V forgings employed in the construction of USSR light-water VVER-440 reactor pressure vessels (RPVs) before and after 1980, respectively. The primary difference between the two materials is phosphorus content (0.019% vs. 0.007% P) consistent with their respective USSR Steel Specifications 15Kh2MFA and 15Kh2MFA-A. Specimens for post-irradiation property determinations were irradiated in the Ford Nuclear Reactor in a controlled-temperature assembly at an average fluence rate of 5.6×10^{12} n/cm^2-s, E > 1 MeV. The post-irradiation Charpy V-notch 41 J (30 ft-lb) transition temperature elevation for the material representing pre-1980 RPVs was 31°C (55°F). This elevation was accompanied by a 27% reduction in Charpy V-notch upper-shelf energy level. For the material representing the post-1980 RPVs, the transition temperature elevation was ≤ 8°C (15°F); the concomitant post-irradiation reduction of upper-shelf energy was not established.

The observed transition temperature elevations are considerably less than the elevations predicted by NRC Regulatory Guide 1.99, Rev. 2. The converse is true for the reduction in upper-shelf energy level found for the pre-1980 RPV construction material. A higher fluence test is required for full qualification of the radiation resistance capabilities of the materials.

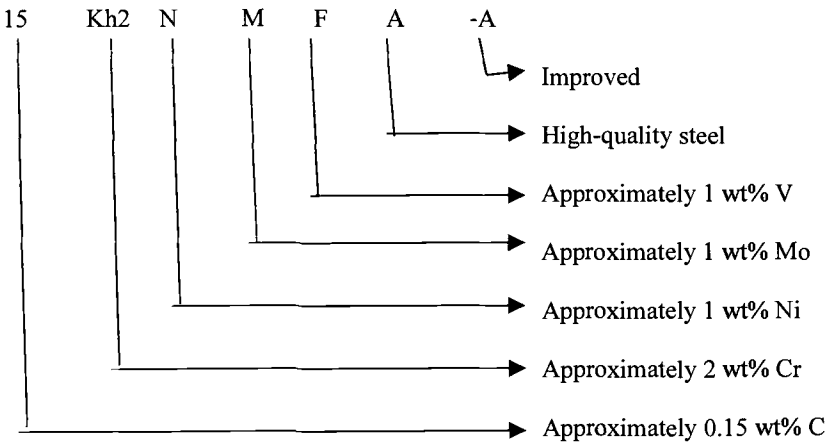
Keywords: Russian steels, irradiation, transition temperature, upper-shelf energy

[1] Consultant, 111 Mel Mara Drive, Oxon Hill, MD 20745.
[2] Staff Member, Oak Ridge National Laboratory, P.O. Box 2008, Oak Ridge, TN 37830.
[3] President, ATI Consulting, P.O. Box 5769, 24 Glenbarr Court, Pinehurst, NC 28374.

Copyright© 2000 by ASTM International www.astm.org

A major difference between the primary pressure vessels of commercial nuclear power reactors of the former Union of Soviet Socialist Republics (USSR) and the United States of America (USA) is the steel type used for the beltline region opposite the fuel core. For the USSR reactor pressure vessels (RPVs), chromium-molybdenum-vanadium steels similar to ASTM A 542 Type B steel have been employed, whereas in the USA, a manganese-molybdenum-nickel steel (ASTM A 533B-1), its forging equivalent (ASTM A 508-3), or a manganese-molybdenum-chromium forging steel (ASTM A 508-2) are the steels of choice. The selection of chromium-molybdenum-vanadium steel by the USSR for its early RPVs was a natural carryover from their fabricators' experience with petroleum industry hydrocracker vessels.

The USSR designation for the steel type used in the early systems (VVER-440's) is 15Kh2MFA. The alphanumeric designations of USSR steels cited in this report are explained for the reader below. For systems of the same size built after about 1980, the specification 15Kh2MFA-A was used. Paralleling USA practice, this specification places special restrictions on phosphorus content and copper content for improved radiation embrittlement resistance at the service temperature (Table 1). Additional restrictions are placed on other impurity elements including sulfur, arsenic, antimony, and tin with the same objective. It is noted that, with normal melting practice, the phosphorus contents of USSR steels tend to be higher than those of USA steels, presumably due to the difference in original raw materials (ores). Currently, a nickel modification of the 15Kh2MFA-A composition, designated 15Kh2NMFA-A, is being applied in the new, higher power systems (VVER-1000's). The USSR designation signifies the following:



In a like manner, the designation 15Kh2MFA and 15Kh2MFA-A can be interpreted. The nickel addition with 15Kh2NMFA-A is for improved as-fabricated properties in the thicker vessels; note however that the nickel addition is being held to less than 1.5 wt% in the newest 15Kh2NMFA-A construction vessels in view of the tendency for enhanced radiation-induced embrittlement in higher nickel steels. The 15Kh2NMFA-A specification places even tighter restrictions on phosphorus, sulfur, antimony, and tin content, than the other two specifications (Table 1).

Table 1 - *Chemical Compositions for Code OB and Code NB Materials Compared to USSR and USA RPV Forging Steel Specifications*

Material/ Specification	Chemical Composition, wt-%														
	C	Si	Mn	Cr	Mo	V	Ni	Cu	Co	As	S	P	Sb	Sn	P+Sb +Sn
Code OB[a]	0.15	0.29	0.42	2.64	0.67	0.29	0.15	0.10	--[b]	--[b]	0.012	0.019	--[b]	--[b]	--[b]
Specification 15Kh2MFA (VVER-440)[cd]	0.13 0.18	0.17 0.37	0.30 0.60	2.50 3.00	0.60 0.80	0.25 0.35	0.40 Max.	0.30 Max.	0.025 Max.	0.040 Max.	0.020 Max.	0.020 Max.	--	--	--
Code NB[e]	0.14	0.22	0.40	2.70	0.67	0.22	0.12	0.10	--[b]	--[b]	0.011	0.007	--[b]	--[b]	--[b]
Specification 15Kh2MFA-A (VVER-440)[df]	0.13 0.18	0.17 0.37	0.30 0.60	2.50 3.00	0.60 0.80	0.25 0.35	0.40 Max.	0.10 Max.	0.025 Max.	0.010 Max.	0.015 Max.	0.012 Max.	0.05 Max.	0.05 Max.	0.015 Max.
Specification 15Kh2NMFA-A (VVER-1000)	0.13 0.18	0.17 0.37	0.30 0.60	1.80 2.30	0.50 0.70	0.10 0.12	1.0[g] 1.5	0.10 Max.	0.03 Max.	0.010 Max.	0.012 Max.	0.010 Max.	0.005 Max.	0.005 Max.	0.015 Max.
Specification ASTM A508-2[h] (A508 Grade 2 Class 1, formerly A508 Class 2)	0.27 Max.	0.15 0.40	0.50 1.00	0.25 0.45	0.55 0.70	0.05 Max.	0.50 1.00	0.10[i] Max.	--	--	0.018[i] Max.	0.015[i] Max.	--	--	--
Specification ASTM A508-3[h] (A508 Grade 3 Class 1, formerly A508 Class 3)	0.25 Max.	0.15 0.40	1.20 1.50	0.25 Max.	0.45 0.60	0.05 Max.	0.40 1.00	0.10[i] Max.	--	--	0.018[i] Max.	0.015[i] Max.	--	--	--
Specification ASTM A542 Type B[h]	0.09 0.18	0.50 Max.	0.25 0.66	1.88 2.62	0.85 1.15	0.03 Max.	0.28 Max.	0.28 Max.	--	--	0.015 Max.	0.015 Max.	--	--	--

a EPRI Series No. 2 (I.D. Stamp 2)
b Not analyzed
c Early construction
d Typical heat treatment for RPV forgings made to this specification: 1000°C ± 10°C (1832°F ± 18°F) for 7 - 8 hours at temperature; water quenching; 680-720°C (1256-1328°F) for 13-15 hours. PWHT (final) typically is at 670°C ± 10°C (1238°F ± 18°F)
e EPRI Series No. 1 (I.D. Stamp 6.1); also applies to I.D. Stamp 1
f Later construction (since approximately 1980)
g Values now being used are below this level due to enhanced embrittlement
h USA steel specification; heat treatment for these steels is typically lower in temperature than for the Russian RPV forging steels
i Restrictive product chemistry requirements

The present study had two primary objectives. One was to perform an independent test of the radiation resistance of two prototypic materials produced "commercially" in the USSR, wherein one material represents the early VVER-440 vessel construction and the second represents the USSR steel specification and production practice for post-1980 VVER-440's. Radiation resistance was to be judged from the magnitude of the change in Charpy V-notch (C_v) ductility produced by irradiation at 288°C (550°F). A second objective was to compare the observed change in properties to the projection of notch ductility change given by the Nuclear Regulatory Commission (NRC) Guide 1.99. The present version of the Guide, Revision 2 [*1*], was derived solely from USA reactor vessel surveillance data for ASTM A 302B, A 533B-1, A 508-2, and A 508-3 steels and their weld metals pertaining to 274°-310°C (525°-590°F) service conditions. Also, property changes found in the present irradiation test were to be compared to post-irradiation observations made previously by USSR laboratories. In this regard, the irradiation test reported here employed USA experimental methods, irradiation facilities, and post-irradiation evaluation procedures only.

The study was made possible, through the donation of finish-machined C_v specimens to the Electric Power Research Institute (EPRI), by the USSR's Kurchatov Institute. The donation was made under the umbrella of an USA-USSR technology exchange agreement conceived by the NRC; the agreement has been implemented by forming the Joint Coordinating Committee on Civilian Nuclear Reactor Safety (JCCCNRS). The irradiation tests were funded by EPRI and Materials Engineering Associates, Inc. (MEA). Indirect support was received from Yankee Atomic Electric Company (YAEC); in particular, the C_V specimens of this study were irradiated in an MEA-YAEC experiment assembly on a space-available basis, courtesy of YAEC.

Materials

Table 1 lists the results of composition determinations by MEA on the specimen materials and the required composition ranges by the USSR specifications 15Kh2MFA and 15Kh2MFA-A. The 15Kh2MFA specification specimens (EPRI Series No. 2) carried a digit 2 stamp mark for identification when received; the specification 15Kh2MFA-A specimens (EPRI Series No. 1) carried a digit 1 or digit 6.1 stamp marking. The digit 1 specimens were used for the irradiation; the digit 6.1 specimens were used for unirradiated condition (reference) tests. In Table 1, the individual materials are found to be in compliance with their respective steel specifications on chemistry. Information on specific material heat treatments is provided in Table 2. The Charpy V-notch (C_V) specimens designated for irradiation were checked dimensionally upon their receipt at MEA since the MEA irradiation capsule requires uniform dimensions in specimens. Small but undesirable differences in specimen lengths were observed. The specimens subsequently were re-machined to a uniform length of 54.38 mm (2.141 in.) or 54.33 mm (2.147 in.) depending on the specimen series. Both length dimensions are within the specification on allowable length given by ASTM Test Method for Notched Bar Impact Testing of Metallic Materials (E 23).

Specimen thickness and width dimensions also showed variations, which could preclude good capsule fit-up and, in turn, the development of uniform specimen temperatures during irradiation. Three of the four major specimen surfaces were re-

machined. The surface containing the V-notch and the V-notch itself were left "as-is". The final thicknesses of the specimens of both groups, with one exception, were in conformance with ASTM E 23. Of necessity, the width dimensions of the EPRI Series No. 1 specimens (but not Series No. 2) had to be machined slightly smaller than the ASTM E 23 specified minimum by 0.075 mm (0.003 in.). It is the opinion of the authors that this disparity does not impact the conclusions of this study. Dimension checks were made for the specimen group stamped 6.1 tested at MEA in the unirradiated condition; these specimens were not re-machined prior to testing.

Table 2 - *Heat Treatments of the Code OB and NB Forging Materials*

Material	Heat Treatment
Code OB	1000°C (1832°F) for 15h 0:1 quench 680°C (1256°F) for 29h Air cool
Code NB	1000°C (1832°F) for 12h 0:1 quench 690-700°C (1274-1292°F) for 19h Air cool 660-670°C (1220-1238°F) for 50h Air cool

Referring to the notch radius measurements of all specimens, it appears that the notch tip was produced by a method other than milling or grinding. The notch radius at one end of the V-notch in most cases is slightly smaller than the radius found at the opposite end. ASTM E 23 calls for a notch radius of 0.25 mm (0.010 in.) $\pm$ 0.025 mm (0.001 in.). The observed radii are equal to or slightly smaller than this specification, i.e., the notch is "sharper" than the ASTM E 23 specified notch. In general, the brittle/ductile transition of low alloy steels increases in temperature with increasing notch sharpness [*2*].

Material Irradiation

The specimens were irradiated in a controlled-temperature assembly (MEA FNR-9A3) in the 2MW Ford Nuclear Reactor (FNR) at the University of Michigan at Ann Arbor. C_v and tensile specimens for a separate MEA-YAEC irradiation effects study also were included in the assembly. The irradiation was conducted in the FNR's L-67 fuel lattice position; the target irradiation temperature was 288°C (550°F). The duration of the irradiation (hours at full reactor power) was 492.7 hours. The average neutron fluence, E > 1 MeV, for Assembly FNR-9A3 was 1.03 x 10^{19} n/cm^2 based on iron wire dosimeters placed within the specimen array. The average fluence rate for the Code OB and Code NB specimens was 5.6 x 10^{12} n/cm^2 -s. Typically, the thermocouples were welded to the C_v specimens at points within 3.2 mm (0.12 in.) of the V-notch.

Experimental Results

Unirradiated Condition

Data developed by MEA for the unirradiated condition are illustrated in Figures 1 and 2 (open circles). The 41-J (30-ft-lb) temperatures for the Series No. 2 material (Code OB-Old Base) and the Series No. 6.1 (and Series No. 1) material (Code NB-New Base) are reasonably well established and are -15°C (5°F) and -51°C (-60°F), respectively. A small uncertainty in 41 J (30 ft-lb) temperature of the Code NB material exists as signified by the dashed rather than solid trend curve. The difference in properties between the two materials is probably due to material processing differences since the compositions of the materials are very similar (Table 1).

The upper-shelf energy (USE) level was not established for the Code NB material due to a lack of specimens. The USE appears to be at least 216 J (159 ft-lb) judging from the post-irradiation data values. Irradiation typically tends to cause a reduction in the USE level. The USE level of the Code OB material is 159 J (117 ft-lb). While lower than that of the Code NB material, it nonetheless can be considered "high" if viewed against the minimum USE level for the pre-irradiation TL or LC orientation condition (102 J, 75 ft-lb) indicated in the Code of Federal Regulations 10CFR50, Appendix G. In the present case, the test specimens are believed to be C-R (strong) orientation specimens.

The pre-irradiation properties of the Code OB material are roughly comparable to those of current production A 533B-1 plate materials and A 508-2/A 508-3 forging counterparts.

Irradiated Condition

Test results for the irradiated condition are included in Figures 1 and 2 (filled data points). Referring first to the Code OB material (Figure 1), a significant increase in 41 J (30 ft-lb) temperature and a large (27%) decrease in USE after irradiation was produced by the irradiation treatment. The phosphorus content of this steel is significantly higher than that of the Code NB material. The copper contents, however, are the same (Table 1). The irradiation exposure of the Code OB material also produced a very marked reduction in the slope of the brittle/ductile transition curve. The increase in the 68 J (50 ft-lb) transition temperature is 64% greater than the increase in the 41 J (30 ft-lb) transition temperature (~50°C vs. 31°C, ~90°F vs. 56°F). In comparison, USA RPV steels generally do not exhibit a substantial change in slope at a fluence of 1 x 10^{19} n/cm^2 at 288°C, but may at higher fluences.

Unlike the Code OB material, the Code NB material showed essentially no change in its 41 J (30 ft-lb) temperature and presumably no change in its USE level. The 8°C (15°F) increase in the transition temperature assumes the -15°C (5°F) pre-irradiation value to be correct (see the dotted curve in Figure 2). At energy levels above about 105 J (77 ft-lb), the pre- and post-irradiation condition data reside in a common data scatter band.

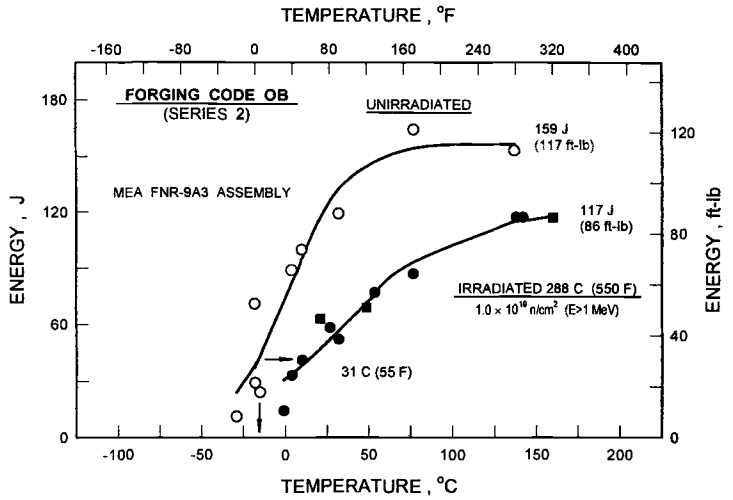


Figure 1 – C_v *Notch Ductility of the Code OB Material (EPRI Series No. 2 Specimens)*

The filled square data points in Figures 1 and 2 identify results from specimens whose irradiation temperatures nominally were between 274°C and 277°C (525°F and 530°F), i.e., lower than the filled circle data points representing the 288°C (550°F) ± 8°C (15°F) target temperature. These data do not describe a different level of radiation resistance. A similar radiation temperature insensitivity at a fluence of ~0.8 x 10^{19} n/cm^2 is suggested by results of another study of USA RPV materials [*3*]. Whether or not the insensitivity extends to higher fluences cannot be ascertained from the present data.

Prior Experimental Results of Kurchatov Institute

Unirradiated Condition

USSR experimental results for both forging steels were obtained from the Kurchatov Institute after the irradiation and testing were completed by MEA. Data developed by the Kurchatov Institute for portion(s) of the Code OB and Code NB are shown in Figures 3 and 4. The Code OB data were developed in 1991 and 1989, respectively. The latter data apparently refer to a different test orientation in view of the much lower USE level described. Perhaps the data for the 1989 tests are for a transverse (weak) test orientation, such as L-C, while the data for the 1991 tests are for a longitudinal (strong) test

orientation, such as C-L. Another possible explanation for the data difference would be material inhomogeneity.

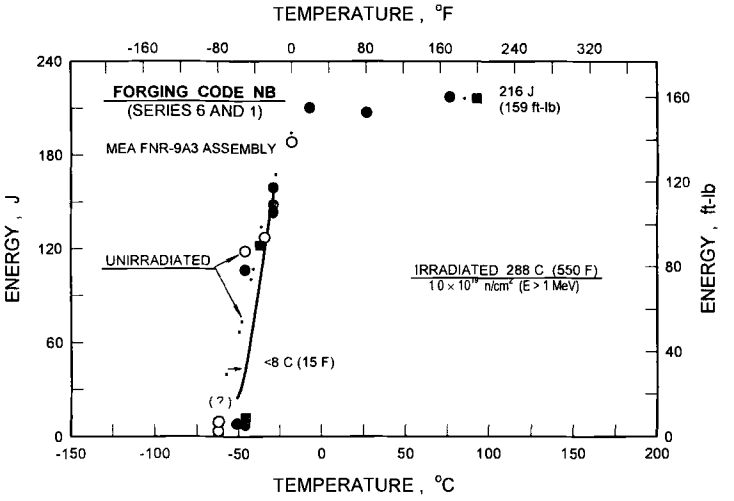


Figure 2 – *C_v Notch Ductility of the Code NB Material (EPRI Series Nos. 1 and 6.1 Specimens)*

The data developed by MEA for the Code OB material have been included in Figure 3 for comparison. Notice that the MEA data reside along the left-hand edge of the scatter band enclosing the 1991 data of the Kurchatov Institute. From the relative USE indications, it appears that the Kurchatov Institute data set produced in 1991 is more representative of the present interlaboratory data comparison. The 41 J (30 ft-lb) transition temperatures indicated by the MEA results and the Kurchatov Institute 1991 results are -15°C (5°F) and -1°C (30°F) respectively. The USE levels are in close agreement. The noted difference in transition temperature points up the potential problem of inhomogeneity of forging material properties. Much greater mechanical property inhomogeneity has been observed in other studies. A well-known example of material having a wide range of inhomogeneity is the Code FF forging material of the IAEA-coordinated program on reactor vessel steels [*4*]. Significant differences between inner wall and outer wall quarter-thickness location properties have also been observed or found suspect [*5*] in forging studies. Inhomogeneity has major implications to the suitability of data from one section of material for indexing irradiation data from another section. This aspect of forgings should be assessed as a precaution if two test sections are considerably displaced from one another.

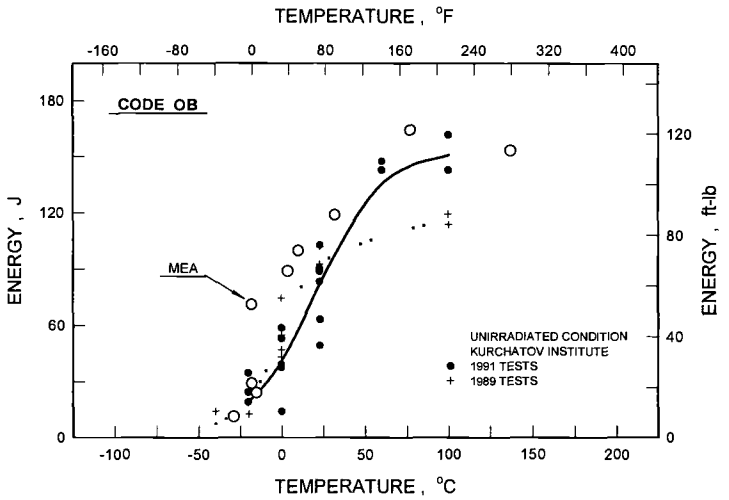


Figure 3 – *C_v Notch Ductility Determinations by the Kurchatov Institute for the Code OB Material as Compared to the MEA Unirradiated Data*

Referring next to the Code NB material (Figure 4), the properties of several locations through the thickness were investigated in 1991 by the Kurchatov Institute. Ten (10) layers, total, were taken between the one-quarter and the three-quarter thickness planes. Uniformity of unirradiated condition properties was exhibited in the results for Layers No. 2, 4, 5 and 6. The MEA data and dotted trend line from Figure 2 are included in Figure 4; MEA specimens were from thickness regions corresponding to Layers No. 4 and No. 6, but the specimens were from a different section of the forging which appears to exhibit property inhomogeneity. Also, it is unclear whether these specimens had the same test orientation as the Kurchatov-tested specimens. The 41 J (30 ft-lb) transition temperature indications provided by the two unirradiated condition data sets differ insignificantly.

All testing was in compliance with ASTM Test Method E 23 both at MEA and at the Kurchatov Institute, except for pendulum strikers. The striker used on the MEA machine was the ASTM 8-mm striker, while an ISO 2-mm striker was used at the Kurchatov Institute. The 8-mm striker is expected to provide higher absorbed energy values compared to the 2-mm striker data at temperatures where the specimen bending and plastic deformation are relatively high. Usually, this difference is observed at absorbed energy levels above 200 J (148 ft-lb). For purposes of the present study, the results of

comparative Charpy tests performed at Kurchatov Institute with the ISO 2-mm striker and at Oak Ridge National Laboratory with the ASTM 8-mm striker on three reactor pressure vessel steels are of interest [*6*]. Two of the materials were an A 533B-1 plate and a submerged-arc weld. The third material was the 15Kh2MFA-A forging used in the present study, except for the notch orientation. Results show good agreement between the two laboratories [*6*], even though the data for the 15Kh2MFA-A forging were highly scattered.

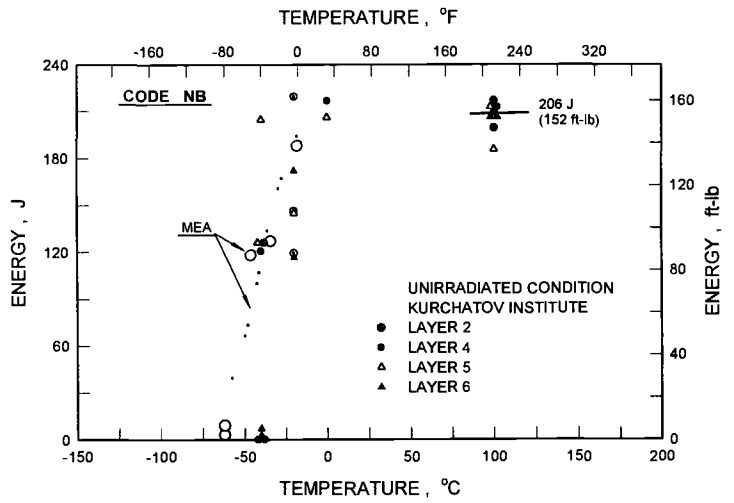


Figure 4 - *C_v Notch Ductility Determinations by the Kurchatov Institute for the Code NB Material as Compared to the MEA Unirradiated Data*

Overall, the cited difference between data sets can be considered material-based and not particular reflections of the test equipment or procedures used by the respective laboratories.

Irradiated Condition

Irradiated condition data obtained by the Kurchatov Institute for the Code OB forging are illustrated in Figure 5. The fluence, 0.6 x 10^{19} n/cm^2, E > 1 MeV, is less than that of the present study, 1.0 x 10^{19} n/cm^2, E > 1 MeV; however, in terms of irradiation effect, the lower fluence would tend to be offset by greater radiation sensitivity at the lower irradiation temperature (270°C, 518°F vs. 288°C, 550°F). The transition temperature elevation of 33°C (60°F) is reasonable compared to the 31°C (55°F) transition temperature elevation shown for

the 288°C (550°F) irradiation in Figure 1. (Note: It is assumed here that the data being compared are for the same test orientation.) The degradation of USE by irradiation was found to be quite large in both the 270°C (518°F) experiment and the 288°C (550°F) experiment; USE reductions were identical at 42 J (31 ft-lb).

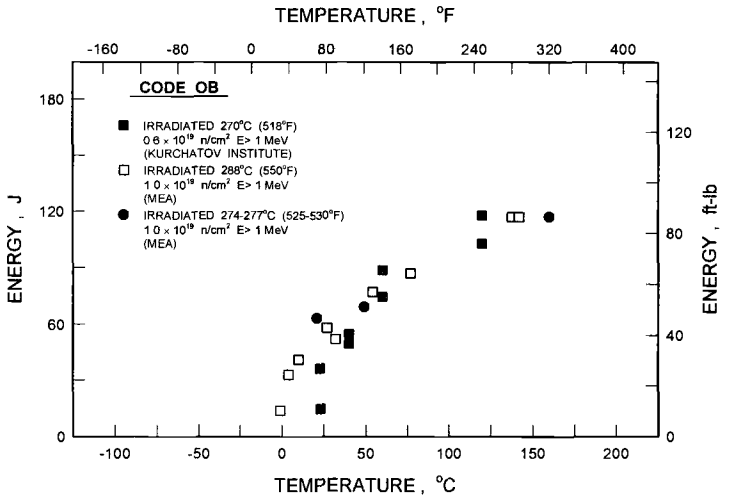


Figure 5 – *Post–Irradiation C_v Notch Ductility Determinations by the Kurchatov Institute and by MEA for the Code OB Material*

The Code NB irradiated condition data of the two laboratories are given in Figure 6. This forging notch ductility following 288°C (550°F) irradiation appears superior to that following 270°C (518°F) irradiation to about 1 x 10^{19} n/cm^2. Material inhomogeneity and/or an irradiation temperature dependency may be the suspected explanation. Since only a few specimens in the current experiment were irradiated in the range of 274°C to 277°C (525°F to 530°F) instead of 288°C (550°F), the data are not sufficient to confirm or deny an irradiation temperature effect. Both sets of data, however, describe good post-irradiation notch ductility for the two conditions evaluated.

Procedure for Projecting Transition Temperature Elevation (Former-USSR Method)

The main properties of steel used in USSR design determinations of RPV resistance to brittle fracture are the critical value of the stress intensity factor (K_{Ic}), the ductile-to-brittle transition temperature (T_K) and the yield strength ($R_p{}^T{}_{0.2}$). Resistance to brittle fracture is

ensured if, for a "postulated" defect taken to be a semi-elliptic flaw or crack, the following condition is fulfilled:

$$K_I \leq [K_I]_i \quad (1)$$

where $[K_I]_i$ is the permissible value of the stress intensity factor taken as the value of K_{Ic}/n_k; n_k is the safety factor. The permissible value of the stress intensity factor depends on the reference temperature ($T-T_K$) and the design condition (Index i). The definition of T_K is described later.

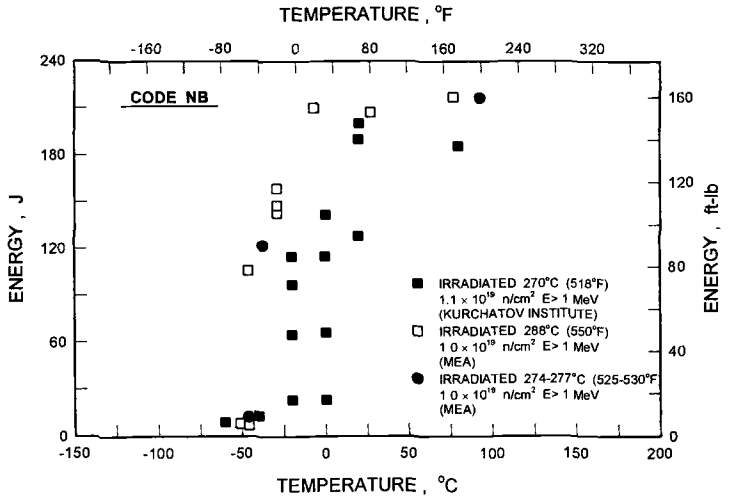


Figure 6 – *Post–Irradiation C_v Notch Ductility Determinations by the Kurchatov Institute and by MEA for the Code NB Material*

The dependence of $[K_I]_i$ on ($T-T_K$) is determined by shifting the initial temperature dependence of K_{Ic}, as follows: The ordinate of the initial temperature dependence of K_{Ic} is divided by the safety factor n_k and then shifted on the x-axis by the value of a temperature margin, ΔT. The effect of irradiation on T_K is then added as ΔT_F (described later). It is assumed that:

- Safety factor $n_k = 2$ and $\Delta T = 30°C$ (54°F) for normal service conditions (Index i = 1)
- Safety factor $n_k = 1.5$ and $\Delta T = 30°C$ (54°F) for violation of normal service conditions and for hydraulic tests (Index i = 2)
- Safety factor $n_k = 1.0$ and $\Delta T = 0°C$ for emergency conditions (Index i = 3).

The temperature dependence of $[K_I]_i$ for steel grades 15Kh2MFA and 15Kh2MFA-A, is described in Russian calculation standards [7]. The toughness-temperature equations are:

- $i = 1$: $[K_I]_1 = 17.5 + 22.5 \cdot \exp\{0.02 (T-T_k)\}$
- $i = 2$: $[K_I]_2 = 23.5 + 30 \cdot \exp\{0.02 (T-T_k)\}$
- $i = 3$: $[K_I]_3 = 35 + 45 \cdot \exp\{0.02 (T-T_k)\}$.

The toughness values are in MPa-$m^{1/2}$ and temperature is in degrees Centigrade.

The projected change in material properties during service life takes into consideration the effects of different service conditions. The irradiation-induced shift of the ductile-to-brittle transition temperature (ΔT_F) is determined by the equation:

$$\Delta T_F = A_F \cdot (\Phi\tau/F_o)^{1/3} \quad (2)$$

where: A_F is the irradiation embrittlement factor in °C;
$\Phi\tau$ is the neutron fluence (E > 0.5 MeV) in neutron /cm^2; and
F_o is a constant having the value of 1 x 10^{18} neutron/cm^2.
Note: $\Phi\tau$ (E > 1 MeV) is taken as approximately 0.6 $\Phi\tau$ (E > 0.5 MeV)

The value of A_F depends on the irradiation temperature and the impurities content of the metal including phosphorus content. Table 3 presents the value of A_F used in the USSR Standard [7] for steel grades 15Kh2MFA, and 15Kh2MFA-A and weld deposits. The irradiation embrittlement factor, like the Chemistry Factor (CF) of NRC Regulatory Guide 1.99, describes the sensitivity of the particular steel to irradiation.

Table 3 - *Irradiation Embrittlement factor A_F [7] for four USSR-Material Types*

Material	Irradiation Temperature	A_F, (°C)
FORGING Grade 15Kh2MFA	270°C (518°F) 290°C (554°F)	18 14
WELD DEPOSIT (Weld Wire Sv-10KhMFT)	250°C (482°F) 270°C (518°F)	800 · (P+0.07Cu) +8 800 · (P+0.07Cu)*
FORGING Grade 15Kh2MFA-A	270°C (518°F) 290°C (554°F)	12 9
WELD DEPOSIT (Weld Wire Sv-10KhMFTU)	270°C (518°F) 290°C (554°F)	15 12

* P and Cu are phosphorus and copper content in wt%, respectively.

The value of the ductile-to-brittle transition temperature is obtained by C_v specimen impact tests. The C_v energy test results are curve-fitted using the hyperbolic tangent method, which employs the equation:

$$KCV = A + B\tanh\left(\frac{T - T_o}{C}\right) \quad (3)$$

where KCV is the absorbed impact energy, T is the temperature, and A,B,C, and T_o are fitting parameters.

The criterion value of absorbed energy for determination of the ductile-to-brittle transition temperature, KCV_1, is established by reference to the yield strength, $R_p^T{}_{0.2}$, at 20°C (68°F) according to Table 4 [7]. By definition, the value of temperature corresponding to the KCV_1 is identified as T_1 and the value of temperature corresponding to 1.5 KCV_1 is identified as T_2. The temperature T_1 is assumed to be the ductile-to-brittle transition temperature, T_K, if the difference, T_2-T_1, is smaller than 30°C (54°F). Otherwise, the value of (T_2 - 30°C) is taken to be the ductile-to-brittle transition temperature, T_K. In most cases, for the USSR reactor pressure vessel steels and weld metals, the value of KCV_1 is equal to 47 J (34.7 ft-lb).

Table 4 - *Criterion Values of Absorbed Energy KCV_1 for Various Yield Strengths.*

Yield Strength At 20°C, (68°F)	Energy Criterion, KCV_1
Up to 304 MPa (44.1 ksi)	23 J (16.9 ft-lb)
More than 304 to 402 MPa (44.1 to 58.3 ksi)	31 J (22.8 ft-lb)
More than 402 to 549 MPa (58.3 to 79.6 ksi)	39 J (28.7 ft-lb)
More than 549 MPa (79.6 ksi)	47 J (34.6 ft-lb)

The Russian Standard [7] does not provide direct provisions for a reduction in C_V upper-shelf energy. However indirectly, it requires USE to be higher than 1.5 KCV_1 or 71 J (51.8 ft-lb) in order to determine the ductile-to-brittle transition temperature T_K.

Measurements vs. Projections of Transition Temperature Elevation (NRC Regulatory Guide 1.99 Method)

The NRC Regulatory Guide 1.99 and its methodology for projecting radiation-induced changes to C_v notch ductility were developed for application to ASTM A 302-B and A 533B-1 plate materials and ASTM A 508-2 and A 508-3 forging materials and their weld metals. The Regulatory Guide is founded on a database for these materials and *not* the steel types and grades studied here. However, the suitability of the Regulatory Guide for projecting the radiation embrittlement of chromium-molybdenum-vanadium pressure vessel steels produced and used in the former USSR is of both practical and scientific interest. Scientific interest in the conservatism (or non-conservatism) of the Guide for these steels stems in part from the issue of how well all key variables governing radiation embrittlement sensitivity are presently known and the issue of how well key variables are being acknowledged in the various projection methodologies.

The elevation in 41 J (30 ft-lb) temperature projected by NRC Regulatory Guide 1.99, Revision 2 [1] for the Code NB material is 43°C (77°F); the projected upper-shelf reduction

is 19%, maximum, for the cited exposure condition. The experimentally-measured 41 J (30 ft-lb) elevation was < 8°C (15°F). The USE reduction appeared to be much less than 19%. Accordingly, the Guide projections are conservative from a fracture safe reliability standpoint.

A parallel assessment of the results for the Code OB (old production) material can be made, but interpretation of the data significance is difficult in view of the large change in slope of the brittle/ductile transition curve. The 31°C (55°F) elevation of the 41 J (30 ft-lb) temperature is not large from an operations standpoint. The 68 J (50 ft-lb) transition temperature elevation of 50°C (90°F), on the other hand, can be viewed as quite appreciable. The projection of the 41 J (30 ft-lb) temperature elevation by irradiation, according to Regulatory Guide1.99, Revision 2, is 43.6°C (78°F) for the Code OB material. This shift amount is about the same as that for the Code NB material, since the Revision 2 methodology makes no allowance for the particular phosphorus content of the steel. The preceding version of the Regulatory Guide, Revision 1 [*8*] did take into account the amount of this impurity element in its projection of transition temperature elevation, A:

$$A = [40 + 1000\ (\%Cu-0.08) + 5000\ (\%P-0.008)]\ [f/10^{19}]^{1/2} \qquad (4)$$

where f is the neutron fluence, E > 1 MeV. For the Code OB material, the computed value of A is 64°C (115°F); A for the Code NB material is 33°C (60°F). It should be noted that the measured 41 J (30 ft-lb) temperature elevations are less than the Revision 1 or Revision 2 projections minus the value of two standard deviations (2σ), i.e., 2 x [9.4°C (17°F)] = 18.8°C (34°F).

The large reduction in USE level observed for the Code OB material (27%) is much greater than the USE reduction projected by the Guide (19%) for the fluence received and this material's copper content of 0.10% Cu. The observed reduction is more consistent for steel having a copper content of (about) 0.20% Cu. The phosphorus content of the Code OB material is believed to have a bearing on this non-conservatism of the Regulatory Guide.

Discussion

The benefit from the post-1980 15Kh2MFA-A specification and steel production practice toward improved pre-service notch ductility and improved radiation embrittlement resistance at 288°C (550°F) is evident in the results from the FNR-9A3 irradiation test. The improved radiation embrittlement resistance can be attributed to the lower phosphorus content [*9*]. Obviously, a high fluence test more indicative of end-of-life (EOL) conditions will be required to fully qualify the radiation resistance capabilities of the Code NB (new production) material. It is noted that design EOL fluences projected for USSR VVER-440 vessels in general are higher than those of USA vessels.

The results for the Code OB material highlight the question of the best energy-level index for weighing the probable RT_{NDT} temperature elevation for those steels showing a change in the slope of the C_v curve with irradiation. The issue is the same for USSR steels as for USA steels. Historically, the 41 J (30 ft-lb) transition temperature elevation has been used as an indirect measure of the reference temperature, RT_{NDT}, elevation. This usage is founded in early experimental correlations of nil-ductility transition temperature (NDT) and Charpy energy transition temperature. The selection of 41 J (30 ft-lb) as a convenient index

for irradiation resistance comparisons was arbitrary and has no founding in structure performance except through test method correlations.

Summary and Conclusions

The primary observations and conclusions of this exploratory study with specimens reported to be ASTM C-R (strong) orientation specimens are:

- The material representing pre-1980 RPV construction had a higher C_V 41 J (30 ft-lb) transition temperature and a lower C_V upper-shelf energy level than the material representing post-1980 RPV construction. The difference in properties is believed due to material processing and not material composition.
- Material compositions proved very similar for the ten elements analyzed, except for phosphorus content (0.019% vs. 0.007% P).
- Notch ductility properties of the materials are similar to those of current USA production A 508-2 and A 508-3 RPV forging materials.
- Both materials exhibited good resistance to 288°C (550°F) irradiation to 1.0×10^{19} n/cm^2, E > 1 MeV, in terms of 41 J (30 ft-lb) transition temperature retention. Transition temperature elevations were ≤ 31°C (55°F).
- Measured transition temperature elevations were less than those projected for the fluence condition and the material copper and nickel contents by NRC Regulatory Guide 1.99, Rev. 2.
- The measured post-irradiation upper-shelf energy for the material representing post-1980 RPV construction was 216 J (159 ft-lb). The pre-irradiation upper-shelf energy level for this material was not established (too few specimens available).
- The measured post-irradiation upper-shelf energy for the material representing pre-1980 RPV construction was 117 J (86 ft-lb) and was 73% of the pre-irradiation value. The 27% reduction by the irradiation exposure is indicative of relatively poor upper-shelf energy resistance to fluence.
- Irradiation reduced the slope of the brittle/ductile transition curve of the material representing the pre-1980 RPV construction appreciably.
- A full assessment of the relative radiation resistance capabilities of the USSR-produced steels will require higher fluence (e.g., > 3×10^{19} n/cm^2, E > 1 MeV) irradiation tests approaching current EOL conditions.
- The available data indicate that the material representing post-1980 RPV construction is at least comparable to USA current production RPV forging and plate materials in terms of 288°C (550°F) neutron radiation resistance.

Acknowledgments

This study was conducted with the encouragement of the USA-USSR Joint Coordinating Committee on Civilian Nuclear Reactors. The authors thank the Kurchatov Institute (Professor Amaev) for providing the test materials and the Yankee Atomic Electric Company (Mr. E. Biemiller) for providing significant indirect support for certain portions of the experimental effort. The authors also appreciate the efforts of Mr. Tim Griesbach (currently at ATI Consulting) who participated in the USA-USSR Joint Coordinating

Committee as a representative of EPRI and who initiated the work at MEA. The report was prepared with the encouragement of Mr. R. Carter, the EPRI Project Manager who succeeded Mr. Griesbach.

References

[1] U.S. Nuclear Regulatory Commission Regulatory Guide 1.99, Revision 2, "Radiation Embrittlement of Reactor Vessel Materials", Washington, DC, May 1988.

[2] Tetelman, A. S. and McEvily, A. J., Jr., *Fracture of Structural Materials,* John Wiley and Sons, New York, 1967, p.326.

[3] Hawthorne, J. R., "Exploratory Studies of Effects of Irradiation Temperature on Mechanical Properties of Structural Steels and Welds", *Effects of Radiation on Materials: 16th International Symposium*; *ASTM STP 1175*, A.S. Kumar, D.S. Gelles, R.K. Nanstad, and E.A. Little, Eds., American Society for Testing and Materials, 1993, pp 306 - 331.

[4] Soulat, P., Houssin, B., Bocquet, P., and Bethmont, M., "Analysis of Radiation Embrittlement Results from a French Forging Examined in the Second Phase of an IAEA-Coordinated Research Program", *Radiation Embrittlement of Nuclear Reactor Pressure Vessel Steels: An International Review (Fourth Volume)*, *ASTM STP 1170*, L.E. Steele, Ed., American Society for Testing and Materials, 1993, pp. 249-265.

[5] Hawthorne, J. R., "Accelerated Irradiation Test of Gundremmingen Reactor Vessel Trepan Material", NUREG/CR-5891, Nuclear Regulatory Commission, Washington, DC, August 1992.

[6] Nanstad, R. K. and Sokolov, M. A., "Charpy Impact Test Results on Five Materials and NIST Verification Specimens Using Instrumented 2-mm and 8-mm Strikers", *Pendulum Impact Machines: Procedures and Specimens for Verification*; *ASTM STP 1248,* T.A. Siewert and A.K. Schmieder, Eds, American Society for Testing and Materials, 1995, pp. 111-139.

[7] "Calculation Standards for Strength of Equipment and Pipes of Nuclear Power Units", PNAE-G-7-002-86, Energoatomizdat, NGA-01-85-1, NIKIET, 1989 (In Russian).

[8] U.S. Nuclear Regulatory Commission Regulatory Guide 1.99, Rev. 1, "Effects of Residual Elements on Predicted Radiation Damage to Reactor Vessel Materials", Washington, DC, April 1977.

[9] Potapovs, U. and Hawthorne, J. R., "The Effect of Residual Elements on 550°F Irradiation Response of Selected Pressure Vessel Steels and Weldments", *Nuclear Applications*, Vol. 6, No. 1, 1969, p. 27.

J. A. Wang[1]

Analysis of Irradiation Data for A302B and A533B Correlation Monitor Materials

Reference: Wang, J. A., "**Analysis of Irradiation Data for A302B and A533B Correlation Monitor Materials,**" *Effects of Radiation on Materials: 19th International Symposium, ASTM STP 1366,* M. L. Hamilton, A. S. Kumar, S. T. Rosinski, and M. L. Grossbeck, Eds., American Society for Testing and Materials, West Conshohocken, PA, 2000.

Abstract: The results of Charpy V-notch impact tests for A302B and A533B-1 Correlation Monitor Materials (CMM) listed in the surveillance power reactor database (PR-EDB) and material test reactor database (TR-EDB) are analyzed. The shift of the transition temperature at 30 ft-lb (T_{30}) is considered as the primary measure of radiation embrittlement in this paper. The hyperbolic tangent fitting model and uncertainty of the fitting parameters for Charpy impact tests are presented. For the surveillance CMM data, the transition temperature shifts at 30 ft-lb (ΔT_{30}) generally follow the predictions provided by Regulatory Guide 1.99, Revision 2, (R.G. 1.99/2) and draft E900-98. Difference in capsule temperatures is a likely explanation for large deviations from R.G. 1.99/2 and ASTM E900-98. Deviations from the R.G. 1.99/2 predictions are correlated to similar deviations for the accompanying materials in the same capsules, but large random fluctuations prevent precise quantitative determination. Significant scatter is noted in the surveillance data. The major contributions to the uncertainty of the prediction models, and the overall data scatter, are from mechanical test results, chemical analysis, difference in effective copper content resulting from the different post weld heat treatment, irradiation environments, fluence evaluation, and inhomogeneous material properties. Thus the prediction model can be improved if the above-mentioned error sources are controlled. In general, the embrittlement behavior of both the A302B and A533B-1 plate materials is similar. There is evidence for a flux effect in the CMM data irradiated in test reactors; thus its implication for power reactor surveillance programs deserves special attention.

Keywords: radiation embrittlement, power reactor, database, LWR, reference materials

1 Introduction

The success of reactor technology depends critically on the choice of materials that have satisfactory resistance to radiation-induced changes in material properties. Presently, interest focuses on radiation damage and its effect on RPV materials. The aging and degradation of light-water-reactor (LWR) pressure vessels are of particular concern because the magnitude

[1]Research Scientist, Oak Ridge National Laboratory, Oak Ridge, TN 37831-6370.

Copyright© 2000 by ASTM International www.astm.org

of the potential embrittlement is important to plant safety. Property changes in materials due to neutron-induced displacement damage are a function of neutron energy, neutron flux, and temperature, as well as the pre-irradiation material history, material chemical composition and microstructure, since each of these influence radiation-induced microstructural evolution [1-3]. These factors must be consider to reliably predict RPV embrittlement and to ensure the structural integrity of the reactor. Based on embrittlement predictions, decisions must be made concerning operating parameters, low-leakage-fuel management, possible life extension, and the potential role of pressure vessel annealing [4]. Large amounts of data obtained from surveillance capsules and test reactor experiments and comprising many different materials and different irradiation conditions are needed to develop generally applicable damage prediction models that can be used for industry standards and regulatory guides. The U.S. Nuclear Regulatory Commission (NRC)/Oak Ridge National Laboratory (ORNL) embrittlement data base (EDB) [5] is such a comprehensive collection of data resulting from the merging of the Power Reactor Embrittlement Data Base (PR-EDB) [6] and the Test Reactor Embrittlement Data Base (TR-EDB) [7]. Three major categories of data are included in the EDB, namely, pre-irradiation material history, irradiation environments, and mechanical test results. This computerized data base for base material and weldments was compiled from surveillance reports of operating power reactors and available technical reports. All data are traceable to the reference sources, including page numbers. Most of the surveillance data have been verified by the reactor vendors responsible for the insertion of the material into surveillance capsules, and any changes and corrections have been documented in special files for future reference.

Generally, the surveillance programs of commercial power reactors include correlation monitor materials (CMM) in addition to base, weld, and HAZ of actual pressure vessel steels. These specimens are fabricated from standard reference steel plates that are similar in most cases in composition and heat treatment to the base material in the respective RPV and are supposed to serve as a reference for comparing the radiation embrittlement of the plant-specific material with the reference material and for detecting anomalies in the radiation environment of the surveillance capsules. In order to use these materials as a reference, the "normal" behavior in regard to fluence, flux, and irradiation temperature must be established first. This procedure requires the collection of data from a sufficient number of irradiations of the material in different irradiation environments, such as different fluxes and temperatures. Such data, obtained from irradiations in surveillance capsules and test reactors, are presently collected in the EDB, and the information is used for this study. The majority of surveillance programs use one of two sources for the reference material, depending on the material in the pressure vessel. One source is the 6-in.-thick ASTM A302 grade B (A302B) reference plate fabricated by U.S. Steel, and the other source consists of three 12-in.-thick A533 grade B class 1 (A533B-1) plates fabricated by Lukens Steel and heat treated by Combustion Engineering (CE). These three plates were fabricated for the Heavy-Section Steel Technology (HSST) program in the late 1960s. Most surveillance data come from the second plate (HSST02); however, the first plate (HSST01) and third plate (HSTT03) are also used in surveillance capsules. The results obtained from the surveillance capsules and material test reactor experiments from these plates are included in this paper. Detailed information of the heat treatments and chemistry compositions for the CMM are listed in Tables 1-5.

Table 1 – *Heat treatment of CMM*

Plate ID	Heat No.	Mat. ID	Thickness	
ASTM	A0421	A302B	14.24 cm	Austenized at 1650°F 6 h, water quenched to 300°F; tempered at 1200°F 6 h, air cooled (heated to 1200°F at 63°F per hour maximum).
HSST01	A1008-1	A533B-Class 1	30.48 cm	Normalized at 1670-01700°F 4h, air cooled; austenized at 1550-1650°F 4 h, water quenched to 300°F; tempered at 1200-1250°F 4 h, furnace cooled to 600°F; stress relieved at 1125-1175°F 40 h, furnace cooled to 600°F.
HSST02	A1195-1	A533B-Class 1	30.48 cm	Normalized at 1650-1700°F 4 h, air cooled; austenized at 1575-1625°F 4 h, water quenched to 300°F; tempered at 1200-1250°F 4 h, furnace cooled to 500°F; stress relieved at 1125-1175°F 40 h, furnace cooled to 600°F.
HSST03	C2702	A533B-Class 1	30.48 cm	Normalized at 1650-1700°F 12 h, air cooled; austenized at 1550-1650°F, 12 h, water quenched to 400°F; tempered at 1200-1250°F 18 h, furnace cooled to 600°F; stress relieved at 1100-1150°F 40 h, furnace cooled to 600°F, at 1020-1035°F 12 h, furnace cooled to 600°F.

Table 2 – *A302B (ASTM) CMM chemical compositions*

Plant/				Chemistry Composition (wt %)								
Exp. ID	HEAT_ID	CHEM_LAB	SPEC_ID	C	Mn	P	S	Si	Cr	Mo	Ni	Cu
	SASTM	U.S. Steel	HEAT	0.24	1.34	0.01	0.02	0.23	0.11	0.51	0.18	0.200
GAR	SASTM S2		HEAT	0.22	1.39	0.01	0.01	0.26		0.60		0.230
IP2	SASTM	SWRI	R-60			0.01						0.170
IP2	SASTM	SWRI	R-62			0.02						0.190
IP2	SASTM	SWRI	R-33								0.28	0.350
IP2	SASTM	SWRI	R-2									0.250
IP2	SASTM	SWRI	R-36								0.27	0.310
IP2	SASTM	SWRI	R-40								0.21	0.210
IP2	SASTM	SWRI	R-56								0.18	0.200
IP2	SASTM	SWRI	R-52								0.27	0.180
NRL-1	SASTM	NRL		0.23	1.35	0.01	0.02	0.22	0.12	0.52	0.22	0.220
RRA	SASTM		@3-11	0.24	1.42	0.01	0.02	0.23	0.11	0.49	0.17	0.182
SRM	SASTM	U.S. Steel	LADLE	0.20	1.31	0.01	0.02	0.23		0.48	0.18	0.180

Table 3 – *A533B (HSST01) CMM chemical compositions*

Plant/				Chemistry Composition (wt %)								
Exp. ID	HEAT_ID	CHEM_LAB	SPEC_ID	C	Mn	P	S	Si	Cr	Mo	Ni	Cu
	SHSS01	NRL	HEAT	0.220	1.370	0.008	0.008	0.220	0.150	0.540	0.660	0.18
	SHSS01	Lukens	CHECK	0.220	1.480	0.012	0.018	0.250		0.520	0.680	
	SHSS01	Lukens	LADLE	0.220	1.450	0.011	0.019	0.220		0.530	0.620	
MY	SHSS01	Westinghouse	61E	0.221	1.524	.0112	.0174	0.198	0.080	0.577	0.665	0.17
MY	SHSS01	Westinghouse	61D	0.215	1.487	.0104	.0174	0.077	0.080	0.556	0.654	0.17
HSST-0	SHSS01K 0T[a]	ORNL		0.230	1.430	0.012	0.013	0.240		0.550	0.810	
HSST-0	SHSS01K 12[a]	ORNL		0.260	1.240	0.021	0.012	0.240		0.550	0.730	
HSST-0	SHSS01K 14[a]	ORNL		0.230	1.440	0.010	0.015	0.230		0.540	0.840	
HSST-0	SHSS01K 18[a]	ORNL		0.220	1.410	0.010	0.014	0.230		0.520	0.830	
HSST-0	SHSS01K 1T[a]	ORNL		0.240	1.370	0.015	0.013	0.230		0.540	0.810	
HSST-0	SHSS01K 34[a]	ORNL		0.260	1.380	0.021	0.014	0.230		0.530	0.840	
HSST-0	SHSS01K 38[a]	ORNL		0.230	1.450	0.015	0.012	0.240		0.560	0.770	
HSST-0	SHSS01K 58[a]	ORNL		0.260	1.180	0.017	0.013	0.230		0.560	0.740	
HSST-0	SHSS01K 78[a]	ORNL		0.240	1.300	0.016	0.014	0.230		0.530	0.800	
HSST-0	SHSS01MU0	ORNL		0.230	1.440	0.014	0.014	0.260		0.540	0.670	
HSST-0	SHSS01MU12	ORNL		0.200	1.380	0.010	0.011	0.220		0.520	0.670	
HSST-0	SHSS01MU14	ORNL		0.230	1.390	0.010	0.012	0.260		0.530	0.680	

[a]The last two digits of HEAT_ID are used to specify the specimen location in parent material, OT - inner surface, 12 - ½ thickness, 14 - 1/4 thickness, 18 - 1/8 thickness, 1T - outer surface, 34 - 3/4 thickness, 38 - 3/8 thickness, 58 - 5/8 thickness, 78 - 7/8 thickness.

Table 4 – *A533B (HSST02) CMM chemical compositions*

Plant/				Chemistry Composition (wt %)								
Exp. ID	HEAT_ID	CHEM_LAB	SPEC_ID	C	Mn	P	S	Si	Cr	Mo	Ni	Cu
	SHSS02		HEAT	0.23	1.39	0.01	0.01	0.21		0.50	0.64	0.170
	SHSS02	Lukens	LADLE	0.22	1.45	0.01	0.01	0.22		0.53	0.62	
DCI	SHSS02		R47	0.20	1.56	0.00	0.01	0.19	0.11	0.47	0.65	0.150
SA1	SHSS02	Westinghous	HEAT	0.22	1.48	0.01	0.01	0.25	0.08	0.52	0.68	0.140
HSST-0	SHSS02	ORNL	CHECK	0.24	1.42	0.01	0.01	0.22	0.12	0.50	0.70	0.140
HSST-0	SHSS02FB0	ORNL		0.27	1.50	0.01	0.01	0.21		0.50	0.72	
HSST-0	SHSS02FB1	ORNL		0.26	1.48	0.01	0.01	0.23		0.49	0.64	
HSST-0	SHSS02FB1	ORNL		0.27	1.49	0.01	0.01	0.21		0.50	0.64	
HSST-4	SHSS02GA			0.23	1.55	0.00	0.01	0.20	0.04	0.53	0.67	0.140
NRL-2	SHSS02	NRL	HEAT	0.23	1.48	0.00	0.01	0.19	0.12	0.51	0.68	0.140
VDE	SHSS02A			0.22	1.44	0.01	0.00	0.30	0.12	0.51	0.63	0.120

[a]The last two digits of HEAT_ID are used to specify the specimen location in parent material, OT - inner surface, 12 - ½ thickness, 14 - 1/4 thickness.

Table 5 – *A533B (HSST03) CMM chemical compositions*

Plant/				Chemistry Composition (wt %)								
Exp. ID	HEAT_ID	CHEM_LAB	SPEC_ID	C	Mn	P	S	Si	Cr	Mo	Ni	Cu
HSST-0	SHSS03	Lukens	CHECK	0.200	1.260	0.011	0.018	0.250	0.100	0.450	0.560	0.120
HSST-0	SHSS03	Lukens	LADLE	0.210	1.310	0.012	0.018	0.240	0.150	0.500	0 600	0.130
HSST-0	SHSS03E 0T[a]	ORNL		0.260	1.330	0.011	0.016	0.240		0.510	0.650	
HSST-0	SHSS03E 12[a]	ORNL		0.250	1.270	0.010	0.020	0.280		0.490	0.700	
HSST-0	SHSS03E 14[a]	ORNL		0.260	1.360	0.011	0.015	0.260		0.520	0.620	
HSST-0	SHSS03E 1T[a]	ORNL		0.250	1.410	0.010	0.016	0.280		0.500	0.610	
HSST-0	SHSS03E 34[a]	ORNL		0.260	1.370	0.010	0.019	0.250		0.430	0.620	

[a]The last two digits of HEAT_ID are used to specify the specimen location in parent material, OT - inner surface, 12 - ½ thickness, 14 - 1/4 thickness, IT - outer surface, 34 - 3/4 thickness.

2 Procedures Used In Embrittlement Analysis

The CMMs are used in the surveillance program in the form of Charpy and tensile specimens. The majority of data are from the Charpy impact test, and limited tensile test data are available only from General Electric's (GE) boiling-water-reactor (BWR) surveillance program. Thus only the Charpy test results are considered here, and the ΔT_{30} is considered as the primary measure for radiation embrittlement.

Computer curve fitting of Charpy V-notch transition temperature test data could promote more consistent analytical interpretation of Charpy data, particularly those obtained from reactor materials surveillance programs. The use of computerized methods is preferable to hand fitting, which was widely practiced in the past. It eliminates some of the arbitrariness of the hand-fitted curve and allows calculation of the variance and covariance of the model parameters. Among the curve-fitting methods available are the four-parameter hyperbolic tangent method [8], the four-parameter exponential curve method [9], the five-parameter exponential term, the six-parameter Gauss-Integral method [10], and the polynomial curve fit [11]. A mathematical expression of the hyperbolic tangent-shaped curves, typical of most Charpy impact energy, lateral expansion, and ductile fracture appearance versus test temperature data, requires at least four adjustable parameters to provide a useful characterization.

2.1 *Description of the EDB Charpy Curve-Fitting Procedures*

In order to have a uniform and consistent determination of the ΔT_{30} for the surveillance reference materials, the raw Charpy data are fitted to a hyperbolic tangent model. It relates impact energy E to the test temperature T according to the formula

$$E = (LSE + USE)/2 + [(USE - LSE)/2] \bullet \tanh(SLOPE(T - TM)) \quad (1)$$

with USE and LSE the upper- and lower-shelf energy, respectively, with TM as the midpoint of the transition temperature region, and SLOPE as the slope of the curve at TM. This model is purely phenomenological but well characterizes the general shape of a Charpy curve in four basic parameters: USE, LSE, TM, and SLOPE. Currently, this hyperbolic tangent function is the most widely used fitting procedure next to hand (eyeball) fitting. The fitting parameters in this paper were obtained from the EDB data-fitting procedures, which use the IMSL subroutine ZXSSQ. This subroutine is based on the Levenberg-Marquardt algorithm to solve nonlinear least-squares problems. In the EDB Charpy curve-fitting utility, initial values for the fitting parameters were determined by first separating the two shelf energies from the transition region using fracture appearance and the relative magnitude of the impact energy as criteria. From the test data in the transition region, crude estimates are obtained for TM and SLOPE.

In the fitting procedure, an additional constraint is introduced for USE, and LSE is assigned to 3 joules [12], which restrains the variation in these parameters. It avoids runaway values for USE and negative LSE if data points in these regions are missing. With these precautions, any reasonable set of Charpy data can be fitted as well and more consistently than by a human evaluator. The procedure is completely automated, with no operator intervention required or allowed. However, visual inspection is made to ensure that the fitting is properly performed. When the procedure fails, it is generally the result of outliers, which must be removed, or the data are such that no reasonable fit can be made. The simplicity and appeal of the least-squares method brings with it the danger that it may be used inappropriately, which was pointed out in Ref. 13. In any use, the underlying assumption and limitations should clearly be kept in mind, and the "best estimates" are good only within the bounds of their statistical uncertainties.

Uncertainties for the fitting parameters are needed to determine accuracy and credibility of the transition temperature and upper shelf data. A covariance matrix of the fitting parameters is part of any least-squares procedure, but these covariances are not used for uncertainty analysis in the EDB fitting program. The unavoidable linearization used for the determination of the covariances disregards second-order effects, and there is no possibility to account for uncertainties in test temperature. A more reliable procedure is the use of random variations of the input data (Monte Carlo procedure); such variations can be applied to both impact energy and test temperature, and the results reflect more accurately the influences of nonlinearities. The generated fitting parameters with corresponding plots of the Charpy curves and uncertainty analyses are demonstrated in Ref. 14. Both the hyperbolic tangent fit and hyperbolic tangent fit plus Monte Carlo procedure (which assigns 10 J uncertainty for the impact energy and 4°C uncertainty for the testing temperature) show good agreement in the determination of T_{30}. The trend curves of raw Charpy data generated by the hyperbolic tangent fit plus Monte Carlo procedure seem to be more representative than that of the hyperbolic tangent fit alone, especially for those data sets with large data scatter.

2.2 *Determination of Trend Curves for Radiation Embrittlement*

The dependency of the ΔT_{30} on the damage fluence (i.e., the trend curve) for the two materials needs to be determined. Two trend curves were evaluated in this study. The transition temperature shift values, ΔRT_{NDT}, predicted by R.G. 1.99/2 are used for the determination of the trend curve, which is given by the formula [15]

$$\Delta RT_{NDT} = [CF] \bullet f^{(0.28 - 0.10 \log f)} \qquad (2)$$

where [CF] is a "chemistry factor" which is given in tabular form, depending on the copper and nickel content, and separately for base material and welds. The symbol f stands for fluence, E > 1.0 MeV in 10^{19} n/cm². ΔRT_{NDT} is in degrees Fahrenheit at 30 ft-lb energy level.

The recently developed transition temperature models of the draft E900-98, "ASTM Standard Guide for Predicting Neutron Radiation Damage to Reactor Vessel Materials, April 1998," were also incorporated into the residual study for power reactor data. "Residual" is defined as the measured ΔT_{30} minus draft E900-98's predictions. This transition temperature model is listed in equation 3.

$$\begin{gathered}
\Delta T_{30p} = ff_1(\phi t) + ff_2(\phi t)\ f(cc), \quad [°F] \\
ff_1(\phi t) = A \bullet \exp\left[\frac{1.906 \bullet 10^4}{T_c + 460}\right](1 + 57.7P)\left[\frac{\phi t}{10^{19}}\right]^a \\
ff_2(\phi t) = \frac{1}{2} + \frac{1}{2}\tanh\left[\frac{\log(\phi t + 5.48 \bullet 10^{12}\ t_i) - 18.29}{0.600}\right] \\
ff(cc) = B(Cu - 0.72)^{0.678}(1 + 2.56\ Ni^{1.358}) \\
where, a = 0.4449 + 0.0597 \bullet \log\left[\frac{\phi t}{10^{19}}\right] \\
Welds: A = 1.10 \bullet 10^{-7},\ B = 209,\ Plates: A = 1.23 \bullet 10^{-7},\ B = 172 \\
Forgings: A = 8.98 \bullet 10^{-8},\ B = 135,\ T_c \text{ is coolant temperature, } °F
\end{gathered} \qquad (3)$$

2.3 *Basis of CMM and Its Implication on Radiation Embrittlement*

The use of CMMs is based on the idea that anomalous conditions with regard to fluence, flux, and irradiation temperature can be detected by correspondingly anomalous behavior of the CMM. The difficulty is that it is not easy to determine whether anomalous embrittlement is caused by: the radiation environment, such as neutron energy spectrum, flux, fluence, irradiation temperature, and reactor operation history; or by the inherent inhomogeneous material properties of the CMM; or uncertainties in the determination of the trend curve for the reference material, and uncertainties in the determination of the ΔT_{30}. Significant errors in the trend curve determination will show up as systematic biases. These biases may be either independent of the fluence (e.g., due to an incorrect chemistry factor) or fluence dependent, indicating errors in the fluence factor. Such systematic biases can never be completely separated from random errors, but using relatively large numbers of data will guard against neglecting large inconsistencies with the trend curve model.

The variation of material properties, such as mechanical test results and chemical

compositions, within the reference material is a more serious problem. Tests made from different sets of specimens for the unirradiated material reveal considerable differences in the baseline T_{30} for the ASTM A302B plate as well as the three HSST plates (HSST01, HSST02, and HSST03). The test specimens used for the baseline of the A302B reference material (LT orientation) have the range of T_{30} from 4 to 32°F, and the range of chemistry composition for copper and nickel is 0.17-0.31wt % and 0.17-0.27wt %, respectively. For the HSST01 plate, the LT baseline specimens have the range of T_{30} from -20 to 36°F at one-quarter thickness; and the range of copper and nickel contents are 0.17-0.18 wt % and 0.62-0.84 wt %, respectively. For the HSST02 plate, the LT baseline specimens have the range of T_{30} from -3 to 47°F; and the range of copper and nickel contents are 0.12-0.17 wt % and 0.62-0.72 wt %, respectively. For the HSST03 plate, the TL baseline specimens have the range of T_{30} from 31 to 42°F at one-quarter thickness and from 17 to 29°F for LT orientation; and the range of copper and nickel contents are 0.12-0.13 wt % and 0.56-0.70 wt %, respectively. The possible fluctuations in the material properties from one specimen set to another can be detected only as random deviations, and these deviations cannot be clearly separated from other random errors.

The standard method used to determine the uncertainty for the T_{30} is based on the uncertainties in determining the fitting parameters in the least-squares fit and the mean-square difference between model and experimental data. However, this procedure does not consider possible deviations between the idealized model and the actual physical mechanism, and this may lead to serious underestimation of the uncertainties, the more so the more restrictive the model is. It can be assumed that the information for determining T_{30} is based on mean values and the slope of the relevant data regardless of what model is actually used, and that this information or the lack of it determines the uncertainties. However, the estimated values of T_{30} and USE as well as the experimental uncertainties are still based on a specific model. From past studies of several fitting models [16], it appears that differences among selected fit models are mostly within uncertainty bounds. Hyperbolic tangent fit results for CMM data are listed in Tables 6-8 for surveillance data, together with the values reported by the original investigation. The index transition temperature at the 30 ft-lb energy level is used in the study, which is the index temperature required by ASTM E-185 for the determination of the transition temperature shift. The 30 ft-lb energy level was used in preference to the old standard of 50 ft-lb because the higher energy is too close to or above the upper shelf for some of the materials used. From the reported surveillance data, there are over 40 data points whose irradiated upper shelf are less than 50 ft-lb. In a few cases, suspect Charpy tests have been eliminated from the fitting and determination of uncertainties. This procedure is rather subjective, but the results are more reasonable.

If the deviations from the expected radiation damage exceed the uncertainties described above, anomalies in the capsule environment (i.e., fluence, flux, irradiation temperature), or plant operation history must be suspected. Errors in fluence determination are generally too small to significantly influence the damage prediction, perhaps with the exception of very low fluences or very high fluences. For example, at a fluence of 1.0×10^{19} n/cm², a 35% uncertainty in the fluence evaluation will result in only an 8% uncertainty in the shift predicted from R.G. 1.99/2. This same uncertainty leads to a 6% uncertainty in the trend curve contained in the draft E900-98 for ASTM CMM irradiated at 550°F for 10 EFPY. From the present investigation of power reactor data, the dependency of radiation damage on the flux cannot be confirmed nor ruled out. Whenever the radiation damage is larger or

Table 6 – *Summary of A302B surveillance CMM*

	Fluence	Flux	C_v transition temp. °F at 30-ft-lb, unirradiated				C_v transition temp. °F at 30-ft lb, irradiated				C_v transition temp. °F shift at 30-ft lb					
	E > 1 MeV	E > 1 MeV														
Orient.	10^{19} n/cm^2	10^{11} n/cm^{2}s	R	T	MT	U	R	T	MT	U	R	P	T	MT	U	E
LT	0.572	0.682	36	32	33	6.1	144	135	135	11.5	108	84	103	102	13.0	
LT	0.277	0.776	36	32	33	6.1	81	81	82	19.5	45	65	35	49	20.4	
LT	1.400		40	32	33	6.1	160	131	128	20.2	120	109	99	95	21.1	
LT	3.680	1.579	40	32	33	6.1	195	168	168	15.6	155	134	136	135	16.8	151
LT	1.430		40	32	33	6.1	178	164	163	12.0	138	110	132	130	13.5	
LT	0.259	0.486	40	32	33	6.1	125	133	134	13.4	85	63	101	101	14.7	80
LT	2.280	0.665	40	32	33	6.1	180	170	165	17.3	140	122	138	132	18.3	150
LT	0.463	0.604	40	32	33	6.1	120	124	123	13.1	80	79	92	90	14.5	102
LT	1.550	0.646	40	32	33	6.1	167	169	166	12.0	127	112	137	133	13.5	138
LT	1.100	0.414	27	32	33	6.1	153	140	140	12.5	126	103	108	107	13.9	
LT	0.737	0.547	27	32	33	6.1	133				106	91				
LT	4.650	4.947	27	32	33	6.1	194				167	139				
LT	2.210	5.725	27	32	33	6.1	142				115	121				
LT	5.470	8.238	27	32	33	6.1	178				151	142				
LT	1.100	1.368	40	32	33	6.1	136	134	132	13.4	96	103	102	99	14.7	119
LT	1.910	0.880	40	32	33	6.1	180	167	165	16.7	140	118	135	132	17.8	134
LT	0.585	1.315	40	32	33	6.1	130	128	128	10.9	90	85	96	95	12.5	102
TL	0.506	1.253	64	64	64	13.0	141	138	142	20.0	77	81	74	78	23.9	100
TL	4.420	1.930	65	64	64	13	215	228	232	28.4	150	138	164	168	31.2	162
TL	0.601	0.595	64	64	64	13	169	135	135	20.0	105	86	71	71	23.9	106
LT	0.243	0.542	38	32	33	6.1	110	106	107	11.7	72	62	74	74	13.2	79
LT	0.506	0.186	38	32	33	6.1	128	132	132	13.5	90	81	100	99	14.8	115
LT	0.453	0.615	38	32	33	6.1	108	106	106	10.7	70	78	74	73	12.3	106
LT	1.080	0.663	38	32	33	6.1	138	120	117	16.6	100	102	88	84	17.7	139
LT	2.360	1.466	40	32	33	6.1	150	156	154	10.3	110	123	124	121	12.0	146
LT	0.798	0.700	40	32	33	6.1	135	126	126	13.8	95	94	94	93	15.1	116
LT	2.370	0.809	40	32	33	6.1	160	162	162	13.1	120	123	130	129	14.5	146
LT	0.524	1.117	40	32	33	6.1	135	132	131	11.3	95	82	100	98	12.8	103
LT	1.750	2.986	40	32	33	6.1	155	148	146	11.8	115	115	116	113	13.3	130
LT	3.480	3.910	40	32	33	6.1	190	186	187	13.7	150	133	154	154	15.0	149
LT	3.850	1.584	40	32	33	6.1	170	162	160	14.3	130	135	130	127	15.5	152
LT	1.720	1.578	35	32	33	6.1	160	156	150	14.3	125	115	124	117	15.5	132
LT	0.739	2.041	35	32	33	6.1	117	118	115	15.4	82	92	86	82	16.6	110
LT	1.530	0.602	35	32	33	6.1	160	132	131	14.9	125	112	100	98	16.1	130
	9.000	32.847	15	32	33	6.1	325				310	150				420
	9.000	30.928	15	32	33	6.1	325				310	150				420
	7.000	25.830	15	32	33	6.1	275				260	146				377
	5.000	17.007	15	32	33	6.1	240				225	140				330

R - as reported; T - hyperbolic tangent model; MT - hyperbolic tangent model plus Monte Carlo method;
U - uncertainty (1 standard deviation); P - R.G. 1.99, Rev.2, prediction; E - E900-98's prediction

smaller than expected, fluxes have not differed significantly from other capsules that behave normally. This leaves irradiation temperature as the most likely cause for variations with comparable fluence, excluding the very low and very high fluence range. Temperature monitors within the surveillance capsules give only the upper bound and, in case of melting, do not indicate whether any high temperature was transient or sustained. The investigation of the material test reactor data, which cover wider ranges of fluence, flux, and irradiation temperature compared with that of power reactor data, seems to reveal the flux effect and the synergistic effect of irradiation temperature and fluence and flux. Both the power reactor and test reactor data show the strong influence of the irradiation temperature on the radiation embrittlement.

Table 7 – *Summary of A533B, HSST01, surveillance CMM*

Orient.	Fluence E > 1 MeV	Flux E > 1 MeV	C_v transition temp. °F at 30 ft-lb, unirradiated				C_v transition temp. °F at 30 ft-lb, irradiated				C_v transition temp. °F shift at 30 ft-lb					
	10^{19} n/cm^2	10^{11} n/cm^2 s	R	T	MT	U	R	T	MT	U	R	P	T	MT	U	E
LT	0.590	0.636	39	32	31	5.4	127	132	132	7.9	88	116	100	101	9.6	106.
LT	0.814	0.564	25	24	23	6.7	153	151	153	8.5	128	128	127	130	10.8	115.
LT	0.583	0.711	27	14	13	7.4	151	147	146	8.6	124	115	133	133	11.3	117.
LT	1.280	0.298	27	14	13	7.4	168	186	186	19.	141	145	172	173	20.9	132.
LT	0.884	0.282	24	30	30	7.7	165	165	163	8.8	141	131	135	133	11.7	115.
LT	1.300	4.348	15	14	13	7.4	165	169	168	11.	150	146	155	155	13.5	149.
LT	1.250	0.339	15	14	13	7.4	175	180	179	8.6	160	144	166	166	11.3	128.
LT	0.407	0.284	3	14	13	7.4	120	110	110	14.	117	102	96	97	16.3	91.6
LT	1.779	0.567	15	14	13	7.4	163	169	169	9.2	148	158	155	156	11.8	147.
LT	0.716	0.239	39	36	36	5.6	149	160	160	9.5	110	123	124	124	11.0	112.

R - as reported; T - hyperbolic tangent model; MT - hyperbolic tangent model plus Monte Carlo method;
U - uncertainty (1 standard deviation); P - R.G. 1.99, Rev.2, prediction; E - E900-98's prediction.

It is a good indication that capsule anomalies are the cause for deviation from the expected radiation damage of the reference material if other materials in the capsules show similar deviations. For this reason, the radiation damage for all materials in a given capsule from the reported surveillance data is investigated in this paper; excluded were the HAZ materials and the materials where the copper and nickel content were not determined. Based on EDB reported data, the new 2σ uncertainties per R.G. 1.99/2 for base and weld metals, are determined as 56 and 63°F, respectively, but absolute residuals greater than 100°F, which has uncertainty greater than 3σ, were not included in the uncertainty study. The manufacturer's chemistry data were used in the residual study.

3 Results

The manufacturer's chemistry is used for the determination of the trend curves of R.G. 1.99/2 and draft E900-98; the copper, nickel, and phosphorous contents, and the chemistry factor according to R.G. 1.99/2 are listed below.

Material	Cu (wt. %)	Ni (wt. %)	P (wt. %)	Chemistry Factor(°F)
ASTM	0.200	0.180	0.011	100
HSST01	0.180	0.660	0.011	136
HSST02	0.170	0.640	0.013	128
HSST03	0.120	0.560	0.011	82

3.1 *Power Reactor Surveillance Data*

3.1.1 *A302B (ASTM) CMM*

Table 8 – *Summary of A 533B, HSST02, surveillance CMM*

	Fluence	Flux	C_v transition temp. °F at 30 ft-lb, unirradiated				C_v transition temp. °F at 30 ft-lb, irradiated				C_v transition temp. °F at 30 ft-lb, unirradiated					
	E > 1 MeV	E > 1 MeV														
Orient.	10^{19} n/cm^2	10^{11} n/cm^2 s	R	T	MT	U	R	T	MT	U	R	P	T	MT	U	E
LT	1.030		48	47	46	5	94	121	116	16	46	129	74	70	17	109
LT	0.428		48	47	46	5	98	97	98	10	50	98	50	52	12	86
LT	1.460		48	47	46	5	11	122	121	13	68	141	75	75	14	117
LT	0.073	0.244	56	47	46	5		75	73	12	40*	46	28	27	13	29
LT	0.269	0.673	45	47	46	5	10	106	105	13	60	82	59	59	14	78
LT	1.770	0.610	45	47	46	5	16	186	186	10.0	120	148	139	140	11	138
LT	0.813	0.760	45	47	46	5	14	148	149	9.6	100	121	101	103	11	115
LT	1.230	0.788	45	47	46	5	15	156	156	11	110	135	109	110	12	127
LT	0.656	0.513	48	47	46	5	12	130	129	14	73	113	83	83	15	98
LT	1.290	1.230	48	47	46	5	15	160	160	14	106	137	113	114	15	114
LT	0.284	0.714	46	47	46	5	11	112	113	9.2	66	84	65	67	11	79
LT	0.941	0.509	46	47	46	5	15	160	160	11	112	126	113	114	12	117
LT	0.724	0.690	50	47	46	5	19	194	191	11	140	116	147	145	13	110
LT	2.840	0.809	45	47	46	5	20	201	201	11	155	164	154	155	12	161
LT	1.900	1.301	45	47	46	5	18	202	194	10	140	150	155	148	12	146
LT	0.608	1.498	45	47	46	5	14	143	141	12	95	110	96	95	13	110
LT	0.895		56	47	46	5	14	130	131	11	88	124	83	85	13	106
LT	0.986		48	47	46	5	11	122	121	13	68	194	75	75	14	108
LT	0.150	0.289	56	47	46	5		78	77	14	64*	64	31	31	15	50
LT	0.057	0.213	56	47	46	5		56	56	12	28*	40	9	10	13	24
LT	0.337		48	47	46	5	11	116	115	7.6	71	90	69	69	9.2	78
LT	0.094	0.248	56	47	46	5		74	73	11	42*	52	27	27	13	36
LT	1.210		48	47	46	5	14	170	168	17	95	135	123	122	18	113
LT	0.312		56	47	46	5	95	99	99	8.6	39	87	52	53	10.0	75.7
LT	1.450		32	47	46	5	15	153	150	17	119	141	106	104	17	117
LT	2.520	1.537	49	47	46	5	20	201	200	12.0	151	160	154	154	13.0	144.
LT	3.760	0.807	49	47	46	5	19	198	197	13	145	172	151	151	14	158
LT	1.010	0.927	49	47	46	5	15	168	168	13	105	128	121	122	14	118
LT	0.585	1.216	45	47	46	5	13	141	141	11	90	109	94	95	12	102
LT	1.460	0.807	49	47	46	5	20	208	207	8.1	156	141	161	161	9.6	143
LT	3.950	1.463	49	47	46	5	23	241	240	9.9	186	173	194	194	11	186
LT	0.540	1.280	49	47	46	5	15	151	150	11.0	110	106	104	104	12	110
LT	4.050	1.457	45	47	46	5	22	230	229	10	180	174	183	183	12	187
LT	1.090	0.838	45	47	46	5	20	205	204	8.7	160	131	158	158	10	133
LT	0.578	1.314	45	47	46	5	17	170	169	11	125	108	123	123	12	112
LT	0.256	0.738	50	47	46	5	11	113	114	12	60	81	66	68	13	75
LT	0.930	0.823	50	47	46	5.1	17	180	180	8.9	125	125	133	134	10.3	118.
LT	1.230	0.644	50	47	46	5.1	18	182	182	8.4	135	135	135	136	9.8	126.
LT	0.282	0.834	45	47	46	5.1	11	119	117	10.9	70	84	72	71	12.0	81.4
LT	1.970	0.779	45	47	46	5.1	19	189	189	10.2	145	152	142	143	11.4	141.
LT	1.750	0.663	45	47	46	5.1	16	152	150	12.2	120	148	105	104	13.2	135.
LT	0.294	0.797	40	47	46	5.1	10	109	108	9.8	60	85	62	62	11.0	82.6
LT	0.866		48	47	46	5.1	12	126	125	9.9	77	123	79	79	11.1	105.
LT	0.107	0.263	56	47	46	5.1		90	89	9.2	44*	55	43	43	10.5	39.4
LT	1.430	1.324	45	47	46	5.1		152	151	9.2	115	141	105	105	10.5	123.
LT	0.708	1.914	45	47	46	5.1	13	136	136	12.1	90	116	89	90	13.1	105.
LT	0.325	0.846	42	47	46	5.1	10	113	113	8.8	66	88	66	67	10.2	90.0
LT	0.964	0.853	42	47	46	5.1	17	175	170	12.6	130	127	128	124	13.6	127.
LT	1.330	0.816	42	47	46	5.1	16	166	165	10.1	120	138	119	119	11.3	138.
LT	1.780	0.657	42	47	46	5.1	17	169	169	11.9	129	148	122	123	12.9	148.
LT	0.840	0.743	50	47	46	5.1	15	147	146	10.6	100	122	100	100	11.8	124.
LT	0.282	0.676	50	47	46	5.1	10	95	96	9.4	50	84	48	50	10.7	85.0
LT	1.670	0.576	50	47	46	5.1	18	183	183	8.6	135	146	136	137	10.0	147.

* 50 ft-lb transition temperature shift. Refer to Table 7 for the notes.

The results from 33 capsules in 10 Westinghouse plants, and 5 capsules in one GE plant, have been investigated. The capsules in the H.B. Robinson Reactor contain specimens fabricated in the TL orientation; all others are fabricated in the LT orientation. The Yankee Rowe surveillance data exhibit a much greater shift than predicted by R.G. 1.99/2, and much lower shift than predicted by draft E900-98. This may be due to the relative low operation temperature (450~525°F) and high flux ($1.7 \times 10^{12} \sim 3.2 \times 10^{12}$ n/cm^2·s) [6] compared with that of the data used to develop R.G. 1.99/2 and draft E900-98, and are, therefore, excluded from the uncertainty study. Please note that the vendor plant surveillance data will now be referred to as the vendor data.

Compared to the R.G. 1.99/2, the 2σ uncertainty of the data scatter band around the Regulatory Guide's trend curve is 30°F for EDB hyperbolic tangent fit results; and a bias of 6.1% (6°F) is detected for CMM [i.e., the measured ΔT_{30} are on the average 6.1% larger than the Regulatory Guide predicted values (see Fig. 1)]. These values indicate that R.G. 1.99/2 gave fairly good predictions for the radiation embrittlement of the ASTM CMM under different irradiation environments. The trend curve of the draft E900-98 for the ASTM CMM is also shown in Fig. 1, which indicates that E900-98 overestimates the ΔT_{30}. The average coolant inlet temperature of ASTM CMM, 542°F, and 10 EFPY are used in the evaluation of draft E900-98. Compared to draft E900-98 with EDB tangent fit results, a bias of -12% (-15°F) and 2σ uncertainty of 30°F is detected [measured ΔT_{30} are on the average 12% less than the E900-98's predicted values]. The above phenomena are demonstrated in a residual plot, see Fig 2.

From Table 6, the average absolute difference between the reported shift and EDB hyperbolic tangent fit results is 12%. The bias and 2σ uncertainty per R.G. 1.99/2's predictions determined by the reported shift data are 7.5% and 24°F, respectively. A similar bias, namely 6.9%, is found from all capsules that contain the A302B CMM per PR-EDB reported data, but with a relatively large data scatter band, and a 2σ uncertainty of 50°F. For the A302B RPV steels, the majority of ASTM CMM shifts are greater than that of the base materials loaded in the same capsule due to the higher copper content of the CMM plate. This may serve as an upper bound for the irradiated A302B plate materials. One special case, Yankee Rowe, has a base metal that appears to be much more sensitive to the radiation embrittlement than ASTM CMM material. The Yankee Rowe steel has less reported copper content, 0.18 wt %, compared with that of ASTM CMM, 0.20 wt %, but with higher phosphorous content than that of the ASTM CMM material.

Although the general underprediction of radiation damage per R.G. 1.99/2 for the CMM parallels the underprediction for companion materials in the same capsules, there are many exceptions to this observation. Only 12 out of 23 underpredicted surveillance capsules have good correlations between the behavior of the reference and plant-specific materials. This situation may be due to (1) deviation of the trend curve for plant-specific material from R.G. 1.99/2, (2) uncertainties in the chemistry of the plant-specific material, (3) differences in temperature and fluence within the capsule, and (4) sample-to-sample variations in both plant-specific materials and CMM. Overall, in 23 out of 37 surveillance capsules that contained both CMM and A302B base metals, the base metals showed a similar deviation from the R.G. 1.99/2 predicted values as did the CMM. Findings with large deviations from the R.G. 1.99/2 trend curve, for example greater than 2σ uncertainty, are useful as warning flags that invite further investigation.

3.1.2 *533B (HSST) CMM*

Results obtained from HSST01 plate in 10 capsules from 8 CE plants, and HSST02 plate in 53 capsules from 7 B&W plants and 13 Westinghouse plants were investigated.

3.1.2.1 *HSST01 CMM Data*

The results of a comparison of CE plants' HSST01 data with R.G. 1.99/2 trend curves are demonstrated in Fig.3 for EDB hyperbolic tangent fit results. On the average, from table 7, R.G. 1.99/2 underpredicted the experimental values for all surveillance capsules by 3.6% (5°F) according to the EDB hyperbolic tangent fit results; and the 2σ uncertainty of the data scatter bands per the R.G. 1.99/2 trend curve is 25.2°F. From Fig. 3, the trend curve indicates that E900-98 underestimates the ΔT_{30} of HSST01 CMM at a time of 10 EFPY and the average 540°F coolant inlet temperature of CE CMM data. Draft E900-98 underestimated the measured shift for HSST01 data by an average of 12% (15°F) with 2σ uncertainty of 28°F, as shown in the residual plot in Fig. 4.

3.1.2.2 *HSST02 CMM Data*

A comparison of the HSST02 data with the R.G. 1.99/2 and E900-98 trend curves is illustrated in Fig. 5. It was found that R.G. 1.99/2 overpredicted the experimental values for all surveillance capsules by an average of 18% (-19°F); and the 2σ uncertainty of the data scatter bands for R.G. 1.99/2 trend curve is 48°F. In order to determine whether this is capsule-specific (or vendor-specific), the biases are determined separately for the B&W and Westinghouse plants with the result that the average bias for B&W plants is -38% (38°F) and -9.0% (-10°F) for Westinghouse (see Fig. 5). In Fig. 5, two trend curves of draft E900-98 were developed for Westinghouse and B&W's data, respectively. The trend curve for Westinghouse data is estimated with 10 EFPY and with 535°F average coolant inlet temperature of Westinghouse's HSST02 CMM [5]. The trend curve for B&W data is estimated with 10 EFPY and with 556°F mean coolant inlet temperature of B&W's HSST02 CMM [5]. Fig. 5 clearly indicates that E900-98 overestimates the ΔT_{30} of B&W data. A residual study provided estimated biases for B&W and Westinghouse data of -22% (-17°F) and -6.2% (-6°F), respectively, which is demonstrated in Fig 6. These values indicate a tendency for overprediction in the B&W capsules. The most likely reason is the capsule temperature; in the B&W capsules, significant melting of the thermal monitors is consistently reported. Even though this may well be due to transients, as stated in the reports, the average nominal capsule temperature is about 608°F [5] based on melting wire, which is higher than that of the other vendors. Additionally, the B&W plants follow a unique heatup curve for plant operation. The nominal coolant inlet temperature for B&W plants is 556°F. Thus, further modifications may be needed, in plant-specific trend curve determinations from surveillance data if the measured damage is substantially less than predicted. If similar overpredictions are found for the companion CMM, corrections need to be made to the plant-specific trend curve to avoid nonconservative predictions.

From the analysis of data in Table 8, the mean absolute difference between EDB hyperbolic tangent fit results and reported shift data is 22% for B&W and 4% for Westinghouse. Similar to the findings for the A302B CMM, large deviations between measured ΔT_{30} and their Regulatory Guide predictions for the CMM are correlated with similar deviations for the companion materials in the same capsules, for example, B&W's surveillance capsules. Overall, in 13 out of 35 surveillance capsules that contained both the CMM and A533B base metals, the base metals showed the similar deviation from the R.G.

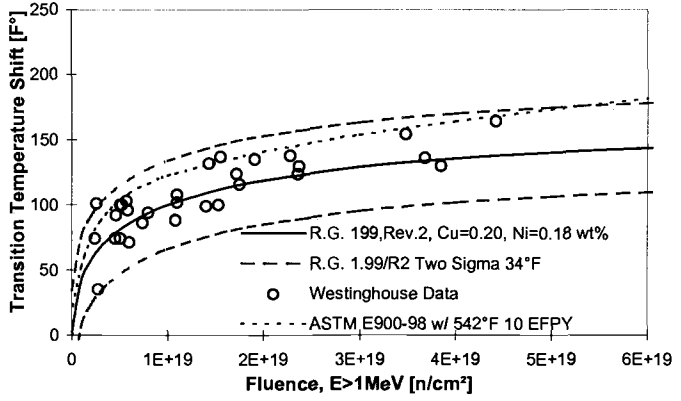


Fig. 1 - *Embrittlement of A302B ASTM CMM relative to R.G. 1.99, Rev.2 , and ASTM E900-98 from PR-EDB hyperbolic tangent fit data.*

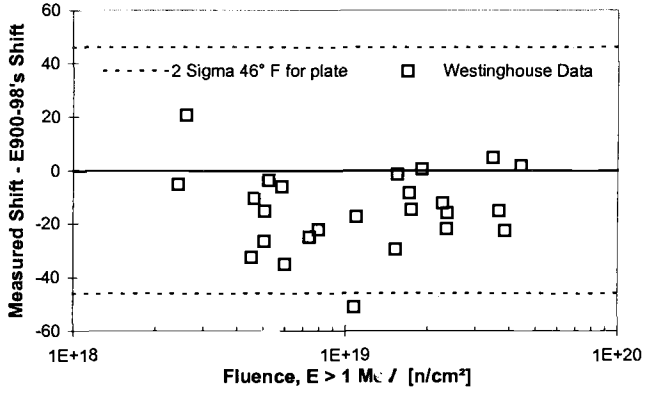


Fig. 2 - *Residual of ASTM E900-98's models per PR-EDB hyperbolic tangent fit data for A302B CMM.*

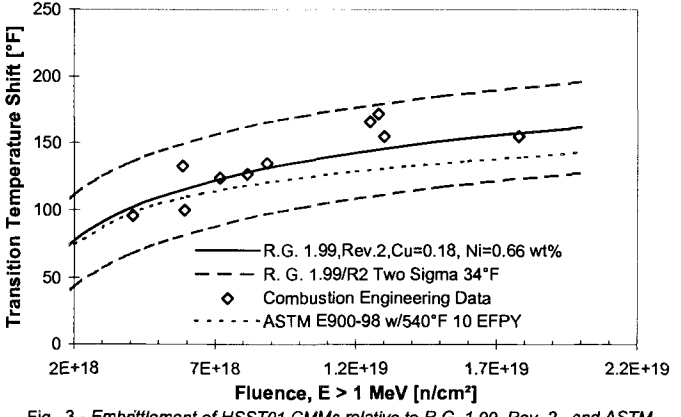


Fig. 3 - *Embrittlement of HSST01 CMMs relative to R.G. 1.99, Rev. 2, and ASTM E900-98 from PR- EDB hyperbolic tangent fit data.*

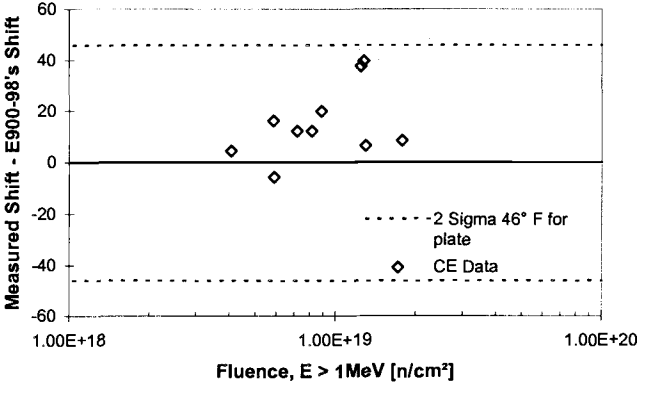


Fig. 4 - *Residual of ASTM E900-98's models per PR-EDB hyperbolic tangent fit data for HSST01 CMM*

1.99/2 predicted values as did the CMM; in 22 out of 31 surveillance capsules that contained both the CMM and weld metals, the weld metals showed a similar deviation from the R.G. 1.99/2 predicted values as did the CMM. The fluctuations for the A533B-1 materials (including plate and weld materials) appear to be the same as those of the A302B material (including plate and weld materials); both have about 50°F 2σ uncertainty per the R.G. 1.99/2 prediction and the biases are -9°F and 6°F for A533B-1 and A302B materials, respectively. These values indicate that R.G. 1.99/2 under-predicted the A302B materials and over predicted the A533B-1 materials. In general, for RPV made of A302B materials, all the CMM shifts are greater than that of A302B plate materials, except those of Indian Point Unit 2. The majority of the CMM shift data are greater than that of the R.G. 1.99/2 prediction, with the exceptions of B&W and GE's CMM data. Forging material shows considerably less sensitivity to radiation embrittlement compared with that of companion CMM, except the Garigliano A336 forging.

3.1.3 *Comparison of the A302B and A533B-1 Plate Materials*

Plate materials in all the RPVs of the U.S. commercial power plants are either A302B or A533B-1, where the older plants were made of A302B materials, and the newer plants were made of A533B-1 materials. The data trend of surveillance plates for the A302B and A533B-1 CMM, from Westinghouse and CE plants, are shown in Fig. 7, and the scatter bands of ΔT_{30} data for both CMM completely overlap. Therefore, the sensitivity of A302B materials to radiation embrittlement appears to be equivalent to that of A533B material. Further investigation was performed using all A302B and A533B-1 Westinghouse plates data that have similar copper contents comparing to that of A302B and A533B CMM, respectively, see Fig. 8. Similar behavior to that of Fig. 7 was observed from Fig. 8.

3.2 *Material Test Reactor Data*

3.2.1 *A302B (ASTM) CMM*

The results of 113 irradiated data sets from the Charpy impact test have been investigated. The trend curve and ΔT_{30} data are shown in Fig. 9. The trend curve for A302B ASTM CMM calculated by R.G. 1.99/2 was used as a reference for ΔT_{30} at 550°F irradiation temperature. The ΔT_{30} data were divided into eight subgroups based on the different irradiation temperature ranges. Fig. 9 clearly shows the effect of irradiation temperature. At the same fluence, the irradiated specimen with a lower irradiation temperature exhibits more radiation embrittlement. At irradiation temperatures less than 300°F, embrittlement develops quite rapidly up to a fluence of about 1.0×10^{19} n/cm². Above 1.0×10^{19} n/cm², embrittlement buildup is less rapid, and some indication of embrittlement saturation appears. At a 550°F irradiation temperature and fluence greater than 1.5×10^{19} n/cm², a clear bias can be detected compared with the predictions of R.G. 1.99/2. R.G. 1.99/2 underpredicts the ΔT_{30} by about 19.3%. This may be a flux effect; higher fluxes are expected to lead to higher values for the ΔT_{30} at high fluences [3, 17, 18].

The specimens irradiated in a material test reactor normally experience a 1- to 2-orders of magnitude higher flux compared with that of commercial power reactors. However, flux and spectral effects are difficult to separate experimentally. Variations in flux are usually obtained by varying the irradiation position in a reactor or by employing different reactors. These flux changes are invariably accompanied by changes in the neutron spectrum. A clearer picture for ASTM CMM data irradiated at 550°F with fluence greater than 1.5×10^{19} n/cm² is demonstrated in Fig. 10. The power reactor surveillance data are also included in

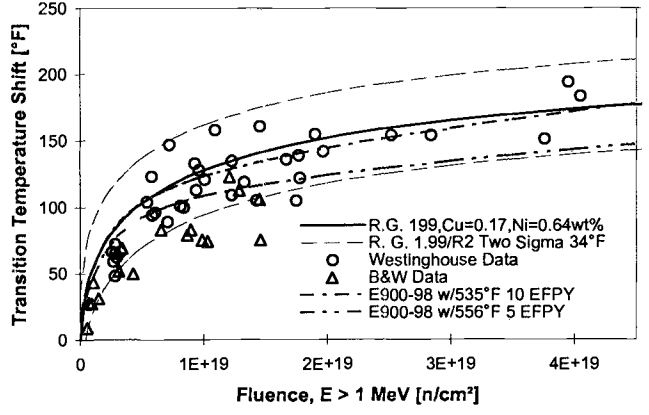


Fig. 5 - *Embrittlement of HSST02 CMMs relative to R.G. 1.99/R2, and ASTM E900-98. Significant bias toward overprediction of the Babcock and Wilcox data.*

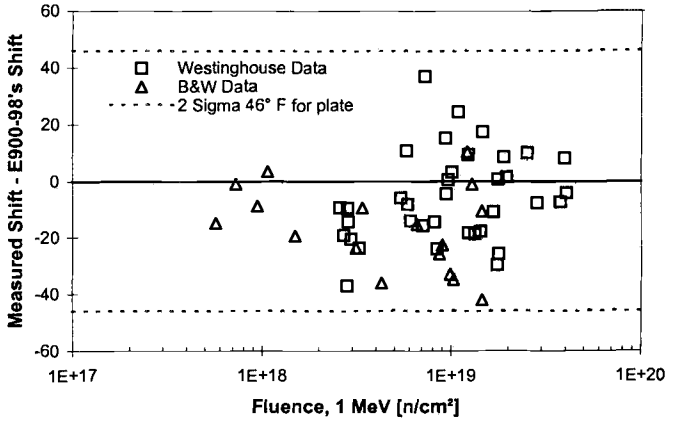


Fig. 6 - *Residual of ASTM E900-98 models per PR-EDB hyperbolic tangent fit data for HSST02 CMM.*

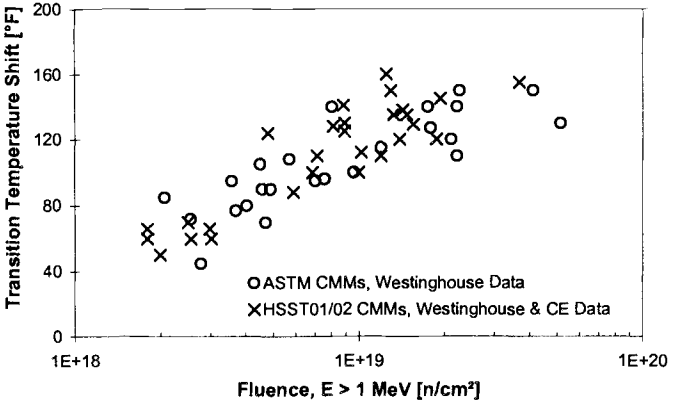


Fig. 7- *Embrittlement of ASTM CMM, HSST01 and HSST02 CMMs, PR-EDB reported data.*

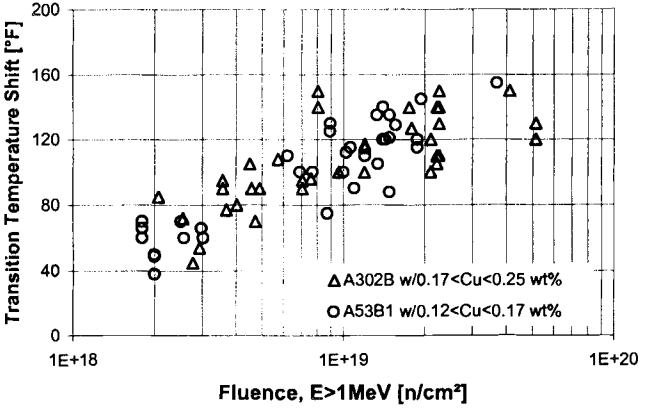


Fig. 8 - *Embrittlement of A302B and A533B1 plates from PR-EDB, Westinghouse data.*

the figure; the average flux for these data is 1.55×10^{11} n/cm^2·s. This shows that R.G. 1.99/2 under-predicted the ΔT_{30} for ASTM CMM data with higher fluence for power reactor data also. In Fig. 10, test reactor data were further subdivided into two subgroups for flux less than 1.1×10^{11} n/cm^2·s and fluxes greater than 2.5×10^{11} n/cm^2·s, respectively. From Fig. 10, it appears that the ΔT_{30} for lower fluxes formed a lower bound for the test reactor data. This may indicate that the flux effect or the combined effect of flux and spectral effect do exist in the test reactor data. In order to further investigate this issue, the test reactor data plotted in Fig. 10 were subdivided into three subgroups, namely, test reactor data irradiated in-core position, test reactor data irradiated at core-edge position, and test reactor data from the simulated surveillance and through-wall specimen capsules irradiated at Oak Ridge Research Reactor Pool Side Facility (ORRPSF) [19]. The data were plotted in Fig. 11. The ORRPSF data on Fig. 11 were not from the in-core positions, two ΔT_{30} data were from simulated surveillance capsule (SSC) positions, one ΔT_{30} data from wall surface (0T) capsule position, and one from a quarter thickness wall (1/4T) capsule position. The two SCC data (which have higher fluxes) show larger ΔT_{30} compared with that of 0T and 1/4T data. The effect of the spectral difference between the SSC and 1/4T positions is negligible for ORRPSF experiments. Thus the flux effect may be supported from the ORRPSF data.

Three of the ΔT_{30} data in Fig. 11 have a fluence of about 5.4×10^{19} n/cm^2: two were from ORRPSF data, and one was a test reactor data irradiated in an in-core position with the flux of about 4×10^{12} n/cm^2·s. The test reactor data at in-core position gave the largest ΔT_{30}; however, its flux was less than that of ORRPSF data at the SCC position, which has 6.95×10^{12} n/cm^2·s flux. A possible cause for this situation may be the different physical locations of the irradiated specimens in the test reactors; in this case, one was at the in-core position and one was at the out-of-core position. There is a difference in neutron energy spectrum between the in-core and out-of-core positions. This example may imply that differences due to the combined effect of the flux and spectral effects at in-core positions are greater than that induced by the flux effect alone for ORRPSF data from the out-of-core position.

3.2.2 *A533B-1 (HSST01) CMM*

The results of 24 irradiated Charpy sets, where 22 sets were irradiated in the Oak Ridge Research Reactor, have been investigated. The results show a strong dependence of the unirradiated T_{30} on specimen location in the original parent plate; for example, the lowest T_{30} is from the specimen position near the surface (0T) of the parent plate. The ΔT_{30} data also show a similar dependence on the specimen position. Irradiated specimens originally located near the surface of the parent plate appear to be the least sensitive to radiation embrittlement. This specimen position effect on transition temperature shift is demonstrated in Fig. 12, where the ΔT_{30} of the 0T specimens are identified by solid symbols.

3.2.3 *A533B-1 (HSST02) CMM*

The results of 21 irradiated Charpy sets have been investigated. The R.G. 1.99/2 prediction for the HSST02 plate is used as the trend curve for the 550°F irradiation temperature. The trend curve and reported ΔT_{30} data are shown in Fig. 13, where the reported ΔT_{30} data were divided into four subgroups for different ranges of irradiation temperatures. The data trend shows the strong influence of irradiation temperature on ΔT_{30}. The ΔT_{30} data irradiated at 572°F and 752°F are from the German VDE experiments [7], and the test specimens were exposed at a high flux of about 2.3×10^{13} n/cm^2·s. The VDE HSST02 CMM has reported copper content as 0.12 wt %. Thus the VDE ΔT_{30} data were normalized to a copper content of 0.17 wt % in Fig. 13. The data trend of the normalized VDE data irradiated

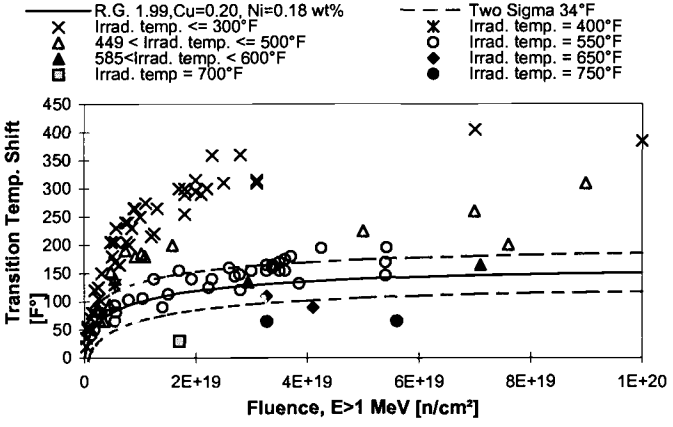


Fig. 9 - *Embrittlement of A302B ASTM CMM relative to R.G. 1.99, Rev. 2, from TR-EDB.*

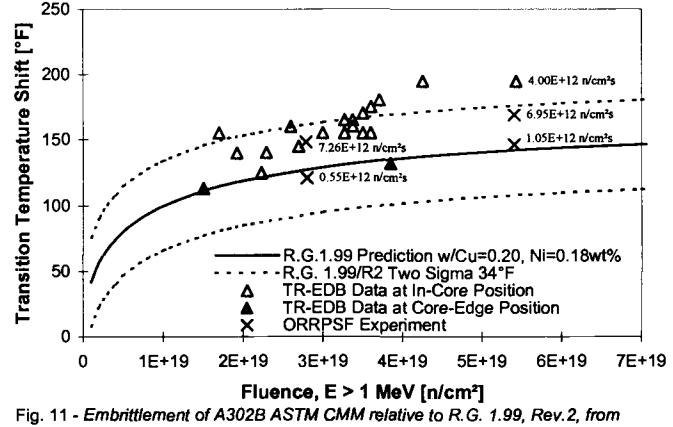


Fig. 11 - *Embrittlement of A302B ASTM CMM relative to R.G. 1.99, Rev.2, from TR-EDB for fluence>1.5E+19 n/cm² irradiated at 550°F.*

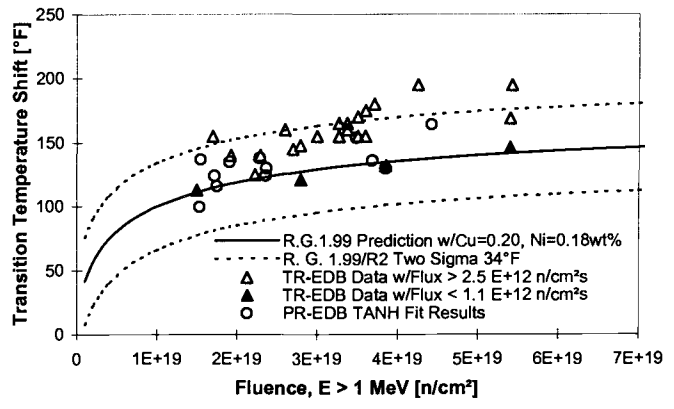


Fig. 10 - *Embrittlement of A302B ASTM CMM irradiated at 550°F relative to R.G. 1.99 Rev. 2 from both TR and PR-EDB for fluence >1.5E+19 n/cm².*

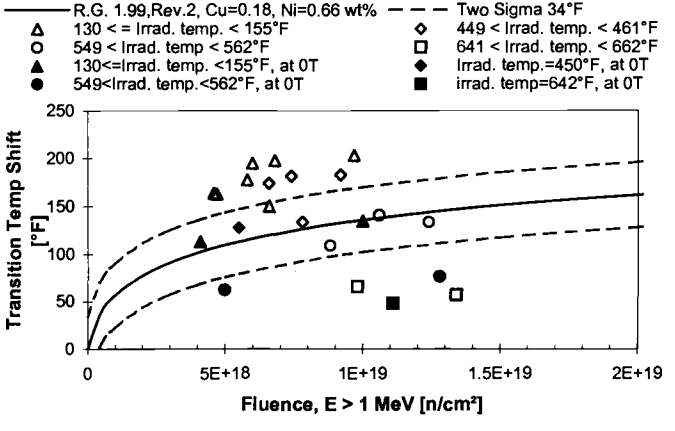


Fig. 12 - *Embrittlement of HSST01 CMM relative to R.G. 1.99, TR-EDB tangent fit data.*

at 572°F seems to be consistent with the conclusion drawn on the flux effect from ASTM CMM data irradiated at 550°F, and a higher irradiation temperature of the VDE experiment at 572°F seems to delay the incubation time of flux effect at higher fluence. This may imply that the flux effect strongly depends on neutron fluence, irradiation temperature, and material chemical composition. There are indications that a higher flux may lead to higher shifts at relatively high fluence, depending on copper content [20].

3.2.4 *A533B-1 (HSST03) CMM*

The results of 39 irradiated Charpy sets have been investigated. The trend curve and ΔT_{30} data are illustrated in Fig. 14. The value predicted by R.G. 1.99/2 for HSST03 was used as a reference curve for ΔT_{30} at the 550°F irradiation temperature. The ΔT_{30} data were divided into five subgroups, based on four ranges of irradiation temperatures and two ranges of flux. Figure 14 clearly shows the irradiation temperature effect, that is a specimen irradiated at a lower temperature will exhibit more radiation embrittlement. At a 550°F irradiation temperature, a clear bias can be detected, compared with the trend curve for HSST03 CMM; that is, R.G. 1.99/2 underpredicted the ΔT_{30} for fluences greater than 2.4×10^{19} n/cm^2 and over predicted the ΔT_{30} for fluences less than 2.4×10^{19} n/cm^2, especially for flux greater than 2.0×10^{12} n/cm^2·s. This may be a flux effect; higher fluxes are expected to lead to higher values for the ΔT_{30} at relatively high fluences and lower values for the ΔT_{30} at relatively low fluences. In order to have a better picture for flux effect on the CMM data irradiated at 550°F, an additional plot was generated for the trend curve of HSST03 CMM with shift data irradiated at 550°F (see Fig. 15), where the ORRPSF and other test reactor data were identified with different symbols.

3.3 *G.E. A302B Reference Material*

Specimens made from Humbolt pressure vessel A302B steel, which is identified as SHM3 material in EDB, were irradiated in several other G.E. plants to serve as an aid in data correlation among BWRs. Residuals obtained from the R.G. 1.99/2 and draft E900-98 were evaluated and shown in Fig. 16. Both of the above embrittlement models overestimated the transition temperature shift for SHM3 CMM irradiated in a BWR environment.

4 Conclusions

The results from the surveillance capsules show that the trend curves for the A302B (ASTM) and A533B (HSST) CMM closely follow the models of the R.G. 1.99/2 and draft E900-98. Significant scatter is noted in the data, some of which may be attributed to variations from one specimen set to another. The major contributions to the uncertainty of the R.G. 1.99/2 and draft E900-98 prediction models and the overall data scatter are from mechanical test results, chemical analysis, irradiation environments, fluence evaluation, and inhomogeneous material properties. The prediction models can be further improved, if the above-mentioned error sources are controlled. Thus properly documented information on mechanical testing procedures, material properties and material history, irradiation environments, reactor power-time history, and neutronic analysis are vital for the development of an embrittlement model. For example, information as to the exact location of the test specimens within the parent material should be provided.

4.1 *Data Fitting Procedure*

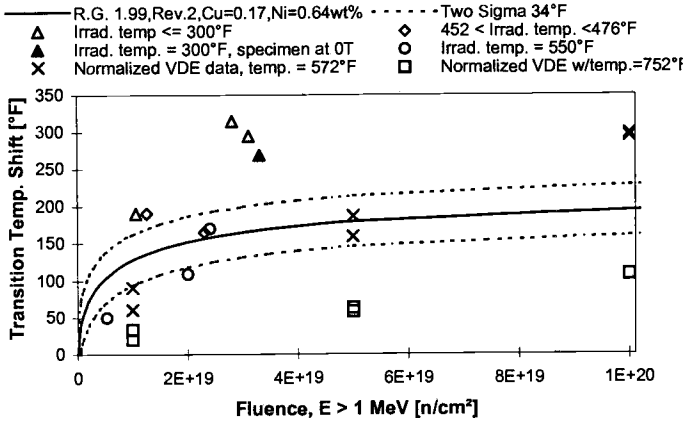


Fig. 13 - *Embrittlement of HSST02 CMM relative to R.G. 1.99, Rev.2, TR-EDB data.*

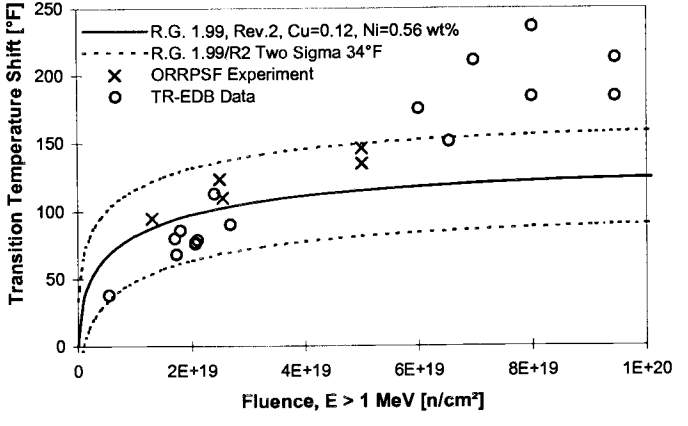


Fig. 15 - *Embrittlement of HSST03 CMM at 550°F relative to R.G. 1.99/R2, TR-EDB data.*

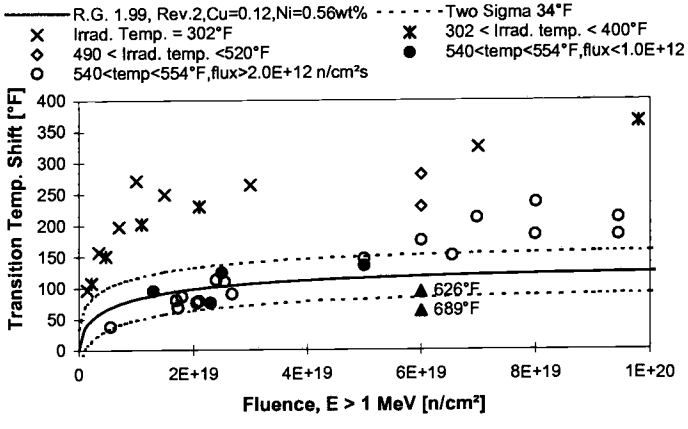


Fig. 14 - *Embrittlement of HSST03 CMM relative to R.G. 1.99,Rev.2, TR-EDB data.*

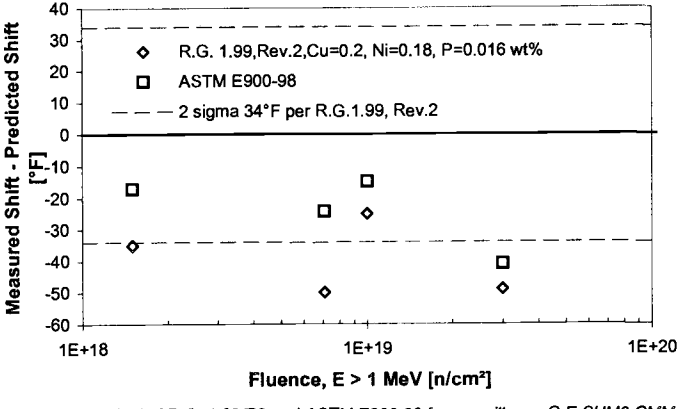


Fig. 16 - *Residual of R.G. 1.99/R2 and ASTM E900-98 for surveillance G.E.SHM3 CMM, where two accelerated data at near core position were omitted from the plot.*

In this paper, the data fitting procedure was also demonstrated to be another independent source contributing to the uncertainty. For example, the mean absolute difference between EDB hyperbolic tangent fit results and reported ΔT_{30} for B&W data can be up to 22%. Thus a unified data-fitting procedure is essential to generate consistent results among different laboratories. Furthermore, in order to minimize the impact of material inhomogeneity on the Charpy curve fitting, a revised fitting procedure may need to be developed that accounts for variables such as specimen chemical compositions in addition to impact energy and test temperature.

4.2 *Irradiation Temperature Effect*

For surveillance data, significant deviations of the measured shift from the trend curve (i.e., more or less than 34°F for plate materials) should be considered as a warning flag pointing to a possible anomalous capsule environment. The most likely reason for deviations from the trend curve is the capsule temperature; fluence and flux can be determined fairly accurately, and possible effects from these sources are relatively small in a power reactor environment. A quantitative relation between irradiation temperature and ΔT_{30} has been established in the past [21], based on the nominal capsule temperature determined by the melt wires loaded in the irradiation capsule. The results show that the weld materials are the most sensitive and the forging materials are the least sensitive to the irradiation temperature. However, on the issue regarding irradiation temperature for the surveillance specimens, a more thorough investigation needs to be done based on detailed neutronic and thermal analysis for specific capsule and specimen loading configuration. These effects must be considered if material- and reactor-specific trend curves are established.

Currently, draft E900-98 incorporates the coolant inlet temperature into embrittlement model to simulate the irradiation temperature for pressurized light-water reactor. However, Figs 5-6 demonstrate a large bias can still be identified for surveillance data from a higher irradiation temperature environment, and the bias is similar to that of R.G. 1.99/2. This may indicate that the coolant inlet temperature is not equivalent to the irradiation temperature experienced by the surveillance specimens. Based on the irradiation temperature studies [22,23], approximate calculations of the temperature increase due to gamma heating in a surveillance capsule were performed for the two-loop Westinghouse plant. The capsule was located in the downcomer and was mounted on the outer side of the thermal shield. The gamma-induced heat source obtained from the calculated gamma field was ~0.117 W/cm^3 in the capsule. The capsule had a square cross-section (4.3 cm × 4.3 cm). The maximum increase of the temperature of the specimens occurred at the center of the capsule and was calculated to be ~0.6°C, if specimens were in good thermal contact with the surveillance capsule. In the case where an air gap was assumed between the capsule and the specimens, the increases in the temperature at the center were ~3°C, 12°C, and 25°C for gap thickness of 0.1 mm, 0.5 mm and 1.0 mm, respectively. Note that it was assumed that the gap completely separates the specimens from the capsule (e.g., there is gap between the capsule and the specimens on all sides of the specimens), which is certainly the most severe case.

Temperature monitors (melting wires) within the surveillance capsules give only the upper bound and, in the case of melting, do not indicate whether the high temperature was transient or sustained. Moreover, an even greater uncertainty for capsule temperature exists for the surveillance capsules that are without thermal monitors. Thus, on the issue regarding irradiation temperature for the surveillance specimens, a more thorough investigation is needed, based on detailed neutronic, thermal, and mechanical analysis for a specific capsule

configuration under the specific service environment. A more precise estimate of the heat transfer across the interface between the container and the specimen, with or without gap, is needed. This will require accurate estimates of the contact pressure distribution, radiation heat transfer coefficients, gas conditions, and the size of the gap for a specific specimen/container design and for specific operating conditions.

4.3 *Flux Effect*

There is some evidence for a flux effect in the CMM data irradiated in test reactors. The existence of a flux effect has important implications for the U.S. commercial power industries, since accelerated locations have almost invariably been used in RPV surveillance programs. For example, the GE surveillance data have a large range of flux, from 1.8×10^8 to 4.6×10^{12} n/cm^2·s, whereas for B&W data it ranges from 2.4×10^{10} to 1.54×10^{11} n/cm^2·s, for CE data, 2.3×10^{10} to 6.2×10^{11} n/cm^2·s, and for Westinghouse data (not including Yankee Rowe data) 1.6×10^{10} to 4.8×10^{11} n/cm^2·s. Thus, the implication of a flux effect in a nuclear commercial power reactor environment deserves special attention, especially for GE BWR surveillance data. If the fluence-rate effect is significant over the range of interest, use of surveillance data with a high lead factor may result in a conservative or non-conservative prediction of vessel embrittlement, depending on the particular fluence range. Thus, depending on the lead factor involved, it may be prudent to apply some correction to the surveillance data in application to the prediction of vessel embrittlement. Based on the available data, however, definition of a "high" lead factor and the development of such correction factors are not yet practicable. Additional data from the CMMs irradiated over a range of flux are needed to establish the flux effects with confidence.

4.4 *Embrittlement Modeling*

All residual defects created from displacive irradiation can contribute to the microstructural evolution that produces the final macroscopic material property changes. The nature of the radiation-induced defect structure is a function of neutron energy, neutron flux, exposure temperature, and unirradiated microstructure. Thus, temperature, neutron flux, neutron energy spectrum, and material composition and processing history all contribute to radiation embrittlement. Insufficient consideration of these conditions may result in misleading correlation and thus incorrect prediction of material state and material behavior, as well as incorrect end-of-life determinations. It was proposed that one way to tackle the problem of dealing with insufficient information, and the lack of complete damage mechanism modeling is to classify the embrittlement data into groups that have similar radiation environments. An Embrittlement study was done based on this criteria [24], and more realistic embrittlement models were developed which exhibited smaller residuals compared to that of R.G. 1.99/2 and draft E900-98.

This investigation shows that results from CMMs can be used to detect anomalies in the surveillance capsule irradiation. Nominal values for the ΔT_{30} in the CMM for a given fluence can be determined from R.G. 1.99/2. Any significant deviation from the trend curve should be investigated as to the possible causes. The exact location of the test samples within the plate should be ascertained, if possible, and variations in the baseline values between samples should be considered. If material inhomogeneity is a suspect for a particular test set, detailed chemical compositions from the broken specimens are needed to generate a more accurate embrittlement index. Influence of irradiation temperature may be inferred from the results of the CMM and should be considered whenever material- and reactor-specific trend

curves are to be established.

Acknowledgments

The author is grateful to Dr. R. K. Nanstad, Dr. I. Remec, and Dr. R. E. Stoller for reviewing this paper and providing helpful suggestions. Research sponsored jointly by the Nuclear Regulatory Commission under Interagency Agreement DOE 1886-8616-4W, and the U.S. Department of Energy, under contract DE-AC05-96OR22464 with Lockheed Martin Energy Research.

5 References

[1] Mansur, L. K., "Mechanisms and Kinetics of Radiation Effects in Metals and Alloys," *Kinetics of Nohomogeneous Processes*, ed. by Gorden R. Freeman, 1987.

[2] Odette, G. R., Lombrozo, P. M., and Wullaert, R. A., "Relationship Between Irradiation Hardening and Embrittlement of Pressure Vessel Steels," *Effects of Radiation on Materials, Twelfth International Symposium, ASTM STP 870*, Eds. F. A. Garner and J. S. Perrin, American Society for Testing and Materials, Philadelphia, 1985, pp. 840-860.

[3] Lucas, G. E., Odette, G. R., Lombrozo, P. M., and Sheckherd, J. W., "Effects of Composition, Microstructure, and Temperature on Irradiation Harding of Pressure Vessel Steels," *Effects of Radiation on Materials, Twelfth International Symposium, ASTM STP 870*, Eds. A. Garner, and J. Perrin, American Society for Testing and Materials, Philadelphia, 1985, pp. 900-930.

[4] Shah, V. N., Server, W. L., Odette, G. R., and Kumar, A. S., "Residual Life Assessment of Light Water Reactor Pressure Vessels, "*Effects of Radiation on Materials, ASTM STP 1011*, American Society for Testing and Materials, Philadelphia, 1989, pp. 161-175.

[5] Wang, J. A., "Embrittlement Data Base, version 1," NUREG/CR-6506 (ORNL/TM-13327), U.S. Nuclear Regulatory Commission, August 1997.

[6] Stallmann, F. W., Wang, J. A., Kam, F. B. K., and Taylor, B. J., "PR-EDB: Power Reactor Embrittlement Data Base, Version 2," NUREG/CR-4816 (ORNL/TM-10328/R2), U.S. NRC, 1994.

[7] Stallmann, F. W., Wang, J. A., and Kam, F. B. K., "TR-EDB: Test Reactor Embrittlement Data Base, Version 1," NUREG/CR-6076 (ORNL/ TM-12415), U.S. Nuclear Regulatory Commission, 1994.

[8] Oldfield, W., "Fitting Curves to Toughness Data," *ASTM J. Testing and Evaluation* Vol. 7 No. 6, November 1979.

[9] Pachur, D., "Radiation Annealing Mechanisms of Low-Alloy Reactor Pressure Vessel Steels Dependent on Irradiation Temperature and Neutron Fluence," *Nucl. Technol.* Vol. 59, 1982, pp. 463-475.

[10] Hofer, G., Hung, C. C., Guenews, U., "A Mathematical Function for Describing the Results of Charpy Impact Tests," *Zeitscrift Fuer Wekstoffenhnick J. Fo Mat. Tech.* 8(4), April 1977, pp. 109-111.

[11] . Hood, W. G., "Polynomial Curve Fitter," *Byte*, June 1987, pp. 155.

[12] Nanstad, R. K., Haggag, F. M., McCabe, D. E., Iskander, S. K., Bowman, K. O., and Menke, B. M., "Irradiation Effects on Fracture Toughness of two High Copper Submerged-Arc Welds, HSSI Series 5," NUREG/CR-5913, ORNL/TM-12156, U.S.

Nuclear Regulatory Commission, October 1992.

[13] Stallmann, F. W., "Theory and Practice of General Adjustment and Model Fitting Procedures," NUREG/CR-2222 (ORNL/TM-7896), U.S. Nuclear Regulatory Commission, December 1981.

[14] Wang, J. A., "Analysis of the Irradiated Data for A302B and A533B Correlation Monitor Materials," NUREG/CR-6413 (ORNL/TM-13133), U.S. Nuclear Regulatory Commission, April 1996.

[15] Randall, P. N., "Basis for Revision 2 of the U.S. Nuclear Regulatory Commission Regulatory Guide 199," *Radiation Embrittlement of Nuclear Reactor Pressure Vessel Steels: An International Review (Second Volume), ASTM STP 909*, L.E. Steele, Ed., 1986, pp. 149-162.

[16] Stallmann, F. W., "Analysis of the A302B and A533B Standard Reference Materials in Surveillance Capsules of Commercial Power Reactors," NUREG/CR-4947 (ORNL/TM-10459), U.S. Nuclear Regulatory Commission, January 1988.

[17] McElroy, W. N., Gold, R., Simons, R. L., and Roberts, J. H., "Trend Curve Data Development and Testing," *Influence of Radiation on Material Properties: 13th International Symposium, ASTM STP 956,* F. A. Garner, C. H. Henager, and N. Igata, Eds., American Society for Testing and Materials, Philadelphia, 1987, pp. 505-534.

[18] Simons, R. L., "Damage Rate and Spectrum Effects in Ferritic Steel ΔNDTT Data," *Influence of Radiation on Material Properties: 13th Inter-national Symposium, ASTM STP 956,* F. A. Garner, C. H. Henager, and N. Igata, Eds., American Society for Testing and Materials, 1987, pp. 535-551.

[19] Hawthorne, J. R., Menke, B. K., "Light Water Reactor Pressure Vessel Surveillance Dosimetry Improvement Program: Postirradiation Notch Ductility and Tensile Strength Determinations for PSF Simulated Surveillance and Through-Wall Specimen Capsules," NUREG/CR-3295 (MEA-2017), U.S. Nuclear Regulatory Commission, April 1984.

[20] Odette, G. R., Mader, E. V., Lucas, G. E., Phythian, W. J., English, C. A., "The Effect of Flux on the Irradiation Hardening of Pressure Vessel Steels," *Effects of Radiation on Materials: 16th Inter-national Symposium, ASTM STP 1175*, A. S. Kumar, D. S. Gelles, R. K. Nanstad, and E. A. Litle, Eds., American Society for Testing and Materials, Philadelphia, 1993, pp. 373-393.

[21] Wang, J. A., Kam, F. B. K., Stallmann, F. W., The Embrittlement Data Base (EDB) and Its Applications," *Effects of Radiation on Materials: 17th Symposium, ASTM STP 1270*, David S. Gelles, Randy K. Nanstad, Arvind S. Kumar, and Edward A. Little, Editors, American Society for Testing and Materials, Philadelphia, 1996.

[22] Private Communications, Dr. Remec, I., Oak Ridge National Laboratory, Computational Physics and Engineering Division, Oak Ridge, Tennessee.

[23] Siman-Tov, I. I., "Heat Transfer Analysis of the LWR Pressure Vessel Steel Irradiation Capsules in the Oak Ridge Research Reactor-Pressure Vessel Benchmark Facility," NRUEG/CR-2053 (ORNL/TM-427), U.S. Nuclear Regulatory Commission, April 1982.

[24] Wang, J. A., "Development of Embrittlement Prediction Models for U.S. Power Reactors and The Impact of the Heat-Affected Zone to Thermal Annealing," *Effects of Radiation on Materials: 18th International Symposium, ASTM STP 1325*, R. K. Nanstad, M. L. Hamilton, F. A. Garner, and A. S. Kumar, Eds., American Society for Testing and Materials, Philadelphia, 1998, in press.

M. Brumovsky,[1] M. Falcnik,[1] M. Kytka,[1] J. Malek,[1] and P. Novosad[1]

Comparison of Static and Dynamic Transition Temperature Shifts in VVER Reactor Pressure Vessel Steels

Reference: Brumovsky, M., Falcnik, M., Kytka, M., Malek, J., and Novosad, P., **"Comparison of Static and Dynamic Transition Temperature Shifts in VVER Reactor Pressure Vessel Steels,"** *Effects of Radiation on Materials: 19th International Symposium, ASTM STP 1366,* M. L. Hamilton, A. S. Kumar, S. T. Rosinski, and M. L. Grossbeck, Eds., American Society for Testing and Materials, West Conshohocken, PA, 2000.

Abstract: This paper summarizes results from surveillance specimen programs of VVER-440/V-213C type reactors. Transition temperature shifts, induced by irradiation, and determined from impact Charpy V-notch toughness as well as from static fracture toughness tests on pre-cracked Charpy size specimens, (COD) are compared. Two methods have been used for determination of static fracture toughness shifts - standard COD type specimens from standard surveillance programs and reconstituted COD type specimens from broken halves of Charpy V-notch specimens; thus identical irradiation conditions have been assured. Results obtained are discussed from the point of view of irradiation conditions as well as of different type of testing. Additional tests have been performed on different heats from VVER-1000 type steel, where Charpy V-notch impact and static as well as dynamic fracture toughness tests have been performed to determine transition temperature shifts. Results are discussed and show that transition temperature shifts from static tests are, generally, larger than those from dynamic tests.

Keywords: reactor pressure vessel, surveillance specimen programs, static fracture toughness, transition temperature shifts, Charpy notch toughness, specimen reconstitution, VVER steels

Introduction

This integrity assessment of RPVs is connected with a *principal paradox* : the whole assessment is based on fracture mechanics, i.e., on some sort of fracture toughness while practically all material testing is based on Charpy impact notch toughness. These Charpy tests are commonly performed not only in initial state of RPV materials, but also, in degraded state of material during RPVs operation. The paradox is clear from the very beginning, but it has a very historical background: Charpy impact

[1]Research Staff, Division of Integrity and Materials, Nuclear Research Institute Řež plc, 250 68 Řež near Prague, Czech Republic.

Copyright© 2000 by ASTM International www.astm.org

tests are old and commonly used as a "technological" type of tests for fast characterization of materials, and also for acceptance tests of materials and components. These tests are much older than fracture mechanics; thus a very large database of material properties including effects of different variables exists for different type of materials. At the same time, these tests are relatively cheap, at least in comparison with fracture mechanics tests, require a small quantity of material, and a very simple testing machine. Finally, these tests have been fully standardized for a long time while fracture mechanics test methods are still under development.
Main differences of both types of testing are seen from the following comparison:

	Charpy impact	*fracture mechanics*
initial concentrator	notch	fatigue crack
loading rate and measured values	dynamical/impact energy necessary for crack initiation, propagation and arrest	K_{IC} - quasistatic initiation of crack propagation K_{Id} - dynamic initiation of crack propagation K_{IA} - arrest of running crack

The most important part of linear elastic fracture mechanics evaluation is using static fracture toughness, K_{IC} (or K_{JC}), which characterizes conditions for an unstable propagation of an initial fatigue crack. Charpy impact test is dynamic and measures energy, which is necessary for conversion of a notch into crack, then to crack propagation and in some cases also to crack arrest and final failure. Thus, fracture mode must be brittle/semi-brittle (cleavage) for determination of K_{IC} (or K_{JC}) values. Both cleavage as well as ductile modes can be present during Charpy tests. Due to the sensitivity of ferritic type materials on loading rate, there are also differences between static (K_{IC}) and dynamic fracture toughness (K_{Id} , K_{IA}) dependencies. The most important common property is a transition behavior of their temperature dependencies. Some intercorrelation between both these type of properties can be made and is generally used, even though both functions have different shapes.

To overcome the paradox between testing procedures and calculation approach, some normalization of fracture toughness temperature dependence is usually performed using so-called ***"reference temperature"*** which is determined on the basis of acceptance type of tests. ASME and similar PWR codes require determination of RT_{NDT} temperature, based on Nil Ductility Temperature, T_{NDT} , as a result of Drop Weight Test (DWT) and additional Charpy impact tests (according to ASME Pressure Vessel and Boiler Code, Section III, Division 1, Edition 1995[2]). On the other side, VVER Code for Strength Analysis of Components and Piping in NPPs, PNAE G-7-002-86,

Energoatomizdat Moscow (1989) [1] defined Critical Temperature of Brittleness, T_{K0} , based only from Charpy impact tests (according to standard ISO/DIN 1248-76 Steel - Charpy impact test, V-notch [3]).

Comparison of both criteria are given in the following Table 1:

Table 1. *Comparison of transition temperatures definition*

<table>
<tr><th colspan="3">VVER Code [1]</th><th>ASME Code [2]</th></tr>
<tr><td colspan="3">Critical Temperature of Brittleness - T_{KO}</td><td>Reference Nil Ductility Temperature - RT_{NDT}</td></tr>
<tr><td colspan="3">Required critical mean Charpy energy value depends on room temperature yield strength. Requirements at temperature equal to $T=T_{KO}$:</td><td></td></tr>
<tr><td>Rp [MPa]</td><td>$(KCV)_C$ [$J.cm^{-2}$]</td><td>$(KV)_C$ [$J.cm^{-2}$]</td><td rowspan="5">Required critical Charpy energy value at temperature $T = T_{NDT}$:
$KCV \geq (KCV)_C = 50\ J.cm^{-2}$
$(KCV)_{min} \geq 0.7\ (KCV)_C$
$(KV)_{min} \geq 28\ J.cm^{-2}$</td></tr>
<tr><td>< 300</td><td>30</td><td>24</td></tr>
<tr><td>300-400</td><td>40</td><td>32</td></tr>
<tr><td>400-550</td><td>50</td><td>40</td></tr>
<tr><td>550-700</td><td>60</td><td>48</td></tr>
<tr><td colspan="3">Requirements at temperature
$T = T_{KO} + 30\ ^{o}C$:
$KCV_{mean} \geq 1.5\ (KCV)C=75\ J.cm^{-2}$
$(KCV)_{min} \geq 52.2$ J.cm-2
$(S.F.A)_{min} \geq 50\%$(fibrous fracture, %)
or
$KV_{mean} \geq 1.5\ (KV)_C = 60\ J.cm^{-2}$
$(KV)_{min} \geq 43$ J</td><td>Requirements at temperature
$T = T_{NDT} + 300C$:
$(KCV)_{min} \geq 85$ J.cm-2
$(KV)_{min} \geq 68$ J = 50 ft.lb
$(\Delta B)_{min} \geq 0.91$ mm = 35 mils
(lateral expansion)</td></tr>
</table>

The temperature dependence of fracture toughness values can be expressed in a form:

$$K_{IC},\ K_{Id},\ K_{IA} = A + B\ .\ \exp\ (C.\ T_R\ ) \qquad (1)$$

where A, B, and C are material constants,

and $$T_R = T - TT \quad (2)$$

is a normalized temperature with respect to a reference transition temperature, TT, which can be either RT_{NDT} or T_{k0}.

Definition of both types of reference temperature theoretically excludes a direct application of ASME curves to VVER materials, even though real dependencies are relatively close to each other.

This definition brings some consequences : RPV materials are degraded during operation - by radiation damage, thermal aging and fatigue damage, as the most important mechanisms. All of them result in some changes in material properties, the most important for integrity evaluation is their embrittlement fraction. Embrittlement is expressed by some changes in temperature dependencies, both of Charpy impact as well as fracture toughness : principal change can be described as a shift of the whole curves to high temperatures, but also some changes in their shape are usually observed. Thus, using only one defined transition temperature cannot fully described the process fully. Moreover, due to different type of testing (especially of loading rate), these transition temperature shifts must not be the same for different type of testing, as it is generally suggested in all existed Codes. Even though wide experimental programs are realized in many countries, no final solution has been yet found: it seems, that with a high probability, **transition temperature shifts** from static fracture toughness testing could be larger than from any dynamic type tests - dynamic and arrest fracture toughness on one side and Charpy impact on the other one - see for example Fig. 1.

Current Code describes the effect of operational material degradation by the following equation (in more general form):

$$TT(t) = TT(0) + \Delta T_F + \Delta T_T + \Delta T_N \quad (3)$$

where TT(0) is initial value of transition temperature,
TT(t) is value of transition temperature after time *t* of operation,
ΔT_F is a shift due to radiation embrittlement,
ΔT_T is a shift due to thermal aging,
ΔT_N is a shift due to fatigue damage.

Definition and determination of all these component shifts is given in the following Table 2.

Main differences are seen in two ways - different definitions of transition temperature and difference between number of factors included into calculation. It must be said, that in RPV regions, where radiation embrittlement is a dominant degradation mechanism, the other two mechanisms are negligible. For RPV integrity, beltline region is of the highest importance, thus the exclusion of thermal aging and fatigue damage in ASME Code is understandable.

It is again clearly seen from this table that practically only shifts of Charpy impact temperature dependencies are taken into account. This is supported by the fact that most of the surveillance specimen programs for PWR reactors have no fracture mechanics specimens. This is a tax from the history and time of reactors design.

Table 2. *Comparison of transition temperature shifts definition*

VVER Code [1]	ASME Code [2]
$K_{IC} = f(T_R)$	K_{IR} , $K_{IC} = f(T_R)$
$T_R = T - T_k$ $T_k = T_{k0} + \Delta T_F + \Delta T_T + \Delta T_N$	T_R = T-ART; ART = RT+RTNDT+Δ(see Reg. Guide 1.99 Rev. 2)
irradiation embrittlement: $\Delta T_F = A_F (F.10^{-22})^{1/3}$ A_F = f(Cu, P) for 15Kh2MFA steel = f(Cu, P, Ni) for 15Kh2NMFA steel = upper bound F ≥ 0.5 MeV *source:* accelerated irradiation in experimental reactors	*irradiation embrittlement* RT = f (Cu, Ni, F) = mean value F ≥ 1 MeV *source :* RPV surveillance programs
fatigue damage: $\Delta T_N = 20\ A$; $A = \Sigma$ Ni /Σ [Ni]	*fatigue damage:* not mentioned- independently on usage factor
thermal aging: $\Delta T_T = 0$ for VVER RPV steels	*thermal aging*: not mentioned

Nevertheless, none of the existing codes has any comment of the possibility to take into account such data (from fracture mechanics testing) if they really exist, generic for a given material or specific for a given RPV.

Looking on results from Fig. 1 or similar graphs from other programs, it can be concluded that evaluation of integrity based only on Charpy impact shifts may not be conservative every time.

Experimental Program

Fig. 1 shows some results obtained from tests of a standard surveillance program of VVER-440/V-213C reactor pressure vessels. This program has several peculiarities, mainly:

- specimens are located in containers in a long chain (approx. 2.5 m) and thus some of them (determined for static fracture toughness testing) are located in a steep neutron flux gradient,
- lead factor (ratio between the neutron flux in surveillance specimens location and in the inner RPV wall) of Charpy specimens located in a central part of

chains (adjacent to the center of active core) is very high - 13 for base metals and 18 for weld metals.

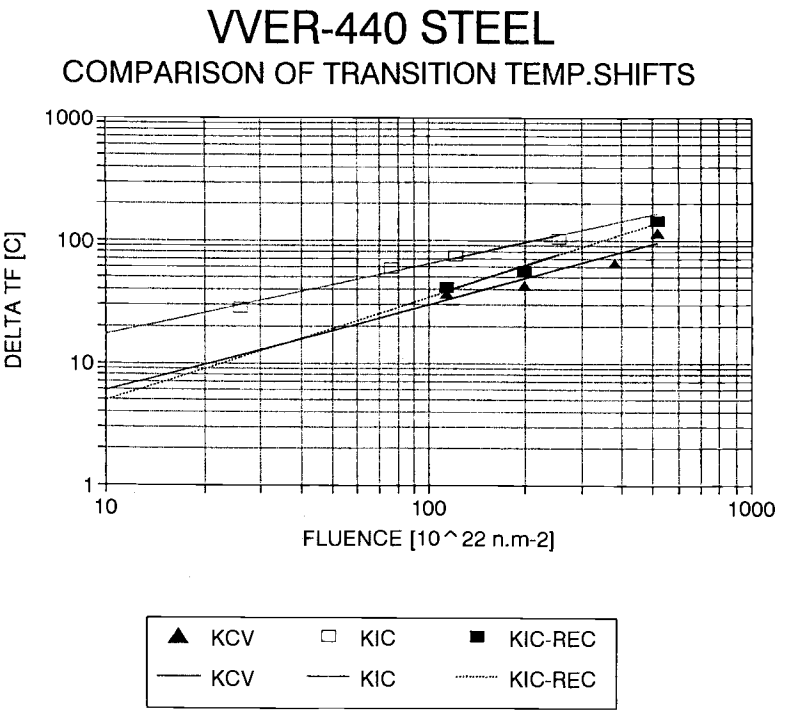


Fig. 1 *Comparison of transition temperature shifts from a standard and re-evaluated surveillance program for one typical VVER-440/V-213C type reactor pressure vessel - base metals*

Direct comparison of transition temperature shifts are thus impossible, as different neutron fluences are obtained.

Such a noncompatibility initiated a re-evaluation of a standard surveillance program : halves of broken Charpy specimens were reconstituted into Charpy pre-cracked specimens and then tested to determine static fracture toughness. Thus, the same specimens (irradiated in one identical condition) are used for both type of testing and comparison of results is quite clear.

Specimens of a standard surveillance programs were manufactured from a steel of 15Kh2MFAA (Cr-Mo-V) type with chemical composition given in the following Table 3.

Table 3. *Chemical composition of surveillance specimens of 15Kh2MFA type steel*

MATERIAL	BASE METAL	WELD METAL
C	0.13	0.031
Mn	0.40	1.13
Si	0.25	0.60
P	0.009-0.012	0.010
S	0.012	0.015
Cr	2.77	1.31
Ni	0.16	0.05
Mo	0.62	0.52
V	0.30	0.19
Cu	0.08-0.10	0.06

These specimens were irradiated up to 5 years (base metals) and 10 years (weld metal) in NPP at temperature equal to 270 °C; their neutron fluences range cover approx. (1 to 6) x 10^{24} n.m^{-2} (neutrons with energies higher than 0.5 MeV; spectral index $F_{1MeV}/F_{0.5MeV} \approx 0.6$).

Second part of the program was concentrated in the steel of VVER-1000/V-320C type reactor pressure vessels - 15Kh2NMFA (Ni-Cr-Mo-V) type. Several laboratory heats were irradiated in the experimental reactor LVR-15 (Nuclear Research Institute) at temperature 288 °C to a neutron fluence equal to 2.6 x 10^{24} n.m^{-2} (neutrons with energies higher than 0.5 MeV). The main reason of this study was to ascertain an effect of different contents of copper and phosphorus in steels, but different type of tests on Charpy size specimens were performed. Their chemical composition if given in Table 4.

Table 4. *Chemical composition of experimental heats of 15Kh2NMFA type steel*

	HEAT 1	HEAT 2	HEAT 3	HEAT 4	HEAT 5	HEAT 6
C	0.15 - 0.16					
Mn	0.48		0.34			
Si	0.17 - 0.21					
P	0.012	0.018	0.015	0.021	0.014	0.021
S	0.010					
Cr	2.06		1.89		2.14	
Ni	1.28					
Mo	0.56					
Cu	0.30		0.52		0.08	
V	0.10					

The following tests were performed and transition temperatures and their shifts determined :

- Charpy V-notch impact (KCV) testing according to ISO standard [3], transition temperature T_{40J} and its shift using tanh curve fitting was determined,

- static fracture toughness (K_{CJ}) testing on pre-cracked Charpy size specimens according to Czech standard Fracture toughness of metals on static loading, CSN in Czech), Prague (1991) [4] (similar to ASTM Standard Test Method for Determination of the Reference Temperature, T_0, for Ferritic Steels in the Transition Range, ASTM E 1921-97 [5] and European ESIS Procedure for Determining the Fracture Toughness Behavior of Materials, ESIS P2-92 [6]), transition temperature $T_{100MPa.m0.5}$ and its shifts using exp curve fitting were determined,
- dynamic fracture toughness (K_{Id}) testing on pre-cracked Charpy size specimens according to Czech standard proposal [7](similar to European ESIS Proposed Standard Methods for Instrumented Pre-cracked Charpy Impact Testing of Steels, Combined K_{Id}, J_{Id} and CTOD Test Methods, ESIS, Draft 6 (1996) [8]), transition temperature $T_{100MPa.m0.5}$ and its shifts using exp curve fitting were determined.

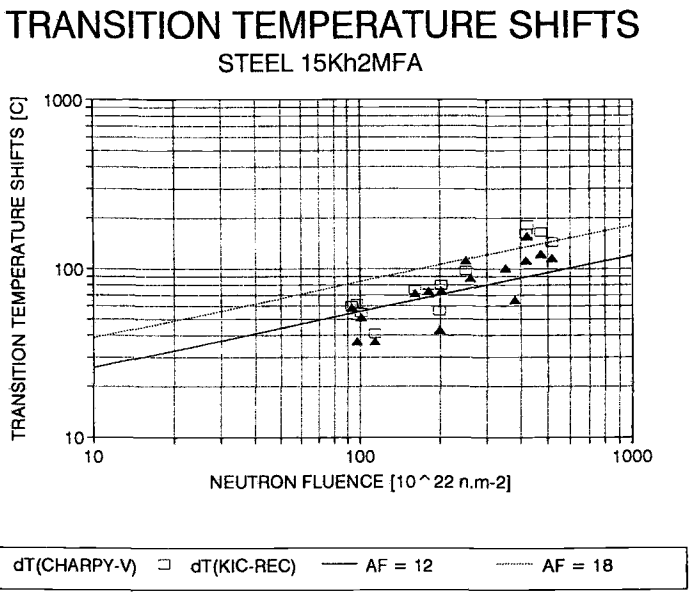


Fig. 2 *Comparison of transition temperature shifts for VVER-440/V-213C type reactor pressure vessels*

Experimental Results and Discussion

First information about different values of transition temperature shifts determined by Charpy impact testing and static fracture toughness values has been obtained only after several years of operation and following testing. The reason is given by the fact that containers with specimens of pre-cracked Charpy type are located in a

steep neutron flux gradient (see Fig. 3), i.e. from base metal in containers Nos. 1-6 (resp. 20-25 from heat-affected zone), and from weld metal in Nos. 17-19 and 37-39, respectively. In these locations, there is a ratio equal up to about 20 in neutron fluxes with respect to the center of active core. Thus, direct comparison of results cannot be made till the time when specimens from different chains (i.e. after different years of irradiation) can be coupled together to reach 12 specimens with a similar or close neutron fluence for one testing curve. Their fluences are much lower than fluences of Charpy impact specimens, as they are located in a maximum of neutron flux in the area adjacent to the center of reactor core. Typical results from both these tests of base metal of one pressure vessel are shown in Fig. 1. It is clearly seen that transition temperature shifts from static fracture toughness tests are much higher than from Charpy impact ones.

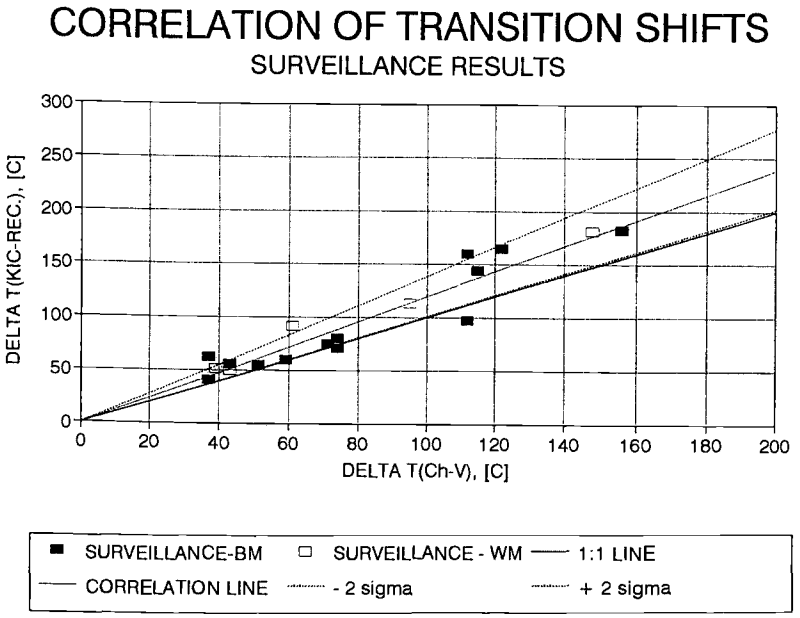


Fig. 3 *Correlation between static fracture toughness and Charpy notch impact toughness transition temperature shifts tested for VVER-440 steels*

This fact has been properly analyzed: re-evaluation of neutron fluences has been also performed. Then, to find out if this effect is given by uncertainties in neutron fluences or by real testing conditions, the decision about use of reconstitution technique was accepted. Broken halves of Charpy impact specimens have been reconstituted using an electron beam welding method. This method was validated according to the ASTM standard [6] and also within the ASTM round robin program. Results obtained are also shown in Fig. 1. Even though differences between both shifts are now closer,

nevertheless, some difference still exist and cannot be neglected. Then, this reconstitution technique has been applied to material of all units tested in NRI and results from base metals are shown in following Fig. 2. There are results from four different heats of 15Kh2MFA steels with a somewhat different chemical composition, thus some scatter of results exists. For comparison with existing codes [1], lines representing maximum design values of shifts, ΔT_F , are also given - coefficient A_F is defined by a formula

$$\Delta T_F = A_F \, . \, (F \, . \, 10^{-22} \,)^{1/3} \tag{3}$$

where F is a neutron fluence with energies larger than 0.5 MeV [$n.m^{-2}$].
It is seen that this formula is applicable to fluences up to about 4×10^{24} $n.m^{-2}$ which is higher than End-of-Life fluence for these reactor pressure vessels.

A comparison of both these transition temperature shifts is shown in Fig. 3, where results from base as well as from weld metals testing are summarized. It is seen that a linear dependence between these two shifts exists, but the following approximate formula has been found :

$$\Delta T_{100MPa.m0.5} \approx 1.2 \; \Delta T_{CHV} \tag{4}$$

This dependence is statistically important and differs from a proportional line 1:1, as even scatter band for 2 σ is higher then this 1:1 line. There is also practically no difference between behavior of base and weld metals.

Fig. 4 shows a dependence of the difference between these two shifts (i.e. ΔT - ΔT_{CHV}) on neutron fluence. Even though a large scatter of results has a relatively low correlation coefficient ($R^2 \cong 0.6$), some tendency of linear dependence can be observed , when maximum values of this difference reach values up to about 50 °C. It must be also stated that up to EOL fluences for these vessels, differences can be defined as close to a scatter of experimental data, as mostly they are lower than 25 °C.

Results from an experimental irradiation program of 15Kh2NMFA type of steel, determined for reactor pressure vessels of VVER-1000/V-320 type reactors, have been also used for this study. Specimens from experimental heats have been irradiated in identical conditions, thus comparison of the results is obvious.

Fig. 5 summarizes comparison of both types of shifts, i.e. from Charpy impact and static fracture toughness tests. Six different heats with different contents of copper and phosphorus were irradiated, thus different shifts have been found even for one irradiation fluence. Again, linear dependence between these two shifts is found, but with a higher proportional coefficient :

$$\Delta T_{100MPa.m0.5} \approx 1.4 \; \Delta T_{CHV} \tag{5}$$

All results from both materials are summarized in Fig. 6 where existence of larger shifts from static fracture toughness tests in comparison with Charpy impact ones are clearly seen. It is also clearly seen that shifts from 15Kh2NMFA type steel are higher than from 15Kh2MFA type of material. The reason of such a different behavior cannot be found from these limited data, but one possible explanation could be in different tensile properties - yield strength of steel 15Kh2NMFA is higher (approx. 520 MPa) than of 15Kh2MFA grade (440 MPa).

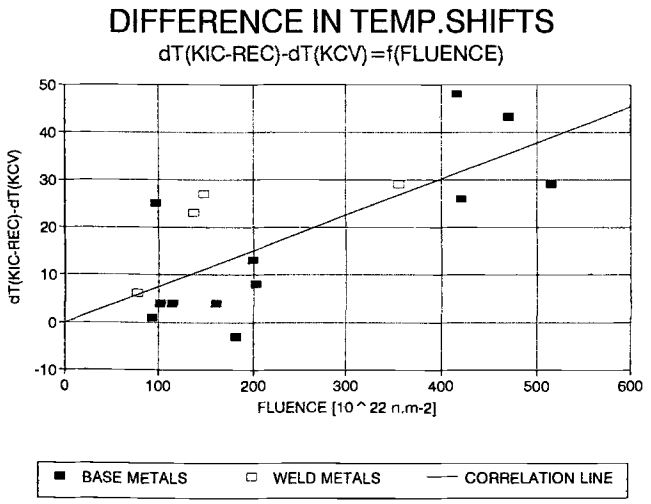


Fig. 4 *Difference between static fracture toughness (re-constituted Charpy) and Charpy notch impact toughness transition temperature shifts for 15Kh2MFA type steels*

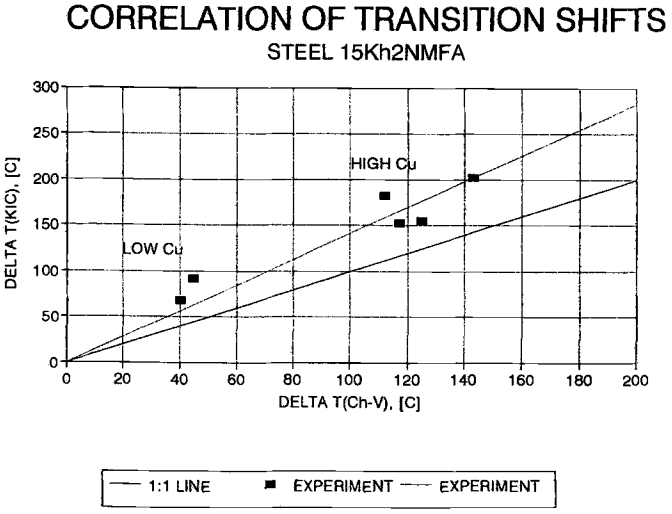


Fig. 5 *Correlation between static fracture toughness (K_{IC}) and Charpy notch impact toughness (Ch-V) transition temperature shifts for 15Kh2NMFA type experimental heats*

Similar picture can be seen in Fig. 6, where results of shifts from dynamic (Charpy impact = ChV, and dynamic fracture toughness = KId) tests are compared with static fracture toughness tests. Again, there is practically no difference between this dependence and Fig. 5, as shifts in both dynamic type tests are practically identical, independent of the type of dynamic testing.

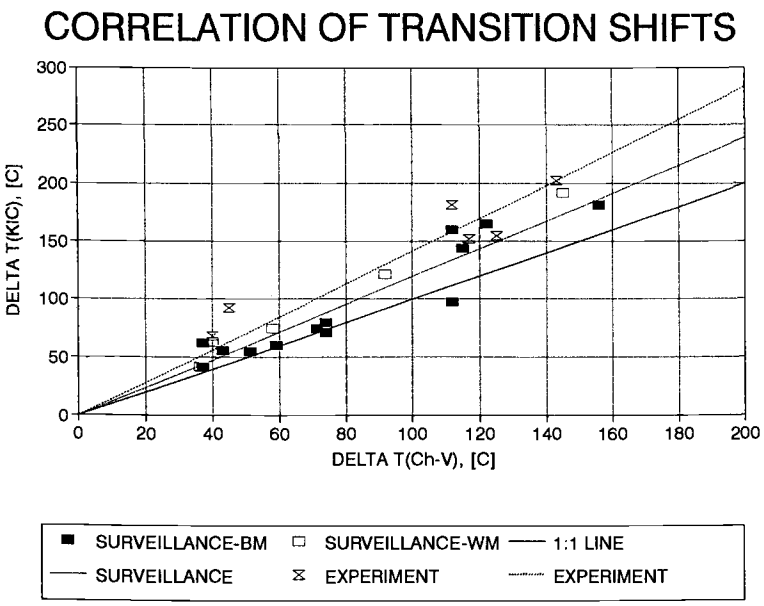


Fig. 6 *Correlation between static fracture toughness and Charpy notch impact toughness transition temperature shifts tested for VVER RPV materials*

Conclusions

Even though a limited set of data exists, some conclusions could be proposed:

- reconstitution technique was proven as a very effective and valuable method for re-evaluation of specimens from the standard surveillance programs;
  use of this method is very important mainly for determination of different material parameters from the same specimens (fully identical conditions for the different tests can be assured);
- differences between static fracture toughness transition temperatures can be described as a linear dependence on neutron fluence or on transition temperature shifts values - the higher is transition temperature shift, the higher is a difference between static and dynamic transition temperature shifts, even though quite different fracture mechanisms are present in these different tests :
  - static vs. dynamic,

- initiation load for unstable crack propagation vs. work necessary for crack initiation, propagation and arrest;
- these differences can be practically neglected up to VVER-440 EOL design neutron fluence (approx. 2×10^{24} n.m^{-2});
- these differences can reach values up to about 50 °C for neutron fluences equal to about 5×10^{24} n.m^{-2} , i.e. for double RPV design lifetime;
- there is practically no difference between transition shifts from different dynamic type tests, i.e. shifts from Charpy impact and dynamic fracture toughness tests are close to each other,
- Charpy impact transition temperature shifts can be used for VVER RPV integrity assessment up to EOL neutron fluence.

Reconstitution of specimens from standard surveillance program gives very important results and shows some dependencies between static and dynamic type transition temperature shifts. Nevertheless, great difference still exists between static transition shifts from reconstituted specimens and from direct tests of pre-cracked Charpy specimens within the surveillance program. One possible explanation could be an existence of flux rate effect which could increase these shifts compared to shifts from specimens irradiated by much higher neutron flux. This question has been one of the reasons why a Supplementary Surveillance Program for RPVs in NPP Dukovany has been designed and finally realized.

References

[1] Code for Strength Analysis of Components and Piping in NPPs, PNAE G-7-002-86, Energoatomizdat Moscow (1989)

[2] ASME Pressure Vessel and Boiler Code, Section III, Division 1, Edition 1995

[3] ISO/DIN 1248-76 Steel - Charpy impact test, V-notch

[4] Fracture toughness of metals on static loading, CSN 420347 (Czech standard, in Czech), Prague (1991)

[5] Standard Test Method for Determination of the Reference Temperature, T_0, for Ferritic Steels in the Transition Range, ASTM E 1921-97

[6] ESIS Procedure for Determining the Fracture Toughness Behavior of Materials, ESIS P2-92

[7] J. Man, M. Holzmann, B. Vlach : Dynamic fracture toughness - method of testing and evaluation (Proposal Czech Standard), Zváranie 36 (1987), 10, pp. 291-294, 323- 356, (In Czech)

[8] Proposed Standard Methods for Instrumented Pre-cracked Charpy Impact Testing of Steels, Combined K_{Id}, J_{Id} and CTOD Test Methods, ESIS, Draft 6 (1996)

Xuejun Jia,[1] Yuanchao Xu,[1] Wendou Yang, [1]and Changyi Zhang[1]

Effect of Radiation on Material Used for 600MW Chinese Nuclear Power Plant Reactor Pressure Vessel

Reference: Jia, X., Xu, Y., Yang, W., and Zhang, C., **"Effect of Radiation on Material Used for 600MW Chinese Nuclear Power Plant Reactor Pressure Vessel,"** *Effects of Radiation on Materials: 19th International Symposium, ASTM STP 1366,* M. L. Hamilton, A. S. Kumar, S. T. Rosinski, and M. L. Grossbeck, Eds., American Society for Testing and Materials, West Conshohocken, PA, 2000.

Abstract: Irradiation experiments were conducted to determine the effect of radiation on the properties of 16MnD5 material from a simulate Chinese 600 MW nuclear power plant reactor pressure vessel ring forging. Irradiation experiments were conducted to compare the performance of the 16MnD5 samples to samples of American Society for Testing and Materials Specification A508-class 3 material. The results showed that the radiation effects on the 16MnD5 material were less than those exhibited by the A505-class 3 material.

Keywords: nuclear power plant, reactor pressure, irradiation embrittlement, reference temperature, charpy-V test, ΔRT_{NDT}, ΔT_{41J}

Introduction

It is expected that additional nuclear power plant (NPPs) will be constructed in China in the coming years because of increasing energy requirements. Since the reactor pressure vessel(RPV) is a component of principle interest in designing any new facilities, Shanghai Heavy Machinery Factory (SHMF) made a simulated forged cylinder for the core (beltline) section of a 600 MW NPP RPV in order to improve the domestic manufacturing of this component. Material samples were taken from this forging and subjected to neutron irradiation to investigate the performance of the 16MnD5 forging material of which it was constructed.

Test Material

The forging material was 16MnD5,with the composition shown in Table 1. In order to

[1]Senior Engineer, Professor, Professor, Assistant Engineer, respectively, Institute of Atomic Energy, P.O. Box 275(51), Beijing, 102413, China.

Copyright© 2000 by ASTM International www.astm.org

Table.1 Chemical composition(wt%)

	C	Mn	Si	S	P	Cr	Ni	Mo
Lable analysis	0.18	1.47	0.14	0.001	0.005	0.13	0.73	0.49
Check analysis	0.20	1.45	0.16	0.001	0.006	0.14	0.75	0.45
A508-class.3	0.18	1.45	0.19	0.001	0.004	0.14	0.75	0.49
	Cu	Al	V	Co	Sn	As	Ta	Sb
Lable analysis	0.025	0.028	0.005					
Check analysis	0.032	0.028	0.005	0.006	0.005	0.005	0.005	0.006
A508-class.3	0.03	0.027	0.003	0.013	0.005	0.005		0.001

compare with the A508-class 3 forging materials, the chemical composition for the A508-class 3 forging is also listed in Table.1. The forging was manufactured with the following heat treatment history: melting and electro-slag remelting, forging, 920℃ normalizing and 670 ℃ tempering, 870-890 ℃ water quenching and 650 ℃ tempering, simulated post-weld heat treatment: 550℃ 55hrs.+ 600℃ 20hrs.+ 600 ℃ 10hrs.

The test specimens were removed from the forging according to the Procedures of French Specification RCC_M2111.The manufacturing information on the A508-class 3 samples were similar.

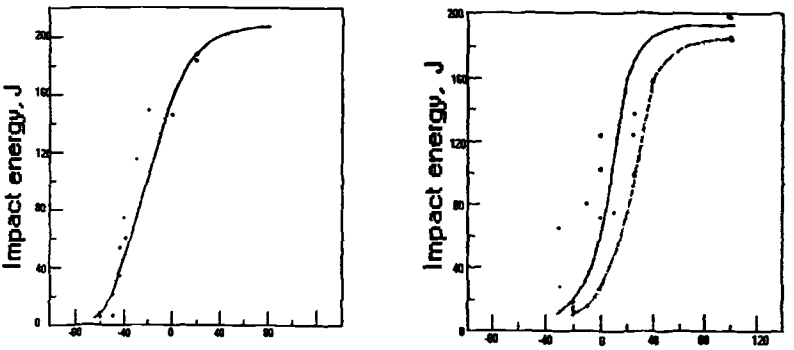
Experimental Procedure

Charpy V-notch specimens were prepared from the 16MnD5 and A508-class 3 steels in accordance with ASTM Notched Bar Impact Testing of Metallic Materials Specification E23. The specimens were inserted in a reusable capsule designed by the authors for simulating low or high temperature (50 ℃-350 ℃) irradiations. Three electric furnaces were installed in capsule to maintain the irradiation temperature at 275+10 ℃, and NiCr-NiAl thermcouples were installed on an imitation specimen in the capsule to monitor the irradiation temperature. The capsule was irradiated in the 3.5 KW swimming pool-type reactor at the China Institute of Atomic Energy with the neutron flux at the capsule location being 4.12 x 10^{12} n/cm^2 s (E>1.0MeV). The capsule was irradiated to a neutron fluence of 4.1 x 10^{19} n/cm^2.

Charpy V-notch impact testing was conducted in a hot cell using a Tinius Olsen's T-84 instrumented Charpy impact testing machine. The energy of the pendulum was 41.5 kg m with an impact velocity of 5.46 m/s. For each test specimen, measurements of the impact energy, lateral expansion, and percent shear fracture surface appearance were taken along with load-versus-time records. The transfer of the specimens to the testing machine and the heating and cooling capabilities of the machine controlled the specimen's temperature to ±1℃. The lateral expansion of the specimens was measured to a precision of ± 0.02 mm.

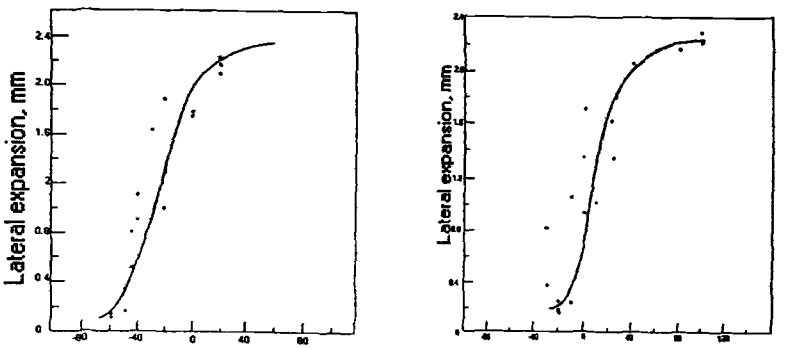
Test Results

The Charpy-V notch impact energy versus temperature (A_k – T) curves before and after irradiation were plotted in Figure 1 for the 16MnD5 steel and the lateral expansion versus temperature (LE-T) curves before and after irradiation for this material are plotted in Figure 2. The A_k-T curves and the LE-T curves before and after irradiation for the A508-class 3 steel are plotted in Figure 3. The curves shown were fit to the data by a statistical method using a hyperbolic tangent function form. The 41J, 68J, and 0.89mm lateral expansion index temperature before and after irradiation and the shifts in the index temperatures are given in Table 2.



a. before irradiation b. after irradiation

Fig.1 — Charpy V-notch impact energy curves before and after irradiation



a. before irradiation b.after irradiation

Fig.2 — Later expansion curves before and after irradiation

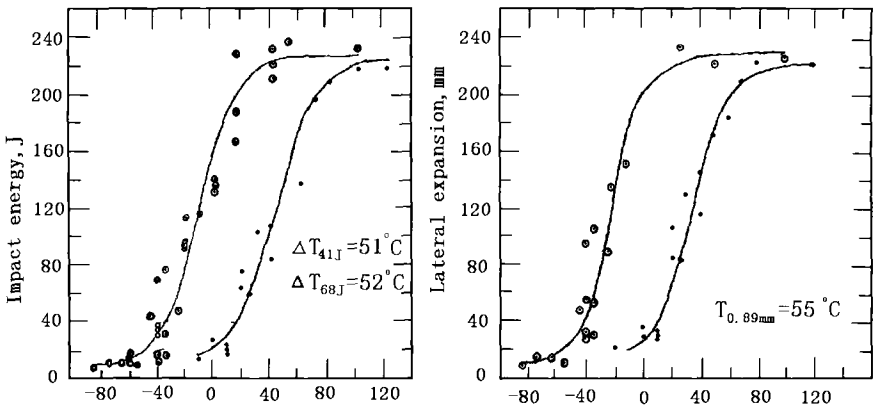


Fig.3 The A_k-T curves and the LE-T curves before and after irradiation for the A508-class 3 steel

Table 2-The brittle-ductile transition temperature before and after irradiation and index temperature shift

Materials			16MnD5		A508-class 3		
Neutron flux(E>1MeV)			0	3.44×10^{12} n/cm^2.s	0	2.70×10^{12} n/cm^2.s	3.85×10^{12} n/cm^2.s
Neutron fluence(E>1MeV)			0	4.1×10^{19} n/cm^2	0	3.23×10^{19} n/cm^2	4.62×10^{19} n/cm^2
USE (J)			206	193	240	220	230
Index temperature	T_{41J} (℃)	Sv.*	-6	-44	-34	17	18
		Sd**	±7	±7	±7	±6	±5
	T_{68J} ℃		24	-32	-24	28	29
	$T_{0.89mm}$ ℃			-30	-28	27	27
	$T_{50\%FATT}$ ℃			-9			
Shift	ΔT_{41J} ℃			38		51	52
	ΔT_{68J} ℃			34		52	53
	$\Delta T_{0.89mm}$ ℃			34		55	55

Discussion

The irradiation embrittlement of RPV steel has been conventionally measured by the shifts in RT_{NDT} or T_{41J}. The chemical composition of a material is known to significantly affect its rate of irradiation embrittlement, especially the copper (Cu), nickel (Ni), and phosphorous (P) content. The low Cu content (0.032wt%) in the

16MnD5 forging is close to the solubility of copper in steels at a temperature 300 ℃ and thus results in little copper precipitation during irradiation. At this low Cu value, the effect of the Ni in the forging is also reduced. The Ni content of the forging was 0.79 wt%, below the value (>1.2wt%) at which a significant effect would be expected given the low Cu content. The P content was also less the value recommended by ASME.

In evaluating the observed embrittlement of the 16MnD5 samples, a comparison can be made to the methodology recommended by the United States Nuclear Regulatory Commission in Regulatory Guide (RG) 1.99, Revision 2 [3] for predicting embrittlement in U.S. reactor steels:

$$\Delta RT_{NDT} = \Delta T_{41J} = CF \times f^{0.28 - 0.10 \log f}$$

Where CF = the chemistry factor and f = the neutron fluence in (10^{19} n/cm^2, E>1MeV).
According the figure in RG1.99, Revision 2, the CF of the 16MnD5 forging would be 11.7 and the predicted ΔRT_{NDT} would be 16 ℃. In the temperature range of 275 ℃. to 300℃ with neutron fluences in the range of 1 x 10^{18} to 6 x 10^{19} (E>1MeV), we also calculate ΔRT_{NDT} using the French RCC-MZG3430 model,

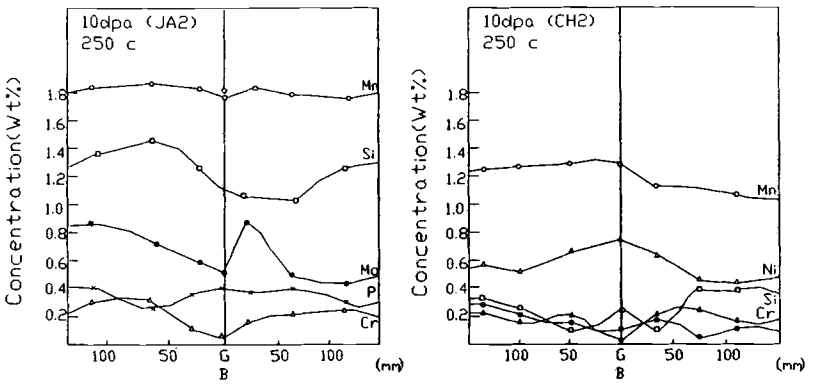
$$\Delta RT_{NDT} = (22 + 556(\%Cu - 0.08) + 2778(\%P - 0.008)) \times (f/10^{19})0.5$$
$$= 45 \text{ ℃}.$$

Where f = the neutron fluence in (n/cm^2, E>1MeV).
This model predicts a ΔRT_{NDT} for the 16MnD5 forging of 45 ℃.

The response of a material to neutron irradiation is also related the neutron flux, the irradiation temperature, the neutron spectrum, and the fluence. The irradiation embrittlement parameter ΔT_{41J} decreases with increasing irradiation temperature in the range of 0.4 to 2.0 ℃/℃ for irradiation temperature in the range of 250 to 310 ℃, with the majority of data sets around an average value of 1 ±0.2 ℃/℃.

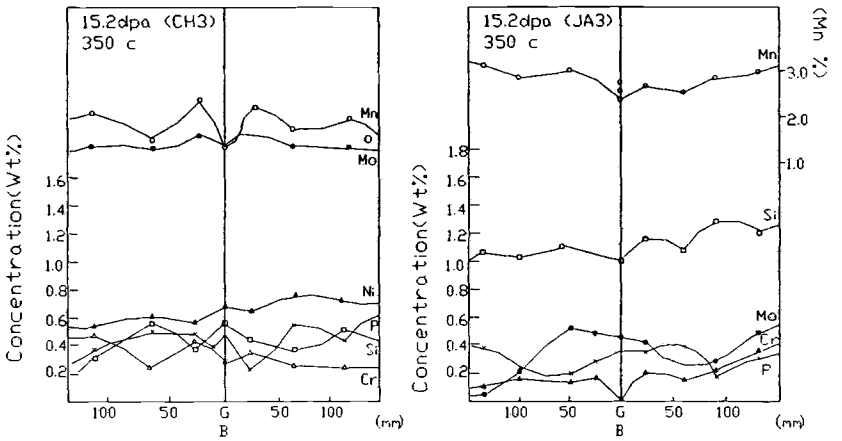
The prediction model in Regulatory Guide 1.99, Rev.2 was based on the surveillance results from capsules irradiated in commercial nuclear power plants. Without correcting for the lower irradiation temperature and high neutron flux, the irradiation embrittlement behavior of the 16MnD5 specimens appears too greater than that predicted by the model. After correcting for these differences, the test results were more consistent with the RG1.99, Rev.2 model prediction. In contrast, the prediction of the RCC-MZG3430 model appears to be high when compared to the observed shifts. The test results can also be compared directly to the shifts observed in the A508-class 3 material. The results indicated the 16MnD5 samples exhibited less irradiation embrittlement than the A508-class 3 material for the same neutron irradiation condition.

In order to make a thorough investigation or the effects of irradiation on the 16MnD5 material, specimens of 16MnD5 and A508-class 3 materials were also irradiated in the super-high voltage electron microscope (H-1300) at the University of Hokkaido. The specimens were irradiated with 1 MeV electron beams to 10 displacements per atom at 250 ℃ and 15.2 displacements per atom at 350 ℃ with an average electron flux of 3 x 10^{23} electrons/cm^2. The results in Figure 4 and Figure 5 show that for the 250 ℃ irradiation the concentrations of manganese (Mn), silicon(Si), and phosphorous (P) near the grain boundaries has changed little while the chromium (Cr) concentration has dropped slightly. In comparison with the A508-class 3 material,



a) 16MnD5 b)A508-class 3

Figure.4 – Concentration of alloy elements after irradiated to 10dpa,250 ℃



a) 16MnD5 b)A508-class 3

Figure.5 – Concentration of alloy elements after irradiated to 15.2dpa,350 ℃

however, the drop in the Cr concentration for 16MnD5 material is small. At an irradiation temperature of 350 ℃, the 16MnD5 samples showed segregation of Mn

from the grain boundary while the Si, P, Ni, and Cr concentrations were not reduced. Under these conditions, the A508-class 3 samples demonstrated segregation of Cr from the grain boundary.

In comparing the microstructures of the materials, the amount of carbide on the grain boundaries was greater for the 16MnD5 material and its grain size was smaller than that of the A508-class 3 material. This may provide more sinks locations for vacancies and thus limit the amount of radiation enhanced diffusion experienced by the 16MnD5 material. At least, it has been shown that the irradiation effects on 16MnD5 steels irradiated by 1.0 MeV electron beams at 350 ℃.

Conclusion

The test results show that the irradiation effects on 16MnD5 steels irradiated either by neutron or by 1.0 MeV electron beams are less than that on A508-class 3 steels.

References

(1) Xu,Y., Jia, X., Experimental Research on Radiation Embrittlement of Low-copper Nuclear Power Plant Reactor Pressure Vessel Steels. *Chinese Journal of Nuclear Science and Engineering, Vol.18, No.2. 1998.*
(2) U. S. NRC. 1.99. Rev.2. 1998
(3) G.R.odetle and G.R.lucas., Irradiation Embrittlement of Reactor Pressure Vessel Steels. ASTM STP909 (1986) P206.
(4) Hu. Benfu, Yang Wendou., Research on the Microstructure of Reactor Pressure Vessel Steels Irradiated by Electron Beams. CIAE, Work Reports, 1992.

Kenneth K. Yoon[1] and Wayne A. Pavinich[1]

Comparison of Fracture Toughness of Irradiated Reactor Vessel Welds - Predicted by ASTM E 900 and Measured

Reference: Yoon, K. K. and Pavinich, W. A., **"Comparison of Fracture Toughness of Irradiated Reactor Vessel Welds - Predicted by ASTM E 900 and Measured,"** *Effects of Radiation on Materials: 19th International Symposium, ASTM STP 1366,* M. L. Hamilton, A. S. Kumar, S. T. Rosinski, and M. L. Grossbeck, Eds., American Society for Testing and Materials, West Conshohocken, PA, 2000.

Abstract: Recently, a new predictive model has been developed by the NRC and is being implemented in ASTM Standard E 900, that addresses radiation-induced embrittlement of ferritic steels. The model is based on extensive Charpy impact energy data of irradiated reactor vessel steels obtained from surveillance programs. The final application of this new method is to predict fracture toughness of irradiated materials to determine pressure-temperature curves for nuclear power plant operation and RT_{PTS} values in compliance with the current regulatory rules for the nuclear-utility industry.

In this paper, the predicted fracture toughness of irradiated reactor vessel welds is compared with that of irradiated material. The degree of conservatism in the Charpy impact energy based predictive model is assessed by comparison with the actual fracture toughness of irradiated materials.

Keywords: fracture toughness, irradiated material, ASTM E 900

Introduction

The ASTM Committee on Radiation Effects, E10, is revising the E 900, "Standard Guide for Predicting Neutron Radiation Damage to Reactor Vessel Materials," which addresses radiation-induced embrittlement of ferritic steels. A new NRC developed predictive model is being incorporated into this standard. The model is based on extensive Charpy impact energy data of irradiated reactor vessel steels from reactor vessel surveillance programs. The final application of this new method is to predict fracture toughness of irradiated materials.

In this paper, the predicted effect of radiation embrittlement on fracture toughness of

[1]Technical Consultant and Advisory Engineer, respectively, Framatome Technologies, Lynchburg, VA 24501.

Copyright© 2000 by ASTM International www.astm.org

irradiated reactor vessel welds is compared with the fracture toughness of reactor vessel welds is compared with the measured fracture toughness of irradiated material. It is intended to investigate the degree of conservatism in the Charpy impact energy based predictive models compared with actual fracture toughness of irradiated materials.

Fracture Toughness Prediction Model for Irradiated Materials

There are two reference fracture toughness curves in the ASME Boiler and Pressure Vessel Code [1], K_{Ic} and K_{Ia}:

$$K_{Ic} = 2.806 \exp[0.02(T - RT_{NDT} + 100)] + 33.2, \ ksi\sqrt{in} \qquad (1)$$

$$K_{Ia} = 1.223 \exp[0.0145(T - RT_{NDT} + 160)] + 26.78, \ ksi\sqrt{in} \qquad (2)$$

where T is crack tip temperature and RT_{NDT} is reference nil-ductility transition temperature, both in ^0F. The RT_{NDT} is used to index the degree of radiation induced embrittlement for irradiated materials. The ASME Code defines the initial RT_{NDT} (IRT_{NDT}), however, the shift in the RT_{NDT} due to radiation induced embrittlement is not addressed in the Code. The NRC Regulatory Guide 1.99, Revision 2 (RG 1.99) [2] provides a method to calculate the shift and mandates use of an additional margin term. When the RT_{NDT} values are determined, the corresponding fracture toughness of irradiated material is determined by equations 1 and 2.

Regulatory Guide 1.99

The RT_{NDT} is determined according to Regulatory Guide 1.99, Revision 2 as follows:

$$\text{Adjusted } RT_{NDT} \text{ (ART)} = IRT_{NDT} + \Delta RT_{NDT} + \text{Margin}$$

where IRT_{NDT} is the initial RT_{NDT} determined from Section NB in Section III of the ASME Code. The ΔRT_{NDT} is determined by RG1.99 as a function of fluence and chemical compositions of the material under consideration or by evaluation of surveillance capsule data. The Margin term is defined as

$$\text{Margin} = 2\sqrt{\sigma_I^2 + \sigma_\Delta^2}$$

where σ_I and σ_Δ are standard deviations of the initial RT_{NDT} data and the shift data, respectively. σ_I is dependent on each material and σ_Δ is 28°F for welds according to RG 1.99, Revision 2.

Proposed ASTM Standard E 900 Method

The ART in E 900 for each heat of material in the reactor vessel beltline is given by the following expression:

$$ART = \text{Initial RT} + \Delta T_{30p} + U$$

where Initial RT is the reference temperature for the unirradiated material. Initial RT may be defined as the RT_{NDT} in Subsection NB of Section III of the ASME Boiler and Pressure Vessel Code for the unirradiated material or alternative means justified by the user.

ΔT_{30p} is defined as follows:

$$\Delta T_{30p} = ff_1(\phi t)f_1(cc) + ff_2(\phi t)f_2(cc)$$

$$ff_1(\phi t) = A \exp[1.906 \times 10^4/(T_c + 460)][\phi t \times 10^{-19}]^a$$

where: $a = 0.4449 + 0.0597 \log(\phi t \times 10^{-19})$

$$ff_2(\phi t) = \{1/2 + \tfrac{1}{2} \tanh \{ [\log(\phi t + 6.48 \times 10^{12}\, t_{irr}) - 18.29]/0.6\}\}$$

$$f_1(cc) = (1 + 57.7)\, P$$

$$f_2(cc) = B\,(Cu - 0.072)^{0.678}\,(1 + 2.56\, Ni^{1.358})$$

where Cu = 0.072 is used where Cu $\leq$ 0.072 wt%
Cu = 0.3 is used where Cu $\geq$ 0.3 wt%
T_c is coolant temperature: cold leg temperature for PWRs and recirculation temperature for BWRs (max. $T_c = 570^0F$)
ΔT_{30} and T_c are in ^0F
Fluence (ϕt) is in n/cm^2 (E> 1 MeV)
Cu = copper content, wt%
Ni = nickel content, wt%
P = phosphorus content, wt%
t_{irr} = irradiation time, effective full power hours
σ_e = standard error = 24^0F
$A = 1.23 \times 10^{-7}$ for plates, ^0F
$A = 8.98 \times 10^{-8}$ for forging, ^0F
$A = 1.10 \times 10^{-7}$ for welds, ^0F
B = 172 for plates, ^0F
B = 135 for forging, ^0F
B = 209 for welds, ^0F

All chemical composition values to be used in the above equation are weld wire heat or base metal heat best estimate values. The value "U" is $2\sigma_e$ (48^oF) except that "U"

need not exceed the mean value of ΔT_{30p}.

Fracture Toughness Data of Irradiated Reactor Vessel Welds

The fracture toughness data sets of irradiated weld materials are examined in this paper to investigate the impact of the new proposed ASTM Standard E 900.

The Linde 80 WF-70 weld has high copper and nickel content and exhibits lower upper-shelf toughness when irradiated. Because of that, it has been the most tested and studied weld material. The 72W and 73W weld materials are simulated welds and were extensively tested under the NRC regulatory research program. In addition, two Linde 80 weld materials, BW WF-70 and BW WF-67, irradiated in the B&W Owners Group surveillance programs, are included for comparison. Table 1 lists pertinent input data.

Table 1. Selected Irradiated Weld Material Data

Weld Material Identification	Fluence E-19 n/cm^2	Tc ^{0}F	P Wt%	Cu Wt%	Ni Wt%	Irr. Time (hrs)	RG1.9 9CF	References
WF-70	0.5	550	0.016	0.32	0.59	720*	202	[4]
WF-70	1.0	550	0.016	0.32	0.59	1440*	202	
72W	1.5	550	0.006	0.23	0.59	1440*	169	[5]
73W	1.5	550	0.005	0.31	0.59	1440*	198	
BW WF-70	1.89	556	0.016	0.32	0.60	105120	202	[6]
BW WF-67	1.89	556	0.016	0.26	0.60	105120	180	

* Estimated.

Comparison between Predicted Fracture Toughness and Data

Using the data from Table 1, adjusted RT_{NDT} values are determined for each weld metal data set as shown in Table 2. Although the irradiation time was estimated from the test report, its effect for these data sets in Table 1 is minimal at these fluence levels. The effect of irradiation time for these data sets is minimal at these fluence levels. For a fluence level greater than 10^{19}n/cm^2, the contribution from the irradiation time term is negligible.

The ΔRT_{NDT} calculated by the E 900 method are lower than the values obtained using the RG 1.99 method as shown in Figure 1. However, a major contributor to the reduction in ART comes from the initial RT_{NDT} for WF-70 welds. E 900 allows the use of a mean Initial RT value instead of the mean minus 2σ mandated by RG 1.99.

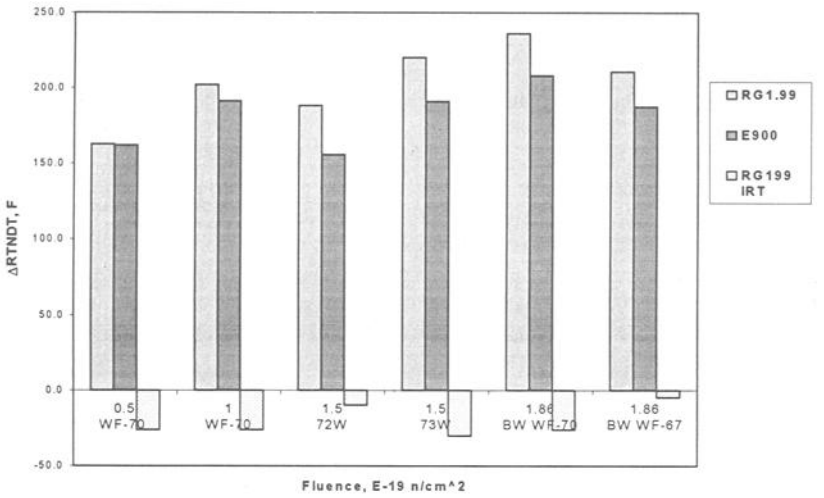


FIG. 1—ΔRT_{NDT} by RG 1.99 and by E 900 for Welds

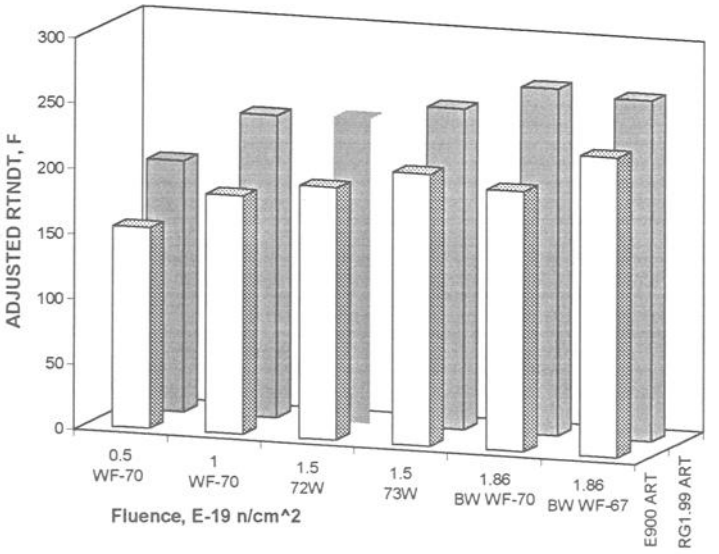


FIG. 2—Adjusted RT_{NDT} by RG 1.99 and by E 900 for Welds

Table 2 Predicted RT_{NDT}

Material ID	Fluence $x10^{-19}$ n/cm^2	RG 1.99				E 900			
		Pos. 1 IRT, ^{0}F	ΔRT_{NDT} ^{0}F	Margin ^{0}F	ART ^{0}F	IRT ^{0}F	ΔRT_{NDT} ^{0}F	Uncer-tainty, ^{0}F	ART ^{0}F
WF-70	0.5	-26	162.9	56	193	-56	162.2	48	154
WF-70	1	-26	202.0	56	232	-56	191.0	48	183
72W	1.5	-10	188.0	56	234	-10	155.9	48	194
73W	1.5	-30	220.2	56	246	-30	190.8	48	209
BW WF-70	1.86	-26	236.3	56	266	-56	208.2	48	200
BW WF-67	1.86	-5	210.6	56	262	-5	187.5	48	231

Figure 2 shows the ART predictions by the proposed E 900 Standard method are all lower than those by the current RG 1.99 Rev. 2, by as much as 60^{0}F for the high copper weld at a fluence of 1.89 $x10^{19}$ n/cm^2. The fluence level of 1.89 $x10^{19}$ n/cm^2 is approximately equivalent to the end-of-design-life value for the beltline region of B&W designed nuclear power reactors. For some other plants that have end-of-design-life fluence twice this level or higher, the benefit would be greater.

Using the predicted ART, the predicted K_{Ic} curves are shown with the fracture data of irradiated welds in Figures 3 through 6. Figure 3 shows the fracture toughness data for irradiated WF-70 at a fluence of $0.5x10^{19}$ n/cm^2, with two data sets at the same test temperature. Figure 4 shows the same weld material at a fluence level of 1 $x10^{19}$ n/cm^2 and shows fracture toughness data obtained at several test temperatures. The 72W and 73W weld metal data sets [5] also have significant number of fracture toughness data from several test temperatures, which cover the entire brittle-to-ductile transition range. From these figures, it is evident that the predictive models are very conservative. In the temperature range of interest, e.g. 200~300^{0}F, to nuclear power plant pressurized-thermal-shock (PTS) analyses, the actual fracture toughness data are more than twice the predicted toughness values. This additional margin is not accounted for in the current rules for the PTS analyses.

Fracture toughness data from WF-70 welds irradiated in a test reactor (high flux) and a power reactor (low flux) are shown in Figure 7. The power reactor fracture toughness data are higher than the test reactor data. However, there are only four data points for BW WF-70 and another set of four data points for BW WF-67, resulting in insufficient data to address the flux effect on fracture toughness at this time.

Potential Benefit from the Master Curve Method

The ASTM Committee on Fatigue and Fracture, E08, developed a new ASTM Standard Test Method for the Determination of a Reference Temperature, T_0, for Ferritic Steels in the Transition Range E 1921-97. This method defines the procedure to obtain a reference temperature, T_0, and a "Master Curve" that characterizes the fracture toughness

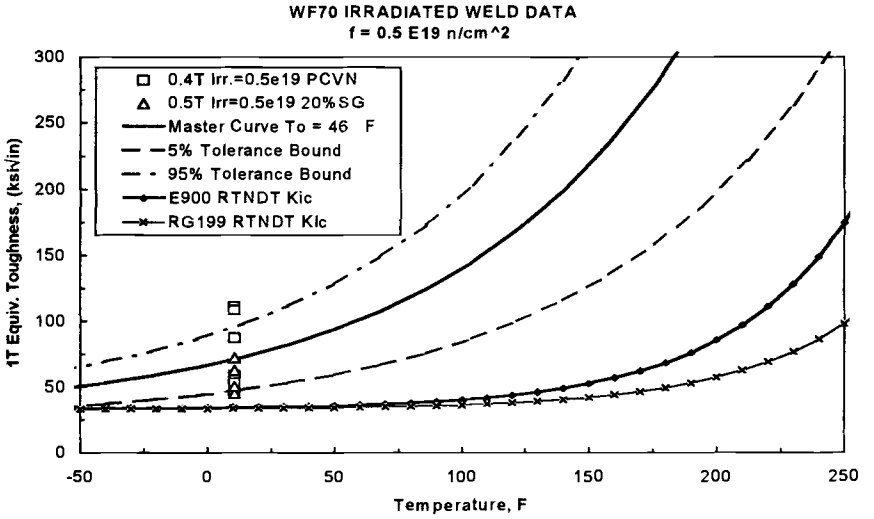


FIG. 3—Irradiated Weld Material WF-70 Data Compared with Various K_{Ic} Curves

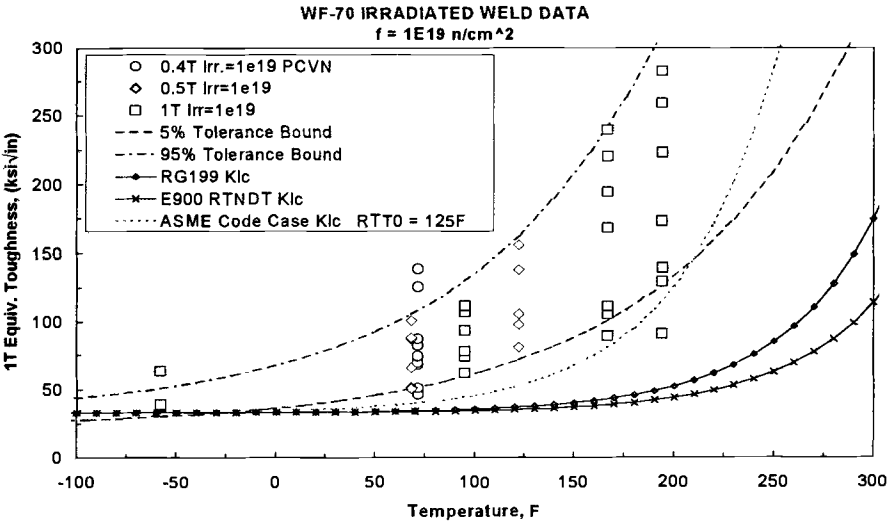


FIG. 4—Irradiated Weld Material WF-70 Data Compared with Various K_{Ic} Curves

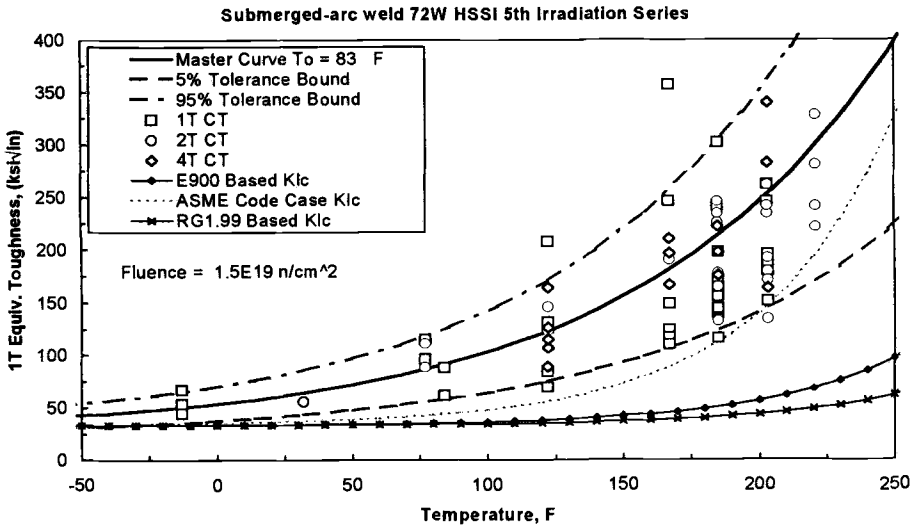


FIG. 5—Irradiated Weld Material 72W Data Compared with Various K_{Ic} Curves

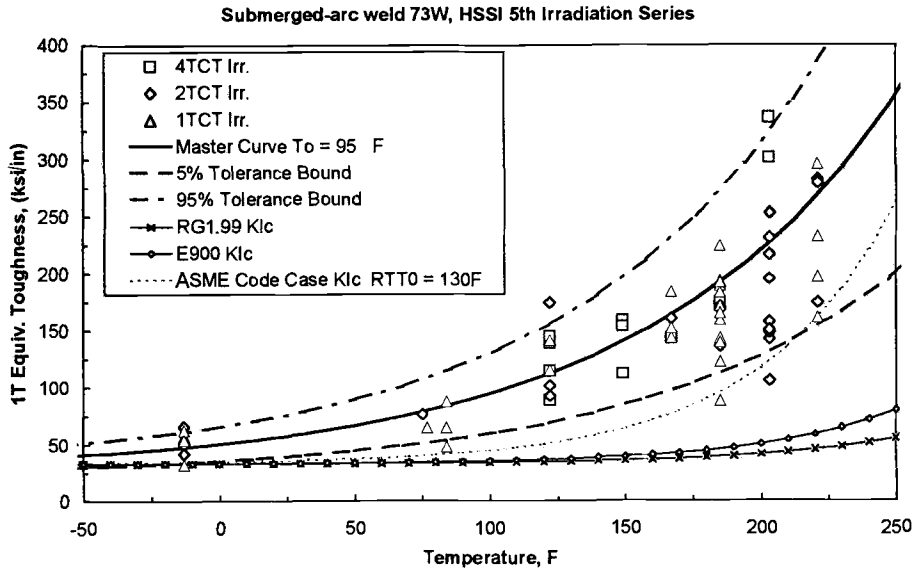


FIG. 6—Irradiated Weld Material 73W Data Compared with Various K_{Ic} Curves

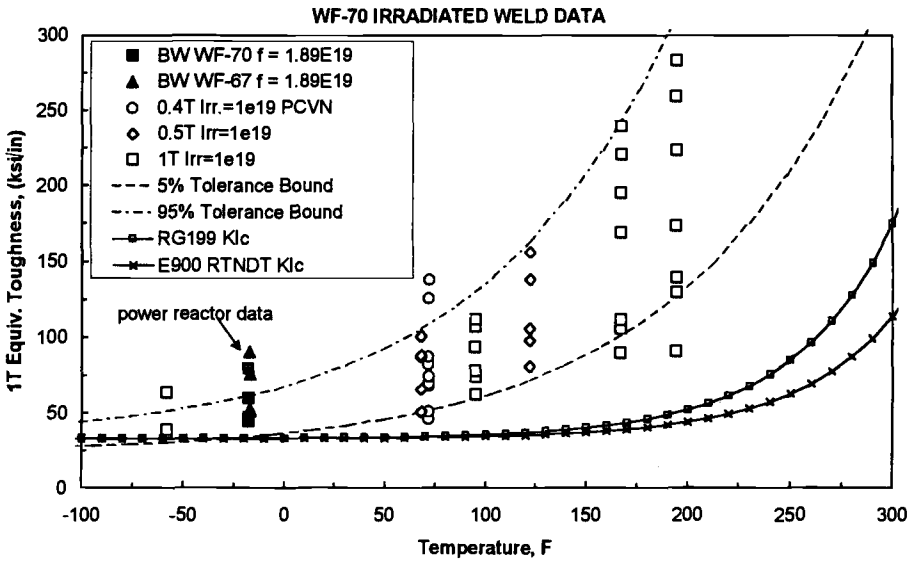


FIG. 7—Power Reactor Data Compared with Test Reactor Data – WF-70

of a ferritic material in the brittle-to-ductile transition temperature range. ASME Code adopted a Code Case [7] to implement the use of this new technology into the ASME Code.

In Figures 4 through 6, another K_{Ic} curve is plotted and designated as ASME Code Case K_{Ic}. This curve is drawn based on an equivalent RT_{NDT} currently defined in the proposed Code Case for use of the Master Curve method. The Master Curve method is based on direct measurement of fracture toughness using ASTM Standard E 1921-98.

The proposed Code Case method appears to be appropriately representing the actual material toughness. This new method is very promising for improving the prediction of fracture toughness of irradiated materials.

Conclusions

1. ART predictions by the proposed E 900 Standard method are lower than those by the current RG 1.99 Rev. 2 , as much as 60^0F for high copper weld and fluence of 1.89×10^{19} n/cm^2. For the WF-70 weld metal, the initial RT_{NDT} term is a major contributor to the difference.
2. When compared with the actual fracture toughness, the current method for prediction using E 900 is still very conservative, by more than a factor of two. This is an additional margin not accounted for the current method of the PTS analyses and pressure-temperature limits for nuclear power plants.
3. A new method based on direct fracture toughness measurement through the Master Curve method should be incorporated to obtain improved fracture toughness values for irradiated materials in the future.

Acknowledgment

The authors gratefully acknowledge the support provided by the B&W Owners Group for this work

References

[1] 1998 ASME Boiler and Pressure Vessel Code, Section XI, *Rules for Inservice Inspection of Nuclear Power Plant Components*, the American Society of Mechanical Engineers, New York, New York, July 1,1998.

[2] Draft Revision of ASTM Standard E 900, "Standard Guide for Predicting Neutron Radiation Damage to Reactor Vessel Materials," ASTM Ballot, April 28, 1998.

[3] U. S. Regulatory Commission, "Radiation Embrittlement Damage to Reactor Vessel

Materials," *Regulatory Guide* 1.99, Rev. 2, May 1988.

[4] Nanstad, R. K., Haggag, F. M., McCabe, D. E., Iskander, S. K., Bowman, K. O., and Menke, B. H., 1992, "Irradiation Effects on Fracture Toughness of Two High Copper Submerged-Arc Welds, HSSI Series 5," NUREG/CR-5913, Oak Ridge National Laboratory.

[5] McCabe, D. E., Sokolov, M. A., Nanstad, R. K., and R.L. Swain, "Effects of Irradiation to 0.5 and 1.0e19 neutrons/cm**2 (>1MeV) on the Midland Reactor Low Upper-shelf Weld: Capsules 10.01, 10.02, and 10.05 in the Heavy-Section Steel Irradiation Program 10th Irradiation Series," August 1995, ORNL/NRC/LTR-95/18.

[6] BAW-2254P, "Test Results of Capsule CR3-LG2 B&W Owners Group," Framatome Technologies, Inc., October 1995.

[7] Code Case N-629, Boiler and Pressure Vessel Code, American Society of Mechanical Engineer, 1999.

Christian Pichon,[1] Christian Brillaud,[2] Denis Deydier,[1] Alain Alberman,[3] and Pierre Soulat[4]

Neutron Spectrum Effect and Damage Analysis on Pressure Vessel Steel Irradiation Behaviour

Reference: Pichon, C., Brillaud, C., Deydier, D., Alberman, A., and Soulat, P., **"Neutron Spectrum Effect and Damage Analysis on Pressure Vessel Steel Irradiation Behaviour,"** *Effects of Radiation on Materials: 19th International Symposium, ASTM STP 1366,* M. L. Hamilton, A. S. Kumar, S. T. Rosinski, and M. L. Grossbeck, Eds., American Society for Testing and Materials, West Conshohocken, PA, 2000.

Abstract: A comprehensive program on pressure vessel irradiation behaviour has been carried out by the Commissariat à l'Energie Atomique (CEA) and Electricité de France (EDF) from 1989 until 1995. This program is a key approach to EDF plant life assessment strategy. It is based on experimental correlations between pressure vessel steel irradiation behaviour with regard to fluences obtained in two very different irradiation spectra specially designed in the OSIRIS and SILOE CEA test reactors. The aims of this program were to assess a potential neutron spectrum effect in the range met in a Pressurised Water Reactor (PWR) between the vessel (internal surface, 1/4 thickness) and the surveillance capsules and correlatively to define the most appropriate exposure parameter for low alloy steel embrittlement.

In order to fulfill this objective, all experimental parameters had to be accurately controlled. New high-capacity irradiation rigs have been therefore developed by the CEA to test two materials in parallel with a large number of Charpy-V specimens in well-defined conditions (temperature, neutronic environment). Two weld materials were specifically manufactured from low alloy Mn Ni Mo steel .In terms of embrittling elements (Cu, Ni, P), these materials are representative of average and upper bound chemical compositions found in French nuclear power reactor vessel welds. Target fluences were 0.1 dpa in both reactors, corresponding to 7.10^{19} n.cm^{-2} ($\Phi_{E>1MeV}$) in the OSIRIS standard spectrum and to 4.10^{19} n.cm^{-2} ($\Phi_{E>1MeV}$) in the SILOE "distorted" spectrum. The spectra characteristics were derived both by damage monitor dosimetry and neutron transport calculations. For each material in each state, Charpy-V transition curves were defined.

The results in terms of Charpy-V transition shifts and fluences ($\Phi_{E>1MeV}$, $\Phi_{E>0.1MeV}$ and Φ_{dpa}) are presented then discussed. In the range considered, no spectrum effect and a very good correlation using fluence $\Phi_{E>1MeV}$ were found.

Keywords: neutron spectrum effect, irradiation damage, pressure vessel steel irradiation, experimental irradiation, fluences, surveillance capsules, exposure parameter $\Phi_{E>1MeV}$, low alloy steel embrittlement, weld materials, Charpy-V transition curves

[1] Deputy Head of Reactor Section and Senior Engineer respectively, Electricité De France/ DE/SEPTEN, Basic Design Departement, 12-14, Av. Dutrievoz, 69628 Villeurbanne FRANCE.

[2] Senior Engineer, Electricité De France - GDL/SECH, Departement of Expertise of Chinon, BP 23, 37420 Avoine FRANCE.

[3] Deputy Manager Experimental Reactors Department, Commissariat à l'Energie Atomique - DRN/DRE, BP 2, 91191 Gif Sur Yvette FRANCE.

[4] Senior Engineer, Metallurgical Departement, Commissariat à l'Energie Atomique - DTA/ DECM/SRMA, BP 2, 91191 Gif Sur Yvette FRANCE.

Copyright© 2000 by ASTM International www.astm.org

Scope of the Program

Power plant life assessment obviously depends on the life-time of the pressure vessel (PV). Therefore, as most utilities, Electricité de France is running a surveillance program for all its nuclear power plant pressure vessels [1, 2].

This program is based on the use of 4 capsules which were installed in the reactor at the beginning of service and then removed periodically. The capsules contain materials representative of the vessel, i.e. base metal, weld and heat affected zone, and are monitored in terms of dosimetry and temperature. Their positions in the reactor are along the core barrel, so they are irradiated at a shorter distance from the fuel assemblies than the vessel. These particularities in irradiation conditions between the vessel and the capsules lead to spectrum differences and are characterised by a flux factor, also called the lead factor, which determines the capsule/vessel embrittlement rate. In France, it is mandatorily limited to a value of 3.

Lead factors depend upon neutron fluences, such as fluence of neutrons with an energy above 1 MeV ($\Phi_{E>1MeV}$), fluence of neutrons with an energy above 0.1 MeV ($\Phi_{E>0.1MeV}$) or displacements per atom (Φ_{dpa}), accounting for spectrum differences. The vessel life-time assessment is therefore dependent on adequate fluence determination. The fluence $\Phi_{E>1MeV}$ is conventionally used in embrittlement prediction formulae [3].

The program called ESTEREL was designed to derive an experimental correlation between embrittlement and various measures of neutron exposure [4, 5]. Complementary calculations were made to assess the neutron spectrum influence on embrittlement, and furthermore on surveillance spectra. Started in 1989, this program and its subsequent analysis were completed in 1995.

Irradiation Program

Description

According to the aims of the program, it was proposed to irradiate two low alloy steel materials with a different behaviour under irradiation in two different neutronic conditions. The main principles were as follows :

- the neutronic conditions must be as representative as possible to those seen by the capsules and the vessel at the inner surface and at 1/4 its thickness,
- as for the surveillance programs, the shift induced by irradiation and measured with the Charpy V test will be the mechanical parameter taken into account in the correlation between embrittlement and fluence,
- in order to well analyse the results, all the experimental parameters have to be accurately well known. In particular, all the parameters which are of a great importance for irradiation embrittlement such as temperature, or which are a source of uncertainties such as heterogeneity of materials or Charpy V test scattering, must be well controlled.

Therefore it was decided to use two CEA test reactors, SILOE on the Grenoble site and OSIRIS on the Saclay site. A standard spectrum for PV steels irradiation can be found in the reflector of the OSIRIS reactor, where most irradiation programs are carried out. A "distorted" spectrum was designed by means of a steel block located in the pool of the SILOE reactor.

Irradiation Devices

A new high capacity irradiation device, the IRMA rig, was specifically designed to meet the ESTEREL program loadings requirements : 60 Charpy-V specimens + 20 tensile specimens + 30 neutron flux monitors. A very careful control of temperatures was needed (288±5°C) to ensure relevant and accurate data from 2 irradiation runs. Two IRMA rigs were manufactured, one for each reactor. Irradiation temperature accuracy was part of the IRMA rig design. Validation of thermal gradients in different gamma environments was obtained through thermal mock-up irradiation runs, featuring dummy steel loadings.

Validation of the Dosimetry

Establishing neutron spectrum effects implies excluding any interfering effects, such as the dose rate effect. The latter was addressed by parallel design : target flux level of 6.10^{-9} dpa.s^{-1} in both irradiation locations of OSIRIS and SILOE. The irradiations could be limited to about 1 calendar year each. Dosimetry was performed with neutronic mock-ups in the SILOE and ISIS reactors [5].

Extensive dosimetry in the irradiation rigs featured Fe, Ni, Cu, Nb activation monitors and, in addition, ^{238}U, ^{237}Np fissile monitors similar to the flux monitors used in power plant surveillance capsules [6, 7].

Materials

Two materials were prepared by FRAMATOME from low alloy Mn Ni Mo steel using an automatic submerged arc welding process. Weld material type was chosen because of better metallurgical and mechanical homogeneity compared to base metal. After welding, the materials were heat treated at 600°C for 15 hours to simulate the stress relief treatment of the vessel. As indicated in Tables 1 and 2, these materials meet the requirements of the French Code RCC-M ed. 1995, except for the embrittling elements (Cu, P) of material M2. In fact, material M1 represents average chemical composition of weld materials found in French nuclear power plants whereas material M2 corresponds to the upper bound composition found on the oldest ones, where RCC-M was not in application [1].

Table 1 - *Chemical Contents of Materials (Weight %)*

%	C	Si	Mn	P	S	Ni	Cr	Mo	Co	Cu	V
RCC-M ed. 95	< 0.100	0.15 0.60	0.80 1.80	< 0.010	< 0.025	< 1.20	< 0.30	0.35 0.65	< 0.03	< 0.07	< 0.02
M1	0.073	0.43	1.59	0.008	0.008	0.76	0.16	0.58	0.010	0.048	0.003
M2	0.058	0.49	1.48	0.020	0.009	0.68	0.04	0.54	0.017	0.095	0.001

The Temperatures at Nil Ductility Transition (TNDT) have been determined for each material : -55°C for M1 and -50°C for M2. They are in the same range of those measured on PV welds.

Table 2 - *Tensile Properties of Materials*

Tests at 20°C	Y.S. (MPa)	U.T.S. (MPa)	Elong. (%)
RCC-M ed95	> 400	550 - 700	> 20
M1	560	646	24.3
M2	553	636	25.2

Charpy-V impact energies were measured on each material at 0°C (M1 : 12.7daJ.cm^{-2}, M2 : 11.2 daJ.cm^{-2}) and -20°C (M1 : 8daJ.cm^{-2}, M2 : 7.4 daJ.cm^{-2}) following the code requirements (0°C : 7 daJ.cm^{-2} and -20°C : 5 daJ.cm^{-2}). For this program, it was initially decided to establish transition curves for each material using a large number of Charpy-V specimens (30), in order to get well-defined and accurate transition temperatures.

Irradiation Runs

Both irradiation runs started in January 1992. The SILOE run ended in October 1992, after 185 Effective Full Power Days (EFPD) (35 MW). The OSIRIS run was extended to November 1993 after 187 EFPD (65 MW). The delay in the latter was due to a leak on the primary cooling system interrupting reactor operation.

On-line temperature monitoring in each irradiation device was carried out by means of 15 thermocouples. The histogram follow-up ensures temperature requirements that were met on all Charpy-V specimens, during more than 95% of the irradiation time.

Physics-Dosimetry Results

Spectrum Calculations

Specific TRIPOLI-3 Monte-Carlo neutron transport calculations were performed for the 2 irradiations using the ENDF/B-VI library. Calculations of fluxes and spectrum indices are given in table 3 and are compared to the results achieved on mock-up through GAMIN and tungsten damage monitors [5], based on electrical resistivity measurements [8]. The GAMIN damage monitor response is very close to $\Phi_{E>0.1MeV}$ whereas the tungsten damage monitor responds closer to Φ_{dpa} [9].

Table 3 - *Responses Obtained with Neutronic Calculations*

Flux & Indexes	OSIRIS		SILOE	
	Tripoli B6	Dosimetry	Tripoli B6	Dosimetry
$\Phi_{E>1MeV}$ (n.cm^{-2}.s^{-1})	3.99 10^{12}		2.97 10^{12}	
$\Phi_{E>0.1MeV}$ (n.cm^{-2}.s^{-1})	8.56 10^{12}	10.02 10^{12}	14.80 10^{12}	15.20 10^{12}
Φdpa_{Fe} (dpa.s^{-1})	5.59 10^{-9}	6.04 10^{-9}	6.12 10^{-9}	5.82 10^{-9}
$\Phi_{dpa}/\Phi_{E>1MeV}$ (dpa.barn)	1401		2059	

The computed spectral indexes were found to be in good agreement, within 10% of experiment. The ratios $\Phi_{dpa}/\Phi_{E>1MeV}$ are significantly different, from 1400 in the OSIRIS standard spectrum, to 2050 in the SILOE distorted spectrum. In comparison, values of 1450 for the vessel at the peak-flux (1650 at the 1/4 thickness) and of 1630 for the capsules are calculated in the French 3 loop PWRs.

Table 4 gives the relative fluence response in 3 energy groups obtained from TRIPOLI calculations : a very high neutron flux density is found below 1 MeV at SILOE.

Table 4 - *Relative Fluence Response*

Response (%)		0.01-0.1 MeV	0.1-1 MeV	>1MeV
$\Phi_{E>1MeV}$	Osiris	0	0	100
	Siloe	0	0	100
$\Phi_{E>0.1MeV}$	Osiris	0	59	41
	Siloe	0	81	19
Φdpa_{Fe}	Osiris	3	26	71
	Siloe	8	57	35

Figure 1 compares normalised calculated spectra obtained in this program with those met in the French 3 loop PWR vessel at the inner surface and at the capsules.

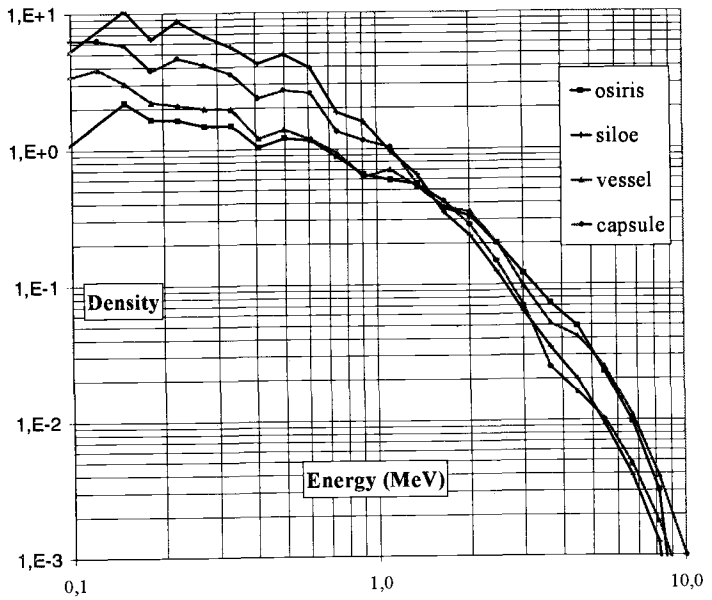


Figure 1 - *Normalised Spectra - ESTEREL Program & PWR 900 MWe Vessel and Capsules*

We can observe very similar spectra between the vessel at its inner surface and OSIRIS and the enveloping feature of the neutron (E<1MeV) density in SILOE with regard to the capsules. This indicates proper relevance of the ESTEREL program in relation with surveillance positions and peak flux at the belt-line up to ½ thickness.

Final Irradiation Fluences

After counting the activity of the flux monitors present in both irradiation rigs, the fluences were processed once with damage dosimetry calibration ($\Phi_{E>0.1MeV}$ and Φ_{dpa}) and once following the PWR surveillance standard practice for $\Phi_{E>1MeV}$. This choice was made to provide "experimentally derived" data, although the $\Phi_{E>1MeV}$ derivation requires a TRIPOLI spectrum analysis and adjustment procedure [6, 7].

Table 5 gives the maximum fluences obtained in the OSIRIS and SILOE irradiation runs (core mid-plane).

Table 5 clearly shows that the spectra met the initial requirements in terms of significant difference in $\Phi_{E>1MeV}$ whereas a similar Φ_{dpa} is reached. Note, however, Φ_{dpa} was found some 15% too low with regard to the specification in SILOE. It is assumed that a constant flux level in the steel block was difficult to be guaranteed, cycle after cycle, in a multipurpose test reactor. An important feature is also that $\Phi_{E>0.1MeV}$ is some 20% higher in SILOE.

Table 5 - *Maximum Fluences (core mid-plane)*

Reactor	Fluence	Damage Dosimetry	"Surveillance" Dosimetry	Uncertainty (1 σ)
OSIRIS	$\Phi_{E>1MeV}$ (n.cm^{-2})		$7.08\ 10^{19}$	± 7,6 %
	$\Phi_{E>0.1MeV}$ (n.cm^{-2})	$1.70\ 10^{20}$		± 4,0 %
	Φ_{dpa} (dpa)	0.102		± 3,2 %
SILOE	$\Phi_{E>1MeV}$ (n.cm^{-2})		$4.26\ 10^{19}$	± 7,6 %
	$\Phi_{E>0.1MeV}$ (n.cm^{-2})	$2.21\ 10^{20}$		± 4,7 %
	Φ_{dpa} (dpa)	0.085		± 5,9 %

Metallurgical Results

The M2 specimens were located in the OSIRIS and SILOE core mid planes, where the axial profile of the flux is nearly flat. Mechanical tests were performed at CEA Saclay.

The M1 specimens were located in the lower and upper part of the experiments. Consequently, the average flux and fluences were some 15 % lower than for the M2 specimens. Mechanical tests were performed at the EDF hot laboratory in Chinon.

Accurate temperature and fluence values were assigned to each Charpy-V specimen, to ensure a sound data analysis. From 30 specimens used in each curve, the 15 best - in terms of irradiation temperature history - were assigned to be tested in the transition zone (average irradiation temperatures and fluences refer to the latter). The Charpy-V curves obtained for both materials M1 and M2 are displayed in Figures 2 and 3.

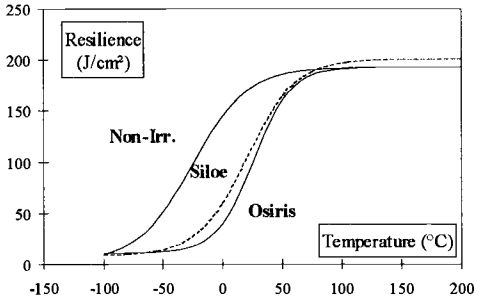


Figure 2 - *Transition Temperature Curves - Material M1*

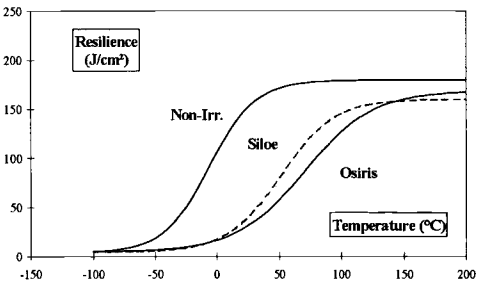


Figure 3 - *Transition Temperature Curves - Material M2*

All the curve shapes are similar. As usual on French materials, no major irradiation effect on the level of the ductile plateau is observed. Greater shifts are obtained for material M2, as expected, and, for each material, in the OSIRIS reactor.

The transition temperature shift (ΔTK_7) is conventionally measured in France at the 56 J (7 daJ.cm^{-2}) level[2]. It is compared with the predicted value given by the FIM mean formula fitted to the behaviours of French used materials [3].

$$\Delta RTNDT\ (°C) = (17.3 + 1537\ (P-0.008) + 238\ (Cu-0.08) + 191.Ni^{2}.Cu)(\Phi_{E>1MeV}/10^{19})^{0.35}$$

with : - if %P < 0.008, then P-0.008=0
- if %Cu < 0.08, then Cu-0.08=0

Table 6 gives the difference (OSIRIS-SILOE) in transition temperature shifts at 56 J with regard to fluence. A primary analysis indicates that the higher embrittlement in OSIRIS is consistent with higher $\Phi_{E>1MeV}$ and Φ_{dpa}. But $\Phi_{E>0.1MeV}$ is lower by 20% in OSIRIS, indicating that this candidate fluence is totally inadequate for embrittlement prediction.

Table 6 - *Differences in Transition Temperature Shifts and Fluences (OSIRIS-SILOE)*

	Transition Temperature Shift Difference		Fluence Difference		
Materials	ΔTK_7 (°C)	Prediction (°C)	Φ_{dpa} (mdpa)	$\Phi_{E>1MeV}$ (10^{19}n.cm^{-2})	$\Phi_{E>0.1MeV}$ (10^{19}n.cm^{-2})
M1	+ 9	+ 7	+ 17	+ 2.47	- 3.7
M2	+ 14	+ 15	+ 18.5	+ 2.77	- 4.5

Despite a lower embrittlement sensitivity, the weld material M1 behaves similar to weld material M2.

The difference predicted by the FIM formula was found to be very close to the observed one.

Damage Analysis

An experimental correlation between embrittlement and fluence has been assessed. Also an attempt to correlate embrittlement and neutron spectrum through numerical analysis has been made. The TRIPOLI Monte-Carlo computations were normalised on actual fluence measurements.

Correlation between Embrittlement and Fluences

As $\Phi_{E>0.1MeV}$ was discarded (see section Metallurgical Results), a more refined analysis is needed to determine whether $\Phi_{E>1MeV}$ or Φ_{dpa} is the most appropriate correlation parameter.

The initial aim was a direct comparison of the OSIRIS and SILOE measured embrittlement at the same Φ_{dpa}. In spite of quite closed Φ_{dpa} reached in OSIRIS and SILOE, the embrittlement in SILOE is significantly lower than the embrittlement in OSIRIS. As Φ_{dpa} is some 15 % lower in the SILOE irradiation, further analysis is required : the embrittlement in SILOE can be derived at an OSIRIS equivalent Φ_{dpa} level using a $(\text{fluence})^n$ dependence. This dependence is generally observed, n value is between 0.35 and 0.50, and is consistent with the EDF surveillance program experience for this type of materials.

Similar derivation was made to compare the embrittlement at the same $\Phi_{E>1MeV}$. Both correlations at the same fluence level are given in Table 7. In this table, a n value of 0.4 is displayed but any other value in the range mentioned above leads to similar conclusions.

Table 7 - *Comparison between the Embrittlements in OSIRIS and SILOE at the same Fluence [Difference in ΔTK_7 (OSIRIS-SILOE)]*

Materials	same Φ_{dpa}	same $\Phi_{E>1\,MeV}$
M1	+ 5°C	- 2°C
M2	+ 9°C	0°C

As seen in Table 7, the same Φ_{dpa} in OSIRIS and SILOE, leads to higher embrittlement in OSIRIS. Note that + 9°C difference in weld material M2 was indeed considered to be significant with regard to Charpy test statistics obtained with 30 specimens.

In terms of exposure parameter, $\Phi_{E>1MeV}$ gives a very good correlation for both weld materials. Reasonable fits are also possible using dpa, however use of this parameter did not exhibit any improvement in fitting.

Correlation between Embrittlement and Spectrum

From computed spectra, two simple models were used to correlate embrittlement with neutron energies.

First, a 2 group - below and above 1 MeV - model was applied for evaluating the contribution of each group to the embrittlement of the materials. Table 8 provides embrittlement (in term of ΔTK_7) percentage for a factor n = 0.4.

Table 8 - *Energy Group Contribution to Embrittlement*

	0.1 - 1 MeV		> 1 MeV	
Materials	OSIRIS	SILOE	OSIRIS	SILOE
M1	4 %	12 %	96 %	88 %
M2	0	0	100 %	100 %

It must be noted that for both spectra, contribution of neutrons below 1 MeV to embrittlement is much lesser than predicted by $\Phi_{E>0.1MeV}$ or Φ_{dpa} (see Table 4) and is almost negligible in the case of material M2.

A second approach consisted of deriving a suitable neutron energy threshold E_s such as the embrittlement is correlated to the neutrons with an energy greater than E_s. For n = 0.4, thresholds were found to be 0.93 MeV for material M1 and 1.04 MeV for material M2. Again, these "effective" energy thresholds are very close to 1 MeV.

Conclusions

An extensive irradiation and physics/dosimetry program was carried out in France by EDF and CEA to obtain an experimental correlation between French PV steel embrittlement, and fluence $\Phi_{E>1MeV}$, $\Phi_{E>0.1MeV}$ or Φ_{dpa}, in order to assess a potential neutron spectrum effect.

In order to fulfill this objective, all experimental parameters were accurately controlled, in particular the neutron and gamma environments.

New high-capacity irradiation rigs have been developed by CEA to test 2 materials in parallel with a large number of Charpy-V specimens. Two irradiations runs were successfully carried out in the SILOE and OSIRIS test reactors. Full thermal and neutronic validation programs were achieved. Two different irradiation spectra were used.

- a standard spectrum in OSIRIS where 70% of damage response in dpa come from neutrons with an energy higher than 1 MeV,
- a "distorted" spectrum in SILOE where conversely 60% of the damage response in dpa come from neutrons with an energy lower than 1 MeV.

Two weld materials used exhibited the same embrittlement behaviour. In terms of damage analysis, $\Phi_{E>0.1MeV}$ didn't work as well as a measure of embrittlement behaviour, $\Phi_{E>1MeV}$ provided a reasonable description of embrittlement, while Φ_{dpa} did not bring any better correlation.

In spite of the enhanced low energy neutron spectrum designed for the purpose of this program, it was not possible to observe a significant neutron influence below 1 MeV on low Cu steels (%CU $\leq$ 0.1). This has to be taken into account for the application of available displacement damage models and should lead to further work in this matter. It would be interesting to have more data in order to demonstrate if there is or not any significant influence of intermediate energy neutrons.

This program allowed obtaining important results concerning the vessel life assessment of French PWRs, which is checked by an adequate regulatory surveillance program. The results on two French PV representative materials have been obtained in test reactors under well-defined conditions (temperature, neutronic environment). An approach similar to a surveillance program (dosimetry, mechanical tests) was used.

The results can be summarised as follows:

- $\Phi_{E>1MeV}$ is confirmed as being the most appropriate exposure parameter for PV steel embrittlement,
- no spectrum effect on embrittlement in the range of spectra found in a PWR (vessel - internal surface, ¼ thickness - and capsules) has to be taken into account,
- good consistency has been obtained between the different ways for assessing the neutronic parameters (calculations, damage dosimetry, "surveillance type" dosimetry) of two different environments.

In terms of relevant neutronic parameters used (and the way to get them) and neutronic representativity of surveillance program, these conclusions strengthen the methodology applied in France for assessing PV life-time.

References

[1] Pichon C., Soulat P., Houssin B. and al., "Radiation embrittlement of EDF pressure vessels steel," *Fontevraud III - Contribution of materials investigation to the resolution of problems encountered in PWR,* Fontevraud, Volume 2, p 616 (1994)

[2] Pichon C., Brillaud C., and al., "Pressure vessel steel surveillance program : developments, experience feed-back and perspectives," *OCDE-NEA-CSNI,* Espoo (1990)

[3] Guionnet C., Houssin B., and al., "Radiation embrittlement of PWR reactor vessel weld metals - Nickel and copper synergism effects," *ASTM-STP 782* (1982)

[4] Nimal J.C., Bourdet L., and al., "Neutron spectrum effect on pressure vessel embrittlement in PWRs," *7th International Symposium ASTM-EURATOM on Reactor Dosimetry,* Strasbourg, EUR 14356, p. 31 (1992)

[5] Alberman A., Béretz D., Bourdet L., Hédin F., Rieg C., Soulat P., "Neutron spectrum effect on pressure vessel embrittlement : dosimetry and qualification of irradiation locations in OSIRIS and SILOE," *8th International Symposium ASTM-EURATOM on Reactor Dosimetry*, Vail, ASTM-STP 1228 , p. 472 (1993)

[6] Nimal J.C., Bourdet L., and al., "Neutronic characteristics assessment of French 900 MWe PWR surveillance program," *7th International Symposium ASTM-EURATOM on Reactor Dosimetry*, Strasbourg, EUR 14356, p. 161 (1992)

[7] Bévilacqua A., Brillaud C., and al., "Pressure vessel surveillance dosimetry improvement in new EDF PWRs," *6th International Symposium ASTM-EURATOM on Reactor Dosimetry*, Jackson Hole, ASTM-STP 1001, p. 62 (1988)

[8] Alberman A., Genthon J.P., Zijp W.L., Nolthenius H.J., "New damage dosimetry development using tungsten technic," *4th International Symposium ASTM-EURATOM on Reactor Dosimetry,* Washington, NUREG CP-0029, p. 321 (1982)

[9] Alberman A., and al., "Dosimetry experiment "DOMPAC" - Neutronic simulation of the PWR pressure vessel thickness - Irradiation damage characterization," *3th International Symposium ASTM-EURATOM on Reactor Dosimetry,* Ispra, EUR 6813, p. 407 (1980)

Matti J. Valo,[1] Amir D. Amaev,[3] Ralf Ahlstrand,[2] Dmitry A. Chistiakov,[4] Eugene Krasikov,[3] Aleksander Kryukov,[3] Anatoly M. Morosov,[4] Vladimir A. Nikolaev,[4] Pavel Platonov,[3] Rauno Rintamaa,[1] Valery V. Rybin,[4] Yaroslav Shtrombakh,[3] and Kim Wallin[1]

Characterization of the Decommissioned Novovoronesh-1 Pressure Vessel Wall Materials by Through-Wall Trepans

Reference: Valo, M. J., Amaev, A. D., Ahlstrand, R., Chistiakov, D. A., Krasikov, E., Kruykov, A., Morosov, A. M., Nikolaev, V. A., Platonov, P., Rintamaa, R., Rybin, V. V., Shtrombakh, Y., and Wallin, K., **"Characterization of the Decommissioned Novovoronesh-1 Pressure Vessel Wall Materials by Through-Wall Trepans,"** *Effects of Radiation on Materials: 19th International Symposium, ASTM STP 1366*, M. L. Hamilton, A. S. Kumar, S. T. Rosinski, and M. L. Grossbeck, Eds., American Society for Testing and Materials, West Conshohocken, PA, 2000.

Abstract: Material properties of the Novovoronesh-1 pressure vessel were characterized after 20 years of plant operation. The unit was the first commercial PWR unit in Russia producing 210 MW electric power. It was commissioned in 1964 and shut down in 1984. Wall thickness of the vessel is 120 mm, including 20 mm of cladding. The vessel contained only circumferential welds. The coolant temperature was 250°C. Nine through-wall trepans of outer diameter 120 mm were cut out from the vessel both from the weld seams and the base metal forging rings. The trepans were studied by RRC-KI, PROMETEY and VTT. The paper is focusing on the Charpy-V and fracture toughness test data of the critical core weld. Due to the lack of archive material the unirradiated material condition was estimated by a reference annealing procedure.

Keywords: irradiation embrittlement, pressure vessel, Charpy-V, fracture toughness, trepan, annealing, VVER

Introduction

Pressure vessel embrittlement is an essential phenomenon to be taken into account in the integrity assessment of pressure vessels. Especially estimation of the effect of

[1]Group Manager, Research Manager and Research Professor, respectively, VTT Manufacturing Technology, P.O. BOX 17042, FIN-02044 VTT, Finland.
[2]Manager, IVO Power Engineering LTD, FIN-01019 IVO, Finland.
[3]Russian Research Centre-Kurchatov Institute, Kurchatov sq. 1, 123182 Moscow, Russia.
[4]PROMETEY, Institute of Structural Materials, 193167, St. Petersburg, Monastyrka riv. emb., 1, Russia.

Copyright© 2000 by ASTM International www.astm.org

long-term, low-flux irradiation on material properties is often experimentally non-feasible and hence one has to rely on studies of trepans taken from decommissioned plants. The study of Novovoronesh-1 trepans was the first attempt in Russia in this direction. Novovoronesh-1 was the first commercial PWR plant in Russia, which was in operation twenty years from 1964 to 1984. The output of the plant was 210 MW and the vessel wall temperature 250°C. At the end of the operation cycle for a short period the vessel wall temperature could have decreased even down to 228°C. The forging rings of the vessel were made of 15Kh2MFA steel and the circumferential weld seams were prepared with welding wire Sv-10KhMFT. The vessel had a 20 mm thick cladding.

No archive vessel material was available and hence the initial material state was estimated by simulating heat treatments. Seven through-wall trepans were taken from the critical core weld and two outside the weld. Only toughness data, i.e., ISO Charpy-V and fracture toughness, of the weld seam and the adjacent base metals are reported in this paper. The institutes *Russian Research Centre-Kurchatov Institute* (RRC-KI) and *PROMETEY* from Russia and *VTT* and *IVO Power Engineering* from Finland took part in the material characterization. The experimental study was performed during the years 1990-1991.

Experimental Procedures

Cutting of Trepans and Preparation of Specimens

The through-wall trepans of dimensions 120 mm x D110 mm were cut by circular drills from the vessel wall. The locations of the trepans in the critical core weld, which lies below the core mid-plane, is shown in Figure 1. The reactor core has a 60° circumferential symmetry but the trepans were not taken at symmetric positions.

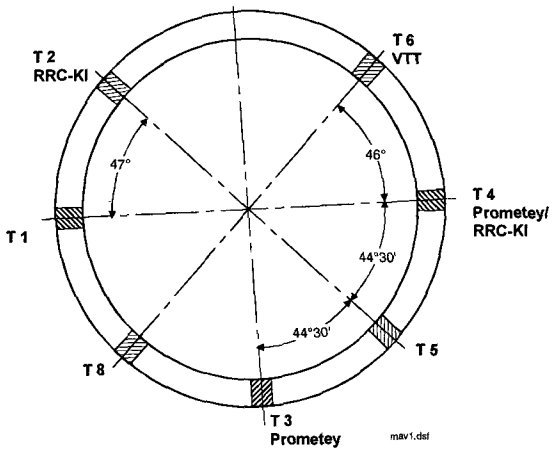


Figure 1 - *Locations of trepans in the reactor core weld. A base metal trepan T 7 was cut 300 mm below trepan T8*

RRC-KI studied the trepan T2, PROMETEY the trepan T3, RRC-KI and PROMETEY jointly the trepans T4 and T7 and VTT the trepan T6. The weld seam of trepan T6 contained a repair weld, which comprised the outer half of the weld seam. The repair weld was not studied.

VTT and RRC-KI used only ISO Charpy-size specimens but PROMETEY used, in addition, also 12.5 mm CT-specimens. RRC-KI and PROMETEY used standard specimens but VTT prepared all specimens by reconstitution from 16 mm inserts [1]. The cutting schedule of the trepans is shown in Figures 2-4. RRC-KI and PROMETEY used mechanical tools for cutting and VTT an electric wire discharge machine.

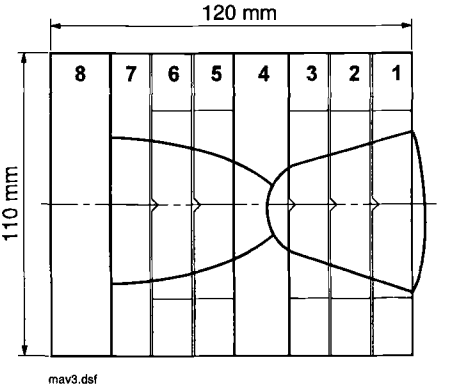


Figure 2 - *Sectioning scheme of trepan T 2 studied by RRC-KI*

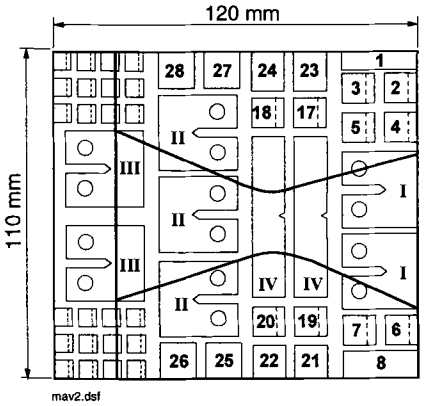


Figure 3 - *Sectioning scheme of trepan T 3 studied by PROMETEY*

Testing

The Charpy-V tests were performed following the guidelines of ASTM E 23-92 except that a DIN tup was used in the tests.

Each partner made the fracture toughness tests following his own procedure. Only fracture toughness values referring to cleavage initiation are reported in this work. The data reported by the partners are used as such and no round robin exercises or harmonization of testing or analyzing methods were undertaken between the partners.

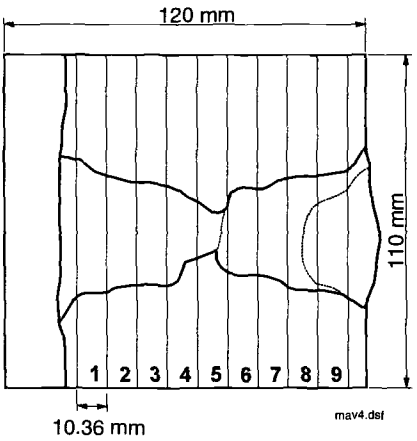


Figure 4 - *Sectioning scheme of trepan T6 studied by VTT. The outer portion of the weld seam consisted of a repair weld, which was not characterized*

Notation of Specimen Orientations

The ASTM notation of specimen orientations for forging is used in the paper also for the weld. Both the metallurgical and the vessel cylindrical coordinates are used i.e. TS = ZR and LS = CR.

Data Analyses

The Charpy-V transition temperatures were defined by the conventional TANH-fitting procedure.

$$E = \frac{A}{2} * \left\{ 1 + TANH\left[\frac{T - T_0}{C} \right] \right\} \quad (1)$$

where E is the impact energy, A the upper shelf energy and the lower shelf energy is assumed to be zero.

Fracture toughness data was analyzed following the basic ideas of ASTM Test method for the determination of reference temperature, T_0, for ferritic steels in the

transition range (E1921-1997). The K-values are first normalized to the B = 25 mm specimens size by applying the size correction (2), where K_{min} = 20 MPa√m.

$$K_{B2} = K_{min} + (K_{B1} - K_{min}) \cdot \left(\frac{B_1}{B_2} \right)^{0.25} \tag{2}$$

The reference transition temperatures T_0 corresponding to the median fracture toughness of 100 MPa√m for the B = 25mm specimen size are estimated from the maximum likelihood formula enabling data censoring.

$$\sum_{i=1}^{n} \frac{\delta_i \cdot \exp\{c \cdot [T_i - T_0]\}}{a - K_{min} + b \cdot \exp\{c \cdot [T_i - T_0]\}} - \sum_{i=1}^{n} \frac{(K_{Jc_i} - K_{min})^4 \cdot \exp\{c \cdot [T_i - T_0]\}}{\left(a - K_{min} + b \cdot \exp\{c \cdot [T_i - T_0]\}\right)^5} = 0 \tag{3}$$

where a = 31 MPa√m, b = 77 MPa√m and c = 0.019 1/°C. Factor δ_i = 1 when the test has ended in brittle fracture and δ_i = 0 when no brittle fracture has occurred in the test or the value is censored.

The model has been developed to characterize the ductile-to-brittle transition regime, rather than the lower-shelf or totally ductile fracture behavior. The model may therefore give inaccurate results in the lower-shelf regime, which should in particular be notified if only low-temperature data are available.

The basic testing requirement is that cleavage fracture initiation will occur in the test [2]. However, the reliability of the estimation is improved if an upper bound (4) for the accepted measured K_{Jc}-values is given according to ASTM E1921-1997. All the test values, which exceeded (4) were censored to the limit value.

$$K_{Jc\,lim} = \left(\frac{Eb\sigma_{ys}}{30} \right)^{0.5} \tag{4}$$

When ductile end of test values are included in the analyses (with δ_i = 0) the K_{Jclim}-limit should always be followed.

Chemical Analyses

VTT used the *Spectrolab-S Optical* Emission spectrometer, RRC-KI the Spectrovac FSQ Optical Emission spectrometer and PROMETEY wet chemistry methods for chemical analyses. The measured chemistry profiles are shown in Figures 5-6. The values given by the partners are used as such in the analyses.

Neutron Dosimetry

Gidropress provided the neutron spectrum in five energy groups at six radial positions in the vessel wall based on ANIS calculations, where the CASK cross-section library was used. Each partner made independent fluence evaluations for their trepans. The evaluation was based on the specific Mn-54 activity of the carbon steel and on the

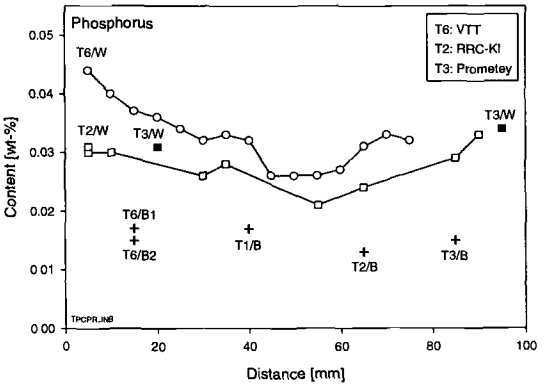


Figure 5 - *Through-wall phosphorus profiles in the weld seam. The distance is measured outwards from the cladding-carbon steel fusion line. Base metal values are not located at the sampling positions*

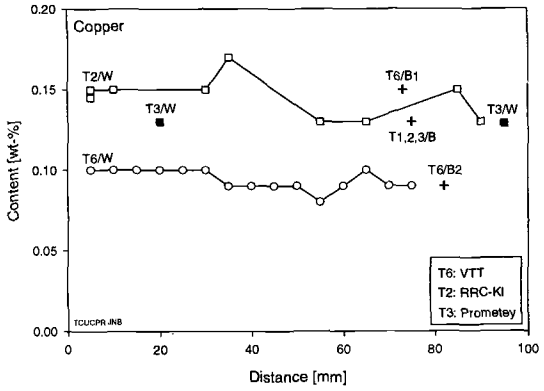


Figure 6 - *Through-wall copper profiles in the weld seam. The distance is measured outwards from the cladding-carbon steel fusion line. Base metal values are not located at the sampling positions*

Nb activity of the cladding. The evaluated fluence profiles are given in Figure 7. Trepans T2 and T3 were taken from equal positions regarding the 60° core symmetry and the trepan T6 from a 30° off-phase position. Because the trepan positions are not fixed to the absolute core coordinates (Figure 1) no conclusion on the consistency of the fluence estimates can be made except that the fluence estimates for T2 and T3 deviate slightly from each others.

The fluence values given by the partners are used as such in the analyses. The fluences in the report are given in units of [$x10^{19}$ n/cm^2, E > 0.5 MeV], if not otherwise indicated. The ratio of the units [E > 1 MeV] / [E > 0.5 MeV] in the vessel wall is near 2.0.

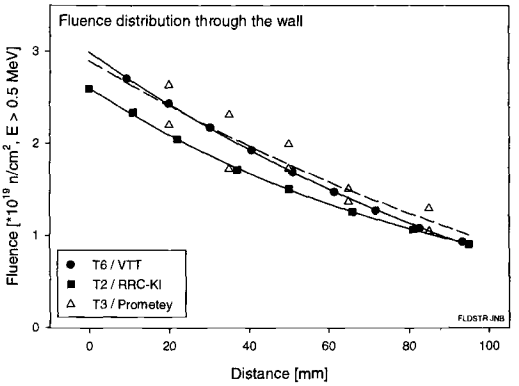


Figure 7 - *Estimated through wall neutron fluence distributions in the trepans No. 2, 3 and 6. Origin of the x-axis is the cladding fusion line*

Experimental Results

Tensile Data

Room temperature tensile test values measured by Prometey for trepan T3 are given below (Table 1).

Table 1 - *Yield Strength of Trepan T3 at 20°C, Prometey Data*

Material	Condition	Fluence	$R_{p0.2\%}$ / MPa
base	as received	2.5	690
base	as received	1.3	605
base	650°C/ 2h	2.5	525
base	650°C/ 2h	1.3	525
weld	as received	1.1	620
weld	650°C/ 2h	1.1	570

Charpy-V Data

Only Charpy-V impact energy data is discussed in the paper. The transition curves (Figures 8-14) and the transition temperature values (Tables 2-3) are given below.

Table 2 - *Charpy-V Data for Base and Weld Metals, Trepan T6, VTT Data*

Material	Condition	n	Plate	Fluence	T_{47J}/°C	P %	Cu %
B1-CR	as received	19	2,4,6	1.5-2.4	33	0.016	0.16
B1-CR	470°C/168h	13	6	1.5	-7	0.016	0.16
B1-CR	650°C/2h	10	4,5	1.7-1.9	-30	0.016	0.16
B1-ZR	as received	25	1,3,5	1.7-2.7	54	0.016	0.16

Material	Condition	n	Plate	Fluence	T_{47J}/°C	P %	Cu %
B1-ZR	as received	8	9	0.9	35	0.016	0.16
B1-ZR	470°C/168h	22	3,5,9	0.9-2.2	25	0.016	0.16
B2-ZR	as received	19	4,7,9	0.9-1.9	30	0.015	0.12
B2-ZR	470°C/168h	10	4,8	1.1-1.9	7	0.015	0.12
B2-ZR	650°C/2h	7	3	2.2	-25	0.015	0.12
W-ZR	as received	9	1	2.7	72	0.044	0.10
W-ZR	as received	8	2	2.4	155	0.037	0.10
W-ZR	as received	7	4	1.9	107	0.033	0.09
W-ZR	as received	5	5	1.7	65	0.026	0.09
W-ZR	470°C/168h	14	1,4,5	1.7-2.7	15	0.030	0.09
W-ZR	650°C/2h	9	2	2.4	-5	0.037	0.10

n number of specimens

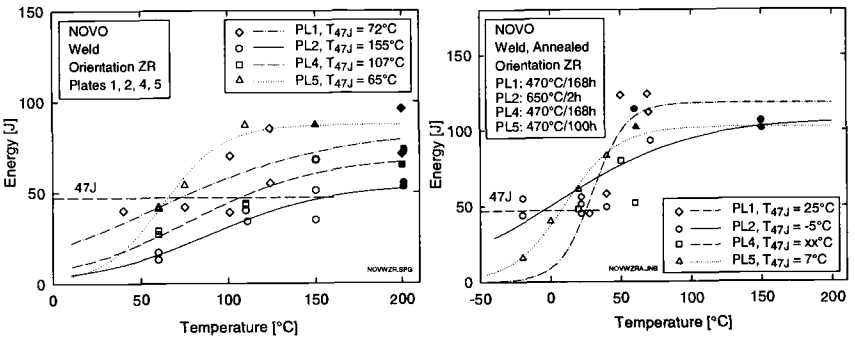


Figure 8 - *Charpy-V data for weld in the as-received and annealed conditions, TS orientation, VTT data*

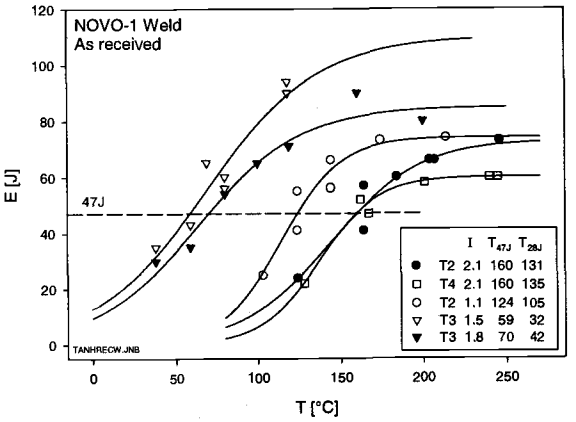


Figure 9 - *Charpy-V data for weld in the as-received condition, TS-orientation, RRC-KI and Prometey data*

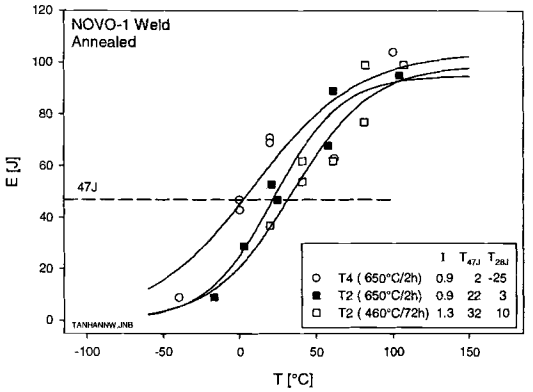


Figure 10 - *Charpy-V data for weld in the annealed conditions, TS-orientation, RRC-KI and Prometey data.*

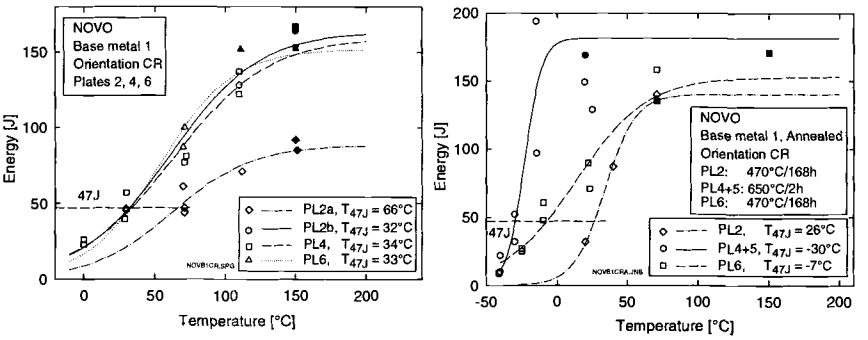


Figure 11 - *Charpy-V data, base metal-1 in the as-received and annealed conditions, (CR) LS-orientation, VTT data*

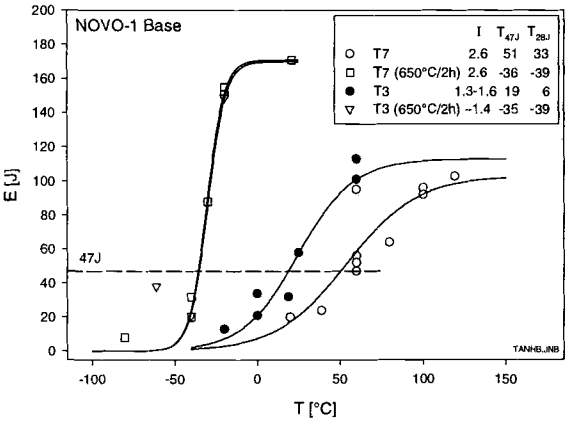


Figure 12 - *Charpy-V data for base metals, RRC-KI and Prometey data*

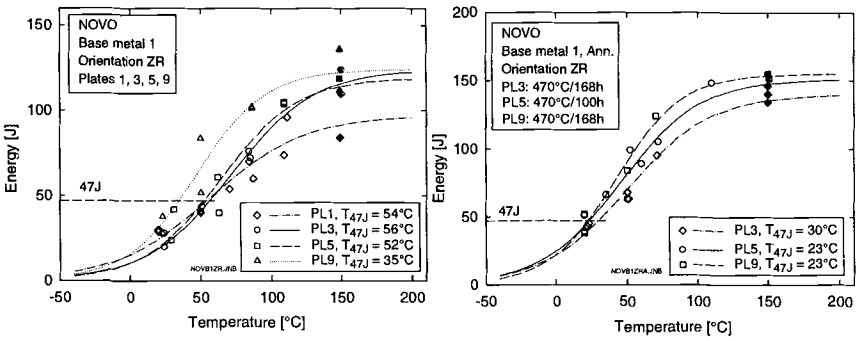


Figure 13 - *Charpy-V data, base metal-1 in the as-received and annealed conditions, (ZR) TS-orientation, VTT data*

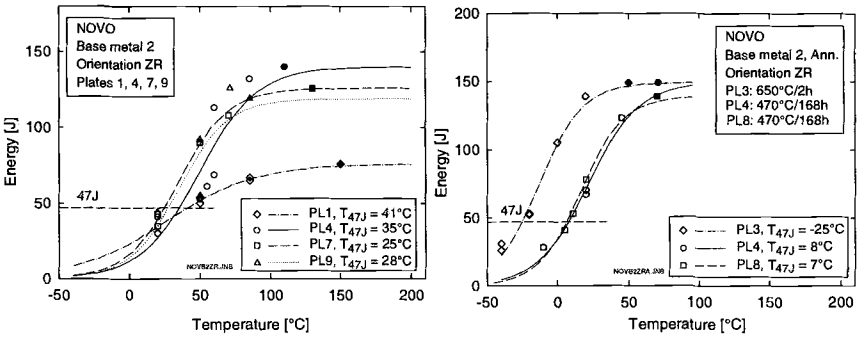


Figure 14 - *Charpy-V data, base metal-2 in the as-received and annealed conditions, (ZR) TS-orientation, VTT data*

Table 3 - *Charpy-V Data for Base and Weld Metals, RRC-KI and PROMETEY Data*

Material	trepan	condition	n	plate	fluence	T_{47J} °C	P wt-%	Cu wt-%
base	T7	as received	10	-	2.6	51	0.015	0.13
base	T7	650°C/2h	7	-	2.6	-36	0.015	0.13
base	T3	as received	7	IV	1.3-1.6	19	0.015	0.13
base	T3	650°C/2h	3	IV	c. 1.4	-35	0.015	0.13
weld	T2	as received	7	5	2.1	160	0.028	0.15
weld	T2	as received	7	2	1.1	124	0.028	0.15
weld	T2	650°C/2h	7	1	0.9	22	0.033	0.13
weld	T2	460°C/72h	7	3	1.3	32	0.024	0.13
weld	T3	as received	7	IV	1.5	59	0.025	0.13
weld	T3	as received	6	IV	1.8	70	0.025	0.13
weld	T4	as received	6	5	2.1	160	0.028	0.15
weld	T4	650°C/h	6	1	0.9	2	0.033	0.13

Fracture Toughness Data

The fracture toughness transition curves (Figures 15-20) and the transition temperatures (Tables 4-5) are given below.

Table 4 - *Fracture Toughness of Base and Weld Metals, VTT Data, Charpy-size Specimens, trepan T6*

Material	condition	n	plate	fluence	T_0	P %	Cu %
B1-CR	as received	12	8	1.1	-73	0.016	0.16
B1-ZR	as received	7	7	1.3	-63	0.016	0.16
B1-ZR	650°C/2h	8	7	1.3	-98	0.016	0.16
B2-ZR	as received	7	2	2.4	-63	0.015	0.12
B2-ZR	as received	11	5	1.7	-76	0.015	0.12
B2-ZR	650°C/2h	8	6	1.5	-121	0.015	0.12
W-ZR	as received	8	3	2.2	77	0.034	0.10
W-ZR	470°C/168h	8	6	1.5	-6	0.026	0.08
W-ZR	650°C/2h	8	3	2.2	-26	0.034	0.10

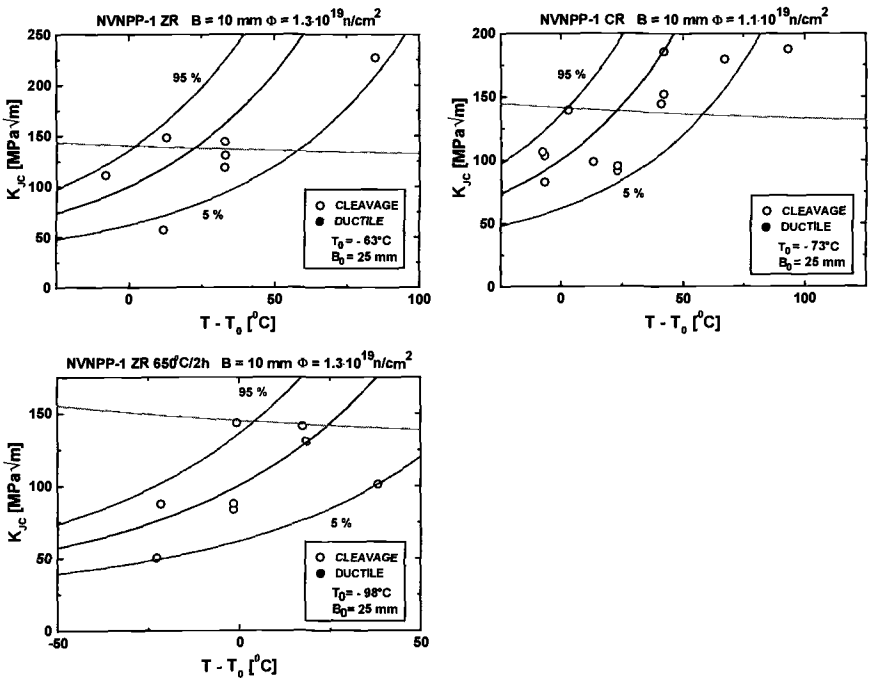
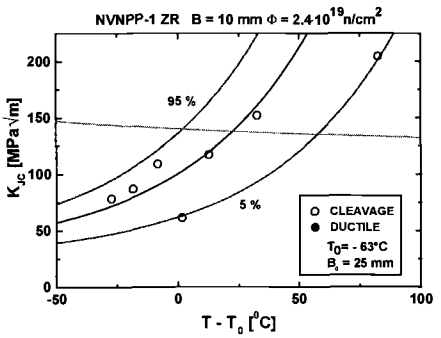
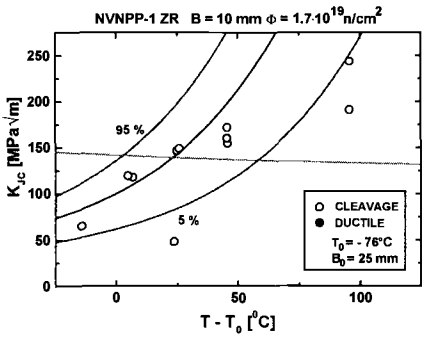


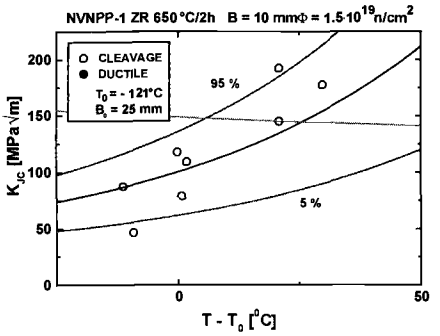
Figure 15 - *Fracture toughness of base metal-1, TS (ZR) - and LS (CR)- orientations, VTT data. The horizontal curve refer to size criterion (eq. 4)*

Table 5 - *Fracture Toughness Data for Base and Weld Metals, RRC-KI and PROMETEY Data*

Material	Condition	n	Plate	Trepan	Fluence	T_0/ °C	P %	Cu %
base	as received	8	-	T7	2.6	-48	0.015	0.13
base	650°C/2h	9	-	T7	2.6	-98	0.015	0.13
base	as received	4	II	T3	2.4	-18	0.015	0.13
base	650°C/2h	5	II	T3	2.4	-98	0.015	0.13
weld	as received	6	I	T3	1.0	+77	0.034	0.13
weld	650°C/2h	6	I	T3	1.0	+12	0.034	0.13
weld	as received	5	II	T3	2.4	+109	0.031	0.13
weld	as received	5	III	T3	2.8	+89	0.031	0.13







Discussion

The definition of the Charpy-V based critical brittleness transition temperature Tk in the Russian code [3] is rather complicated. The transition temperature criterion depends on the yield strength of the material and in addition requirements are set for the mean

and minimum impact energy values at Tk and at Tk+30°C. Because the data points in the measured transition curves are few and the criteria can not be applied properly T_{47J} is used for all materials as Tk. According to the code the T_{47J} criterion is applied for materials having Rp0.2% in the range of 549 - 687 MPa.

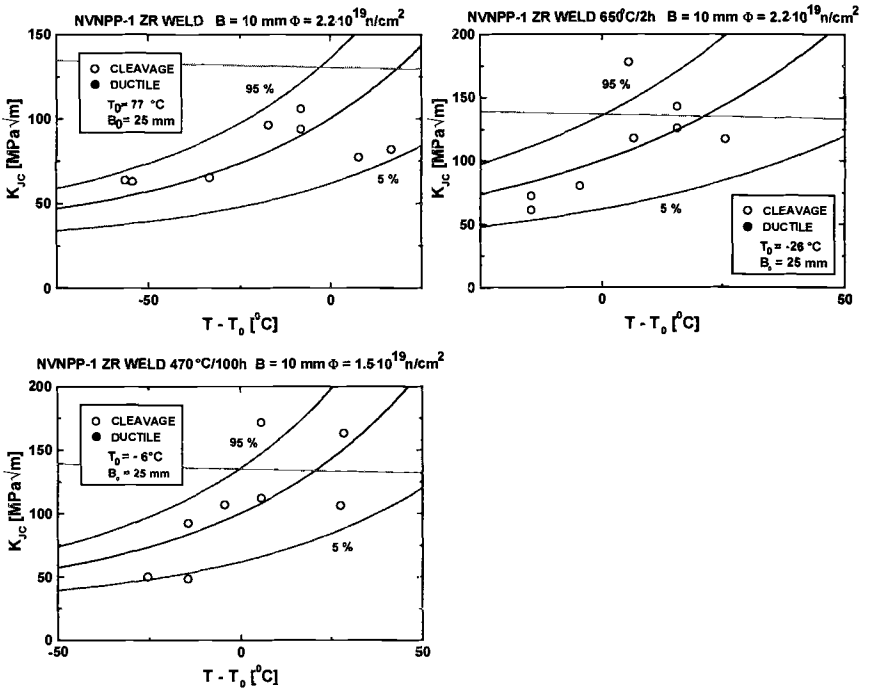


Figure 17 - *Fracture toughness of weld metal, TS-orientation, VTT data. The horizontal curve refer to size criterion (eq. 4)*

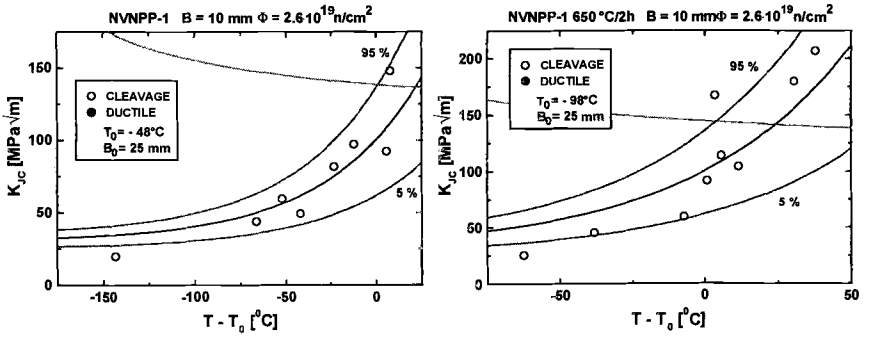


Figure 18 - *Fracture toughness of base metal in the as received and annealed conditions, TS-orientation, RRC-KI data. The horizontal curve refer to size criterion (eq. 4)*

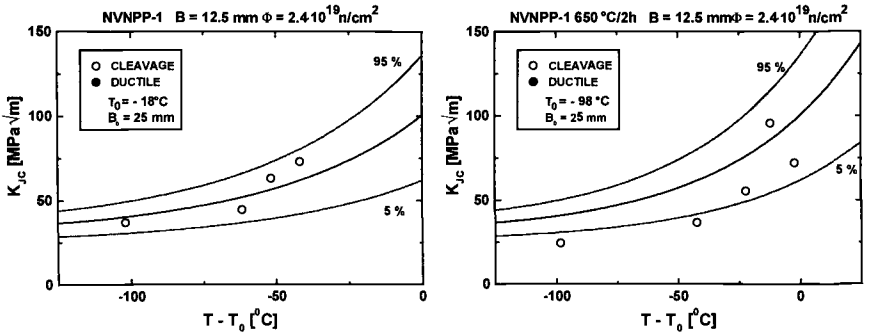


Figure 19 - *Fracture toughness of base metal, TS-orientation, PROMETEY data. The horizontal curve refer to size criterion (eq. 4)*

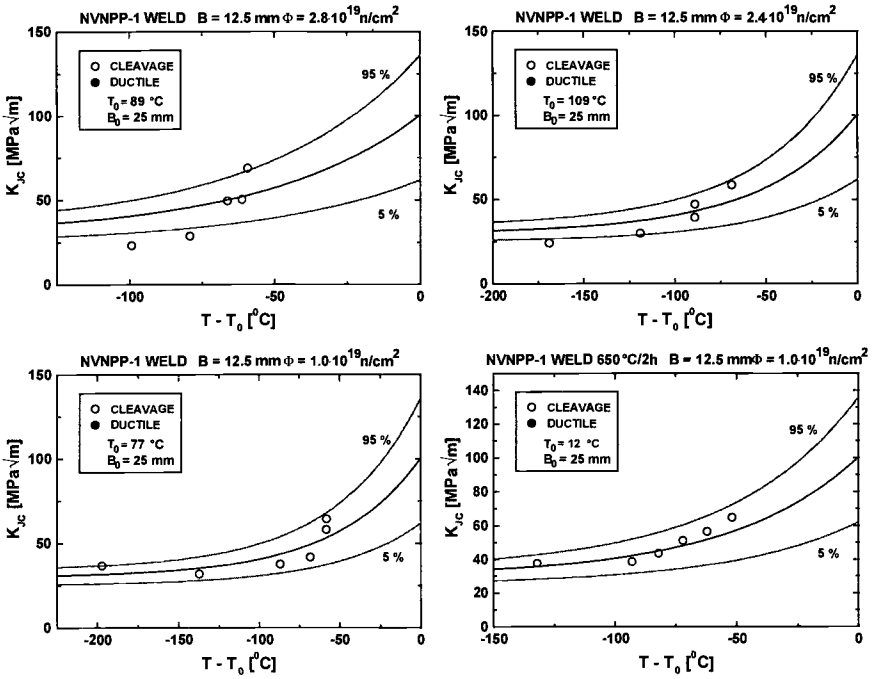


Figure 20 - *Fracture toughness of weld, TS-orientation, PROMETEY data. The horizontal curve refer to size criterion (eq. 4)*

The measured T_{47} and T_0 transition temperatures for all trepan materials and material conditions are shown in Figures 21-23. The annealing recovery of the VVER-type base and weld materials is in general relatively good [4] and the residual embrittlement is not sensitive to the impurity level (P < 0.04 %) or the irradiation fluence of the material in test reactor or surveillance irradiation. Hence an estimation

for the unknown unirradiated material condition can be made by a thermal heat treatment. Both the 470°C and the 650°C heat treatments have been applied for same materials in five cases. The 650°C heat treatment gives in average 20°C lower transition temperatures (ranging from 8°C to 32°C) than the 470°C heat treatment. The 650°C/2h - annealed condition is used as the reference condition for the data. Tko is also assumed to be uniform through the trepan sample.

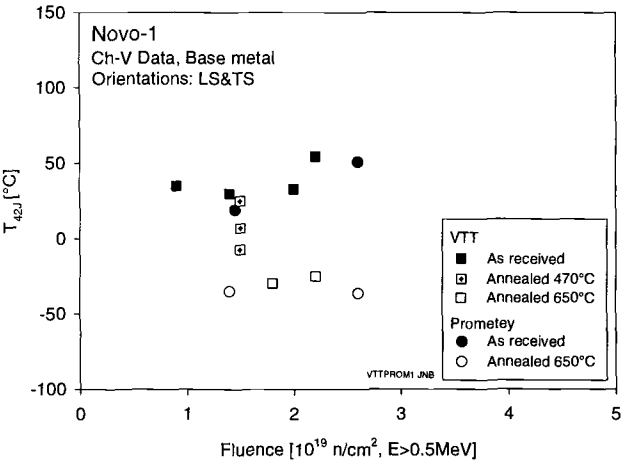


Figure 21 - *The Charpy-V 47J transition temperatures versus fluence for the base metals*

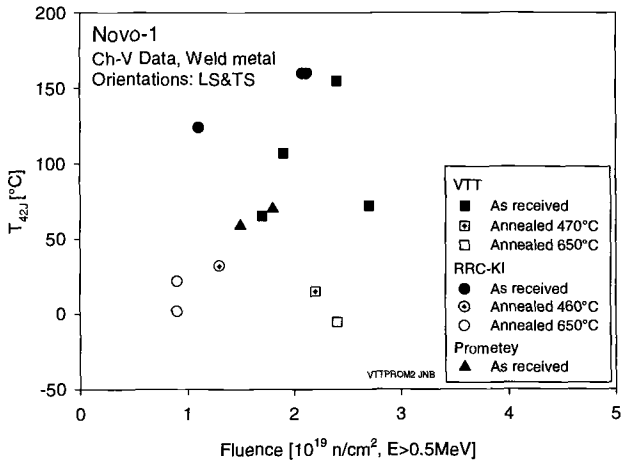


Figure 22 - *The Charpy-V 47J transition temperatures versus fluence for the weld metal*

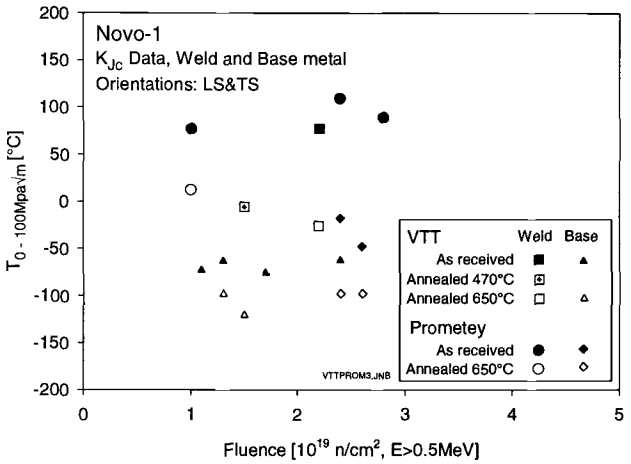


Figure 23 - *The T_o-transition temperatures for base and weld metals*

The measured transition temperature shifts versus fluence for all materials are given in Figure 24. Figure 24 indicates rather large and inconsistent scatter in the Charpy-V weld data. An evident reason for this is the low upper shelf (54 J-70 J) of the irradiated weld in relation to the applied transition temperature criterion E = 47 J as well as the low number of data points in each transition curve (around 5-7). The Charpy-V weld metal transition temperature shifts are roughly divided into two groups i.e. high shifts near 150°C and small shifts near 60°C. The small shifts are measured with specimens located near the weld root, where the weld seam phosphorus impurity has its minimum

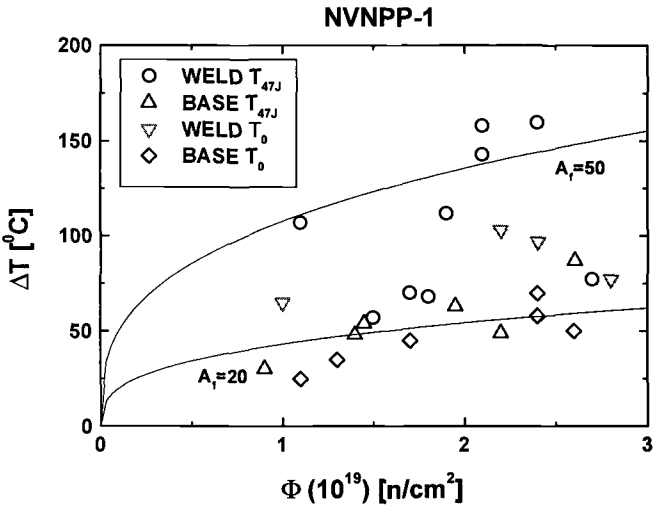


Figure 24 - *Transition temperature shifts versus fluence*

value. The fracture toughness of the weld behaves more uniformly even if the number of data points in each transition curve is comparable to the number of Charpy-data points and even if the Prometey weld data is measured near the lower shelf of K_{JC}, where temperature sensitivity is low and hence the estimation of the T_0-value should be inaccurate. Figure 24 indicates only a slight fluence dependence in the transition temperature shifts. In the base metal there is practically no measured embrittlement gradient in the vessel wall as is clearly seen in Figures 12-14. Figures 12 and 14 include also some divergent base metal curves, which are measured with specimens located near (app. 5mm) the cladding or weld seam fusion lines.

Phosphorus and copper impurities explain part of the measured embrittlement. The current Russian code expression for embrittlement of weld metal at 250°C irradiation is

$$\Delta T_F = A_F * \left(\frac{F_n}{F_o}\right)^{1/3} \tag{5}$$

$$A_F = 800 \cdot (P[\%] + 0.07 \cdot Cu[\%]) + 8$$

where F_0 is 10^{18} n/cm^2, E>0.5MeV.

An essential feature of the Novovoronesh-1 weld is the variation of impurity contents in the weld seam. The code equation is checked against the measured data in Figure 25 by plotting $\Delta T/A_F$ versus fluence. The high shift weld metal Charpy-V data and one base metal data point exceed the prediction of the code. The weld metal points remain over the curve even if the 470°C annealing is used for defining Tko. The weld shifts remain below the code curve if T_0 is used as the toughness parameter.

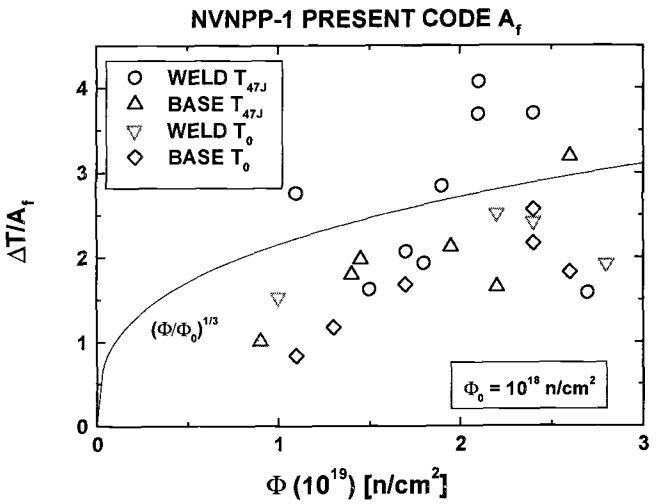


Figure 25 - *$\Delta T/A_F$ versus fluence, the points located above the curve indicate higher embrittlement than the code prediction*

The Russian code PNAE G-7 is based on the Charpy test as most other regulatory codes. The correlation of the Charpy-V based Tk (T_{47J}) and the directly measured fracture toughness T_0 is shown in Figure 26 for the Novovoronesh-1 trepan data. The use of Tk instead of the directly measured fracture toughness is a conservative approach especially for base metal. The data also indicate that base and weld metals behave as separate subgroups. In ASTM E1921-97 a correlation between 27 J Charpy-energy and T_0 is given. This correlation for Novovoronesh-1 data is given in Figure 27. This later correlation even emphasizes the difference between the base metal and weld metal behaviors.

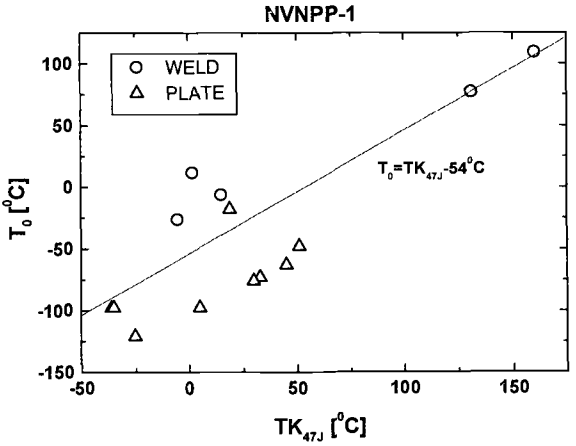


Figure 26 - *Comparison between T_k and the master curve T_0 for the Novovoronesh 1 trepan results. The correlation T = Tk-54°C is derived from a large VVER database*

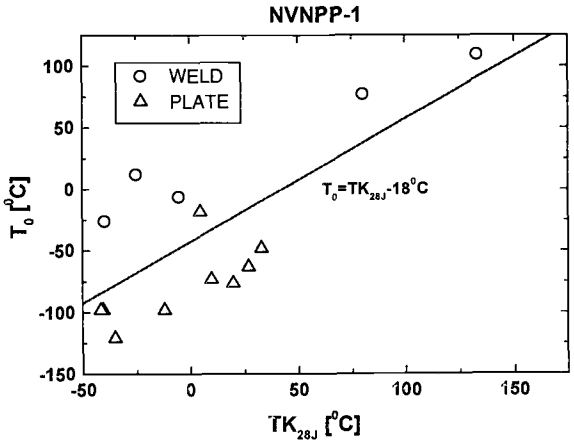


Figure 27 - *Correlation of Tk-28J and the master curve T_0 for the Novovoronesh-1 trepan data*

Conclusions

The Novovoronesh-1 trepan study was the first attempt to characterize VVER vessel material properties after plant decommissioning. Because unirradiated archive material was not available Tko could be estimated by simulating heat treatments only. This can lead to systematic errors in the data. The simulation procedure works rather satisfactory with materials irradiated in test reactors or surveillance positions but the process has not been validated for materials irradiated during 20 years. It was also noticed that phosphorus content of the weld seam varies considerably, which would require a detailed characterization of the weld seam i.e. the measurement of Tko, T_0 and Tk in many weld seam locations but it was not feasible due to the limited amount of trepan material. Scarcity of the trepan material necessitated also the determination of transition temperatures with relatively small number of specimens with the inherent statistical uncertainty. Nevertheless the following conclusions can be made based on the measured data.

- The estimated irradiation embrittlement of the weld metal exceeds the current code description as is seen in Figure 25. The embrittlement is excessive only when described by the T_{47J} parameter. The directly measured fracture toughness T_0 is within the code description. It is clear that the high Charpy-V impact energy criterion used for Tk is not applicable to low upper shelf materials.

- The data reveals practically no through wall attenuation of toughness. In case of base metal the difference of absolute through wall Tk values is small and it can not be separated from the overall scatter. In weld the inhomogeneities due to variation of chemistry and possibly due to the difference between the weld root and the weld properties obscure the observation of the fluence effect.

- The correlation between the Charpy-V based Tk and the directly measured T_0 parameters is poor as is the case also in the ASME code between T_0 and T_{RTNDT} [5]. There is also a large difference between the weld metal and base metal behavior. Tk-estimates for base metal are largely conservative whereas in the case of weld metal there is no excessive conservatism. The situation emphasizes the importance to measure fracture toughness T_0 directly if precise estimations are required.

- Weld metal is the critical vessel wall material. No indication is seen in the base metal data of excessive aging due to grain boundary segregation.

References

[1] Valo, M. and Ahlstrand, R., "Application of Reconstitution Welding Technique for Studying Base Metal of a Novovoronesh Unit-1 Trepan Sample," *Small Specimen Test Techniques Applied to Nuclear Reactor Vessel Thermal Annealing and Plant Life Extension, ASTM STP 1204*, W. R. Corwin, F. M. Haggag, and W. L. Server, Eds., American Society for Testing and Materials, Philadelphia, 1993.

[2] Wallin, K., "Validity of small specimen fracture toughness estimates neglecting constraint corrections", *Constraint Effects in Fracture: Theory and applications. ASTM STP 1244,* Mark Kirk and Ad Bakker, Eds., American Society for Testing and Materials, Philadelphia, 1994.

[3] Regulatory Document PNAE G-7-002-86 (Strength analysis standards for equipment and piping at nuclear power plants). Moscow: Energoatomizdat. 527 p. (Translated by SCITRAN, Santa Barbara, California, USA).

[4] Amayev, A. D., Kryukov, A. M., Levit, V. I., Platonov, P. A., Rogov, M. F. & Skolov, M. A. Radiation Damage and recovery in WWER-440 Vessels materials. Power Plant Life Extension 93, Zurich, 1993. 48 p.

[5] Wallin, K. & Rintamaa, R., Statistical Re-Evaluation of the ASME K_{Ic} and K_{IR} Fracture Toughness Reference Curves, 23. MPA-Seminar, October 1 – 2, 1997.

Yuanchao Xu,[1] Xuejun Jia,[1] Changyi Zhang, [1] Guangshen Ning ,[1] and Qingkai Yu [2]

The Effects of Flux on Radiation Embrittlement of Low-Copper Pressure Vessel Steels

Reference: Xu, Y., Jia, X., Zhang, C., Ning, G., and Yu, Q., **"The Effects of Flux on Radiation Embrittlement of Low-Copper Pressure Vessel Steels,"** *Effects of Radiation on Materials: 19th International Symposium, ASTM STP 1366,* M. L. Hamilton, A. S. Kumar, S. T. Rosinski, and M. L. Grossbeck, Eds., American Society for Testing and Materials, West Conshohocken, PA, 2000.

Abstract: The effects of neutron flux (E>1MeV) on the radiation embrittlement of the low-copper RPV steels are investigated. Tested materials include the forging matrix (JF) weld (JW) of Japan's SA 508-3 steel as well as the matrix (CF) and weld (CW) of China's domestic RPV steel. JF and CF were irradiated to fluences from 3.2 to 4.9×10^{23}n/m^2(E>1MeV) at 280±5℃, JW and CW irradiated to fluences of 1.4 and 1.5×10^{23}n/m^2 at 290±5℃, respectively, in the test reactor. JF and JW are also used as surveillance specimens for PWR RPV, and two sets of surveillance data have been acquired. The experimental results indicate that the transition temperature shifts (ΔRT_{NDT}) for JF irradiated in the test reactor are larger than those from surveillance specimens, when these ΔRT_{NDT} are normalized to an effective fluence of 2×10^{23}n/m^2 (E>1MeV) and an effective temperature of 290℃. This shows notably the influence of neutron flux on ΔRT_{NDT}. The mean ΔRT_{NDT} for CF and CW is about 0.7 times that for JF and JW in terms of the normalized data, which imply the influences of the impurities besides Cu and microstructures on radiation embrittlement of low-copper RPV steels.

Keywords: reactor pressure vessels, low-copper steels, irradiation, neutron flux, test reactor, surveillance, effective fluence, Charpy V-norch impact, transition temperature shift, matrix defects

[1] Professor and Engineers, respectively, Nuclear Materials Laboratory, China Institute of Atomic Energy.

[2] Graduate student, China Nuclear Industry Graduate School.

Copyright© 2000 by ASTM International www.astm.org

Introduction

In order to predict reactor pressure vessel (RPV) lifetime, it is necessary that the RPV steel for which an integral database from a surveillance program has not been collected will be irradiated to high fluence in test reactors. The exposure conditions e.g. flux and temperature, in test reactors are different from those of power reactors (PWR); they significantly affect the embrittlement of RPV steels[1-4]. The influences of irradiation conditions on the embrittlement of variant type of RPV steels are different in a degree. The RPV steels, for example Japanese SA 508-3 steel and Chinese domestic RPV steel (similar to SA 508-3 steel), which have been used for nuclear power plants built in recent years, have a lower content of copper. It is of interest to study the effects of exposure conditions on the embrittlement of these steels to manage RPV lifetime [5,6].

Materials

The forging matrix (JF) and weld (JW) compositions of Japanese SA508-3 steel and Chinese RPV matrix (CF) and weld (CW) are listed in Table 1.

Japanese steel heat treatment process: normalized at 900/950℃and tempered at 600/660℃; quenched at 870/895℃and tempered at 650/665℃; simulated post weld heat treatment at 595/610℃. It's grain size No. 7 or finer, the initial RT_{NDT}<-20℃[7].

The manufacturing process and initial data of CF are referred to [8]. The following specifications and parameters were employed for CW:

Test plate dimensions: 210×370×1200mm

Weld groove width: 22mm at the bottom and 29mm at the top

Welding wires: 4mm-dia. H10Mn2NiMoA

Amperage: 450 to 550 A

Voltage: 30 to 35V

Travel speed: 25 to 33m/hr.

Postweld stress relief treatment at 550 to 610℃. The reference transition temperature: RT_{NDT}≤-20℃.

Irradiation and Charpy Impact Test

JF, JW, CF and CW were irradiated in the light-water pool type reactor of China Institute at Atomic Energy. The uncertainties of fluence (E>1MeV) reported in Table 2 are about ±10%. The irradiation temperature for JF and CF is 280±5℃, that for JW and CW is 290±5℃.

The same JF and JW were used as surveillance specimens for PWR RPV, the flux and fluences are listed in Table 3.

Table 1 —*Chemical Composition of JF, FW, CF and CW*

Materials	Elements		Chemical composition(wt%) C	Si	Mn	P	S	Ni	Cr	Cu
JF	Spec.	Max.	0.23	0.30	1.50	0.012	0.015	0.90	0.25	0.05
		Min.	0.17	0.15	1.20	—	—	0.60	—	—
	Ladle		0.18	0.19	1.45	0.004	0.001	0.75	0.14	0.03
JW			0.08	0.45	1.23	0.009	0.006	0.38	0.02	0.03
	Guarantee		0.10	0.30 —0.65	0.90 —1.40	0.012	0.015	0.20 —0.50	0.30	0.05
CF			0.20	0.16	1.45	0.006	0.001	0.75	0.14	0.03
CW	First layer		0.06	0.17	1.48	0.01	0.006	0.94	0.03	≤0.05
	Second layer		0.06	0.20	1.52	0.01	0.004	0.91	0.03	≤0.05

Materials	Elements		Mo	V	Co	Al	Sn	As	Sb
JF	Spec.	Max.	0.65	0.01	0.02	0.04	0.01	0.01	0.002
		Min.	0.45	—	—	—	—	—	—
	Ladle		0.49	0.003	0.013	0.027	0.005	0.005	0.001
JW			0.53	<0.01	0.01	—	0.001	0.002	0.001
	Guarantee		0.45 — 0.65	0.05	0.02	—	0.01	0.01	0.004
CF			0.45	0.005	—	0.28	—	—	—
CW	First layer		0.56	0.01	≤0.02	—	≤0.01	≤0.01	≤0.005
	Second layer		0.57	0.01	≤0.02	—	≤0.01	≤0.01	≤0.005

Charpy impact tests were performed by type T-84 instrumented impact test machine with facilities for automatic-sending tested specimens to the anvil from heating or refrigerating devices. The deviations of test temperatures from the setting ones were within ±2℃.

Experimental Results

The temperature transition curves of the impact energy and lateral expansion for JF unirradiated and irradiated to the fluence of 3.2×10^{23}n/m^2 (E>1MeV) are shown in Fig.1.

Charpy V-notch impact test results for the materials before and after irradiation in the test reactor are listed in Table 2. The results from PWR RPV surveillance test are given in Table 3.

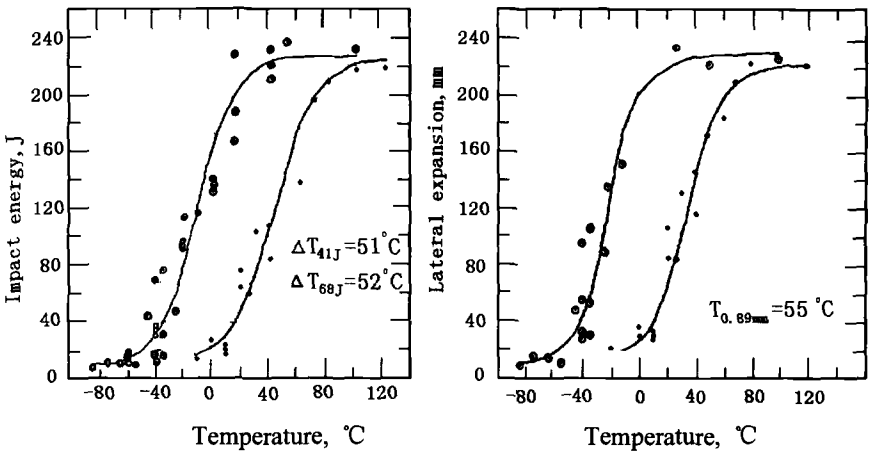


Fig.1 —*Charpy V-Notch Temperature Transition Curves for JF*

⊙—unirradiated; •—irradiated to a fluence of 3.2×10^{23}n/m^2 (E>1MeV)

Comparison of Test Reactor and Surveillance Results

To compare test reactor irradiation results with those from power reactor RPV surveillance, results predicted by NUREG/CR-6551 Equation 4-1 [9] and RG 1.99 (2) [10], respectively, are given in Table 4. The two models were developed by analysis of power reactor surveillance data [9,11]. Experimental results were normalized by means of NUREG/CR-6551 Eq. 4-1 to an effective fluence of 2×10^{23}n/cm^2 (E>1MeV), the results for JF and CF irradiated in the test reactor were adjusted to an effective temperature of 290℃ in terms of dependence of about -0.5℃/℃ for low-copper RPV steels [3], the transition temperature shifts for JF and CF were decreased by about 5℃. The normalized results are listed in Table 4 and shown in Fig.2.

The results indicate the mean ΔRT_{NDT} measured for JF and JW irradiated in the test reactor is about 2 times as much as that predicted by the Eq.4-1, for CF and CW about 1.5 times. The mean ΔT_{41J} normalized by the Eq.4-1 for JF and JW irradiated in the test reactor is also about 2 times that for the surveillance results. The surveillance data for JF and JW are in good agreement with results predicted by the Eq. 4-1 and RG 1.99(2), respectively, minus a little measured bias. The mean ΔRT_{NDT} predicted by RG 1.99(2) is about 0.6 times that by the Eq. 4-1 for JF and CF irradiated to the fluences above 3×10^{23}n/m^2 (E>1MeV).

Table 2 —*Charpy Impact Test Results for JF,JW,CF and CW before and after Irradiation in the Test Reactor*

Materials		JF				JW		CF		CW	
Set No. of specimens		Unirrad.	1#	2#	3#	Unirrad.	Irrad.	Unirrad.	Irrad.	Unirrad.	Irrad.
Flux (E>1MeV), $n/m^2 \cdot s$		0	2.7×10^{16}	3.8×10^{16}	4.1×10^{16}	0	4.2×10^{16}	0	3.4×10^{16}	0	4.6×10^{16}
Fluence (E>1MeV), n/m^2		0	3.2×10^{23}	4.6×10^{23}	4.9×10^{23}	0	1.4×10^{23}	0	4.1×10^{23}	0	1.5×10^{23}
USE, J		238	226	229	217	224	215	206	193	174	160
ΔUSE, J			12	9	21		14		13		14
Index temperature, ℃	T_{41J}	-34	17	18	24	-39	-4	-44	-6	-63	-40
	T_{41J} S.D.*	±7	±6	±5	±7	±8	±9			±12	±9
	T_{68J}	-24	28	29	35	-25	9	-32	2	-50	-27
	$T_{0.89mm}$	-28	27	27	33	-30	11	-30	4	-53	-27
Transition temperature shift, ℃	ΔT_{41J}		51	52	58		35		38		23
	ΔT_{68J}		52	53	59		34		34		23
	$\Delta T_{0.89mm}$		55	55	61		41		34		26

* Standard Deviation(σ)

Table 3 —*Results for PWR RPV Surveillance Tests of JF and JW*

Materials	Set No. of spec.	Flux (E>1MeV), $n/m^2 \cdot s$	Fluence (E>1MeV), n/m^2	USE, J	ΔUSE, J	Index temperature, ℃			Transition temperature shift, ℃		
						T_{41J}	T_{68J}	$T_{0.89mm}$	ΔT_{41J}	ΔT_{68J}	$\Delta T_{0.89mm}$
JF	Unirrad.	0	0	238		-36	-25	-26			
	1#	3.3×10^{14}	1.9×10^{22}	234	4	-30	-20	-21	6	5	5
	2#	3.6×10^{14}	3.1×10^{22}	234	4	-27	-13	-16	9	12	10
JW	Unirrad.	0	0	215		-39	-25	-32			
	1#	3.2×10^{13}	1.8×10^{21}	208	7	-37	-24	-27	2	1	5
	2#	4.2×10^{13}	3.5×10^{21}	206	9	-32	-20	-19	7	5	13

Table 4 —*Comparison of Test Results With Predicted and Normalized Ones by Models*[9,10]

Exposure conditions	Materials	ϕ $\times 10^{14}$ n/m^2·s	f $\times 10^{23}$ n/m^2	ΔRT_{NDT}, ℃			
				Test results	NUREG/ CR-6551	RG 1.99(2)	Normalized to 2×10^{23}n/m^2
Test reactor	JF	270	3.2	51	22	14	36
		380	4.6	52	26	15	31
		410	4.9	58	27	16	34
	JW	420	1.4	35	16	12	41
	CF	340	4.1	38	27	15	24
	CW	460	1.5	23	17	19	26
Power reactor	JF	3.3	0.19	6	5	6	16
		3.6	0.31	9	6	8	20
	JW	0.32	0.018	2	3	4	
		0.42	0.035	7	4	5	

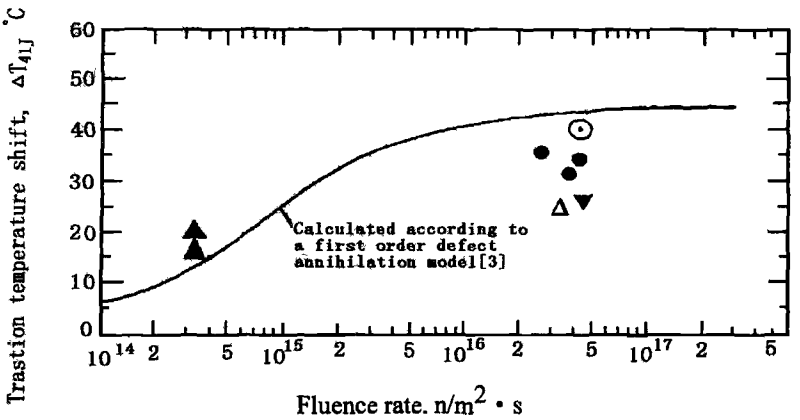


Fig. 2 — *Transition Temperature Shifts as A Function of Fluence Rate for Low-Copper RPV Steels (Normalized to 2×10^{23}n/m^2, E>1MeV)*

• —Data for JF irradiated in the test reactor

⊙—Data for JW irradiated in the test reactor

Δ—Data for CF irradiated in the test reactor

▼—Data for CW irradiated in the test reactor

▲—Data from surveillance tests for JF

The experimental data normalized to $2x10^{23}$n/m^2 (E>1MeV) by the Eq. 4-1 are larger than resules calculated according to a first order defect annihilation model[3] at about $3.5x10^{14}$n/m^2· s (E>1MeV), and smaller than those calculated at above 2.5×10^{16}n/m^2· s (E>1MeV).

Discussion

For irradiated low-copper RPV steels, the influence of rich-copper precipitates on the embrittlement of the materials is secondary, the effects of matrix defects on strengthening and embrittling of materials are notable. The effects of stable matrix defects including dislocation loops[12-14], vacancy clusters[15] and vacancy-impurity complexes[16] on strengthening of low copper steels irradiated to high fluence at intermediate or high flux at 290℃ is outstanding; the influences of unstable matrix defects including steady point defects are less important. The vacancy clusters of 4—10 empty atomic volumes in the RPV steel irradiated at 288℃were observed by positron life spectrum measurements[13]. The results of the calculation in terms of theoretical model[2] indicate that the strengthening induced by stable matrix defects at irradiation temperature of 288℃ linearly increase with flux increasing at fixed fluence, or with fluence increasing at fixed flux.

For low-copper steels exposed in PWR radiation environment where the flux is low, there is a little influence of unstable matrix defects on the embrittlement in low fluence region, the strengthening induced by stable matrix defects significantly enhance with fluence increasing in intermediate and high fluence regions.

The results from the model[1] demonstrate both hardenings of low-copper RPV steels irradiated at low flux and at high flux nearly-parallel enhance in certain proportion with fluence increasing. The results from this study appear a tendency that the increment rate of ΔRT_{NDT} decrease with fluence increasing when fluence $>1\times 10^{23}$ n/m^2 (E>1MeV) and the embrittlement tend towards a saturation.

Even though Japanese SA 508-3 and Chinese RPV steele were irradiated under the same conditions in the test reactor and their copper and nickel contents are nearly equal, the results normalized to same effective fluence are different, the mean ΔRT_{NDT} for CF and CW is about 0.7 times those for JF and JW. Since Chinese steel was refined by ESR technology, the contents of impurities which act a role on non-hardening embrittlement as their segregating at grain boundaries are less than those of Japanese steel. There is a difference in some degree on the microstructures of two steels, as their heat treatment processes are not completely identical.

Conclusion

The results from this study indicate that the effects of neutron flux on the embrittlement of low-copper RPV steels are notable. Normalized to the effective fluence, the mean ΔRT_{NDT} for JF irradiated to the fluence above $4x10^{23}$n/m^2 (E>1MeV) in the test reactor is about 2 times that for PWR RPV surveillance data. More test reactor data that cover the wide ranges of fluences for JF are needed to verify the above statement with confidence.

The experimental results also imply that there are influences of the impurities

besides copper and microstructures on radiation embrittlement of low-copper RPV steels.

Acknowledgments

Research sponsored by the International Atomic Energy Agency Under IAEA Research Contract No. : 9949.

References

[1] Odette, G. R., Mader, E. V. Lucas, G. E., Phythian, and English, G. A., "The Effect of Flux on the Irradiation Hardening of Pressure Vessel Steels, " *Effects of Radiation on Materials: 16th International Symposium, ASTM STP 1175*, A. S. Kumar, D. S. Gelles, R. K. Nanstad and E. A. Little, Eds., Americal Society for Testing and Malerials, Philadelphia, 1993,pp. 373—393.

[2] Stoller, R. E., "Modeling the Influence of Irradiation Temperature and Displacement Rate on Radiation-Induced Hardening in Ferritic Steels, " *Effects of Radiation on Materials: 16th International Symposium, ASTM STP 1175*, A. S. Kumar, D. S. Gelles, P. K. Nanstad and E.A. Little, Eds., Americal Society for Testing and Materials, Philadelphia, pp. 394—423.

[3] Analysis of the Behaviour of Advanced Reactor Pressure Vessel Steels Under Neutron Irradiation, Technical Reports Series No.265, IAEA, Vienna, 1986.

[4] Haggag, F. M., "Effects of Irradiation Temperature on Embrittlement of Nuclear Pressure Vessel Steels, " *Effects of Radiation on Materials: 16th International Symposium, ASTM STP 1175*, A.S.Kumar, D.S.Gelles, R.K.Nanstad and E.A.Little, Eds., American Society for Testing and Materials, Philadelphia, 1993, pp. 172—185.

[5] Tipping, Ph., "Lifetime and Ageing Management of Nuclear Power Plants: a Brief Overview of Some Light Water Reactor Component Ageing Degradation Problems and Ways of mitigation, " *Int. J. Pres. Ves. & Piping* **66** (1996) 17–25.

[6] Sung-yull Hong, Ill-Seok Jeong and Tae Eun Jin, "Recent Strategy and Progress in Korean Nuclear PLIM Program, " *Nuclear Engineering and Design* 174 (1997) 25—32.

[7] XU,Y., Jia, X., Zhang, C., Yang, J., and Yang, W., "Experimental Research on Radiation Embrittlement of Low-Copper Pressure Vessel Steels, " *Chinese Journal of Nuclear Science and Engineering*, Vol. 18, No. 2, 1998. pp. 146-152.

[8] Jia, X., Xu, Y., Zhang, C. and Yang, W., "Effect of Irradiation on Material of 600MW NPP-RPV, " *Effects of Radiation on Materials, 19th International Symposium, ASTM STP 1366*, M. L. Hamilton, A. S. Kumar, S. T. Rosinski and M. L. Grossbeck, Eds, American Society for Testing and Materials, West Conshohocken, PA, 1999.

[9] Eason, E. D., Odette, G. R., and Wright, J. E., "Improved Embrittlement Correlations for Reactor Pressure Vessel Steels," *NUREG/CR-6551*, Nuclear Regulatory Commission, Washington, D. C., 1998.

[10] "Radiation Embrittlement of Reactor Vessel Materials" , *Regulatory Guide 1.99(Rev.2)*. U. S. Nuclear Regulatory Commission, Washington, D. C., May 1988.

[11] Randall, P. N., "Basis for Revision 2 of the U. S. Nuclear Regulatory Commission's Regulatory Guide 1.99," *Radiation Embrittlement of Nuclear Reactor Pressure Vessel Steels: An International Review (second Volume), ASTM STP 909*, L. E. Steels, Ed., American Society for Testing and Materials, Philadelphia, 1986, pp. 149−162.

[12] Buswell, J. T., Phythin, W. J., McElroy, J. J., Dumbill, S., Ray, P. H. N., Mace, J., and Sinclair, R. N., " Irradiation-Induced Microstructural Changes, and Hardening Mechanisms, in Model PWR Reactor Pressure Vessel Steels, " *Journal of Nuclear Materials*, 225, 1995, p.196.

[13] valo, M., Krause, R., Saarinen, K., Hautojarvi, P., and Hawthorne, J. R., *Effects of Radiation on Materials: 15th International Symposium, ASTM STP 1125*, R. Stoller, A. Kumar and H. Packen, Eds. American Society for Testing and Materials, 1992 p. 93.

[14] Buswell, J. T., Bischler, P. J. E., Fenton, S. T., Ward, A. E., and Phythian, W. J., *Journal of Nuclear Materials*, 205, 1993, p.198.

[15] Moser, P., Li, X. H., Akamatsu, M. and Van Duysen , J. C., "Vacancy Defects in Electron Irradiated RPV Steels Study by Positron Lifetime, " *Materials Science Forum*, Vols.175 −178, 1995, pp.453−456.

[16] Akamatsu, M., Van Duysen, J. C., Pareige, P., and Auger, P., "Experimental Evidence of Severalc Contributions to the Radiation Damage in Ferritic Alloys," *Journal of Nuclear Materials*, 225,1995, pp.192−195.

William L. Server[1] and Stan T. Rosinski[2]

Technical Basis for Application of the Master Curve Approach to Reactor Pressure Vessel Integrity Assessment

Reference: Server, W. L. and Rosinski, S. T., **"Technical Basis for Application of the Master Curve Approach to Reactor Pressure Vessel Integrity Assessment,"** *Effects of Radiation on Materials: 19th International Symposium, ASTM STP 1366*, M. L. Hamilton, A. S. Kumar, S. T. Rosinski, and M. L. Grossbeck, Eds., American Society for Testing and Materials, West Conshohocken, PA, 2000.

Abstract: The American Society of Mechanical Engineers (ASME) Boiler and Pressure Vessel Code reference toughness curves are based upon an approach which utilizes a material normalizing and indexing parameter, RT_{NDT}. This parameter is based upon the combined results from Charpy V-notch and drop-weight nil-ductility transition temperature tests as defined in the ASME Code. In many cases, this indexing parameter is overly conservative relative to the real toughness of ferritic reactor pressure vessel (RPV) steels, and a more direct index and measure of the true fracture toughness is desired. The Master Curve fracture toughness method, recently issued as ASTM Standard Test Method E 1921-97, is a better indicator of fracture toughness behavior in terms of a directly measured toughness index, T_o, and statistically-derived tolerance bounds. This method is technically more sound than the RT_{NDT} approach and provides use of the statistical nature of measured fracture toughness properties (including use of surveillance materials). The Pressure Vessel Research Council (PVRC) is presently investigating application of the Master Curve approach for implementation in the ASME Code. The Electric Power Research Institute (EPRI) is supporting development of alternative RPV integrity assessment approaches, which includes documentation of the technical basis for application of the Master Curve approach. An EPRI document has been written that supports the ASME Code activities to allow utility use of the Master Curve approach. The results of that document for application of the Master Curve approach to RPV integrity assessment are summarized in this paper. Examples illustrating applicability of the Master Curve approach are presented.

Keywords: fracture toughness, master curve, reactor pressure vessel steels, ASME Code, reference temperature, nuclear pressure vessel

Introduction

Recent nuclear industry attention has been focused on the direct use of measured fracture toughness properties in the assessment of reactor pressure vessel (RPV) integrity. Specifically, efforts have been initiated to develop procedures for determining a material transition temperature, designated as T_o, based on measured fracture toughness testing using the Master Curve approach. This is in contrast to the historically utilized approach

[1] President, ATI Consulting, P.O. Box 5769, 24 Glenbarr Court, Pinehurst, NC 28374.
[2] Program Manager, EPRI, 1300 Harris Boulevard, Charlotte, NC 28269.

Copyright© 2000 by ASTM International www.astm.org

to determine a reference temperature, RT_{NDT}, based on a combination of Charpy V-notch and drop-weight nil-ductility transition (NDT) temperature test methods. The direct determination of material fracture toughness, and a transition temperature associated with measured fracture toughness, represents a more precise measure of material resistance to crack initiation than earlier methods and should provide a more realistic assessment of RPV integrity.

Significant efforts are presently underway in the research, codes and standards, and regulatory arenas to:

- Collect all relevant available fracture toughness data and generate additional data for RPV materials,
- Develop consensus procedures for the determination of T_o,
- Demonstrate the validity of using T_o as a fracture toughness transition reference temperature, and
- Incorporate the new approach into appropriate codes, standards, and regulations.

These activities involve the participation of all aspects of the nuclear industry including individual utilities, nuclear steam supply system (NSSS) vendors, vendor Owners Groups, EPRI, research laboratories, the U.S. Nuclear Regulatory Commission (NRC), and other domestic and international experts. An alternative approach for determining RT_{NDT}, specifically using T_o via the Master Curve methodology, is discussed in this paper. Coordination activities of industry groups to demonstrate the validity of the Master Curve approach also are described.

In October 1995, the PVRC initiated a Master Curve project to assemble a database of available domestic and international fracture toughness testing results on pressure vessel materials. The objective of this effort was to evaluate the use of the Master Curve approach from the recently approved ASTM Test Method for the Determination of Reference Temperature, T_o, for Ferritic Steels in the Transition Range (E 1921-97), and its application to RPV materials. The database will be used to validate the T_o (Master Curve) approach for RPV steels. It is anticipated that the database will contain sufficient data from various size test specimens that the variability in T_o can be shown to be independent of specimen size and test temperature.

A task group under the PVRC Committee on Failure Modes of Components was formed to serve as a focal point for information sharing and to assist in coordination of industry activities to maximize resources and resolve technical issues associated with the Master Curve approach. Task group membership included domestic and international experts on the Master Curve approach, nuclear utilities, NSSS vendors, EPRI, and the NRC (and its contractors). The coordination role of the PVRC Task Group on the Master Curve Approach is illustrated in Figure 1.

The overall goal of the PVRC Task Group is to make recommendations to the ASME Boiler & Pressure Vessel Code Committee on rules to implement use of the Master Curve approach following ASTM E 1921-97. The short-range objective of the task group is to develop an alternative method using T_o as a fracture toughness indexing parameter instead of RT_{NDT}. A significant amount of fracture toughness data from both large and small test specimens has been collected and compared using the T_o and RT_{NDT} indexing approaches. Additionally, various testing programs presently are underway or

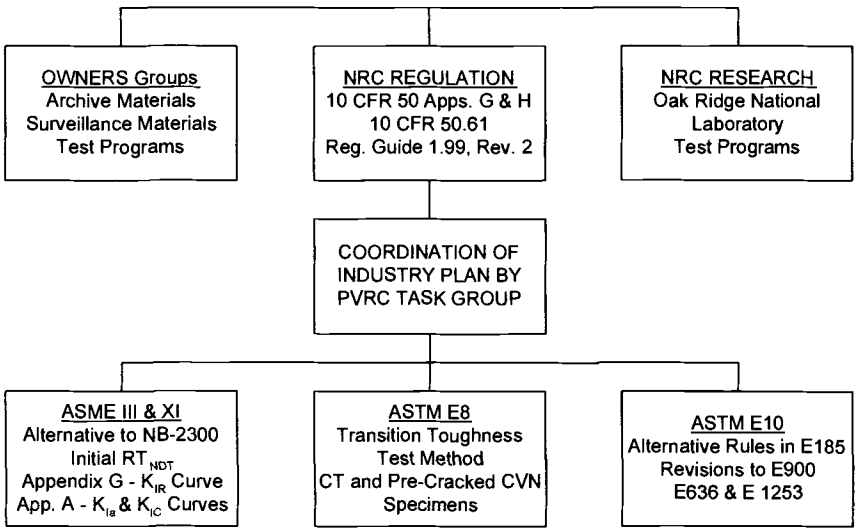


Figure 1 - *Industry Activities for Implementation of Direct Measurement of Fracture Toughness*

planned through the Materials Property Council (MPC) and the International Atomic Energy Agency (IAEA). The results from these testing programs will provide T_o values for a number of pressure vessel materials in order to further evaluate the use of T_o as an alternate indexing parameter. Technical issues regarding specimen constraint, multiple test temperatures, and shape change of the Master Curve must be addressed in order to meet the short-range task group objective. Many of the members of the PVRC Task Group are also members of the ASME Code Section III and XI Committees, who have responsibility for drafting an ASME Code Case[3] that will contain recommended rules for implementing T_o as an indexing parameter. The PVRC Task Group will forward this approach, and other recommendations, to appropriate ASME Code Committees.

The long-range objective of the PVRC Task Group is to develop rules for direct measurement of irradiated fracture toughness using the Master Curve approach. The direct assessment of fracture toughness on irradiated materials potentially will reduce present conservatism associated with the use of the current RT_{NDT} reference toughness approach. The application to irradiated materials appears to be analogous to the unirradiated case, especially for fluence conditions matching those needing evaluation for service (e.g., end of operating life fluence). The database available for irradiated materials is at least as large as that available for the unirradiated ASME Code K_{IC} materials.

[3] The ASME Code Case was under development at the time that this paper was written, and now it is approved as Code Case N-629; see the appendix in Reference *1*.

This paper is intended to describe the technical basis for application of the T_0 fracture toughness methodology for ferritic reactor pressure vessel materials. The methodology is being developed for use in the ASME Code and has been documented in an EPRI report [*1*]. Activities are presently underway through various organizations to document the technical basis of ASTM E 1921-97 and to document the data analyses used to validate the Master Curve approach. In summary, ASTM Test Method E 1921-97 adequately covers aspects related to bias and accuracy in the determination of T_0 [*2*] and provides a technically sound approach for defining a unique fracture toughness transition temperature (T_0) for ferritic steels. The new Master Curve methodology is a revolutionary advance in our understanding of cleavage fracture initiation and ductile-brittle transition behavior in ferritic steels. It is clearly superior to the old RT_{NDT} approach, since it is based upon measurement of actual fracture toughness properties rather than Charpy V-notch and drop weight results. Since the new approach is more technically sound and is based on statistics, the degree of margin needed for vessel integrity evaluations can be better understood and quantified.

Theoretical Basis of the Master Curve

The Master Curve approach to describing fracture of ferritic steels in the ductile-to-brittle transition range is based on the observation that the initiation of cleavage fracture is a metallurgical process that is highly scattered due to the microstructure inherent in ferritic steels. It has been shown [*3-6*] that, by treating cleavage fracture as a statistical phenomenon, cleavage fracture can be modeled using a three-parameter Weibull distribution. As a result, it is possible to determine median values and appropriate bounds for fracture toughness measurements in the transition region. Wallin [*5*] has used this technique to determine median fracture toughness values as a function of temperature and observed that, for a variety of ferritic steels, these fracture toughness transition curves had a characteristic shape. This fixed shape suggested that the fracture toughness for these materials could be described by a series of curves that differed only in their location on the temperature scale; this is the origin of the term "Master Curve." Under the Master Curve method, a fracture toughness curve is determined by a single parameter that establishes the position of the Master Curve on the temperature scale. This parameter is termed T_0 and is defined as the temperature at which the median fracture toughness for a 1T (25.4 mm; 1.00 in. thick) fracture toughness specimen equals 91 ksi-in$^{1/2}$ (100 MPa-m$^{1/2}$). A fracture toughness curve for any ASME Code ferritic pressure vessel material (within specified limits), which is tested in the transition range, can be uniquely determined by this reference temperature. The use of a reference temperature to locate a standard curve on the temperature scale is in many ways analogous to the use of RT_{NDT} to adjust the ASME Code curves. However, the ASME Code fracture toughness curves, K_{IC} and K_{IR}, are lower bound curves that are *not* based on probability assessment.

ASTM Test Method E 1921-97 uses the Master Curve methodology to establish a fracture toughness transition temperature. This methodology is based on four basic observations about cleavage initiation toughness in the transition region. These observations are:

- It is possible to use elastic-plastic, J-integral technology to measure cleavage initiation fracture toughness in small specimens.

- Repeated measurements at one temperature using identical specimens will produce a well-defined distribution of toughness values.
- The distribution of measured values is related to the length of the crack front in a statistical manner based on a weakest link theory.
- The shape of the fracture toughness transition curve is the same for all ferritic steels with yield strength ranging from about 275 to 825 MPa (40 to 120 ksi).

The technical community has extensively examined the validity of these observations, and further work to substantiate the overall technical basis for the Master Curve methodology is continuing.

Basis for Using T_0 to Define Fracture Toughness Reference Curve

The fundamental premise underlying the draft ASME Code Case approach is: if it is possible to define a new indexing temperature (RT_{To}) for the K_{IC} curve that assures that the reference K_{IC} curve will provide an adequae bound to the actual material fracture toughness data, then RT_{To} must be the functional equivalent of RT_{NDT}. The requirement for functional equivalency eliminates the need for an empirical correlation because it relates directly to the intent of the ASME reference curves. It is feasible to define a functionally equivalent indexing temperature because both the K_{IC} curve and the Master Curve describe the ductile-to-brittle transition for static crack initiation tests in pressure vessel steels. However, the Master Curve approach is attractive because it relates the toughness curve from actual toughness measurements rather than the combination of Charpy and drop-weight tests, as used to determine RT_{NDT}. As illustrated in Figure 2, the Master Curve approach can be used to describe both the temperature dependence of the original K_{IC} curve data set and the variability inherent in the data [7]; note that T_o is identified as T_{100} in this figure.

A demonstration of functional equivalency requires a precise examination of both the current technology and the proposed alternative. In order to provide an objective evaluation of the proposed alternative, standards of acceptability must be determined. To be functionally equivalent, the K_{IC} curve, as indexed to RT_{To}, must continue to appropriately bound the fracture toughness data. In order to define a standard of acceptability for the proposed approach, an objective definition of the meaning of the phrase "appropriately bound" is required. This standard can be stated in terms of the probability that a measured toughness value will fall below the K_{IC} curve as it is currently defined (that is, indexed to RT_{NDT}). This standard is used as a basis of comparison in later discussion of the ASME Code Case.

The proposed alternate procedure for using Master Curve technology requires a definition of RT_{To} that meets the functional equivalency requirement. It is feasible to consider such a definition because the Master Curve technology allows construction of a or confidence limit for any flaw size as a function of $T-T_o$. The 95% confidence limit (which is really the 5% lower tolerance bound) for the 1T flaw size is illustrated in Figure 3. If the value of RT_{To} is set such that the corresponding K_{IC} curve falls below the Master Curve 95% confidence limit, at least 95% of the data generated with specimens of 1T size

will be bounded by the K_{IC} curve. In practice, a lower bound Master Curve and the K_{IC} curve have slightly different shapes. Therefore, any definition of RT_{To} also implies an intersection point between the two curves. Figure 3 illustrates the relationship between the two curves for the ASME Code Case assumed relationship:

$$RT_{To} = T_o + 35^oF. \quad (1)$$

In this case, the two curves intersect at a $T-T_o$ value of 115^oF (64^oC). Below this temperature the K_{IC} curve would be expected to bound more than 95% of the 1T toughness data. Above this temperature the K_{IC} curve would bound less than 95% of the data. This intersection temperature corresponds to a toughness of 137 ksi-in$^{1/2}$ (151 MPa-m$^{1/2}$) on the K_{IC} curve. Also, at temperatures on the lower shelf, the K_{IC} curve may bound less than 95% of the data due to the second crossover of the two curves.

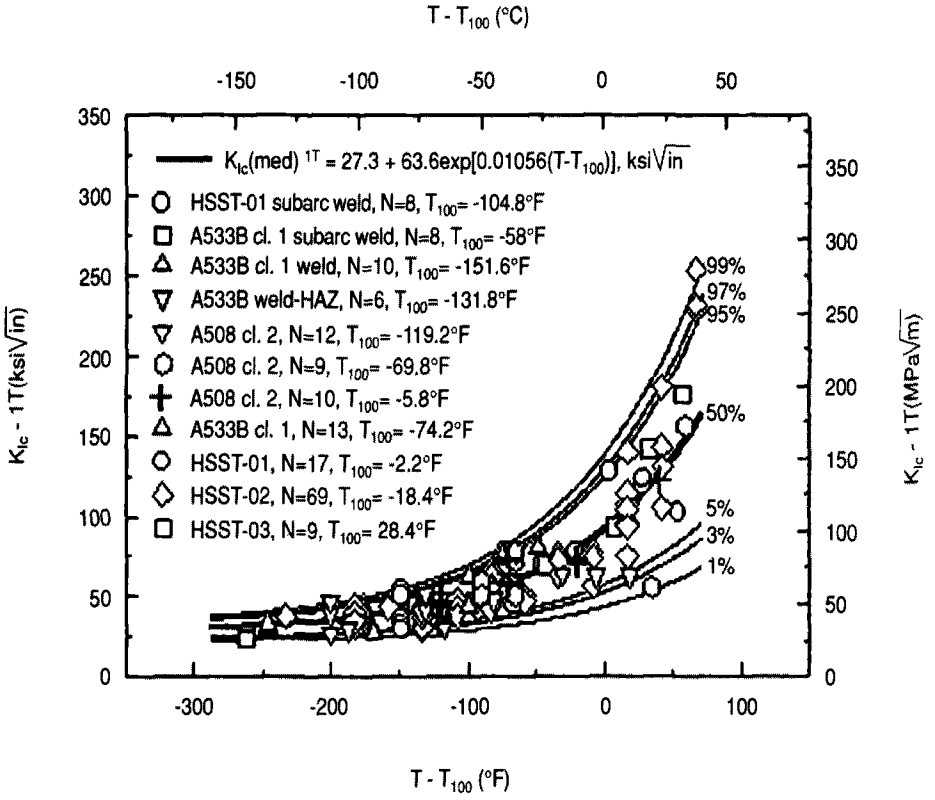


Figure 2 - *Comparison of Original K_{IC} Data to Master Curve (Data Adjusted to 1T)*

The Master Curve approach is based on a new understanding of the statistics of cleavage fracture that was not available at the time the ASME Code curves were developed. Subsequent to the development of the ASME Code curves, it was observed that measured values of elastic-plastic fracture toughness in the transition region exhibit generally reproducible size dependence [*5*]. This size dependence was not apparent in the original linear elastic data set, because the critical specimens were relatively large (making the size correction less obvious) and the number of specimens was limited. Use of size dependence is a significant departure from traditional linear elastic fracture mechanics (LEFM), where the toughness transition data are held to be size-invariant material property values. This size effect is incorporated in the Master Curve, but not in the definition of the K_{IC} curve. In the Master Curve, the size independent parameter is T_o, not the toughness. The K_{IC} curve is applied to the analysis of many different flaws, with different size parameters. The use of the Master Curve to estimate RT_{NDT} as RT_{To}, therefore, requires the selection of an appropriate flaw size. In testing and evaluation using ASTM E 1921-97, it is common practice to adjust all fracture toughness data to the 1T-equivalent value for the purpose of calculating T_o.

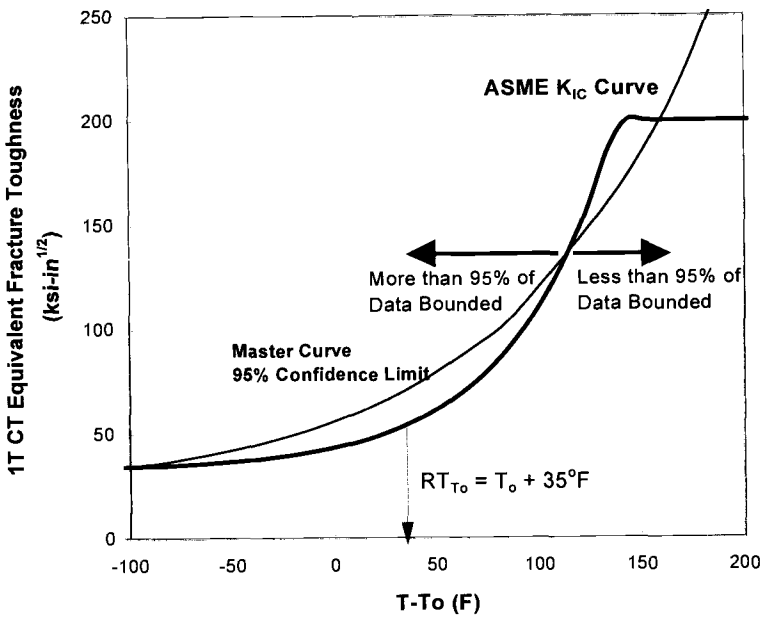


Figure 3 – *Relationship Between Master Curve 95% Confidence Limit (5% Lower Tolerance Bound) and ASME K_{IC} Curve Adjusted Using RT_{To}*

The original K_{IC} curve was drawn as a lower bound to as-measured fracture toughness values. There is a flaw size inherent in the use of RT_{NDT} as a referencing temperature for the K_{IC} curve approach that is related to the specimen size distribution in the original data set. In order to be functionally equivalent, RT_{To} should be based on similar specimen size assumptions. A simple means of assuring that the definitions of RT_{NDT} and RT_{To} contain similar implicit size assumptions is to make all comparisons on a common data set that contains a wide variety of specimen sizes. This manner of comparison has been used in developing the ASME Code Case.

Master Curve Analysis and Statistical Treatment of Code K_{IC} Data

The current procedure for determining the ASME K_{IC} reference toughness curve provides highly conservative values for many materials. There is a certain "confidence level" that arises from the knowledge that the reference curve significantly underpredicts the toughness in most cases. However, the inconsistent correspondence between RT_{NDT} and fracture toughness makes it difficult to quantify the level of conservatism. This inability to quantify the level of conservatism can result in an unreasonably conservative assessment of RPV integrity that unnecessarily restricts plant operations. The ASTM Master Curve methodology provides a value of T_o that relates the reference toughness curve directly to the measured fracture toughness data. The "confidence level" in applying the ASTM test method arises from the knowledge that the reference curve is directly related to measurements of the relevant property, rather than indirectly using the RT_{NDT} approach. The statistical basis of the procedure allows a consistent level of conservatism to be set by selecting an appropriate level of confidence. The ASTM procedure incorporates advances in fracture mechanics technology that were not available when the ASME reference curve was adopted.

The existing ASME reference curve is based on an empirical relationship between RT_{NDT} and fracture toughness. Although subsequent testing has indicated that the ASME K_{IC} curve continues to bound an overwhelming majority of the existing data, RT_{NDT} has proven to be a relatively poor predictor of the fracture toughness transition temperature [*8*]. Wallin also has performed a statistical analysis of the empirical relationship between RT_{NDT} and fracture toughness.[4] Wallin's analysis indicates that the Code K_{IC} curve is equivalent to a mean minus 2 standard deviation curve, and the 5% tolerance bound using the Master Curve is equivalent to a mean minus 2.2 standard deviation curve. This similarity in the statistical distribution suggests that the use of the 5% tolerance bound to the Master Curve, in place of the existing K_{IC} curve, will result in a curve that is equal to or slightly more conservative. The original K_{IC} curve was constructed by drawing a lower bound to the as-measured (non-size corrected) valid fracture toughness data available in 1971. While it is always possible to draw an absolute lower bound to a finite data set, there still remains the possibility that the next measurement will produce a value below the bound. Wallin and Rintamaa [*9*] performed an analysis that can be used to estimate the probability that the next measurement will fall below the ASME K_{IC} curve. Using the original data set, which was limited in size, they found this probability of failure to be 2.5%. It is entirely possible that an independent measurement would give a

[4] Unpublished evaluation performed by K. Wallin and presented at a short course in Denver 1997.

higher value. However, the relationship between the original fracture toughness data and the K_{IC} curve provides an objective measure of degree of conservatism inherent in the original analysis. This measure might then be used as a standard of acceptability for a proposed alternate definition of reference temperature. Wallin and Rintamaa [*9*] also found that, when the original K_{IC} data set was converted to 1T-equivalent toughness values, the probability of a point falling below the Master Curve 5% confidence bound was 1.5%. This analysis confirms the earlier observation that matching the K_{IC} curve with the Master Curve 5% tolerance bound will give a level of confidence in the bounding curve that is at least consistent with the intent of the current ASME Code.

Application of the Master Curve Methodology for the ASME Code Case

As described earlier, the short-term objective of the PVRC Task Group on the Toughness Master Curve is to develop recommendations for an alternative definition of a reference indexing temperature, similar to RT_{NDT}, using measured fracture toughness data. The consensus of the task group was that this first step was the most reasonable approach to obtain near-term benefit from fracture toughness data, rather than trying to immediately replace the existing ASME Code fracture toughness (K_{IC} and K_{IR}) curves, which is a longer-term objective. The application of the Master Curve methodology as an alternative determination of RT_{NDT} (termed RT_{To}) was, in part, based on NRC acceptance of a similar alternative definition of RT_{NDT} for the Zion RPV weld metal as supported by Master Curve fracture toughness data [*10*].

The short-term objective is to take advantage of improved fracture toughness measurements, without losing the historical link to the fracture toughness data that was the basis of the Code K_{IC} and K_{IR} curves. It is anticipated that as the technology further develops, the Master Curve, with an appropriate statistical bound, will eventually replace the current ASME reference curves.

There are many similarities between the process originally used to define the K_{IC} curve and the Master Curve approach. Both curves are determined from static crack initiation tests of pressure vessel steels. The K_{IC} curve is based on linear-elastic fracture mechanics (valid plane strain fracture toughness measurements) and the Master Curve is determined by using either linear-elastic fracture toughness or, more commonly, using small specimen elastic-plastic J-integral fracture toughness and statistical concepts. Both approaches characterize a material in terms of measured fracture toughness leading to a transition temperature. RT_{NDT} is determined by a combination of drop-weight and Charpy results. T_o is determined with multiple measurements of fracture toughness using the J-integral calculation method. The two transition temperatures, RT_{NDT} and T_o, provide the linkage between the two procedures.

The fundamental assumption underlying the proposed approach is that any alternative means of indexing a lower bound to the static fracture toughness data must serve the same purpose as the currently defined RT_{NDT}. Thus, the proposed alternative reference temperature must assure that the reference K_{IC} curve, when indexed by the alternative reference temperature, will properly bound the appropriate fracture toughness of the material. Note that the relationship between RT_{NDT} and fracture toughness is somewhat tenuous as discussed earlier, and a one-to-one correspondence between the value of reference transition temperature determined using this alternative approach

(RT_{To}) and RT_{NDT} might not be directly correlated as currently defined. However, this alternative approach is attractive because it relates the toughness curve to actual measured fracture toughness values rather than the indirect combination of Charpy and drop-weight tests.

There should be and is a fundamental relationship between the K_{IC} curve and the Master Curve. Both curves bound static crack initiation fracture toughness results. Therefore, it should be possible to use T_o to define a value of RT_{To} such that the K_{IC} curve appropriately bounds the fracture toughness data. A key factor in selecting this approach to achieve the short-term objectives is the ability to rely on the existing relationship between the static K_{IC} curve and the K_{IR} curve, which is based on dynamic and crack arrest data. By maintaining this established relationship between the K_{IC} and K_{IR} curves, the procedure developed to index the static Master Curve fracture toughness curve can be appropriately applied to both curves. This process eliminates the need to develop additional dynamic and crack arrest data to establish separate correlations for static and dynamic fracture toughness behavior.

The K_{IC} curve is an empirical lower bound curve while the Master Curve method fits the median of the measured fracture toughness data. The Master Curve approach provides a means of determining tolerance bounds on the toughness prediction, which can be used to construct a statistical lower bound. One feature of the Master Curve approach, which should be considered in vessel integrity analysis when applied directly meeting the PVRC long-term goal, is the size dependence of the data and the lower tolerance bounds. This size dependence is a departure from traditional linear elastic fracture mechanics, where the valid data and transition curve are generally held to be fundamental material properties that are size invariant. The key parameters required to determine the Master Curve-based lower bound structural curve are T_o and the appropriate statistical lower tolerance bound level. The bounding curve for the Master Curve technique is defined for a specific specimen size. In determining T_o, ASTM E 1921-97 requires a size adjustment for the fracture toughness data to the one-inch (25.4 mm) thickness (1T) equivalent, even though the actual test specimens might be either larger or smaller. This procedural approach does not imply that the 1T curve is a universal toughness curve for use in any direct application; the appropriate tolerance bound curve may need to be size-adjusted (or a different tolerance bound selected) to reflect the particular application.

The current ASME Code K_{IC} curve has been applied to the analysis of many different flaws with different size parameters since it has been assumed to be size invariant. The appropriate flaw size and specimen size correction factors need to be developed to establish the indexing relationship for T_o to the K_{IC} curve. Since most users will likely be testing limited numbers of specimens, which will be size corrected to the 1T Master Curve in accordance with ASTM E 1921-97, any additional factors to account for specimen size must be included in the definition of RT_{To}.

The determination of RT_{To} using the ASME Code Case is, in most simple terms, T_o plus an additional temperature increment to account for uncertainties and the general scatter in the measured fracture toughness data. The currently proposed relationship for RT_{To}, for indexing both the K_{IC} and K_{IR} curves was given earlier in Eq. 1. Figure 4 illustrates the data from three large data sets [*11,12*] evaluated in the PVRC Task Group activities: materials 72W, 73W, and HSST Plate 02 (which is essentially the basis for the

Code K_{IC} curve). The data are plotted in terms of temperature (T) minus T_o so that all of the data can be plotted together on a single plot. The data, as shown in Figure 4, have been normalized to 1T size, and the corresponding alternate K_{IC} curve indexed using (T_o+35°F; T_o+19°C) is shown relative to the data.

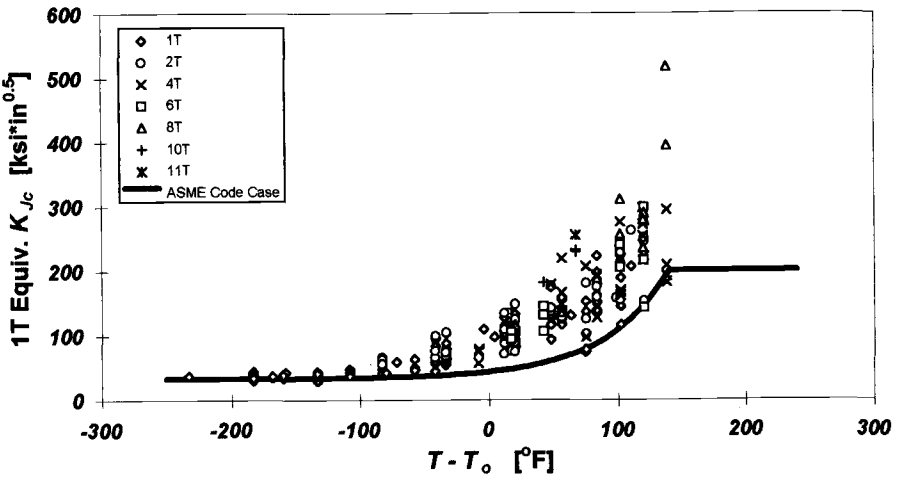


Figure 4 – Fracture *Toughness Data Normalized to 1T and Compared to the ASME Code Case Curve*

Very few of the data points barely transgress the K_{IC} curve. As indicated earlier, the actual fracture toughness data from large test specimens shift to lower toughness values than the 1T-normalized data. Figure 5 shows the same data, without the data being size-corrected to 1T. The (RT_{To})-indexed K_{IC} curve is shown, and a few more data points are shown to transgress the curve. The number of data points to the right of the K_{IC} curve is essentially consistent with a 5% lower tolerance bound. These data points are considered acceptable, since they are few in number and reflect a crack-front size larger than four inches (4T; 102 mm) or greater. This size is significantly larger than any real flaws that could go undetected in a reactor pressure vessel, based on engineering judgment and advances in nondestructive examination technology. Also, there is no need to have an absolute lower bound. If all of the original data used to derive the Code K_{IC} curve were included in Figures 4 and 5 (i.e., see the data in Figure 2), the conclusions drawn here would be the same.

Emphasis on the HSST Plate 02 data set has been made since it is a very large set of data and determined the lower bound for the Code K_{IC} curve. The K_{IC} curve, based on the RT_{To} definition, is compared to this HSST Plate 02 in Figure 6. The newly defined curve continues to encompass the original data set. In fact, for the HSST Plate 02 material, the new definition is even more conservative than using RT_{NDT}. RT_{To} is approximately 25°F (14°C) higher than the corresponding RT_{NDT}. However, a significant amount of data has been generated since the adoption of the original curve and most of

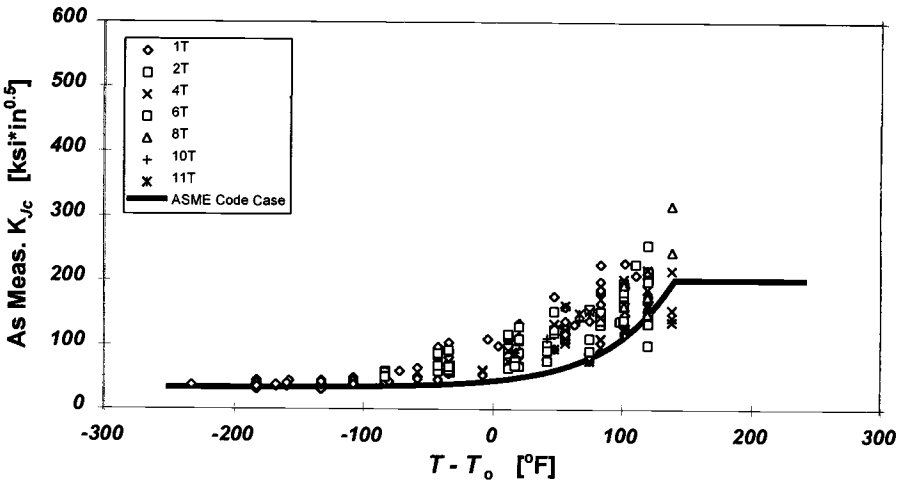


Figure 5 – *As-Measured Fracture Toughness Data Compared to the ASME Code Case Curve*

these additional measurements have been based on elastic-plastic toughness results, consistent with the new Master Curve Test Method. Based upon recent unpublished analyses by Westinghouse (for a significant portion of a large fracture toughness database, which is very similar to the PVRC database)[5], the inherent margin in the original analysis for RT_{NDT} is compared with the inherent margin using the new RT_{To} methodology. Figure 7 illustrates the overall results from the Westinghouse evaluation, which follows the probability of failure method of Wallin. This method determines the probability of a particular valid test result transgressing the resulting K_{IC} curve as a function of crack-front size. In Figure 7, note that for a temperature shift of 35°F (19°C) for a 1T specimen, the probability of failure predicted is approximately 5%. This value is essentially equivalent to the failure probability for the lower bound curve as determined through the Master Curve approach. The results suggest similar levels of statistical significance between the current RT_{NDT} method and the new approach using RT_{To}.

The advantage of the Master Curve T_0 approach is that it allows the reference curve to be keyed directly to fracture toughness measurements. There is a large material-to-material variability in the implied margin terms in the traditional approach. The transition portion of the original K_{IC} curve was determined primarily by one material (HSST Plate 02). The data for the majority of other materials exhibit toughness levels well above the K_{IC} curve and the implied margins are large. The Master Curve approach to defining the toughness reference curve can be used to even out this variability in implied margin.

[5] Personal communication with M. Kirk and R. Lott of Westinghouse, Science and Technology Center, Pittsburgh, PA.

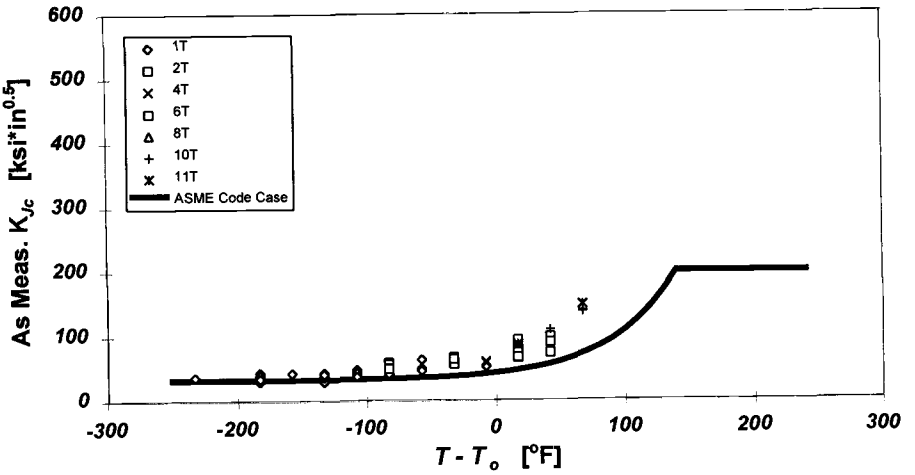


Figure 6 – *HSST Plate 02 Fracture Toughness Data Compared to Draft ASME Code Case Curve*

The ASME Code Case is based on a shift of 35°F (19°C) between RT_{To} and T_o. This implies a higher value of RT_{To} (and therefore a larger implied margin) for HSST Plate 02. However, many materials that now have excessively large margins will have lower values of RT_{To}. The selection of the shift value is effectively a determination of the appropriate level of implied margin. The ASME Code Case sets this value in a manner that is consistent with the intent of the current practice. Figure 7 also indicates a relationship to size. The curve for "as-measured" indicates the non-size-corrected results as compared to the different size-corrected (or scaled) results. The measured data covering a range of specimen sizes falls between the 1T and 2T size-corrected ranges, which indicates that the overall data trend is very similar to the range in which T_o is determined in ASTM E 1921-97. This crack-front size of 1-2 in. (25-51 mm) is also consistent with the size of flaws that should not be missed during inservice inspections of reactor pressure vessels.

As additional testing is performed and analysis of the fracture toughness database continues, there might be other applications of Master Curve fracture toughness properties that will be identified. For example, the petrochemical and petroleum refining industry has initiated an industry-sponsored project to develop applications of the Master Curve methodology for the steels and environmental situations of interest to these industry segments. The long-term objective of the PVRC Task Group and other nuclear power industry groups is to be able to utilize direct measurement of fracture toughness on irradiated materials from RPV surveillance programs. Testing of both unirradiated and irradiated material will enable alternative definition of the toughness curves for assessing RPV integrity.

There are several ways fracture toughness data might be utilized. If existing surveillance capsules include specimens from controlling vessel materials, fracture toughness testing might be performed to generate a value of T_o for the irradiated material.

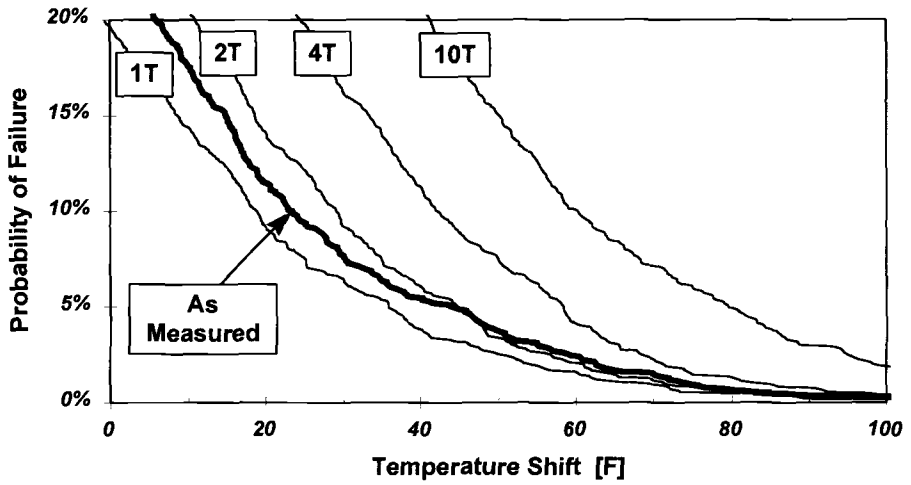


Figure 7 – K_{IC} *Failure Probability Curve as a Function of Temperature Above* T_o *for Different Scale Sizes*

The irradiated properties might be used in a manner similar to the approach described above for unirradiated material. In order to fully utilize irradiated data, a method will have to be developed to project the T_o value measured from specimens irradiated to a particular neutron fluence to other fluence levels. ASTM Subcommittee E10.02 is considering this approach for inclusion in ASTM Standards E 185 and E 900.

Another potential use of fracture toughness data will be to modify or replace the current ASME Code K_{IC} and K_{IR} curves. New fracture toughness curves might be developed to represent pressure vessel materials. A number of different toughness curves might be developed to represent specific subgroups of pressure vessel steels, for example, Linde 80 welds, Linde 1092 welds, SA533 Gr. B, Cl. 1 plate, and so on. A substantial amount of data will be needed to support the development of these generic fracture toughness properties. Such curves could have significant value because many pressure vessel materials have no sources of archive material for additional testing. Fracture toughness data on archive materials that are available could be used to generate fracture toughness curves that have broader application than a single specific material. Data from both unirradiated and irradiated materials from reactor vessel surveillance programs, as well as from archive materials, are currently being generated.

Summary and Conclusions

The following summary and conclusions can be made based upon the review of the technical basis for the draft ASME Code Case:

- The new Master Curve methodology is a revolutionary advance in our understanding of cleavage fracture initiation and ductile-brittle transition behavior in ferritic steels. It is clearly superior to the old RT_{NDT} approach since it is based

upon measurement of actual fracture toughness, rather than Charpy V-notch and drop weight results.

- Application of the ASME Code Case to the HSST Plate 02 data, which dominated the current Code K_{IC} curve (referenced to RT_{NDT}), results in *more* conservatism than before for this specific heat of material. Other materials that exhibited a much larger degree of conservatism using an RT_{NDT} index can show more appropriate levels of conservatism when normalized using RT_{To}.
- The proposed ASME Code Case relationship, $RT_{To} = T_o+35°F$, adequately bounds existing evaluated data and is a technically sound approximation for determining RT_{To}.
- The 5% lower tolerance bound curve determined through ASTM Standard Test Method E 1921-97 for all data evaluated in this study supports the use of the proposed ASME Code Case relationship, $RT_{To} = T_o+35°F$.
- Since the new Master Curve approach is more sound technically and statistically-based, the degree of margin needed for vessel integrity evaluations can be better understood and quantified.
- The PVRC Task Group activities, as well as other industry, international, and NRC programs, are moving forward to codify this methodology. Technical issues exist that will require further research and test data, but these issues are well defined and joint activities are proposed in the industry to clarify existing results and resolve these issues.
- ASTM E 1921-97 adequately covers aspects related to bias and accuracy in the determination of T_o, and the methodology provides a technically sound approach for defining a unique fracture toughness transition temperature (T_o) for ferritic steels applicable to ASME Code adoption.

Acknowledgments

The authors would like to thank the co-authors of the EPRI summary report [*1*] who assisted in this review of the technical basis for the ASME Code Case: Chris Hoffmann and Steve Byrne of ABB-Combustion Engineering, Ken Yoon of Framatome Technologies, and Randy Lott and Mark Kirk of Westinghouse. The efforts of the Toughness Master Curve Task Group are gratefully acknowledged, especially Alan Van der Sluys of McDermott Technology and Sumio Yukawa, Consultant, for their review and leadership efforts. Mark Kirk of Westinghouse is acknowledged for providing review comments and comparison results from unpublished studies. The three pressurized water reactor Owners Groups were instrumental in contributing to the completion of this report and in supporting the development of the technology upon which this report is based. The encouragement of the utility Owners Groups' reactor vessel representatives (Robert Hardies, Baltimore Gas and Electric Company, Charles Tomes, Wisconsin Public Service Corporation, James Pfefferle, Wisconsin Electric Power Company, and John Harrell, Virginia Power Company), who promoted this activity, are especially acknowledged.

References

[1] Server, W. L., et al., *Application of Master Curve Fracture Toughness Methodology for Ferritic Steels*, EPRI TR-108390, April 1998.

[2] Kirk, M., et al., "Bias and Precision of T_0 Values Determined Using ASTM Standard E 1921-97 for Nuclear Reactor Pressure Vessel Steels," *Effects of Radiation on Materials, 19th International Symposium, ASTM STP 1366,* M. L. Hamilton, A. S. Kumar, S. T. Rosinski, and M. L. Grossbeck, Eds., American Society for Testing and Materials (this symposium).

[3] Wallin, K., "The Scatter in K_{IC} Results," *Engineering Fracture Mechanics, Vol. 19, No. 6,* pp. 1085-1093, 1984.

[4] Wallin, K., "The Size Effect in K_{IC} Results," *Engineering Fracture Mechanics, Vol. 22, No. 1*, pp. 149-163, 1985.

[5] Stienstra, D. A., *Stochastic Micromechanical Modeling of Cleavage Fracture in the Ductile-Brittle Transition Region*, Texas A&M University, 1990.

[6] Anderson, T. and Stienstra, D. A., *Probabilistic Fracture Analysis of Reactor Pressure Vessel Steels; Joint EPRI-CRIEPI RPV Embrittlement Studies*, EPRI TR-107027, October 1995.

[7] Sokolov, M. A., "Statistical Analysis of the ASME K_{IC} Database," *Journal of Pressure Vessel Technology, Vol. 120*, Feb. 1998.

[8] *Reference Fracture Toughness Procedures Applied to Pressure Vessel Materials,* American Society of Mechanical Engineers, 1984.

[9] Wallin, K. and Rintamaa, R., "Statistical Definition of the ASME Reference Curves," In *Proceedings of MPC Seminar*, University of Stuttgart, October 1977.

[10] Yoon., K. K., "Alternative Method of RT_{NDT} Determination for Some Reactor Vessel Weld Metals Validated by Fracture Toughness Data", *Journal of Pressure Vessel Technology, Vol. 117*, November 1995.

[11] Nanstad, R. K., et al., *Irradiation Effects on Fracture Toughness of Two High-Copper Submerged-Arc Welds, HSSI Series 5,* NUREG/CR-5913, U.S. Nuclear Regulatory Commission, October 1992.

[12] ASME Section XI Task Group on Flaw Evaluation, *Flaw Evaluation Procedures: Background and Application of ASME Section XI Appendix A*, EPRI NP-719-SR, August 1978.

Mark Kirk,[1] Randy Lott,[1] William L. Server,[2] Robert Hardies,[3] and Stan Rosinski[4]

Bias and Precision of T_o Values Determined Using ASTM Standard E 1921-97 for Nuclear Reactor Pressure Vessel Steels

Reference: Kirk, M., Lott, R., Server, W. L., Hardies, R., and Rosinski, S., **"Bias and Precision of T_o Values Determined Using ASTM Standard E 1921-97 for Nuclear Reactor Pressure Vessel Steels,"** *Effects of Radiation on Materials: 19th International Symposium, ASTM STP 1366,* M. L. Hamilton, A. S. Kumar, S. T. Rosinski, and M. L. Grossbeck, Eds., American Society for Testing and Materials, West Conshohocken, PA, 2000.

Abstract: Recently ASTM adopted a Test Method for the Determination of Reference Temperature, T_o, for Ferritic Steels in the Transition Range (E1921-97). This test method quantifies the variation of fracture toughness with temperature throughout the transition regime based on limited replicate testing at a single temperature. Advances in elastic plastic fracture mechanics enabled adoption of size requirements in E1921-97 that permit testing of specimens as small as 10 mm cross section. Thus, E1921-97 presents the first opportunity to measure directly the fracture toughness of samples removed from surveillance capsules, rather than inferring toughness using RT_{NDT} indexed K_{IC} curve.

We assemble a database of fracture toughness values for reactor pressure vessel steels, including over 1,600 E1921-97 valid fracture toughness values for both irradiated and un-irradiated steels. In this paper, we use this database to address concerns regarding the bias and pecision of T_o values determined by ASTM E1921-97, and regarding the use of T_o as an index temperature for the ASME K_{IC} curve. When the requirements of E1921-97 are satisfied, neither the temperature at which the fracture toughness tests are conducted nor the level of deformation prior to fracture bias the estimate of T_o. Furthermore, the recently proposed T_o-based index for the K_{IC} curve ($RT_{To} \equiv T_o + 35°F$) reduces considerably the degree of scatter in facture toughness data, and contains implicit margins on toughness that are consistent for every steel considered. RT_{To} is superior to RT_{NDT} as an index temperature for the K_{IC} curve, and also provides for a more conservative assessment of vessel safety than does RT_{NDT}.

Keywords: master curve, T_o, RT_{NDT}, RT_{To}, reactor pressure vessel steels, ASME K_{IC} curve, nuclear pressure vessels

[1]Senior and Advisory Engineer, respectively, Westinghouse Electric Company, 1310 Beulah Rd., Pittsburgh, PA 15235.

[2]President, ATI Consulting, P.O. Box 5769, Pinehurst, NC 28374.

[3]Metallurgical Consultant, Baltimore Gas and Electric Company, Calvert Cliffs Nuclear Power Plant, 1650 Calvert Cliffs Pkwy., Lusby, MD 20657.

[4]Project Manager, EPRI, 1300 Harris Blvd., Charlotte, NC 28262.

Copyright© 2000 by ASTM International www.astm.org

Federal law [1] requires nuclear licensees to demonstrate that the effects of neutron irradiation embrittlement do not compromise the safe operation of their reactor pressure vessel (RPV). The variation of the RPV steel's fracture toughness with temperature provides a key input to analyses performed to this end (e.g., pressure-temperature limit analysis, pressurized thermal shock analysis). Currently, the ASME K_{IC} curve, indexed to the state of vessel embrittlement using a RT_{NDT} value adjusted for irradiation effects, provides this toughness characterization. The K_{IC} curve was developed in 1973 [2] as a lower bound to a database of valid linear elastic fracture mechanics (*LEFM*) toughness values for a variety of un-irradiated RPV steels. RT_{NDT} is adjusted for the effects of irradiation by testing Charpy V-notch (CVN) specimens removed from surveillance capsules. Use of this indirect process to quantify the effect of irradiation on toughness was necessitated by the large specimen size once considered necessary to produce "valid" fracture toughness values.

Technological advancements in the past 25 years set the scene for a more direct approach to the characterization of irradiation effects on RPV toughness. Developments in the mathematical description of fracture, and in the physical understanding of the cleavage fracture process combine to enable the direct measurement of fracture toughness. These advancements are reviewed briefly here:

- Mathematical Description of Fracture: Current ASME code relies on linear elastic fracture mechanics (*LEFM*) for both toughness characterization and structural assessment. While *LEFM* provides an adequate description of the driving force to fracture in a thick-section RPV, its requirements for contained plasticity at fracture confound efforts to measure toughness using small specimens. Advancements in elastic plastic fracture mechanics, or *EPFM*, enable the testing of smaller fracture toughness specimens while still ensuring the applicability of these results to heavy-section structures.
- Physical Understanding of Fracture: Advances in understanding of the micro-mechanisms responsible for cleavage fracture enable definition of the entire lower transition curve based on limited replicate fracture tests conducted at a single temperature. The theoretical background for these advances is attributable to the work of many investigators [3-6]. Wallin, Saario, and Törrönen (WST) [7] have combined this physical understanding into a predictive tool. Their technique is commonly referred to as the Master Curve, which is based on the following three premises:
    1. The variation of median toughness with temperature is identical for all ferritic steels,
    2. The effects of crack front length on fracture toughness are explicitly accounted for using a weakest link model, and
    3. The dispersion of toughness about the median is described using a Weibull distribution with a constant slope value of 4.

  In situations where these premises hold, one can uniquely define the variation of fracture toughness with temperature in the transition regime, complete with statistical tolerance bounds, simply by estimating the Master Curve index temperature T_o.

Recently ASTM adopted E1921-97, which combines these advancements to provide an estimation protocol for T_o. E1921-97 includes the following *EPFM*-based size requirement:

$$MIN(b,a,B) \geq \frac{30 \cdot K_{Jc}^2}{\sigma_{ys} \cdot E} \quad (1)$$

where b is the specimen ligament, a is the crack length, B is the specimen thickness, σ_{ys} is the yield strength, and E is the elastic modulus. This size requirement permits determination of valid K_{Jc} values for most RPV steels using specimens as small as 10mm cross section. Currently, CVN specimens are removed from surveillance capsules and tested to estimate RT_{NDT}, a value *correlated* with fracture toughness. Equation (1) suggests that these samples can instead be tested as small fracture toughness specimens to *measure directly* the effects of irradiation on toughness using the temperature index T_o. Thus, the adoption of E1921-97 and the demonstrated appropriateness of the Master Curve to RPV steels [8] together provide a basis for eliminating inaccuracies inherent to current correlative approaches to toughness estimation.

Scope of Investigation

Proposals for use of T_o to assess nuclear RPV integrity have raised the following concerns:

1. T_o Estimate Bias and Precision: E1921-97 permits determination of T_o values based on limited replication. Tests may be conducted over a wide temperature range, and over deformation conditions ranging from well-contained plasticity to full ligament yielding. Concerns have been raised that this flexibility may produce a systematic variation of T_o with test conditions, even when T_o is determined in accord with the requirements of E1921-97.
2. T_o as an Index Temperature for Reference Toughness Curves: T_o provides a means to index the variation of fracture toughness with temperature in the same way that RT_{NDT} indexes the ASME K_{IC} curve. Recently, ASME Section XI passed a Code Case that permits use of a T_o-based reference temperature (termed RT_{To}) as an alternative to RT_{NDT} [9]. This Code Case has raised concerns regarding the technical superiority of RT_{To} relative to RT_{NDT}, and regarding the appropriate relationship between the two index temperatures.

In this investigation we assemble a fracture toughness database for reactor pressure vessel steels (both irradiated and un-irradiated), and use this database to address these concerns.

Fracture Toughness Database

A database of fracture toughness values for ASTM A533B and ASTM A508 steels (and their weldments) is assembled from the literature. Table 1 describes this database, which includes the following data groupings:

- 27 un-irradiated steels (8 plates, 11 welds, 1 HAZ, 7 forgings)
- 2 un-irradiated non-RPV steels (1 plate, 1 forging)

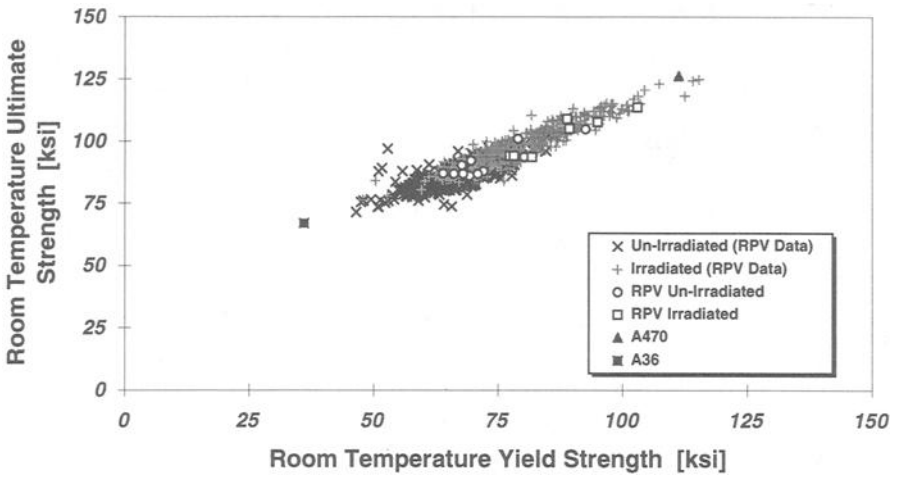


FIGURE 1 – *Variation of ultimate tensile strength with yield strength for steels in the fracture toughness database (filled and open symbols) compared with those characteristic of the operating nuclear vessels (plusses and crosses).*

- 10 Irradiated RPV steels (1 plate, 9 welds)
- 2,043 fracture toughness values (1,664 E1921-97 valid)
  - Un-Irradiated RPV: 1,431 values (1,115 E1921-97 valid)
  - Un-Irradiated non-RPV: 300 values (247 E1921-97 valid)
  - Irradiated RPV: 312 values (302 E1921-97 valid)
- Specimen sizes range from fatigue precracked CVNs to 11T compact tension specimens.

While this database focuses on RPV steels and their weldments, the range of chemistry, tensile properties, and product forms included may not fully represent the diversity of conditions in all operating nuclear vessels. For this reason, we carry two non-RPV steel data sets through the analysis. These non-RPV steels differ more from each other, and from RPV steels, than any two RPV steels differ from one another. Consequently, the data for non-RPV steels supports the argument that the Master Curve applies to *all* RPV steels by providing evidence that steels of strength and chemical composition that extend beyond those characteristic of nuclear grade RPV steels are still modeled well by the Master Curve. The two non-RPV steels are A470 (a high strength / high alloy rotor forging) and A36 (a low strength / low alloy plate used in civil structures). Figure 1 demonstrates that the tensile properties of these two non-RPV steels differ markedly from each other, and bound the range of tensile properties of commercial nuclear RPVs, both before and after irradiation.

When ASME adopted the K_{IC} curve in 1973, the data basis consisted of 173 quasi-static fracture toughness values for 11 un-irradiated heats of RPV steel (and their weldments). The number of un-irradiated fracture toughness data summarized in Table 1 exceeds this original basis by a factor of 5.8. Moreover, a significant quantity of fracture toughness data is now available for irradiated steels (302 values, or 1.75 times more than

the original 173 *un-irradiated* datum). These data provide an empirical basis for the Master Curve that exceeds considerably that used to justify the original K_{IC} curve.

TABLE 1 – *Fracture toughness database for RPV steels.*

					T_{TEST}-T_o Range		Specimen Sizes		No. of Specimens	
Ref.	Material ID	Product Form	RT_{NDT} [°F]	T_o [°F]	Min [°F]	Max [°F]	Min	Max	Total	E1921 Valid
Un-Irradiated RPV Steels										
[2]	A508 Cl. 2	Forging	51	-60	-90	60	2T	6T	9	9
[2]	A508 Cl. 2	Forging	65	-55	-120	41	2T	8T	10	10
[2]	A508 Cl. 2	Forging	50	-124	-196	24	1T	2T	13	13
[2]	A533B Cl. 1	Plate	65	-74	-247	77	1T	2T	13	13
[2]	A533B Cl. 1	HAZ	0	-132	-118	68	1T	2T	6	6
[2]	A533B Cl. 1	Weld	0	-57	-264	57	1T	8T	8	8
[2]	A533B Cl. 1	Weld	-45	-151	-169	-49	1T	2T	10	10
[2]	HSST-01	Plate	20	-1	-149	-149	1T	1T	17	17
[2]	HSST-01	Weld	0	-105	-70	55	1T	6T	8	8
[2]	HSST-02	Plate	0	-17	-233	67	1T	11T	60	60
[2]	HSST-03	Plate	20	31	-181	-181	1T	1T	9	9
[14]	72W	0124 Weld	-9.4	-70	-168	138	1T	8T	74	74
[14]	73W	0124 Weld	-29.2	-78	-160	119	1T	8T	77	77
[15]	A508 Cl. 3	Forging	-22	-157	9	99	1T	1T	155	143
[16]	A533B Cl. 1	Plate	5	-149	19	163	1/2T	1T	157	88
[17]	A508 Cl. 2	Forging	149	-2	-97	52	1T	4T	33	33
[18]	A533B Cl.1	Plate	-9.4	-109	-129	184	1/2T	4T	121	118
[19]	A533B Cl. 1	Plate	5	-159	29	227	CVN	9T	217	87
[20]	WF70 Beltline	80 Weld	27	-71	-77	103	1/2T	4T	57	51
[20]	WF70 Nozzle	80 Weld	27	-34	-114	66	1/2T	1T	32	32
[21]	HSST-02	Plate		-8	-140	82	1T	1T	25	23
[21]	68W	0091 Weld		-133	-79	111	1T	1T	10	10
[21]	69W	0091 Weld		5	-153	70	1T	1T	21	19
[21]	70W	0124 Weld		-77	-134	46	1T	1T	10	10
[21]	71W	80 Weld		-41	-98	55	1T	1T	7	7
[22]	A508 Cl. 3	Forging	-13	-46	-192	60	1/2T	4T	153	109
[23]	A508 Cl. 3	Forging		-159	2	225	CVN	8T	119	71
Non RPV Steels										
[22]	A470	Forging	-31	-116	-204	94	1/2T	4T	124	123
[24]	A36	Plate		-68	-252	100	1/2T	1.25T	176	124
Irradiated RPV Steels										
[14]	72W	0124 Weld	138	85	-187	118	1T	4T	70	69
[14]	73W	0124 Weld	179	99	-202	122	1T	4T	66	61
**	WF70 Beltline	80 Weld		88	-146	106	CVN	1T	50	47
**	WF70 Beltline	80 Weld		37	-26	-26	CVN	CVN	7	7
**	WF70 Nozzle	80 Weld		135	-57	32	CVN	1T	28	28
[21]	HSST-02	Plate		127	-140	49	1T	1T	28	28
[21]	68W	0091 Weld		-111	-90	53	1T	1T	15	15
[21]	69W	0091 Weld		66	-98	56	1T	1T	16	16
[21]	70W	0124 Weld		-33	-160	38	1T	1T	16	16
[21]	71W	80 Weld		2	-101	30	1T	1T	16	15

** - R. Nanstad, personal communication.

T_o Estimate Bias and Precision

ASTM E1921-97 employs K_{Jc} tests to determine T_o provided two conditions are satisfied:

1. The estimated median K_{Jc} value exceeds 46 ksi$\sqrt{}$in, and
2. Between 6 and 10 of the measured K_{Jc} values satisfy the size requirement of Eq. (1).

This latitude of permissible test conditions, and the limited required replication has led to concerns regarding the possibility of a systematic variation of T_o within the limits allowed by E1921-97 [10]. Here we address these concerns using the fracture toughness database.

Table 2 summarizes T_o values estimated using E1921-97. T_o values for all iso-temperature data groupings that meet ASTM requirements (44 for un-irradiated RPV steels, 14 for non-RPV steels, and 17 for irradiated RPV steels) are calculated. Table 2 includes T_o values calculated using the multi-temperature (MT) technique of Moskovic [11]. While both the MT and E1921-97 T_o values are estimates, the MT T_o values are regarded as a best experimental estimate because they are based on much larger data sets than E1921-97 T_o values (77 values for MT T_o estimates *vs.* 10 for E1921-97 T_o estimates, on average). These data are used to examine the effects of the following variables on the precision and bias of E1921-97 T_o estimates.

1. Test temperature
2. Deformation prior to fracture
   a) Maximum deformation
   b) Proportion of "highly" deformed specimens
3. Data replication

The following statistical test is employed:

1. The deviation of an E1921-97 T_o estimate from the best experimental estimate of T_o is calculated (see the next to the last column in Table 2).
2. These deviations are plotted as a function of the variables listed above.
3. The E1921-97 T_o values are considered accurate (i.e. differing by no more than the scatter inherent to the data) relative to the best experimental estimate of T_o provided that both the slope and intercept of a line fit through the data are statistically indistinguishable from zero (based on a Student's-T test at a 99% confidence level).

The results of this evaluation are as follows:

- Test Temperature (Fig. 2): The test temperature at which K_{Jc} experiments are conducted exerts no systematic influence on the value of T_o over the entire temperature range for which experimental data is available ($-50°F < T - T_o < +175°$ F).
- Maximum Deformation Prior to Fracture (Fig. 3): The deformation characteristic of an E1921-97 data set is quantified as follows:

$$M_{MINIMUM} = \frac{E \cdot b \cdot \sigma_{ys}}{K^2_{Jc|Maximum}} \qquad (2)$$

TABLE 2 – *T_o values for RPV steels.*

					K_{Jc} Specimen Counts				ASTM E1921-97 T_o Calculation			Multi-Temperature T_o Calculation		Comparisons	
Ref	Material ID	B [in]	W/B	T_{TEST} [°F]	Total	E1921 Valid	Reqd. by E1921	# w/ M<50	K_{JclMed} [ksi*in$^{0.5}$]	T_o [°F]	σ [°F]	T_o [°F]	# of Specimens	$T_o\|_{E1921}$ - $T_o\|_{MT}$ [°F]	#Specl$_{MT}$ / #Specl$_{E1921}$
Un-Irradiated RPV Steels															
[2]	HSST-02	2	2	-50	7	7	7	0	69	-10	13	-17	60	7	8.6
[14]	72W	1	2	-112	6	6	6	0	77	-89	13	-70	74	-19	12.3
[14]	72W	1	2	-58	6	6	6	0	100	-71	13	-70	74	-1	12.3
[14]	73W	1	2	-112	9	9	7	0	73	-82	11	-78	77	-4	8.6
[14]	73W	1	2	-58	6	6	6	0	100	-71	13	-78	77	7	12.8
[14]	73W	1	2	5	8	7	6	2	195	-87	12	-78	77	-9	9.6
[17]	A508 Cl. 2	1	2	0	10	10	6	0	81	15	10	-2	33	17	3.3
[18]	A533B Cl.1 (13A)	0.5	2	-103	20	20	6	3	97	-112	7	-109	121	-3	6.1
[18]	A533B Cl.1 (13A)	1	2	-103	26	26	6	0	101	-117	6	-109	121	-8	4.7
[18]	A533B Cl.1 (13A)	2	2	-103	12	12	6	0	108	-125	9	-109	121	-16	10.1
[18]	A533B Cl.1 (13A)	4	2	-103	6	6	6	0	105	-122	13	-109	121	-13	20.2
[19]	A533B Cl. 1	0.98	1	-92	12	10	6	7	161	-163	10	-159	217	-4	18.1
[19]	A533B Cl. 1	1.97	1	-58	12	12	6	2	208	-157	9	-159	217	2	18.1
[19]	A533B Cl. 1	3.94	1	-60	6	6	6	0	174	-139	13	-159	217	20	36.2
[19]	A533B Cl. 1	3.94	1	14	9	7	6	4	429	-161	12	-159	217	-2	24.1
[19]	A533B Cl. 1	9.06	1	14	6	6	6	0	325	-132	13	-159	217	27	36.2
[15]	A508 Cl. 3	1	2	-148	50	50	6	0	99	-159	5	-157	155	-2	3.1
[15]	A508 Cl. 3	1	2	-103	55	55	6	0	133	-151	4	-157	155	6	2.8
[15]	A508 Cl. 3	1	2	-58	50	38	6	28	203	-154	5	-157	155	3	3.1
[16]	A533B Cl. 1	0.49	2	-94	12	9	6	6	147	-154	11	-149	157	-5	13.1
[16]	A533B Cl. 1	0.49	2	-130	6	6	6	0	88	-125	13	-149	157	24	26.2
[16]	A533B Cl. 1	0.49	2	-94	10	7	6	5	149	-156	12	-149	157	-7	15.7
[16]	A533B Cl. 1	0.98	2	-94	10	10	6	0	116	-125	10	-149	157	24	15.7
[16]	A533B Cl. 1	0.98	2	-94	8	8	6	0	164	-166	11	-149	157	-17	19.6
[16]	A533B Cl. 1	0.98	2	-94	10	10	6	1	155	-160	10	-149	157	-11	15.7
[20]	WF70 Beltline	0.5	2	-58	6	6	6	1	102	-73	13	-71	57	-2	9.5
[20]	WF70 Beltline	1	2	-13	7	7	6	1	160	-83	12	-71	57	-12	8.1
[20]	WF70 Beltline	1	2	-58	6	6	6	0	89	-54	13	-71	57	17	9.5

TABLE 2 (cont.) – *T_o values for RPV steels.*

					K_{Jc} Specimen Counts				ASTM E1921-97 T_o Calculation			Multi-Temperature T_o Calculation		Comparisons	
Ref	Material ID	*B* [in]	*W/B*	T_{TEST} [°F]	Total	E1921 Valid	Reqd. by E1921	# w/ *M*<50	K_{JcIMed} [ksi*in$^{0.5}$]	T_o [°F]	σ [°F]	T_o [°F]	# of Specimens	$T_o\|_{E1921}$ - $T_o\|_{MT}$ [°F]	#Specl$_{MT}$ / #Specl$_{E1921}$
Un-Irradiated RPV Steels (Continued)															
[20]	WF70 Nozzle	0.5	2	-58	7	7	6	0	79	-38	12	-34	32	-4	4.6
[20]	WF70 Nozzle	1	2	-13	8	8	6	0	98	-23	11	-34	32	11	4.0
[23]	A508 Cl. 3	3.15	1	5	20	16	6	18	403	-163	8	-159	119	-4	6.0
[23]	A508 Cl. 3	3.15	1	-22	10	10	6	0	270	-149	10	-159	119	10	11.9
[23]	A508 Cl. 3	3.15	1	-49	11	11	6	0	199	-143	10	-159	119	17	10.8
[23]	A508 Cl. 3	3.15	1	-85	8	8	6	0	153	-150	11	-159	119	10	14.9
[23]	A508 Cl. 3	7.87	1	5	8	8	6	0	318	-139	11	-159	119	20	14.9
[22]	A508 Cl. 3	0.5	2	-148	7	7	7	0	62	-91	13	-46	153	-44	21.9
[22]	A508 Cl. 3	0.5	2	-76	30	30	7	0	73	-45	6	-46	153	2	5.1
[22]	A508 Cl. 3	1	2	-76	8	8	7	0	74	-46	12	-46	153	0	19.1
[22]	A508 Cl. 3	0.5	2	-4	13	13	6	3	97	-13	9	-46	153	33	11.8
[22]	A508 Cl. 3	0.5	2	-4	27	21	6	14	119	-38	7	-46	153	8	5.7
[22]	A508 Cl. 3	1	2	-4	12	12	6	0	113	-33	9	-46	153	14	12.8
[22]	A508 Cl. 3	1	2	-4	12	12	6	0	112	-31	9	-46	153	16	12.8
[22]	A508 Cl. 3	2	2	-4	6	6	6	0	135	-54	13	-46	153	-8	25.5
[22]	A508 Cl. 3	1	2	14	10	10	6	4	166	-60	10	-46	153	-13	15.3
Non-RPV Steels															
[22]	A470	0.5	2	-148	28	28	6	0	77	-124	6	-116	124	-8	4.4
[22]	A470	3	2	-148	7	7	6	0	85	-139	12	-116	124	-23	17.7
[22]	A470	0.5	2	-76	8	8	6	0	105	-96	11	-116	124	21	15.5
[22]	A470	0.5	2	-76	27	26	6	3	116	-108	6	-116	124	8	4.6
[22]	A470	1	2	-76	8	8	6	0	121	-112	11	-116	124	4	15.5

TABLE 2 (cont.) – *T_o values for RPV steels.*

					K_{Jc} Specimen Counts				ASTM E1921-97 T_o Calculation			Multi-Temperature T_o Calculation		Comparisons	
Ref	Material ID	B [in]	W/B	T_{TEST} [°F]	Total	E1921 Valid	Reqd. by E1921	# w/ M<50	K_{JcMed} [ksi*in$^{0.5}$]	T_o [°F]	σ [°F]	T_o [°F]	# of Specimens	$T_o\|_{E1921}$ - $T_o\|_{MT}$ [°F]	#Specl$_{MT}$ / #Specl$_{E1921}$
Non-RPV Steels (Continued)															
[24]	A36	0.5	1	-105	16	16	7	5	69	-66	8	-68	176	2	11.0
[24]	A36	1.25	1	-45	8	8	6	0	97	-54	11	-68	176	14	22.0
[24]	A36	1.25	1	-18	8	8	6	6	127	-61	11	-68	176	7	22.0
[24]	A36	0.49	2	-105	14	14	7	1	68	-63	9	-68	176	4	12.6
[24]	A36	1.25	2	-105	8	8	7	0	62	-47	12	-68	176	20	22.0
[24]	A36	0.49	2	-45	17	12	6	9	107	-67	9	-68	176	1	10.4
[24]	A36	1.25	2	-45	7	7	7	0	75	-18	13	-68	176	49	25.1
[24]	A36	1.25	2	0	22	9	6	17	155	-66	11	-68	176	1	8.0
Irradiated RPV Steels															
[14]	72W	1	2	185	9	9	6	1	166	111	11	85	70	26	7.8
[14]	72W	1	2	203	6	6	6	0	173	124	13	85	70	39	11.7
[14]	72W	2	2	185	6	6	6	0	197	92	13	85	70	7	11.7
[14]	72W	2	2	203	6	6	6	0	199	109	13	85	70	24	11.7
[14]	73W	1	2	185	10	10	6	0	159	116	10	99	61	17	6.1
[14]	73W	2	2	203	10	10	6	0	186	116	10	99	61	17	6.1
**	WF70 Nozzle	1	2	167	6	6	6	0	113	139	13	135	28	4	4.7
**	WF70 Nozzle	0.5	2	149	6	6	6	0	88	154	13	135	28	19	4.7
**	WF70 Nozzle	1	2	113	7	7	6	0	76	137	12	135	28	2	4.0
**	WF70 Nozzle	0.394	1	77	9	9	7	0	71	113	11	135	28	-22	3.1
**	WF70 Beltline	0.5	2	68	6	6	6	0	82	83	13	88	50	-5	8.3
**	WF70 Beltline	1	2	95	6	6	6	0	95	89	13	88	50	1	8.3
**	WF70 Beltline	0.394	1	71.6	10	8	6	3	86	79	11	88	50	-9	5.0
**	WF70 Beltline	0.394	1	32	8	8	8	0	57	104	13	88	50	16	6.3
**	WF70 Beltline	0.394	1	10.4	7	7	7	3	76	35	12	37	50	-2	7.1
[21]	HSST-02	1	2	122	10	10	6	0	85	131	10	127	28	4	2.8
[21]	HSST-02	1	2	176	10	10	6	0	136	126	10	127	28	-1	2.8

** - R. Nanstad, personal communication.

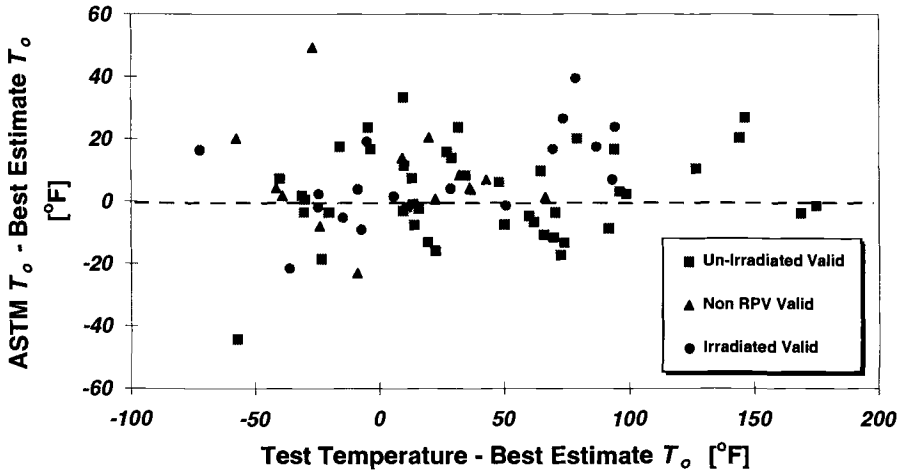


FIGURE 2 – *Effect of test temperature on T_o.*

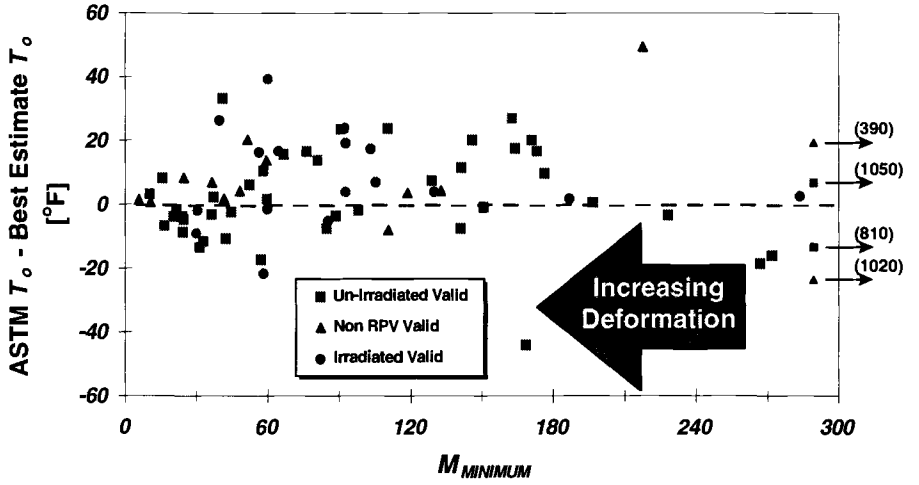


FIGURE 3 – *Effect of deformation level on T_o.*

As $E\sigma_{ys}/K_{Jc}^2$ is proportional to $1/CTOD$, M is proportional to the ratio of the remaining ligament to the crack tip opening displacement at cleavage fracture. The information in Fig. 3 demonstrates that the deformation prior to fracture experienced by K_{Jc} experiments conducted exerts no systematic influence over the resultant value of T_o covering the entire deformation range for which experimental data is available ($30 < M_{MINIMUM} < 1{,}100$). Evaluations based on average and maximum values of M produce the same conclusions.

- Number of "High" Deformation Values (Fig. 4): During the development of E1921-97, considerable debate focused on selection of the value of the numeric

coefficient (M-value) in eq. (1). Candidate values of 30 and 50 were considered, with 30 being adopted in the standard. Nevertheless, certain portions of the technical community remain concerned that M=30 is not sufficiently restrictive to ensure that T_o estimates are specimen size insensitive. Use of the M=50 value, which is demonstrated by Dodds, et al. [12,13] to limit the deformation prior to fracture to the small-scale yielding regime, would have been more acceptable to these constituencies. The comparison in Fig. 3 illustrates that data sets that have single specimens deformed to M=30 (or more) do not exhibit biased T_o estimates. However, if a sizable proportion of the K_{Jc} values in a data set experienced "high" deformation (defined as M<50), T_o may be influenced. Figure 4 demonstrates that available empirical evidence for RPV steels provides no basis for this concern.

- Data Replication (Fig. 5): As illustrated in Fig. 5, increased data replication reduces T_o uncertainty. Appendix B of E1921-97 provides the following estimate for 85% tolerance bounds on T_o uncertainty:

$$T_o = T_o|_{E1921} \pm \frac{Z\beta}{\sqrt{N}} \tag{3}$$

where β depends on the median toughness (β increases as median toughness reduces from 91 ksi$\sqrt{\text{in}}$), Z=1.44 for an 85% tolerance bound, and N is the number of samples tested. Figure 6 superimposes these tolerance limits on the data of Fig. 5 for two different levels of median toughness. This comparison demonstrates that the uncertainty estimate of E1921-97, Appendix B, is appropriate for RPV steels.

Table 3 summarizes the results of the Student's T-test applied to the following data groupings: all data, un-irradiated RPV steels, non-RPV steels, and irradiated RPV steels. These data demonstrate that neither test temperature nor the degree of deformation prior to fracture exerts a systematic influence on T_o values. Thus, we find no empirical basis for concerns regarding systematic influences of these variables on T_o, provided T_o is determined in accordance with the requirements of E1921-97.

Temperature Index Parameters

T_o indexes the variation of fracture toughness with temperature. Recently, ASME Section XI passed a Code Case that permits use of a T_o-based reference temperature (termed RT_{To}) as an alternative to RT_{NDT} [9]. The Code Case includes the following relationship:

$$RT_{To} \equiv T_o + \Delta \tag{4}$$

The proposed Δ value of 35°F has raised questions regarding the technical superiority of RT_{To} relative to RT_{NDT}, and regarding the appropriate relationship between these two index temperatures. Both of these concerns are evaluated using the fracture toughness database.

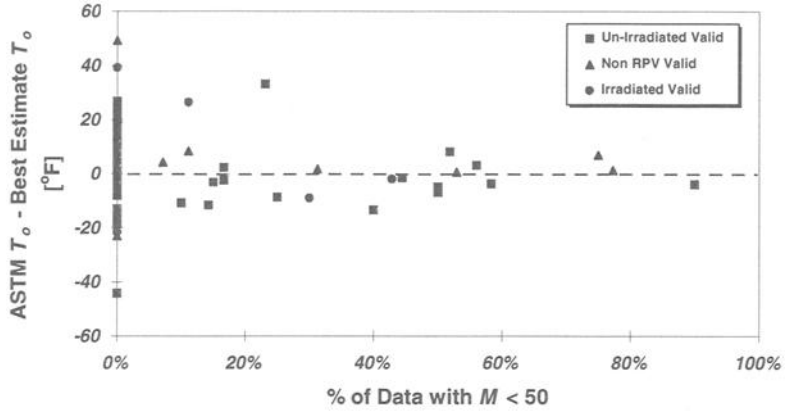


FIGURE 4 – *Effect of the number of "highly" deformed specimens in a data set on T_o.*

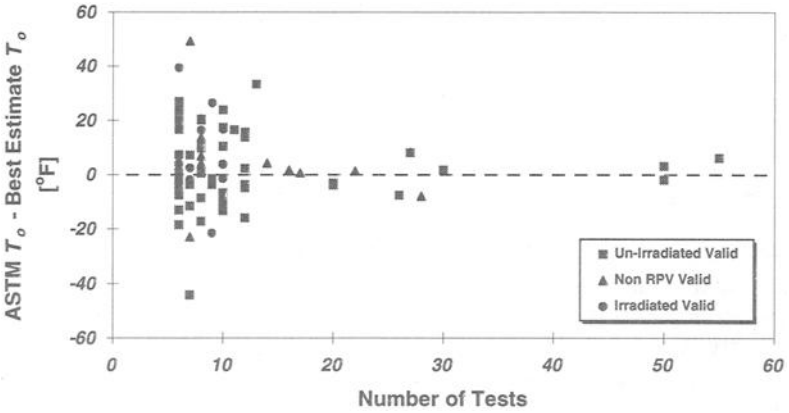


FIGURE 5 – *Effect of data set size on T_o.*

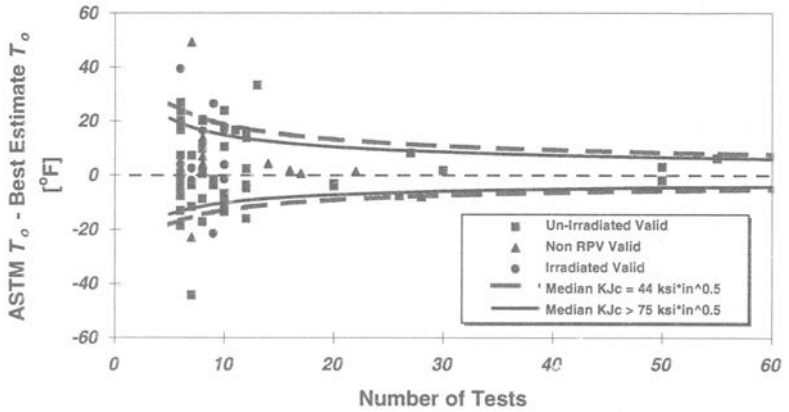


FIGURE 6 – *Effect of data set size on T_o overlaid with E1921-97 85% tolerance bounds.*

TABLE 3 – *Statistical tests on T_o bias.*

		Test on Intercept			Test on Slope		
Variation of T_o Error with	**Data Set**	**T stat**	**T for 99%**	**Signif?**	**T stat**	**T for 99%**	**Signif?**
$M_{Minimum}$	**All Data**	**2.74**	**2.326**	**Yes**	**1.15**	**2.326**	**No**
	Un-Irradiated RPV	0.96	2.33	No	0.36	2.33	No
	Non-RPV	2.11	2.65	No	1.20	2.65	No
	Irradiated RPV	1.45	2.58	No	0.30	2.58	No
Test Temp. - T_o	**All Data**	**1.57**	**2.33**	**No**	**1.28**	**2.33**	**No**
	Un-Irradiated RPV	0.07	2.33	No	1.11	2.33	No
	Non-RPV	1.72	2.65	No	0.60	2.65	No
	Irradiated RPV	1.32	2.58	No	2.66	2.58	Yes

Comparison of Candidate Index Temperatures

An index temperature is used to ensure that an appropriately large proportion of fracture toughness data lie above the K_{IC} curve. Thus, an index temperature should have the following characteristics:

- Scatter Reduction: An index temperature should reduce the scatter in toughness data relative to that exhibited by toughness data plotted *vs.* temperature with no index temperature. The best candidate index temperature will reduce scatter the most.
- Implicit Margins: An index temperature should place all data sets in the same position relative to the K_{IC} curve so that a consistent implicit toughness margin (that is, degree of toughness under-prediction) occurs for every steel considered.

Here we evaluate RT_{To} and RT_{NDT} relative to these criteria.

Data sets in Table 1 having measured values of both RT_{NDT} and RT_{To} were used in this evaluation. Results of the evaluation are as follows:

- Scatter Reduction: Figure 7 illustrates that use of RT_{NDT} as an index temperature increases slightly the scatter in un-irradiated fracture toughness data relative to the scatter when no index temperature is used. Conversely, use of RT_{To} compresses dramatically the data scatter.
- Implicit Margins: Figure 8 illustrates that, among the data summarized in Table 1, considerable variability exists in the correspondence between measured values of RT_{NDT} and T_o. The following data sets are selected for illustration:
  - RT_{To} above RT_{NDT}: HSST-02 [2], $RT_{To} - RT_{NDT} = +18°F$
  - RT_{To} far below RT_{NDT}: A508 Cl. 3 forging [15], $RT_{To} - RT_{NDT} = -100°F$

  Figure 9 shows these data sets plotted *vs.* temperature indexed to RT_{NDT}. The distance between the fracture toughness data and the K_{IC} curve differs for each case. However, when these data sets are plotted *vs.* temperature indexed to RT_{To} (Fig. 10) a different picture emerges. Here a consistent distance between the fracture toughness data and the K_{IC} curve occurs for both steels.

In summary, the current ASME toughness estimation methodology (RT_{NDT}-based) increases the degree of scatter in fracture toughness data, and contains implicit margins on toughness that vary considerably for different RPV steels. Conversely, the proposed

alternative methodology (T_o-based) reduces considerably the degree of scatter in fracture toughness data, and contains implicit margins on toughness that are consistent for every steel considered. Thus, RT_{To} emerges as a superior index temperature to RT_{NDT} for use with the K_{IC} curve.

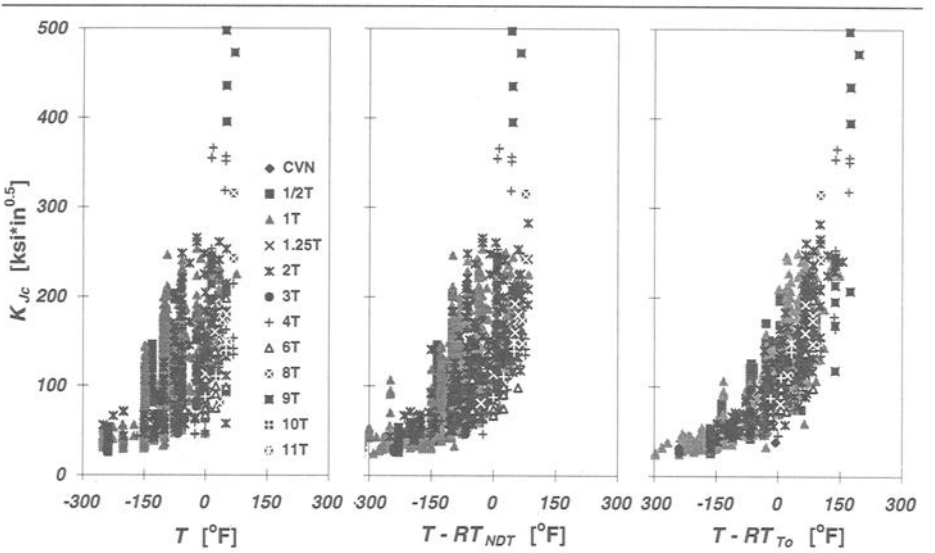


FIGURE 7 – *The scatter reduction characteristics of RT_{NDT} (center) and RT_{To} (right) relative to non-indexed data (left) for un-irradiated RPV steels.*

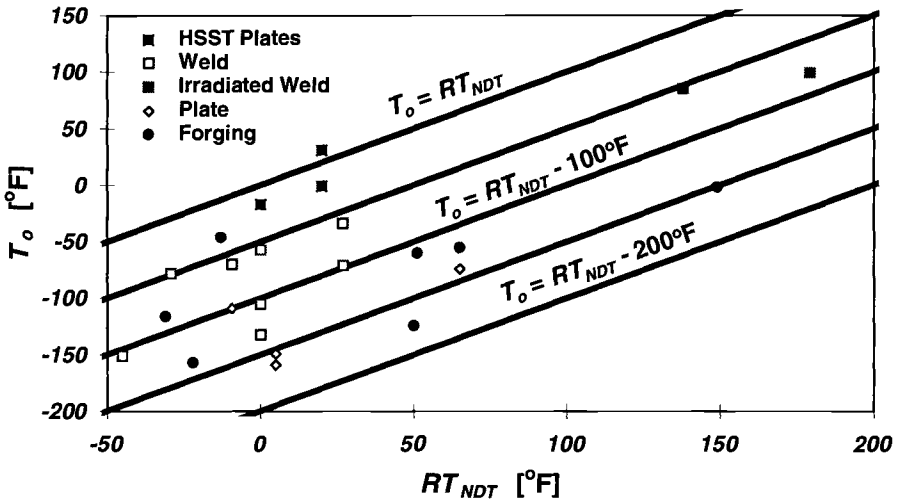


FIGURE 8 – *Relationship between T_o and RT_{NDT} for RPV steels.*

Selection of a Value for Δ

The information presented in the preceding section demonstrates the technical superiority of RT_{To} to RT_{NDT} as an index temperature. Nevertheless, the need to select a value for Δ in the definition of RT_{To} (eq. (4)) remains. To maintain linkage with historically accepted safety margins, a value of Δ is selected such that the K_{IC} curve, when indexed to RT_{To}, bounds available fracture toughness data in a manner functionally equivalent to how the K_{IC} curve indexed to RT_{NDT} bounds available fracture toughness data. The data detailed in Table 1 are again used.

To perform this evaluation, an objective definition of the term "functionally equivalent" is needed. Here we explore the following possibilities:

1. Δ can be defined to ensure that the data set which established the position of the K_{IC} curve when indexed to RT_{NDT} (HSST-02 [2]) has the same implicit margin (that is, proximity of toughness data to the bounding curve) when the K_{IC} curve is indexed to RT_{To}.
2. Δ can be defined to ensure that all of the margin implicit to the original K_{IC} database is maintained.
3. Δ can be defined to ensure that a K_{IC} curve indexed to RT_{To} provides an absolute bound to all data not on the lower shelf (that is, at temperatures exceeding T-RT_{NDT} = -100°F). This definition is consistent with the approach used to establish the K_{IC} curve. However, increases in the amount of toughness data available (173 values when the K_{IC} curve was established *vs.* 1196 values today) produce a six-fold reduction in the proportion of future data expected to lie below the bounding curve (0.6% historically *vs.* 0.1% now). Such a reduction may be neither needed nor justified.

One other definition of "functionally equivalent" cannot be pursued. As illustrated in Fig. 9, implicit margins on toughness vary considerably for the current RT_{NDT}-based methodology. Therefore, it is not possible to define Δ to maintain ***the*** margin implicit to a RT_{NDT} indexed K_{IC} curve because no single, unique, margin exists in the current methodology.

The first and second values of Δ are determined as follows:

1. Calculate the mean sum of squares of K_{Jc} residuals between the K_{IC} curve (indexed to RT_{NDT}) and the data set.
2. Vary Δ until the mean sum of squares of K_{Jc} residuals between the K_{IC} curve (indexed to RT_{To}) and the data set becomes equivalent to the value calculated in Step 1.

The third value of Δ is determined by increasing Δ until all data not on the lower shelf are bounded by the K_{IC} curve. Δ values based on the three candidate definitions of "functionally equivalent" are as follows:

1. Implicit margin maintained for HSST-02: Δ = 17°F
2. Implicit margin maintained for original K_{IC} database: Δ = 33°F
3. A RT_{To} indexed K_{IC} curve that bounds all currently available data: Δ = 105°F

The level of margin implicit to the current assessment methodology (i.e., a RT_{NDT} indexed K_{IC} curve) varies considerably (Fig. 9). Therefore, in the past one could rely only on a level of implicit margin consistent with that of the most limiting material.

Consequently, it is the historical margin implicit to HSST-02 (Definition 1) that the newly proposed T_o-based methodology must maintain to align with the current licensing basis for commercial nuclear plants. As mentioned previously, ASME Code Case N-629 advocates a Δ value of 35°F. This Δ value exceeds that needed to maintain consistency with the current licensing basis (Definition 1) by 18°F. Consequently, RT_{To} emerges as an indexing parameter for the K_{IC} curve that is simultaneously technically superior to, and more conservative than, current approaches that are based on RT_{NDT}.

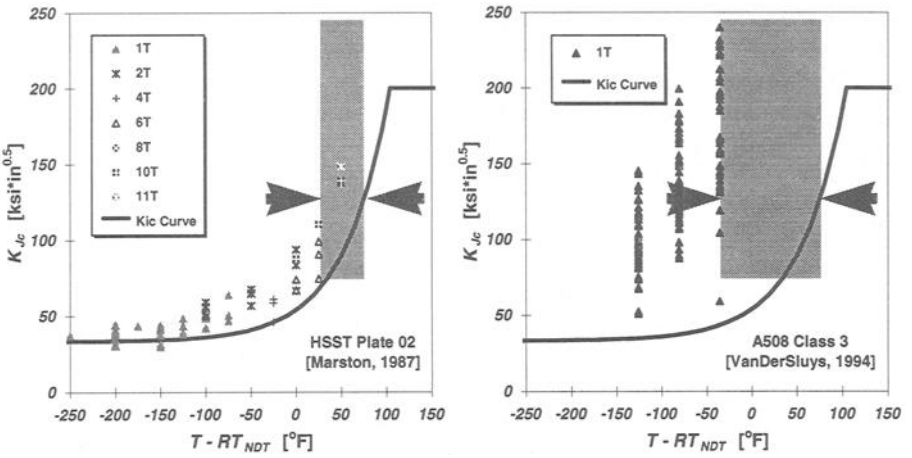


FIGURE 9 – *Margins implicit to existing (RT_{NDT}-based) methodology.*

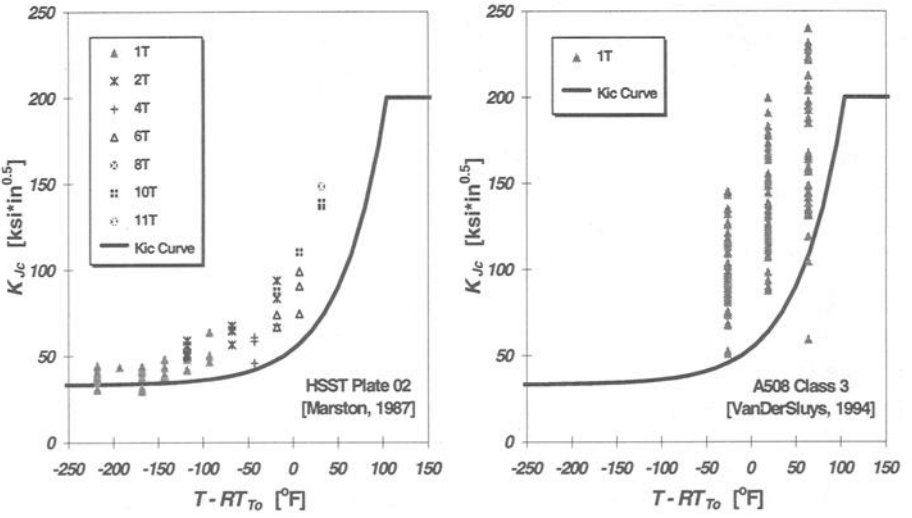


FIGURE 10 – *Margins implicit to proposed (RT_{To}-based) methodology.*

Summary and Conclusions

In this investigation we use a database of fracture toughness values for reactor pressure vessel steels (both irradiated and un-irradiated) to address concerns regarding the bias and precision of T_o values determined by ASTM E1921-97, and regarding the use of T_o as an index temperature for the K_{IC} curve. This database includes over 1,600 E1921-97 valid fracture toughness values from plates, welds, and forgings. These data provide empirical evidence that supports the following conclusions:

Regarding T_o Bias and Precision

a) Provided T_o is estimated in accord with the requirements of E1921-97, the test temperature at which the fracture toughness tests are conducted does not bias the estimate of T_o.
b) Provided T_o is estimated in accord with the requirements of E1921-97, the level of deformation experienced by the fracture toughness tests does not bias the estimate of T_o. Furthermore, even the presence of a large number of K_{Jc} values that exceed the K_{Jc} limit does not bias the T_o estimate.
c) The tolerance bounds on T_o proposed in E1921-97, Appendix B, are appropriate for RPV steels.
d) The standard deviation of E1921-97 T_o estimates relative to T_o estimates determined using considerably larger data sets is 14°F for the RPV steels considered.

Regarding Use of T_o as an Index Temperature for the K_{IC} Curve

a) A ASME Code Case N-629 advocates addition of 35°F to T_o (determined by E1921-97 to establish a temperature to index the ASME K_{IC} curve. This index temperature is called RT_{To}. The value of 35°F exceeds that needed to maintain consistency with the current licensing basis by 18°F. Consequently, use of RT_{To} as an indexing parameter for the K_{IC} curve is more conservative than use of RT_{NDT}.
b) The T_o-based toughness estimation methodology reduces considerably the degree of scatter in fracture toughness data, and contains implicit margins on toughness that are consistent for each steel considered. RT_{To} is therefore superior to RT_{NDT} as an index temperature for the K_{IC} curve.

Acknowledgments

The authors wish to acknowledge the assistance of Dr.'s. D. McCabe, G. Wardle, T. Iwadate, and D. Lidbury who provided fracture toughness data in tabular or spreadsheet form. Additionally, Ms. A. Blayden of the Westinghouse STC library provided invaluable assistance with locating literature references. Finally we would like to thank Prof. R. Dodds for his many helpful discussions on this topic. This work was supported by the Westinghouse Electric Company.

References

[1] 10 CFR Part 50, "Fracture Toughness Requirements for Light Water Reactor Pressure Vessels."

[2] Marston, T.U., "Flaw Evaluation Procedures, Background and Application of ASME Section XI Appendix A," EPRI Report NP-719-SR, Electric Power Research Institute, 1978.

[3] "The Phenomena of Rupture and Flow in Solids," *Philosophical Transactions, Series A*, Vol. 221, 1920, pp. 163-198.

[4] Ritchie, Knott, and Rice, "On the Relationship Between Critical Tensile Stress and Fracture Stress in Mild Steels, *Journal of the Mechanics and Physics of Solids.*, **21**, 1973, pp. 395-410.

[5] Curry, D., and Knott, J., *Metal Science,* **12**, 1978, pp. 511-514.

[6] Curry, D., and Knott, J., *Metal Science,* Metal Science, **13**, 1979, pp. 341-345.

[7] Wallin, Saario, and Törrönen, "Statistical Model for Carbide Induced Brittle Fracture in Steel," *Metal Science*, **18**, 1984, pp.13-16.

[8] Kirk, M., Lott, R., Kim, C., and Server, W., "Empirical Validation Of The Master Curve For Irradiated And Unirradiated Reactor Pressure Vessel Steels," Presented at the 1998 ASME/JSME Pressure Vessel and Piping Symposium, July 26-30, 1998 - San Diego, California, USA.

[9] ASME Code Case N-629, "Use of Fracture Toughness Test Data to Establish Reference Temperature for Pressure Retaining Materials for Section XI."

[10] Mayfield, M.E., et al., "Application of Revised Fracture Toughness Curves in Pressure Vessel Integrity Analysis," Paper #106, SMIRT Conference, Lyon, France, August, 1997.

[11] Moskovic, R., "Statistical Analysis of Censored Fracture Toughness Data in the Ductile to Brittle Transition Temperature Region," *Engineering Fracture Mechanics*, Vol. 44, No. 1, 1993, pp. 21-41.

[12] Nevalainen, M., and Dodds, R.H., "Numerical Investigation of 3-D Constraint Effects on Brittle Fracture in SE(B) and C(T) Specimens," University of Illinois Civil Engineering Studies Structural Research Series Report # 598, UILU-ENG-95-2001, February 1995.

[13] Ruggieri, C., Dodds, R.H., and Wallin, K., "Constraint Effects on Reference Temperature, T_o, for Ferritic Steels in the Transition Region," *Engineering Fracture Mechanics*, to appear.

[14] Nanstad, R.K., et al., "Irradiation Effects on Fracture Toughness of Two High-Copper Submerged-Arc Welds, HSSI Series 5., NUREG/CR-5913, U.S. Nuclear Regulatory Commission, 1992.

[15] VanDerSluys, W.A. and Miglin, M.T., "Results of MPC/JSPS Cooperative Testing Program in the Ductile-to-Brittle Transition Region," *Fracture Mechanics: 24th Volume, ASTM STP 1207,* J.D. Landes, D.E. McCabe, and J.A.M. Boulet, Eds., American Society for Testing and Materials, 1994, pp. 308-324.

[16] Morland, E., "Fracture Toughness in the Transition Regime for A533B-1 Steel: The Effect of Specimen Sidegrooving," *Fracture Mechanics 21st Symposium, ASTM STP 1074,* J.P. Gudas, J.A. Joyce, and E.M. Hackett, Eds., American Society for Testing and Materials, 1990, pp. 215-237.

[17] Alexander, D.J., and Cheverton, R.D., "Fracture Properties of Specially Heat Treated ASTM A508 Cl. 2 Pressure Vessel Steel," *Fracture Mechanics 23rd Symposium, ASTM STP 1189,* Ravinder Chona, Ed., American Society for Testing and Materials, 1993, pp. 365-380.

[18] McCabe, D.E., "A Comparison of Weibull and β_{Ic} Analysis of Transition Range Data," *Fracture Mechanics, 23rd Symposium, ASTM STP 1189,* Ravinder Chona, Ed., American Society for Testing and Materials, Philadelphia, PA, 1984, pp. 80-94.

[19] Ingham, T., et al., "Fracture Toughness in the Transition Regime for A533B Steel: Prediction of Large Specimen Results from Small Specimen Tests," *Fracture Mechanics: Perspectives and Directions (20th Symposium), ASTM STP 1020,* R.P. Wei and R.P. Gangloff, Eds., American Society for Testing and Materials, 1989, pp. 369-389.

[20] McCabe, D.E., et al., "Unirradiated Material Properties of Midland Weld WF-70," NUREG/CR-6249, U.S. Nuclear Regulatory Commission, 1994.

[21] McGowan, et al., "Characterization of Irradiated Current-Practice Welds and A533 Grade B Class 1 Plate for Nuclear Pressure Vessel Service, NUREG/CR-4880, U.S. Nuclear Regulatory Commission, 1988.

[22] Iwadate, T., Tanaka, Y., Ono, S., and Watanabe, J., "An Analysis of Elastic Plastic Fracture Toughness Behavior for J_{IC} Measurement in the Transition Region", *Elastic-Plastic Fracture: Second Symposium, Volume II-Fracture Resistance Curves and Engineering Applications, ASTM STP 803,* C.F. Shih and J.P. Gudas, Eds., American Society for Testing and Materials, 1983, pp. II-531-II-561.

[23] Lidbury, D. and Moskovic, R., "Assessment of the Ductile-to-Brittle Transition Toughness Behavior of an A508 Cl. 3 PWR Pressure Vessel Steel by a Statistical Approach," American Society of Mechanical Engineers Pressure Vessel and Piping Conference Proceedings, Vol. 250: Pressure Vessel Integrity, 1993, pp. 283-294.

[24] Sorem, W.A., "The Effect of Specimen Size and Crack Depth on the Elastic-Plastic Fracture Toughness of a Low-Strength High-Strain Hardening Steel," Ph.D. Dissertation, University of Kansas, 1989.

Rachid Chaouadi,[1] Albert Fabry,[1] Eric van Walle,[1] and José Van de Velde[1]

Fracture Toughness of the Ni-Modified A302-B Plate of the BR3 Reactor Pressure Vessel

Reference: Chaouadi, R., Fabry, A., van Walle, E., and Van de Velde, J., **"Fracture Toughness of the Ni-Modified A302-B Plate of the BR3 Reactor Pressure Vessel,"** *Effects of Radiation on Materials: 19th International Symposium, ASTM STP 1366,* M. L. Hamilton, A. S. Kumar, S. T. Rosinski, and M. L. Grossbeck, Eds., American Society for Testing and Materials, West Conshohocken, PA, 2000.

Abstract: The present paper aims to compare regulatory predictions of fracture toughness to direct measurements using precracked Charpy specimens tested in three-point bending. Trepans were extracted from the vessel of the BR3 reactor in order to perform fracture toughness tests in addition to Charpy impact and tensile testing. This vessel was successfully wet-annealed at 343°C during 1 week after a maximum neutron fluence of 3.3 10^{19} n/cm². The reactor is presently under decommissioning after a maximum neutron fluence of 4.0 10^{19} n/cm². The trepans (base metal and weld) were taken from two regions: vessel mid-plane and nozzle elevation (no neutrons, negligible thermal aging). Here, the base metal (Ni-modified A-302 grade B) is investigated: Tensile, Charpy impact and fracture toughness tests were performed at thickness ranging from 1/4T to 1/2T.

The determination of the reference temperature, T_0, is performed according to the ASTM E1921 standard.

It is found that the 41J-shift of the Charpy impact transition curve is similar to the T_0-shift of the master curve: ΔT_{41J}=96°C and ΔT_0=115°C. This is an important result as current regulation is based on the 41J-shift. This regulation indexes the ASME fracture toughness curve to the initial RT_{NDT} for the baseline condition and is increased by the 41J-energy shift for the irradiated condition. This results in an over-conservatism of about 40°C. It is found also that the T_{41J} and T_0 shifts fall within the regulatory predictive bounds based on the chemistry factor (Cu and Ni-content) and neutron fluence.

Keywords: fracture toughness, Charpy impact, tensile, transition, irradiation, Ni-modified A-302 grade B reactor pressure vessel steel, reference temperature

[1] SCK•CEN, Reactor Materials Research, Boeretang 200, 2400 Mol, Belgium.

Copyright© 2000 by ASTM International www.astm.org

The BR3 reactor, the sister of the Yankee Rowe PWR reactor, was put into operation in 1963 and was shutdown in 1987, at 86000 EFPH corresponding to a cumulative maximum neutron fluence of about 4 10^{19} n/cm² (E>1MeV). The vessel was successfully wet annealed in 1984 at 72000 EFPH corresponding to a maximum fluence of 3.3 10^{19} n/cm² (E>1MeV). The operation temperature was 260°C.

In 1995, the BR3 vessel was sampled in the frame of a mechanical test project aimed at characterizing the vessel materials. Boat-type trepans of 10 cm thickness by 15 cm diameter (see Figure 1) were extracted from the vessel by electro-discharge machining in cooperation with PCI Energy Services. Both base metal and weld were sampled in two locations: at midplane (maximum fluence) level as well as at nozzle elevation where neutron exposure is negligible, thus providing a relevant baseline condition. Indeed, thermal ageing effects were found to be negligible [1]. More information can be found in references 1-3.

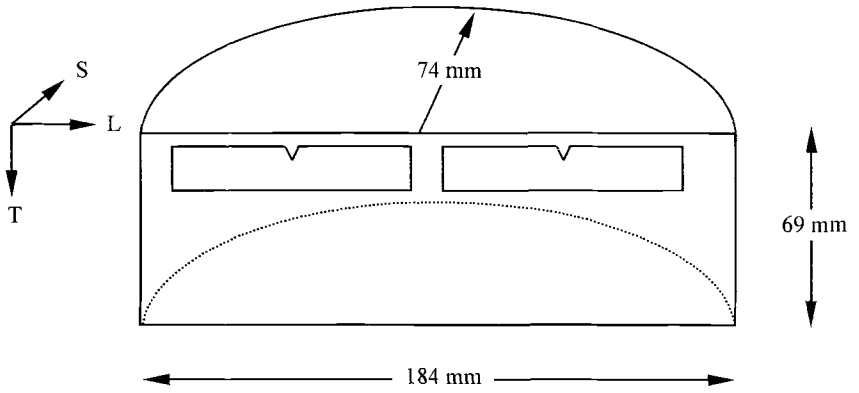


Figure 1--*Trepan as extracted from the vessel*

Current regulatory evaluation of the fracture toughness of pressure vessel steels in the transition region is established through empirical correlations based on the Charpy transition curve. The irradiation-induced shift of the K_{Ic} and K_{Id} Charpy transition curve at the specific energy level of 41J is assumed identical to the shift of the ASME fracture toughness transition curve by indexing ASME curves. In the un-irradiated (baseline) condition, the ASME curves are furthermore indexed to a reference temperature of nil ductility, RT_{NDT}, derived from Charpy and Pellini drop weight tests [4].

Direct fracture toughness measurements are usually excluded because of the specimen size requirements. Recent extensive efforts have been devoted to use small samples in order to determine the fracture toughness behaviour. The recent ASTM Standard Test Method for Determination of Reference Temperature, T_0, for Ferritic Steels in the Transition Range (E1921) allows to determine a so-called reference

temperature that characterizes the transition behaviour based on a simple generic master curve equation [5-7]. This single parameter determines the median fracture toughness behaviour and its confidence interval (usually 5% and 95% bounds).

The test program includes tensile, Charpy impact and fracture toughness tests. For the latter, the precracked Charpy geometry is selected for these tests. The capability to use small Charpy samples to characterize the fracture toughness in the transition regime was demonstrated on the HSSI Weld 73W [8,9].

This work reports Charpy impact, tensile and fracture toughness tests performed on specimens machined from the trepans taken from the BR3 vessel. The specimen size does not exceed the Charpy size (10×10×55 mm).

Material and Testing

The reactor pressure vessel at the BR3 reactor was built in 1958 by Babcock and Wilcox Company together with the Yankee Rowe reactor vessel. The BR3 base metal is a Ni-modified A302-B of chemical composition given in Table 1.

Table 1--*Chemical composition (%-wt)[1]*

C	Si	Mn	P	S	Cr	Cu	Mo	Ni
0.28	0.26	1.25	0.02	0.02	0.06	0.19	0.47	0.56

All tests are carried out according to the prevailing ASTM standards: ASTM E23 for the Charpy impact tests, E8 for the tensile tests and E1921 for the fracture toughness tests.

The tensile specimens were taken in the L-orientation (rolling direction). The tests were performed on small cylindrical geometries (D_0=3.6 mm, L_0=18 mm). The specimens are pulled at a constant crosshead velocity of 0.2 mm/min.

The Charpy samples were taken in the L-T orientation. The impact tests were performed on a 300J instrumented impact hammer equipped with an ASTM tup.

Fracture toughness measurements were performed on Charpy specimens (L-T orientation) that were precracked at ambient temperature and 20% side-grooved prior to testing. The final K_{max} during precracking was maintained below 25 MPa$\sqrt{m}$. In all cases, it was verified that the K_{max}, including temperature effect, is well below 60% of K_{Jc}-value after fracture. The tests were conducted under displacement control at a constant crosshead speed of 0.2 mm/min. The specimen notch sides were machined to allow fixation of the clip gage. The applied load and the crack mouth opening displacement were continuously recorded up to fracture. A computer routine allows calculation of the fracture toughness at cleavage initiation. After testing, the specimens are heat tinted at 260°C for 15 min and further broken at liquid nitrogen temperature. The fracture surfaces are then photographed to measure the initial and final crack length by the 9-point average method.

For fracture toughness testing, the test temperatures were selected such that at least 6 samples are tested in the neighborhood of a K_J-level of 100 MPa$\sqrt{m}$. Test temperature

range is estimated from the 28 J energy level of Charpy V-notch impact data with an additional margin of –50°C for precracked Charpy specimens [ASTM E1921].

Results

Tensile Data

Figure 2 shows the evolution of the yield and ultimate stresses with test temperature. The yield increase induced by irradiation is also shown. The yield stress, σ_y, is fitted throughout the temperature range [-200 to +300°C] by the following equation:

$$\sigma_y \text{ (MPa)} = C_1 + C_2 \exp [\, C_3 \, T(°C)]$$

where the constants C_1, C_2 and C_3 are given in Table 2.

Table 2-- Fitting constants to represent the evolution of the yield stress as a function of test temperature.

condition	C_1	C_2	C_3
nozzle elevation	391	33	-0.014
beltline level	518	99	-0.009

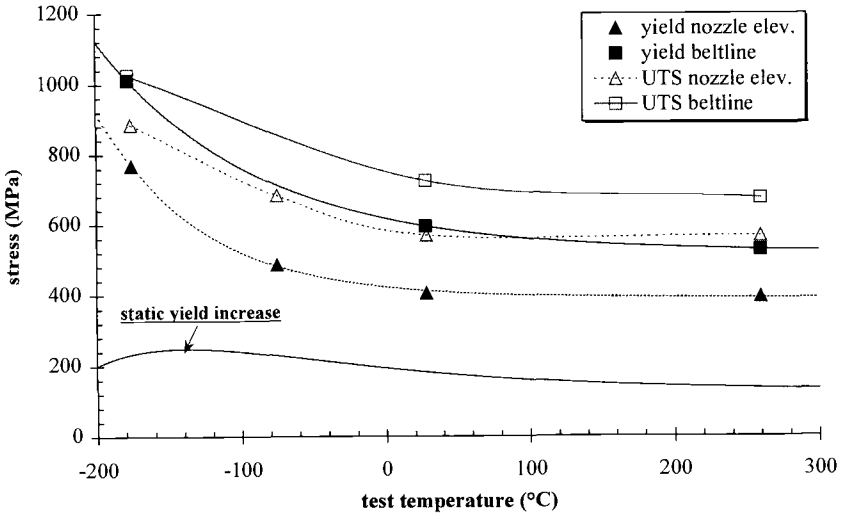


Figure 2--*Tensile properties of the BR3 base metal.*

Charpy Impact Data

The Charpy impact test data obtained at vessel 1/4T-position were previously published [2]. Due to the limited amount of material at 1/4T, tensile and fracture toughness testing was done at 1/2T. Additional Charpy impact tests were also performed at this location. The energy, shear fracture appearance and lateral expansion versus test temperature are plotted in Figure 3 to 5, respectively. As can be seen, no significant difference is found between the two locations 1/4T and 1/2T.

The main parameters characterizing the Charpy impact transition curve are gathered in Table 3. The irradiation results in a loss of upper shelf energy of about 40% while the 41J-shift is 96°C. The SFA shift is smaller than the 41J-energy and 0.89 mm lateral expansion shifts. The RT_{NDT} in the irradiated condition is determined from:

$$RT_{NDT} = RT^{0}_{NDT} + \Delta T_{41J}$$

where $RT^{0}_{NDT} = -12\,^{\circ}C$ [2].

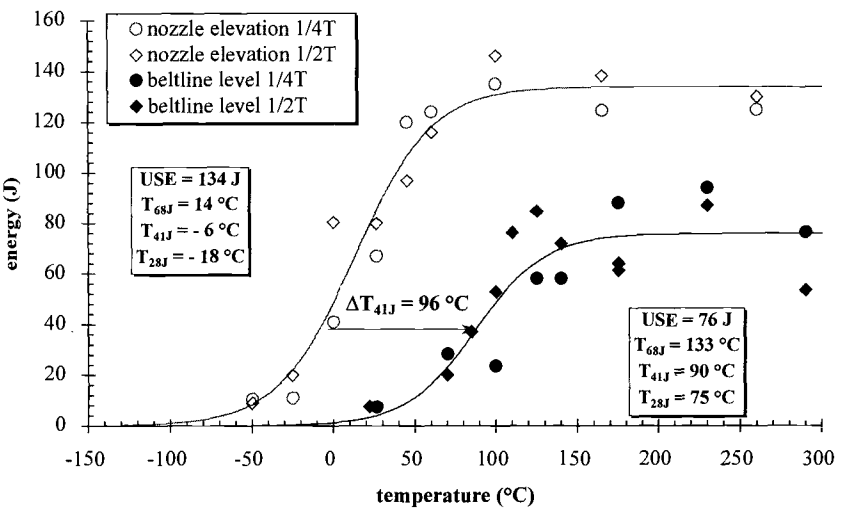


Figure 3--*Energy transition curves for the BR3 base metal. The 41J- energy shift is 96°C.*

Evaluation of these data with the load diagram approach results in the characteristic temperatures and yield stresses given in Table 4. In the irradiated condition, only the samples taken from the 1/4T thickness were considered. Figure 6 shows the evolution of the static and dynamic yield stress with test temperature. Irradiation induces a yield increase in the athermal range of about 160 MPa. The curves shown in Figure 6 are trend fits through the experimental data.

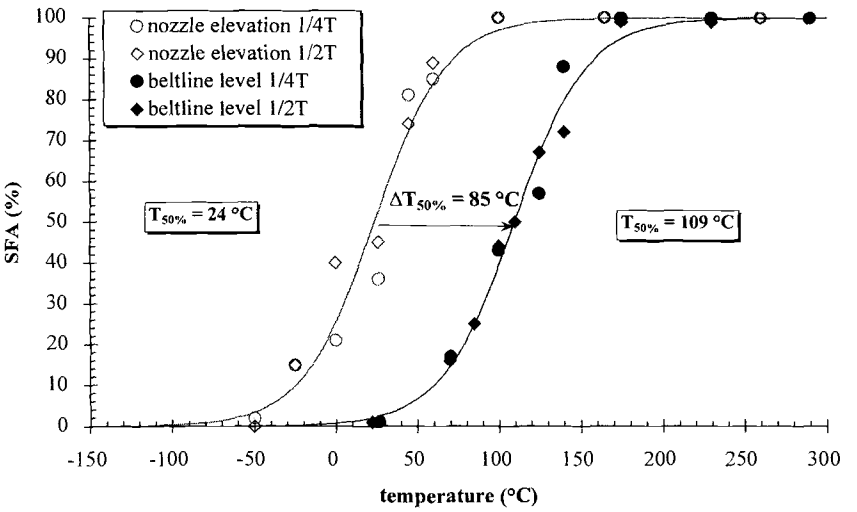


Figure 4--*Shear fracture appearance transition curves for the BR3 base metal.*

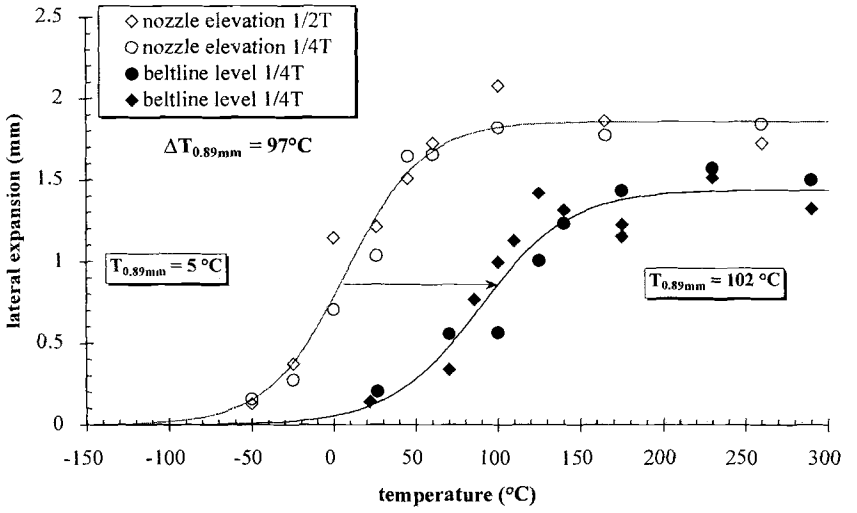


Figure 5--*Lateral expansion transition curves for the BR3 base metal.*

Table 3--*Charpy impact properties*

condition	USE (J)	T_{68J} (°C)	T_{41J} (°C)	T_{28J} (°C)	$T_{50\%}$ (°C)	$T_{0\,89mm}$ (°C)	RT_{NDT} (°C)
nozzle elevation	134	14	-6	-18	24	5	-12 (†)
beltline level	76	134	90	75	109	102	84
shift	58	120	96	93	85	97	96

(†) from [2]

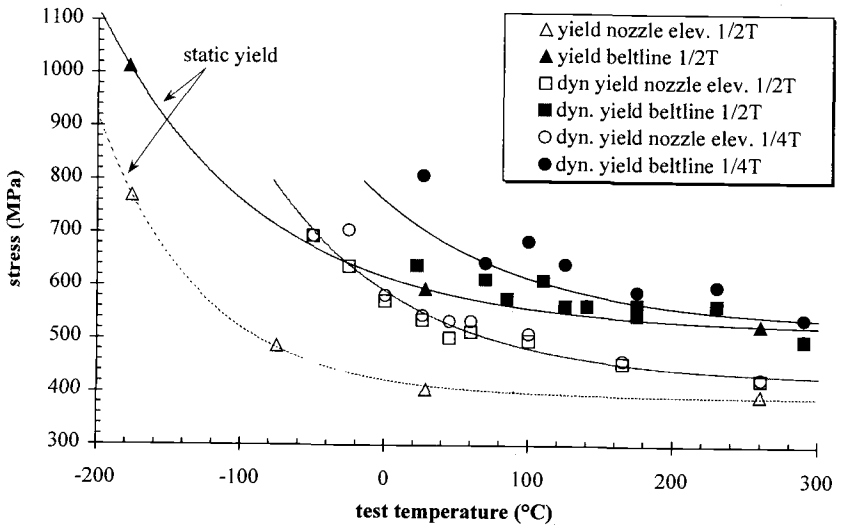


Figure 6--*Combined CVN/tensile load - temperature diagram: the yield (static as well as dynamic) increases by ~140 MPa. The curves are not derived from modelling but fitted through the data.*

Fracture Toughness Data

The fracture toughness is determined using the J-integral concept transformed into an equivalent K_J through the relation:

$$K_J = \sqrt{J\,E}$$

where J-integral is calculated from:

$$J = \frac{K^2}{E} + \frac{\eta U_{pl}}{B_n (W - a_0)}$$

where $\eta = 1.9$, a_0 is the initial crack length, B_n and W are respectively the specimen net thickness and width, E is the Young modulus (E is taken equal to 210 GPa). U_{pl} is derived

from area under the load versus load point displacement curve from which the elastic part is subtracted. For the SENB geometry, the load point displacement (LPD) is derived from the crack mouth opening displacement (CMOD) using the following relation:

$$LPD = \frac{CMOD \quad S/4}{r_p (W - a_0) + a_0}$$

where S is the span and the rotational factor r_p=0.44.

Table 4--*CVN/tensile load - temperature characterization (from [3]).*

condition	T_I (J)	T_A (°C)	T_O (°C)	FATT (°C)	RT static yield (MPa)	RT dynamic yield (MPa)
nozzle elevation	-55	20	55	31	433	554
beltline level	15	103	142	119	592	716
shift	70	83	87	88	159	162

T_I = temperature from which the SFA becomes > 0%
T_A = temperature for K_{Ia}=100 MPa$\sqrt{m}$ defined from the Charpy arrest loads
T_O = temperature at which the SFA reachs 100%
FATT = temperature at which SFA = 50%

The ASTM E1921 procedure allows to estimate the test temperatures from the T_{28J} temperature. In our case, this leads to –68°C and +39°C for the baseline and irradiated condition, respectively. At these test temperatures, the expected median K_J would be around 100 MPa$\sqrt{m}$. As will be seen, this is the case in both the baseline and the irradiated condition.

The fracture toughness test results are given in Table 5 and 6 for the baseline and the irradiated condition, respectively. The analysis of the fracture toughness data was performed according to the E1921 procedure. The data are normalized to 1T size and the reference temperature is then determined. K_0 and m (Weibull modulus) are also determined but no data censoring is applied. The results, summarized in Table 7, indicate that for each condition the parameters are in very good agreement. It is interesting to note that, despite the non-validity of the data of specimens tested at -60 and -40°C in the baseline condition and at +55°C in the irradiated condition, the derived reference temperatures are still consistent with those determined with valid data. Figure 7 shows the 1T-adjusted fracture toughness data and their master curves associated to the 5 % and 95% bounds.

Table 5—*Fracture toughness test results at nozzle elevation, (¼T location).*

Id.	T (°C)	W	B	B_n	a_0	J_c	Δa	K_{Jc}	remark
D3-3	-75	10.02	10.01	7.804	5.184	41.10	0	92.90	--
D3-1	-75	10.09	9.98	7.868	5.381	42.57	0	94.55	--
D3-2	-75	10.07	10.03	7.977	5.196	45.45	0	97.70	--
D3-6	-75	10.03	10.12	7.948	4.926	53.75	0	106.24	--
D3-4	-75	10.00	10.05	7.947	5.265	63.26	0	115.26	--
D3-5	-75	10.02	10.16	7.926	5.133	68.54	0	119.97	--
B3-7	-60	10.05	9.99	7.952	5.644	27.12	0	75.47	--
B3-8	-60	10.12	9.96	7.908	5.478	30.81	0	80.44	--
B3-9	-60	10.11	10.02	7.959	5.608	36.76	0	87.86	--
D3-10	-60	10.04	10.15	7.942	5.117	54.22	0	106.71	--
D3-9	-60	10.09	10.04	7.785	5.285	71.32	0	122.38	--
B3-5	-60	10.10	9.99	7.874	5.584	72.47	0	123.36	$K_J > K_{J\ limit}$
B3-10	-60	10.05	9.99	7.93	5.592	77.28	0	127.39	$K_J > K_{J\ limit}$
D3-11	-60	10.02	10.05	7.76	5.201	82.40	0	131.54	$K_J > K_{J\ limit}$
D3-12	-60	10.03	10.04	7.846	5.075	86.73	0	134.96	$K_J > K_{J\ limit}$
B3-6	-60	10.07	9.99	7.846	5.749	97.52	0	143.10	$K_J > K_{J\ limit}$
B3-11	-40	10.05	9.99	7.903	5.722	87.83	0	135.81	$K_J > K_{J\ limit}$
B3-12	-40	10.08	9.95	7.847	5.493	93.60	0	140.20	$K_J > K_{J\ limit}$
B3-2	-40	10.07	9.96	7.941	5.51	104.66	0	148.25	$K_J > K_{J\ limit}$
B3-3	-40	10.05	9.95	7.897	5.491	132.48	0.172	166.80	$K_J > K_{J\ limit}$
B3-1	-40	10.01	9.82	7.636	5.707	150.98	0.143	178.06	$K_J > K_{J\ limit}$
B3-4	-40	10.12	9.99	7.838	5.585	207.32	0.234	208.65	$K_J > K_{J\ limit}$

Table 6--*Fracture toughness test results at beltline level, (¼T location).*

Sp. Id.	T (°C)	W	B	B_n	a_0	J_c	Δa	K_{Jc}	remark
E3-13	40	10.16	9.97	7.951	5.105	16.52	0	58.90	--
E3-7	40	9.91	9.89	7.878	5.263	21.63	0	67.40	--
E3-4	40	10.02	9.99	7.942	5.146	29.15	0	78.24	--
E3-14	40	9.98	9.99	7.849	4.712	37.78	0	89.07	--
E3-1	40	10.08	9.93	7.928	5.249	68.48	0	119.92	--
E3-11	40	10.10	10.06	7.898	5.571	70.57	0	121.74	--
E3-9	40	9.96	9.93	7.658	5.264	81.53	0	130.85	--
E3-2	55	9.94	9.94	7.918	5.428	31.44	0	81.26	--
E3-3	55	9.90	9.97	7.792	5.093	34.98	0	85.71	--
E3-6	55	9.78	9.87	7.729	5.159	43.92	0	96.04	--
E3-10	55	9.95	9.83	7.571	5.308	91.69	0.143	138.76	$K_J > K_{J\ limit}$
E3-12	55	9.91	9.86	7.450	4.998	95.69	0.103	141.76	$K_J > K_{J\ limit}$
E3-8	55	9.93	9.96	7.681	5.271	101.97	0.09	146.33	$K_J > K_{J\ limit}$

Table 7--*Determination of the reference temperature T_0. Also indicated are m and K_0.*

Condition	T	N	r	T_0	K_0	m	remark
nozzle elevation	-75	6	6	-60.7	89.4	8.9	T_0 E1921 (†)
	-60	10	5	-54.5	100.1	5.1	all data, no censoring
	-40	6	0	-58.5	139.9	5.9	all data, no censoring
				$T_{0\ nozzle}$ = - 61 °C (†)			
beltline level	40	7	7	54.2	89.5	3.2	T_0 E1921 (†)
	55	6	3	57.7	103.8	4.0	all data, no censoring
				$T_{0\ beltline}$ = + 54 °C (†)			

(†) : T_0 valid data according to ASTM E1921 criteria
N : total number of specimens
r : number of data satisfying the ASTM E1921 size requirements
T : test temperature (°C)
K_0: normalization toughness (MPa$\sqrt{m}$)
m : Weibull shape parameter

Discussion

It is interesting to compare the 5% lower bound of the master curve to the ASME K_{Ic} curve. The latter represents the lower bound of fracture toughness data as a function of temperature indexed by the reference nil-ductility temperature, RT_{NDT}. Figure 8 and Table 8 illustrate this comparison. In the baseline and irradiated conditions, a margin of 47 and 29°C respectively, is found between the 5% bound and the ASME curve, the latter being too conservative.

It is also relevant to briefly discuss the present results in the context of long standing regulatory concerns for both the BR3 and Yankee Rowe vessel plates. It must be recalled that the Yankee nickel-modified A-302B lower shell plate and the BR3 plate are similar, while the surveillance plate specimens at both plants were not nickel-modified and are representative of the Yankee A-302B upper shell plate.

The discussion can be made in the light of Figure 9, which compares the measured transition temperature shifts to some selected predictions. The ASTM E509-97 Standard Guide for In-Service Annealing of Light-Water Cooled Nuclear Reactor Vessels has been used to establish the range of "1998 regulatory uncertainties". The pre-anneal irradiation path relies on Regulatory Guide 1.99 Revision 2, but incorporates a correction (increase) of +29°C to account for the detrimental effect of irradiation temperature of 260°C. The anneal recovery predicted by Eason's et al. [10] correlation is of 22%. Note that re-annealing the BR3 plate to examine the IARA condition gives negligible recovery of the 41J shift, while the recovery of the load diagram parameters (yield stress, characteristic temperatures) ranges from 7% to 16%. Finally, the post-anneal re-embrittlement (IAR) path is based on the so-called "vertical shift" method. A 2σ uncertainty of ±24°C has been applied, across-the-board, to the entire range of the prediction. Good concurrence with experiment is

observed. It can be seen that embrittlement is rather uniform from the vessel surface to the vessel half-thickness. The upper bound curve obtained by this procedure can now be compared to previous upper bound estimates. The 1991 ORNL/UCSB [11] evaluation performed on behalf of the USNRC (shift of 180°C at 2.3 10^{19} n/cm²) is similar to the above I-path assessment, but furthermore incorporates a significant penalizing correction. This was done to account for the fact that the 41J CVN-shift of the A302-B Yankee surveillance plate at both BR3 and Yankee Rowe largely exceeds the shift of the A302-B reference ASTM plate as well as the predictions of the Regulatory Guide 1.99 Revision 2. This was attributed to the unusually coarse microstructure of this surveillance plate, resulting from its higher-than-usual austenization temperature. The 1991 SCK•CEN Mol evaluation, dotted curve on Figure 9, accepted the same irradiation temperature effect as the above evaluations, but argued that the outlier behavior of the Yankee A302-B plate is a 41J indexing artefact [1] and that this could not affect fracture toughness; it was also contended that there is no influence of the nickel addition. These 1991 views are confirmed by the present work and by direct comparative BR2 irradiation of the BR3 plate together with Yankee A302-B and A533-B surrogate plate [2,3].

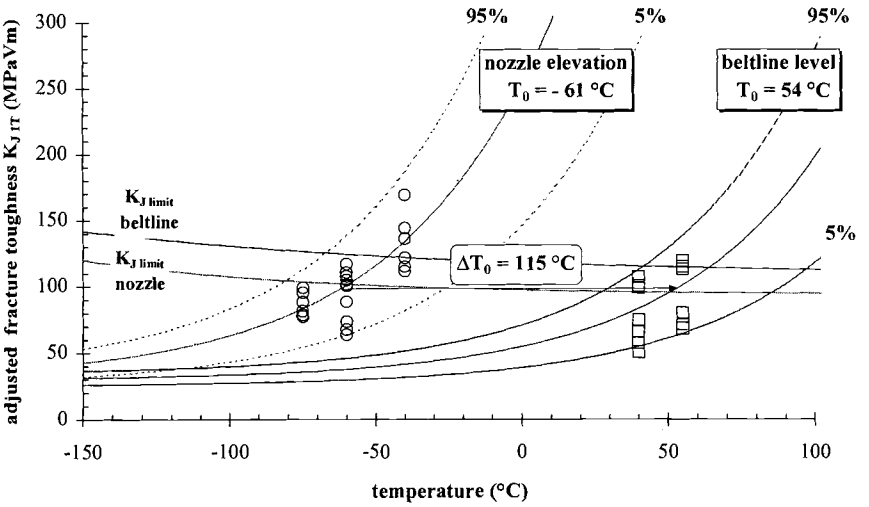


Figure 7--*Master curve and associated 90% confidence interval for the BR3 base metal. Data are normalized to 1T-size.*

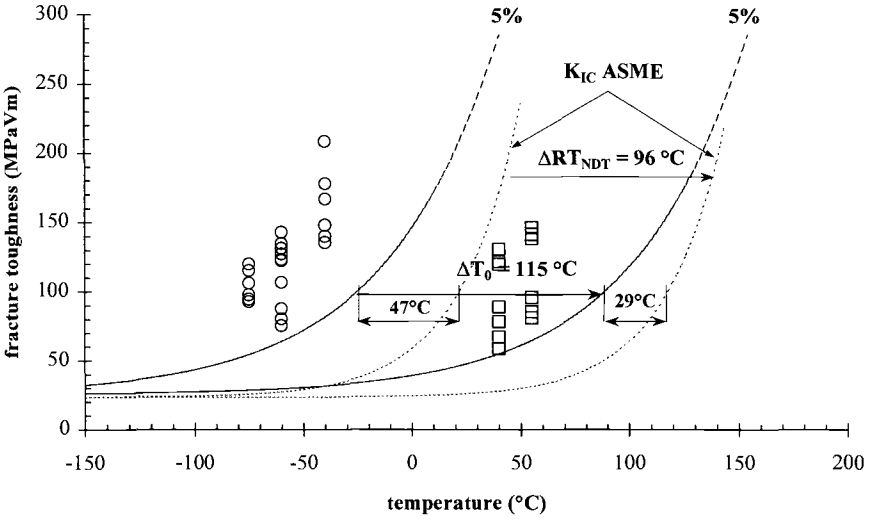


Figure 8--*5%-master curve versus K_{Ic} ASME lower bound fracture toughness curve comparison: although the shift is similar, the ASME curves are more conservative.*

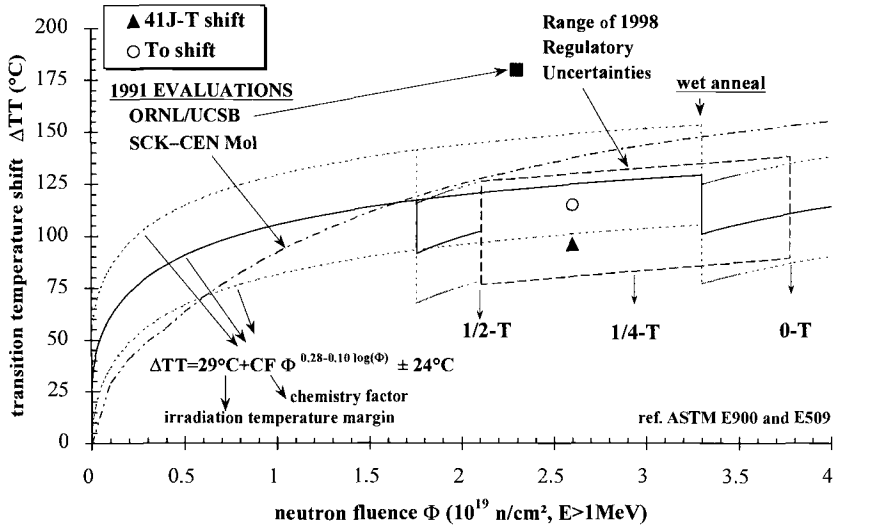


Figure 9--*Comparison of T_{41J} and T_0 shifts to predicted temperature shift. Previous evaluations [1,10] are also included for comparison.*

Table 8--*Comparison between regulation and direct fracture toughness measurements. Although the temperature shifts are very similar, the regulatory curves are much more conservative (about 40°C).*

condition	T_0 (°C)	RT_{NDT}
nozzle elevation	−61	−12
beltline level	+54	+84
shift	115	96

Summary and Conclusions

This work gives the opportunity to test material that is taken from a real pressure vessel irradiated, wet-annealed and re-irradiated up to a cumulated fast neutron fluence of 4 10^{19} n/cm². It compares fracture toughness projections to direct measurements using precracked Charpy specimens tested in three-point bending. Two regions of the vessel were investigated: at vessel mid-plane and at nozzle elevation (no neutron, negligible thermal ageing). The base metal (Ni-modified A-302 grade B) is investigated here through tensile, Charpy impact and fracture toughness testing.

The determination of the reference temperature according to the ASTM E1921 standard has shown that within the considered temperature range and for each material condition, T_0 does not seem to depend on the test temperature. This was surprising as at the highest test temperatures, most of the data fall out the validity range of the above mentioned standard.

It was found that the 41J-shift of the Charpy impact transition curve is quite similar to the T_0-shift of the master curve: ΔT_{41J}=96°C and ΔT_0=115°C. This is an important result as current regulation is based on the 41J-shift. However, this regulation indexes the ASME fracture toughness curve to the initial RT_{NDT} for the baseline condition and is shifted by the same 41J-energy shift for the irradiated condition. This results in a conservatism of about 40°C for the static initiation fracture toughness. It is found also that the T_{41J} and T_0 shifts fall within the regulatory predictive bounds based on the chemistry factor (Cu and Ni-content) and neutron fluence.

Acknowledgments

The work reported here is co-sponsored by Tractebel Energy Engineering. The authors are indebted to R. Gérard for his strong interest and support. Special acknowledgments to P. Beckers (tensile specimens fabrication), G. Bes (dimensional control), M. Eykmans (Charpy specimens fabrication), T. Noels (tensile tests), L. Van Houdt (fracture toughness tests) and R. Vosch (Charpy impact tests) who performed the work with competence and diligence.

References

[1] Fabry, A., Van de Velde, J., Puzzolante, J.L., Van Ransbeeck, T., Verstrepen, A., Biemiller, E.C., Carter, R.G. and Petrova, T., "Research to Understand the Embrittlement Behavior of Yankee/BR3 Surveillance Plate and Other Outlier RPV Steels", *Effect of Radiation on Materials,: 17th International Symposium, ASTM STP 1270*, D.S. Gelles, R.K Nanstad, A.S. Kumar and E.A. Little, Eds., American Society for Testing and Materials, 1995.

[2] Fabry, A, van Walle, E., Gérard, R., Van de Velde, J., Chaouadi, R., Van Ransbeeck, T., Puzzolante, J.L., de Bakker, P., Bodart, S., Dadoumont, J., Massaut, V., Mc Gough, H., Kwech, H., and Smith, G., "Enhanced Surveillance of Nuclear Reactor Pressure Vessels", *Materials Ageing and Component Life Time Extension, Proceedings of an International Symposium,* Milan, Italy, Oct. 10-13, 1995, V. Bicego, A. Nitta and R. Viswanathan, Eds., EMAS, 1995, pp. 577-588.

[3] Fabry, A, Chaouadi, R., Puzzolante, J.L., Van de Velde, J., Biemiller, E.C., Rosinski, S.T. and Carter, R.G., "Embrittlement and Annealing of Reactor Pressure Vessel Steels: Comparison of BR3 Surveillance and Vessel Plates to the Surrogate Plates Representative of the Yankee Rowe Vessel", *Effect of Radiation on Materials,: 18th International Symposium, ASTM STP 1325*, R.K. Nanstad, M.L. Hamilton, F.A. Garner and A.S. Kumar, Eds., American Society for Testing and Materials, West Conshohocken, PA, 1999, pp. 452-481.

[4] 10CFR50, Code of Federal Regulation, Title 10, Appendix G: "Fracture Toughness Requirements", Federal Register, Vol. 60, December, 1995.

[5] Wallin, K., "Fracture Toughness Transition Curve Shape for Ferritic Structural Steels", *Joint FEFG/ICF International Conference on Fracture of Engineering Materials and Structures*, Singapore, 1991, pp. 83-88.

[6] Wallin, K., "Statistical Modelling of Fracture in the Ductile-to-Brittle Transition Region", *Defect Assessment in Components - Fundamentals and Applications, ESIS/EGF9*, Edited by J.G. Blauel and K.-H. Schwalbe, Mechanical Engineering Publications, London, 1991, pp. 415-445.

[7] Wallin, K., "Recommendations for the Application of Fracture Toughness Data for Structural Integrity Assessments", IAEA/CSNI Specialists' Meeting on Fracture Mechanics Verification by Large Scale Testing, Oak Ridge, Tennessee, October 26-28, 1992.

[8] Chaouadi, R., "Fracture Toughness Testing in the Transition Regime using Small Size Samples", *Small Specimen Test Techniques, ASTM STP 1329*, W.R. Corwin, S.M. Rosinski and E. van Walle, Eds., American Society for Testing and Materials, 1998, pp. 214-237.

[9] Chaouadi, R., van Walle E., Fabry A. and Van de Velde J., "Fracture Toughness of Precracked Charpy Specimens of Irradiated 73W Weld Material", *Effect of Radiation on Materials,: 19th International Symposium, ASTM STP 1366*, M.L. Hamilton, A.S. Kumar, S.T. Rosinski and M.L. Grossbeck, Eds, American Society for Testing and Materials, West Conshohocken, PA, 1999.

[10] Eason, E.D., Wright J.E. and Odette G.R., "Models for Embrittlement Recovery due to Annealing of Reactor Pressure Vessel Steels", NUREG/CR-6327, Feb. 1995.

[11] Nanstad, R.K and Odette, G.R., "Review of Yankee Rowe embrittlement", Nov. 18, 1991.

James A. Joyce,[1] Robert L. Tregoning,[2] and X. Jie Zhang[2]

Application of Master Curve Technology to Biaxial and Shallow Crack Fracture Data for A533B Steels

Reference: Joyce, J. A., Tregoning, R. L., and Zhang, X. J., **"Application of Master Curve Technology to Biaxial and Shallow Crack Fracture Data for A533B Steels,"** *Effects of Radiation on Materials: 19th International Symposium, ASTM STP 1366,* M. L. Hamilton, A. S. Kumar, S. T. Rosinski, and M. L. Grossbeck, Eds., American Society for Testing and Materials, West Conshohocken, PA, 2000.

Abstract: The Master Curve approach has recently been proposed by Wallin [1] to define the expected toughness of ferritic steels in the ductile-to-brittle transition. This method has been standardized in ASTM E1921-98 using deeply cracked fracture toughness specimens tested quasistatically in the lower transition regime. However, the commercial nuclear power industry will often use this method to infer structural performance where the critical crack of interest is shallow, rather than deep, and the loading is biaxial rather than uniaxial. Research has been funded by the U.S. Nuclear Regulatory Commission (NRC) and conducted at the Oak Ridge National Laboratory (ORNL), the U.S. Naval Academy (USNA), and the Naval Surface Warfare Center (NSWC) to address potential shortcomings of the present ASTM Standard Master Curve method for such applications.

Low-constraint specimens of A533B steel were tested to measure performance under more realistic crack tip constraint conditions, and results were analyzed using the Master Curve approach. The A533B steel plate was heat treated to simulate the elevation of the material yield strength and reduction in toughness which results from extended aging due to neutron irradiation. ORNL conducted shallow crack (a/W = 0.1), uniaxially and biaxially-loaded cruciform specimen testing, while USNA performed shallow crack (a/W = 0.1), uniaxially-loaded SE(B) testing. Both laboratories also utilized additional deeply cracked (a/W > 0.5) specimens to fully characterize the A533B steel plate tested as per ASTM E1921. ORNL conducted 1/2T C(T) specimens, while USNA tested both 1/2T C(T) and 1T SE(B) specimens. The standardized master curve approach has been used for analysis in most cases, but this technique was augmented with the maximum

[1]Professor, U.S. Naval Academy, Annapolis, MD, 21402, USA.
[2]Mechanical and Materials Engineers respectively, Naval Surface Warfare Center, West Bethesda, MD, USA.

Copyright© 2000 by ASTM International www.astm.org

likelihood, multi-temperature method [2] when data at a single temperature was sparse.

Results indicate that larger variability in K_{Jc} (fracture toughness at onset of cleavage initiation) is present in the shallow cracked specimens compared with deeply cracked specimens tested at the same temperature. This result is expected due to interaction between the gross section and crack-tip plasticity which lowers constraint and reduces the opening mode stress magnitude within the crack-tip process zone. Surprisingly, however, the 1T SE(B) shallow crack specimens exhibited a distinct reduction in the median K_{Jc} in comparison with the deeply cracked specimens tested using the same material. This trend is counter to historical short-crack data which exhibits an increase in the median K_{Jc} [3, 4].

Stereo-Section fractography was performed to reveal the microstructure near the cleavage crack initiation sites of several shallow and deeply cracked A533B specimens. More intense carbide bands are present in the USNA shallow cracked SE(B) specimens than in the other specimens tested. This implies that the *local* carbon content and hardness is higher in these specimens and lead to the low median K_{Jc} [5-8]. This effect has recently been more rigorously quantified [9]. The variation of the carbide band density in the A533B material tested is a cause of considerable concern. The ability of surrogate, surveillance capsule specimens to accurately capture the reduced toughness due to banding is questionable in light of the relatively small amount of material available for testing, the highly localized nature of the banding, and the inability to predict where it will occur.

Keywords: Shallow crack, cleavage, ductile-to-brittle transition, ferritic steel, elastic-plastic fracture, fracture mechanics, master curve, carbide banding, biaxial loading, stereo-section fractography.

Objective

Experimental results [10] obtained at the Oak Ridge National Laboratory (ORNL) as part of their Biaxial Shallow Flaw Fracture Toughness Test Program initially indicated that the biaxial loading ratio (ratio of through-thickness to opening mode stress) had some effect on the median K_{Jc} at cleavage initiation within the ductile-to-brittle transition region. This initial conclusion was based on a relatively small number of tests (three or less) at a unique temperature and biaxiality ratio due to the complexity and expense of these tests. Therefore, it was not clear from these initial tests that the observed biaxial effect was statistically justified.

Since uniaxial bending tests conducted on deeply cracked 1T SE(B) A533B specimens exhibit wide variability in the ductile-to-brittle transition region [3], further additional uniaxial testing was planned to benchmark the biaxial test series. It was decided that USNA would test eight deeply cracked ($a/W = 0.55$) 1T SE(B) specimens, and eight shallow cracked ($a/W = 0.1$) 1T SE(B) specimens. It was also decided that ORNL would conduct further cruciform specimen biaxial tests in order to obtain six data-points at one temperature under each of the two extreme biaxial loading ratios. All tests were to be conducted at $-5^{\circ}C$ to coincide with the principal temperature where the biaxial

effect appeared to be the most pronounced. The objective of the USNA testing was to characterize the expected variability of this reactor pressure vessel steel using both deep and shallow crack uniaxial load fracture mechanics specimens. The shallow cracked uniaxial specimens would be benchmarked against previous and additional cruciform specimen testing conducted at ORNL under uniaxial loading. The additional USNA and ORNL information would then allow the magnitude of the biaxial loading effect to be more clearly defined.

Analysis

Evaluation of the J Integral

The J-integral value for each SE(B) specimen was calculated using an η_{pl} factor based on the plastic crack opening displacement ($\eta_{J\text{-}C}$) instead of the load-line displacement. A numerical study by Kirk and Dodds [11] has shown that if the J-integral is calculated from the crack opening displacement (COD) instead of the load-line displacement, the result is virtually insensitive to the material strain hardening exponent for shallow cracked (a/W < 0.29) SE(B) specimens. It is also equivalent to the J-integral calculated in the standardized manner using load-line displacement for deeply cracked (a/W > 0.4) specimen as long as no ductile tearing precedes cleavage initiation. At this time, no γ function has been developed to correct the J-integral from COD for crack growth. However, minimal ductile tearing was expected for the bulk of the SE(B) specimens.

Measuring only the COD has an additional benefit. Fracture toughness tests of 1/2T and 1T SE(B) specimens which are interrupted by cleavage involve the release of a large amount of stored energy which can damage the experimental apparatus, especially the load line displacement transducer. This is especially true in shallow crack SE(B) specimens.

For the SE(B) experiments conducted in this study, the following analysis was used to evaluate J. The J-integral at the onset of cleavage is determined as the sum of elastic and plastic components:

$$J_c = J_{el} + J_{pl} \tag{1}$$

with J_{el} given by:

$$J_{el} = \frac{K_e^2}{E} \tag{2}$$

where, for the SE(B) specimen:

$$K_e = \frac{PSf(a_o/W)}{(BB_N)^{1/2}W^{3/2}} \tag{3}$$

and:

$$f(a_o/W) = \frac{3(a_o/W)^{1/2}}{2[1+2(a_o/W)]} \frac{[1.99-(a_o/W)(1-a_o/W))(2.15-3.93(a_o/W)+2.7(a_o/W)^2)]}{(1-a_o/W)^{3/2}} \quad (4)$$

where: a_o = initial crack length,
P = specimen load,
S = specimen span,
W = specimen width,
B = nominal specimen thickness,.and
B_N = net section thickness of the crack plane.

The plastic component of J is given by:

$$J_{pl} = \frac{\eta_{J-C} A_p}{B_N (W-a_o)} \quad (5)$$

where: $A_p = A - C_o P^2/2$,
and: A = area under the load versus COD curve up to the cleavage initiation point,
C_o = the elastic COD compliance, and
$\eta_{J-C} = 3.785 - 3.101(a_o/W) + 2.018(a_o/W)^2$ from Kirk and Dodds [11].

The critical stress intensity (K_{Jc}) at cleavage initiation is evaluated from

$$K_{Jc} = \sqrt{J_c E} \quad (6)$$

where J_c is the J integral at cleavage initiation and E is the plane stress elastic modulus of the material. In order to directly compare toughness results measured from different thickness specimens, a statistical size correction is employed to equilibrate the amount of highly stressed material sampled by the crack tip at cleavage. By convention, the measured median toughness value [$K_{Jc(med)}$] for a given distribution is converted to an equivalent value for a 1T specimen [$K_{Jc(med)1T}$] using the following equation adopted from ASME 1921:

$$K_{Jc(med)1T} = K_{min} + [K_{Jc(med)} - K_{min}]\left(\frac{B}{B_{1T}}\right)^{1/4} \quad (7)$$

where: B_{1T}= 25 mm (thickness of a 1T specimen), and
K_{min}= 20 MPa$\sqrt{m}$ (Weibull threshold stress).

The $K_{Jc(med)}$ value is evaluated as per ASTM E1921 and represents the median fracture toughness of each data-set. This analysis assumes that the toughness distribution follows a three-parameter Weibull distribution with a slope of 4 and has a threshold stress

intensity factor (K_{min}) of 20 MPa$\sqrt{m}$. A value of T_o, the temperature at which $K_{Jc(med)1T}$ = 100 MPa$\sqrt{m}$, is also found using the empirical "master curve" shape for the toughness vs. temperature relationship as specified in ASTM E1921. This calculated T_o value is utilized to compare the toughness performance of deep crack specimens with uniaxial and biaxial shallow crack specimens conducted at USNA and ORNL.

Analysis of the shallow crack specimens is not within the scope of ASTM E1921 as the governing assumptions are violated when small scale yielding is lost. Loss of small-scale yielding causes the toughness distribution to skew towards higher values as increased J_c values are required for cleavage. This causes the measured T_o for the shallow crack distribution to be lower than the value measured in deep crack specimens for the same material [12]. Therefore, a shallow crack T_o value does not represent a material property as intended in ASTM E1921, but is a measure of the material's performance under low-constraint conditions.

Multi-temperature Master Curve

When cleavage fracture toughness data are available at a range of test temperatures, rather than at a single temperature as required by E1921-98, a multi-temperature maximum likelihood approach, originally proposed by Wallin [2], can be used to evaluate the reference temperature T_o. This method requires an iterative solution for T_o satisfying the following equation:

$$\sum_{i=1}^{n} \frac{\delta_i \exp\{c[T_i - T_o]\}}{a - K_{min} + b\exp\{c[T_i - T_o]\}} - \sum_{i=1}^{n} \frac{(K_{Jc} - K_{min})^4 \exp\{c[T_i - T_o]\}}{(a - K_{min} + b\exp\{c[T_i - T_o]\})^5} = 0 \qquad (8)$$

where: δ_i = 0 (test terminates without cleavage), or 1 (test terminates with cleavage),
a = 31 MPa$\sqrt{m}$,
b = 77 MPa$\sqrt{m}$, and
c = 0.019 $°C^{-1}$.

Here a, b, and c are the "master curve" toughness vs. temperature coefficients for K_o, the mean toughness value of the distribution. K_{Jc} values substituted into Eq. (8) must first be converted to their 1T equivalent values using Eq. (7). Eq. (8) reduces to the form used in E1921-98 for single temperature data sets [2].

Description of Experiments

Material Properties

The material tested was an A533B steel designated HSST Plate 14 that had been heat treated by ORNL to simulate the effects of neutron irradiation on yield stress. The tensile mechanical properties of this approximately 228 mm thick plate are described in reference [10] both before and after heat treatment. Nominal properties after the heat treatment are presented in Table 1. The material utilized for the uniaxial SE(B) testing by USNA was taken from block P16A (Figure 1). Sixteen 1T SE(B) specimens were prepared from this block (Figure 2). Eight shallow crack specimens were cut from the 50

mm of the piece closest to the center of the original plate, and the eight deep crack specimens were machined from the top 50 mm of the original plate surface as shown.

Table 1 *Average tensile mechanical properties within center portion of HSST Plate 14*

Material ID	Temp. (°C)	0.2% σ_{ys} (MPa)	σ_{UTS} (MPa)	% Elongation (51 mm)	NDT (°C)
Plate 14	40	617	775	16	40

The crack starter notch for the shallow SE(B) specimens were machined from the original plate centerline to place the cracks in these specimen as closely as possible to the crack location of the biaxial cruciform tests run at ORNL. The deep crack specimens were all notched from the original plate surface so that the remaining ligament in these specimens was at least 30 mm from the original plate surface. ORNL testing [10] has indicated that the tensile properties within central portion of the original plate are uniform, and that through-thickness variability only occurs within 10 mm from the plate surface. Therefore, it is expected that the properties within the shallow crack SE(B) specimens are uniform, along with the properties within the remaining ligament of the deep crack SE(B) specimens. All of these specimens were machined as standard 1T SE(B) specimens according to ASTM E1737 with W = 50.8 mm, and a bend span of 203 mm. All cracks were oriented in the L-S orientation as defined by ASTM E399 to match the orientation in the ORNL biaxial tests. No side grooves were used for these tests except for the one deep cracked specimen that was tested using unloading compliance to establish the upper shelf J_{Ic} and J-R curve for this material.

The shallow crack specimens were notched to a depth of 3.8 mm using a sharpened circular saw with a thickness of 1.57 mm. The specimens were reverse bend loaded once to a load of 100 kN to aid in final fatigue crack straightness, and then cyclically loaded at room temperature to grow a sharp fatigue crack. The reverse loading plastic zone was estimated from Irwin's plane strain estimation formula [13] for cracks to be approximately 0.5 mm. The fatigue crack was grown using a constant ΔK of 18 $MPa\sqrt{m}$ and R = 0.1 to a length of approximately 1.9 mm, for a total crack length of 5.7 mm or a/W = 0.1. The deep crack 1T SE(B) specimens were saw cut to an initial depth of 24 mm, and then cycled in fatigue using a constant ΔK of 18 $MPa\sqrt{m}$ and R = 0.1 until a fatigue crack extended to 29.2 mm, for an initial a/W = 0.57.

All specimens were tested in a 250 kN screw driven testing machine using an unloading compliance technique. The test temperature was established through convective cooling using liquid nitrogen spray within an insulating environmental chamber. The temperature was maintained within 2°C as measured by a thermocouple inserted into each sample near the crack. For most samples, only the crack opening displacement (COD) was measured, though when it was found that the deeply cracked samples remained intact after cleavage, the final two deeply cracked SE(B) samples were

tested with a "flex-bar" apparatus so that the load line displacement could be measured. The COD was measured on the shallow crack samples using a ring type displacement gage mounted in the notch opening. For the deep crack specimens, a standard E399 type COD gage was utilized. This gage was mounted between two razor blades which were spot welded to the specimen surface across the crack mouth.

Eighteen additional 1/2T C(T) specimens were machined from the bend arms of the 1T SE(B) specimens after these tests were concluded. The relative location of the C(T) specimens with respect to the original SE(B) specimens is indicated in Figure 2. The objectives of the C(T) testing were twofold: to provide a direct comparison with similar ORNL testing, and also to determine if there were measurable differences between material located near the plate centerline and near the surface of the USNA test piece (Fig. 2). However, the test section of these 1/2T C(T) specimens was never located within the top 25 mm of the original plate surface, where through-thickness mechanical property variability has previously been measured [10]. The C(T) specimens were machined about the 1/4 span point of the original 1T SE(B) specimens and had the same crack orientation (L-S) as in the earlier SE(B) tests. Nine C(T) specimens each were machined from shallow crack and deeply cracked SE(B) specimens. These specimens were all precracked to a/W = 0.6 and tested statically at –30°C using the same temperature control apparatus as in the larger specimen testing. Displacement control testing was employed using an actuator speed of 0.025 mm per second. Loading was applied monotonically, without any elastic unloading sequences.

Presentation of the USNA Results

Results of the eighteen 1/2T C(T) specimens are presented in Table 2. The specimen ID suffix (Table 2) indicates if the specimens were machined from "S"hallow or "D"eep crack SE(B) specimens. The J at onset of cleavage instability (J_c) varies widely for these nominally identical tests, as is typical of tests conducted in the mid-transition region. J_c varies here from 26.6 kJ/m^2 to 281.4 kJ/m^2, a range of an order of magnitude in spite of efforts made to keep the specimens and test conditions unchanged for all tests. K_{Jc} was calculated for these tests using Eq. 6, and E = 199 MPa, while conversion to a common, 1T thickness toughness ($K_{Jc(1T)}$) measure for each test result was accomplished using Eq. 7. Ductile crack extension prior to cleavage initiation was negligible in these specimens. Test results from the deep and shallow 1T SE(B) specimens are shown in Table 3, with calculations done in a similar fashion except that no statistical size correction was necessary. For these data, J_c values ranged from 12.1 to 447.6 kJ/m^2, or a ratio of maximum J_c to minimum J_c of approximately 37. The extreme values occurred for the shallow crack tests, which is consistent with previous shallow crack tests of this type by Link and Joyce [3] on a similar A533B material. The wide range of J_c results is attributable to the lower constraint present in these specimens. In some cases the cleavage initiation point can be in an ideal position and the failure can occur at as low a J_c value as found in a deep crack specimen. In most cases, however, extended plasticity will develop out to the crack free surface, causing a relaxation

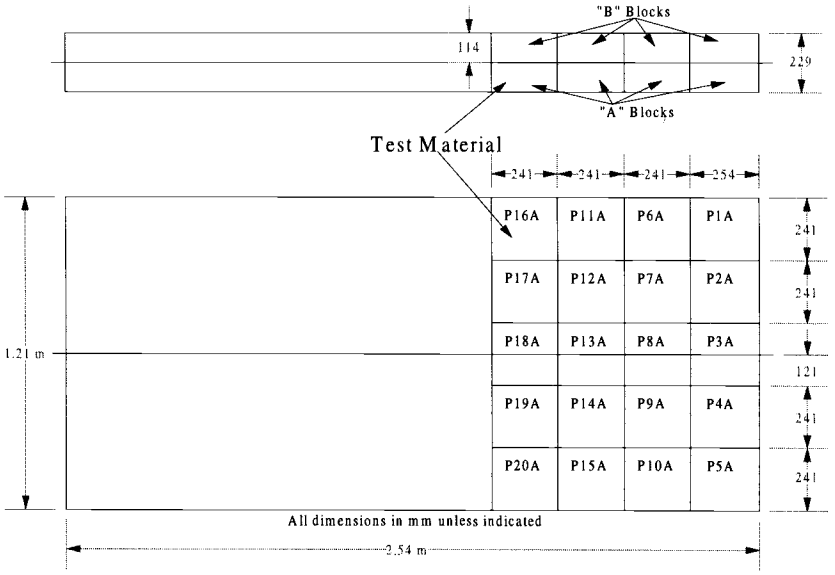


Figure 1 *Location of Block P16A within A533B HSST Plate 14*

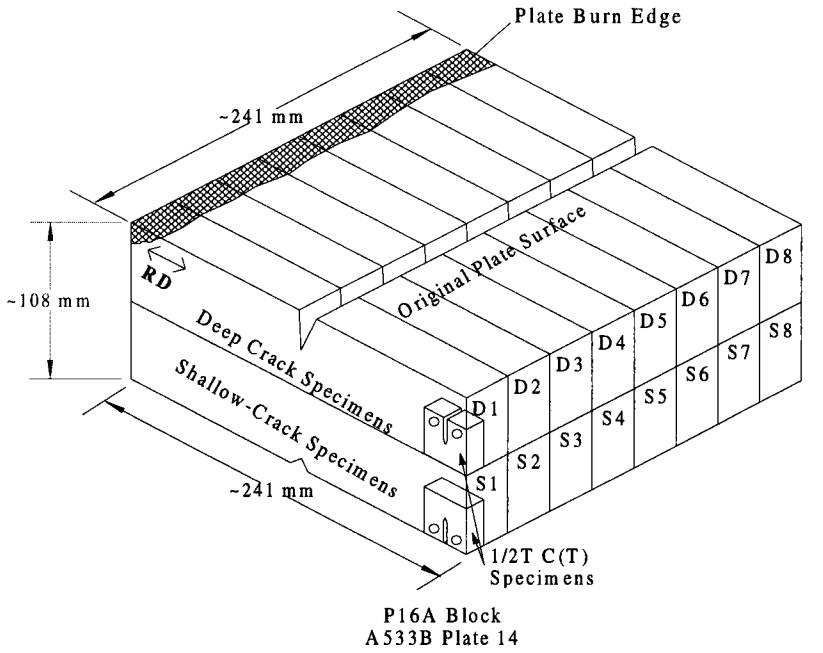


Figure 2 *Test material showing SE(B) specimen location and orientation.*

in the crack-tip constraint for a given remote load, and delays the onset of cleavage fracture. A series of load versus COD curves for some of these shallow crack SE(B) specimens is presented in Figure 3.

Table 2 *USNA 1/2T C(T) fracture toughness results at -30°C*

Specimen ID	a_o/W	P_c kN	COD_c mm	J_c kJ/m^2	K_{Jc} MPa$\sqrt{m}$	$K_{Jc(1T)}$ MPa$\sqrt{m}$
P14-CS1	0.60	15.0	0.78	143.5	168.	144.
P14-CS2	0.59	12.3	0.37	46.4	96.	84.
P14-CS3	0.60	13.7	0.58	92.6	135.	117.
P14-CS4	0.60	13.8	0.51	77.4	123.	107
P14-CS5	0.59	13.7	0.47	69.7	117.	102.
P14-CS6	0.60	15.0	1.09	221.3	209.	179.
P14-CS7	0.60	15.0	0.69	121.3	155.	133.
P14-CS8	0.59	15.5	0.81	158.5	177.	152.
P14-CS9	0.59	13.5	0.48	68.8	116.	101.
P14-CD1	0.51	15.4	0.96	187.4	192.	164.
P14-CD2	0.58	10.4	0.27	26.6	73.	64.
P14-CD3	0.60	10.4	0.30	29.9	77.	68.
P14-CD4	0.60	9.67	0.28	26.4	72.	64.
P14-CD5	0.60	13.4	0.56	86.7	131.	113.
P14-CD6	0.60	14.0	0.71	121.3	155.	133.
P14-CD7	0.60	10.5	0.31	32.5	80.	70.
P14-CD8	0.60	15.6	1.30	281.4	235.	201.
P14-CD9	0.60	12.6	0.44	58.7	108.	94.

One of the deep crack 1T SE(B) specimens, P14-D6, was side-grooved (20% total thickness reduction) and tested at 120°C using unloading compliance to obtain an upper shelf J-R curve for this material (Figure 4). The resulting J-R curve is somewhat lower than the –5°C deep-crack SE(B) J_c values and measured crack extensions shown in columns 5 and 6 of Table 3. These differences could be due to the effects of temperature and side grooving on the resulting J-R curve. Both lower temperatures and side grooving typically elevate the tearing resistance. The results obtained from the shallow crack 1T SE(B) specimens are similar to the deep crack data at -5°C. Since there is little tearing or constraint loss evident, this result is consistent with previous observations by Link and Joyce [3] for a similar A533B material.

Presentation of ORNL Data

Fracture Toughness Data

ORNL tested 27 1/2T C(T) specimens at various temperatures to characterize the

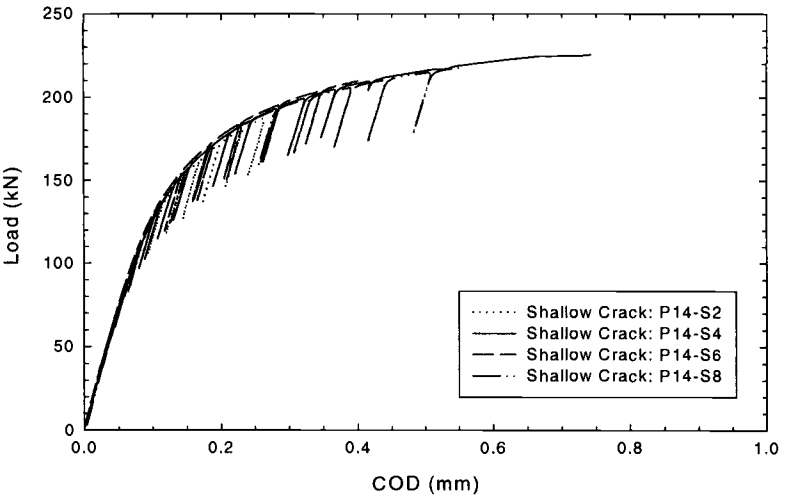


Figure 3 *Sample load vs. COD behavior of shallow crack 1T SE(B) tests*

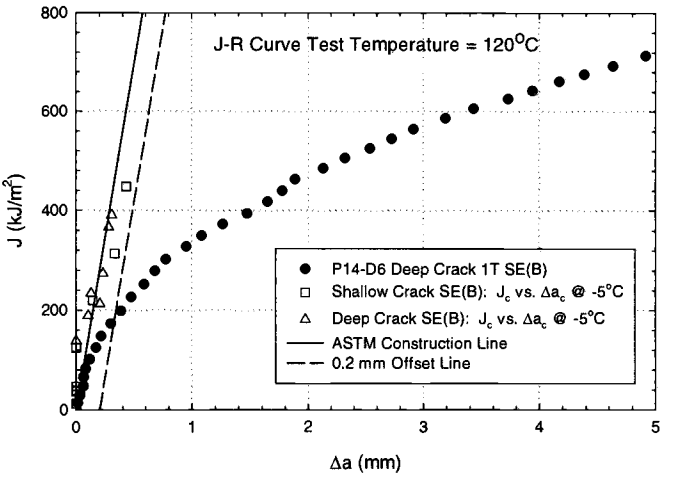


Figure 4 *Plate 14 upper shelf J-R curve behavior at 120°C and transition regime J_c results*

HSST Plate 14 material fracture toughness behavior within the ductile-to-brittle transition regime [10]. These results are summarized in Table 4. These specimens were not side grooved, the crack orientation was L-S, and all testing was conducted according to ASTM E813 [10]. Not all specimens were tested to cleavage failure, as is indicated in Table 4. The non-cleavage results are not valid K_{Jc} measures as defined by ASTM E1921; however the final J (J_f) at test termination can still be transformed to a K_{Jf} value using Eq. 6 with J_f substituted for J_c. All K_{Jf} and K_{Jc} values were then converted to a 1T equivalent toughness value using Eq. 7.

Table 3 *Deep and shallow crack toughness results for 1T SE(B) specimens at –5°C*

Specimen ID	a_o/W	P_c kN	COD_c Mm	J_c kJ/m^2	Δa_{meas} mm	K_{Jc} MPa$\sqrt{m}$
P14-D1	0.57	58.6	1.75	390.3	0.305	290.
P14-D2	0.57	57.9	1.33	273.2	0.229	243.
P14-D3	0.57	55.7	1.13	212.6	0.203	214.
P14-D4	0.57	58.4	1.63	366.3	0.279	281.
P14-D5	0.57	56.8	1.18	233.8	0.127	225
P14-D7	0.57	54.9	1.02	188.9	0.102	202.
P14-D8	0.57	49.8	0.83	138.5	0.0	172.
P14-S1	0.11	146.3	0.13	46.9	0.0	101.
P14-S2	0.11	185.9	0.26	124.5	0.0	166.
P14-S3	0.11	136.3	0.11	38.7	0.0	91.
P14-S4	0.11	225.8	0.74	447.6	0.432	311.
P14-S5	0.11	133.2	0.11	36.8	0.0	90.
P14-S6	0.11	210.3	0.40	219.4	0.142	218
P14-S7	0.11	82.4	0.06	12.1	0.0	51.
P14-S8	0.11	217.8	0.55	313.6	0.33	260.

Biaxial Data

ORNL has developed their biaxial test apparatus over the past few years [14-15] and the available data[3] from this testing on the HSST Plate 14 material is shown in Table 5. A cruciform type specimen geometry was utilized with a/W = 0.1, W = 100 mm. The crack orientation was once again L-S. These specimens are tested with controlled out-of plane to opening mode load ratios by varying the applied pressure ratio between the transverse and longitudinal cruciform arms. The following out-of-plane to opening mode load ratios were tested: 0:1 (uniaxial), 0.6:1, and 1:1 (fully biaxial). The J_c values were computed from CMOD based η-factors, which were developed from finite element

[3] All data from [5], and from personal communication with W.E. Pennell and W.J. McAfee, ORNL.

Table 4 *ORNL 1/2T C(T) Plate 14 Fracture Toughness Results*

Specimen ID	Temperature °C	K_{Jc} (or K_{Jf}) MPa$\sqrt{m}$	$K_{Jc(1T)}$ (or $K_{Jf(1T)}$) MPa$\sqrt{m}$	Cleave? n=0, y=1
W1	-30	95.9	83.8	1
W8	-30	102.3	89.2	1
W4	-30	118.2	102.6	1
W5	-30	129.5	112.1	1
W3	-30	147.9	127.6	1
W6	-30	170.4	146.5	1
W2	-30	178.7	153.5	1
W7	-30	194.0	166.3	1
TC6	-80	113.4	98.5	1
TC10	-80	51.3	46.3	1
TC18	-80	87.9	77.1	1
TC21	-10	211.1	180.7	0
TC17	-10	179.9	154.5	1
TC14	-10	171.8	147.6	1
TC13	-10	153.0	131.8	1
TC7	-10	156.8	135.0	1
TC8	-10	236.9	202.4	0
TC5	0	269.3	229.6	0
TC11	0	107.7	93.7	1
TC19	0	277.8	236.8	0
TC4	23	325.0	276.5	0
TC12	23	328.4	279.3	0
TC20	23	277.4	236.4	0
TC1	-130	59.5	53.2	1
TC2	-130	85.1	74.7	1
TC3	-130	55.3	49.7	1
TC4	-130	56.4	50.6	1

results of the cruciform test geometry. As shown in Table 5, all specimens were loaded until cleavage. For a more complete description of these tests the reader is referred to the above references or to reference [10].

Discussion of the Results

The ORNL 1/2T C(T) $K_{Jc(1T)}$ results are shown in Figure 5. The median master

curve has been developed using the multi-temperature analysis of Eq. 8, while the 5% and 95% confidence interval bounds, and K_{Jc} limit, have been calculated using the analysis of E1921-98. All the C(T) data has been used in the analysis except the data tested at –130 °C as these values are too close to the lower shelf. The reference temperature calculated is T_o = -51°C, and this test series is summarized, along with all subsequent testing, as Case 1 in Table 6. The data are reasonably well defined by the master curve and well bounded by the confidence interval, except for the single outlying point at 0°C. Since this result is defined by such a large data set it will be used as the baseline reference temperature and master curve for subsequent comparisons.

There is sufficient replication at two separate temperatures (eight tests at -30 °C and six tests at –10 °C) to allow calculation of T_o using the ASTM E1921-98 procedure for these 1/2T C(T) data-sets. The results of these calculations give T_o = -46 °C and T_o = –40°C , respectively. Based on the good agreement between the single and multi-temperature master curve approaches, the multi-temperature method should be the better tool for assessment purposes. A trial test temperature can be chosen for testing to determine a preliminary T_o value. Then, follow-on testing can be conducted at this T_o for maximum accuracy. Using the multi-temperature approach, all data can then be used to determine a single T_o with lower uncertainty than is possible with only one single temperature data-set.

Figure 6 illustrates the comparison among the two USNA 1/2T C(T) data sets (Cases 4 and 5 in Table 6) and the multi-temperature master curve and confidence interval illustrated in Figure 5. As shown in Table 6, the T_o values calculated for the two USNA 1/2T C(T) data sets are consistent. A T_o of –48 °C was calculated for the specimens machined from the top 50 mm of the test plate, and a T_o of -47 °C was found for the specimens taken from the center-most 50 mm. These values are also in excellent agreement with the ORNL multi-temperature T_o value of –51 °C (Case 1 in Table 6). The lack of difference in these median USNA C(T) T_o values implies that the centerline and near-surface material are uniform. However, closer examination of the data indicates that five of the nine (56%) results obtained from the near-surface specimens fall outside the 90% confidence band, with four of the five outliers falling below the 5% bound. All nine of the specimen test results obtained from specimens near the plate centerline fall within the 90% confidence interval determined from the ORNL data. The increased specimen scatter present in the near-surface data may be an indication that greater material variability exists at this location. However, this assertion can only be verified with metallographic evidence.

Table 5 *ORNL Biaxial Cruciform Fracture Toughness Results*

Specimen ID	Temperature °C	K_{Jc} MPa$\sqrt{m}$	$K_{Jc(1T)}$ MPa$\sqrt{m}$	Cleave? n=0, y=1
Biaxiality Ratio = 0:1				
P12B	-30	88.0	116.2	1
P3A	-31	103.0	137.4	1
P2B.1	-4	261.5	361.5	1
P2B.2	-3	379.7	528.7	1
P9A	-3	399.8	557.1	1
P13A	-6	184.2	252.2	1
P18A	-3	280.5	388.4	1
P17A	-2	321.7	446.7	1
P19B	-2	302.3	419.2	1
Biaxiality Ratio = 0.6:1				
P14B	-31	70.3	91.1	1
P7B	-30	136.3	184.5	1
P3B	-4	269.8	373.3	1
P12A	-6	225.8	311.0	1
P15B	-4	232.4	320.4	1
P6A	4	195.2	267.8	1
P10A	8	297.4	412.3	1
P9B	15	281.9	390.4	1
Biaxiality Ratio = 1:1				
P13B	-28	112.1	150.2	1
P4A	-29	141.2	191.4	1
P6B	-4	162.3	221.2	1
P15A	-4	154.6	210.4	1
P10B	-6	204.6	281.1	1
P17B	-5	129.5	174.8	1
P5A	-3	210.0	288.7	1
P5B	-4	316.1	438.7	1
P4B	6	167.5	228.6	1
P7A	15	229.3	316.0	1
P11A	15	234.1	322.8	1
P11B	17	325.5	452.0	1

Table 6 *Summary of the T_o Reference Temperature Results*

Case No.	Specimen Data Set	No. of Data Points	Test Temp. °C	$K_{o(1T)}$ MPa√m	$K_{Jc\ (med)1T}$ MPa √m	T_o °C
1	ORNL 1/2T C(T) Multi-Temp.	23	Various			-51
2	ORNL 1/2T C(T)	8	-30	134.5	124.5	-46
3	ORNL 1/2T C(T)	6	-10	167.6	154.6	-40
4	USNA 1/2T C(T) – Surface 50 mm.	9	-30	140.4	129.5	-48
5	USNA 1/2T C(T) – Center 50 mm	9	-30	136.9	127.7	-47
6	USNA 1T SE(B) Deep Crack	7	-5	245.0	225.6	-59
7	USNA 1T SE(B) Shallow Crack	8	-5	221.0	203.4	-53
8	ORNL Biaxial 0:1 Multi-Temp.	9	Various			-89
9	ORNL Biaxial 0:1.	7	-5	456.8	418.6	-93
10	ORNL Biaxial 0.6:1 Multi-Temp.	8	Various			-71
11	ORNL Biaxial 1:1 Multi-Temp.	12	Various			-68
12	ORNL Biaxial 1:1	6	-5	316.7	290.7	-73

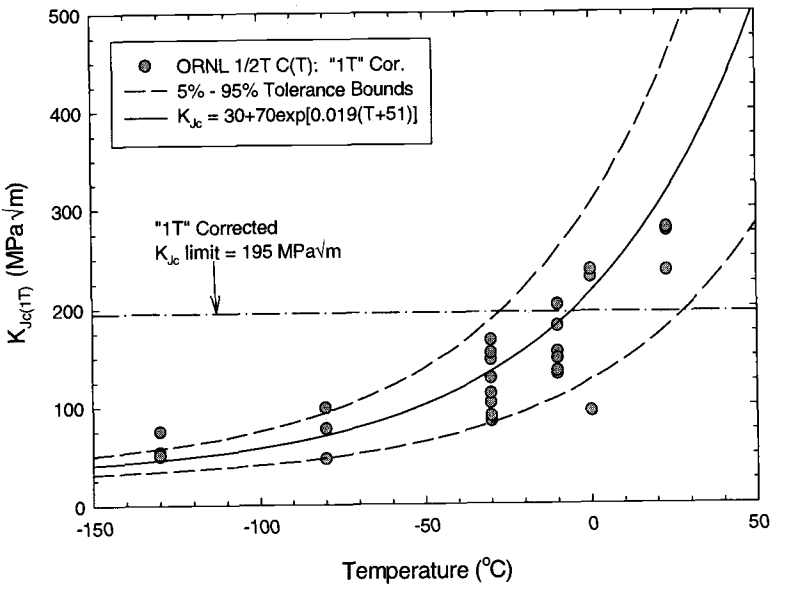


Figure 5 *Multi-temperature deep crack master curve for Plate 14*

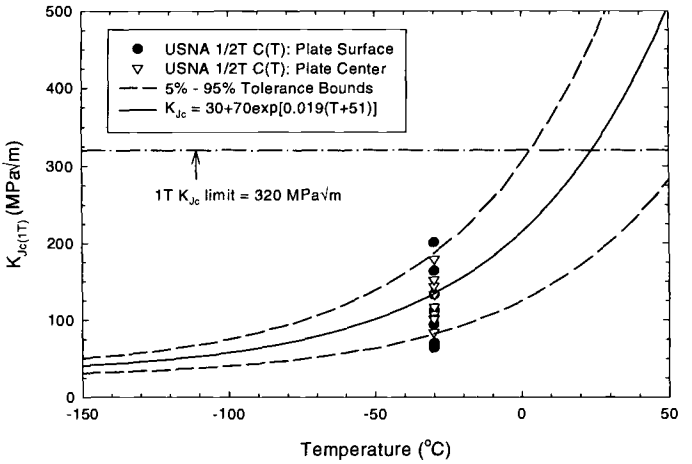


Figure 6 *USNA deep crack C(T) results superimposed on the multi-temperature master curve*

The USNA shallow and deep crack 1T SE(B) results are superimposed on the USNA 1/2T C(T) data in Figure 7. As described earlier, the deep crack specimens were all machined from the top 50 mm of plate, although the remaining ligament was more than 25 mm from the original plate surface. The deep crack data set T_o, calculated using

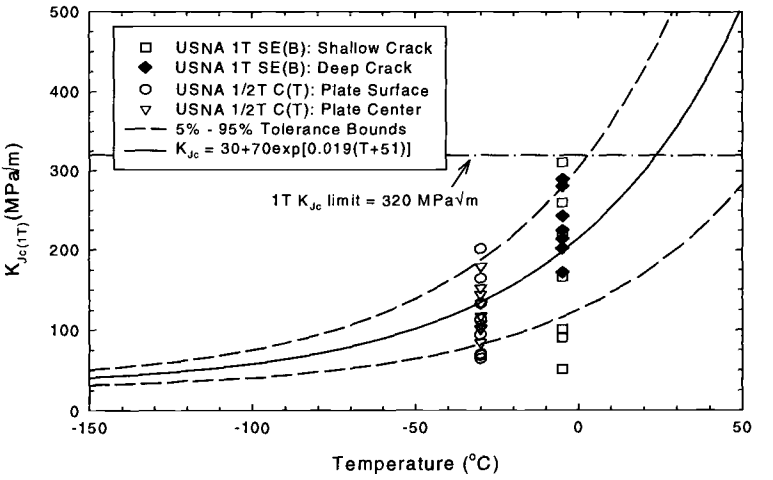


Figure 7 *USNA SE(B) results and comparison to earlier deep crack test results*

the E1921 procedure, is -59 °C (Case 6 in Table 6). While these data predominantly fall above the median curve from the ORNL C(T) specimens, all data are largely within the expected confidence interval. The roughly 10 °C difference between the deep crack SE(B) and various C(T) specimen results is well with the experimental uncertainty associated with T_0 measurement from a small-data set as outlined in E1921.

The shallow crack specimen results, however, were initially puzzling because they do not exhibit the behavior expected. First, the T_0 for these data are higher than calculated for the deep crack specimens (Case 7 in Table 6), which indicates that the corresponding median toughness of the shallow crack specimens is ***lower***. Additionally, four out of eight (50%) shallow crack results ***fall below*** the 5% confidence bound. This behavior is counter to other studies [3, 4] which have shown that constraint loss in the shallow crack specimens leads to an ***increase*** in the median toughness compared to deep-crack testing. The absolute lower bound of both deep and shallow crack specimen data is often similar [3] due to the finite possibility that a particularly weak cleavage initiation site (CIS) fails prior to the development of gross plasticity within the short crack SE(B). However, there is no mechanical reason to explain why the shallow crack lower bound falls below deep crack lower bound data for these specimens. Additional metallographic and fractographic work was performed to identify an underlying material cause for this phenomenon. This work will be described subsequently.

The primary goals of the shallow cracked SE(B) testing were to cheaply assess the expected variability and median toughness of the 0:1 cruciform biaxial tests, and provide a benchmark for judging the statistical significance of any measured biaxial effect. Recall that the 0:1 tests are loaded uniaxially and the a/W ratio for these cruciform tests is 0.1 which is similar to the shallow crack SE(B) specimens. The cruciform specimen has the following primary differences with the SE(B) tests: the crack length is approximately 100 mm, the specimen has unloaded transverse arms which may cause some slight constraint elevation, the specimen utilizes all but the top 20 mm of the test piece, and the crack depth is physically twice the crack length present in the SE(B) specimen. These latter two differences are only important if the material properties exhibit any gross thickness dependence. As mentioned earlier, testing by ORNL has indicated consistent through-thickness mechanical properties. The differences in crack front length are accounted for by converting the cruciform results to an equivalent 1T thickness using Eq. 8. Therefore, it is expected that the shallow crack SE(B) and 0:1 biaxial tests should provide consistent results.

The deep and shallow crack SE(B) and 0:1 cruciform tests conducted near –5 °C are summarized in Figure 8. The reference temperature for all the 0:1 tests is –89 °C when Eq. 8 is used to analyze the multi-temperature data-set (Case 8 in Table 6). The cruciform 0:1 data-set illustrates behavior expected of short crack specimens. It's 1T corrected median toughness at –5 °C is elevated compared with the deep crack data (419 MPa$\sqrt{m}$ vs 226 MPa$\sqrt{m}$), and the scatter is increased. In Figure 8, the median toughness and extreme values for each data series are connected with trends lines to emphasize the median toughness differences. The trend lines also illustrate that scatter in the cruciform and shallow crack SE(B) data is similar, and much greater than the deep-crack data scatter due to constraint loss. However, the median toughness of the shallow crack data set is much less than the cruciform data (203 MPa$\sqrt{m}$ vs. 418 MPa$\sqrt{m}$). It is apparent

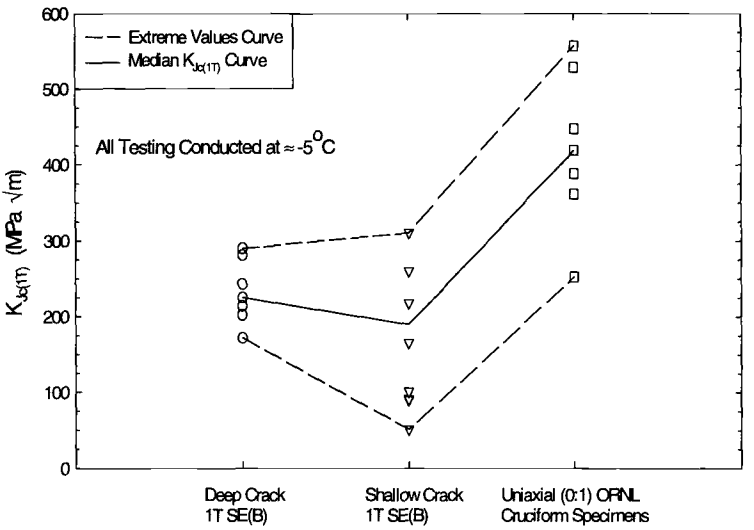


Figure 8 *SE(B) and uniaxial cruciform toughness distributions*

from these data that the shallow crack SE(B) tests do not adequately simulate the 0:1 cruciform tests as originally intended.

The shallow crack toughness data measured in the ORNL biaxial tests conducted at -5°C are plotted as a function of biaxiality ratio in Figure 9, along with the uniaxial shallow crack 1T SE(B) results. All cruciform results have been converted to 1T equivalent values for comparison. It is evident from this figure that the median toughness does decrease with increased biaxial loading ratio if the shallow crack SE(B) results are neglected. This trend is also evident in the single and multi-temperature reference temperature results reported in Table 6. The reference temperature for the 1:1 tests is approximately 20 °C higher than that for the 0:1 results (Case 11 in Table 6). This difference, while not large, has remained consistent with additional testing and is thought to represent a physical effect.

The shallow crack 1:1 biaxial cruciform and SE(B) results illustrated in Figure 9 are plotted as a function of temperature in Figure 10 and compared to the deep crack confidence bounds. The ASME K_{Ic} curve for this material is also illustrated in Figure 10. This curve is based on a RT_{NDT} of 40 °C for this material as measured by ORNL [10]. Also shown in Figure 10 is an ASME code case design curve which is a proposed modification to the existing ASME K_{Ic} design curve. The code case curve utilizes the same shape as the ASME K_{Ic} curve, but replaces the RT_{NDT} reference temperature with RT_{To} which is $T_o + 35°C$.

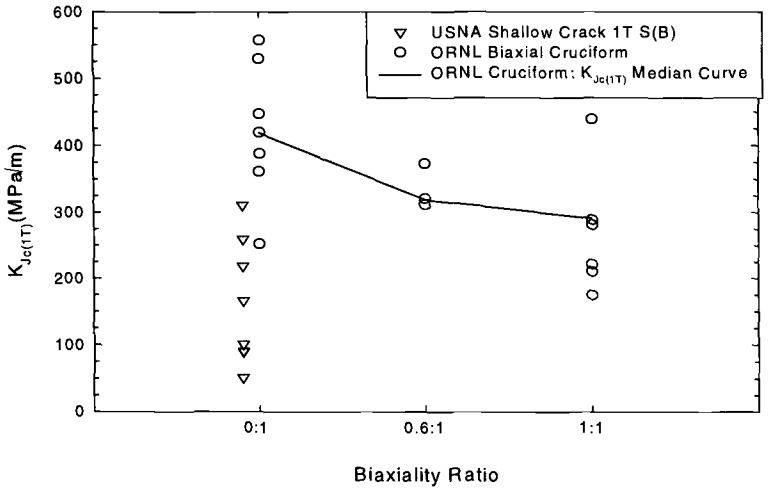


Figure 9 *Effect of biaxiality ratio on shallow crack toughness distribution*

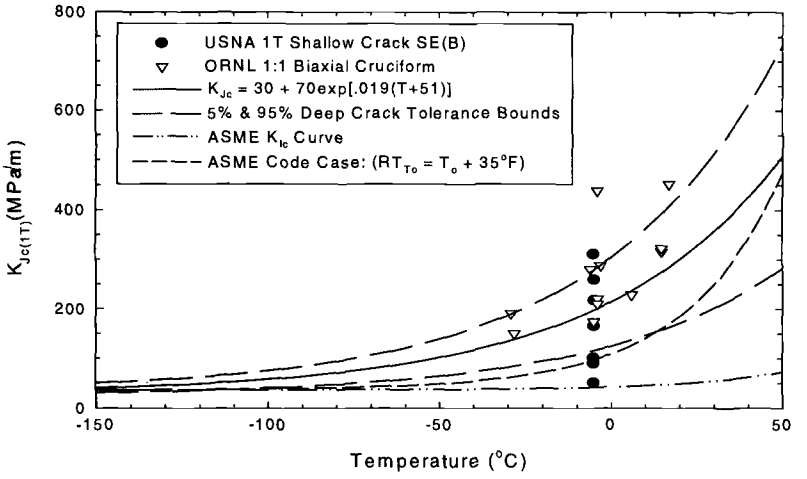


Figure. 10 *The relationship between low constraint 1:1 cruciform and shallow crack SE(B) results and several different tolerance bounds based on previous deep crack data*

Two salient points are apparent in this figure. The first is that the lowest shallow crack SE(B) data point at –5 °C (K_{Jc} = 51 MPa$\sqrt{m}$) nearly falls on the lower bound K_{Ic} curve (ASME K_{Ic} = 41 MPa$\sqrt{m}$), and is lower than the code case design curve (Code case K_{Ic} = 71 MPa$\sqrt{m}$). Two other points in the shallow crack distribution having $K_{Jc} \approx 90$ MPa$\sqrt{m}$ also are close to the code case design curve. Further, as mentioned earlier, a large percentage of these shallow crack SE(B) data fall below the 5% deep crack confidence bound which is counter to expectations and experience. The second point is that while the 1:1 biaxial results do exhibit an increase in constraint when compared with the 0:1 results, the measured toughness values are still well above either of the K_{Ic} design curves or the deep crack confidence bounds. Therefore, structural predictions based on deep crack data remain conservative. If any benefit is to be gained by considering the increased toughness within short-cracked structures due to constraint loss, this gain must be mitigated accordingly by an appropriate toughness decrease due to biaxial loading effects.

Metallography/Fractography

Metallography and fractography study were combined to identify an underlying reason for the low median toughness of the shallow crack 1T SE(B) data-set compared to the remainder of the deep crack uniaxial and shallow crack biaxial data. A stereo-section fractography (SSF) technique [7, 8] was utilized to simultaneously observe the fracture surface and underlying microstructure very close to the CIS. A schematic of the process is indicated in Figure 11. The primary CIS is first identified and then repeated transverse sectioning, polishing, and etching is performed until the transverse plane is sufficiently close to the CIS in order to reveal the microstructural features associated with cleavage. In this study, four specimens tested near –5 °C were chosen to represent the extreme data points within the shallow crack SE(B) (USNA P14S4 and P14S7) and the 0:1 biaxial (ORNL P9A and P13A) data-sets.

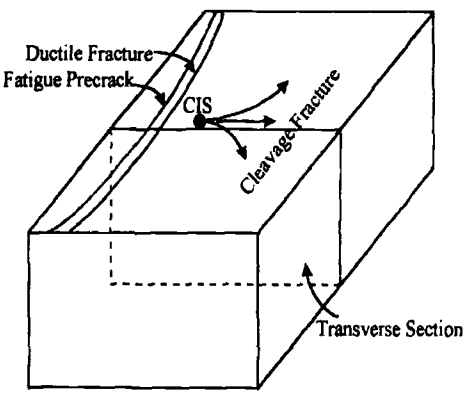


Figure. 11 *Sectioning plane and location relative to cleavage initiation for the SSF technique*

Since toughness variation is related to local microstructural inhomogeneity, only specimens demonstrating extreme toughness results were studied to uncover the range of microstructural differences expected within these samples. An additional deep crack specimen (USNA P14D3) was selected to represent typical deep-crack SE(B) data. A

primary CIS was evident on specimens USNA P14S4, ORNL P13A, and USNA P14D3. An initial transverse section was made within 50 – 100 μm of the primary cleavage site for these specimens. Multiple initiation sites were present on specimens USNA P14S7 and ORNL P9A. Therefore, these specimens were randomly sectioned. The metallographic preparation procedures of these transverse sections were kept as similar as possible. Each section was polished to a 6 μm finish and then etched for 20 seconds using a 2% nital solution. SSF observations then were utilized to locate the tip of the fatigue precrack, the ductile crack extension, and the CIS with respect to the underlying microstructural features.

The metallography at the CIS for each specimen is summarized in Figures 12 and 13. As indicated by these figures, each group of specimens exhibited vastly different levels of attack under similar etching conditions. Specifically, the USNA shallow crack specimens exhibited a duller general appearance and had a much higher concentration of dark bands than either the ORNL 0:1 specimens or the USNA deep crack specimen. Previous work has verified that the dark bands consist of carbide particles [6-9]. USNA deep crack specimen P14D3 responded the slowest to the etching process; carbide banding was only revealed in this specimen by utilizing a longer etching time than is illustrated in Figure 12. The different etching responses exhibited within these groups stem from material inhomogeneity. The overall surface dullness is related to the average chemical composition and microstructural scale. Carbide particle size and density is a likely contributor to the overall dullness since it etches dark. The most striking difference is the intensity and density of the carbide banded regions within the shallow crack SE(B) specimens compared to the other specimens. Close examination of metallographic surfaces within Figures 12 and 13 reveals that the high density of carbide clusters within these bands often triggers cleavage initiation. These dendritic carbide bands form during the initial solidification of the A533B plate and do not dissipate during the secondary quenching and tempering performed to simulate radiation embrittlement. A microhardness survey was conducted on specimen USNA P14S5 (Figure 14). Indentations placed within the dark carbide band had a hardness of 390 Hv (40 HRC), while the surrounding matrix hardness was 230 Hv (20 HRC). This hardness difference is indicative of a tremendous strength and toughness discrepancy between these regions.

Therefore, it appears as if a primary cause for the scatter in the cleavage initiation toughness distribution for this steel stems from the variability in the proximity of the fatigue precrack to one of these strong, brittle carbide bands. USNA P14S7 and ORNL P13A had the lowest toughness values of their respective series, and the fatigue precrack tip in each was located near high carbon bands. Conversely, specimens USNA P14S4 and ORNL P9A had the highest toughness values within each series due to the fact that the crack appears to have grown substantially to locate one of these trigger regions.

The higher density of carbide bands within the USNA shallow crack series also explains the low median toughness value measured for this series. Banding within these specimens is generally more severe than either the ORNL 0:1 specimens or the USNA

specimen P14D3. It is informative to compare the lowest 0:1 biaxial specimen (ORNL P13A) to the highest shallow crack SE(B) specimen (USNA P14S4). Although the measured toughness of P14S4 is higher than P13A (311 MPa$\sqrt{m}$ vs. 184 MPa$\sqrt{m}$), the banding structure within P14S4 is clearly more severe. The higher toughness for this specimen is merely a function of probability; the fatigue precrack happened to reside relatively far away from a banded region. It is also informative to note that the deep crack USNA and ORNL microstructures appear more similar than the shallow crack SE(B) structure and therefore should be expected to result in the generally similar properties measured among the deep-crack USNA C(T), USNA SE(B), and ORNL C(T) specimens, and the consistent performance of the shallow crack ORNL biaxial tests.

In terms of this study, the microstructural differences explain the peculiarities among the fracture toughness distributions noted earlier. Metallography has indicated that the central section of piece 16A had a preponderance of carbide bands compared to the surface section and likely the bulk of the A533B plate 14. These bands are localized throughout the plate thickness. Deep crack SE(B) specimens adjacent to the highly banded shallow crack SE(B) specimens were relatively free from banding. Further study also indicated that the worst concentration of banding in the shallow crack 1T SE(B) specimens was mainly confined near the crack plane. This explains why the measured median toughness values are consistent between the C(T) specimens machined from the ends of the shallow crack specimens and those taken from the end of the deep-crack specimens. However, banding may explain the greater variability (especially the preponderance of low toughness results) in the C(T) specimens machined from the end of the P14 shallow crack SE(B) specimens compared to the confidence bounds from the ORNL tests.

Banding also explains the principal reason why the shallow crack SE(B) results do not coincide with the 0:1 biaxial tests. Specimen constraint is similar in these two geometries and the measured toughness distributions should be consistent once differences in the crack front length are accounted for using Eq. 7. Further, these microstructural differences do not allow the shallow crack SE(B) results to serve as a good benchmark to the biaxial test series as originally intended. The biaxial effect can only be rigorously demonstrated among specimens with a constant microstructure. Work is ongoing at ORNL to ensure that the microstructure within the biaxial specimen data-set is indeed consistent.

A more troubling ramification is that these heavily carbide banded regions exist and can lead to demonstrably lower toughness performance than the bulk of the plate material. The shallow crack SE(B) results, which more closely simulate cracking in structures, is just slightly above the K_{IC} curve. Further, this material degradation was not exhibited by either T_o or RT_{NDT} screening tests. The end result is that the additional expected margin due to shallow crack constraint loss is completely erased by the banding microstructure. Design and assessment procedures must either explicitly or implicitly include some margin to account for the possibility that banding may exist within a critical region, and that it also unlikely that surrogate screening material will capture this feature. Work is currently in progress to assess the prevalence of banding in prototypical thick-section A533B plate.

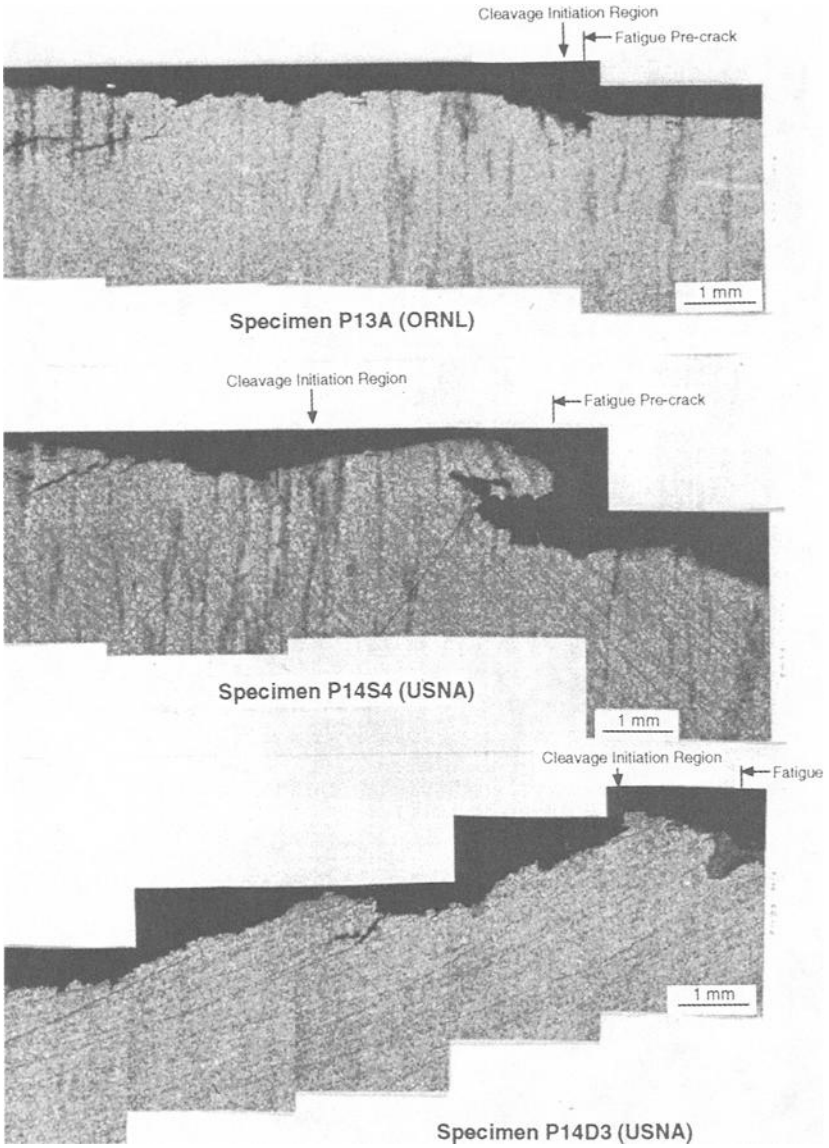


Figure 12 *Transverse section for (a) 0:1 cruciform lower bound specimen (ORNL P13A), (b) shallow crack SE(B) upper bound specimen (USNA P14S4), and (c) a typical deep crack SE(B) specimen (USNA P14D3)*

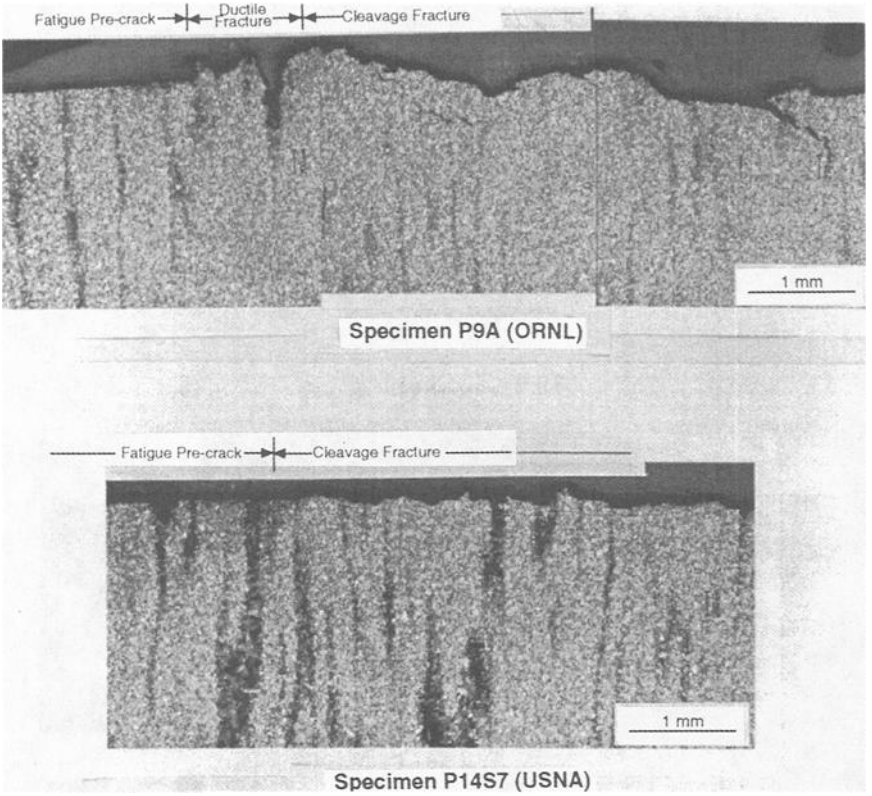


Figure 13 *Transverse section for (a) 0:1 cruciform upper bound specimens (ORNL P9A), and (b) shallow-crack SE(B) lower bound specimen (USNA P14S7)*

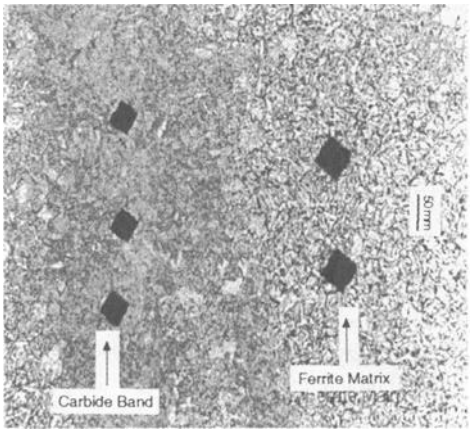


Figure 14 *Microhardness indentations within high density and low density carbide regions* deep crack

Conclusions

Several different types of tests were conducted on a single thick-section plate of A533B (HSST Plate 14) within the ductile-to-brittle transition region in order to characterize the material and to simulate structural performance using shallow cracks specimens under uniaxial and biaxial loading. Several important points have been illustrated by this testing.

- In standard specimens, the maximum likelihood approach provides good correspondence between multi-temperature estimations of T_0 and single temperature assessment as per ASTM E1921. The multi-temperature approach is recommended for assessment purposes. A trial test temperature can be chosen for testing to determine the material's T_0 value. Then, follow-on testing can be conducted at T_0 for maximum accuracy. Using the multi-temperature approach, all data can then be used to determine T_0 with lower uncertainty.

- Multiple screening tests to determine the T_0 of Plate 14 using different specimen types all yielded consistent values of approximately –50 °C. These tests also illustrated that there are no gross material differences between the center, and near-surface region of this plate.

- The C(T) specimens purposely machined near regions of intense carbide banding did result in a large number of specimens (56%) which fell outside the 90% confidence bounds. This increased scatter was mainly manifested by low toughness values and is thought to be indicative of local carbide banding.

- The variability measured within the cruciform biaxial testing is typical for cleavage crack initiation of these low-constraint specimens within the ductile-to-brittle transition region. Comparison of the 0:1 and 1:1 tests illustrates that a measurable biaxial effect does exist. The high toughness values are reduced in the 1:1 tests as plasticity remains confined to higher levels of remote loading, while the absolute lower toughness bound is not affected.

- Shallow crack SE(B) tests were conducted to determine the variability expected within these tests, and to provide a benchmark for quantifying the effect of the biaxiality ratio on fracture toughness. While the scatter in the SE(B) tests was consistent with the 0:1 biaxial testing, the median toughness of these tests was not elevated compared to high constraint results as should be expected. Intense carbide banding was identified within the crack plane of the shallow crack SE(B) specimens that was not present in any other series of tests examined. The presence of these carbide bands is troubling because they are localized, occur randomly within the plate, and are not easily measured with screening tests.

- Constraint loss due to the shallow crack effect is still evident in the 1:1 biaxial specimens, and the corresponding toughness distribution remains higher than the deep

crack data. The current ASME design approach is based on deep crack specimen results, and this approach remains conservative for assessing shallow flaw structural performance under biaxial loading.

- Metallurgy should be conducted as part of screening programs to ensure that the surrogate test material is representative of the service component. Further, some margin should exist within structural assessment methodologies to account for potential material variability within the service component. While the large existing ASME K_{Ic}/K_{IR} design curve margin implicitly covers this variability, any proposed modifications to this curve should consider material inhomogeneity. Work is needed to identify the prevalence and cause of these bands in thick-section A533B plate to rationally determine appropriate margins for use within the master curve approach.

Acknowledgement

The work described in this investigation was performed as a part of the "Elastic-Plastic Fracture Mechanics Technology for LWR Alloys Program sponsored by the U.S. Nuclear Regulatory Commission (USNRC). at the Naval Surface Warfare Center, Carderock Division and at the U.S. Naval Academy. The support of the materials branch at the USNRC, especially the Program Technical Monitor, Dr. Shah Malik, is gratefully acknowledged. The authors would like to thank Derek Baker of the USNA for machining the test specimens.

References

[1] Wallin, K., Fracture Toughness Transition Curve Shape for Ferritic Structural Steel, *Fracture of Engineering Materials & Structures*, S.T. Teoh and K.H. Lee, eds., Elsevier Applied Science, 1991, pp. 83-88.

[2] Wallin, K., "Validity of Small Specimen Fracture Toughness Estimates Neglecting Constraint Corrections," *Constraint Effects in Fracture Theory and Applications: Second Volume*, ASTM STP 1244, Mark Kirk and Ad Bakker, Eds., American Society for Testing and Materials, 1995.

[3] Link, R.E., and Joyce, J.A., "Experimental Investigation of Fracture Toughness Scaling Models," *Constraint Effects in Fracture: Theory and Applications*, ASTM STP 1244, Mark Kirk and Ad Bakker Eds., American Society for Testing and Materials, 1994.

[4] Sumpter, J.D.G., "An Experimental Investigation of the T Stress Approach," *Constraint Effects in Fracture*, ASTM STP 1171, E.M. Hackett, K.H. Schwalbe, and R.H. Dodds, Eds., American Society for Testing and Materials, 1993, pp. 492-502.

[5] Zhang, X.J., "Cleavage-Fibrous Transition Behavior of Structural Steels," Ph.D.

Thesis, University of Maryland, (1985).

[6] Irwin, G.R., Zhang, X.J., and Armstrong, R.W., "Isolated Cleavage Region in the Ductile Fracturing Transition of Nuclear – Vessel Steels and their Weld Metals," *Journal of Material Science Letters*, Vol. 8, 844-848, 1989.

[7] Zhang, X.J., Armstrong, R.W., and Irwin, G.R., "Stereo (SEM) Section Fractography of Isolated Cleavage Regions in Nuclear Vessel Steels," *Metallurgical Transactions*, 20A, pp. 2862-2868, 1989.

[8] Zhang, X.J., Tregoning, R.L., Armstrong, R.W., and Irwin, G.R., "SEM Stereo-Section Fractography (SSF) Observations," *Proceedings for George R. Irwin Symposium on Cleavage Fracture*, K.S. Chan, Ed., pp. 69-79, 1997.

[9] Zhang, X.J., and Tregoning, R.L., "The Effect of Localized Carbide Banding on the Fracture Toughness of Heavy Section A533B Steel," submitted to *Materials Solution '99*, ASM.

[10] McAfee, W.J., Bass, B.R., and Bryson, J.W., "Development of a Methodology for the Assessment of Shallow-Flaw Fracture in Nuclear Reactor Pressure Vessels: Generation of Biaxial Shallow-Flaw Fracture Toughness Data," ORNL/NRC/LTR-97/4, Oak Ridge National Laboratory, April 1997.

[11] Kirk, M.T., and Dodds, R.H., "J and CTOD Estimation Equations for Shallow Cracks in Single Edge Notch Bend Specimens," *Proceedings of TWI/EWI International Conference on Shallow Crack Fracture Mechanics, Toughness Tests and Applications*, Cambridge, UK, 1992.

[12] Ruggieri, C., Dodds, R.H., Jr., and Wallin, K., "Constraint Effects on Reference Temperature, T_0, for Ferritic Steels in the Transition Region," *Engineering Fracture Mechanics*, to be published.

[13] Irwin, G.R., "Plastic Zone Near a Crack and Fracture Toughness," *Sagamore Research Conference Proceedings*, Vol. 4, 1961.

[14] Bass, B.R., Bryson, J.W., Theiss, T.J., and Rao, M.C., "Biaxial Loading and Shallow-Flaw Effects on Crack-Tip Constraint and Fracture Toughness," NUREG/CR-6132 (or ORNL/TM-12498), Oak Ridge National Laboratory, January 1994.

[15] McAfee, W.J., Bass, B.R., Bryson, J.W., Jr., and Pennell, W.E., "Biaxial Loading Effects on Fracture Toughness of Reactor Pressure Vessel Steel,", NUREG/CR-6273 (or ORNL/TM-12866), Oak Ridge National Laboratory, March 1995.

Kunio Onizawa,[1] Tohru Tobita,[1] and Masahide Suzuki[1]

Effect of Irradiation on Fracture Toughness in the Transition Range of RPV Steels

Reference: Onizawa, K., Tobita, T., and Suzuki, M., **"Effect of Irradiation on Fracture Toughness in the Transition Range of RPV Steels,"** *Effects of Radiation on Materials: 19th International Symposium, ASTM STP 1366,* M. L. Hamilton, A. S. Kumar, S. T. Rosinski, and M. L. Grossbeck, Eds., American Society for Testing and Materials, West Conshohocken, PA, 2000.

Abstract: The effect of irradiation on cleavage fracture toughness in the ductile-brittle transition range of RPV steels was studied using precracked Charpy-V (PCCv) specimens. Four kinds of RPV steels of ASTM A533B class 1 made by Japanese steel makers were used for this study. Neutron irradiation to PCCv specimens was carried out at JMTR. An approach based on the weakest link theory was applied to analyze the specimen size effect and the scatter of fracture toughness. The scatter of fracture toughness was confirmed to have a Weibull type distribution. Irradiation effect on the scatter was found insignificant. The fracture toughness transition curves were determined by PCCv data according to the master curve approach and the Japanese code. The shift of the master curve due to neutron irradiation was somewhat greater than the Charpy 41J shift. The scheme to estimate the lower bound of fracture toughness was also studied.

Keywords: reactor pressure vessel, surveillance, structural integrity, irradiation embrittlement, fracture toughness, precracked Charpy, master curve, lower bound

Introduction

The brittle fracture of a reactor pressure vessel (RPV) must be prevented, because it may lead to a catastrophic accident. Therefore, the ductile-to-brittle transition index temperature of the RPV steel should be appropriately lower than the operating temperature of the reactor. However, fast neutrons from the reactor core during operation can increase the transition temperature, i.e., cause irradiation embrittlement. To assure RPV structural integrity throughout its operational life, fracture toughness after neutron irradiation is needed. To do this, the surveillance program for the RPV is performed according to regulations. The results obtained from the Charpy impact tests in the surveillance program are used for the estimation of fracture toughness after irradiation[1,2]. Most codes related to the surveillance program assume that the degree of irradiation embrittlement obtained from Charpy impact tests is equivalent to that of fracture toughness for the material concerned. Recent research, however, has indicated that the correlation is not always conservative in predicting the degree of irradiation

[1]Senior Engineer, Research Engineer and Head, respectively, Reactor Component Reliability Laboratory, Japan Atomic Energy Research Institute, Tokai-mura, Ibaraki-ken, 319-1195, Japan.

Copyright© 2000 by ASTM International www.astm.org

embrittlement in terms of fracture toughness[3,4]. Fracture mechanics methodology is, therefore, necessary for the precise evaluation of irradiation embrittlement to assure the structural integrity of an RPV.

A methodology to evaluate fracture toughness of RPV steels has not been established completely, particularly in the transition temperature range. Since fracture toughness values from test specimens of RPV steels show a large scatter in the transition temperature range, fracture toughness should be evaluated statistically. This means that a certain statistical approach is necessary for the evaluation of fracture toughness. Although intensive research[e.g. 4] has been conducted to establish the statistical treatment and the evaluation method of specimen size effect in the past, the methods need a large number of specimens and/or relatively large size specimens[5]. Since only a small number of small size specimens are available from a surveillance capsule, further research is desired to establish an improved test and evaluation method for surveillance program specimens to evaluate the irradiation effect on fracture toughness.

The objective of this paper is to evaluate the irradiation effect on fracture toughness for RPV steels made by Japanese steel fabricators. Based on the results of the fracture toughness tests by precracked Charpy (PCCv) specimens, and standard size 1T-CT and 4T-CT specimens, a statistical analysis is performed to evaluate the irradiation effect on the median value and the scatter of fracture toughness in the transition temperature range. The evaluation schemes for the lower bound of fracture toughness are compared with the experimental data.

Experiments

Materials

Four kinds of RPV steels of ASTM A533B class 1 were used in this study. One is designated as JRQ, which was used as a correlation monitor material in the IAEA CRP[6,7]. Two other kinds of A533B-1 steels, called Steel A and Steel B, were also used. These steels correspond to RPV steels of the 1970's and the late 1980's, respectively. The last material was chosen because of its large database of cleavage fracture toughness for small size specimens to large ones. The material is designated as JSPS A533B-1 and was used in the round robin study organized by The Japan Society for Promoting of Science (JSPS)[8]. Chemical compositions of the materials are summarized in Table 1. Mechanical properties at room temperature for the materials are listed in Table 2.

Fracture Toughness Tests

Four types of specimens were used in this study, namely PCCv, 0.5T-DCT, 1T-CT and 4T-CT[9]. Table 3 indicates the test matrix. In most cases, the specimens were side-grooved by 10% on each side of the specimen after precracking. For JSPS A533B-1 steel, one of the authors performed fracture toughness tests using PCCv specimens machined from halves of broken 2T-CT specimens at SCK•CEN[10]. The notch orientation is T-L direction for all specimens. Each specimen was machined from the

approximately quarter thickness position of the material. Fracture toughness tests were performed at mainly lower transition temperatures where a cleavage fracture was observed before the maximum load of the specimen.

Testing and evaluation for fracture toughness were performed according to the ASTM Standard Test Method for Plane-Strain Fracture Toughness of Metallic Materials (E399) and Standard Test Method for J_{IC}, A Measure of Fracture Toughness (E813). A valid fracture toughness, K_{IC}, was obtained only from some 4T-CT specimens. The following method was applied to obtain fracture toughness values from the other specimens. Fracture toughness values at cleavage fracture, J_C, were calculated based on the area under the load-displacement curve up to the sudden load drop and the cleavage fracture load (see eq. 1). Fracture toughness K_{JC} values were then converted from J_C by the equation (2). Elastic modulus E and Poisson's ratio ν were fixed to 206 GPa and 0.3 in this study, respectively.

$$J_C = J_{el} + J_{pl} = \frac{K_C^{\,2}}{E'} + \frac{\eta A_{pl}}{B_N b_0} \tag{1}$$

where Kc: Stress intensity factor at the cleavage fracture,
η=2+0.522(a_0/W) for compact tension specimens,
η=2 for PCCv specimens,
A_{pl}: Plastic part of the area under load-displacement curve,
B_N: Net thickness, b_0: Initial ligament (=W-a_0),
a_0: Initial crack length, W: Specimen width,
E'=E for ASTM, E'=E/(1-ν^2) for JEAC.

$$K_{JC} = \sqrt{E' J_C} \tag{2}$$

In the new ASTM standard[11], η factor has been changed from 2.0 to 1.9 based on the 3-D detailed analysis for PCCv specimen[12]. This makes the fracture toughness value lower by approximately 5% in terms of J-integral. When some equations in the new ASTM standard, which are described later, are applied, the new η factor is used.

Table 1--*Chemical Compositions of Materials Used in This Study* (wt.%)

Material	C	Si	Mn	P	S	Ni	Cr	Cu	Mo
JRQ	0.18	0.24	1.42	0.017	0.004	0.84	0.12	0.14	0.51
Steel A	0.19	0.30	1.30	0.015	0.010	0.68	0.17	0.16	0.53
Steel B	0.19	0.19	1.43	0.004	0.001	0.65	0.13	0.04	0.50
JSPS A533B-1	0.24	0.41	1.52	0.028	0.023	0.43	0.08	0.19	0.49

Table 2--*Tensile Properties at Room Temperature of Materials Used in This Study*

Material	σ_{ys} (MPa)	σ_{uts} (MPa)	Elongation (%)	Note
JRQ	477	615	22.2	
JSPS A533B-1	504	692	20.2	Ref. [8]
Steel A	469	612	26.4	
Steel B	462	597	24.9	

Table 3—*Specimens Used for Fracture Toughness Testing in This Study*

Specimen / Material	PCCv	0.5T-CT	1T-CT	2T-CT	4T-CT
JRQ	×	$\times^{+}$	×		
Steel A	×		×		×
Steel B	×		×		×
JSPS A533B-1	$\times^{++}$	$\times^{+++}$	$\times^{+++}$	$\times^{+++}$	$\times^{+++}$

$^{+}$: 0.5T-DCT, $^{++}$: Reference [10], +++: Reference [8]

Irradiation

PCCv and 0.5T-DCT specimens of JRQ were irradiated in Japan Materials Testing Reactor (JMTR, thermal output 50MW). Fast neutron fluence for each specimen was calculated to be within the range from 1.9 to 2.5 x 10^{19} n/cm^2 (E>1 MeV). The displacement per atom (dpa) for iron by the irradiation to 2 x 10^{19} n/cm^2 (E>1 MeV) was about 3 x 10^{-2}. Fast neutron flux was about 1.2 x 10^{13} n/cm^{2}s (E>1 MeV). Temperature for the specimens during irradiation was controlled in the range from 280°C to 300°C.

Sixteen PCCv specimens together with ten Charpy-V specimens of Steel A and Steel B were irradiated at the JMTR in the range from 285°C to 295°C. Mean neutron fluence values for Steel A and Steel B are approximately 13x10^{19} and 11x10^{19} n/cm^2 (E>1 MeV), respectively. The shifts of Charpy transition temperatures by neutron irradiation are summarized in Table 4.

Table 4--*Charpy Transition Temperature Shifts by Neutron Irradiation at JMTR*

Material	Neutron fluence (n/cm^2, E>1MeV)	Irradiation temperature (°C)	ΔT_{41J} (°C)	ΔT_{68J} (°C)	$\Delta T_{0.9mm}$ (°C)
JRQ	2.3 x 10^{19}	291	88	90	87
Steel A	12.9 x 10^{19}	287	155	162	144
Steel B	11.3 x 10^{19}	288	71	73	66

Results and Discussion

Specimen Size Effect on Cleavage Fracture Toughness

The validity limit for K_{JC} values has been stipulated in the new ASTM standard as follows;

$$K_{JC\_limit} = \sqrt{Eb_0\sigma_{ys}/30} \tag{3}$$

PCCv specimens were tested in the range from T_{28J}-50°C to T_{28J}-10°C. In all cases, invalid data violating equation (3) were found from PCCv data sets. The larger specimens

provided no invalid data in the range tested.

As is known well, the scatter of cleavage fracture in the transition temperature range is significant. The scatter has been explained by the weakest link theory[13,14] that is based on the local inhomogeneity in the material. The theory treats the probability of finding a particle located randomly in the material and leads to the fracture of the specimen. In addition to this, a fracture toughness value from a small specimen can be higher than that from a large specimen. The reason is that the small specimen has insufficient thickness to assure small scale yielding and maintain a certain level of constraint at a crack tip, as compared with a large size specimen or a real heavy-section structure[15].

Figure 1 shows fracture toughness as a function of specimen thickness. Each fracture toughness value was normalized by K_{IC} obtained at each testing condition. This figure clearly shows the size dependence of the fracture toughness value. The highest PCCv data was four times larger than the K_{IC}. The mean values of PCCv data except for invalid data were 1.5 to 2.2 compared to K_{IC}. On the other hand, the lowest value of PCCv data was approximately the same as the K_{IC}.

To obtain a reliable fracture toughness value from a small size specimen, several correction schemes have been proposed. Wallin[16] proposed the following equation for correcting specimen size applicable to RPV steels;

$$K_{JC\_y} = K_{\min} + (K_{JC\_x} - K_{\min}) \cdot (B_x / B_y)^{1/b} \tag{4}$$

where $K_{JC\_x \text{ or } y}$: K_{JC} for specimens of thickness, $B_{x \text{ or } y}$,

$K_{\min} = 20\ MPa\sqrt{m}$,

b = 4.

Figure 1 includes the size effect correction curve for PCCv (B=10 mm) based on the equation (4). The upper curve corresponds to Steel B, the lower curve is to Steel A and JSPS A533B-1. The correction curve for Steel B overestimated K_{IC} of 4T-CT specimen by 40%, while the curves for Steel A and JSPS A533B-1 agreed well with K_{IC}. To verify the correction equation, we need more data including a sufficient number of PCCv data.

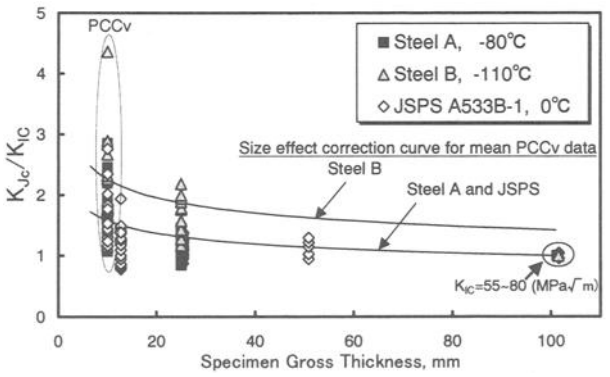


Figure 1--*Normalized Fracture Toughness as a Function of Specimen Gross Thickness*

Irradiation Effect on the Scatter of Fracture Toughness

The equation (4) is based on the weakest link theory. The theory assumes that the distribution of the fracture toughness values of a material can be described using Weibull type statistics. Using three parameters, K_{min}, b and K_0, the fracture probability based on Weibull statistics can be expressed by the following equation[16].

$$P_f = 1 - \exp\left(-\left(\frac{K_{JC\_1T} - K_{min}}{K_0 - K_{min}}\right)^b\right) = 1 - \exp\left(-\left(\frac{K_{JC\_1T} - 20}{K_0 - 20}\right)^b\right) \quad (5)$$

where P_f: Cumulative fracture probability ($= (i-0.3)/(N+0.4)$),
b, K_0: Fitting parameters.

All data obtained by the same-size specimens at a certain temperature can be analyzed by the equations (4) and (5). The equation (5) has also been incorporated into the new ASTM standard to describe the statistics of cleavage fracture toughness.

Figures 2 to 4 compare Weibull plots of PCCv data and 1T-CT data. PCCv data were corrected by equation (4) to 1T-CT thickness for comparison. These figures also include the fitting curve by equation (5). Figure 2 indicates that the size-corrected PCCv data and 1T-CT data of unirradiated JRQ are in good agreement. The fitted parameter b in equation (5) was 2.3 and 2.5 for the corrected PCCv data and 1T-CT data, respectively. These values were much less than the theoretical value of four. Figure 3 shows the Weibull plots of PCCv data of irradiated JRQ. The b values were 2.8 and 3.1 for the data tested at 17°C and 35°C, respectively. The slopes were again smaller than the theoretical values. The reason of difference between the experimental slope b and the theoretical b is not clear for the moment. It may come from a statistically insufficient number of data, and/or an inhomogeneity of the material. However, it is noted that the b value became a bit large after irradiation. In other words, neutron irradiation could make the data scatter smaller. This means that the scatter after irradiation may be estimated conservatively by applying the scatter before irradiation.

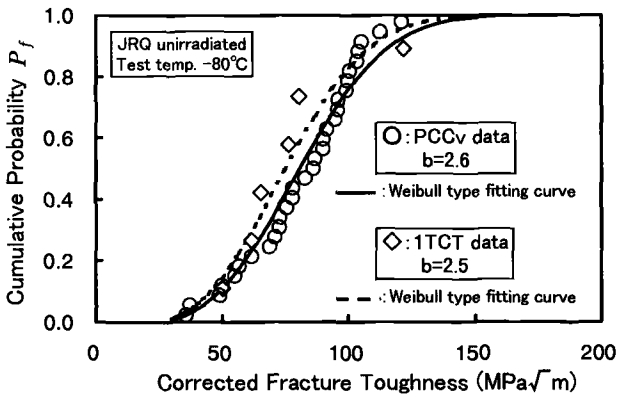


Figure 2--*Weibull Plots of Unirradiated Specimens of JRQ Tested at -80°C*

Figure 4 shows Weibull plot of steels A. In this case, the b value of 1T-CT data was approximately coincident with the theoretical value. The mean value of corrected PCCv data was higher than that of 1T-CT data. Concerning the data scatter, the corrected PCCv data showed the b value was smaller than that of 1T-CT data. For the lower bound data, however, approximately the same trend was seen between both data below 5% fracture probability. If the theoretical b value was used for data fitting, the lower tail of PCCv data is much higher than that of 1T-CT data.

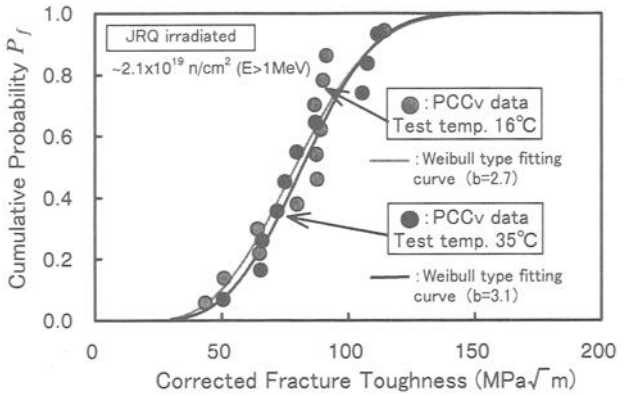


Figure 3--*Weibull Plots of Data from Irradiated PCCv Specimens of JRQ Tested at 17°C and 35°C*

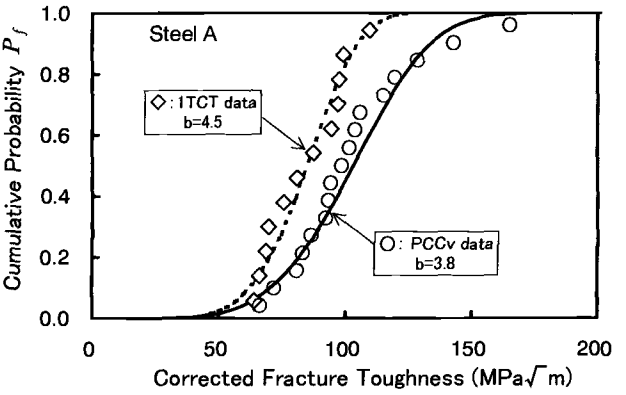


Figure 4--*Weibull Plots of Data from Unirradiated Specimens of Steel A Tested at –80°C*

Shift of Fracture Toughness Transition Curve

The median value of the data can be calculated by K_0 from equation (5) and the following equation as a fracture probability P_f=0.5.

$$K_{JC\_1T(med)} = (K_0 - 20)[\ln(2)]^{1/4} + 20 \quad (6)$$

Using the median value, the temperature dependence of cleavage fracture toughness within the transition range is expressed by the following equation[11,16].

$$K_{JC\_1T(med)} = 30 + 70 \cdot \exp\{0.019 \cdot (T - T_0)\} \quad (7)$$

This equation has been established by statistical analyses using a huge database including unirradiated and irradiated RPV steels. This equation, which is called a master curve, uniquely defines the cleavage fracture toughness transition curve by a reference temperature, T_0.

Table 5 lists the T_0 values before and after neutron irradiation that were obtained from materials used in this study. Figure 5 shows the values of T_0 based on the method above as a function of specimen thickness. The values of T_0 from JRQ showed no effect of specimen thickness, while the other steels showed the effect to some extent. The T_0 values from PCCv data were 10~20°C lower than those values from 1T-CT and 2T-CT data. The deviation is slightly larger than the reported values of 5~10°C for some RPV steels in reference [17]. The reason of the large deviation is not clear for the moment. Since the number of valid data from PCCv specimens of other steels were relatively small (≤10), additional tests might help to understand the reason. For this, the better test temperature for PCCv specimens may be lower than the present temperature.

To identify the effect of irradiation on T_0, we obtain the shift of fracture toughness by comparing the T_0 before and after irradiation. Figure 6 shows the master curve for JRQ steel before and after irradiation. Before irradiation, the T_0 value was determined by the average of PCCv data tested at –80°C and –50°C. The T_0 value after irradiation was also the average of two T_0 values from two PCCv data sets tested at 17°C and 35°C. The shift of T_0 by irradiation to JRQ was then calculated as 105°C. This shift is larger than the Charpy shift listed in Table 4 by about 20°C.

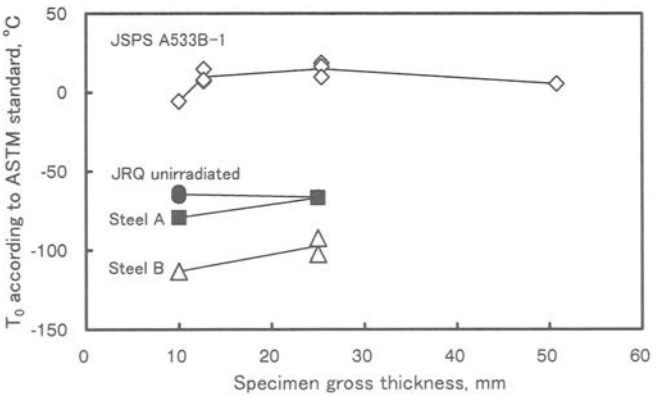


Figure 5--*Comparison of Reference Temperature, T_0, According to the New ASTM Standard as a Function of Specimen Gross Thickness*

Table 5--*Comparison of T_0 Values before and after Neutron Irradiation Determined by the ASTM Standard*

Material		Specimen type	B (mm)	T_0 (°C)	N	r	Test Temp. (°C)	SG (%)
JRQ	Unirradiated	PCCv	10.0	−66	31	30	−80	0/20
		PCCv	10.0	−63	16	9	−50	0
		1TCT	25.0	−66	6	6	−80	20
	Irradiated	PCCv	10.0	32	12	11	17	0
		PCCv	10.0	48	10	10	35	0
Steel A	Unirradiated	PCCv	10.0	−79	17	12	−80	20
		1TCT	25.0	−67	12	12	−80	20
		1TCT	25.0	−67	12	12	−50	20
	Irradiated	PCCv	10.0	72	8	8	50	20
Steel B	Unirradiated	PCCv	10.0	−113	10	7	−110	20
		1TCT	25.0	−102	12	12	−110	20
		1TCT	25.0	−92	12	12	−80	20
	Irradiated	PCCv	10.0	−25	7	7	−50	20
JSPS A533B-1	Unirradiated	PCCv	10.0	−6	20	10	0	0/20
		0.5TCT	12.7	7	16	16	−25	20
		0.5TCT	12.7	15	23	23	0	0/20
		0.5TCT	12.7	8	12	11	25	20
		1TCT	25.4	19	18	18	−25	20
		1TCT	25.4	16	18	18	0	0/20
		1TCT	25.4	10	12	12	25	20
		2TCT	50.8	5	6	6	0	20

B: Specimen thickness
N: Total number of data used
r: Number of valid data
SG: Side grooving

Figures 7 and 8 show the effect of irradiation on the fracture toughness of Steels A and B. The T_0 values after irradiation were determined by only eight and seven PCCv specimens for Steel A and Steel B, respectively. The master curves together with 5% and 95% tolerance bounds before and after irradiation were indicated in those figures. For Steel A, the highest datum after irradiation was significantly higher than the other data. When the highest datum is excepted from the data set, the T_0 moves to higher temperature by about 30°C, as shown in Figure 7 by dotted lines. After the exception, the data scatter was fitted well in the tolerance bounds. Although this exception is not a standard practice, it could lead to a conservative evaluation.

Figure 9 compares the shifts of T_0 and Charpy 41J transition temperature by neutron irradiation. As mentioned above, the T_0 shift is somewhat larger than the Charpy 41J shift. This suggests that the prediction of irradiation embrittlement based on Charpy shift may underestimate the change in fracture toughness, which is directly related to RPV integrity.

Figure 10 shows all data obtained in this study as a function of the difference

between test temperature and T_0 determined by PCCv data. The fracture toughness values were size-corrected to 1T thickness by equation (4). Below 30°C of T-T_0, the master curve agrees well with the data. At higher transition temperature range, the master curve tends to overestimate the data. Of course, the determination of the master curve at such a higher temperature should be restricted because the PCCv data is no longer valid above ~150 MPa$\sqrt{m}$. Therefore, we need the data from larger specimens to verify the shape of the master curve.

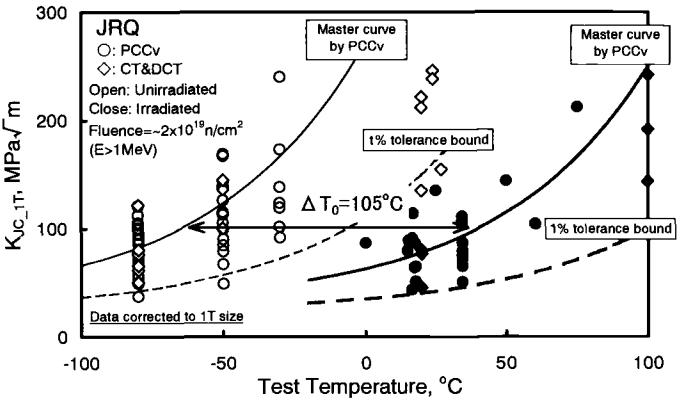


Figure 6—*Master Curves According to the ASTM Draft Standard Before and After Irradiation of JRQ*

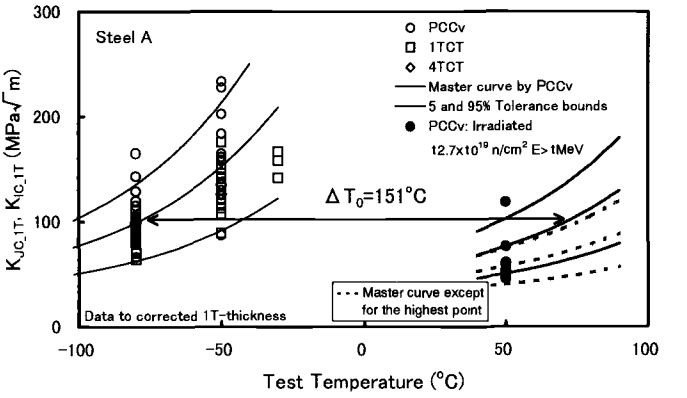


Figure 7—*Master Curves According to the ASTM Draft Standard Before and After Irradiation of Steel A*

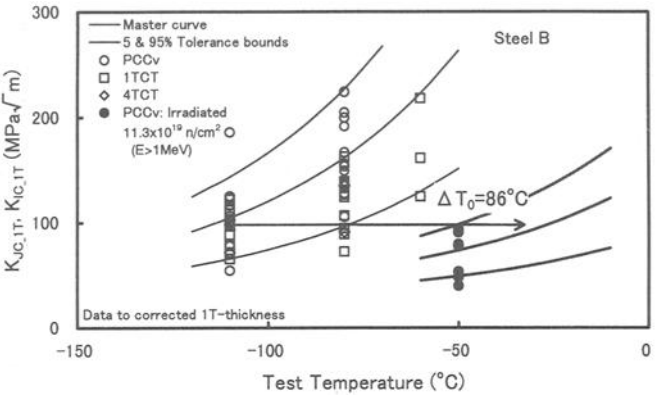


Figure 8— *Master Curves According to the ASTM Draft Standard Before and After Irradiation of Steel B*

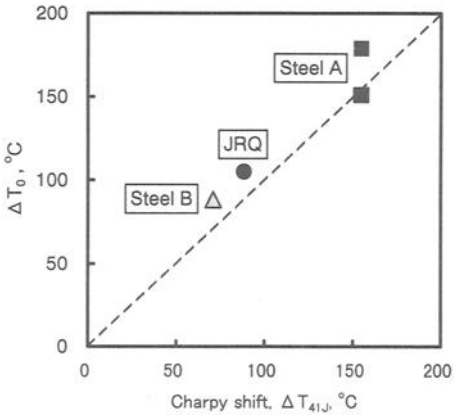


Figure 9—*Comparison of Shifts of Master Curve and Charpy Transition Temperature*

Estimation of Lower Bound Toughness

Based on Weibull statistics, tolerance bounds for the master curve can be drawn. Assuming the Weibull slope b=4, the parameter K_{min}=20 and an infinite sampling size, a lower bound curve in the same form as equation (7) has been calculated in the new ASTM standard. Figure 10 indicates the lower tolerance bound curves. As mentioned before, the experimental data indicated larger scatter than the theory. The 5% lower bound curve is not enough to bound 95% of the experimental data. The 1% bound curve is in good agreement with the lower bound data in the whole temperature range.

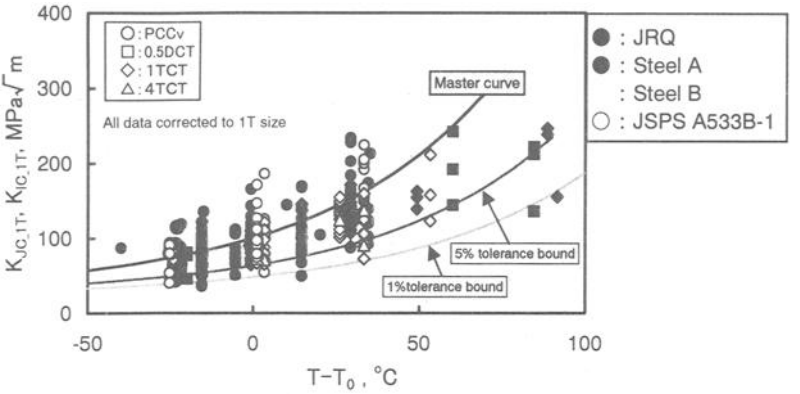


Figure 10--*Size Corrected Data to 1T, The Master Curve and the 1% and 5% Tolerance Bound Curves Determined by PCCv Data*

The Japanese code on the method for the fracture toughness test and evaluation, JEAC 4206[18], stipulates the method to obtain the lower bound toughness curve for the integrity assessment of RPV during a PTS transient. To estimate the fracture toughness at the time to be assessed, all fracture toughness data obtained from surveillance tests are shifted by the amount of predicted or measured Charpy shift. The lower bound curve can be defined as the lowest envelope of all the fracture toughness data points. The form of the curve is expressed by the following:

$$K_{JC} = 20.16 + 129.9 \cdot \exp\{0.0161 \cdot (T - T_{0J})\} \quad (8)$$

By adjusting T_{0J} according to the fracture toughness data, the plant specific K_{IC} curve is determined. Applying equation (8) to the data of JRQ unirradiated specimen, we obtained the T_{0J} and the corresponding JEAC K_{IC} curve before irradiation. The K_{IC} curve after irradiation was determined by shifting the K_{IC} curve before irradiation by the amount of Charpy shift. Figure 11 indicates the JEAC K_{IC} curves before and after irradiation together with all test data. The lower bound curves agreed well with the data up to the upper transition range, which leads to a conservative evaluation. When we apply equation (8) to the test data after irradiation, we obtain the shift of T_{0J} value by irradiation of ~80°C. This value was slightly less than the Charpy shift. Therefore, the K_{IC} curve after irradiation became conservative. However, this result may depend on the statistical treatment of the data. If we took more data from irradiated specimens or less data from unirradiated specimens, we would get a less conservative K_{IC} curve after irradiation.

Figure 12 shows the JEAC K_{IC} curve together with 1% tolerance bound curve based on the weakest link theory. To compare all data with those curves, the data points without size-correction were plotted as a function of $T-T_0$. The JEAC curve was defined from unirradiated JRQ datum as the lowest point of all data. The shape of JEAC K_{IC} curve coincides well with the lowest data points. The 1% tolerance bound curve agrees with the JEAC K_{IC} curve in the lower transition range but tends to become higher at the

upper transition range. This comparison is limited to only four materials and mainly small specimen data. The sparse data in the upper transition range also makes the verification of those curves difficult. For the moment, both the JEAC K_{IC} curve and the 1% tolerance bound seem to be the conservative estimation of the lower bound fracture toughness.

The following equation (9) is the K_{IC} curve in the ASME Sec. XI[1] to describe the lower bound fracture toughness of RPV steels.

$$K_{IC} = 36.5 + 22.8 \cdot \exp\{0.036 \cdot (T - RT_{NDT})\} \quad (9)$$

In this case, we need an RT_{NDT} of the steel to define the K_{IC} curve. The RT_{NDT} is determined by the combination of the results from drop weight test and Charpy impact test. The drop weight test can not be done after irradiation because the test requires relatively large size specimens. Therefore, Charpy impact test results are used instead of the results of drop weight test to determine the irradiation effects. The adjusted RT_{NDT} value after neutron irradiation is then calculated with the Charpy shift added to the initial RT_{NDT}. The K_{IC} curve after irradiation is defined by the equation (9) using the adjusted value. This means that the irradiation effect on Charpy property and fracture toughness should be equivalent. Figure 13 shows the comparison of the experimental data and the ASME K_{IC} curves. This figure clearly shows that the data from both unirradiated and irradiated specimens are bounded by the ASME K_{IC} curve based on RT_{NDT}. For the data investigated, the ASME method gave a good approximation of the lower bound curve. However, the shift of fracture toughness can be larger than Charpy shift as obtained from this study. The lower bound curve for highly irradiated material should be carefully checked by fracture toughness tests.

Summary and Conclusions

To establish the method to evaluate fracture toughness in the transition range, fracture toughness tests were performed using various specimens from PCCv to 4T-CT of four Japanese RPV steels. Based on JMTR irradiation and post-irradiation tests for JRQ, Steels A and B, the following conclusions were drawn for the evaluation of fracture toughness after irradiation;

(1) The size effect correction based on the weakest link theory was not always sufficient to obtain an equivalent value from a PCCv specimen to a large specimen.
(2) For data scatter, the experimental value of Weibull slope was not much affected and slightly decreased by neutron irradiation.
(3) According to the master curve approach, the shift of the fracture toughness curve by irradiation was evaluated to be somewhat greater than the Charpy 41J shift.
(4) The JEAC K_{IC} curve after irradiation could be conservative. However, large number of data before irradiation would be necessary.

Acknowledgments

A part of this work was carried out under the contract between JAERI and

Science and Technology Agency of Japan under the auspices of the special account law for electric power development promotion. A part of this report was also performed at JAERI in the framework of the IAEA Coordinated Research Program[7]. The authors would like to thank Dr. K. Shibata, Dr. T. Isozaki and Mr. Y. Nishiyama, JAERI for their encouragement and helpful discussion, and many staffs at Hot Laboratory of JAERI for their careful testing of irradiated specimens. They are also grateful to Dr. T. Iwadate and Dr. Y. Tanaka of the Japan Steel Works, Ltd. for providing the JSPS A533B-1 material. The tests of PCCv specimens of JSPS A533B-1 were done at SCK•CEN, Belgium during the period when one of the authors stayed.

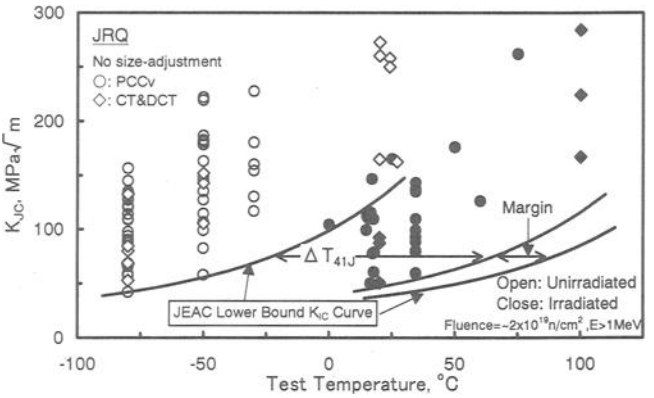


Figure 11--*Lower Bound Curves of JRQ Before and After Irradiation According to the JEAC Method*

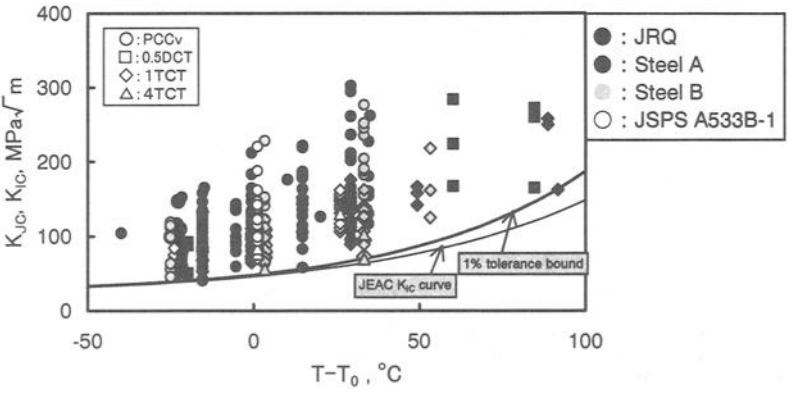


Figure 12--*Comparison of the JEAC K_{IC} Curve and the ASTM 1% Tolerance Bound Curve*

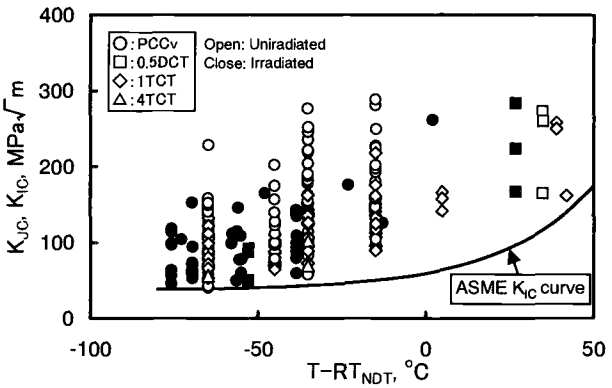


Figure 13--*Comparison of Experimental Data and the ASME K_{IC} Curve as a Function of T-RT_{NDT}*

References

[1] ASME Boiler and Pressure Vessel Code, Section XI, "Inservice Inspection of Nuclear Power Plant," American Society for Mechanical Engineers, 1995.

[2] Japanese Electric Association, "Methods of Surveillance Tests for Structural Materials of Nuclear Reactors," JEAC 4201-1991. (in Japanese)

[3] Nanstad, R. K., Haggag, F. M., McCabe, D. E., Iskander, S. K., Bowman, K. O., and Menke, B. H., "Irradiation Effects on Fracture Toughness of Two High-Copper Submerged-arc Welds, HSSI Series 5," NUREG/CR-5913 Vol.1, U. S. NRC., October 1992.

[4] Miglin, M. T., Oberjohn, L. A., and Van Der Sluys, W. A., "Analysis of Results from the MPC/JSPS Round Robin Testing Program in the Ductile-to-Brittle Transition Region," *Fracture Mechanics: Twenty-fourth Volume, ASTM STP 1207*, J.D. Landes, D. E. McCabe and J. A. M. Boulet, Eds., American Society for Testing and Materials, Philadelphia, 1994, pp. 342-354.

[5] Iwadate, T., Tanaka, Y., Ono, S., and Watanabe, J., "An Analysis of Elastic-Plastic Fracture Toughness Behavior for J_{IC} Measurement in the Transition Region," *Elastic-Plastic Fracture: Second Symposium, Volume II-Fracture Resistance Curves and Engineering Applications, ASTM STP 803*, C. F. Shi and J. P. Gudas, Eds., American Society for Testing and Materials, 1983, pp. II-531-II-561.

[6] CRP Sub-Committee, "Manufacturing History and Mechanical Properties of Japanese Materials Provided for The International Atomic Energy Agency," Japan Welding Engineering Society, Oct. 1986.

[7] Onizawa, K., Suzuki, M., and Ueda, S., "JAERI Contribution for the IAEA Coordinated Research Program Phase III on Optimizing of Reactor Pressure Vessel Surveillance Programmes and Their Analysis," JAERI-M 93-201, Japan Atomic Energy Research Institute, October 1993.

[8] JSPS 129 Committee, "Standard Test Method for Fracture Toughness within Ductile-Brittle Transition Range," Japan Society for Promoting Science, 1995.

[9] Onizawa, K., Tobita, T., and Suzuki, M., "Investigation on the Evaluation of Cleavage Fracture Toughness Using PCCv Specimens in the Ductile-Brittle Transition Range of Reactor Pressure Vessel Steels," JAERI-Research 97-081, Japan Atomic Energy Research Institute, November 1997.

[10] Chaouadi, R., "Fracture Toughness Measurements in the Transition Regime Using Small Size Samples," *Small Specimen Test Techniques, ASTM STP 1329*, W. R. Corwin, S. T. Rosinski, and E. van Walle, Eds., American Society for Testing and Materials, 1998, pp. 214-237.

[11] ASTM Draft 15, "Test Method for The Determination of Reference Temperature, T_0, for Ferritic Steels in the Transition Range," Rev. 6-13-97, American Society for Testing and Materials, 1997.

[12] Nevalainen, M., and Dodds, R., "Numerical Investigation of 3-D Constraint Effects on Brittle Fracture in SE(B) and C(T) Specimens," NUREG/CR-6317, UILU-ENG-95-2001, July 1996.

[13] Landes, J. D., and Shaffer, D. H., "Statistical Characterization of Fracture in the Transition region," *Fracture Mechanics: Twelfth Conference, ASTM STP 700*, American Society for Testing and Materials, 1980, pp. 368-382.

[14] Wallin, K., "The Scatter in K_{IC}-Results," *Engineering Fracture Mechanics*, Vol. 19, No.6, 1984, pp.1085-1093.

[15] Anderson, T., and Dodds, R., "Specimen Size requirements for Fracture Toughness Testing in the Ductile-Brittle Transition Region," *Journal of Testing and Evaluation*, Vol. 19, 1991, pp. 123-134.

[16] Wallin, K., "Irradiation Damage Effects on the Fracture Toughness Transition Curve Shape for Reactor Pressure Vessel Steels," *International Journal of Pressure Vessel and Piping*, 55(1993) pp.61-79.

[17] Wallin, K., "Validity of Small Specimen Fracture Toughness Estimates Neglecting Constraint Corrections," *Constraint Effects in Fracture Theory and Applications: Second Volume, ASTM STP 1244*, M. Kirk and Ad Bakker, Eds. American Society for Testing and Materials, 1995.

[18] Japanese Electric Association, "Fracture Toughness Test Methods for Nuclear Power Plant Components," JEAC 4206-1991, (in Japanese).

M. Brumovsky,[1] O. Erben,[2] and P. Novosad[1]

Supplementary Surveillance Program for Reactor Pressure Vessels of VVER-440/V-213C Type Reactors in NPP Dukovany

Reference: Brumovsky, M., Erben, O., and Novosad, P., **"Supplementary Surveillance Program for Reactor Pressure Vessels of VVER-440/V-213C Type Reactors in NPP Dukovany,"** *Effects of Radiation on Materials: 19th International Symposium, ASTM STP 1366,* M. L. Hamilton, A. S. Kumar, S. T. Rosinski, and M. L. Grossbeck, Eds., American Society for Testing and Materials, West Conshohocken, PA, 2000.

Abstract: Standard surveillance specimen programs for materials in the reactor pressure vessels of VVER-440/V-213 type reactors were designed with a high lead factor (approx. equal to 12 for base metal and 18 for weld metal). Thus, end-of-life neutron fluence levels are obtained within the first three years of operation. The maximum irradiation time is five years after which there is no active monitoring of neutron fluence inside reactor pressure vessels. Also, the distribution of neutron flux along surveillance specimen chains creates a large difficulty in grouping of specimens for static fracture toughness testing.

A reevaluation of the standard surveillance program for NPP Dukovany has been performed. This reevaluation includes additional irradiations and a very detailed analysis of all results, and provides a basis for a design of a Supplementary Surveillance Program. Its realization started in 1997 by loading the first chains with specimens.

The principles of this Program are explained in this paper. This program will provide: 1) new results under a realistically low lead factor, 2) new data on cladding properties under irradiation as well as after annealing and re-irradiation, and 3) data on the re-irradiation rate of vessel materials. Also the fourth part of the Program will provide a permanent neutron monitoring through the real vessel end-of-life. Within the whole program, the IAEA reference material JRQ will be also used, and this material will serve as a correlation monitor with other irradiation experiments.

Keywords: pressure vessel steels, surveillance specimen program, VVER-440/V-213 type reactor, neutron monitoring, IAEA reference material JRQ, 15Kh2MFA type steel

[1]Research Staff, Division of Integrity and Materials, Nuclear Research Institute Řež plc, 250 68 Řež near Prague, Czech Republic.

[2]Research Staff, Division of Reactor Services, Nuclear Research Institute Řež plc, 250 68 Řež near Prague, Czech Republic.

Copyright© 2000 by ASTM International www.astm.org

Introduction

Surveillance specimen programs from reactor pressure vessel materials are one of the most important parts of in-service monitoring that is necessary for the realistic and reliable assessment of reactor pressure vessel residual lifetime.

Structure, volume, type of specimens, withdrawal schedule and testing procedures depend, first of all, on the date when the reactor was designed, and also, on capsule volume and other possibilities of reactor pressure vessel construction. Thus, these surveillance programs represent, on one side, knowledge (State-of-the-Art) of assessment of resistance against failure and of irradiation embrittlement, and on the other side, possibilities of individual pressure vessel internal part locations.

Reactor pressure vessels of VVER-440/213 type reactors are characterized by small diameters that enabled them to be transported by train. This diameter also resulted in smaller thicknesses of water reflector and relatively high neutron fluxes and fluences on the inner vessel wall.

This type of reactor was primarily designed in the late 1960s, even though some of them (for NPP in Czech and Slovak Republics as well as in Hungary) were manufactured in ŠKODA Nuclear Machinery, Plzen, Czech Republic as a modification V-213C only in the late 1970s or in the beginning of 1980s. Thus, their design does not satisfy current requirements. A wide and detailed analysis was performed by the Nuclear Research Institute Rez that resulted in a project for "Supplementary Surveillance Program", as an addition to the Standard Surveillance Program.

Description of a Standard Surveillance Program [1]

The following describes a standard surveillance program in VVER-440/213 type reactors.

Test materials

Test specimens were manufactured from the following materials used in pressure vessels :

- base metal (steel 15Kh2MFA) from a ring used for beltline region,
- weld metal (submerged arc weld - Sv-10KhMFTA) from a welding coupon representing the weld in the lower part of beltline region (weld 0.1.4),
- heat affected zone material from this welding joint;

all materials are of Cr-Mo-V type.

Test specimens

Three type of specimens are part of the program :

- static tensile (dia 3 mm x 30 mm) specimens
- Charpy V-notch specimens for impact testing
- COD (pre-cracked Charpy) type specimens for static fracture toughness testing

In all cases specimens were cut from the central part of material thickness not closer than 1/4 of thickness to pressure vessel surface.

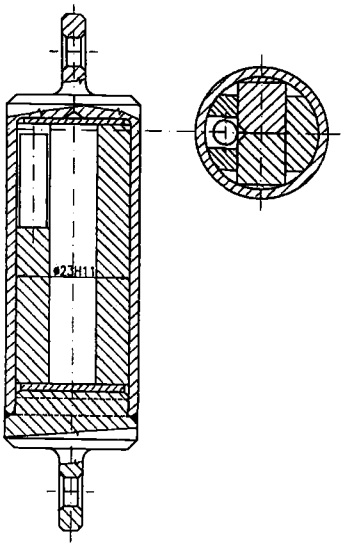


Fig. 1 Scheme of a container from the Standard Surveillance Program

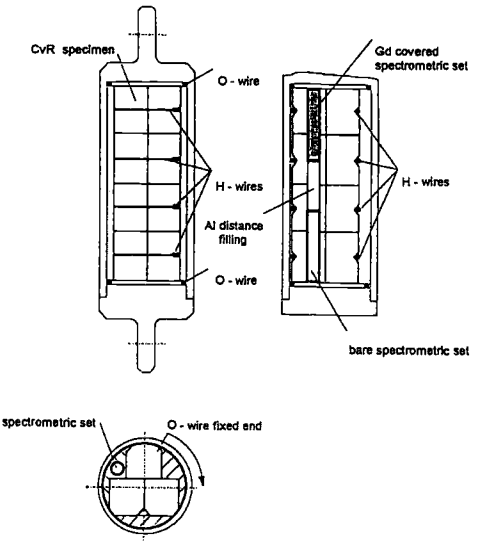


Fig. 2 Scheme of a container from the Supplementary Surveillance Program

Neutron flux monitors

Fast neutron flux (and fluence) measurements are based on measurement of the following activation monitors (which are used according to their lifetime):

^{54}Fe (n,p), ^{63}Cu (n, alpha), ^{93}Nb (n,n`)

There are 18 containers with neutron flux monitors in each set irradiated up to two years, and 6 containers for sets that are irradiated for longer times. Monitors are made from thin foils that are put into aluminum tubes and located in the upper part of the specimen container.

Temperature monitors

Powder natural diamond is used as a temperature monitor. Principle of its use is given by the fact that :

- crystal lattice parameters are increased by irradiation,
- this change can be removed by following annealing at temperature higher that was the irradiation one.

Thus, using X-ray diffraction method, change in crystal lattice parameters is determined just after irradiation, and consequently after annealing is performed at several temperatures higher than the supposed one.

Capsule assemblies

The test specimens are placed into capsules made from austenitic stainless steel that prevents corrosion effects on specimens. The scheme of such capsules is given in

Fig.1. Each capsule contains either 6 tensile specimens or 2 specimens of Charpy type. Some of them also contain neutron flux monitors. Capsules are assembled into chains - each contain 19 or 20 capsules in active core position. Two chains also contain another 13 capsules that are located in the upper part of the reactor pressure vessel (out of neutron field) and these specimens are included for determination of thermal aging effects.

Two chains of capsules represent one set of specimens, that are located on the outer surface of active core basket and symmetric to the corner of the hexagonal active core structure. Thus, six sets of chains are placed into each pressure vessel. Capsules with the same type of specimens are located in chains in such a way to reach approximately the same neutron fluence. In some cases they are located in one chain in one row, in other way in two chains in the same location.

Removal schedule

Removal schedule is given by operation schedule of reactor, i.e. by fuel elements reloading. Interval between these changes is approximately one year, thus modified schedule of withdrawal with respect to lead factors are as follows :

1, 2, 3, 5 years of operation + 1 set for 10 to 20 years,

one set is withdrawn after 5 years of operation, annealed and then tested.

Disadvantages of a Standard Surveillance Program

The Nuclear Research Institute Rez is responsible for testing of all surveillance specimens from VVER NPPs in Czech and Slovak Republics. Thus, during the years a wide experience has been collected, results have been analyzed and necessary steps for improvement of surveillance programs are accepted.

The most important disadvantages of a standard surveillance programs of this type of reactor are as follows:

Test materials

Base material specimens are taken from cutoff material from the real beltline region ring, weld metals are taken from test coupons, made by the same technology and from the same materials as a critical weld, which is located in the lower part of the active core region of the vessel.

Specimens from heat-affected zone do not fully represent material from the active core region as welding coupons are made from special manufactured plates, only.

Test specimens

The type and form of tensile specimens is not fully convenient for testing in "hot cells", also their 10-times gauge length is not in full agreement with normally used tensile standards.

There are no free specimens for testing by dynamic fracture toughness test.

Neutron flux monitors and neutron fluences

There are only a limited number of fast neutron flux monitors and no thermal neutron monitor.

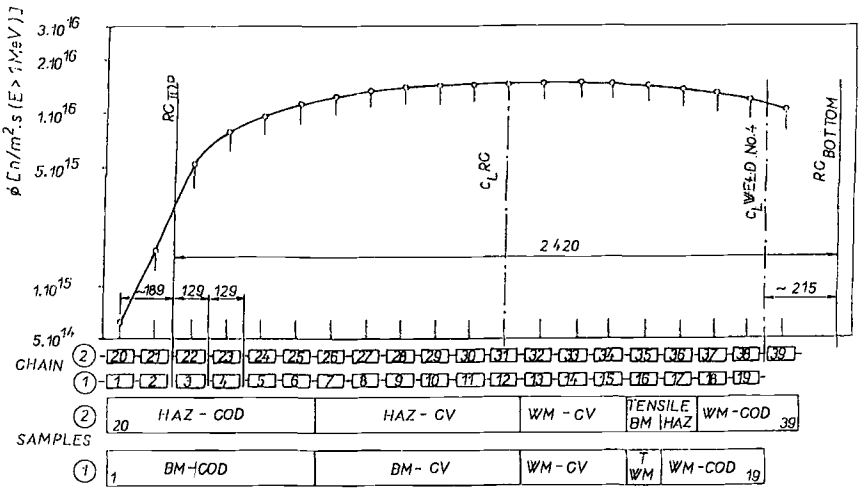


Fig. 3 Typical distribution of neutron flux along irradiation chain with containers

The location of these monitors in capsules does not permit a determination of an exact neutron fluence on each specimen: its location in the capsule does not allow an exact determination of the orientation of the capsule with respect to the reactor core. Moreover, capsules are located in a very high radial gradient of neutron flux, which has an influence not only on relative fluences on both (or six) specimens, but also on a capsule as a whole.

The design of capsules in long chains (2,550 mm) results in an asymmetrical axial gradient of neutron flux, where differences between the central and outer part of a chain represent a factor more than 10 - see Fig. 3. Only a limited number of containers in the central part receive similar neutron fluence, in the outer parts there is a steep gradient even for one set of specimens. This design also does not allow a comparison of results from different type of tests, for example of Charpy impact (located in central part) and static fracture toughness tests (located in upper or lower boundary).

Because of the location of capsules on the outer surface of the active core basket, a high lead factor with respect to the pressure vessel wall is received: between the capsules and the pressure vessel wall there is a water reflector, even though it is not as thick as for PWR type reactors. Thus, the lead factor for base material is about 12 and for weld metal even up to about 16. As a result, the problem of flux intensity effect is very important and under very frequent discussions.

Temperature monitors

Temperature monitors of diamond type were shown to be practically unusable, as changes in its lattice parameter depend also on neutron flux (not only on fluence). This effect also influences its behavior during annealing. Some correction factors may have to be applied but their uncertainties are quite still quite large.

Some experiments performed with irradiation of "opened" capsules (i.e. with specimens that were in contact with water) did not show any observable effect on material properties. Similar results have been obtained also by direct measurement of irradiation temperature of specimens in special chains using thermocouples.

Capsule assemblies

Capsules were designed only for two Charpy type specimens, thus at least 6 capsules are necessary for testing of one set of specimens - this represents a relatively long part of the chain, and in outer parts is complicated by a steep neutron flux gradient.

The design of these capsules does not permit an exact determination of the orientation of specimens with respect to the reactor active core, and thus also limits an exact determination of fluence on each of the specimens.

Removal schedule

The high lead factor requires very early removal schedule - irradiation in about 3 years of operation represents practically the full design lifetime of the vessel material. Thus, a maximum of 5 years of operation was chosen to obtain some reliable trend lines, even though it does not accurately represent the neutron flux intensity effect.

There is only one remaining set irradiated in each reactor - it is designed to be removed after not less than 10 years of operation, as this data is important for examining thermal aging.

There is no neutron monitoring the surveillance capsules or at the inner pressure vessel wall: only ex-vessel neutron measurements in cavity are performed. These measurements serve as the only information on neutron fluxes on vessel wall.

Static fracture toughness testing

Reactor pressure vessel integrity assessment is fully based on fracture mechanics, i.e. on knowledge of fracture toughness of RPV materials and their changes due to irradiation damage. Nevertheless, the most importance in older design surveillance programs has been concentrated in testing of Charpy V-notch specimens for determination of impact notch toughness, KV or KCV, and its transition temperature. In the standard surveillance program for these RPVs specimens for static fracture toughness (or COD) determination had been planned, but their location is fully unfavorable for such determination (i.e., specimens were to be located in the periphery of chains - see Fig. 3). Thus, each set of two specimens (located in one container)would receive different neutron fluences, even in one chain. The grouping of these specimens into one testing set is quite impossible. To overcome this problem, a modified procedure has been applied; that is, specimens with similar neutron fluences but from chains irradiated by different times are grouped together to obtain one transition curve. Typical results from static fracture toughness testing for one RPV are shown in Fig. 4, together with Charpy transition temperature shifts. In the same figure a comparison of results from different types of specimens are also shown - halves of broken Charpy specimens were reconstituted and tested for static fracture toughness. A comparison of the transition temperature shifts from both static fracture toughness testing measurements shows a substantial difference. The reason for this difference can be attributed either to uncertainties in neutron fluence determination or to neutron flux effect. Thus, in the supplementary program a modified

design of capsules is used - each capsule contains twelve inserts for further reconstitution of one set of specimens to cover the whole transition curve.

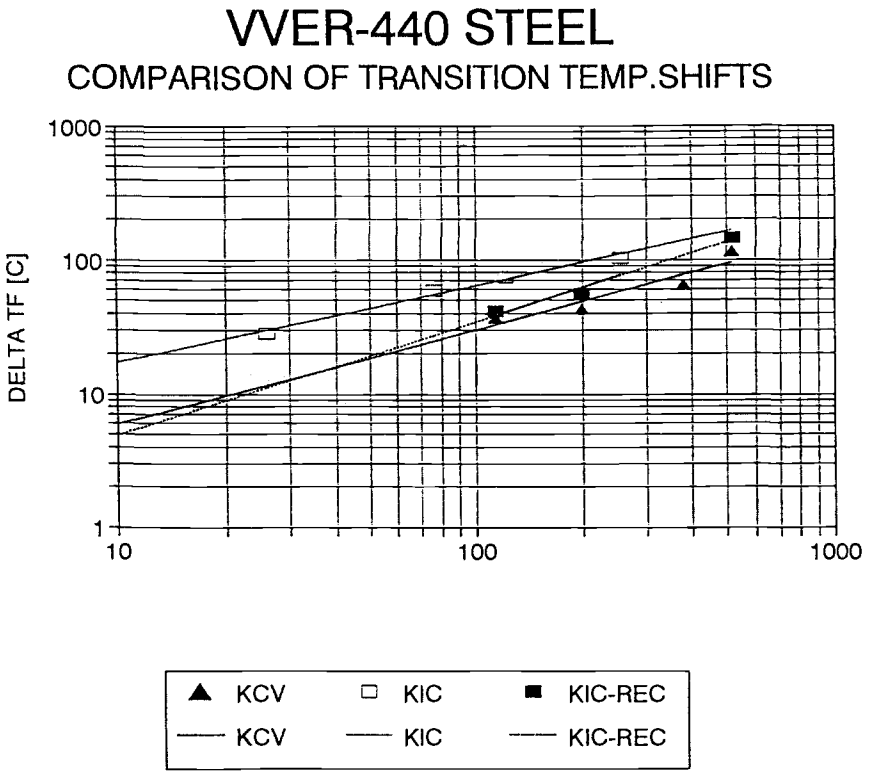


Fig. 4 Comparison of transition temperature shifts from different type of testing

Principles of a Supplementary Surveillance Program

Using an experience from a standard surveillance program, requirements for reliable assessment of reactor pressure vessel residual lifetime, as well as requirements, given by a trend of the combination of VVER standards and procedures with PWR ones, the following requirements for supplementary surveillance programs has been established:

Program objective

Ensure monitoring of neutron fluences and changes in material properties during the whole remaining reactor pressure vessel lifetime.

Specimens materials

Materials for specimens must be of archive type, i.e. the same as for standard surveillance program. Even though some archive materials still exist in manufacturer

store, halves of tested specimens in unirradiated state from standard surveillance programs will be used. Specimens put into program will be manufactured from base and weld metals, only.

Use of reconstitution technique for these specimens after their irradiation allows irradiation of a whole set of specimens in one capsule, only. For this case, specimens of 10x10x14 mm will be used, in three rows in one capsule = 12 specimens together in one capsule.

Moreover, some reference material (ASTM A 533-B type JRQ from the IAEA program) will be used for comparison of results in different reactors and with different materials.

Irradiation temperature

New design of capsules will contain small gaps between specimens and capsule walls and/or aluminum inserts.

Capsules will contain melting monitors according with ASTM Standard Guide for Use of Melt Wire Temperature Monitors for Reactor Vessel Surveillance (ASTM E 1214-87) and with KTA Überwachung der Strahlenversprödung von Werkstoffen des Reaktordruckbehälters von Leichtwasserreaktoren (In German) (KTA 3203 -1984), and these monitors will be placed in each of the capsules.

Neutron fluence

Proper determination of neutron fluences as well as placing capsules in locations with lower neutron fluxes is the main reason of this supplementary program.

Capsules will be located in such places where lead factor would be much lower than for a standard surveillance program, at least in the range between 2 and 3. This can be reached by placing the capsules in the upper position of capsules, i.e. in place of current capsules nos., 3 and 4.

Set A of activation monitors (including fast as well as thermal neutrons) and also fission monitors will be placed into each capsule. These monitors will be made from foils as well as from wires that will be placed in axial and also azimuthal direction in capsules as it is shown in Fig. 2. Choice of these monitors allow the determination of neutron fluences during the whole residual lifetime of vessels.

These measurements will be extended by gamma scanning of all specimens after their withdrawal.

Moreover, ex-vessel neutron measurements in cavity will be realized during each reactor campaign to be able to compare results from surveillance as well as from ex-vessel position every year of operation and supplementary calculations.

Experimental Verification of a Supplementary Surveillance Program Design

Even though this supplementary program was prepared using a wide experience from standard programs, some problems must be resolved:

- exact irradiation temperature of specimens,
- neutron flux gradient within a capsule (in axial as well as in radial and azimuthal directions), especially in outer positions,

- neutron flux and spectrum in capsules located in outer positions.

For this purpose a special measuring set of two chains was designed and prepared. These two chains contain capsules from standard (see Fig. 1) as well from supplementary program (12 specimens of 10x10x14 mm) (see Fig. 2). Both chains included the following monitors :

- neutron activation monitors (Fe, Cu, Nb, Ni, Al-Co) in all capsules - these monitors are used in a form of a foil and also as a wires, located in full axial as well as azimuthal directions inside a capsule,
- fission (U, Np) monitors in six capsules,
- melting wire type of temperature monitors almost in all capsules,

Computer codes, based on neutron transport codes, were developed for the interpretation of measured values and to extend their validity.

The other purpose of this set was to verify a reconstitution methods for testing static and dynamic fracture toughness for comparison with impact testing. All these methods were applied to base and weld metals as well as to austenitic cladding metal.

Results from this experimental verification were analyzed, experience from testing and evaluation collected, and the information was used for the supplementary surveillance program planning.

Supplementary Surveillance Program Design and Planning

The supplementary surveillance program has been designed by taking into account requirements given in Section 4 as well as the experience from the verification program, given in Section 5:

- monitoring of RPV during the rest of lifetime, i.e. not only of material degradation but also of neutron field on RPV,
- use of only archive materials, each container contains twelve inserts for further reconstitution either to Charpy V-notch toughness or static fracture toughness type specimens,
- irradiation with a low lead factor to be able to fully apply results from surveillance program to RPV embrittlement assessment,
- irradiation of cladding materials as this material was not inserted into the standard surveillance program and its behavior is important for RPV integrity assessment during PTS regimes ,
- determination of an annealing efficiency and a re-embrittlement rate of real RPV materials after annealing as a useful and effective tool for potential Plant (RPV) Life Extension,
- use of IAEA reference JRQ material for qualification of irradiation conditions - these specimens are placed in one container in the central part of each chain (i.e. in the same irradiation conditions). Charpy impact tests will be performed to compare irradiation conditions in individual chains - neutron fluences and irradiation temperatures. Thus, this material will also serve as reference solid state neutron monitors.

The monitoring of individual containers has been modified with respect to the experience from the Standard Surveillance Program as follows:

- neutron fluence monitors :
  two spectrometric sets of monitors are placed in each container : Fe, Ni, Nb, Al-0.1%Co, Ti, Cu and Np - one set is inserted in Al-tube while the other in Gd-tube to be able to determine a correction factor for thermal neutrons;
  wire type monitors for determination of relative neutron field in each container and for each specimen - O-wire (in both ends of container) to determine azimuthal distribution (and also the orientation of container with respect to the reactor active core), and I-wire (in specimens corners) to determine an axial distribution of neutron flux ; wires are made either from Fe (for short irradiation) or Nb (for long irradiation),
- temperature monitors :
  two sets of temperature monitors are placed at least into three containers of each chain (upper, middle and lower part),
  one set is prepared according to ASTM standard (wires in quartz tubes) and contains (inlet water temperature is equal to 268 °C) :
  Bi (melting temperature = 271 °C) , Pb-12.5 In (280 °C) and Pb-10 In (291 °C),
  a second set is prepared according to the KTA standard (with hollow rings located in Al-fillings of containers) :
  Bi (271°C), Pb-1.9 Ag-5 Sb (272 °C), Pb-12.5 Sn (278 °C), Pb-2 Ag-3 Sb (288 °C), Pb-10 In (291°C).

The **supplementary surveillance program** is divided into four parts:

(1) *irradiation with low lead factor:*
irradiation of archive materials - base and weld metals - are prepared in all four units with such a schedule to cover the whole planned residual lifetime of RPVs; individual chains are prepared for base metals and other for weld metals- position of containers with base metals are slightly different than those with weld metals in such a way that their lead factors will be the same for both materials (fluence on weld metal is equal to about 70 % of base metal in beltline region),
the following locations of containers have been chosen :

-	base metal : containers position	2 - Charpy impact
		4 - static fracture toughness
		6 - tensile
-	weld metal : containers position	1 - Charpy impact
		3 - static fracture toughness
		5 - tensile
-	reference steel JRQ : containers position	12 - center of active core
		19 - weld No. 4

this locations is used also in all parts of the program, principal time schedule for their withdrawal is as follows:
1, 2, 3, 5, 10 and some also 15 years of operation,
specimens will be tested for notch impact toughness as well as static fracture toughness determination (a limited number of tensile specimens is also included)

(2) *determination of re-embrittlement rate:*
a portion of specimens from base and weld metals irradiated within the standard surveillance program has been annealed by a standard regime (475 °C-100 h) in the laboratory and then inserted into the RPV in similar positions as non-irradiated

specimens, i.e. in positions with low lead factor (between 2 and 3) to be fully applicable to RPV embrittlement; irradiated and annealed specimens will be withdrawn in one, three and five years intervals to assess re-embrittlement rate of RPV archive materials in real RPV irradiation conditions,
both types of testing (notch impact as well as static fracture toughness) will be performed on both materials

(3) *irradiation of cladding materials:*
inserts cut from outer and inner cladding layers as well as from the heat-affected zone in the base metal are part of the program, (this cladding material comes from an archive part of vessel - nozzle bottoms after their removal from vessel) cladding materials will be irradiated in two groups: one group in a low lead factor position to obtain RPV end-of-life fluence (with similar schedule as base and weld materials, i.e. up to 15 years), the second group will be irradiated for 3 years in high lead factor, then it will be annealed and again inserted into the reactor. Further withdrawal is planned to cover an assessment of re-embrittlement rate after annealing for another 3 years of operation (representing more than 30 normal operating years),
only static fracture toughness tests will be performed for these materials

(4) *neutron dosimetry chains*
even though some of chains within parts (1) to (3) will cover practically the whole remaining RPV lifetime, their long term irradiation will not allow the determination of real neutron fluences in all operation years; thus, special chains with only a limited number of containers are inserted into reactors practically through the whole lifetime beginning five years from now; these chains are intended for intermediate irradiation (for two years only, in principle) will contain only IAEA reference material (JRQ steel) and neutron monitors in the position of maximum neutron fluence and weld metal locations - both reference material and neutron monitors will serve for determination/precisioning of neutron fluxes and irradiation temperatures.
JRQ specimens will be tested by the notch impact method, only

Thus, all four parts of the supplementary surveillance program will ensure necessary and reliable information about RPV materials behavior, mainly about their irradiation embrittlement under conditions very close to real ones - similar irradiation temperature as well as close neutron flux values. At the same time, information for potential RPV life extension - without and/or with thermal annealing - will be gathered well in advance of the designed RPV lifetime.

This program was started in 1997 but not all chains were inserted immediately - there is a time schedule prepared in such a way to cover their whole remaining design lifetime of reactor pressure vessels.

Conclusion

Experience gained from the standard surveillance program was compared with current requirements for reactor pressure vessel residual lifetime assessment. This review showed the necessity for reevaluation and also of implementation of a new - supplementary program.

This supplementary surveillance program started in 1997 and will continue through the whole remaining residual lifetime for :

- surveillance of vessel materials changes,
- surveillance of neutron dosimetry in- as well as ex-vessel positions,
- monitoring of cladding materials,
- information about annealing efficiency and re-embrittlement rate.

The supplementary surveillance program is based on the use of archive material, mainly from the standard program, and it uses a reconstitution method for testing irradiated specimens. IAEA reference JRQ material is widely used for qualification of results not only for monitoring irradiation embrittlement but also for neutron dosimetry.

Literature

[1] Brumovsky, M. and Pav, T. - "Surveillance of VVER-440C Reactor Pressure Vessels," in *"Radiation Embrittlement of Nuclear Reactor Pressure Vessel Steels. An International Review," ASTM STP 1170,* 1993, pp. 57-70.

Pressure Vessel Welds—Mechanical Properties

Reinhard Langer,[1] Reinhard Bartsch,[2] and Gerhard Nagel[3]

Irradiation Behavior of Submerged Arc Welding Materials with Different Copper Content

Reference: Langer, R., Bartsch, R., and Nagel, G., **"Irradiation Behavior of Submerged Arc Welding Materials with Different Copper Content,"** *Effects of Radiation on Materials: 19th International Symposium, ASTM STP 1366,* M. L. Hamilton, A. S. Kumar, S. T. Rosinski, and M. L. Grossbeck, Eds., American Society for Testing and Materials, West Conshohocken, PA, 2000.

Abstract: In Germany there are two first generation commercial nuclear power plants in operation, Obrigheim NPP (KWO) and Stade NPP (KKS). The reactor pressure vessels of both plants were fabricated of forged rings, joined with submerged arc welds. These welds were performed with a flux of the first generation, produced in license of Linde, and with copper-coated wires. When the first results of the irradiation surveillance programs were available, it became obvious that the neutron-induced embrittlement of the welding materials would be higher than expected at design of the power stations in the late sixties.

To evaluate the neutron irradiation response, additional irradiation programs were performed. In the scope of these programs, submerged arc test welds were produced, corresponding in chemical composition, mechanical properties and Charpy toughness in the unirradiated condition of the core-welds of the two NPPs concerned. It was intended to assess also K_{Ic},T-curves of the welding material established on fracture toughness tests of large specimens.

This report presents some results of unirradiated and irradiated tensile, C_v, K_{Ic} specimens and E208 drop weight specimens according to ASTM E208 taken from submerged arc welds with different copper content up to 0.42 wt.%. Irradiation was performed in the RPVs concerned and in the VAK RPV with different fluxes and fluences up to about 3.3E19 cm^{-2} (E > 1MeV).

The irradiation behavior of the welding material in general is shown, especially the influence of the copper content. At a copper content of about 0.30 wt. %. saturation in in the T_{41} shift was found. The results show no influence of the irradiation facilities and of the different fluxes. With results on irradiated C_v, E208 drop weight, and WOL X specimens the conservatism of the use of the T_{41} shift according to the RT_{NDT} concept could be confirmed.

[1] Siemens AG KWU/NT13, Freyeslebenstraße 1, D-91050 Erlangen, Federal Republic of Germany.
[2] Kernkraftwerk Obrigheim GmbH.
[3] PreussenElektra AG.

Copyright© 2000 by ASTM International www.astm.org

Keywords: irradiation behavior, submerged arc welding materials, copper influence, dose rate effect, tensile tests, impact testing, K_{Ic}-tests, reconstituted C_v tests

Introduction

In Germany there are two first generation commercial nuclear power plants in operation, Obrigheim NPP (KWO) and Stade NPP (KKS). The reactor pressure vessels of both plants were fabricated of forged rings, joined with submerged arc welds (SAW). These welds were performed with a flux of the first generation, produced in license of Linde, and with copper coated wires. When the first results of the irradiation surveillance programs were available, it was seen that the neutron induced embrittlement of the welding materials would be higher than expected at design of the power stations in the late sixties.

In order to provide additional assurance of the integrity of the reactor pressure vessels, two test welds were produced using the submerged arc welding method. These test welds corresponding in chemical composition, mechanical properties and Charpy - toughness to the unirradiated circumferential core-welds of the two NPPs. It was intended to assess also K_{Ic},T-curves of the welding materials from fracture toughness tests with large specimens.

Manufacturing of the Welds

The weld 510 and weld S were produced as monitoring test coupons for acceptance testing of the circumferential core welds. The test welds were identified as weld 390 and 370. The last comprised four deposits with copper contents in the range of 0.14% up to 0.42% marked with A, B, C and D. For the various copper contents specific electrolytic copper coatings of the welding wires were applied, having the wire and flux combination and the welding parameters unchanged. The main investigations were performed on the deposits of weld 390 and weld D. Table 1 presents a compilation of the production parameters used.

Table 1 - *Production Parameters of the Submerged Arc Welds*

	Wire	Wire Diam. mm	Flux	Current A	Voltage V	Rate of Travel mm/min	Preheating Temp. °C	Post Weld Heat Treatm. [°C/h]
Weld S	SW 121 *)	5	Grau Lo	600	30	420-450	180/200	600±15°C/20h
Weld 510	SW121 *)	5	GrauH/UM81	650	32	400	200	600±15°C/12 h
Weld 370 A, B, C, D	SW437 **)	5	LW320/330	600	32	450	180/200	600±15°C/11 h
Weld 390	NiCrMo1-UP	5	LW 320	650	30	420	180/230	600±15°C/11 h

*) SW121: Predecessor of NiCrMo1-U **) SW437: NiCrMo1 UP mod

Baseline Testing in the Unirradiated Initial Condition

The chemical composition of the welds was determined in extensive chemical analyses by means of various methods. The chemical composition of the weld deposits is shown in Table 2. Mean values were applied for the copper content of the welds A, B, C, and D. No relevant scatter was realized to the other elements.

Table 2 - *Chemical Composition of the Weld Deposits*

	C %	Si %	Mn %	P %	S %	Cr %	Mo %	Ni %	Cu %
Weld S	0.060	0.23	1.83	0.009	0.009	0.38	0.62	1	0.23
Weld 510	0.085	0.12	1.10	0.014	0.010	0.37	0.61	1.21	≤ 0.25
Weld A	0.080	0.14	1.17	0.014	0.012	0.74	0.59	1.10	0.14
Weld B	0.080	0.14	1.17	0.014	0.012	0.74	0.59	1.10	0.30
Weld C	0.080	0.14	1.17	0.014	0.012	0.74	0.59	1.10	0.42
Weld D	0.080	0.14	1.17	0.014	0.012	0.74	0.59	1.10	0.22
Weld 390	0.070	0.17	1.79	0.012	0.007	0.40	0.63	0.92	0.28

The seven welds available have nearly the same content of carbon, molybdenum and nickel. They differ in the content of manganese from 1.10 up to 1.83 wt.%, of chromium from 0.37 up to 0.74 wt.%, and cover a range of 0.14 up to 0.42 wt.% of copper.

Table 3 presents the results of tensile tests at room temperature, the T_{NDT} according to ASTM E208 and the RT_{NDT} according to ASME III NB 2300 of the welds in the unirradiated initial state. The values of T_{41}, T_{68} and the level of the upper shelf energy (USE) of best fit Charpy impact transition curves [1] are listed in Table 3, too.

Table 3 - *Results of Tensile Tests at RT; Charpy T_{41}, T_{68} and USE; T_{NDT} and RT_{NDT} of the Different Welds in the Unirradiated State*

Weld	Yield Strength [N/mm²]	Tensile Strength [N/mm²]	Elon-gation [%]	Red. of Area [%]	T_{NDT} [°C]	RT_{NDT} [°C]	ISO v-Specim. Orient.	T_{41} [°C]	T_{68} [°C]	USE [J]
Weld S	559	640	25	71.5	-15	-15	L	-28	-10	160
Weld 510	650	725	22	71	-15	-7	L	-12	4	128
Weld A	556	649	22	70	-	-	T	-20	-10	140
Weld B	588	672	21	68	-	-	T	-34	-11	150
Weld C	595	675	23	68	-	-	T	-31	-6	142
Weld D	604	696	20	70	-35	-28	T	-12	-1	144
Weld 390	604	686	24	71	-35	0	T	-7	12	128

K_{Ic},T-curves were evaluated additionally from weld 390 and weld D. They will be shown and discussed later, together with those of the irradiated state.

Irradiation Facilities

Three reactors were available for irradiation, the KWO RPV, the KKS RPV and the VAK RPV. Whereas KWO RPV and Stade RPV are PWRs the VAK was an Experimental Boiling Water Reactor, now out of operation, capable of irradiation capsules of a square of 100 mm x 146,5 mm corresponding in dimensions to WOL 100 X specimens. In the irradiation positions of the KWO RPV the maximum diameter of capsules was 70 mm whereas in the KKS RPV only small specimens could be irradiated with a maximum dimension of 25 mm x 25 mm. Beside the different size of capsules the neutron flux of the VAK was much higher than that of the commercial RPVs (Table 4). The irradiation temperature of all three facilities was in the same range, verified by temperature monitors within the capsules and 3 dimensional finite element temperature calculations of the capsules. The fluence of the specimens was calculated, and the calculation verified by Fe- and Nb- fluence detectors. For evaluation of the test results the calculated fluences were applied. The relevant interesting data of the RPVs is shown in Table 4.

Table 4 - *Comparison of the NPPs Applied for Irradiation of the Specimens*

VAK NPP	KWO NPP	Stade NPP
BWR, 16 MW electric power	PWR, 357 MW electric power	PWR, 640 MW electric power
irradiation temperature 285°C (adapted to PWRs)	irradiation temperature 283°C	irradiation temperature 285°C
flux: 2 E12 cm^{-2} s^{-1}	flux 4 - 6 E10 cm^{-2} s^{-1}	flux 6 E11 $^{cm-2}$ s^{-1}
capsule dimension: 100mm x 146.5mm x length	capsule dimension: ø 70mm x length	capsule dimension: 25mm x 25mm x length

Irradiation Experiments

Tensile test specimens and Charpy impact test specimens were irradiated in all three reactors. Additional tests were performed on E208 drop weight and WOL X specimens fabricated of weld 390 and weld D in the VAK. WOL X specimens were also irradiated of weld D in the KWO RPV.

Tests and Results

Tensile Tests

Tensile tests were performed on specimens with fluences up to 5.4E19 cm^{-2} (E>1MeV). The yield strength as a function of the fluence is shown in Fig. 1. Weld 510

has the highest yield and tensile strength in the unirradiated condition. After irradiation the welds with the highest copper content show the highest irradiation effect. In the fluence range of 1E19 to 3E19 (E > 1MeV) the results of the welds with a higher copper content are in one scatterband, while the results of weld A (low copper content) is placed distinct below that scatterband.

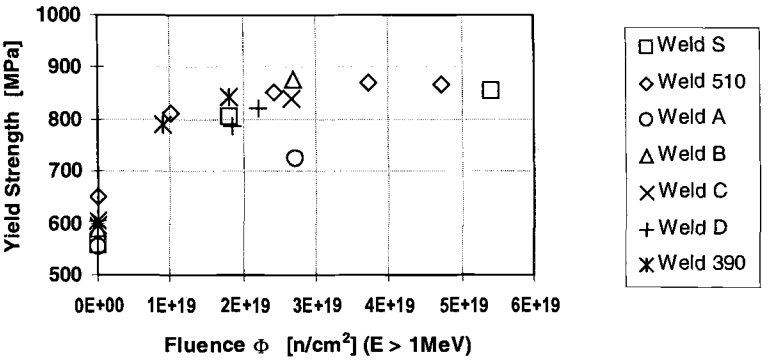


Fig. 1 - *SAW; Yield Strength as a Function of the Fluence Φ (E>1MeV)*

Charpy Impact Tests

The ΔT_{41} values obtained from Charpy impact curves as a measure of the "ductile to brittle transition temperature" (DBTT) are plotted in Fig. 2, as a function of the fluence Φ, (E>1MeV).

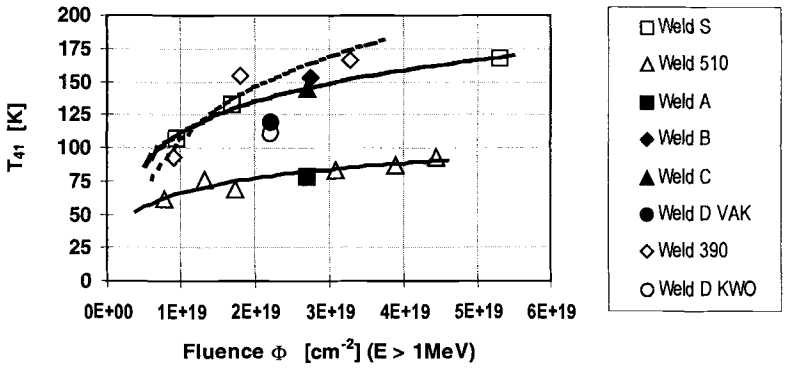


Fig. 2 - *SAW; Comparison of the Shift of Impact Transition Curves ΔT_{41} as a Function of the Fluence Φ (E>1MeV)*

Results are available from the weld S, weld 390 and weld 510 at different fluences, so best fit curves could be evaluated. Weld 390 shows the highest shift. The ΔT values of the welds B and C are on the same level with Weld S, though the copper content of

weld B and C is leading, (Table 2). Similar appearance show the results of weld 510 and weld A. The results of weld D are between the upper and lower scatter band.

Fracture Mechanics (K_{Ic}) Tests

WOL X specimens were irradiated and tested from the welds D and 390. Fig. 3 shows the results of the K_{Ic}-tests of weld D on specimens unirradiated and irradiated in the VAK- and KWO-RPV and the lower bound K_{Ic},T-curves established according to [2].

The shift of the lower bound K_{Ic},T-curve is not exactly comparable with the ΔT_{41}, but obviously it is in the same range like the estimated T_{41} shift of weld D (Fig. 2).

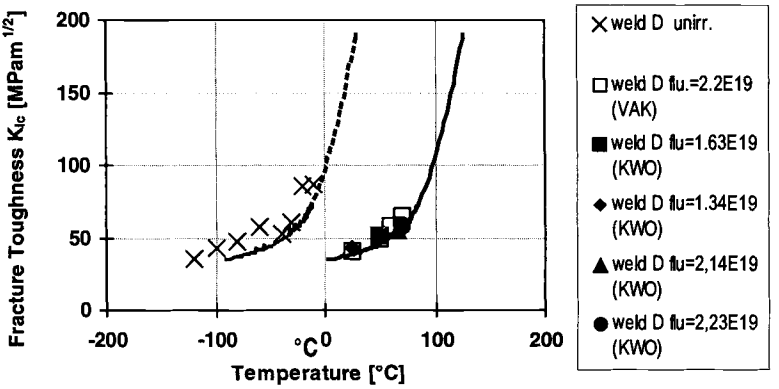


Fig. 3 - *SAW-D; K_{Ic}-Values, K_{Ic},T-Curve; Unirr. and Irr.; VAK and KWO-RPV*

Four sets of irradiated K_{Ic}-specimens are available from weld 390. The results of the tests and the K_{Ic},T-curves obtained are shown in Fig. 4. Two K_{Ic},T-curves were

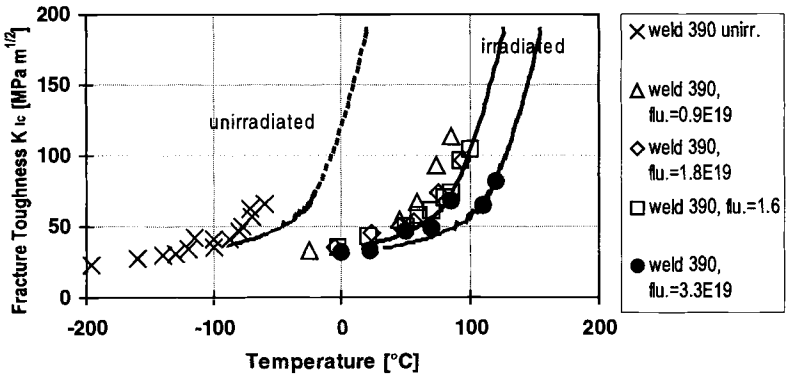


Fig. 4 - *SAW-390; K_{Ic}-Values, K_{Ic},T-Curve; Unirr. and Irr. (VAK, $\Phi \leq 1.8E19$, $\Phi \leq 3.3E19$ cm^{-2}, E>1MeV)*

evaluated from the four specimen sets. The first curve covers specimens irradiated to a fluence up to $\Phi \leq 1.8E19$ cm^{-2} the second one up to $\Phi \leq 3.3E19$ cm^{-2} (E> 1MeV). The shifts of the K_{Ic},T-curves and the ΔT_{41}-values are in the same range, too.

Evaluation of the Test Results

Influence of Copper Content

As seen in Fig. 1, Fig. 2 and Table 5, the effect of neutron irradiation is dependent on the copper content but there are additional influences. In Fig. 5 the Charpy shift ΔT_{41} is plotted as a function of the copper content for a fluence of 2.2E19 (E> 1MeV). This

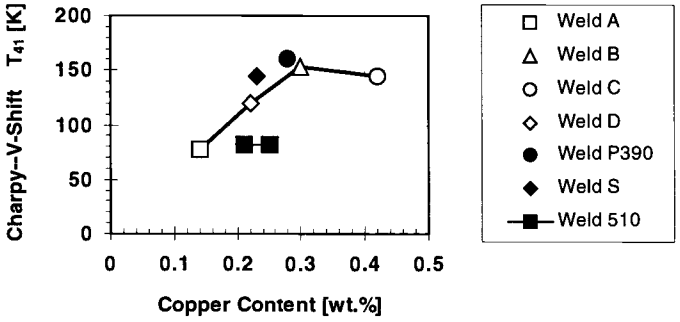


Fig. 5 - *SAW; shift of impact transition curves ΔT_{41} as a function of the copper content*

figure demonstrates a saturation of the irradiation embrittlement at a copper content of about 0.3% for welds produced by the applied parameters. At 0.30 wt.% the limit of the solubility for copper at post weld heat treatment temperature of 600±15°C seems to be reached [3].

Dose Rate Effect

In scope of these programs tensile test specimens, C_v specimens and WOL X specimens of weld D were irradiated in the KWO vessel and in the VAK RPV. Fig. 6 presents strength values from tensile testing as a function of the test temperature for some of the specimens with almost the same fluence.

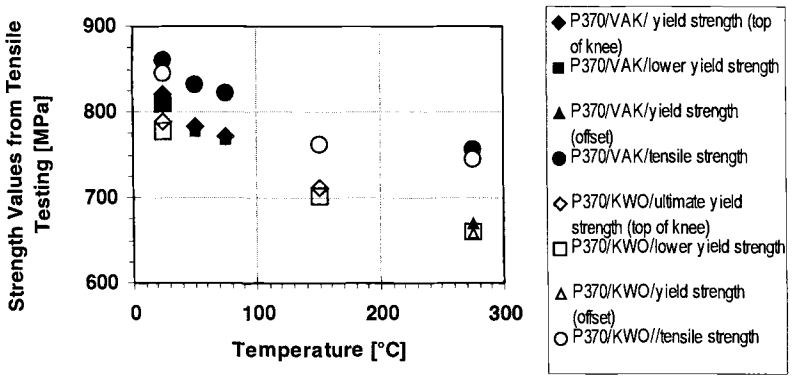


Fig. 6 - *SAW-D; Comparison of Results on Tensile Tests, Specimens Irr. in VAK- and KWO-RPV*

It is obvious that the measured test results are in good agreement despite the remarkable different neutron fluxes of the RPVs with a relation of 1:33 (Table 4).

The results of impact testing of C_v specimens and C_v compound specimens as a function of the test temperature are plotted in Fig. 7.

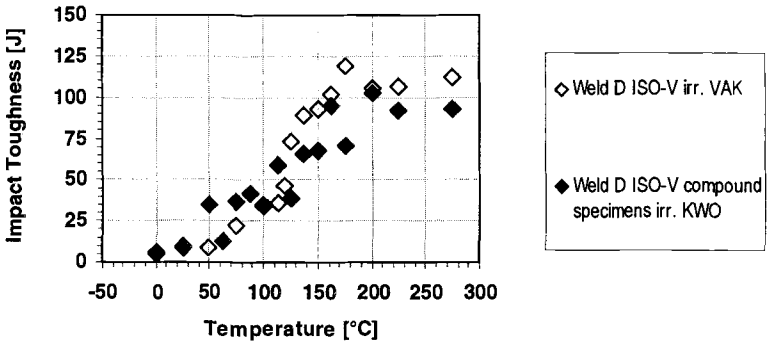


Fig. 7 - *SAW -D; Comparison of Charpy Test Results, Irr. at the VAK-RPV, (Compact Specimens, Φ=2,25E19 cm^{-2}) and the KWO-RPV, (Compound Specimens, Φ = 2,22E19 cm^{-2}) (E>1MeV)*

The inserts for compound specimens were irradiated in the KWO RPV whereas the compact specimens were irradiated in the VAK RPV. Constitution of the compound specimens was performed by electron beam welding [4] of the irradiated inserts to base metal ends specially heat treated to adjust strength properties comparable to those of the irradiated weld metal.

The impact toughness values presented in Fig. 7 show the results of the C_v compact and C_v compound specimens forming one trend band.

The results of WOL X-40 specimens irradiated in the KWO RPV and those of WOL X-50 specimens irradiated in the VAK vessel together with a covering K_{Ic},T-curve are shown in Fig. 3. The fluence of two of the specimens irradiated in KWO NPP is in a lower range than the other ones. These specimens were tested at the lower temperatures. All results are in a narrow trend band, proving that there is no dose rate effect in the flux density range considered.

Conservatism of T_{41} shift according to the RT_{NDT}-Concept

Table 5 shows the irradiation induced shift values of the Charpy tests and E208 drop weight tests comparable. The comparison shows that the shift values of the Charpy tests are in the same range or higher than those of the E208 drop weight tests. A statistical evaluation of the K_{Ic} tests was not yet performed, but the shifts of the lower bound curves (Fig.3 and Fig.4) are in the same range as the Charpy shifts and the ΔT_{NDT}.

The lower bound K_{Ic},T-curves evaluated on measured K_{Ic}-values of irradiated specimens according to [2], (Fig. 3 and Fig. 4) are located at lower temperatures than those based on the RT_{NDT} concept using the ΔT_{41} values.

Table 5 - SAW-D, SAW-390; *Results of Charpy Shift ΔT_{41} and Shift of T_{NDT}*

Weld	Specimen Orientation	Irradiation	Fluence (cm^{-2}) (E>1MeV)	ΔT_{41} [K]	ΔT_{NDT} [K]
Weld D	T - L	VAK	2.20E+19	119	
Weld D		VAK	2.69E+19		115
Weld D *)	T - L	KWO	2.22E+19	111	
Weld 390	T - L	VAK	9.00E+18	93	95
Weld 390	T - L	VAK	1.80E+19	154	125
Weld 390	T - L	VAK	3.30E+19	166	165

These results obtained by C_v -, E208 drop weight and WOL X specimens demonstrate the conservatism of the T_{41} shift according to the RT_{NDT}-concept.

Summary

Several welds were manufactured using fabrication parameters representative to those of the RPV core welds considered but with different copper content and comparable nickel content. These welds were irradiated to varying fluence levels in

NPPs with different neutron fluxes. Tensile , E208 drop weight, C_v compact and C_v compound specimens were tested in the unirradiated and irradiated condition. K_{Ic} tests were also performed and lower bound K_{Ic},T-curves were determined in the unirradiated and irradiated condition.

The data compiled from these investigations prove that

- The irradiation response of the welds in general is dependent on copper content and fluence.
- A saturation of irradiation embrittlement was detected for copper content above 0.30 wt.% within the examined fluence range.
- No dose-rate effect or irradiation-time influence is existent within the respective fluence/flux range.
- C_v compound specimens constituted by electron beam welding lead to comparable results as C_v compact specimens.
- The use of the ΔT_{41} according to the RT_{NDT}-concept as the DBTT shift for the core belt materials of a RPV is conservative and leads to a safe valuation of the RPV.

References

[1] Hofer, G. , Günes Ü. "Zur Auswertung der beim instrumentierten Kerbschlagbiegeversuche anfallenden Signale" *Materialprüfung* 27, (1985), Nr. 8

[2] Vazoukis, G., R. Langer, "Covering of the Complete Fracture Toughness (K_{Ic}) Curve as a Function of Temperature by Determination of K_{Ic}-Values in the Lower Shelf Region",, *Kerntechnik* 578 (1992) No. 6, p. 347-352

[3] English, C. A. "Microstructure Research in RPV Steel: Techniques versus Invormation", Topical Day-19.3.1999, MOL Belgium

[4] Klausnitzer, E., and G. Hofmann, "Reconstituted Impact Specimens with Small Inserts", *Effect of Radiation and Materials: 15th International Symposium, ASTM STP 1125,* R.E. Stoller, A.S. Kumar, and D.S. Gelles, Eds., American Society for Testing and Matererials, West Conshohocken, PA, 1992, pp.76-90.

Shafik K. Iskander,[1] Randy K. Nanstad,[1] Donald E. McCabe,[1] and Ronald L. Swain[1]

Effects of Irradiation on Crack-Arrest Toughness of a Low Upper-Shelf Energy, High-Copper Weld

Reference: Iskander, S. K., Nanstad, R. K., McCabe, D. E., and Swain, R. L., **"Effects of Irradiation on Crack-Arrest Toughness of a Low Upper-Shelf Energy, High-Copper Weld,"** *Effects of Radiation on Materials: 19th International Symposium, ASTM STP 1366*, M. L. Hamilton, A. S. Kumar, S. T. Rosinski, and M. L. Grossbeck, Eds., American Society for Testing and Materials, West Conshohocken, PA, 2000.

Abstract: The crack-arrest fracture toughness (K_a) of unirradiated and irradiated specimens machined from a low upper-shelf, high-copper weld was determined. The specimens were machined from the beltline weld of the Midland Unit 1 nuclear reactor pressure vessel (RPV). This weld was fabricated from one heat of weld wire and one lot of welding flux and bears the designation WF-70. It is of particular interest because it has been used in several RPVs that may still be in operation. The effect of irradiation has been measured in terms of the shift of the mean and lower-bound crack-arrest fracture toughness versus temperature curves. These shifts are compared to (1) 41-J transition temperature shift from Charpy V-notch (CVN) tests, $\Delta TT_{41\text{-}J}$; (2) shift in the Master Curve transition temperature, T_0, at the 100 MPa·√m level, ΔT_0; and (3) shift of the "arrest force" F_a temperature determined from instrumented CVN testing, ΔTF_a. Preliminary results indicate that the shift of K_a of this low upper-shelf energy weld is approximately the same as the shift $\Delta TT_{41\text{-}J}$, larger than ΔT_0, and significantly larger than ΔTF_a.

Keywords: low upper-shelf energy weld, crack arrest, fracture toughness, irradiation, nil-ductility transition temperature, NDT, radiation damage, reactor pressure vessel steels, transition temperature shift

Nomenclature

Acronyms

ART	Adjusted reference temperature value of RT_{NDT}
ASME	American Society of Mechanical Engineers
ASTM	American Society for Testing and Materials

[1]Metals and Ceramics Division, Oak Ridge National Laboratory, Oak Ridge, TN 37831-6151.

Copyright© 2000 by ASTM International www.astm.org

CMOD	Crack-mouth-opening displacement
CVN	Charpy V-notch
EPRI	Electric Power Research Institute
HAZ	Heat-affected zone
HSSI	Heavy-Section Steel Irradiation
NDT	Nil-ductility-transition temperature, determined according to ASTM Standard Test Method for Conducting Drop-Weight Test to Determine Nil-Ductility Transition Temperature of Ferritic Steels (ASTM E 208-95a)
NRC	U.S. Nuclear Regulatory Commission
ORNL	Oak Ridge National Laboratory, Oak Ridge, TN
RPV	Reactor pressure vessel
USE	Upper-shelf energy

Symbols

$1\text{-}\sigma$	One standard deviation on the error
a_a	Arrested crack length
ΔTF_a	Shift in arrest force temperature
ΔT_0	Shift in the Master Curve transition temperature T_0
$\Delta TT_{41\text{-}J}$	Shift in the 41-J CVN-impact energy level
F_a	Arrest force determined from instrumented CVN testing
K_a	The value of the stress intensity factor shortly after arrest[2]
K_{Ia}	The value of the crack-arrest fracture toughness K_a for a crack that arrests under conditions of crack-front plane strain[2]
K_{Ic}	Plane-strain fracture toughness
RT_{NDT}	Reference nil-ductility-transition temperature
T	Temperature
TF_a	Arrest force temperature determined from instrumented CVN testing
T_{LB}	Lower-bound temperature
T_0	Master Curve transition temperature at the 100-MPa·√m level determined according to ASTM Standard Test Method for Determination of Reference Temperature, T_0, for Ferritic Steels in the Transition Range (ASTM E 1921-97)

[2] Excerpted from Standard Test for Determining Plane-Strain Crack-Arrest Fracture Toughness, K_{Ia}, of Ferritic Steels (ASTM E 1221-96).

Introduction

In the fracture mechanics integrity analysis of reactor pressure vessels (RPVs), the initiation and arrest fracture toughness curves as described in Section XI of the *ASME Boiler and Pressure Vessel Code* (ASME Code) are used for the normal operation of RPVs. The effects of neutron irradiation on toughness are accounted for by shifting the curves upward in temperature by an amount equal to the transition temperature shift of the Charpy V-notch (CVN) impact energy curve at the 41-J level ($\Delta TT_{41\text{-}J}$) without changing the shapes of the curves. Such a procedure implies that the shifts in the fracture toughness curves are the same as the $\Delta TT_{41\text{-}J}$ and that irradiation does not change the shape of the fracture toughness curves.

As is well known, irradiation of some RPV ferritic steels to fluences on the order of 1×10^{19} n·cm^{-2} (>1 MeV) causes changes in the shape of the CVN impact energy curve. Similar changes in shape could occur in the fracture mechanics toughness curves, and such changes could lead to nonconservative determinations of the irradiated fracture toughness. For these reasons, research programs have been sponsored by the U.S. Nuclear Regulatory Commission (NRC) within the Heavy-Section Steel Irradiation (HSSI) Program at the Oak Ridge National Laboratory (ORNL).

Some of these programs are the Fifth, Sixth, and Tenth Irradiation Series. The objective of the Fifth Series was to determine the effect of neutron irradiation on the shift and shape of the K_{Ic} versus ($T - RT_{NDT}$) curve, where K_{Ic} is the plane-strain fracture toughness, T is the temperature, and RT_{NDT} is the reference nil-ductility transition temperature.[3] The objective of the Sixth Series was similar but investigated the effect on K_{Ia}, the plane-strain crack-arrest fracture toughness. The Fifth and Sixth Irradiation Series used commercially produced submerged-arc welds with copper contents of 0.23 and 0.31 wt %. The welds were specially fabricated for the HSSI Program in 220-mm-thick plate [1],[2],[3]. The copper was added to the weld wire melt, resulting in a weldment with a standard deviation (1-σ) in copper of about 0.01 wt %. The average upper-shelf energy (USE) of the welds used in the Fifth and Sixth Series is approximately 135 J.

The material used for the Tenth Series is a low-USE weld with a copper content that varies between 0.21 and 0.46 wt % and an average USE of 90 J. The objective of the Tenth Series was similar to those of the Fifth and Sixth Series. All three series investigated the effects of irradiation on the fracture toughness of welds because several nuclear RPVs in operation have welds with copper contents that make them susceptible to severe degradation in toughness at end-of-life fluence levels.

This paper investigates the effects of irradiation on crack-arrest toughness by measuring the irradiation-induced shifts of the mean and lower-bound crack-arrest fracture toughness versus temperature curves. These shifts are compared to (1) 41-J impact energy transition temperature shifts from CVN tests, $\Delta TT_{41\text{-}J}$; (2) shift in the Master Curve T_0 transition temperature, ΔT_0; and (3) shift of the "arrest force" temperature, ΔTF_a, determined from instrumented Charpy testing. The results are also

---

[3]The reference temperature, RT_{NDT}, is determined in accordance with the ASME Code, Section III, Subarticle NB-2330.

compared to the small amount of other published experimental data on the effects of irradiation on crack-arrest fracture toughness.

Description of Materials And Procedures

Crack-arrest testing was performed according to the American Society for Testing and Materials (ASTM) Test for Determining Plane-Strain Crack-Arrest Fracture Toughness, K_{Ia}, of Ferritic Steels (E 1221-96). Crack-arrest specimens for both unirradiated and irradiated evaluation were machined from the beltline weld of the nuclear RPV of the canceled Midland Unit 1. Thirty weld-embrittled specimens and six duplex crack-arrest specimens were fabricated; their dimensions are shown in Figs. 1(a) and 1(b), respectively. The crack-starter bead of the weld-embrittled specimens was prepared with a McKay DWT welding electrode. The same electrode is used at ORNL to produce crack-starter beads in test specimens for the ASTM Standard Test Method for Conducting Drop-Weight Test to Determine Nil-Ductility Transition Temperature of Ferritic Steels (E 208-95a), which is also a crack-arrest test. During the testing at the relatively higher temperatures, loading and unloading had to be continued well beyond the E 1221-96 guidelines. The crack front propagated in a stable tearing mode to the end of the heat-affected zone (HAZ) of the weld (Fig. 2). Such tearing was visible also on the fracture surfaces; it occurred in many of the unirradiated specimens and to a lesser extent in the irradiated ones. Once the crack front progressed to the end of the HAZ, a rapid run-arrest event took place. However, by that time the energy stored in the specimen was sufficient to drive the crack to such an extent that the remaining ligament was too small to satisfy E 1221-96 validity criteria (A) and (B). This result indicated that the specimen length of 127 mm (5 in.) was somewhat small [Fig. (1a)]; thus, larger (152-mm-long) duplex specimens [Fig. 1(b)] were fabricated.

Duplex specimens are much costlier to fabricate than weld-embrittled specimens. However, the decision to fabricate duplex specimens was dictated by the limited amount of remaining material available, sufficient for only six duplex specimens. Duplex specimens require less material than weld-embrittled ones. The other advantage of duplex specimens is that they can be tested at higher temperatures than weld-embrittled ones. The 4 valid unirradiated values out of 21 specimens tested were from the 6 duplex specimens.

The WF-70 material used in fabricating the crack-arrest specimens is of particular interest because it was used in several RPVs that may still be in operation. The subject beltline weld has been extensively studied [4], [5], and [6]. The chemistry and the mechanical properties in the unirradiated and irradiated conditions are given in Tables 1 and 2, respectively.

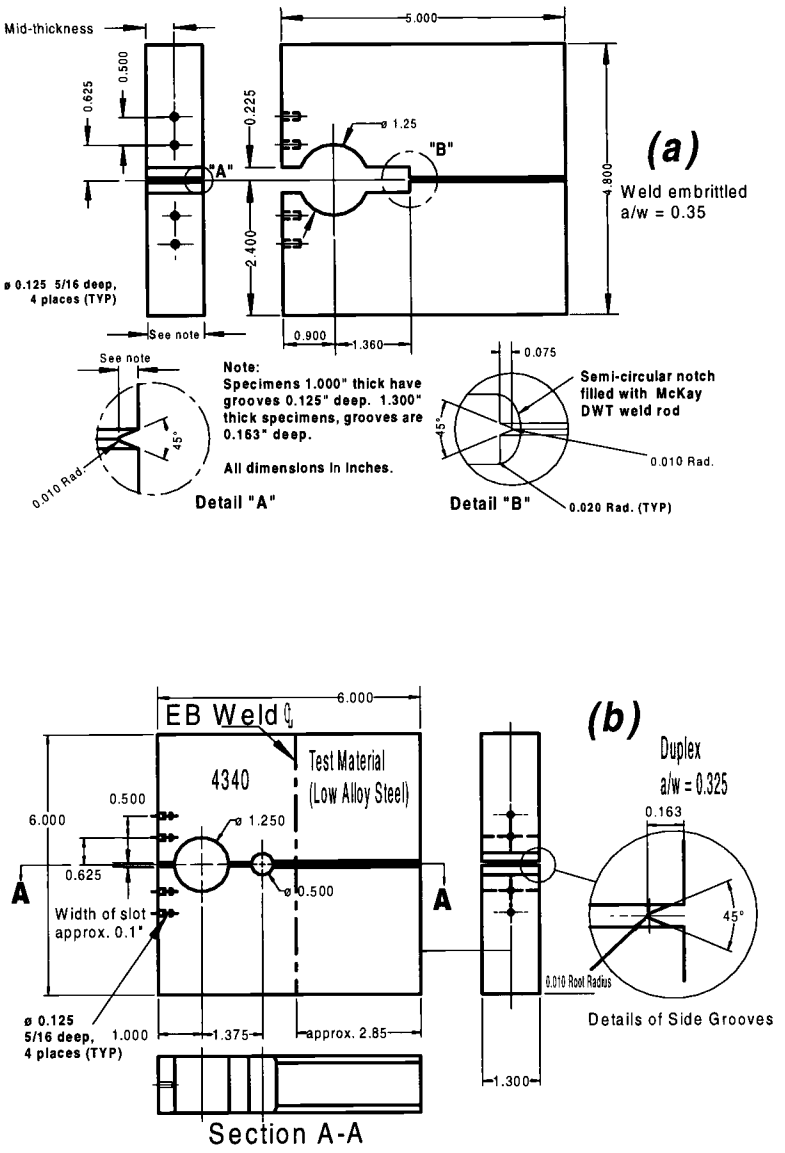


Fig. 1. Dimensions of crack-arrest specimens. (a) Weld-embrittled used in unirradiated and irradiated testing. (b) Duplex crack-arrest specimens used in the unirradiated testing.

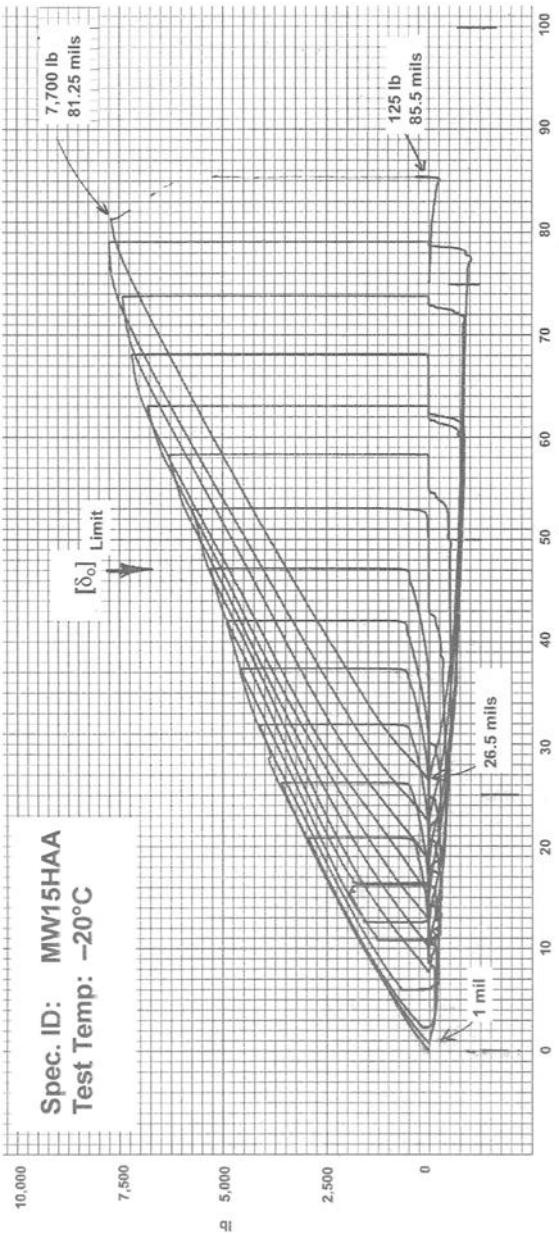


Fig. 2. Loading and unloading had to be continued well beyond the ASTM E 1221-96 guidelines until the crack front propagated in a stable tearing mode to the end of the heat-affected zone of the weld.

Table 1—*Chemical composition of Midland beltline weld*

Composition (wt %)									
C	Mn	P	S	Si	Cr	Ni	Mo	Cu	V
0.084	1.61	0.017	0.007	0.62	0.10	0.57	0.41	0.21–0.34	0.004

Table 2—*Mechanical properties of the beltline WF-70 unirradiated weld material (tensile specimens oriented transverse to the welding direction and Charpy specimens in the T-L orientation)*

Drop-weight NDT (°C)	CVN 41-J transition temperature (°C)	CVN impact USE (J)	Reference temperature, RT_{NDT} (°C)	Room-temperature tensile strength (MPa)	
				Yield	Ultimate
−60 to −45[a]	−22 to 14[b]	78 to 108[b]	−20 to 37[b]	523	628

[a]From eight locations.
[b]From 19 sets of Charpy curves from different depths and azimuthal locations.

The yield strength as a function of temperature is required in crack-arrest testing to determine the crack-mouth-opening displacements (CMODs) during the loading and unloading test procedure as specified in E 1221-96. It is also required to evaluate whether the measured value of the crack-arrest toughness, K_a, qualifies as a value of plane-strain crack-arrest toughness, K_{Ia}. There are five validity tests that K_a values must satisfy to qualify as K_{Ia} (see E 1221-96). The unirradiated and irradiated values of the yield strengths used in this study are shown as a function of temperature in Fig. 3. Tests on unirradiated tensile specimens oriented transverse to the welding direction, and in the same T-L orientation[4] of crack-arrest specimens, fractured in the specimen shoulder. More tensile specimens in both longitunal and transverse orientations were prepared and tested. The yield strengths obtained from both orientations were significantly higher than the initially obtained values from transverse-orientation specimens that failed in the shoulder region. The reason for the initially prepared specimens failing in the shoulder was not pursued. There is little difference between the unirradiated longitudinal and transverse orientation yield strengths (Fig. 3). The curves shown in Fig. 3 are regression

[4]The nomenclature for crack-plane orientation is given in many ASTM standards; e.g., ASTM Standard Test Method for Plane-Strain Fracture Toughness of Metallic Materials (E 399).

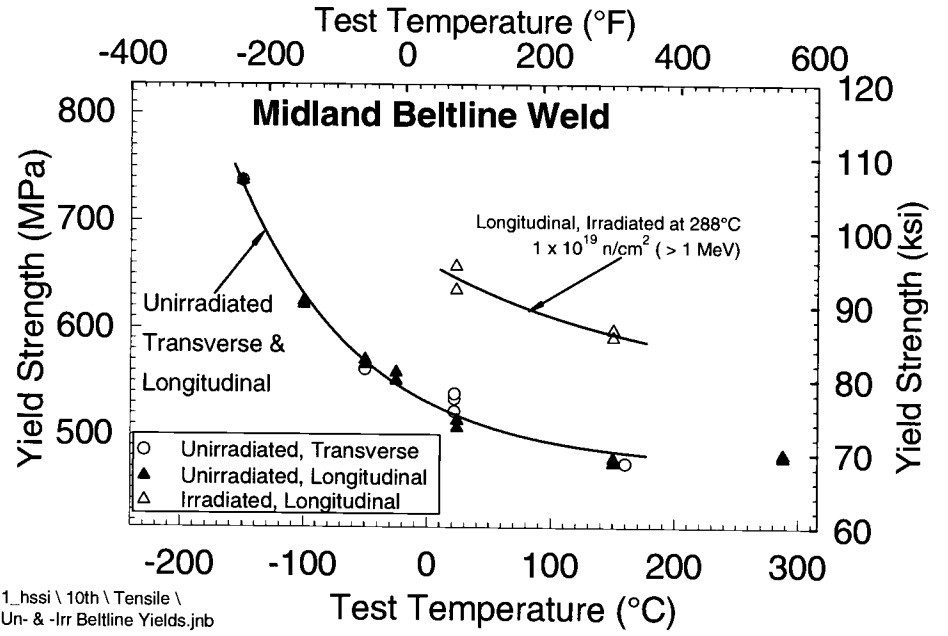


Fig. 3. Tensile yield strength of WF-70 weld metal before and after irradiation.

fits to the transverse and longitudinal orientations for the unirradiated and irradiated conditions, respectively, and the resulting expressions were used to interpolate for the yield strengths at the required temperature. The reason for this choice is that the transverse orientation is the same as the T-L orientation of the crack-arrest specimens, while only longitudinal-orientation tensile specimens were available in the irradiated condition. It is assumed that the differences in yield strength between the two orientations in the irradiated condition are also insignificant. The values of the yield strength have an impact on the K_{Ia} validity limits.

According to E 1221, the modulus of elasticity, or Young's modulus, as a function of temperature is needed in calculating the stress intensity factors. Values for Young's modulus given in the 1989 ASME Code, Section III, Div. 1, Table I-6.0, Appendix I, for carbon-molybdenum steels were regression fit; the resulting expressions were used to interpolate for Young's modulus at the required temperature.

The 41-J impact energy level is used as an index to determine the CVN transition temperature shift, $\Delta TT_{41\text{-}J}$. Thus it is of interest to examine the CVN impact energy data obtained from testing 276 specimens obtained from 19 different depths and azimuthal locations (Fig. 4). All the available data on the WF-70 welds tested at ORNL are included in Fig. 4. In Ref. [4], the Charpy results from each location were regression fit with separate "mean" curves, and the CVN 41-J transition temperature values obtained from the mean curves ranged from –22 to 14 °C, a spread of 36 °C, as given in Table 2. A

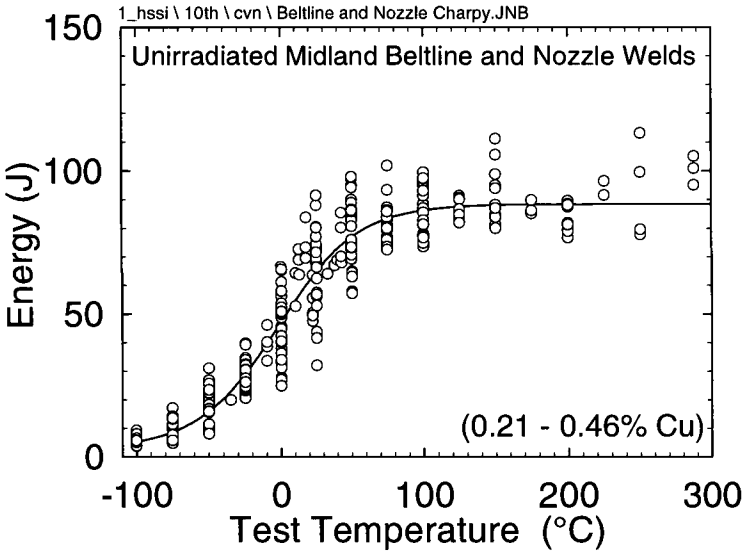


Fig. 4. Charpy V-notch impact energy data of WF-70 weld metal obtained from testing 276 specimens obtained from 19 different depths and azimuthal locations.

similar spread was indicated by simulation analysis of HSSI Welds 72W and 73W [7]. The scatter that is inherent in CVN testing and CVN evaluations could benefit from employing statistical methods to quantify the uncertainty.

The 41-J energy-indexing level used in determining shifts for low-USE welds in particular should be reevaluated as well. As noted by McElroy and Lowe [8], the drop in an already low USE with the consequent shape change could distort the 41-J indexing level, particularly in the irradiated condition. In addition to such a distortion, the large uncertainty in the value of the 41-J energy-level temperature results in a larger uncertainty in $\Delta TT_{41\text{-}J}$. Other measures of fracture toughness shifts should be considered, such as that in T_0, determined according to ASTM Method for the Determination of Reference Temperature, T_0, for Ferritic Steels in the Transition Range (E 1921-98). Other measures, such as the shift in Charpy lateral expansion or the shift in 50% shear percent fracture appearance, should also be considered.

Fifteen weld-embrittled crack-arrest specimens were included in the specimen complement of an HSSI irradiation capsule, denoted as Capsule 10.06, which was irradiated in the University of Michigan Ford Nuclear Reactor. The crack-arrest specimens were irradiated at a nominal temperature of 288°C to a fluence that varied between 0.54 and 1.35×10^{19} n·cm^2 (>1 MeV). The total irradiation time was 4936 h at full reactor core power; thus the average flux was approximately 5×10^{11} n·cm^2·s^{-1} and the 1-σ uncertainty associated with the fast neutron fluence and other irradiation

parameters was ~8%. The Charpy specimens whose $\Delta TT_{41\text{-}J}$ shift is used for comparison were irradiated in an earlier capsule, and their average fluence was approximately 1.31×10^{19} n·cm^{-2} (>1 MeV). Because of the different fluences, an adjustment to the test temperature, described in detail in Ref. [9], was made to the data to compare the crack-arrest toughness shifts to the $\Delta TT_{41\text{-}J}$.

Testing Procedures

A detailed description of the testing procedure, equipment, analysis procedure, and error analysis is given in Ref. [10] and [11]. The measurement of the final crack length, a_a, is performed according to E 1221-96. Because it is rare that an arrested crack front is straight (see Fig. 5), it is difficult to estimate crack extension without subjective influences affecting such a determination. To obtain an upper bound on the error, the expression for K_a given in E 1221-96 (details given in Ref. [10]) and the maximum valid value of an arrested crack length, a_a, in a specimen were used to estimate the uncertainty in K_a. The total uncertainty in K_a from all sources for 152-mm long specimens is estimated to be approximately ±5%.

Results And Discussion

Tests on Material in the Unirradiated Condition

The variations of crack-arrest toughness values with test temperature of unirradiated specimens are shown in Fig. 6. According to E 1221-96, the values of K_a must fulfill five validity criteria, and only four of the duplex specimens were "valid." None of the 127-mm-wide weld-embrittled specimens fulfilled all five validity criteria. In particular, violations associated with insufficient unbroken ligament length were prevalent. For this reason, larger, 152-mm-wide duplex crack-arrest specimens were used. The specimen identifications have been placed beside their corresponding K_a values in Fig. 6 as an aid in analyzing the validity criteria to determine whether a trend exists for either the valid or invalid values[5]. The valid values appear to be generally smaller than the invalid values; however, there are occasional invalid values that are below the valid values. This suggests that the validity requirement for the unbroken ligament could be relaxed with the justification that the *dynamic* values of yield strength used are conservative and that the requirement for a 15% remaining ligament can be justifiably relaxed. The dynamic value used is formally prescribed by ASTM 1221-96 as 207 MPa (30 ksi) higher than the value measured in the quasi-static mode according to ASTM Standard Test Methods for Tension Testing of Metallic Materials (ASTM E 8). A sufficient relaxation of the unbroken ligament requirement would result in 13 of the 14 values of the weld-embrittled specimens being valid. If such a relaxation were to be made, the only remaining invalid result, from specimen MW12FBB ("12FBB" in Fig. 6), would give a crack-arrest toughness value of 159 MPa·√m at a test temperature of -20°C, which seems to be associated with test temperatures 40°C higher.

---

[5]For purpose of conciseness, the "MW" prefixes of the specimen identification numbers were omitted in Fig. 6.

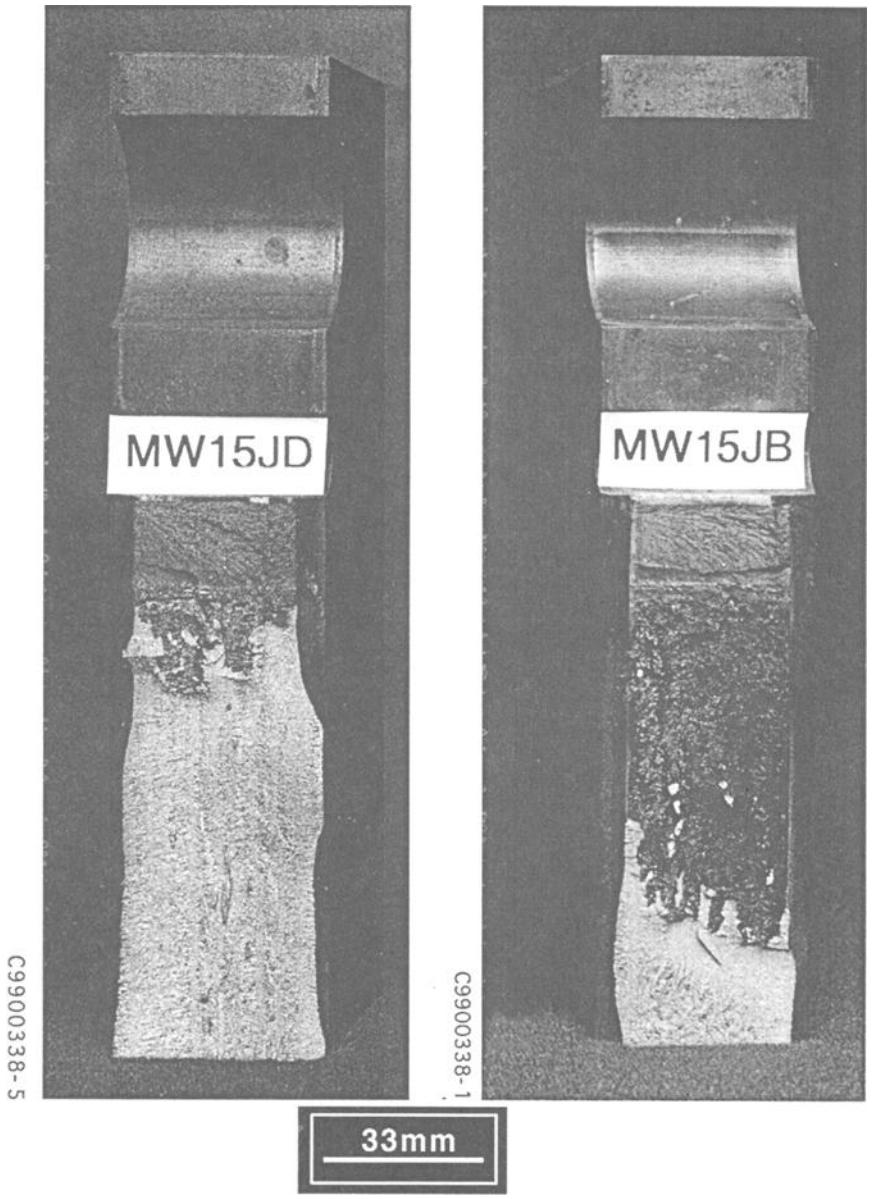


Fig. 5. Typical fracture surfaces for two unirradiated 127-mm-wide crack-arrest WF-70 weld metal specimens.

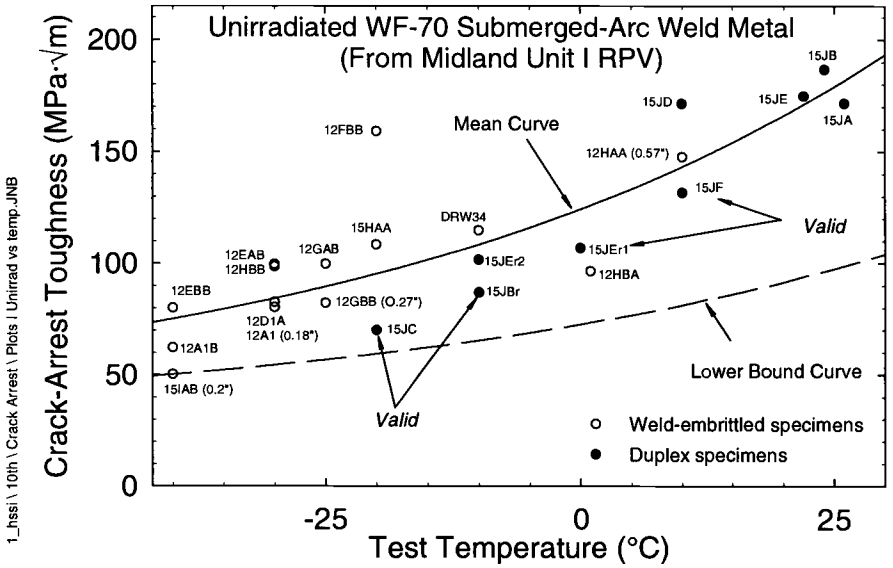


Fig. 6. Unirradiated crack-arrest toughness values K_a versus test temperature for the WF-70 weldment. The two curves are the mean and lower bound to the data. Note: For the purpose of conciseness, the "MW" prefixes were omitted from the specimen identification numbers.

The task group responsible for the ASTM crack-arrest test procedure E 1221 recognized the need for the data to be under plane-strain conditions. Conservative validity criteria were selected based on existing analytical and experimental results [12] to ensure that specimens that met those criteria would indeed be representative of plane-strain conditions. Even at that time, however, it was recognized that those criteria might be overly restrictive. They were chosen nonetheless to be utilized until more evidence justifying their relaxation could be amassed. More data are now available; for example, Ref. [13] presents crack-arrest test results that clearly violate the size criteria of E 1221-96 but that still accurately predict the arrest behavior of a thick-walled RPV under simulated pressurized thermal-shock loading. Based on these and other considerations, the ASTM task group will be asked to reconsider the relaxation of the validity criteria.

The curves in Fig. 6 were obtained by regression fitting an ASME K_{Ia}-type expression of the form

$$K_a = 29.4 + 94.8 \exp [0.01825 (T - T_x)] \quad (1)$$

where the asymptotic value of 29.4 from the ASME K_{Ia} curve was used and the values 94.8 and 0.01825 were obtained by fitting the unirradiated data with $T_x = 0$, and T is the

test temperature. The lower-bound curve is shown in Fig. 6 as a dashed curve; it was obtained by shifting the curve for Eq. (1) upward in temperature until it passed through the lowest value of K_a. This shift resulted in a lower-bound curve with $T_x = T_{LB} = 43.1\,°C$. It should be emphasized that there are insufficient data for these results to be transferred to other cases; they have been given here only for purposes of documenting the methods used.

The bounding values of the drop-weight nil-ductility temperature (NDT) and the RT_{NDT} values for this weld given in Table 2 were used to plot ASME K_{Ia} curves together with the experimental unirradiated crack-arrest toughness values (Fig. 7). The ASME K_{Ia} curves that were referenced to NDT values are in better agreement with the measured unirradiated values than those referenced to RT_{NDT}. A likely reason for this is the shape of the low-USE Charpy curves, which resulted in the relatively high temperatures necessary to fulfill the 68-J requirements for the determination of RT_{NDT}. There appears to be considerable conservatism in the values of RT_{NDT}. However, it is important to consider the relationship between the *irradiated* values of crack-arrest toughness and the ASME K_{Ia} curves that were referenced to an adjusted value of RT_{NDT}, and this will be discussed in the following section.

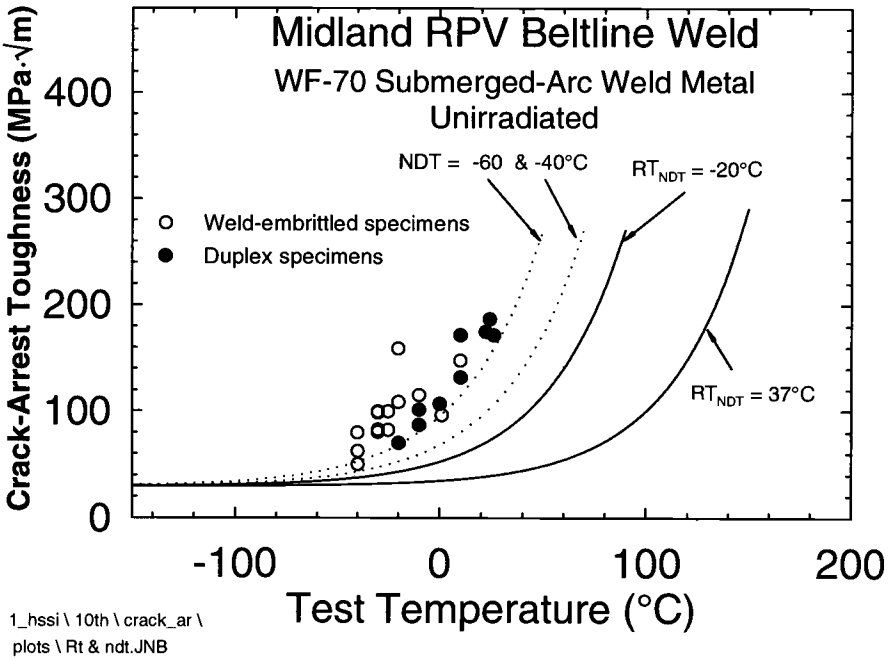


Fig. 7. Unirradiated crack-arrest toughness K_a versus test temperature for the WF-70 weldment and ASME K_{Ia} curves referenced to ***bounds*** *of NDT and RT_{NDT}.*

Tests on Material in the Irradiated Condition

The results of the tests on the irradiated crack-arrest specimens from the WF-70 weldment are presented in Fig. 8, which also includes the unirradiated data. Because of the different fluence levels of the crack-arrest specimens and the comparison Charpy results, all the irradiated crack-arrest results are referenced to the fluence level of the Charpy specimens. The method used is described in detail in Ref. [9] and is an "adjustment" to the test temperature. The mean curve for the irradiated values was obtained by fitting Eq. (1) to the data; the adjusted test temperatures for the values of T were used, which resulted in T_x = 110.5°C as the shift due to irradiation in the crack-arrest toughness mean curve. Lower-bound curves to the unirradiated and irradiated test results have also been plotted as dotted curves, and the shift between the lower-bound curves was approximately the same as that between the mean curves.

To quantitatively compare the margins between the ASME K_{Ia} curves and the experimental data, the ASME K_{Ia} curves were referenced to the bounding values of unirradiated and irradiated values of NDT and RT_{NDT}, and are shown in Fig. 9. To account for effects of irradiation, the ASME K_{Ia} curves based on NDT and RT_{NDT} have

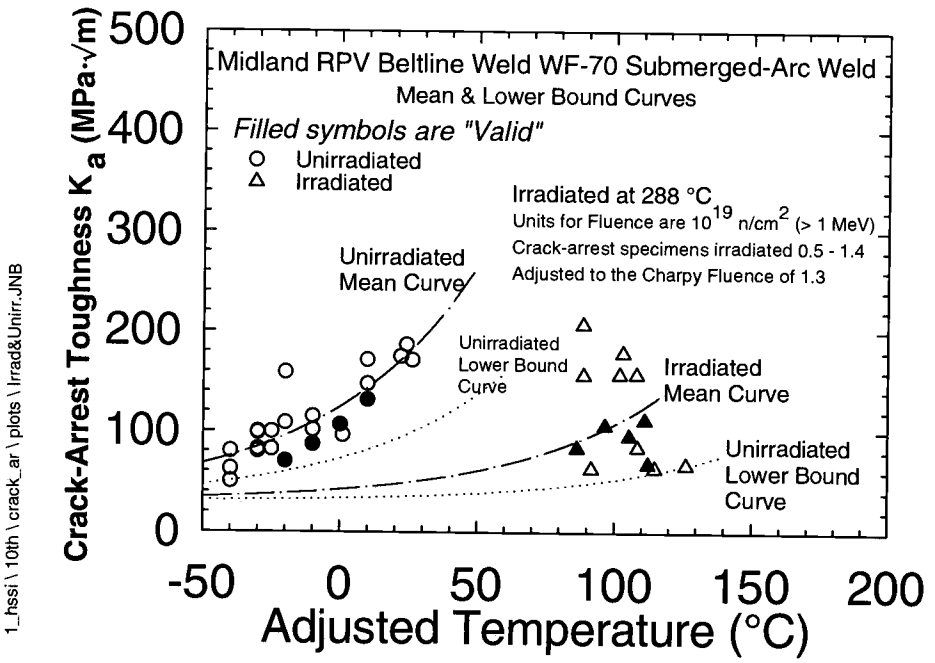


Fig. 8. Unirradiated and irradiated crack arrest toughness K_a versus test temperature for the WF-70 weldment. The dotted curves are lower bounds to the data obtained by shifting the mean curves to a higher temperature by the amounts shown.

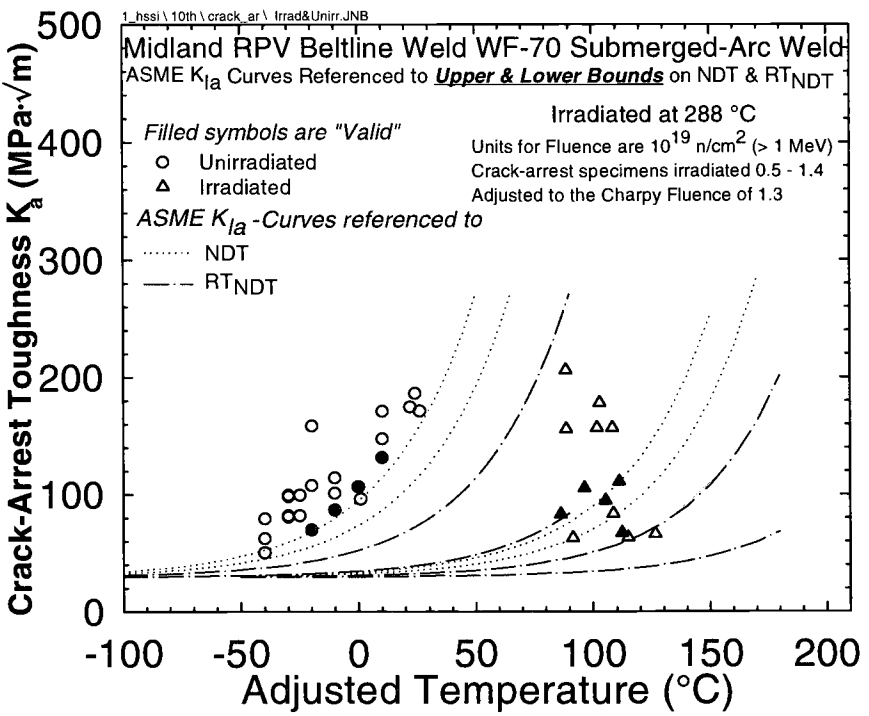


Fig. 9. Unirradiated and irradiated crack-arrest toughness values and ASME K_{Ia} curves referenced to ***bounds*** *of NDT and RT_{NDT}.*

been shifted by $\Delta TT_{41\text{-}J}$. The resulting adjusted value of RT_{NDT} is referred to as the "ART." The conservatism exhibited between the unirradiated data and the RT_{NDT}-based curve has diminished significantly in the irradiated case. The curve referenced to a lower-bound ART is now an approximate lower bound to the toughness values. The upper-bound ART curve has a substantial amount of conservatism between it and the data. In actual practice, only one value of ART is available, and a margin is applied to it.

It is also useful to determine whether any of the above shifts can be related to the shift in the arrest force F_a as estimated from the trace of an instrumented Charpy test (Fig. 10). The values of the arrest force F_a estimated from traces of Charpy impact energy tests of unirradiated and irradiated specimens are shown in Fig. 11. The temperature at which the value of K_a = 100 MPa·√m is attained is approximately −15°C (see Fig. 8). The value of F_a at this temperature is approximately 6.5 kN, and the temperature at this level of arrest force estimated from the beltline irradiated Charpy tests is ~40°C, indicating a shift of F_a of ~55°C, significantly less than the shift of the K_a curves (110.5°C).

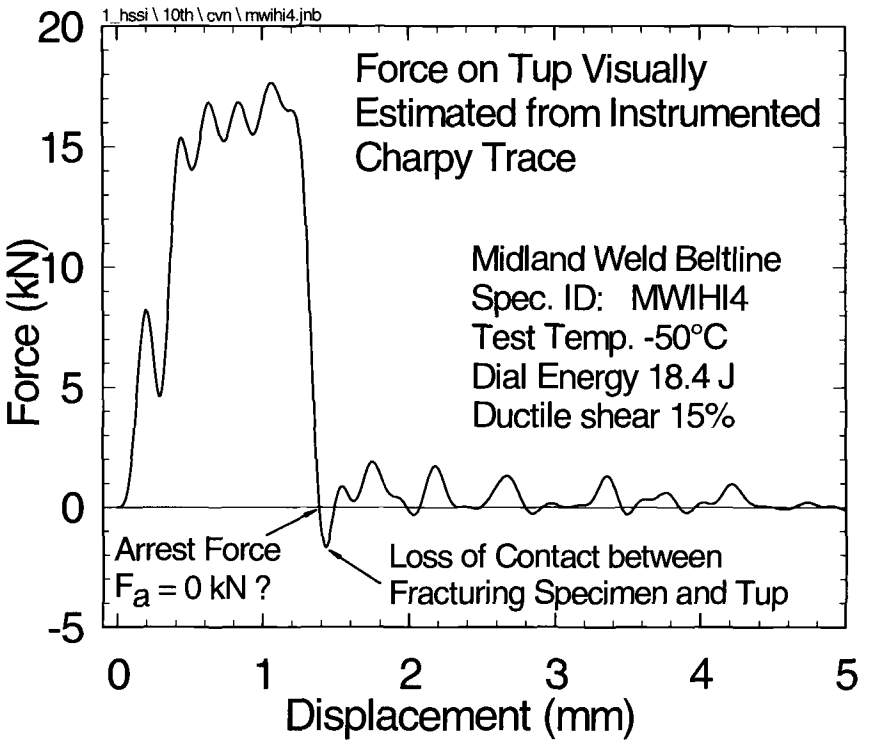


Fig. 10. The arrest force F_a as estimated from the trace of an instrumented Charpy test.

Comparison with Other Data

Much of the published data on the effect of irradiation on crack-arrest toughness are contained in a paper by Marschall and Rosenfield [14] and in an Electric Power Research Institute (EPRI) report by Mager and Marschall [15]. Four steels were tested in the EPRI project: two welds and two plate materials. Both the plates and the welds included a low-copper as well as a high-copper steel. Six to 12 specimens were tested from each of the 4 materials, for a total of 36 and 34 specimens in the unirradiated and irradiated condition, respectively. The results of the irradiated crack-arrest toughness were compared to the unirradiated data by shifting the irradiated data downward in temperature to achieve an approximate data coincidence. The EPRI downward shift is approximately comparable to the lower-bound shift used in this paper (obtained by shifting the ASME K_{Ia} curve upward in temperature until the first data point is encountered). The EPRI shift in K_{Ia} due

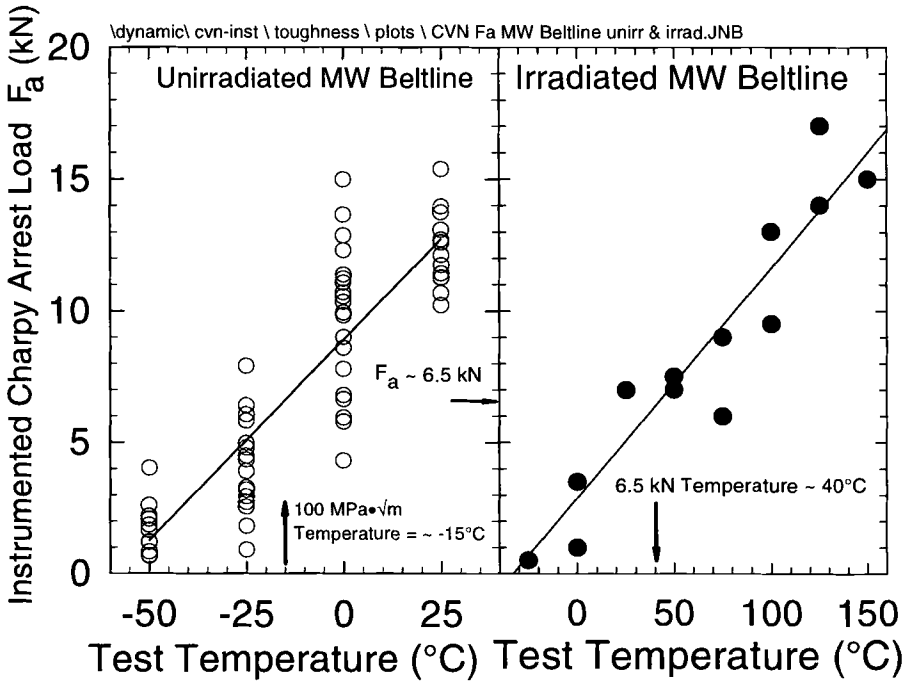


Fig. 11. Shift of the temperatures at a force level F_a = 6.5 kN of unirradiated and irradiated instrumented Charpy tests.

to irradiation for high-copper materials is less than the $\Delta TT_{41\text{-}J}$, whereas for the low-copper materials, the shift in K_{Ia} is slightly greater than or equal to $\Delta TT_{41\text{-}J}$. (In the EPRI program, the CVN shifts were also evaluated in several ways.)

Since the time of the above-mentioned investigations, ORNL has obtained irradiation K_a values for HSSI 72W and 73W welds and for the ASTM A 508 class 3 forging [9],[10],[11],[16],[17]. Shifts in the mean K_a curves, approximately equal to $\Delta TT_{41\text{-}J}$, obtained in those investigations are quite similar to those in this paper, although the mechanical properties and the range of copper content in the samples were quite different (see Table 3).

Table 3—*Comparison of copper contents, fluence ranges, and mean and lower-bound shifts of ORNL-tested crack-arrest specimens*

Sample	Copper content (%)	Adjusted $\Delta TT_{41\text{-}J}$ (°C)	K_a curve shifts (°C)		Fluence[a]
			Mean	Lower-bound	
HSSI 72W weld[b]	0.23	80	84	88	1.5–1.9
HSSI 73W weld[b]	0.31	93	80	82	1.5–1.9
ASTM A 508 class 3 forging	0.06	11	8	4	3.5
WF-70 beltline weld	0.21–0.32	110.5	107	105	1.3

[a]Fluence is given in units of 10^{19} n·cm^{-2} (> 1 MeV).
[b]These reported values are higher than those in Refs. [1] and [2] because the fluence of the subject crack-arrest specimens is higher.

Summary

Crack-arrest testing of high-copper submerged-arc welds has been performed on 25- and 33-mm-thick unirradiated and irradiated weld-embrittled specimens. Many of the crack-arrest test results are invalid according to E 1221-96, and yet they appear to be in a reasonable relationship with the valid data and consequently may be considered to be of value. Preliminary observations are as follows.

1. Values of irradiated crack-arrest toughness K_a were obtained for the submerged-arc WF-70 weld.

2. The shifts of mean and lower-bound K_a curves for the WF-70 weld are approximately the same as the corresponding 41-J CVN-impact energy level shifts.

3. The degree of conservatism of the ASME K_{Ia} curve referenced to the adjusted RT_{NDT} (ART) for the irradiated condition has decreased significantly from that exhibited in the unirradiated condition.

4. Further studies are needed to use the arrest force deduced from irradiated Charpy-instrumented data as an alternative means of estimating irradiated crack-arrest toughness.

Acknowledgments

This research is sponsored by the Office of Nuclear Regulatory Research, U.S. Nuclear Regulatory Commission, under Interagency Agreement DOE 1886-N695-3W with the U.S. Department of Energy under Contract No. DE-AC05-96OR22464 with Lockheed Martin Energy Research Corp. The authors appreciate the financial support and encouragement of the U.S. Nuclear Regulatory Commission.

In any task dealing with irradiated materials, many individuals are involved. The following individuals not only contributed to the various tasks but also made many useful suggestions and, without their able and enthusiastic assistance, this task would not have been completed. The authors acknowledge Dennis Heatherly for capsule design and operation, and Igor Remec and Chuck Baldwin for dosimetry. The authors also wish to acknowledge John J. Henry, Jr., and Eric T. Manneschmidt for specimen fabrication and testing of the unirradiated specimens and for test fixture assembly and shakedown; Joey Weaver and David Thomas for assistance with equipment; Pat Bishop, Gary Parks, Steve Childs, Pat Howard, Charlie DeVore, Tom Kenny, and Lloyd Turner for coordination of activities in the hot cell; Mikhail Sokolov for peer review; Julia Bishop for preparation of the manuscript; Judy Benton for electronic publishing; and Walter Koncinski for editing.

References

[1]. Nanstad, R. K., McCabe, D. E. , Menke, B. H., Iskander, S. K., and Haggag, F. M., "Effects of Irradiation on K_{Ic} Curves for High-Copper Welds," in *Effects of Radiation on Materials, 14th International Symposium (Volume II), ASTM STP 1046,* N. H. Packan, R. E. Stoller, and A. S. Kumar, Eds., American Society for Testing and Materials, West Conshohocken, PA, 1990, pp. 214–333.

[2]. Nanstad, R. K., Haggag, F. M., and Iskander, S. K., "Radiation-Induced Temperature Shift of the ASME K_{Ic} Curve," in *Transactions of the 10th International Conference on Structural Mechanics in Reactor Technology (SMiRT),* Vol. S, A. H. Hadgjian, Ed., Anaheim, CA, August 1989, pp. 143–48.

[3]. Nanstad, R. K., Haggag, F. M., McCabe, D. E., Iskander, S. K., Bowman, K. O., and Menke, B. H., *Irradiation Effects on Fracture Toughness of Two High-Copper Submerged-Arc Welds, HSSI Series 5,* NUREG/CR-5913, Vol. 1 (ORNL/TM-12156/V1), Martin Marietta Energy Systems, Inc., Oak Ridge Natl. Lab., October 1992.

[4]. Nanstad, R. K., McCabe, D. E., Swain, R. L., and Miller, M. K., *Chemical Composition and RT_{NDT} Determinations for Midland Weld WF-70,* NUREG/CR-5914 (ORNL-6740), Martin Marietta Energy Systems, Inc., Oak Ridge Natl. Lab., December 1992.

[5]. McCabe, D. E., Nanstad, R. K., Iskander, S. K., and Swain, R. L., *Unirradiated Material Properties of Midland Weld WF-70,* NUREG/CR-6249, (ORNL/TM-12777), Martin Marietta Energy Systems, Inc., Oak Ridge Natl. Lab., October 1994.

[6]. McCabe, D. E., Nanstad, R. K., Iskander, S. K., Heatherly, D. W., and Swain, R. L., *Evaluation of WF-70 Weld Metal from the Midland Unit 1 Reactor Vessel—Final Report,* NUREG/CR-5736 (ORNL/TM-13748), Lockheed Martin Energy Research Corporation, Oak Ridge Natl. Lab. (in preparation).

[7]. Nanstad, R. K., McCabe, D. E., and Swain, R. L., "Evaluation of Variability in Material Properties and Chemical Composition for Midland Reactor Weld WF-70," in *Effects of Radiation on Materials, 18th International Symposium, ASTM STP 1325*, R. K. Nanstad, M. L. Hamilton, F. A. Garner, and A. S. Kumar, Eds., American Society for Testing and Materials, West Conshohocken, PA, 1998, pp. 125–56.

[8]. McElroy, R. J., and Lowe, A. L., Jr., "Irradiation Embrittlement Modeling of Linde 80 Weld Metals," in *Effects of Radiation on Materials: 17th International Symposium, ASTM STP 1270,* D. S. Gelles, R. K. Nanstad, A. S. Kumar, and E. A. Little, Eds., American Society for Testing and Materials, West Conshohocken, PA, 1996, pp. 68–85.

[9]. Iskander, S. K., Milella, P. P., and Pini, A., *Results of Crack-Arrest Tests on Irradiated A508 Class 3 Steel*, NUREG/CR-6447 (ORNL-6894), Lockheed Martin Energy Research Corp., Oak Ridge Natl. Lab., February 1998.

[10]. Iskander, S. K., Corwin, W. R., and Nanstad, R. K., "Effects of Irradiation on Crack-Arrest Toughness of Two High-Copper Welds," in *Effects of Radiation on Materials: 15th International Symposium, ASTM STP 1125,* R. E. Stoller, A. S. Kumar, and D. S. Gelles, Eds., American Society for Testing and Materials, Philadelphia, 1992, pp. 251–69.

[11]. Iskander, S. K., Corwin, W. R., and Nanstad, R. K., *Results of Crack-Arrest Tests on Two Irradiated High-Copper Welds*, NUREG/CR-5584 (ORNL/TM-11575), Martin Marietta Energy Systems, Inc., Oak Ridge Natl. Lab., December 1990.

[12]. Barker, D. B., Chona, R., Fourney, W. L., and Irwin, G. R., *A Report on the Round Robin Program Conducted To Evaluate the Proposed ASTM Standard Test Method for Determining the Plane-Strain Crack-Arrest Fracture Toughness, K_{Ia}, of Ferritic Materials*, NUREG/CR-4996 (ORNL/Sub/79-7778/4), Martin Marietta Energy Systems, Inc., Oak Ridge Natl. Lab., January 1988.

[13]. Bryan, R. H., et al., *Pressurized-Thermal-Shock Test of 6-in.-Thick Pressure Vessels. PTSE-2: Investigation of Low Tearing Resistance and Warm Prestressing*, NUREG/CR-4888 (ORNL-6377), Martin Marietta Energy Systems, Inc., Oak Ridge Natl. Lab., December 1987.

[14]. Marschall, C. W., and Rosenfield, A. R., "Crack-Arrest Tests of Irradiated High-Copper ASTM A508 Submerged-Arc Weld Metal," in *International Conference on Fracture, Advances in Fracture Research*, Vol. 5, April 1981, pp. 2467–75.

[15]. Mager, T. R., and Marschall, C. W., *Development of a Crack Arrest Toughness Data Bank for Irradiated Reactor Pressure Vessel Materials*, EPRI NP-3616, Electric Power Research Institute, July 1984.

[16]. Iskander, S. K., Corwin, W. R., and Nanstad, R. K., *Crack-Arrest Tests on Two Irradiated High-Copper Welds. Phase II: Results of Duplex-Type Specimens*, NUREG/CR-6139 (ORNL/TM-12513), Martin Marietta Energy Systems, Inc., Oak Ridge Natl. Lab., March 1994.

[17]. Iskander, S. K., Milella, P. P., Pini, A., and Manneschmidt, E. T., "Crack-Arrest Testing of Irradiated Nuclear Reactor Pressure Vessel Steels at the Oak Ridge National Laboratory," *Journal of Testing and Evaluation*, Vol. 26, No. 6, November 1998, pp. 546–54.

Tetsuya Suzuki,[1] Keisuke Itoh,[2] Yoshinobu Naruse,[2] Hideki Matsui,[3] and Akihiko Kimura[1]

Effect of Location of V-Notch on Neutron Irradiation-Induced Shift in DBTT of HAZ of Welded Pressure Vessel Steel

Reference: Suzuki, T., Itoh, K., Naruse, Y., Matsui, H., and Kimura, A., **"Effect of Location of V-Notch on Neutron Irradiation-Induced Shift in DBTT of HAZ of Welded Pressure Vessel Steel,"** *Effects of Radiation on Materials: 19th International Symposium, ASTM STP 1366,* M. L. Hamilton, A. S. Kumar, S. T. Rosinski, and M. L. Grossbeck, Eds., American Society for Testing and Materials, West Conshohocken, PA, 2000.

Abstract: The effect of the location of the V-notch in the heat affected zone (HAZ) on the ductile-brittle transition behavior of neutron-irradiated welded A533B pressure vessel steel has been investigated utilizing the small specimen technique. Standard size, one-third size and 1.5 mm size Charpy V-notch specimens were prepared by changing the distance from the fusion boundary, so that a V-notch was located in the position to be evaluated. Neutron irradiation was performed in JMTR at 290℃ up to 0.75 and 1.3 x 10^{24} n/m^2. In both the cases before and after the irradiations, ductile-brittle transition temperature (DBTT) is lower and the upper-shelf energy is higher for so-called HAZ(M1) specimen, which has a V-notch 1mm away from the fusion boundary, than base metal and deposit. However, the DBTT of the HAZ(M4) specimen, with a V-notch 4 mm away from the boundary, is higher than that of base metal. As for the ΔDBTT, the HAZ(M1) and HAZ(M4) specimens showed equivalent and considerably larger ΔDBTT, respectively, than the base metal specimen; hence the HAZ(M4) specimen shows rather higher DBTT, that is, lower toughness. Micro-Vickers hardness measurements revealed that the M1 and M4 site showed the highest and lowest hardness, respectively.

Keywords: Charpy test, sub-sized specimen, heat affected zone, irradiation embrittlement, ductile-brittle transition temperature, pressure vessel steel

[1] Graduate Student and Professor, respectively, Institute of Advanced Energy, Kyoto University, Gokasho, Uji, Kyoto 611-0011, Japan.

[2] Research scientist, Chubu Electric Power Company, Inc., Nagoya 459, Japan.

[3] Professor, Institute for Materials Research, Tohoku University, Sendai 980-77, Japan.

Copyright© 2000 by ASTM International www.astm.org

Introduction

Welded joints of pressure vessel steel (PVS) for nuclear reactors have a complex metallographical structure and as a result have different mechanical properties depending on the location in the heat affected zone (HAZ). Hence, irradiation effects on weld joint are expected to be diverse and will depend on the location around the welded joints. Impact properties are known to be influenced by the notch conditions such as shape and depth. Impact fracture behavior will also depend on the microstructure at the notch position. The small specimen technique is useful in evaluating irradiation effects of the material in a localized area such as HAZ of welded joint[1]. Development of sub-sized Charpy V-notch specimen techniques has been done extensively[1-9] and it can be a promising option for RPV surveillance test of light water reactors, since the plant life extension program of a nuclear power reactor will demand supplemental surveillance specimens for monitoring irradiation embrittlement of PVS during extended operation. The Japanese standard for reactor surveillance requires HAZ specimens which have a V-notch at 1 mm inside of the base metal from the fusion boundary and the irradiation effect of these specimens have been investigated thoroughly. However, little research has been done to investigate the effects of V-notch location in the HAZ on the post-neutron irradiation impact properties of welded PVS. In this study, the effects of V-notch location in HAZ on the irradiation-induced shift in the ductile-brittle transition temperature (DBTT) are investigated, utilizing the small specimen technique in the evaluation of irradiation embrittlement of welded A533B.

Experimental Procedure

The material used in the present study was A533B PVS, a material used for nuclear reactor pressure vessels, produced by Japan Steel Works, LTD. The chemical composition of the material is shown in Table 1 with heat treatment conditions. Two steel plates of 183 mm thickness were welded by using the narrow gap submerged-arc welding method. Welding conditions are as follows: Arc voltage: 32V, Beam current: 630A, Traveling speed: 650mm/min, Pre-heat: done.

TABLE1--*Chemical composition of A533B cl.1 steel and deposit*

	C	Si	Mn	P	S	Ni	Cr	Cu	Mo	V	Al	N
Base	0.17	0.16	1.42	<0.003	<0.003	0.63	0.13	0.03	0.51	<0.01	0.026	0.0093
Deposit	0.10	0.07	1.27	0.008	<0.003	0.82	0.03	0.08	0.44	<0.01	0.006	0.0047

Quenching: 1163 K, 4 hr, water quench.
Tempering: 933 K, 4 hr, air cooled.

After post-weld heat treatment (898K, 15 hr), ultrasonic flaw detection was carried out and no significant defects were detected at the fusion boundaries. All these procedures of material preparations followed the method to fabricate the actual pressure vessel. Charpy V-notch(CVN) specimens, tensile specimens and TEM disks were cut out of the welded joint at the quarter thickness (1/4T) location. The procedure for specimen preparation followed the Japan Electric Association Criteria (JEAC4201), which specifies reactor surveillance procedures in Japan. In the Charpy tests, three different sizes of specimens were used; standard size, one-third size and 1.5 mm size specimens as shown in Fig. 1, to investigate the effects of specimen size on the impact properties. The anvil spaces of each specimen are 40, 15 and 12.5 mm, respectively. In order to determine the mechanical properties precisely at a given localized area, miniaturized specimens were used. Miniaturized Charpy V-notch specimens were prepared by changing the location of

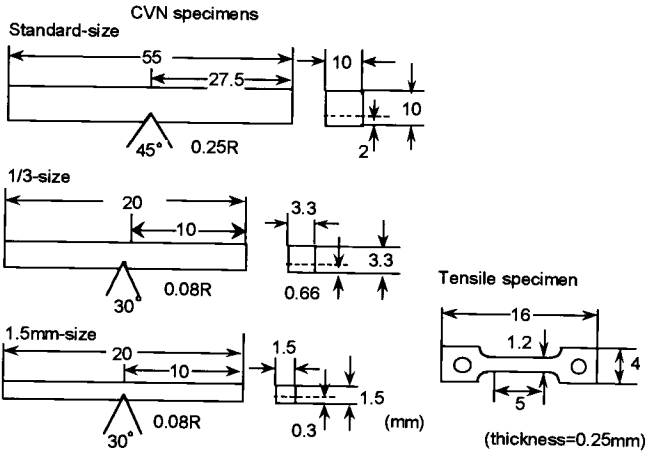


Fig.1--*Specimen geometries*

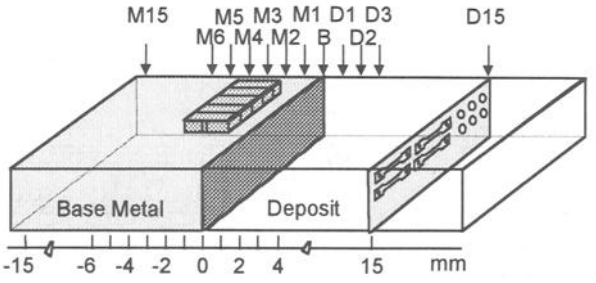


Fig.2--*Sampling position in the welded plate*

the V-notch, so that a V-notch was located at different distances from the fusion boundary as shown in Fig. 2. The V-notch was made on the specimen surface parallel to the fusion boundary, with crack growth parallel to the welding direction. For each specimen, a V-notch was fabricated after confirming the location of the fusion boundary by etching the surface. Specimens are identified by the symbols M forbase metal, D for deposit and B for fusion boundary. Thus, Mx denotes the specimen which is sampled from the position located at x mm away from the fusion boundary in the HAZ of base metal. Tensile specimens and TEM disks were punched out from the sheets, cut parallel to the fusion boundary by a multi-wire saw. The miniaturized specimens were fabricated from broken pieces of unirradiated standard size specimens fractured in a brittle manner in the lower shelf temperature region. Figure 3 is a flow chart of the present experiment, showing the procedure reproducing small specimens from standard size specimens. Four one-third size specimens or sixteen of 1.5mm size specimens can be produced from half of a standard size specimen.

Neutron irradiations for small specimens were performed utilizing the temperature controlled irradiation capsule in JMTR, with fluences up to 0.75 and 1.5 $\times$ 10^{24} n/m^2, at temperatures between 277 and 304℃, which depended on the position in the capsule.

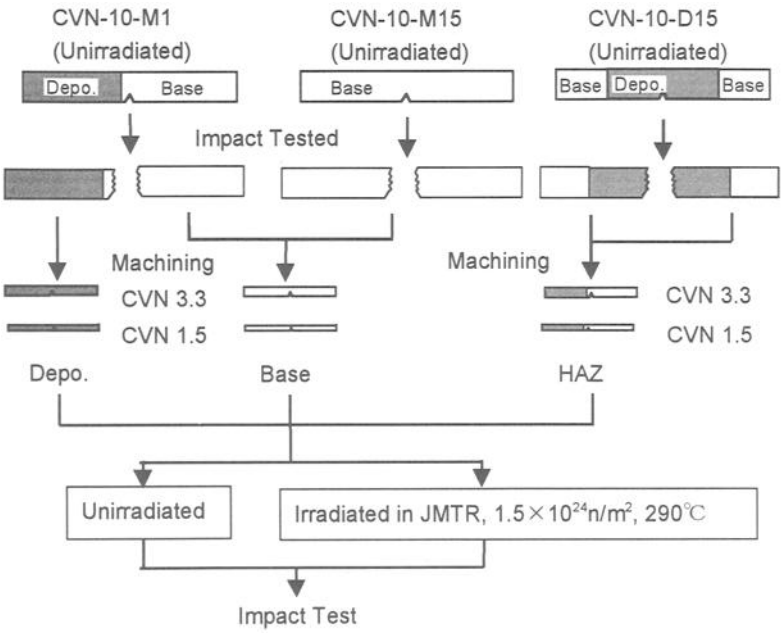


Fig.3--*General scheme of specimen preparation*

To evaluate the impact properties, Charpy impact tests were conducted using an instrumented drop-tower type impact testing machine with a maximum force capacity of 5 tons. The test temperature was measured by a thermocouple in contact with the specimen in the cold bath and controlled within an error of ± 0.5 K during tests. Impact load and displacement were measured by a load washer of quartz piezo-oscillator and a linear voltage differencial transducer (LVDT), respectively. The impact-absorbed energies were determined by measuring the total area under the load versus displacement curve. Each individual Charpy data set was fitted to the following hyperbolic function for obtaining the DBTT and the USE:

$$R(T)=a+b \tanh\{(T-T_0)/c\} \quad (1)$$

where T is test temperature and a, b, c and T_0 are regression coefficients. In this study, DBTT is defined to be T_0, which is the temperature corresponding to the mean value of upper-shelf and lower-shelf energy, since the traditional method of defining the DBTT at a given energy (e.g., 68 or 41 J) cannot apply to the sub-size specimen. The USE is defined to be (a+b). All the specimens tested in the upper shelf region did not break but just bent.

Hardness measurements were also carried out using a Vickers hardness testing machine with a load of 200 g.

Results and Discussion

1. Dependence of impact properties on the location of the V-notch in HAZ of unirradiated material

The dependence of the ductile-brittle transition temperature(DBTT) and the upper-shelf energy (USE) on the V-notch location of specimens obtained from three different sizes of specimens is shown in Fig. 4. As shown in this figure, the test results using standard size specimens indicate that the DBTT of HAZ(M1) specimens is lower than those of the base metal or weld, and there is no significant difference in DBTTs between the base metal(M15) and the deposit(D15). As for the USE, the highest energy was again observed for HAZ(M1) and the lowest one for deposit. The test results using miniaturized CVN specimens indicate almost the same relative relationship of DBTTs and USEs as the standard size specimens, as shown in Fig.4.

More extensive investigations were carried out for one-third size specimens. Although the DBTTs and the USEs of the M1 specimens are the lowest and the highest, respectively, it should be noted that the M4 specimen shows the highest DBTT, namely the lowest toughness among the specimens. In general, the USEs of the specimens in the deposit are smaller than those in the base metal and even in the HAZ region. In order to investigate the effects of neutron irradiation on the above results, especially for the M4

and M1 specimen, sub-sized specimens were fabricated from the broken pieces of the standard size specimens and irradiated in the JMTR.

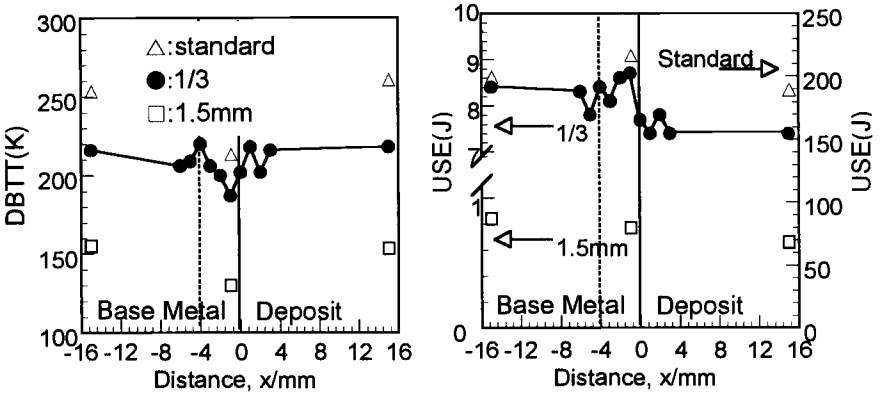


Fig.4--*Size effect of unirradiated material*

2. Effects of neutron irradiation

1) Comparison of irradiation embrittlement among base metal, deposit and HAZ

The ductile-brittle transition curves of base metal(M15), deposit(D15) and HAZ(M1) specimen before and after irradiation ($\phi_n = 1.3 \times 10^{24} n/m^2$) are shown in Fig.5 with the plots of DBTTs and USEs obtained from the 1.5 mm and one-third size specimens. The numerical data are also shown in Table 2. As shown in the figure, neutron irradiation induces a shift in the DBTT of 43K, 64K and 56K for the 1.5mm size M15, M1 and D15 specimens, respectively. The one-third size M15, M1 and D15 specimens also show an irradiation-induced shift in the DBTT of 26K, 42K, and 43K respectively. In both the size of specimens, the ΔDBTT of M1 specimen is larger than that of M15 specimen.

Before irradiation, the DBTT of the M1 specimen is lower than those of the M15 and D15 specimen, and the M1 and D15 specimen show a comparable ΔDBTT, as shown in the figure. The DBTT of the M1 specimen, however, is still lower than that of the M15 specimen after the irradiation. It is apparent that the M15(base metal) specimen indicate the smallest ΔDBTT among the specimens independent of specimen size. Finally, the D15 specimen indicates the highest DBTT after irradiation; that is, the lowest toughness. The 1.5 mm size specimens show little change in the USEs, while that of the one- third size specimens remarkably reduced by the irradiation. The reason of this behavior is under consideration and will be reported elsewhere. The USE obtained from the one-third

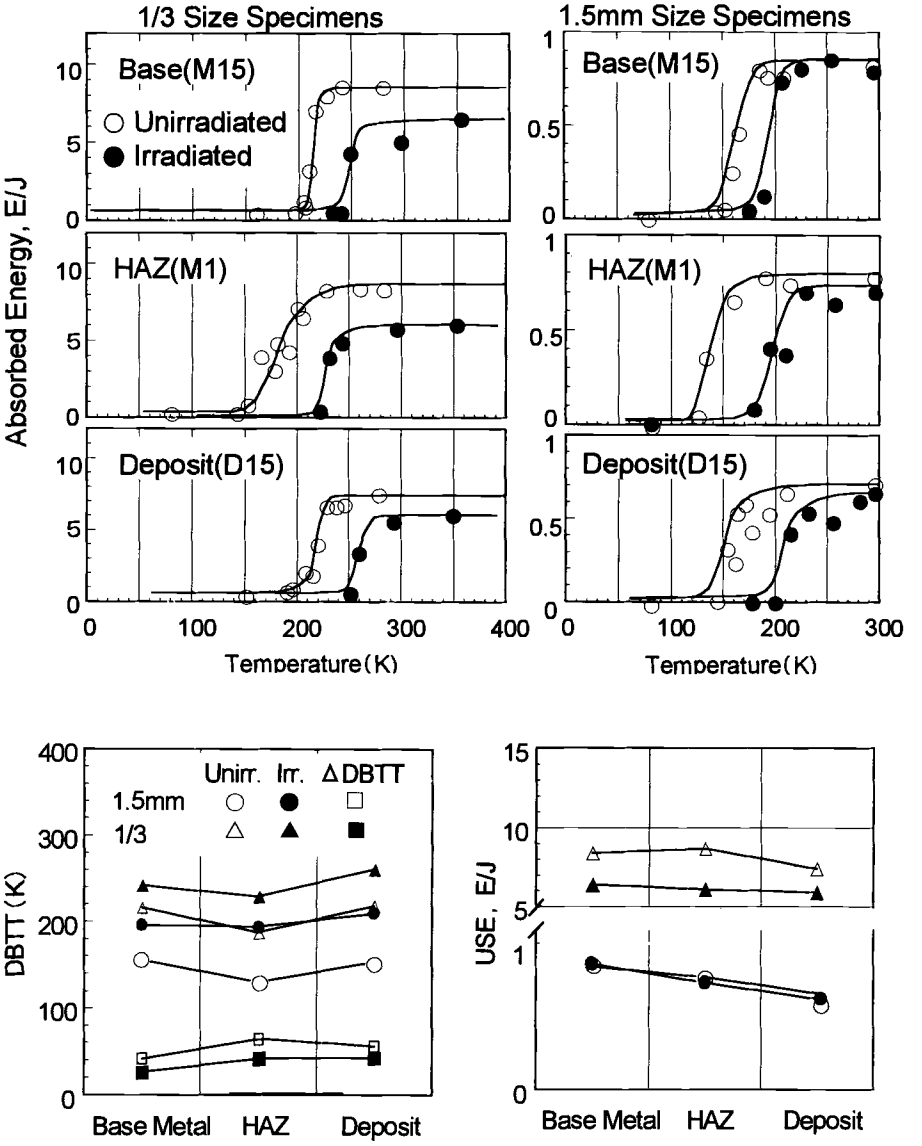


Fig.5--*Effect of neutron irradiation on the DBT behavior of base metal(M15), deposit(D15) and HAZ(M1) of 1.5mm and 1/3 size specimens(top). Comparison of DBTTs and USEs among those three materials (bottom) (Φ_n=1.3x10^{24}n/m^2). The DBTT of M1 specimen is the lowest, although the ΔDBTT is the largest among the specimens.*

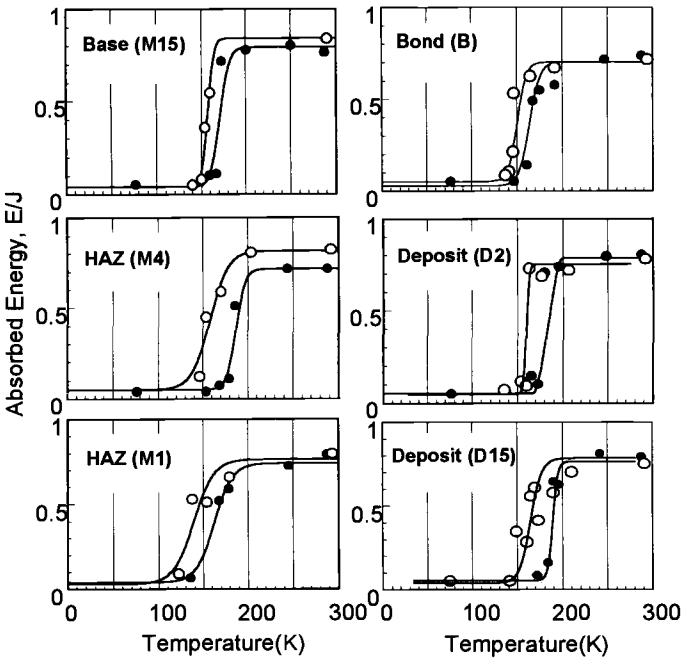


Fig.6--*Ductile-brittle transition behavior of base metal(M15), deposit(D2,D15) and HAZ(M1,M4) measured by 1.5 mm CVN specimens. (Φ_n=0.75x10^{24}n/m^2)*

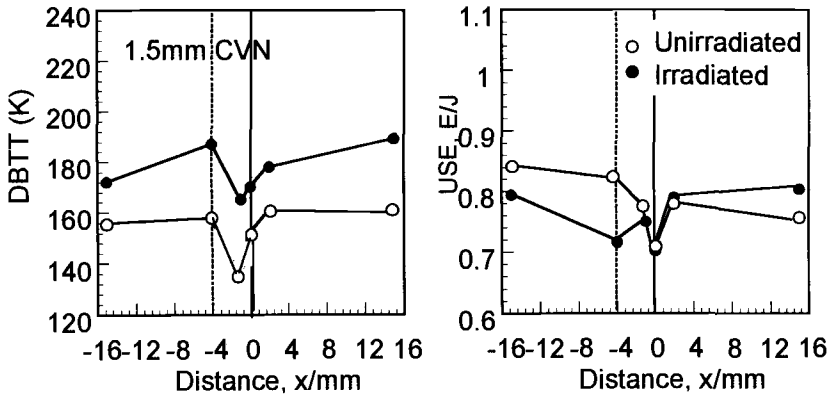


Fig.7--*Dependence of DBTT and USE on the location of notch (Φ_n=0.75x10^{24}n/m^2)*

size specimens is the lowest for deposit(D15) before and after irradiation. On the other hand the irradiation-induced drop in the USE obtained from the one-third size specimens is the most significant for the HAZ (M1) specimens as shown in the figure.

Although the irradiation embrittlement characterized by the shift in the DBTT and the drop in the USE is the most significant for the HAZ(M1) specimen among base metal, deposit and HAZ(M1), the toughness of the HAZ(M1) specimen is still higher than those of the D15 and M15 specimens after irradiation; that is, surveillance of the impact properties of base metal (M15) can be representative to those of HAZ(M1) specimen from the view of safety operation of the reactor. This result supports the ASTM Standard E185 that omitted the HAZ(M1) specimen from the reactor surveillance program. However, the tests of deposit should not be omitted from the surveillance program.

2) Dependence of DBTT and USE on the location of notch at welded joint

In order to investigate the dependence of post-irradiation DBT behavior on the location of the V-notch at the weld joint, six different specimen locations were selected for neutron irradiation (Φ_n=0.75x10^{24}n/m^2, Tirr.=290°C), using CVN 1.5 mm size specimens. The DBT behaviors of base metal (M15), deposit (D2 and D15), fusion boundary (B) and HAZ (M1 and M4) before and after the JMTR irradiation are shown in Fig. 6. In all of the specimens, the irradiation caused the shift of the DBT curves to higher temperatures, although the reduction of USE is rather small or even not observed. Plots of DBTTs and the USEs before and after irradiation are shown in Fig. 7. The numerical data are shown in Table 2. There are two sets of data for unirradiated specimens of M15, M1 and D15 and some numerical data are different from each other, although they are not too large. The difference is considered to be due to scatter of the obtained data. In general, the neutron irradiation always increases the DBTT of each specimens independent of the V-notch location. Before the irradiation, the DBTT of 1.5 mm size specimens was rather high for the M4 specimens and it was the lowest for the M1 specimens, which is similar to the results of one-third size specimen described above. As for the effects of irradiation, the M1, M4 and D15 specimens shows larger ΔDBTT than the others, although the dependence of DBTT on the location of V-notch is almost the same as before irradiation. Worthy of notice is that the ΔDBTT of M4 specimens is revealed to be rather large and resultantly the DBTT of irradiated M4 specimen is higher than M1 specimen, clearly indicating the importance of the M4 site rather than the M1 site. The M15 (base metal) specimen resulted in the smallest ΔDBTT among the specimens. As for the USE, again the irradiation effects was not reflected in the measured values, suggesting the ineffectiveness of the 1.5mm size specimens for evaluating the effect of irradiation on USE of A533B PVS.

3) Hardness measurements

Micro-Vickers hardness measurements across the fusion boundary were carried out for a one-third size CVN specimen before impact test. Figure 8 shows the line profiles of the hardness across the fusion boundary of unirradiated and irradiated (ϕ_n = $1.3x10^{24}n/m^2$) specimen. Before and after irradiation, the M1 site is the hardest and almost same as the sites in deposit. As clearly shown in the figure, the M4 site shows the lowest hardness before the irradiation. Neutron irradiation induces the increase in hardness by 85, 110 and 110 for M6, M1 and D6 sites, respectively. That is, the irradiation hardening is larger at the M1 site than the M6 and D6 sites (M6 and D6 can be considered to be the same as base metal and deposit, respectively). The M4 site and the M1 site shows equivalent increase in the hardness. Again the hardness of the M4 site is rather smaller than the M1 and M6 site after the irradiation. This tendency of irradiation hardening shows no good agreement with the shift in the DBTT described above. That is, the M4 and M1 specimens showed equivalent and considerably larger ΔDBTT in comparison with base metal (M6) as shown in Fig.6. Relationship between DBTT and Hv of six different specimen locations is shown in Fig. 9, indicating that there are two groups of plots: 1) the DBTT increases with increase in the Hv (M15, D15) as usual , 2) while the DBTT decreases with increase in the Hv (M4, B, M1). It is considered that a reverse relationship between DBTT and Hv of different location in HAZ is due to the reduction of cleavage fracture stress accompanied by the reduction of yield stress. An examination of microstructure by TEM revealed that the precipitation morphology of carbides depended on the location in HAZ and the density and size of carbides are lower and larger in the M4 than in the M1. The detail of TEM study will be reported else where.

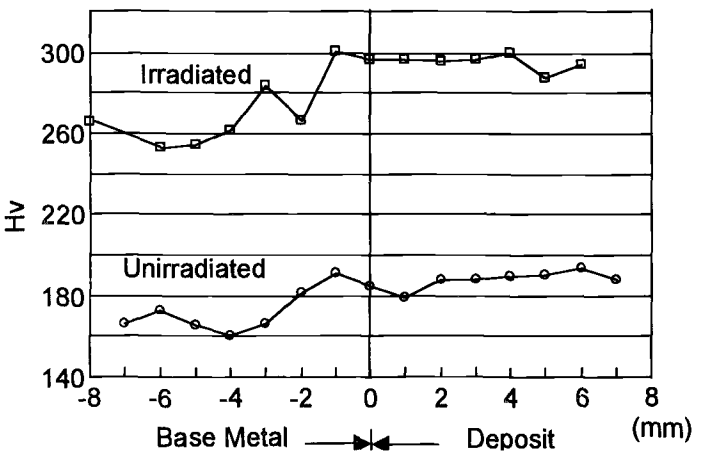


Fig.8--*Hardness property of welded joint*

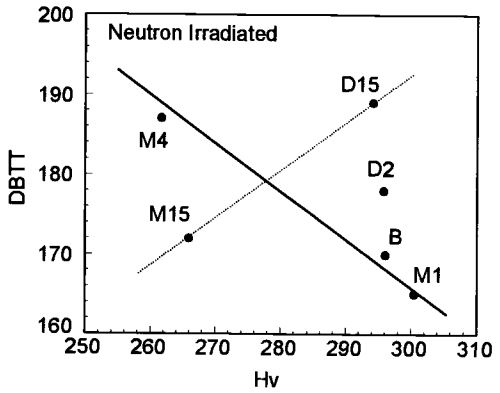


Fig.9—*Relationship between ΔDBTT and ΔHv of six different specimen locations*

3. A consideration of size effect

In the previous work[10], it was shown that there was a linear relationship between DBTTs of 1.5 mm sub-sized specimen and standard size specimen:

$$\text{DBTT (standard)} = 1.62 \times \text{DBTT (1.5mm)}$$

Although there is no evidence that the relationship holds for the specimens in HAZ, the DBTT of standard size HAZ specimens can be roughly estimated from the equation. The DBTT of M4 specimen is higher than base metal (M15) after neutron irradiation to 0.75×10^{24}n/m^2 by 15 K using 1.5 mm size CVN specimens, which corresponds to 24 K higher DBTT in standard size specimens. This amount of difference is considered to be significant.

TABLE 2--*Summary of mechanical properties.*

	1.5mm size (ϕ =0.75x10^{24}n/m^2)				1.5mm size (ϕ =1.3x10^{24}n/m^2)				1/3 size (ϕ =1.3x10^{24}n/m^2)			
	DBTT(K)		USE(J)		DBTT(K)		USE(J)		DBTT(K)		USE(J)	
	Unirr.	Irr.	Unirr.	Irr.	Unirr.	Irr.	Unirr.	Irr.	Unirr.	Irr.	Unirr.	Irr.
M15	155	172	0.84	0.79	155	196	0.84	0.86	216	242	8.4	6.4
M4	157	187	0.82	0.72	—	—	—	—	—	—	—	—
M1	135	165	0.79	0.75	130	194	0.77	0.73	187	229	8.7	6.1
B	151	170	0.70	0.70	—	—	—	—	—	—	—	—
D2	160	178	0.78	0.79	—	—	—	—	—	—	—	—
D15	159	189	0.75	0.80	154	210	0.75	0.62	218	261	7.4	5.9

Irradiation temperature:290℃

Conclusion

The dependence of DBT behavior on the location of the V-notch in the HAZ of welded A533B was investigated before and after neutron irradiation in JMTR. Primary results are:

1) Before irradiation, the highest toughness is observed in the HAZ(M1) specimen which have V-notch at 1mm away from the fusion boundary, while the lowest is observed for the M4 specimen which have V-notch at 4 mm away from the fusion boundary.
2) The irradiation embrittlement characterized by the shift in the DBTT and the drop in the USE is the most significant for the HAZ(M1) specimen among base metal, deposit and HAZ(M1), although the toughness of the HAZ(M1) specimen is still higher than those of the D15 and M15 specimen even after the irradiation.
3) The HAZ(M1) and HAZ(M4) specimens showed equivalent and considerably larger ΔDBTT; hence after irradiation, the HAZ(M4) specimens show the higher DBTT than M1 and M15 specimens.
4) Before and after irradiation, the hardness is the highest at M1 site and lowest at around M4 site.
5) The 1.5 mm size specimen is not suitable for the evaluation of the effect of irradiation on USE of A533B PVS studied in this work.

It is concluded that in surveillance tests of welded joints of PVS, the impact tests of so-called HAZ specimens having a V-notch at 1mm away from the fusion boundary can be represented by the tests of base metal. Definition of HAZ specimen could be reconsidered for surveillance tests, since the M4 site is lower in fracture toughness and shows rather higher DBTT than the M1 and M15 site both before and after neutron irradiation.

References

[1] Hu, W. D. and Gelles, D. S., "Miniature Charpy Impact Test Results for the Irradiated Ferritic Alloys HT-9 and Modified 9Cr-1Mo," *Proc. Topical. Conf. on Ferritc Alloys for Use in Nuclear Energy Technologies.* 1983, pp. 631-645.

[2] Corwin, W. R. and Hougland, A. M., "Effect of Specimen Size and Material Condition on the Charpy Impact Properties of 9Cr-1Mo-V-Nb Steel," *The Use of Small-Scale Specimens for Testing Irradiated Material. ASTM STP 888,* 1986, pp. 325-338.

[3] Lucas, G. E., Odette, G. R., Sheckherd, J. W., McConnel, P. and Perrin, J., "Subsized Bend and Charpy V-Notch Specimens for Irradiated Testing," *The Use of Small-Scale Specimens for Testing Irradiated Material. ASTMSTP 888,* 1986, pp. 304-324.

[4] Abe, F., Noda, T., Araki, H., Okada, M., Narui, M. and Kayano, H., "Effects of Specimen Size on the Ductile-Brittle Transition Behavior and the Fracture Sequence of 9Cr-W Steels," J. Nucl. Mater., 159, 1987, pp. 292-301.

[5] Alexander, D. J. and Klueh, R. L., "Specimen Size Effects in Charpy Impact Testing," *Charpy Impact Test: Factors and Variables, ASTM STP 1072*, 1990, pp. 179-191.

[6] Kumar, A. S., Louden, B. S., Garner, F. A. and Hamilton, M. L., "Recent Improvements in Size Effects Correlations for DBTT and Upper Shelf Energy of Ferritic Steels," *Small Specimen Test Techniques Applied to Nuclear Reactor Vessel Thermal Annealing and Plant Life Extension, ASTMSTP 1204*, 1993, pp. 47-61.

[7] Kurishita, H., Kayano, H., Narui, M., Yamazaki, M., Kano, Y., and Shibahara, I., "Effects of V-Notch Dimensions on Charpy Impact Test Results for Differently Sized Miniature Specimen of Ferritic Steel," Mater. Trans., JIM, 34(11), 1993, pp. 1042-1052.

[8] Sokolov, M. A. and Nanstad, R. K.,, "On Impact Testing of Subsize Charpy V-Notch Type Specimens," *Effects of Radiation on Materials: 17th Int. Symp., ASTM STP 1270*, 1996. Pp. 384-414.

[9] Kurishita, H., Shibahara, I., Narui, M., Mizuta, S. and Kayano, H., "Evaluation of the Upper Shelf Energy for Ferritic Steels from Miniaturized Charpy Specimen Data, " *Effects of Radiation on Materials: 17th Int. Symp., ASTM STP 1270*, 1996, pp775-789.

[10] Kimura, A., Suzuki,T., Jincho,M. and Matsui,H., "Dependence of Ductile-Brittle Transition Behavior on the Specimen Size and Location of Notch in the HAZ of Welded A533B PVS", Small Specimen Test Technique, ASTM STP 1329, 1997, pp. 110.

Rachid Chaouadi,[1] Eric van Walle,[1] Albert Fabry,[1] Marc Scibetta,[1] and José Van de Velde[1]

Fracture Toughness Test Results of Precracked Charpy Specimens of Irradiated 73W Weld Material

Reference: Chaouadi, R., van Walle, E., Fabry, A., Scibetta, M., and Van de Velde, J., **"Fracture Toughness Test Results of Precracked Charpy Specimens of Irradiated 73W Weld Material,"** *Effects of Radiation on Materials: 19th International Symposium, ASTM STP 1366,* M. L. Hamilton, A. S. Kumar, S. T. Rosinski, and M. L. Grossbeck, Eds., American Society for Testing and Materials, West Conshohocken, PA, 2000.

Abstract: This work investigates the use of precracked Charpy specimens to predict fracture toughness behaviour of reactor pressure vessel steels. Fracture toughness measurements were performed on the 73W weld material previously tested by Oak Ridge National Laboratories (ORNL). Charpy-size specimens were tested in three-point bend and compared with the original data obtained on large compact tension (CT) samples. Fracture toughness tests were performed in both unirradiated and irradiated ($T_{irrad} \approx 288°C$ and $\Phi \approx 1.5\ 10^{19}$ n/cm², E>1MeV) conditions. Most of the Charpy size samples were reconstituted from broken CT specimens. Fracture toughness data obtained using Charpy size samples are in good agreement with results from large CT samples. Moreover, the various temperature shifts measured by the Charpy impact test data are in agreement with the fracture toughness shifts. Reconstitution results in a decrease of the upper shelf energy but has little effect on the other transition parameters.

Keywords: fracture toughness, Charpy, transition, reconstitution, reactor pressure vessel steel, reference temperature, master curve

Introduction

Recently, there was a major worldwide effort in support of the use of the master curve approach to characterize ferritic steels in the transition regime. In the nuclear field, current evaluation of the fracture toughness of pressure vessel steels in the transition region is established through empirical correlations based on the Charpy transition curve; the irradiation-induced shift of the Charpy transition curve is empirically correlated to the shift of the ASME fracture toughness transition reference curve. More specifically, the shift of the fracture toughness transition curve is postulated to be the shift of the Charpy impact transition curve at the specific energy index of 41 J. This procedure may penalize some reactors that demonstrate a so-called 'outlier behaviour' in regard of this methodology. Therefore, direct fracture toughness measurements are desirable. However, the necessary specimen size of irradiated material often prohibits such measurements. Recent

[1] SCK•CEN, Reactor Materials Research, Boeretang 200, 2400 Mol, Belgium.

Copyright© 2000 by ASTM International www.astm.org

developments on size adjustment allow attractive use of small samples to determine the fracture toughness behaviour. In particular, the Charpy geometry as it is used in surveillance capsules to monitor vessel degradation gives a good opportunity to verify such methodologies.

Reconstitution technology allows Charpy specimens to be remanufactured from broken halves. Therefore, the interest in using Charpy samples to measure fracture toughness became obvious but a sound demonstration of its ability to provide relevant data is needed.

In the present work, fracture toughness measurements were performed on precracked Charpy specimens loaded in three-point slow bending. Attention was given to irradiated samples. The 73W weld material, irradiated and well characterized at Oak Ridge National Laboratories (ORNL), offers a good opportunity to demonstrate the ability of the Charpy sample to measure the fracture toughness. The fracture toughness data were then analyzed in terms of the master curve concept following the recommendations given in the ASTM Standard Test Method for Determination of Reference Temperature, T_0, for Ferritic Steels in the Transition Range (E1921-98).

Materials and Testing

The 73W reference weld material was selected as it was well characterized and documented at ORNL: tensile, drop weight, Charpy impact, fracture toughness and crack arrest data in both unirradiated and irradiated conditions are available [1-3]. The chemical composition and tensile properties are given in Tables 1 and 2.

Broken 2T- and 4T- compact tension specimens were supplied by ORNL for further investigation. From the remaining weld material (typically 12 to 16 mm thick) Charpy size specimens were reconstituted (one side only) using the arc stud welding technique [4]. The crack orientation was taken identical to the original CT specimen. In addition, a weld block was also provided for Charpy size fabrication (not reconstituted).

The 73W weld material was irradiated at ORNL at 288°C up to an average fluence of 1.5 10^{19}n/cm^2. Complete characterization of this material can be found in [1-3].

Tensile, Charpy impact and fracture toughness tests were performed according to prevailing standards. Tensile tests were performed in 3 orientations, namely, T (transverse), L (longitudinal or welding direction) and S (short-transverse). All Charpy specimens are manufactured in the T-L orientation. The Charpy tests are carried out in a 300 J impact machine with an instrumented ASTM tup. For fracture toughness measurements, the Charpy specimens are first precracked and 20% side-grooved before testing. The precracking and testing were carried out on a servohydraulic tensile machine equipped with an environmental chamber allowing testing in the range -200° to +600°C. The final K_{max} during precracking was maintained below 20 MPa$\sqrt{m}$. The tests were conducted under displacement control at a constant crosshead speed of 0.1 mm/min. The specimen front surface, where the notch is located, was machined to allow fixation of the clip gauge. The applied load, crosshead displacement and crack mouth opening displacement were continuously recorded up to fracture. A computer routine allowed calculation of the fracture toughness at cleavage initiation. After testing, the specimens are heat tinted at 300°C for 15 min and further broken at liquid nitrogen temperature. From the fracture surfaces, the initial and final crack lengths were measured with the 9-point average method.

Table 1--*Chemical composition (%-wt).*

C	Si	Mn	P	S	Cr	Cu	Mo	Ni
0.10	0.45	1.56	0.005	0.005	0.25	0.31	0.58	0.60

Table 2--*Tensile properties at ambient temperature.*

yield stress σ_y (MPa)	ultimate stress σ_u (MPa)	uniform elongation ε_u (%)	total elongation ε_t (%)	reduction of area RA (%)
490	600	12	22	68

The 4T-CT specimens used here were 73W-18 and 73W-21, previously irradiated to a fast neutron fluence of 1.64 10^{19} n/cm^2 and tested at 50°C and 65°C, respectively. Figure 1 shows how the specimens were extracted from the broken CT specimen. The specimens were identified as 18XYZ where 18 indicates the original specimen number, X is the part of the CT specimen (L or R), Y for the layer (A to M) and Z for the position in the layer (1 to 8). After reconstitution, the remaining 73W weld material at the notch position is between 7 and 12 mm in length.

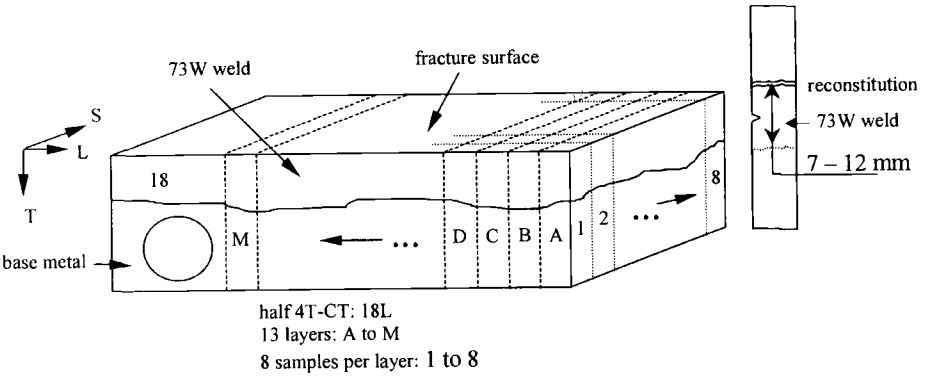


Figure 1--*Cutting scheme of the 10×10×40 mm inserts of the half 4T-CT labeled 73W-18. 104 specimens were obtained from this block. The remaining weld length is between 10 and 15 mm.*

Results and Discussion

Tensile Data

For tensile testing, a small cylindrical geometry of 3 to 3.6 mm diameter and 18 mm gauge length was selected. Specimens were taken in the three orientations, L, T and S. Within the experimental scatter, no orientation effect is observed (see Table 3). Figure 2 shows that these results are consistent with ORNL data obtained on standardized samples.

Table 3--*Tensile test results in the baseline condition. No orientation effect is found.*

Sp. Id.	orientation	T	σ_y	σ_u	ε_u	ε_t	RA
73W-L2	L	-184	857	921	17	27	56
73W-L5	L	-150	736	840	17	26	57
73W-L3	L	-100	604	734	15	27	64
73W-L6	L	-50	537	665	14	22	65
73W-L1	L	22	516	625	12	21	71
73W-L7	L	100	472	581	10	18	66
73W-L8	L	200	468	581	9	16	63
73W-L4	L	288	474	607	10	16	59
73W-S2	S	-184	847	915	16	25	53
73W-S5	S	-150	720	826	17	26	58
73W-S3	S	-100	587	726	15	24	64
73W-S6	S	-50	539	669	13	21	64
73W-S1	S	22	501	617	12	20	69
73W-S2	S	150	462	569	9	16	65
73W-S4	S	288	462	590	9	16	60
73W-D11	T	-184	847	911	18	26	48
73W-F6	T	-100	567	709	15	25	66
73W-D10	T	22	487	599	11	21	71
73W-F7	T	288	468	590	9	16	60

σ_y: 0.2%-yield stress (MPa) ε_u: uniform elongation (%)
σ_u: ultimate tensile strength (MPa) ε_t: total elongation (%)
RA: reduction of area (%)

Similarly, in the irradiated condition, the tensile properties are in good agreement with ORNL data (see Table 4 and Figure 2). Again, no orientation effect was found.

Table 4--*Tensile test results in the irradiated condition (Φ=1.64 10^{19} n/cm², E>1 MeV). No orientation effect is found.*

Sp. Id.	orientation	T	σ_y	σ_u	ε_u	ε_t	RA
73W-18R-A3	T	-178	993	1012	12	15	33
73W-18R-A2	T	-75	697	785	7	13	60
73W-18R-A1	T	26	631	720	6	13	59
73W-18R-A5	T	125	571	651	5	16	56
73W-18R-A6	T	288	584	683	6	13	50
73W-21L-H5	S	-175	1018	1043	9	13	34
73W-21L-H4	S	-75	738	840	8	15	60
73W-21L-H1	S	22	655	744	6	13	64
73W-21L-H3	S	260	605	696	4	9	52

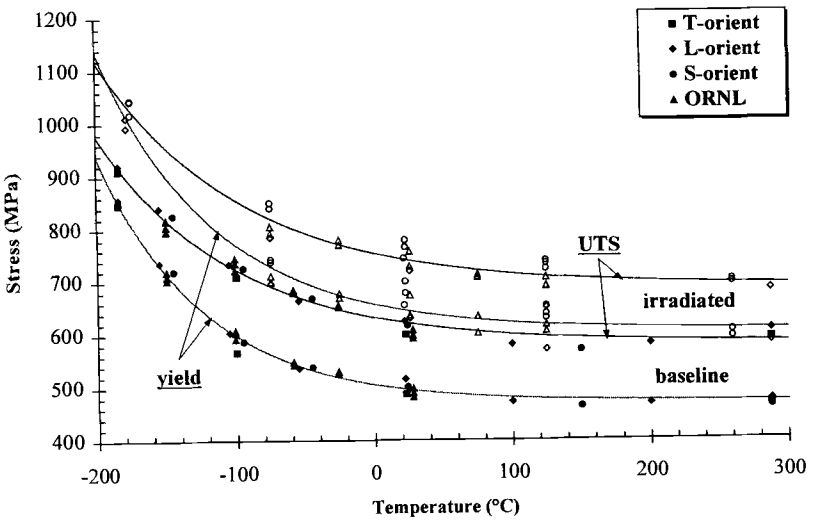


Figure 2--*Tensile properties: no effect of specimen orientation is found on the yield or tensile strengths. These data are in good agreement with ORNL ones [1,2].*

The yield stress, σ_y, is fitted throughout the temperature range [-200 to +300°C] by the following equation:

$$\sigma_y \text{ (MPa)} = C_1 + C_2 \exp [\, C_3 \, T(°C)]$$

where the constants C_1, C_2 and C_3 are given in Table 5.

Table 5-- *Fitting constants to represent the evolution of the yield stress as a function of test temperature.*

condition	C_1	C_2	C_3
baseline	467	36	-0.0129
irradiated Φ=1.64 10^{19}	594	55	-0.0113

Charpy Impact Tests

In the baseline condition, two series of Charpy specimens were impact tested: one series was reconstituted from a broken half CT while the other was taken from a weld block (full weld thickness). The test results are given in Tables 6 and 7, respectively.

The energy, shear fracture appearance and lateral expansion as a function of test temperature are shown in Figures 3 to 5, respectively. A loss of upper shelf energy was noticed with the reconstituted specimens. Details on the effect of insert length on the loss of the upper- shelf energy can be found in [4]. In the meantime, no effect is found in the transition region. The ORNL data are also shown in Figures 3 to 5 together with the 1σ confidence bounds relative to the mean tanh fit curves. Globally, despite the small number of specimens tested here in comparison to ORNL, the SCK•CEN data are in agreement with ORNL data.

Table 6-- *Charpy impact test results in the baseline condition: reconstituted specimens.*

Sp. Id.	T (°C)	E (J)	SFA (%)	LE (mm)
73W-2	-100	5.4	0	0.069
73W-3	-81	4.1	0	0.051
73W-6	-61	35.4	8	0.521
73W-5	-26	66.4	33	1.082
73W-4	0	77.2	55	1.279
73W-8	24	100.5	81	1.710
73W-9	24	96.0	84	1.568
73W-7	38	105.7	89	1.824
73W-10	100	109.4	100	1.953
73W-1	150	119.6	100	2.162
73W-11	200	112.0	100	2.090
73W-12	300	124.6	100	2.262

T: test temperature SFA: shear fracture appearance
E: dial energy LE: lateral expansion

Table 7-- *Charpy impact test results in the baseline condition: standard specimens.*

Sp. Id.	T (°C)	E (J)	SFA (%)	LE (mm)
73W-B6	-100	3.76	0	0.100
73W-B11	-90	15.0	1	0.260
73W-B15	-70	18.6	6	0.230
73W-B08	-40	13.4	10	0.370
73W-B07	-30	56.4	23	0.950
73W-B14	-20	64.7	45	1.130
73W-B10	-10	88.1	56	1.430
73W-B12	0	95.1	63	1.640
73W-B13	24	132.7	89	2.170
73W-B16	100	139.5	100	2.190
73W-B09	190	133.0	100	2.170
73W-B17	288	151.3	100	2.560

In the irradiated condition, only reconstituted samples were available. The test results are given in Table 8. Unlike the unirradiated condition, the upper-shelf energy does not seem to be affected by reconstitution, in agreement with [4] (see Figure 11 of [4]). As for unirradiated condition, good agreement was found between SCK•CEN and ORNL data (see Figures 3 to 5).

The usual parameters characterizing the Charpy impact transition behaviour are summarized in Table 9: N is the number of Charpy specimens, USE is the upper shelf energy, T_{68J}, T_{41J}, T_{28J}, $T_{50\%}$ and $T_{0.89mm}$ are the temperatures corresponding to 68 J, 41 J and 28 J energy, 50% shear fracture appearance and 0.89 mm lateral expansion, respectively. As can be seen, a drop of upper-shelf energy is observed with reconstituted samples but does not become significant for low upper shelf energy (~100 J). By contrast shear fracture appearance and lateral expansion remain unaffected by the reconstitution process. The other transition parameters are almost unaffected although some small differences are observed, for example the 68 J energy level of irradiated material. However, this can be associated with experimental uncertainties related to the small number of test specimens and the material variability. Otherwise, the overall agreement between SCK•CEN and ORNL data is very satisfactory. The temperature shifts of SCK•CEN and ORNL data, given in Table 9, are also consistent.

Table 8-- *Charpy impact test results in the irradiated condition: reconstituted specimens.*

Sp. Id.	T (°C)	E (J)	SFA (%)	LE (mm)
18-RE-3	-40	2.59	2	0.041
18-RB-7	-20	11.18	6	0.317
18-RB-6	0	25.5	11	0.537
18-LC-3	24	34.65	17	0.386
18-LC-6	50	36.59	35	0.693
18-RE-1	65	28.67	20	0.310
18-RE-6	70	45.48	45	0.682
18-RE-7	75	70.03	75	1.081
18-RA-8	100	68.67	70	0.982
18-RE-2	125	64.8	85	1.033
18-RB-3	150	64.38	92	1.155
18-RE-4	165	90.52	100	1.451
18-RE-8	185	96.02	100	1.481
18-RA-7	225	79.13	100	1.407
18-RE-5	255	89.52	100	1.474
18-LD-1	288	72.51	100	1.320

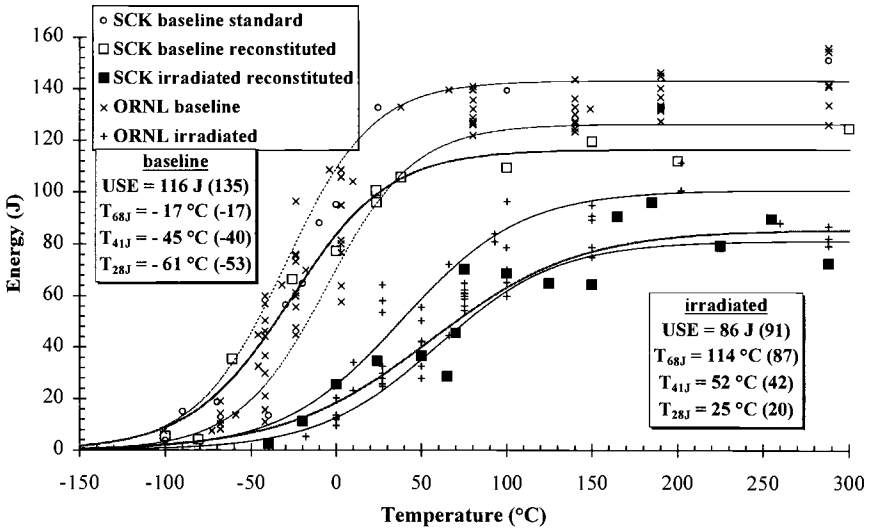


Figure 3--*Charpy impact test results: transition curve for energy. ORNL and SCK•CEN data are very similar although the upper shelf is affected by reconstitution. Values given in parentheses refer to ORNL data. Dotted lines correspond to the 1σ (standard deviation) confidence bounds on the mean tanh fit curves. Full lines refer to the tanh fit curves of SCK•CEN data.*

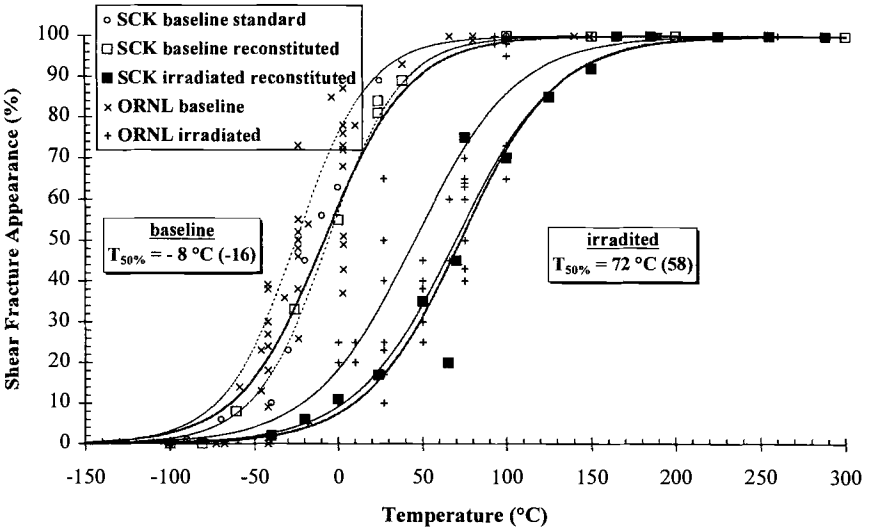


Figure 4--*Charpy impact test results: transition curve for SFA. Although the small number of reconstituted specimens, the agreement is good. $T_{50\%}$ from ORNL data are given between parentheses.*

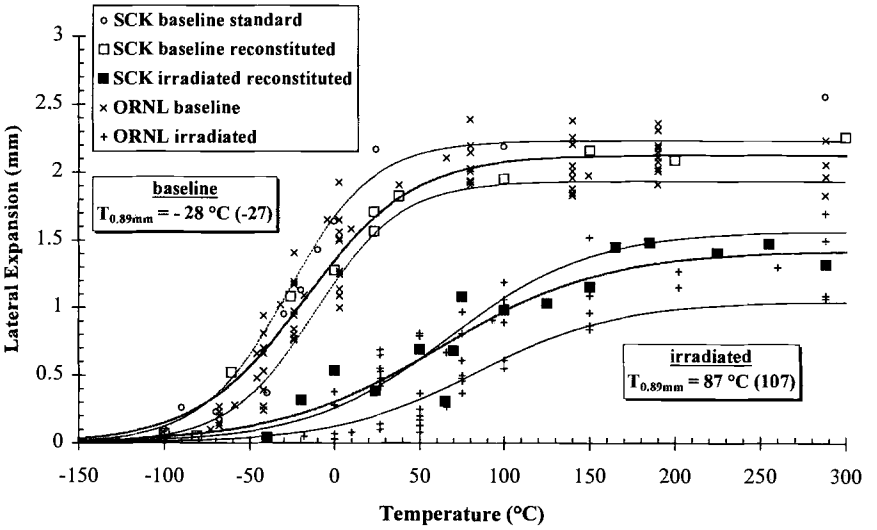


Figure 5--*Charpy impact test results: transition behaviour for lateral expansion. As for energy and SFA, the test data are close to the ORNL ones. $T_{0.89mm}$ from ORNL data are given in parentheses for comparison.*

Table 9-- *Summary of the Charpy impact test data: reconstitution and irradiation effects.*

Lab.	specimen	condition	N	USE J	T_{68J} °C	T_{41J} °C	T_{28J} °C	$T_{50\%}$ °C	$T_{0.89mm}$ °C
SCK data	standard	baseline	12	142	-18	-34	-43	-12	-28
SCK data	reconstituted	baseline	12	116	-17	-45	-61	-8	-28
ORNL data	standard	baseline	83	135	-17	-40	-53	-16	-27
SCK data	reconstituted	irradiated	16	86	114	52	25	72	87
ORNL data	standard	irradiated	56	91	87	42	20	57	107
ORNL data	standard	shift	--	44	104	82	73	73	134
SCK data	reconstituted	shift	--	30	131	97	86	80	115

Fracture Toughness Tests

Fracture toughness tests were performed on Charpy size samples. The results obtained on reconstituted specimens in the baseline condition have already been published [5]. A new series of unirradiated standard Charpy samples was tested and the results are given in Table 10. The test and evaluation procedure is according to the ASTM E1921-98 standard except for a minor modification related to K-J conversion: here, the plane strain rather than plane stress elasticity modulus is used. The Young modulus (E) and Poisson ratio (ν) are taken equal to:

$$E\,(\text{GPa}) = 207 - 0.06 \times T\,(^{\circ}\text{C})$$
$$\nu = 0.3$$

Table 10-- *Fracture toughness test results in the baseline condition: standard specimens.*

Id.	T (°C)	$K_{fatigue}$ (MPa√m)	W (mm)	B (mm)	B_n (mm)	a_0 (mm)	J_c (kJ/m²)	Δa (mm)	K_{Jc} (MPa√m)	remark
73W-A13	-100	14.27	9.977	10.002	8.008	4.410	17.55	0	62.54	
73W-A18	-100	15.02	9.986	9.992	7.900	4.594	21.61	0	69.41	
73W-A11	-100	14.46	9.981	9.987	8.039	4.454	30.59	0	82.58	
73W-A12	-100	14.83	9.986	9.992	7.987	4.549	31.55	0	83.87	
73W-A17	-100	15.01	9.995	9.994	7.866	4.621	31.67	0	84.03	
73W-A15	-100	14.46	9.970	9.985	7.948	4.441	37.80	0	91.74	
73W-A14	-100	14.90	9.986	9.990	7.952	4.568	38.79	0	92.95	
73W-A10	-100	14.91	9.978	9.984	7.998	4.559	45.48	0	100.70	
73W-A06	-80	15.07	9.980	9.998	7.939	4.608	15.86	0	59.46	
73W-A04	-80	15.33	9.980	9.989	7.904	4.656	37.01	0	90.84	
73W-A07	-80	15.44	9.956	9.984	7.942	4.657	42.96	0	97.87	
73W-A09	-80	14.75	9.964	9.995	7.959	4.508	44.96	0	100.12	
73W-D17	-80	15.08	9.982	10.000	7.805	4.606	46.47	0	101.79	
73W-D13	-80	15.29	9.980	10.001	7.813	4.652	56.17	0	111.91	
73W-D16	-80	14.89	9.977	10.014	7.878	4.561	83.64	0	136.55	
73W-A08	-80	15.25	9.960	9.996	7.968	4.622	106.86	0	154.35	(1)
73W-D12	-80	15.19	9.981	10.040	7.873	4.642	129.42	0	169.86	(1)
73W-A16	-80	14.74	9.967	9.981	7.890	4.505	143.93	0	178.97	(1)
73W-A05	-80	15.22	9.974	9.984	7.818	4.623	180.64	0.245	200.68	(1) (2)

(1) : K_{Jc} exceeds the ASTM E1921-98 limit value given by $\sqrt{\dfrac{\sigma_y E\left(W-a_0\right)}{30}}$

(2) : Δa exceeds the ASTM E1921 limit value given by $0.05\left(W-a_0\right)$

In the irradiated condition, all samples were reconstituted from the broken 4T-CT half labeled 18 (tested at 50°C [1]). The results are given in Table 11. Three typical load-displacement traces were found in these tests and are illustrated in Figure 6. In the baseline condition, when unstable fracture (cleavage type) occurs, the load drops to a very low load value (typically less than 1 kN). By contrast, in the irradiated condition, crack arrest occurs for many samples after 10 to 50% load drop. Besides, many samples exhibited a pop-in behaviour. This was also reported in [1] where 25% of the specimens tested exhibited significant pop-in. This indicates that pop-in events are promoted by irradiation. It should be mentioned that most of the tests were performed until a significant load drop was observed. The load-displacement trace was then analyzed and if any significant pop-in was found, the fracture parameter, K_{Jc}, is calculated for the observed pop-in.

Table 11-- *Fracture toughness test results of reconstituted irradiated specimens.*

Id.	T (°C)	$K_{fatigue}$ (MPa$\sqrt{m}$)	W (mm)	B (mm)	B_n (mm)	a_0 (mm)	J_c (kJ/m²)	Δa (mm)	K_{Jc} (MPa$\sqrt{m}$)	remark
73W-18LE1	-5	20.90	10.08	10.05	7.946	5.027	4.73	0	33.05	(3)
73W-18LE6	-5	20.90	10.05	10.12	8.012	5.024	25.85	0	77.24	
73W-18LE3	-5	22.10	10.02	10.03	7.822	5.138	29.75	0	82.86	
73W-18LE4	-5	20.90	10.02	10.05	7.842	4.980	37.11	0	92.54	
73W-18LE5	-5	22.20	10.09	10	7.75	5.218	44.53	0	101.38	
73W-18LK7	-5	20.30	9.99	9.99	8.051	4.836	64.40	0	121.91	
73W-18LE2	-5	20.50	10.01	10.08	8.047	4.912	71.84	0.106	128.76	
73W-18LC1	10	21.91	10.04	10.02	7.822	5.133	11.11	0	50.63	
73W-18LD4	10	23.20	9.87	9.99	7.672	5.134	24.51	0	75.20	
73W-18LD5	10	22.67	9.87	9.99	7.737	5.063	27.32	0	79.40	
73W-18LD2	10	22.79	9.86	9.91	7.6	5.045	42.37	0	98.88	
73W-18LC7	10	24.78	9.84	9.84	7.537	5.255	43.02	0.102	99.64	
73W-18RB5	10	22.79	9.92	9.91	7.694	5.104	49.75	0	107.15	
73W-18LC2	10	22.09	9.91	9.83	7.646	4.973	58.07	0.121	115.76	
73W-18RB1	25	29.08	9.90	9.91	7.945	5.780	5.95	0	37.06	(3)
73W-18LC5	25	23.74	9.92	9.85	7.689	5.209	18.60	0	65.51	
73W-18LB6	25	21.5	10.08	10.05	8.023	5.125	20.71	0	69.13	(3)
73W-18LD3	25	22.28	9.83	9.98	7.796	4.968	24.45	0	75.12	
73W-18LB5	25	21.60	10.01	9.98	7.942	5.054	39.36	0	95.30	
73W-18LD7	25	24.63	9.92	9.89	7.678	5.329	58.15	0.109	115.84	
73W-18LD6	25	22.94	9.87	9.86	7.594	5.060	30.15	0	83.42	(3)
73W-18LC4	25	22.85	9.96	9.88	7.484	5.141	98.92	0.166	151.09	(1)
73W-18LD8	25	23.04	9.91	9.9	7.571	5.124	99.87	0.161	151.81	(1)
73W-18RB2	25	26.16	9.93	9.91	7.412	5.519	132.53	0.314	174.88	(1) (2)
73W-18LC8	40	23.32	10.03	9.92	7.753	5.285	55.07	0	112.74	(3)
73W-18LB2	40	23.60	9.83	9.83	7.434	5.093	64.26	0.134	121.77	
73W-18RB4	40	23.27	9.92	9.91	7.745	5.167	89.99	0.186	144.11	(1)
73W-18RB8	40	22.84	9.91	9.87	7.508	5.088	113.93	0.205	162.15	(1)
73W-18LB4	40	23.10	9.82	9.81	7.321	5.017	158.85	0.325	191.46	(1) (2)
73W-18LB3	40	22.20	9.93	9.82	7.554	4.999	163.52	0.412	194.26	(1) (2)

(1) and (2) = as defined before (Table 10); (3) = pop-in.

Finite element calculations have shown that the effect of reconstitution on the J-level as well as on the stress-strain distribution ahead of the crack tip is negligible even

when inserts as small as 3 mm are considered [6]. Here, the region of interest is larger than 8 mm and therefore, no influence of reconstitution is expected.

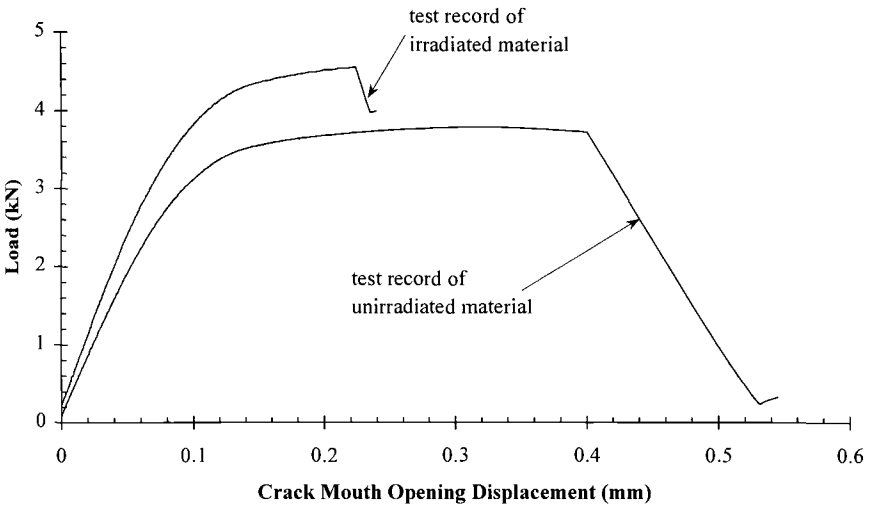


Figure 6--*Typical load-displacement records showing that unstable fracture results almost in specimen separation for the unirradiated material while crack arrest occurs in the irradiated material.*

The master curve concept was then applied to the data of Tables 10 and 11. The results are given in Table 12 where T_0, K_0 and m are given for each series of data.

Table 12-- *Data analysis of the PCCv specimens according to the master curve concept, ASTM E1921-98.*

condition	T	N	T_0	K_0	m	remark
baseline	-100	8	-68.6	73.2	6.6	valid
	-80	11	-89.0	122.0	2.8	all data (no censoring)
	-80	7	-66.1	89.9	4.2	only valid
	-80	11	-77.7	104.4	4.2	censor with N=r=11
	-80	11	-84.7	114.9	4.2	censor per E1921
		$T_{0\ average}$	-76.7			
irradiated	-5	7	11.2	86.7	2.6	valid per E1921
	10	7	33.3	80.2	4.1	valid per E1921
	25	10	28.1	103.3	2.0	all
	25	10	56.0	73.6	2.7	only valid r=N=7
	25	10	33.9	95.7	2.3	censor with N=r=10
	25	10	28.3	103.1	2.3	censor per E1921
	40	6	25.2	132.5	5.0	all
		$T_{0\ average}$	24.3			

In the baseline condition, two series of specimens were used to determine T_0. At −100°C, all samples satisfied the size requirements of ASTM E1921. T_0 is found equal to

–68°C. At –80°C, 4 among 11 samples were above the $K_{J\ limit}$ according to E1921, requiring data censoring. Three censoring procedures were applied:

- only data satisfying the E1921 requirements are taken into account (invalid data are omitted);
- censoring procedure as per E1921;
- the invalid data points are taken equal to $K_{J\ limit}$ and N = r (N = total number of specimens and r = number of valid data) in the maximum likelihood expression.

Application of the various procedures to the –80°C data show that the E1921 censoring procedure does not significantly modify the results in comparison to no censoring. The most conservative procedure is the one that considers only valid data, rejecting all invalid data in the T_0 determination procedure. Based on the E1921 standard, the $T_{0\ average}$ is –77°C.

In the irradiated condition, four test temperatures were selected: –5, 10, 25 and 40°C. At –5 and 10°C, all data points were below the $K_{J\ limit}$ while this limit was exceeded by some of the samples tested at 25 and 40°C, therefore, necessitating data censoring. Table 12 gives a $T_{0\ average}$ = 24°C.

The size adjusted fracture toughness data of the PCCv specimens are shown in Figure 7 together with the master curve and associated confidence bounds. Reconstituted PCCv data taken from [5] were also added in the baseline condition. The radiation-induced shift of the reference temperature is ΔT_0 = 101°C.

Similarly, the ORNL data [1,2] were also analyzed with the master curve procedure. Here, as various CT sizes were tested, the size correction was first applied prior to the determination of the reference temperature T_0. This allows the number of specimens to increase per test temperature. The results are depicted in Table 13. The resulting T_0-shift is ΔT_0=100°C. Figure 7 shows the 1T-adjusted fracture toughness versus temperature of all available test data. Although the positions of the master curves (defined by the reference temperature, T_0) are slightly different, the temperature shifts are very close (see Table 14). The slight differences observed on T_0 can be associated with experimental uncertainties although the censoring procedure may be non conservative in determining T_0.

Table 13--*Determination of T_0 from ORNL data (all data normalized to 1T).*

	T	-80°C	-50°C	-30°C	-15°C	-5°C	+5°C		average
baseline	n	13	13	11	14	10	6		
	T_0	-69.5	-63.7	-65.0	-57.6	-67.4	-62.8		-64
	T	-25°C	29°C	50°C	75°C	85°C	95°C	105°C	average
Irradiated	n	5	5	6	6	13	6	5	
	T_0	16.2	46.0	34.1	38.2	42.5	28.6	42.7	36

Table 14--*Comparison of temperature shifts as determined with PCCv and CT. Despite the slight difference in T_0-absolute values, the shifts are about the same.*

T_0 (°C)	baseline	irradiated	T_0-shift
CT (ORNL)	-64	34	98
PCCv (SCK)	-77	24	101

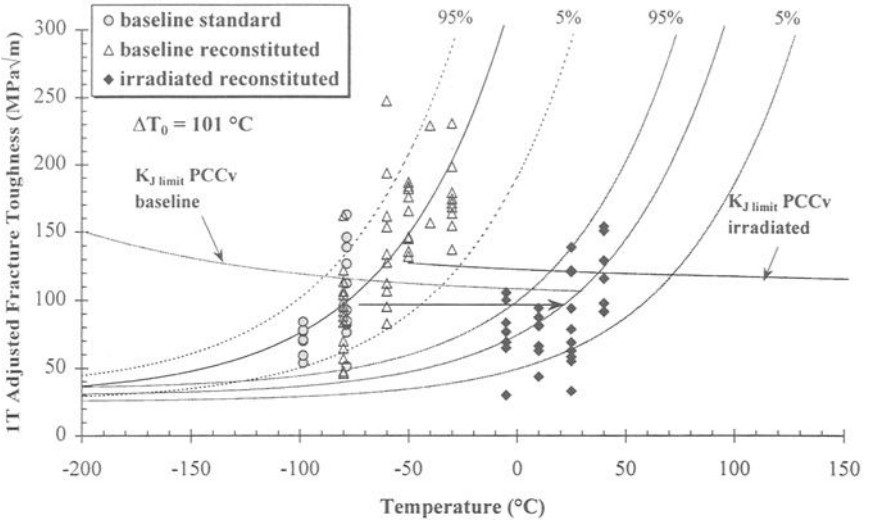


Figure 7-- *Normalized fracture toughness as a function of test temperature. The data are adjusted to 1T reference size. The radiation damage expressed by the 100 MPa √m K_J-level shift is equal to 101°C.*

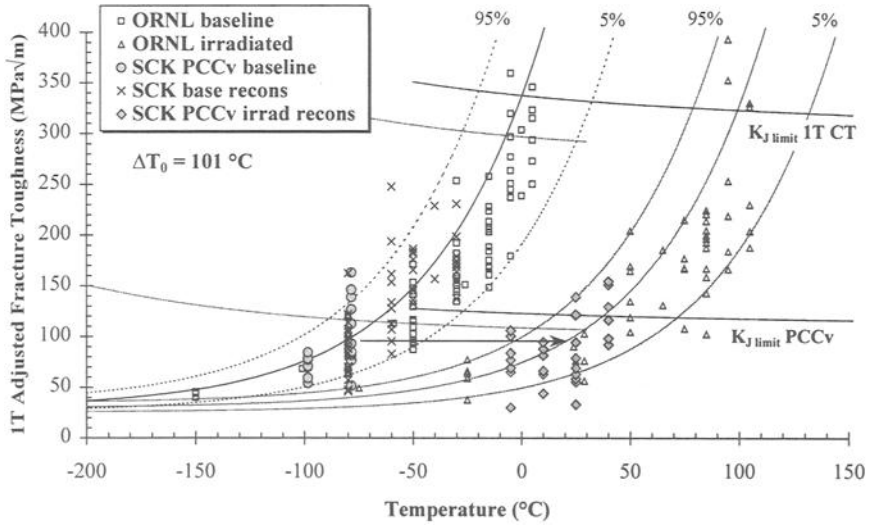


Figure 8--*The SCK•CEN and ORNL data are well described by the master curves.*

Current nuclear regulatory procedure relies on the Charpy impact test data to estimate the fracture toughness of the irradiated vessel. One of the major aspects of fracture toughness in the transition regime is the so-called lower bound toughness curve, which is used for safety assessment purposes. This K_{IC} lower bound curve represents the minimum possible toughness that is not affected by specimen size, geometry or any statistical consideration. The K_{IC} curve of the ASME code represents the lower bound of fracture toughness data as a function of temperature normalized to the reference nil-ductility temperature, RT_{NDT}. This K_{IC} curve is given by:

$$K_{Ic}^{ASME} = 36.48 + 22.783 \exp\left[0.036\left(T - RT_{NDT}\right)\right].$$

In the irradiated condition, the RT_{NDT} shift is taken equal to the 41 J shift of the Charpy impact transition curve. Therefore,

$$RT_{NDT} = RT_{NDT}^{0} + \Delta T_{41J}$$

where RT_{NDT}^{0} is the initial RT_{NDT}.

The parameters characterizing the transition behaviour and the resulting shift as determined from Charpy impact and fracture toughness data are given in Table 15. Figure 9 shows how the ASME curves compare to the 5% and 1% bounds derived from the master curve. The agreement between the 1% bound and the ASME curve is very good.

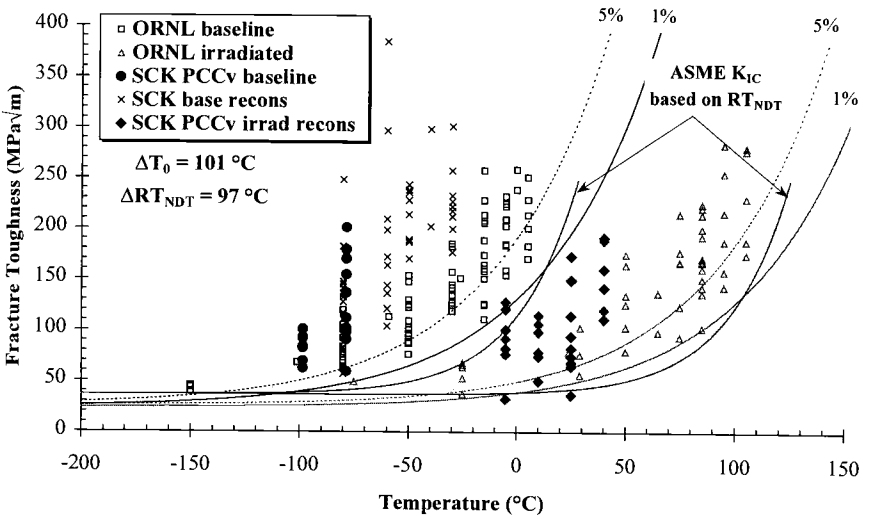


Figure 9--*Comparison of 1T-adjusted fracture toughness data to the ASME lower bound, and the 5% and 1% master curve bounds.*

It is demonstrated here that the precracked Charpy specimen associated to the master curve approach can be confidently used for fracture toughness characterization. For the 73W material, it is found that the nuclear regulatory approach based on the 41 J shift gives similar results in comparison to fracture toughness data.

Table 15—*Comparison of irradiation-shift measures of the transition behaviour: 41 J regulatory shift versus fracture toughness shift based on ORNL and SCK•CEN data.*

T in °C	T_0		T_{41J} from CVN	
	SCK (PCCv)	ORNL (CT)	SCK	ORNL
baseline	-77	-64	-45	-40
irradiated	24	36	52	42
shift ΔT	101	100	97	82

Summary and Conclusions

In this paper, the use of the Charpy size sample to characterize the fracture toughness behaviour of reactor pressure vessel steels in the transition range is investigated. A well-characterized and documented material was selected, namely the 73W weld material thoroughly investigated at ORNL. The reconstitution technology allowed the fabrication of small size samples from broken CT specimens. Tensile, Charpy impact and precracked Charpy specimens were tested in both baseline and irradiated conditions.

Flow properties determined from small size samples were found to be in very good agreement with ORNL data and no orientation effect was found. For the Charpy impact data, reconstitution did not show a significant effect on the results although a small drop of upper shelf was observed in the baseline condition. Within the experimental uncertainties, the various parameters characterizing the transition regime for both SCK•CEN and ORNL data are in full agreement. When size correction is taken into account, fracture toughness test results obtained with precracked Charpy specimens are in good agreement with compact tension specimens tested at ORNL. The application of the master curve approach allows for the definition of the transition curve with one single parameter, the reference temperature T_0. The shift of the transition curve was found to be almost identical although T_0 determined with PCCv lies about 10°C lower than with CT specimens. The 1% bound and K_{IC} ASME curves are very close to the actual experimental lower bound. In this case, the regulatory approach based on the 41 J shift gives results similar to direct fracture toughness measurements. Consequently, the precracked Charpy specimen can confidently be used for fracture toughness determination and characterization of the transition behaviour of reactor pressure vessel steels.

Acknowledgments

The work reported here is co-sponsored by Electrabel. The authors are indebted to R. Gérard from Tractebel Energy Engineering for his strong interest and support. The authors are grateful to R. K. Nanstad from ORNL for his strong interest and for providing the 73W weld material (without him this work would not be possible). Special thanks go to L. Van Houdt (fracture toughness tests), R. Vosch (Charpy impact tests), J. Verachtert and T. Noels (tensile tests), G. Bes (dimensional control), P. Beckers, M. Eyckmans and R. Mertens (Charpy specimens reconstitution and fabrication) for performing the work most competently and diligently.

References

[1] Nanstad, R. K., Haggag F. M., McCabe D. E., Iskander S. K., Bowman K. O., and Menke B. H., **"Irradiation Effects on Fracture Toughness of Two High-copper Submerged-arc Welds, HSSI Series 5"**, NUREG/CR-5913, ORNL/TM-12156/V1, 1992.

[2] Nanstad, R. K., McCabe D. E., Haggag F. M., Bowman K. O., and Downing D.J., **"Statistical Analyses of Fracture Toughness Results for Two Irradiated High-Copper Welds"**, *Effects of Radiation on Materials, 15th International Sympsium, ASTM STP 1125*, R.E. Stoller, A.S. Kumar and D.S. Gelles, Eds., American Society for Testing and Materials, 1992, pp. 270-291.

[3] Iskander, S. K., Corwin, W. R. and Nanstad, R. K., **"Effects of Irradiation on Crack-Arrest Toughness of Two High-Copper Welds"**, *Effects of Radiation on Materials, 17th International Sympsium, ASTM STP 1125*, R.E. Stoller, A.S. Kumar and D.S. Gelles, Eds., American Society for Testing and Materials, 1992, pp. 251-269.

[4] van Walle, E., **"Reconstitution: where do we stand?"**, *Effects of Radiation on Materials, 17th International Sympsium, ASTM STP 1270*, D.S. Gelles, R.K. Nanstad, A.S. Kumar and E.A. Little, Eds., American Society for Testing and Materials, 1996, pp. 415-441.

[5] Chaouadi, R., **"Fracture toughness testing in the transition regime using small size samples"**, *Small Specimen Test Techniques, ASTM STP 1329*, W.R. Corwin, S.M. Rosinski and E. van Walle, Eds., American Society for Testing and Materials, 1998, pp. 214-237.

[6] Scibetta, M. and Chaouadi, R., **"Effect of reconstitution on fracture toughness measured with PCCv"**, SCK•CEN Report BLG-749, April 1997.

Philip J. E. Bischler,[1] Malcolm R. Wootton,[1] and Christopher J. Bolton[1]

Fracture Toughness of Submerged-Arc Weld Samples from a Decommissioned Magnox Reactor Pressure Vessel: Initial Results

Reference: Bischler, P. J. E., Wootton, M. R., and Bolton, C. J., **"Fracture Toughness of Submerged-Arc Weld Samples from a Decommissioned Magnox Reactor Pressure Vessel: Initial Results,"** *Effects of Radiation on Materials: 19th International Symposium, ASTM STP 1366,* M. L. Hamilton, A. S. Kumar, S. T. Rosinski, and M. L. Grossbeck, Eds., American Society for Testing and Materials, West Conshohocken, PA, 2000.

Abstract: BNFL Magnox Generation Group is sampling irradiated submerged-arc weld metal from the reactor pressure vessel at Trawsfynydd Power Station, which is currently being decommissioned. Chemical analysis has shown that the sampled weld is typical of previously sampled submerged-arc weld. There are no significant variations either through the weld thickness or along the weld, indicating high quality and uniformity of construction. Dosimetry measurements are in line with predictions, and show significant attenuation through the vessel thickness. Fracture toughness measurements are being made using pre-cracked Charpy specimens machined from four different depths in the through-wall thickness, with reconstituted material from failed Charpy halves being used to augment the test data. The data from the layer of the first weld furthest from the reactor core have been compared with predictions made by the methodology used in assessing continuing RPV integrity, and support the methodology.

Keywords: pressure vessels, submerged-arc weld metal, irradiation, fracture toughness, chemical analysis

Introduction

Six of BNFL Magnox Generation Group's eight operational Magnox power stations have steel pressure circuits. In four of these stations, the reactor cores are housed within spherical steel vessels of approximately 20 m diameter and thickness in the range 75 to

[1] Research Officers and Group Head respectively, Materials Group, Integrity and Engineering Branch, BNFL Magnox Generation, Berkeley, Gloucestershire, GL13 9PB, UK.

Copyright© 2000 by ASTM International www.astm.org

100 mm. Pressures of the carbon dioxide coolant gas range between 10 and 20 bar depending upon the particular design, whilst the core inlet and outlet temperatures are approximately 190 °C and 360 °C. The reactor cores in the remaining two, earlier stations are contained in cylindrical pressure vessels, approximately 11 m in diameter and 50 mm thick. The pressure of the carbon dioxide in these older stations is only 7 bar whilst the core inlet and outlet temperatures (150 °C and 350 °C respectively) are similar to those in the more modern plant.

Magnox Generation Group has recognised that embrittlement of the steel in the reactor pressure vessels (RPVs) is the main ageing phenomenon which is ultimately likely to limit the lives of the Magnox stations. Regular testing of tensile and Charpy specimens of structural materials loaded into monitoring schemes at the time of construction of the stations has shown that the submerged-arc (SMA) weld metal shows the greatest sensitivity to neutron irradiation [*1-4*].

As part of the ongoing programme of activities to support the continued operation of its four stations with steel RPVs, a major project has been undertaken to remove SMA weld samples from four different welds contained in an RPV at Trawsfynydd Power Station, which is currently being decommissioned. The objective of the project is to measure the fracture toughness of irradiated SMA weld metal in order to make comparisons with the predictions made by the RPV assessment methodology. In addition, since the neutron dose attenuates through the RPV wall, the acquisition of specimens from different depths of the sample can give mechanical property data as a function of neutron dose.

All of the samples have been successfully removed from the RPV, and testing is proceeding. This paper outlines the methodology for removing the weld samples and presents the initial fracture toughness results. These results are from the first weld only and are from the layer furthest from the reactor core. The results are compared with the methodology used to predict fracture toughness of irradiated RPV material [*5*]. In addition, the chemical analysis of the weld and the dosimetry measurements are also discussed.

Vessel Construction

The Magnox RPVs were fabricated from carbon steel plates and forgings joined together by either manual or machine (SMA) welds. The plates consisted of simple grain refined carbon-manganese ferritic steels in the normalised and stress relieved condition. The earlier cylindrical RPVs were constructed using manual metal arc welds alone. The construction process for the later spherical RPVs involved factory assembly of two or three curved plate panels using a submerged arc welding process with copper covered electrodes. Duct forgings were attached to holes cut in the plates using the same welding process. These segments were then transported to site and assembled using a manual metal arc welding process. The entire vessel was then slowly heated, stress relieved for up to ten hours at temperatures within the range 600±40 °C and slowly cooled at 2-5

°C/hour. A schematic diagram of a typical RPV sitting on its support skirt is shown in Figure 1.

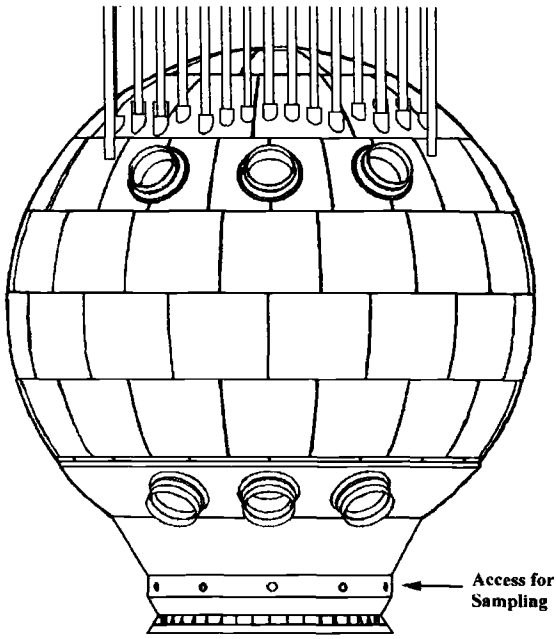


Figure 1 - *Schematic representation of reactor pressure vessel.*

Sampling and Testing Procedures

The sampling procedure involves removing four through-thickness slightly tapered trepan samples (nominally 165 mm diameter and 90 mm thickness) from each of four SMA welds from the south pole region of the Trawsfynydd Reactor 2 RPV. These welds were inaccessible during the operation of the station, and could only be accessed following decommissioning from the outside of the vessel using remotely operated vehicles deploying long reach arms through existing ventilation ports in the side of the support skirt on which the RPV sits as shown in Figure 1. The underside of the vessel and the skirt were clad in asbestos which had to be removed prior to sampling. A detailed description of the sampling vehicle and the operational procedure can be found elsewhere [*6*]. However, it is worth noting that cutting the samples had to be done at temperatures sufficiently low to avoid altering the material properties under consideration and that the long term safety case of the decommissioned vessel had to be maintained.

Each of the samples removed from the RPV contained a length of SMA weld metal with a double 'V' cross section. The welding had been carried out by multiple machine

passes on both sides of the original double 'V' preparation. The cross section of one of the welds removed from the RPV is shown in Figure 2. The appearance is typical of all of the sections.

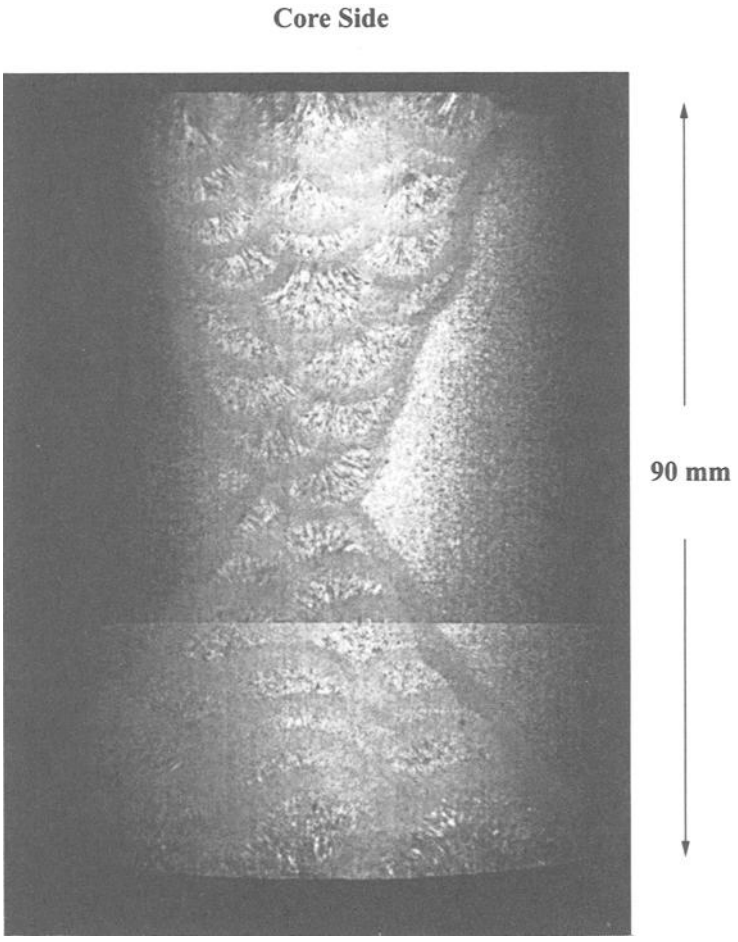


Figure 2 – *Cross section of Trawsfynydd RPV weld.*

A standard orientation procedure was adopted during trepanning so that the orientation of each trepanned sample relative to the other samples and the south pole of the RPV was unambiguously defined. Following removal of the trepan sample from the reactor, a 10 mm slice was taken from the centre of the weld parallel to the welding direction, thereby ensuring maximum use of the available material. Charpy sized specimens were cut from four different layers within each sample. The positions of these layers relative to the line of the weld are shown schematically in Figure 3, with layer 1 being the core-side of the sample. The positions of the layers were chosen to provide maximum information on property changes as a function of dose attenuation through the vessel wall.

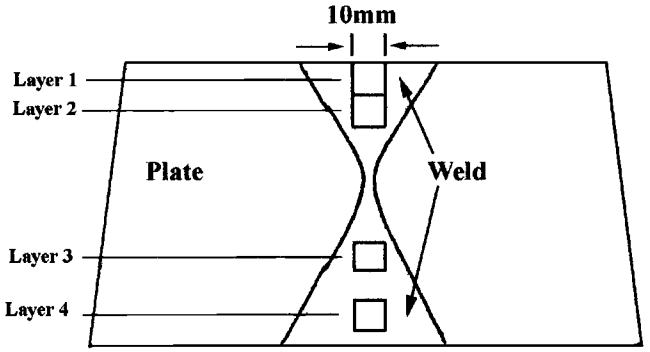


Figure 3 – *Position of Charpy specimens along the weld.*

One end of the 10 mm slice was trimmed to produce a perpendicular face. This face was always cut with the same orientation with respect to the south pole of the RPV. This meant that the position and orientation of each sample within the slice relative to the geometry of the RPV was unambiguously defined.

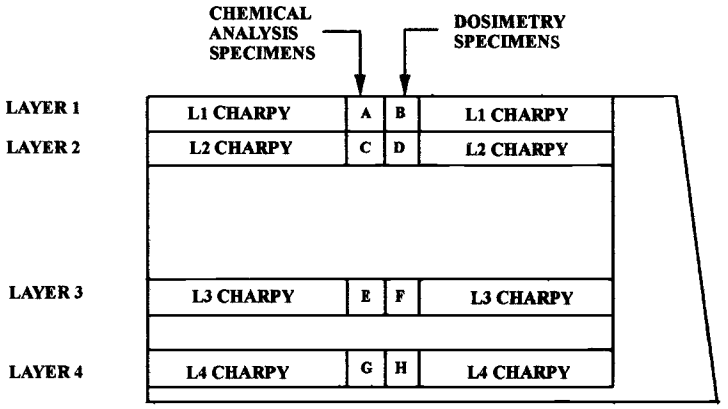


Figure 4 – *Position of Charpy specimens along the 10 mm weld slice.*

Charpy sized specimens were then cut from each layer as indicated in Figure 4. In addition, 10 mm cubes of metal were machined per layer between the two Charpy specimens (see Figure 4) for chemical analysis and dosimetry measurements.

Each specimen was numbered on the same through-thickness face which uniquely identified the location of the specimen within the slice. This numbering sequence combined with the orientation procedure adopted when machining the trepanned samples unambiguously identified the position of each specimen relative to the geometry of sample in the RPV.

The cutting of the 10 mm slice from the original trepanned sample and the subsequent machining of the Charpy specimens inevitably produced a substantial quantity of unused reactor pedigree material. This has been archived for future use.

Chemical Analysis

Table 1 contains a summary of the chemical analysis data from the various trepan samples of weld 1 for layers 1, 2, 3 and 4.

Table 1 - *Chemical Analysis (wt %) of Trawsfynydd RPV Weld 1*

Sample	Layer	C	Si	Mn	S	P	Cu	Ni	Cr	Co
	1	...	...	...	...	...	...	...	...	...
1	2	...	...	...	...	...	...	...	...	...
	3	0.076	0.427	1.34	0.042	0.040	0.264	0.108	0.066	0.015
	4	0.069	0.529	1.36	0.051	0.041	0.280	0.108	0.066	0.015
	1	0.069	0.431	1.40	0.040	0.034	0.268	0.111	0.073	0.016
2	2	0.083	0.424	1 41	0.041	0.034	0.265	0.119	0 078	0.016
	3	0.064	0.465	1.32	0.039	0.038	0.281	0.103	0.070	0.016
	4	0.064	0.572	1.32	0.045	0.039	0.280	0.107	0.068	0.015
	1	0.069	0.440	1.42	0.040	0.037	0.269	0 115	0.073	0.016
3	2	0.070	0.456	1.42	0.042	0.041	0.259	0.119	0.075	0.016
	3	0.072	0.455	1.34	0.040	0.038	0.261	0.110	0.071	0.016
	4	0.068	0.568	1.36	0.047	0.043	0.280	0.115	0.070	0.016
	1	0.063	0.479	1.38	0.043	0.036	0.270	0.114	0.072	0.016
4	2	0.074	0.476	1.40	0.043	0.038	0.265	0.117	0.074	0.016
	3	0.073	0.460	1.31	0.040	0.033	0.238	0.106	0.067	0.015
	4	0.064	0.600	1.36	0.048	0.039	0.272	0.115	0.069	0.016
Submerged-arc Weld Cut-out and Surveillance Database Values										
Mean		0.088	0.519	1.486	0.037	0.031	0.233	0.096	0.086	n/a
Max.		0.170	0.740	1.84	0.051	0.054	0.310	0.270	0.160	n/a
Min.		0.057	0.140	0.95	0.021	0.015	0.100	0.060	0.020	n/a

[1] Measured Nb, Mo and Ti all <0.015%.

This table also includes for comparison purposes the chemical analysis of SMA weld metal from duct cut-outs and surveillance specimens held in an analysis database compiled by Magnox Generation. There are no composition data available for trepan sample 1 layers 1 and 2 since this particular sample had a repair weld of manual metal

arc weld metal. Despite this, the totality of the chemical analysis data from this weld confirms that the weld material has a composition within the range previously observed in SMA weld metal found in duct cut-outs and surveillance specimens. In addition, the results from the different samples and layers show no significant compositional variations along the weld or through the thickness of the weld. These results provide significant confirmation of the high quality and uniformity of construction.

Dosimetry

A single averaged neutron dose has been calculated for each layer from the samples available using the same approach as is used for all RPV locations. This method combines experimental flux determinations and the results of computer modelling of the four samples. The principal method of calculation used to predict nickel fission equivalent fluxes and dpa rates is the MCBEND computer code [7]. It is a general purpose, Monte Carlo, radiation transport code for evaluating neutron fluxes and spectra in fixed source systems.

Experimental values of the fast neutron flux for each layer were measured from one of the small cubes of material cut from the region immediately between the two full Charpy specimens in each layer. The measurements were obtained by counting the activity of the Mn-54 activation product from the reaction Fe-54(n,p)Mn-54. However, in order to quantify the Mn-54 after the long delay period between the reactor being shut down and the vessel being sampled (approximately 7 years), it was necessary to separate it from the Co-60 which dominates the activity of the samples.

The Mn-54 results were compared with the MCBEND predictions for all of the Charpy specimen locations in all four samples removed from weld 1. The average value of the ratio of the calculated Mn-54 flux to the measured Mn-54 flux was 1.034 with a standard deviation of 3.35%, which indicates that the dosimetry measurements are in good agreement with predictions. In addition, comparing the results from the different samples along the weld shows no evidence of variation in dose along the length of weld sampled.

The predicted neutron doses (E>1keV) in dpa x 10^5 for layers 1, 2 3 and 4 are presented in Table 2, and as expected show a significant attenuation in dose through the vessel. For comparison purposes, the highest doses to a PWR pressure vessel are typically an order of magnitude higher than those to a Magnox vessel.

Table 2 - *Predicted Neutron Doses (E>1keV)*

Layer Number	Predicted Neutron Dose Dose (dpa x 10^5) (E>1keV)
4	147
3	192
2	308
1	339

Fracture Toughness Testing

Test Procedure

On receipt of the specimens, a standard Charpy notch was cut in the face of each specimen opposite the numbered side. This is the same notch orientation as surveillance specimens. The specimens were then side-grooved along each flank to depth of 1mm using a cutter with a standard Charpy V-notch profile. They were then fatigue cracked to a nominal crack length to specimen width ratio of 0.5 which provided conformity with the fracture toughness output from the prediction programme. Single specimen fracture toughness tests were then carried out at series of test temperatures using the unloading compliance technique for crack length measurements.

On completion of a test, the fracture surface was heat tinted by heating at 185°C for ~24 hours and the specimen was then broken open at liquid nitrogen temperatures. The as-fractured surfaces were then photographed and scanned to produce electronic images for crack growth measurements. The heat tinting temperature is less than the irradiation temperature (187°C) and hence guarantees that the prolonged heat tinting does not modify the as-irradiated microstructure. This is important since each broken half needed to be reconstituted in order to provide two extra fracture toughness specimens. Hence, each original Charpy specimen can yield potentially three fracture toughness results.

After the fracture faces of each original specimen had been photographed, these were cut from each half specimen and retained for future examination. The remaining pieces of the specimen were then reconstituted using a modified stud welder. Each reconstituted specimen retained its original number with the addition of the suffix 'R' or 'RA'. After numbering, each specimen was notched and side grooved in the same way as the parent specimens, and tested according to the same testing schedule. The use of the low heat tinting temperature for reconstituted specimens means that samples from these specimens can be used to investigate micostructural features introduced during irradiation.

As the test programme proceeded, new test temperatures were selected after reviewing the results to date. The objectives underlying the choice of test temperature were as follows:

1. the three results from an original Charpy specimen would be obtained at different temperatures;

2. several tests would be performed at each of about four temperatures in the transition region;

3. a small number of tests would be done at intermediate temperatures in the transition region;

4. a small number of tests would be done on the upper shelf;

5. the results would be used to guide tests aimed at the upper 'knee' of the fracture toughness/temperature curve.

Results

The first fracture toughness tests were carried out on specimens from the layer furthest from the reactor core (layer 4 in Figure 3). These specimens were chosen since the estimated dose levels to this layer were similar to those in the surveillance database. Test results from specimens from other layers are not yet available. The fracture toughness data obtained from the layer 4 specimens are shown in Figure 5 as a function of test temperature. The toughness values plotted are the linear elastic fracture toughness (K_C),

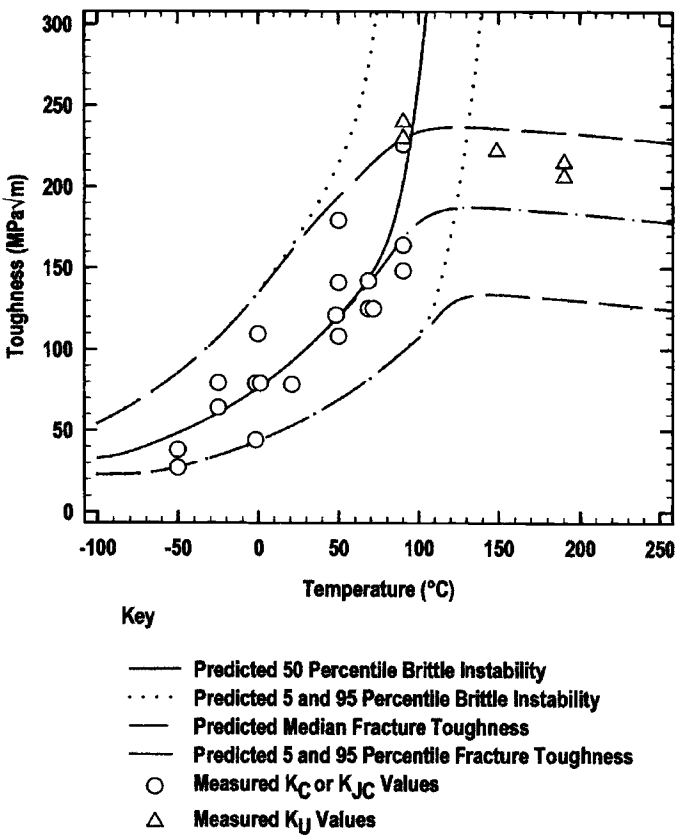


Figure 5 – *Toughness Results for Layer 4 Specimens*

the elastic-plastic fracture toughness (K_{JC}) and the fracture toughness at the termination of the test after ductile crack growth but without brittle instability (K_U). All toughness measurements are in MPa$\sqrt{m}$. The figure also includes the predicted fracture toughness of irradiated submerged-arc weld metal for 5, 50 and 95 % probabilities. The dose is assumed to be the average value for layer 4. In order to compare the results with the predictive methodology for the size of specimen being tested, the start of life fracture toughness values were calculated for a specimen thickness of 10mm. It can be seen from this figure that the results compare well with the prediction, bearing in mind that so far data are only available from one layer in one weld. Furthermore, all of the samples tested at normal operating conditions have exhibited ductile behaviour, providing further confidence in the assessment process.

A detailed description of the procedure (CUSURV) used to predict the irradiated toughness of ferritic materials used in the construction of Magnox RPVs can be found elsewhere [*5*]. For each material, a start of life toughness-temperature curve with an associated 90% confidence interval is produced based on values of toughness measured on metal, in this case submerged-arc weld metal, from station cut-outs. The major effect of irradiation on toughness for these materials is in the transition region and this is estimated by using the change in the 100 MPa$\sqrt{m}$ temperature which varies linearly with the Charpy 40 joule transition temperature [*5*]. Uncertainties in the irradiation shifts arise from the Charpy curve fitting programs, from uncertainties in irradiation temperature and irradiation dose, and from scatter in the irradiation response of the metal caused by variation in composition, microstructure and other mechanical properties. In order to estimate mean toughness and the 90% confidence interval for the irradiated metal, CUSURV makes assumptions about the independence of each source of uncertainty, and then samples and combines them using a stratified statistical sampling method. As far as lower and upper shelf toughness are concerned, the lower shelf toughness is assumed to be insensitive to irradiation; for upper shelf toughness, the dose dependence of the ratio of irradiated toughness to unirradiated toughness is estimated and applied to the unirradiated toughness.

Conclusions

BNFL Magnox Generation Group have successfully removed samples of submerged-arc (SMA) weld metal from the reactor pressure vessel of the Magnox power station at Trawsfynydd. Chemical analysis has demonstrated that the sampled material is typical of SMA weld metal which has been previously sampled and supports the claims of high quality of construction of the pressure vessel as there are no variations through the thickness or along the weld. Dose measurements are in line with prediction and show significant attenuation through the vessel thickness. The fracture toughness test data from early tests supports the methodology used to predict fracture toughness.

Acknowledgment

This paper is published by permission of BNFL Magnox Generation Group.

References

[1] Buswell, J. T., Bolton, C. J., Wootton, M. R., Bischler, P. J. E., Jones, R. B., Jones, L. T., Phythian, W., J., and Sinclair, R. N., "The Radiation Hardening and Embrittlement of Mild Steel Submerged-Arc Weld", *Effects of Radiation on Materials: 16th International Symposium, ASTM STP 1175*, A. S. Kumar, D. S. Gelles, R. K. Nanstad, and E. A. Little, Eds., American Society for Testing and Materials, West Conshohocken, PA, 1994, pp 332-351.

[2] Buswell, J. T., and Jones, R. B., "The Modelling of Radiation Hardening and Embrittlement in Magnox Mild Steel Submerged-Arc Welds", *Effects of Radiation on Materials: 16th International Symposium, ASTM STP 1175*, A. S. Kumar, D. S. Gelles, R. K. Nanstad, and E. A. Little, Eds., American Society for Testing and Materials, West Conshohocken, PA, 1994, pp 424-443.

[3] Bolton, C. J., Buswell, J. T., Jones, R. B., Moskovic, R., and Priest, R. H., "The Modelling of Irradiation Embrittlement in Submerged-Arc Welds", *Effects of Radiation on Materials: 17th International Symposium, ASTM STP 1270*, D. S. Gelles, R. K. Nanstad, A. S. Kumar, and E. A. Little, Eds., American Society for Testing and Materials, West Conshohocken, PA, 1996, pp 113-118.

[4] Beere, W. B., Fidler, R. S., Bolton, C. J. Fenton, S. T. and Jones, R. B. "The Ductile-Brittle Transition Behaviour of Submerged-Arc Weldments Following High Temperature Exposure", *Effects of Radiation on Materials: 18th International Symposium, ASTM STP 1325*, R. K. Nanstad, M. L. Hamilton, F.A. Garner, and A. S. Kumar, Eds., American Society for Testing and Materials, West Conshohocken, PA, To Be Published.

[5] Jones, R.B., and Bolton, C. J., "Neutron Irradiation Embrittlement Studies in Support of Continued Operation, and Validation by Sampling of Magnox Reactor Steel Pressure Vessels and Components", *Twenty-Fourth Water Reactor Safety Information Meeting*, Bethesda, NUREG/CP-0157, 1996, pp 25-48.

[6] Bischler, P. J. E., and Curry, A., *International Conference on Plant Life Management and Plant Extension*, Prague 1997 (in press).

[7] Chucas, S. J., "MCBEND, A Monte Carlo Program for General Radiation Transport Solutions", *ANSWERS Software Service*, AEA Technology, ANSWERS/MCBEND(94)15.

Donald E. McCabe,[1] Randy K. Nanstad,[1] and Mikhail A. Sokolov[1]

Effects of Irradiation and Thermal Annealing on Fracture Toughness of the Midland Reactor Weld WF-70

Reference: McCabe, D. E., Nanstad, R. K., and Sokolov, M. A., **"Effects of Irradiation and Thermal Annealing on Fracture Toughness of the Midland Reactor Weld WF-70,"** *Effects of Radiation on Materials: 19th International Symposium, ASTM STP 1366*, M. L. Hamilton, A. S. Kumar, S. T. Rosinski, and M. L. Grossbeck, Eds., American Society for Testing and Materials, West Conshohocken, PA, 2000.

Abstract: The influence of irradiation damage and recovery of properties by thermal annealing for low upper-shelf WF-70 weld metal has been evaluated. The test material was obtained from the beltline and nozzle course girth welds of the Midland Unit 1 reactor pressure vessel. The two welds, ostensibly made with the same heat of weld wire and the same lot of submerged-arc flux, were determined to be separable for evaluations by virtue of differing copper contents. Conventional transition temperature methods of drop-weight nil-ductility transition and Charpy V-notch (CVN) transition curves could not distinguish a difference in transition temperature. However, a recently developed master curve method of data evaluation revealed the difference by virtue of achieving better sensitivity using only fracture mechanics-based test data.

Irradiation embrittlement after a fluence of 1.0×10^{19} n/cm^2 was evaluated by both the conventional American Society of Mechanical Engineers (ASME) Code method and by the more recent American Society for Testing and Materials (ASTM) master curve method. Again, the Code method rated the postirradiation transition temperatures of the two materials the same. The master curve method indicated that the postirradiated properties of the two materials differed significantly. The U.S. Nuclear Regulatory Commission (NRC) *Regulatory Guide 1.99*, Rev. 2, reasonably predicted the experimentally obtained CVN transition temperature shift at the 41 J reference level for the beltline weld.

Postirradiation annealing at 454°C (850°F) for 168 h almost completely restored the as-received transition temperature properties. The recovery of the transition temperature compared to unirradiated values after 343°C (650°F) for 168-h recovery anneal was 52% by the 41 J CVN temperature, which conflicts with the theoretical

[1]Metals and Ceramics Division, Oak Ridge National Laboratory, Oak Ridge, Tennessee 37831-6151.

Copyright© 2000 by ASTM International www.astm.org

recovery of 17% calculated by NRC *Regulatory Guide 1.162*. The ΔT_o from the master curve method indicated 21% recovery of transition temperature.

Keywords: T_o, master curve, ASTM Standard E 1921, transition range, toughness, Weibull, pressure vessel steels

Introduction

A decision made by Consumers Power Company, Midland, Michigan, to abandon plans to operate a newly constructed nuclear power plant provided an opportunity to acquire, for research evaluations, a material of high interest to the nuclear industry *[1]*. In particular, the girth welds in the reactor vessels were WF-70, a low upper-shelf (LUS) weld metal that has been used also in several currently operating power generating reactors. WF-70 is a Babcock and Wilcox identification code that documents the specific weld filler wire and flux used. In this case, the weld wire was from Heat 72105, and the flux was Linde 80, Lot 8669.

This paper will present data and analyses made on weld metal taken from the beltline and nozzle course girth welds of the Unit 1 pressure vessel. Three conditions evaluated were: (1) as-received, (2) irradiated, and (3) irradiated followed by recovery annealing. Two fracture toughness evaluation methods were employed: (1) the conventional ASME practice that uses either drop-weight nil-ductility transition (NDT) tests or Charpy transition curves in the case of LUS steels *[2,3]*, and (2) a relatively new ASTM master curve evaluation method that employs elastic-plastic fracture mechanics test practices and advanced statistical analysis methods. In both cases, a universal transition range curve of fracture toughness is assumed [ASTM Test Method, "Determination of Reference Temperature T_o, for Ferritic Steels in the Transition Range" (E 1921-97)]. The obvious difference is that the ASME curve tracks the lower bound of K_{Ic} data scatter where the master curve tracks the median trend of K_{Jc} fracture toughness for one specific size of test specimen.

Master Curve Description

The following master curve equation expresses the median fracture mechanics-based K_{Jc} toughness trend for 1T size specimens:

$$K_{Jc(med)} = 30 + 70 \exp\left[0.019\,(T - T_o)\right] \quad \text{MPa}\sqrt{\text{m}}\,, \tag{1}$$

where T is test temperature, and T_o is a material-specific reference temperature. When $T = T_o$, the 1T size-corrected median fracture toughness of data scatter is 100 MPa$\sqrt{m}$.

ASME K_{Ic} Curve Method

The following ASME K_{Ic} curve equation is regarded as a specimen size-independent, lower-bound curve, applicable to all base metals and weld metals used in nuclear reactor vessels.

$$K_{Ic} = 36.5 + 23.15 \exp\left[0.036 (T - RT_{NDT})\right] \quad MPa\sqrt{m} , \tag{2}$$

where RT_{NDT} is a reference temperature that is generally set equal to the drop-weight NDT temperature; however, in the case of LUS materials, RT_{NDT} is the temperature corresponding to the 68 J energy point on the Charpy transition temperature curve minus 33°C (60°F).

Material Description

The WF-70 weld metal was sampled from the beltline girth weld of the Midland reactor pressure vessel at seven locations around the circumference. The nozzle course weld was sampled at only two locations spaced about 180° apart around the girth. The wall thickness at the beltline was about 0.2 m (8.75 in.). The nozzle course wall thickness was about 0.3 m (12 in.). Both welds had received stress relief anneal at 607°C (1125°F) for about 24 h. The as-received mechanical properties are given in Table 1 and chemical compositions in Table 2. More detailed information is given in refs. *[4]*, *[5]*, and *[6]*. As can be seen, only the copper content differed significantly between the beltline and nozzle course welds. Since the subjects of principal interest in the present project were irradiation and annealing effects, the difference in copper content dictated that the two materials should be evaluated separately. The weld-fabrication process was submerged-arc, and the shell course plate material was A 508 class 2, as modified by ASME Code Case 1332-4. Crack orientation in fracture-mechanics type specimens was TL; namely, the crack plane was parallel to the plate thickness direction. Charpys were also TL. Drop-weight NDT cracks were TS-oriented.

Technical Approach

Tests were planned to enable a comparison between the ASME Code of fracture-toughness evaluation as applied to LUS steels and the master curve methodology. Again, the three material conditions covered here are unirradiated, irradiated, and irradiation followed by postirradiation anneal. Irradiation was controlled to a nominal fluence of 1×10^{19} n/cm^2 (>1 MeV), and the temperature of exposure was controlled to nominal 288°C (550°F). The temperatures for the postirradiation annealing part of the experiment were either 343 or 454°C (650 or 850°F) for 168 h.

Charpy transition curve shift from irradiation damage is referenced at the 41 J (30 ft-lb) temperature level, as stipulated in ASTM Standard E 185 82, "Conducting Surveillance Tests for Light-Water Cooled Power Reactor Vessels." All CVN data was

Table 1—*Room temperature tensile properties and transition temperature characterizations for WF-70 weld metal*

Material	Tensile tests				Drop-weight NDT (°C)	Charpy V-notch temperatures (°C)		Charpy upper-shelf energy (J)
	Yield strength		Ultimate tensile strength					
	MPa	ksi	MPa	ksi		T_{41J}	T_{68J}	
Beltline	512	74.3	613	88.9	-53	-9	28	89
Nozzle course	545	79.3	655	94.9	-48	-1	44	88

Table 2—*Chemical composition for WF-70 weld metal ± 1 σ range of variation* (irradiation-sensitive elements only)

Material	Composition (wt %)				
	Cu	Ni	P	Mn	Si
Beltline	0.256 ± 0.034	0.57 ± 0.02	0.017 ± 0.002	1.61 ± 0.05	0.62 ± 0.03
Nozzle course	0.396 ± 0.028	0.57 ± 0.02	0.016 ± 0.002	1.60 ± 0.05	0.61 ± 0.05

combined to make one transition curve to represent the unirradiated condition. Beltline CVN curves were generated at four quarter-point positions around the vessel girth and at five selected through-thickness locations. Two nozzle course positions sampled at three through-thickness positions made six nozzle course CVN curves. The results from combined data are the values that appear in Table 1. Reference *[7]* provides detailed results. On the other hand, the irradiated and postirradiation anneal conditions were represented by only one 14-specimen transition curve per condition. Tensile tests were conducted in duplicate for each selected test temperature and/or damage condition.

Fracture-mechanics-based toughness evaluations were made using compact specimens. Sizes varied between 1/2T to 2T in the case of the unirradiated condition. Only 1/2T and 1T sizes were used in the irradiated and the postirradiation anneal experiments. The fracture-mechanics analysis method used was elastic-plastic; namely, J-integral was calculated at the point of cleavage instability, J_c, followed by conversion to its stress-intensity factor equivalence, K_{Jc}, using the following:

$$K_{Jc} = \sqrt{J_c E} \quad . \tag{3}$$

The reference temperature, T_o, that appears in Eq. (1), was obtained using at least six replicate specimens at each selected test temperature. Data scatter within replicate tests was modeled using a three-parameter Weibull distribution model, and from this, the median K_{Jc} of the distribution could be obtained from ASTM Standard E 1921 97. If the test specimens were not 1T size, the data were first converted to 1T size equivalence using a weakest-link size effect model (E 1921 97). Reference temperature, T_o, could then be determined using Eq. (1).

The ASME lower-bound K_{Ic} curve is temperature-normalized with RT_{NDT}, a reference temperature obtained by empirical test methods that are not fracture-mechanics practices. As mentioned previously, the temperature corresponding to 68 J CVN energy, reduced by 33°C (60°F), defines the RT_{NDT} reference temperature for LUS steels. In the present experiment, there were multiple sampling locations for CVN transition data of the unirradiated condition. These data were also evaluated independently at each position using the least-squares fitted hyperbolic tangent curves to establish the range of RT_{NDT} temperatures.

Table 3 presents the fracture-mechanics-based reference temperature, T_o, for unirradiated beltline and nozzle course WF-70 weld metals. Each test temperature/ specimen size group was evaluated separately, and then all data were combined for "grand totals" using a multitemperature analysis model *[8]*.

Irradiation Embrittlement Evaluations

Table 4 is a postirradiation corollary to Table 3. Only the grand total T_o values from Tables 3 and 4 have been used in Table 5, which summarizes the before-and-after irradiation transition temperature and tensile strength data.

Material Fracture Toughness Comparisons

The following information and comparisons will focus principally on the beltline weld properties.

Figure 1 compares the ASME lower-bound K_{Ic} curve representation and the master curve 2% tolerance-bound curves, positioned according to standard practices. The data shown are the K_{Jc} values determined on beltline WF-70 weld that has not been size-adjusted. The ASME curve placement is arguably about 35°C too conservative. In this case, the RT_{NDT} of −5°C came from the combined CVN data set assembled from the 19 transition curve positions *[4* and *7]*. Each curve evaluated individually showed RT_{NDT} ranging from −20° to +37°C. Note in rows 1 and 2 of Table 5 that the Charpy V method of transition temperature establishment, RT_{NDT}, did not indicate any appreciable difference between beltline and nozzle course WF-70 welds, either before or after irradiation.

Transition-curve shift due to irradiation is referenced at the CVN 41 J temperature. See row 9 in Table 5. The Charpy curve shown in Fig. 2 illustrates why ΔT shift measured from Charpy transition curves tends to be a function of the reference energy level. Shape change due to loss of upper-shelf energy is a common problem in accurate representation of embrittlement characterization by Charpy tests. The 2%

Table 3—*Summary tabulation of T_o temperatures for unirradiated specimens*

Material	Specimen size	Test temperature (°C)	T_o (°C)	Grand total T_o (°C)
Beltline	2T	-25	-58	
	1T	-25	-61	
	1/2T	-25	-59	
	2T	-50	-58	
	1T	-50	-47	
	1/2T	-50	-58	
	1T	-75	-44	
	1T	-100	-41	
Grand total[a]				-54
Nozzle course	1T	-25	-30	
	1T	-50	-19	
	1/2T	-50	-38	
	1T	-100	-35	
Grand total[a]				-32

[a]Using the multitemperature analysis method of reference 6.

tolerance bound in Fig. 1 from the master curve appears to represent properly the lower-bound range in the data spread. Also note in Table 5, row 7, that master curve T_o values identify a difference between beltline and nozzle course welds in both unirradiated and irradiated conditions. Figure 3 shows the positions of the master curves. Unlike Charpy curves, master curves do not change shape with irradiation damage.

NRC *Regulatory Guide 1.99 [9]* can be used to calculate ΔTT_{41J} shift, provided material chemistry, neutron fluence, and operating temperature are known. Revision 2 of *Regulatory Guide 1.99* is currently the accepted method. A third revision is under consideration at the present time *[10]*. The Eason, Wright, Odette equation to calculate ΔTT_{41J} will diminish the high-copper impact (above 0.3 wt %) on ΔTT_{41J}. The impact of these predictions for WF-70 are displayed by the last two rows of Table 5. As ball park estimates, these results are acceptable. Accuracy error is introduced by the initial or unirradiated K_{Ic} curve positioning. Obviously, the proposed refinement provides no relief from the RT_{NDT} error.

For temperature/pressure operating condition control during normal transient conditions, and for pressurized thermal-shock conditions, the ASME lower-bound K_{Ic} curve is currently used. Master curve could some day replace this lower-bound curve using the following 2% cumulative probability equation:

$$K_{Jc(0.02)} = 24.3 + 30 \exp\left[0.019\,(T - T_o)\right] \quad MPa\sqrt{m} \; . \tag{4}$$

Table 4—*Summary tabulation of T_o values for irradiated specimens*

Material	Irradiation (n/cm^2)	Specimen size	Test temperature (°C)	T_o (°C)	Grand total T_o (°C)
Beltline	1×10^{19}	1T	75	22.5	
		1/2T	50	29.9	
		1T	35	33.0	
		1/2T	20	29.2	
Grand total[a]					27.4
Nozzle course	1×10^{19}	1T	75	60.4	
		1/2T	65	68.8	
		1T	45	59.5	
Grand total[a]					62.2

[a]Using the multitemperature model of reference 8.

Table 6 compares the ASME/master curve operating stress intensity factors for two examples of intermediate transient temperatures: 100°C and 150°C; specifically for irradiated WF-70 weld metal after 1×10^{19} n/cm^2 fluence. At 100°C, the determinations are relevant to intermediate reactor start-up transient conditions, and the 40 to 240% lower fracture toughness imposed by the present ASME code can unnecessarily cause temperature control difficulties for start-up and shut-down operations. At 150°C, the extension of the transition curves from both methods falsely indicate toughness levels that exceed upper-shelf capability, as had been defined by R-curves, for WF-70 weld metal *[6]*.

Postirradiation Annealing

Two groups of irradiated specimens were arranged, each consisting of 1T C(T) compact specimens, CVN bars, and tensile specimens. One group was postirradiation annealed at 343°C (650°F) for 168 h, and the other was annealed at 454°C (850°F) for 168 h.

Recovery of properties was measured experimentally, and the results are compared here to predictions using NRC *Regulatory Guide 1.162,* Rev. 2 *[11]*. Table 7 lists the post-anneal transition temperatures for the WF-70 beltline material. The

Table 5—*Unirradiated and irradiated properties for WF-70 weld metal at a fluence of 1 × 10^{19} n/cm² (>1 MeV)*

	Beltline		Nozzle course	
	Unirradiated	Irradiated	Unirradiated	Irradiated
RT_{NDT}	–5°C (23°F)		11°C (51.8°F)	
$RT_{NDT} + \Delta TT_{41J}$		98°C (208°F)		101°C (214°F)
Yield strength	512 MPa (74.3 ksi)	634 MPa (91.9 ksi)	547 MPa (79.3 ksi)	596 MPa (86.4 ksi)
Ultimate tensile strength	613 MPa (88.9 ksi)	717 MPa (104.0 ksi)	654 MPa (94.9 ksi)	709 MPa (102.9 ksi)
CVN T_{41J}	–9°C (16°F)	94°C (201°F)	–1°C (30°F)	89°C (192°F)
NDT	–53°C (-63°F)		–48°C (-54°F)	
T_o	–54°C (-65°F)	27°C (81°F)	–32°C (-26°F)	62°C (144°F)
ΔT_o		81°C (146°F)		94°C (169°F)
ΔTT_{41J}[a]		103°C (185°F)		90°C (162°F)
ΔTT_{41J} by predictive models:				
Reg. Guide 1.99, Rev. 2		99°C (178°F)		126°C (227°F)
Eason, Wright, Odette (NUREG/CR-6551)		98°C (176°F)		107°C (193°F)

[a]By experiment.

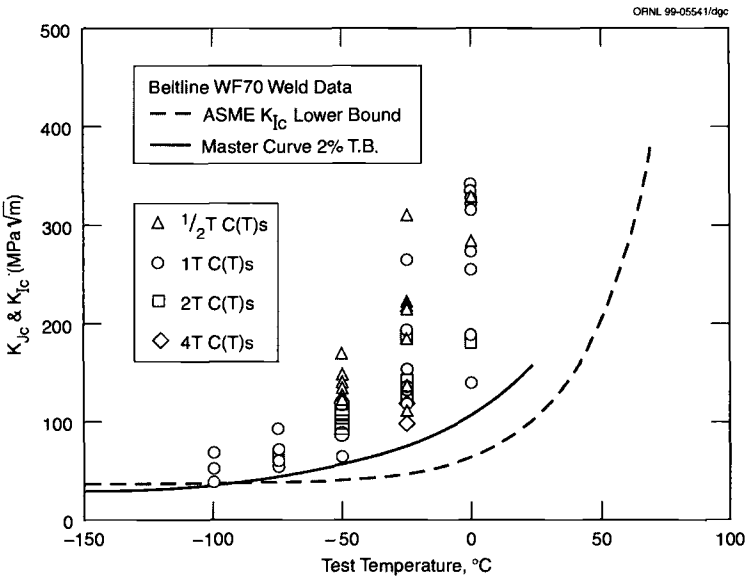


Fig. 1—*The lower-bound K_{Ic} curve of ASME code and the master curve 2% tolerance-bound curve positions relative to the experimental data.*

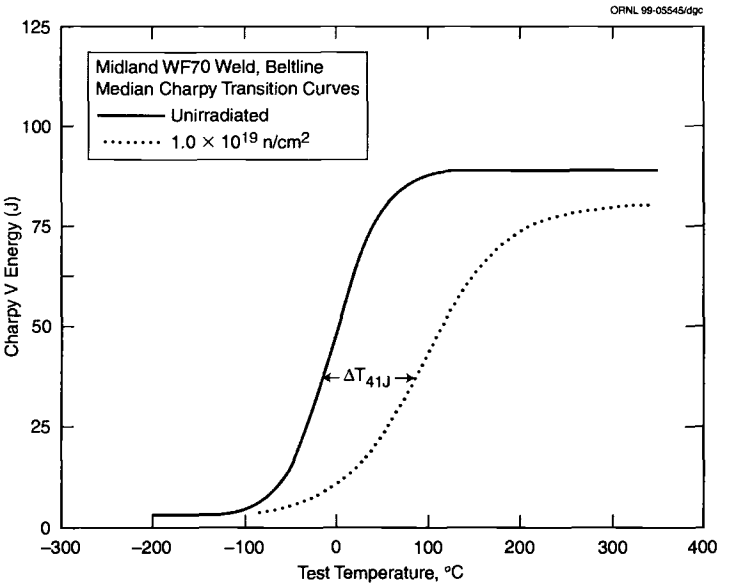


Fig. 2—*Before-and-after irradiation Charpy transition temperature curves for Midland beltline weld metal.*

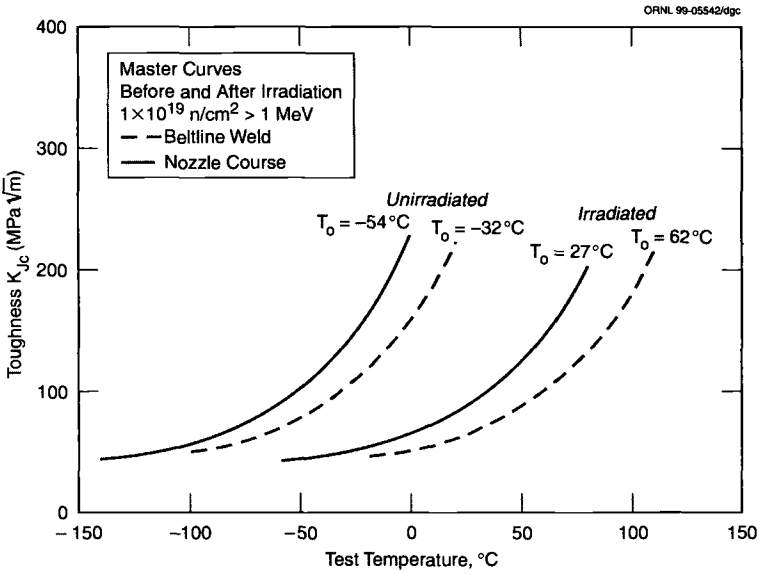


Fig. 3—*Before-and-after irradiation (1×10^{19} n/cm^2) location of master curves for beltline and nozzle course WF-70 weld metal.*

unirradiated 41 J temperature was -5°C so that the 454°C postirradiation anneal resulted in 75% recovery. This is compared to the 80% predicted.

For upper-shelf CVN energy, the initial USE was 89 J, and postirradiation USE was a nominal 81 J so that a predicted recovery of 300% based on USE loss of 8 J was in agreement with the experiment (Fig. 4). Three data points that appear in this figure indicate that the as-received USE was also improved with 454°C anneal, suggesting that WF-70 has some potential to be relieved from the LUS classification using such preirradiation treatments.

For the 343°C postirradiation anneal, the CVN curve shift by experiment indicated 52% recovery of unirradiated transition temperature and 125% recovery of USE. These compare poorly to *NRC Regulatory Guide 1.162 [11]* predictions of 17% and 62% respective recoveries.

Master curve T_0 reference temperature recoveries apply only to transition temperature shift. At 454°C, the experimental result was 91% recovery as opposed to the 1.162 *Regulatory Guide* prediction of 80%. At 343°C recovery anneal temperature, the experimental result was 21% as opposed to the predicted 17%.

Table 8 shows initial, irradiated, and postirradiation annealed tensile properties. In this case, the 454°C anneal had just about fully restored the tensile properties, and the 343°C anneal proved to be ineffective. Hence, in this case, tensile property changes prove to be of lower sensitivity than transition temperature changes.

Table 6—*Postirradiation fracture toughness comparison between ASME and master curve methods at 100 and 150 °C*

Method	Material	Lower-bound K_{Jc} (MPa√m)	
		100°C	150°C
ASME	Beltline and nozzle	60	187
Master curve[a]	Beltline	144	335
Master curve[a]	Nozzle	86	184

[a]2% tolerance bound.

Table 7—*Post-recovery anneal temperatures and upper-shelf energies of WF-70 beltline weld metal*

Method	Annealing temperature, °C (°F)	Postanneal properties	
		Experimental	Predicted
Charpy 41 J	454 (850)	15°C (59°F)	10.8°C (51°F)
Charpy USE	454 (850)	106-J (77 ft-lb)	105-J (77 ft-lb)
Charpy 41 J	343 (650)	44°C (111°F)	80.4°C (117°F)
Charpy USE	343 (650)	91-J (66 ft-lb)	86-J (63 ft-lb)
Master curve T_0	454 (850)	-47°C (-53°F)	-41°C (-43°F)
Master curve T_0	343 (650)	10°C (50°F)	13°C (55°F)

Conclusions

The impact of irradiation damage on the performance of WF-70 LUS weld metal was evaluated. The transition temperature shift in fracture toughness and increased tensile properties due to irradiation damage and recovery of properties with postirradiation annealing was evaluated experimentally and compared to predicted effects using NRC *Regulatory Guides 1.99* and *1.162*.

The weld metal from the beltline girth has nominally 0.25 wt % Cu; the nozzle course girth has nominally 0.40 wt % Cu. Consequently, the two were evaluated as separate materials. The as-received condition evaluated by CVN and drop-weight NDT temperatures showed no clear difference between the two materials. Likewise, the ASME

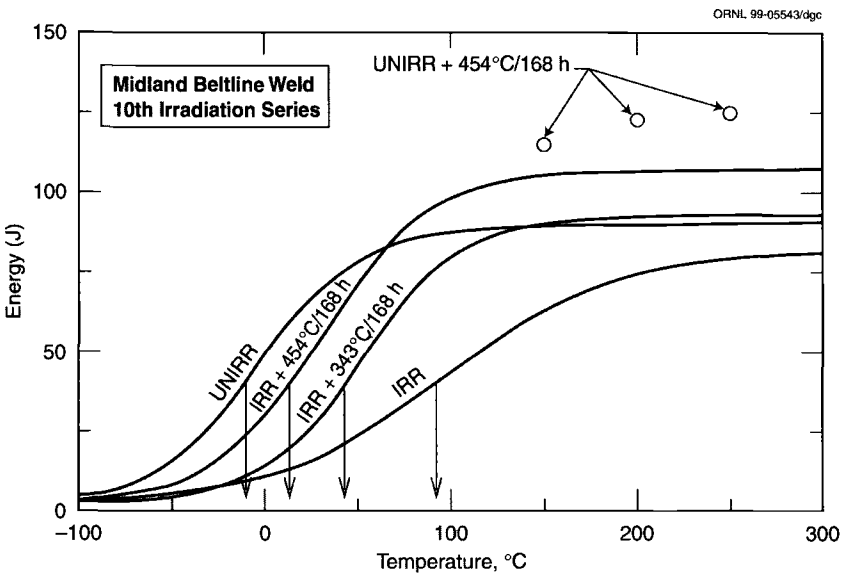


Fig. 4—*Charpy transition curves for as-received, irradiated, and postirradiation anneals. Note three datum for USE after preirradiation anneal.*

Table 8—*Recovery of tensile properties, postirradiation annealing*

Material (strength)	As-received, MPa (ksi)	Irradiated at 1×10^{19} n/cm^2, MPa (ksi)	Irradiated + 454 °C anneal, MPa (ksi)	Irradiated + 343 °C anneal, MPa (ksi)
Beltline yield	512 (74.3)	634 (91.9)	525 (76.2)	634 (92)
Beltline tensile	613 (88.9)	717 (104.0)	629 (91.2)	734 (106.5)
Nozzle yield	547 (79.3)	596 (86.4)	534 (77.5)	617 (89.5)
Nozzle tensile	654 (94.9)	709 (102.9)	636 (92.3)	708 (102.7)

method that uses CVN 41 J transition temperature shift after 1×10^{19} n/cm^2 did not show the expected difference between the two materials from the irradiation-damaged standpoint.

The master curve, T_o, reference temperature method showed that these two welds had distinctly different transition temperatures in both the unirradiated and irradiated conditions. The improved precision of measurement by master curve was used to show how the presently used code estimates for lower-bound K_{Ic} can significantly overestimate the true fracture-toughness temperatures that are critical for the control of normal transient conditions of reactor start-up and cool-down operations.

Postirradiation annealing of the WF-70 beltline material at 454°C for 168 h resulted in 75 and 91% recovery of the unirradiated transition temperature properties, as measured by the 41 J CVN criterion and the T_0 criteria, respectively. *Regulatory Guide 1.162* predicted 80% recovery. Postirradiation anneal at 343°C for 168 h resulted in 52 and 21% recovery by 41 J Charpy and T_0 temperatures, respectively. The *Regulatory Guide 1.162* prediction was 17% recovery. The more accurate master curve representation appears in Fig. 5. Tensile properties were 100% recovered after 454°C anneal but exhibited no recovery by the anneal at 343°C.

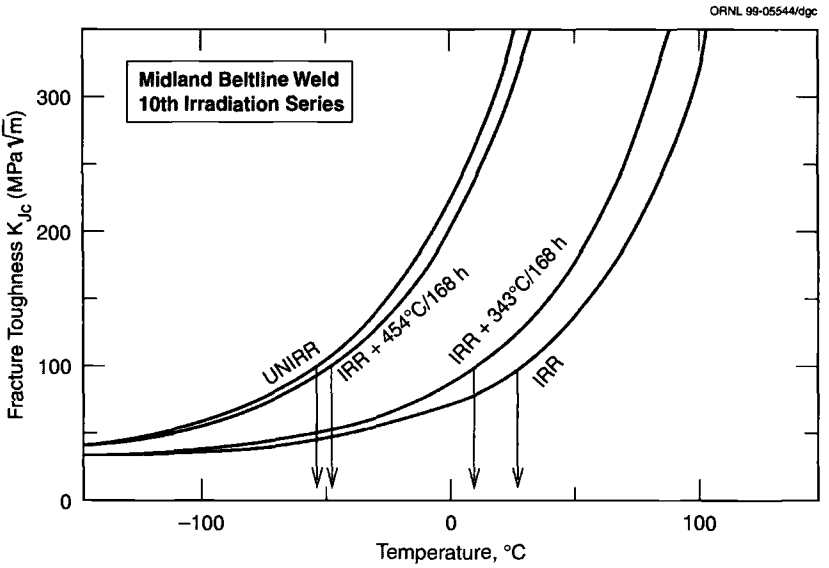


Fig. 5—*Master curves for preirradiation and postirradiation anneals. Temperatures corresponding to 100 MPa$\sqrt{m}$ fracture toughness are marked by arrows.*

Acknowledgments

This research is sponsored by the Division of Engineering Technology, Office of Nuclear Regulatory Research, U.S. Nuclear Regulatory Commission, under Interagency Agreement DOE 1886-N695-3W with the U.S. Department of Energy under Contract DE-AC05-96OR22464 with Lockheed Martin Energy Research Corporation.

References

[1] Babcock and Wilcox, *Material Documentation Report for the Weld Material Removed from the Consumers Power (Midland) Reactor Vessel* (620-0012-51), BAW-2070, Babcock and Wilcox, January 1989.

[2] *ASME Boiler and Pressure Vessel Code, An American National Standard*, Section III, Division I-NB, Article 2330, "Test Requirements and Acceptance Standards," American Society of Mechanical Engineers, 1992.

[3] *ASME Boiler and Pressure Vessel Code, An American National Standard*, Section XI, Article G2000, "Rules for Inservice Inspection of Nuclear Power Plant Components," American Society of Mechanical Engineers, 1992.

[4] R. K. Nanstad, D. E. McCabe, R. L. Swain, and M. K. Miller, *Chemical Composition and RT_{NDT} Determinations for Midland Weld WF-70*, NUREG/CR-5914 (ORNL-6740), December 1992.

[5] D. E. McCabe, R. K. Nanstad, S. K. Iskander, and R. L. Swain, *Unirradiated Material Properties of Midland Weld WF-70*, NUREG/CR-6249 (ORNL/TM-12777), October 1994.

[6] D. E. McCabe, R. K. Nanstad, S. K. Iskander, D. W. Heatherly, and R. L. Sweden, "Evaluation of WF-70 Weld Metal from the Midland Unit 1 Reactor Vessel-Final Report," p. 7, Nuclear Regulatory Commission report NUREG/CR5736, to be published.

[7] R. K. Nanstad, D. E. McCabe, and R. L. Swain, "Evaluation of Variability in Material Properties and Chemical Composition for Midland Reactor Weld WF-70," *Effects of Radiation on Materials: 18th International Symposium, ASTM STP 1325*, R. K. Nanstad, M. L. Hamilton, F. A. Garner, and A. S. Kumar, Eds., American Society for Testing and Materials, West Conshohocken, PA, 1999.

[8] K. Wallin, "Validity of Small Specimen Fracture Toughness Estimates Neglecting Constraint Corrections," pp. 519-537 in *Constraint Effects in Fracture Theory and Applications: Second Volume, ASTM STP 1244*, M. Kirk and A. Baker, Eds., American Society for Testing and Materials, 1995.

[9] U.S. Nuclear Regulatory Commission, *Regulatory Guide 1.99, Revision 2*, "Radiation Embrittlement of Reactor Vessel Materials," May 1988.

[10] E. D. Eason, J. E. Wright, and G. R. Odette, *Improved Embrittlement Correlations for Reactor Pressure Vessel Steels*, NUREG/CR-6551 (MCS 970501), November 1998.

[11] U.S. Nuclear Regulatory Commission, *Regulatory Guide 1.162*, "Format Content of Report for Thermal Annealing of Reactor Pressure Vessels," February 1996.

Pressure Vessel Steels—
Segregation and Microstructure

Mirco Grosse[1] and Jürgen Böhmert[2]

Irradiation Damage Structure in VVER-440 Steels after Irradiation at Different Temperatures and Post-Irradiation Annealing

Reference: Grosse, M. and Böhmert, J., **"Irradiation Damage Structure in VVER-440 Steels after Irradiation at Different Temperatures and Post-Irradiation Annealing,"** *Effects of Radiation on Materials: 19th International Symposium, ASTM STP 1366,* M. L. Hamilton, A. S. Kumar, S. T. Rosinski, and M. L. Grossbeck, Eds., American Society for Testing and Materials, West Conshohocken, PA, 2000.

Abstract: Neutron irradiation of the VVER-440-type reactor pressure vessel steel 15Kh2MFA at lower temperature causes an increase of the content of point defects in the iron lattice. The ratio between the magnetic and nuclear scattering of these point defects shows that not only vacancies are formed but also the number of foreign atoms in solution is increased. Additionally, small precipitates grow. These precipitates are smaller and have a weaker thermal stability than the precipitates grown in this steel after neutron irradiation at service temperature. In some cases the number of precipitates which can be found in the unirradiated state decreases significantly by irradiation at 60°C. Annealing at 475°C/1h provokes coarsening of the precipitates and re-dissolution of the precipitates formed by irradiation at lower temperature.

Keywords: pressure vessel steel, neutron embrittlement, annealing, small angle neutron scattering, microstructure, irradiation temperature

Introduction

The microstructural damage process causing neutron embrittlement of reactor pressure vessel (RPV) steels proceeds in two general stages:

1. formation phase of displacement cascades and
2. diffusional interaction phase.

[1] Research scientists and [2]leader of the Neutron Embrittlement Division of the Institute of Safety Research at the Forschungszentrum Rossendorf Inc.; P.O. Box 510119, D-01314 Dresden, Germany.

Copyright© 2000 by ASTM International www.astm.org

In the first stage atoms are removed from their places in the iron lattice and in the precipitates by multiple collosion. A part of the lattice defects is spontaneously annihilated or rearranged during the subsequent cascade cooling [1,2]. The individual formation process lasts ≤ 10 ps and does not or hardly depend on the temperature. At the end a large number of Frenkel pairs or isolated defects (vacancies, interstitials) and a vacancy-rich displacement cascade core are produced.

In the second stage the surviving point defects and super-small clusters can be rearranged within and outside of the cascade region by thermal diffusion [2]. They can be annihilated by recombination, can be trapped in sinks like grain boundaries, voids, interfaces or dislocations, and can form dislocation loops. Furthermore, the defect migration is connected with the transport of solute atoms and produces a radiation-induced solute redistribution [3]. The processes in the second stages are strongly influenced by the irradiation temperature.

During the irradiation, both stages take place simultaneously, averaged spatially and temporally, and are competitive. The first stage produces a configuration far from thermal equilibrium, the second one approaches the system to the thermal equilibrium [3,4]. As numerical model calculations have shown [5], the resulting damage structure strongly depends on the relevance of these two stages. For a given material (composition, metallurgical variables) the main parameter which controls the microstructural evolution is the ratio between dose rate (neutron flux ϕ) and irradiation temperature T_{irr}. High flux and low temperature encourage the far-from-thermal equilibrium configuration with high point defect supersaturation, low flux and high temperature favours microstructures near the thermal equilibrium. As a consequence very diverse microstructural phenomena, that kind of irradiation-induced or irradiation-enhanced precipitation, dissolution of precipitates and irradiation-induced segregation, can be observed for different materials and under different irradiation conditions.

Up until now microstructural studies of RPV steels have preferentially been focussed on the irradiation near reactor operating temperature. Additional insights could, however, be gained by irradiation under high neutron flux and at low temperatures. Such investigations have been rather seldom.

Recently, attention has been centred on the low temperature radiation embrittlement because the surveillance specimens of the High Flux Isotope Reactor (HFIR) at the Oak Ridge National Laboratory operating at a temperature of 50 °C showed an accelerated embrittlement [6,7]. In a comprehensive programme the influence of metallurgical variables, flux and fluence on the irradiation response at 60 °C was investigated with different RPV steels and model iron alloys [8]. The formation of small defect-solute cluster or complexes due to local intracascade processes is considered to be the most relevant microstructrual evolution process. The features have not been imaged by TEM but could be indentified by small angle neutron scattering (SANS) measurements.

Experiments with A 588 RPV support structure steel irradiated up to a fluence of 3.7×10^{19} ncm^{-2} ($E > 1$ MeV) at about 70 °C showed a large irradiation-induced shift in transition temperature but failed to provide clear evidence of microstructural changes [8]. The irradiation embrittlement was interpreted as matrix damage and the copper content was considered to be unimportant.

Stoller [10] has estimated the influence of the irradiation temperature on the relative importance of point defect clusters and copper-rich precipites by a kinetic rate theory model.

The results confirm that point defect clusters are the major type of the microstructural change due to neutron irradiation at low temperatures. This is consistent with the above-mentioned experimental findings.

The irradiation-induced structural changes of A 533 B cl. 1 RPV steel were studied by SANS, anomalous small angle X-ray scattering (ASAXS) and positron annihilation spectroscopy (PAS) in [11]. The material was irradiated up to fluences of $1 \cdot 10^{18}$ ncm^{-2} [E > 1 MeV] at temperatures of 60, 121 and 288 °C. The structural changes as well as the differences in the mechanical properties were found to be small and only relevant after irradiation at 60 °C. An influence of the copper content in the range from 0.07 to 0.14 wt.-%. could not be detected. The results were explained by the assumption of inhomogenities, which differ from the iron matrix only in the number density.

This paper concerns small angle neutron scattering (SANS) analysis of the microstructure of original and laboratory heats of VVER-440-type RPV steel after neutron irradiation in the Rossendorf research reactor RFR. For comparison results of SANS investigations of the same steel irradiated in a power reactor with a flux of $\phi \approx 2 \cdot 10^{15}$ s^{-1}m^{-2} and at a temperature of about 270°C are given. Analyses of annealed specimens give information about thermal stability of the irradiation defects and about the possibility to conclude from the damage state formed after research reactor irradiation on the state after power reactor irradiation.

Materials and Measurements

The investigation involves an original heat and two laboratory heats of the VVER-440-type RPV steel 15Kh2MFA. Material KAB was manufactured from a test plate of an original heat used in the Greifswald nuclear power plant (Germany) . The thermal treatment was:

- austenitization 0.5 h / 1000°C, cooling in oil
- annealing 10 h / 700°C, cooling on air.

The materials ESW-A and -C are laboratory heats with the same thermal treatment. The chemical composition and the irradiation conditions of the investigated materials are given in Tables 1 and 2. The samples were irradiated at the Rossendorf Research Reactor (RFR). For the comparison with the real service conditions a sample of the KAB material, irradiated in the Rheinsberg VVER-2 nuclear power plant (Germany) was investigated, too. Samples with a thickness of 1 mm were cut from half Charpy-V specimens of these materials in the unirradiated and irradiated state. Some irradiated samples were annealed over 1 h at 270°C and 475°C.

The small angle neutron scattering (SANS) investigations were performed at the PAXE facility at the Orphee research reactor of the LLB Saclay (France) [12] and at the SANS-V4 facility at the BER-II research reactor of the Berlin neutron scattering center BENSC [13]. During the measurements, the samples were magnetized in a magnetic field of 1.4 T. This magnetic field is strong enough to generate a saturated magnetization in the samples [14]. Table 3 gives the experimental conditions of the SANS measurements.

Tables 1 Chemical composition (in wt.-%) of the investigated materials, Fe - balance

	C	Si	P	V	Cr	Mn	Ni	Cu	Mo
ESW-A	0.145	0,12	0,018	0,23	2,35	0,28	0,07	0,14	0,70
ESW-C	0,145	0,18	0,018	0,30	2,60	0,36	0,07	0,34	0,67
KAB-B	0,150	0,24	0,011	0,28	2,60	0,52	0,24	0,22	0,62

Tables 2 Irradiation conditions of the investigated materials

material	reactor	neutron flux [$10^{15}m^{-2}s^{-1}$] (E > 1 MeV)	fluence [$10^{22}m^{-2}$] (E > 1 MeV)	dpa [10^{-2}]	irradiation temperature [°C]
KAB-B	VVER-2	1.38	3.3	0.6	270
	RFR, Rossendorf	185	19	2,6	60
ESW-A		224	23	3,1	
ESW-C		26,8	11	1,5	

Tables 3 Experimental conditions of the SANS measurements

	SANS-V4 (BENSC)		PAXE (LLB)	
wavelength [nm]	5	5	5	6
collimation length [m]	1	4	1	5
sample - detector - distance [m]	1.09	4.0	1.5	5
Q - range [nm^{-1}]	0.2 - 3.0		0.3 - 2.6	
Investigated specimens	ESW-A unirradiated irradiated 60°C irrad. 60°C, ann. 270°C ESW-C unirradiated irradiated 60°C irrad. 60°C, ann 270°C KAB unirradiated irradiated 60°C		ESW-C unirradiated KAB unirradiated irrradiated 60°C irrad. 60°C, ann 270°C irrad. 60°C, ann. 475°C irrad. 270°C irrad. 270°C, ann. 475°C	

For the background correction the empty holders were measured. The absolute calibration was performed as usual at these facilities, for the measurements at the SANS-V4 facility by measurements of a water standard, at the PAXE facility by a direct calibration method [15]. In both experiments two dimensional position sensitive detectors consisting of 64 x 64 cells with a size of 1 cm x 1 cm were applied. The data analysis was done using software packages of the LLB and BENSC, respectively, including the calibration, correction of the detector sensitivity and for background and the radial averaging (reduction of the two dimensional scattering data to intensity I vs. scattering vector Q - datasets). The differential magnetic scattering cross section depends $d\Sigma(Q)_{mag}/d\Omega$ on the azimuthal angle α between the scattering vector $\underline{Q}$ and vector of the sample magnetization $\underline{M}$, whereas the differential nuclear scattering cross section $d\Sigma(Q)_{nuc}/d\Omega$ is independent of α. This difference was used for the separation between magnetic and nuclear scattering cross section [14]:

$$\left(\frac{d\Sigma(Q)}{d\Omega}\right) = \left(\frac{d\Sigma(Q)_{nuc}}{d\Omega}\right) + \left(\frac{d\Sigma(Q)_{mag}}{d\Omega}\right) \quad (1)$$

$$\left(\frac{d\Sigma(Q)_{nuc}}{d\Omega}\right) \sim \Delta\eta^2_{nuc} \quad (2)$$

$$\left(\frac{d\Sigma(Q,\alpha)_{mag}}{d\Omega}\right) \sim \Delta\eta^2_{mag}\cdot\sin^2(\alpha) \quad (3)$$

$\Delta\eta$ is the difference between the mean scattering densities of inhomogeneities and of the matrix which is given by:

$$\Delta\eta = n_I \cdot b_I - n_M \cdot b_M \quad (4)$$

$n_{I,M}$ are the mean number densities of atoms, $b_{I,M}$ are the mean scattering lengths in the inhomogeneity and in the matrix, respectively. In dia- or paramagnetic phases the magnetic moments are disordered. $b_{I,mag}$ is in this case 0. It means that the scattering density of nonferromagnetic phases in a ferromagnetic matrix is 0 and the magnetic scattering does not depend on the structure and composition of this phase, only on the known structure of the matrix.

The small angle scattering curve can be divided into two ranges:

- the Guinier-range at $QxR \approx 1$ and
- the Porod-range at $QxR \geq 4$.

In the normalised (multiplied by R) Q-range between 1.5 and 4 an undefined mixing according to both Guinier- and Porod scattering law occurs. In the lower part the Guinier scattering law dominates whereas with increasing normalised Q-value the Porod scattering law becomes more and more dominant. At Q-values of $Q \geq 4/R$ the differential scattering cross section for inhomogeneities with a well-defined interface to the matrix (no fractal structures or dislocations) and without preferred orientation decreases with increasing Q according to the power law:

$$\left(\frac{d\Sigma}{d\Omega}\right)_{SAS} = \frac{2\pi \cdot c \cdot \Delta\eta^2 \cdot S}{Q^4} = P \cdot Q^{-4}, \tag{5}$$

where c is the concentration and S the specific surface of the inhomogeneities. P is the well-known Porod constant.

From the whole scattering data the size distribution function represented as volume distribution $D_V(R)$ (volume fraction of the inhomogeneities with a size in the range from R to R+ΔR) were calculated from the differential scattering cross section $d\Sigma(Q)/d\Omega$ using the indirect transformation method developed by Glatter [16]:

$$\left(\frac{d\Sigma(Q)_{mag,nuc}}{d\Omega}\right) = k \cdot \int_0^\infty D_V(R) \cdot R^3 \cdot \Delta\eta^2(R)_{mag,nuc} \cdot S(Q,R)\, dR \tag{6}$$

k is a constant depending on the shape of the inhomogeneities, R the characteristic dimension of them. The so-called shape factor S(Q,R) is the Fourier transform of the shape of the inhomogeneities. This method describes $D_v(R)$ as a linear combination of splin functions Φ_n:

$$D_V(R) * \Delta\eta^2(R) = \sum_n c_n * \Phi_n(R) \tag{7}$$

c_n are the weight factors of the linear composition. $\Psi_n(Q)$ are the Fourier transforms from Φ_n. Using the property of Fourier transformation that constant factors do not change the transformation, the differential scattering cross section can be fitted by a linear combination of $\Psi_n(Q)$ and c_n can be obtained:

$$\frac{d\Sigma(Q)}{d\Omega} = f * \sum_n c_n * \Psi_n(Q) \tag{8}$$

f is a calibration factor. An exact Fourier transformation can be performed only by integration over an infinitely large Q- and R-ranges, respectively. Such an infinite Q-Range is not measurable. A limited Q-range effects oscilations around the correct curve and formation of so-called ghost peaks. Applying different Q-ranges in the analysis ghost peaks can be detected. They change their position and intensity whereas real peaks are not changed significantly. However, the used program ITP92 takes into account the limited Q-range of small angle scattering experiments. It minimizes the effects of the limited Q-range by

- defining of a limit for R_{max} using the sampling theorem of the Fourier transformation: $R_{max} = 4\,\pi\,/\,Q_{min}$
- damping the oscilations by the Lagrange algorism.

If there are more than one type of inhomogeneities with different sizes and structures then Δη depends on R. Eq. (6) is only properly valid if inhomogeneities seen by the nuclear scattering are identical in shape and size with the inhomogeneities seen by the magnetic

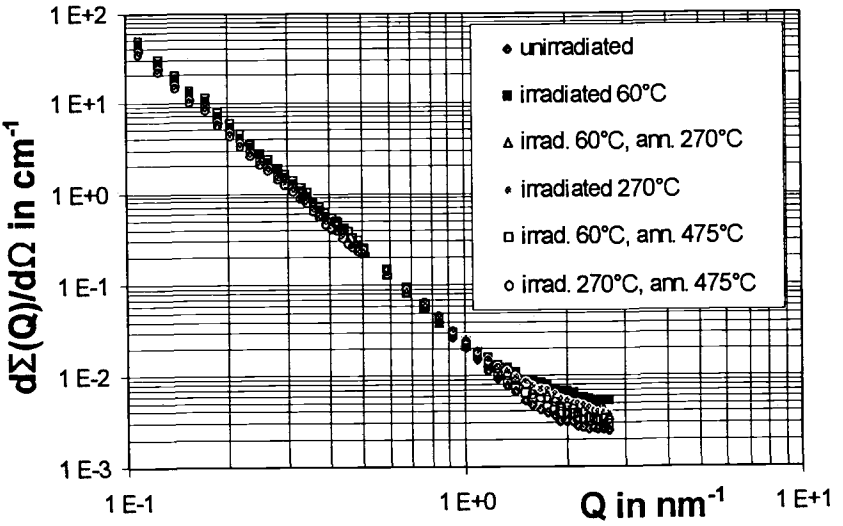


Fig. 1 Comparison of the SANS cross section perpendicular to the external magnetic field for different states of materials KAB

scattering. Otherwise different functions for $D_V(R)$ and $S(Q,R)$ have to be taken into account.The indirect transformation method estimates D_V under the boundary condition that $D_V(R)$ is unequal to zero only in the range $0 \leq R \leq 4\pi/Q_{min}$ and for a supposed shape of the inhomogeneities. For this analysis Glatters ITP92 software was used. D_V was calculated assuming spherical inhomogeneities.

Results

Fig. 1 shows the differential SANS cross section perpendicular to the external magnetic field of the different irradiation and annealing states of the material KAB. Differences in both directions were preferentially found at higher values of Q (Fig.2).

The measured differential scattering cross section $(d\Sigma(Q)/d\Omega)_{mes}$ does not only contain the Q-dependent small angle neutron scattering $(d\Sigma(Q)/d\Omega)_{SAS}$, but also a constant contribution $(d\Sigma/d\Omega)_c$. This constant contribution is caused by the incoherent scattering, mainly at the different iron isotopes, and by the monotonic Laue scattering at point defects in the matrix. In order to seperate $(d\Sigma/d\Omega)_c$ from $(d\Sigma(Q)/d\Omega)_{SAS}$ the asymptotic behaviour of $(d\Sigma(Q)/d\Omega)_{SAS}$ (see Eq. (5)) can be utilized.

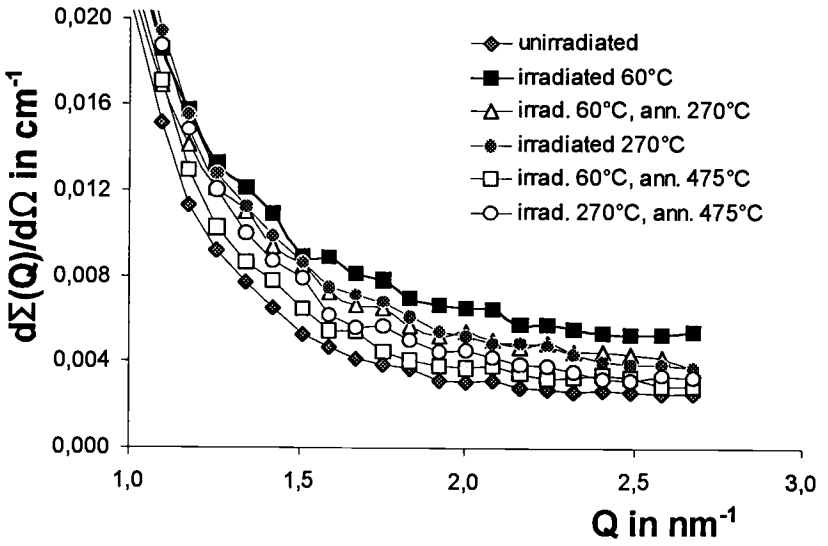


Fig. 2 Linear plot of the high Q side of the scattering pattern perpendicular to the magnetic field

The measured differential scattering cross section $(d\Sigma(Q)/d\Omega)_{mes} = (d\Sigma(Q)/d\Omega)_{SAS} + (d\Sigma/d\Omega)_c$ can be multiplied by Q^4:

$$\left(\frac{d\Sigma(Q)}{d\Omega}\right)_{mes} \cdot Q^4 = \left(\frac{d\Sigma(Q)}{d\Omega}\right)_{SAS} \cdot Q^4 + \left(\frac{d\Sigma}{d\Omega}\right)_c \cdot Q^4$$

$$= P + \left(\frac{d\Sigma}{d\Omega}\right)_c \cdot Q^4 \qquad (9)$$

The slope of the $d\Sigma(Q)/d\Omega \cdot Q^4$ vs. Q^4 plot gives the constant scattering contribution.

For the estimation of the constant scattering contribution a Q-range between 1.77 and 2.6 or 1.77 and 3.0 nm^{-1}, respectively, was used in the Porod plot. It means that the method is exact for inhomogeneities with a size $R > 2.25$ nm. From TEM investigations at comparable materials [18] it is known that the material contains an relatively high content of vanadium-rich carbides with a size $R > 10$ nm. The volume fraction and, thus, the scattering contribution of these larger objects are expected to be much higher than the fraction of the smaller objects. For smaller objects an additional "Guinier-scattering" occurs. If it is fulfilled that the Porod scattering of the larger objects and the Laue scattering dominate, the intensity in the Q-range used for this analysis then a linear dependence of $d\Sigma(Q)/d\Omega \cdot Q^4$ on Q^4 is expected. Otherwise the plot $d\Sigma(Q)/d\Omega \cdot Q^4$ vs. Q^4 is significantly curved. Then the slope of the plot becomes smaller with increasing Q^4.

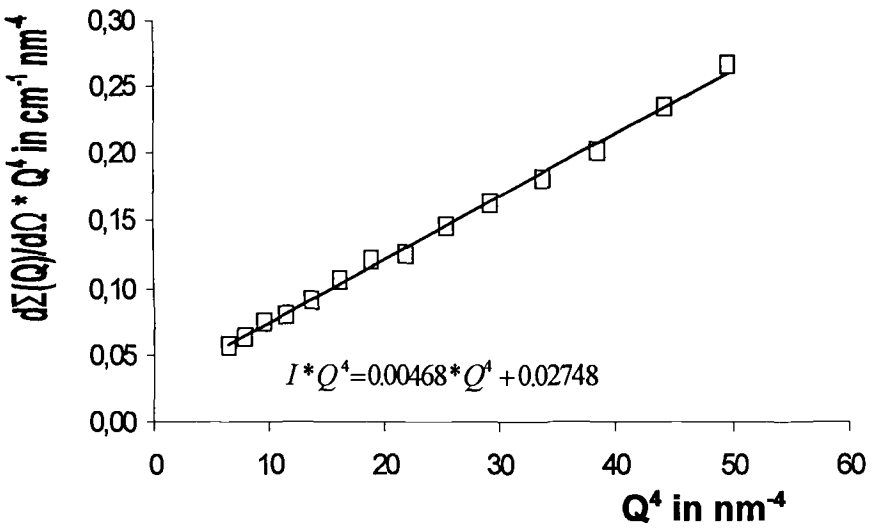


Fig. 3 Porod plot of the SANS cross section perpendicular to the magnetic field of material KAB irradiated at 60°C

As one can be seen in Fig. 3, there is no change in the slope of the Porod-curve. It shows that Porod scattering of larger objects and monotonic Laue scattering are dominating over the whole Q-range used for this analysis.

The Figures. 4 a through 4c compare the values of the constant scattering contribution of the different irradiation and annealing states for the three materials. The following can be found:

- The magnetic constant scattering of the unirradiated state is low and differs only slightly for the different materials. The nuclear constant scattering is nearly the same in the unirradiated state for the two laboratory heats but is significantly smaller for material KAB.
- Irradiation provokes an increase of both the nuclear and magnetic constant scattering. This increase is the higher the lower the irradiation temperature. The magnetic constant scattering increase relatively stronger than the nuclear one.
- Annealing at 270°C/1h of the materials irradiated at 60°C decreases both the magnetic and nuclear constant scattering. The values measured for the sample irradiated under service condition are not fully reached by this thermal treatment.
- The results of a post-irradiation annealing at 475°C/1h depend on the irradiation temperature. At the sample irradiated at 60°C the decrease of the magnetic constant scattering is stronger than the decrease in the nuclear one. It reaches the value of the unirradiated state, whereas the nuclear constant scattering keeps significantly higher than the value for the unirradiated state. At the sample irradiated at 270°C the nuclear constant scattering decreases and reaches the value for the unirradiated state whereas the magnetic constant scattering does not decrease significantly.

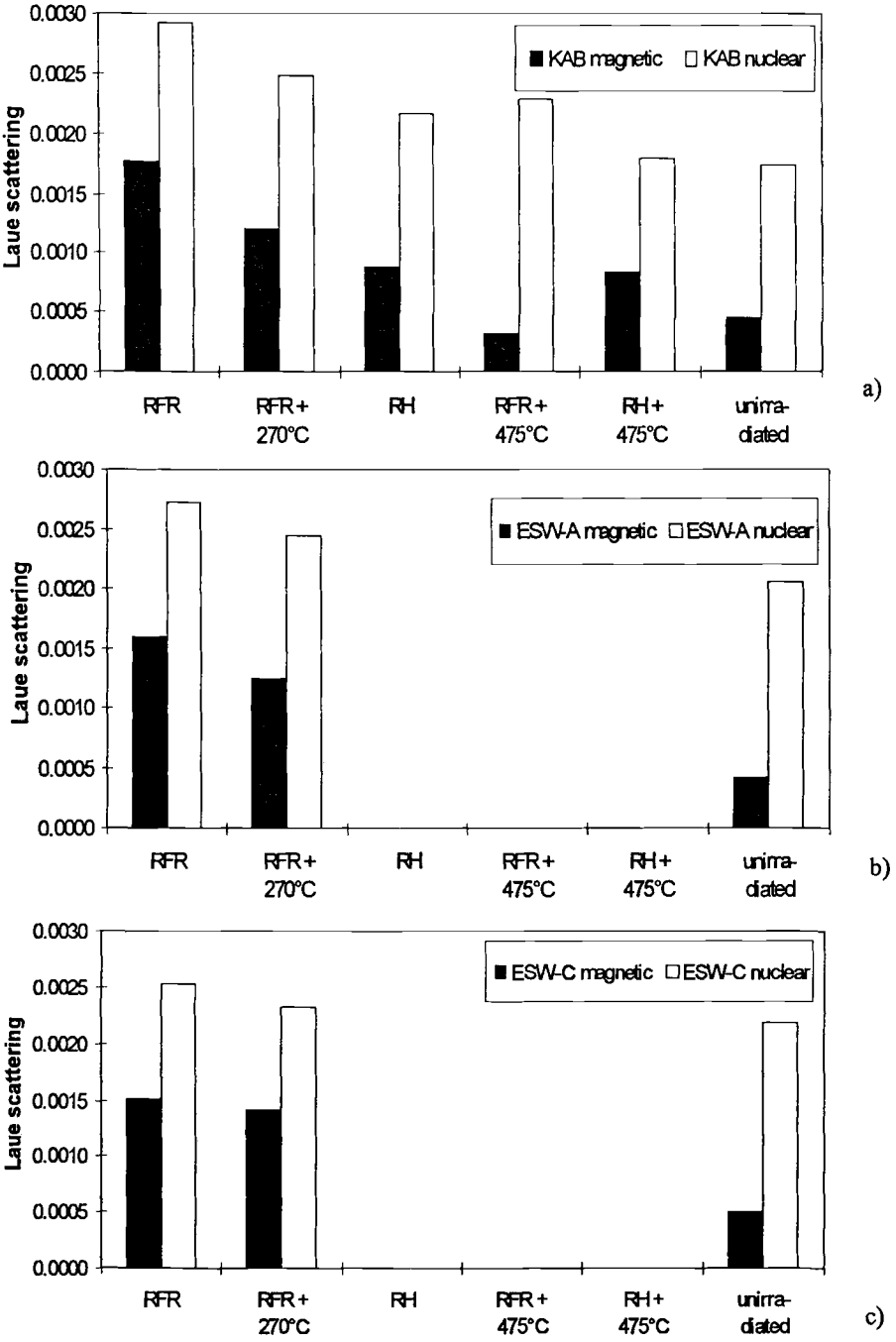


Fig. 4 Comparison of the monotonic Laue scattering for the different irradiation and annealing states of the materials a) KAB b) ESW-A and c) ESW-C

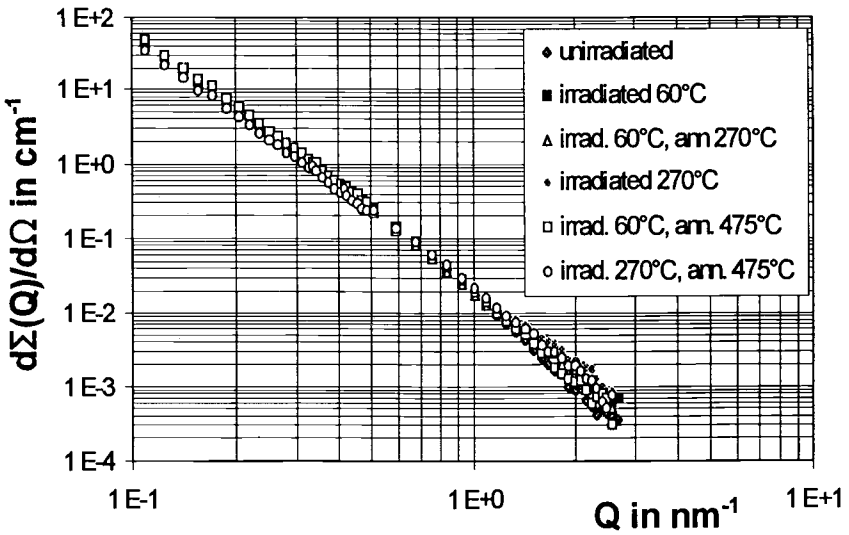


Fig. 5 True SANS cross section of the different irradiation and annealing states of material KAB after subtraction of constant scattering

The subtraction of the constant scattering contribution from the measured differential scattering cross section yields the true small angle scattering cross section (see Fig. 5). From these SANS data the uncalibrated volume distribution functions H(R) for the several material states are calculated using the indirect transformation method. The results are given as the function H(R), which is related with the product of difference in the scattering density $\Delta\eta(R)$ and volume distribution function $D_V(R)$ by an unknown calibration factor f:

$$H(R) = f \cdot \Delta\eta \cdot D_V(R) \tag{10}$$

Tests with intensity distributions of given size distribution functions performed by Glatter and also own test show that the results of ITP92 agree very well with the input size distribution functions.

Most of the structures that have to be taken into account for the irradiation defects are non-ferromagnetic. In this case, the difference in the magnetic scattering density $\Delta\eta_m(R)$ is constant and equal to the scattering density of the iron matrix. Then in good approximation H(R) depends only on the size distribution $D_V(R)$. The results for the magnetic inhomogeneities in the different states of the materials investigated are given in Figs. 6 a) and b). The upper limits of the size distribution functions at 12 nm are set by the boundary condition of the indirect transformation method [16].

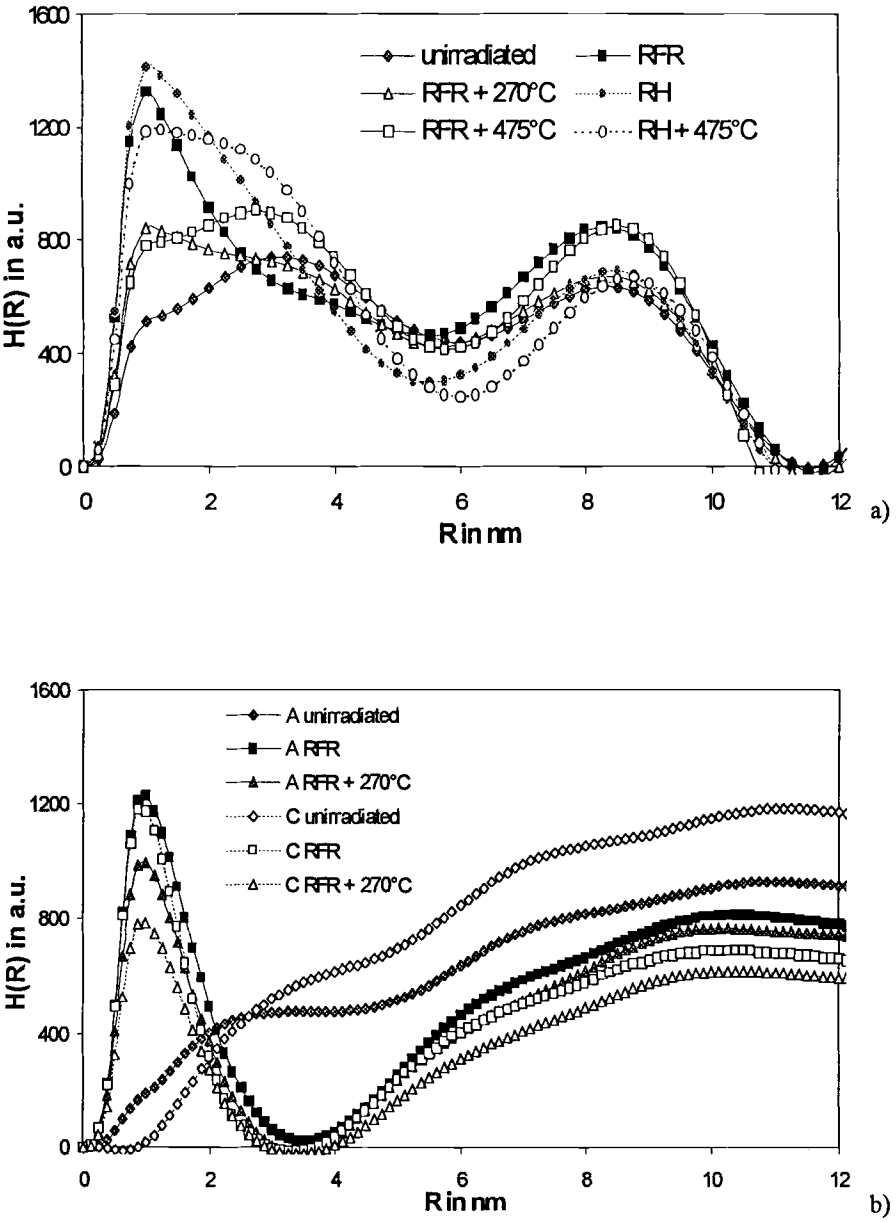


Fig. 6 Size distribution functions for the different irradiation and annealing states of the materials a) KAB and b) ESW-A and ESW-C calculated from the magnetic small angle neutron scattering

Discussion

Constant scattering contribution

The constant scattering contribution can be estimated by [17]:

$$\left(\frac{d\Sigma}{d\Omega}\right)_c = \frac{\rho}{2}\cdot\sum_{\mu,\nu}(b_\mu - b_\nu)^2\cdot c_\mu c_\nu \qquad (11)$$

$$= \rho\cdot(\overline{b^2} - \overline{b}^2)$$

$$\overline{b}^2 = (\sum_\mu b_\mu\cdot c_\mu)^2$$

$$\overline{b^2} = \sum_\mu b_\mu^2\cdot c_\mu$$

ρ is the number density of the atoms in the lattice, μ and ν are the indices of the different isotopes, b is the scattering length of the isotopes and c is their concentration.

In the unirradiated state, the constant scattering is mainly caused by the incoherent scattering of the different iron isotopes. The different iron isotopes only cause nuclear scattering as they have the same magnetic behaviour. The theoretical value of this nuclear scattering should be $(d\Sigma/d\Omega)_{c\text{-}Fe} = 0.0027\ cm^{-1}$. The upper limit is $0.0037\ cm^{-1}$ for the case that each foreign atom is solved but there are no vacances in the iron lattice.

The estimated values are smaller than the theoretical lower limit given by the incoherent scattering of iron. It shows that the absolute value of the monotonic Laue scattering are incorrect. The estimation of the Laue scattering is influenced by some instrumental uncertainities. The instrumental uncertainities can effect that the Laue scattering is underestimated by the following reasons:

- It was assumed that the one half of the instrumental background intensity comes from the range ahead the sample and the other half comes from other ranges.Therefore the separately measured background intensity was multiplied with a factor (1+T)/2. T is the transmission of the sample. If the assumption is not fulfilled and the instrumental background intensity comes only from ranges ahead the sample, the instrumental background is overestimated and to much "instrumental background" is subtracted.
- The counting rate of the instrumental background intensity measurement (measurement without sample) is low. It is not excluded that the counting effectivity of the detector is a bit higher for the instrumental background measurement than for the SANS measurement because the effective dead time depends on the counting rate. The effect results in an overestimation of the instrumental background as well.

However, the uncertainities are systematical and for all material states the same. This allows the discussion of the changes in the Laue scattering.

The very small value of the magnetic constant scattering contribution confirms that the constant scattering in the unirradiated state is mainly caused by the iron isotopes.

The isotope composition is not significantly changed by the irradiation. Consequently, the increase of the constant scattering contributions after the irradiation at low temperature is due to the increase of the number of point defects. The differences between the increase in the magnetic and the nuclear scattering can provide clues about the kind of point defects. The

stronger increase of the constant magnetic scattering in comparison to the constant nuclear scattering can be caused by the formation of new point defects which stronger differ from the iron matrix in the magnetic scattering length b_m than in the nuclear scattering length b_n. It means that not only the formation of vacancies but also of interstitials and substitutional atoms has to be taken into account. The formation of vacancies would cause a stronger increase of the nuclear scattering than of the magnetic scattering. However, the formation of vacancies cannot be excluded.

Size distribution of precipitates

In the following the discussion is focused on the size distribution function calculated from the magnetic scattering. As already mentioned, these distribution functions are less influenced in the scattering density $\Delta\eta(R)$. Nevertheless, the ratio between nuclear + magnetic and nuclear scattering, the so-called A-ratio [14], can provide information about the type of inhomogeneities. It is defined as follows:

$$A = \frac{\left(\frac{d\sigma(Q)_{nuc}}{d\Omega}\right)_{SAS} + \left(\frac{d\sigma(Q)_{mag}}{d\Omega}\right)_{SAS}}{\left(\frac{d\sigma(Q)_{nuc}}{d\Omega}\right)_{SAS}} \qquad (12)$$

For a system with only one type of inhomogeneities the A-ratio follows from Eq.(2,3):

$$A = \frac{\Delta\eta^2_{nuc} + \Delta\eta^2_{mag}}{\Delta\eta^2_{nuc}} \qquad (13)$$

For systems with different types of inhomogeneities $\Delta\eta$ depends on R. Then A also depends on R and, thus, also on Q. The A-ratio for the different types of inhomogeneities can be estimated from the ratio of the size distribution functions H calculated from the nuclear and the magnetic scattering. This calculation is based on the assumption that the magnetic and the nuclear scattering see objects which are identical in volume fraction and size. Otherwise no constant A-ratio over some R-ranges would be found. Fig. 7 shows the R dependence of the A-ratio for the investigated material states. A constant A-ratio means that in this R-range only one type of inhomogeneities exists. Such regions with constant A-ratio can be found for instance for the size range of the irradiation-induced peak in the size distribution function of the as-irradiated and the irradiated and annealed state of the laboratory heats ESW-A and -C. In the unirradiated state there are small differences between the size ranges 2 nm $\leq$ R $\leq$ 5 nm and 7 nm $\leq$ R $\leq$ 12 nm. Both in the irradiated state and in the annealed state, the A-ratio is not constant over the size range from 5 to 12 nm. This means that the nuclear scattering density of the precipitates is changed with their size. Beside the peaks the A-ratio is very uncertain and, therefore, should not be discussed in further detail.

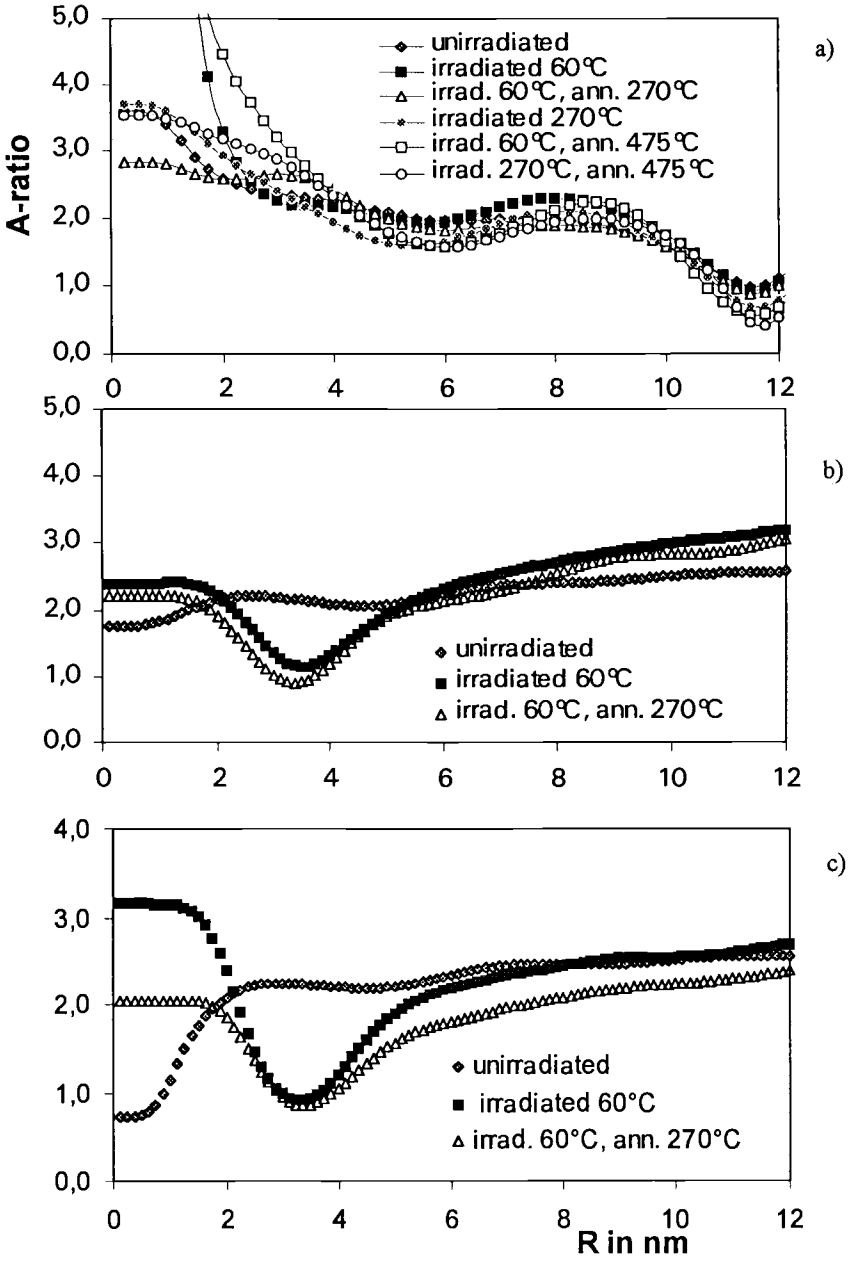


Fig 7 R dependence of the A-ratio for a) KAB, b) ESW-A and c) ESW-C

The shape of the size distribution functions differs between the original material KAB and the laboratory heats ESW-A and -C. It shows that the structure of this material is more complex. There are no essential differences between the shape of the size distribution functions calculated from the nuclear and the magnetic small angle scattering.

In the unirradiated state, the material KAB shows a wide distribution over the size range between 0.8 and 11.0 nm with two maxima at about 3.0 and 8.5 nm. For the laboratory heats ESW-A and -C the distribution is smooth without a sharp peak. At high R-values the H(R) is not equal to zero. This proves the existence of larger inhomogenities. Such larger inhomogeneities are detected by transmission electron microscopy (TEM) as vanadium-rich MC or M_4C_3 precipitates [18]. In [18], the maximum of the size distribution of these carbides was estimated with D = 17 nm for a 15Kh2MFA steel. The differences between KAB and ESW show that metallurgical differences influence the inhomogeneities in the size range between 0 and 12 nm very strongly. The higher content of vanadium in ESW-C effects a higher number of vanadium-rich precipitates in this heat than in ESW-A. For the wide distribution found in the unirradiated state of the materials ESW-A and -C a constant A-ratio of 2.5 was calculated for both materials. For material KAB the A-ratio slightly decreases from 2.5 to 2.0 in the size range between 0.8 and about 5 nm and keeps constant up to 10 nm. However, the estimated values are close to the theoretical value of vanadium carbide VC (A=2.4).

After irradiation a new peak occurs in all the investigated materials at small R-values. The maxima of these new peaks in the size distribution functions are at about 1 nm. It is in correspondence with TEM results where non-resolvable black dots with a size between 1 an 8 nm were found [19]. The width of the peaks for the materials irradiated at 60°C is approximately the same whereas the peak for KAB irradiated in VVER-2 is significantly broader. It means that in materials irradiated at 270°C the irradiation-induced inhomogeneities can be larger than in material irradiated at 60°C. In spite of the significantly smaller fluence the material KAB irradiated in VVER-2 shows the highest amount of irradiation-induced inhomogeneities in this size range. Taking into account that for this irradiation state the amount of foreign atoms in the iron lattice is lower than in the materials irradiated at 60°C this finding can be understood. The higher temperature increases the mobility of the solute atoms dissolved due to the collision cascade process. Due to the high mobility they can form clusters and precipitates. The A-ratio of the inhomogeneities of the first peak is 3.7 for KAB-VVER-2, 3.2 for ESW-C and 2.4 for ESW-A. The A-ratios show that the irradiation-induced inhomogeneities are precipitates. As previous ASAXS investigations [20] have shown, the irradiation-induced precipitates are vanadium-rich in this kind of steel. A comparison with A-ratios calculated for ideal structures of some phases shows that vanadium rich mixing carbides (A-ratio 2.7)for $V_{0.86}Cr_{0.09}Mo_{0.04}Fe_{0.01}C$ which was found by EDX analysis of replica foils at unirradiated 15Kh2MFA specimens [21]), vanadium nitrides (4.4 for VN, 2.5 for V_4N_3) or vanadium-rich carbo-nitrides and even copper phosphides (4.8 for Cu_3P) might be the constituents of the irradiation-induced precipitates. The estimation of the A-ratio was not successful for KAB-RFR. At very low R-values the portion of the magnetic inhomogeneities is much higher than the portion of the nuclear inhomogeneities. Maybe, the premise that the inhomogeneities are non-ferromagnetic and the same inhomogenities are detected by magnetic and nuclear scattering are injured and, thus, the analysis is not correct in this case.

The effect of the irradiation on inhomogenities with higher size is uncertain. For the material KAB-RFR even a higher number of inhomogeneities with sizes between 6 and 10 nm can be detected whereas for the laboratory heats and KAB-VVER-2 the number of these precipitates decreases. In contrast to the R-region between 0 and 4 nm the principal shape of the size distribution function is not changed in the higher R-range. It is presumed that local differences in the carbide content, which do not result from the irradiation, are the reasons for that.

The annealing at service temperature of 270°C of the material irradiated in the RFR causes a decrease of the number of irradiation-induced inhomogeneities in the size range between 0.8 and 3.0 nm. In material KAB this effect is very strong and connected with a coarsening of these precipitates. The size distribution function for KAB-RFR-270 strongly differs from the size distribution function for KAB-VVER-2. It shows that not only the irradiation temperature but also the higher neutron flux has to be taken into account. In the materials ESW-A and -C the decrease of the objects smaller than 3.0 nm is not so strong as in material KAB-RFR and no coarsening can be found. The A-ratios of these particles decrease down to 2.6 for KAB-RFR, 2.2 and 2.0 for ESW-A and ESW-C, respectively. It shows that in addition to the decreasing number of inhomogeneities an increase of the mean value of $\Delta\eta_{nucl}$ occurs. This effect can be caused by an annealing of small voids as well as by a change of the composition of the irradiation-induced precipitates, for instance, by decreasing of the iron content of small carbides. The increase in the mean value of $\Delta\eta_{nucl}$ is strongest for KAB, and still stronger for ESW-C than for ESW-A.

Annealing at 475°C yields a coarsening of the irradiation-induced precipitates of the first peak of the size distribution function. As well as for the as-irradiated at 60°C state for this annealed state of KAB-RFR no A-ratio can be estimated for the first peak. For the material irradiated at 270°C (VVER-2) the A-ratios are similar to the as-irradiated state. The second peaks of the size distribution functions decrease at lower R and is comparable to the as-irradiated state near to the maximum and at higher R. The A-ratio is constant over this R-range.

The results can be explained by a partial dissolution of precipitates formed by the processes in the collision cascade. Vacancies are also formed in the iron lattice. Some of the atoms which are knocked out from the precipitates by the collision process remain in the iron lattice as point defects. The others with a higher mobility can rearrange to new small precipitates or voids. At higher temperatures point defects are trapped. Some of the surviving foreign atoms in the iron matrixs attain to the newly formed precipitates, coarsen them, change their composition and stabilize them. However, some of the newly formed inhomogeneities are dissolved.

Conclusions

The effect of low temperature neutron irradiation on the formation of precipitates and point defects was studied by small angle neutron scattering for an original heat and two laboratory heats of the VVER-440-type RPV steel 15Kh2MFA. On condition that the Porod scattering of large objects and the monotonic Laue scattering are the dominating intensity contributions at Q values > 1.8 nm^{-1} the following results were found :

1. The number of point defects is increased by the irradiation at low temperature. The point defects are not only vacancies but also re-solved atoms from precipitates formed in the metallurgical process. A partial dissolution of these precipitates is possible. Smaller inhomogeneities with sizes between 0.3 and 3.0 nm are formed.
2. Irradiation at service temperature produces a smaller content of point defect but a greater number of irradiation-induced precipitates. These precipitates can be larger than the precipitates formed at lower temperature.
3. Annealing at 270°C of the material irradiated at lower temperature does not reproduce the structure of the material irradiated under service conditions. It shows that also the neutron flux influences the formation of irradiation defects.
4. Annealing at 475°C shows that the irradiation-induced inhomogeneities differ in their stability for the different irradiation temperature. While the inhomogeneities found after irradiation at 60°C partially disappear, the volume fraction of the precipitates (size < 5 nm) formed after irradiation at 270°C does not change significantly. However, a coarsening of the irradiation-induced defects can be found after annealing at 475°C for both irradiation states.

Acknowledgement

The authors thanks Mrs M.-H. Mathon from LLB Saclay and Mr. R.Gilles from HMI Berlin for their support during the experiments and their helpful discussion of the results.

References

[1] T. Diaz de la Rubia, M.W. Guinan, Mater. Res. Forum 97-99 (1992) 23.

[2] S.J. Zinkle, B.N. Sing, J. Nucl. Mat. 199 (1993) 173.

[3] G. Martin, F. Soisson, P. Bellon, J. Nucl. Mater. 205 (1993) 301.

[4] F. Sousson, P. Bellon, A. Barbu, G. Martin, Mat. Res. Soc. Symp. Proc. Vol. 373, 1995, Materials Research Society, p. 89.

[5] S. Matsumura, M. Okudaiva, C. Kinoshita, J. Nucl. Mater. 251 (1997) 145.

[6] R.K. Nanstadt, K. Farrell, D.N. Braski, J. Corwin, J. Nucl. Mater. 158 (1988) 1.

[7] K. Farrell, S.T. Mahmod, R.E. Stoller, L.K. Mansur, J. Nucl. Mat. 210 (1994) 268.

[8] G.R. Odette, G.E. Lucag, R.D. Klingesmith, R.E. Stoller, *Effects of Radiation on Materials: 17th International Symposium, ASTM STP 1270,* D.S. Gelles, R.K. Nanstad, A.S. Kumar, E.A. Little (Eds.), American Society for Testing and Materials, 1996, p. 547.

[9] F.M. Boyolon, R.J. McElroy, S. Gage, W.J. Phythian, *Effects of Radiation on Materials: 17th International Symposium, ASTM STP 1270,* D.S. Gelles, R.K. Nanstad, A.S. Kumar, E.A. Little (Eds.), American Society for Testing and Materials, 1996. p. 331.

[10] R.E. Stoller, *Effects of Radiation on Materials: 17th International Symposium, ASTM STP 1270,* D.S. Gelles, R.K. Nanstad, A.S. Kumar, E.A. Little, Eds., American Society for Testing and Materials, 1996, p. 28.

[11] M. Groβe, A. Hempel, J. Böhmert, G. Brauer, F.M. Haggag: Proc. Material Research Society Symposium Proceedings Vol 439, Pittsburgh (1997), 515.

[12] Laboratoire Leon Brillouin: "Equipments Experimentaux" Edition LLB (1995) 69.

[13] "Neutron-Scattering Instrumentation at the Research Reactor BER II," Berlin Neutron Scattering Center - BENSC, May 1996.

[14] G. Brauer, F. Eichhorn, F. Frisius, R. Kampmann, *Effects of Radiation on Materials: 16th International Symposium, ASTM STP 1175,* A.S. Kumar, D.S. Gelles, R.K. Nanstad (Eds.), American Society for Testing and Materials, Philadelphia, 1993, p. 503.

[15] J.P. Cotton, "Initial Data Treatment in Neutron X-ray and Light Scattering," Eds. P. Lindner and T. Zemb, North Holland Delta Series (1991) 19.

[16] O. Glatter, J. Appl. Cryst. 13 (1980) 7.

[17] W. Schilling, "Einführung in die Röntgenstreuung in Synchrotronstrahlung zur Erforschung kondensierter Materie," Forschungszentrum Jülich, ISBN 3-89336-088-3, 1992, 19.1.

[18] K. Törrönen, "Microstructural Parameters and Yielding in a Quenched and Tempered Cr-Mo-V Pressure Vessel Steel," Materials and Processing Technology Publication 22, Technical Research Centre of Finland, Espoo 1979.

[19] J. Kocik, E. Keilova, J. Nucl. Mater. 172 (1990) 126.

[20] M. Grosse, F. Eichhorn, J. Boehmert, G. Brauer, *Effects of Radiation on Materials: 17th Volume, ASTM STP 1270,* David S. Gelles, Randy K. Nanstad, Arvind S. Kumar and Edward A. Little, Eds., American Society for Testing and Materials, Philadelphia, 1996, ASTM STP 1270 (1996), p. 1123.

[21] J. Janovec, A. Güth, A. Vyrostkava, B. Stefan: Neue Hütte 34, (1989), p. 91.

Shenhua Song,[1] Roy G. Faulkner,[1] Peter E. J. Flewitt,[2] Pierre Marmy,[3] and Max Victoria[3]

Grain Boundary Phosphorus Segregation under Neutron Irradiation and Aging in 2.25Cr1Mo Steel

Reference: Song, S., Faulkner, R. G., Flewitt, P. E. J., Marmy, P., and Victoria, M., **"Grain Boundary Phosphorus Segregation under Neutron Irradiation and Aging in 2.25Cr1Mo Steel,"** *Effects of Radiation on Materials: 19th International Symposium, ASTM STP 1366,* M. L. Hamilton, A. S. Kumar, S. T. Rosinski, and M. L. Grossbeck, Eds., American Society for Testing and Materials, West Conshohocken, PA, 2000.

Abstract: Impurity segregation to grain boundaries under irradiation is one of the important radiation effects on materials. For this reason, phosphorus segregation to prior austenite grain boundaries in a P-doped 2.25Cr1Mo steel subjected to neutron irradiation and aging is examined using field emission gun scanning transmission electron microscopy (FEGSTEM) with energy dispersive X-ray microanalysis (EDX). The steel samples are irradiated and aged around 270 °C and 400 °C, respectively. The irradiation dose rate and dose are ~1.05×10^{-8} dpa/s and ~0.042 dpa respectively for 270 °C irradiation, and ~1.75×10^{-8} dpa/s and ~0.13 dpa respectively for 400 °C irradiation. The FEGSTEM results indicate that there is no apparent phosphorus segregation during 270 °C irradiation but there is some during 400 °C irradiation.

Keywords: neutron irradiation, segregation, grain boundary, phosphorus

Introduction

Over the past two decades, a great deal of research has been carried out on irradiation-induced segregation because of its considerable importance to nuclear engineering applications [*1*]. However, much attention has been paid to austenitic materials such as nickel alloys [*2-5*] and austenitic stainless steels [*6-10*] while only a little to ferritic materials [*11*].

Changes in mechanical properties during service of low-alloy steel components used in the nuclear power industry are clearly of great importance in the safe operation of reactor systems and play an important part in plant life extension studies. Neutron irradiation of these low-alloy ferritic steel components gives rise to an increase in ductile-

[1] Researcher and Professor, respectively, Institute of Polymer Technology and Materials Engineering, Loughborough University, Loughborough, LE11 3TU, UK.
[2] Structural Integrity Manager, Berkeley Centre, Magnox Electric plc, Berkeley, Gloucestershire GL13 9PB, UK.
[3] Senior Scientists, EPFL-CRPP, Fusion Technology, CH-5232 Villigen PSI, Switzerland.

Copyright© 2000 by ASTM International www.astm.org

brittle transition temperature (DBTT) with a decrease in upper shelf energy [*12,13*]. Of most concern is the possibility that, with large DBTT shifts, the brittle behaviour may be encountered in the temperature regime of normal reactor operation or of reactor shutdown.

It is clear [*14*] that embrittlement of low-alloy steels is classified into non-hardening embrittlement and hardening embrittlement. The non-hardening embrittlement is generally associated with intergranular failure stemming from grain boundary segregation of impurities such as P, S, As, Sn and Sb. The hardening embrittlement arises from the production of hardening centres, both precipitates and matrix defects.

As is well known, 2.25Cr1Mo steel is one of the important low-alloy steels in the power industry. It has been found [*15-17*] that the grain boundary segregation of phosphorus has considerable contributions to temper embrittlement or intergranular stress corrosion cracking in this steel. Similar embrittlement may be prediced to be correlated with irradiation-induced phosphorus segregation to grain boundaries.

In the work presented here, phosphorus segregation to prior austenite grain boundaries in a P-doped 2.25Cr1Mo steel subjected to neutron irradiation and aging was examined using field emission gun scanning transmission electron microscopy (FEGSTEM).

Experimental Procedure

Experimental Material and Specimen Preparation

A nominal 2.25Cr1Mo steel doped with 0.077 wt%P was prepared by induction melting of the base elements under an argon atmosphere. The resulting ingots were hot rolled to 10 mm diameter rods and they were then austenitised for two hours at 1150 °C, furnace-cooled to an intermediate temperature of 950 °C, held there for half an hour and then air-cooled to room temperature. All the rod samples pre-treated above were finally austenitised for two hours at 1050 °C and then water-quenched. Chemical composition of the steel is shown in Table 1.

Because of the problems associated with radioactive material handling, before irradiation the specimens were quasi-prepared TEM discs. In order to reduce γ-ray emission from radioactive specimens which affects energy dispersive X-ray microanalysis, the 2 mm diameter discs were cut and trepanned by a Spark erosion machine and then mechanically polished to about 0.1 mm thick. In order to have indentical specimen size conditions the thermal control specimens are the same as those for irradiation in size.

Irradiation and Thermal Aging

Material irradiation was performed in a thermal light-water research reactor, named SAPHIR, operated by the Swiss Federal Institute for Reactor Research in Villigen (Switzerland). This reactor operates at a thermal power of 10 MW. The thermal neutron flux is 8×10^{13} neutrons/(cm^2.s) at the core surface and up to 1.2×10^{14} neutrons/(cm^2.s) in the central irradiation positions. In this work, the specimens were irradiated to about 0.042 dpa (fast neutron energy > 1 MeV) with a neutron dose rate of about 1.05×10^{-8}

dpa/s around 270 °C and to about 0.13 dpa (fast neutron energy > 1 MeV) with a neutron dose rate of about 1.75×10^{-8} dpa/s around 400 °C, respectively. However, owing to the limited cooling capability of the system the irradiation temperature has some fluctuations during irradiation. The irradiation temperature is illustrated in Figure 1 as a function of irradiation time for both 270 °C (curve C1) and 400 °C (curve C2) irradiations.

Table 1— *Chemical composition of the experimental steel*

	C	Mn	S	P	Si	Cr	Ni	Mo	Sn	As	Sb
wt%	0.086	0.46	0.009	0.077	0.29	2.28	0.15	1.00	0.011	0.005	0.021
at%	0.40	0.47	0.016	0.14	0.57	2.44	0.14	0.58	0.005	0.004	0.010

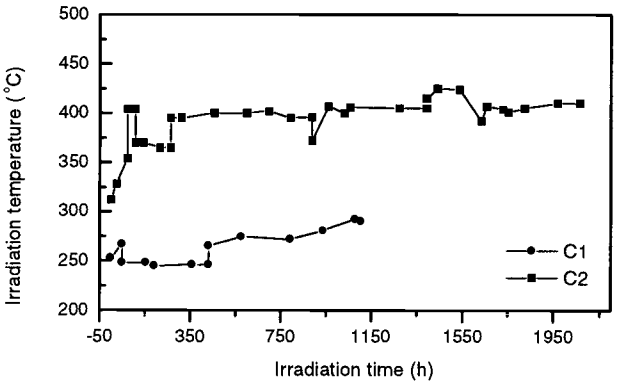


Figure 1 —*Irradiation temperature as a function of irradiation time.*

To enable radiation effects to be distinguished from any purely thermal effects generated during irradiation, thermal control specimens were produced and aged by simulating the irradiation process (see Figure 1). Henceforth, thermally aged samples are called unirradiated samples.

Thin Foil Preparation and Microanalysis

Irradiated and thermally aged 2 mm dia. discs were slightly polished on fine grade silicon carbide paper to clean the specimen surfaces and then electropolished by using a Struers Tenupol dual-jet electropolishing machine to achieve thin foil regions that are electron-transparent. Good thin foils were found to be consistently produced by employing an electrolyte of 5% perchloric acid and 95% methanol, cooled by liquid

nitrogen to -60 °C. The operating voltage used was about 25 V. The electrolyte flow was set to maximum for the first minute of electropolishing to dimple the disc, and then reduced to a lower rate until perforation took place. The thin foils were then cleaned in acetone and stored under absolute alcohol.

The thin foils were examined in a Philips EM 400 transmission electron microscope (TEM) equipped with a LaB6 source, operating at 120 kV. Ten foils prepared for each material condition were initially assessed according to their suitability for subsequent segregation analysis with regard to the presence of the desired sink types within the thin area. The three best foils for each material condition were selected for further analysis using the FEGSTEM.

The instrument used to determine spatial chemical composition distributions was the Vacuum Generators HB501 field emission gun scanning transmission electron microscope (FEGSTEM) with a Link systems energy dispersive X-ray (EDX) spectrometer. It offers advantages over conventionally illuminated STEMs for high resolution microanalysis.

The specimen under examination was, whenever possible, taken from storage under absolute ethanol, mounted in the holder and inserted into the specimen stage of the microscope at the night before intended analysis. This may allow the specimen to settle down and minimise drift at the start of analysis in the next day. For analysis, a suitable interface of the desired type was selected and oriented so that its plane was parallel to the incident electron beam. For each grain boundary, three positions were analysed and the arithmetic mean of data points obtained was taken as the measured value. 2-3 grain boundaries were analysed for each kind of sample. Spatial compositional data around the boundary were obtained by placing the stationary electron probe at the required analysis point and collecting an EDX spectrum for proper time (usually ~100 seconds). Spectra were achieved for points on the boundary and at distances of 1.25, 2.5, 5 and 10 nm on either side of the boundary within precipitate-free regions.

Results and Discussion

Microstructure

Optical metallography showed that all the 2.25Cr1Mo steel samples in the water-quenched condition, following the austenitising heat treatment, had a lath martensite microstructure, with a prior austenite grain size of ~100 μm (mean linear intercept, see Ref. [*18*]). Figure 2 represents TEM image of the martensite microstructure for the water-quenched 2.25Cr1Mo steel. Transmission electron microscopy demonstrated that there was a very small amount of carbide precipitation for the 270 °C-irradiated and -aged samples and some amount of carbide precipitation for the 400 °C-irradiated and -aged samples, and that microstructures for the irradiated samples were similar to those for the thermally aged samples. A FEGSTEM image of a typical grain boundary analysed is shown in Figure 3, demonstrating that the grain boundary is parallel to the incident electron beam, which is necessary for FEGSTEM microanalysis.

Microanalysis Results

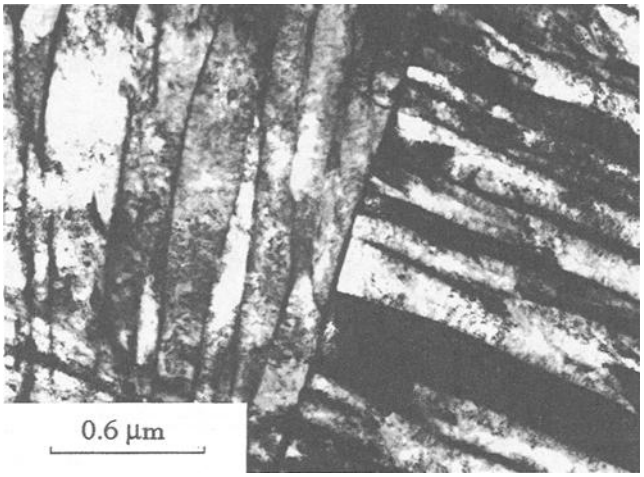


Figure 2 — *TEM image of the martensite microstructure for the water-quenched 2.25Cr1Mo steel.*

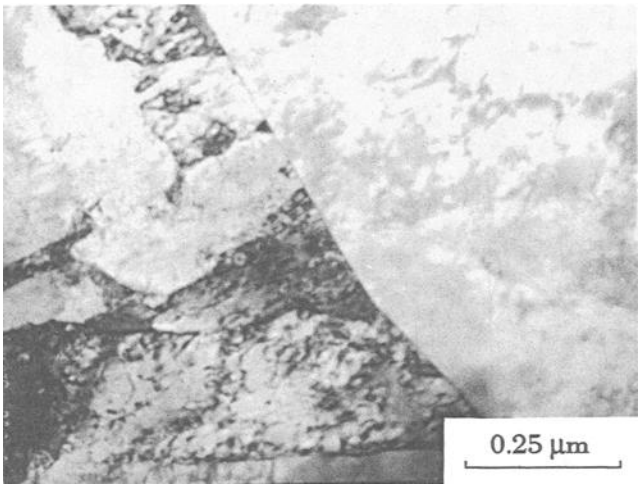


Figure 3 — *FEGSTEM image showing a typical grain boundary analysed.*

The phosphorus concentration profiles around the grain boundary, determined by FEGSTEM microanalysis, are shown in Figures 4 and 5 for irradiated and unirradiated materials. Clearly, there is no apparent irradiation effect for phosphorus segregation during 270 °C-irradiation (see Figure 4). The mean value of the measured results for the irradiated samples is about 1.9 at% at the grain boundary, which is almost the same as that for the unirradiated samples (about 2.0 at%). Owing to the fact that little thermal segregation of phosphorus occurs below 300 °C, the grain boundary segregation of

phosphorus in the 270 °C irradiated or aged samples should be produced in the pre-irradiation heat-treatment process. This has been confirmed in Ref. [*19*].

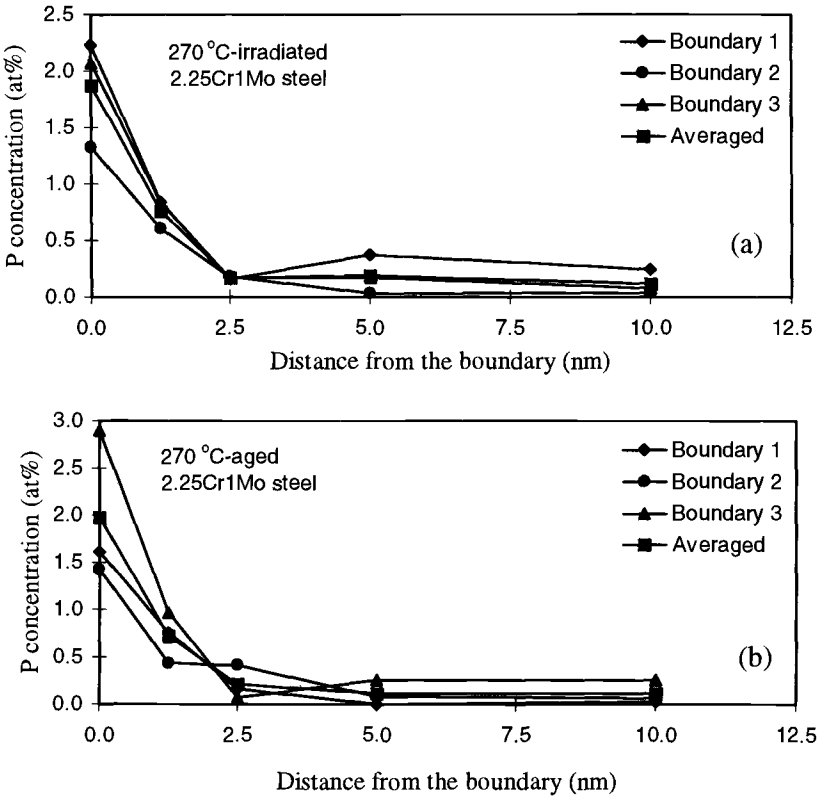


Figure 4 — *Phosphorus concentration profiles from the grain boundary to the matrix for (a) 270 °C-irradiated and (b) 270 °C-aged samples, determined by FEGSTEM microanalysis (Data points away from the boundary plane are produced by averaging the measured values from both sides of the boundary).*

For 400 °C irradiation, there is some irradiation effect for phosphorus segregation. After 400 °C irradiation, the mean value of the measured results is about 3.05 at% at the grain boundary. This value is approximately 0.33 at% higher than that for the unirradiated samples (see Figure 5).

It should be recognised that the value of the experimental measurement for the grain boundary segregation using the X-ray microanalysis technique is determined by the following factors: (i) the probe size; (ii) the grain boundary orientation; (iii) the overall stability and accuracy of the location of the analysing electron beam; and (iv) the

magnitude and spatial extent of the segregant profile. Apart from these parameters there is a variability of segregation concentration due to the specific orientation of the particular grain boundary selected for microanalysis. This has been discussed by Laws and Goodhew [*20*] with respect to chromium depletions observed in a sensitised austenitic stainless steel.

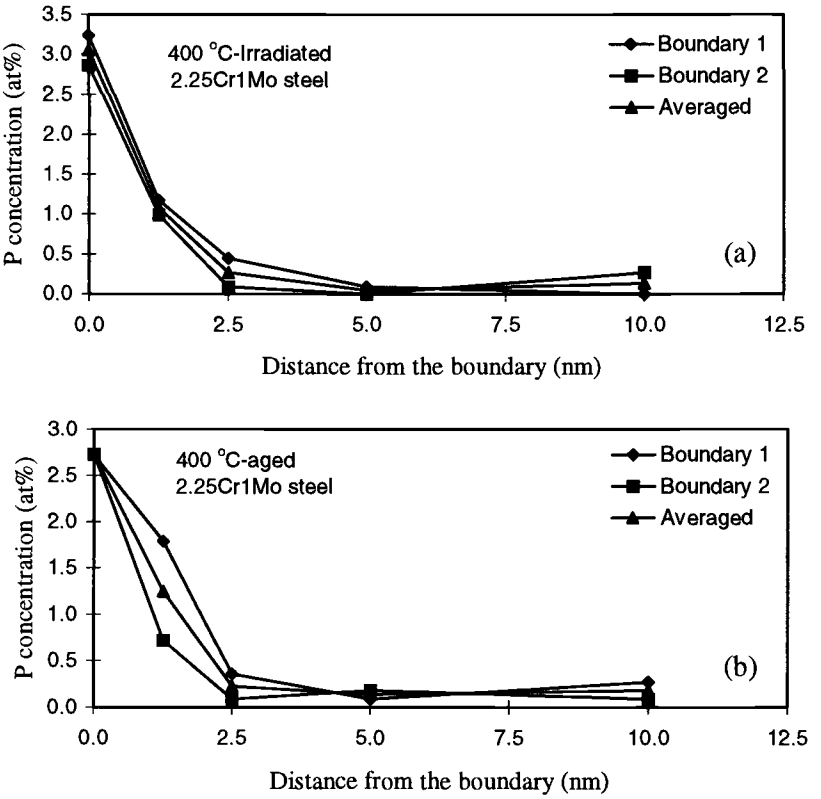


Figure 5 — *Phosphorus concentration profiles from the grain boundary to the matrix for (a) 400 °C-irradiated and (b) 400 °C-aged samples, determined by FEGSTEM microanalysis (Data points away from the boundary plane are produced by averaging the measured values from both sides of the boundary).*

The concentration at a given grain boundary depends on the overall misorientation but there is clearly an enhancement for specific orientations that result in those termed special grain boundaries. Therefore, the boundary concentration varies from boundary to boundary. In microanalysis, grain boundaries were selected that had the capability to be oriented parallel to the analysing electron beam to produce larger X-ray signal with respect to elements of interest. As a consequence, for this particular microanalysis

techinque the selection of the grain boundaries is limited. This would affect the measured results.

The preceding experimental results may be explained by a site-competition mechanism [*21*]. Since the binding energies of carbon with grain boundaries and point defects are much higher than those of phosphorus, the capabilities of competition for segregation sites and for the formation of point defect-solute complexes are much stronger for carbon than for phosphorus. The segregation of phosphorus is therefore suppressed during irradiation by the competition effect. This effect has also been found in C-Mn submerged-arc weld metals [*22*].

It is worthy of note that the actual grain boundary concentration of phosphorus should be much higher than that determined by FEGSTEM microanalysis because of its limited spatial resolution. The actual spatial resolution of FEGSTEM microanalysis is much lower than its nominal spatial resolution of ~1-1.5 nm due to the specimen-electron beam interaction leading to beam broading within the specimen [*23*]. This situation needs to be taken into account in the evaluation of grain boundary segregation by means of FEGSTEM microanalysis.

Faulkner *et al.* [*24*] established an analytical convolution method to quantify the true solute grain boundary segregation. Its application in Ref. [*24*] demonstrated that it worked quite reasonably. This method is to convolute an assumed electron probe current distribution with an assumed segregant distribution to provide a measure of the best profile that could be created by the geometric interaction of the electron probe and segregant distributions. The electron probe current is assumed to be radially normally distributed, with a mean of zero [*i.e.* centred at (0,0)] and a variance represented by σ^2. For a solute distribution of concentration C_b in the segregated layer (the concentration gradient is assumed to be zero within the layer) and C_0 in the adjacent matrix, the derived concentration, C, generated from an electron probe at a distance x_d from the centre of the segregated layer of width d_0, is given by [*24*]

$$C = C_o + \tfrac{1}{2}(C_b - C_o) \times [erf(\frac{x_d + \frac{1}{2}d_o}{\sigma\sqrt{2}}) - erf(\frac{x_d - \frac{1}{2}d_o}{\sigma\sqrt{2}})] \quad (1)$$

For a fixed width of segregated layer, the derived concentration profile is determined by the standard deviation of the probe distribution, σ. The probe diameter is usually defined by a diameter containing 80% of the total probe current. The relationship between the standard deviation of the normal approximation to the electron distribution (σ) and the beam diameter containing 80% of the current (ϕ_{80}) is given by [*24*]

$$\sigma = 0.279\phi_{80} \quad (2)$$

Equation (1) may be employed in conjunction with Equation (2) to determine the actual boundary concentration of the solute. To obtain this, it is essential to determine the effective probe size. It can be shown [*23*] that the average effective probe size for the α-Fe matrix is about 3.1 nm for an operating valtage of 100 kV, a nominal probe size of 1.5 nm, and a foil thickness of 30 nm. Using the messured boundary concentrations and

assuming that the boundary thickness is 1nm and that the solute concentration in the matrix adjacent to the boundary is equal to the bulk concentration, one may acquire from Equations (1) and (2) that the actual boundary concentrations of phosphorus are about 4, 4, 6, and 7 at% for the 270 °C-aged, 270 °C-irradiated, 400 °C-aged, and 400 °C-irradiated samples, repectively. As mentioned above, the grain boundary segregation of phosphorus in the 270 °C irradiated or aged sample is generated in the pre-irradiation or pre-aging heat-treatment process, i.e. during water-quenching from 1050 °C. An Auger electron spectroscopy study [*25*] has indicated that there is a phosphorus boundary concentration of ~5 at% in a 1300 °C-austenitized and oil-quenched low-alloy steel with a bulk phosphorus concentration similar to that in the steel employed in the present work. This concurs generally with the present study.

Summary

Experimental results on phosphorus segregation to prior austenite grain boundaries are reported for the neutron-irradiated and thermally aged (unirradiated) 2.25Cr1Mo steels. The results clearly demonstrate that there is no apparent irradiation effect for grain boundary segregation of phosphorus under 270 °C-irradiation and nevertheless there is some under 400 °C-irradiation.

Acknowledgements

We are grateful to Mr R. Scowen of the Berkeley Centre of Magnox Electric for the assistance given with the use of VG HB501 FEGSTEM. This work was financially supported by Magnox Electric and is published with the permission of the Director of Technology and Central Engineering of Magnox Electric. Also, we would like to thank Dr. C. C. Goodwin of Loughborough University for commenting on the manuscript.

References

[1] Flewitt, P. E. J., Williams, G. H., and Wright, M. B., "Integrity of Magnox Reactor Steel Pressure-Vessels," *Materials Science and Technology,* Vol. 9, 1993, pp.75-82.

[2] Lam, N. Q., Okamoto, P. R., Wiedersich, H., and Taylor, A., "Radiation-Induced Solute Segregation and Precipitation in Alloys," *Metallurgical Transactions*, Vol. 9A, 1978, pp. 1707-1714.

[3] Rehn, L. E., Okamoto, P. R., Potter, D. I., and Wiedersich, H., "Effect of Solute Misfit and Temperature on Irradiation-Induced Segregation in Binary Ni Alloys," *Journal of Nuclear Materials,* Vol. 74, 1978, pp. 242-251.

[4] Okamoto, P. R., and Rehn, L. E., "Radiation-Induced Segregation in Binary and Ternary Alloys," *Journal of Nuclear Materials,* Vol. 83, 1979, pp. 2-23.

[5] Murphy, S. M. and Perks, J. M., "Analysis of Phosphorus Segregation in Ion-Irradiated Nickel," *Journal of Nuclear Materials,* Vol. 171, 1990, pp. 360-372.

[6] Damcott, D. L., Cookson, J. M., Carter, R. D., Martin, J. R., Atzmon, M., and Was, G. S., "Proton-Induced Grain Boundary Segregation in Stainless Steel," *Radiation Effects and Defects in Solids,* Vol. 118, 1991, pp. 383-392.

[7] Cookson, J. M., Carter, R. D., Damcott, D. L., Atzmon, M., and Was, G. S., "Irradiation Assisted Stress-Corrosion Cracking of Controlled Purity 304L Stainless Steel," *Journal of Nuclear Materials,* Vol. 202, 1993, pp. 104-121.

[8] Carter, R. D., Damcott, D. L. Atzmon, M., Was, G. S., and Kenik, E. A., "Effects of Proton Irradiation on the Microstructure and Microchemistry of Type-304L Stainless steel," *Journal of Nuclear Materials,* Vol. 205, 1993, pp. 361-373.

[9] Kenik, E. A., "Application of Analytical Electron Microscopy to Radiation Damage Studies," *Journal of Nuclear Materials,* Vol. 216, 1994, pp. 157-169.

[10] Bruemmer, S. M. and Was, G. S., "Microstructural and Microchemical Mechanisms Controlling Inergranular Stress Corrosion Cracking in Light Water Reactor Systems," *Journal of Nuclear Materials,* Vol. 216, 1994, pp. 348-363.

[11] Little, E. A., "Microstructural Evolution in Irradiated Ferritic-Martensitic Steels – Transitions to High-Dose Behaviour," *Journal of Nuclear Materials,* Vol. 206, 1993, pp. 324-334.

[12] Gage, G. and Little, E. A., "Materials Characterization for Advanced Pressurized-Water Reactor. Part 1 – Mechanical Properties," *Nuclear Energy – Journal of the British Nuclear Energy Society,* Vol. 33, 1994, pp. 153-162.

[13] Little, E. A. and Gage, G., "Materials Characterization for Advanced Pressurized-Water Reactor. Part 2 – Microstructure," *Nuclear Energy – Journal of the British Nuclear Energy Society,* Vol. 33, 1994, pp. 163-172.

[14] Phythian, W. J. and English, C. A., "Microstructural Evolution in Reactor Pressure-Vessel Steels," *Journal of Nuclear Materials,* Vol. 205, 1993, pp.162-177.

[15] Seah, M. P., Spencer, P. J. and Hondros, E.D., "Additive Remedy for Temper Brittleness," *Metal Science,* Vol. 13, 1979, pp. 307-314.

[16] Lea, C., "Stress Corrosion Cracking and Temper Brittleness: Effect of Phosphorus Grain Boundary Segregation in a Low-Alloy Steel," *Metal Science,* Vol. 14, 1980, pp. 107-112.

[17] Yuan, Z.-X., Song, S.-H., Faulkner, R. G., and Xu, T.-D., "Effect of Cerium on Temper Embrittlement of P-Doped Mn Structural Steels," *Acta Metallurgica et Materialia,* Vol. 42, 1994, pp. 127-132.

[18] Vorlicek, V. and Flewitt, P. E. J., "Cooling Induced Segregation of Impurity Elements to Grain Boundaries in Fe-3 wt%Ni Alloys, 2.25Cr1Mo Steel and

Submerged-Arc Weld Metal," *Acta Metallurgica et Materialia,* Vol. 42, 1994, pp. 3309-3320.

[19] Faulkner, R. G., Song, S.-H., and Flewitt, P. E. J., "Combined Quenching and Tempering Induced Phosphorus Segregation to Grain Boundaries in 2.25Cr1Mo Steel," *Materials Science and Technology,* Vol. 12, 1996, pp. 818-822.

[20] Laws, M. S. and Goodhew, P. J., "Grain-Boundary Structure and Chromium Segregation in a 316 Stainless Steel," *Acta Metallurgica et Materialia,* Vol. 39, 1991, pp. 1525-1533.

[21] Faulkner, R. G., Song, S.-H., Flewitt, P. E. J., Victoria, M., and Marmy, P., "Grain Boundary Segregation under Neutron Irradiation in Dilute Alloys," *Journal of Nuclear Materials,* Vol. 255, 1998, pp. 189-209.

[22] Beere, W., "Phosphorus and Carbon Segregation in C-Mn Weld Metal," Technical Report TE/GEN/REP/0152/97, Berkeley Centre, Magnox Electric, Berkeley, Gloucestershire, UK, 1997.

[23] Williams, D. B., *Practical Analytical Electron Microscopy in Materials Science,* Electron Optics Pub. Co., Florida, 1984, p. 83.

[24] Faulkner, R. G., Morgan, T. S., and Little, E. A., "Analytical Electron Microscopy of Thin Segregated Layers," *X-Ray Spectrometry,* Vol. 23, 1994, pp. 195-202.

[25] Ogura, T., McMahon Jr., C.J., Feng, H. C., and Vitek, V, "Structure-Dependent Intergranular Segregation of Phosphorus in Austenite in a Ni-Cr Steel," *Acta Metallurgica* Vol. 26, 1978, pp. 1317-1330.

Jan Kočík,[1] Eliška Keilová,[1] Ivan Procházka,[2] and Jakub Čížek[2]

Microstructure of the Neutron Irradiated VVER-type Reactor Pressure Vessel Steels

Reference: Kočík, J., Keilová, E. Procházka, I., and Čížek, J., **"Microstructure of the Neutron Irradiated VVER-type Reactor Pressure Vessel Steels,"** *Effects of Radiation on Materials: 19th International Symposium, ASTM STP 1366,* M. L. Hamilton, A. S. Kumar, S. T. Rosinski, and M. L. Grossbeck, Eds., American Society for Testing and Materials, West Conshohocken, PA, 2000.

Abstract: Conventional transmission electron microscopy has been used to investigate the radiation-induced changes in the microstructure of VVER-type RPV steels. Specimens irradiated at ≈ 270 °C temperature in both the power light-water reactor (surveillance specimens) and the research reactor have been studied. In addition, the microstructure of the thermally aged specimens was analyzed too. Microstructural analysis has been supplemented by some preliminary results of the Doppler broadening and lifetime positron annihilation measurements.

Radiation-induced matrix defects visible by TEM in power reactor surveillance specimens consist of black dots, small dislocation loops and fine precipitates distributed heterogeneously with a dislocation substructure. Evolution of the radiation damage structure depends on the neutron fluence and the neutron flux. Only hardly discernible black dots were observed in specimens irradiated in the research reactor in NRI Řež. However, also in this case, the presence of a vacancy-rich component in the damage structure was suggested by positron lifetime measurements.

Keywords: microstructure, pressure vessel steels, radiation-induced defects, neutron irradiation, surveillance programmes, TEM, PAS

[1] Research Staff, Division of Integrity and Materials, Nuclear Research Institute Řež plc, 250 68 Řež near Prague, Czech Republic.

[2] Senior Research Worker and PhD Student, Department of Low Temperature Physics, Faculty of Mathematics and Physics, Charles University, V Holešovičkách 7, 170 00 Prague, Czech Republic.

Copyright© 2000 by ASTM International www.astm.org

Introduction

Reactor neutron irradiation results in significant changes in the mechanical properties and the microstructure of light water reactor pressure vessel steels. The mechanical properties degradation - irradiation embrittlement - is generally attributed to the development of fine scale radiation-induced defects which impede the dislocation motion under an applied stress. Defects are formed from vacancies and interstitials created in collision cascades processes. Those point defects surviving the cascades migrate freely through the crystal lattice at the service temperature, interact with each other and with solute atoms in the matrix and also with dislocation substructure and precipitates. These irradiation-induced diffusional processes result in a formation of point defect clusters, dislocation loops, atmospheres, and precipitates. These processes induce rather significant changes in the microstructure of the original material.

Microstructural examination thus plays a significant role in understanding the degradation of RPV steels. The TEM investigation of the VVER-440 type reactor surveillance specimens, reported previously [*1, 2*], has shown the fundamental characteristics of those specimens. The fraction of radiation-induced defects visible in TEM consisted of very fine black dots (unresolvably small defects), small dislocation loops and very fine precipitates probably of VC type. The investigations included the 1 to 5 year irradiation, the effect of accelerated irradiation in the research reactor and also the effect of a post-irradiation annealing. Only hardly discernible black dots were found in specimens irradiated in the research reactor.

In this contribution the VVER-440/213C reactor surveillance specimens are the main concern. It extends the time of irradiation to 10 years, the range of the neutron flux from 1.1×10^{16} m^{-2} to 5.6×10^{18} m^{-2} ($E > 0.5$ MeV), and includes also the standard regeneration annnealing for VVER 440 reactor pressure vessel and, finally, the thermally aged specimens. The microstructural investigations are complemented with preliminary positron annihilation spectroscopy measurements of Doppler broadening and positron lifetime.

Material

The Cr-Mo-V ferritic steel of the 15Kh2MFA type is employed for the RPV of the VVER-440/213C light-water reactors. The smooth ring in the vicinity of the active core of the reactor is made from the steel of the grade AA of higher purity. The chemical composition of the investigated grade AA material is given in Table 1. The material

Table 1 - *Chemical analysis of the melt (in mass %)*

C	Si	Mn	S	P	Cr	Ni	Mo	V	As	Co	Cu
0.16	0.17	0.46	0.016	0.014	2.9	0.07	0.66	0.31	0.008	0.009	0.07

comes from the surveillance material for VVER-440/213C reactor. The specimens used in the investigation represent the microstructure in the middle of the ring wall, approx. 150 mm

thick. The thermal treatment of the base metal includes: quenching from 1000 °C to the oil at 125 °C, tempering at the temperature (690±10) °C for 18 hours and the multiple annealing at the temperature (680±10) °C for 6, 6, 11 and 10.5 hours (it simulates vessel stress relieving treatment after welding).

The samples were irradiated at positions for surveillance specimens in vertical channels welded to the outer surface of the core barrel of the VVER-440 reactor on the nuclear power plant. The lead factor is high, amounting the value ≈ 18 because of the small thickness of water reflector in VVER-440 reactors. The irradiation temperature ≈ 270 °C was considered to be ≈ 10 °C above that of the inlet water. The shift in the C_V transition temperature of material under the study is shown in Figure 1. In addition to that, the specimens of the same material together with the IAEA steel of ASTM A 533-B type of Japanese provenance were irradiated also in the inert gas-filled capsule in the LVR-15 research reactor at Nuclear Research Institute Řež.

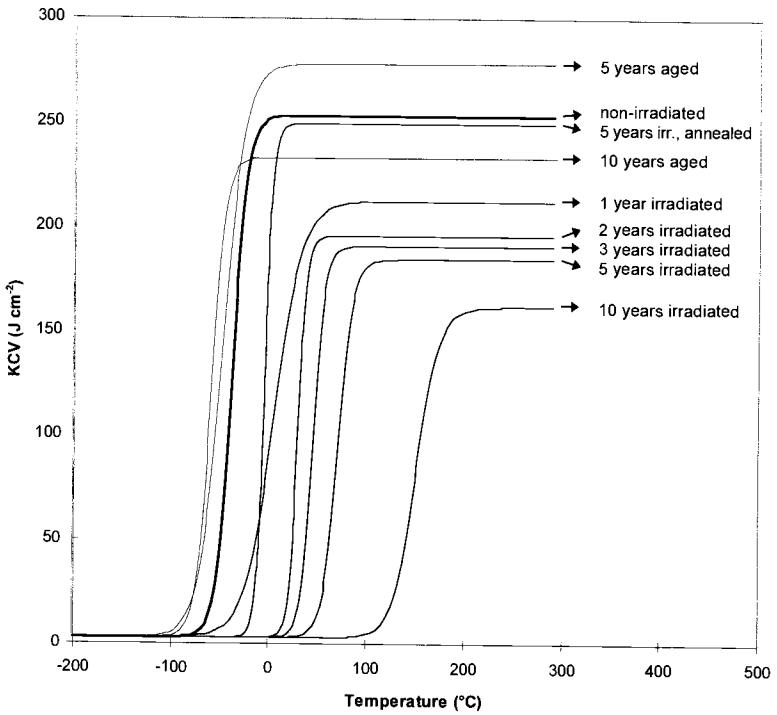


Figure 1 - *The Impact Charpy-V Transition Curves.*

Investigated specimens and their irradiation and/or thermal treatment history are briefly summarized in Table 2.

Table 2 - *Survey of specimens*

Specimen	Irradiation Time (year)	Neutron Flux*/ ($x10^{16}$ $m^{-2}s^{-1}$)	Neutron Fluence*/ ($x10^{24}$ m^{-2})	Conditions
A0	-	-	-	As received
A1	1	3.66	1.12	Power reactor irradiated
A3	2	3.89	2.13	Power reactor irradiated
A4	3	4.18	3.32	Power reactor irradiated
A6	5	4.56	5.89	Power reactor irradiated
A7	10	3.83	9.96	Power reactor irradiated
A12	5	1.16	1.79	Power reactor irradiated
A8	5	1.09	1.41	Power reactor irradiated and annealed 475 °C/165 hours
A10	-	-	-	Thermally aged 270 °C/5 years
A11	-	-	-	Thermally aged 270 °C/10 years
A13	0.03	cca 50	0.5	Research reactor irradiated
A14	0.03	cca 50	0.5	Steel A 533-B, research reactor irradiated

*/ Note: Neutron fluxes and fluences are given for E > 0.5 MeV. The coefficient allowing convert neutron fluxes and fluences for E >1 MeV is 0.6.

Experimental Methods

Transmission electron microscopy (TEM) was used to characterize the dislocation substructure, fine precipitates and to identify second-phase particles.

Thin foils for TEM were prepared from samples cut from fractured Charpy-V specimens using a twin-jet electropolisher at low temperatures. The Tesla BS-540 conventional transmission electron microscope operated at 120 kV was used for the investigation, allowing for a resolution of 2 - 3 nm for studied (ferromagnetic) materials. The two-beam dark-field and bright-field techniques were used to the analysis of dislocation substructures, the selected diffraction area technique was applied for the identification of precipitate particles.

Doppler broadening (DB) of annihilation radiation was used to study the neutron-irradiated RPV steel materials. DB spectra were measured with a high-purity Ge detector (EG&G Ortec) having the energy resolution of ~1.9 keV FWHM and peak-to-Compton ratio of 68:1 for E_γ=1.33 MeV energy. The source (~1.3 MBq of ^{22}Na sealed between the two mylar foils of 2 μm thickness) was sandwiched between the two discs of the studied steel. Auxiliary ^{60}Co sources were put near the detector at proper distances, while the specimen-source sandwich was placed at a constant distance from the detector. In this way different contents of ^{60}Co and ^{54}Mn in specimens, which had undergone different irradiation and/or thermal treatment history, were compensated and loading of the spectrometer electronics

chain was kept constant. At least 2×10^6 counts in the annihilation peak were collected in each run.

The positron lifetime (PL) spectra were measured by means of a BaF_2 lifetime spectrometer similar to that described in [*3*] and providing the timing resolution of 160 ps FWHM for the ^{22}Na positron source. At least 10^7 events were collected in each spectrum. Measured spectra were decomposed into exponential components using a procedure described in [*4*]. At present the measurements on unirradiated specimens were completed.

Specimens for positron annihilation measurements, ∅8×0.25 mm in size, were prepared from fractured Charpy-V bodies. The specimen surfaces were carefully mechanically ground and polished and finally chemically-mechanically polished to minimise the preparation-induced stresses.

PL technique has proven, that an additional weak component with lifetime ≈ 300 ps occurs in the spectrum, originating from an improper preparation. This component appeared to be completely annealed after a 640 °C/2 hours annealing in vacuo. The fraction of positrons affected by an improper preparation of analysed specimens has been estimated to be < 1 %, i.e. reasonably small.

Results and Discussion

Non-irradiated Microstructure

The tempered bainite microstructure consists of recovered and polygonized fine ferrite cells (Figure 2). The evolution of the microstructure during tempering masks original bainite lath-like morphology, which is seen only infrequently. The dislocation density varies markedly area by area. The average dislocation density amounts 2.3 x 10^{14} m^{-2} inside cells. The blocky chromium-rich carbides of the M_7C_3 and $M_{23}C_6$, typically ≈ 0.2 μm in size, precipitate preferably along prior lath boundaries. The fine plate-like and globular VC carbides, < 20 nm in size, precipitates more or less homogeneously within the microstructure and in some boundaries. The microstructure of the as-received state is described in more detail in [*5*].

Microstructure of Irradiated Specimens (TEM)

Effect of the Neutron Fluence - Radiation-induced defects after 1 year exposition in surveillance channel appear as single black dots condensed to dislocation lines. With increasing neutron fluence after 3 and 5 year irradiation their number density as well as size grow and some contrast typical for small dislocation loops and/or precipitates becomes visible. Simultaneously, the tendency to clustering of these defects can be indicated. The clustering becomes evident after 10 year exposition, when density of defects is fairly high. This is illustrated in Figure 3 for areas with well recovered dislocation substructure.

The density of defects grows from ≈ 1.6 x 10^{21} m^{-2} to ≈ 1.9 x 10^{22} m^{-2} and the defect size grows from ≈ 3 to ≈ 10 nm, for 1 and 10 year irradiation, respectively. These values correspond with results published earlier [*2*], and are consisting also with results, measured in templates taken from the VVER-440 power plant [*6*].

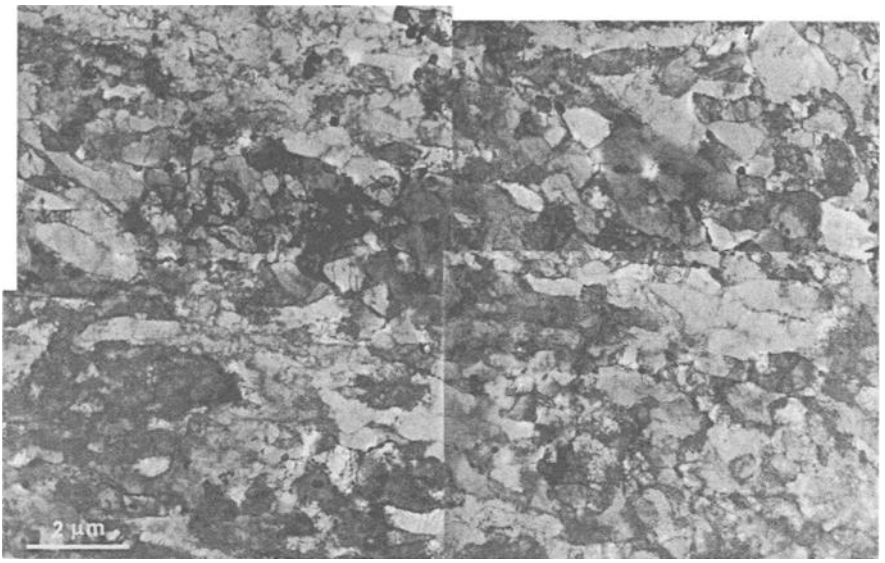


Figure 2 - *Microstructure of the as-received base material, A0.*

It has been already known, the determination of the nature of small radiation-induced clusters (≤ 5 nm) in TEM is very difficult [*7*]. In addition to that, in tempered bainitic microstructures the heterogeneity of the as-received microstructure resulted from the uneven recovery and polygonisation of dislocation substructure is the other detrimental factor. Finally, the annihilation dislocation loops and small VC precipitates occur in the microstructure as a result of previous deformation and annealing treatment and can match to radiation induced defects. In spite of the fact, that the analysis of the defects nature failed, there are generally acceptable reasons to assume, that both, the dislocation loops and small precipitates occur in the radiation-induced population of defects.

Dislocations in highly irradiated specimens show bowed dislocation segments and many large dislocation loops indicating the climb processes take a significant part in an evolution of dislocation substructure under the irrradiation.

No microvoids were found in any surveillance specimen investigated by TEM.

Effect of the Neutron Flux - Black dot type defects were found after the 5 years irradiation in the surveillance channel in the lower flux position (Figure 4). Their amount and distribution corresponds with 1 year irradiation at higher flux position.

Similarly to the previous investigations [*1, 2*], no clearly discernible defects appeared after irradiation in the LVR-15 research reactor in both, the VVER type steel and the IAEA A 533-B steel irradiated to the neutron fluence $\approx 3 \times 10^{23}$ m^{-2}.

It is believed, that above mentioned differences in radiation-induced defects observed in TEM after neutron irradiation under different conditions (power and research reactor) are primarily due to neutron flux.

Effect of the Regeneration Annealing - Defects present in the material after the 5 year irradiation dissappear completely during the 475 °C/165 hours annealing commonly used for

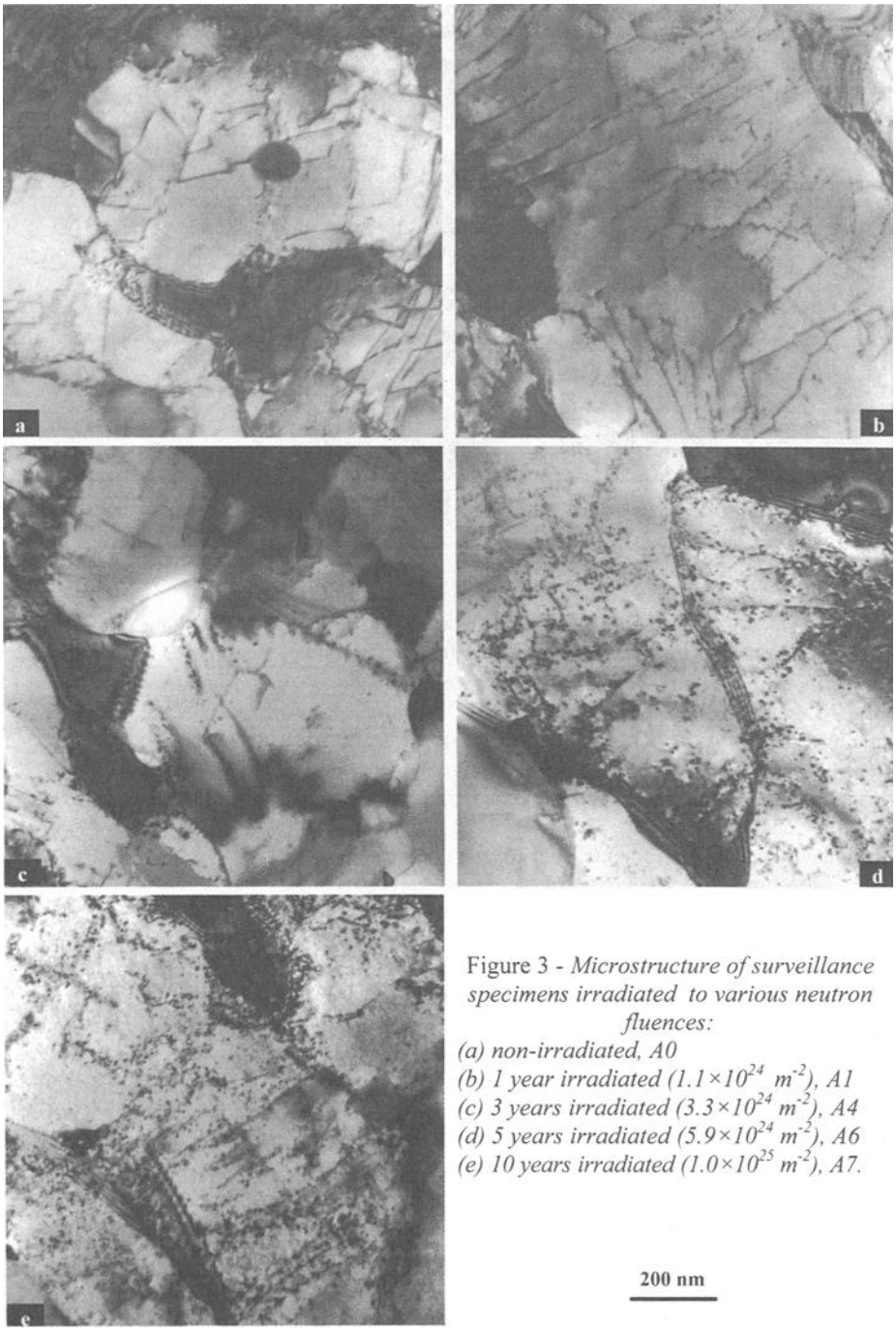


Figure 3 - *Microstructure of surveillance specimens irradiated to various neutron fluences:*
(a) non-irradiated, A0
(b) 1 year irradiated (1.1×10^{24} m^{-2}), A1
(c) 3 years irradiated (3.3×10^{24} m^{-2}), A4
(d) 5 years irradiated (5.9×10^{24} m^{-2}), A6
(e) 10 years irradiated (1.0×10^{25} m^{-2}), A7.

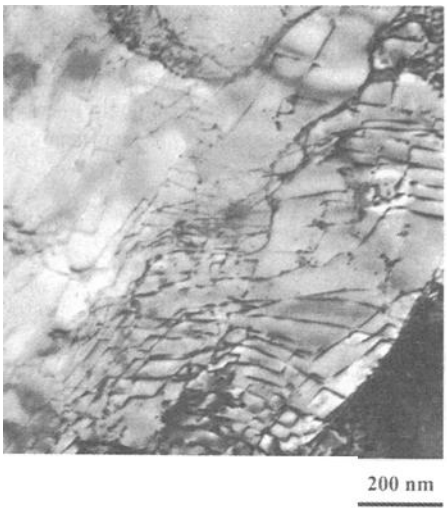


Figure 4 - *Microstructure of the specimen irradiated for 5 years in low neutron flux (~ 1×10^{16} m^{-2} s^{-1}, E > 0.5 MeV), A12.*

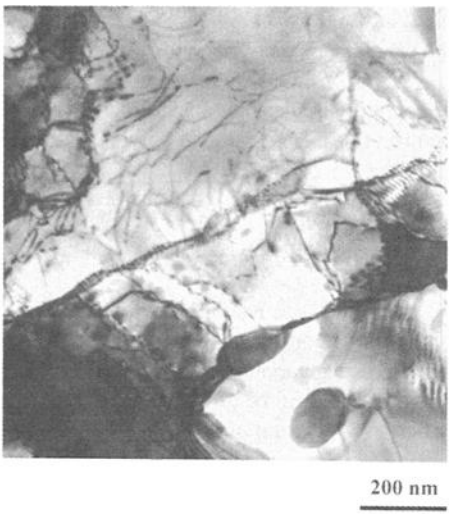


Figure 5 - *Microstructure of the specimen irradiated for 5 years in low neutron flux (~ 1×10^{16} m^{-2} s^{-1}, E > 0.5 MeV) and annealed 475°C/165 h, A8.*

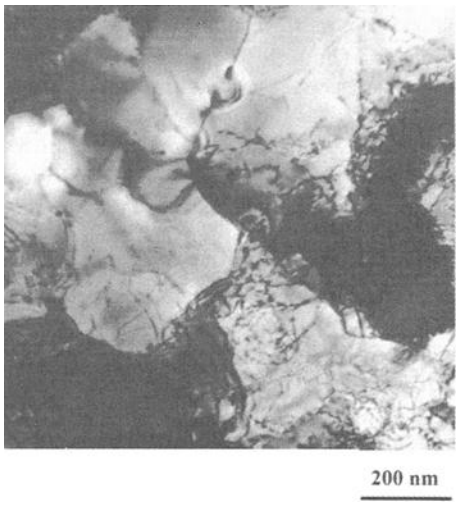


Figure 6 - *Microstructure after 10 year ageing at ≈ 270°C, A11.*

the regeneration of the VVER-440 type reactor pressure vessels (Figure 5). Simultaneously, the pronounced recovery of dislocation substructure occurs.

Effect of Ageing - No defects were seen in a material aged for 10 years at the service temperature in the surveillance channel at a position above the reactor core (in negligible neutron flux). However, the polygonization of the dislocation substructure was significant (Figure 6).

Doppler Broadening

First tentative results of DB measurements are presented. Comparison of the DB spectra obtained for non-irradiated steel with those for steels irradiated for 1 through 10 years revealed an apparent narrowing of the annihilation line occurring for all measured irradiated surveillance specimens. Narrowing of the annihilation line is illustrated in Figure 7 as difference spectrum of normalized counts for the A1 – A0 couple. Thus, due to irradiation effects, positrons in the irradiated VVER steels become localized to a higher degree compared to the non-irradiated material. In terms of the conventional S-parameters, the observed narrowing of the annihilation peak can be quantitatively described through the relative differences $(S_i - S_0)/S_0$, where S_i and S_0 stand for S-parameters referring to the irradiated and non-irradiated materials, respectively. These relative differences turned to be $\approx +(2.5\pm0.3)$ % for all irradiated. The error quoted includes not only the purely statistical one but also the uncertainties due to possible imperfect simulations of the equal loadings and unequivalent geometries of the auxiliary ^{60}Co source. These uncertainties were estimated from a set of separate test runs. Present experimental data clearly suggest (see Figure 8) that the shape of the annihilation line is narrowed mostly in the fluence region below 1×10^{24} m^{-2}, while much less change (increase) of the S-parameter could be observed, and perhaps a certain kind of saturation is approached, when neutron fluence is increased above this value. Within the accuracy attained, the S-parameters may not even exhibit visible changes with the neutron fluence above 1×10^{24} m^{-2}. It can be also seen from Figure 8, that both the approaches to simulation of constant loading gave similar results. Although present data are yet insufficient to give a more detailed evidence about the nature of such a saturation, it seems likely, that further DB measurements can bring a useful complementary information about the effects of neutron irradiation on the RPV steels. Such DB experiments, aimed to receive more extended and accurate data, are currently being in progress.

Positron Lifetime

In PL spectra measured for the non-irradiated steel, the two components (except for the source contribution) could clearly be identified, their lifetimes (intensities) being $\tau_1 = 59\pm5$ ps (12.5±0.5 %) and $\tau_2 = 149.0\pm0.6$ ps (87.5±0.5 %), what can be understood as an evidence of unsaturated trapping in this material. However, application of the simple two-state trapping model to these data reveals the bulk lifetime of 125 ps, which is considerably higher than the well-known value for defect-free α-iron. This may be regarded as an indication that at least two kinds of trapping centers are active in the non-irradiated RPV steel.

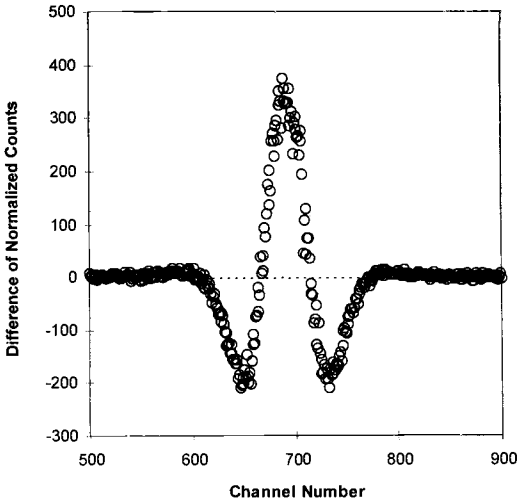


Figure 7 - *The difference of normalized annihilation peak shapes for specimens A1 and A0 (A0 subtracted from A1).*

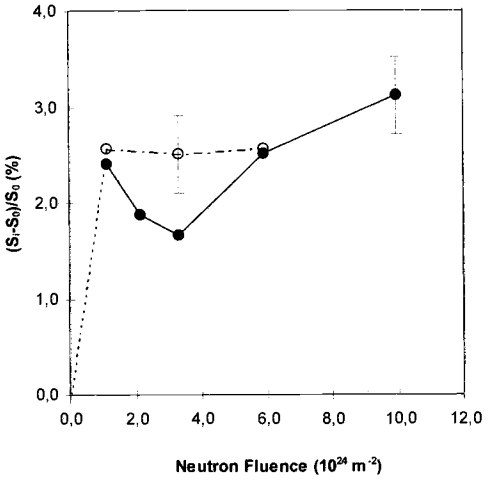


Figure 8 - *The measured S-parameter vs neutron fluence for the irradiated RPV steels. Full circles - auxiliary ^{60}Co source used.*

Conclusions

Conventional transmission electron microscopy has clearly revealed several characteristic features of a radiation damage structure of VVER-440 type reactor pressure vessel steels. Radiation-induced matrix defects visible by TEM in power reactor surveillance specimens consist of black dots, small dislocation loops and fine precipitates concentrated to dislocations, low-angle boundaries (and precipitates). No voids were found in TEM. Only hardly discernible black dots were observed in specimens irradiated in the research reactor in NRI Řež.

Quantitative data for radiation-induced defects obtained in surveillance specimens and in templates taken from the power plant [*6*] are in good agreement.

Dislocation substructure recovery in irradiated surveillance specimens is slow. All radiation-induced defects were annealed out during regeneration annealing 475 °C/165 hours. Simultaneously, a significant recovery of dislocation substructure occurs. Ageing for 10 years at a reactor service temperature results in polygonization of dislocation substructure.

First Doppler broadening spectra revealed an apparent narrowing of the annihilation line occurring for all measured irradiated surveillance specimens. Narrowing occurs mostly in the fluence range below $\approx 1\times10^{24}$ m^{-2}. Further experiments, aimed to receive more extended and accurate data, are currently being in progress.

In addition, the starting positron lifetime measurements have shown, that at least two kinds of trapping centers are active in a non-irradiated VVER-440 reactor pressure vessel steel.

Acknowledgments

Financial support provided by the Czech Academy of Sciences under the grant No. 106/96/1319 is gratefully acknowledged.

References

[1] Kočík, J., Keilová E., "Radiation Damage Structure of WWER-Type RPV Steels," *Nucleon*, NRI Řež Research Bulletin, No 3-4, Řež, 1993, 21.

[2] Kočík, J., Keilová, E., "Radiation Damage Structure in Irradiated and Annealed 440 WWER Reactor Pressure Vessel Steels," Joint IAEA/NEA Specialists' Meeting on Irradiation Embrittlement and Optimization of Annealing, Paris, September 1993.

[3] Bečvář F., Lešták L., Novotný I., Procházka I., Šebesta F. and Vrzal J., *Materials Science Forum*, 175-178, 1995, 947.

[4] Procházka I., Novotný I., Bečvář F., *Materials Science Forum*, 255-257, 1997, 772-775.

[5] Kočík, J., Keilová E., "Microstructure of Cr-Mo-V reactor pressure vessel steels", *Nucleon*, NRI Řež Research Bulletin, No. 3, Řež, 1998, 19.

[6] Gorynin, I.V., Nesterova, E.V., Nikolajev, V.A., Rybin, V.V., "Microstructure and Mechanical Properties of WWER-440 Reactor Vessel Metal after Service Life Expiration and Recovery Anneal," *Effects of Radiation on Materials: 17th International Symposium, ASTM STP 1270,* D.S. Gelles, R.K. Nanstad, A.S. Kumar and E.A. Little, Eds., ASTM, 1996, p. 248.

[7] Jenkins, M.L., Fukushima, H., Kirk, M.A., "On the determination of loop nature in the TEM," *Microstructure Evolution During Irradiation*, I.M. Robertson, G.S. Was, L.W. Hobbs, T.D. de la Rubia, Eds, Symposium Proceedings Volume 439, Materials Research Society, Pittsburgh, 1997, p. 289.

R. Barry Jones,[1] Derek J. Edens,[2] and Malcolm R. Wootton[1]

Influence of Thermal Neutrons on the Hardening and Embrittlement of Plate Steels

Reference: Jones, R. B., Edens, D. J., and Wootton, M. R., **"Influence of Thermal Neutrons on the Hardening and Embrittlement of Plate Steels,"** *Effects of Radiation on Materials: 19th International Symposium, ASTM STP 1366,* M. L. Hamilton, A. S. Kumar, S. T. Rosinski, and M. L. Grossbeck, Eds., American Society for Testing and Materials, West Conshohocken, PA, 2000.

Abstract: A series of C-Mn pressure vessel plates and other steels containing various levels of copper, phosphorus and boron were irradiated at 240°C in two differing neutron spectra in the Halden reactor. Hardening and embrittlement data obtained after exposure in a highly thermalised neutron spectrum with $dpa_{thermal}(>1keV)/dpa_{fast}(<1keV) = 2$ were compared with data obtained after exposure to a cadmium-shielded spectrum with $dpa_{thermal}/dpa_{fast} = 0.01$. Exposure times varied from 85 to 251 days at a mean fast dpa dose rate of 6×10^{-11}dpa/second. For C-Mn plate steels containing low levels of impurity boron, the respective shifts in yield stress and Charpy transition temperature were always greater after exposure to the thermalised spectrum when compared with exposures to the cadmium-shielded spectrum. The shifts in the cadmium shielded spectrum agreed with data trend predictions from many surveillance and accelerated irradiations where thermal dpa doses were small. The influence of thermal neutrons was incorporated into trend curves by using an "effective" dpa dose, i.e. $dpa_{effective} = dpa_{fast} + k\ dpa_{thermal}$ where k is a thermal neutron efficiency factor. For doses $<300 \times 10^{-5} dpa_{thermal}$ the value of k was 2.0 ± 0.5. In a C-Mn steel containing an increased level of impurity boron, an allowance was required for the additional dpa generated by the thermal neutron-induced transmutation of boron-10. For thermal doses where the burn-out of boron-10 was not too great, the value of k in the embrittlement equation increased to $2.0 + 0.3(B-1) \pm 0.5$ for steels containing B weight ppm of natural boron. For a high copper C-Mn-Mo steel, hardening and embrittlement shifts arose due to irradiation-enhanced copper precipitation. Over the thermal dose range examined, thermal neutrons did not change the dose dependence of copper precipitation hardening.

Keywords: thermal neutrons, neutron spectra, plate steels, hardening, embrittlement, boron transmutation, copper precipitation, trend curves

[1]Irradiation Team Leader and Research Officer respectively, Materials Group, Integrity and Engineering Branch.

[2]Group Head, Reactor Analysis, Nuclear Technology Branch at BNFL Magnox Generation, Berkeley Centre, Berkeley, Glos, GL13 9PB, UK.

Copyright© 2000 by ASTM International www.astm.org

The programme for assuring the structural integrity of Magnox gas-cooled reactor steel pressure vessels involves the periodic withdrawal from the reactors of surveillance canisters, exposed from start-of-life, which contain a variety of plate and weld samples for subsequent Charpy impact and tensile testing. The locations of the canisters in the reactors were chosen to be representative of the differing ranges of irradiation temperature (150°C to 360°C) and neutron dose rate ($9x10^{-14}$ to $5x10^{-12}$ dpa/second) received by the spherical steel vessels and involve canister lead-factors which are close to unity [1]. The exposure-induced changes in the mechanical properties of the steel samples are expressed as functions of irradiation temperature, neutron dose or time in trend curves; these are subsequently used for predicting the current and future mechanical state of the reactor pressure vessel (RPV).

There is no fundamental quantitative model which is capable of directly predicting material properties based on nuclear interactions in the steels, rather the approach is to correlate properties against some particular measure of the neutron dose. Several measures may be used. For example, damage may be expressed in terms of neutrons of energies exceeding 1MeV or 0.1MeV, or in terms of the resulting number of displacements produced per atom of iron (dpa). The latter unit is obtained by calculation of the atoms displaced due to the kinetic energy of a recoil atom resulting from a nuclear interaction. As the spectrum of neutron energies impinging on Magnox RPVs varies with position on the vessel, due to differing thicknesses of graphite moderator or from the presence of in-vessel structural components, the use of dpa is favoured because this unit includes the damaging capability of neutrons of all energies. Figure 1 shows the currently recommended atom displacement cross-section as a function of neutron energy (see "Nuclear Standards, Standard Practice for Characterising Neutron Exposures in Ferritic Steels in Terms of Displacements-per-atom," ASTM E693-79, Re-approved 1985). Although the cross-section is greatest for high energy neutrons it is also significant for neutrons of thermal energies. In this respect, the estimates of dpa may be divided into regimes >1keV ("fast" dpa) and <1keV ("thermal" dpa).

The use of modern neutron transport codes like MCBEND [2] permits neutron spectra to be calculated at the inner wall surface of the RPV, i.e. the location specified for integrity assessment. The code calculations themselves are validated against measurements made on specially installed flux monitor packs, from surveillance dosimetry, and from drillings taken out of reactor components or reactor debris. In accord with MCBEND prediction, it was found that the fractional dpa contribution from thermal neutrons was much higher at the RPV side-core positions, being between 50% and 100%, compared to its magnitude at the top or bottom of the RPV, namely 0.5% to 5% [1]. However, at side-core positions, the rapid attenuation of thermal neutrons through the walls of the surveillance canisters, through the steel tube supporting the canisters, and from effects of inter-canister neutron shielding, meant that the thermal doses received by these particular surveillance samples were significantly less than those of the adjacent inner RPV surface.

Studies of the irradiation damage process using molecular dynamics modelling calculations [3, 4] have predicted a much higher fraction of atom displacements which survive compared with the model assumed in Figure 1. These extra displacements came from the lower energy recoils (of about 500eV) associated with thermal neutron $Fe^{56}(n,\gamma)$ interactions. Accordingly an additional parameter, termed neutron effectiveness (k), has been introduced to modify the calculation of the damage dose parameter such that

$$dpa_{total} = dpa_{fast} + k\, dpa_{thermal} \quad (1)$$

Earlier work [5,6] had shown that for steels containing about 30ppm by weight of natural boron, exposure in a thermalised neutron spectrum resulted in greater hardening and embrittlement than would have been the case in a spectrum with few thermal neutrons. This effect was attributed to the B^{10} (n,α) reaction producing Li^7 and He^4 transmutation products with energies of 0.87MeV and 1.53MeV respectively, so generating a large number of atom displacements within a few microns of the transmutation site. It follows that any experiments performed in thermalised neutron spectra with the aim of determining k in equation (1) must also take into account the magnitude of the concurrent thermal neutron effect arising from boron transmutations.

In order to assess both the magnitude of k and the role of boron in affecting materials trend curves, an experiment was mounted in the highly thermalised neutron spectrum in the reflector of the heavy water moderated reactor at Halden in Norway. This paper describes the results obtained on the various plate steels included in the rig payloads.

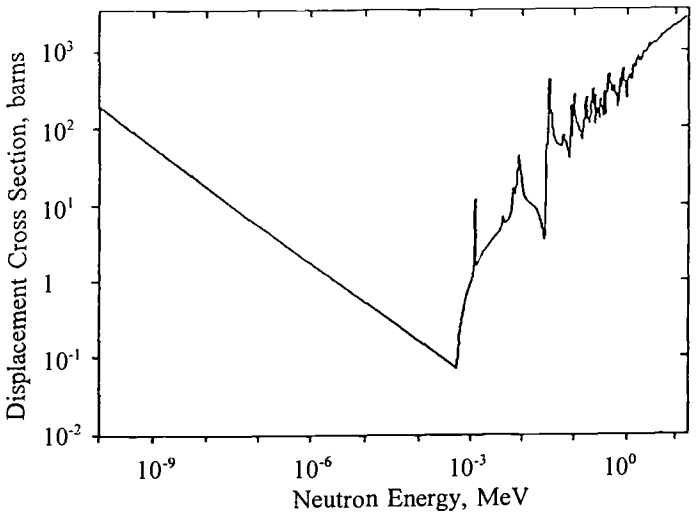


Figure 1 - *The currently recommended ASTM dpa cross-section for iron*

Experimental Details

Materials

The plate steels were selected to be representative of C-Mn plates used in the RPVs, and to evaluate particular effects of thermal neutrons on impurities (e.g. Cu, P, Mo, B) known to influence post-irradiation mechanical properties. The steel compositions are in Table 1. BW78A and BW78C steels were Si-killed plates from RPV duct cut-outs removed during

reactor construction; the Bearcomo plate was also typical of other Magnox RPVs. All plates had low levels of Ni, and varying amounts of Cu and P but Bearcomo also contained Mo and had a much higher Cu content. A special split melt to the BW78 specification was also manufactured; VSA had low residual impurites while VSB had an addition of 41 wt ppm of natural boron. The RPV-representative plates were irradiated in the normalised and 600°C stress relieved condition; VSA and VSB were irradiated only in the normalised state. An experiment to examine the role of thermal neutrons on P in Fe is described elsewhere [7].

Table 1 - *Compositions (weight%) of Plate Steels*

Steel	C	Si	Mn	S	P	Cu	Al	B*(ppm)	Mo
BW78A	0.18	0.23	1.09	0 030	0.017	0.15	0.003	0.90 ±0.3	0.007
BW78C	0.13	0.15	1.22	0.024	0.011	0 044	<0.005	1.32 ±0.1	0.011
VSA	0.13	0.18	1.34	0 002	0.005	<0.02	0.006	0.93	<0.005
VSB	0.13	0.18	1.33	0.002	0.005	<0.02	0.006	40.6	<0.005
Bear-como	0 145	0.16	1.24	0.034	0.056	0.55	<0.010	0.87	0.29

* B determined by the irradiation/He mass spectrometry method (Ref 8); the ± values reflect between-layer variations in the plates compared to a 5% variation within a layer.

Test Pieces and Procedures

Standard Charpy samples 10mm x 10mm x 55mm were employed for measuring embrittlement. Batches of Charpy samples were cut from different layers through the RPV plate cut-outs. To avoid any small layer-to-layer variations in mechanical properties, layer-specific unirradiated control samples were always tested for comparison with irradiated samples. Testing was performed on an instrumented machine with an automatic sample heating and transfer mechanism. To augment the number of irradiated impact tests performed, reconstituted Charpy samples were made using 20mm lengths from broken, low ductility, Charpy samples. Transition temperatures for 40J and 50% fibrosity (i.e. 50% shear fracture area) were obtained from *tanh* fits [9] to the energy-absorbed/test temperature or fibrosity/test temperature data. Tensile test data were obtained from the broken halves of lower shelf Charpy samples that had been remotely machined into mini-tensile samples with a gauge diameter of 4.5 mm and gauge length of 16 mm; these were tested to failure at ambient temperature using an Instron 1273 machine at a strain rate of 3.4×10^{-4} sec^{-1}.

Irradiation Conditions

Irradiations were performed under accelerated conditions in the reflector of the Halden

heavy-water moderated reactor in Norway. The Charpy samples of the plate steels, and of other programme materials [7], were loaded axially, one upon the other, inside sealed, helium-filled zirconium alloy tubes (termed "pins"). Close-fitting aluminium packing pieces were inserted between the Charpy samples and the inside of the pins to maintain good thermal contact. Six zirconium alloy pins were arranged in a rig. The exposure temperature was assessed to be 240 °C from the measured reactor coolant temperature of 235 °C plus an upper bound estimate of the nuclear heating received by the Charpy samples of 5 °C. Exposure to several dose levels was achieved using two types of reactor spectra which had widely differing thermal/fast neutron ratios. Spectra were characterised by high ratios of thermal dpa/fast dpa of 1.5-3.3 and a low ratio of 0.012 respectively; details are given in Table 2. For the low ratio spectrum the thermal neutrons were absorbed by a thin axial cadmium shield located between the zirconium pin and the aluminium packing.

Table 2 - *Summary of the Halden Irradiation Experiment*

Rig	Low B plate steels	High B plate	Days exposure	Notes
Rig 1	BW78A, BW78C, VSA, Bearcomo	VSB	97	6 pins
Rig 2i	BW78A, BW78C, VSA	VSB	166	2 pins
Rig 2	BW78A, BW78C, VSA, Bearcomo	-	251	4 pins
Rig 2A	BW78A, BW78C, VSA, Bearcomo	VSB	85	2 pins
Rig 3 Cd-shield	BW78A, BW78C, VSA, Bearcomo	VSB	154	6 pins

Some loadings were sufficient only for tensile test samples.

The neutron doses were measured using wires of Al-Co alloy (thermal dose) and pure Fe or Ni (fast dose). The wires ran axially along the whole length of the pins and were located on opposite sides of the Charpy samples in holes drilled in the Al packing. Dose determinations were made at intervals of 25-50mm along the wires and the values interpolated to give the dose at each Charpy notch. The measured Fe^{54} fast neutron activation was converted into fast (>1keV) dpa dose using a scale factor obtained from a MCBEND model of the Halden reactor. The thermal (<1keV) dpa doses were obtained from the cobalt activation, using the Westcott neutron dose and a cross section of 10.9 barns plus a small contribution from epithermal resonance events. The centre-to-end axial dose profile varied from 1.5:1 for thermal doses to 2:1 for fast doses. Across the rig the dose gradients were ±15% thermal and ±30% fast respectively. By careful choice of the location of the batches of samples within the pins it was possible to restrict the dose variations. For the mini-tensile samples the doses of the individual source Charpy samples were quoted. For each combination of material and neutron exposure the Charpy sample doses were averaged. Attempts were made to test those samples having doses most divergent from the mean value

on the upper or lower Charpy shelves. The fast dpa dose rates lay in the range from 2.5-10x10^{-11}dpa/second for all samples.

Results

Charpy Tests

Irradiation caused an upward temperature shift in the impact energy curves, compared to start-of-life, and also caused a reduction in the upper shelf energy in a some of the plates examined. Figure 2 shows a comparison between the 40J Charpy impact transition temperature (T_{40J}) and that for 50% fibrosity ($T_{50\%}$) for all the plates. The results for the high boron steel VSB lay systematically below the data for the other plates. The data on BW78A, BW78C, VSA and Bearcomo in Figure 2 has been analysed to give the equation

$$T_{40J} = 1.03T_{50\%} - 7.22\ °C \quad (2)$$

This shows that the test temperature distribution of the fibrosity data is consistent with that of the energy data and that conclusions drawn about the influence of thermal neutrons on behaviour should be robust to changes in the transition temperature criterion.

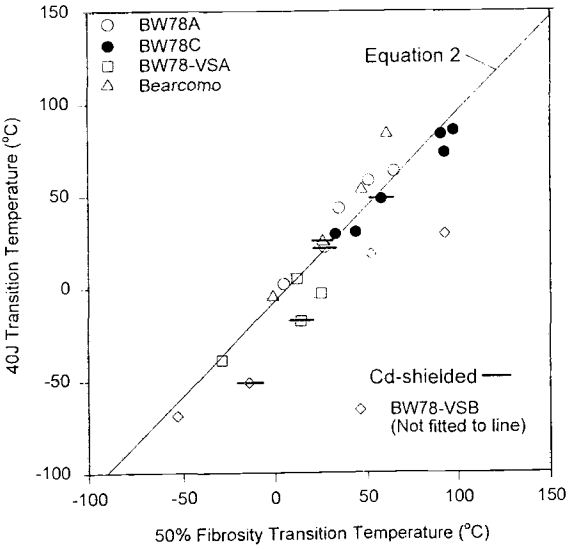


Figure 2 - *Comparison of plate steel 40J and 50% fibrosity transition temperatures*

Table 3 lists the 40J transition tempersature shifts for each plate and irradiation exposure. Inspection of the results shows that the minimum shift is always found for the Cd-shielded

Rig 3 results, even though the Rig 3 exposures are not usually at the lowest fast dpa dose. Secondly, the highest shift is found in the high boron steel VSB although it has not been exposed to the highest combination of fast and thermal dpa doses.

Table 3 - *Charpy Shifts for Plate Steels Irradiated at 240°C in Halden*

Identity	fast dpa $x10^5$	thermal dpa $x10^5$	ΔT_{40J}°C	Identity	fast dpa $x10^5$	thermal dpa $x10^5$	ΔT_{40J}°C
BW78A				**BW78C**			
H1	34	77	28	H1	43	90	53
H1	55	92	43	H2	95	199	56
H2	150	271	61	H2A	57	88	44
H3 (Cd)	67	0.8	20	H3 (Cd)	56	0.6	29
VSA				**VSB**			
H1	44	83	45	H1	34	79	87
H2i	81	162	36	H2	73	149	99
H3 (Cd)	88	1.2	22	H3 (Cd)	64	0.9	19
Bearco'o				-	-	-	-
H1	80	110	58				
H2	154	244	88				
H3 (Cd)	48	0.6	30				

Tensile Tests

Irradiation increased the lower yield stress (or 0.2% proof stress) and the ultimate tensile stress of all the plate steels. The yield stress shifts are shown in Table 4 for the differing exposure conditions; in general duplicate results were available. Inspection of the data shows that, in common with the Charpy shifts, the lowest shifts are found in the results for the Cd-shielded Rig 3 even though it is not at the lowest fast dpa dose. However, in contrast to the Charpy data, the hardening of the high boron steel VSB is the lowest of all the plates, is not particularly sensitive to dose, and does not show a marked dependence on the thermal neutron fraction in the spectrum.

Analysis and Discussion of Results

Comparison with Trend Curves

The results of surveillance and accelerated irradiation exposures on BW78 Si-killed C-Mn steels are available and the property changes incorporated into trend curves [1]. The data used in such derivations come predominantly from irradiations in neutron spectra where the

Table 4 - *Yield Stress Increases for Plate Steels Irradiated at 240°C*

Identity	fast dpa x10^5	thermal dpa x10^5	$\Delta\sigma_y$ MPa	Identity	fast dpa x10^5	thermal dpa x10^5	$\Delta\sigma_y$ MPa
BW78A				**BW78C**			
H1	62	95	74, 77	H1	48	92	82, 79
H1	30	77	55, 55	H1	21	67	83, 72
H2i	87	169	107, 112	H2i	56	136	41*123*
H2i	64	149	99, 104	H2	96	203	109, 106
H2	126	282	125, 129	H2A	46	79	63, 66
H2a	40	81	62, 67	H3 (Cd)	47	0.5	52, 51
H3 (Cd)	58	0.7	42,49	-	-	-	-
VSA				**VSB**			
H1	40	85	66, 78	H1	40	81	53, 61
H2i	106	180	95, 89	H1	22	67	59, 51
H2A	56	96	67, 67	H2i	91	164	60, 66
H3 (Cd)	94	1.3	73, 72	H2A	61	99	52, 54
				H3 (Cd)	83	0.9	55, 53
Bearco'o				–	–	–	–
H1	73	107	166, 166				
H2	152	236	209, 213				
H2A	33	76	132, 131				
H3 (Cd)	51	0.6	142, 135				

fraction of thermal neutrons is small (i.e. thermal dpa/fast dpa <5%). Consequently one of the easiest ways to assess the current results is in relation to the respective trend curves for Charpy and yield stress shifts. Figure 3 shows the mean value and the 90% prediction interval for the Charpy 40J shift in a low Cu Si-killed plate steel as a function of the product of the square root of the fast dpa irradiation dose (D_{fast} in units of dpa x10^5) and a factor (F_T) compensating for differing irradiation temperatures (T_i), as given by Jones and Williams [10], namely

$$F_T = 1.869 - 4.57 \times 10^{-3} T_i \quad (3)$$

Figure 3 shows all the current ΔT_{40J} data on BW78A, BW78C, BW78-VSA and BW78-VSB. Each data point is labelled with the irradiation rig from which it was derived. The first observation is that the data points from Rig 3, with a low thermal neutron fraction (thermal/fast dpa ratios of 0.011-0.014), lie close to the mean trend line and comfortably within the prediction interval. There are some other points on this figure for the *same plates* of BW78A and BW78C, labelled H and CX respectively. These refer to other, earlier, accelerated irradiations performed in spectra with low thermal fractions in the UK reactors Herald [11] and Chapelcross [12]; as expected these results are also in good agreement with the trend curve. The second observation is that data on the BW78 plates from Halden rigs 1, 2, 2i, and 2A with thermalised spectra (thermal/fast dpa ratios of 1.5-2.3) always lie above the mean trend line and six out of the eight observations lie above the upper prediction interval. This points to a consistent enhancement of embrittlement by thermal

neutrons. The final observation is that BW78-VSB plate, with 41 ppm boron, exhibits greatly enhanced embrittlement when compared to the other, low boron, steels in the thermalised spectra, but shows embrittlement close to the mean trend line when exposed in a spectrum with thermal/fast dpa ratio of only 0.014. This confirms that there is an additional boron transmutation effect with thermal neutrons which can embrittle ferritic steels [5, 6].

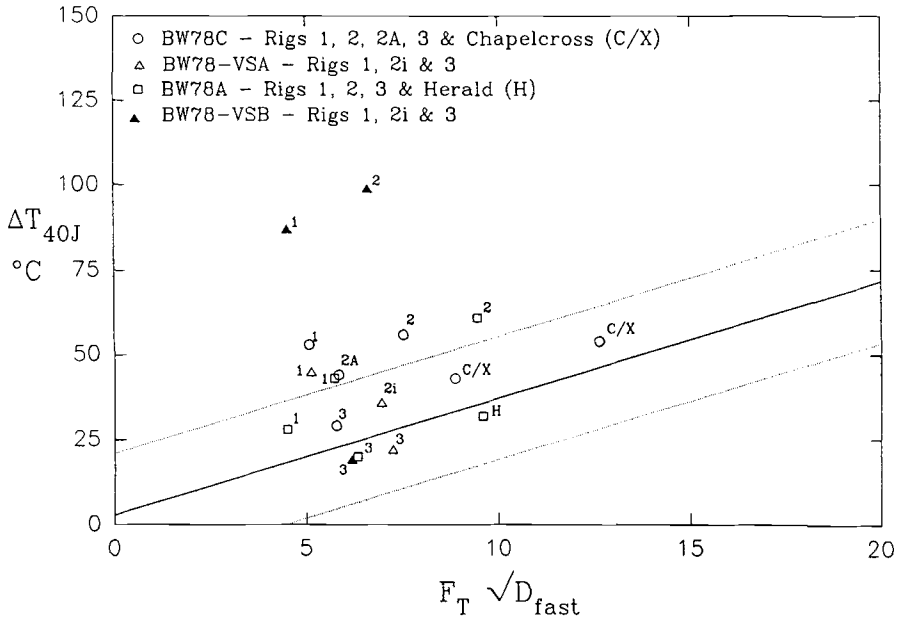


Figure 3 - *Comparison of all BW78 ΔT_{40J} values with the low Cu plate trend curve. The irradiation locations are indicated; the Halden Rig 3 location is Cd-shielded.*

The equivalent comparison between the various BW78 plate steel yield stress shifts and the yield stress shift trend curve for a low Cu, Si-killed steel is shown in Figure 4. Once again, the data points from Rig 3, with low thermal neutron fractions (thermal/fast dpa ratios of 0.011-0.014), lie close to the mean trend line and comfortably within the prediction interval. As for the Charpy data above, there are additional points on Figure 4 for the same BW78A and BW78C plates exposed in other low fractional thermal neutron irradiations, labelled H and CX, which conform to the trend line. In line with the findings for Charpy data, the yield stress shifts for BW78A, BW78C and BW78-VSA plates from Halden rigs 1, 2, 2i, and 2A with thermalised spectra (thermal/fast dpa ratios of 1.5-3.3) always lie above the mean trend line and the majority of the observations lie above the upper prediction interval. This confirms that there is an enhancement of irradiation hardening by thermal neutrons. However, as noted earlier, there is a marked difference between the Charpy shift and the yield stress shift behaviour of the high boron steel VSB. Figure 4 shows that all the

results for VSB, irrespective of the thermal/fast dpa ratio, lie within the prediction interval, indicating an insensitivity to thermal neutron effects. Indeed, as a function of $F_T \sqrt{D_{fast}}$, the results appear to have a lower slope than that for the trend line. Currently no explanation for the divergent behaviour of the tensile samples of VSB behaviour has been found.

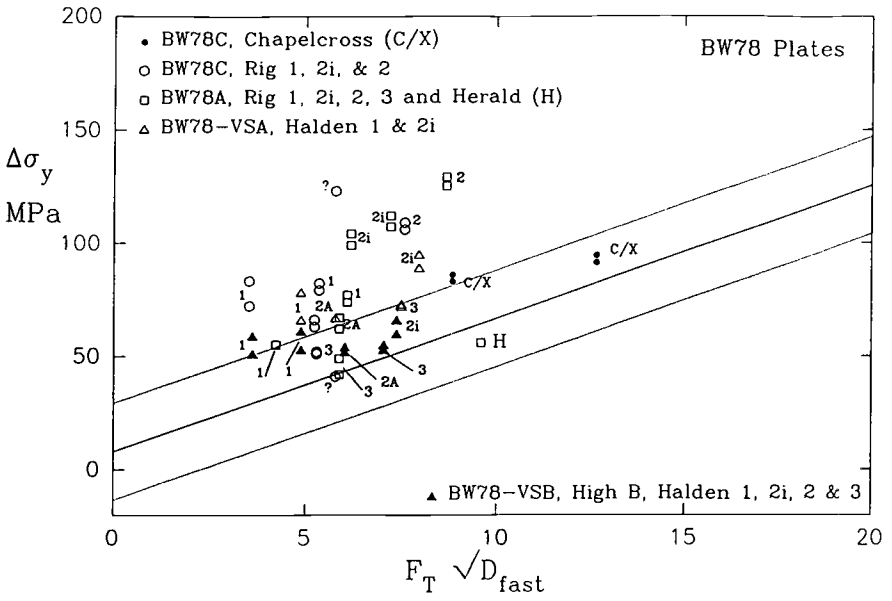


Figure 4 - *Comparison of all BW78 $\Delta\sigma_y$ values with the low Cu plate trend curve. The irradiation locations are indicated; the Halden Rig 3 location is Cd-shielded.*

Trend Curve Analysis for k in Low Boron Steels

For a thermalised neutron spectrum

$$\Delta T_{40J} = B + AF_T\sqrt{[D_{fast} + \alpha D_{thermal} + \beta(\text{boron-10 events})]} \quad (4)$$

where α and β are efficiency coefficients. When the boron burn-out is not great the terms in α and β may be combined as $kD_{thermal}$ as below

$$\Delta T_{40J} = B + AF_T\sqrt{[D_{fast} + kD_{thermal}]} \quad (5)$$

For neutron spectra with a low thermal neutron fraction, a conventional trend curve predicts

$$\Delta T_{Trend} = B + AF_T\sqrt{[D_{fast}]} \quad (6)$$

so that with $\Delta(\Delta T) = \Delta T - \Delta T_{Trend}$

$$k = [1/D_{thermal}]\,[\{\Delta(\Delta T)/AF_T\} + \sqrt{D_{fast}})^2 - D_{fast} \quad (7)$$

A similar analysis can be performed for $\Delta\sigma_y$, the yield stress shift. Further simplifications can be made if the respective temperature shift or yield stress shift intercept values in the trend curve are assumed to be zero, as would be the case for a low Cu steel. With this assumption, and using the data for BW78A, BW78C and BW78-VSA, the values for k in Table 5 have been obtained. These can be viewed in various ways but, simplistically, it is relevant to average the values appropriate to the mechanical property measured. For the ΔT analyses $k = 2.38 \pm 1.14$ (7 results), while for the $\Delta\sigma$ analyses $k = 2.43 \pm 0.7$ (19 results).

Table 5 - *Values of k Evaluated by the Trend Curve Method*

Irradiation rig & property used		k for BW78A	k for BW78C	k for BW78-VSA
Rig 1	ΔT	3.2, 1.8	3.9	2.9
Rig 2i	ΔT	-	-	0.8 (2.2*)
Rig 2	ΔT	1.7	2.1	-
Rig 1	$\Delta\sigma$	2.1, 2.3	2.1, 2.3	
Rig 1	$\Delta\sigma$	2.2, 1.5	3.4, 4.7	2.5
Rig 2i	$\Delta\sigma$	2.6, 2.9, 2.6, 3.0	-	1.5, 1.7
Rig 2A	$\Delta\sigma$	na	na	na
Rig 2	$\Delta\sigma$	2.1, 2.3	2.1, 2.3	-

* tanh (or by-eye) fits used on Charpy data na = not available

The magnitude of k depends on a number of factors but the main uncertainty is in deciding if all of $\Delta(\Delta T)$ is arising from thermal neutron-induced irradiation damage in the matrix or whether grain boundary embrittlement is also contributing. In Table 5 the assumption has been made that a matrix effect (i.e. additional hardening centres produced from low energy recoils) is predominant, otherwise the tabulated values of k would be overestimates. Consequently the main problem for this type of k analysis is whether there is a zero effect of thermal neutrons on the intercept B. As B would be small anyway for the low Cu steels BW78C and BW78-VSA then it seems reasonable to ignore any additional thermal neutron influence. This assumption is less secure for the higher Cu-content BW78A. However it is noteworthy that although BW78A would be expected to exhibit additional embrittlement and hardening effects due to Cu, such effects are not observed either in the Halden tests or in the additional irradiation results included in Figures 3 and 4. This indicates that the Cu in BW78A may not be held in solution and available to precipitate-out during irradiation. Although this aspect requires further examination it is not unreasonable

to ignore any thermal neutron influence on B for BW78A also. An alternative analysis for k is now explored which does not involve trend curve comparisons.

Multiple Regression of BW78 Shift Data

In an attempt to isolate the effect of thermal neutrons from other variables, a separate analysis was made of all available yield stress shift and transition shift measurements on BW78-type plate steels following accelerated irradiations in spectra with both high and low thermal/fast dose ratios. In order to maximise the size of the dataset, data were included from exposures in the Herald [11] and Chapelcross [12] reactors in addition to the Halden exposures (with and without Cd shields).

The model initially chosen was a modified form of the basic dose-damage relationship, namely, for yield stress shifts

$$\Delta\sigma_y = AF_T\sqrt{(D_F + kD_T)} + B(1+C(D_T/D_F)) \quad (8)$$

In this equation, the association of a regression constant 'C' with the normally dose independent intercept term 'B' was to allow for the possibility of a different intercept for the two subsets of data described above. A statistically significant value for 'C' would indicate the presence of a saturating effect associated with thermal neutron irradiation in addition to any such effect arising from predominantly fast neutron irradiations. A series of regression analyses were carried out using the SAS® statistical analysis package 'PROC NLIN' [13]. The analysis was made in a number of stages.

Separate analyses of the two data subsets (fast dpa predominant: Herald, Chapelcross and Halden Rig 3, thermal dpa predominant: Halden Rigs 1, 2i 2A and 2) failed to determine a statistically significant value of k in either case. It is believed that this arose from the relatively small variation of the thermal/fast dose ratio in each subset.

The datasets were combined and examined for a spectrum dependent intercept (B). This analysis produced a statistically significant value for k (2.4±1.0). In contrast, the value for 'C' was statistically insignificant (-0.1±0.2), indicating that B was independent of the thermal/fast dpa ratio. Hence a single, spectrum independent, value of B was adopted for analysis of the data,

$$\Delta\sigma_y = AF_T\sqrt{(D_F + kD_T)} + B \quad (9)$$

rather than using equation (8). Furthermore, it was concluded that the yield stress shifts for BW78-type steels showed no evidence for a separate saturating thermal neutron irradiation induced mechanism at the dose levels explored here.

With a combined dataset, a single intercept and using equation (9), the value of k was estimated as 1.8±0.4 However, the predicted values of yield stress shift versus the measured values strongly supported the conclusion that two yield stress shift values from BW78C irradiated in Rig 2i were outliers (these are the queried points in Figure 4 and the asterisked entries in Table 4). For this reason, the analysis was repeated with these two shifts omitted.

In the resulting analysis, the value for k was estimated to be 1.9±0.3, with the uncertainties for the other regression coefficients also showing reductions. A plot of predicted values of yield stress shift versus the measured values is shown in Figure 5; the data compare favourably with a 1:1 line. The regression constants in equation (9) have values A=5.0±0.4MPa/√(dpax10^5), B=19.9±4.8MPa and k=1.9±0.3. These values were also robust to small changes to the database.

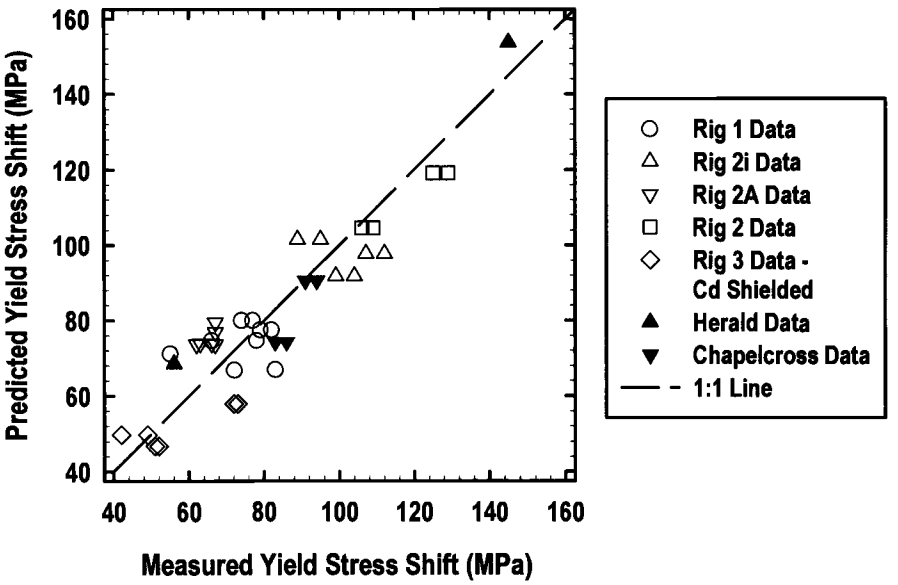


Figure 5 - *Predicted versus measured yield stress shifts for BW78 steels in differing neutron spectra*

A similar analysis was performed on the Charpy 40J shift data using an equation of the same form as equation (8). There were fewer data, namely eight with high thermal dpa contributions and seven with predominantly fast dpa, so the parameters were less well defined. Using the same analysis sequence as before, C was insignificant. Without C, a significant value for k was found but B was insignificant. Employing a fixed value of A=3.23°C/√(dpax10^5), from the Figure 3 trend curve, and omitting both parameters B and C gave k=2.1±0.5. Omitting the highest dose BW78A point (from Herald [11]) and C, produced A_{40J}=2.8±1.0°C/√(dpax10^5), B_{40J}=9±10°C, and k_{40J}=1.8±1.0.

Both the Charpy shift and yield stress shift regression analyses are conclusive in obtaining similar values of k (1.9±0.3 and 1.8±1.0 respectively). In addition sensible values are found for the ratios A_{40J}/A = 0.56, and B_{40J}/B = 0.45, since Charpy shifts (in °C) and hardening shifts (in MPa) for plate steels are commonly found to be in the ratio 0.5 in the absence of grain boundary embrittlement effects. However the magnitudes of B and B_{40J} are somewhat larger than anticipated bearing in mind the low Cu contents of the majority of the steels examined.

In conclusion, both the regression method and the trend curve method for determining k suffer from drawbacks and these are both connected to the magnitude of the Cu precipitate hardening and embrittlement contribution anticipated in the plate steels. With this in mind, and noting the uncertainties on the values of k determined, it is concluded that a representative value, to be used for both embrittlement and hardening assessments, is given by $k = 2.0 \pm 0.5$.

Role of Boron Transmutations

The discrepancy between the 40J shifts for steel VSB and the low boron plate trend curve (Figure 3) is due to the presence of 41ppm of natural boron in VSB. Assuming a uniform distribution of boron in VSB, an equation may be derived for the additional dpa dose produced by the transmutation. The combined damaging effects of fast neutron atom displacements, boron transmutation-induced atom displacement reactions and (n,γ) matrix atom displacements (equation 4) can be re-written as

$$\Delta T_{40J} = B + AF_T [D_{fast} + \alpha D_{thermal} + \beta n^0_{B10} \{1 - \exp(-\sigma^0_{B10} \Phi_W t)\}]^{1/2} \quad (10)$$

where n^0_{B10} is the initial atom fraction of boron-10 (i.e. 1.028 x weight fraction of natural boron), σ^0_{B10} is the thermal neutron cross section for boron-10 of $3838 \times 10^{-24} cm^{-2}$, and $\Phi_W t$ is the Westcott thermal dose (product of Westcott flux and time in seconds). Using equation (10), with $\alpha = k$, β may be evaluated. Note that in the earlier evaluations of k there was a small contribution from boron transmutation effects, because the steels used had typical boron contents of 1ppm. Additionally, the value of β determined from data on VSB will depend on the actual values of the other parameters (A, B and k) used in equation 10. The general trend of the VSB Charpy results supports the experimentally based value of $\beta = 900$ $(x10^5)$* displacements per transmutation that was derived from an earlier, unpublished, analysis of data on boron-containing steels [5, 6]. Using equation 10 and the mean values of the embrittlement parameters determined above by multiple regression, four estimates of β have been obtained for VSB; these range from 690 to 1100 $(x10^5)$ with a mean β value of 898 (the $x10^5$ term arises because the trend equation doses are expressed in units of dpa $x10^5$). If equation 10 is altered to express the boron effect in terms of $dpa_{thermal}$, rather than Westcott dose, the thermal neutron terms may be unified. This gives a simplified general expression for k, applicable in equation (1) at thermal doses where the extent of boron-10 burn-out by transmutation is not too great, and relevant for steels of any boron level, namely

$$k = 2.0 + 0.3 (B-1) \pm 0.5 \quad (11)$$

where B is the natural boron content in ppm by weight. The term in boron vanishes for steels with 1ppm of boron.

Role of Thermal Neutrons on Copper Precipitation

The purpose of irradiating the high Cu Bearcomo steel was to establish whether the presence of additional thermal neutrons could change the development of Cu precipitation as a function of dose. There is no doubt that the current exposures have produced large property shifts due to Cu because the yield stress shifts in Bearcomo are the largest observed in all the low boron steels irradiated in these experiments. The excess in hardening shifts for the Bearcomo steel (eight data) over the shifts in the similarly irradiated BW78 steels was about 80MPa. However, as these excess shifts were detected in Bearcomo in both the low thermal/fast dpa ratio spectrum as well as in the high ratio spectra, it would seem that Cu precipitation hardening is not affected by neutron spectrum for the dose range examined, i.e. at total effective doses between 52×10^{-5} and 624×10^{-5}dpa (or $F_T\sqrt{[D_{fast} + 2.0D_{thermal}]}$values from 7 to 19) in these tests.

Although all Bearcomo embrittlement shifts exceeded those for the similarly irradiated low boron BW78 steels, the sizes of the excess shifts were rather small and appeared to increase with higher effective doses. However there is less confidence in this conclusion as it is based on only three results.

Overall, there is little convincing evidence to support any influence of thermal neutrons on Cu precipitation in the dose range examined in these tests.

Conclusions

1. The irradiation-induced Charpy transition temperature shifts and yield stress shifts for 1 ppm boron, C-Mn plate steels from irradiation rigs exposed to highly thermalised neutron spectra at 240°C were all greater than those obtained under equivalent irradiation temperature and fast neutron doses in cadmium-shielded rigs with spectra having low fractions of thermal neutrons.

2. The magnitudes of the transition temperature and yield stress shifts for the Cd-shielded irradiated plates were in agreement with predictions based on dpa-based plate trend curves derived from surveillance or accelerated experiments in spectra with low thermal neutron fractions.

3. The additional embrittlement and hardening produced by exposure to thermal neutrons may be incorporated into the trend curves by modifying the dose term so that $dpa_{total} = dpa_{fast} + k\, dpa_{thermal}$, where the fast dpa are calculated for neutrons >1keV, and thermal dpa are calculated for neutrons < 1keV.

4. Using two different methods, the average damaging efficiency of thermal neutrons (k) was determined to be $k = 2.0 \pm 0.5$ for low boron plate steels, for thermal doses $<300 \times 10^{-5}$dpa in spectra with ratios of $dpa_{thermal}/dpa_{fast} < 3.3$.

5. Large transition temperature shifts, but not hardening shifts, were found in a C-Mn plate steel containing 41 weight ppm of boron when exposed at 240°C in a thermalised neutron spectrum. In a low thermal fraction spectrum the shifts were small. About 900 additional atom displacements were calculated to occur for each atom of boron-10 transmuted. For embrittlement estimates at doses where the burn-out of boron-10 by transmutation is not too great $k = 2.0 + 0.3\ (B\text{-}1) \pm 0.5$, where B is the ppm content (by weight) of natural boron in the steel.

6. For a high copper content, C-Mn-Mo steel the yield stress shifts and the embrittlement shifts were always larger than those in low Cu C-Mn steel due to the influence of irradiation-enhanced Cu precipitation at 240°C. For the doses and neutron spectra examined here thermal neutrons did not alter the dose dependence of irradiation-induced Cu precipitation hardening.

Acknowledgement

This paper is published by permission of BNFL Magnox Generation, Berkeley Centre, Glos, UK.

References

[1] Jones, R.B., and Bolton, C.J., "Neutron Radiation Embrittlement Studies in Support of Continued Operation, and Validation by Sampling of Magnox Reactor Steel Pressure Vessels and Components," 24th Water Reactor Safety Meeting, 1996, NUREG/CP-0157, Vol 2, 1997, USNRC, pp25-48.

[2] Chuckas, S.J., "MCBEND User Guide to Version 9," AEA Technology Report, ANSWERS/MCBEND (94), 15, 1994.

[3] Phythian, W.J., Stoller, R.E., Foreman, A.E.J., Calder,A.F., and Bacon, D.J., "A Comparison of Displacement Cascades in Copper and Iron by Molecular Dynamics and its Application to Microstructural Evolution," Journal of Nuclear Materials, Vol 223, 1995, pp245-261.

[4] Norgett, M.J., Robinson, M.T., and Torrens, I.M., "A Method of Calculating the Number of Atom Displacements in Irradiated Metals," Nuclear Engineering and Design, vol 33, 1975, p50.

[5] Harries, D.R., and Eyre, B.,L., "Effects of Irradiation in Iron and Steels," *Flow and Fracture of Metals and Alloys in Nuclear Environments, ASTM STP 380,* American Society for Testing and Materials, 1965, pp105-119.

[6] Grounes, M., "Review of Swedish Work on Irradiation Effects in Pressure Vessel Steels and on the Significance of the Data Obtained," *Effects of Radiation on Structural Materials, ASTM STP 426*, American Society for Testing and Materials, 1967, pp224-259.

[7] Jones, R.B., Cowan, J.R., Corcoran, R.C. and Walmsley, J.R., "Embrittlement, Hardening and Grain Boundary Composition in an Irradiated and Thermally Aged Fe-P-C Alloy," *Effects of Radiation on Materials, 19th International Symposium, ASTM STP 1366,* M. L. Hamilton, A. S. Kumar, S. T. Rosinski and M. L. Grossbeck, Eds., American Society for Testing and Materials, 1999.

[8] Oliver, B.M., McElroy, W.N., Kellog, L.S., and Farrar IV, H., "Boron Determinations in Pressure Vessel Steels," Reactor Dosimetry, ASTM STP 1228, 1994.

[9] Oldfield, W., "Curve Fitting Impact Test Data: A Statistical Procedure," ASTM Standardisation News, no 3 (11) 1975, pp24-29.

[10] Jones, R.B., and Williams, T.J., "The Dependence of Radiation Hardening and Embrittlement on Irradiation Temperature," *Effects of Radiation on Materials: 17th International Symposium, ASTM STP 1270*, D S Gelles, R K Nanstad, A S Kumar and E A Little, Eds., American Society for Testing and Materials, 1996, pp569-590

[11] Priest, R.H., Charnock, W., and Stewart, A.T., "The Effect of Accelerated Irradiation on Fracture Behaviour", *Effects of Radiation on Materials: 11th Conference, ASTM STP 782*, H R Brager and J S Perrin, Eds, American Society for Testing and Materials, 1982, pp475-491.

[12] Fenton, S.T., Jones. R.B., and Morri, J.R., "Accelerated Irradiation of Sizewell "A" BW78C Duct Cut-Out Plate Specimens in Chapelcross", Nuclear Electric plc Memorandum TEM/MEM/0134/94, Rev 1, 1995.

[13] SAS User's Guide: Statistics, Version 5, Chapter 25, 1985, pp575-606.

Duncan Meade,[1] Roy G. Faulkner,[1] and David Ellis[2]

Radiation-Induced Grain Boundary Segregation of Phosphorus in ASME SA533B Ferritic Pressure Vessel Steel

Reference: Meade, D., Faulkner, R. G., and Ellis, D., **"Radiation-Induced Grain Boundary Segregation of Phosphorus in ASME SA533B Ferritic Pressure Vessel Steel,"** *Effects of Radiation on Materials: 19th International Symposium, ASTM STP 1366,* M. L. Hamilton, A. S. Kumar, S. T. Rosinski, and M. L. Grossbeck, Eds., American Society for Testing and Materials, West Conshohocken, PA, 2000.

Abstract: The segregation of phosphorus to grain boundaries is well known to cause embrittlement in a range of ferritic pressure vessel steels. Modelling of segregation is therefore useful in predicting the service life of pressure vessels, particularly in those pressure vessels used in nuclear reactor power generating plant where significant cost savings can be made. In this paper, predictions of the radiation induced grain boundary segregation of phosphorus in ASME SA533B pressure vessel steels are made using an analytical model for impurity segregation in dilute ternary alloys. The model takes into account equilibrium-type segregation, together with a newly adopted approach incorporating the site competition effects that exist between phosphorus and carbon. The site competition effect causes the predicted phosphorus segregation to fall to levels significantly lower than the predictions obtained from models of dilute binary alloys. The predictions are compared to FEGSTEM results of samples irradiated at between 255°C and 315°C, doses between 1.5 and 38mdpa and dose rates ranging from $6x10^{-9}$ to $8.9x10^{-11}$ dpa/s. The predictions obtained from the model are in close agreement to the experimentally observed segregated phosphorus results.

Keywords: Radiation-induced segregation, site competition, grain boundary segregation, phosphorus segregation, analytical modelling, FEGSTEM analysis

[1] Research student and Professor of Physical Metallurgy, respectively, Power & Aerospace Materials Group, Institute of Polymer Technology and Materials Engineering, Loughborough University, Leicestershire, Leicestershire, LE11 3TU, UK.
[2] Rolls Royce and Associates, PO Box 31, Derby DE2 8BJ, UK.

Copyright© 2000 by ASTM International www.astm.org

Introduction

Temper embrittlement of steels is a well documented phenomenon and has been discussed in some detail [*1-6*]. Its effect is known to be caused by the segregation of phosphorus to grain boundaries whilst the material is held for long times at constant temperature. Typically, the embrittlement is most severe in alloys held in the temperature range 350 to 600°C, and the process of segregation has become known as *Thermal Equilibrium Segregation (TES)*. Theoretically, McLean [*7*] derived a model for TES that accurately predicted the degree of segregation of phosphorus to grain boundaries at different temperatures for infinite times. Following McLean, Seah [*2*] incorporated time dependence into the model so that more accurate predictions could be made for shorter periods.

In addition to phosphorus, elements such as boron and carbon are known to be active thermal segregants to grain boundaries. These elements, however, make the cohesive strength of the grain boundaries increase, thus reducing the degree of embrittlement due to the phosphorus present at the boundary. Authors have suggested that there exists some degree of atomic site competition at the grain boundaries between the elements phosphorus, carbon and boron [*8-11*]. Authors have also suggested some degree of site competition between phosphorus and nitrogen [*12*] and between sulphur and carbon [*13*].

In irradiated materials, phosphorus has also been shown to segregate to grain boundaries [*14-18*]. Analytical models have been developed based on theories of *Non-Equilibrium Segregation (NES)* to predict the degree of segregation as a function of the irradiation conditions of irradiation temperature, neutron dose and neutron dose rate [*14, 17, 19-23*]. Microstructural parameters have also been incorporated into these analytical models. Thus far, however, only predictions for binary alloys have been obtainable from these *Radiation Induced Segregation (RIS)* models. No allowance has been made for the effects of atomic site competition at the grain boundaries during irradiation, nor co-segregation due to chemical interactions, as in the TES models developed by Guttmann and co-workers [*1, 5, 6*]. In this paper, an approach is made to incorporate a site competition effect into an already existing RIS model to predict the magnitude of segregation of these impurity elements. The predictions obtained from the model are compared with experimental observations of segregation in different heats of ASME type SA533B pressure vessel steel.

Experimental

Six different heats, alloys A through F, of varying composition were obtained and analysed. The nominal compositions of the alloys used can be found in (Table 1), with composition expressed in terms of weight percent. The alloys can be sub-categorised many ways. Examining the phosphorus contents of the alloys shows that alloys A, B and C all have similar concentrations (approx. 0.024wt%), with alloys D and E showing slightly lower concentrations (approx. 0.016wt%) and alloy F showing the lowest concentration of 0.010wt%. Carbon contents range from 0.048wt% in alloys A and E to 0.062wt% in alloys C and D.

TABLE 1-*Material composition (wt.%)*

Element	A	B	C	D	E	F
C	0.048	0.051	0.062	0.062	0.048	0.051
Mn	1.46	1.50	1.58	1.63	1.5	1.36
Mo	0.49	0.48	0.52	0.48	0.48	0.42
Si	0.48	0.41	0.38	0.44	0.38	0.34
P	0.023	0.024	0.023	0.017	0.016	0.010
Cr	0.040	0.044	0.013	0.04	0.04	0.05
Al	<0.005	<0.005	0.005	0.006	-	-
V	<0.005	<0.005	0.003	0.01	-	-
Sn	0.024	0.024	0.002	0.01	0.01	0.002
As	0.010	0.010	0.014	0.018	0.02	0.03
Sb	<0.002	<0.002	0.002	0.002	0.002	0.002
Cu	0.243	0.48	0.071	0.118	0.56	0.56
S	0.024	0.024	0.0135	0.013	0.012	0.010
Ni	0.25	0.31	0.063	0.087	0.08	1.7

However, there are other significant differences between these alloys. The copper concentrations vary greatly between alloys, with the highest concentration of 0.48wt% found in alloy B. The lowest concentration is 0.071wt%, found in alloy C. These differences may influence the precipitation behaviour of the material, an area that lies outside the scope of this paper but would be worth considering for later work. In particular, it has been shown by Miller and co-workers [*15, 16, 18*], that considerable copper clustering has been found in typical Western pressure vessel steels, and that these copper clusters were also rich in the elements manganese, silicon and phosphorus. The effect of this clustering behaviour could reduce the magnitude of phosphorus segregation to grain boundaries. Nickel contents also vary considerably, ranging from a high 1.7wt% in alloy F down to 0.063wt% in alloy C.

The irradiated samples were examined using *Field Emission Gun Scanning Transmission Electron Microscopy (FEGSTEM)*, using a VG HB501 system based at Harwell Laboratories, UK. A number of grain boundaries from each sample were analysed for possible phosphorus segregation. The results obtained from the analyses are tabulated in the results section of this paper. These results will be used for comparison of the predictions obtained from the theoretical model developed in the following section. Discussion of the relative merits of using the technique of FEGSTEM will be made following these comparisons.

Theoretical modelling

The theoretical model developed here is based on the RIS model of Faulkner and co-workers [*14, 17, 20-23*]. The model adopts an analytical approach, and incorporates the microstructural features of dislocation density and grain size, which experimentally have shown to significantly affect the segregation behaviour of various impurity elements. The material parameters that are used in the model are readily obtainable from available literature [*17,22,23*]. Those used in the calculations are shown in (Tables 2-4).

TABLE 2-*Phosphorus parameters*

Parameter	Notation	Value
Activation energy for solute diffusion (eV)	E_a	2.68
Pre-exp. constant for solute diffusion (m^2/s)	D_{OS}	$7.12x10^{-3}$
Solute-interstitial (S-I) complex binding energy (eV)	E_{bI}	0.57
Migration energy for diffusion of S-I complexes (eV)	E_{mC}	0.87
Pre-exp. constant for diffusion of S-I complexes (m^2/s)	D_{OC}	$8.0x10^{-7}$
Equilibrium segregation energy (eV)	Q_P	0.54

TABLE 3-*Carbon parameters*

Parameter	Notation	Value
Activation energy for solute diffusion (eV)	E_a	0.83
Pre-exp. Constant for solute diffusion (m^2/s)	D_{OS}	$3.94x10^{-7}$
Solute-interstitial (S-I) complex binding energy (eV)	E_{bI}	1.12
Migration energy for diffusion of S-I complexes (eV)	E_{mC}	1.42
Pre-exp. Constant for diffusion of S-I complexes (m^2/s)	D_{OC}	$8.0x10^{-7}$
Equilibrium segregation energy (eV)	Q_C	0.829

TABLE 4-*Material specific parameters*

Parameter	Notation	Value
Migration energy for diffusion of interstitials (eV)	E_{MI}	0.3
Pre-exp. constant for diffusion of interstitials (m^2/s)	D_{OI}	$5.0x10^{-6}$
Migration energy for vacancy diffusion (eV)	E_{MV}	1.24
Pre-exp. constant for vacancy diffusion (m^2/s)	D_{OV}	$5.0x10^{-5}$
Vacancy formation energy (eV)	E_{FV}	1.4
Interstitial atom formation energy (eV)	E_{FI}	3.0
Activation energy for dislocation recovery (eV)	E_d	0.1
Interstitial bias parameter	Z_I	1.1
Grain boundary width (m)	d	$1.0x10^{-9}$
Interstitial jump distance (m)	B	$1.43x10^{-10}$
Vibrational entropy of atoms around interstitial	A_I	1.0
Vibrational entropy of atoms around vacancy	A_V	1.0
Numerical constant for critical time calculation	δ	0.05
Dose rate correction factor	B	0.05

The model presented here is an extension of the *Thermal Non-Equilibrium Segregation (TNES)* theory of Faulkner [*20*]. The TNES theory assumes that there exists a difference in concentration of species between the grain centre and the 'sinks', where vacancies and interstitials are considered to become annihilated. These sinks, for the purposes of modelling, are primarily the grain boundaries, although experimental work has been shown that segregation to dislocations, intragranular precipitates and voids also occurs. This concentration gradient is due to the formation of a supersaturation of point defects within the bulk of the material, for example, the formation of vacancies during rapid quenching. During continued irradiation, both vacancies and self-interstitials are formed. However, in the RIS model extended here only the behaviour of the interstitials

formed. However, in the RIS model extended here only the behaviour of the interstitials will be considered. The reasons for this will be discussed in more detail later. This supersaturation of interstitials is maintained within the bulk of the material. However, at the sink, the concentration of interstitials is maintained at the thermal equilibrium. Thus, there exists a concentration gradient, which forms the driving force for the migration of these point defects. During irradiation, it has been shown that impurity atoms will preferentially bind to these freely migrating point defects. Thus, any migration of point defects will also mean the migration of interstitial – impurity atom complexes. This will eventually redistribute the impurity atoms in such a way as to cause localised enrichment in the vicinity of the sinks. The following equations from the original RIS model of Faulkner [*14,22*] present this situation.

The concentration of impurity-interstitial complexes, C_C, can be determined from:

$$C_c = k_c C_d C_g^P \exp\left(\frac{E_b^{IP}}{kT}\right) \tag{1}$$

where:
k_c = geometrical constant
C_g^P = bulk phosphorus content
E_b^{IP} = phosphorus-interstitial binding energy
k = Boltzmann's constant
T = absolute irradiation temperature
C_d = interstitial concentration, from:

$$C_d = A_I \exp\left(\frac{-E_f^I}{kT}\right) \tag{2}$$

where:
A_I = constant associated with the vibrational entropy of atoms around an interstitial
E_f^I = interstitial formation energy

Thus, the ratio of the complex concentration, C_C, to the impurity concentration, C_g^P, at the grain boundary can be expressed as:

$$\left(\frac{C_c}{C_g^P}\right)_{GB} = k_c A_I \exp\left(\frac{E_b^{IP} - E_f^I}{kT}\right) \tag{3}$$

During irradiation, however, the concentration of defects within the grain is continually in a state of change, since the neutron bombardment is causing further point defects to be produced. Thus, the point defect concentration within the grain needs to be adjusted to allow for this defect production rate:

$$C_d = A_I \exp\left(\frac{-E_f^I}{kT}\right) + \left(\frac{G}{D_I k_{dI}^2}\right) \tag{4}$$

where:
G = defect production rate, more commonly known as the dose rate
D_I = diffusion coefficient of interstitials in the matrix

Since the model is only considering the migration of interstitial – impurity complexes, the interstitial sink strength, k_{dI}^2, can be evaluated from the following equation:

$$k_{dI}^2 = \sqrt{Z_I \rho}\left(\frac{6}{R} + \sqrt{Z_I \rho}\right) \tag{5}$$

where:
Z_I = interstitial bias parameter
R = grain size of the material
ρ = temperature dependent dislocation density, from:

$$\rho = \rho_0 \exp\left(\frac{E_d}{kT}\right) \tag{6}$$

where:
ρ_0 = initial irradiation dislocation density
E_d = activation energy for dislocation recovery

Note here that microstructural parameters are included in these equations. The effect of grain size is incorporated, since larger grains effectively mean that there is a greater impurity supply to a given grain boundary. Higher dislocation densities, on the other hand, cause lower segregation of impurity atoms, since segregation occurring at dislocations will reduce the segregation occurring at grain boundaries.

Therefore, allowing for the effect of a continual production of point defects within the grain, the ratio of the complex concentration, C_c, to the impurity concentration, C_g^P, within the grains can be expressed as:

$$\left(\frac{C_c}{C_g}\right)_m = k_c A_I \exp\left(\frac{E_b^{IP} - E_f^I}{kT}\right) + \frac{k_c G}{D_I k_{dI}^2} \exp\left(\frac{E_b^{IP}}{kT}\right) \tag{7}$$

If the ratio of the matrix concentration to the grain boundary concentration is now calculated, the following expression can be determined:

$$\frac{\left(\frac{C_g^P}{C_c}\right)_{GB}}{\left(\frac{C_g^P}{C_c}\right)_{m}} = 1 + \frac{G}{A_I D_I k_{dI}^2} \exp\left(\frac{E_f^I}{kT}\right) \tag{8}$$

Expanding this equation, and incorporating factors to allow for both the absolute magnitude of the size of misfit of the segregating atoms and the fraction of displacement cascades that give rise to freely migrating point defects, gives the RIS of phosphorus to grain boundaries in a binary Fe-P alloy, $C_b^{P\max}$, as:

$$C_b^{P\max} = C_g^P \frac{E_b^{IP}}{E_f^I}\left[1 + \frac{BGF(\eta)}{A_I D_I k_{dI}^2} \exp\left(\frac{E_f^I}{kT}\right)\right] \tag{9}$$

where:
B = dose rate correction factor
$F(\eta)$ = a function of the long range recombination coefficient of freely migrating point defects, evaluated in reference [*23*].

The equations described thus far describe the maximum level of phosphorus segregation in a binary system assuming that there are no other processes occurring. This situation is somewhat unrealistic. In all pressure vessel steels, the alloys used are complex, containing many alloying elements. Some of these elements are known not to segregate actively. Other elements, however, segregate actively but behave differently depending upon the concentration of certain other alloying elements that may be present. The modifications to the model presented aim to highlight the behaviour of elements that are known to segregate to grain boundaries, but once there would be competing for the same atomic sites. Thus, the model not only considers ternary alloys, it also considers how the grain boundary plane influences the behaviour of the segregating elements. The following equations are used to determine the final level of RIS to grain boundaries allowing for the site competition effects discussed.

$$C_b^{P\max} = C_g^P \frac{E_b^{IP}}{E_f^I}\left(\frac{C_g^P \exp\left(\frac{E_b^{IP}}{kT}\right)}{C_g^C \exp\left(\frac{E_b^{IC}}{kT}\right) + C_g^P \exp\left(\frac{E_b^{IP}}{kT}\right)}\right)\left[1 + \frac{BGF(\eta)}{A_I D_I k_{dI}^2} \exp\left(\frac{E_f^I}{kT}\right)\right] \tag{10}$$

This equation describes the maximum predicted segregation of phosphorus using a thermodynamic relationship. Kinetically, a finite time, t, will be needed for the elements to segregate to the grain boundaries. This time is determined by the irradiation conditions set up by the reactor. Thus, it is possible to determine the radiation exposure time from the total irradiation dose and the dose rate at which the radiation has been affecting the material. The model follows on from previous work [*14,20,22*] in that a

critical time for desegregation needs to be calculated. For times up to this critical time, it is assumed that segregation processes are continually occurring. However, beyond this critical time, a steady state is reached where the magnitude of segregation is maintained. This differs from thermal non-equilibrium segregation models which assume that de-segregation occurs in the region adjacent to the boundary. The critical time relationship employed in the model incorporates the grain size of the material, together with the diffusivities of both the impurity and the impurity-interstitial complexes, thus:

$$t_{crit} = \frac{\delta R^2 \ln\left(\frac{D_C^P}{D_I}\right)}{4\left(D_C^P - D_I\right)} \tag{11}$$

where:
δ = numerical constant
D_C^P = diffusion coefficient of phosphorus-interstitial complexes

For times less that the critical time, t_{crit}, it is assumed that segregation processes can happen, and that solute enrichment or depletion at the grain boundary occurs. However, for times exceeding the critical time, the rate of desegregation of solute away from the boundary is equal to the rate of solute build-up at the grain boundary. Thus, a steady state of segregation is reached, and this value remains constant for all times greater than t_{crit}. Kinetically, this can be expressed using McLean's derivation [7] as:

$$\frac{C_b^P(t) - C_g^P}{C_b^{P\max} - C_g^P} = 1 - \exp\left(\frac{4D_C^P t}{\alpha^2 d^2}\right) erfc\left(\frac{2\sqrt{D_C^P t}}{\alpha d}\right) \tag{12}$$

where:
d = width of the grain boundary
α = ratio of the maximum predicted RIS of phosphorus to the matrix concentration of phosphorus

The model assumes that the final level of segregation depends upon some form of competition for atomic sites at the grain boundary. It is therefore assumed that the competing atoms will redistribute in proportion to the concentration present in the material and the relative grain boundary binding energies of the competing species. The following equation modifies the predicted segregated concentration, $C_b^P(t)$, by a factor containing both the concentrations and grain boundary binding energies for the competing species of phosphorus and carbon.

$$C_b^{P*} = C_b^P(t)\left(\frac{C_g^P \exp\left(\frac{Q_P}{kT}\right)}{C_g^P \exp\left(\frac{Q_P}{kT}\right) + C_g^C \exp\left(\frac{Q_C}{kT}\right)}\right) \tag{13}$$

where:
Q_P, Q_C = grain boundary binding energies of phosphorus and carbon respectively

Note here that when the concentration of the competing segregant is zero, the predicted concentration the primary segregant is unchanged from that predicted by the pure binary model, described earlier. Likewise, as the concentration of the competing segregant diminishes, its effect on the primary segregant diminishes accordingly.

Modelling the TES of both elements in a ternary system assumes a modification of the basic theoretical approach of Guttmann [*1*]. It is necessary to include the effects of TES since the material being irradiated is being held at constant temperature for a long period of time, and thus the mechanism needs to be allowed for. In the ternary Fe-P-C alloy, the maximum predicted TES of phosphorus can be determined from:

$$C_{ES}^{P\max} = \frac{C_g^P \exp\left(\frac{Q_P}{kT}\right)}{1 + C_g^P \exp\left(\frac{Q_P}{kT}\right) + C_g^C \exp\left(\frac{Q_C}{kT}\right)} \tag{14}$$

As with the RIS model, a finite time needs to be incorporated to more accurately predict the segregation following the approach of McLean [*7*], thus:

$$\frac{C_{ES}^P(t) - C_g^P}{C_{ES}^{P\max} - C_g^P} = 1 - \exp\left(\frac{4D_i t}{\alpha^2 d^2}\right) erfc\left(\frac{2\sqrt{D_i t}}{\alpha d}\right) \tag{15}$$

This final equation is used to calculate the final level segregation, $C_{ES}^P(t)$, at any time, t.

Results

The results obtained from the FEGSTEM analysis of the irradiated samples are shown in (Table 5). The data indicates the irradiation conditions of temperature, dose and dose rate. Also expressed are the dislocation densities of the alloys which is required for the theoretical predictions. The results obtained from the theoretical model using the parameters shown earlier and the irradiation conditions expressed in (Table 7) are shown in (Figures 1 to 5). The graphs show the theoretical predictions of phosphorus segregation using the original binary model, together with predictions obtained from the newly developed ternary model. The graphs also show the experimentally observed results for each alloy obtained from the FEGSTEM analyses.

The data for the dislocation densities of samples E1 and F1 have not yet been determined. This prevents the prediction of the RIS with the newly modified model, since the dislocation density is required in determining the sink strength in equation 5.

TABLE 5-Results of irradiated samples

Sample	P	Dose	Flux	T_{irr}	ρ	GB P (at. %)		
	(at.%)	(mdpa)	(dpa/s)	(°C)	(m^{-2})	Min	mean	Max
B1	0.043	1.5	$8.9x10^{-11}$	255	$4.2x10^{14}$	0.75	2.75	4.5
B2	0.043	12.34	$6.4x10^{-10}$	255	$4.2x10^{14}$	2.75	3.2	3.75
B3	0.043	29	$6x10^{-9}$	255	$4.2x10^{14}$	0	1.5	3
C1	0.041	38	$6x10^{-9}$	255	$3.16x10^{14}$	1.5	1.875	2.75
D1	0.03	26.62	$6.3x10^{-9}$	315	$1.5x10^{14}$	3	3.75	4.25
E1	0.028	32.3	$5.8x10^{-9}$	255	-	1.5	2	2.75
F1	0.018	30.1	$6.2x10^{-9}$	255	-	0.5	1.5	4.25

However, comparison of the observed phosphorus segregation values with those figures obtained from the other alloys shows that there is a significant amount of segregation in both alloys. It is also worth noting that sample F1 has the lowest phosphorus content of those analysed and exhibits a mean boundary concentration of 1.5 at.%, an enrichment in the order of 100 times. The maximum figure of phosphorus found in this sample was 4.25 at.%, which is an enrichment of around 250 times the bulk figure.

Also of note in the data presented are the irradiation temperatures. All alloys were irradiated at 255°C, with the exception of Sample D1 which was irradiated at the higher temperature of 315°C. This may explain the higher concentration of phosphorus that this alloy exhibits at the grain boundaries. The predictions obtained for this alloy tend to have underpredicted somewhat the actual observed segregation.

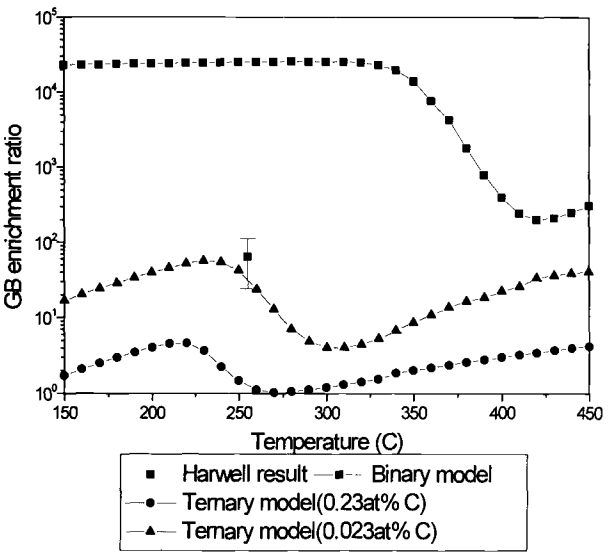


FIGURE 1-*Sample B1, Dose = 1.5mdpa, Flux = $8.9x10^{-11}$dpa/s, $\rho = 4.2x10^{14}m^{-2}$*

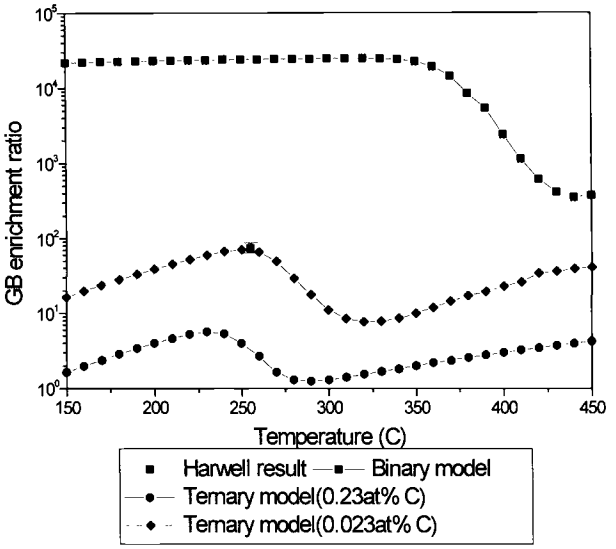


FIGURE 2-*Sample B2, Dose = 12.34mdpa, Flux = 6.4x10^{-10}dpa/s, ρ= 4.2x10^{14}m^{-2}*

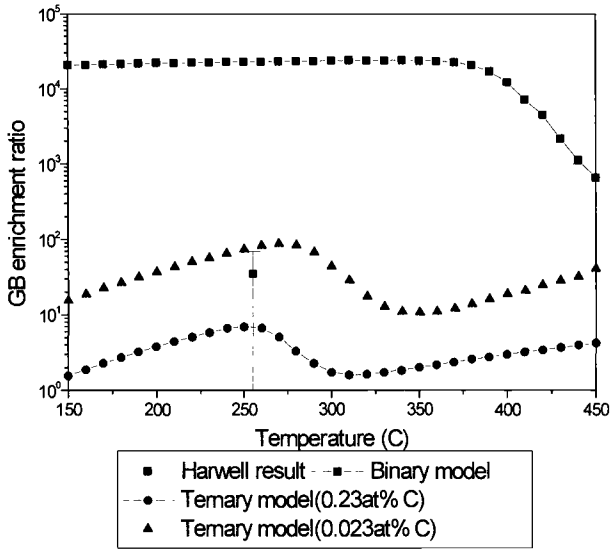


FIGURE 3-*Sample B3, Dose = 29mdpa, Flux = 6x10^{-9}dpa/s, ρ= 4.2x10^{14}m^{-2}*

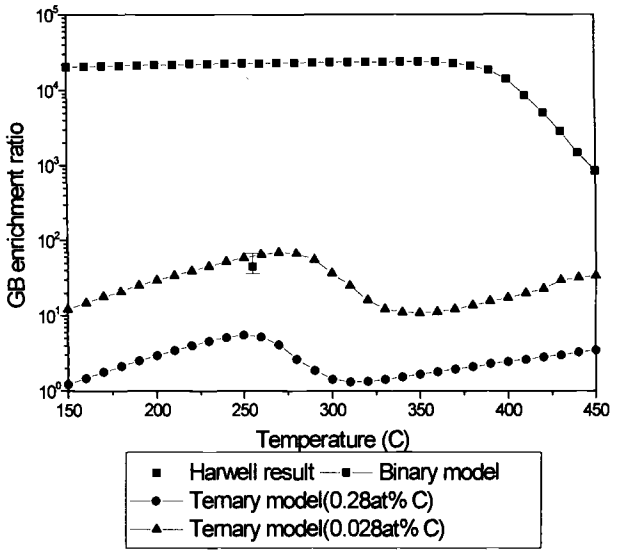


FIGURE 4-*Sample C1, Dose = 38mdpa, Flux = $6x10^{-9}$dpa/s, $\rho = 3.16x10^{14}m^{-2}$*

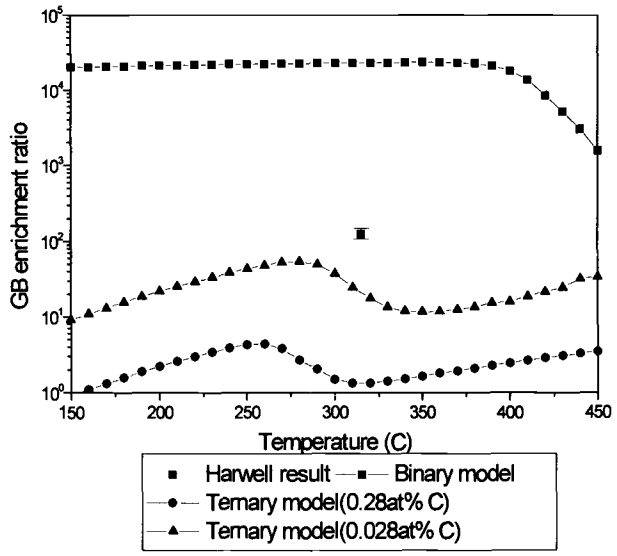


FIGURE 5-*Sample D1, Dose = 26.62mdpa, Flux = $6.3x10^{-9}$dpa/s, $\rho = 1.5x10^{14}m^{-2}$*

Discussion

The results obtained from the newly improved model show that the inclusion of carbon dramatically alters the predicted RIS behaviour of phosphorus. Compared to the previously used binary model, the magnitude of phosphorus segregation drops dramatically, and falls in proportion to the carbon content that is considered to be mobile and able to participate in segregation. Considering the situation being modelled, this is entirely realistic. Carbon is a rapidly segregating element. This is shown through its propensity to form carbides both inter- and intra- granularly in many alloy systems. Therefore, it is to be expected that carbon would more easily segregate and remain at grain boundaries compared to phosphorus. Comparing the predictions to the experimentally obtained figures for phosphorus segregation shows good agreement between the results.

The experimental results themselves are subject to some degree of error. As mentioned earlier, the results were obtained using the technique of FEGSTEM. This technique has been shown to be very appropriate to the analysis of irradiated materials that exhibit impurity element segregation [*24*]. However, the technique tends to underpredict the true magnitude of segregation, owing to the finite beam size, together with the effect of beam broadening within the sample. In addition, any misalignment of the grain boundary will influence the accuracy of the result.

Alternative techniques that have been used to analyse segregated grain boundaries are *Auger Electron Spectroscopy (AES)* [*25, 26*] and *Atom Probe Field Ion Microscopy (APFIM)* [*15, 16, 18*]. These techniques also have their limitations, however. For example, AES samples need to be fractured in order to expose suitable grain boundaries. However, those grain boundaries that are exposed during low temperature fracture may not be entirely representative of the majority of the material, and thus the results obtained would be somewhat biased.

Likewise, APFIM suffers from difficult sample preparation, since the sample is the form of a needle tip and would thus require a representative grain boundary to be located within this small volume of material in order to analyse for any segregation. Experimentally, all three techniques would be useful in order to complement each other, and in order to gain a more accurate representation of what is actually happening at the grain boundaries. Until a technique is developed that can analyse to atomic resolution without any error, modelling techniques will always be required to predict atomic behaviour on a very fine scale.

The model presented here is also somewhat limited even though it has extended a previously accepted approach. The model only predicts the effect of carbon on the behaviour of phosphorus on the grain boundary plane. Here, it is assumed that phosphorus and carbon compete for the same atomic sites at the grain boundary plane. No consideration at present is made for synergistic co-segregation due to chemical interactions, which has been found to occur in thermally aged materials containing, for example, nickel, chromium, manganese and phosphorus [*27*], molybdenum and phosphorus [*28*], chromium and phosphorus [*29*] and phosphorus, carbon, manganese and chromium [*30*].

In order to allow for any synergistic co-segregation effect, chemical interaction parameters for segregating elements need to be determined, similar to those used in the ternary TES models of Guttmann [*1, 5, 6*]. However, since the mechanism that is assumed to be dominant in RIS is that of interstitial complex migration, a method of possible tri-complex migration may need consideration.

Additionally, the model assumes that all grain boundaries are identical. Although microstructural parameters are included in the predictions, no allowance is made for grain boundary structure or grain alignment. These two factors would significantly alter the number of available atomic sites that are present at the grain boundary, which in turn would affect the potential for segregating atoms to remain at the boundary. The predictions obtained from the model can only be used as a maximum value.

The model also generalises about the prior to irradiation condition of the material. It has been assumed that the starting condition of the material is uniform and that no segregation has occurred. This is clearly unrealistic since the material would have experienced some heat treatment process, which would have induced some degree of segregation. In order to take this effect into account, the model needs to incorporate some sort of additive effect, whereby any segregation due to RIS is added on to the prior thermally induced segregation. A graphic representation of how the prior to irradiation heat treatment affects the material can be found in the segregation behaviour of chromium in austenitic stainless steels [*31*]. In this situation, the material the pre-irradiated material exhibits enrichment of chromium at grain boundaries. However, during irradiation, depletion of chromium occurs, causing the deleterious effect of irradiation assisted stress corrosion cracking. The binary model discussed in this paper has been used successfully to model this behaviour [*32*].

Conclusions

The ternary model for RIS presented here would appear to predict more accurately the behaviour of phosphorus segregation observed in the irradiated samples examined. The improvements show that carbon suppresses the degree of phosphorus segregation at grain boundaries in proportion to the carbon concentration that is assumed to be in solution in the material and able to segregate. The model is limited, however, since it generalises about the structure of the grain boundary. Work to characterise more fully the boundaries and the carbides present would be required to make a more accurate comparison between the model predictions and the actual magnitude of segregation.

Acknowledgements

Duncan Meade would like to take this opportunity to thank Dr. David Ellis and Rolls Royce and Associates for their continued help and support throughout this project. Duncan Meade would also like to acknowledge Prof. Roy Faulkner for valuable guidance and advice, and Dr. Colin Goodwin and Dr. Shenhua Song for their fruitful discussions.

References

[1] M. Guttmann, "Equilibrium Segregation in a Ternary Solution: a Model for Temper Embrittlement", *Surface Science*, Vol. 53, pp. 213-227, 1975

[2] M.P. Seah, "Grain Boundary Segregation and the T-t Dependence of Temper Brittleness", *Acta Metallurgica*, Vol. 25, pp. 345-357, 1977

[3] P. Lemble, A. Pineau, J.L. Castagne, P. Dumoulin, M. Guttmann, "Temper Embrittlement in 12% Cr Martensitic Steel", *Metal Science*, August 1979, pp. 496-502

[4] Ph. Dumoulin, M. Guttmann, M. Foucault, M. Palmier, M. Wayman, M. Biscondi, "Role of molybdenum in phosphorus-induced temper embrittlement", *Metal Science*, January 1980, pp.1-15

[5] R. Guillou, M. Guttman, Ph. Dumoulin, "Role of Molybdenum in Phosphorus-Induced Temper Embrittlement of 12%Cr", *Metal Science*, February 1981, pp.63-72

[6] M. Guttman, Ph. Dumoulin, M. Wayman, "The Thermodynamics of Interactive Co-Segregation of Phosphorus and Alloying Elements in Iron and Temper-Brittle Steels", *Metallurgical Transactions A*, Vol. 13A, pp. 1693-1711, 1982

[7] D. McLean, from "*Grain Boundaries in Metals*", Oxford University Press, 1957

[8] H. Erhart, H.J. Grabke, "Equilibrium Segregation of Phosphorus at Grain Boundaries of Fe-P, Fe-C-P, Fe-Cr-P and Fe-Cr-C-P alloys", *Metal Science*, Vol. 15, pp. 401-408, 1981

[9] R.R. de Avillez, P.R. Rios, "The Influence of Carbon on the Phosphorus Segregation in Iron Alloys", *Scripta Metallurgica*, Vol. 17, pp. 677-680, 1983

[10] H. Hansel, H.J. Grabke, "Grain Boundary Segregation of Phosphorus and Carbon in Ferritic Steels", *Scripta Metallurgica*, Vol. 20, pp. 1641-1644, 1986

[11] T. Mega, J. Shimomura, E. Yasuhara, "Grain Boundary Segregation of Phosphorus, Boron and Manganese in High Tensile Strength Steel Sheet", *Materials Transactions*, JIM, Vol. 36, No. 10, pp. 1206-1213, 1995

[12] H. Erhart, H.J. Grabke, "Site Competition in Grain Boundary Segregation of Phosphorus and Nitrogen in Iron", *Scripta Metallurgica*, Vol. 15, pp. 531-534,1981

[13] S. Suzuki, S. Tanii, K. Abiko, H. Kimura, "Site Competition Between Sulphur and Carbon at Grain Boundaries and Their Effect on the Grain Boundary Cohesion", *Metallurgical Transactions*, Vol. 18A, pp. 1109-1115, 1987

[14] R.G. Faulkner, E.A. Little, T.S. Morgan, "Irradiation Induced Grain and Lath Boundary Segregation in Ferritic-Martensitic Steel", *Journal of Nuclear Materials*, Vols. 191-194, pp. 858-861, 1992

[15] M.K. Miller, M.G. Burke, "An Atom Probe Field Ion Microscopy Study of Neutron-Irradiated Pressure Vessel Steels", *Journal of Nuclear Materials*, Vol. 195, pp. 68-82, 1992

[16] M.K. Miller, R. Jayaram, K.F. Russell, "Characterisation of Phosphorus Segregation in Neutron Irradiated Russian Pressure Vessel Steel Weld", *Journal of Nuclear Materials*, Vol. 225, pp. 215-224, 1995

[17] R.G. Faulkner, S. Song, P.E.J. Flewitt, "A Model Describing Neutron Irradiation-Induced Segregation to Grain Boundaries in Dilute Alloys", *Metallurgical Transactions*, Vol. 27A, No. 11, pp. 3381-3390,1996

[18] M.K. Miller, K.F. Russell, "APFIM Characterisation of a High Phosphorus Russian RPV Weld", *Applied Surface Science*, Vols. 94-95, pp. 378-383, 1996
[19] R.G. Faulkner, "Nonequilibrium Grain-Boundary Segregation in Austenitic Alloys", *Journal of Materials Science*, Vol. 16, pp. 373-383, 1981
[20] R.G. Faulkner, "Combined Grain Boundary Equilibrium and Non-Equilibrium Segregation in Ferritic/Martensitic Steels", *Acta Metallurgica*, Vol. 35, No. 12, pp. 2905-2914, 1987
[21] R.G. Faulkner, N.C. Waite, E.A. Little, T.S. Morgan, "Radiation Induced Grain Boundary Segregation in Dilute Alloys", *Materials Science and Engineering*, Vol. A171, pp. 241-248, 1993
[22] R.G. Faulkner, S. Song, P.E.J. Flewitt, "Irradiation-Induced Silicon Segregation in Ferritic Steels", *Journal of Nuclear Materials*, Vols. 212-215, pp. 608-611, 1994
[23] R.G. Faulkner, S. Song, P.E.J. Flewitt, S.B. Fisher, "Irradiation-Enhanced Solute Diffusion in Alloys", *Journal of Materials Science Letters*, Vol. 16, pp. 1191-1194, 1997
[24] T.S. Morgan, E.A. Little, R.G. Faulkner, J.M. Titchmarsh, "Microstructural Studies in Fast Reactor Irradiated FV448 Ferritic-Martensitic Alloy Plate and Weldment", *Effects of Radiation on Materials: 15th International Symposium, ASTM STP 1125*, American Society for Testing and Materials, West Conshohocken, PA, 1994, pp. 607-621
[25] P. Doig, P.E.J. Flewitt, R.K. Wild, "A Comparison of X-Ray (STEM) and Auger Spectroscopy for the Microanalysis of Grain Boundary Segregation", *Philosophical Magazine A*, Vol. 37, No. 6, pp. 759-768, 1978
[26] P. Lejcek, S. Hofmann, "Auger Electron Spectroscopy on Both Fracture Surfaces of an (001)/(011) Asymmetrical Grain Boundary", *Surface Science*, Vol. 307-309, pp. 798-803, 1994
[27] C.L. Briant, "The Effect of Nickel, Chromium and Manganese on Phosphorus Segregation in Low Alloy Steels", *Scripta Metallurgica*, Vol. 15, pp. 1013-1018, 1981
[28] R. Moller, S.S. Brenner, H.J. Grabke, "The Effect of Molybdenum on the Grain Boundary Segregation of Phosphorus in Steel", *Scripta Metallurgica*, Vol. 20, pp.587-592, 1986
[29] S. Suzuki, "Influence of Chromium on Solubility and Grain Boundary Segregation of Phosphorus in Ferritic Iron", *Zeitschrift fuer Metallkunde*, Vol. 82, Pt. 11, pp.883-887, 1991
[30] Weng Yu-Qing, C.J. McMahon Jr., "Interaction of Phosphorus, Carbon, Manganese and Chromium in Intergranular Embrittlement of Iron", *Materials Science and Technology*, Vol. 3, pp. 207-216, 1987
[31] A. Jenssen, L.G. Ljungberg, J. Walmsley, S. Fisher, "Importance of Molybdenum on Irradiation-Assisted Stress Corrosion Cracking in Austenitic Stainless Steel", Corrosion '96, Paper 101
[32] C.C. Goodwin, "Mathematical Modelling of Irradiation Induced Grain Boundary Segregation in Austenitic Stainless Steels", Ph.D. Thesis, Loughborough University, 1998

Alla V. Nikolaeva,[1] Yuri R. Kevorkyan,[2] and Yuri A. Nikolaev[2]

Comparison of Observed and Predicted Data on Radiation Induced Grain Boundary Phosphorus Segregation in VVER Type Steels

Reference: Nikolaeva, A. V., Kevorkyan, Y. R., and Nikolaev, Y. A., **"Comparison of Observed and Predicted Data on Radiation Induced Grain Boundary Phosphorus Segregation in VVER Type Steels,"** *Effects of Radiation on Materials: 19th International Symposium, ASTM STP 1366,* M. L. Hamilton, A. S. Kumar, S. T. Rosinski, and M. L. Grossbeck, Eds., American Society for Testing and Materials, West Conshohocken, PA, 2000.

Abstract: The influence of impurity grain boundary segregation on mechanical properties of low-alloy Cr-Ni-Mo steels is discussed. Mechanisms of impurity and alloying effects on grain boundary embrittlement of low-alloy steels are considered. An approach for estimation of radiation enhanced grain boundary segregation kinetics is proposed. The approach takes into account the reduction of dislocation density (from 1×10^{14} to 1×10^{13} m^{-2}) due to irradiation that was observed for low-alloy Cr-Ni-Mo steels. The influence of collision cascades on the radiation damage is also considered. Auger spectroscopy is used for grain boundary segregation detection. The contribution of grain boundary embrittlement to mechanical property degradation due to neutron irradiation is assessed.

Keywords: reactor pressure vessel, grain boundary segregation, radiation embrittlement, ductile-to-brittle transition temperature.

Introduction

In developing of kinetic models of radiation damage of reactor pressure vessel (RPV) steels, the approach of homogeneous generation of point defects is usually used. Such simplification is reasonable at high temperature and partly at low neutron flux, when the average lifetimes of vacancy complexes formed in cascade volumes is short in comparison with the characteristic time of formation and growth of point defect complexes from supersaturated solution of vacancies and interstitial atoms. The cascade mechanism of point defect generation plays an important role in formation of damage structure of steels. Vacancy clusters are formed in displacement cascades, not by means of a long-term fluctuation mechanism, but form in an extremely short time ($\sim10^{-8}$ s).

[1]Senior research scientist, Nuclear Safety Institute, Russian Academy of Sciences, B.Tulskaya 52, 113191 Moscow, Russia.

[2]Leading research scientists, Russian Research Center "Kurchatov Institute", ORM, Kurchatov Sq. 1, 123182 Moscow, Russia.

Copyright© 2000 by ASTM International www.astm.org

Inclusion account of the cascade mechanism of point defect generation opposed to homogeneous defect generation brings in a number of substantial changes to the kinetic model: firstly, the number of generating point defects decreases because of recombination during the post-dynamic (relaxation) stage of cascade volume development; secondly, immobile clusters of point defects are formed in cascades (mainly of vacancy type), therefore, the generation rates of free (not incorporated in immobile clusters) interstitial atoms (G_i) and vacancies (G_v) are not equal to each other ($G_i > G_v$). These factors can affect the evolving point defect diffusive fluxes, which define the character and the rate of defect microstructural evolution as well as rate of the solid solution decay and impurity segregation. The role of the cascade mechanism of point defect generation during the formation of vacancy agglomerations obviously increases for RPV operation conditions, that is, rather low irradiation temperature and small dose rate.

The formation of interstitial atom agglomerations in cascades as nuclei of dislocation loops, etc., is possible as well. However, due to the peripheral arrangement and interstitial atom density, the probability of their clustering is much lower than for vacancies. Formation of interstitial clusters in displacement cascade volume is neglected in the present work and all interstitials that escape in-cascade recombination are assumed to be free. Then the ratio of free vacancy and interstitial atom generation rates can be given as follows:

$$G_v/G_i = (1 - \varepsilon),\ G_i = \eta G, \tag{1}$$

where ε is vacancy fraction incorporated in immobile complexes; η is the cascade efficiency, i.e. point defect fraction survived after in-cascade recombination; G is displacement rate.

Damage Structure of Displacement Cascade Volume

Since the cascade structure apparently has high importance under development of a radiation damage model of RPV steel, it is expedient to discuss the modern concepts of cascade formation. According to these concepts, formation and the evolution of cascade volume microstructure has three stages: a dynamic stage with duration (τ) of $\sim 10^{-13}$ s, a short-term annealing stage (relaxation) ($\tau \sim 10^{-11} - 10^{-8}$ s) and a long-term annealing stage ($\tau > 10^{-8}$ s). The characteristic times of radiation damage evolution in a kinetic model of radiation damage correspond only to the latter stage, thus, cascade structure after short-term annealing represents the initial information for the kinetic model.

The basic experimental technique of cascade structure investigation is atom probe/field ion microscopy (APFIM). This method, however, is reliably applicable only for refractory materials. If relaxation of the vacancy structure in cascades results in formation of dislocation-vacancy loops or stacking faults, electron microscopy can be used. As for other materials and arbitrary vacancy clusters, studies are only possible using computer simulation methods. There is extensive literature on the study of cascades. Consideration of a minimal number of original and survey works is sufficient for the purposes of the present work.

Computer Simulation

Molecular dynamics simulations provide the most detailed information on cascade formation. Other methods, including the approach of pair-wise collisions for dynamic processes and ill defined "thermal spikes" for relaxation processes have restrictions. Nevertheless they correctly describe the basic qualitative tendencies of displacement cascade evolution. Application of molecular dynamics for high-energy atoms is limited to a computer's capacity. The 5 keV cascade in copper was completely simulated by molecular dynamics (including relaxation) in Ref. [1]. The analyses of those calculations have shown that before times of $\sim 10^{-13}$ s the approach of pair-wise collisions is applicable. However after long times the of knock-on energy is rapidly transferred to all atoms in the volume, resulting in quasi-equilibrium state with average kinetic energy considerably higher than the energy appropriate for irradiation temperature. A disordered volume is formed in the central part of the displacement cascade. A comparison of pair correlation functions for this area and molten copper gives the basis for assuming that the liquid-like phase is formed at the center of displacement cascade. This phase appears at $\tau \sim 10^{-13}$ s, grows up to $\tau \sim 10^{-9}$ s and then diminishes. After $\tau \sim 6\times10^{-9}$ s the cascade volume is completely recrystallized. At $\tau \sim 10^{-8}$ s (at this time the modeling was interrupted) the average temperature in cascade volume fell to ~ 50 K.

A rather long time of existence of the liquid-like phase in copper (more than 10-20 atom fluctuations in the lattice) and subsequent crystallization results in essential transformation of cascade volume structure. All interstitials incorporated in the liquid-like phase are unstable and completely absent after recrystallization. During the relaxation stage interstitials located outside of the liquid-like phase can migrate and can partially incorporate with each other. Almost all vacancies concentrate in the liquid-like phase mainly agglomerate. The following process of vacancy clustering was offered in [1]. Vacancies formed at the dynamic stage as discrete free defects lose their individuality at the relaxation stage when in the central volume quasi-melting occurs. Due to the thermal expansion of the central volume and presence of vacancies, the density of the central volume decreases by 15 % [1]. During the cascade cooling, crystallization of the liquid-like phase occurs radially inside from its surface. Density fluctuations in the surface layers are insufficient for quenching of vacancies in the recrystallizated state. These vacancy are superseded into the central part of the liquid-like phase where density fluctuations are higher and vacancies become "frozen" in solid state. Such as mechanism of displacement of vacancies from peripheral regions to the center explains the increased density of vacancies and their tendency to clustering.

Since extensive study of displacement cascades using molecular dynamics simulations for a wide energy range of primary knock-on atoms for various materials are limited by a computer's capacity, nowadays there are no similar data on vacancy structure of cascades in the matrix material (α-iron) of RPV steel. For some purposes less precise methods of computer simulation can be used: the method of pair-wise collisions for the dynamic stage of a cascade and the Monte-Carlo method for the relaxation stage [2]. Using the pair-wise collision method enables to estimate cascade volume, distribution of heat release and point defects, and the number of point defects formed in the cascade by the end of the dynamic stage ($\sim 10^{-13}$ s). Similar studies of α-iron were carried out for instance in Ref. [3]. The cascade functions for metals (model "TRN-Standard") assessed using the method of pair-wise collisions are used for

calculation of defect generation rates. In the majority of the early studies the essential influence of heat release in displacement cascades ("thermal spikes") on redistribution of vacancies was excluded. However, because of the high density of point defects, the existence of rather fast relaxation stage proceeding under the environmental temperature was included. According to the data of calculations by the Monte-Carlo Doran method [4] and more recent studies [3], during $\tau \sim 10^{-8}$ s at a temperature of 800 K the general number of point defect pairs in cascades decreased by 5 times as a result of mutual recombination, and the relative size distribution of vacancy agglomerations was displaced to the larger sizes.

It is worth noting that the model of short-term annealing mentioned above, in which the role heat release in cascades was not taken into account and does not correspond to the described above of relaxation process of 5 keV cascade in copper. The discrepancy consists in the estimation of an opportunity of liquid-like phase formation and time of its existence, which are probably connected with cascade volume size, heat release density and corresponding vacancy density. If it is correct, it is necessary to expect the relaxation process in cascades by means of the mechanism of liquid-like phase formation, in high-energy cascades formed in heavy metals, and by means of the model of short-term annealing - in lighter materials and low-energy cascades.

Experiment.

As already mentioned, the only experimental method suitable for the study of detailed defective structure of cascades is the APFIM. This method is the most applicable to refractory materials (W, Mo, Pt). There is a lot of data on cascades study in these materials caused by particles of various energies and masses. It is worth noting that all these data have more scientific than applied importance. They serve the proof of theoretical concepts and confirm the adequacy of computer models. APFIM data do not contradict the conclusions of the theory and computer simulation, though the quantitative comparison is complicated because of the absence of statistically representative data (both experimental and calculated) for identical materials and energies of primary knock-on atoms. In the vacancy structure of cascades in refractory materials investigated by APFIM, both uncollapsed defective structures representing vacancy clusters, and two dimensional structural defects such as dislocation vacancy loops and stacking faults from collapse of initial vacancy structure were observed [1]. These validate the theoretical assumption that in heavier materials and under irradiation by more massive particles the probability of formation of vacancy clusters and subsequent collapse is higher.

The experimental analysis of collapsed vacancy structures is possible using standard methods of electron microscopy, since the character of diffraction contrast created by dislocation vacancy loops and stacking faults, enables resolution of smaller vacancy clusters. The early experimental data on study of collapsed vacancy structures were generalized in Ref. [5]. From more recent works it worth to note Refs. [6, 7]. According to these studies, in a number of rather heavy FCC and BCC metals (Au, Cu, Mo) after ion or neutron irradiation at temperatures below the thermal migration of vacancies, extended defects such as dislocation vacancy loops and stacking faults were observed. These defects were attributed to collapse of vacancy structures in cascades. Dislocation vacancy loops of small size were observed in α-iron only under rather high irradiation doses (more then 10^{17} ion/m^2 under irradiation by the same ions with energies

of 40-100 keV). This gives the basis for assuming that in ferritic alloys, vacancy structures of isolated cascades do not collapse, and the opportunity of collapse arises only due to overlapping cascades. The probability of such overlapping is important for high damage doses and rather low temperatures.

On the basis of the given brief analyses it is possible to suppose with a sufficient probability that the vacancy structures of cascades, generated in RPV steel under neutron irradiation represent volumetric vacancy agglomerations. Since the representative data on displacement cascade simulation in α-iron are absent, and collapsed vacancy structures probably connected with formation of liquid-like phase in the relaxation stage of cascade evolution have not been observed experimentally for characteristic irradiation doses for RPV steel. In the further analyses the results of cascade simulations using the approach of pair-wise collisions and results of simulation of short-term annealing of cascades by the Monte-Carlo technique will be used.

Analyses of Radiation Damage of RPV Materials

The spectrum of primary knock-on atoms ψ(T) under irradiation of material by fast neutrons with spectral distribution φ(E) is defined by the following expression:

$$\psi(T) = \int_0^\infty \varphi(E)\sigma(E)K(E,T)dE \tag{2}$$

where σ(E) is the complete microscopic section of interaction of neutrons with atoms of material; K(E, T) is the probability of nucleation of a primary knock-on atom with energy T by a neutron with energy E.

If φ(E) is normalized on a real value of neutron flux then $\int_{E_d}^\infty \psi(T)dT$, where E_d is a threshold energy of atom displacement (40 eV for Fe), gives the value of primary knock-on atom production rate, per atom of material. The generation rate of all displaced atoms in terms of dpa/s (dpa - displacement per atom) is given by the expression:

$$G = \int_{E_d}^{T_M} \psi(T)\nu(T)dT \tag{3}$$

where ν(T) is the cascade function; $T_M \approx 4E/A$ (A is the atomic mass) is the maximal energy of primary knock-on atoms, transmitted by a neutron with energy E.

Values of fluxes and calculated values of G for the typical irradiation conditions of a RPV steel [8] are given in Table 1.

The data given in Table 1 correspond to thermal reactor capacities of 1375 MW for VVER-440 and 3000 MW for VVER-1000. The data on displacement rates were obtained for the cascade function $\nu = 10\ T_{Dam}$ (T_{Dam} is a fraction of primary knock-on atom energy in keV, spent in elastic collisions) which defines the number of the atoms displaced in a cascade, at the end of the dynamic stage and is known as the TRN-Standard.

TABLE 1 - *Density of Fast Neutron Fluxes and Point Defect Production Rates*

Reactor	Position	Flux (E≥0.5MeV) 10^{14} m^{-2} s^{-1}	Displacement rate 10^{-11} dpa/s
MR	Working channel	4000	3000
VVER-440	Internal surface RPV	34	30
	Surveillance position	350	280
VVER-1000	Internal surface RPV	5.7	8
	Surveillance position	24	28

The results of calculations of primary knock-on atom spectra for neutron spectra for VVER and MR reactors were not published, because of more practical interest in calculations of the number of displaced atoms. However, if it is necessary, the primary knock-on atom spectra can be obtained as a by-product of these calculations. Some data on primary knock-on atom spectra were published in Ref. [9]. Particularly in Ref. [9] a spectrum of primary knock-on atoms in α-iron for neutron flux with energy of 1 MeV was given. An average energy of primary knock-on atoms in characteristic spectra of VVER and MR can be estimated using those data. This energy was estimated to be approximately 30 keV. In the first approach it is possible to limit the model to point defects generated only by primary knock-on atoms with energy of 30 keV.

The general number of pairs of point defects in a 30 keV cascade after the dynamic stage is ~ 260, the primary knock-on atom generation rate per atom ranges approximately from 1 to 100×10^{-12} s^{-1} which corresponds to the range of displacement rate given in Table 1. As a result of a short-term annealing a portion of point defects in the cascade recombines, another portion is conglomerated in immobile clusters, another portion escapes the cascade and freely migrates in the material. As follows from the results of short-term annealing simulation [3], the in-cascade recombination results in a two-fold decrease in the point defect number at a temperature of 300 K (interstitial atoms are mobile only) and in a five-fold decrease at a temperature of 800 K (both interstitial atoms and vacancies are mobile). Thus, for the quantitative calculations at irradiation temperatures of RPV service (~550 K) a three-fold reduction of point defects due to the in-cascade recombination can be assumed ($\eta = 1/3$ in Eq. 1).

Calculations showed that the lifetime of voids with less than 9 vacancies is very short in comparison with the recombination rate and vacancies incorporated in those voids can be considered as free. Thus, it will be assumed that only the vacancy clusters containing more than 8 vacancies have a steady immobile configuration. Because of the high density of agglomerations in the cascade volume it is possible to expect that in the initial stage of long-term annealing the conglomerate of vacancies has an intermediate stage of integration. Therefore, it is possible to suppose that only one microvoid nucleates in each cascade volume. For a 30 keV cascade such a microvoid contains ~60 vacancies that corresponds ~65% of the vacancies survived after in-cascade recombination [3] ($\varepsilon = 0.65$ in Eq. 1). The others vacancies are free.

Kinetic Model

The kinetic model of radiation damage described below takes into account processes of formation and decay of vacancy clusters. The influence of irradiation on the change of dislocation structure is not considered.

The concentration of the cascade microvoids N_{z0} is determined by the following equation:

$$\partial N_{z0}/\partial\tau = G_{z0} - N_{z0}/\tau_{z0} \quad (4)$$

where G_{z0} is the generation rate of cascade microvoids and τ_{z0} is their lifetime.

The lifetime of microvoid can be determined from the equation describing the rate of change of its radius r_z in diffusive approach:

$$\partial r_z/\partial t = -(D_iC_i - D_vC_v)/r_z - D_vC_{ve}\exp[\Delta E(z)/kT]/r_z \quad (5)$$

where D_v and D_i are diffusion coefficients of vacancies and interstitials, respectively; C_v and C_i are concentrations of vacancies and interstitials, respectively; C_{ve} is equilibrium concentration of thermal vacancies; $\Delta E(z) = E(z+1) - E(z)$; $E(z)$ is convertible formation energy of microvoid containing z vacancies ($z\times\Omega = 4\pi r_z^3/3$). In the approach of the capillary model of binding $\Delta E(z) = 2\gamma\Omega/r_z$, where γ is the surface energy of α-iron.

The first term in the Eq. (5) describes the rate of r_z change caused by the difference in diffusive fluxes of vacancies and interstitials, the second term corresponds to the thermal decay of microvoids. Under the cascade mechanism of point defect generation $(D_iC_i - D_vC_v) > 0$ due to various generation rates of free vacancies and interstitial atoms (Eq. 1).

The following equations can be derived from Eq. (5) for the rate, P (z), of microvoid growth from size z to z+1 and the rate Q (z) of microvoid transition from size z to z-1:

$$P(z) = 3\,(4\pi/3\Omega)^{2/3}\, z^{1/3}\, D_vC_v \quad (6a)$$

$$Q(z) = 3\,(4\pi/3\Omega)^{2/3}\, z^{1/3}\, \{D_iC_i + D_vC_{ve}\exp[\Delta E(z)/kT]\} \quad (6b)$$

The equations of point defect balance are as follows:

$$\partial C_i/\partial t = G_i - \mu D_iC_iC_v - S_iD_iC_i \quad (7a)$$

$$\partial C_v/\partial t = G_i(1-\varepsilon) + G_{th} - \mu D_iC_iC_v - S_vD_vC_v \quad (7b)$$

where G_{th} is the rate of vacancy evaporation from microvoids; S_α is the point defect sink strength ($\alpha = i$ or v). $S_\alpha = S_0 + S_{void}(t)$, S_0 is the initial sink strength (dislocations, grain boundaries etc.), $S_{void}(t)$ is the strength of microvoids as sinks for point defects:

$$S_{void}(t) = 4\pi/\Omega \int r_z N_z dz\ , \quad (8)$$

where N_z is a size distribution function of microvoids:

$$\int_{9}^{z_0} N_z dz = N_0 \tag{9}$$

G_{th} can be defined as follows:

$$G_{th}(t) = 4\pi/\Omega \, D_v C_v \int r_z N_z \exp[\Delta E(z)/kT] dz \tag{10}$$

The steady state of the point defect equations (7) in the case of $G_i \neq Gv$ and $S_i = S_v$ gives:

$$D_i C_i - D_v C_v = (G_i - G_v)/S_\alpha = (\varepsilon G_i - G_{th})/S_\alpha \tag{11}$$

S_α is a function of time determined by the kinetics of evolution of microvoids and dislocation structure. Therefore, Eqs. (4) and (5) are nonlinear. Their solution is possible only by numerical methods if the time dependence of the difference of diffusive fluxes ($D_iC_i - D_vC_v$) determined by Eq. (11) is known.

As can be seen from Eqs. (4) - (6), the equation for N_z is as follows:

$$\partial N_z / \partial t = G_{z0}\delta(z - z_0) - \frac{\partial}{\partial z}[(P(z) - Q(z))N_z] \tag{12}$$

The Eqs. (4) - (12) form a closed system, which can be solved only by numerical methods.

Results of Numerical Calculations

The parameters used in the following calculations are listed in Table 2. Justification of the choice of these parameters was given in Ref. [10]. Result of computer simulations of microvoid evolution and corresponding diffusive fluxes of point defects under neutron irradiation of RPV steel in Figs. 1 - 7. The dependence of vacancy concentration on dislocation density is shown in Fig. 1. A peak in vacancy concentration with increasing dislocation density is due to high recombination rate at low dislocation density and increasing dislocation sink strength with dislocation density. The dependence of diffusive fluxes of interstitials and vacancies on damage dose is shown in Fig. 2. As seen from Fig. 2, the diffusive fluxes essentially depend on displacement rate. The dependence of the difference between point defect fluxes on damage dose is shown in Fig. 3. Usually in calculations the void radius is considered to be fixed. In Ref. [17] it was assumed to be 0.5 nm (~44 vacancies). As seen from Fig. 4 the mean void radius ranges at least from 0.45 to 0.55 nm that results in variation of void sink strength (Fig. 6). The dependence of the thermal decay rate of microvoids on damage dose is shown in Fig. 5. The increase in S_{void} with displacement rate (Fig. 6) doesn't contradict the decrease of $\bar{z}$ with increase of G (Fig. 4) because of increase of void density with G (Fig. 7). Since the slope of the dependence of vacancy diffusive fluxes on displacement rate for

uniform generation model is higher that the model discussed (Fig. 8) the cascade generation model can be used for flux effect explanation.

TABLE 2 - *Parameters Used in Calculations*

Irradiation temperature (T_{irr})	270°C
Point defect production rate (G)	10^{-8} - 10^{-11} dpa/s
Cascade efficiency (η)	1/3
Vacancy fraction incorporated in microvoids (ε)	0.65
End-of-life neutron irradiation dose (F_l)	10^{24} m^{-2}
Dislocation density (ρ)	10^{13} - 10^{14} m^{-2}
Recombination factor (μ)	3.3×10^{20} m^{-2} [10]
Surface energy of α-iron (γ)	1.5 J/m^2 [11]
Diffusivity pre-exponential:	
α-iron	2.0×10^{-4} m^2/s [12]
vacancy in α-iron	5.0×10^{-5} m^2/s [13, 14]
interstitial α-iron	5.0×10^{-6} м^2/с [14];
Activation energy of α-iron self-diffusion	2.75 Ev [12]
Vacancy migration energy (E_m)	1.25 eV [14]
α-iron lattice parameter	0.28665 nm [15, 16]

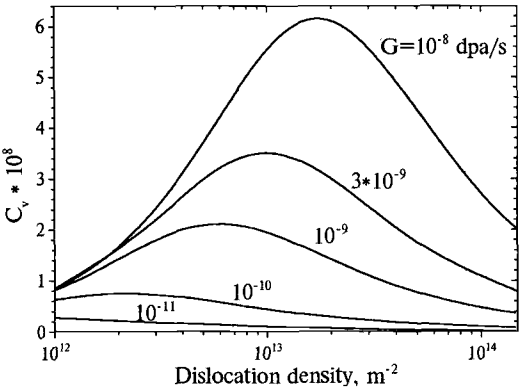


Figure 1 - *Dependence of Vacancy Concentration on Dislocation Density*

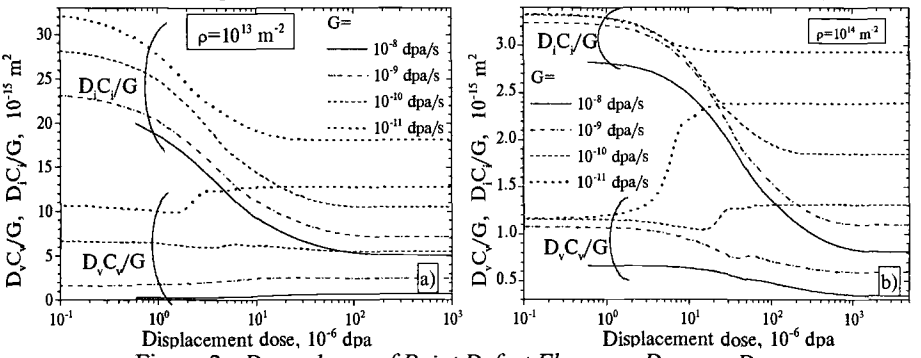


Figure 2 - *Dependence of Point Defect Fluxes on Damage Dose*

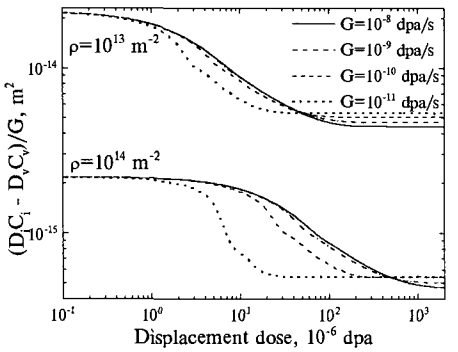


Figure 3 - *Dependence of the Difference Between Point Defect Fluxes on Damage Dose*

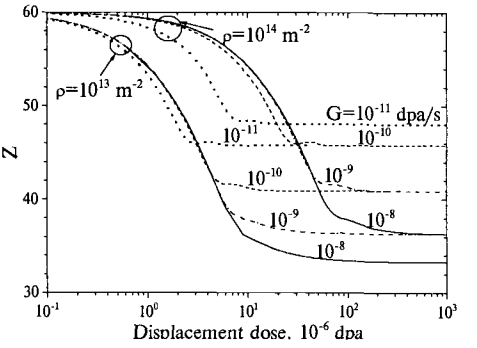


Figure 4 – *Dependence of Mean Number of Vacancies in Microvoids on Damage Dose*

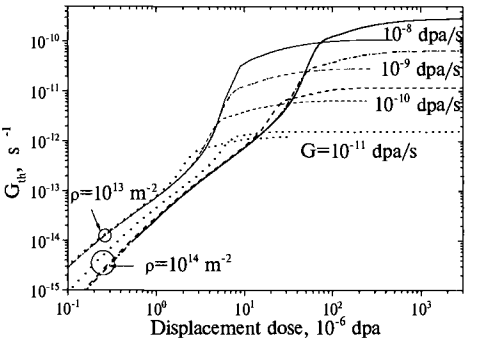


Figure 5 – *Dependence of Thermal Decay Rate of Microvoids on Damage Dose*

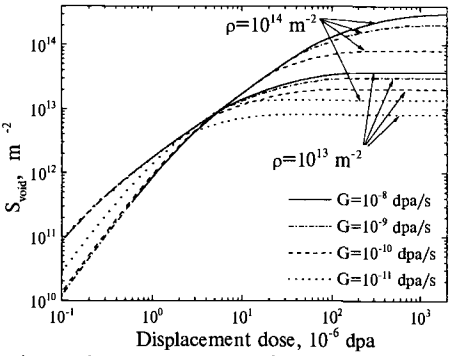


Figure 6 – *Dependence of Microvoid Sink Strength on Damage Dose*

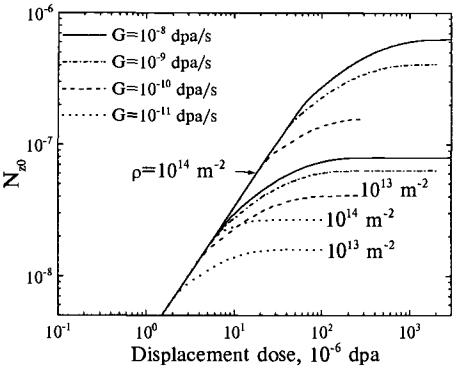


Figure 7 - *Dependence of Microvoid Density on Damage Dose*

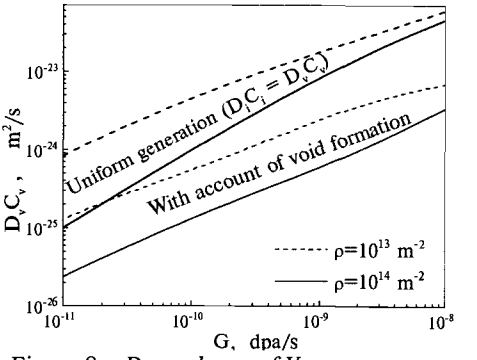


Figure 8 – *Dependence of Vacancy Diffusive Fluxes on Displacement Rate*

Radiation Induced Phosphorus Grain Boundary Segregation

A low-alloy RPV steel was irradiated to fast neutron fluences ranging from 14 to 65×10^{22} n/m^2 (E > 0.5 MeV) at ~275°C. The duration of the irradiation was of about 60,000 h. Chemical composition of the steel is as follows (in wt.%): 0.25%C, 0.31%Si, 0.47%Mn, 3.30%Cr, 1.07%Ni, 0.37%Mo, 0.040%S, 0.018%P and 0.10%Cu.

The tendency of the steel for brittle fracture was estimated by the ductile-to-brittle transition temperature (DBTT). A 47 J reference energy was used for determination of the DBTT. 165°C DBTT shift was determined for the steel irradiated to 14×10^{22} n/m^2. For the steel irradiated to 62×10^{22} n/m^2 the DBTT shift increased up to 310°C.

A fractographic examination using a scanning electron microscope revealed appearance of some intergranular fracture mode on the fracture surfaces of specimens in irradiated conditions (in unirradiated condition intergranular fracture mode was vanishing). Up to 80 % of intergranular fracture was observed on the fracture surface of Charpy specimens irradiated to a fluence of 62×10^{22} n/m^2. In the case of the irradiation exposure of 14×10^{22} n/m^2 a fraction of intergranular fracture was found to be about two times less.

Auger spectroscopy along with McLeen theoretical approach were used for characterization of grain boundary chemistry. The research was carried out at the facility MICROLAB Mk II with an electron beam energy of 5 keV. The samples with a cross section of 1 mm^2 were broken in the vacuum cell of the facility. Auger spectroscopic examination revealed an increase in phosphorus grain boundary concentration with damage dose. Changes in the phosphorus peak height ratio (PHR) as a function of neutron fluence are shown in Fig. 9. Thus, the conception of irradiation induced intergranular segregation was confirmed. An acceleration of grain boundary phosphorus segregation after a fluence of 42×10^{22} n/m^2 was observed.

In Ref. [17] the dependence of transition temperature shift on PHR was obtained based on the thermal ageing condition

$$\Delta TT = 1300\ PHR + Const,\ °C \qquad (13)$$

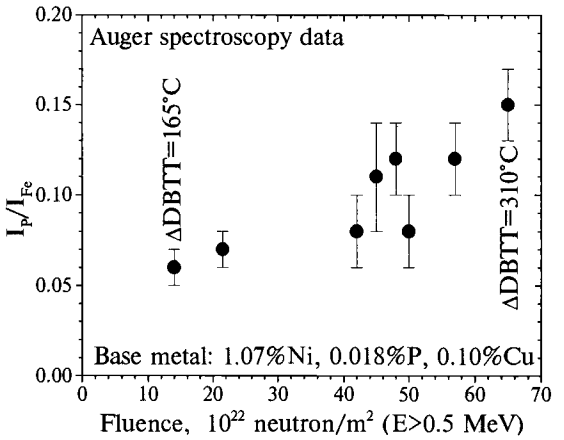


Figure 9 - *Auger Spectroscopy Data on Grain Boundary Phosphorus Segregation*

where ΔTT is the DBTT shift. Eq. (13) underestimates change in transition temperature due to irradiation from 14 to 62×10^{22} n/m^2 in composition with the observed value being 20% (Table 3) more than expected from Eq. (13).

The following expression was developed in [18]:

$$\Delta DBTT = 82\ \Delta C_P^{GB} \ln (d/d_o) \qquad (14)$$

where d is the prior austenitic grain size, d_0 is a characteristic value equal to 1 μm and ΔC_P^{GB} is the change in phosphorus grain boundary segregation. Results of Eq. (13) and (14) are very close. That suggests that the embrittlement was predominantly controlled by phosphorus segregation.

An approach developed in Refs. [10, 19] combined with the kinetic model of radiation damage developed in the present work was used for prediction of radiation enhanced grain boundary phosphorus segregation. A comparison of experimental and predicted data on radiation enhanced grain boundary phosphorus segregation is shown in Fig. 10. Good correlation between experiment and prediction for a dislocation density of 10^{14} m^{-2} for lower fluence range and prediction for a dislocation density of 10^{13} m^{-2} for higher fluence range confirms the fact of the dislocation density reduction in RPV steels during irradiation [19].

TABLE 3. Observed and calculated data on DBTT shift.

Fluence	ΔTT_F, °C		
10^{22} n·m^{-2}	Observed	Eq. (13)	Eq. (14) (d = 120 μm)
14	165		40
62	310		146
ΔTT_F(**62**)-ΔTT_F(**14**)	**145**	**117**	**106**

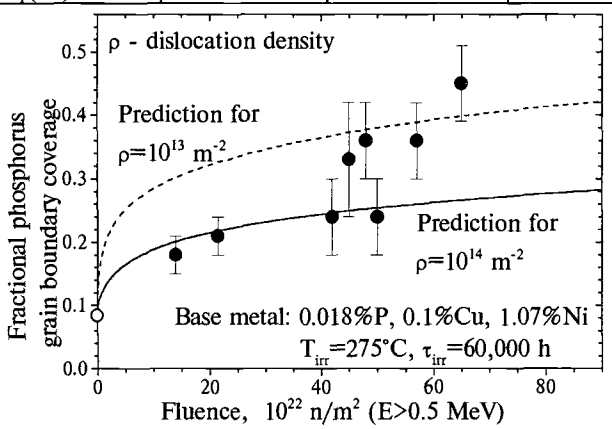


Figure 10 - *Comparison of Experimental and Predicted Data on Radiation Enhanced Grain Boundary Phosphorus Segregation*

References

[1] Seidman, D.N., Averbach, R.C. and Benedek, R. Displacement cascades. Dynamic and atomic structure. *Phys. Status Solidi (b),* 1987, v. 144, pp. 85-104.

[2] Beeler, J.R. Radiation effects computer experiments. Amsterdam - New-York - Oxford, 1983.

[3] Platonov, P.A., Krasnoshtanov, V.F., Kevorkyan, Yu.R. Simulation of the processes of nucleation and annealing of defects in displacement cascade areas in alfa-iron. *Atomnaya Energiya*, 1975, v. 39, No. 4, pp. 260-264.
[4] Doran, D.G. *Radiation Effects*, 1970, v. 2, p. 249.
[5] Kevorkyan, Yu.R. Some questions of cascade mechanism of point defect generation in materials. *Voprosy Atomnoy Nauki i Techniki, Radiation Material Science Series*, 1979, v. 1, No. 9, pp. 24-30.
[6] Kitagawa, K., Yamakawa, K., Fukushima, H., et al. Ion-irradiation experiment for the fundamental studies of damage evolution of fusion materials. *Journal of Nuclear Materials*, 1985, v. 133-134, pp. 395-399.
[7] Kirk, M.A., Robertson, I.M., Jenkins M.L., et al. The collapse of defect cascades to dislocation loops. *Journal of Nuclear Materials*, 1987, v. 149, pp. 21-28.
[8] Brodkin, E.B., Borodin, A.V., Vikhrov, V.I. and Khrustalev, A.V. Calculated and experimental parameters of fast neutron field in the region near RVP wall of VVER-440 and VVER-1000. Proceedings of 4th Soviet Union Wide Scientific Conference on Protection from Irradiation of Nuclear Equipment, Tomsk, 1985.
[9] Kevorkyan, Yu.R. Computer simulation of structure damage processes in iron under neutron irradiation. *Ph. D. Thesis*, RRC "Kurchatov Institute", Moscow, 1975.
[10] Nikolaeva, A. V., Nikolaev, Yu. A. and Kryukov, A.M. The contribution of grain boundary effects to low-alloy steel irradiation embrittlement. *Journal of Nuclear Materials*, 1994, v. 218, pp. 85-93.
[11] Samsonov, G.I., Pryadko, I.F. and Pryadko, L.F. Configuration model of solids. Naukova Dumka, Kiev, 1971.
[12] Oikawa, M. Review of lattice diffusion of substitutional impurity in iron. A summary report. *Technology Reports*, Tohoku Univ., 1982, v. 47, pp. 215-224.
[13] Simonen, E. P. Predicted irradiation effects on alloy aging kinetics. In: International conference on nuclear power plant, aging, availability reactor and reliability analysis. 1985, San Diego, USA.
[14] Stoller, R.E. Pressure vessel embrittlement predictions based on a composite model of copper precipitation and point defect clustering. In: Effects of Radiation on Materials: 17th International Symposium, *ASTM STP 1270*, Eds. D.S.Gelles, R.K.Nanstad, A.S.Kumar and E.A.Little (ASTM, Philadelphia 1996) pp. 25-58.
[15] Finnis, M.W. and Sinclair, J.E. A simple empirical N-body potential for transition metals. *Philosophical Magazine A*, 1984, v. 50, No. 1, pp. 45-55.
[16] Huntington, H.B. Solid State Physics, v. 7, Eds. F.Seitz and D.Turnbull, (Academic Press, Inc., N.-Y.) p. 274.
[17] Hudson, J.A., Druce, S.G., Gage, G. and Wall, M. Thermal ageing effects in structural steels. *Theoretical and Application Fracture Mechanics*, 1988, v. 10, pp. 123-133.
[18] Nikolaeva, A.V., Nikolaev, Yu.A. and Kryukov, A.M. Grain boundary embrittlement due to reactor pressure vessel annealing. *Journal of Nuclear Materials*, 1994, v. 211, pp. 236-243.
[19] Nikolaev, Yu.A., Nikolaeva, A.V., Zabusov, O.O., Gurovich, B.A., Kuleshova, E.A. and Chernobaeva, A.A. Radiation and thermo-induced adsorbtion of phosphorus on grain boundaries in low-alloy steels. *Fizica Metallov i Metallovedenie*, 1996, v. 81, No. 1, pp. 120-128.

Ferritic and Ferritic/Martensitic Steels—Annealing and Reirradiation Behavior

M. A. Sokolov,[1] A. A. Chernobaeva,[2] R. K. Nanstad,[1] Yu. A. Nikolaev,[2] and Yu. N. Korolev[2]

Irradiation, Annealing, and Reirradiation Effects on American and Russian Reactor Pressure Vessel Steels

Reference: Sokolov, M. A., Chernobaeva, A. A., Nanstad, R. K., Nikolaev, Y. A., and Korolev, Y. N., **"Irradiation, Annealing, and Reirradiation Effects on American and Russian Reactor Pressure Vessel Steels,"** *Effects of Radiation on Materials: 19th International Symposium, ASTM STP 1366,* M. L. Hamilton, A. S. Kumar, S. T. Rosinski, and M. L. Grossbeck, Eds., American Society for Testing and Materials, West Conshohocken, PA, 2000.

Abstract: One of the options to mitigate the effects of irradiation on reactor pressure vessels (RPVs) is to thermally anneal them to restore the toughness properties that have been degraded by neutron irradiation. Even though a postirradiation anneal may be deemed successful, a critical aspect of continued RPV operation is the rate of embrittlement upon reirradiation. There are insufficient data available to allow for verification of available models of reirradiation embrittlement or for the development of a reliable predictive methodology. This is especially true in the case of fracture toughness data. Under the U.S.-Russia Joint Coordinating Committee for Civilian Nuclear Reactor Safety (JCCCNRS), Working Group 3 on Radiation Embrittlement, Structural Integrity, and Life Extension of Reactor Vessels and Supports agreed to conduct a comparative study of annealing and reirradiation effects on RPV steels. The Working Group agreed that each side would irradiate, anneal, reirradiate (if feasible), and test two materials of the other. Charpy V-notch (CVN) and tensile specimens were included. Oak Ridge National Laboratory (ORNL) conducted such a program (irradiation and annealing, including static fracture toughness) with two weld metals representative of VVER-440 and VVER-1000 RPVs, while the Russian Research Center-Kurchatov Institute (RRC-KI) conducted a program (irradiation, annealing, reirradiation, and reannealing) with Heavy-Section Steel Technology (HSST) Program Plate 02 and Heavy-Section Steel Irradiation (HSSI) Program Weld 73W. The results for each material from each laboratory are compared with those from the other laboratory. The ORNL experiments with the VVER welds included irradiation to about 1×10^{19} n/cm^2 (>1 MeV), while the RRC-KI experiments with the U.S. materials included irradiations from about 2 to 18×10^{19} n/cm^2 (>1 MeV). In both cases, irradiations were conducted at ~290°C and annealing treatments were

[1]Oak Ridge National Laboratory, P.O. Box 2008, Oak Ridge, TN 37831-6151.

[2]Russian Research Center-Kurchatov Institute, 123182 Moscow, Russia.

Copyright© 2000 by ASTM International www.astm.org

conducted at ~454°C. The ORNL and RRC-KI experiments have shown generally good agreement for both the Russian and U.S. steels. While recoveries of the Charpy 41-J transition temperatures were substantial in all cases, significantly less recovery of the lateral expansion and shear fracture in some cases (no recovery in one case) deserves further attention. The RRC-KI results for the U.S. steels showed reirradiation embrittlement rates which are conservative relative to the lateral shift prediction based on Charpy impact energy.

Keywords: Charpy, embrittlement, annealing, reirradiation, reactor pressure vessel

Introduction

One of the options to mitigate the effects of irradiation on RPVs is to thermally anneal them to restore the toughness properties that have been degraded by neutron irradiation. Even though a postirradiation anneal may be deemed successful, a critical aspect of continued RPV operation is the rate of embrittlement upon reirradiation. There are insufficient data available to allow for verification of available models of reirradiation embrittlement or for the development of a reliable predictive methodology. This is especially true in the case of fracture toughness data. Under the U.S.-Russia JCCCNRS, Working Group 3 on Radiation Embrittlement, Structural Integrity, and Life Extension of Reactor Vessels and Supports agreed to conduct a comparative study of annealing and reirradiation effects on RPV steels. The Working Group agreed that each side would irradiate, anneal, reirradiate (if feasible), and test two materials of the other. CVN and tensile specimens have been included. ORNL conducted such a program (irradiation and annealing) with two weld metals representative of VVER-440 and VVER-1000 RPVs including static three-point bend tests of precracked CVN (PCVN) specimens, while the RRC-KI conducted a program (irradiation, annealing, reirradiation, and reannealing) with HSST Plate 02 and HSSI Weld 73W. The results for each material from each laboratory are compared with those from the other laboratory.

Materials

Three welds and one base metal were characterized in the present study. The chemical compositions and mechanical properties in the unirradiated condition are listed in Tables 1 and 2, respectively. The base metal was American Society for Testing and Materials (ASTM) A 533 grade B class 1 plate, designated HSST Plate 02, portions of which have been used in many investigations around the world. The plate was edge-quenched in water after austenitizing at 871°C, then tempered at 663°C for 4 h and furnace cooled. The final stress relief was performed at 621°C for 40 h [1]. One of the welds, designated HSSI Weld 73W, was specially produced for the HSSI Program by Combustion Engineering, Inc., using the submerged-arc process with Linde 0124 flux. The weld was postweld heat treated at 607°C for 40 h [2,3]. The weld is known to be a high-copper (radiation-sensitive) weld.

The two other welds were specially produced by the Izhora Plant to exemplify radiation-sensitive welds of two Russian-made commercial reactors, VVER-440 and

VVER-1000. Both welds were made using the submerged-arc process. The VVER-440 weld, designated Weld 502, was made by weld wire Sv-10KhMFT with flux AN-42M. It is characterized by low nickel and high phosphorus contents (<0.20 and ~0.030%, respectively), typical for older VVER-440 vessel welds. The weld was heat treated at 675°C for 34 h. The VVER-1000 weld, designated Weld 260, was made by weld wire Sv-12Kh2N2MAA with flux FTs-16. The VVER-1000 materials, including the Weld 260, have low copper and phosphorus contents (<0.10 and <0.012%, respectively). Weld 260 is also characterized by high nickel content (1.64%), which is typical for old VVER-1000 vessel welds. The weld was heat treated at 620°C for 17.5 h, furnace cooled, then heat treated at 640°C for 9.5 h.

Test Procedures

The test program concentrated on comparison of changes in Charpy impact properties due to irradiation and annealing. RRC-KI performed tests using the RKP-300 pendulum-type Amsler impact testing machine. A ISO-type instrumented striker with a 2-mm radius was used for tests at RRC-KI. Charpy tests at ORNL were conducted in accordance with ASTM Standard E-23, using an 8-mm radius instrumented striker.

Additionally, ORNL performed a limited number of tensile and static fracture toughness tests. Round tensile specimens with a gage section 4.52 mm in diameter and 31.75 mm in length were tested, while compact and PCVN specimens were used for fracture toughness characterization of irradiated and annealed material.

Analysis of Charpy Data

Charpy absorbed energy data of the four materials studied in the unirradiated condition are presented in Figure 1(a) through (d). Charpy data from both laboratories are in good agreement, despite the difference in the strikers used.

ORNL has been involved in a number of cross-comparison Charpy testing exercises with 2- and 8-mm radii instrumented strikers (including one with RRC-KI) and summarized the comparison results [4]. The overall results have showed generally good agreement in absorbed energy measurements by the two strikers in the energy range below 200 J. The current data are consistent with that observation. Therefore, the unirradiated data from the two laboratories for each material in this study were combined and these results [shown in Fig. 1(a) through (d)] were used as the reference Charpy data set for each material. Charpy data for each material/condition were fit to the hyperbolic tangent function:

$$E = \frac{USE + LSE}{2} + \frac{USE - LSE}{2} \times \tanh\left(\frac{T - T_{TM}}{C}\right), \quad \textbf{(1)}$$

where E is absorbed energy, lateral expansion, or shear fracture; US and LS are upper- and lower-shelf values of E; T_{MT} is the temperature at the middle of the transition range; and C is the slope of the curve in the transition range at T_{MT}. Fitting was performed with

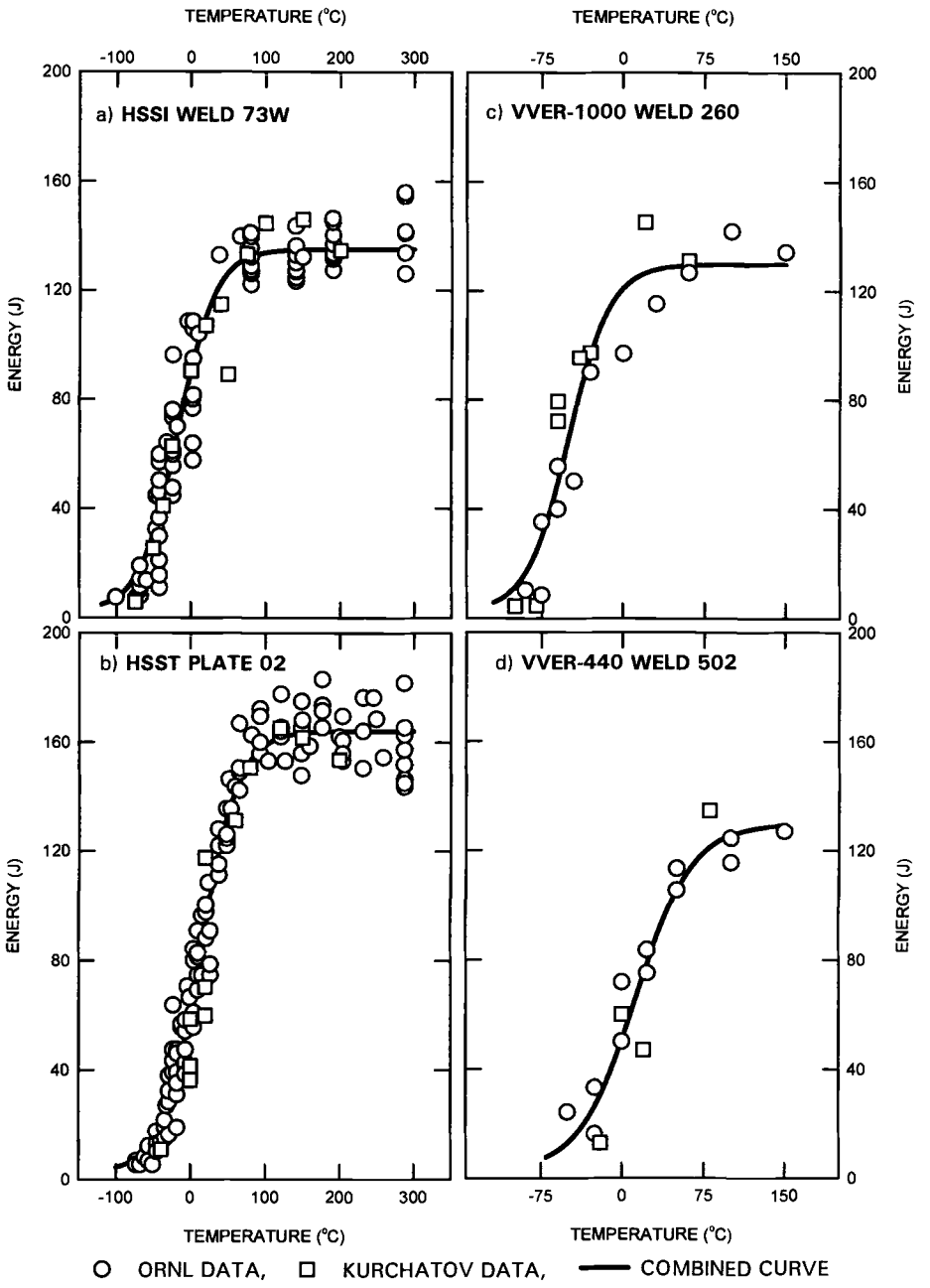


Fig. 1. Charpy data from materials studied in the unirradiated condition tested at ORNL and RRC-KI. Solid line is the best fit to combined data using a hyperbolic tangent function.

LSE fixed at 2.7 J for energy, 0.061 mm for lateral expansion, and 0% for shear, respectively [2]. Additionally, the upper-shelf value for shear was fixed at 100%.

The transition temperature is the main parameter derived from the Charpy tests. It defines a temperature which corresponds to a certain level of energy, lateral expansion, or shear. This level is accepted to be 0.9 mm for lateral expansion and 50% for shear according to the current practices in both countries. However, the radiation-induced transition temperature shift is measured at the level of 41 J in the U.S., while it is measured at 47 J in Russia. Indexing at 41 or 47 J reflects a difference of a historical practice rather than a technical one. The 41-J level corresponds to 30 ft-lb, while 47 J corresponds to 6 kgf·m/cm^2, commonly used indices in the United States and Russia, respectively. But practically, they are from about the same neighborhood in the transition range for RPV materials. In order to provide data according to the relevant national practice, the shifts of transition temperature due to irradiation or annealing will be reported as measured at 47 J for Russian welds, and at 41 J for the U.S. steels, regardless of the test laboratory.

Irradiation Conditions

The ORNL experiments with the VVER welds included irradiation to about 1×10^{19} n/cm^2 (>1 MeV) in the University of Michigan Ford Reactor, while the RRC-KI experiments with the U.S. materials included irradiations from about 2 to 18×10^{19} n/cm^2 (>1 MeV) in Unit 5 of the Novo-Voronezh Nuclear Power Plant (NVNPP-5), a VVER-1000 type reactor. In both cases, irradiations were conducted at ~290°C. Additionally, Charpy and tensile specimens of Weld 502 were irradiated by ORNL at 275°C, a temperature which is closer to the operating temperature (270°C) of VVER-440 reactor vessels.

Besides the differences between U.S. and Russian practices in indexing absorbed energy for determination of the transition temperature, there is also a difference in the measures of neutron fluence used. In the United States, neutron fluence for RPVs is measured for neutrons having energies greater than 1 MeV, while in Russia it is for neutrons having energies greater than 0.5 MeV. Thus, the values of neutron fluence for U.S. and Russian materials in this paper will be reported for neutrons with energies greater than 1.0 and 0.5 MeV, respectively, regardless of the source of irradiation. However, because the dosimetric procedures for each source were performed in the standard manner, estimates for adjustment must be determined. To determine the neutron irradiation exposure parameters, each country uses a neutron spectrum adjustment procedure that combines transport calculations of the neutron field and measurements using neutron monitors from irradiation capsules. The values of neutron fluence with >0.5 MeV for Russian welds irradiated by ORNL as well as the values of neutron fluence with >1 MeV for American steels irradiated by the RRC-KI given in this paper should be considered as the best currently available estimates. ORNL made this estimate by using a ratio, of flux of neutrons with >0.5 MeV to those with >1 MeV, equal to 1.76 for the capsule irradiated in the Ford Reactor, while RRC-KI used a ratio of 2.11 for their capsules irradiated in NVNPP-5.

Table 1 - Chemical Composition of Materials Used in the Annealing and Reirradiation Studies

Material	Composition (wt %)								
	C	Mn	P	S	Cr	Ni	Mo	Cu	V
HSST Plate 02	0.23	1.55	0.009	0.014	0.04	0.67	0.53	0.14	0.003
HSSI Weld 73W	0.098	1.56	0.005	0.005	0.25	0.60	0.58	0.31	0.003
Weld 502 (VVER-440)	0.03	1.16	0.030	0.013	1.60	0.12	0.48	0.15	0.24
Weld 260 (VVER-1000)	0.08	0.85	0.009	0.015	1.83	1.64	0.61	0.07	—

Table 2 - Mechanical Properties of Materials Studied in the Unirradiated Condition

Material	Transition temperature (°C)				USE (J)	Room temperature tensile strength (MPa)	
	at 41 J	at 47 J	at 0.9 mm	at 50%		Yield	Ultimate
Plate 02	-14	NA	-1	27	164	467	622
Weld 73W	-39	NA	-27	-15	135	494	604
Weld 502 (VVER-440)	NA	-3	2	20	130	437	546
Weld 260 (VVER-1000)	NA	-62	-51	-39	130	490	583

Table 3 - Fitting Coefficient (A) Compared with Chemistry Factor (CF) from RG 1.99 for U.S. Materials and Embritttlement Coefficient (A_F) from CS-86 for Russian Welds

Material	Composition (wt %)			(°C)		
	P	Cu	Ni	A	CF	A_F
Plate 02	0.009	0.14	0.67	65.6	56	NA
Weld 73W	0.005	0.31	0.60	86.7	110	NA
Weld 502 (VVER-440)	0.030	0.15	0.12	16.6	NA	32.4
Weld 260 (VVER-1000)	0.009	0.07	1.64	22.0	NA	20

Irradiation and Annealing Results

Results from the primary irradiation experiments with HSST Plate 02 and HSSI Weld 73W performed by ORNL were previously published [3,5,6]. Fracture toughness characterization of these steels has been also performed in these studies. Recently, cleavage fracture toughness data (K_{Jc}) for these steels were reevaluated using the master curve analysis procedure [7]. The procedure applies a statistical distribution function to characterize scatter of fracture toughness in the transition range and weakest-link theory to account for size effects, see Ref. [7] for details. It introduces the reference fracture toughness temperature, T_{100}, as a temperature at which the median fracture toughness equals 100 MPa·m$^{1/2}$. The shift of T_{100} is used in the present work to characterize effects of irradiation and/or annealing on cleavage fracture toughness. In the present study, PCVN specimens of VVER-440 Weld 502 were tested in three-point bending by ORNL to provide fracture toughness characterization of this weld in the unirradiated, irradiated, and irradiated/annealed conditions.

Irradiation and annealing results are summarized in Fig. 2(a) through (d) for both the U.S. and Russian steels. The materials studied were irradiated to a wide range of neutron fluences. In general, the irradiation and annealing experiments conducted by RRC-KI and ORNL show reasonable agreement. Two different fitting functions were used to represent the embrittlement path (I) for the materials studied. For Plate 02 and Weld 73W it is

$$\Delta TT = A \cdot F^{(0.28 - 0.1 \log F)} , \quad (2)$$

where ΔTT is the shift of Charpy energy at 41 J or fracture toughness at 100 MPa·m$^{1/2}$; F is neutron fluence in units of 10^{19} n/cm^2 (>1 MeV); and A is a fitting parameter. This fitting function has the same form and the same constants in the exponent as the one in U.S. Nuclear Regulatory Commission (NRC) *Regulatory Guide 1.99* (RG 1.99), Revision 2 [8]. For VVER-440 and VVER-1000 welds it is

$$\Delta TT = A \cdot F^{1/3} , \quad (3)$$

where F is neutron fluence in units of 10^{18} n/cm^2 (>0.5 MeV). This fitting function has the same form and the same constant in the exponent as the one in the Russian Standards (CS-86) [9].

The fitting parameters are compared with chemistry factors (CF) from RG 1.99 for Plate 02 and Weld 73W and embrittlement coefficients (A_F) from CS-86 for VVER-1000 Weld 260 in Table 3. Weld 502 represents the materials for the older generation of VVER-440 reactors which operate at 270°C and CS-86 provides the embrittlement coefficient calculation procedure for this irradiation temperature as well as for 250°C, but not for an irradiation temperature of 290°C. However, ORNL performed irradiation of this weld at 275°C in addition to irradiation at 290°C. This allowed for a possibility to

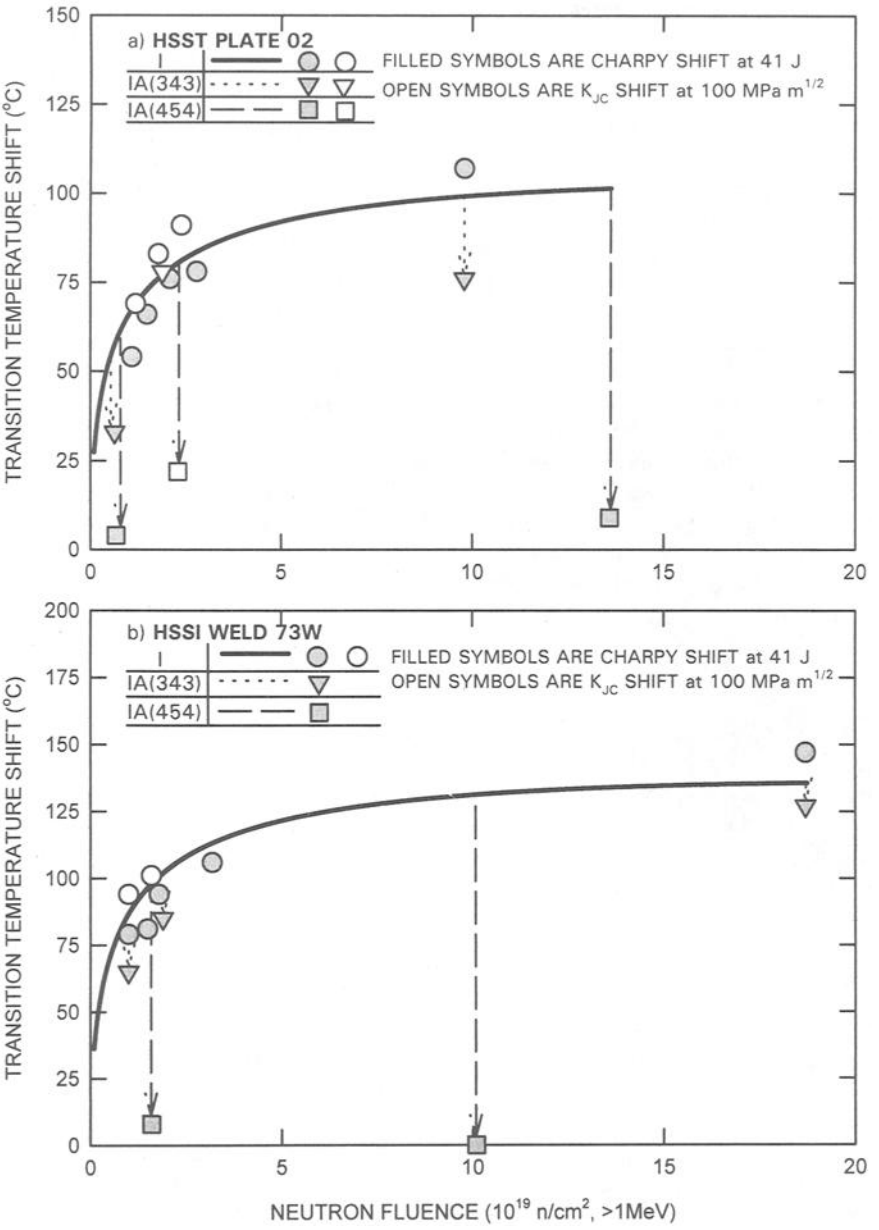


Fig. 2. Shift of the transition temperature due to irradiation and annealing.
(a) HSST Plate 02, (b) HSSI Weld 73W.

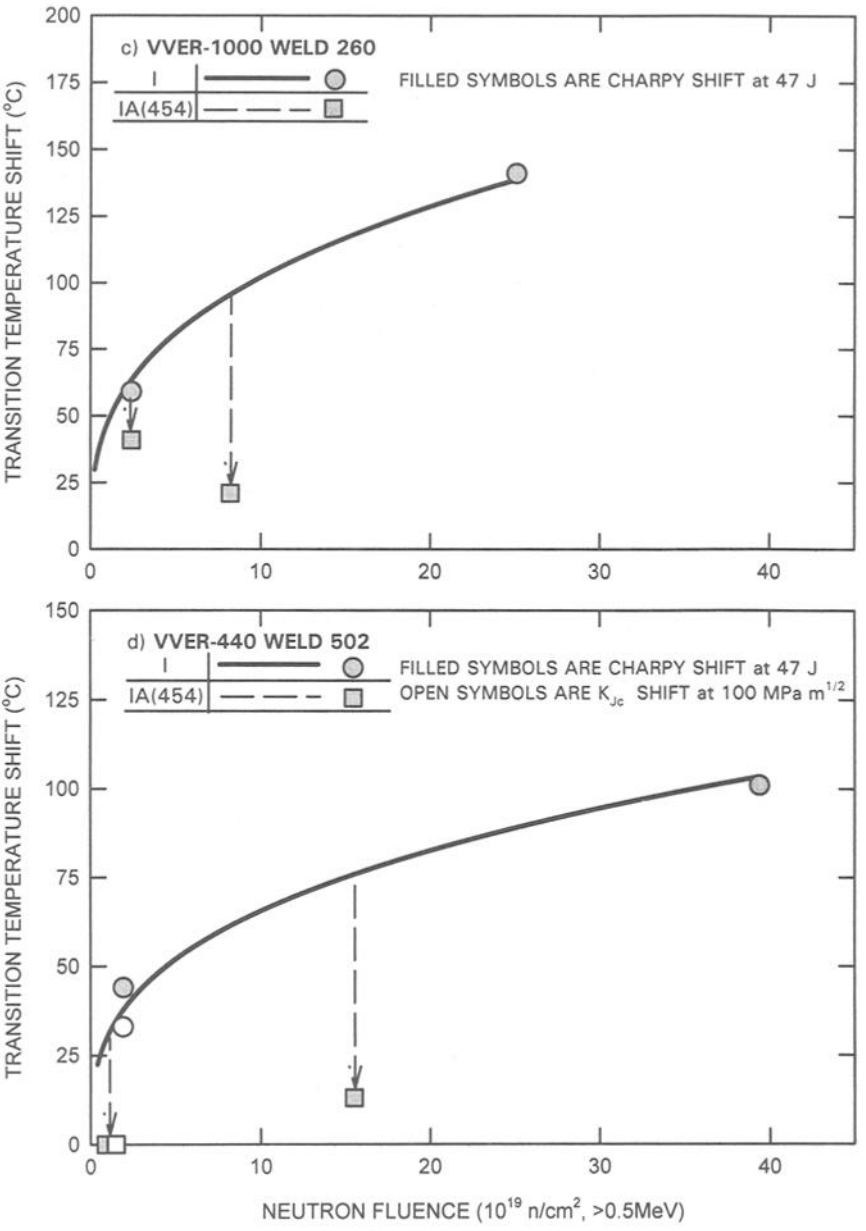


Fig. 2. Shift of the transition temperature due to irradiation and annealing.
(c) VVER-1000 Weld 260, (d) VVER-440 Weld 502.

compare A_F predicted from CS-86 to the one determined from the Charpy data irradiated at 275°C. These values of A_F for the Weld 502 are also presented in Table 3. Figure 3 shows the Charpy energy data for Weld 502 irradiated at two temperatures.

The data in Table 3 show that the CS-86 provides a very conservative value of A_F for the VVER-440 Weld 502 compared to the fitting coefficient from the present study. Contrary to that, however, the high-nickel VVER-1000 weld exhibited an embrittlement coefficient higher than that from the CS-86. That raises concerns regarding the ability of the current Russian practice to adequately predict the radiation embrittlement of high-nickel welds in VVER-1000 reactor vessels. For HSST Plate 02 and HSSI Weld 73W, the fitting coefficients are within 2 standard deviations of the mean CF parameters from RG 1.99.

A significant difference in the experiments is that those conducted by RRC-KI involved much higher neutron fluences than those conducted by ORNL. These results are extremely important for Plate 02 and Weld 73W in that they show neither material exhibits unexpected radiation sensitivity at very high fluences and, further, that both highly irradiated materials show nearly full recovery of Charpy toughness after annealing at 454°C.

ORNL also performed tensile tests of VVER-440 and VVER-1000 welds in the irradiated and annealed conditions. Tensile properties of Plate 02 and Weld 73W in the irradiated condition have been previously reported [2,5]. The radiation-induced changes in yield strength for the materials studied were compared to the shifts of Charpy transition temperature. The data are in very good agreement with the large Power Reactor Embrittlement Data Base (PR-EDB) maintained at ORNL for the NRC (Fig. 4).

Two annealing temperatures were involved in the present study. Annealing temperature 343°C was applied to Plate 02 and Weld 73W only, while all four materials were annealed at 454°C. In general, annealing at 454°C provides more complete recovery of the transition temperature than that at 343°C. The residual shift of transition temperature (the difference between transition temperatures of a material after annealing and in the unirradiated condition) increases with increase in neutron fluence for the 343°C annealing temperature.

It was noticed that fracture toughness shifts [Fig. 2(a) and (b)] are slightly higher than the Charpy shifts for Plate 02 and Weld 73W. Additionally, recovery of the fracture toughness shift seems to be less than the Charpy shift recovery at both annealing temperatures for Plate 02. The difference is relatively small. Contrarily, fracture toughness shifts for VVER-440 Weld 502 were slightly less than Charpy shifts and full recovery after annealing at 454°C was observed for both transition temperatures. Observed differences between Charpy and fracture toughness shifts are within the scatter reported in Refs. [10,11].

According to the present data, the annealing temperature of 454°C is high enough to provide nearly complete recoveries of the transition temperatures even after irradiation to very high fluences. Moreover, RRC-KI has reirradiated some Charpy specimens of Plate 02 and Weld 73W which were annealed at 454°C and then performed additional annealing of reirradiated specimens at 454°C (see the following section). Altogether, the data indicate very positive recovery of transition temperature after annealing at 454°C and that residual shift does not accumulate with neutron fluence or with cycling of irradiation

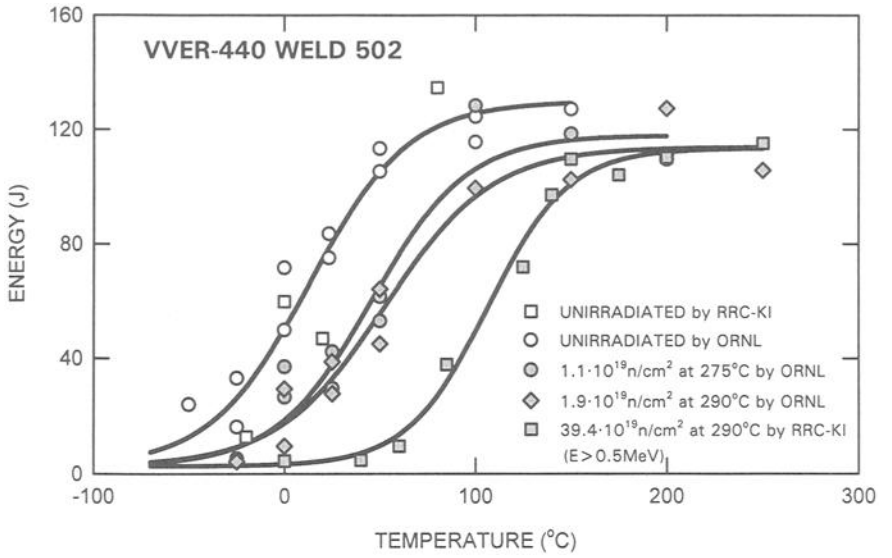


Fig. 3. ORNL and RRC-KI Charpy data of VVER-440 Weld 502 in the unirradiated condition and after irradiation at 275 and 290°C.

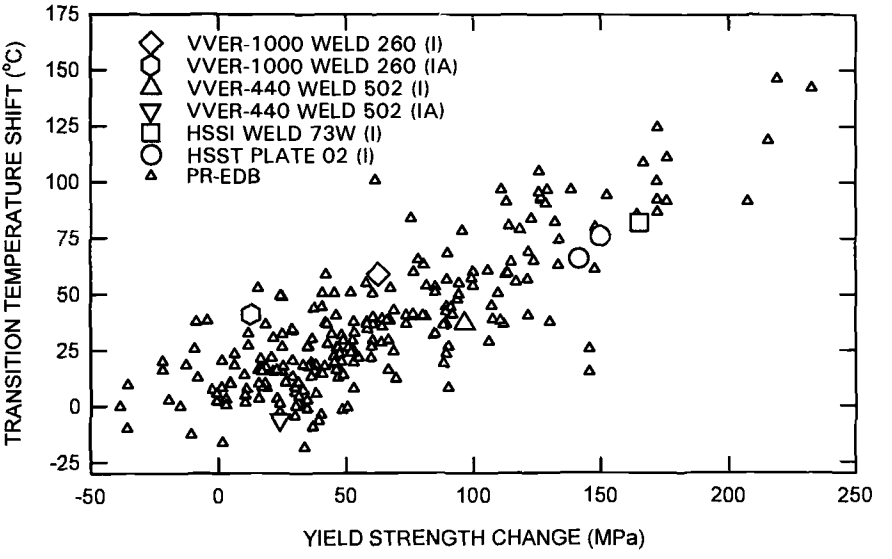


Fig. 4. Transition temperature shift versus change in yield strength for the materials studied by ORNL in comparison with PR-EDB data.

and annealing at 454°C. This observation is in a good agreement with earlier work on VVER-440 materials [12].

Recovery of the Charpy energy transition temperature was the primary objective in the present study. However, it was observed that other Charpy specimen measurements react differently on annealing at 454°C. Figures 5 through 8 present absorbed energy, lateral expansion, and percent shear data of specimens tested after annealing at 454°C for Plate 02 and Welds 73W, 502, and 260, respectively. Specimens were irradiated to different fluences, including those annealed after irradiation-annealing-reirradiation cycle. The data are plotted against the unirradiated curves to observe the degree of recovery after annealing. For each material in general, the annealed data tend to group into one data set regardless of irradiation and annealing history. Among the three Charpy toughness parameters, absorbed energy appears to recover the most, lateral expansion the least, and percent shear is somewhat in between in the transition region.

On the upper-shelf, energy values of all four materials rise above the unirradiated level after annealing, similarly to results reported in Refs. [10,13], while none of the materials exhibited complete recovery of lateral expansion. A limited number of unirradiated specimens of Plate 02 and Weld 502 were annealed at 454°C. Plate 02 specimens were tested on the upper-shelf only, while Weld 502 specimens were tested over a wide temperature range. For unirradiated/annealed specimens of Plate 02, the upper-shelf values of absorbed energy and lateral expansion are within scatter of the unirradiated values. Unirradiated/annealed specimens of Weld 502 showed slightly different behavior; the upper-shelf energy increased to the same level shown by the irradiated/annealed specimens, while lateral expansion did not change as a result of annealing.

The need for direct fracture toughness measurements is critical, especially in light of the present results where different Charpy parameters showed mixed response to annealing.

Reirradiation Results

RRC-KI also performed reirradiation of Charpy specimens of Plate 02 and Weld 73W which had been irradiated and annealed at 454°C. Moreover, some of the reirradiated specimens were subjected to additional post-reirradiation annealing at 454°C. The data are summarized in Fig. 9. The solid line represents the embrittlement path (I) as shown earlier in Fig. 2. Specimens of both materials were initially irradiated to about 2.1×10^{19} n/cm^2 (>1 MeV), then annealed at 454°C for 72 h (dashed line in Fig. 9). After annealing (IA), specimens were loaded back into NVNPP-5 reactor for reirradiation. The total neutron fluence was about 4.7×10^{19} n/cm^2 (>1 MeV) for Plate 02 and about 5.0×10^{19} n/cm^2 for Weld 73W. The measured shifts of transition temperature following reirradiation (IAR) were compared to those predicted by NRC *Regulatory Guide 1.162* (RG 1.162) [14]. According to this guide, the reembrittlement path can be predicted by the scheme of lateral shift (dotted lines in Fig. 9). The present data show that experimentally measured shifts of transition temperature after reirradiation are well below primary embrittlement path proving benefits of annealing for RPV steels. Even the lateral shift approach provides conservative predictions of the transition temperature shifts after

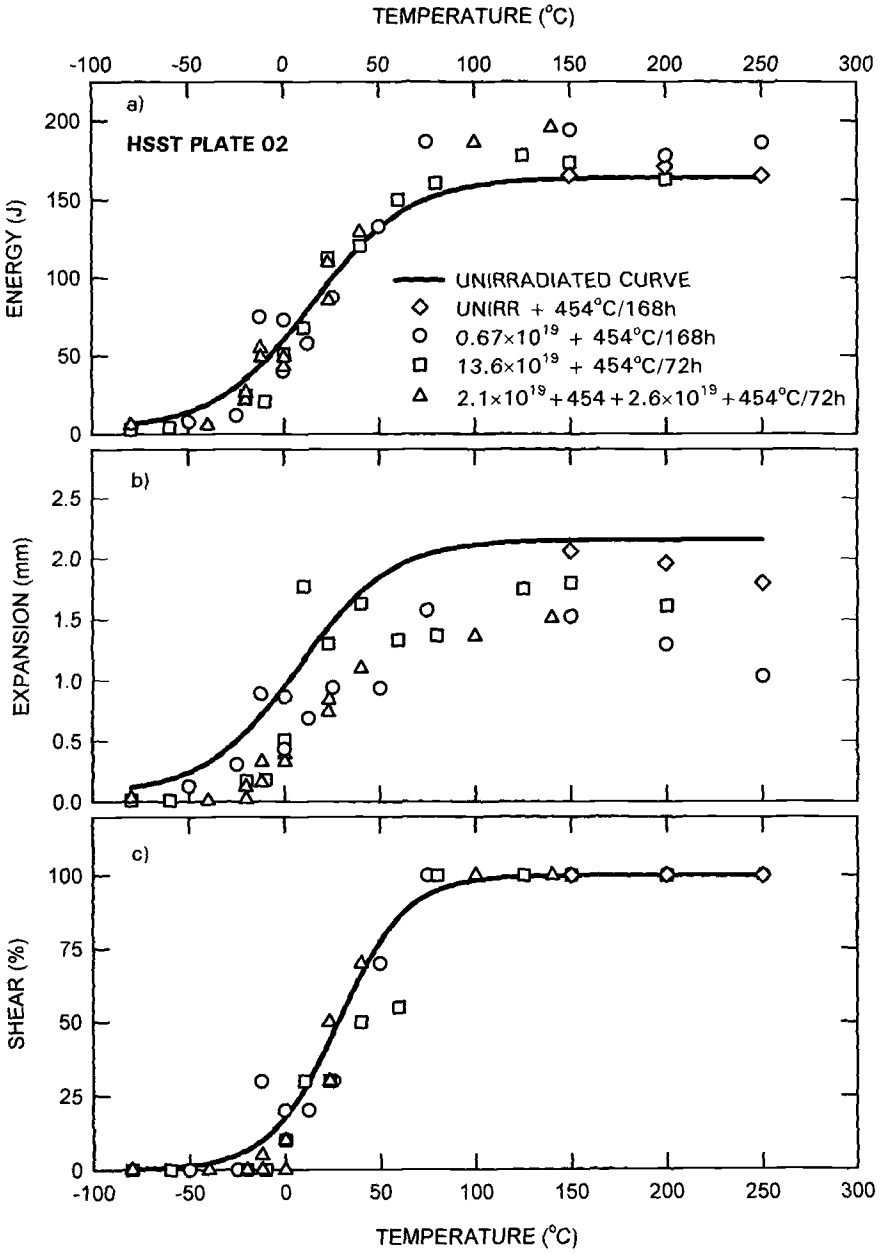


Fig. 5. Charpy data of Plate 02 in the annealed condition compared with the combined unirradiated curves. The legends in (a) apply to all three plots.

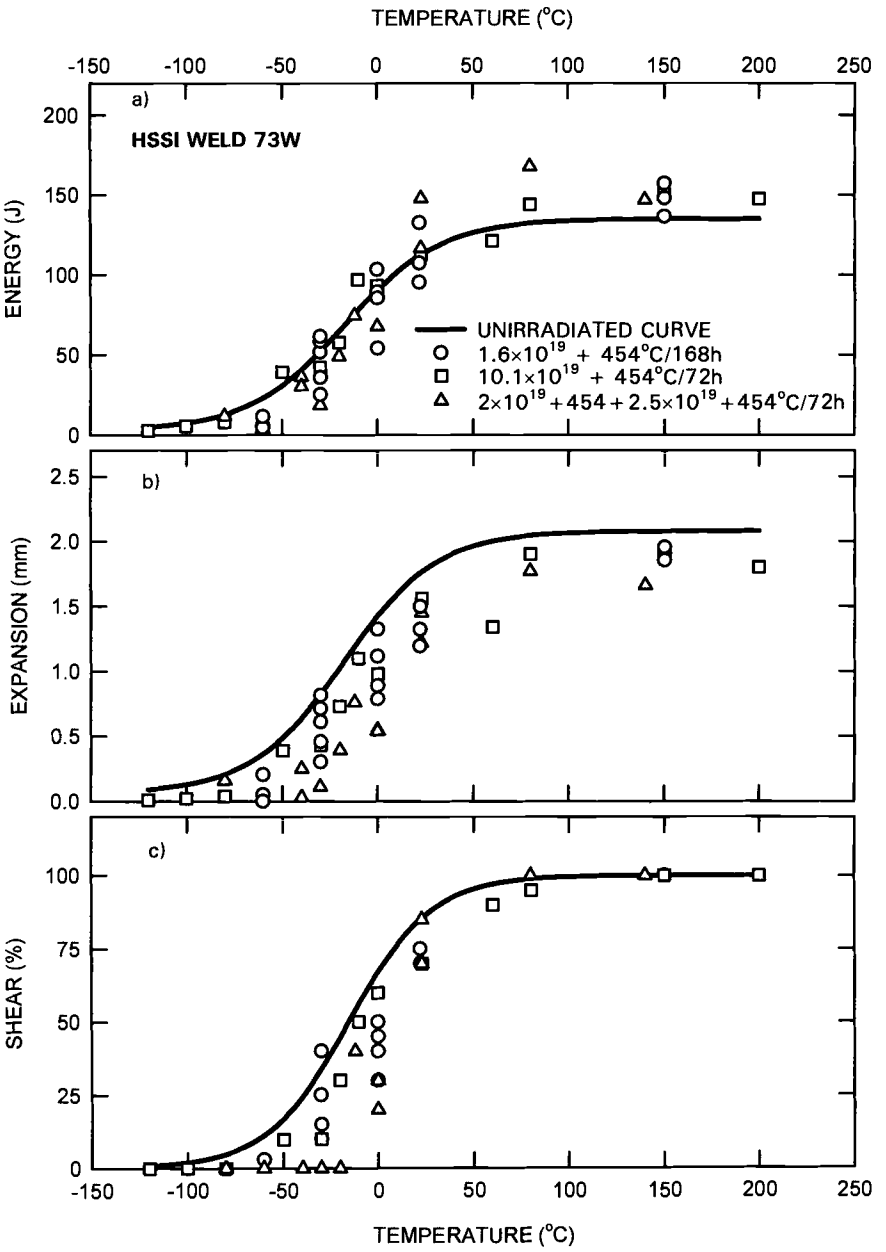


Fig. 6. Charpy data of Weld 73W in the annealed conditions compared with the combined unirradiated curves. The legends in (a) apply to all three plots.

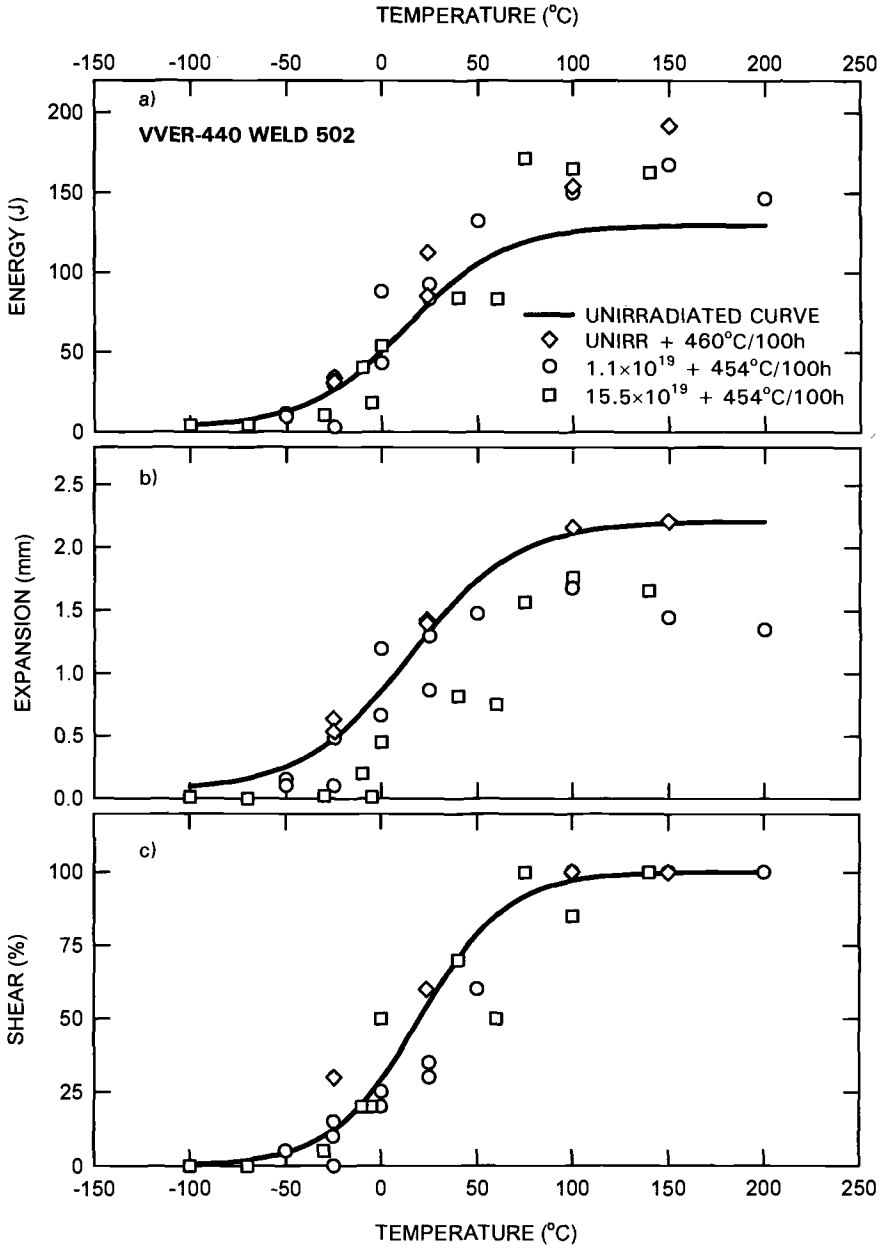


Fig. 7. Charpy data of Weld 502 in the annealed conditions compared with the combined unirradiated curves. The legends in (a) apply to all three plots.

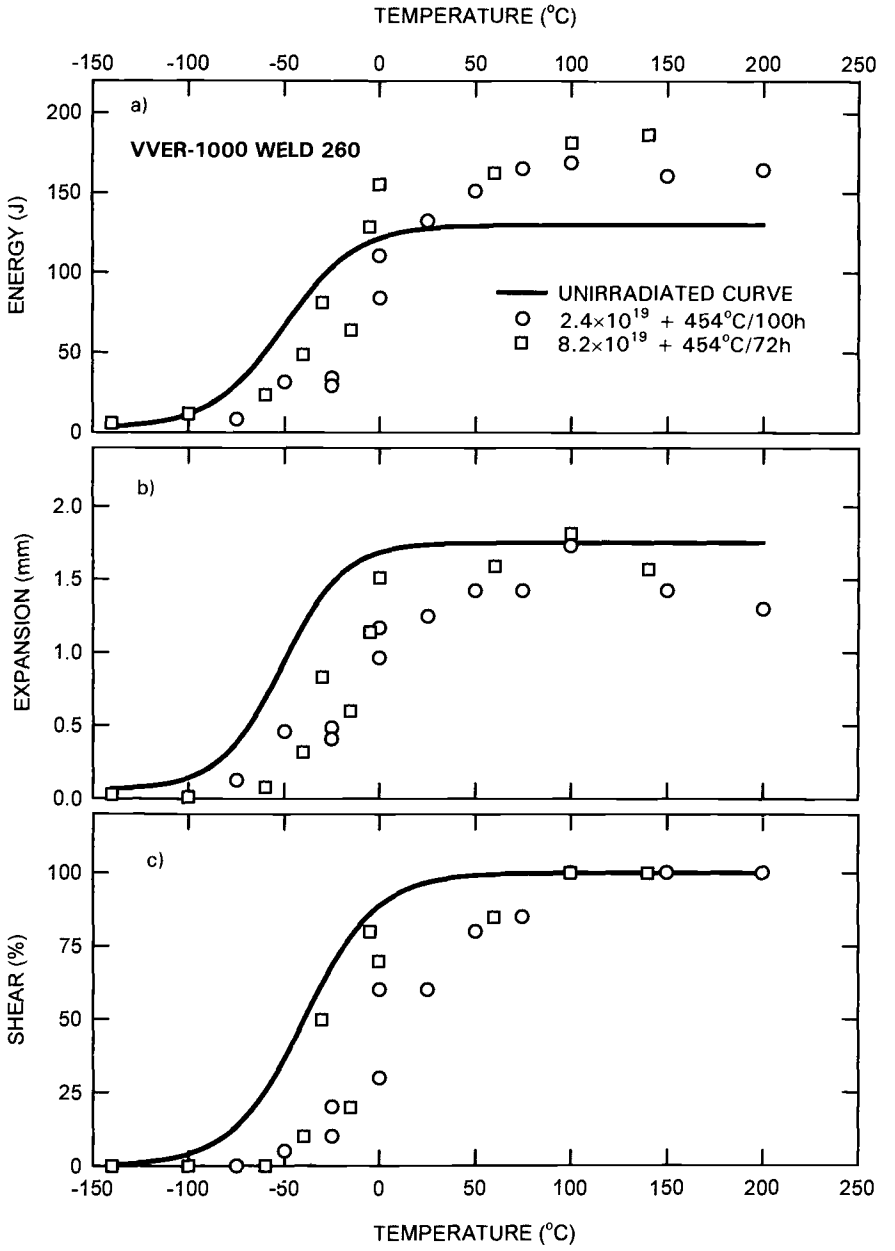


Fig. 8. Charpy data of Weld 260 in the annealed conditions compare with the combined unirradiated curves. The legends in (a) apply to all three plots.

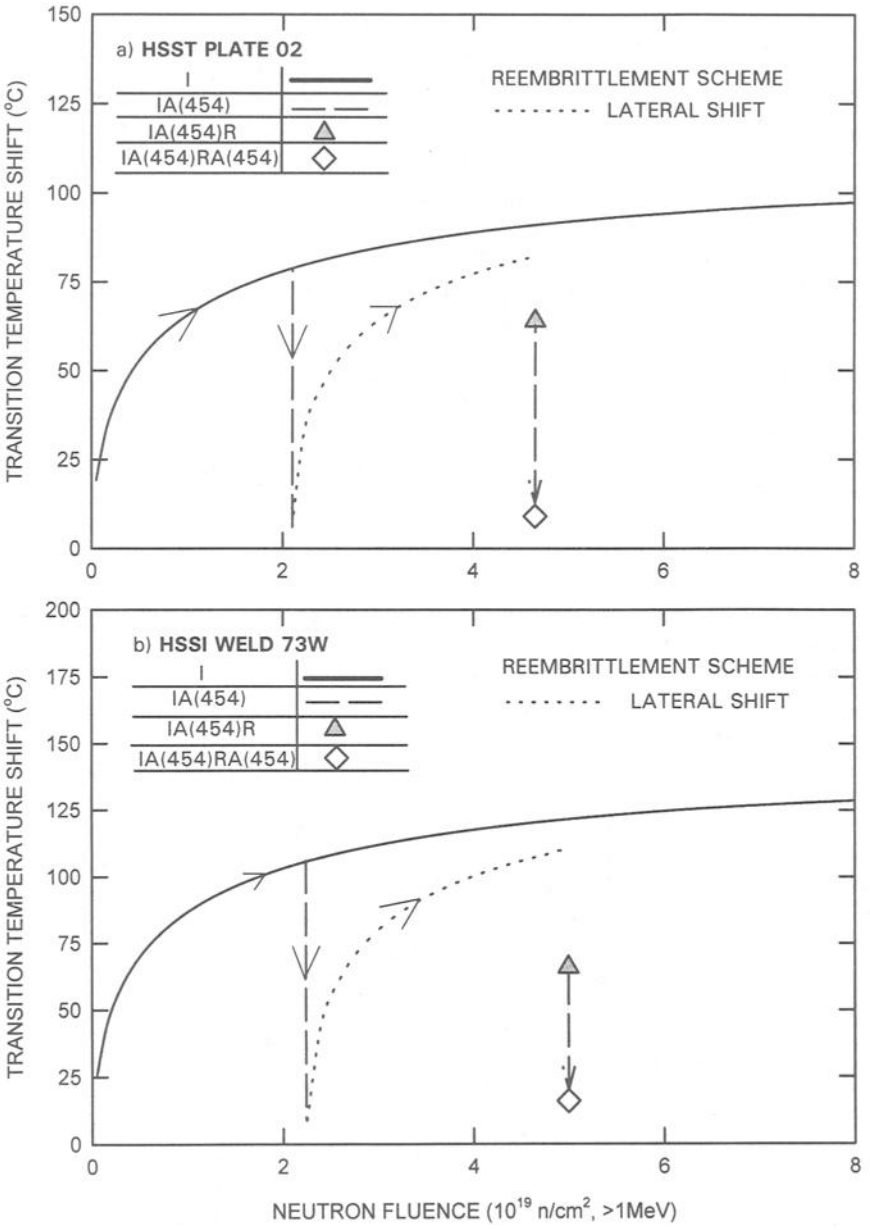


Fig. 9. Reirradiation data of (a) HSST Plate 02 and (b) HSSI Weld 73W.

reirradiation. Reirradiation data for Weld 73W are in agreement with a prediction made in Ref. [15] based on a small-angle neutron scattering (SANS) study of this weld in the irradiated and irradiated/annealed conditions. SANS measurements showed a large number of very fine copper-rich precipitates in this weld. A simple correlation between Charpy shifts and square root of volume fraction of these precipitates was shown in that study. Annealing at 454°C results in a significant drop of number density and volume fraction of precipitates, which corresponds well with recovery of Charpy transition temperature. However, it was found that, in addition to a decrease in number density and volume fraction, annealing results in a radius increase of these precipitates. Thus, annealing coarsens the copper-rich precipitates. As a result of these observations, it was concluded that the irradiated/annealed weld had less copper in solution that before irradiation; therefore, the reembrittlement rate of this weld should be less that it was in the primary irradiation cycle. From a radiation sensitivity point of view, the irradiated/annealed weld is microstructurally different than it was before irradiation. The present results support these conclusions. Annealing of the reirradiated materials showed the same degree of transition temperature recoveries as those achieved for the first annealings [16].

Observations and Conclusions

1. Two U.S. steels, one plate of A 533 grade B class 1 and one submerged-arc weld (with Linde 0124 flux), and two Russian welds, one representative of older VVER-440 RPVs and the other representative of older VVER-1000 RPVs, were irradiated at a wide range of neutron fluences. All four materials were annealed following irradiation, while the U.S. steels were also reirradiated and annealed following reirradiation. The experiments with the U.S. steels were conducted in Russia and those for the Russian steels in the United States.

2. The ORNL and RRC-KI experiments showed generally good agreement for both the Russian and U.S. steels.

3. While transition temperature recovery following annealing of the Charpy 41-J transition temperature was substantial in all cases, significantly less recovery of the Charpy lateral expansion and percent shear fracture were observed. On the upper shelf, energy values of all four materials recovered to values above those of the unirradiated condition, while none of the materials exhibited complete recovery of lateral expansion.

4. Neither HSST Plate nor HSSI Weld 73W exhibited unexpected radiation sensitivity at very high neutron fluences; i.e., greater than 1×10^{20} n/cm^2 (>1 MeV); furthermore, both highly irradiated materials exhibit nearly full recovery of CVN transition temperature after thermal annealing at 454°C.

5. The reirradiation embrittlement rates for both HSST Plate 02 and HSSI Weld 73W are conservative relative to the "lateral shift" method for reembrittlement prediction.

Acknowledgments

This research is sponsored by the Division of Engineering Technology, Office of Nuclear Regulatory Research, U.S. Nuclear Regulatory Commission, under Interagency Agreement DOE 1886-N695-3W with the U.S. Department of Energy under Contract DE-AC05-96OR22464 with Lockheed Martin Energy Research Corporation.

References

[1] W. J. Stelzman, R. G. Berggren, and T. N. Jones, Jr., *ORNL Characterization of Heavy-Section Steel Technology Program Plates 01,02, and 03*, NUREG/CR-4092 (ORNL/TM-9491), Oak Ridge National Laboratory, Oak Ridge, Tenn., 1985.

[2] R. K. Nanstad, F. M. Haggag, D. E. McCabe, S. K. Iskander, K. O. Bowman, and B. H. Menke, *Irradiation Effects on Fracture Toughness of Two High-Copper Submerged-Arc Welds, HSSI Series 5*, NUREG/CR-5913, Vol. 1 (ORNL/TM-12156/V1), Oak Ridge National Laboratory, Oak Ridge, Tenn., 1992.

[3] R. K. Nanstad, D. E. McCabe, B. H. Menke, S. K. Iskander, and F. M. Haggag, "Effects of Radiation on K_{Ic} Curves for High Copper Welds," pp. 214-233 in *Effects of Radiation on Materials: 14th International Symposium, ASTM STP 1046*, N. H. Packan, R. E. Stoller, and A. S. Kumar, Eds., American Society for Testing and Materials, Philadelphia, 1990.

[4] R. K. Nanstad and M. A. Sokolov, "Charpy Impact Test Results on Five Materials and NIST Verification Specimens Using Instrumented 2-mm and 8-mm Strikers," pp. 111-139 in *Pendulum Impact Machines: Procedures and Specimens for Verification, ASTM STP 1248*, T. A. Siewert and A. K. Schmieder, Eds., American Society for Testing and Materials, Philadelphia, 1995.

[5] R. G. Berggren, J. R. Hawthorne, and R. K. Nanstad, "Analysis of Charpy V-Notch Impact Toughness of Irradiated A533-B Class 1 Plate and Four Submerged-Arc Welds," pp. 1094-1110 in *Effects of Radiation on Materials: 12th International Symposium, ASTM STP 870*, F. A. Garner and J. S. Perrin, Eds., American Society for Testing and Materials, Philadelphia, 1985.

[6] B. H. Menke, J. J. McGowan, R. G. Berggren, R. K. Nanstad, and K. C. Miller, "Effects of Neutron Irradiation on Fracture Toughness of A533-B Class 1 Plate and Four Submerged-Arc Welds," pp. 1111-1130 in *Effects of Radiation on Materials: 12th International Symposium, ASTM STP 870*, F. A. Garner and J. S. Perrin, Eds., American Society for Testing and Materials, Philadelphia, 1985.

[7] M. A. Sokolov and D. E. McCabe, *Comparison of Irradiation-Induced Shifts of K_{Jc} and Charpy Curves: Analysis of Heavy-Section Steel Irradiation Program Data*, ORNL/NRC/LTR-95/4, Oak Ridge National Laboratory, Oak Ridge, Tenn., 1995.

[8] *Regulatory Guide 1.99*, "Radiation Embrittlement of Reactor Vessel Materials," Revision 2, U.S. Nuclear Regulatory Commission, Washington, D.C., May 1988.

[9] *Calculation Standards for Strength of Equipment and Pipes of Nuclear Power Units*, PNAE-G-002-86, Energoatomizdat, NGA-01-85-1, NIKIET (in Russian), 1989.

[10] M. A. Sokolov, D. E. McCabe, S. K. Iskander, and R. K. Nanstad, "Comparison of Fracture Toughness and Charpy Impact Properties Recovery by Thermal Annealing of Irradiated Reactor Pressure Vessel Steels," pp. 771-781 in *7th International Symposium on Environmental Degradation of Materials in Nuclear Power Systems - Water Reactors*, Vol. 2, American Nuclear Society, La Grange Park, Ill., 1995.

[11] M. A. Sokolov and R. K. Nanstad, "Comparison of Irradiation-Induced Shifts of K_{Jc} and Charpy Impact Toughness for Reactor Pressure Vessel Steels," pp. 167-190 in *Effects of Radiation on Materials, 18th International Symposium, ASTM STP 1325*, R. K. Nanstad, M. L. Hamilton, F. A. Garner, and A. S. Kumar, Eds., American Society for Testing and Materials, West Conshohocken, Pa., 1999.

[12] A. D. Amayev, A. M. Kryukov, and M. A. Sokolov, "Recovery of the Transition Temperature of Irradiated WWER-440 Vessel Metal by Annealing," pp. 369-379 in *Radiation Embrittlement of Nuclear Reactor Pressure Vessel Steels: An International Review (Fourth Volume), ASTM STP 1170*, L. E. Steele, Ed., American Society for Testing and Materials, Philadelphia, 1993.

[13] S. K. Iskander, M. A. Sokolov, and R. K. Nanstad, "Effects of Annealing Time on the Recovery of Charpy V-Notch Properties of Irradiated High-Copper Weld Metal," pp. 277-293 in *Effects of Radiation on Materials: 17th International Symposium, ASTM STP 1270*, D. S. Gelles, R. K. Nanstad, A. S. Kumar, and E. A. Little, Eds., American Society for Testing and Materials, Philadelphia, 1996.

[14] *Regulatory Guide 1.162*, "Format and Content of Report for Thermal Annealing of Reactor Pressure Vessels," U.S. Nuclear Regulatory Commission, February 1996.

[15] M. A. Sokolov, S. Spooner, G. R. Odette, B. D. Wirth, and G. E. Lucas, "SANS Study of High-Copper RPV Welds in Irradiated and Annealed Conditions," pp. 333-345 in *Effects of Radiation on Materials, 18th International Symposium, ASTM STP 1325*, R. K. Nanstad, M. L. Hamilton, F. A. Garner, and A. S. Kumar, Eds., American Society for Testing and Materials, West Conshohocken, Pa., 1999.

[16] A. A. Chernobaeva, M. A. Sokolov, R. K. Nanstad, A. M. Kryukov, Y. A. Nikolaev, and Yu. N. Korolev, "Exploratory Study of Irradiation, Annealing, and Reirradiation Effects on American and Russian Reactor Pressure Vessel Steels," pp. 871-882 in *Proceedings of the Eighth International Symposium on Environmental Degradation of Materials in Nuclear Power Systems - Water Reactors, August 10-14, 1997, Amelia Island, Florida*, American Nuclear Society, La Grange Park, Ill., 1997.

Philippe Pareige,[1] Pierre Auger,[1] Stephen Welzel,[1,2] Jean-Claude Van Duysen,[3] and Salem Miloudi[3]

Annealing of a Low Copper Steel: Hardness, SANS, Atom Probe, and Thermoelectric Power Investigations

Reference: Pareige, P., Auger, P., Welzel, S., Van Duysen, J.-C., and Miloudi, S., **"Annealing of a Low Copper Steel: Hardness, SANS, Atom Probe, and Thermoelectric Power Investigations,"** *Effects of Radiation on Materials: 19th International Symposium, ASTM STP 1366,* M. L. Hamilton, A. S. Kumar, S. T. Rosinski, and M. L. Grossbeck, Eds., American Society for Testing and Materials, West Conshohocken, PA, 2000.

Abstract: The evolution of the microstructure of the French Chooz A pressure vessel steel (characterized by a low copper content (<0.1 at.% Cu)) has been studied during annealing at 450°C. The irradiated material (fluence: 0.5 to 16×10^{23} $n.m^{-2}$, flux : 2×10^{15} $n.m^{-2}.s^{-1}$, temperature : 275°C) shows a quick recovery of hardness after 20 h of aging. The intensity of the SANS scattered signal as well, as the thermoelectric power one, decreases with annealing time. In addition, 3D images, at the atomic scale, given by the Tomographic Atom Probe show that during the first hours of annealing, the neutron-induced Cu-Ni-Mn-Si clusters formed during the in-service irradiation are "dissolved" while copper precipitates are formed. Their low number density is in agreement with the full recovery of the hardness.

These results are of primary importance for prediction of recovery of an irradiation embrittled steel and also for prediction of its behavior during reirradiation. This work also shows that the nondestructive technique, thermoelectric power, may be used to "follow" the microstructural evolution of materials during annealing treatments.

Keywords: low copper steel, neutron irradiation, annealing, recovery, hardness, SANS, 3D atom probe, thermoelectric power, nondestructive technique

[1]Groupe de Métallurgie Physique, UMR CNRS-6634, Université et INSA de Rouen, 76821 Mont Saint Aignan, France.

[2]Now at Hahn-Meitner-Institut Berlin GmbH, Glienickerstrasse 100, D-14109 Berlin , Germany.

[3]EDF, Département EMA "Les Renardières", 77250 Moret sur Loing, France.

Copyright© 2000 by ASTM International www.astm.org

Introduction

Thermal annealing treatments at low temperature (343 to 454°C) have been identified as a suitable means to recover mechanical properties of embrittled neutron-irradiated nuclear reactor pressure vessels [*1 -8*].

Although the mechanical properties of these annealed materials are relatively well-known, little information is available as far as microstructural changes are concerned. Nevertheless, this information is of primary importance in order to predict and to understand the evolution of the mechanical properties (and of course the microstructure) after reirradiation under service conditions. Characterization of the microstructure of irradiated and annealed high copper welds (0.2 to 0.3 at.% Cu) may be found in the literature [*9-10*]. It appears that embrittlement is reduced by coarsening the neutron-induced copper-enriched precipitates. In this work, a microstructural characterization of a low copper (<0.1at.% Cu) forging irradiated and annealed material is presented. The small amount of as-irradiated materials (broken Charpy specimens) does not allow standard mechanical tests to be performed. This is the reason why hardness measurements were chosen to follow the mechanical behavior of materials during annealing heat treatments. Two different but complementary techniques, namely Small Angle Neutron Scattering (SANS) and Atom-Probe (conventional Atom-Probe (AP) and Three Dimensional Atom-Probe (3DAP)), were used to follow the evolution of the microstructures. In addition, a nondestructive technique, the Thermo-Electric Power (TEP), was also applied and results were directly compared with those of previous techniques.

In the first part, we describe the low copper forging material from the Chooz A nuclear reactor pressure vessel in the as-received and as-irradiated states. A brief description of each of the technique used is given in the second part. The third part is dedicated to Hardness, SANS and AP results, which are described and compared with TEP measurements in a last paragraph.

Material

The investigated material was the C core shell metal of the Chooz A reactor, whose chemical composition is described in Table 1. The concentration of highly embrittling elements (Cu=0.09wt.%, Ni=0.57wt.% and P=0.012wt.%) is rather low. The samples were taken from irradiated Charpy V notch impact specimens tested in the EDF surveillance program.

Table 1 – *Nominal Composition of the Pressure Vessel C Shell Material*

Elt	C	S	P	Si	Cr	Mo	Mn	Ni	V	Al	Co	Cu	Fe
at.%	0.74	0.009	0.021	0.63	0.17	0.22	1.26	0.53	0.021	0.049	0.018	0.078	Bal.
wt.%	0.16	0.006	0.012	0.32	0.16	0.39	1.26	0.57	0.02	0.024	0.02	0.09	Bal.

All Charpy V specimens have been machined from a overlength of the C shell after the

following heat treatments: 1h at 910°C, water quench, then 4 h at 660 – 670°C and at least 28 h at 600°C. The neutron flux on the irradiated specimens was about 3.4×10^{14} $n.m^{-2}$ s^{-1} (E > 1 MeV); the irradiation temperature was 265°C. The steel contains a mixture of ferrite and bainite. In some areas, the structure is entirely bainitic while others contain about 60% bainite and 40% ferrite.

The microstructure of this material after different neutron irradiations, up to fluence of 16×10^{23} $n.m^{-2}$ (E > 1MeV), has been clearly characterized in previous works [*11-14*].

Though the concentrations of reputed embrittling residual elements are rather low the increase in the Charpy transition temperature reaches 145°C for a fluence close to 10^{24} $n.m^{-2}$. Both conventional and Tomographic Atom Probes as well as SANS experiments clearly indicate that, in the case of this low copper steel (< 0.1wt%), neutron irradiation induces the formation of solute clusters containing Si (3 at.%), Ni (4 at.%), Mn (5 at.%) and Cu (1 at.%) in the ferritic matrix. The size and the composition of these solute enrichments do not change with increasing fluences. In contrast, their number density increases with fluence.

The annealing heat treatments (2, 20 and 100h at 450°C) were performed on materials irradiated under different neutron fluences. Table 2 summarized those neutron irradiation conditions and annealing times for specimens prepared for the four techniques.

Table 2 – *Initial Neutron Fluences and Annealing Times (at 450°C) of the Studied Materials Prepared for Hardness, SANS, Atom-Probe and TEP Techniques. Corresponding dpa Values are Reported*

Hardness (500g) (Annealing time: 2, 20 and 100 h at 450°C)					
Fluence, 10^{23} $n.m^{-2}$	0.5	4	9.7	12	15.8
dpa (10^{-2})	0.7	5.4	14	16.5	23.4
+ *hardness measurements on a thermally aged unirradiated specimen: 500 h at 455°C*					
SANS (Annealing time: 2 – 20 – 100 h at 450°C)					
Fluence, 10^{23} $n.m^{-2}$	15.8				
dpa (10^{-2})	22.8				
Tomographic Atom Probe (Annealing time: 2 and 100 h at 450°C)					
Fluence, 10^{23} $n.m^{-2}$	12				
dpa (10^{-2})	16.5				
Thermo Electric Power (Annealing time: 2, 20 and 100 h at 450°C)					
Fluence, 10^{23} $n.m^{-2}$	0.4	3	8	15	
dpa (10^{-2})	0.6	4	11	21	
+ *TEP measurements on a thermally aged unirradiated specimen: 500 h at 455°C*					

Techniques

In order to follow the evolution of the microstructure during the annealing treatments, hardness measurements associated to AP, TAP and SANS experiments were performed. In addition, investigations with TEP were also performed in order to test the sensitivity of this non destruction technique to the microstructural evolution.

SANS experiments have been performed at the Institut Laue Langevin (Grenoble – France). Measurements were made at room temperature with 0.8 nm wave length neutrons. These experiments have been carried out with an applied magnetic field (H = 1.4 T). A two dimensional position sensitive detector allowed to cover a scattering vector ($\vec{q}$) from 0.17 to 1.3 nm^{-1}. Absolute scattering cross-sections $d\sigma / d\Omega$ were obtained by calibration with a water standard.

Due to both high spatial and mass resolutions, the atom probe is recognized as one of the most suited tools to characterize the early stages of phase separation occurring in metallic alloys [*15*]. Two different configurations of the instrument have been used in this study. An Energy Compensated Atom Probe (ECAP) [*16*], having a high mass resolution ($m / \Delta m = 2000$) was used. The result of an ECAP analysis is a linear concentration profile with a lateral resolution kept constant to 1.5 nm. The depth resolution is strictly one atomic layer and the probed depth for a specimen is about 0.7 μm representing about 6×10^4 ions individually collected. The high mass resolution is necessary to identify unambiguously all chemical species, particularly Ni, Mo and Cu ions, of which are observed in mass spectra with mass to charge ratio difference of 1/6 of an atomic mass unit. Because of the mono-dimensional nature of the analysis results, convolution effects may occur between matrix and particles. That is the reason why the Tomographic Atom Probe was used. It allows 3D images of the microstructure to be obtained by means of a position sensitive detector [*17,18*]. The mass resolution is degraded ($m / \Delta m = 200$) but the analyzed surface is enlarged while the spatial resolution is enhanced; the depth resolution is still one atomic layer, but the lateral resolution is better than half a nanometer over 10×10 nm^2. This configuration gives access to small precipitate size and composition free of convolution bias. Atom probe experiments were performed at Rouen University in the Groupe de Métallurgie Physique – UMR CNRS 6634 (France).

Hardness measurements were performed at the Service Contrôle Matériaux Irradiés – EDF (Chinon – France) with a Leitz RZD – DO instrument. Indentation was performed applying a 0.5 kg load (4.903 N). Uncertainties are ± 8 Hv.

The thermoelectricity technique has already been successfully applied to follow the evolution of the stability of the ferritic phase of duplex stainless steels [*19-22*]. In the framework of this study, thermoelectricity has been used to study the evolution of ferritic phases under irradiation. A precise description of the technique and its calibration as well as application on ferritic materials (mainly Fe-Cu alloys) are given in a companion paper [*23*]. These works have shown that Thermoelectric Power (TEP) is able to accurately follow copper depletion (or copper precipitation) in alloys aged under thermal or irradiation (electrons) conditions. The high sensitivity to phase evolutions and the relative simplicity of operating conditions of TEP have motivated its use to commercial materials.

Experimental Results

Hardness measurements performed during the thermal aging of the unirradiated specimen (up to 500 h at 455°C) do not reveal any hardening of the material. Thus, the hardness evolution of the irradiated materials will be only attributed to the recovery of irradiation damages.

Recovery kinetics are depicted on Figure 1 for the five studied fluences. Hardness measurements are reported as a function of the square root of time to clearly reveal the hardness behavior at short aging times. Uncertainties, not reported, are ± 8 Hv.

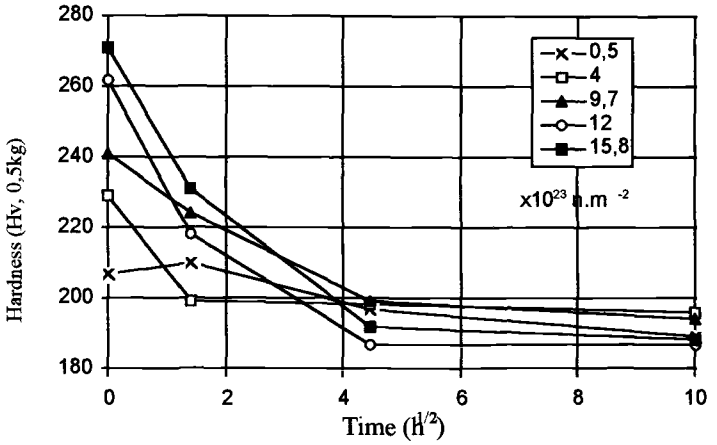


Figure 1– *Hardness in the As-Irradiated and Annealed (450°C) Conditions*

Recovery of the hardness does not depend on the fluence and is already significant after 2 hours of aging for the highest fluences. The material recovery is almost complete after 20 h at 450°C (i-e: 185 Hv for the unirradiated state) and complete after 100 h. This result is in agreement with previous one performed on materials with a higher copper content (0.2 to 0.4 at.% Cu) [*24, 25*].

SANS results are presented in figures 2 and 3, for materials irradiated (15.8×10^{23} $n.m^{-2}$) and annealed 2 h, 20 h and 100 h at 450°C. The Guinier analysis was performed for q values above 1 nm^{-1}. The results from the Guinier analysis of these data are reported in Table 3.

Table 3 – *Guinier Analysis of SANS Data for the Chooz A Material Irradiated (15.8×10^{23} $n.m^{-2}$) and Annealed at 450°C*

	R, nm [1]	I(q=0) [2], cm^{-1}	q_{min} - q_{max} [3], nm^{-1}
Irradiated materials	1.80 ± 0.01	0.180 ± 0.006	1.06 – 1.34
2h annealing	2.05 ± 0.01	0.120 ± 0.005	1.00 – 1.31
20h annealing	2.00 ± 0.02	0.030 ± 0.005	1.03 – 1.34
100h annealing	2.30 ± 0.09	0.020 ± 0.003	1.00 – 1.31

[1] $R = \sqrt{5/3}\ R_g$ [2] I value at q=0 following the Guinier line [3] q interval

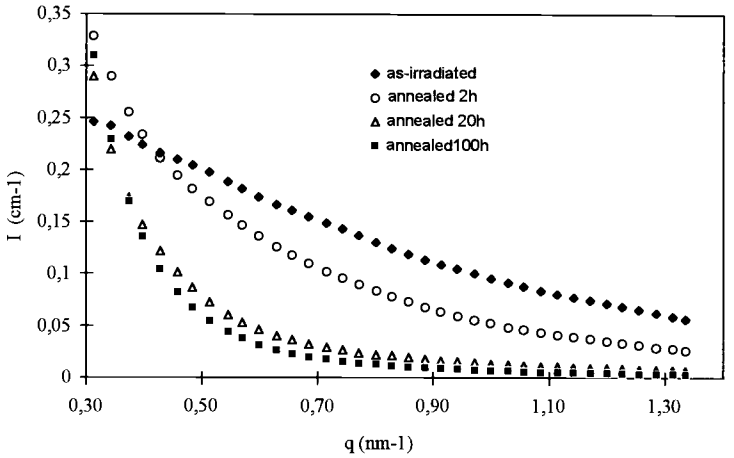


Figure 2 – *SANS Results ($I_\perp = f(q)$) for the Chooz A Material Irradiated (15.8×10^{23} n.m^{-2}) and Annealed 2, 10 and 100 h at 450°C*

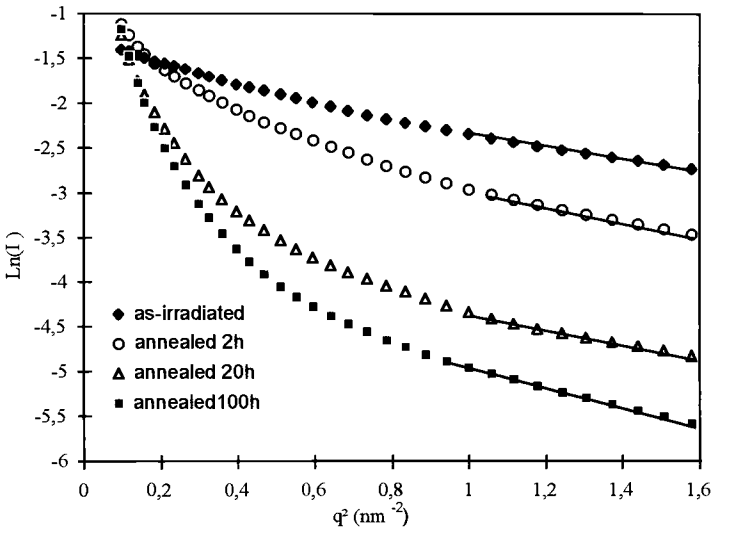


Figure 3 – *SANS Results ($Ln(I_\perp) = f(q^2)$) for the Chooz A Material Irradiated (15.8×10^{23} n.m^{-2}) and Annealed 2, 10 and 100 h at 450°C*

The decrease of the I(q=0) values with the increasing annealing times indicates a drop of the volume fraction of the scattering centers. An estimation of the number density of the scattering centers are : $35 \pm 7 \times 10^{23}$ m^{-3} in the as-irradiated specimen, $2.6 \pm 0.5 \times 10^{23}$

m^{-3} after 2 h of annealing and $0.5\pm0.2\times10^{23}$ m^{-3} after 100 h of annealing. This number density evolution is associated to a weak but noticeable increase of the radius of the scattering centers which are supposed to be spherical in the Guinier approximation.

These results are in agreement to previous SANS data from studies concerning the annealing effects. Solt [*26*] and Lucas [*27*] have reported that annealing steels with high copper levels (0.17 wt.% - 0.4 wt.% Cu) leads to an increase of the size of the scattering centers associated to a copper enrichment of the pre-existing neutron induced copper clusters and a copper depletion of the ferritic matrix.

In case of the French Chooz A steel, the neutron-induced clusters are Si, Ni, Mn and Cu enriched (80% of iron). In order to understand the chemical and structural evolution of these induced features under annealing conditions, atom probe experiments were performed.

The studied materials using atom probe techniques have been irradiated to a fluence up to 12×10^{23} $n.m^{-2}$ ($E > 1$ MeV) prior to annealing heat treatments. Under these irradiation conditions, previous atom probe experiments have determined a number density of neutron-induced clusters of the order of 9×10^{23} m^{-3}. The copper content in the ferritic matrix was depleted down to 0.04 at.% Cu. Table 4 summarized the chemical composition of the ferrite matrix of the unirradiated, irradiated (12×10^{23} $n.m^{-2}$), irradiated and annealed 2h and 100h at 450°C materials. In any composition, particles, clusters or any phase different from the ferritic matrix (small carbides...) have been subtracted. The nominal composition (bulk chemistry) is also reported for comparison.

Table 4 - *Chooz A Pressure Vessel Steel. Chemical Composition of the Ferrite Matrix Measured with the Atom Probe Technique in As Received, As-Irradiated (12×10^{23} $n.m^{-2}$) and Irradiated and Annealed (2 h and 100 h at 450°C) Conditions. Bulk Chemistry is also Reported*

		Si	Cr	Ni	Mo	C	P	Cu	Mn	Fe
Bulk chemistry	%at.	0.63	0.17	0.53	0.22	0.74	0.02	0.08	1.26	bal.
Un-irradiated	%at.	0.80	0.15	0.68	0.26	0.05	0.02	0.08	1.32	bal.
	2σ	0.10	0.04	0.10	0.06	0.02	0.01	0.03	0.13	-
Irradiated	%at.	0.62	0.13	0.66	0.22	0.05	0.02	0.04	1.00	bal.
	2σ	0.05	0.02	0.05	0.03	0.01	0.008	0.01	0.05	-
Irradiated and annealed 2h at 450°C	%at.	0.59	0.10	0.64	0.12	0.02	0.02	0.05	1.1	Bal.
	2σ	0.06	0.03	0.05	0.03	0.01	0.01	0.01	0.08	bal.
Irradiated and annealed 100h at 450°C	%at.	0.57	0.16	0.75	0.17	0.01	0.01	0.04	1.2	Bal.
	2σ	0.05	0.03	0.05	0.03	0.01	0.01	0.01	0.07	-

As far as the copper level in solid solution is concerned, a low value (0.04 at.% Cu) has been measured. This value is equal to the copper solubility limit in the Fe-Cu system given by the SGTE (Scientific Group Thermodata Europe) data base [*28*] for a

temperature of 450°C. This value has also been observed in the TEP studies of Fe-Cu model alloys [*23*] and in studies of irradiated and annealed weld materials (Babcock and Wilcox [*9*] and Midland [*10*]).

Concerning the microstructure, on the one hand, no more neutron-induced clusters (Si, Ni, Mn and Cu) have been detected in the ferrite matrix after 2 h of annealing. On the other hand, tiny copper clusters (1 to 2 nm in diameter) have been observed with a copper concentration of about 30 at.% Cu. No Si, Mn and Ni is associated to these copper clusters. It must be noted that this copper concentration is already 30 times higher than the copper content detected in the clusters of the as-irradiated material. After 100 h of aging, a copper rich particle (%Cu > 60 at.% Cu) was observed (Figure 4).

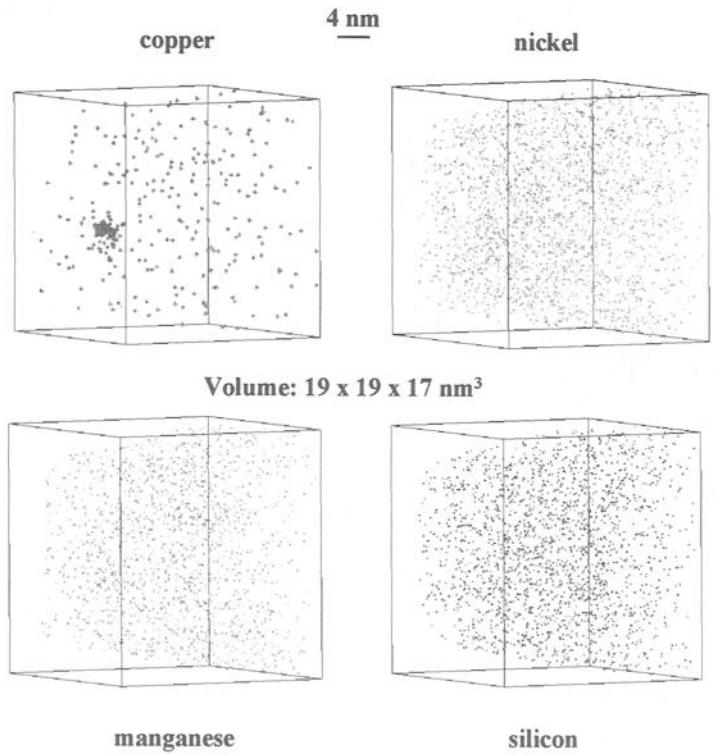


Figure 4 - *Three Dimensional Reconstruction of a Small Volume (19×19×17 nm³) of the Ferrite of the Irradiated and Annealed Chooz A Material (12×10²³ n.m⁻² and 100 h at 450°C) Obtained with Tomographic Atom Probe. One Dot is One Atom*

In all the sets of experiments performed on this material aged during 100 h, only one copper particle has been detected. Of course this result is too poor to give quantitative results but is, nevertheless, relatively important for the understanding of the evolution of

the microstructure. The characteristics of the clusters and particles detected in the different materials are summarized in Table 5.

This combination of results (Hardness, SANS and Atom-Probe) clearly indicates that annealing this low copper irradiated material at 450°C promotes the "dissolution" of the neutron induced clusters (Si, Ni, Mn and Cu) on behalf of copper particles. Copper clusters observed after two hours of annealing may be seen as copper pre-precipitates and may act as nuclei for growth and coarsening of copper pure particles. The number density of these later particles (bigger and richer) is sufficiently low to have no influence on the hardness measurements. SANS and Atom-Probe results show a similar decrease in the number density of scattering centers or particles between the as-irradiated and long time annealed specimens. These results suggest a very quick "dissolution" of the neutron-induced clusters, at least for the associated elements with exception of copper (Si, Ni and Mn return to the solid solution). This very fast evolution (in less than two hours) could be explained by the presence of freely migrating point defects in the neutron-induced clusters.

Table 5 - *Atom-Probe and Tomographic Atom-Probe Results Concerning Neutron-Induced Clusters as well as Copper Clusters and Precipitates Detected in the As-Irradiated Material (Fluence: 12×10^{23} n.m^{-2} (E>1MeV)) and Annealed Materials (2 and 100 h at 450°C)*

	Radius (nm)	Chemical composition (at.%)	Number density (10^{23} m^{-3})
Irradiated	1.5-2	Cu~1 – Ni~4 Mn~5 – Si~3	9
Irradiated and annealed 2h	0.5-1	Cu~30	Not determined
Irradiated and annealed 100h	1.5-2	Cu > 60	< 0.1

As it was previously mentioned, TEP is able to follow the evolution of the ferritic phase in the case of Fe-Cu model alloys. It was thus interesting to test this non destructive technique on these irradiated and annealed pressure vessel steels. First, TEP measurements were performed on thermal heat treated unirradiated specimen (500 h at 450°C). Then, irradiated and irradiated + annealed materials (see Table 2 for conditions) were investigated.

Aging the unirradiated material at 455°C up to 500 h has no influence on TEP evolution. The reference value (unaged material) stayed constant from 0 to 500 h of thermal aging. This indicates that if TEP variations are observed on the irradiated and annealed specimens it would only be attributed to the recovery of the irradiation damage.

Figure 5 shows TEP variations as a function of the neutron fluence. The evolution of the hardness of the same samples is also reported on the graph.

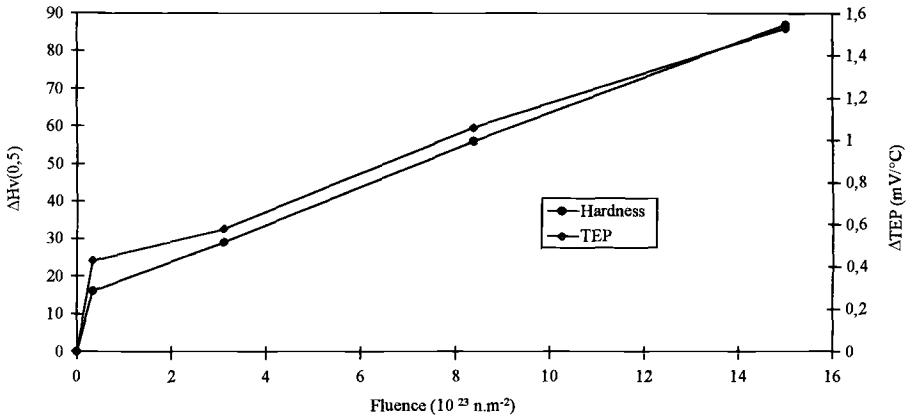


Figure 5 - *Evolution of TEP and Hardness as a Function of Neutron Fluences (Chooz A)*

It is known [*11,12*] that, in this neutron-irradiated low copper steel, the increase of the hardness is associated to (in addition to matrix point defects and impurities segregations) the presence of small clusters which have a constant size and chemical composition but an increasing number density as a function of fluence. Thus, evidence of a correlation between irradiation damages and TEP variations is observed. Of course, the contribution of each neutron irradiation damage cannot be assessed using TEP. Additional experiments with more appropriate techniques are required.

Figure 6 shows TEP measured values for the irradiated and annealed specimens aged for 2, 10 and 100 h at 450°C.

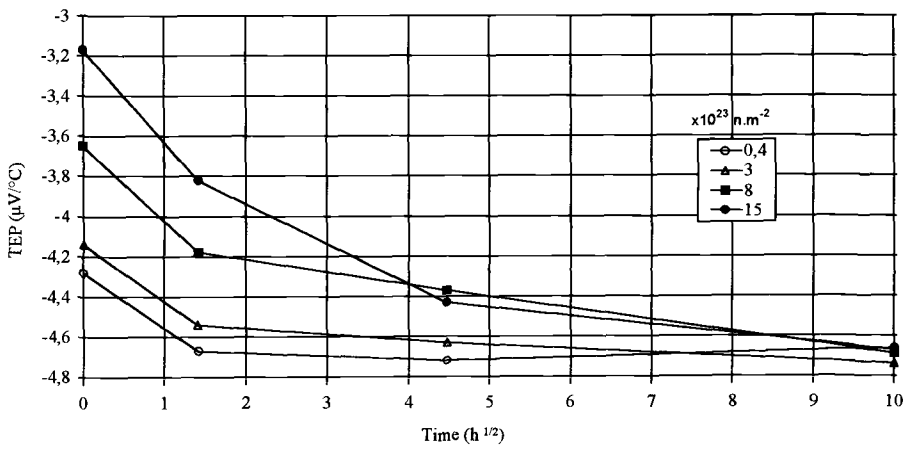


Figure 6 - *Evolution of TEP During Annealing Heat Treatments (450°C) as a Function of Time for Different Initial Neutron Irradiation Fluences*

It has been observed that under neutron irradiation conditions, TEP values follow

exactly the hardness curves (see Figure 1), regardless of the initial neutron dose.

These preliminary investigations and results, strongly suggest that TEP may be an appropriate non destructive, simple and in-situ technique, to follow the degree of recovery of the mechanical properties during annealing heat treatments of embrittled pressure vessel steels.

Conclusion

The evolution of the microstructure of the French Chooz A pressure vessel steel (characterized by a low copper content (<0.1 at.% Cu)) has been studied during annealing at 450°C. Hardness, SANS and Atom-Probe (conventional Atom-Probe and Tomographic Atom-Probe) were used. The irradiated material (fluence: 0.5 to 16×10^{23} $n.m^{-2}$, flux : 2×10^{15} $n.m^{-2}.s^{-1}$, temperature : 275°C) shows a quick recovery of hardness after 20 h of aging. The intensity of the SANS scattered signal decreases with annealing time. 3D images of the microstructure, at the atomic scale, given by the Tomographic Atom Probe show that during the first hours of annealing, the neutron induced Cu-Ni-Mn-Si clusters formed during the in-service irradiation, are "dissolved" while copper precipitates are formed. Their low number density is in agreement with the full recovery of the hardness.

These results are of primary importance for prediction of recovery of an irradiation embrittled steel and also for prediction of its behavior during re-irradiation. Since the copper level is a factor 2 less than that in the matrix after the stress relief heat treatment, these studies predict that the amount of re-irradiation embrittlement should be significantly less than during the initial neutron irradiation, as mentioned in previous works [*9*] for American high copper welds. Of course, this suggestion will be of interest if copper is really the major element in the process of the neutron-induced formation of the tiny clusters (Cu, Si, Ni, Mn).

This work also shows that the non-destructive technique, Thermoelectric Power, may be used to "follow" the microstructural evolution of materials during annealing treatments. Indeed, TEP evolution is consistent with the hardness measurements. This suggest a strong correlation between TEP variations and recovery of neutron irradiation damage.

Acknowledgments

This research was financially supported by Electricité de France (EDF), Département des Matériaux, under contract EDF/CNRS n°. 508914.

References

[1] Amayev, A. D., Kryukov, A. M., and Sokolov, M. A., *Radiation Embrittlement of Nuclear Reactor Pressure Vessel Steels: An International Review, ASTM STP 1170*, E. L Steele, Ed., American Society for Testing and Materials, Philadelphia, PA , vol. 4, 1993, p. 369.

[2] Kryukov, A. M., and Sokolov, M. A., *Small specimen test Techniques Applied to Nuclear Reactor Vessel Thermal Annealing and Plant Life Extension, ASTM STP 1204*, W. R. F. M. Haggag and W. L. Server, Ed., American Society for Testing and Materials, Philadelphia, PA, 1993, p. 147.

[3] Iskander, S. K., Sokolov, M. A., and Nanstad R. K., *Effects of Radiation on Materials: 17th Int. Symp., ASTM STP 1270*, A. S. Kumar, D. S. Gelles, R. K. Nanstad and E. A. Little, Ed., American Society for Testing and Materials, Philadelphia, PA, 1994, p. 277.

[4] Hawthorne, J. R., and Hiser, A. L., *Environmental Degradation of Materials in Nuclear Power Systems-Water Reactors, Fifth Int. Symp., American Nuclear Society*, Lagrange Park, IL, 1992, p. 671.

[5] Hawthorne, J. R.,*Influence of Radiation on Materials Properties Part II, ASTM STP 956*, F. A. Garner, C. H. Hanager, and N. Igata, Ed., American Society for Testing and Materials, Philadelphia, 1987, p. 461.

[6] Lott, R. G., Mager, T. R., Shogan, R. P., and Yamichko, S. E., *Radiation Embrittlement of Nuclear Reactor Pressure vessel Steels: An international review, ASTM STP 909*, E. Lendell Steele Ed., American Society for Testing and Materials, Philadelphia, PA, vol. 2, 1986, p. 242.

[7] Hawthorne, J. R., Watson, H. E., and Loss, F. L., *Proc. 10th Conf. on Effects of Radiation in Materials, ASTM STP 725*, D. Kramer, H. R. Prager, J. S. Perrin, Ed.,.American Society for Testing and Materials, Philadelphia, PA, 1981, p. 63.

[8] Hawthorne, J. R., Watson, H. E., and Loss, F. L., *Effects of Radiation on Structural Materials, ASTM STP 683*, J. A. Sprague, D. Kramer, Ed., American Society for Testing and Materials, Philadelphia, PA, 1987, p. 278.

[9] Pareige, P., Stoller, R. E., Russell, K. F., and Miller, M. K., *Journal of Nuclear Materials*, 249, 1997, p. 165.

[10] Miller, M. K. and Russell, K. F., *Journal of Nuclear Materials*, 250, 1997, p. 223.

[11] Pareige, P., Van Duysen, J.-C., and Auger, P., *Applied Surface Science*, 67, 1993, pp. 342-347.

[12 Auger, P., Pareige, P., Akamatsu, M., and Blavette, D., *Journal of Nuclear Materials*, 225, 1995, p. 225.

[13] Pareige, P., Doctoral Thesis, Rouen University, France, October 1994

[14] Pareige, P., Auger, P., Miloudi S., Van Duysen, J.-C., and Akamatsu, M., *Annale de Physique*, C2, 22, 1997, pp. 117-125.

[15] Miller, M. K., Cerezo, A., Hetherington, M. G., and Smith, G. D. W., Atom Probe

Field Ion Microscopy, Oxford Science Publications, Clarendon Press, Oxford, 1996.

[16] Sarrau, J. M., Danoix, F., Deconihout, B., Bouet, M., Menand, A., and Blavette, D., *Applied Surface Science*, 76/77, 1994, p.363.

[17] Blavette, D., Bostel, A., Sarrau, J. M., Deconihout, B. and Menand A., *Nature*, 363, 1993, 432.

[18] Blavette, D., Deconihout, B., Bostel, A., Sarrau, J. M. and Menand, A., *Revue of Scientific Instrument*, 64, 1993, p. 2911.

[19] Pollock, D. P., *Thermoelectricity: Theory, Thermometry, Tool, ASTM STP 852*, 1985.

[20] Borrely, R., Pelletier, J. M. and Gobin, P. F., *Acta Metallurgica*, vol. 26, 1978, p. 1863.

[21] Pelletier, J. M., Borrely, and R., Pernoux, E., *Phys. Stat. Sol. A*, vol. 39, 1977, p.525.

[22] Pelletier, J. M., Borrely, R., and Gobin, P. F., *Scripta Metallurgica*, vol. 11, n°7 1977, p.553.

[23] Miloudi, S., Van Duysen, J-C., Jumel, S., and Pareige, P., *Effects of radiation on materials: 19th International Symposium, ASTM STP 1366*, M. L. Hamilton, A. S. Kumar, S. T. Rosinski and M. L. Grossbeck, Ed., American Society for Testing and Materials, 1999.

[24] Mader, E., Lucas, G.E., Odette, G.R., *Effects of Radiation on Materials: 15th International Symposium, ASTM STP 1125*, R. E. Stoller, A. S. Kumar, and D. S. Gelles, Eds., American Society for Testing and Materials, 1990, p. 151.

[25] Lott, R. G., and Mager, T. R., *International Journal of Pressure Vessel Piping*, 34 (1988) p. 155.

[26] Solt, G., Frisius, F., and Waeber, W. B., *ASTM STP 1011*, 1989, p. 229.

[27] Lucas, G. E., Odette, G. R., Wirth, B., Mader, E., Klingensuith, D., *IGRDM 6*, Prague, 1995.

[28] Miller, M. K., Russell, K. F., Jostons, A., and Blake, R. G., *Appl. Surf. Sci.*, 87&88 1995, p. 216.

Ryuta Kasada,[1] Taro Morimura,[2] Hideki Matsui,[3] Minoru Narui,[4] and Akihiko Kimura[5]

Two-Step Recovery Process of Irradiation Hardening in 1%Ni Doped 9%Cr-2%W Martensitic Steel

---

Reference: Kasada, R., Morimura, T., Matsui, H., Narui M., and Kimura, A., **"Two-Step Recovery Process of Irradiation Hardening in 1%Ni Doped 9%Cr-2%W Martensitic Steel,"** *Effects of Radiation on Materials: 19th International Symposium, ASTM STP 1366,* M. L. Hamilton, A. S. Kumar, S. T. Rosinski, and M. L. Grossbeck, Eds., American Society for Testing and Materials, West Conshohocken, PA, 2000.

Abstract: The effect of nickel addition on irradiation-induced hardening has been investigated for reduced-activation martensitic steel (RAMS). Specimens were irradiated in the JMTR at 80°C and 220°C up to 0.15 dpa. There was no significant difference in the tensile properties between the steels with and without Ni addition after the irradiation at 220°C, while in the case of the irradiation below 170°C, the Ni-added RAMS showed a more than four times larger irradiation hardening than the steel without Ni addition. The recovery behavior of the irradiation hardening of Ni-added steel on post-irradiation annealing showed two-step recovery behavior; the first step was around 200°C and the second one was around 350°C, while only the single step of recovery was observed around 350°C in the steel without Ni addition. The mechanism of the recovery process of the tremendous irradiation hardening in Ni-added steel is discussed along with the behavior of vacancies, carbon atoms and their complexes investigated by means of positron annihilation lifetime spectrometry.

Keywords: irradiation hardening, effects of nickel, reduced-activation martensitic steels, helium embrittlement, post-irradiation annealing

---

[1]Graduate student, and [5]Professor, Institute of Advanced Energy, Kyoto University, Gokasho, Uji, Kyoto 611-0011, Japan.

[2]Graduate student, [3]Professor, and [4]Assistant researcher, Institute for Materials Research, Tohoku University, Katahira, Aoba-ku, Sendai 980-77, Japan.

Copyright© 2000 by ASTM International www.astm.org

Introduction

Reduced-activation martensitic steels (RAMS), JLF-1 (Monbusho) [*1-4*] and F82H (JAERI) [*4-6*], have excellent irradiation resistance, therefore, they have been the prime candidates for structural materials of the DEMO reactor and beyond. It has been very important to investigate helium effects in fusion neutron irradiated materials, because the structural materials may suffer not only displacement damages but also effects of transmutation helium such as enhancement of void swelling and helium induced embrittlement [*7-9*]. However, no available source of fusion neutrons exists at this moment, and it must be carried out to simulate the irradiation conditions in the fusion environment. As one of these simulations, isotope tailoring experiments for ferritic steels with an addition of several percentages of nickel, has been done using a mixed-spectrum fission reactor, such as the HFIR (High Flux Isotope Reactor) [*7,10-13*]. It has been known that nickel produces helium by a two-step transmutation reaction with thermal neutrons of $^{58}Ni(n, \gamma)^{59}Ni$ followed by ^{59}Ni $(n, \alpha)^{56}Fe$. R. L. Klueh et al. reported that 2%Ni-added 9Cr-1Mo steel irradiated up to 40 dpa at 400°C in the HFIR produced 32 appm helium, and the DBTT of the steel increased by 200°C [*13*]. It was very serious irradiation embrittlement compared to the steel without any addition of nickel and was interpreted in terms of transmutation helium-induced embrittlement. On the other hand, our previous study showed that more than two times larger irradiation hardening was induced in the 1%Ni-added 9Cr RAMS than the steel without Ni addition after irradiation below 170°C in the JMTR (Japan Materials Testing Reactor) [*14*]. The amount of helium production during irradiation in the JMTR was 10^{-2} appm at most, indicating that nickel in itself affects the irradiation hardening in the steels.

In this paper, we investigate the recovery behavior and its mechanism of the tremendous irradiation hardening of Ni-added RAMS, and discuss the role of nickel addition in the irradiation hardening and embrittlement.

Table 1- *Chemical compositions and heat treatment conditions*

9Cr-2W steels (wt.%)

	C	Si	Mn	P	S	*Ni*	Cr	V	Ti	W	Ta
Mod. JLF-1/LSM	0.12	0.01	0.01	0.003	0.001	***0.02***	8.91	0.26	0.05	2.03	0.069
Mod. JLF-1/LSM/Ni	0.10	0.01	0.01	0.004	0.001	***1.00***	8.92	0.26	0.04	2.02	0.069

Heat treatment condition: normalized at 1050°C for 30 min and then tempered at 700°C for 1 h, followed by air cooling.

Experimental Procedure

The materials used in this study were reduced activation 9%Cr-2%W martensitic steels with and without 1 wt.% of nickel addition. These steels were mod. JLF-1 lowered silicon and manganese which is written as Mod. JLF-1/LSM in this paper, and Ni-added Mod. JLF-1/LSM as Mod. JLF-1/LSM/Ni. The chemical compositions of the steels are given in Table 1. The steels were under the following heat treatment conditions; normalized at 1050°C for 30 min and then tempered at 700°C for 30 min (or 750°C in 1 hour), followed by air cooling. Specimens were punched out from the steel plates into mini-sized tensile specimens of $4 \times 16 \times 0.25$ mm and disk specimens of 3 mm diameter. The specimens were irradiated in the JMTR (Japan Materials Test Reactor) at the following irradiation conditions. The first irradiation was performed in the multi-section and multi-division controlled irradiation rig at 220°C up to 0.15 dpa [*15*]. A part of the specimens was irradiated in the capsule out of the reactor core where the irradiation temperature was lower than 170°C and the total irradiation dose was less than 0.15 dpa. The second irradiation was performed in the porous capsule to irradiate at temperature of water coolant (80°C), and the total dose was 0.11 dpa. The amount of transmutation helium was the order of 10^{-2} at.ppm at most for all the specimens.

After the irradiations, tensile tests were carried out at a cross-head speed of 0.2 mm/min at room temperature. Micro-Vickers hardness and positron annihilation lifetime measurements (PA) were carried out after post-irradiation annealing in a vacuum of 5.0×10^{-7} torr. The lifetime spectra of PA was decomposed into two components, that is a matrix component (τ_1, I_1) and a microvoid component (τ_2, I_2), where τ_i and I_i were the lifetime and intensity of i-th component, respectively.

Results

Tensile Properties

The effects of 1%Ni addition on the tensile properties of the RAMS after the irradiation at 220°C and below 170°C is shown in Fig. 1. There was no significant difference in the tensile properties between the steels with and without Ni addition after the irradiation at 220°C, while in the case of the irradiation below 170°C, the Ni-added RAMS showed a more than four times larger irradiation hardening than the steel without Ni addition. In order to make clear the effect of low temperature irradiation on the irradiation-induced hardening, the specimens were irradiated in a porous capsule so as to

irradiate the specimens at the water coolant temperature of 80°C. The stress-strain curves of Ni-added RAMS are shown in Fig. 2, indicating that the Ni-added steel irradiated at 80°C shows smaller irradiation hardening than the steel irradiated below 170°C. The dependence of irradiation hardening of the Ni-added steel on the irradiation temperature is shown in Fig. 3, which was obtained for the steels irradiated in JMTR[14,16]. There seems to be a peak of the hardening at a temperature between 80 and 170°C.

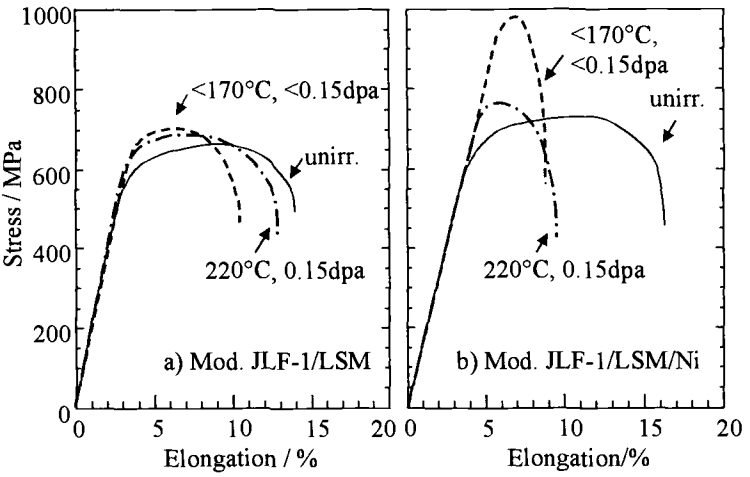


Fig.1- *Stress-strain curves of (a) Mod. JLF-1/LSM and (b) Mod. JLF-1/LSM/Ni, unirradiated, irradiated at 220℃ and below 170℃.*

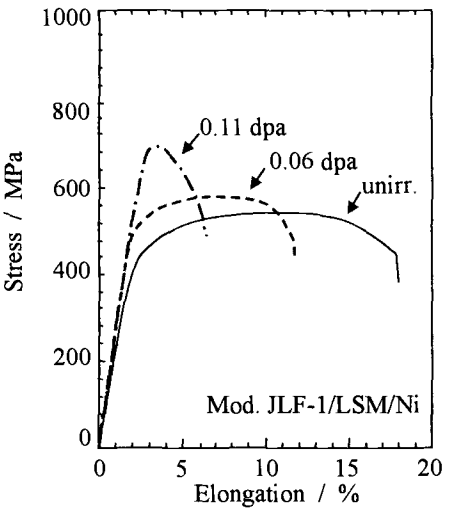


Fig.2- *Stress-strain curves of Mod. JLF-1/LSM/Ni irradiated at 80℃.*

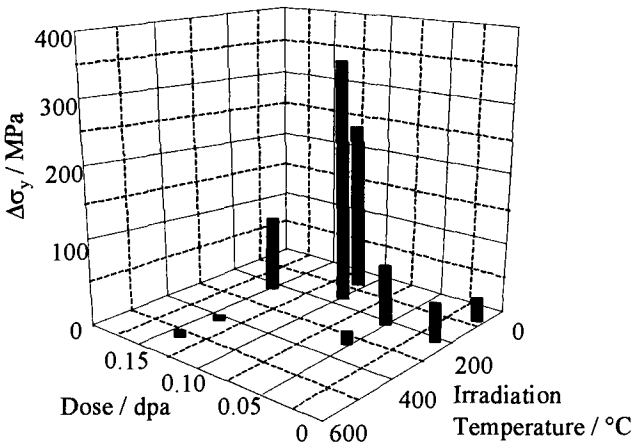


Fig. 3- *Dependence of irradiation hardening of Mod. JLF-1/LSM/Ni irradiated in JMTR on irradiation temperature and dose.*

Post-irradiation Annealing Behavior

Isochronal Annealing Experiment- The recovery process of the irradiation hardening upon post-irradiation annealing was investigated by means of micro-Vickers hardness and PA measurements to clarify the effect of the Ni addition and the irradiation temperature on the irradiation hardening. Figure 4 shows the isochronal annealing curves of RAMSs of three different conditions; a) RAMS and b) Ni-added RAMS irradiated below 170°C, c) Ni-added RAMS irradiated at 220°C. After the irradiation below 170°C, the amount of irradiation hardening is much larger in the nickel-added steel. However, the irradiation hardening of nickel-added steel is considerably reduced when the irradiation temperature is 220°C. As for the recovery behavior, two-step recovery behavior was observed in the nickel added steel after the irradiation below 170°C, while the steel without nickel addition shows the single step recovery. The second recovery stage in the Ni-added steel, which is located above 300°C, is considered to be the same stage as observed in the steel without nickel addition. The first recovery stage in the Ni-added steel observed at temperatures above 200°C disappeared when the irradiation temperature was 220°C. This shows that the nickel-added martensitic steel has an additional component of irradiation hardening after the irradiation below 170°C.

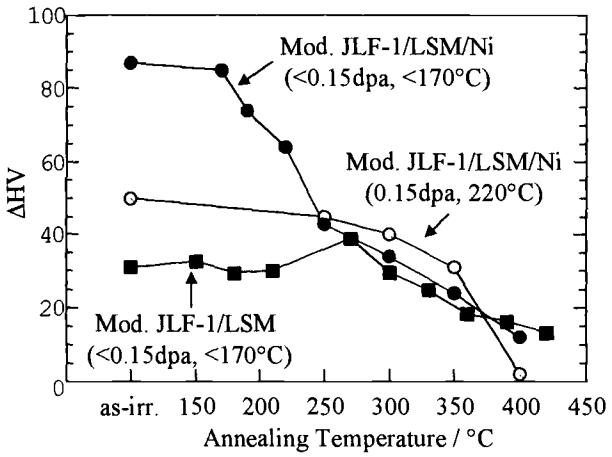


Fig. 4- *Vickers hardness change on isochronal annealing for 1 hour of Mod. JLF-1/LSM irradiated below 170℃, and Mod. JLF-1/LSM/Ni irradiated at 220℃ and below 170℃.*

Isothermal Annealing Experiment- In order to investigate the annealing behavior of the enhanced irradiation hardening of Ni-added RAMS more in detail, isothermal annealing experiments were carried out at temperatures between 170 and 400°C for the Ni-added RAMS irradiated at 80°C, as shown in Fig. 5. In the annealing temperature above 300°C, almost all the irradiation hardening recovered after 20 min of annealing. At

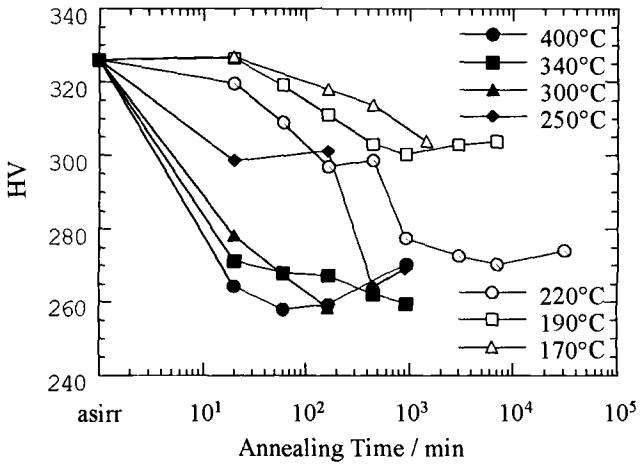


Fig. 5- *Vickers hardness change on isothermal annealing from 170℃ to 400℃ of 1%Ni irradiated at 80℃.*

the annealing temperatures of 220 and 250°C, a two-step recovery process of the irradiation hardening is clearly shown. Below 190°C, only the first stage was observed because of the low temperature annealing. From the thermal annealing data, the apparent activation energies of each recovery stage have been estimated to recognize that the two-step recovery is a thermal activation process, although the recovery process of the irradiation hardening involves many elemental processes. Figure 6 shows the normalized plots of the hardness data in Fig.5, where the normalization was performed on each recovery stage. The Arrhenius plot was attempted and shown in Fig. 7, indicating that some plots are out of the straight lines. The obtained activation energies are 0.93 and 1.4 eV for the first and second recovery stage, respectively.

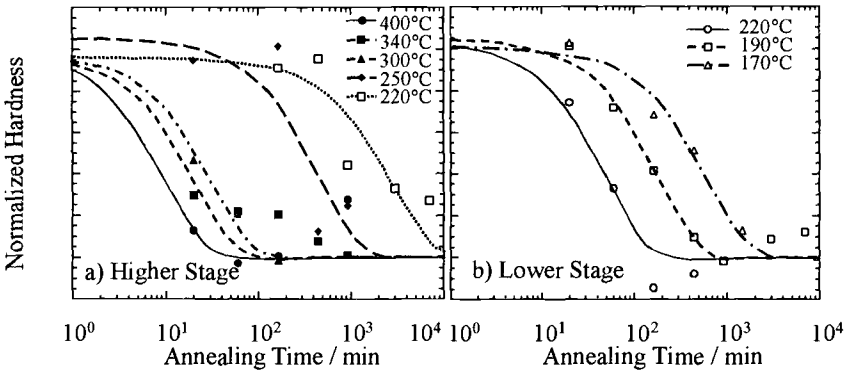


Fig. 6- *Normalized hardness of a) Higher Stage and b) Lower Stage of the recovery of the irradiation hardening shown in Fig. 5.*

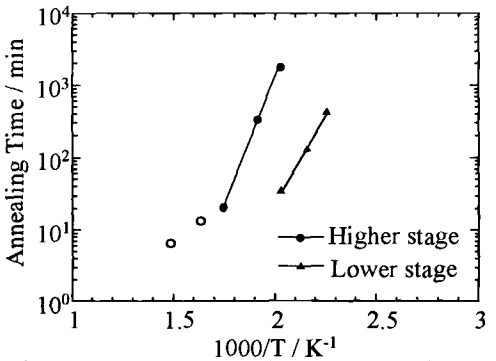


Fig. 7- *Arrhenius plots of the recovery of the irradiation hardening in Mod. JLF-1/LSM/Ni.*

Positron Annihilation Lifetime Spectrometry- Positron annihilation lifetime spectrometry was carried out for a) the steel without nickel addition irradiated below 170°C, b) the Ni-added steel irradiated at 80°C upon isochronal annealings, as shown in Fig. 8. In both of the steels, the irradiation results in the appearance of the longer life time component (τ_2 = 400 to 500 psec), namely formation of microvoids[*17*], and at the annealing temperature above 300°C, the τ_2 decreased to 200 psec. This suggests the decomposition of microvoids by the thermal annealing above 300°C, and the decomposition stage of the microvoids corresponds to the second recovery stage of the irradiation hardening of the steels. As for the first stage, PA spectra give no reflection of the recovery of the irradiation hardening. In the previous study[*14,16*], we indicated that microvoids did not contribute directly to irradiation hardening in RAMS, which is in agreement with the results concerning the first recovery stage, so it is considered that the vacancies released by the decomposition of microvoids are closely related to the recovery of the other damage structure such as interstitial type of clusters which is considered to be the cause of irradiation hardening in RAMS.

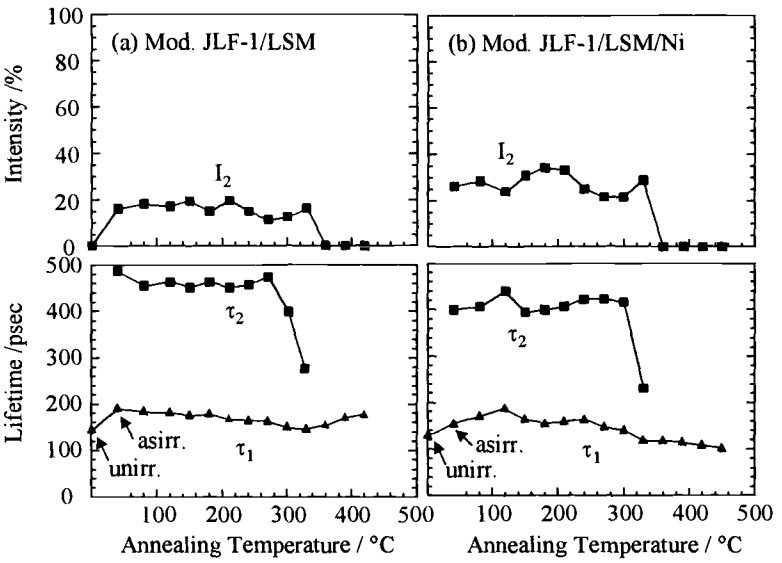


Fig. 8- *Two component analysis of PA spectra on isochronal annealing for (a) Mod. JLF-1/LSM irradiated below 170 °C and (b)Mod. JLF-1/LSM/Ni irradiated at 80 °C.*

Discussion

The two-step recovery of irradiation hardening in the Ni-added steel indicates that the Ni-added RAMS has an two-component source of the irradiation hardening caused by nickel addition in itself. Appearance of the extra hardening of Ni-added steel depends on the irradiation temperature; it is observed below 220°C and seems to show peak at a temperature between 80 and 170°C. The PA results indicated the disappearance of τ_2 occurred above 300°C. These results almost agreed with that of the resistivity measurement of electron irradiated high purity iron and its carbon-doped alloys by S. Takaki et al.[*18*], where the recovery stage of 320°C was attributed to the resolution or rearrangements of small clusters, which was suggested as carbon-vacancies (C-V) complex. It is considered that the disappearance of τ_2 by the annealing above 300°C in PA measurement corresponds to the vacancy evaporation from C-V complexes or microvoids. The recovery of irradiation hardening is interpreted in terms of shrinkage and/or annihilation of interstitial loops by the absorption of freely migrating vacancies which evaporates from microvoids. The extra component of the irradiation hardening observed in the Ni-added steel is considered to be due to the formation of nickel rich interstitial type loops which is unstable above 220°C[*19*].

Thus, the nickel addition to the RAMS significantly enhances the irradiation hardening or embrittlement at the following irradiation conditions;

1) irradiation temperature is below 220°C

2) irradiation dose is as much as 0.1dpa

As the irradiation hardening of RAMS is remarkably influenced by the addition of 1%Ni, the post-irradiation DBTT of the steel is considered to be also influenced by the nickel addition. A significant hardening will result in a significant shift in the DBTT. Since the extra hardening caused by the nickel in itself is obtained by the irradiation up to only 0.1 dpa so on, the irradiation temperature during the shut down of the reactor with high flux should be kept above 220°C in order to perform isotope tailoring experiment by means of nickel addition.

Conclusion

The effects of nickel addition on the post-irradiation tensile properties, micro-Vickers hardness and PA lifetime were investigated for the reduced-activation martensitic steels after the neutron irradiation up to 0.15 dpa with estimated transmutation helium concentration of 0.01 at.ppm. The main results were:

1) In spite of no difference in the irradiation hardening behavior between the steels with and without nickel addition irradiated at 220°C, a tremendous irradiation hardening was observed in Ni-added steel irradiated below 170°C.
2) The tremendous irradiation hardening observed in the Ni-added steel irradiated at 80°C showed a two-step recovery upon isochronal annealing; the first stage is around 200°C and the second is around 350°C, which indicates that Ni-added RAMSs have an extra irradiation hardening caused by nickel in itself when the irradiation temperature is below 170°C.
3) It is recommended for the research on helium effects utilizing nickel isotope tailoring technique that the irradiation temperature during shut down of the reactor with high flux is strictly kept above 220°C.

Acknowledgement

We would like to thank M. Hasegawa for his advice about positron annihilation lifetime spectrometry. This research was partly supported by the Japan-US collaboration program of irradiation effects on fusion materials (JUPITER).

References

[1] Kimura, A., Morimura, T., Narui, M., and Matsui, H., "Irradiation Hardening of Reduced Activation Martensitic Steels," *Journal of Nuclear Materials*, vols.233-237, 1996, pp. 319-325.

[2] Morimura, T., Kimura, A., Matsui, H., "Void Swelling of Japanese Candidate Martensitic Steels under FFTF / MOTA Irradiation," *Journal of Nuclear Materials*, vol. 239, 1996, pp. 118-125.

[3] Kimura, A., Narui, M., Misawa, T., Matsui, H., and Kohyama, A., *Journal of Nuclear Materials*, in press

[4] Kohyama, A., Hishinuma, A., Gelles, D. S., Klueh, R. L., Dietz, W., Ehrlich, K., "Low-Activation Ferritic and Martensitic Steels for Fusion Application," *Journal of Nuclear Materials*, vols. 233-237, 1996, pp. 138-147

[5] Shiba, K., Suzuki, M., Hishinuma, A., and Pawel, J. E., "Effect of Boron on Post Irradiation Tensile Properties of Reduced Activation Ferritic Steel (F-82H) Irradiated in HFIR," *Effects of Radiation on Materials: 17th International Symposium, ASTM STP 1270*, David S. Gelles, Randy K. Nanstad, Arvind S. Kumar, and Edward A. Little, Eds., American Society for Testing and Materials, 1996, pp. 753-760

[6] Shiba, K., Suzuki, M., Hishinuma, A., "Irradiation Response on Mechanical Properties of Neutron Irradiated F82H," *Journal of Nuclear Materials*, vols. 233-237, 1996, pp. 309-312

[7] Klueh, R. L., Maziasz, P. J., "Helium Effects on Neutron-Irradiated Cr-Mo Ferritic Steels: A Review of Recent Results," *Effects of Radiation on Materials, Volume I, ASTM STP 1046*, M. H. Packan, R. E. Stoller, and A. S. Kumar, Eds., American Society for Testing and Materials, Philadelphia, 1989, pp. 246-262

[8] Hasegawa, A., Yamamoto, N., and Shiraishi, H., "Effect of Helium Implantation at 533-573 K on Tensile Properties of 9Cr Martensitic Steels," *Journal of Nuclear Materials*, vol. 202, 1993, pp. 266-274

[9] Ullmaier, H., Camus, E., "Low Temperature Mechanical Properties of Steels Containing High Concentrations of Helium," *Journal of Nuclear Materials*, vol. 251, 1997, pp. 262-268

[10] Maziasz, P. J., and Klueh, R. L., "Void Formation and Helium Effects in 9Cr-1MoVNb and 12Cr-1MoVW Steels Irradiated in HFIR and FFTF at 400°C," *Effects of Radiation on Materials: 14th International Symposium, Volume I, ASTM STP 1046*, 1989, pp. 35-60

[11] Klueh, R. L., and Alexander, D. J., "Impact Behavior of 9Cr-1MoVNb and 12Cr-1MoVW Steels Irradiated in HFIR," *Journal of Nuclear Materials*, vols. 179-181, 1991, pp. 733-736

[12] Klueh, R. L., and Maziasz, P. J., "Effect of Irradiation in HFIR on Tensile Properties of Cr-Mo Steels," *Journal of Nuclear Materials*, vol. 187, 1992, pp. 43-54

[13] Klueh, R. L., and Alexander, D. J., "Embrittlement of Cr-Mo Steels after Low Fluence Irradiation in HFIR," *Journal of Nuclear Materials*, vol. 218, 1995, pp. 151-160

[14] Kasada, R., Kimura, A., Matsui, H., and Narui, M., "Enhancement of Irradiation Hardening by Nickel Addition in the Reduced-Activation 9Cr-2W Martensitic Steel," *Journal of Nuclear Materials*, vols. 258-263, 1998, pp. 1199-1203

[15] Kiritani, M., Yoshiie, T., Kojima, S., Satoh Y., and Hamada, K., "Fission-Fusion Correlation by Fission Reactor Irradiation with Improved Control," *Journal of Nuclear Materials*, vol. 174, 1990, pp. 327-351

[16] Kasada, R., Kimura, A., Matsui, H., Hasegawa, M., and Narui, M., "Effects of Varying Temperature Irradiation on the Neutron Irradiation Hardening of Reduced-Activation 9Cr-2W Martensitic Steels," *Journal of Nuclear Materials*, in press.

[17] Kuramoto, E., Takano, Y., Kikuchi, N., and Takenaka, M., "Positron Annihilation Lifetime Measurements of Irradiated Iron and Iron-Chromium Alloys," *Journal of Nuclear Materials*, vols. 141-143, 1986, pp. 829-836

[18] Takaki, S., Fuss, J., Kugler, H., Dedek U., and Schultz, H., "The Resistivity Recovery of High Purity and Carbon Doped Iron Following Low Temperature Electron Irradiation," *Radiation Effects*, vol. 79, 1983, pp. 87-122

[19] Yoshida, N., Yamaguchi, A., Muroga, T., Miyamoto, Y., and Kitajima, K., "Characteristics of Point Defects and Their Clustering in Pure Ferritic Steels," *Journal of Nuclear Materials*, vols. 155-157, 1988, pp. 1232-1236

Yuri A. Nikolaev[1] and Alla V. Nikolaeva[2]

Application of the Floating Curve Model for Estimation of Re-Irradiation Embrittlement of VVER-440 RPV Steels

Reference: Nikolaev, Y. A. and Nikolaeva, A. V., **"Application of the Floating Curve Model for Estimation of Re-Irradiation Embrittlement of VVER-440 RPV Steels,"** *Effects of Radiation on Materials: 19th International Symposium, ASTM STP 1366,* M. L. Hamilton, A. S. Kumar, S. T. Rosinski, and M. L. Grossbeck, Eds., American Society for Testing and Materials, West Conshohocken, PA, 2000.

Abstract: Radiation embrittlement and its mitigation by annealing of VVER-440 reactor pressure vessel steels are studied. The Russian regulatory approach for prediction of radiation embrittlement of VVER-440 steels is considered. Results of an investigation of materials cut out of operating nuclear power plants are discussed. Different models of re-irradiation embrittlement are compared. A new model for assessment of embrittlement under re-irradiation is developed.

Keywords: reactor pressure vessel, radiation embrittlement, post-irradiation annealing, re-irradiation, ductile-to-brittle transition temperature

Introduction

A reactor pressure vessel (RPV) is considered to be a lifetime limiting component for nuclear power plants (NPPs) with pressurized water reactors (PWR). Neutron irradiation of RPV steels increases density of point defects, enhances diffusivity of all atoms in solid solution and produces phase transformations, precipitation, microvoids, etc. that result in considerable change in the mechanical properties of materials. Investigations carried out in the second part of 1970s confirmed that phosphorus and copper in low concentrations tremendously increase the sensitivity of VVER-440 RPV steels to irradiation embrittlement [1]. The content of these impurities was not checked in welds of the first generation of VVER RPVs during manufacture. Phosphorus contents in the core weld of the majority of VVER RPVs of the first generation is rather high (up to 0.046-0.050 wt. %) [2, 3]. Investigation of VVER-440/213 surveillance specimens showed that the embrittlement of weld metal occurs much sooner than estimated in design. Namely the core welds control the lifetime of the VVER RPVs. Re-estimated lifetime of some welds was found to be essentially shorter than design life. At that time, the only way to provide RPV design lifetime was to anneal the RPVs [4].

[1]Leading research scientists, Russian Research Center "Kurchatov Institute", ORM, Kurchatov Sq. 1, 123182 Moscow, Russia.

[2]Senior research scientist, Nuclear Safety Institute, Russian Academy of Sciences, B.Tulskaya 52, 113191 Moscow, Russia.

Copyright© 2000 by ASTM International www.astm.org

Thermodynamic instability of various radiation defects at temperatures exceeding the irradiation temperature (T_{irr}) leads to the recombination of point defects, reducing the density of dislocations, dislocation loops and irradiation-induced precipitates. These give rise to mitigation of radiation embrittlement. The mechanical property recovery depends on temperature and duration of post-irradiation annealing [4, 5]. Re-embrittlement kinetics of VVER-440 type steels and other types of RPV steels was studied in the recent years highly insufficiently. In the present paper a new approach for estimation of re-irradiation kinetics of VVER-440 RPV steels is developed.

Embrittlement of VVER-440 RPV Steels Under Irradiation

The irradiation embrittlement in RPV steels is known to be defined by metallurgical factors (alloying and impurity contents, microstructure) and by irradiation conditions (temperature, neutron flux parameters, damage dose) [1, 6, 7]. The radiation behavior of different types of RPV steels is specified in national guides by trend curves. The trend curves establish relation between radiation embrittlement estimated by the shift of ductile-to-brittle transition temperature (DBTT) due to irradiation (ΔTT_F) and fast neutron fluence (F) and chemical composition of steels. Typically these dependences have the following form:

$$\Delta TT_F = TT_F - TT_0 = A_F \times F^n , \quad (1)$$

where TT_0 and TT_F are DBTT in unirradiated and as-irradiated conditions, respectively; A_F is a parameter dependent on the chemical composition of steel ("chemistry factor"); n is an exponent which can depend on the chemical composition and damage dose (n=1/3 for VVER-440 steels).

All trend curves for VVER-440 RPV steels were generally developed on the basis of regression analysis of the Russian VVER-440 surveillance data base and predict the irradiation response rather reliably. In accordance with the Russian Guide DBTT increase of VVER-440 welds caused by neutron irradiation is connected with damage dose by the following equation:

$$\Delta TT_F = 800\ (C_P + 0.07\ C_{Cu})\ F^{1/3}, \quad (2)$$

where C_P and C_{Cu} are phosphorus and copper contents in wt. %, respectively; F is neutron fluence in terms of 10^{22} neutron/m^2 (E > 0.5 MeV). Regression analyses of the test results of VVER-440 surveillance welds (Fig. 1) give very close result to Eq. (2):

$$\Delta TT_F = 750\ (C_P + 0.063\ C_{Cu})\ F^{1/3}, \quad (3)$$

The trend curve specified in the Russian Guide is very close to the regression line and significantly underestimates radiation embrittlement for some materials. To make Eq. (2) to be a 95% conservative estimation of radiation embrittlement of VVER-440 welds a correction of 5.7 should be added to A_F (2):

$$\Delta TT_F = [5.7 + 800(C_P + 0.07C_{Cu})]\ F^{1/3} = 800\ (0.0071 + C_P + 0.07C_{Cu})\ F^{1/3} \quad (4)$$

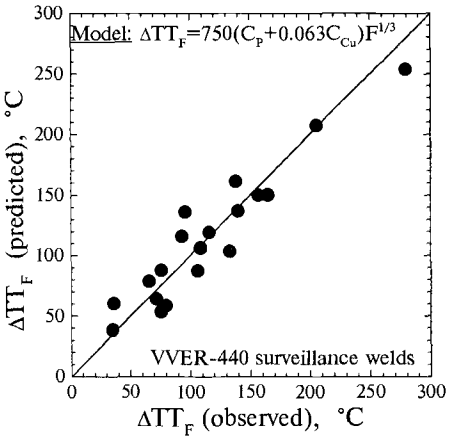


Figure 1 - *Comparison of Observed and Predicted Values of Radiation Induced DBTT Shift for VVER-440 Surveillance Welds*

A great part of VVER-440 surveillance materials was irradiated at a "high" flux of ~3×10^{16} neutron·m^{-2}s^{-1} (E > 0.5 MeV) that is more than ten times higher than the flux at the core region of RPV wall. This can produce some additional unconservatism of the trend curve (2). The dependence of Charpy curve shift per fluence unit on neutron flux value is the flux effect. The importance of the flux effect becomes evident from the following experiment. A VVER-440 surveillance weld (0.028%P, 0.18%Cu) was irradiated in the unit 2 of Armenia NPP at the high flux and in the unit 1 of Rovno NPP at a "low" flux of ~4×10^{15} neutron·m^{-2}s^{-1} (E > 0.5 MeV). As it can be seen in Fig. 2, irradiation at the low flux produces much higher DBTT shifts than irradiation at the high flux. The difference between DBTT shift produced by irradiation at the low and high flux at the fluence region of (1-1.6)$\times10^{22}$ neutron/m^2 (the end-of-life fluence for weld No. 4 of VVER-440/230 RPVs) is approximately 40°C.

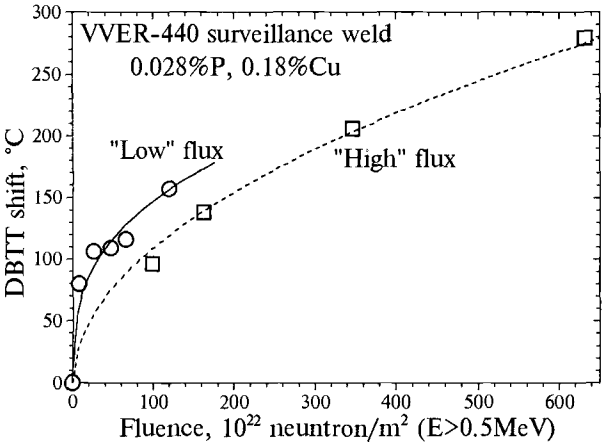


Figure 2 - *Irradiation Embrittlement of a VVER-440 Surveillance Weld Irradiated at the Low and the High Fluxes*

From 1990 until 1996 from internal surfaces of RPVs of units 2, 3 and 4 of the Novovoronezh NPP (NV) and also units 1 and 2 of the Kozloduy NPP (KZY) small samples (templets) were cut out to evaluate the actual condition of RPV materials [2, 3]. For core welds of NV-4 and KZY-2 the DBTT values corresponding to the 1st cycle of irradiation were determined (Fig. 3). The actual values of irradiation embrittlement for NV-4 and KZY-2 were found to be higher than those calculated using the trend curve (2) and lower than the corresponding DBTT values estimated by trend curve (4), that is, by the upper 95% tolerance bound of the trend curve (2) for VVER-440 surveillance welds.

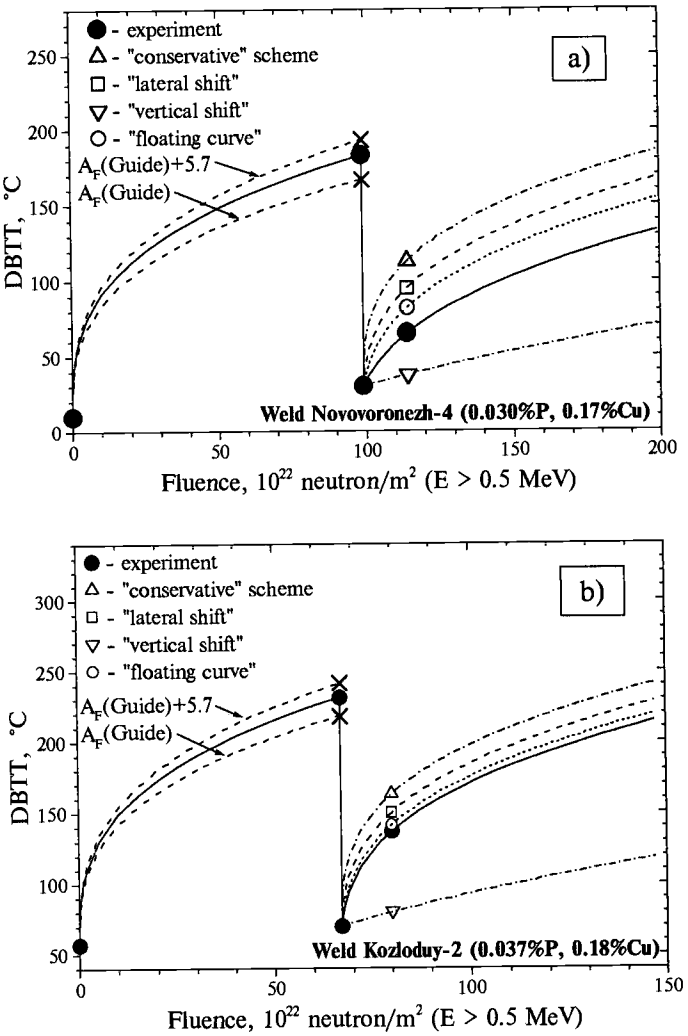


Figure 3 - *Comparison of the Experimental and Calculated DBTT Values of RPV Welds in Unirradiated, Irradiated, Annealed and Re-Irradiated Conditions. a) NV-4; b) KZY-2*

Embrittlement of VVER-440 RPV Steels under Re-Irradiation

Efficiency of post-irradiation annealing and, consequently, the lifetime of RPV materials in units operating after the annealing is defined by the following two factors:

1) by the degree of DBTT recovery or the residual irradiation embrittlement:

$$\Delta TT_{res} = TT_A - TT_0 , \quad (5)$$

where TT_A is DBTT of steel after post-irradiation annealing;

2) by the rate of embrittlement under re-irradiation:

$$\Delta TT_R = TT_R - TT_A , \quad (6)$$

where TT_R is DBTT of steel after re-irradiation.

From the beginning of 1988, VVER-440/230 RPVs were undergoing annealing with the minimum temperature of 460°C (12 pressure vessels including the repeated annealing of the unit 3 of the Novovoronezh NPP in 1991) at first for 150 and then for 100 hours. All the investigations carried out by the present time justified that annealing at a minimum temperature of 460°C for 100 h enables to achieve practically complete recovery of DBTT [2-5]. For steels with the phosphorus content less than 0.040% the residual shift after that regime of post-irradiation annealing does not exceed 20°C [4]. Thus, the DBTT of steel after annealing is defined by the following equation:

$$TT_A \leq TT_0 + 20°C. \quad (7)$$

It was also shown that annealing at 560°C for 2 hours resulted in complete recovery and sometimes to over-recovery of DBTT [8]. Since TT_0 values for VVER-440/230 RPV steels were not determined before beginning the NPP operation and the reference materials are not available it seems to be reasonable to assess TT_0 for those steels as the highest value between ($TT_A^{475°C}$ - 20°C) and $TT_A^{560°C}$. The TT_0 values used in Fig. 3 were determined by this way.

Nowadays, there are three standard approaches for assessment of re-irradiation embrittlement:

(I) The rate of embrittlement during re-irradiation at least is not higher than during the irradiation before annealing. Thus, the upper limit for re-irradiation kinetics is the "conservative" scheme (Fig. 4). In accordance with this scheme embrittlement rates under initial irradiation and re-irradiation are the same:

$$TT_R^C = TT_0 + \Delta TT_{res} + A_F \times \Delta F_R^{1/3}, \quad \Delta F_R = F_R - F_{irr} , \quad (8)$$

This equation has been applied in Russia in calculations of lifetime for RPVs annealed since 1987. However, this approach contradicts the mechanistic conceptions concerning the nature of irradiation embrittlement in RPV steels, because it does not follow adequately the processes of radiation damage and annealing of RPV steels.

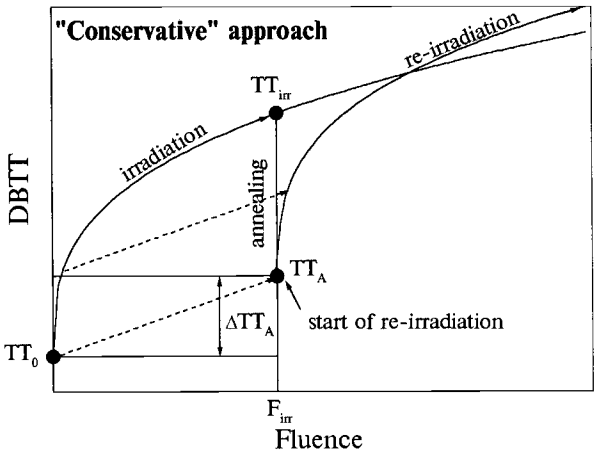


Figure 4 - *The "Conservative" Model of Embrittlement under Re-Irradiation*

(II) The re-embrittlement kinetics is hardly lower than the radiation embrittlement rate at the moment of annealing. This is the lower limit for re-irradiation embrittlement kinetics, known as the vertical shift approach (Fig. 5). According to the vertical shift approach:

$$TT_R^V = TT_0 + \Delta TT_{res} + A_F \times (F_R^{1/3} - F_{irr}^{1/3}) . \quad (9)$$

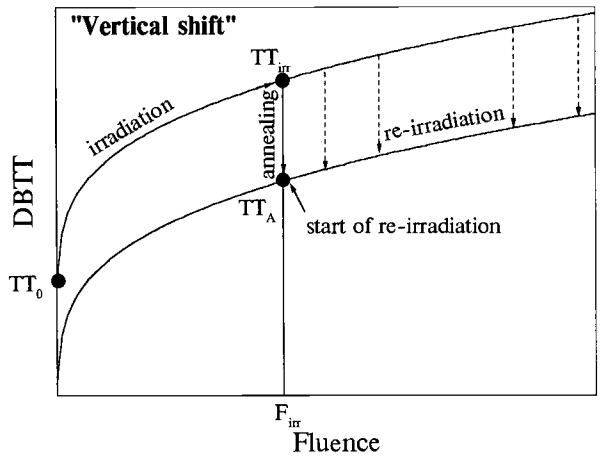


Figure 5 – *The Vertical Shift Model of Embrittlement under Re-Irradiation*

(III) An intermediate approach for re-irradiation embrittlement is the lateral shift model (Fig. 6). This model assumes that re-irradiation kinetics corresponds to the irradiation rate starting from the point when radiation embrittlement equal to the residual DBTT shift:

$$TT_R^L = TT_0 + A_F \times \{(\Delta TT_{res}/A_F)^3 + \Delta F_R\}^{1/3} = TT_0 + \{\Delta TT_{res}^3 + A_F^3 \Delta F_R\}^{1/3}. \quad (10)$$

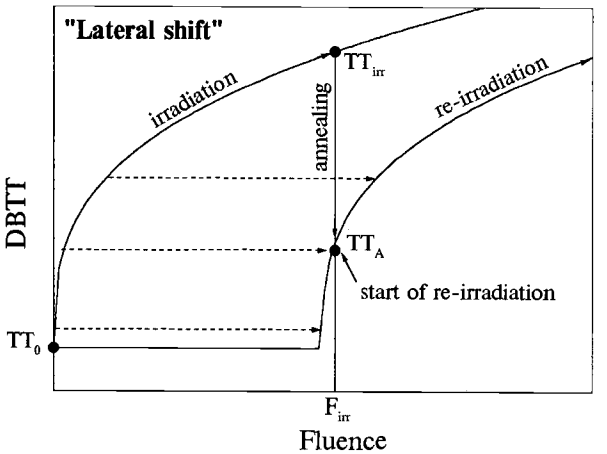


Figure 6 - *The Lateral Shift Model of Embrittlement under Re-Irradiation*

Re-irradiation behavior of RPV welds shown in Fig. 3 conforms with all other re-irradiation results:

1) the conservative approach (Fig. 7) and the lateral shift model (Fig. 8) estimate re-irradiation embrittlement completely conservatively;
2) the lateral shift model is less conservative than the conservative approach;
3) the vertical shift model (Fig. 9) completely underestimates re-irradiation embrittlement and cannot be used for prediction of re-irradiation embrittlement.

The best knowledge about the character of re-embrittlement kinetics can be obtained by numerical analysis in which experimental values of re-irradiation embrittlement are compared with the corresponding values calculated by different models. The results of such analysis are given in Table 1.

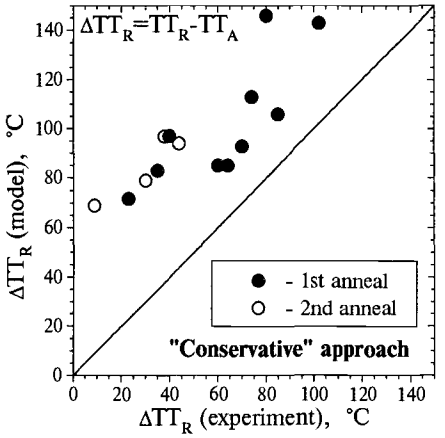


Figure 7 - *Comparison of Experimental Data on Re-Irradiation with Those Predicted Using the Conservative Model*

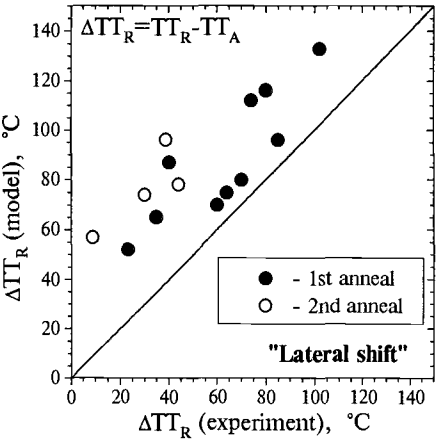


Figure 8 - *Comparison of Experimental Data on Re-Irradiation with Those Predicted Using the Lateral Shift Model*

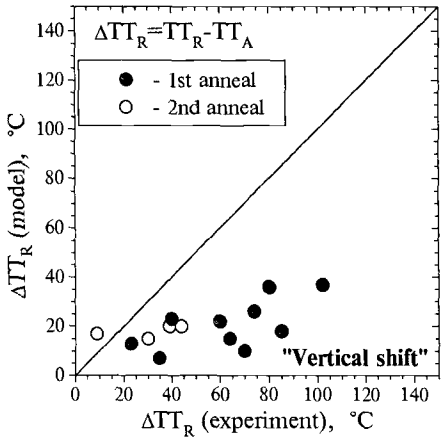


Figure 9 - *Comparison of Experimental Data on Re-Irradiation with Those Predicted Using the Vertical Shift Model*

TABLE 1 - *Comparison of the Quality of Different Models for Estimation of Re-Irradiation Embrittlement**

Model	1st cycle of re-irradiation (1st anneal) 10 experimental points		1st and 2nd cycle of re-irradiation (1st and 2nd anneal) 14 experimental points	
	σ, °C	$(\sigma/\sigma_{"C"})^2$ $(\sigma/\sigma_{"L"})^2$	σ, °C	$(\sigma/\sigma_{"C"})^2$ $(\sigma/\sigma_{"L"})^2$
Conservative scheme ("C")	44	1	47	1
Lateral shift ("L")	30	2.14 1	36	1.75 1
Floating curve ("FC") $\Delta T_S=\Delta T_{res}\times\exp[-(C_{Cu}-C_{Cu0})/A]$ C_{Cu0} = 0.24 %, A = 0.125%	20	4.99 2.33	27	3.19 1.83
floating curve with $\Delta T_S = \Delta T_{res} \times (C_{Cu0}/C_{Cu})$ C_{Cu0} = 0.30 %	20	4.99 2.33	27	3.15 1.81

* σ is standard deviation. $\sigma^2 = \frac{1}{N-1}\sum_1^N \left(\Delta TT_R^{experimen} - \Delta TT_R^{model}\right)^2$, where N is number of experimental points. $\sigma_{"C"}$ is σ for the conservative scheme, $\sigma_{"L"}$ is σ for the lateral shift model. Two models can be compared using the Fisher distribution. Fisher distribution coefficients for 9 and 13 degrees of freedom and for confidence levels of 0.05 and 0.20 are F(0.05,9,9) = 3.18 and F(0.05,13,13) = 2.58, F(0.20,9,9) = 1.79 and F(0.20,13,13)= 1.61. Model "A" is statistically significantly better than model "B" if $(\sigma_{"B"}/\sigma_{"A"})^2 > F$.

High rate of re-irradiation embrittlement, expected for core welds of some operating VVER-440/230 RPVs (unit 2 of Kola NPP), makes it necessary to develop a less conservative and more physically justified model of re-irradiation embrittlement. The common feature of the three approaches considered above is the same "chemistry factor" for irradiation before and after post-irradiation annealing. All these approaches are discrete in relation to the starting point of re-irradiation on the curve Eq. (1) used for estimation of initial irradiation embrittlement. At the present paper it was developed a new approach (Fig. 10) in which that point is not discrete but depend on chemical composition of steel (the floating curve model):

$$TT_R^{FC} = TT_0 + \Delta TT_{res} + \{-\Delta TT_S + A_F \times (\Delta F_S + \Delta F_R)^{1/3}\}, \quad (11)$$

$$\Delta TT_S = TT_A - TT_S = A_F \times \Delta F_S^{1/3}$$

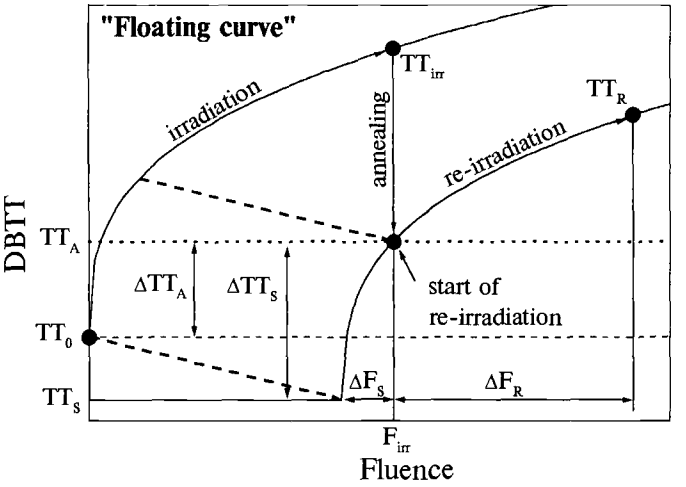


Figure 10 - *The Floating Curve Model of Embrittlement under Re-Irradiation*

ΔTT_S was found to be a function of copper content. The following basic functional forms were used for ΔTT_S fitting:

$$\Delta T_S = \Delta T_{res} \times \exp[-(C_{Cu}-C_{Cu0})/A] \quad (12)$$

$$\Delta T_S = \Delta T_{res} \times (C_{Cu0}/C_{Cu}) \quad (13)$$

The fitting parameters of the functions (12) and (13) were chosen to provide a conservative assessment of re-irradiation embrittlement. Two sets of experimental data were used for fitting these parameters. The first set included only results of the 1st cycle of re-irradiation (10 points including the results shown in Fig. 3) and the second set additionally included 4 results of the 2nd cycle of re-irradiation (14 points altogether). $\sigma_{"FC"}$ was found to be tolerant to variation of the fitting parameters of Eq. (12) in the region 0.23-0.25% for C_{Cu0} and 0.117-0.147% for A (Fig. 11). The parameters were chosen at the centre of this region. ΔT_S in the forms (12) and (13) provides nearly the

same results (Figs. 12a and 12b, respectively). Thus, ΔT_S slightly depends on functional form. The only common feature of Eq. (12) and (13) is dependence of ΔT_S on copper contents that results in increasing re-irradiation embrittlement with increasing copper contents.

The floating curve model provides better description of re-irradiation embrittlement than the conservative scheme and the lateral shift model (Fig. 12, Table 1). Thus, for evaluation of radiation embrittlement after post-irradiation annealing at 460-475°C the most appropriate model, describing dependence of transition temperature shift on damage dose, is the floating curve model.

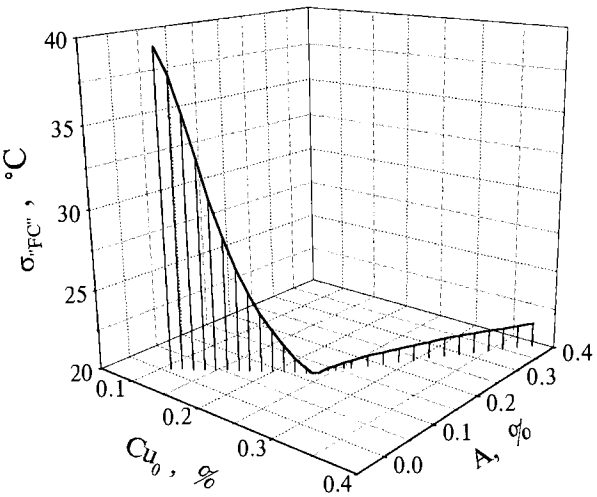


Figure 11 - *Variation of Standard Deviation $\sigma_{"FC"}$ for the Floating Curve Model with Variation of the Fitting Parameters of Eq. (12)*

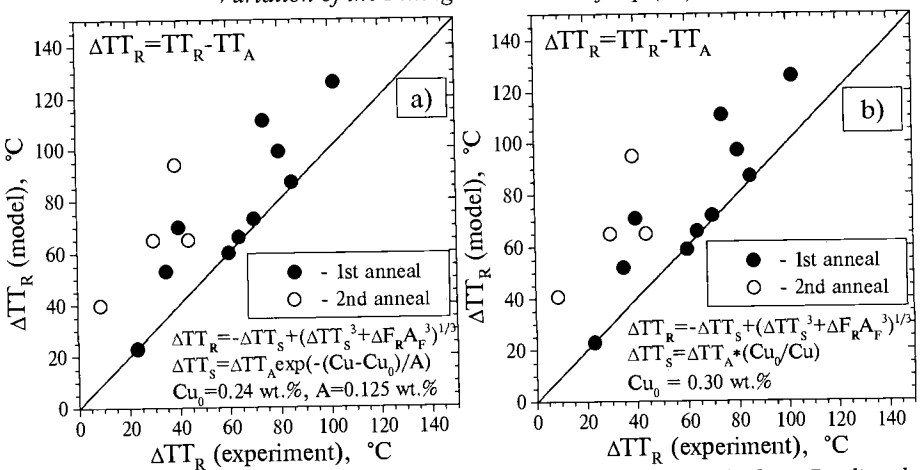


Figure 12 - *Comparison of Experimental Data on Re-Irradiation with Those Predicted Using the Floating Curve Model*

Conclusions

1. The trend curve specified in the Russian Guide for VVER-400 welds underestimates radiation embrittlement of VVER-440 surveillance welds.
2. A significant increase of irradiation embrittlement of a VVER-440 surveillance weld with decreasing neutron flux was observed.
3. A new approach (the floating curve model) for projecting re-embrittlement behavior after thermal annealing was proposed.
4. An increase of re-irradiation embrittlement with increasing copper content was suggested.
5. It was shown that the floating curve model estimates re-irradiation embrittlement better than the conservative approach and the lateral shift model.

References

[1] Alexeyenko, N.N., Amaev, A.D., Gorynin, I.V. and Nikolaev, V.A. *Irradiation damage of water-water reactor vessel steels.* Russia, Moscow, Energoatomizdat, 1981.

[2] Korolev, Yu.N., Kryukov, A.M., Nikolaev Yu.A., et al. Assessment of irradiation response of WWER-440 welds using samples taken from Novovoronezh unit 3 and 4 reactor pressure vessels. *Nuclear Engineering and Design*, 1998, v. 185, pp. 309-317.

[3] Korolev, Yu.N., Kryukov, A.M., Nikolaev, Yu.A., et al. The actual properties of WWER-440 reactor pressure vessel materials obtained by impact tests of subsize specimens fabricated out of samples taken from the RPV. *Small Specimen Test Techniques, ASTM STP 1329*, W.R.Corwin, S.T.Rosinski, and E. van Walle, Eds. American Society for Testing and Materials, Philadelphia, 1998, pp. 145-159.

[4] Amaev, A.D., Kryukov, A.M. and Sokolov, M.A. Recovery of transition temperature of irradiated WWER-440 vessel metal by annealing. *Radiation Embrittlement of Nuclear Reactor Pressure Vessel Steels. ASTM STP 1170*, L.E. Steele, Ed., American Society for Testing and Materials, Philadelphia, 1993, pp. 369-379.

[5] Kryukov, A.M., Nikolaev, Yu.A. and Nikolaeva, A.V. Behavior of mechanical properties of nickel-alloyed reactor pressure vessel steel under neutron irradiation and post-irradiation annealing. *Nuclear Engineering and Design*, 1998, v. 186, p. 353-359

[6] Hawthorne, J.R. Irradiation embrittlement. *Treatise on Materials Science and Technology*, C.L.Briant and S.K.Bunerji, Eds., 1983, v. 25, pp. 461-524.

[7] Nikolaeva, A. V., Nikolaev, Yu. A. and Kryukov, A.M. The contribution of grain boundary effects to low-alloy steel irradiation embrittlement. *Journal of Nuclear Materials*, 1994, v. 218, pp. 85-93.

[8] Leitz, C., Klausnitzer, E. and Hofmann, G. Annealing experiments on irradiated NiMoCr weld metal. *Effects of Radiation on Materials. ASTM STP 1175*, A.S.Kumar, D.S.Gelles, R.K.Nanstad and E.A.Little, Eds., American Society for Testing and Materials, Philadelphia, 1993, pp. 352-362.

Irradiation-Induced Behavior of Iron, Model Alloys, and Ferritic/Martensitic Alloys

R. Barry Jones,[1] James R. Cowan,[1] Robin C. Corcoran,[2] and John C. Walmsley[3]

Embrittlement, Hardening, and Grain Boundary Composition in an Fe-P-C Alloy after Irradiation or Thermal Aging

Reference: Jones, R. B., Cowan, J. R., Corcoran, R. C., and Walmsley, J. C., **"Embrittlement, Hardening, and Grain Boundary Composition in an Fe-P-C Alloy after Irradiation or Thermal Aging,"** *Effects of Radiation on Materials: 19th International Symposium, ASTM STP 1366,* M. L. Hamilton, A. S. Kumar, S. T. Rosinski, and M. L. Grossbeck, Eds., American Society for Testing and Materials, West Conshohocken, PA, 2000.

Abstract: An Fe-1200ppmP-30ppmC alloy has been examined after aging and irradiation exposure at 240°C. Thermal aging for 97 days reduced the yield stress by 10% but increased the 40J Charpy transition temperature by 50°C. Irradiation for a similar duration, in a highly thermalised neutron spectrum at $5.8 \pm 1.7 \times 10^{-11}$dpa/sec, increased both the yield stress by 15% and the transition temperature by 70°C. Longer irradiation, in spectra with or without the high thermal fraction, produced additional hardening but little extra embrittlement. Irradiation and aging gave a fivefold increase in the fraction of brittle intergranular fracture. Auger Spectroscopy showed that the P grain boundary monolayer coverage was virtually unchanged for all start-of-life, aging and irradiation conditions. In contrast, the C coverage reduced by 50% during the initial aging or irradiation, but changed little after longer irradiations. Grain boundary N increased initially but then stabilised. No grain boundary S occurred. Transmission microscopy revealed some dislocation loops and small regions of strain contrast in the grains after irradiation but no P-rich precipitates were seen. From this, and other published work, it is concluded that irradiation hardening arises from dislocation loops and possibly from P-rich cluster formation. Embrittlement developed due to loss of C from the grain boundaries, rather than from changes to the boundary P content. Loss of C reduced the boundary fracture stress but embrittlement was independent of the matrix strength. For the irradiation conditions examined, there was no evidence of irradiation-induced grain boundary P segregation.

Keywords: Embrittlement, hardening, irradiation, neutron spectra, thermal aging, iron alloy, phosphorus, carbon, intergranular fracture, grain boundary composition

[1]Irradiation Team Leader and Research Officer respectively, Materials Group, Integrity and Engineering Branch.
[2]Research Officer, Electron Optics Team, Nuclear Facilities Branch at BNFL Magnox Generation, Berkeley Centre, Berkeley, Glos, GL13 9PB, UK.
[3]Formerly at Berkeley Centre, now at SINTEF Materialteknologi, Trondheim, Norway.

Copyright© 2000 by ASTM International www.astm.org

The development of intergranular fracture during service exposure of ferritic steels in reactor pressure vessels (RPVs) and boilers is an important topic in assessing safety and future lifetime. Many studies have been made of the grain boundary segregation of phosphorus and the development of intergranular fracture in ferritic steels following high temperature exposure [1]. In order to understand the underlying mechanisms, intergranular embrittlement in Fe-P-C alloys during thermal aging at temperature >450°C has been extensively studied [2, 3, 4]. In addition, neutron irradiation of Fe-P-C alloys increased phosphorus segregation after a high dose exposure (9.94×10^{19} n/cm^2) at 395°C [5].

Significant intergranular embrittlement by phosphorus segregation in RPV submerged-arc weld surveillance samples has been detected after exposure for >20 years at temperatures of 360-392°C, these samples concurrently received a low neutron dose of about 20×10^{-5}dpa [6]. Subsequent examination of small submerged-arc weld and manual metal-arc weld samples removed from the inside surface of a high temperature region on an operational Magnox gas-cooled RPV has confirmed the occurrence of comparable high levels of intergranular phosphorus segregation after somewhat longer exposure times, at slightly higher dose levels and marginally lower temperatures [7]. Examination of the temperature dependence of the kinetics of phosphorus segregation and consideration of the minimum phosphorus level required to initiate intergranular embrittlement suggests that segregation by thermal diffusion of phosphorus is unlikely to be a problem for service exposures at 300°C, in accord with available long term data [6].

The possibility that grain boundary phosphorus segregation could occur by irradiation-enhanced phosphorus segregation processes during RPV operation at much lower exposure temperatures has been explored theoretically [8], by embrittlement modelling [9] and by the examination of surveillance and re-irradiated submerged-arc weld samples [10]. However, the levels of intergranular phosphorus observed [10] are lower than those found after higher temperature thermal exposure [6, 7]. In some cases the levels may be comparable with those determined on start-of-life weld samples that have been subjected to vessel post-weld stress-relief treatments at temperatures of 550-600°C followed by slow cooling at 4.5°C/hour [11]. Consequently, the evidence for irradiation-enhanced intergranular phosphorus segregation is less well established and further work is needed.

A series of irradiation and thermal aging experiments have been performed on a high purity Fe-P-C alloy to examine the irradiation-enhanced phosphorus segregation mechanism and its influence on embrittlement. Pre-exposure and post-exposure tensile, hardness and Charpy impact tests have been combined with transmission electron microscopy of the grains, scanning electron microscopy of fracture surfaces and determinations of grain boundary composition using scanning Auger electron spectroscopy.

Experimental Details

Alloy Fabrication and Composition

An iron alloy containing about 30ppm carbon and 1200 ppm phosphorus was fabricated

as one half of a split melt prepared from Japanese high purity iron stock by British Steel Technology, Rotherham, UK. An ingot of 25 kg was vacuum cast, surface ground, upended by 50%, hot forged to a section size of 50mm x 100mm at 1030°C, hot rolled from 1180°C to 30mm x 100mm x 380mm plate and air cooled. The composition, in weight percent, is shown in Table 1 below.

Table 1 - *Compositions (weight %) of the Fe-P-C alloy*

Alloy	C	Si	Mn	P	S	Cr	Mo	Al
B	0.003	0.01	<0.02	0.12	<0.002	<0.02	<0.005	<0.005

In addition for the original iron stock: Ni = 0.03%, Cu = 0.006%, Nb, Sn, V, W each <0.005%, Ti and O each = 0.03%, and N < 0.0015%. For alloy B the use of the neutron irradiation/He mass spectometry analytical method for boron [12] gave B = 0.15ppm.

Test Piece and Procedures

Standard Charpy samples 10mm x 10mm x 55mm were machined from two layers in the plate with the long axes of the samples parallel to the plate rolling direction. Layer 1 samples came from the top and layer 2 samples from the bottom of the plate. The notches were cut in the top (layer 1) and bottom (layer 2) plate surfaces. Charpy tests were performed on unirradiated, aged or irradiated samples at temperatures ranging from -50°C to +150°C using an instrumented machine. After testing, some of the broken halves of brittle Charpy samples were machined into mini-tensile samples with a gauge diameter of 4.5 mm and gauge length of 16 mm; these were tested to failure at ambient temperature on a shielded Instron 1273 machine at a strain rate of 3.4×10^{-4} sec^{-1}.

Irradiation and Aging Conditions

Irradiations were performed under accelerated conditions in the reflector of the Halden heavy-water moderated reactor in Norway. The Fe-P-C Charpy samples, were loaded axially in contact with alumimium bodies in close-fitting zirconium alloy tubes together with full length dosimeter wires and other ferritic materials as part of a wider irradiation programme [13]. The sample tubes were immersed in the moderator water which was at 231-238°C; the maximum irradiation temperature of the samples was 240°C after including a calculated allowance for nuclear heating. Exposures were made in neutron spectra characterised by both high thermal dpa/fast dpa ratios of 1.5-2.3 and low ratios of 0.012, where "fast" dpa were calculated from the ASTM dpa cross-section for iron using neutrons >1keV in energy, and "thermal" dpa from those with energies <1keV (see "Nuclear

Standards, Standard Practice for Characterising Neutron Exposures in Ferritic Steels in Terms of Displacements-per-Atom," ASTM E693-79, Re-Approved 1985). To obtain the low ratio spectra the thermal neutrons were absorbed by a thin axial cadmium shield located between the zirconium tube and the aluminium bodies holding the samples.

Irradiation exposures in the high ratio spectra were made in Rigs 1, 2A and 2 for 97, 85 and 251 days respectively; for the Cd-shielded low ratio spectrum used for Rig 3 the exposure was for 154 days. The fast dpa dose rate for all the rigs was in the range $5.8\pm1.7\times10^{-11}$ dpa/sec. At the end of an irradiation the samples were allowed to cool to room temperature over about 23 hours inside the reactor and then discharged. Although the dose to each Charpy sample was determined, average doses are quoted for the batches used for impact testing; for the mini-tensiles the individual doses of the source Charpy samples are used.

Thermal aging exposures on Charpy samples were performed at 240±3 °C for times of 100 and 97 days respectively followed by cooling in the furnace to reproduce the cooling rate experienced by the irradiated samples. During the 100 day exposure the furnace records showed that a heating and cooling transient to <320 °C over a period of several hours had occurred; to remove uncertainty, a repeat treatment for 97 days was performed on new specimens.

Microstructural Examination

Optical examination revealed that the mean linear intercept grain size was 80μm. Scanning electron microscope (SEM) examination was used to determine the respective proportions of cleavage, intergranular and ductile microvoid coalescence fracture modes present on the broken Charpy samples using the method described by Bischler and Wild [10]. Charpy samples fractured on the lower shelf of the transition curve were used in this investigation. Transmission electron microscopy (TEM) was performed on thin foil samples prepared from both as-received and irradiated samples using a JEOL 3010 operated at 300kV.

Auger Electron Spectroscopy (AES)

Auger Electron Spectroscopy (AES) has been used for analysis of grain boundary fracture surfaces because of its surface sensitivity (3-10 atomic layers) for elements of interest (mainly P, C, N, S and Fe). Analysis has been performed using a Vacuum Generators 310-F Scanning Auger Microprobe fitted with a Field Emission Gun source (FEG) calibrated using known standards for P, C, Fe and other elements. Specimens, in the form of $2\times2\times10$ mm^3 'matchsticks', were cut from the undeformed ends of the unaged, aged or irradiated Charpy samples and notched to facilitate low temperature brittle fracture. Samples were fractured, using an impact fracture stage operated under high vacuum conditions, at liquid nitrogen temperatures to give a brittle fracture surface. Auger analysis

was performed on several areas on the specimen, approximately 6 intergranular and 6 cleavage facets being analysed per area. Facets were identified either by observation, i.e cleavage fractures contained river lines and intergranular fractures were featureless, or by the use of P mapping techniques. The resulting spectra were recorded in the direct form, with quantitative analysis being carried out by determining the areas under the peaks [14].

Carbon contamination of the sample may occur during examination and this may be allowed for by making carbon measurements periodically on cleavage facets. In practice low levels of carbon contamination are found; the data are used to remove any contamination contribution in the intergranular carbon measurements permitting a true carbon segregation level to be measured [14].

Results and Analysis

Charpy Tests

Figure 1 shows all the available Charpy energy-absorbed results plotted against the test temperature for the respective start-of-life, aged and irradiated conditions. As the Charpy data for the various irradiated samples were quite similar, a single line has been used to represent the data trend in Figure 1. In general, within a narrow test temperature range the Charpy curves show a steep energy transition from ductile, high energy failure to brittle, low energy failure. There appears to be no change in the shape of the Charpy curve as the thermal or irradiation exposures are altered but the curves are shifted to higher test temperatures compared to start-of-life. The high energy upper shelf is not degraded by the treatment received but the upper shelf energy falls continuously as the test temperature is raised. The variation of the 40J transition temperature with aging or irradiation exposure is shown in Table 2. These transition temperatures have been obtained by fitting the test result with the tanh function [15]; in the analysis the observed slight reduction in upper shelf with test temperature was approximated by an upper shelf which was independent of test temperature. Because the 40J temperature is so close to the lower shelf in some instances, values are also quoted in Table 2 for a mid-transition temperature criterion (i.e. the temperature at the energy mid-way between upper and lower shelf values) obtained from the tanh fits.

The results show that thermal aging at 240°C produces a large change in the transition temperature criteria, a **total** transition shift of 50°C being found. This implies that the start-of-life material was not in a stable metallurgical condition when subjected to the various irradiation exposures, which is an important conclusion affecting the subsequent interpretation of the irradiated data. In relation to the data for the aged material, then the Rig 1 exposure has only produced an **additional** shift of 21°C. When the results for the other irradiation exposures are considered then it is found that the additional shifts are all similar to those for Rig 1. In other words, more than doubling the dose (as in Rig 2) or changing the spectrum (as in Rig 3) has not altered the transition temperatures significantly from those obtained in Rig 1. This implies that the transition temperature shift has saturated. This

behaviour is illustrated in Figure 2 by plotting total transition shift as a function of the exposure time, and in Figure 3 by plotting the additional shift as a function of dose.

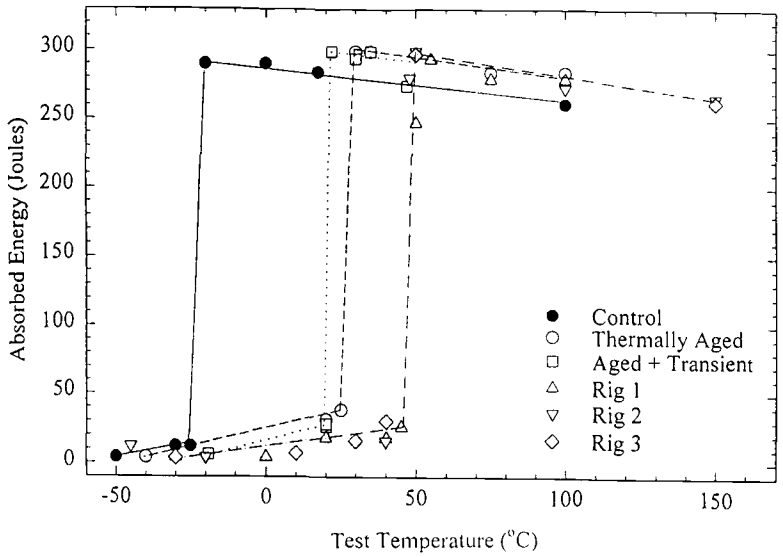


Figure 1 - *Charpy curves for start-of-life, aged, and irradiated Fe-P-C. For clarity, the irradiated data have been approximated by a single Charpy curve.*

Table 2 - *Charpy Transition Temperatures for Fe - 1200ppm P - 30ppmC*

Samples	Aging or dose (dpa x10^5) fast thermal	T_{40J} °C	T_{mid} °C	ΔT_{40J} °C	ΔT_{mid} °C
As fabricated	--	-25	-24	0	0
Aged*	100 days	21	21	46	45
Aged	97 days	25	25	50	49
Rig 1	47 86	46	48	71	72
Rig 2	119 242	41	41	66	65
Rig 3	80 1.0	40	41	65	65

*Includes a brief thermal transient

Fracture Mode

The data from the SEM examination of lower shelf Charpy sample fracture surfaces are

listed in Table 3. In the as-fabricated condition a significant level (10%) of intergranular fracture is present. After either aging or irradiation exposures a significant increase in the intergranular fracture component was found to levels of about 50%.

Auger Spectroscopy

Auger analyses for intergranular levels of P, C and N on the samples are shown in Table 4. The P and C results are expressed as monolayer coverages whereas the level of N is given in atomic % as there is no specific monolayer conversion factor. Grain boundary segregation of S was not detected. The compositional trends for P and C are illustrated in Figure 2, as a function of the respective aging or irradiation exposure times and the trends may be compared with that for the Charpy shifts. The monolayer coverage of P is close to 0.40 and does not change significantly with either aging or irradiation exposure. In contrast the monolayer coverage of C shows a progressive reduction in magnitude from 0.44, in the unirradiated as-fabricated condition, to 0.16 for the highest dose sample with a clear trend towards the coverage stabilising. The intergranular N (representative of one grain face) also showed an similar trend towards a stabilising value with exposure but in this case it increased markedly to saturate at 1.47atom %N, i.e. about sixteen times its start-of-life level of 0.09 atom %N. The intergranular C:N atom ratios in the higher dose samples are about 2.5-2.8.

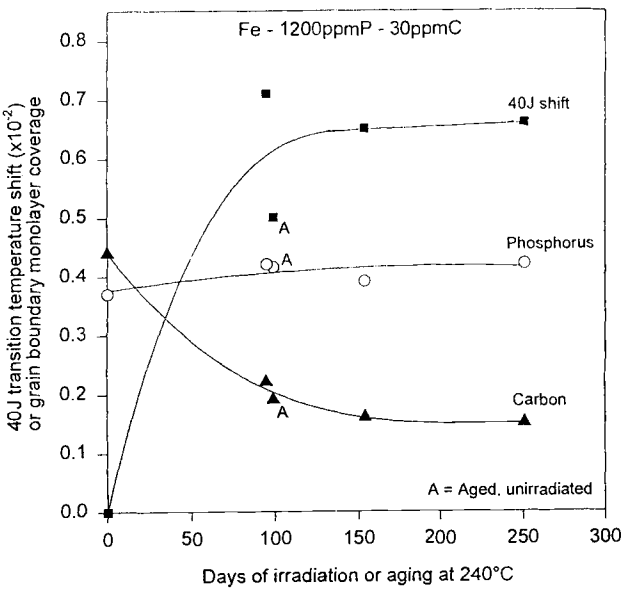


Figure 2 - *Effect of irradiation or aging exposure on the shift in 40J Charpy transition temperature and on the respective grain boundary monolayer coverages of P and C*

Table 3 - *Analysis of the Fracture Modes in Fe - 1200ppmP - 30ppmC*

240°C exposure	Sample, 10^{-5}dpa dose & test °C	Intergranular %	Cleavage %	Micro-void coalescence %	Other %
As fabricated	2/8, zero -50°C	10.4	86.1	2.9	0.6
Rig 1	1/1, 49f, 89th 40°C	48	49	1	1.5
Aged* 100days	1/21, zero -19°C	34.8	62.7	1.2	1.3
Aged 97 days	2/15, zero -40°C	46.9	42.3	9.6	1.2

* Aging includes thermal transient

Table 4 - *Auger Analysis of Grain Boundaries in Fe - 1200ppmP - 30ppmC*

Sample layer/number	Dpa ($x10^5$) or aging time at 240°C	P_{true} monolayer	C_{true} monolayer	N_{true} atom%
FeP 2/8-1 Fe/P2/8-2	Unirradiated, as fabricated	0.38 ± 0.07 0.36 ± 0.06	0.44 ± 0.09 0.43 ± 0.06	0.26 ± 0.15 0.09 ± 0.08
FeP 1/18	100days*	0.44 ± 0.09	0.19 ± 0.07	1.32 ± 0.62
FeP 2/21-1 FeP 2/21-2	97 days	0.42 ± 0.10 0.39 ± 0.08	0.18 ± 0.08 0.20 ± 0.09	1.08 ± 0.57 1.41 ± 0.58
FeP 1/1a FeP 1/1b (Rig 1)	89_{fast} $+ 49_{thermal}$	0.43 ± 0.08 0.41 ± 0.06	0.18 ± 0.06 0.24 ± 0.10	1.43 ± 0.48 1.86 ± 0.83
FeP2/4-1 FeP2/4-2 (Rig 2)	131_{fast} $+276_{thermal}$	0.40 ± 0.06 0.46 ± 0.07	0.13± 0.06 0.17 ± 0.08	1.60 ± 0.68 1.22 ± 0.63
FeP2/13-1 FeP2/13-2 (Rig 3 + Cd)	74_{fast} $+ 0.9_{thermal}$	0.42 ± 0.09 0.40 ± 0.04	0.18 ± 0.05 0.18 ± 0.08	1.51 ± 0.56 1.62 ± 1.01

* Aging includes brief thermal transient

Tensile Properties

The load extension diagrams on all the Fe-P samples tested at ambient temperature showed upper and lower yield points associated with Luders extension. The yield, ultimate strength, hardness and ductility properties are shown in Table 5. All samples showed considerable ductility and this property seemed to be only marginally degraded by thermal aging or irradiation. Prolonged aging at 240°C produced a slight reduction in both the hardness and yield stress of the unirradiated samples; consequently the mean value of the four **aged** yield stress values is used as the unirradiated control for comparison with the irradiated values. A similar procedure was used for the UTS values.

Table 5 - *Tensile and Hardness Properties for Fe-1200ppmP-30ppmC*

Alloy Layer and Treatment	Spec	σ_y MPa	$\Delta\sigma_y$** MPa	σ_u MPa	$\Delta\sigma_u$**	ϵ_u %	ϵ_T %	VHN
layer 1	1/9	205	-	336	-	25.9	50.3	126.4
	1/9a	208	-	338	-	23.9	47.8	
layer 2	2/10	196	-	334	-	25.7	48.3	-
	2/10a	204	-	338	-	23.1	48.3	
Irrad 1, layer 1	1/4	218	27	n/a	-	n/a	n/a	
60f, 94th	1/4a	224	33	354	17	20.6	36.2	
Irrad 1, layer 1	1/7	219	28	348	11	20.6	43.1	-
34f, 79th	1/7a	216	25	346	9	21.4	40.9	-
Irrad 2, layer 2	2/1	243	52	358	21	19.2	47.4	-
158f, 243 th	2/1a	247	56	362	25	18.2	39.4	-
Irrad 2A, layer 2	2/17	220	29	337	0	19.7	40.6	-
55f, 91th	2/17a	220	29	339	2	20.1	41.1	-
Irrad 3, layer 1	1/12	210	19	334	-3	21.2	45.9	-
85f, 1.0 th	1/12a	216	25	338	1	20.8	43.4	-
Th-aged, layer 1		194	-	341	-			111.0
240°C 100		194	-	338	-			
days*								
Th-aged, layer 2		192	-	335	-			116.5
240°C 97 days		184	-	334	-			

*Includes brief thermal transient.

**Control values obtained from the 97-100 day thermal aging data, i.e σ_y = 191 MPa, σ_u = 337 MPa.

Irradiation exposure produced increases in yield stress that were dependent on both the neutron spectrum used and the dose received. The dose dependence of the yield stress increase ($\Delta\sigma_y$) is commonly expressed using a square root of dose law (7, 9), however if only the "fast" dpa component of the dose (D_{fast} with D in units of 10^{-5} dpa) is employed,

the Fe-P-C values do not conform to a single dose relationship. Although the hardening response of the samples exposed to highly thermalised neutron spectra conform to a simple dose law, those from the Rig 3 Cd-shielded experiment exhibit significantly smaller hardening. Other work [13] has shown that the hardening produced from thermal dpa damage is additional to that from fast dpa; the most appropriate way of adding the damage is by combining the doses in the form ($D_{fast} + 2.0D_{thermal}$). If the yield stress shift is replotted in this way the irradiation hardening at 240°C is given by the equation

$$\Delta\sigma_y = -1.01 + 2.09\sqrt{(D_{fast} + 2.0D_{thermal})} \quad (1)$$

as shown in Figure 3. This gives a good fit to all the results and it is clear that there is no sign of any saturation in the "square root of dose" dependence of the irradiation hardening at the higher dose levels.

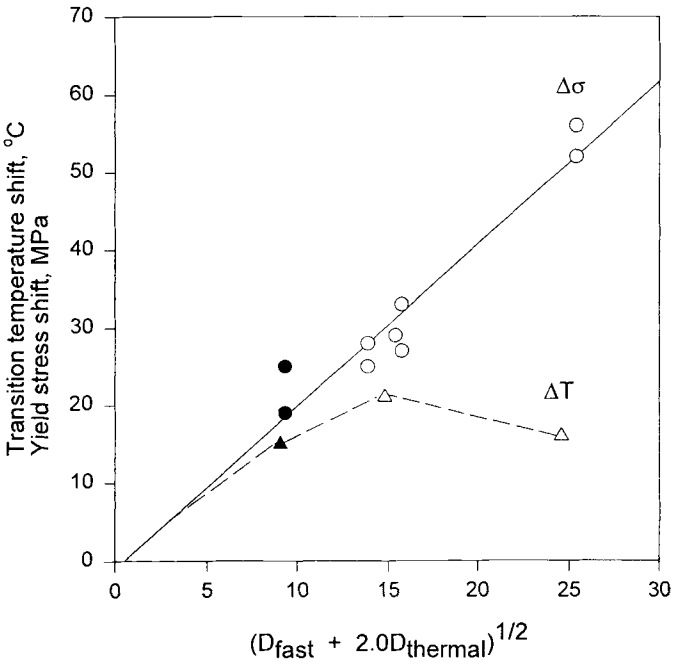


Figure 3 - *Yield stress shift and transition temperature shift plotted as a function of the square root of the "effective" dpa dose, where effective dpa = $dpa_{fast} + 2dpa_{thermal}$. Both sets of shifts have been calculated using control values derived from thermally aged samples. The filled symbols refer to data from Cd-shielded irradiations. A regression line is shown for the yield stress shifts while a data trend line is shown for the Charpy shifts.*

Electron Microscopy

Some preliminary observations have been made on thin foils prepared from the unirradiated material (FeP2/8) and from the Rig 1 irradiation exposure (FeP1/1). The unirradiated microstructure is free of matrix and grain boundary precipitation. Some small dislocation loops were seen, with a mean diameter (d) of 13nm and a number density (N_v) of $0.7x10^{20}m^{-3}$, which exhibited inside-to-outside contrast behaviour on reversal of the diffraction vector. The irradiated sample, see Figure 4, exhibited a rather irregular distribution of larger dislocation loops, d = 21nm, $N_v = 1.7x10^{20}m^{-3}$ together with dislocation pinning at unresolved obstacles. Dark field imaging showed the presence of features which exhibited distinct strain-contrast but were too small to allow their structure to be resolved. FEGSTEM analysis confirmed the presence of small dislocation loops but failed to find any phosphorus-rich precipitates.

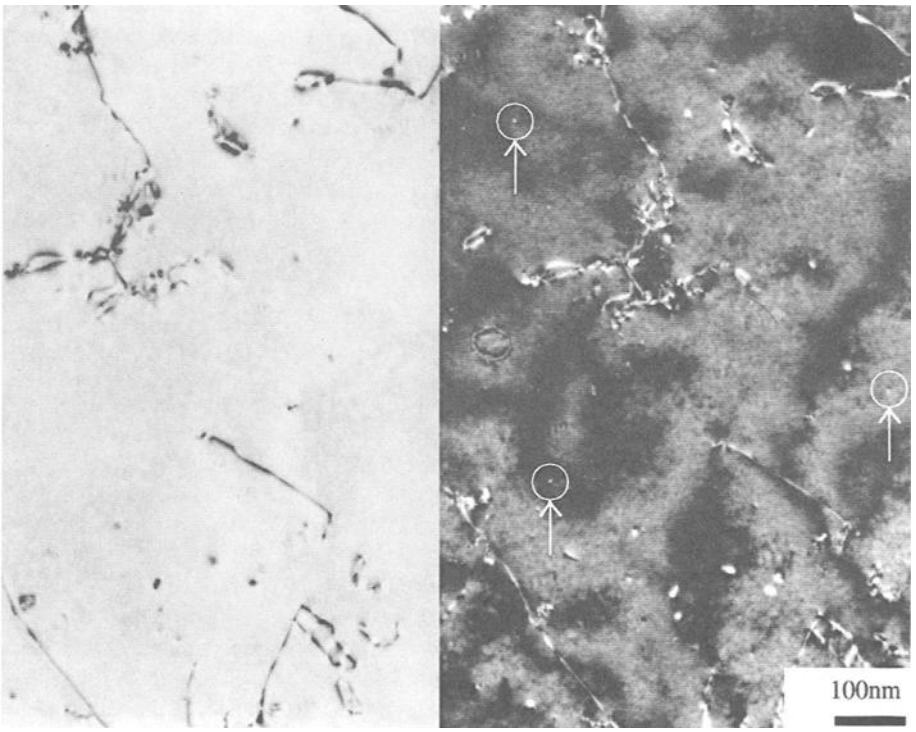


Figure 4 - *Bright (a) and dark field (b) images of irradiated FeP-C alloy. Line dislocations, dislocation loops and regions of strain contrast (arrowed) are visible.*

Discussion

Yield Strength Changes

The analysis of yield stress as a function of neutron dose is based on the assumption that thermal aging for time periods longer than 100 days does not result in any further change in the unirradiated yield stress. Although this seems reasonable, on the basis that, compared with start-of-life values, aging-induced reductions in yield stress were relatively small (13MPa) compared with the increases due to irradiation (25-40MPa), it would be prudent to obtain tensile or hardness data after 250 days aging to support this view.

To address the question of whether P is affecting the irradiation hardening it is important to distinguish between effects due to solute clustering or precipitation and processes influencing the matrix. Although no P-rich precipitation could be detected in the present Fe-P-C alloy, observations of P-rich clusters using FIM techniques have been made in low Cu, P-containing steels by Pareige et al [16] or in P-doped Fe alloys by Miller et al [17] respectively, after irradiation at 288°C to doses between ten and one hundred times in excess of those in the current work. At high doses the number density of solute-rich clusters generally increased with additional irradiation [16]; this implies that the number density of any P-rich clusters in Fe-P-C would be small at the doses characteristic of the current experiments.

With regard to the possible influence of P-rich clusters on matrix hardening it is useful to compare the current results with the data of Miller et al [17] and Takeyama et al [18] on Fe-P-C alloys irradiated to differing doses at 288°C and 200°C respectively. It is possible to compensate for the differing irradiation conditions using the equation

$$\Delta\sigma_y = AF_T\sqrt{(D)} \qquad (2)$$

where D is dpa dose (expressed in units of dpa $x10^5$) and $F_T = 1.869\text{-}4.57x10^{-3}T_{irrad}$ [19]. With regard to the dose units, dpa may be calculated using the conversion dpa = $(E>1MeV)n/cm^2$ x 2.14 $x10^{-21}$ for water reactor spectra [17, 18]. In Table 6 the values of A (from equation 2) are evaluated for all the results and are shown in relation to the levels of C and P in the alloys. The results indicate that the value of the matrix hardening coefficient (A) is affected by both C and P contents. At low P contents of 0.001%, reducing the C content reduces the irradiation hardening coefficient, while at low levels of C (0.003-0.008%), increasing P from 0.001% to 0.12% increases the irradiation hardening coefficient by at least a factor of three. The available data is insufficient to establish the precise compositional dependencies of the irradiation hardening for these elements but it can be concluded that for Fe with 30ppmC there is a strong P-dependence of the hardening coefficient.

The observed irradiation hardening may also be examined in relation to the microstructural features observed by TEM. The irradiation hardening due to a population of loops of diameter d and number density N_v is given by the equation

$$\Delta\sigma_y = \alpha\mu b\,(N_v d)^{1/2} \qquad (3)$$

as used by Takeyama et al [18] with $\alpha = 0.5$, shear modulus $\mu = 8.3 \times 10^4$ MPa, and Burgers vector b = 0.248 nm. The irradiation hardened Fe-C used by Miller et al [17] has been examined by Hoelzer and Ebrahimi [20] and the loop population characterised. Similarly, data is available on the irradiation-induced loops in the Fe-C studied by Takeyama et al [18]. These results, together with the initial data available on the current Fe-P-C alloy, are listed in Table 7 along with a calculation of the hardening predicted from equation (3) and comparisons with observed values.

Table 6 - *Irradiation Hardening Data for Fe-P-C Alloys*

Source	C wt%	P wt%	T_{irrad} °C	n/cm^2 >1MeV	D, dpa x10^5	$\Delta\sigma_y$ MPa	A value (eq 2)
Miller* [17]	0.013	0.003	288	4.63 x10^{19}	9908	105	1.91
Take'ma [18]	0.012	0.001	200	6.4 x10^{18}	1370	91	2.57
Take'ma [18]	<0.008	0.001	200	6.4 x10^{18}	1370	30	0.85
This work	0.003	0.12	240	-	644 max**	56 max	2.71***

* More modern data from [20] used for chemical compositions
** combined thermal and fast dpa *** derived from equation 2

Table 7 - *Comparison of Predicted and Observed Hardening*

Alloy/Ref	Mean loop diameter, nm	Loop number density, m^{-3}	Predicted $\Delta\sigma_y$, MPa	Observed $\Delta\sigma_y$, MPa
Miller [17], Hoelzer [20] Fe-0.013%C	8.6	3.7 x 10^{21}	58	105
Takeyama et al [18] Fe-0.012%C	33	1.0 x 10^{21}	59	91
Fe-P-C, this work, Rig 1	21	1.7 x 10^{20}	10-17*	25-33

*depending on whether the $(N_v d)^{1/2}$ unirradiated loop correction was performed by the linear or root sum of squares method

In general, the calculated loop hardening is between 59% and 65% of that observed in both the irradiated Fe-C alloys. For the Fe-P-C the limited loop data shows that the loop

size is similar to that in the Fe-C alloys with no evidence for the significant reductions in loop diameter found after neutron or electron irradiation when other solutes (such as Mn, Cu or Ni) are added to Fe [17, 18]. The predicted irradiation hardening in Fe-P-C is of the correct magnitude but again is less than that actually measured. With the limitations in the current microscopy data it is not possible to judge the degree of hardening underprediction; with more comprehensive data (from both Rig 1and higher dose exposures in Rigs 2 and 3) it might be possible to decide if the evidence from the loops supported the possibility of an additional hardening contribution from small P-rich clusters.

Embrittlement

Irradiation embrittlement (ΔT_{40J}) is often related to the irradiation hardening ($\Delta\sigma_y$) by [19]

$$\Delta T_{40J} = K \Delta\sigma_y \quad (4)$$

where K = 0.5 for plate steels and Fe alloys. For the Fe-P-C alloy this simple behavioural pattern is not observed. Initially, the irradiation embrittlement is large but the irradiation hardening of the grains is comparatively small. Although the irradiation hardening continues to develop steadily at higher irradiation doses, the increments of embrittlement become smaller and appear to saturate (see Figure 3). In contrast, thermally aged samples show significant embrittlement but this is associated with a reduction in grain strength. The main conclusion from these observations is that embrittlement is occurring by processes which are largely independent of the strength of the grains. The embrittlement mechanism responsible is associated with an increasing incidence of intergranular fracture that is brought about by a reduction in the fracture strength of the grain boundaries due to changes in the grain boundary concentration of various impurity elements. The elements of importance in this context are C and N as grain boundary strengtheners compared with P and S as grain boundary embrittlers. These elements need to be considered both individually and in combination.

The current investigation has shown three main changes in the grain boundary segregation levels for the Fe-P-C alloy following isothermal aging or irradiation exposure at 240°C. Firstly, there was no significant variation in grain boundary P segregation, with the final levels similar to those present at start-at-life. Secondly, there was a progressive decrease in the level of grain boundary C compared with levels at start-of-life. Finally, there was a significant increase in the level of grain boundary N compared with start-of-life.

It is instructive to compare these findings with previous work on Fe-P-C alloys after both thermal aging and irradiation exposures. The well documented antagonistic reaction between P and C at grain boundaries during aging in Fe alloys, which has been explained in terms of either P and C site competition [21] or a repulsive chemical interaction between P and C [22], results in one solute displacing the other from grain boundary sites. Following aging or irradiation, the observed reduction in grain boundary C should have lead to an increase in the observed grain boundary P coverage, but this did not occur. In the thermally aged condition the absence of any increase in the grain boundary P is not surprising because of the low thermal diffusion coefficient of P at 240°C. In order for P segregation to

increase within reasonable timescales at this temperatures, it is necessary to enhance the diffusion rate of P. It is generally expected that any effect of irradiation on P segregation should be manifest through a kinetic effect [8] resulting in increased transport of P to grain boundaries. However, there was no apparent increase in P segregation after irradiation at 240°C.

One possible explanation of this finding is that any irradiation enhancement of P segregation in the current work is too small to significantly change the level of grain boundary segregation. Given that the irradiation enhancement of grain boundary P found in the work of Kameda et al [5] came from the use of higher temperatures and higher neutron doses, this may not be surprising. Another possibility is that the level of grain boundary segregation at 240°C is already saturated at the equilbrium level (for a bulk P content of 1200ppm); this seems unlikely given that equilibrium grain boundary P levels increase as the aging temperature decreases, and P levels exceeding 0.56 monolayers have been measured in a related Fe-600ppmP-20ppmC alloy after aging at 475°C [4]. An alternative explanation is that the equilibrium level of free P, in solid solution and available to segregate, may have been reduced by irradiation exposure due to the removal of P from solid solution to form P-rich clusters [16, 17]. Currently, there is no direct evidence for P-rich clusters in the Fe-P-C alloy under the particular 240°C irradiation conditions considered. Without information on cluster size or number density the latter possibility cannot be evaluated further.

The effect of irradiation on P and C segregation has been examined by Kameda et al [5] using Fe-base alloys with comparable levels of S (0.002wt%) and containing a range of P levels from 0.004 - 0.054%, which had been irradiated to a larger dose ($9.4x10^{18}n/cm^2$ E>0.1MeV) and at a higher irradiation temperature of 395°C compared with the current investigation. In irradiated alloys with high bulk P levels intergranular P segregation was shown to occur, possibly at the expense of S segregation (which itself occurred in alloys with low bulk P). An increase in the bulk C content from 10ppm to 912 ppm changed the brittle fracture mode from intergranular to cleavage in an irradiated high P alloy, presumably due to a P-C competition effect. Irradiation had no effect on the grain boundary N content. The current results are somewhat different, with no effect of irradiation on P segregation, the absence of any significant S segregation and an increase in N segregation. However, both pieces of work show similar effects due to C; the current work demonstrating an increase in intergranular brittleness with decreasing C levels on the grain boundaries while that of Kameda et al showed a reduction in intergranular brittleness with an increase in bulk C and, by implication, an increase in grain boundary C level.

The increasing levels of intergranular fracture, and the resulting upward shift in Charpy transition temperature, are clearly related to the loss of C from the grain boundaries with the consequent reduction in the grain boundary fracture stress [1]. The mechanism by which C is being removed from the grain boundaries is not clear. Under thermal aging conditions the possible precipitation of carbides in the grains might be a mechanism for removing previously segregated C from the grain boundaries, but the results of the current electron microscope examinations, and the absence of age hardening effects, have not provided convincing supporting evidence. For the irradiated specimens there may be an additional mechanism for reducing the grain boundary C; this arises from the report [16] that significant levels of C have been detected by atom probe measurements on irradiation-

induced P-rich clusters.

Conclusions

1. The Charpy impact transition temperature of an Fe-0.12%P-0.003%C alloy increased by 50°C and the yield stress decreased by 20MPa after thermal aging for 97 days at 240°C. An irradiation of similar duration at an average dose rate of 5.8×10^{-11} dpa/sec in a spectrum where $dpa_{thermal}/ dpa_{fast} = 2$, produced a 70°C Charpy transition temperature increase and about 30MPa irradiation hardening.

2. Higher dose irradiations in neutron spectra, both with and without the thermal neutrons, produced additional irradiation hardening but little further embrittlement. Hardening increased with the square root of the effective neutron dose given by $dpa_{fast} + 2dpa_{thermal}$.

3. Both thermal embrittlement and irradiation embrittlement were associated with an increase from 10% to 50% in the fraction of intergranular fracture detected on the brittle fracture surfaces of lower Charpy shelf samples.

4. Auger spectroscopy showed that the grain boundary monolayer coverage of P remained close to 0.40 for all start-of-life, thermal aging and irradiation conditions. However the monolayer coverage of C decreased from 0.40 to about 0.20 during a 97 days aging or irradiation period, but then remained almost constant for longer irradiation periods. Some nitrogen, but no sulphur, segregation to grain boundaries was detected.

5. Transmission microscopy failed to find evidence of P-rich precipitates after irradiation but some dislocation loops and small regions of strain contrast were detected in the grains.

6. From comparisons with published work and from measurements on the loop density and size, it was concluded that only part of the irradiation hardening could be attributed to the loops detected. It is suggested that there might be a hardening contribution from P-rich clusters forming under irradiation.

7. Embrittlement is thought to arise from the reduction in grain boundary fracture stress due to loss of carbon from the boundaries. There was no evidence to support the radiation enhanced grain boundary segregation of P under these experimental conditions.

Acknowledgement

This paper is published by permission of BNFL Magnox Generation, Berkeley Centre, Glos, UK.

References

[1] Briant, C.L., and Grabke, H.J., "Grain Boundary Segregation in Iron and its Effect on Intergranular Fracture," *Material Science Forum*, Vol 46, 1989, pp253-276.

[2] Erhart, H., amd Grabke H.J., "Equilibrium Segregation of Phosphorus at Grain Boundaries of Fe-P, Fe-P-C, Fe-Cr-P, and Fe-Cr-C-P Alloys," *Metal Science*, Vol 15, 1981, pp401-408.

[3] Abiko, K. and Liu, C.M., "Role of Solute Atoms on Intergranular Fracture in High Purity Iron Alloys," *Proc R I Jaffe Symposium on Clean Materials Technology, ASM Materials Week*, Chicago, Illinois, USA 2-5 November 1992.

[4] Cowan, J.R., "The Role of Stress, Microstructure and Cooling Rate on the Grain Boundary Segregation of Phosphorus and Carbon in an Fe-P-C Alloy," *PhD Thesis, University of Birmingham*, UK, 1998.

[5] Kameda, J., and Bevolo, A.J., "Neutron Irradiation-Induced Intergranular Solute Segregation in Iron-Base Alloys," *Acta Metallurgica*, Vol 37, 12, 1989, pp3283-3296.

[6] Beere, W.B., Fidler, R.S., Bolton, C.J., Fenton, S.T., and Jones, R.B., "The Ductile-Brittle Transition Behaviour of Submerged-Arc Weldments Following High Temperature Exposure," *Effects of Radiation on Materials: 18th International Symposium, ASTM STP 1325*, R. K. Nanstad, M. L. Hamilton, F. A. Garner and A. S. Kumar, Eds., American Society for Testing and Materials, West Conshohocken, PA, 1997,pp 223-232.

[7] Jones, R.B., and Bolton, C.J., "Neutron Radiation Embrittlement Studies in Support of Continued Operation, and Validation by Sampling of Magnox Reactor Steel Pressure Vessels and Components," *24th Water Reactor Safety Meeting, 1996*, NUREG/CP-0157, Vol 2, 1997, USNRC, pp25-48.

[8] Druce, S.G., English, C.A., Foreman, A.J.E., McElroy, R.J., Vatter, E.A, Bolton, C.J, Buswell, J.T, and Jones, R.B., "The Modelling of Irradiation-Enhanced Phosphorus Segregation in Neutron Irradiated Reactor Pressure Vessel Submerged-Arc Welds," *Effects of Radiation on Materials: 17th International Symposium, ASTM STP 1270*, D. S. Gelles, R. K. Nanstad, A. .S Kumar and E. A. Little, Eds., American Society for Testing and Materials, West Conshohocken, PA, 1996, pp 119-137.

[9] Bolton, C.J., Buswell, J.T., Jones, R.B., Moskovic, R., and Priest, R.H., "The Modelling of Irradiation Embrittlement in Submerged-Arc Welds," *Effects of Radiation on Materials: 17th International Symposium, ASTM STP 1270*, D. S. Gelles, R. K. Nanstad, A. S. Kumar and E. A. Little, Eds., American Society for

Testing and Materials, West Conshohocken, PA, 1996, pp 103-118.

[10] Bischler, P.J.E., and Wild, R.K., "A Microstructural Study of Phosphorus Segregation amd Intergranular Fracture in Neutron Irradiated Submerged-Arc Welds," *Effects of Radiation on Materials: 17th International Symposium, ASTM STP 1270*, D. S. Gelles, R. K. Nanstad, A. S. Kumar and E. A. Little, Eds., American Society for Testing and Materials, West Conshohocken, PA, 1996, pp 260-273.

[11] Beere, W.B., and Buswell, J.T., "The Effect of Heat Treatment on Phosphorus Segregation in Submerged-Arc Weld Metal," *Effects of Radiation on Materials: 18th International Symposium, ASTM STP 1325*, R. K. Nanstad, M. L. Hamilton, F. A. Garner and A. S. Kumar, Eds., American Society for Testing and Materials, West Conshohocken, PA, 1997, pp317-330.

[12] Oliver, B.M., McElroy, W.N., Kellog, L.S., and Farrar IV, H., "Boron Determinations in Pressure Vessel Steels," *Reactor Dosimetry, ASTM STP 1228*, H. Farrar IV, E. P. Lippincott, and J. G Williams, Eds., American Society for Testing and Materials, West Conshohocken, PA, 1994.

[13] Jones, R.B., Edens, D.J., and Wootton, M.R., "Influence of Thermal Neutrons on the Hardening and Embrittlement of Plate Steels," *Effects of Radiation on Materials: 19th International Symposium, ASTM STP 1366*, M. L. Hamilton, A. S. Kumar, S. T. Rosinsky, and M. L. Grossbeck, Eds., American Society for Testing and Materials, West Conshohocken, PA, 1999.

[14] Fisher, S.B., Knowles, G. And Lee, B., "Auger Spectroscopy of Magnox Pressure Vessel Steels," *Effects of Radiation on Materials: 18th International Symposium, ASTM STP 1325*, R. K. Nanstad, M. L. Hamilton, F. A. Garner, and A. S. Kumar, Eds., American Society for Testing and Materials, West Conshohocken, PA, 1999, pp 249-259.

[15] Oldfield, W., "Curve Fitting Impact Test Data: A Statistical Procedure," *ASTM Standardisation News*, no 3 (11) 1975, pp24-29.

[16] Pareige, P., Stoller, R.E., Russell, K.F., and Miller, M.K., "Atom Probe Characteristion of the Microstructure of Nuclear Pressure Vessel Surveillance Materials After Neutron Irradiation and After Annealing Treatments," *Journal of Nuclear Materials*, Vol 249, 1997, pp165-174.

[17] Miller, M.K., Hoelzer, D.T., Ebrahimi, F., Hawthorne, J.R., and Burke, M.G., "Microstructural Characterisation of Fe-Cu-Ni-P Model Steels," *Proc 3rd Int Conf on Environmental Degradation of Materials in Nuclear Power Systems-Water Reactors*, Traverse City, USA, 1988, G J Theus and J R Weeks, Eds, TMS, pp 133-139.

[18] Takeyama, T., Ohnuki, S., and Takahashi, H., "Effect of Neutron and Electron Irradiation on Low Manganese Steels," *Transactions of the Iron and Steel Institute of Japan*, Vol 21, 1981, pp326-331.

[19] Jones, R.B., and Williams, T J., "The Dependence of Radiation Hardening and Embrittlement on Irradiation Temperature," *Effects of Radiation on Materials: 17th International Symposium, ASTM STP 1270*, D. S. Gelles, R. K. Nanstad, A. S. Kumar and E. A. Little, Eds., American Society for Testing and Materials, West Conshohocken, PA, 1996, pp 569-590.

[20] Hoelzer, D.T., and Ebrahimi, F., "Effect of Copper and Nickel on the Neutron Irradiation Damage in Iron Alloys," *Materials Research Society Symposium Proceedings*, The Materials Research Society, Vol 373, 1995, pp 57-62.

[21] Hansel, H., and Grabke, H.J., "Grain Boundary Segregation of Phosphorus and Carbon in Ferritic Iron," *Scripta Metallurgica*, Vol 20, 1986, pp 1641-1644.

[22] Guttmann, M., Dumoulin, Ph., and Wayman, M., "The Thermodynamics of Interactive Co-Segregation of Phosphorus and Alloying Elements in Iron and Temper-Brittle Steels," *Metallurgical Transactions A*, vol 13A, 1982, pp 1693-1711.

Hiroshi Kawanishi[1] and Masahide Suzuki[2]

Microstructure and Hardening in Thermally Aged and Neutron-Irradiated Fe-Cu Model Alloy

Reference: Kawanishi, H. and Suzuki, M., **"Microstructure and Hardening in Thermally Aged and Neutron-Irradiated Fe-Cu Model Alloy,"** *Effects of Radiation on Materials: 19th International Symposium, ASTM STP 1366,* M. L. Hamilton, A. S. Kumar, S. T. Rosinski, and M. L. Grossbeck, Eds., American Society for Testing and Materials, West Conshohocken, PA, 2000.

Abstract: The microstructure of Fe-0.6 wt.% Cu alloys irradiated at 290°C to 0.0055 dpa in the Japan Materials Testing Reactor was examined using a conventional electron microscopy technique to study the precipitation behavior of copper in α-iron, in addition to those thermally aged at 500°C for 1000 h and unalloyed Fe. Hardness measurements were also carried out. Results showed that there were two kinds of copper precipitates in thermally aged alloys. The first one was an ultrathin untwinned precipitate that increased in thickness with aging, decreasing in size and number density. The second was small with twinning, that grew little until peak hardness. Age hardening, thus, was attributed to ultrathin copper precipitate. Irradiation, which induced a dramatic hardening in the alloys, eliminated the ultrathin precipitates while the small-twinned ones survived. Two (111) patterns appeared on a (110) selected area diffraction pattern of the α-iron matrix in the irradiated specimens with one (111) pattern analyzed to be due to $(110)_{Cu_3Fe}$ reflections (forbidden reflections in fcc crystals) and the other (111) pattern to $(220)_{Fe_3O_4}$ reflections. It was concluded that irradiation induced the formation of short range ordered domains of Cu_3Fe-superlattice ($L1_2$-type) in Fe-Cu alloys, resulting in the dramatic hardening. The precipitation of FeSi was recognized to be enhanced by irradiations in unalloyed iron.

Keywords: Fe-Cu alloy, pressure vessel steel, hardening, aging, twinning, copper precipitate, superlattice, short range order, Cu_3Fe, FeSi

[1]Research Associate, Department of Quantum Engineering and Systems Science, University of Tokyo, 7-3-1 Hongo, Bunkyo-ku, Tokyo 113-8656, Japan.

[2]Senior Engineer, Tokai Establishment, Japan Atomic Energy Research Institute, Tokai-mura, Naka-gun, Ibaraki-ken 319-1195, Japan.

Copyright© 2000 by ASTM International www.astm.org

Introduction

Significant hardening has been recognized at low doses in Fe-Cu alloys as well as in ferritic reactor pressure vessel (RPV) steels containing copper. The radiation-induced hardening or embrittlement has long been attributed to the formation of copper-rich precipitates[*1-7*]. However, it appears that no microstructural change responsible for the hardening has been identified completely by transmission electron microscopy (TEM) studies. This may arise from the magnetic effects of ferritic steels and the oxide produced on the specimen surfaces during electropolishing TEM specimens. A Fe-Cu model alloy provides good specimens for understanding or modeling the hardening as a consequence of the evolution of copper precipitates under thermal aging and neutron irradiations. TEM analysis is expected to become possibly easier in the model alloys since the alloying system is simpler than that in commercial RPV steels.

We have reported through a conventional TEM study in the previous work [*8*] that copper precipitates that were ultrathin disk ($\leq$ 0.4 nm in thickness and ~ 20 nm in diameter) formed in a Fe-0.6 wt.% Cu model alloy water-quenched from 850°C, and that the precipitates increased in thickness with thermal aging at 500°C, reducing in size and number density. Furthermore, the precipitate was found to remain disk-shaped in the over-aged conditions following 1000 h at 500°C. A chemical hardening mechanism has been proposed to interpret the hardening due to the disk-shaped precipitates with thermal aging, and it has been demonstrated that the model can successfully explain the hardening in terms of the change in the thickness and number density of the precipitates with thermal aging. In addition, the habit plane of the copper precipitates has been determined to be the (112) plane of the matrix, meaning that there are the twelve equivalent habit planes in the matrix. It appeared that this made it rather difficult to analyze the selected area diffraction patterns (SADP) from a small area with copper precipitates. In addition, it was confirmed that Fe_3O_4 was inevitably formed in the model alloys with some level of oxygen as impurity, resulting often in complicated contrast for the dark field imaging.

Recently, it has been revealed that twinning on (111) twining planes and $<11\bar{2}>$ twining directions, which is common to materials of face centered cubic (fcc) crystal, formed within the copper precipitates in over-aged conditions [*9*]. This result was entirely different from those obtained by high-resolution electron microscopy (HREM) [*10-12*], suggesting strongly that copper precipitates had fcc structure even at the stage of nucleation.

In the present paper, we first report some new results of copper precipitates obtained by continuing TEM examinations of thermally aged Fe-0.6 wt.% Cu. Next, data are presented on the characterization of the microstructural change in the alloys irradiated in the Japan Materials Testing Reactor (JMTR).

Experimental Procedure

The details in the specimen preparation, heat-treatments and chemical compositions for Fe-0.6 wt.% Cu model alloys as well as unalloyed Fe used in the present study have been previously described [*8*]. The 3 mm-diameter disks, 0.25 mm thick, were cut from rods which were thermally aged for 1000 h at 500°C after solution-annealing at 930°C for 1 h and homogenization treatments at 850°C for 2 h, followed by water-quenching. Vickers

hardness measurements were made with a load of 1 kg. Conventional transmission electron microscope (CTEM) examinations were made on three kinds of specimens using a JEM 200CX electron microscope. Those were, as water-quenched, 100 h-aged and 1000 h-aged one. The irradiation was carried out on these three conditions in the JMTR at 290°C for 6 days to 4.2 x 10^{18} n/cm^2 (E >1MeV) using a hydraulic rabbit where the specimens were set within a can of aluminum filled with helium. The dose was calculated to be 0.0055 dpa by taking account of neutrons of E ≤1MeV. Hardness measurements and CTEM examinations were done after the irradiations. Dark field contrast images were carefully analyzed with the help of the corresponding SADPs in the CTEM study.

Results

Hardness Measurements

Fig. 1 shows the change in the hardness with thermal aging and neutron irradiation for Fe-0.6 wt.% Cu alloys and unalloyed Fe. Two points should be pointed out from Fig.1. First, compared to that in thermally-aged specimens, a dramatic increase in the hardness can be seen in the specimen water-quenched and then irradiated to a dose as low as 0.0055 dpa. The second is that the increment of the hardness with irradiation is reduced with the aging period, namely, the hardening is greatest in the water-quenched specimens and is lowest in the over-aged specimens. Hardening also occurs in unalloyed Fe due to irradiation, but it is less.

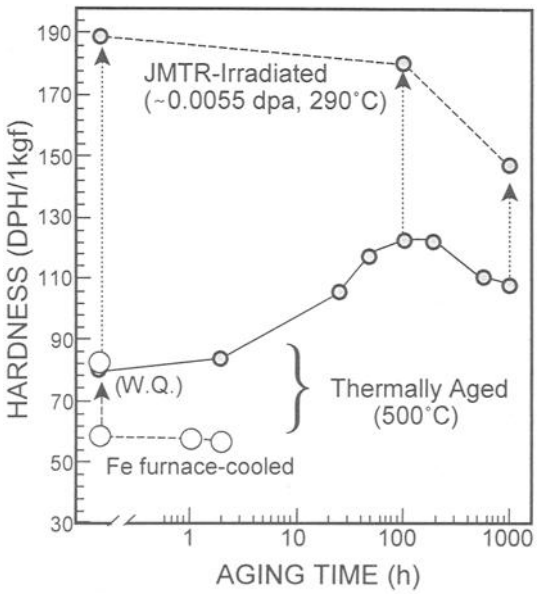


Figure 1 - *Hardness in Fe-0.6 wt.% Cu alloys and unalloyed Fe with thermal aging and irradiation in the JMTR.*

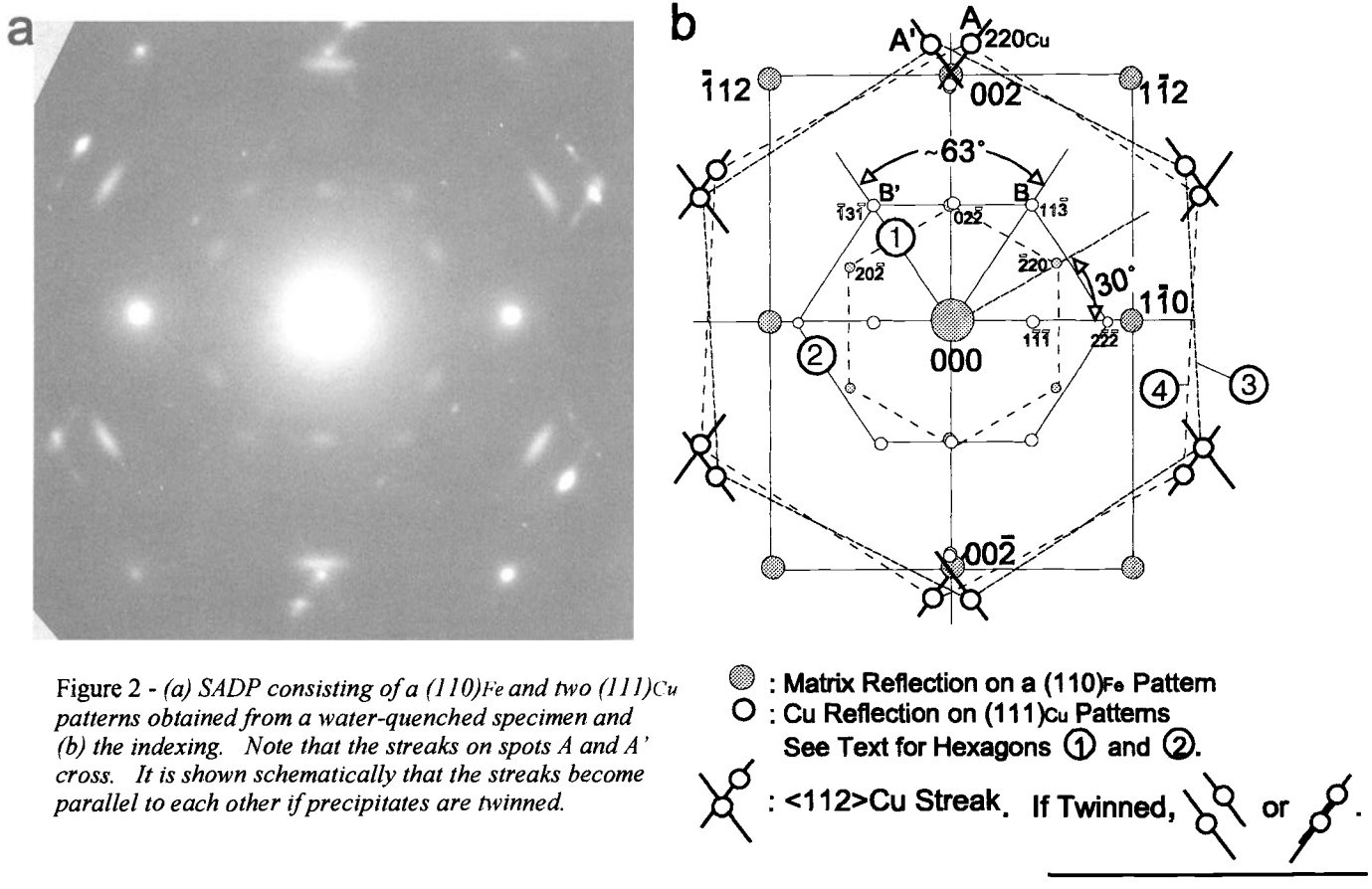


Figure 2 - *(a) SADP consisting of a (110)Fe and two (111)Cu patterns obtained from a water-quenched specimen and (b) the indexing. Note that the streaks on spots A and A' cross. It is shown schematically that the streaks become parallel to each other if precipitates are twinned.*

CTEM Examinations in Thermal Aged Specimens

Ultrathin precipitates of copper were observed by displacement fringe contrast in the water-quenched and 100 h-aged specimens when a coherent interface exists between the matrix and precipitate, and the image was made using two reflections of the matrix and the precipitate in the corresponding SADP (e.g., the combination of $(002)_{Fe}$ and $(220)_{Cu}$ reflections, or $(110)_{Fe}$ and $(111)_{Cu}$ reflections). The details for the imaging have been described in the previous paper [*8*]. Fig. 2(a) shows one example of a SADP consisting of one $(110)_{Fe}$ and two $(111)_{Cu}$ patterns taken from a water-quenched specimen. The indexing is presented in Fig. 2(b). The $(111)_{Cu}$ patterns form the regular hexagons ③ and ④ as shown in Fig. 2(b), indicating that a Kurdjumov-Sacks (K-S) orientation relationship exists between the matrix and the precipitates (i.e., $(110)_{Fe}$ // $(111)_{Cu}$ and $[1\bar{1}1]_{Fe}$ // $[1\bar{1}0]_{Cu}$). It should be noted in Fig. 2(a) that the $(220)_{Cu}$ spots on hexagons ③ and ④ are always associated with streaks, and the thickness of the precipitates can be deduced from the length of the streaks and has been estimated to be ≤ 0.4 nm for the water-quenched specimens, since the streak length is approximately in inverse proportional to the precipitate thickness [*8*]. In Fig. 2, the streaks (// $[\bar{1}12]_{Fe}$) on hexagon ③ never become parallel to those (// $[1\bar{1}2]_{Fe}$) for the hexagon ④. This shows that the normals of the surface of these two precipitates of disk-type are directed towards either the $<1\bar{1}2>_{Fe}$ or $<\bar{1}12>_{Fe}$ directions, because the streak inevitably takes place normal to the precipitate surface, leading to the conclusion that no ultrathin precipitates are twinned. This can be explained as follows. If twinning takes place, there must be more than two sections in a single precipitate where each section belongs to either hexagon ③ or ④. Therefore, in such cases, the directions of the streaks become parallel as shown in the lower part of Fig. 2 (b).

In addition to the spots of the matrix and the precipitates, there are two sets of extra spots in Fig. 2(a), and the sets form the hexagons denoted ① and ② in Fig. 2(b), though the intensities are rather low. The hexagon ① forms a regular hexagon, which is analyzed to be a (111) pattern of Fe_3O_4. The reflections B and B' on the hexagon ② make an angle of ~ 63° and are indexed as the spots for $(11\bar{3})$ and $(\bar{1}3\bar{1})$ of Fe_3O_4, respectively, and the hexagon ② forms a $(112)_{Fe_3O_4}$ pattern. Based on the orientation relationship of $(110)_{Fe}$ // $(100)_{Fe_3O_4}$ and $[001]_{Fe}$ // $[001]_{Fe_3O_4}$ between the matrix and Fe_3O_4 [*8*], it is calculated that the planes of $(111)_{Fe_3O_4}$ and $(112)_{Fe_3O_4}$ make an angle of ± 9°44' to a $(110)_{Fe}$ plane under the above relationship. Therefore, the $(111)_{Fe_3O_4}$ and $(112)_{Fe_3O_4}$ patterns do not appear probably when the electron beam is parallel to an exact $<110>_{Fe}$ direction, but the patterns are often observed in practice due to a shift of the electron beam from an exact $<110>_{Fe}$ direction even if a $(110)_{Fe}$ pattern appears.

Fig. 3 shows the example of dark field images for ultrathin copper precipitates in (a) the water-quenched and (b) 100 h-aged specimens using reflections of $(110)_{Fe}$ and two $(111)_{Cu}$ on a $(110)_{Fe}$ SADP as shown in Fig. 2(a) where two $(111)_{Cu}$ spots are not seen. However, the analysis of the reflection spots due to copper precipitates in reciprocal lattice space shows that there are inevitably two $(111)_{Cu}$ spots at a position very close to a $(110)_{Fe}$ spot where the spacing of $(110)_{Fe}$ and $111)_{Cu}$ planes is 0.2027 and 0.2087 nm, respectively. This arises from the twelve habit planes for copper precipitate in the Fe-matrix, i.e, $(112)_{Cu}$ planes where $(112)_{Cu}$ // $(112)_{Fe}$. Though it is usually impossible to distinguish these $(111)_{Cu}$ spots from the $(110)_{Fe}$ spot on the corresponding $(110)_{Fe}$ SADP, they contribute to imaging [*8*]. However, the existence of two $(111)_{Cu}$ spots near a $(110)_{Fe}$

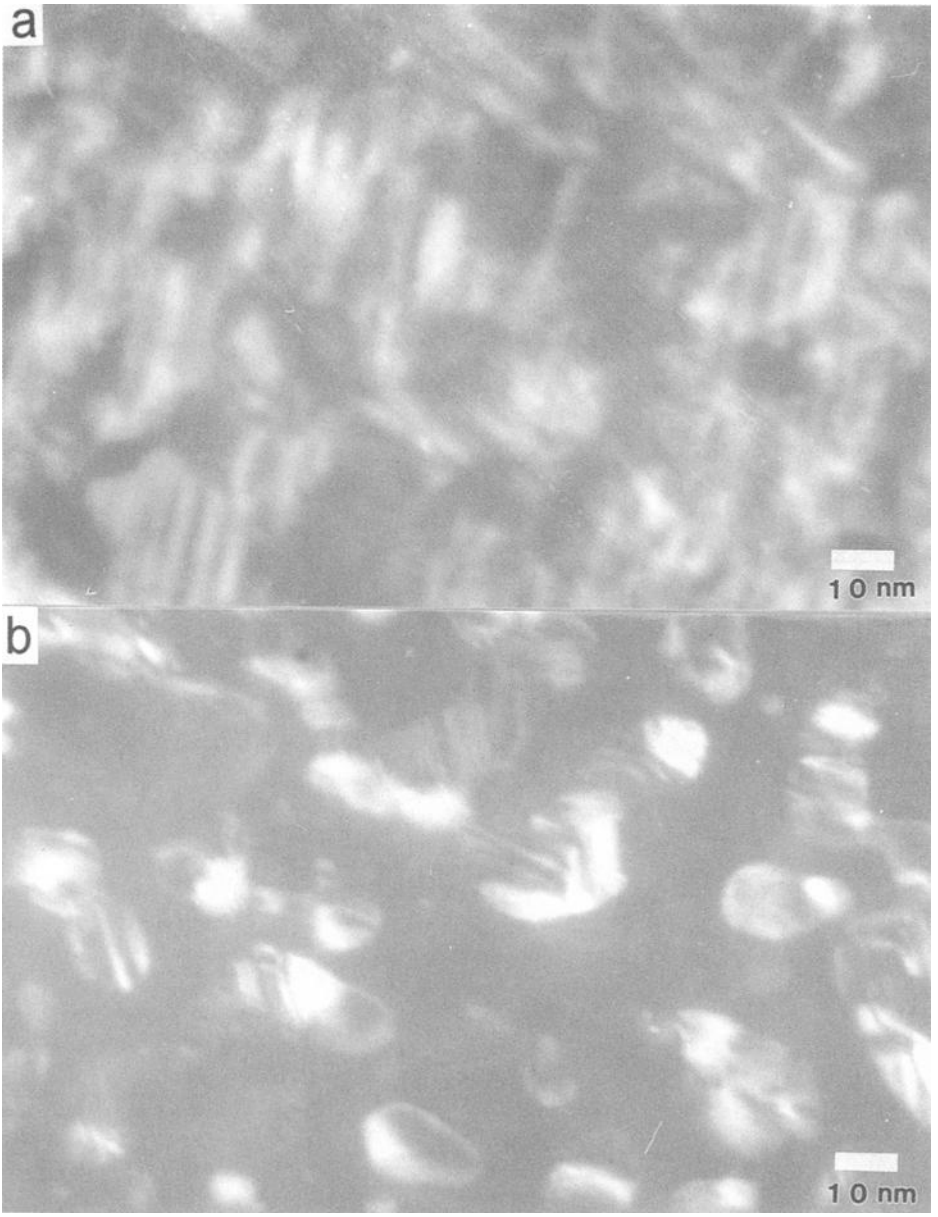


Figure 3 - *Ultrathin copper precipitates in (a) water-quenched and (b) 100 h-aged specimen imaged using the matrix reflection, $(1\bar{1}0)_{Fe}$ from a $(110)_{Fe}$ SADP.*

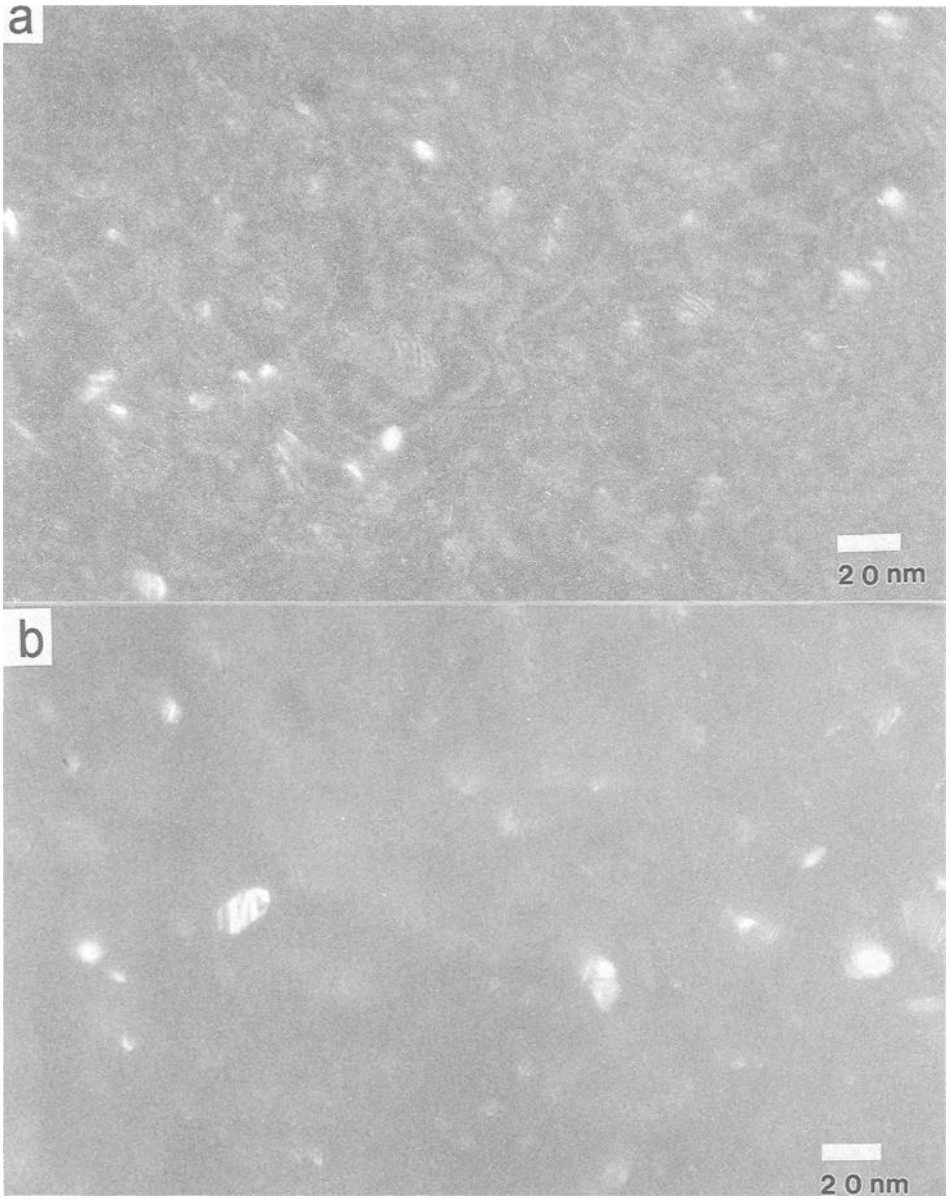


Figure 4 - *Small copper precipitates in (a) the water-quenched and (b) the 100 h-aged specimen taken by using a (110)Fe reflection.*

spot may be recognized as two streaks on the (110)Fe spot [see Figs. 2(b) and (c) in ref. *8*]. The precipitates in the 1000 h-aged specimens were easily observed even in the bright field images. This was considered to be due to an increase in thickness. No streaks were observed in the 1000 h-aged specimens and it was impossible to directly determine precipitate thickness. Instead, thickness was determined to be about 2 nm by the width of the no-contrast-line associated with the precipitates in dark field contrast [*8*].

The displacement fringe contrast corresponding to copper precipitates was observed in the relatively thin area near the edge of the hole produced by electropolishing. Here, it must be mentioned that for a (110)Fe matrix SADP, the (111)Cu pattern for copper precipitates does not always appear concurrently on the (110)Fe pattern with the K-S orientation relationship. For example, the $(11\bar{2})$Cu pattern is positioned close to the $(1\bar{1}0)$Fe pattern, but both patterns are not parallel to each other, making an angle of 5°16'. In a practical case, the (112)Cu pattern might be superimposed on the (110)Fe and (111)Cu patterns, resulting in a complicated SADP. The probability that the (111)Cu pattern will be superimposed on a (110)Fe pattern is one in six because there are the six equivalent planes of (110)Fe-type in a cubic crystal. This is another reason for making it complicated to examine copper precipitates.

In addition to ultrathin precipitates, small copper precipitates were often observed in the water-quenched and 100 h-aged specimens by using a (110)Fe reflection in a relatively thick area of the specimen. Figs. 4 (a) and (b) are examples of such precipitates in the water-quenched and 100 h-aged specimen, respectively. White contrast of copper precipitate is believed to result from the (111)Cu reflections which overlap the (110)Fe reflections as described above. These precipitates are about nm in size and increase little in both size and number density during the 100 h-aging. Therefore, the hardening to peak hardness, which occurs by ~ 100 h-aging, can not be due to these precipitates. Fringe contrast can be seen in larger examples, e.g., > 5 nm in diameter. The fringe contrast of this type was considered to be different from the displacement fringe contrast corresponding to ultrathin precipitates (Fig. 2(a)) though the contrast is weak, but was due to the growth twins formed within a precipitate. The formation of growth twins in the 1000 h-aged specimens can be demonstrates by consideration of the SADPs consisting of (111)Fe and (110)Cu patterns [*9*], emphasizing that the fringe is not due to 9R-twinning [*10-12*], but to growth twins as described below. To detect these small precipitates from their reflections usually becomes rather difficult due to the weak intensity of the reflections. The intensity of the displacement fringe contrast basically oscillates with depth in the foil and the oscillation term takes the form

$$\cos^2(\Delta t/\xi g)$$

while the intensity for twinning, I(zone), can be expressed as

$$I(\text{zone}) = \begin{cases} k & \text{(for parent zone),} \\ 0 & \text{(for twinned zone) and vice versa,} \end{cases}$$

where t is the foil thickness, ξg the extinction distance and k a constant [*13*]. Strictly speaking, the intensity for the parent zone is not constant, but it can be regarded approximately as a constant for small and thin precipitates. This feature may help us to determine whether the fringe contrast is due to displacement fringe contrast or growth twins. The smallest size of the precipitates associated with fringes was observed to be ~ 3

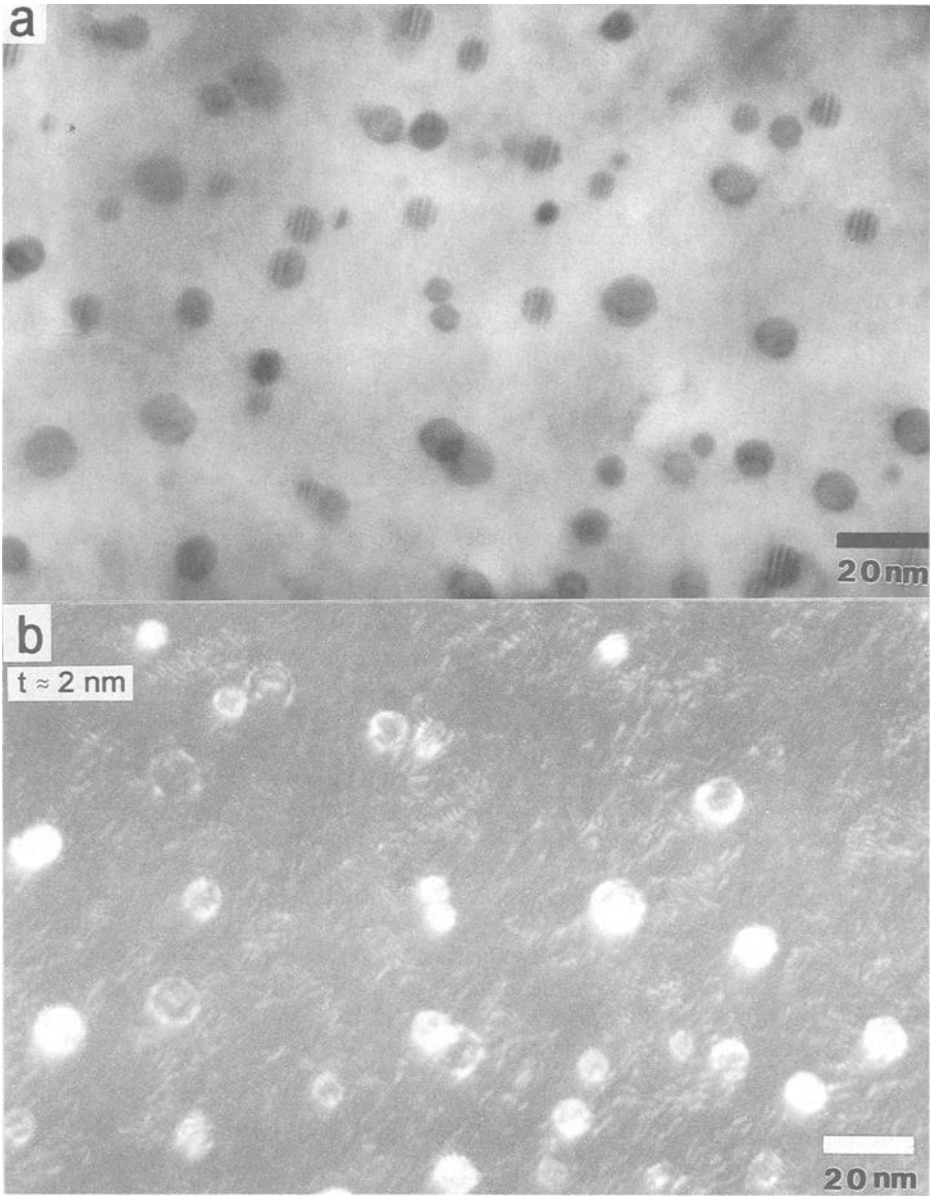


Figure 5 - *(a) Bright field image of copper precipitates in the 1000 h-aged specimen, and (b) the corresponding dark field image using a (110)Fe reflection on a (110)Fe SADP.*

nm in the present study, which was found in a water-quenched specimen.

In the 1000 h-aged specimens, the copper precipitates are easily observable in both bright and dark field contrast as shown in Fig. 5. Many of the precipitates show fringe contrast which can be clearly recognized in the bright field image (Fig. 5(a)). These fringes can be shown to be due not to 9R-twinning, but to growth twins developed during the growth of the precipitates with aging, which is often observed for precipitates in a f.c.c. crystal where the twinning plane is $(111)_{Cu}$ and the twinning direction is $<11\bar{2}>_{Cu}$. Those results have been presented elsewhere [9]. The examinations showed that all precipitates of copper were associated with twinning in the over-aged specimens. On the other hand, the ultrathin precipitates of copper were considered to have been eliminated during the 1000 h-aging.

It is shown above that there are two kinds of copper precipitates in the water-quenched condition; one is associated with twinning and the other without twins. Fig. 6 shows the change in the number density of the precipitates with thermal aging, where the precipitates without twins is expected to disappear after 100 h as indicated by a dash line in Fig. 6, whereas those with twins increase to 1000 h. Fig. 7 shows the change in the average diameter of the precipitates with thermal aging. It can be noted in Fig. 7 that the precipitates without twins decrease with thermal aging while those with twins increase. The precipitates with twins in the water-quenched and 100 h-aged specimens appeared to be rather thin since the precipitates were often observed as images similar to dislocation loops. However, it was difficult to accurately measure their thickness.

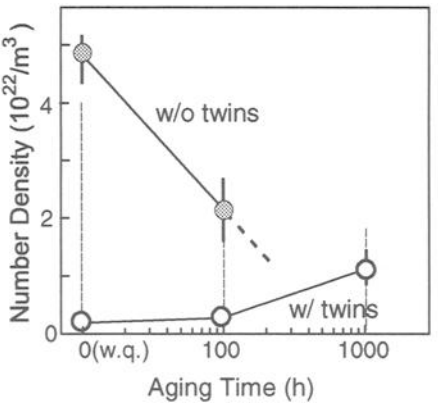


Figure 6 - *Change in number density for two kinds of copper precipitates with thermal aging, where one is without twins and the other with twins.*

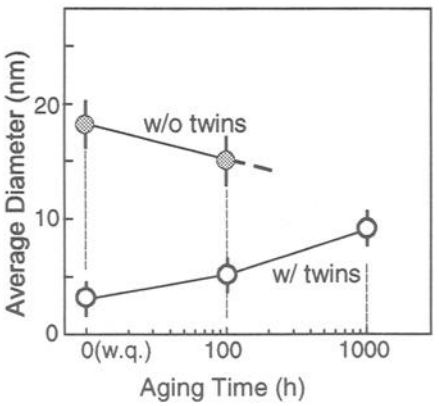


Figure 7 - *Change in average diameter for the two kinds of copper precipitates with thermal aging.*

CTEM Examinations in the Specimens Irradiated in the JMTR

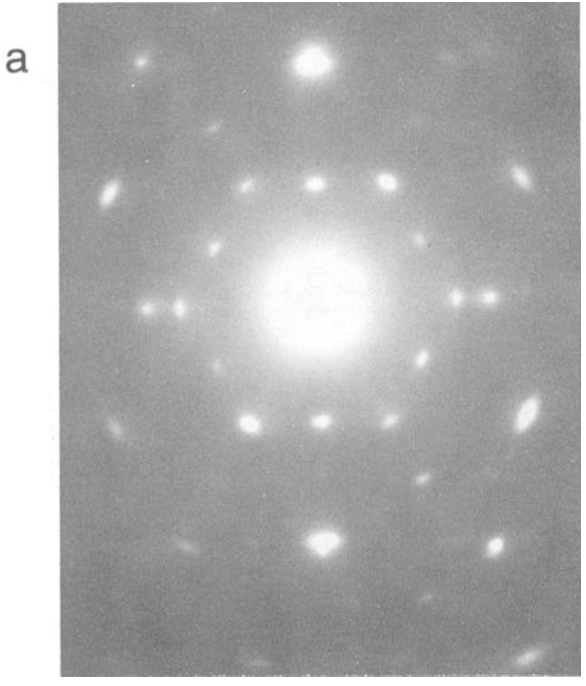
A typical example of the SADP from Fe-0.6 wt.% Cu alloy irradiated in the JMTR after water-quenching is shown in Fig. 8, with two hexagons denoted as ② and ①, judged to be regular hexagons that appear to represent a (111) pattern. This pattern, it can be concluded, can be analyzed the superimposition of $(110)_{Fe}$, $(111)_{SRO}$ and $(111)_{Fe_3O_4}$ patterns where the suffix SRO means the short range order of Cu_3Fe-superlattice. Short range order is defined as local ordered-domain. By assuming that the irradiation induces the ordering in Fe-Cu alloys where the lattice parameter of superlattice can be expected to be close to that of the parents, i.e., a solid solution of Fe and Cu, the spots forming the hexagons ① and ② are tentatively indexed as (110) or (220) reflections. The (110) reflections, which do not occur in f.c.c. crystals, are well known as forbidden reflections; only the reflections with either all odd or all even indices such as (111) or (022) are allowed to occur in the reciprocal lattice space. However, the occurrence of the forbidden reflections is proof of the formation of a superlattice. The spacing of (110) or (220) planes for hexagon ② and ① was measured in Fig. 8 to be about 0.249 and 0.294 nm, respectively. Table 1 gives the lattice parameter of superlattices which are anticipated to form in Fe-Cu alloys, and the spacing of (110) planes together with those for Fe_3O_4 by assuming that Regard's law is valid for the superlattice. Hexagons ② and ① are found from Table 1 to fit in a (111) pattern for Cu-25Fe (Cu_3Fe) and Fe_3O_4, respectively. Fig. 8 indicates, furthermore, that there is an orientation relationship between the matrix and the short range order, which is expressed as $(110)_{Fe}$ // $(111)_{SRO}$ and $[002]_{Fe}$ // $[\bar{1}\bar{1}2]_{SRO}$.

Table 1 - *Lattice Parameter and Spacing of (110) Planes in the Fe-Cu System and Fe_3O_4*

Alloy(in atomic %)	Cu	Cu-25Fe	CuFe	Cu-75Fe	Fe	Fe3O4
Lattice Parameter(a_o; nm)	0.3615	0.3427	0.3240	0.3054	0.2866	0.8394
Spacing of (110) plane	0.2556	0.2423	0.2291	0.2160	0.2027	0.2968*

* spacing of d_{220}

The precipitation of Fe_3O_4 was already reported to be formed in thermally aged Fe-Cu alloys [*8,14*]. Fe_3O_4 has a f.c.c. structure of spinel-type and the lattice parameter is 0.8394 nm where the spacing of $(220)_{Fe_3O_4}$ plane is 0.2968 nm. It appears that $(110)_{Fe}$ // $(111)_{Fe_3O_4}$ and $[002]_{Fe}$ // $[1\bar{1}0]_{Fe_3O_4}$ in Fig. 8, which is the well known Nishiyama-Wasserman's (N-W) orientation relationship [*15,16*]. However, the orientation relationship between the matrix and Fe_3O_4 is reported as $(110)_{Fe}$ // $(100)_{Fe_3O_4}$ and $[001]_{Fe}$ // $[001]_{Fe_3O_4}$ [*8,14*]. According to this orientation relationship, the planes of $(110)_{Fe}$ and $(111)_{Fe_3O_4}$ never become parallel and one of the equivalent $(110)_{Fe}$ planes makes an angle of 9°44' to a $(111)_{Fe_3O_4}$ plane. Two possibilities exist with regard to the occurrence of a $(111)_{Fe_3O_4}$ pattern on a $(110)_{Fe}$ pattern. The first is that the $(111)_{Fe_3O_4}$ pattern appears readily since $(220)_{Fe_3O_4}$ spots are close to the $(110)_{Fe}$ reciprocal lattice plane when the electron beam is not exactly parallel to a $<110>_{Fe}$ direction. The second is that the orientation relationship between the matrix and Fe_3O_4 precipitate change during



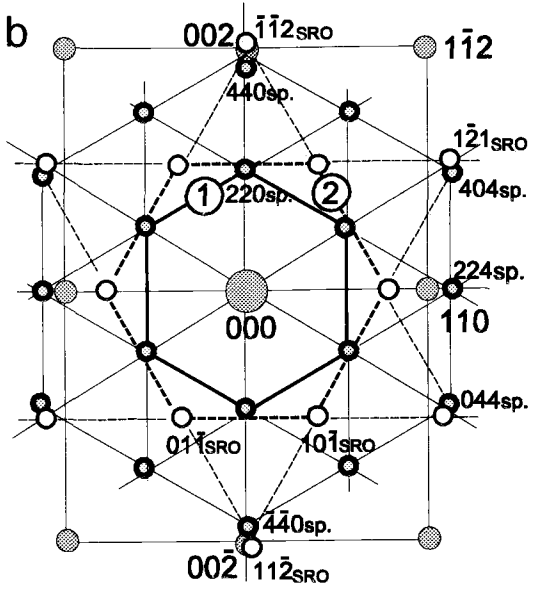


Figure 8 - *(a) SADP from Fe-0.6 wt.% Cu irradiated in the JMTR following water-quenching, and (b) the indexing. The pattern consists of (110)Fe, (111)Fe_3O_4 (hexagons ①) and (111)SRO(Cu_3Fe-superlattice) pattern (hexagon ②).*

: Matrix Reflection on a (110)Fe Pattern; hkl
: Cu-Superlattice (Short Range Order) Reflection on a (111)Cu_3Fe Pattern; hkl_{SRO}.
: Fe_3O_4 Spot on a (111)Fe_3O_4 (Spinel-type) Pattern ; hkl_{sp}.

irradiation. In some SADPs away from the $(110)_{Fe}$ orientation, the reflections from Fe_3O_4 could be found just at the positions which were expected from the relationship given by ref. 14. It, thus, appears that the $(111)_{Fe_3O_4}$ pattern in Fig. 8 occurs by a shift of the electron beam from an exact $<110>_{Fe}$ direction.

Fig. 9 shows dark field contrast of (a) short range ordered domains by imaging one $(1\bar{1}0)_{SRO}$ reflection in a $(110)_{Fe}$ orientation as shown Fig. 8, and (b) Fe_3O_4 precipitates by using a $(220)_{Fe_3O_4}$ reflection. The contrast from short range order consists of small white dots (a few nm in size), which occur in bands or ribbons against a low intensity background, and the plate- or disk-contrast (10-20 nm in size with shaded background). It can be pointed out that the density of white contrast in Fig. 9(a) increases with the specimen thickness, being almost proportional to the distance from the edge of the hole. This indicates that the contrast is not due to surface deposits such as oxide, but due to a substance embedded in the matrix. This contrast could not be observed in bright field conditions. Neither fringe contrast (Fig. 3) nor the streak (Fig. 2) as seen in the water-quenched conditions has been observed in the specimens irradiated in the JMTR, indicating that the ultrathin copper precipitates were eliminated by irradiation. The $(220)_{Fe_3O_4}$ reflection essentially produced disk-like images of several nm distributed uniformly through the matrix, and the images often were similar to that from a $(110)_{SRO}$ reflection. Similar images were often recognized in thermally aged alloys as well. The reason for this is thought to be due to the overlapping effects of Fe_3O_4 particles, disk-shaped copper precipitate and/or short range order domains. It was difficult in some case to distinguish the dark field images due to ordered domain and Fe_3O_4. Irradiation, however, appeared to slightly increase the size of Fe_3O_4.

In addition to the images of short range ordered domains shown in Fig. 9(a), small disks were often observed in the specimens irradiated in the JMTR to 0.0055 dpa at 290°C after water-quenching or thermal aging at 500°C for 100 h. The shape of the disks was deduced to be from the fringe contrast arising from twinning as described below. Figs. 10(a) and (b) are examples of such precipitates in the specimens irradiated in the JMTR, which are taken by using a $(110)_{Fe}$ reflection. Although we can recognize the precipitates as white contrast in the dark field image, so-called extra precipitate-spots contributing to the imaging usually were not identified around the $(110)_{Fe}$ spot in the SADP. This may be partially due to their small size and low number density, resulting in low intensity of the reflected beam; the observations showed that the precipitates of this type were not distributed uniformly through the matrix, but usually localized. This contrast is believed to be due to two $(111)_{Cu}$ spots which are always close to a $(110)_{Fe}$ spot as described above, supposing that there is still the K-S orientation relationship between the precipitate and the matrix. The size appears to increase with the period of thermal aging before irradiation. In Fig. 10(b), it can be seen that the precipitate shows fringe contrast. Fig. 11 is the magnified micrograph of such fringe contrast. These observations lead us to the conclusion that the precipitates are associated with twinning and identical to copper precipitates observed in the specimens water-quenched or thermally aged (Fig. 4). The size and number density of these precipitates appeared to be less affected by irradiation, although results were strongly influenced by the diffraction conditions. Thus, these small precipitates are believed to survive without reduction in size during irradiation.

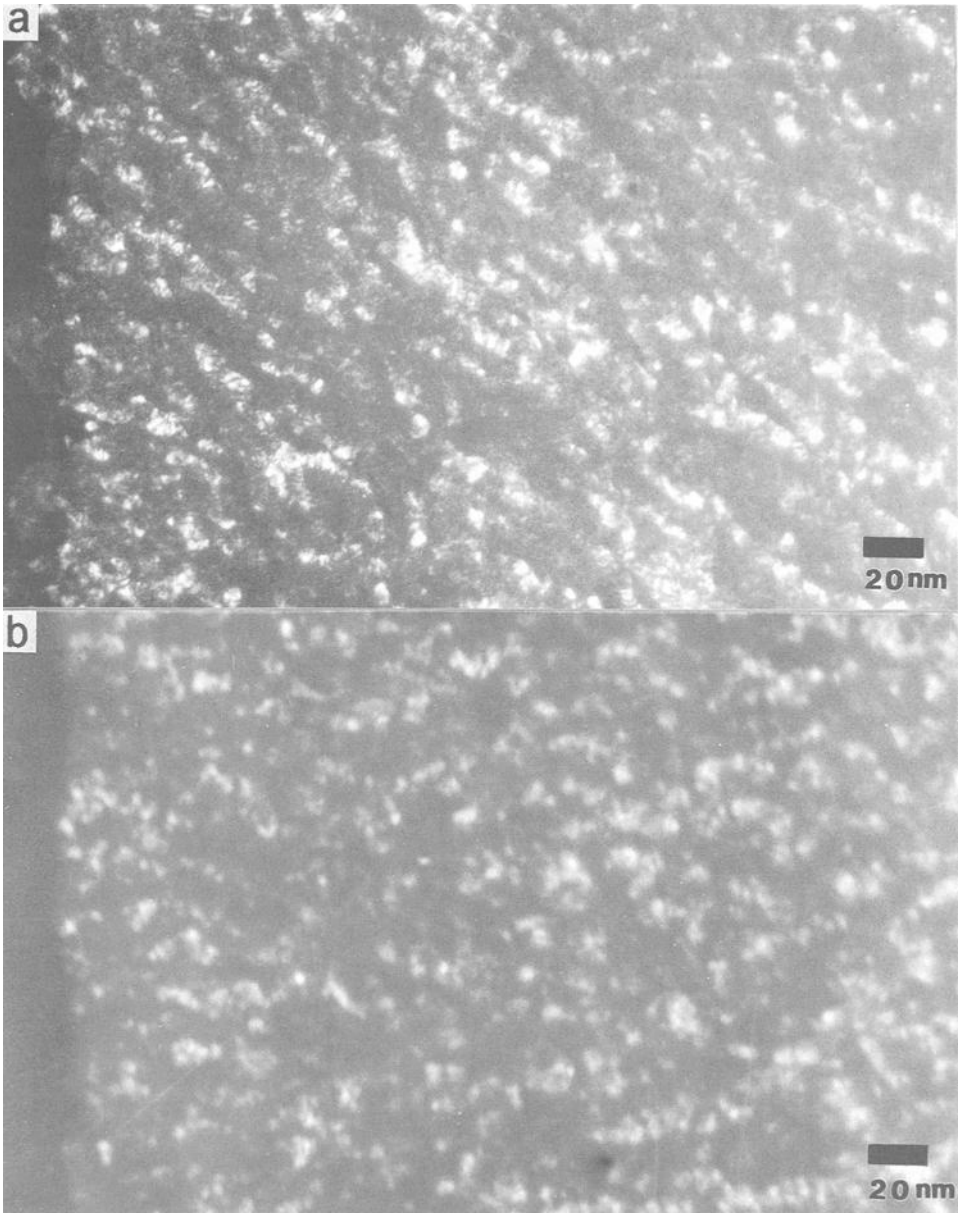


Figure 9 - *(a) Short range ordered domains in a specimen irradiated in the JMTR to 0.0055 dpa at 290°C after water-quenching using a reflection of* $(110)_{SRO}$ *in a* $(110)_{Fe}$ *pattern and (b)* Fe_3O_4 *precipitates using a* $(220)_{Fe_3O_4}$ *reflection.*

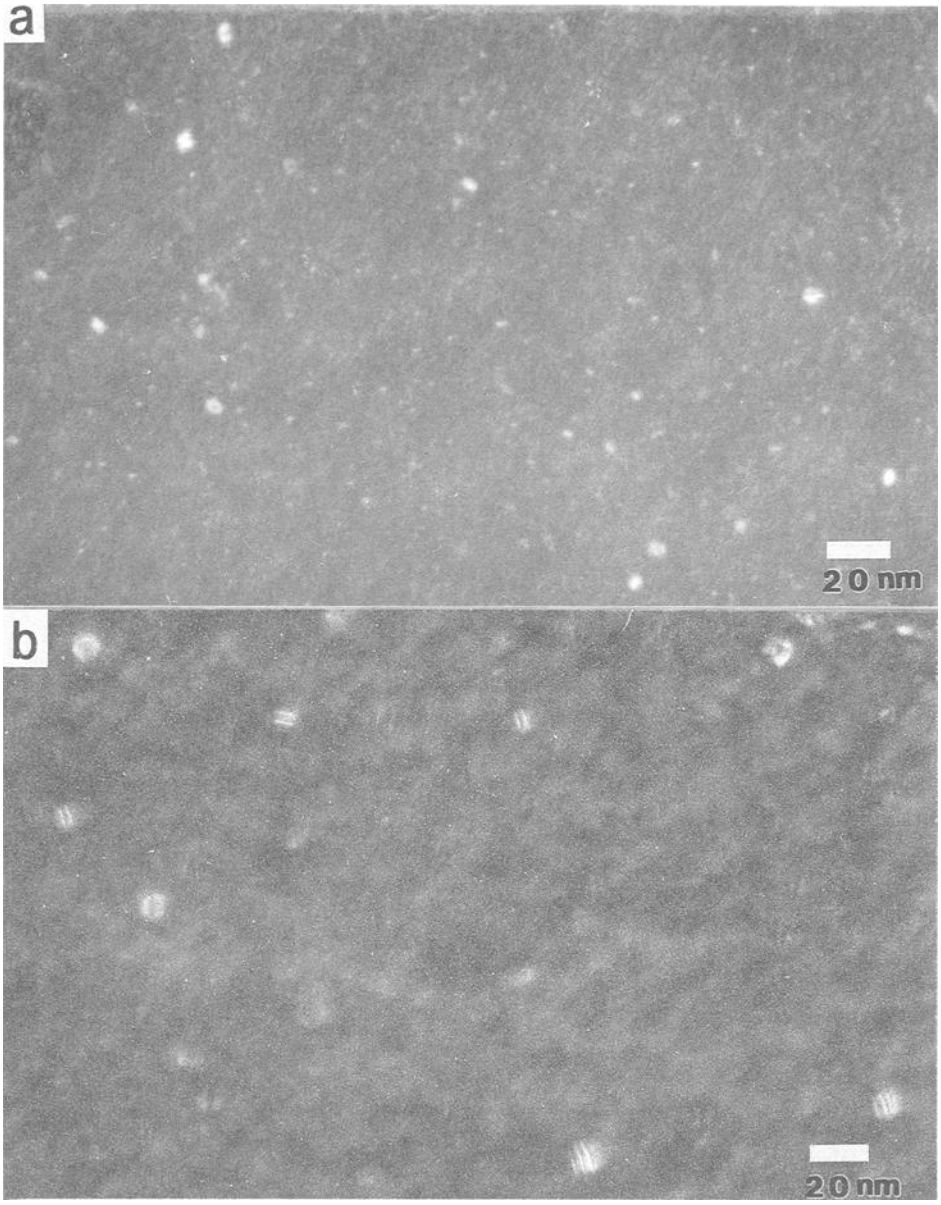


Figure 10 - *Small copper precipitates in specimens irradiated in the JMTR after (a) water-quenching and (b) 100 h-aging where fringes are due to twinning.*

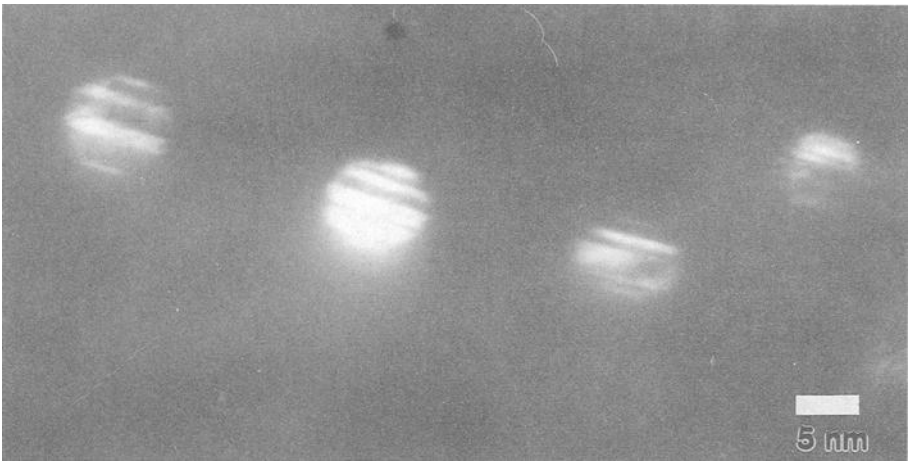


Figure 11 - *An example of fringe contrast associated with small copper precipitates in the specimen irradiated in the JMTR following 100 h-aging, indicating the existence of twinning.*

Unalloyed Fe Irradiated in the JMTR

In the unalloyed iron (Fe-0.0033Si-0.0042Cu-0.004C-0.006O in wt.%) irradiated in the JMTR, new precipitates of disk-shape were formed as shown in Fig. 12. Though those are observed using contrast similar to that for dislocation loops in dark field (Fig. 12(a)), these are not dislocation loops, but precipitates since they often precipitate on residual dislocations as seen in Fig. 12(b), indicating the precipitates with strain field (Fig. 12 (c)). The analysis of the corresponding SADP show that the precipitate lies along the $<001>_{Fe}$ direction, and that there are orientation relationships between the matrix and the precipitate such as $(001)_{Fe}$ // (001)ppt and $[100]_{Fe}$ // [100]ppt. Takeyama et al. observed the preferential precipitation of FeSi (ϵ-phase)-plates on dislocations in a high purity of Fe (Fe-0.003Si-0.01O-0.03C-0.01N-0.0001Cu in wt.%) which was thermally aged at 100°C for 30 m [*17*]. Si-content in the present specimen is similar to that for Takeyama et al. Also, the preferential precipitation on dislocations, the orientation relationship and the precipitate shape in the present specimen are the same as those from Takeyama et al. The plate precipitates observed in our irradiated Fe, therefore, appear to be FeSi (ϵ-phase). Since precipitates of this type have not been observed in the thermally aged specimens, the precipitation is considered to be enhanced by neutron irradiation.

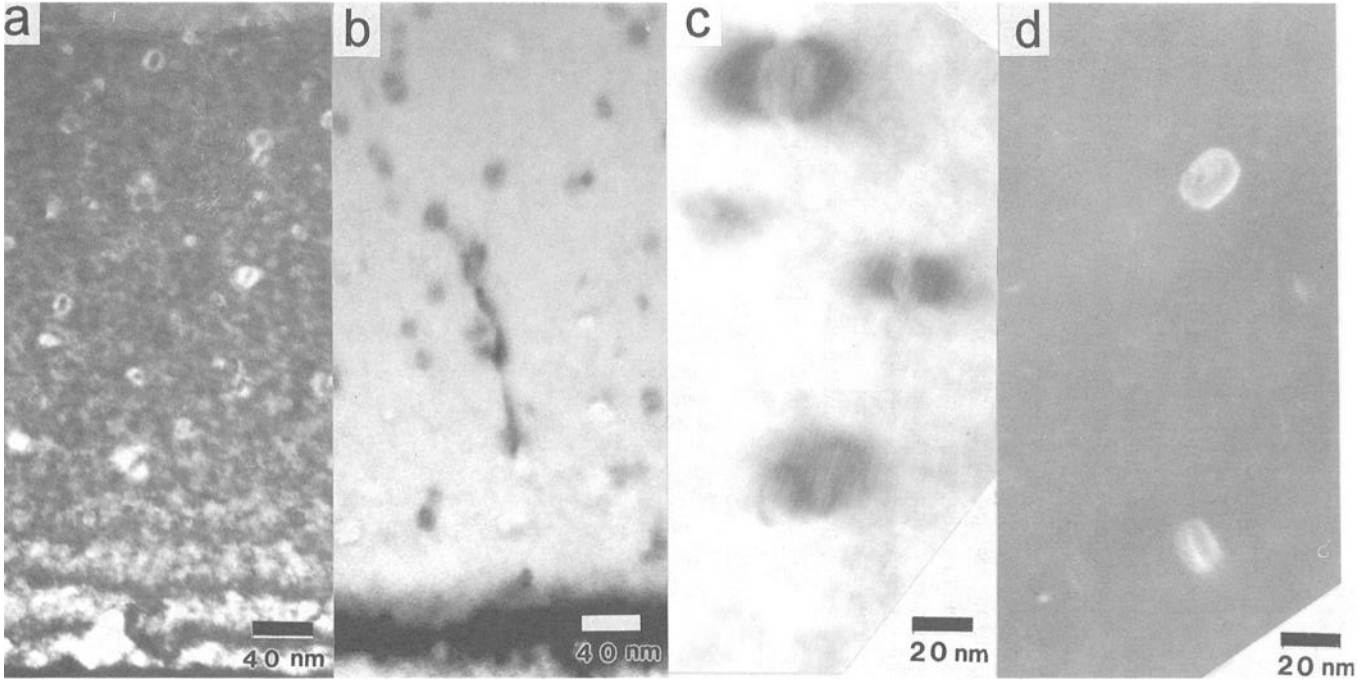


Figure 12 - *Precipitates in unalloyed Fe irradiated in the JMTR. (a) Dark field image using a (112)$_{Fe}$ reflection. (b) Bright field image of the precipitates. Note some predipitates on a dislocation. (c) Halo contrast showing strain fields around the precipitates. (d) Dark field image of the precipitates from an extra reflection presumed to be (002)$_{FeSi}$. The precipitate is believed to be FeSi (ϵ-phase).*

Discussion

The Effects of Pre-Aging on Hardening in Fe-0.6 wt.% Cu Irradiated in the JMTR

It can be readily understood in Fig. 1 that the degree of the hardening was reduced with the period of pre-aging. The specimen thermally aged for 1000 h prior to the JMTR-irradiation shows the least hardening. This suggests that copper precipitates with twinning, which developed during thermal aging, might delay the formation of short range ordered domains. The observations indicated that the ultrathin precipitates without twins (Fig. 3), which were formed in the water-quenched and 100 h-aged conditions, were eliminated by neutron irradiation while only small precipitates with twins (Fig. 10) still persisted after the irradiation. Thus, it may be reasonable that the precipitate with twins plays the important role of delaying the formation of ordered domains. It is possible that the pre-aging delays the formation of the ordered domain by increasing the precipitate-thickness or reducing the concentration of copper in solute in the matrix, resulting in less hardening. Though the above description means that ultrathin precipitate is preferential for ordering, the reason remains to be investigated further.

Fe_3O_4 and FeSi for Unalloyed Fe Irradiated in the JMTR

Figs. 13(a) and (b) demonstrate the precipitation of Fe_3O_4 in (a) the unalloyed Fe irradiated at 290°C to 0.0055 dpa in the JMTR, and (b) the Fe-0.6 wt.% Cu alloy thermally aged for 1000 h at 500°C. In general, it was rather difficult to accurately define the size and shape of Fe_3O_4 precipitates due to the overlapping effects of Fe_3O_4 precipitates, copper precipitates and superlattice images. Moreover, the contrast is very sensitive to how each reflection operates in a given condition. In unalloyed Fe, Fe_3O_4 could be observed as particle in dark field contrast by using a $(2\bar{2}0)_{Fe_3O_4}$ reflection (Fig. 13(a)), where Fe_3O_4 particle as small spots are distributed uniformly in the matrix. On the other hand, in addition to Fe_3O_4 particles, there are a group of Fe_3O_4 particles in Fe-0.6 wt.% Cu specimens as seen in Fig. 13(b). These oxide precipitates seem to form a plate or disk consisting of localized Fe_3O_4 particles, but images probably result from the overlapping effects just described above since such plate-like contrast becomes weak or disappears when only an Fe_3O_4 reflection operates. It is evidence from our TEM observations that the size of Fe_3O_4 particles in unalloyed Fe was larger than that in Fe-Cu alloys, and that irradiation increased their size slightly. No precipitation of FeSi (Fig. 12) has been observed in the thermally aged Fe, indicating the enhancement of the precipitation by neutron irradiations. Neither defect clusters nor dislocation loops were observed in our irradiated specimens. The precipitation of FeSi is considered to contribute in some degree to the hardening of the unalloyed Fe irradiated in the JMTR, but the present data are insufficient for specifying what induces the hardening precisely.

Short Range Ordered Domains of Cu_3Fe-Superlattice

It has been known that superlattice is created from a random solid solution with little or no deformation of the lattice. This means that every lattice spacing or lattice parameter is changed little on transformation between an ordered and disordered solid solution. By

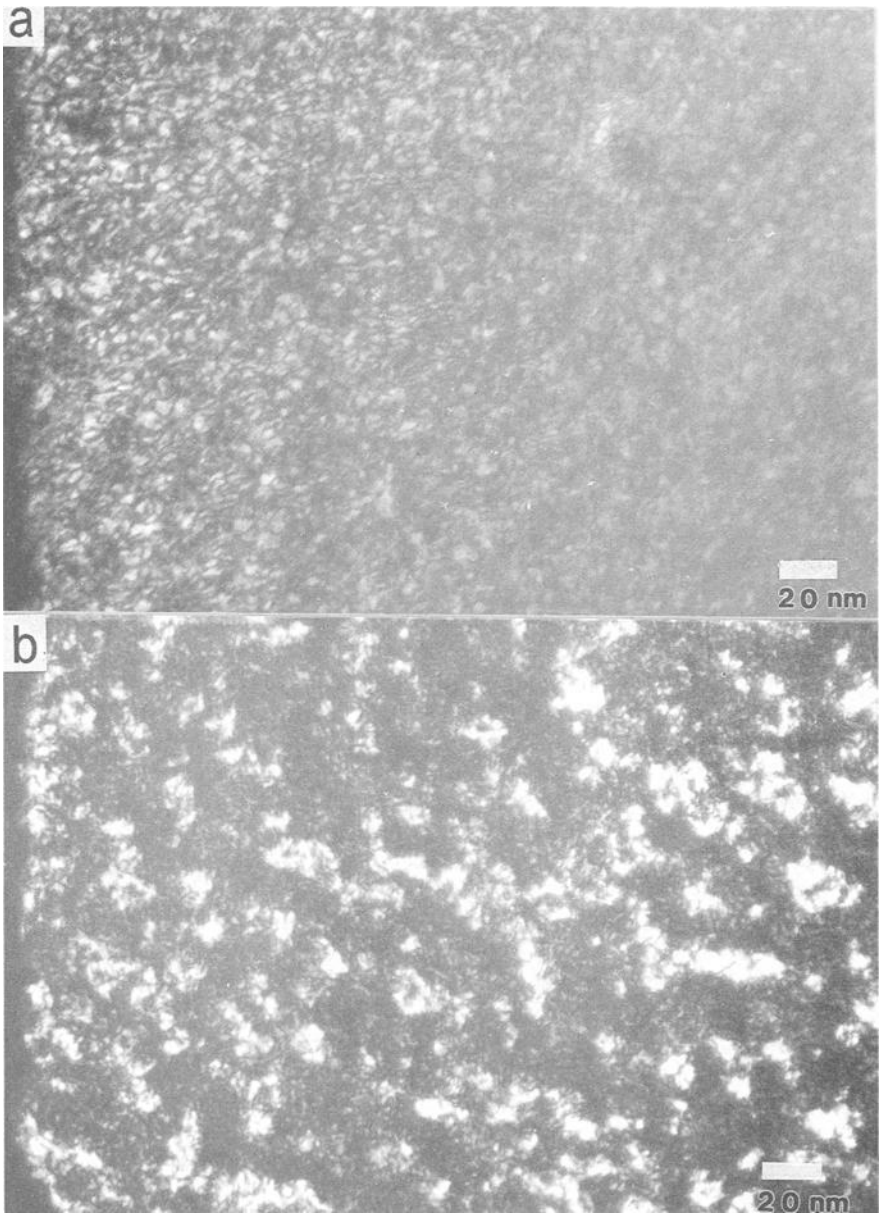


Figure 13 - *Dark field image of Fe_3O_4 precipitates in (a) unalloyed Fe irradiated in the JMTR and (b) Fe-0.6 wt.% Cu thermally aged for 1000 h at 500°C.*

assuming a linear relation for the lattice parameter (Vegard's law) in the Fe-Cu system, the hexagon ② in Fig. 8 has been determined to be a $(111)_{Cu_3Fe}$ pattern from the analysis of lattice parameter and the spacing of (110) planes (Table 1) where Cu_3Fe is believed to have the same structure as Cu_3Au (superlattice of $L1_2$-type). Caution, here, must be paid to the fact that there might be reflections or spots due to Fe_3O_4 near those of Cu_3Fe, e.g., $(113)_{Fe_3O_4}$-spot near a $(110)_{Cu_3Fe}$-spot. Compared two hexagons ② in Figs. 2 and 8, hexagon ② in Fig. 8(b) is a regular hexagon while hexagon ② in Fig. 2(b) is not. Thus, hexagons ② in Figs. 2(b) and 8(b) are determined to be $(112)_{Fe_3O_4}$ and $(111)_{Cu_3Fe}$ diffraction patterns, respectively. There are two methods to distinguish two patterns on a $(110)_{Fe}$ diffraction pattern. The first one is to measure the interplanar spacings of spots. The spacings of $(113)_{Fe_3O_4}$ and $(110)_{Cu_3Fe}$ planes are very close; those of $(113)_{Fe_3O_4}$ and $(110)_{Cu_3Fe}$ planes are 0.2531 and 0.2423 nm, respectively. The second is to measure the angle of two spots forming hexagon. The angles for a set of $(113)_{Fe_3O_4}$ and $(110)_{Cu_3Fe}$ spots are 63° and 60°, respectively. It seems that $(112)_{Fe_3O_4}$ pattern do not appear in Fig. 8. However, it is anticipated that $(113)_{Fe_3O_4}$ spots may influence the image contrast when we use $(110)_{Cu_3Fe}$ spots on a $(111)_{Cu_3Fe}$ because $(113)_{Fe_3O_4}$ spots are placed near the $(111)_{Cu_3Fe}$ in reciprocal lattice space. Thus, we must always pay attention to the possibility that the image of Cu_3Fe may be overlapped with that of Fe_3O_4. With experience, it appears very difficult to precisely define the shape of Cu_3Fe-domains; Cu_3Fe and Fe_3O_4 often show similar images (for example, Figs. 13(a) and (b)).

The results strongly suggest that vacancies produced by neutron-irradiation play an important role in ordering. In addition, the image of the ordered domain is observed close to a plate (see Fig. 14), leading to the hypothesis that the replacement of Fe atoms with Cu atoms takes place statistically at the interface between the matrix and thin precipitates (both ultrathin precipitates for water-quenched conditions and disk-typed precipitates with twinning for over-aged conditions) through the migration of vacancies. It can be understood that neutron-irradiation raises the concentration of vacancies, compared to that in thermally aged specimens, and that the exchange between Fe and Cu atoms may be enhanced, resulting in radiation-enhanced ordering. Blewitt and Coltman reported that the electrical resistivity in a disordered Cu_3Au alloy was reduced due to the ordering with the initiation of reactor operation at 200°C, and thought that the ordering was assisted by the enhanced diffusion of both atoms of Cu and Au due to vacancies produced by neutrons [*18-19*]. Ordering of this type was also observed in disordered Cu_3Au alloys with electron irradiation (E = 1MeV) by Dugdale and Green [*20*]. On the other hand, it has been known for a long time that the ordered structure was readily destroyed in various kinds of alloys by irradiation [*21*].

The SADP analysis (Fig. 8) corresponding to short range ordered domains shows the orientation relationship between the matrix and Cu_3Fe-superlattice to be

$$(110)_{Fe} \,//\, (111)_{Cu_3Fe} \text{ and } [002]_{Fe} \,//\, [1\bar{1}2]_{Cu_3Fe},$$

which is different from the K-S relation. It is phenomenally understood from data that the reduction of the lattice parameter of the superlattice, compared to that of the precipitate (Cu), may induce the rotation of the lattice about 24°54' around the <111> axis of a copper precipitate with ordering. The reason why the orientation relationship between Cu_3Fe and the matrix does not coincide with the K-S relation, however, is uncertain and remains to be clarified. The newly determined orientation relationship is drawn stereographically in Fig.

15. A representation of this type is useful to analyze a SADP of different kind from the superimposition of $(110)_{Fe}$ and $(111)_{Cu_3Fe}$ pattern. Fig. 15, for example, can be used to predict the appearance of $\{(110)_{Fe} + (110)_{Cu_3Fe}\}$ or $\{(001)_{Fe} + (112)_{Cu_3Fe}\}$ patterns in a SADP, and also indicate that two patterns of $(111)_{Cu_3Fe}$ and $(110)_{Cu_3Fe}$ may occur simultaneously on a $(110)_{Fe}$ pattern. However, no $(110)_{Cu_3Fe}$ pattern is seen in Fig. 8, maybe as a result of weak corresponding reflections which are very sensitive to diffraction conditions, i.e., depending on the electron beam direction during the observations.

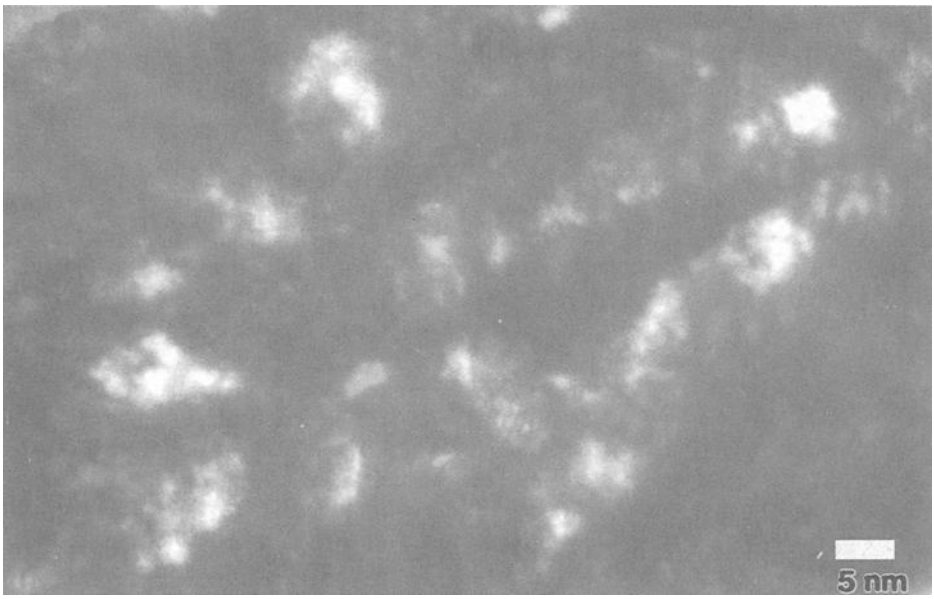
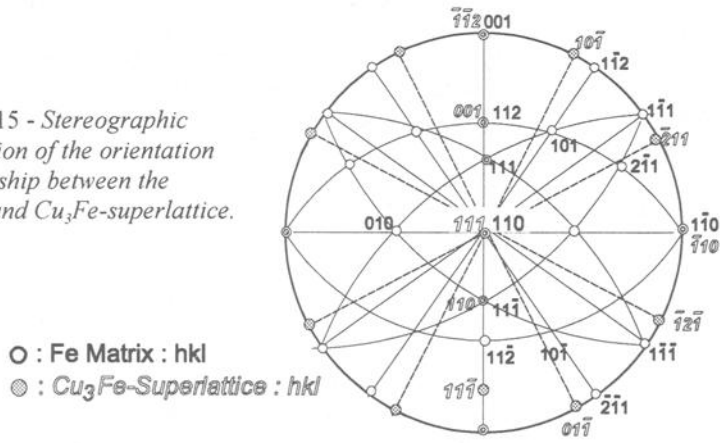


Figure 14 - *Dark field micrograph of ordered-domain by $(110)_{Cu_3Fe}$ reflection. Note that the domain shows a plate-like contrast.*

Figure 15 - *Stereographic projection of the orientation relationship between the matrix and Cu_3Fe-superlattice.*



The Contribution of Cu_3Fe-Superlattice to Hardening

In the present study, the ordered structure was observed to distribute locally and seemed like an island or a group of islands in dark field contrast, indicating that the total volume of the ordered zone was rather small. This was attributed to the low concentration of copper, i.e., 0.6 wt.%. When a dislocation is supposed to slide on a slip plane in Fe-Cu alloys with short range ordered domains, excess work must be done in order to destroy the regular configuration of Fe and Cu atoms, resulting in hardening of the alloy. A treatment of this type was initially done by Fisher [*22*], who proposed the hardening ($\Delta\sigma_{SRO}$) from the ordered domains of short range as follows:

$$\Delta\sigma_{SRO} = \gamma / \boldsymbol{b}$$

where γ is the increase in the interface energy due to the domain from a dislocation (Burgers vector $\boldsymbol{b}$) moving on a slip plane with short range order. This mechanism is very close to the chemical hardening mechanism proposed for a thin precipitate later by Kelly and Fine [*23, 24*]. If we treat the ordered domain as a precipitate, the chemical hardening mechanism can be applied to evaluate the hardening from the ordered domains. However, we were unsuccessful in determining their accurate shape, size and number density in the present experiments and the evaluation of the hardening remained as future work. Though the value of γ is also unknown, it might be much higher than the interface energy of copper precipitates if we assume that all ultrathin copper precipitates convert into the ordered structure and that their size, thickness, and number density are similar for water-quenched and irradiated specimens. A large domain of short range orders with anti-phase boundaries may be formed within an ordered domain and can be expected to contribute to the hardening [*25*]. The anti-phase domain can be identified by the occurrence of satellite spots around superlattice spots in SADP. This also remains in future work.

The present study has focused on the microstructure in neutron-irradiated Fe-Cu model alloys, and we proposed the formation of short range ordred domains, resulting in the dramatic hardening. The structure of the domain is also proposed to be Cu_3Fe by determining the lattice parameter of the domain using the $(1\,1\,0)_{SRO}$ reflections on a SADP. It is desirable to further prove the structure by different techniques (e.g., X-ray diffraction method, neutron scattering techniques or atom probe field ion microscopy). Furthermore, it is interesting to investigate whether or not ordered domains take place in commercial ferritic pressure vessel steels (for example, A-533B) containing copper by neutron irradiations. The work appears to be quite important from the viewpoint of technology.

Conclusions

1. Two kinds of copper precipitates were formed in Fe-Cu model alloys by thermal aging. One was an ultrathin untwinned precipitate that increased in thickness with thermal aging, reducing in diameter and number density. The other was always associated with twinning and grew less until the alloy was over-aged. Both were formed in water-quenched conditions and were disk-shaped.
2. Hardening by thermal aging was attributed mainly to the thickening of the ultrathin

precipitate. Precipitates of other kind were not responsible for the hardening.

3. A remarkable hardening took place in the water-quenched specimens with neutron irradiation with the ultrathin copper precipitates disappearing, while the precipitates with twins persisted. Superlattice, which was speculated to be from Cu_3Fe with a lattice parameter of $\approx$ 0.353 nm, was formed and was considered to be responsible for the hardening due to irradiation. Irradiation is believed to enhance the ordering in Fe-Cu model alloys.
4. Irradiation induced a slight hardening of $\approx$ 20 DPH in unalloyed iron where disk-shaped precipitates (probably, FeSi of ϵ-phase) newly precipitated in addition to Fe_3O_4.

Acknowledgment

Acknowledgments are due to Dr. T. Shikama and Mr. M. Narui of the Oarai Branch, Institute of Materials Research, Tohoku University, for their assistance in carrying out the irradiation experiments.

References

[1] English, C. A.,"Radiation Embrittlement of Nuclear Reactor Pressure Vessel Steels: An International Review(Second Volume)", *ASTM STP-**909***, L. E Steele, Ed., American Society for Testing and Materials, Philadelphia, 1986, pp.187-205.

[2] Lucas, G. E. and Oddete, G. R., in Proc. Second Int. Symposium on Environmental Degradation of Materials in Nuclear Power System-Water Reactors, J. T. A. Roberts, J. R. Weeks and G. Theus, Eds., (American Nuclear Society, Illinois, USA, 1986)p.345.

[3] Buswell, J. T., English, C. A., Hetherington, M. G., Phythian, W. J., Smith, G. D. W. and Worral, G. M., "Effects of Radiation on Materials: the 14th International Symposium (Volume ||), N. H. Packan, R. E. Stoller, and A. S. Kumar, Eds., ASTM *STP-**1046***, American Society for Testing and Materials, Philadelphia, 1990. p.127-153.

[4] Miller, M. A. and Burke, M. G., "Effects of Radiation on Materials: the 14th International Symposium(Volume II)", N. H. Packan, R. E. Stoller, and A. S. Kumar, Eds., ASTM *STP-**1046***, American Society for Testing and Materials, Philadelphia, 1990.pp.107-126.

[5] Little, E. A., Buttle, D. J. and Scruby, C. B., "Effects of Radiation on Materials: the 14th International Symposium(Volume II), N. H. Packan, R. E. Stoller, and A. S. Kumar, Eds., *ASTM STP-**1046***, American Society for Testing and Materials, Philadelphia, 1990. pp.107-126.

[6] Buswell, J. T., Phythian, W. J., McElroy, R. J., Dumbill, S., Ray, P. H. N., Mace, J. and Sinclair, R. N., J. Nuclear Materials, **225**(1995)pp.196-214.

[7] Williams, T. J. and Phythian, W. J., "Effects of Radiation on Materials: the 17th International Symposium(Volume II)", David S. Gelles, Randy K. Nanstad, Arvind S. Kumar and Edward, A. Little, Eds., ASTM *STP-1270*, (American Society for Testing and Materials, Philadelphia, USA, 1996)pp.191-205.

[8] Kawanishi, H., and Suzuki, M., "Effects of Radiation on Materials: the 18th International Symposium", R. K. Nanstad, M. L. Hamilton, F. A. Garner and A. S. Kumar, Eds., *ASTM STP-1325*, American Society for Testing and Materials, West Conshohocken, PA, 1999. pp.945-969.

[9] Kawanishi, H., and Suzuki, M., (to be published).

[10] Othen, P. J., Jenkins, M. L., Smith, G. D. W. and Phythian, W. J., *Philosophical Magazine Letters*, **64**(1991)pp.383-391.

[11] Othen, P. J., Jenkins, M. L. and Smith, G. D. W., *Philosophical Magazine A*, **7**(1994)p.1.

[12] Hardouin Duparc, H. A., Doole, R. C., Jenkins, M. L. and Barbu, A., *Philosophical Magagazine Letters*., **71**(1995)pp.325-333.

[13] Hirsch, P. B., Howie, A., Nicholson, R. B., Pashley, D. W. and Whelan, M. J., *Electron Microscopy of Thin Crystals*, Butterworths, London, 1965, pp. 305-306 and 327-352.

[14] Sakata, S. and Mizushima, S., *Japan Academy*, **41**(1965)p.933.

[15] Nishiyama, Z., *Science Report*, Tohoku University, **23**(1934)p.638.

[16] Wasserman, G., *Arch. fur das Eisenhutt*., **16**(1933)p.647.

[17] Tekeyama, T., Hachinoe, M. and Sato, G., *J. Electron Microscopy*, **15**(1966)269.

[18] Blewitt, T. H. and Coltman, R. R., *Physical Review*, **85**(1952)384.

[19] Blewitt, T. H. and Coltman, R. R., *Acta Metallugica*, **2**(1954)549.

[20] Dugdale, R. A. and Green, A., *Philosophical Magazine*, **45**(1954)163.

[21] For example, Siegel, S., *Physical Review*, **75**(1949)p.1823.

[22] Fisher, J. C., *Acta Metallugica*, **2**(1954)9.

[23] Kelly, A. and Fine, M. E., *Acta Metallugica*, **5**(1957)pp.365-367.

[24] Kelly, A. and Nicholson, R.B., *Progress in Materials Science*, **10**, Eds., B. Charmers, (1963, Pergamon Press, Oxford) pp.323-363.

[25] Brown, N. and Herman, M., *Trans. American Institue of Mining , metallurgy and petroleum Engineers*, **206**(1956)p.1353.

Seiya Yanagita,[1] Qiu Xu,[1] Toshimasa Yoshiie,[1] and Hiromitsu Ino[2]

Neutron Irradiation Rate Dependence of Damage Structures in Fe-Cu Model Alloys

Reference: Yanagita, S., Xu, Q., Yoshiie, T., and Ino, H., **"Neutron Irradiation Rate Dependence of Damage Structures in Fe-Cu Model Alloys,"** *Effects of Radiation on Materials: 19th International Symposium, ASTM STP 1366,* M. L. Hamilton, A. S. Kumar, S. T. Rosinski, and M. L. Grossbeck, Eds., American Society for Testing and Materials, West Conshohocken, PA, 2000.

Abstract: Fe-Cu model alloys and pure iron were irradiated at 573 K under two different neutron flux conditions (9.4×10^{-8} dpa/s and 1.1×10^{-9} dpa/s) up to about 0.008 dpa. Although defect clusters were not detected by TEM in any specimen, the results of positron lifetime measurement and mechanical property tests clearly indicated an irradiation rate dependence on the microvoid formation and mechanical properties. In positron lifetime measurements, the size of microvoids under low flux irradiation was larger than under high flux irradiation. But the number density was lower than high flux irradiation. In mechanical property testing, more hardening occurred by low flux irradiation. The irradiation rate dependence increased with copper content. These results suggest that the dependence is caused by the precipitation of copper. As copper migrates mainly by the vacancy mechanism, the size and the density of precipitates increase with increasing vacancy migration distance, which becomes longer with a decreasing of the irradiation rate.

Keywords: irradiation rate dependence, Fe-Cu model alloy, neutron flux, irradiation hardening

Introduction

In a fission reactor, the pressure vessel is one of the important components because it can not be replaced. So it is necessary to understand property changes of the pressure vessel by neutron irradiation for the evaluation of the safety of the reactor. Property changes of irradiated materials are mainly caused by clustering of point defects and solute atoms. When the reactor pressure vessel steel contains copper, the precipitation of copper occurs during neutron irradiation at lower temperature than under thermal aging. This can cause extreme mechanical property changes. A lot of research has revealed that small copper

[1] Graduate Student, Research Associate and Professor, respectively, Research Reactor Institute, Kyoto University, Kumatori, Osaka 590-0494, Japan.

[2] Professor, Faculty of Engineering, Hosei University, Koganei, Tokyo 184-8584, Japan.

Copyright© 2000 by ASTM International www.astm.org

precipitates play a major role in irradiation hardening and embrittlement in pressure vessel steels. But the effect of irradiation rate on the growth of copper and its precipitates has not been clarified yet. As accelerated irradiation testing has been performed to estimate the lifetime of nuclear materials, the understanding of the effect of irradiation rate is important. In this study, the effect of neutron irradiation rate on the initial stage of damage structure development in Fe-Cu model alloys and pure iron is reported.

Experimental

Specimens of this study were pure iron, Fe-0.15 wt%Cu, Fe-0.3 wt%Cu and Fe-0.6 wt%Cu. They were made from pure iron (purity 99.99 %) and copper (purity 99.9 %) by using the high-frequency induction furnace in a vacuum. After melting, solution treatment was carried out at 1423 K for 24 hours, and then alloys were quenched in water. The resulting alloys were cold-rolled to 0.2 mm (for tensile test) or 0.1 mm (for the other test) in thickness. Disks of 3 mm in diameter were punched out from 0.1 mm plates. Miniature size tensile test specimens (2.3 mm $\times$ 12.5 mm) were punched out from 0.2 mm plates, where the rolling direction was parallel to the long axis of specimens. Finally, all specimens were annealed at 1223 K for 0.5 hours, followed by quenching in water.

Neutron irradiation test was performed at the KUR (Kyoto University Reactor). Irradiation facilities used in this study were the Hydraulic Conveyor (Hyd, Flux ($E > 0.1$ MeV) : 3.9×10^{13} n/(cm^2·s)) and the Slant Exposure Tube (Sl, Flux ($E > 0.1$ MeV) : 4.4×10^{11} n/(cm^2·s)). These flux are equivalent to 9.4×10^{-8} dpa/s (Hyd) and 1.1×10^{-9} dpa/s (Sl). The irradiation temperature of this study was 573 K to approximate the irradiation condition of a power reactor. For carrying out the 573 K irradiation, the special irradiation capsules were employed to control specimen temperature by using an electric heater in all irradiation tests [*1*].

Irradiation times were 5 hours and 24 hours at Hyd and 400 hours at Sl, respectively. The total doses were 7.0×10^{17} n/cm^2 (1.6×10^{-3} dpa) at Hyd for 5 hours, 3.4×10^{18} n/cm^2 (8.1×10^{-3} dpa) at Hyd for 24 hours and 6.3×10^{17} n/cm^2 (1.5×10^{-3} dpa) at Sl for 400 hours. Since the total dose of Hyd irradiation for 5 hours is nearly equal to Sl irradiation for 400 hours, the irradiation rate dependence can be evaluated between them.

Annealing tests were also performed to evaluate the long-time annealing effect. Annealing temperature and time were 573 K and 400 hours, respectively, which were equivalent to Sl irradiation conditions of this study.

After irradiation, TEM observation, positron lifetime measurement, miniature tensile test and hardness test were carried out. Specimens of ϕ 3 mm $\times$ 0.1 mm disk were also used for positron lifetime measurement and hardness test. TEM observation was performed using JEOL-2010 type electron microscope (JEOL Co.) operating at 200 kV. In the specimens of 24 hours irradiation at Hyd, positron lifetime measurement and miniature tensile test were not performed because of its residual activity. The values of hardness shown in this study are the dynamic hardness which is calculated from indented depth, instead of the area of indentation. In the hardness test, a DUH-201 type dynamic hardness tester (Shimadzu Co.) with trigonal pyramid shaped ("Berkovich type") diamond indenter was used. Parameters of the hardness test were as follows: load was 10 gf, load rate and unload rate were 1.35 gf/s and holding time after loading was 5 s. The indented depth was 1500 $\sim$ 2500 nm.

Results

TEM observation

During TEM observation, no point defect clusters were observed in any specimens at any irradiation condition. One of the reason why no defects were observed is considered to be the low dose of this study. For example, in pure iron, defect clusters which can be observed by TEM are not formed until the dose of about 10^{19} n/cm^2. Doses in this study are one order of magnitude lower than that.

Another reason why no defects were observed is considered to be the form of defect clusters. According to our model calculations [2], copper cluster size of Fe-0.6 wt% alloy after Hyd irradiation for 5 hours and SI irradiation for 400 hours are about 0.6 nm and 1.0 nm in diameter, respectively. As copper clusters below 1 nm in diameter are expected to be the bcc structure [3] and its lattice parameter is close to that of iron, it is difficult to detect them in iron. Our model calculations also show that the diameters of interstitial type dislocation loops and voids are almost the same or larger than those of copper clusters but their number density is lower than that of copper clusters.

Positron lifetime measurement

The results of positron lifetime measurement are shown in Table 1 and Figure 1. The lifetime of pure iron is the mean lifetime and others are the longer lifetime components by the two-lifetime-component analysis. In pure iron, the lifetime spectra were not decomposed into two components. The lifetime of pure iron is shorter than that of vacancies. It indicates that the detectable number of microvoids was not formed in pure iron. On the other hand, Xu et al. [1] detected the existence of microvoids in iron by the same irradiation conditions. This discrepancy is considered to arise from the impurity effect because their specimens are made from iron of 99.999 % in purity and decarbonized in hydrogen gas. Impurities may help the nucleation of interstitial clusters, and vacancies are annihilated at these clusters, which prevent the formation of microvoids.

In both irradiation conditions, the lifetime of Fe-Cu alloys indicate the existence of microvoids. By the addition of copper, the impurity effect mentioned above is suppressed. The positron lifetime of SI irradiation for 400 hours is longer than that of Hyd irradiation for 5 hours at the same copper content. But the intensity of Hyd irradiation is higher than that of SI irradiation. These results show that vacancy cluster size of SI irradiation is larger than that of Hyd irradiation, but the number density is lower. According to the theoretical calculation given by Puska and Nieminen [4], the lifetime of 300 ps in Fe-Cu alloys means the microvoids contain about 15 vacancies (0.8 nm in diameter). This result suggests that copper stabilizes the microvoids during irradiation. So it is considered that copper interacts not only with vacancies but also with microvoids.

Hardness measurement

The results of hardness measurements are shown in Table 2, Figure 2 and Figure 3. In the hardness change, SI irradiation for 400 hours is larger than Hyd irradiation for 5 hours. The results of hardness can be approximated by $H = AC_{Cu} + B$, where H is the value of hardness, A and B are the constant and C_{Cu} is the initial copper content (wt%).

Table 1 – *Results of positron lifetime measurement. The two lifetime component analysis was performed. "Mean" represents the mean positron lifetime which is obtained by one lifetime component analysis. "Short" represents the short positron lifetime component (units in ps) and its intensity (units in %, in parenthesis). "Long" represents the long positron lifetime component (units in ps) and its intensity (units in %, in parenthesis).*

	Hyd			Sl		
	Mean	Short	Long	Mean	Short	Long
pure Fe	143	—	—	122	—	—
Fe-0.15%Cu	135	122 (86.0)	293 (14.0)	134	116 (86.4)	344 (13.6)
Fe-0.3%Cu	161	134 (82.6)	270 (17.4)	167	125 (80.9)	339 (19.1)
Fe-0.6%Cu	130	116 (82.2)	230 (17.8)	160	126 (83.3)	322 (16.7)

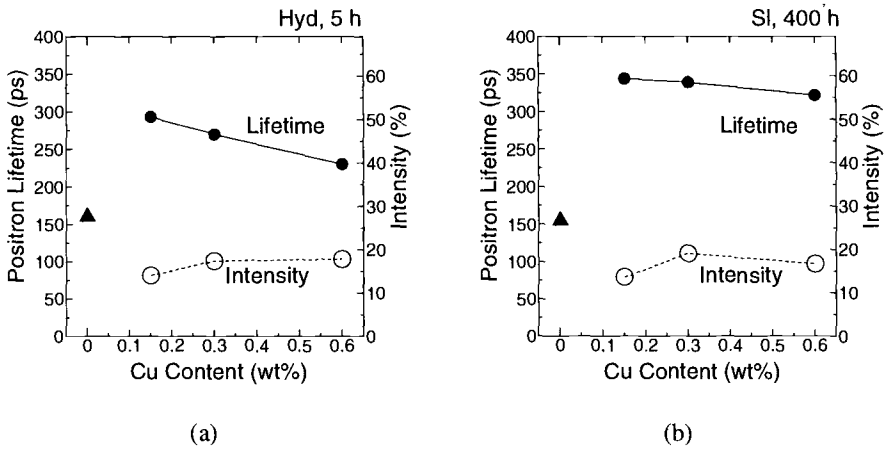


Figure 1 – *Dependence of long positron lifetime component and its intensity on copper content for (a) Hyd irradiation for 5 hours, (b) Sl irradiation for 400 hours. Note that the lifetime of pure iron (solid triangle) in both figures are mean values.*

Values for A and B were obtained by using the method of least squares. Results are shown in Figure 2 and Figure 3 as straight lines. The slopes in Figure 2(a) and Figure 3(a) are 71.8 (as-quenched), 95.9 (Hyd for 5 hours), 97.2 (at Hyd for 24 hours) and 115 (at Sl for 400 hours). The slopes in Figure 2(b) and Figure 3(b) are 24.1 (Hyd for 5 hours), 27.5 (at Hyd for 24 hours) and 43.1 (at Sl for 400 hours). It is obvious that the hardness change increases with copper content. In this study, all specimens are quenched in water after final annealing. So it is considered that increase in hardness with copper content is due to an alloying effect.

In Table 2, results of annealed specimens are also shown. Results of annealed specimens and as-quenched specimens were almost the same, so it can be concluded that the annealing effect is negligible at the test condition in this study (573 K, max. 400 hours).

Table 2 – *Results of hardness measurements.*

Cu content (wt%)	0	0.15	0.3	0.6
as-quenched	79.6	93.4	106	123
annealing, 400 h	81.5	88.8	107	123
SI, 400 h	97.3	120	146	167
Hyd, 5 h	98.1	109	122	155
Hyd, 24 h	104	120	142	163

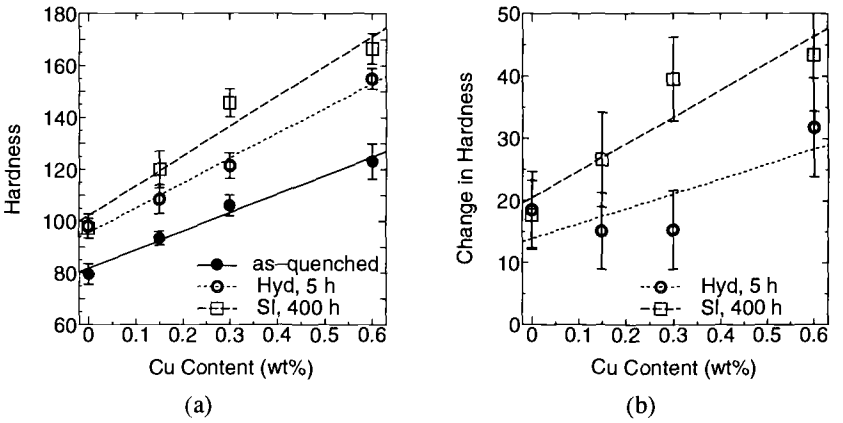


Figure 2 – *(a) Result of hardness test and (b) change in hardness during irradiation as a function of copper content for as-quenched, Hyd irradiation for 5 hours and SI irradiation for 400 hours. Standard deviations are also shown.*

Figure 2(b) indicates that hardening is accelerated under low irradiation rate. Results of a model calculation [2] suggest that the main factor influencing the hardness change is the precipitation of copper clusters and its effect increase with decreasing the irradiation rate. Results shown in Figure 2(b) are qualitatively consistent to the results of the calculation.

Note that the slope of Hyd irradiation for 5 hours is nearly equal to that of Hyd irradiation for 24 hours, as shown in Figure 3, but the hardness change by irradiation is not proportional to the irradiation time. This suggests that the saturation of hardening occurs at a very low dose. It is due to the fact that the hardening is mainly caused by the precipitation of copper in this irradiation stage. At the latter irradiation stage, more hardening is expected by the growth of interstitial type dislocation loops and voids.

Tensile test

The results of miniature size tensile tests are shown in Table 3 and Figure 4. In general, the 0.2% yield stress change and the ultimate tensile stress (UTS) change by irradiation at SI for 400 hours are larger than those at Hyd irradiation for 5 hours. Note that the

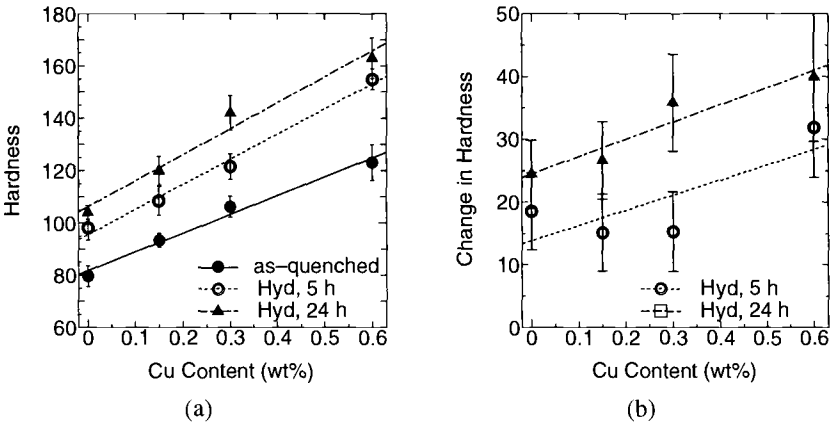


Figure 3 – *(a) Result of hardness test and (b) change in hardness during irradiation as a function of copper content for as-quenched, Hyd irradiation for 5 hours and 24 hours. Standard deviations are also shown.*

Table 3 – *Results of tensile test. "as-q" represents the result of as-quenched (non-irradiated) specimens.*

	0.2% yield stress (MPa)			UTS (MPa)		
Cu content (wt%)	as-q	Hyd, 5h	Sl, 400h	as-q	Hyd, 5h	Sl, 400h
0	111.8	143.2	90.81	146.1	160.8	124.5
0.15	128.5	128.5	146.1	162.8	152.0	171.6
0.3	141.2	149.1	195.2	168.7	160.8	213.8
0.6	206.9	249.1	304.0	209.9	254.0	337.3

irradiation softening seems to occur as shown in Figure 4 in pure Fe, but it can not be concluded because of few test data. Further analysis for this point should be performed. The 0.2% yield stress change and the UTS change by irradiation increase with copper content. These results agree with the result of hardness test. Similar to the hardness measurement, the result of the tensile tests were approximated by $T = AC_{Cu} + B$, where T is the 0.2% yield stress or UTS. These are shown in Figure 4 as straight lines in each figure. The results of TEM observation and positron lifetime measurement indicate the existence of very fine point defect clusters. So it can be considered that these fine clusters are enough to cause the mechanical property change.

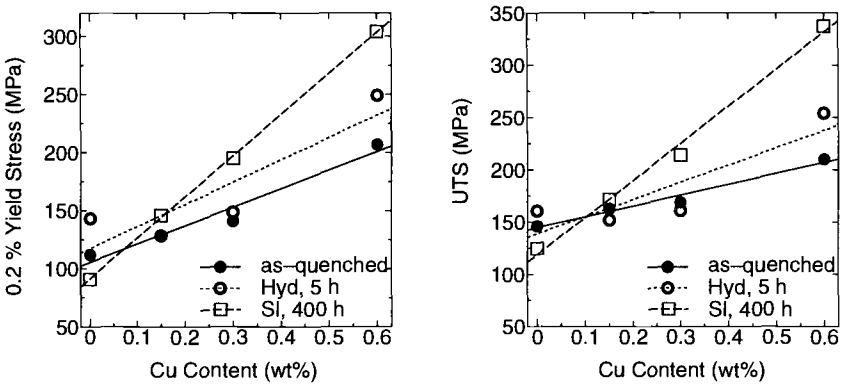


Figure 4 – *Results of tensile test. (a) 0.2% yield stress and (b) ultimate tensile stress are shown as a function of copper content for as-quenched, Hyd irradiation for 5 hours and SI irradiation for 400 hours.*

Discussion

Interaction between copper and vacancies

Copper in iron is a oversized atom, and its volume is about 18 % larger than that of iron [5]. The binding energy between copper and vacancy is reported to be about 0.14 eV [6]. From the results of this study, the following two interactions between copper and vacancies are supposed.

One is the trapping of vacancies by copper. This effect prevents vacancy migration, and many of the vacancies remain in the matrix until the latter stage of irradiation. This effect increases with copper content, and suppresses the effect of impurities, since the concentration of copper is much higher than that of impurities. The situation that vacancies remain in the matrix is favorable for the growth of microvoids.

The other is the gathering of copper around vacancy clusters. As mentioned above, copper in iron is the oversized atom, it is reasonable that copper interacts not only with the vacancy but also with vacancy clusters, such as microvoids. The interaction between copper and microvoids causes the relaxation of void surfaces, so the sink efficiency of microvoid to point defects decreases. This effect increases with copper content. As the result of this effect, microvoid growth is difficult, but they are stabilized by preventing the absorption of interstitials by microvoids. After all, the microvoid size decreases but the number density increases with copper content.

Irradiation rate dependence

In this study, results of three kinds of measurements clearly showed an irradiation rate dependence, i.e., the hardening and the growth of microvoids are enhanced under low irradiation rate. As mentioned above, mechanical property changes by irradiation

increase with copper content. The results of model calculations [2] and positron lifetime test in this study suggest that the behavior of copper is caused by the difference of the migration distance of vacancies, since copper migrates by the vacancy mechanism. In other words, the number of vacancy jumps depends on the irradiation rate. As the sink strength, the number density of defect clusters is more important than the size of them. When the irradiation rate is low, their density is low and the annihilation rate of point defects with defect clusters is low. After all, point defects can migrate at long distance, which is advantageous for copper precipitation.

Kussmaul et al. [7] suggested the possibility of irradiation rate dependence in mechanical property change by comparing the result of irradiation at the Gundremmingen reactor with that at a test reactor at 557 K. From our result, we can conclude that their results is caused by an irradiation rate dependence. On the other hand, Odette et al. [8] reported that the yield stress change is not sensitive to irradiation dose rate at 323 K irradiation. The temperature for 323 K is, however, too low for vacancy migration in a non-high purity iron. Because long range vacancy migration occurs in iron at above 473 K by the effect of impurities [9] except for high purity iron. While the experiments by Kussmaul et al. and by us were performed at 557 K and 573 K where vacancies could migrate easily. From comparison of these three results, it is clear that the irradiation rate dependence is significant at about the vacancy migration temperature.

Conclusion

Neutron irradiation tests following irradiation with well-controlled temperature were performed. Although the total dose of these tests was low, the results showed irradiation rate dependence. These results suggest that the irradiation rate dependence should be taken into consideration for data from accelerated irradiation tests to improve the reliability of interpretations.

Since all specimens used in this study were model alloys, we can not declare that the irradiation rate dependence exists in the commercial materials of the reactor pressure vessel, e.g., A212B and A533B, which contain several alloying elements. For example, it has been reported that nickel interacts with copper after annealing [10]. More experiments using these materials should be performed.

Acknowledgements

This work has been carried out in part under the Visiting Researcher's Program of the Research Reactor Institute, Kyoto University.

References

[1] Xu, Q., Yoshiie, T. and Iseki, M., "Effects of Damage Rate on Nucleation of Voids and Dislocation Loops in Metals", *Effects of Radiation on Materials: 19th International Symposium, ASTM STP 1366*, M. L. Hamilton, A. S. Kumar, S. T. Rosinski and M. L. Grossbeck, Eds., American Society for Testing and Materials, 1999.

[2] Yanagita, S., Yoshiie, T. and Ino, H., "A Model Calculation for Irradiation Rate Dependence of Defect Structure in Fe-Cu Alloy", to be published.

[3] Ludwig, M., Farkas, D., Pedraza, D. and Schmauder, S., "Embedded Atom Potential for Fe-Cu Interactions and Simulations of Precipitate-Matrix Interfaces", *Modeling and Simulation in Materials Science and Engineering*, Vol. 6, No. 1, 1998, p. 19.

[4] Puska, M. J. and Nieminen, R. M., "Defect Spectroscopy with Positrons: A General Calculation Methods", *Journal of Physics F: Metal Physics*, Vol. 13, 1983, p. 333.

[5] King, H. W., "Quantitative Size-Factors for Metallic Solid Solutions", *Journal of Materials Science*, Vol. 1, 1966, p. 79.

[6] Brauer, G. and Popp, K., "Neutron Embrittlement of Reactor Pressure Vessel Steels: A Challenge to Positron Annihilation and Other Methods", *Physica Status Solidi A*, Vol. 102, 1987, p. 79.

[7] Kussmaul, K., Föhl, J. and Weissenberg, T., "Investigation of Materials from a Decommissioned Reactor Pressure Vessel – A Contribution to the Understanding of Irradiation Embrittlement", *Effects of Radiation on Materials: 14th International Symposium (Volume II), ASTM STP 1046*, N. H. Packan, R. E. Stoller and A. S. Kumar, Eds., American Society for Testing and Materials, 1990, p. 80.

[8] Odette, G. R., Lucas, G. E., Klingensmith, R. D. and Stoller, R. E., "On the Effect of Flux and Composition on Irradiation Hardnening at 60°C", *Effects of Radiation on Materials: 17th International Symposium, ASTM STP 1270*, D. S. Gelles, R. K. Nanstad, A. S. Kumar and E. A. Little, Eds., American Society for Testing and Materials, 1996, p. 547.

[9] Kiritani, M., "Nature of Point Defect Clusters and Their Interactions Revealed by Electron-Microscope Observation of Their Clusters", *Proceedings of Yamada Conference on Point Defects and Defect Interactions in Metals*, J. Takamura, M. Doyama and M. Kiritani, Eds., University of Tokyo Press, 1982, p. 59.

[10] Buswell, J. T., English, C. A., Hetherington, M. G., Phythian, W. J., Smith, G. D. W. and Worrall, G. M., "An Analysis of Small Clusters Formed in Thermally Ages and Irradiated FeCu and FeCuNi Model Alloys", *Effects of Radiation on Materials: 14th International Symposium (Volume II), ASTM STP 1046*, N. H. Packan, R. E. Stoller and A. S. Kumar, Eds., American Society for Testing and Materials, 1990, p. 127.

Vladimir I. Karpukhin,[1] Yevgeny A. Krasikov,[1] Vadim A. Nikolaenko,[1] and Yaroslav I. Shtrombakh[1]

Gamma-Radiation Annealing to Mitigate Neutron-Induced Degradation of Both Model and Structural Reactor Materials

Reference: Karpukhin, V. I., Krasikov, Y. A., Nikolaenko, V. A., and Shtrombakh, Y. I., **"Gamma-Radiation Annealing to Mitigate Neutron-Induced Degradation of Both Model and Structural Reactor Materials,"** *Effects of Radiation on Materials: 19th International Symposium, ASTM STP 1366,* M. L. Hamilton, A. S. Kumar, S. T. Rosinski, and M. L. Grossbeck, Eds., American Society for Testing and Materials, West Conshohocken, PA, 2000.

Abstract: Formation and evolution of radiation defects are determined by the irradiation conditions. Some of these conditions do not get sufficient attention. In particular, this is true for the gamma-annealing process whose role in radiation-induced effects have not been considered in detail previously. Reactor experiments have shown that volume expansion of diamond and silicon carbide depends on the γ-radiation flux value: the higher the gamma-flux, the lower is the expansion. Radiation γ-annealing was also discovered in reactor grade graphite. Analysis has shown that this phenomenon is probably operating in reactor pressure vessel materials. This phenomenon opens a new perspective of radiation effects mitigation and reactor materials life cycle management using neutron and gamma-ray intensity control.

Keywords: neutron-induced degradation, gamma-irradiation annealing, model materials, structural materials

The long-term prediction of structural materials operation reliability in radiation fields is sometime inadequate from the modern point of view. This validation has initiated a search for radiation damage mechanisms yet unaccounted for, but essential from the point of view of radiation solid-state physics factors.

Having analysed the role of reactor γ-radiation as a factor inhibiting defect formation, the authors found clear evidence that the rate of the materials radiation degradation simultaneously irradiated by neutrons and γ-quanta depends on the flux of the latter. The γ-ray effect is usually estimated only in terms of heat release. However, between the γ-quanta on the materials properties under irradiation have not been considered in detail so far.

[1] Leading research scientist, Head of Laboratory, Head of Group, Deputy Director respectively, Reactor Materials Division, Russian Research Centre "Kurchatov Institute", 1, Kurchatov Square, Moscow, 123182, Russia.

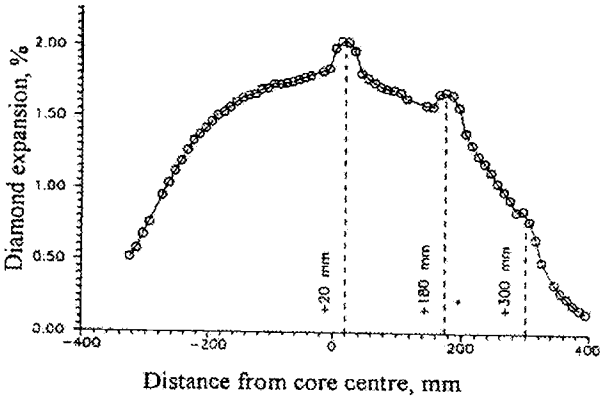
Copyright© 2000 by ASTM International www.astm.org

The effect of γ-quanta on defect formation and annealing is indirect. First, fast electrons are produced by photoeffect, Compton scattering and pairing, and then electrons interact with both regular atoms and defect-lattice atoms. The spectra and intensities of neutrons and γ-quanta in reactor are such that neutrons mainly produce defects, while γ-quanta primarily affect their annealing.

Materials, Experimental Methods and Results

Diamond and Graphite

The expansion results measured in diamond powder, used as a routine model material for in-core irradiation are presented in Fig.1 *[1]*.



The approach employs crystal lattice parameters measured by X-ray methods. The data obtained have been reduced to a relative volume change (expansion) in percent. The error was 0.01 %, unless otherwise specified.

An experiment was carried out in the IR-8 research reactor with lead screens used as γ-radiation absorbers. The capsules were filled with diamond powder and placed in tubes stacked along the core height. Coolant water at a temperature of about 60°C was flowing around the capsules during irradiation. At the elevations of +20, +180 and +300 mm from the core centre lead balls 40 mm in diameter were put on the channel tube which provided a 3-fold attenuation of the γ-radiation.

It follows from Fig.1 that the places where lead screens were situated the diamond expansion increased in magnitude.

To the contrary, when γ amplifying indium screens were used neutron-induced defect mitigation took place (Fig.2)..

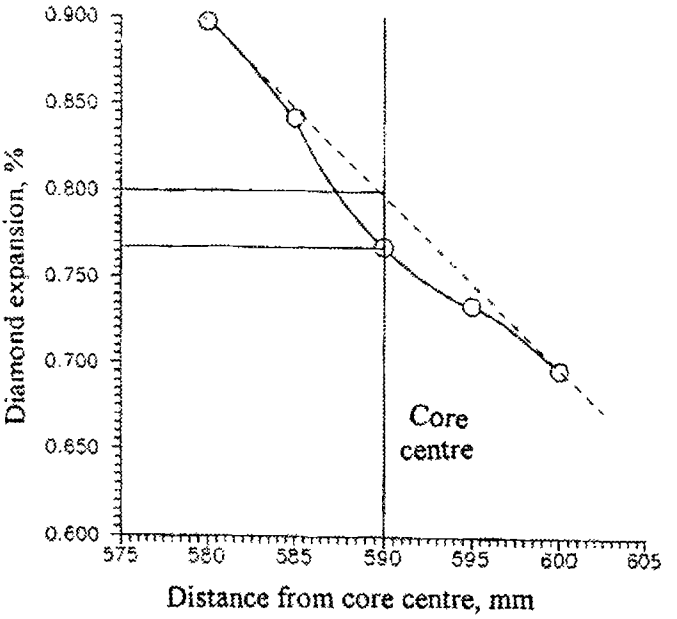


Figure 2 – *Diamond Expansion vs Core Height. An Indium Screen Was Installed at the+590 mm Position*

Furthermore neutron-induced defects in diamond can be mitigated by the following electron irradiation at room temperature (Fig.3) or γ-quanta irradiation *[1]*.

Radiation γ-annealing was discovered in diamond and graphite. This phenomenon is potentially significant for metals as well, however.

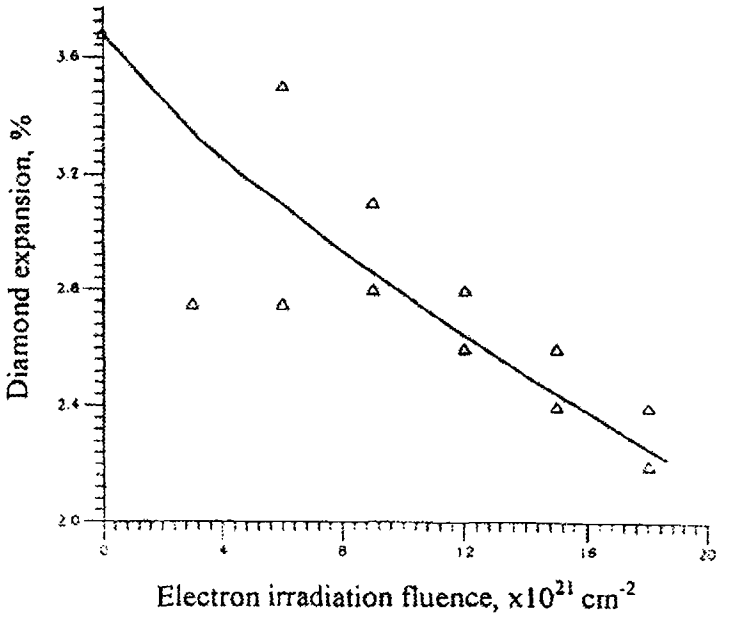


Figure 3 – *Radiation Annealing of Neutron Irradiated Diamond by 200 Electrons*

Reactor Pressure Vessel Steels

Long-term operating Nuclear Power Plant (NPP) Reactor Pressure Vessels (RPV) are subject to multi-factor influences. It is practically impossible to reproduce some of these factors (time, e.g.) in framework of experimental investigations including using study of surveillance specimens. Detailed information that can result from taking samples directly from the decommissioned and operating RPVs is more reliable than received by any other method and therefore should be of highest value.

Analysing that prototype NPP RPVs embrittlement have shown that, as in the case for diamond and graphite mitigation of the degrading neutron influence by radiation gamma-annealing take place.

In Russia, along with routine investigations on radiation embrittlement of experimental and surveillance specimens, systematic study of actual properties of the decommissioned prototype NPP RPV materials by means of through the wall trepans has been carried out. In 1987 the earliest commercial PWR prototype Novovoronezh unit 1 (210 MWe) RPV was trepanned after 20 years (1964-1984) of operation and

decommissioning. Then the Novovoronezh unit 2 (365 MWe, 1969-1990) and the oldest PWR type experimental reactor-prototype EPR (1956-1986) RPVs also were studied using similar sampling.

Trepan cutting – Through the RPV wall samples were cut out using specialised equipment: machine tool with annular drill and anode-mechanical cutting. The typical dimensions of these trepans are 120-140 mm in diameter and 120-140 mm long. Test pieces and specimens were manufactured by means of electrodischarge machine wire cutting.

Irradiation exposure parameters – Experimental investigation included an examination of axial (along trepan axis) and azimuth distribution of relative neutron fluxes that were determined by means of Co-60 activity measurement in small pieces from parts of the trepan. The specific activity of Co-60 was determined using an ORTEC gamma-spectrometer. The absolute value of fast (E>0.5 MeV) neutron fluence for the trepan inner surface was determined by means of gamma-spectrometry of the Nb impurity in steel using the threshold reaction ^{93}Nb(n,n') ^{93m} Nb was applied. To provide ^{93m} Nb specific activity measurement, a radiochemical extraction of Nb from the steel was carried out. The activity of ^{93m}Nb was measured by X-ray spectrometry with a Si(Li) crystal and a beryllium window using an ORTEC spectra analysing system was used.

Chemical content analysis – The optical emission spectrometric method was applied for the determining elements and impurities content. The analysis of samples was carried out using Baird Spectrovac spectrometer. The results of the chemical analysis are presented in Table 1.

Table 1–*RPV materials chemical content (wt. %%)*

RPV Material	C	Mn	Si	S	P	Mo	Ni	Cr	V	Cu
NV1weld	0.05	0.52	0.42	0.019	0.033	0.49	0.12	1.45	0.18	0.15
NV1base	0.17	0.49	0.34	0.020	0.013	0.65	0.15	2.78	0.28	0.18
NV2weld	0.07	1.05	0.37	0.020	0.036	0.50	0.14	1.42	0.20	0.16
NV2base	0.15	0.53	0.31	0.016	0.014	0.66	0.16	2.59	0.16	0.12
EPRbase	0.24	0.49	0.28	0.040	0.018	0.40	1.07	3.30	0.02	0.10

Mechanical properties tests – The RPV steel radiation embrittlement estimation was made by using the ductile-to-brittle transition temperature (DBTT) shift. An RKP-300 impact pendulum test machine for standard Charpy specimens tests was used. Previous investigations gave an opportunity to establish the dependencies and mechanisms of the RPV materials radiation embrittlement necessary for vessel materials condition predicting. The general dependence of radiation embrittlement in terms of DBTT shift is as follows *[2]*:

$$DBTT_{shift} = A_F \times F^n, \qquad (1)$$

where

$A_F = f(P+Cu)$ = the radiation embrittlement coefficient
F = the fast neutron fluence with E>0.5 MeV in 10^{18} cm^{-2} units.

It was shown that the magnitude of ^{n} is close to one–third, while the coefficients of copper and phosphorus differ from each other by about a factor of ten *[2]*.

It was also established that the relation between DBTT $_{shift}$,P, Cu and F is described by:

$$DBTT_{shift} = [A_F(\%P+0.1\%Cu) + B] \times F^{1/3}, ℃ \qquad (2)$$

The results of the Novovoronezh unit 1 weld metal study obtained in Russia and Finland *[3]* are presented in Table 2.

Table 2–*Results of the Novovoronezh unit 1 weld metal study*

Parameter	Distance from the RPV cladding, mm				
	5	15	22	36	81
Neutron fluence, ($10^{23}m^{-2}$)	2.9	2.5	2.3	1.9	1.1
A_F	26	47.5	67	75	54
ICF	0.3	0.45	0.5	1.1	6.1

It can be seen from Table 2 that anomalous distribution of the radiation embrittlement coefficient throughout the RPV thickness was registered, for its maximum does not coincide with the maximum of neutron load (and total content of copper and phosphorus).

The discrepancy between maximum embrittlement and maximum neutron load together with concentration of harmful impurities for weld seam metal can not be ascribed to peculiarities of the work cycle of processing or metallurgical factors. So, it is necessary to return to the analysis of radiation effects for some other cause.

In a few studies the probability of additional defects formation under the influence of thermal neutrons *[4]* and the hard component of γ-irradiation *[5]* was considered. However similar to fast neutrons these concomitant types of radiation can give maximum contribution just at the RPV inner surface, and this circumstance further compounds the discussed experimental paradox.

More or less satisfactory, the phenomenon could be interpreted as a result of neutron irradiation intensity influence (so called 'effect of flux' *[6,7]*), but this is improbable since it was shown that at the reduction of fast neutron flux throughout the RPV wall thickness was only about 20-25 %.

Therefore, among the irradiation conditions, it is necessary to chose the factor, which varies rather sharply throughout the wall thickness. The most suitable one is the gamma-

ray radiation, accompanying the neutron radiation. The thickness of the iron layer within which gammas of 1 MeV energy are reduced ten times is about 4 cm that corresponds rather well to the spatial scale of the phenomenon considered. Therefore, it is reasonable to define a more universal characteristic of irradiation condition, which is combined from intensities of fast neutrons and accompanying gammas fluxes. That is why this characteristic specified as Irradiation Composition Factor (ICF) is included in Table 2. This parameter is the ratio of fluxes of fast (E>0.5 MeV) neutrons and gammas (E>0.2 MeV). In addition to the rate of the defect production due to the neutrons, this parameter takes into account the efficiency of the radiation gamma-annealing, and therefore characterises the number of the conserved defects in the process of cascade evolution.

Table 3 represents the results of the Novovoronezh unit 2 RPV weld metal and base metal study.

Table 3–*Results of the Novovoronezh unit 2 RPV materials study*

Parameter	Distance from the RPV cladding, mm					
	15weld	22base	65weld	88base	105weld	111base
Neutron fluence, ($10^{23}m^{-2}$)	6.8	7.6	4.7	4.0	2.2	3.0
A_F	44	20	48	22	38	18
ICF	0.3	0.4	6.6	15.6	17.9	32.8

One can see that in principle the results of the Novovoronezh unit 2 RPV weld metal and base metal study have confirmed the existence of gamma-annealing effect but it is smoothed-out. It is not surprising thing taking into account the RPV service life histories: during 12 campaigns of 18 RPV of the Novovoronezh unit 1 was in operation without 'thermal shield' (i.e. with high level of γ-flux) and to the contrary during 17 campaigns of 20 RPV of the Novovoronezh unit 2 was in operation with 'thermal shield'.

The results of the EPR RPV base metal study are presented in Table 4. From the Table 4 data, we notice that EPR base metal study does not reveal, however, the gamma annealing effect. It is a result of a gamma-ray radiation suppression by numerous stainless steel shields. So the effect of γ-annealing is not exhibited and the A_F distribution has a monotonic character. To verify the existence of the gamma-annealing effect the EPR RPV base metal specimens were irradiated in the condition with high γ-flux(ICF=0.25). In these circumstances very low value of A_F=18 was obtained. Previously the similar result was obtained during the same material irradiation in the MR

Table 4–*Results of the EPR RPV base metal study*

Parameter	Distance from the RPV cladding, mm			
	7.5	30	90	112.5
Neutron fluence, ($10^{23}m^{-2}$)	6.2	4.1	2.1	1.4
A_F	68	57.4	52.3	63
ICF	3.1	6	42	70

test reactor (A_F=21 at ICF=0.36) *[7]*.

Discussion

Fig. 4 shows the scope of data for A_F of the above-mentioned steels along with A537 and A212 B steels as a function of ICF. These materials were irradiated in different types of reactors that is why ICF range is very wide.

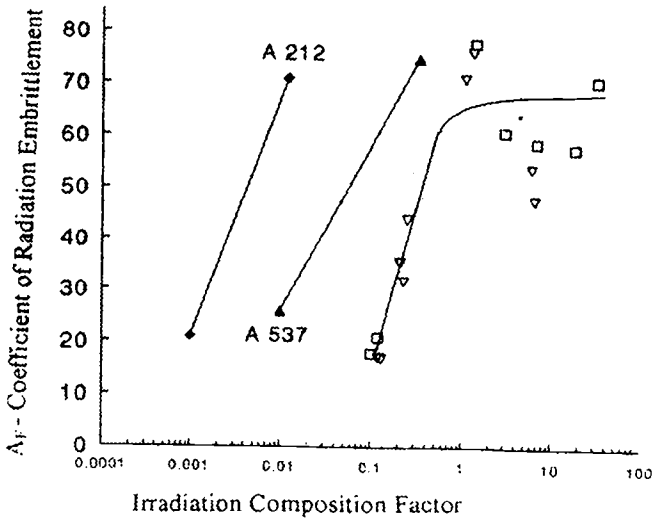


Figure 4 – *Dependence of Radiation Embrittlement Coefficient A_F on Irradiation Composition Factor ICF: V - NV1 and NV2 weld metal, □ - EPR base metal,* ▲ - A537 *steel,* ◆ - *A212 steel.*

The A_F –ICF relationship is of special interest for the U.S. A537 type steel. Irradiation was carried out at the same place of the reactor, but for the case of A_F =22 the specimens were surrounded by cadmium foil *[8]*. This work was performed to evaluate the contribution of thermal neutrons to embrittlement.

We propose to explain the reduction of the embrittlement in this case by the additional γ- radiation flux arising from the (n,γ) reaction and, as a result, by radiation γ-annealing intensification.

The A212 type steel was irradiated in the ORR reactor core and also in the position adjacent to the HFIR reactor vessel *[4]*. The irradiation temperature of both steels was 50-60 °C.

It is reasonable to say that gammas from nuclear reactors have such energy spectrum that the conversion electrons interact mainly with the defects already formed by fast neutrons. Therefore it is necessary to take into account the efficiency of radiation γ-annealing by the conversion electrons of intermediate energies in the defects evolution process.

Probably the increased RPV radiation embrittlement occurring in commercial reactors with wide water gap between the core and the RPV wall may be explained not only by the formation of extra defects induced by hard gammas *[5]* but suppression of radiation γ-annealing because of the gammas of intermediate energies reduction as well. So, optimisation of the core-RPV wall gap structure is a matter of a great importance [9].

Conclusions

Radiation γ-annealing was previously discovered in diamond and graphite. This phenomenon is appeared to be significant for RPV metals as well.

Lower embrittlement at higher fast neutron fluence and also higher concentration of impurities in NV1 RPV weld metal trepans is not an anomaly but a natural phenomenon, i.e. compensation of the degrading neutron influence by radiation γ-annealing. The results of the NV2 and EPR trepan materials study support this conclusion.

The radiation γ-annealing phenomenon opens the perspective of radiation effects mitigation and NPP RPV life cycle management using the control of neutron and γ- ray intensities. Therefore, optimisation of the water gap between the core and RPV wall structure is a matter of a great importance.

Taking into account the gamma-ray radiation densities in reactor experiments is recommended in interpretation and prediction of the effects occurring in materials under irradiation in different types of reactors, including thermonuclear ones.

Acknowledgments

The authors render thanks to colleagues: A.D.Amaev who participated in discussions, and V.N.Kusnetsov who carried out the gamma flux calculations.

The research described in this publication was made possible in part by a Grant N467 from the International Science and Technological Centre.

References

[1] Karpukhin, V.I.,Gordeev V.G., and Nikolaenko, V.A., "Effect of γ-Irradiation on Defect Annealing in Diamond," *Radiation Effects in Solids*, vol.139, 1996, pp.173-182.

[2] Amayev, A.D.,Kryukov, A.M., Levit, V.I., and Sokolov, M.A., "Radiation stability of WWER-440 Vessel Materials," *Radiation Embrittlement of Nuclear Reactor Pressure Vessel Steels: An International Review (Forth Volume), ASTM STP 1170,* Lendell E.Steele, Ed., American Society for Testing Materials, Philadelphia, 1993, pp.9-29.

[3] Ahlstrand, R., and .Valo, M., "Finnish Contribution to Trepan Testing of Novovoronezh I Reactor Pressure Vessel," *Proceedings of the Forth International Conference on Material Science Problems in NPP Equipment Production and Operation*, June 16-23, 1996.

[4] Mansur L.K.and Farrell K., "On Mechanisms by Which a Soft Neutron Spectrum May Induce Accelerated Embrittlement," *Journal of Nuclear Materials*, Vol.170, 1990, pp 236-245.

[5] Alexander D.E. and .Rehn L.E., "The Contribution of High Energy Gamma Rays to Displacement Damage in LWR Pressure Vessels," *Journal of Nuclear Materials*, Vol..209, 1994, pp 212-214.

[6] Nanstad R.K., Farrell K.,Braski D.N. and Corwin W.R., "Accelerated Neutron Embrittlement of Ferrite Steels at Low Fluence, Flux and Spectrum Effects, " *Journal of Nuclear Materials*,Vol.15,1988, pp 1-6.

[7] Platonov P.A.,Kryukov A.M., Shtrombach Ja.I. and Krasikov E.A., "Features of Radiation Embrittlement Kinetics of Steel for VVER-440 Before and After Annealing", *Effects of Radiation on Materials," 18th International Symposium ASTM,1996, ASTM STP 1325,* in press.

[8] Alberman A., Bley G., Pepin P. and Soulat P.,"Influence of Thermal Neutrons on the Brittleness of High-Temperature Gas Cooled Reactor Liner Steel," *Nuclear Technology*, v.66, 1984, pp. 639-646.

[9] Nikolaenko V.A., Amayev A.D., Krasikov E.A., and Shtrombach Ja.I., "The Mode of Radiation Degradation Controlling and Device for Its Implementation," Russian Patent RU 2104314 C1, 6 C 21 D 1/09, 10/00,1998.

David S. Gelles,[1] Akihiko Kimura,[2] and Tamaki Shibayama[3]

Analysis of Stress-Induced Burgers Vector Anisotropy in Pressurized Tube Specimens of Irradiated Ferritic-Martensitic Steels: JFMS and JLF-1

Reference: Gelles, D. S., Kimura, A., and Shibayama, T., **"Analysis of Stress-Induced Burgers Vector Anisotropy in Pressurized Tube Specimens of Irradiated Ferritic-Martensitic Steels: JFMS and JLF-1,"** *Effects of Radiation on Materials: 19th International Symposium, ASTM STP 1366,* M. L. Hamilton, A. S. Kumar, S. T. Rosinski, and M. L. Grossbeck, Eds., American Society for Testing and Materials, West Conshohocken, PA, 2000.

Abstract: A procedure for determining the Burgers vector anisotropy in irradiated ferritic steels is described, allowing identification of all a<100> and all $\frac{a}{2}$<111> dislocations in a region of interest. The necessary micrographs to apply the procedure have been taken of a pressurized tube specimen of JFMS, a duplex ferritic steel following irradiation in FFTF/MOTA at 407°C to 7.5 x 10^{22} n/cm^2 (E > 0.1 MeV) or 37.5 dpa, and a pressurized tube of JLF-1 irradiated at 430°C under similar conditions to 14.3 x 10^{22} n/cm^2 (E > 0.1 MeV) or 60 dpa. Analysis of micrographs indicates that large anisotropy in Burgers vector populations develop during irradiation creep.

Keywords: irradiation creep, dislocations, anisotropy, ferritic steel, microstructure

Introduction

In a previous ASTM Effects of Radiation on Materials Symposium, it was shown that irradiation creep induced Burgers vector anisotropy for perfect dislocations could be determined in pressurized creep tubes of Nimonic PE16, a precipitation strengthened austenitic superalloy [1]. The process required that the Burgers vector type be known (in that case $\frac{a}{2}$<110>) and used an elimination procedure to determine the Burgers vector for each dislocation present in a field of view. This procedure was also used for microstructural evaluation of type 316 austenitic stainless

[1]Staff Engineer, Structural Materials Research, Battelle Pacific Northwest National Laboratory,* Richland, WA 99352.
[2]University of Kyoto, Kyoto, Japan.
[3]Hokkaido University, Sapporo, Japan.
*Operated for the U.S. Department of Energy by Battelle Memorial Institute under Contract DE-AC06-76RLO 1830.

Copyright© 2000 by ASTM International www.astm.org

steel pressurized tubes [2]. That procedure can now be extended to ferritic stainless steels where the Burgers vector type is known to contain both $a<100>$ and $\frac{a}{2}<111>$.

However, the opportunity to examine the effect of stress on microstructural evolution occurs rarely in irradiation experiments because pressurized tubes are reirradiated until failure occurs in order to assess the consequences of increasing dose. However, in early Monbusho experiments in the FFTF/MOTA, a series of pressurized tubes of the Japanese duplex ferritic steel JFMS was irradiated for only one irradiation cycle and was then removed [3]. More recently, after the shutdown of the FFTF, specimens of JLF-1 were made available [4]. JFMS is a Fe-10Cr-2Mo steel containing approximately 25% delta ferrite in Martensite, with moderate carbon, high silicon and nickel, and intentional additions of vanadium and niobium. Two sets of four tubes were irradiated, one at 407°C and the other at 520°C. Each set included one unstressed and three stressed conditions to maximum levels of about 90 MPa. JLF-1 is the first of a series of a low activation Fe-9Cr-2W-0.2V steels which were prepared to exclude nickel and molybdenum additions. Three sets of up to four tubes were irradiated, three tubes at 430°C, four tubes at 460°C and four tubes at 520°C. All sets contained unstressed conditions. Microstructural examination of these pressurized tubes was a part of the Monbusho experimental objectives.

Analysis of Burgers Vector Anisotropy in Ferritic Alloys

It was shown that irradiation creep in Nimonic PE16 and AISI 316 produces anisotropy in the populations of perfect dislocations as a function of the Burgers vectors [1,2]. Such an anisotropic response is to be expected if irradiation creep is controlled by dislocation motion. Orowan was the first to note that the plastic strain rate, $\dot{\epsilon}$, for crystal (c) coordinates must be the sum of all dislocation motion [5]

$$\dot{\epsilon}_{ij}^{(c)} = \sum_K \rho_K b_K v_K (\hat{b}_K \cdot \hat{x}_i)(\hat{b}_K \cdot \hat{x}_j) \qquad (1)$$

where K defines each of the possible dislocation Burgers vectors, ρ is the dislocation density, b is the Burgers vector length, and $\bar{v}$ is the average dislocation velocity, and i and j have their usual directional meaning. Equation (1) shows that for irradiation creep caused by dislocation climb, anisotropy usually exists in the Burgers vector populations (ρ) and / or in the dislocation velocities ($\bar{v}$), and anisotropy in $\bar{v}$ generally leads to anisotropy in ρ.

Procedures similar to those for Burgers vector analysis in austenitic microstructures [1] can be developed for ferritic alloys. It is presumed that a straightforward procedure based on the standard approach requiring two no-contrast conditions ($\vec{g} \cdot \vec{b} = 0$) to identify each Burgers vector is impossible, and that the dislocations present are only of two types, either $a<100>$ or $\frac{a}{2}<111>$. The procedure for ferritic alloys is based on a process of elimination.

Table 1 lists the contrast conditions for the three $a<100>$ and four $\frac{a}{2}<111>$ dislocation possibilities as a function of the low index imaging conditions possible near a (011) foil orientation previously given in reference [6] and similar to that

defined in reference [1] for austenitic steels. Figure 1 provides an indexed Kikuchi map showing the relationships of the $\vec{g}$ vectors given in Table 1. From Table 1, it can be noted that imaging with $\vec{g} = 200$ shows all $\frac{a}{2}<111>$ dislocations, but only a[100] dislocations are in contrast, with a[010] and a[001] dislocations out of contrast. Also, a[100] dislocations should appear in much stronger contrast than $\frac{a}{2}<111>$ dislocations because $\vec{g} \cdot \vec{b}$ is 2 instead of 1, a fact easily verified by experiment. If instead $\vec{g} = 01\bar{1}$ contrast is used, then $\frac{a}{2}[1\bar{1}1]$, $\frac{a}{2}[11\bar{1}]$, a[100], and a[010] dislocations are visible but $\frac{a}{2}[111]$, $\frac{a}{2}[\bar{1}11]$, and a[100] dislocations are not visible. Therefore, all dislocations of type $\frac{a}{2}<111>$ and $a<100>$ are imaged in a series of two such micrographs. Comparing the dislocation structure in micrographs taken with these contrast conditions reveals that images appearing only in $\vec{g} = 200$ contrast must either be $\frac{a}{2}[111]$, $\frac{a}{2}[\bar{1}11]$ or a[100] dislocations (and the a[100] images are much stronger), and images that only appear in $\vec{g} = 01\bar{1}$ must be a[010] or a[001] dislocations. Thus, all the $\frac{a}{2}<111>$ dislocations appearing in $\vec{g} = 200$ contrast can be split into two groups, $\frac{a}{2}[111]$ with $\frac{a}{2}[\bar{1}11]$ and $\frac{a}{2}[1\bar{1}1]$ with $\frac{a}{2}[11\bar{1}]$. When $\vec{g} = \bar{1}01$ contrast is used, then $\frac{a}{2}[\bar{1}11]$, $\frac{a}{2}[11\bar{1}]$, a[100] and a[001] dislocations are visible and $\frac{a}{2}[111]$, $\frac{a}{2}[1\bar{1}1]$, and a[010] dislocations are invisible. Therefore, a micrograph using $\vec{g} = \bar{1}01$ contrast will differentiate between the a[001] and a[001] images identified on the $\vec{g} = 01\bar{1}$ micrograph because only a[001] is visible in both. Thus, with three micrographs, all

Table 1. *The $\vec{g} \cdot \vec{b}$ imaging criteria for various bcc imaging conditions and Burgers vector combinations.*

$\vec{g}$	Burgers vector						
	$\frac{a}{2}[111]$	$\frac{a}{2}[\bar{1}11]$	$\frac{a}{2}[1\bar{1}1]$	$\frac{a}{2}[11\bar{1}]$	a[100]	a[010]	a[001]
200	1	1	1	1	2	0	0
020	1	1	1	1	0	2	0
002	1	1	1	1	0	0	2
$01\bar{1}$	0	0	1	1	0	1	1
$\bar{1}10$	0	1	1	0	1	1	0
$\bar{1}01$	0	1	0	1	1	0	1
101	1	0	1	0	1	0	1
$11\bar{2}$	0	1	1	2	1	2	1
$1\bar{2}1$	0	1	2	1	2	1	1
$2\bar{1}1$	1	1	2	0	2	1	1
$21\bar{1}$	1	1	0	2	2	1	1
$1\bar{1}2$	1	0	2	1	1	1	2
$12\bar{1}$	1	0	1	2	1	2	1

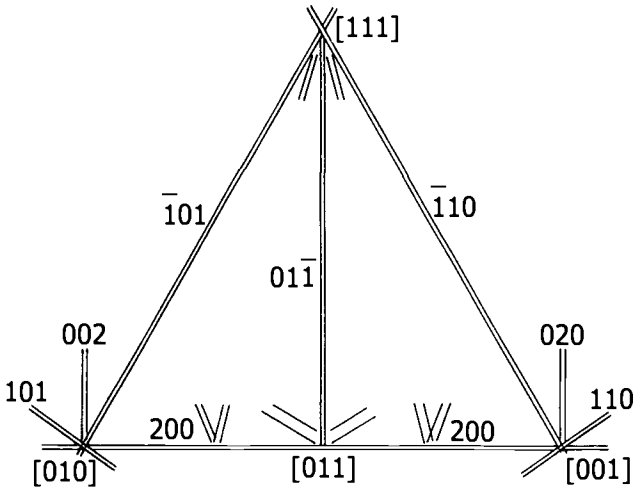


Figure 1. *Definition of notation as represented on a Kikuchi map for bcc dislocation imaging conditions.*

a<100> type dislocations can be identified and separated by Burgers vector. Furthermore, the $\vec{g} = \bar{1}01$ micrograph can also be used to differentiate between the two groups of $\frac{a}{2}$<111> dislocations appearing in $\vec{g} = 200$ contrast, and therefore, all $\frac{a}{2}$<111> dislocations can be identified and separated by Burgers vector. A similar identification sequence can be defined if $\vec{g} = \bar{1}10$ is used instead of $\bar{1}01$.

In practice, however, the large tilt angles required to obtain images using $\vec{g} =$ 200, $01\bar{1}$, and $\bar{1}01$ sufficiently alter the dislocation configurations so that identification becomes difficult. Stereo pair images, taken for each contrast condition that is used, can greatly assist dislocation identification. Therefore, an optimum micrograph series to identify Burgers vector anisotropy in ferritic alloys consists of six micrographs: a stereo pair using $\vec{g} = 200$ contrast near (011), a stereo pair using $\vec{g} = 01\bar{1}$ contrast near (011), and a stereo pair using either $\vec{g} = \bar{1}01$ contrast between (010) and (111) or $\bar{1}10$ contrast between (001) and (111).

Experimental Procedures

Pressurized tubes of JFMS steel were made from tubing fabricated from rod stock. The chemical composition of the rod stock is given in Table 2. Tube segments had dimensions of 0.57 mm outside diameter, 0.20 mm wall thickness, and were 19.8 mm in length. Endcaps of the same material were electron beam welded to both ends of the tubing segments. One endcap had a small (0.13 mm diameter) hole for pressurization to obtain the desired hoop stress at the design irradiation temperature. The pressurization gas was helium. Diameter measurements were made using a non-contacting laser measurement system before and after irradiation. Four specimens were irradiated in level 2 of FFTF/MOTA 1F during cycle 10 at 407°C in canister 2C-3 for an accumulated exposure time of 335.4 equivalent full power days,

Table 2. *Nominal composition of JFMS and JLF-1 (wt%) with balance Fe.*

	Cr	C	Mo	W	Mn	Nb	V
JFMS	9.85	0.05	2.3	na	0.58	0.06	0.12
JLF-1	9.04	.097	>.01	1.97	0.46	na	0.19
	Si	P	S	Ni	N	Ta	Ti
JFMS	0.675	0.009	0.006	0.94	>100ppm	na	na
JLF-1	>0.1	na	na	na	na	0.07	.001

na - not available

over approximately 8050 h. The estimated accumulated damage in these creep specimens during irradiation was 7.5 x 10^{22} n/cm^2 (E > 0.1 MeV) or 37.5 dpa.

Pressurized tubes of JLF-1 steel were similarly made from tubing fabricated from rod stock. The chemical composition of the rod stock is included in Table 2. Three specimens were irradiated in level 2 of FFTF/MOTA 2A in canister 4D-2 and 2B in canister 4D-1 at 430°C for an accumulated exposure time of 503.4 equivalent full power days, over 12082 h. The estimated accumulated damage in these creep specimens during irradiation was 14.3 x 10^{22} n/cm^2 (E > 0.1 MeV) or 61 dpa [4].

Following irradiation and diametral measurement, four JFMS specimens (RR00, RR03, RR04 and RR07), comprising zero and maximum stress conditions for the two irradiation temperatures, and one JLF-1 specimen comprising the maximum stress condition (VA08), were selected for microstructural examination. Burgers vector anisotropy measurements were performed only on specimens RR03 and VA08.

Specimens were sectioned with a slow speed saw by first removing the end caps and then splitting each tube longitudinally. Curved disks 3 mm in diameter were then punched from the central region of each split tube using a punch designed for tubing specimens. The disks were mechanically ground flat and then thinned for transmission electron microscopy using standard procedures. Examinations were performed using a JEOL 1200EX transmission electron microscope with a double tilting goniometer stage. Column realignment was found to be necessary after each change in specimen tilt.

Results and Analysis

Diameter Change and Swelling Measurements

Diameter change measures for the pressurized tube specimens of JFMS and JLF-1 are given in Table 3, and the diametral creep strains are plotted using open symbols and closed diamonds, respectively, as a function of hoop stress in Figure 2, with measurements for HT-9 using closed circles and squares for comparison.

From Figure 2, it can be shown that allowing for differences in dose, JFMS and JLF-1 have similar creep strengths to HT-9, and behavior in JFMS appears to be

Table 3. *Creep data on JFMS and JLF-1 pressurized tubes irradiated in FFTF [3].*

JFMS				JLF-1			
ID	Temp (°C)	Hoop Stress (MPa)	Diam. Strain (%)	ID	Temp (°C)	Hoop Stress (MPa)	Diam. Strain (%)
RR00	407	-0.1	0.11	VA02	430	0	0.04
RR01		25.8	0.09	VA05		30	0.13
RR02		51.3	0.11	VA08		60	0.27
RR03		86.0	0.15	VA01	459	0	0.03
RR04	520	-0.1	0.01	VA04		30	0.08
RR05		26.6	0.05	VA07		60	0.16
RR06		53.3	0.12	VA10		100	0.23
RR07		90.5	0.23	VA00	519	0	na
				VA03		30	0.23
				VA06		60	0.61
				VA09		100.0	0.60

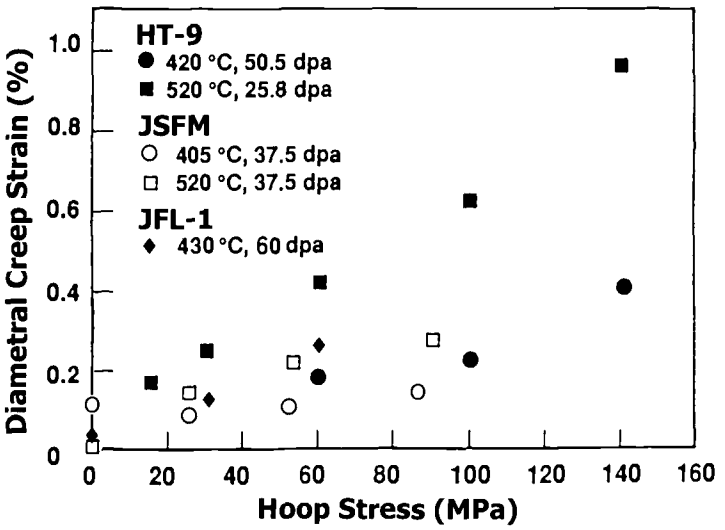


Figure 2. *Irradiation creep response of JFMS and JLF-1 in comparison with HT-9 as a function of hoop stress.*

linear with stress, but with an offset due to apparent diametral change in the zero stress condition. Such offset response can be caused by void swelling or density change due to precipitation. JLF-1 on the other hand shows non-linear behavior with greater curvature than that for HT-9 indicative of complex behavior. A more detailed description of creep response in ferritic steels has recently been published by Toloczko etal. [7].

Swelling as determined from density change was measured only for specimens VA02 and VA08 of JLF-1. Results are provided in Table 4. Table 4 indicates that swelling was 0.658% for unstressed JLF-1 irradiated at 430°C to 61 dpa whereas under a hoop stress of 60 MPA the swelling increased to 0.885%.

Table 4. *Swelling in JLF-1 specimens irradiated at 430°C as a function of stress.*

Specimen ID	Stress	Swelling
VA02	0 MPa	0.66
VA08	60 MPa	0.89

Microstructural Examination

The effect of irradiation on the microstructure of JFMS was found primarily in the precipitate structure. No void swelling was observed. Following irradiation at 407°C, $M_{23}C_6$ was retained at prior austenite grain boundaries and martensite lath subboundaries, but a high density of equiaxed particles formed within grains. Particles on subgrain boundaries were larger than those in the matrix, and the decorated subgrain boundaries had adjacent regions denuded of particles. This precipitate has previously been characterized as G phase [8] or $M_6C(\eta)$ [9]. The precipitate volume fraction appeared to be significantly higher than that found in HT-9, probably a result of the high levels of silicon and nickel in the alloy. Quantitative measurement showed the precipitate volume fraction was 1.14%, with a mean particle size of 6.6 nm and a number density of 8.9×10^{16} cm^{-3}. Precipitate densities approaching 10^{17} cm^{-3} should produce high strength. Following irradiation at 520°C, significant rearrangement of precipitation at prior austenite grain boundaries and martensite lath subboundaries was found. Details of these microstructural changes will be published elsewhere.

Analysis of dislocation structures was limited to specimens irradiated at 407°C. Stress fields associated with precipitation complicated the dislocation analysis due to the added precipitate intensities, but it was found that imaging conditions approaching weak beam dark field were sufficient to unambiguously show $\frac{a}{2}<111>$ dislocations using $\vec{g}$ = 200 contrast. Two types of regions were examined: martensite and delta ferrite, but the latter was easier to work with.

An example of the dislocation structure in a delta ferrite grain in specimen RR03 irradiated at 407°C at a stress level of 86 MPa is shown in Figures 3 and 4. The grain orientation is near [142]. In Figure 3, stereo pair images in dark field using 200, $01\bar{1}$, and $\bar{1}10$ contrast are provided of the same area, but to show the stereo effect, it has been necessary to rotate the field of view. Figure 3a and b show the

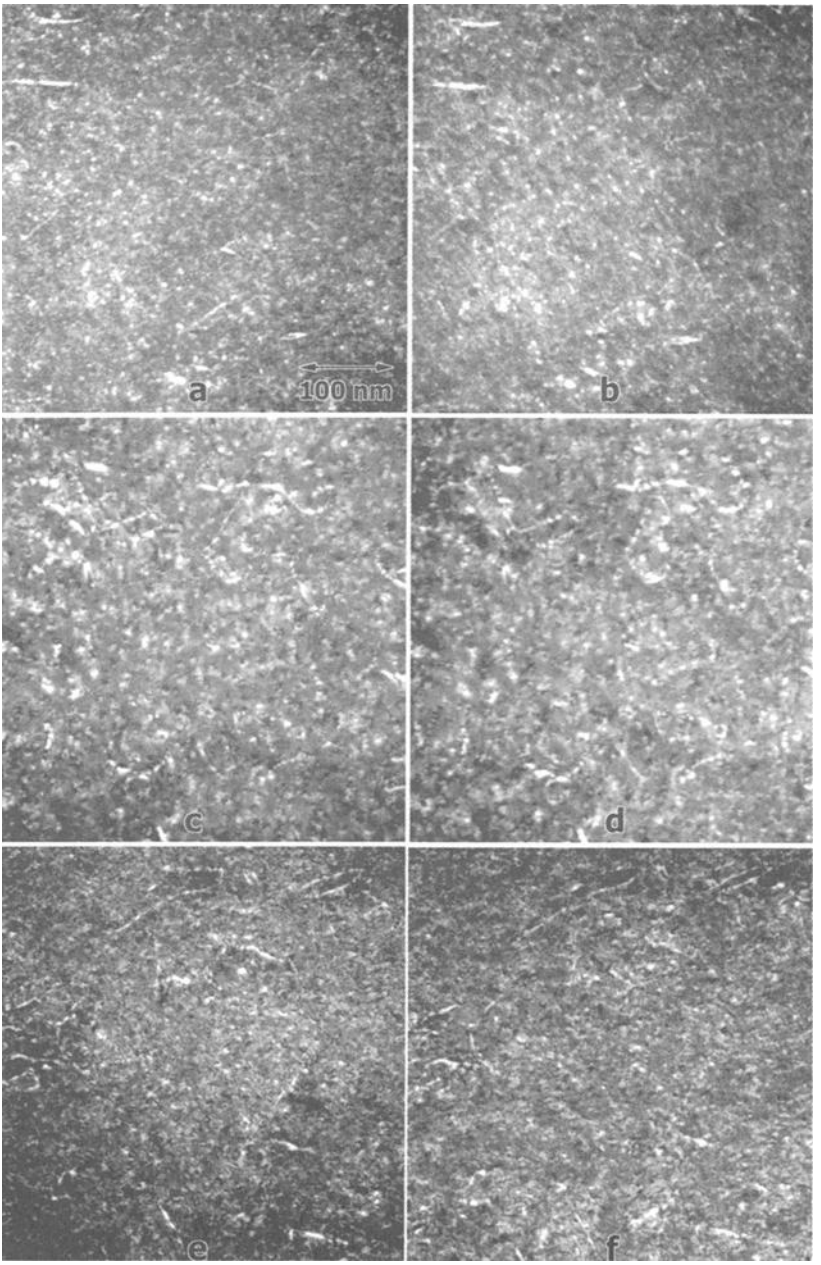


Figure 3. *Weak beam dark field stereo pair micrographs of a ferrite grain in JFMS pressurized tube specimen RR03 irradiated at 407°C to 37.5 dpa, using 200 contrast in a) and b), $0\bar{1}1$ contrast in c) and d), and $\bar{1}10$ contrast in e) and f).*

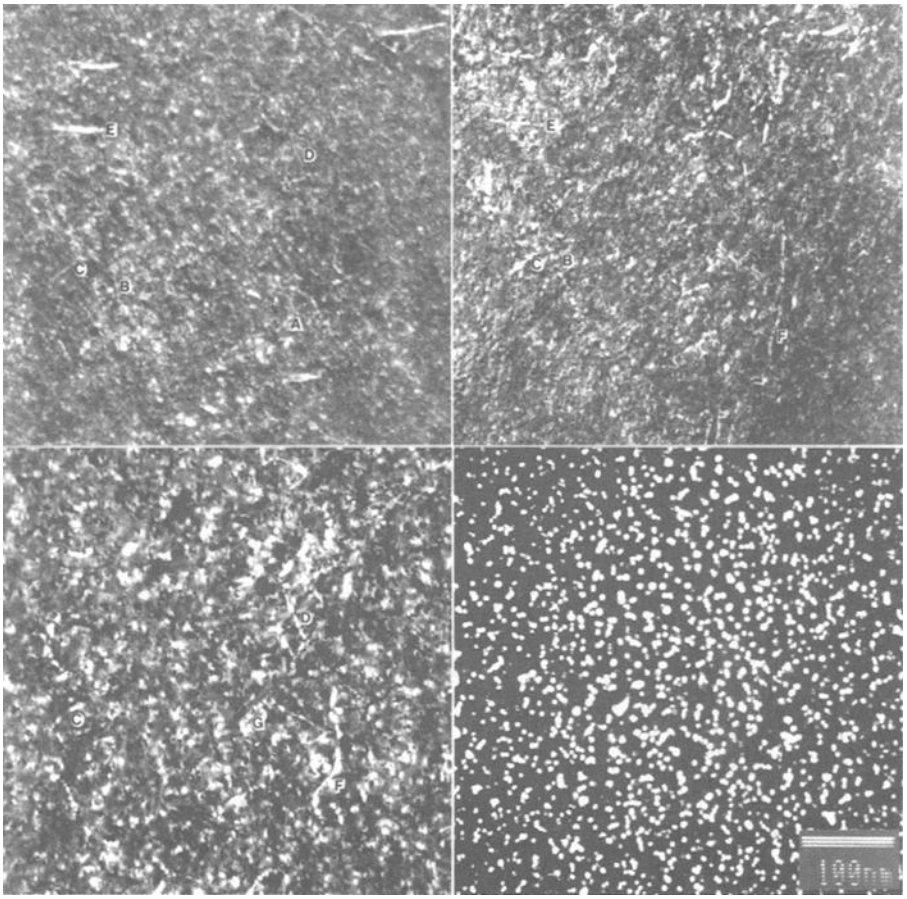


Figure 4. *Weak beam dark field micrographs of the same area as Figure 3 arranged for comparison of dislocation and precipitate structures using 200 contrast in a), $01\bar{1}$ contrast in b), $\bar{1}10$ contrast in c), and precipitate dark field contrast in d). The meaning of the various labels is described in the text.*

region using 200 contrast. Strong horizontal dislocation lines in the upper left and a smaller strong loop image towards the lower right correspond to a[100] dislocations and the remainder of the dislocation images correspond to $\frac{a}{2}<111>$ dislocations. The $\frac{a}{2}<111>$ dislocations are much weaker, often being difficult to distinguish from a background mottling arising from the strain fields of precipitate particles. However, for example, two weaker straight dislocation images can be seen on the central left. Figures 3c and d provide a stereo pair using $01\bar{1}$ contrast, but the images have been rotated 90 degrees counter-clockwise so that the two weak $\frac{a}{2}<111>$ images noted in figures 3a and b should appear at the lower center, but only one is visible. Again, the images are complicated by a background mottling from precipitate strain fields. Figures 3e and f provide stereo pair images using $\bar{1}10$ contrast, with the

images rotated a further 50 degrees counter-clockwise. Image contrast is again similar, complicated by precipitate strain fields. From this series of micrographs, it can be shown that dislocation images tend to be horizontal, and therefore perpendicular to the Burgers vector direction, indicating a strong tendency for edge dislocation character, rather than screw character.

Figure 4 is provided, using the same micrograph series without stereo pairs or rotation, so that the dislocation images can be compared more easily. Figure 4a, b and c use 200, $01\bar{1}$ and $\bar{1}10$ contrast, respectively, and figure 4d gives a precipitate dark field image using $\vec{g}$ = ⅓ <222> for approximately the same area. Each of the dislocation image micrographs has been labelled to show a visible example of each of the types of dislocations, with $\frac{a}{2}[111]$ labelled A", $\frac{a}{2}[\bar{1}11]$ labelled "B", $\frac{a}{2}[1\bar{1}1]$ labelled "C", $\frac{a}{2}[11\bar{1}]$ labelled "D", a[100] labelled "E", a[010] labelled "F", and a[001] labelled "G". All labels are to the right of the respective dislocation images. Note that $\frac{a}{2}[111]$, $\frac{a}{2}[\bar{1}11]$, $\frac{a}{2}[1\bar{1}1]$,$\frac{a}{2}[11\bar{1}]$ and a[100] dislocations can be identified in figure 3a, $\frac{a}{2}[1\bar{1}1]$, $\frac{a}{2}[11\bar{1}]$, a[010] and a[001] can be identified in figure 3b, and $\frac{a}{2}[\bar{1}11]$, $\frac{a}{2}[1\bar{1}1]$, a[100] and a[010] can be identified in figure 3c, based on the labels. Therefore, it is possible to differentiate between all of the dislocations present in this specimen area.

The area shown in Figures 3 and 4 has been analyzed to provide a quantitative estimate for Burgers vector anisotropy. The foil is approximately 67 nm thick, and the field of view for measurement is considerably larger than that shown in figures 3 and 4. Table 5 gives results of the dislocation density measurements. From Table 4, it can be shown that dislocation densities vary between 0.6 and 4.7×10^9 cm^{-2}, corresponding to nearly a factor of eight variation. Anisotropy develops in both the $\frac{a}{2}$<111> and a<100> populations with the populations smallest for those orientations in the tangential direction. Therefore, Burgers vector anisotropy can be measured using a process of elimination technique, and large Burgers vector anisotropy can develop in stress duplex ferritic/martensitic steels.

Table 5. *Dislocation density measurements, showing Burgers vector anisotropy as a function of Burgers vector in specimen RR03 of JFMS irradiated at 407°C with a hoop stress of 86 MPa and VA08 of JLF-1 irradiated at 430°C with a hoop stress of 60 MPa.*

Burgers vector		$\frac{a}{2}[111]$	$\frac{a}{2}[\bar{1}11]$	$\frac{a}{2}[1\bar{1}1]$	$\frac{a}{2}[11\bar{1}]$	a[100]	a[010]	a[001]
$10^9 cm^{-2}$	RR03	1.94	1.02	0.62	4.50	1.77	4.28	4.72
	VA08	9.47	1.38	3.03	2.65	0.89	2.27	4.17

Microstructural examination of JLF-1 was limited to specimen VA08 which had been pressurized to the largest hoop stress of 60 MPa. Furthermore, only dislocation anisotropy was studied in detail. However, irradiation was found to have caused no major changes in microstructure; no void swelling was found and no evidence for further precipitation could be identified. These findings appear contradictory to swelling measurements given in Table 4. A possible explanation lies in the

anticipated precipitation of tungsten in the form of $M_{23}C_6$.

An area was selected for analysis of dislocation anisotropy with orientation near (013) and with the tube length effectively parallel to $[01\bar{1}]$. A sequence of six micrographs was taken using $\vec{g}$ = 200, $01\bar{1}$ and $\bar{1}10$. Three of the images are provided in Figure 5 to show the dislocation structure found within a region bounded by subgrain boundaries. Each of the dislocation image micrographs has been labelled to show a visible example of each of the types of dislocations, with $\frac{a}{2}[111]$ labelled "A", $\frac{a}{2}[\bar{1}11]$ labelled "B", $\frac{a}{2}[1\bar{1}1]$ labelled "C", $\frac{a}{2}[11\bar{1}]$ labelled "D", a[100] labelled "E", a[010] labelled "F", and a[001] labelled "G". The area shown in Figure 5 has also been analyzed to provide a quantitative estimate for Burgers vector anisotropy. The foil is again approximately 67 nm thick, but the field of view for measurement is similar to that shown in order to avoid subgrain boundary effects. From Table 5, it can be shown that dislocation densities vary between 0.9 and 9.5×10^9 cm^{-2}, corresponding to a factor of about ten variation. Anisotropy develops in both the $\frac{a}{2}<111>$ and $a<100>$ populations.

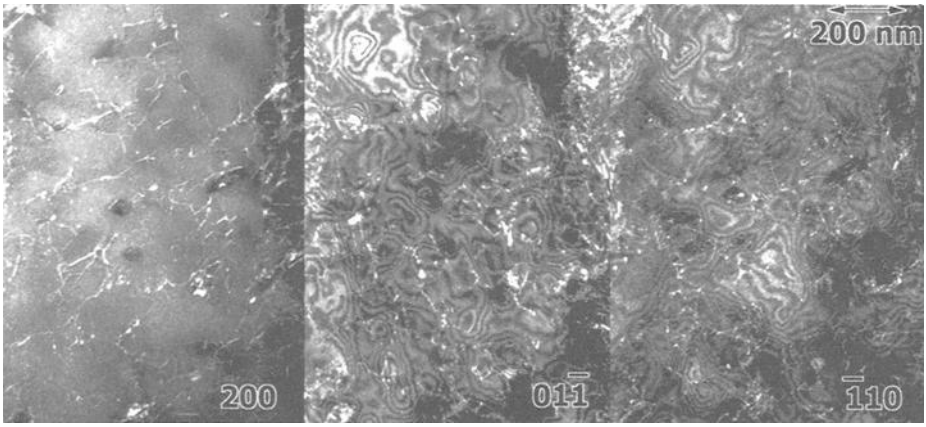


Figure 5. *Weak beam dark field micrographs of an area in specimen VA08 arranged for comparison of dislocations using 200 contrast in a), $01\bar{1}$ contrast in b), $\bar{1}10$ contrast in c). The meaning of the various labels is described in the text.*

Discussion

This work has provided an opportunity to extend Burgers vector anisotropy determination to the ferritic alloy class. Procedures have been established and tested, and results have been generated showing that a significant anisotropy can be generated in ferritic/martensitic steels at 400-430°C for stress levels of 60-86 MPa. This discussion section is intended to cover two topics: limitations of the procedure and significance of the results.

JFMS is found to develop significant precipitation following irradiation. The precipitate is presumed to be due to high levels of silicon and nickel in the steel, resulting in G phase precipitation. The precipitate particles have a strain field associated with them that affects weak beam dark field imaging so that identification

of $\frac{a}{2}<111>$ dislocations using 200 contrast becomes very difficult, and the possibility for errors during analysis exists. A steel with less matrix precipitation, such as a low activation steel, is expected to provide images that are easier to identify. On the other hand, JLF-1 reveals little apparent precipitation resulting during irradiation, but swelling measurements indicated that density has decreased more than 0.6% without any apparent voidage. A possible explanation is precipitation of tungsten in association with precipitate already present in the microstructure prior to irradiation.

The analysis given in Table 5 is based on measurements that may not be statistically significant. The specimen thicknesses were only 67 nm, and only about 40 dislocations were analyzed in the field of view. Dislocation motion may have occurred in such thin foils, although evidence for such motion was not observed. Few dislocation nodes could be found in the analyzed regions to show that the Burgers vector identification did not violated energy balances. Also, dislocation density measurements have not yet been completed on an unstressed specimen.

The results that anisotropy as large as a factor of 8 in JFMS and 10 in JLF-1 between different Burgers vector populations is surprising, given the limited amount of total strain found in the specimens. The strain measured in specimen RR03 was 0.15% and in VA08, it was 0.27%, whereas the unstressed specimen RR00 deformed 0.11% presumably due to precipitation and VA02 deformed 0.04 despite swelling of 0.658%. Therefore, the strain due to irradiation creep may have been as low as 0.04% in RR03 but 0.24% possibly influenced by precipitation in VA08. In comparison, results on austenitic steels provided similar levels of anisotropy in irradiated pressurized tubes, with deformations ranging between -0.02 and 1.255%.[1] The lower value corresponded to a situation where the perfect dislocation population had only just been generated, and therefore the average dislocation velocity was very low. Therefore, it appears that the present results indicate that dislocation motion may have been very limited in the JFMS specimen for the dose level achieved, about 40 dpa possibly caused by the high precipitate density found in the specimen.

Conclusions

Procedures have been developed to determine Burgers vector anisotropy in ferritic/martensitic steels containing both $\frac{a}{2}<111>$ and $a<100>$ Burgers vectors. The procedures have been tried on two irradiated pressurized tube specimens of JFMS steel irradiated in the FFTF/MOTA. Analysis of results for the specimens irradiated at stresses of 60 to 86 MPa indicates differences in Burgers vector anisotropy as large as a factor of 10.

Acknowledgement

This work was supported by JUPITER and the FFTF/MOTA on the US/Japan collaboration program.

References

[1] Gelles, D. S., in *Effects of Radiation on Materials: Twelfth International Symposium,* ASTM STP 870, Vol. I, F. A. Garner and J. S. Perrin, Eds. (ASTM, Philadelphia, 1985) 98-112.

[2] Gelles, D. S.. Journal of Nuclear Materials, Vol. 205, 1993 pp. 146-161.

[3] Kohyama, A., and Puigh, R. J., in *FFTF/MOTA Annual Progress Report, Fusion Year 1988* (National Institute for Fusion Research, Nagoya, June 1989) 180-182.

[4] Kohyama, A., Kohno, Y., Asakura, K., Yoshino, M., Namba, C., and Eiholzer, C. R., Journal of Nuclear Materials, Vol. 212-215, 1994, pp. 751-754.

[5] Orowan, E., Proceedings, Physical Society, Vol. 52, 1940, p. 8.

[6] Gelles, D. S., in *Radiation-Induced Changes in Microstructure: 13th International Symposium* (Part I), ASTM STP 955, F. A. Garner, N. H. Packan and A. S. Kumar, Eds., (ASTM, Philadelphia, 1987) pp. 560-587.

[7] Toloczko, M. B., Garner, F. A., and Eiholzer, C. R., Journal of Nuclear Materials, Vol. 258-263, 1998, pp. 1163-1166.

[8] D. S. Gelles and L. E. Thomas in *Alloy Development for Irradiation Performance Semiannual Progress Report for the Period Ending March 31, 1982,* DOE/ER-0045/8, 343-362.

[9] Maziasz, P. J., Journal of Nuclear Materials, Vol. 169, 1989, pp. 95-115.

Roger E. Stoller[1] and Lawrence R. Greenwood[2]

An Evaluation of Neutron Energy Spectrum Effects in Iron Based on Molecular Dynamics Displacement Cascade Simulations

Reference: Stoller, R. E. and Greenwood, L. R., **"An Evaluation of Neutron Energy Spectrum Effects in Iron Based on Molecular Dynamics Displacement Cascade Simulations,"** *Effects of Radiation on Materials: 19th International Symposium, ASTM STP 1366*, M. L. Hamilton, A. S. Kumar, S. T. Rosinski, and M. L. Grossbeck, Eds., American Society for Testing and Materials, West Conshohocken, PA, 2000.

Abstract: The results of molecular dynamics (MD) displacement cascade simulations in bcc iron have been used to obtain effective cross sections for two measures of primary damage production: (1) the number of surviving point defects expressed as a fraction of the displacements calculated using the standard secondary displacement model of Norgett, Robinson, and Torrens (NRT), and (2) the fraction of the surviving interstitials contained in clusters that formed during the cascade event. Primary knockon atom spectra for iron obtained from the SPECTER code have been used to weight these MD-based damage production cross sections in order to obtain spectrally-averaged values for several locations in commercial fission reactors and materials test reactors. An evaluation of these results indicates that neutron energy spectrum differences between the various environments do not lead to significant differences between the average primary damage formation parameters. In particular, the defect production cross sections obtained for PWR and BWR neutron spectra were not significantly different. The variation of the defect production cross sections as a function of depth into the reactor pressure vessel wall is used as a sample application of the cross sections. A slight difference between the attenuation behavior of the PWR and BWR was noted; this difference could be explained by a subtle difference in the energy dependence of the neutron spectra. Overall, the simulations support the continued use of dpa as a damage correlation parameter.

Keywords: ferritic steels, modeling, molecular dynamics, point defects, pressure vessels, radiation damage, rate theory

Introduction

Radiation-induced embrittlement in reactor pressure vessel (RPV) steels has traditionally been correlated with exposure parameters such as the neutron fluence above 1

1. Senior Research Staff, Oak Ridge National Laboratory, P. O. Box 2008, Oak Ridge, TN 37831-6376.
2. Lead Scientist, Pacific Northwest National Laboratory, P. O. Box 999, Richland, WA 99352.

Copyright© 2000 by ASTM International www.astm.org

MeV or atomic displacements per atom (dpa) [1,2]. One advantage of dpa over fast fluence is that it explicitly accounts for atomic displacements produced by the entire neutron energy spectrum. Therefore, it provides improved correlation when data have been obtained from irradiation facilities with different neutron energy spectra. Differences in neutron energy spectra are manifested as differences in the energy spectra of the primary knockon atoms (PKA) that are produced in elastic collisions with these neutrons. Low energy PKA, such as those produced by thermal neutrons, are somewhat more efficient at net defect production than are high-energy PKA. This suggests that these displacements should be more heavily weighted in dosimetry. Conversely, the lower energy PKA produce fewer point defect clusters that can promote the formation of extended defects that are responsible for mechanical property changes.

The issue of PKA energy effects can be investigated by displacement cascade simulations using the method of molecular dynamics (MD). Although MD simulations can provide a detailed picture of the formation and evolution of displacement cascades, they impose a substantial computational burden. However, recent advances in computing equipment permit the simulation of high energy displacement events involving more than one-million atoms [3-8]; the results presented below will encompass MD cascade simulation energies from near the displacement threshold to as high as 40 keV. These simulations were carried out using the MOLDY code [9], in which the computing time is almost linearly proportional to the number of atoms in the simulation. Higher energy events require a larger atom block as listed in Table 1. Two to three weeks of computer execution time is required to complete the highest energy 40 keV cascade simulations with 1,024,000 atoms for 15 ps on a modern high-speed workstation.

Table 1: Typical MD cascade parameters and required atom block sizes

Neutron Energy (MeV)	Average PKA Energy (keV)	Corresponding E_{MD} (keV)	NRT Displacements	Atoms in Simulation
0.0034	0.116	0.1	1	3,456
0.0058	0.236	0.2	2	6,750
0.014	0.605	0.5	5	6,750
0.036	1.24	1.0	10	54,000
0.074	2.54	2.0	20	54,000
0.19	6.60	5.0	50	128,000
0.40	13.7	10.	100	250,000
0.83	28.8	20	200	250,000
1.8	61.3	40	400	1,024,000

Two parameters have been extracted from the MD simulations: the number of point defects that remain after the displacement event is completed, and the fraction of the surviving interstitials that are contained in clusters. For the purpose of comparison with standard dosimetry, these values have been normalized to the number of atomic displacements calculated with the secondary displacement model by Norgett, Robinson, and Torrens (NRT) [10]. The energy dependence of the two MD defect parameters was used to evaluate the effects of neutron energy spectrum. Simple, energy-dependent

functional fits to the MD results were obtained, and the SPECOMP code [11] was used to compute effective cross sections for point defect survival and point defect clustering. PKA spectra for iron obtained from SPECTER [12] were then used to weight these effective cross sections in order to calculate spectrum-averaged values for various neutron irradiation environments. These include several locations through the wall of RPVs of representative commercial pressurized and boiling water reactors (PWR and BWR), and positions in both water and sodium-cooled materials test reactors.

MD Cascade Simulations

The molecular dynamics code, MOLDY, and the interatomic potential for iron that was used are described in detail in Refs. 9, 13 and 14. Briefly described, the process of conducting a cascade simulation requires two steps. First, a block of atoms of the desired size is thermally equilibrated. This process permits the lattice thermal vibrations (phonon waves) to be established for the simulated temperature, and typically requires a simulation equivalent to approximately 10 ps. This atom block can be saved and used as the starting point for several subsequent cascade simulations. Then, the cascade simulations are initiated by giving one of the atoms a defined amount of kinetic energy, E_{MD}, in a specified direction. This atom is equivalent to the PKA following a collision with a neutron. Statistical variability can be introduced by either further equilibration of the starting block or by choosing either a different primary knockon atom or PKA direction. Based on the magnitude of the calculated standard deviations, at least six different cascades are required to obtain statistically representative average parameters at any one cascade energy and temperature.

The MOLDY code describes only elastic collisions between atoms; it does not account for energy loss mechanisms such as electronic excitation and ionization. Thus, the initial energy E_{MD} given to the simulated MD knockon atom is analogous to the damage energy (T_{dam}) in the NRT model [10]. Using the values of E_{MD} in Table 1, the corresponding E_{PKA} and the NRT defects in iron have been calculated using the procedure described in Ref. 10 with the 40 eV displacement threshold recommended in ASTM E521, Standard Practice for Neutron Radiation Damage Simulation by Charged-Particle Irradiation. These values are also listed in Table 1. Note that the difference between the MD simulation, or damage energy, and the PKA energy increases as the PKA energy increases.

The cascade simulations are continued until in-cascade recombination of vacancies and interstitials is complete and the atom block has returned to near thermal equilibrium. The required simulation time varies from about 5 ps for the low-energy cascades to 15-20 ps for the 40 keV cascades at 100 K. Some further point defect recombination and clustering will take place at the longer times associated with point defect diffusion. However, such times are not accessible by the MD method. These results are thereby strictly representative of primary damage formation only. The range of neutron energies covered by these simulations is also listed in Table 1 and illustrated in Figure 1. The neutron spectra obtained for a typical PWR at the inside of the pressure vessel, and at positions 0.25 (1/4-T) and 0.75 (3/4-T) of the way through the RPV are shown. MD cascade simulation energies are shown that correspond to atomic recoils from elastic collisions with neutrons of the indicated energies.

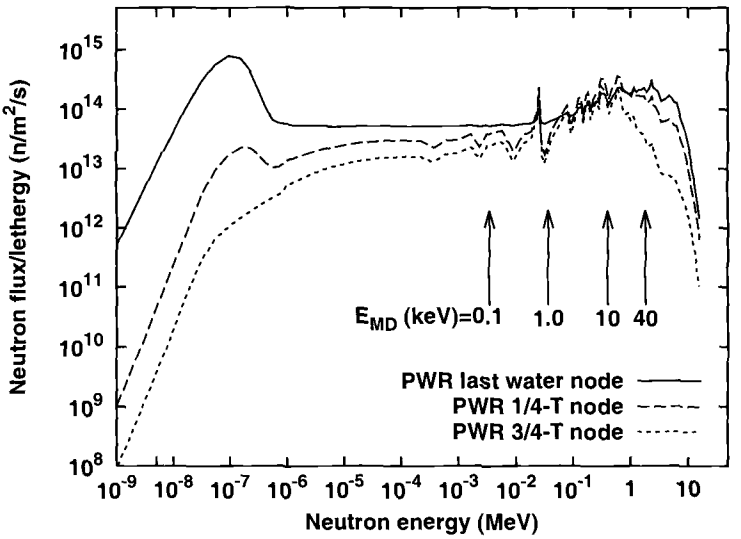


Figure 1 — *Representative PWR neutron spectra at the inside surface of the RPV, and the 1/4-T and 3/4-T RPV locations. Average cascade energies correspond to the indicated neutron energies.*

Two parameters are of primary interest to this work: the number of point defects that survive after in-cascade recombination is complete, and the fraction of the surviving interstitials contained in clusters rather than as isolated defects. The former is important because it is only the surviving point defects that can contribute to radiation-induced microstructural evolution. The latter is significant because these small clusters provide nuclei for the growth of larger defects which can give rise to mechanical property changes. The formation of these small clusters directly within the cascade means that the extended defects can evolve more quickly than if the clusters could only be formed by the much slower process of classical nucleation. For purposes of this work, interstitials were considered clustered if they were within the nearest-neighbor lattice distance of another interstitial. The size distribution of the interstitial clusters produced is a function of the cascade energy [3], and the interstitial clustering fraction is calculated by summing that distribution.

The surviving MD defects can be conveniently described as a fraction of the NRT displacements [10] and the number of clustered interstitials as a fraction of the surviving MD defects. The energy dependence of the surviving defect fraction (η) and the interstitial clustering fraction (f_{icl}) from the MD simulations is shown in Figures 2 and 3, respectively. Since the MD results did not exhibit a strong dependence on irradiation temperature, all of the results obtained at 100, 600, and 900 K are shown [3-7]. The line drawn through the data in each figure is a nonlinear least-squares fit to the data using the following functions:

$$\eta = 0.5608 \cdot E_{MD}^{-0.3029} + 3.227x10^{-3} \cdot E_{MD} \qquad (1)$$

$$f_{icl} = [0.097 \cdot ln(E_{MD} + 0.9)]^{0.3859} - 7x10^{-6} \cdot E_{MD}^{2.5} \quad (2)$$

In both Eqns. (1) and (2), the first term in the function dominates the energy dependence up to about 20 keV. The second term accounts for the effect of subcascade formation at the highest energies [5-7]. Mathematically, this term is responsible for the minimum in the defect survival curve and the maximum in the interstitial clustering curve at about 20 keV. As discussed elsewhere [5,6], this change in the energy dependence occurs because subcascade formation makes a single, high energy cascade appear to be the equivalent of several lower energy cascades. Thus, the defect survival fraction is slightly higher, and the interstitial clustering fraction slightly lower at 40 keV than at 20 keV.

The increase in the defect survival fraction between 20 and 40 keV is slight, but it appears to be statistically significant from the magnitude of the standard deviations that are shown as error bars in Figure 2. These standard deviations are based on the average of 7, 10, and 7 cascades at 10, 20, and 40 keV, respectively. The results of a preliminary analysis of 50 keV cascades is consistent with a slight increase in the cascade survival fraction above 20 keV. However, only four such cascades have been completed at this time and this is too small a number to obtain a reliable average. Additional simulations are underway at 40 and 50 keV to obtain a better statistical estimate of the averages at each energy. Since the standard deviations on the average interstitial clustering fractions are much larger, the significance of the maximum shown in Figure 3 is less clear. Based on the degree of subcascade formation observed in the 40 keV cascade simulations, it appears unlikely that η and f_{icl} will change significantly at higher cascade energies. Therefore, the values calculated from Eqns. (1) and (2) for 40 keV were applied for all the higher energy PKA in the SPECOMP and SPECTER calculations.

Defect Production Calculations Using SPECOMP and SPECTER

Energy-dependent defect production cross sections for surviving MD defects and clustered interstitials, and spectrum-averaged values for several irradiation environments were generated by modifying the SPECOMP [11] and SPECTER [12] computer codes. SPECOMP normally calculates displacement cross sections for compounds using the primary knockon atomic recoil energy distributions contained in a 100-neutron-energy by 100-recoil-energy grid for each of 40 different elements. For the present defect and clustered interstitial calculations, these new functions were used as a factor multiplying the standard displacement cross section equations as a function of the damage energy, T_{dam}. SPECOMP thus produced surviving defect and clustered interstitial cross sections on a 100 point neutron energy grid.

The SPECTER computer code contains libraries of calculated cross sections for displacements, gas production, and total energy distribution, as well as atomic recoil energy distributions for more than 40 elements and various compounds. For a given neutron energy spectrum and irradiation time, the code can be used to calculate the net radiation damage effects, as listed above. In the present case, the SPECOMP calculations for the surviving defect and clustered interstitial cross sections were added to the SPECTER libraries. SPECTER runs for various neutron spectra were then used to produce spectrum-averaged values for the point defect and interstitial clustering fractions.

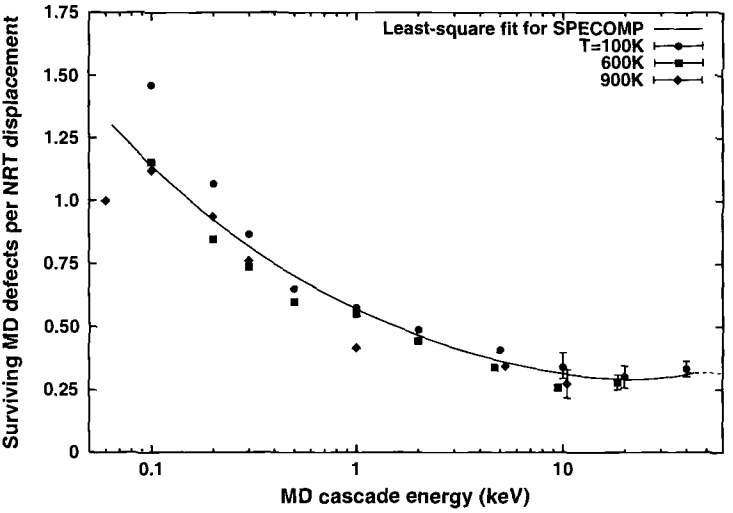


Figure 2 — *Average MD point defect survival fraction as a function of cascade energy; results of MD simulations at 100, 600, and 900K.*

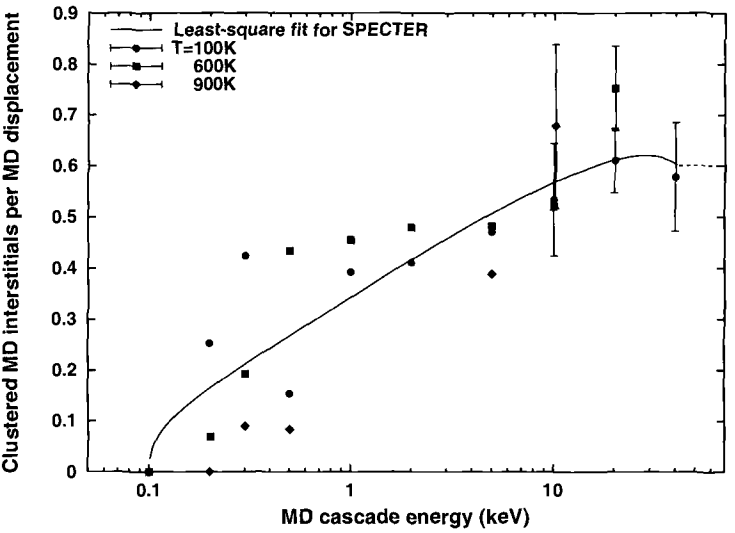


Figure 3 — *Average in-cascade interstitial clustering fraction as a function of cascade energy; results of MD simulations at 100, 600, and 900 K.*

Results and Discussion

The primary results of these calculations are summarized in Figure 4. The PKA-spectrum-averaged defect survival fraction is shown in Figure 4a, and the interstitial

clustering fraction in Figure 4b. In both cases, the effective production cross section has been divided by the NRT dpa cross section. Values are shown for the 1/4-T and 3/4-T RPV positions from representative PWR and BWR neutron spectra [15]. Four additional irradiation sites are also shown. These are: positions located in the peripheral target position (PTP) and removable beryllium reflector (RB*) of the High Flux Isotope Reactor (HFIR) at ORNL, and the mid-core and below-core (BC) positions in the Fast Flux Test Facility (FFTF) at the U.S. DOE Hanford Reservation.

Including the HFIR and FFTF positions provides spectra from two broadly used materials test reactors (although the FFTF is no longer operating). The former is a very high-flux (up to -10^{19} n/m^2), water-moderated test reactor, and the latter is a liquid metal (Na) cooled fast reactor. In spite of the differences between the various neutron energy

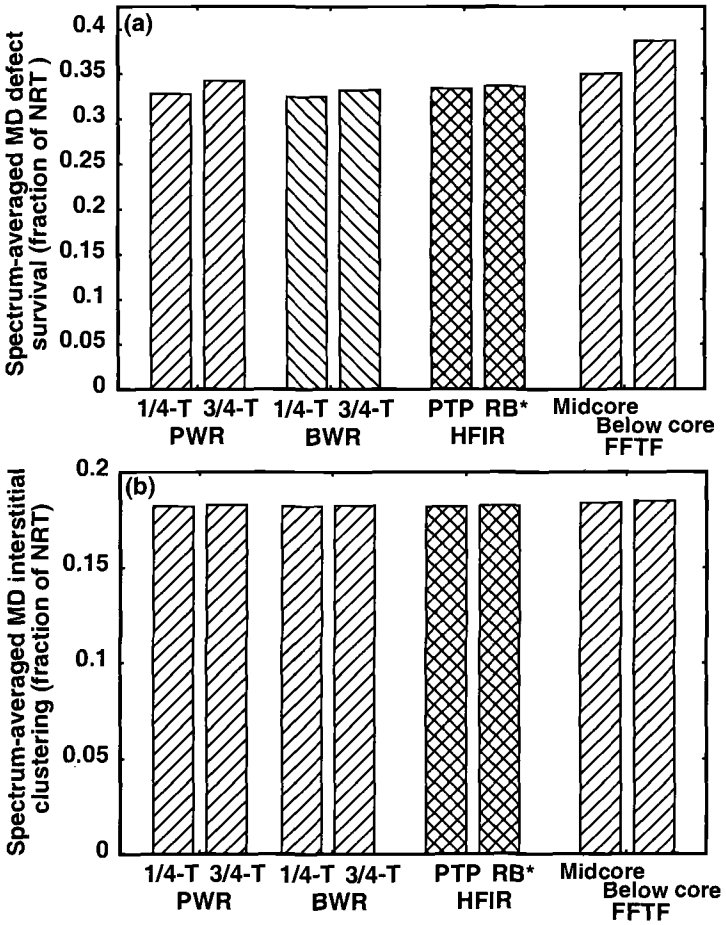


Figure 4 — *Comparison of spectrally-averaged damage production cross sections (per NRT dpa) for various irradiation environments; defect survival ratio is shown in (a) and the interstitial clustering fraction is shown in (b).*

spectra, only relatively small differences are observed in the two spectrum-averaged damage cross sections. This is consistent with the observed iron PKA energy distributions shown in Figure 5. In the region where the PKA probability is highest, i.e. for PKA energies between 1 keV and 0.1 MeV, the PKA spectra are quite similar.

A slight difference between the PWR and BWR spectra can be seen in the way the spectra change as a function of thickness through the pressure vessel. This is illustrated in Figure 6, where the spectrum-averaged defect production cross sections are shown for four positions: the last water node point before the RPV, the 1/4 and 3/4 RPV locations, and the first node point in the cavity beyond the RPV. The values for the two reactor types are most similar at the pressure vessel wall, and diverge somewhat at greater depths. The reason for this modest divergence is a subtle difference in the neutron energy spectra and the way in which neutron attenuation occurs. The BWR spectrum is generally considered to be softer than the PWR, and would be expected to give a higher defect survival fraction based on the results shown in Figure 2. However, the average PKA energy at the 1/4-T and deeper positions is actually somewhat higher for the BWR. This can be rationalized by a comparison of the 1/4-T neutron spectra in Figure 7, where the energy-dependent group fluxes are normalized using their respective peak values. The BWR spectrum shows both a higher relative thermal flux and a higher relative fast flux than the PWR spectrum. Since most of the displacements are generated by the higher energy neutrons, the effective average PKA energy for the BWR spectrum is greater than that of the PWR. Although the details of this comparison may apply only to these particular reference spectra [15], it illustrates how using a dose or correlation parameter that makes use of the complete neutron spectrum can provide more information than is obtained when only a simple fluence greater than a specified energy threshold is used.

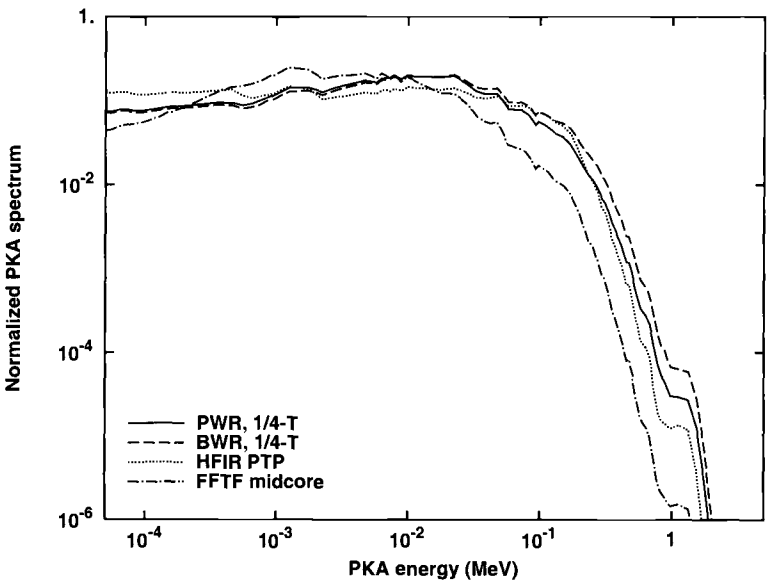


Figure 5 — *Normalized iron PKA energy distributions for PWR and BWR 1/4-T and positions, HFIR PTP, and FFTF midcore position.*

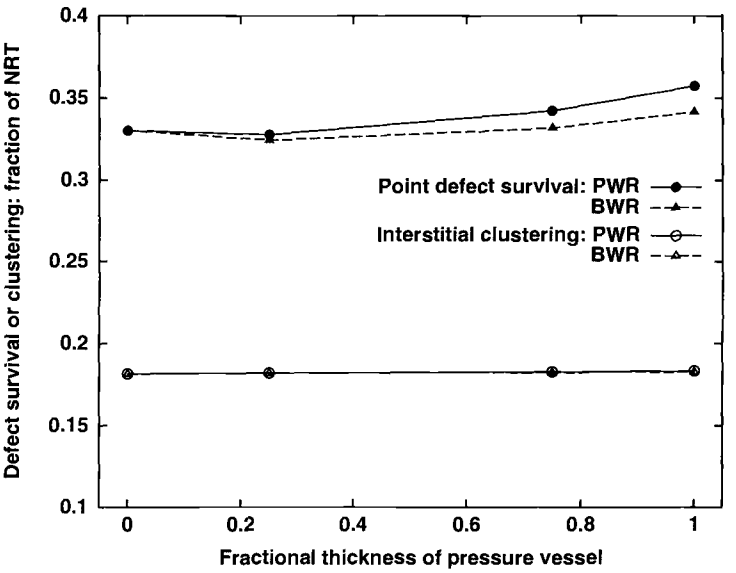


Figure 6 — *Variation of spectrally-averaged damage production cross sections (per NRT dpa) through the RPV for PWR and BWR.*

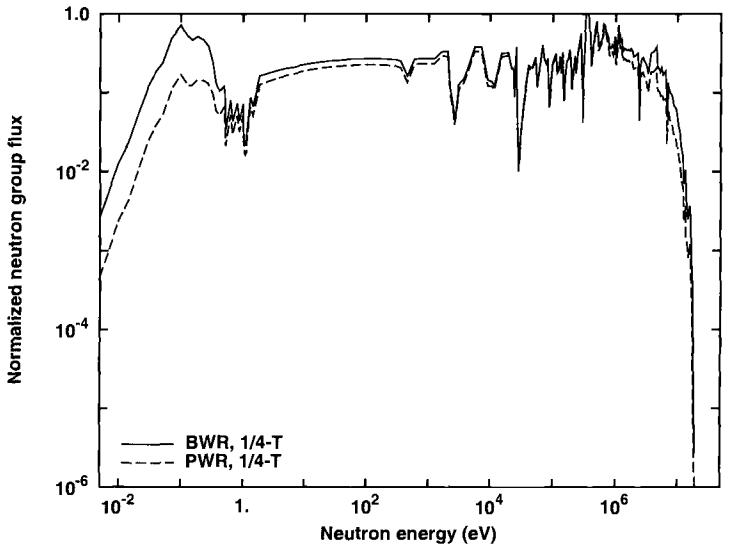


Figure 7 — *Normalized neutron spectra for PWR and BWR at the 1/4-T location. Note that the BWR fluxes are higher at both the lowest and highest energies.*

The projected attenuation of the damage rate through a PWR reactor pressure vessel is shown in Figure 8, in which results based on the MD-based damage cross

sections are compared to neutron fluence (E>1.0 MeV) and dpa. The results are normalized to the value obtained at the first node of the transport calculation inside the RPV. The other four points plotted are the 1/4-T, 3/4-T, the last node in the RPV, and the first node in the reactor cavity. Because an increasing fraction of displacements are caused by lower energy neutrons as the high energy end of the spectrum is lost, dpa is attenuated more slowly than fast fluence. The MD point defect survival is attenuated somewhat more slowly than dpa because of the increased survival fraction at lower energies shown in Figure 2. However, the small difference between dpa and the MD-based results shown in this figure indicates that dpa accounts for nearly all of the spectral shift associated with attenuation through the RPV.

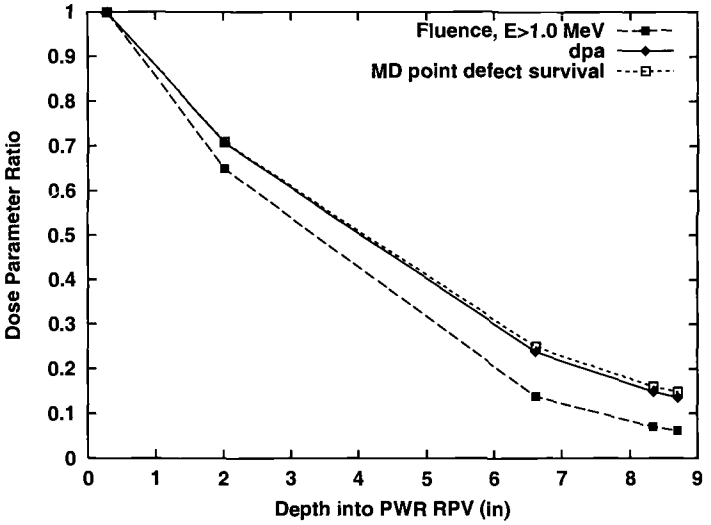


Figure 8 — *Attenuation of fast neutron fluence, dpa, and MD-based point defect survival fraction through the wall of PWR reactor pressure vessel.*

Summary

Although it is not yet possible to simulate the highest energy displacement cascades generated in the materials used in fission reactors, the analysis of MD cascade simulations in bcc iron for energies up to 40 keV are of considerable relevance. For example, while Fig. 5 indicates that there is a significant probability of PKA production at energies above 100 keV for fission reactor neutron spectra, the highest average PKA energy obtained from SPECTER for any of the LWR RPV neutron spectra was only 23 keV.

The primary damage parameters derived from the MD results exhibit a strong dependence on cascade energy up to about 10 keV. At this point, a high degree of subcascade formation leads to nearly asymptotic behavior at higher cascade energies. However, there is also evidence of a minimum in the fractional defect survival curve at ~20 keV. This potential for a slight increase in the cascade survival fraction above 20 keV is being investigated further. Analysis of cascade and subcascade morphology indicates that the primary damage parameters will not significantly change at higher energies, which

implies that the results reported here should be relevant to an evaluation of neutron energy spectrum effects.

Notably, the spectrum-averaged defect production cross sections calculated for several fission reactor neutron spectra were all quite similar. This included locations within the pressure vessels of commercial PWRs and BWRs, as well as locations in light water and liquid metal cooled materials test reactors. Since the cross sections were so similar, it appears unlikely that spectral differences will significantly influence comparisons of PWR and BWR data when dpa is used as a correlation parameter. In addition, an evaluation of damage attenuation through the RPV wall for both reactor types indicates that the spectrum-averaged, MD-based damage production cross sections are attenuated at a rate which is not significantly different from the dpa cross section. This implies that neutron energy spectrum changes due to attenuation should also be well accounted for through the use of dpa.

Finally, the spectrum-averaged defect production cross sections obtained from the MD results can be used to guide the selection of appropriate radiation damage source terms in the kinetic models used to investigate radiation-induced microstructural evolution and embrittlement in pressure vessel steels. It has not been demonstrated that these results are relevant to materials other than ferritic steels; however, a comparison of MD cascades in fcc copper and bcc iron up to 10 keV revealed many similarities between these two materials [3].

Acknowledgments

Research sponsored by the Office of Nuclear Regulatory Research, U.S. Nuclear Regulatory Commission under inter-agency agreement DOE 1886-8109-8L with the U.S. Department of Energy and by the Division of Materials Sciences, U.S. Department of Energy under contract DE-AC05-96OR22464 with Lockheed Martin Energy Research Corp., and the Office of Fusion Energy Sciences, U.S. Department of Energy at the Pacific Northwest National Laboratory.

References

[1] R. E. Stoller and G. R. Odette, *Journal of Nuclear Materials* 186 (1992) 203-205.

[2] Recommendations of IAEA Specialists Meeting on Radiation Damage Units in Graphite and Ferritic and Austenitic Steels, *Nuclear Engineering and Design* 33 (1975) 48.

[3] W. J. Phythian, R. E. Stoller, A. J. E. Foreman, A. F. Calder, and D. J. Bacon, *Journal of Nuclear Materials* 223 (1995) 245-261.

[4] R. E. Stoller, *Journal of Nuclear Materials* 233-237 (1996) 999-1003.

[5] R. E. Stoller, *JOM (formerly Journal of Metals)* 48 (1996) 23-27.

[6] R. E. Stoller, G. R. Odette, and B. D. Wirth, *Journal of Nuclear Materials* 251 (1997) 49-69.

[7] R. E. Stoller, "Molecular Dynamics Simulations of High Energy Cascades in Iron," Microstructure of Irradiated Materials, I. M. Robertson, L. E. Rehn, S. J. Zinkle, and

W. J. Phythian, Editors, Materials Research Society, Pittsburgh, PA, 1995, pp. 21-26.

[8] R. E. Stoller and L. R. Greenwood," *Journal of Nuclear Materials* 271&272 (1999) 57-62.

[9] M. W. Finnis, "MOLDY6-A Molecular Dynamics Program for Simulation of Pure Metals," AERE R-13182, UK AEA Harwell Laboratory (1988).

[10] M. J. Norgett, M. T. Robinson, and I. M. Torrens, *Nuclear Engineering and Design* 33 (1975) 50-54.

[11] L. R. Greenwood, "SPECOMP Calculations of Radiation Damage in Compounds," Reactor Dosimetry: Methods, Applications, and Standardization, ASTM STP 1001, H. Farrar IV and E. P. Lippincott, Eds., American Society of Testing and Materials, West Conshohocken, PA, 1989, pp. 598-602.

[12] L. R. Greenwood and R. K. Smither, "SPECTER: Neutron Damage Calculations for Materials Irradiations," ANL/FPP/TM-197, Argonne National Laboratory, Argonne, IL, January 1985.

[13] M. W. Finnis and J. E. Sinclair, *Philosophical Magazine* A50 (1984) 45-55 and Erratum, *Philosophical Magazine* A53 (1986) 161.

[14] A. F. Calder and D. J. Bacon, *Journal of Nuclear Materials* 207 (1993) 25-45.

[15] T.E. Albert, M.L. Gritzner, G.L. Simmons, and E.A. Straker, "PWR and BWR Radiation Environments for Radiation Damage Studies, "EPRI NP-152, Electric Power Research Institute, Palo Alto, CA, September 1977.

Angela Hempel,[1] Masaaki Saneyasu,[1] Zheng Tang,[1] Masayuki Hasegawa,[1]*
Gerhard Brauer,[2] Fernando Plazaola,[3] Sadae Yamaguchi,[1] Fumihisa Kano,[4] and
Akio Kawai[4]

Effects of Neutron Irradiation on Fe-Cu Model Alloys and RPV Steels Probed by Positron Annihilation and Hardness Measurements

Reference: Hempel, A., Saneyasu, M., Tang, Z., Hasegawa, M., Brauer, G., Plazaola, F., Yamaguchi, S., Kano, F., and Kawai, A., **"Effects of Neutron Irradiation on Fe-Cu Model Alloys and RPV Steels Probed by Positron Annihilation and Hardness Measurements,"** *Effects of Radiation on Materials: 19th International Symposium, ASTM STP 1366,* M. L. Hamilton, A. S. Kumar, S. T. Rosinski, and M. L. Grossbeck, Eds., American Society for Testing and Materials, West Conshohocken, PA, 2000.

Abstract: To study the formation of microvoids and Cu precipitates in Fe-Cu model alloys (0-1.0 wt. % Cu) and A533B reactor pressure vessel (RPV) steel, positron lifetime and Vickers microhardness have been measured after fast neutron irradiation to a fluence of 8.3×10^{18} n/cm^2 below 150°C. Long positron lifetimes for the Fe-Cu alloys ranging from 300 to 420 ps and 270 to 350 ps for A533B RPV steels have been observed, which show microvoid formation. The long lifetimes in the Fe-Cu alloys depend on the Cu content and thermal aging at 550°C before irradiation. This fact suggests incorporation of irradiation-induced vacancies at Cu atoms and their precipitates leading to suppression of the microvoid formation. The long lifetime component for the Fe-Cu alloys recovers around 350°C, while that for A533B steel recovers around 300°C. To estimate the microvoid sizes, superimposed-atom model calculations of positron lifetimes in microvoids consisting of 1 (V_1) to 66 (V_{66}) vacancies have been performed,

1 Visiting Researcher, Graduate Course Student, Research Associate and Professors, Institute for Materials Research, Tohoku University, Sendai 980-8577, Japan.

2 Group Leader, Institut für Ionenstrahlphysik und Materialforschung, Forschungszentrum Rossendorf e.V., Postfach 51 01 19, 01314 Dresden, Germany.

3 Professor, Elektrika eta Elektronika Saila, Euskal Herriko Unibertsitatea, 644 p.k., 48080 Bilbo, Spain.

4 Researchers, Power and Instrumental Systems Research and Development Center, Toshiba Co., 4-1 Ukishima-cho, Kawasaki-ku, Kawasaki 210-0862, Japan.

* Corresponding author

Copyright© 2000 by ASTM International www.astm.org

respectively. Based on these calculations, the formation and post-irradiation annealing behaviour of microvoids are examined.

In addition, irradiation-induced hardening monitored by Vickers microhardness is discussed with reference to positron annihilation experiments.

Keywords: neutron irradiation, positron annihilation, reactor pressure vessel steels, Fe-Cu model alloys, microvoids, isochronal annealing, irradiation-induced hardening

Introduction

Light water reactor pressure vessel (RPV) steels can be embrittled by long-term in-service exposure to neutron irradiation [*1-3*]. Point defects, their clusters and impurity precipitates are induced by neutron-irradiation and are responsible for embrittlement. It has been widely known that copper impurities and microvoids play a significant role in the embrittlement process in RPV. However, a detailed mechanism describing their behavior is not well understood yet [*3-9*].

Therefore a lot of effort has been undertaken to identify the structure and properties of such irradiation-induced precipitates and to describe the behaviour of the defects during isochronal annealing [*3*]. A majority of recent work has focused on the role of copper in RPV steels and Fe-Cu alloys, but has not been successful yet in the clarification of the copper-rich precipitates and their effects on the embrittlement. The critical questions are centered on the factors controlling the nucleation, growth, and precise hardening mechanism due to these copper-rich precipitates. Fluence, flux, irradiation temperature, chemical composition and thermal history before irradiation have been supposed to be critical and important factors. For example, before irradiation peak hardness has been observed after thermal aging at 550°C for 2 hours [*10*]. This peak hardness is due to metastable copper-rich precipitates formed by the thermal aging.

Copper-rich precipitates will be influenced by highly supersaturated irradiation-induced vacancies via vacancy-Cu interactions and radiation-enhanced diffusion. Furthermore, incorporation of the vacancies into the precipitates will suppress the microvoid formation and vacancy-related process under irradiation.

Several microscopic experimental methods have been employed to investigate irradiation embrittlement processes, such as small angle neutron scattering (SANS), atom-probe field ion microscopy (APFIM) and transmission electron microscopy (TEM) [*6*].

The positron lifetime technique is another well-established method for studying atomic defects, such as vacancies, vacancy clusters, dislocations and precipitates. The method is based on the trapping of positrons at open-volume defects, which have lower electron density and hence give a longer positron lifetime compared to the bulk lifetime. Because of the high trapping probability, the positron annihilation method is sensitive to defect concentrations as low as $\sim 10^{-6}$ [*11,12*].

A lifetime longer than that for mono-vacancies proves the presence of defect conglomerates with two and more vacancies, such as three-dimensional vacancy clusters [*13*].

However, to interpret the experimental results, a theoretical model, which gives positron lifetime as function of microvoid size, is very necessary. Based upon a simple superimposed-atom model, Puska and Nieminen [*14*] have performed such calculations for positron lifetimes in microvoids consisting of 1 (V_1) to 15 (V_{15}) vacancies, using a fitting parameter to reproduce the experimental bulk lifetime. To examine larger microvoids, however, ab-initio superimposed-atom model calculations are necessary.

In the present study, positron lifetime and Vickers microhardness measurements are employed to study microvoid formation, copper-rich precipitates and their influence on irradiation hardening. Furthermore we have made a calculation of an ab-initio superimposed-atom model, using supercells with periodic boundary conditions [*15*] to examine the microvoids.

Experimental

Model alloy samples were prepared according to the procedure given in Ref. [*6*]. Mother alloys of Fe-5 wt. % Cu were made from pure iron (ATOMIRON 5N, Showa Denko Co.) and Specure-Copper (99.999%, Johnson Matthey Chem. Ldt.) by arc melting in Ar-gas atmosphere. They were diluted with appropriate amounts of iron by arc melting. The resulting alloys were cold-rolled to about 0.3 mm in thickness and disks of 5 mm in diameter were punched, then mechanically and chemically polished. The disk samples were sealed in evacuated quartz tubes and hold at 825°C for 4 hours, followed by quenching into iced water. A part of the samples was sealed in quartz tubes and then thermally aged at 550°C for 2-312 hours. The specimen and pre-irradiation heat treatments are summarized in Table 1.

Table 1 – *Specimens and their heat treatment before irradiation.*

Material	Cu Content , wt. %	Aging Time at 550°C , hours
Pure Fe*	0.00002	
Fe-0.3Cu	0.31	As-quenched (unaged)
Fe-1.0Cu	1.0	2, 10, 100, 312
RPV steel A533B	0.02	

* For pure Fe, two kinds of samples were used, where the irradiation temperature of sample II was slightly higher than for sample I. Sample I was used for the study of the influence of copper content on positron lifetime and Vickers microhardness measurements. For the annealing experiments sample II was used.

These samples were irradiated with fast neutrons to a fluence of 8.3×10^{18} n/cm^2 (flux $\Phi = 1.6 \times 10^{13}$ n/cm^{2}s) below 150°C in the Irradiation Facility of Hydraulic Rabbit II in Japan Materials Testing Reactor (JMTR).

Positron lifetime measurements were carried out using a lifetime spectrometer with a time resolution of about 260 ps (FWHM) and a positron source of ^{22}Na (0.7 MBq) sealed with a Mylar film. After irradiation, the samples were isochronal annealed from 150°C to 700°C in steps of 25°C or 50°C for 30 min. The spectra were analyzed with the PATFIT-88 program [*16*].

Vickers microhardness was measured with a conventional apparatus with a load of 200 g for 15 seconds. Thereby, an averaged hardness of at least 10 indentations on each sample was obtained.

The chemical composition of the reactor pressure vessel steel is shown in Table 2.

Table 2- *Chemical composition of reactor pressure vessel (RPV) steel A533B.*

Element	Composition, wt %	Element	Composition, wt. %
C	0.180	Cr	0.120
Si	0.250	Mo	0.520
Mn	1.450	V	0.003
P	0.007	As	0.002
S	0.002	Sn	0.001
Cu	0.020	Co	0.003
Ni	0.670	Al	0.013

Results and Discussion

A) Positron Lifetime in Vacancy Clusters – Theoretical Calculation

For an interpretation of positron lifetimes for vacancies and their clusters a theoretical model for the lifetime of positrons trapped by these defects is necessary. Puska and Nieminen [*14*] employed the superimposed-atom model with a fitting parameter for d-electrons in Fe. In the superimposed atom model the spherical averaged charge densities of an isolated free atom were superimposed to obtain the electron density distribution.

In this study to evaluate the positron lifetime from larger vacancy clusters, an improved superimposed-atom model calculation was performed within the framework of a supercell approximation and the two-component (positron and electron) density-functional theory by Boronski and Nieminen [*17*], but without using any fitting parameter [*15*]. A detailed description will be published elsewhere. In Figure 1 the calculated positron lifetimes for iron together with those by Puska and Nieminen are plotted against the number of vacancies (N_V). Although the present results are slightly shorter than those by Puska and Nieminen, general agreement between them is good and it is commonly observed in both studies that the positron lifetime increases rapidly with numbers of vacancies up to $N_V \approx 15$. Furthermore, the present calculation clearly shows that the positron lifetime increases very slowly for large microvoids and is almost saturated at about 420 ps for microvoids of around 66 vacancies ($\sim V_{66}$).

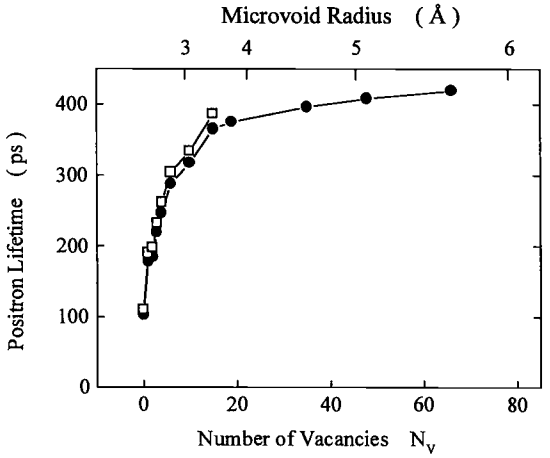


Figure 1 - *Theoretical calculations of positron lifetimes at microvoids in Fe: Puska and Nieminen [14]* (□) *and present work* (•). *Microvoid radius is given by that of sphere with the same volume, which is equal to N_v times the volume of a monovacancy.*

B) Model Alloys

Figure 2 shows typical positron lifetime spectra of Fe-0.3Cu alloy in the as-irradiated state and after post-irradiation annealing at 500°C, which is almost identical to that for the unirradiated state. The lifetime spectrum for the as-irradiated state can be well decomposed into two lifetime components τ_i (i = 1,2) with their relative intensities I_i.

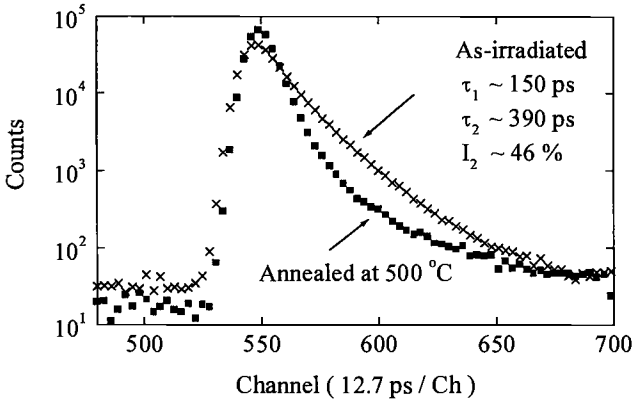


Figure 2 – *Positron lifetime spectra of Fe-0.3 wt. % Cu model alloy in as-irradiated state and after post-irradiation annealing at 500°C. This alloy was aged for 312 hours at 550°C before irradiation.*

Before fast neutron irradiation pure Fe as well as the Fe-0.3Cu alloy show one lifetime which is almost independent of aging time (Figure 3(a)). This lifetime is about 106 ps for pure Fe, while about 111 ps in Fe-0.3Cu. In Fe-1.0Cu, however, the lifetime is found to increase after longer aging time: 127 ps for 100 hours and 144 ps for 312 hours.

In Figure 3(b), the lifetime parameters τ_1, τ_2 and I_2 for the model alloy after irradiation are plotted against thermal aging time before irradiation. Because of a limited time resolution of the spectrometer, the short lifetimes τ_1 ranging from the bulk lifetime τ_B (105 ps) to the monovacancy lifetime τ_{V1} (180 ps) usually represents an average of lifetimes of free positrons in bulk state and of trapped positrons at simple defects such as monovacancies, their complex with impurities and dislocation loops, i.e., other than the three-dimensional vacancy clusters (microvoids). Therefore, the observed lifetime τ_1 (~150 ps) shows that a large part of positrons is trapped at simple defects induced by irradiation.

As-irradiated pure Fe (the sample I) shows almost constant lifetimes τ_2 of about 420 ps for aging for 2-312 hours, demonstrating that the microvoids in pure iron are insensitive to thermal aging in their size of about $\sim V_{66}$ as seen from Figure 1. In the as-irradiated state, the intensity I_2 for pure Fe is about 80 % and much higher than those ones for the Fe-Cu model alloys (I_2 ~ 40 %) as stated below. The intensity I_2 is not exactly proportional to the number density of microvoids, but gives a measure of a relative number density: the higher I_2 corresponds to the higher number density.

The lifetime τ_2 for Fe-0.3Cu markedly depends on thermal aging. The quenched state of this alloy has nearly the same lifetime τ_2 as that of pure Fe. However, τ_2 is about 350 ps after aging for 2-100 hours. These lifetimes are much shorter than those for pure Fe and then are due to much smaller microvoids of about 15 vacancies (V_{15}), compared to the quenched state and pure Fe ($\sim V_{66}$). This strongly suggests that after thermal aging microvoid formation is much suppressed by Cu-doping as seen from τ_2 and I_2 in Figure 3(b). This suppression is attained by incorporation of irradiation-induced vacancies into small metastable Cu-rich precipitates formed by thermal aging and hence by reduction in number of the vacancies forming the microvoids. Further aging for 312 hours has increased τ_2 to about 380 ps ($\sim V_{19}$). This shows the formation of larger microvoids and hence indicates that a larger number of vacancies are incorporated into the microvoids. Then it has to be noticed that the Cu-rich precipitates for the 312 hour aging sample are not so efficient in their incorporation of vacancies as those for the samples after 2-100 hour aging.

In the as-irradiated Fe-1.0Cu alloy, τ_2 is about 300 ps ($\sim V_{10}$) and much shorter than those for pure Fe and Fe-0.3Cu (Figure 3(b)). This reflects that in this alloy with the higher Cu content a large number of vacancies is incorporated into Cu-rich precipitates or is trapped at Cu atoms in solution. However, it is noted that τ_2 for Fe-1.0Cu gradually increases with the aging time, showing the formation of larger microvoids after longer aging.

It is also noted that τ_1 for Fe-1.0Cu is shorter than those for pure Cu and Fe-0.3Cu. This indicates that positrons are trapped in Cu-rich precipitates formed by aging in this alloy. Our preliminary experiment of positron lifetime and coincidence Doppler broadening of annihilation radiation suggests such positron trapping with τ_1 of about 100 ps for Fe-1.0Cu aged for 0-10h. Details will be reported elsewhere.

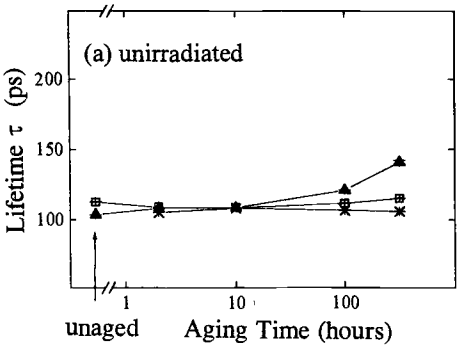


Figure 3a- *Dependence of positron lifetime parameters on copper content and thermal aging time in pure Fe (×), Fe-0.3Cu (□), Fe-1.0Cu (▲) before Irradiation.*

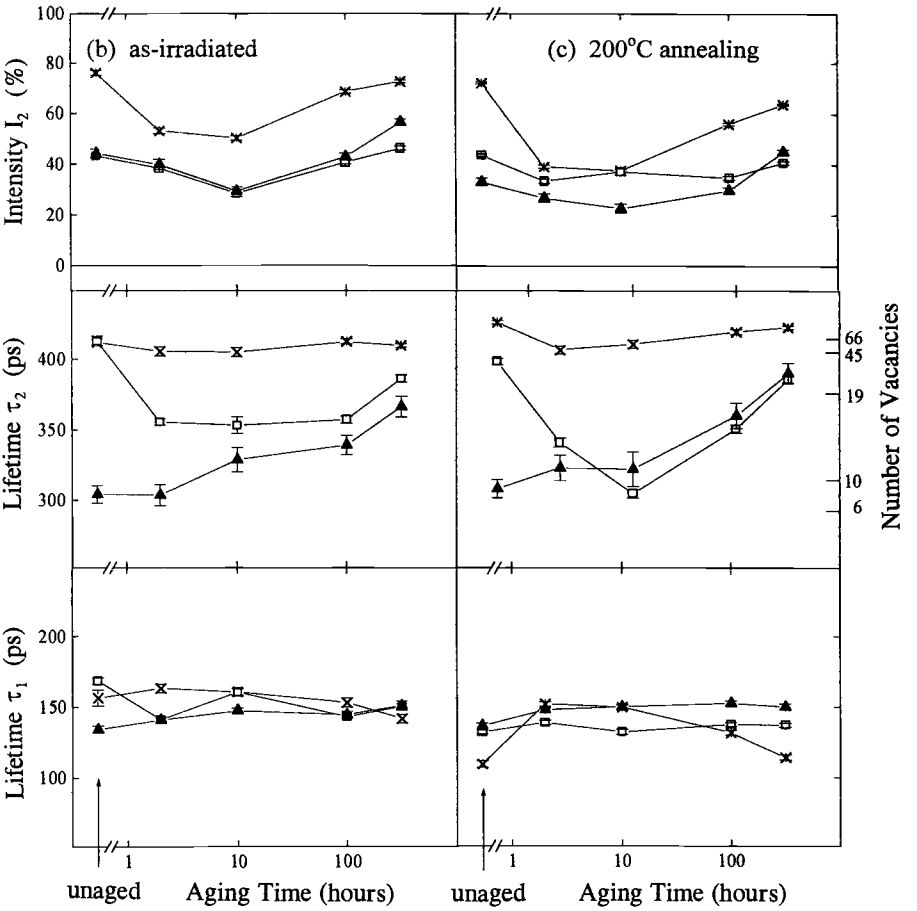


Figure 3b, c – *Dependence of positron lifetime parameters on copper content and thermal aging time in pure Fe (sample I) (×), Fe-0.3Cu (□), Fe-1.0Cu (▲): (b) as-irradiated and (c) after annealing at 200°C for 30 min after irradiation.*

The positron lifetime parameters after post-irradiation annealing are also sensitively dependent on thermal aging. As an example, the parameters after annealing at 200°C are shown in Figure 3(c). By the annealing τ_2 for pure Fe and Fe-1.0Cu are slightly increased or unchanged. However, τ_2 for Fe-0.3Cu of thermal aging for 2-100 hours is decreased by annealing at 200°C, which shows the microvoid size is reduced by the aging in this alloy. Detailed description of annealing behaviour will be presented in a later section.

The presence of copper precipitates comes from the low solubility of Cu in iron at 550°C, which is only 0.074 wt. % [*18*]. Furthermore, TEM studies on Fe-Cu alloys by Othen et al. [*19*], Charleux et al. [*20*] and Phythian [*10*] have reported Cu-precipitates in Fe-0.3Cu and Fe-1.0Cu. High-resolution electron micrograph measurements by Othen et. al. [*19*] on Fe-Cu alloys after thermal aging for 6 hours (at 550°C) have shown Cu-rich precipitates of a size of 4-5 nm with a 9R fringe pattern, following martensitic transformation from bcc Cu structure. After aging time for 10 hours, copper precipitates (diameter ≈13mm) show a multiple twinned 9R particle. Further aging (10-100 hours) leads to growth of the precipitates. A small amount of precipitates with diameters between 7 and 17 nm have a multiply twinned 9R structure.

These Cu-rich precipitates will be responsible for vacancy-incorporation and hence suppression of the microvoids. At this point there is no more detailed information about the effects of neutron irradiation on the state and the size of the precipitates in Fe-Cu alloys with different Cu content. However, further studies are very necessary to understand detailed positron trapping at these precipitates.

From previous Vickers microhardness experiments on unirradiated Fe-Cu alloys it has been reported that the hardness markedly increases with Cu content [*5*]. In Figure 4(a) Vickers microhardness before irradiation is plotted against aging time. Unirradiated pure Fe shows only a small dependence on thermal aging time and an almost constant H_v ~ 75 is found under the given conditions. For Fe-0.3Cu after 10 hours thermal aging a small hardness peak up to H_v ~ 90 was observed. The hardness for Fe-1.0Cu is much higher than those found for Fe-0.3Cu and marked by a dependence on thermal aging, with hardness peak at aging time of about 10 hours. It is seen in the as-irradiated sample (Figure 4(b)) that the hardness increases with Cu content. The irradiation-induced hardening $\Delta H_v = H_v$ (as-irrad.)-H_v (unirrad.) is plotted against aging time in Figure 4(c).

Pure Fe shows the smallest hardening, but this small hardening slightly increases by aging for 2~100 hours, which may be due to some effects between irradiation-induced defects and impurity atoms.

The Fe-0.3Cu alloys show nearly the same hardening for thermal aging. However, it should be noted that the irradiation-induced hardening is much larger than that for pure Fe. This means that the hardening is associated with the Cu-rich precipitates but is insensitive to detailed states of the precipitates in this alloy during thermal aging.

The hardening for Fe-1.0Cu alloys decreases with aging time. The unaged sample shows the highest hardening, which reflects the smallest hardness before irradiation.

The hardness of Fe-1.0Cu after irradiation shows almost the same hardness for aging up to10 hours (at 550°C) but longer aging results in a rapid decrease of hardness. On the other hand the hardness before irradiation shows the marked hardness peak around 10

hour aging (Figure 4(a)). Then the hardening is sensitively dependent on aging as seen in Figure 4(c). These observations on the hardening for both Fe-Cu alloys suggest complex interactions between the irradiation-induced defects and the Cu-rich precipitates. Clarification of these interactions must wait for further detailed studies using e.g. APFIM and high resolution TEM.

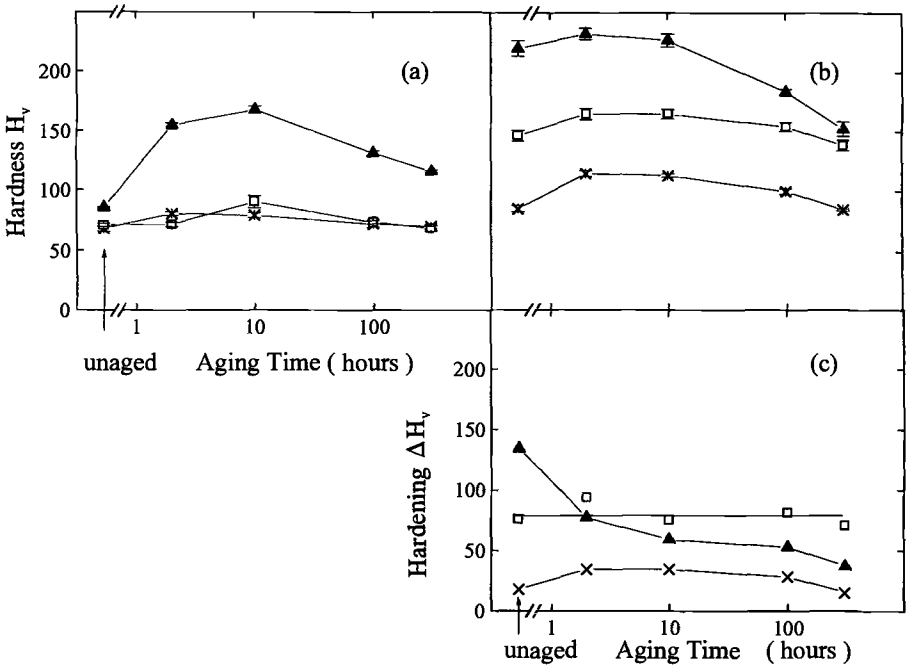


Figure 4 - *Dependence of Vickers microhardness H_v and hardening ΔH_v on copper content and thermal aging time in pure Fe (×), Fe-0.3Cu (□), Fe-1.0Cu (▲): (a) unirradiated, (b) as-irradiated and (c) irradiation-induced hardening, $\Delta H_v = H_v$ (as-irrad.)-H_v (unirrad.).*

C) Annealing Behaviour – Model Alloys

The lifetime parameters for pure Fe (the sample II) are presented in Figure 5. In the as-irradiated state the longer lifetimes τ_2 of about 420 ps suggests the positron-trapping at microvoids consisting of about 66 vacancies ($\sim V_{66}$) as seen in Figure 1.

The lifetime τ_2 and its intensity I_2 are almost constant up to annealing at 200°C. However τ_2 progressively increases with annealing temperature up to 300°C and reaches about 450 ps, while I_2 decreases with temperature. The progressive increase in τ_2 accompanying the decrease in I_2 suggests growth of the microvoids, but with a

decreasing in their number density. Further annealing above 350°C leads to a rapid decrease in τ_2 and I_2 and gives rise to a complete recovery of them at 450°C.

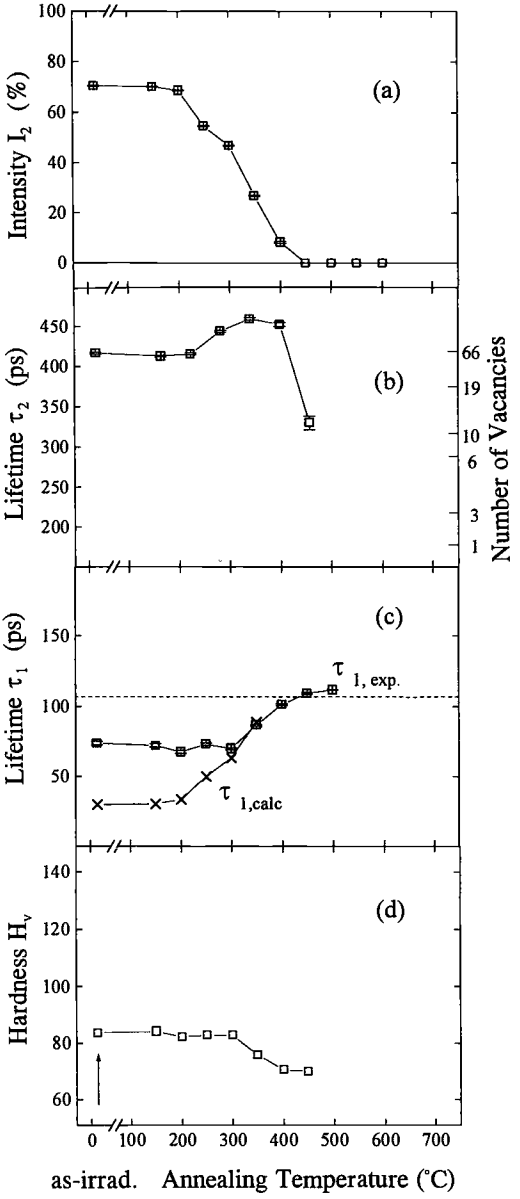


Figure 5 – *Positron lifetime parameters and Vickers microhardness for irradiated pure Fe (sample II). The dashed lines stand for quenched state.*

To check the existence of simple defects in Fe, we calculated the lifetime τ_1 by the two-state trapping model using the observed τ_2, I_2 and τ_B (bulk lifetime). If the calculated τ_1 agrees well with the observed τ_1, we can say that the one-defect state, namely the microvoid-state, is enough to describe the positron trapping. The calculated τ_1 is shown in Figure 5(c), but is found to be much shorter than the observed τ_1 for the as-irradiated and annealed states below 300°C. This disagreement below 300°C indicates the existence of defects, other than the microvoids. However, the calculated τ_1 after annealing higher than 300°C agrees well with the observed one. This suggests that the other kind of defects recover around 300°C.

The Vickers microhardness of pure Fe is almost constant after annealing up to 300°C, but shows a slightly decrease above 300°C and nearly complete recovery to the unirradiated value after annealing at 450°C. This is close to the annealing temperature for the recovery of the microvoids. However, it should be noted that the annealing behaviour of the hardness does not reflect the change in τ_2 and I_2 due to the microvoid growth at 250 – 300°C. The decrease of hardness after annealing at 300°C might be due to the annealing of microvoids, but also due to the recovery of the simple defects. Then it is further suggested that the irradiation hardening is not due to the microvoid but due to interstitial-type defects (such as interstitial dislocation loops). Both kinds of defects will disappear simultaneously around 450°C, resulting in full recovery of the hardening in pure Fe.

The annealing behaviour of the lifetime parameters for Fe-0.3Cu and Fe-1.0Cu is shown in Figure 6(a) and 6(b). As stated above, the lifetime parameters for the as-irradiated state of the model alloys depend on aging before irradiation, which is due to vacancy incorporation into the Cu-rich precipitates and the Cu atoms in supersaturated solution.

In Fe-0.3Cu after being quenched and aged for 312 hours (at 550°C), the lifetime τ_2 of about 400 ps ($\sim V_{40}$) is almost unchanged by annealing up to 300°C, while its intensity I_2 shows gradual decrease. The decrease in I_2 suggests the decrease in the number density of microvoids, while the small decrease in τ_1 means the recovery of the simple defects other than the microvoids. This recovery will be due to dissociation of interstitial type defects and hence cause a decrease in the number density of the microvoids. The longer lifetime component τ_2 vanishes after annealing at 400°C, suggesting the full recovery of the microvoids.

The sample with thermal aging for 10 hours (at 550°C) shows a progressive shortening of τ_2 with annealing temperature up to 300°C and its intensity (I_2) recovers completely at 350°C. It should be mentioned that after annealing at 150°C τ_2 decreases from 350 ps ($\sim V_{15}$) to 320 ps ($\sim V_{10}$) but I_2 increases from 30 % to 40 %. This annealing behaviour of the long lifetime component (τ_2, I_2) is in a contrast to those of the quenched and 312 hours aged samples as seen in Figure 6(a). The decrease in τ_2 accompanying the increase in I_2 suggests smaller microvoids on the average and their higher number densities. This is mostly due to nucleation of smaller microvoids, which are formed from vacancies released from vacancy-impurity complexes and the Cu-rich precipitates. The newly formed small microvoids cause the number density to increase but the average radius of microvoids to decrease. The microvoids in all the Fe-0.3Cu alloys completely disappear after annealing at 400°C.

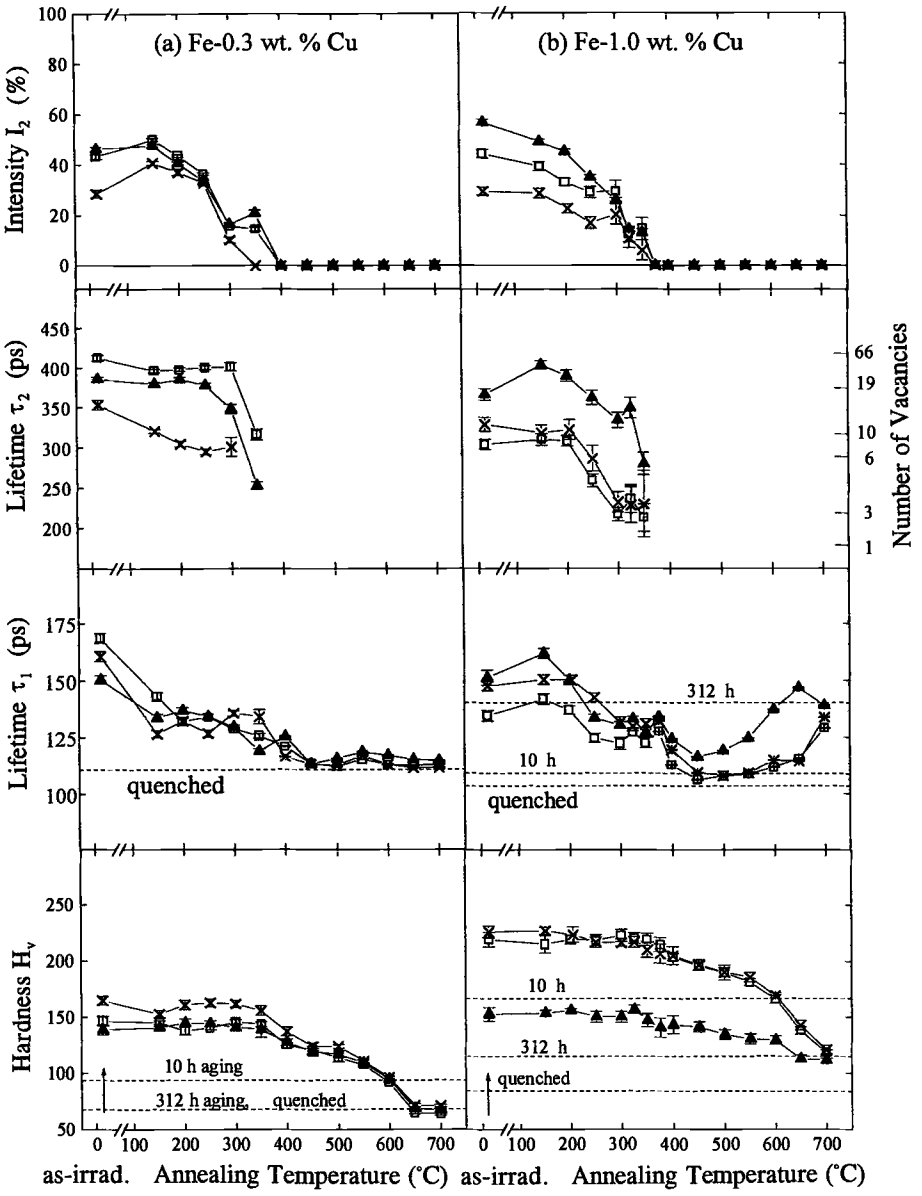


Figure 6 – *Isochronal annealing behaviour of lifetime parameters and Vickers microhardness of the irradiated model alloys: (a) Fe-0.3 wt. % Cu and (b) Fe-1.0wt.% Cu: quenched (□), and thermal aged at 550°C for 10 hours(×) and 312 hours(▲). The dashed lines show the positron lifetime τ_1 or Vickers microhardness for the unirradiated samples.*

The Vickers microhardness for all the Fe-0.3Cu alloys is nearly constant up to annealing at 300°C but shows a recovery stage around 400°C. This recovery stage corresponds to the complete recovery of the microvoids as seen in τ_2 and I_2 in Figure 6. However, this hardening is not due to the microvoids as seen from pure Fe in Figure 5, because the annealing behaviour of the hardness does not reflect the complex annealing behaviour of τ_2 and I_2,.

The residual hardening of Fe-0.3Cu gradually decreases by annealing at 500 - 600°C and completely recovers at 600°C. This residual hardening will be attributed to Cu-rich precipitates formed by irradiation and correlated to thermal age hardening at 550°C. Metastable Cu-precipitates and/or Cu-solute-atoms will be introduced by irradiation and will be transformed into stable Cu-precipitates after post-irradiation annealing around 650°C for 30 min; in the unirradiated samples the age hardening almost recovers after heating at 550°C for 312 hours.

Samples of the quenched and 10h-aged (at 550°C) Fe-1.0Cu show a long lifetime τ_2 of about 320 ps ($\sim V_{10}$), which is almost constant under annealing up to 200°C. But the decrease in I_2 suggests a decrease in the number density of the microvoids. This decrease in I_2 is accompanied by a decrease in τ_1, probably due to the dissociation of simple interstitial type defects and hence to a decrease in the number density of the microvoids as in Fe-0.3Cu. Further annealing below 350°C leads to a gradual decrease in τ_2 and I_2. The long lifetime components completely disappear at 375°C, which suggests full recovery of microvoids. The lifetime τ_1 of both the quenched and 10 hours aged sample starts to increase above 500°C. One possible explanation for this behaviour might be the creation of copper precipitates. A large number of copper atoms is supposed to be in solution in the Fe-matrix. However, with annealing at higher temperatures these copper atoms start to create copper clusters (precipitates).

In Fe-1.0Cu after 312 hour aging (at 550°C), τ_2 increases from about 370 ps ($\sim V_{15}$) to 420 ps ($\sim V_{66}$) by annealing at 150°C, accompanied by the decrease in I_2, suggesting the growth of the microvoids. Further annealing from 200°C to 400°C leads to a decrease in τ_2 and I_2 due to the decomposition of the microvoids. In Fe-1.0Cu of 312 hour aging the longer τ_2 with the higher I_2 in comparison with those for quenched and 10h-aging show the larger microvoids with the higher density. This shows that more irradiation-induced vacancies are agglomerated into the microvoids and then less are incorporated into the Cu-rich precipitates. In the sample aged for 312 hours, the Cu-rich precipitates are more stable and not efficient in vacancy incorporation. This stage shows a decrease in τ_1 to nearly the same as those for the unirradiated samples quenched and aged for 10 hours. Further annealing above 450°C causes τ_1 to increase to that of the unirradiated sample (~140 ps).

After irradiation, Fe-1.0Cu of 312 hour aging shows a much smaller hardness than those for the samples quenched and 10h-aged. The Vickers microhardness is almost constant up to annealing at 350°C. Then it is clearly seen that the hardness is not correlated with lifetime τ_2, I_2 and hence the size and density of microvoids. Further annealing leads to a decrease of hardness to those of the unirradiated sample, accompanied by the increase of lifetime τ_1 to those of the unirradiated state.

D) RPV Steel A533B

Positron annihilation experiments have already been performed to study microvoid formation in neutron-irradiated RPV steels [*3,21,22*]. RPV steels usually are aged for a long time before in-service irradiation. The present results are in good agreement with the previous ones as shown in Figure 7. The lifetimes τ_1 and τ_2 gradually increase with fluence (Figure 7(b)). The lifetime τ_2 of 300~400 ps gives clear evidence of the formation of microvoids (V_{10}~V_{20}) in RPV steels irradiated at about 150°C. The increase in I_2 from 10 to 25% with increase in fluence (Figure 7(a)) indicates that the microvoid density increases with the fluence. It should be noted, however, that no microvoid formation has been observed in RPV steel after irradiation at about 300°C (in-service temperature for RPV steels) [*3,21,22*].

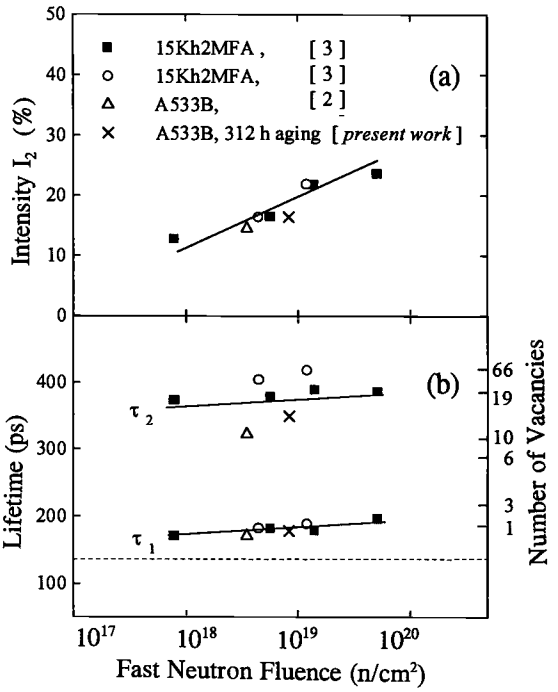


Figure 7 – *Positron lifetime parameters for neutron irradiated RPV steels (at about 150°C) as function of fast neutron fluence. The solid line is only to guide the eye. The dashed line shows τ_1 for the unirradiated A533B sample after 312 hour aging at 550°C.*

In Figure 8, the lifetime parameters for the as-irradiated state and after isochronal annealing are shown. The lifetime τ_2 for the as-irradiated sample increases from 270 ps (~V_5) for the quenched state to about 300 ps (~V_9) for 10 hour aging (at 550°C). Further aging leads to an increase in τ_2 to 350 ps (~V_{15}). These lifetimes, and hence the

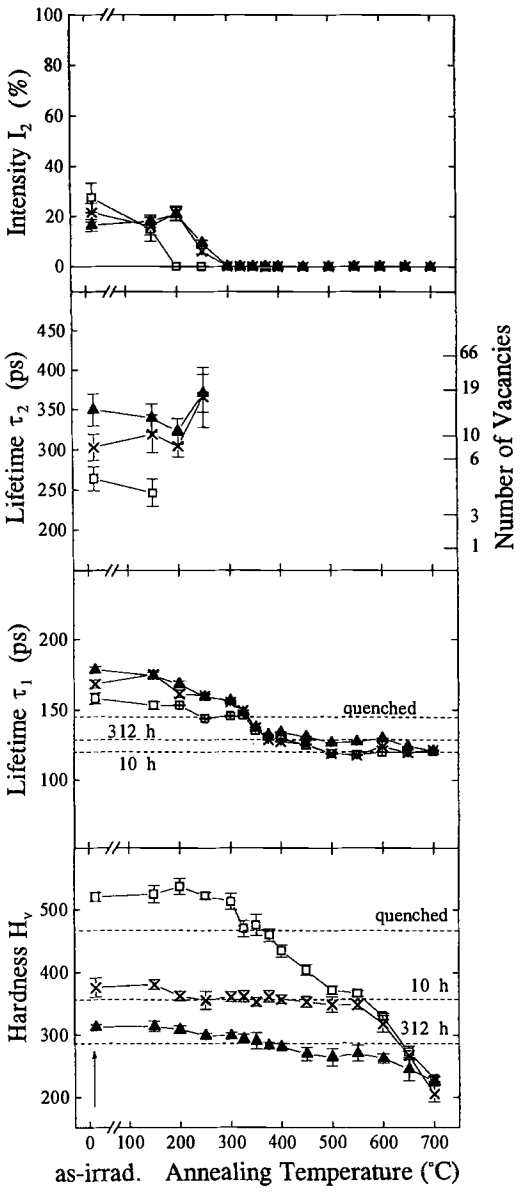


Figure 8 - *Isochronal annealing behaviour of lifetime parameters and Vickers microhardness of A533B RPV steel: quenched (□), and thermal aged at 550°C for 10 hours (×) and 312hours(▲). The dashed lines show the positron lifetime τ_1 or Vickers microhardness for the unirradiated samples.*

microvoids formed, are much smaller than for pure Fe and the Fe-Cu model alloys. The intensity I_2 smaller than 30% indicates that the density of microvoids is much smaller than the ones observed in pure Fe and Fe-Cu model alloys. After isochronal annealing at 250°C, τ_2 has increased to about 370 ps ($\sim V_{18}$) for the aged samples. This shows the formation of larger microvoids and therefore that a larger number of vacancies is incorporated into the microvoids. However, further annealing leads to a rapid decrease of τ_2, and to the full recovery at about 300°C. This behaviour is consistent with earlier findings in [*3*].

A short lifetime τ_1 between 160 and 180 ps shows the presence of simple defects other than microvoids. After annealing around 250°C, a slight decrease in τ_1 for all samples was observed, which will be correlated to the recovery of the τ_2 component and then to the recovery of the microvoids as seen in the Fe-Cu alloys. Around 350°C, τ_1 undergoes further rapid recovery. Especially, for the quenched sample, τ_1 decreases to a value shorter than that for the unirradiated state. These observations show that not only the irradiation-induced defects but also quench-induced defects anneal out around 350°C.

The Vickers microhardness before irradiation decreases with aging time as shown in Figure 8. The irradiation hardening for the quenched sample is larger than that for the aged samples (10 and 312 hour aging). After irradiation the hardness for the quenched sample is almost unchanged up to about 300°C, but recovers to that for the unirradiated state at 350°C. It should be noticed that the further annealing up to 500°C give rise to rapid decrease in the hardness, which corresponds to the thermal aging (softening). However, annealing above 600°C causes further decrease in the hardness. The hardness for the 10 hour aged sample shows the recovery reaching the unirradiated state around 250°C and then an almost constant value up to 550°C. However, it decreases rapidly with annealing at 600~700°C, as seen also for the quenched sample. The hardness for the 312 hour aged sample also shows the recovery reaching the unirradiated state around 300°C, but exhibits a gradual decrease with annealing temperature up to 700°C.

The recovery between 350°C and 500°C will be closely related to that seen in τ_1. However after annealing above 550 °C, such a close correlation between τ_1 and the hardness is not seen; the hardness shows the rapid decrease, but there is almost no change in τ_1 during the annealing above 550°C.

Summary

Pure Fe, Fe-Cu model alloys with 0.3 wt.% and 1.0 wt.% copper, and reactor pressure vessel steel A533B were prepared. All the samples were water-quenched from 825°C, followed by thermal aging at 550°C for 2, 10, 100 or 312 hours, before irradiation.

Positron lifetime and Vickers microhardness measurements were carried out after fast neutron irradiation below 150°C to a fluence of 8.3×10^{18} n/cm^2.

After irradiation, positron lifetime spectra for all the samples reveal the long lifetime (τ_2) components between 300 and 420 ps due to irradiation-induced microvoids. The observed τ_2 demonstrate that the microvoids consist of about 10 vacancies (V_{10}) for τ_2=300 ps and of about 66 vacancies (V_{66}) for τ_2=420 ps. The lifetime τ_2 and its intensity (I_2) are sensitive to copper content and thermal aging before irradiation. The Fe-Cu alloys with thermal aging between 2 and 100 hours show much shorter τ_2 and hence smaller microvoids than those in pure Fe, due to incorporation of irradiation-induced vacancies into Cu-rich precipitates formed during the thermal aging. The short lifetimes τ_1 from 130 to 170 ps after irradiation shows that other defects than microvoids are formed and trap positrons.

In pure Fe the microvoids grow between 200 and 300°C but anneal out rapidly around 450°C.

In the Fe-Cu alloys τ_2 and I_2 gradually decrease with annealing temperature up to 300°C and disappear rapidly around 350°C, which suggests the complete recovery of the microvoids around 350°C. In the Fe-1.0Cu alloys aged before irradiation, marked peak hardness is observed for aging for 10 hours. The irradiation-induced hardening in Fe-0.3Cu is found to be almost unchanged by aging, but that in Fe-1.0Cu decreases with aging time, which reflects complex interaction between the Cu-rich precipitates and the irradiation-induced defects.

The recovery in the hardening of the Fe-Cu alloys takes place in two stages: (1) ~ 350 °C, and (2) ~ 650°C. The recovery temperature for the hardness around 350°C agrees well with that for the microvoids. The second recovery in the hardness up to 650°C is due to thermal aging effects in the irradiated Fe-Cu alloys.

Positron lifetime measurements on A533B steel after irradiation have shown that the irradiation-induced microvoids consist of 5 (V_5) ~ 15 (V_{15}) vacancies, depending on the aging time. Post-irradiation annealing experiments reveal that these microvoids anneal out below 300°C. The prolonged short lifetime (τ_1) suggests that irradiation-induced defects other than microvoids are formed by irradiation.

The hardness of the quenched A533B steel exhibits further marked decrease after annealing up to 700°C, while those of the aged samples show the almost constant value up to 550°C followed by rapid decrease with annealing at 600 ~ 700°C. After annealing at 700°C all the A533B samples show nearly the same hardness which is smaller than those of the unirradiated states.

Acknowledgments

We would like to thank Mr. M. Narui and M. Yamazaki in the Oarai Branch, Institute for Material Research, Tohoku University, for their support hot laboratory work, and are indebted to Prof. H. Matsui for his support with the Vickers microhardness experiments.

References

[1] Odette, G.R., "On the Dominant Mechanism of Irradiation Embrittlement of Reactor Pressure Vessel Steels," *Scripta Metallurgica*, Vol. 17, 1983, pp. 1183-1188.

[2] Mader, E., Lucas, G.E., and Odette, G.R., "The Effect of Metallurgical and Irradiation Variables on the Postirradiation Annealing Kinetics of Pressure Vessel Steels," *Effects of Irradiation on Materials*: 15th International Symposium, *ASTM STP 1125*, R.E. Stoller, A.S. Kumar and D.S. Gelles, Eds., American Society for Testing and Materials, 1992, pp. 151-171.

[3] Brauer, G., Liszkay, L., Molnar, B., and Krause, R., "Microstructural Aspects of Neutron Embrittlement of Reactor Pressure Vessel Steels - A View from Positron Annihilation Spectroscopy," *Nuclear Engineering and Design*, Vol. 127, 1991, pp. 47-68.

[4] Hori, F., Aono, Y., Takenaka, M., and Kuramoto, E., "Positron Annihilation Study of Electron-Irradiated FeCu and FeCuC Alloys," *Scripta Metallurgica et Materialia*, Vol. 29, 1993, pp. 243-248.

[5] Shibamoto, H., Koyama, K., Yuya, H., Hasegawa, M., Kimura, A., Matsui, H. and Yamaguchi, S., "Effects of Proton Irradiation on Positron Annihilation and micro-Vickers Hardness of Fe-C-Cu Model Alloys," *Effects of Radiation on Materials*: 17th International Symposium, *ASTM STP 1270*, David S. Gelles, Randy K. Nanstad, Arvind S. Kumar, and Edward A. Little, Eds., American Society for Testing and Materials, 1996, pp. 623-636.

[6] Brauer, G., and Popp, K., "Neutron Embrittlement of Reactor Pressure Vessel Steels: A Challenge to Positron Annihilation and Other Methods," *Physica Status Solidi (a)*, Vol. 102, 1987, pp. 79-89.

[7] Brauer, G., "Positron Annihilation Studies of VVER Type Reactor Steels," Colloque C1, Supplément au Journal de Physique III, Vol. 5, 1995, pp.143-150.

[8] Stoller, R.E., Odette, G.R., and Wirth, B.D., "Primary Damage Formation in bcc Iron," *Journal of Nuclear Materials*, Vol. 251, 1997, pp. 49-60.

[9] Wirth, B.D., Odette, G.R., Maroudas, D., and Lucas, G.E., "Energetics of Formation and Migration of Self-Interstitials and Self-Interstitial Clusters in α-Iron," *Journal of Nuclear Materials*, Vol. 244, 1997, pp. 185-194.

[10] Phythian, W.J., Foreman, A.J.E., English, C.A., Buswell, J.T., Hetherington, M., Roberts, K., and Pizzini, S., "The Structure and Hardening Mechanism of Copper Precipitation in Thermally Aged or Irradiated Fe-Cu and Fe-Cu-Ni Model Alloys", *Effects of Radiation on Materials*: 15th International Symposium, *ASTM STP 1125*, R.E. Stoller, A.S. Kumar, and D.S. Gelles, Eds., American Society for Testing and Materials, 1992, pp. 131-150.

[11] Korhonen, T., Puska, M.J., and Niemenen, R.M., "First-Principles Calculation of Positron Annihilation Characteristics at Metal Vacancies," *Physical Review B*, Vol. 54, No. 21, 1996, pp. 15016-15024.

[12] Eldrup, M., and Singh, B.N., " Studies of Defects and Defect Agglomerates by Positron Annihilation Spectroscopy," *Journal of Nuclear Materials*, Vol. 251, 1997, pp. 132-138.

[13] Hautojärvi, P., and Corbel, C., "Positron Spectroscopy of Defects in Metals and Semiconductors," Proceedings of the International School of Physics "Enrico Fermi 1993," Course CXXV, Positron Spectroscopy of Solids, A.Dupasquier and A.P. Mills Jr., Eds., IOS Press, OHM Ohmsha, Amsterdam, Oxford, Tokyo, Washington DC, 1995, pp. 491-532.

[14] Puska, M.J., and Nieminen, R.M., "Defect Spectroscopy with Positrons: A General Calculation," *Journal of Physics F: Metal Physics*, Vol. 13, 1983, pp. 333-346.

[15] Plazaola, F., Seitsonen, A.P., and Puska, M.J., "Positron Annihilation in II-V Compound Semiconductors: Theory," *Journal of Physics: Condensed Matter*, Vol. 6, 1994, pp. 8809-8827.

[16] Kirkegaad, P., Pedersen, N.J., and Eldrup, M., "PATFIT-88: A Data-Processing System for PAS on Mainframe and Personal Computers," RisøM-2740, Risø, 1989, pp. 1-132.

[17] Boronski, E., and Nieminen, R.M., "Electron-Positron Density Functional Theory", *Physical Review B*, Vol. 34, No. 6, 1986, pp. 3820-3831.

[18] Salje, G., and Feller-Kniepmeier, M., "The diffusion and solubility of copper in iron," *Journal of Applied Physics*, Vol. 48, No. 5, 1977, pp. 1833-1839.

[20] Othen, P.J., Jenkins, M.L., and Smith, G.D.W., "High-Resolution Electron Microscopy Studies of the Structure of Cu Precipitates in α-Fe", *Philosophical Magazine A*, Vol. 70, No. 1, 1994, pp. 1-24.

[20] Charleux, M., Livet, F., Bley, F, Louchet, F., and Bréchet, Y., "Thermal Aging of an Fe-Cu Alloy: Mircostructural Evolution and Precipitation Hardening", *Philosophical Magazine A*, Vol. 73, No. 4, 1996, pp. 883-897.

[21] Lopes Gil, C., De Lima, A.P, Ayres De Campos, N., Fernandes, J.V., Kögel, G., Sperr, P., Triftshäuser, W., and Pachur, D., "Neutron-Irradiated Reactor Pressure Vessel Steels Investigated by Positron Annihilation," *Journal of Nuclear Materials*, Vol. 161, 1989, pp. 1-12.

[22] Ghazi-Wakili, K., Zimmermann, U., Brunner, J., Tipping, P, Waeber, W.B., and Heinrich, F., "Positron Annihilation Studies on Neutron Irradiated Pressure Vessel Steels," *Physica Status Solidi (a)*, Vol. 102, 1987, pp. 153-163.

Marc G. Horsten,[1] Emile V. van Osch,[1] David S. Gelles,[2] and Margaret L. Hamilton[2]

Irradiation Behavior of Ferritic-Martensitic 9-12%Cr Steels

Reference: Horsten, M. G., van Osch, E. V., Gelles, D. S., and Hamilton, M. L., **"Irradiation Behavior of Ferritic-Martensitic 9-12%Cr Steels,"** *Effects of Radiation on Materials: 19th International Symposium, ASTM STP 1366,* M. L. Hamilton, A. S. Kumar, S. T. Rosinski, and M. L. Grossbeck, Eds., American Society for Testing and Materials, West Conshohocken, PA, 2000.

Abstract: A dedicated series of irradiation experiments has been executed in the high flux reactor (HFR) in Petten (Netherlands) to evaluate the irradiation behavior of ferritic-martensitic 9-12%Cr steels at temperatures in the range of 70°C to 370°C and damage dose levels up to 3 dpa. Materials investigated in the program comprise Mod.9%Cr (9Cr-1Mo-0.2V-0.08Nb), HT9 (12Cr-1Mo-0.5W-0.5Ni-0.3V), MANET type steel (10Cr-0.5Mo-0.6Ni-0.2V-0.15Nb), NF616 (9Cr-2W-0.5Mo-0.2V-0.07Nb) and HCM12A (12Cr-2W-1Cu-0.4Mo-0.3Ni-0.2V-0.05Nb). The 9-12%Cr steels show severe hardening and ductility reduction at room temperature (RT) after neutron irradiation. Strength, ductility and toughness of material irradiated at 70°C gradually recover with increase in test temperature. Similar ductility trends of material irradiated at 300°C are observed as for unirradiated material, but recovery with increase in temperature is not observed below temperatures of 400°C. The 9%Cr steels show less hardening and reduction in ductility than the 10-12%Cr steels. The reduction of area and 0.2% yield stress correlate well with the upper-shelf energy and ductile-to-brittle transition temperature, respectively, both for the unirradiated and irradiated condition. In general, the 9%Cr steels show more resistance to irradiation at 300°C than the 10-12%Cr steels with respect to fracture toughness.

Keywords: neutron irradiation, ferritic-martensitic 9-12%Cr steels, tensile properties, fracture toughness, Charpy impact behavior, embrittlement, hardening, ductility

Introduction

The ferritic-martensitic 9-12%Cr steels have good potential for nuclear applications, both in fission reactors [1-3] and future fusion machines [4]. The martensitic 9-12%Cr steels have good resistance against swelling and He embrittlement [1, 5, 6]. The heat treatability of the material makes it possible to optimize the material for toughness and high temperature properties. One of the main problems in the application of this class of material in nuclear applications is the embrittlement of the material under neutron irradiation at low temperatures [7]. A dedicated series of irradiation experiments has therefore been performed

[1]Materials scientists, NRG (former ECN), PO Box 25, 1755 LE Petten, Netherlands.
[2]Staff scientists, PNNL Materials Research Department , Richland, WA 99352, USA.

Copyright© 2000 by ASTM International www.astm.org

in the HFR Petten, The Netherlands, containing a variety of 9-12%Cr steel heats. The materials are conventional 9-12%Cr steels containing chromium, molybdenum, vanadium, tungsten and niobium. The target irradiation temperatures are 70°C and 300°C, and target damage dose levels are in the range of 1.5 dpa to 2.5 dpa. The aim of the experiments is to evaluate the irradiation behavior of these materials in terms of irradiation hardening and embrittlement at temperatures up to 400°C.

Materials and Specimens

Materials

Five different ferritic-martensitic 9-12%Cr steels have been irradiated in the HFR Petten. The chemical composition of the materials is shown in Table 1. The final heat treatment, Vickers hardness and (prior austenite) grain size are shown in Table 2. The steels are all air cooled (AC), except for the Mod.9%Cr-1 heat which was water quenched (WQ) after austenitizing. The materials are plate steels except HT9, which was delivered as forged rods with a diameter of 50 mm.

Table 1 - *Chemical composition of materials*

Element (wt-%)	MANET-II	HT9	HCM12A	Mod.9%Cr heat 1	Mod.9%Cr heat 2	NF616
C	0.10	0.20	0.10	0.105	0.09	0.101
Si	0.14	0.28	0.09	0.43	0.31	0.036
Mn	0.75	0.51	0.59	0.38	0.46	0.47
P	0.005	0.002	0.015	0.009	0.011	0.011
S	0.005	0.005	0.001	0.003	0.002	0.001
Cr	10.30	11.86	10.82	8.26	8.68	8.96
Ni	0.65	0.54	0.32	0.13	0.12	0.005
Mo	0.57	1.02	0.39	0.95	0.92	0.48
V	0.19	0.30	0.20	0.20	0.21	0.20
W	-	0.54	1.99	0.02	-	1.94
Nb	0.14	0.01	0.05	0.075	0.09	0.065
B	0.0075	-	0.0018	0.0050	-	0.0037
Cu	0.01	0.01	1.0	0.08	0.05	-
N	0.031	0.001	0.061	0.055	0.049	0.045
Ti	-	0.01	-	0.003	0.004	-
Fe	bal.	bal.	bal.	bal.	bal.	bal.

MANET-II was developed for fusion applications and is a modified version of the DIN 1.4914 material. HT9 is a 12%Cr steel developed initially for fast breeder reactor wrapper applications. The HCM12A and NF616 steels are Japanese high temperature steels originally developed as turbine blade material with excellent (high temperature) creep properties. The Mod.9%Cr steels are stabilized 9Cr1Mo steels developed for

instance for heat exchangers, but is considered one of the reference ferritic-martensitic steels for future fusion machines.

Table 2 - *The final heat treatment, hardness and grain size of the FM steels*

	Austenitizing treatment			Temper treatment			Hardness	Grain size
	T (°C)	Time (h)	Quench	T (°C)	Time (h)	Quench	HV5	(μm)
MANET-II[1]	1075	½	AC	750	2	AC	-	-
HT9[2]	1050	1	AC	770	7	AC	249	10
HCM12A	1050	1	AC	770	7	AC	235	-
Mod.9%Cr-1	1070	2½	WQ	765	4¾	AC	214	20
Mod.9%Cr-2	1055	?	AC	760	2	AC	259	8
NF616	1070	1	AC	780	1	AC	300	40

[1] MANET-II has received pre austenitizing treatment: 950°C/½h/AC.
[2] HT9 was delivered as forged rods with a diameter of 50 mm and contains 5% δ-ferrite.

The structure of the HCM12A, MANET-II, NF616 and Mod.9%Cr steels is fully tempered martensitic. The composition is within the Schaeffler diagram α'-martensite. HT9 is aimed to have a duplex structure with retained austenite in a α'-martensitic matrix, resulting in a small amount of 5% δ-ferrite in the final product. The temper treatment of all materials is aimed to obtain good toughness properties while sacrificing the high temperature properties, making the steels suitable for application at lower temperatures.

Specimens

The tensile test specimen, the miniaturized Charpy impact specimen (KLST) and the compact tension (CT) specimens used for the experiments are shown in Figs, 1a-d respectively. The tensile test specimens are taken in the L orientation and the CT and KLST specimens are taken in the L-T orientation. The L orientation is the rolling direction for the plate materials and the principal deformation (forging) direction for the HT9 rods.

Irradiation Experiments

A series of irradiation experiments has been performed in the core of the HFR. The experiments have been performed at target temperatures of 70°C and 300°C. Nominal target damage dose levels range from 1.5 to 2.5 dpa. The irradiation experiments are summarized in Table 3. In the 70°C experiments the specimens are in direct contact with the reactor coolant water. The 300°C experiments are controlled by a gas mixture technique along with vertical displacement of the capsule.

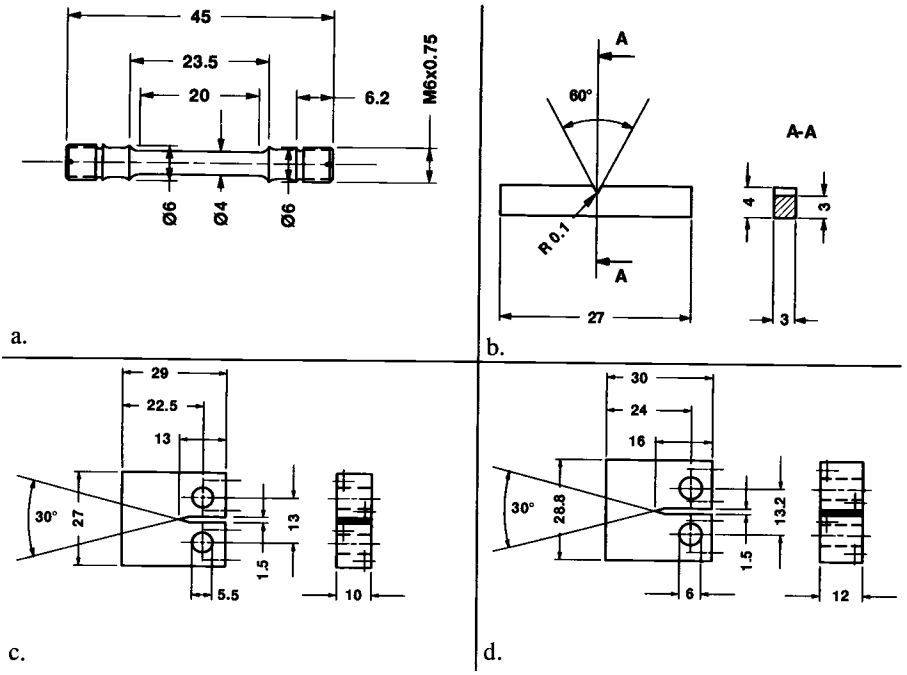


Figure 1 - *Test specimens (a) tensile, (b) KLST, (c) CT-10 mm and (d) CT-12 mm*

The actual temperatures are indicated as ranges and are average values for the different locations within the experiment and are determined either from direct

Table 3 - *Overview of irradiation experiments*

Experiment Name	T_{irr} (°C) Target	Range	Dose (dpa) Target	Range	Materials included	Specimens included
CATETO-I	300	285-309	1.5	0.9-2.0	MANET-II	CT-10mm
CATETO-II	300	279-311	2.5	1.5-3.3	MANET-II, HT9, Mod.9%Cr-1/2	CT-10mm
CHARIOT-3	300	344-368	2.5	2.2-3.1	HCM12A, NF616, Mod.9%Cr-1	CT-10mm, KLST
ILAS-2	300	265-312	2.5	2.0-2.3	HT9, Mod.9%Cr	Tensile
ILAS-5	300	322-352	2.5	2.7-3.1	HCM12A, NF616	Tensile
MANIA	300	277-320	2.5	1.4-2.7	MANET-II, Mod.9%Cr-1	Tensile
SIWAS-5	70	60-80	1.5	1.0-2.3	MANET-II, HT9, Mod.9%Cr-1	CT-12mm, Tensile
SIWAS-6	70	60-80	2	1.3-2.7	HCM12A, NF616	Tensile

measurements on the samples or from calculated values from drum temperature measurements. The actual temperatures range between 265°C up to 368°C for the 300°C irradiation experiments and are around 70°C for the HFR coolant water temperature irradiation experiments.

Mechanical Testing

Mechanical testing is performed in the hot cell laboratory of NRG in Petten. The reference tests on unirradiated material have been performed on the same machine as the irradiated specimens.

Tensile Testing

The tensile specimens have been tested on an electro-mechanical test machine. Elevated temperature tests are performed using a split, two zone resistance furnace mounted around the specimen. Heating of the specimen takes between 1 and 1½ hours depending on the test temperature. The temperature stablilisation period before start of the test is ½ hour. The specimens are tested at a conventional strain rate of $5x10^{-4}$ s^{-1}, which is calculated from a constant machine pull rod displacement rate. The force is registered by a load cell. The engineering stress-strain curve and engineering stress-strain data 0.2%-yield stress (0.2%YS), ultimate tensile strength (UTS), uniform elongation (UE) and total elongation (TE) are derived from the load and machine displacement signals. The reduction of area (RA) and fracture elongation (FE) of the specimens are measured on the broken specimen halves.

Charpy Impact Testing

The KLST specimens have been tested on a pendulum-type Charpy impact machine with a potential energy of 50 J and an impact speed is 3.5 m/s. The machine is installed in a dedicated hot cell and has a fully automatic specimen transportation. The temperature conditioning system allows specimens to be tested in the range of -150°C up to +450°C. The experiments are evaluated in terms of fracture energy (E) in Joule and lateral expansion (LE) in mm. The Charpy impact transition curves are analyzed in terms of ductile to brittle transition temperature (DBTT) and upper shelf energy (USE).

Fracture Toughness Testing

The CT specimens have been tested on a servo-hydraulic test machine. The fracture resistance experiments are based on the ESIS P2-91 [8] procedure with some modifications to meet the special requirements for testing irradiated material. The crack extension during testing is measured by the direct current potential drop (DCPD) technique. The specimens are instrumented with direct current and potential drop wires (4 wires attached to each specimen) and load line displacement measurement bridges. The DCPD wires are carefully isolated from the machine. The specimens are fatigue pre-cracked in the machine at room temperature at a frequency of about 10 Hz using an

R ratio of 0.1. The fatigue pre-cracking is performed in several stages with decreasing ΔK range to optimize the fatigue pre-cracking process. A small stress intensity factor range is used at the final stage of pre-cracking, before the actual fracture resistance test is performed. Elevated temperature tests are performed using a split, two zone resistance furnace which is mounted around the specimen. The force is recorded by a load cell. The specimens are tested at a loading rate where the initial increase in stress intensity is between 0.8 to 1.0 MPa$\sqrt{m}$/s. During the test the load and DCPD signal are recorded as a function of the load line displacement. After testing the fatigue pre-crack length and amount of stable crack extension are measured from the fracture surface of the specimen. These measurements are used to correlate the measured DCPD signal to the actual crack extension. The amount of stable crack extension Δa is determined from the DCPD vs. specimen opening curve. This curve is used to estimate the transition from blunting to stable crack extension. The fracture resistance J is calculated from the load-displacement diagram. The experiments result in fracture resistance J-Δa curves. The various engineering fracture toughness parameters can be determined from this curve.

Results and Discussion

Tensile Properties

The tensile properties after irradiation at low temperature (SIWAS-5: 1.5 dpa at 70°C) and at elevated temperature (ILAS-2: 2.5 dpa at 300°C) are shown in Figs 2 and 3 for HT9 and Mod.9%Cr-1 material, respectively. The 0.2%YS and TE are plotted as a function of test temperature. The unirradiated 0.2%YS data (Figs 2a and 3a) show a moderate decrease with increasing test temperature up to about 400°C; above this temperature the rate of decrease increases.

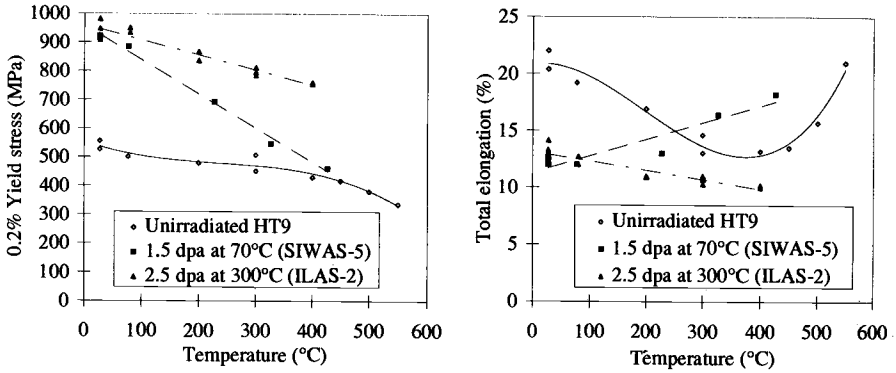


Figure 2 - *Tensile properties of irradiated HT9 material, (a) 0.2% yield stress, (b) total elongation*

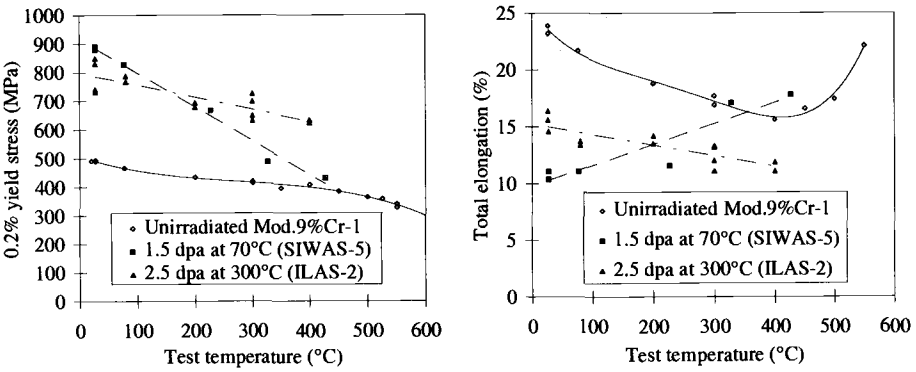


Figure 3 - *Tensile properties of irradiated Mod.9%Cr steel, (a) 0.2%yield stress, (b) total elongation*

The ductility (TE) of unirradiated material (Figs 2b and 3b) decreases up to about 400°C, similar to what is observed for the 0.2%YS. Above this temperature, the recovery of the material results in an increase in ductility. Irradiation at 70°C and 300°C results in an irradiation hardening at RT of about 400 MPa for HT9 and between 225 and 375 MPa for Mod.9%Cr-1 material. The room temperature ductility (TE) decreases by a factor of nearly 0.5 for HT9 and by a factor of about 0.7 for the Mod.9%Cr-1 material, but tensile elongations are still over 10%. Increase in test temperature results in a decrease in 0.2%YS for both materials. However, the level of irradiation hardening of material irradiated at 300°C remains constant over the temperature range up to 400°C. The corresponding ductility decreases gradually with increase in test temperature. At a test temperature of 400°C, the irradiated HT9 and Mod.9%Cr steel still show lower ductility levels than observed for the unirradiated materials. The materials irradiated at 70°C, on the other hand, show a rapid decrease in irradiation hardening with increase in test temperature. The damage structure has recovered fully at a test temperature of 425°C, where the stress levels of irradiated material are similar to that of the unirradiated material. The ductility of the material irradiated at this low temperature increases strongly with test temperature, reflecting the recovery of the damage structure. Surprisingly, the ductility of the irradiated material tested at 300 and 400°C are at or even above the levels observed for unirradiated material. The exact temperatures at which recovery of the damage structure commences can not be given; therefore, only straight/dotted lines are shown to guide the eye.

The radiation response of the various material heats is shown in Fig. 4, where the irradiation hardening (increase in 0.2%YS) and loss of ductility (decrease in TE) is shown as a function of material and irradiation condition.

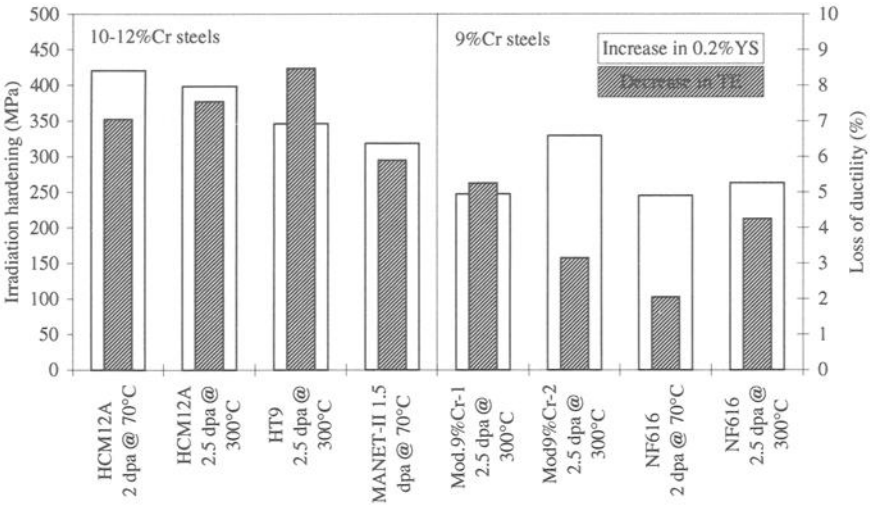


Figure 4 - *Irradiation hardening and loss of ductility of different 9-12%Cr steels*

The test temperature is taken at the irradiation temperature. The irradiation hardening and loss of ductility of the 10-12%Cr steels seem somewhat higher than for the 9%Cr steels. The hardening level of the Mod.9%Cr-2 steel however reaches those of the 10-12%Cr steels. The results and the conclusions on the differences between the 9%Cr and 10-12%Cr steels might be obscured by the fact that the irradiation temperature is not exactly the same for each sample in a capsule. Actual irradiation temperatures in ILAS-2 are in the range of 265 to 312°C, see Table 3. However, the radiation response of Mod.9%Cr-1 material is clearly different from that of the HT9 material. This is also demonstrated in Figs, 2a and 3a. The Mod.9%Cr steel samples irradiated in the center of the capsule show hardening levels of 80-100 MPa lower than samples irradiated at the top/bottom location of the capsule, see Fig. 3a. This is observed for test temperatures of RT and 300°C. The HT9 samples irradiated in the center of the capsule, however, behave identical to the ones irradiated at the top/bottom location of the capsule. This difference in irradiation behavior might even be more pronounced in the ILAS-5 capsule (NF616 and HCM12A material), where irradiation temperatures in the range of 320 to 370°C are reported. Moreover, the high-temperature NF616 material has, even after the temper treatment of 1 hour at 780°C, a 0.2% yield stress of about 750 MPa, which is considerably higher than the 570 MPa of, for instance, of the HCM12A material. The ability of the material to accommodate extra irradiation hardening on top of this high yield stress is limited, resulting in a low level of irradiation hardening, while the absolute yield stress of NF616 material is quite similar to that of HCM12A.

Charpy Impact Behavior

The Charpy impact behavior of three different materials (NF616, Mod.9%Cr-1 and HCM12A) after irradiation to 2.5 dpa at 300°C (CHARIOT-3: 300°C) is shown in Fig. 5.

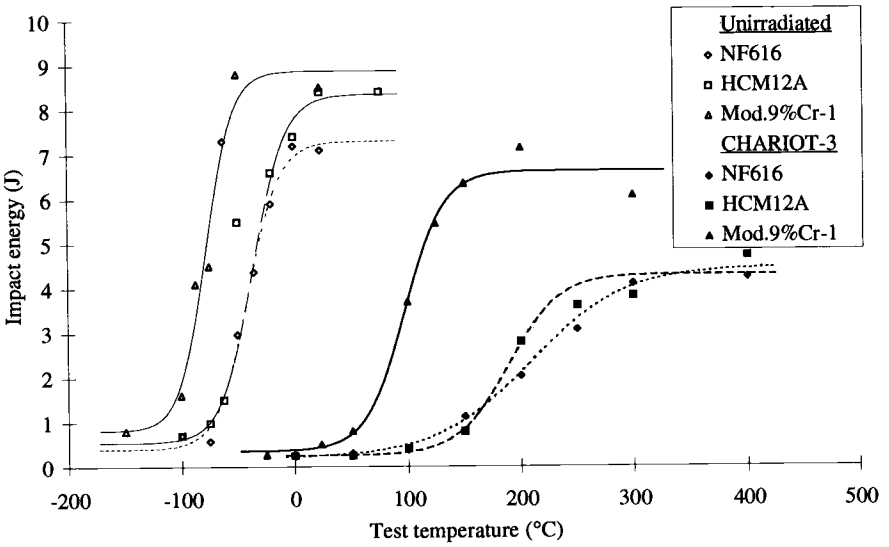


Figure 5 - *Transition curves of different FM steels measured by miniaturized KLST Charpy impact specimens*

The actual irradiation temperature of the miniaturized KLST Charpy-type specimens is estimated to range between 345 and 370°C. The two high-temperature steels NF616 and HCM12A behave quite similar in the unirradiated condition, despite the fact that the 0.2%YS differ considerably for the two materials. Only the USE of the NF616 material is somewhat lower than that of the HCM12A material. The Mod.9%Cr steel has a DBTT that is 30-40°C below those of NF616 and HCM12A. Irradiation even at the relatively high temperatures (around 350°C) results in a remarkable shift in DBTT and decrease in USE of all materials. The DBTT of Mod.9%Cr steel shifts by about 175°C and the USE decreases by 2.2 J. The two high-temperature steels behave again quite similar after irradiation, the DBTT shifts by 225-250°C and the USE decreases by 2.8-4.0 J. Similar DBTT shifts and USE reductions have been reported by [9] after HFIR irradiations of 9%Cr and 12%Cr steels up to 34 to 42 dpa at temperatures in the range of 300-400°C. The behavior of NF616 can be explained by the initial state of the material. The 0.2%YS of the material at RT is about 180 MPa higher than that of HCM12A and about 260 MPa higher than for instance Mod.9%Cr-1. In unirradiated condition this material has a similar transition behavior as HCM12A,

but the USE seems to be somewhat lower. This might reflect the harder state of the NF616 material in unirradiated condition. Irradiating the material to 2.5 dpa at about 350°C has severely embrittled the material, ultimately resulting in the large shift in DBTT and additional reduction in USE as observed for this 9%Cr steel.

There is a positive correlation between the reduction of area and the upper shelf energy (Fig. 6a) and the 0.2% yield stress and the DBTT (Fig. 6b). Compared to the low activation varieties of 9%Cr steels such as F82H material and BS reported in [10, 11], the shifts in DBTT and especially the decrease in USE are considerable.

Table 4 - Summary of miniature Charpy impact results

Material	Unirradiated		CHARIOT-3: 2.5 dpa @ 300°C		Irradiation effect	
	DBTT (°C)	USE (J)	DBTT (°C)	USE (J)	ΔDBTT (°C)	ΔUSE (J)
Mod.9%Cr-1	-78	8.9	97	6.6	175	2.2
NF616	-41	7.3	209	4.5	249	2.8
HCM12A	-36	8.3	189	4.3	225	4.0

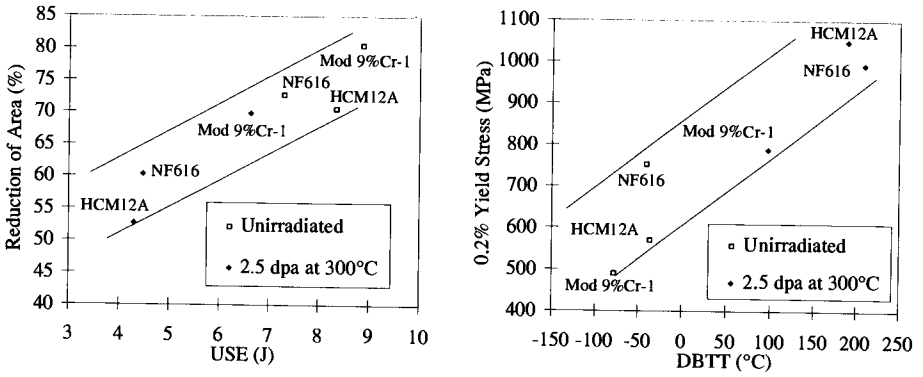


Figure 6 - *Relationship between (a) RA and USE and (b) 0.2%YS and DBTT for three FM steels*

Fracture Toughness Behavior

The static fracture toughness behavior of HT9, MANET-II and Mod.9%Cr steel is shown in Figs 7, 8 and 9 respectively. The fracture toughness K_Q of unirradiated and irradiated material is shown as a function of test temperature. K_Q for the lower bound and transition region is the ASTM linear-elastic qualifier for K_{Ic} evaluation. The type of specimen and the procedure followed for testing the irradiated specimens prevent the determination of a valid K_{Ic} value for these materials. The K_Q for the upper shelf is

determined from the $J_{0.2bl}$ values by application of the equation: $K = \sqrt{J \frac{E}{1-\nu^2}}$, where E is the Young's modulus and ν the Poisson's ratio. The curves and the data must therefore be considered as qualitative information with the main objective to describe the transitional behavior of the (irradiated) material and to evaluate any effect of irradiation on this behavior.

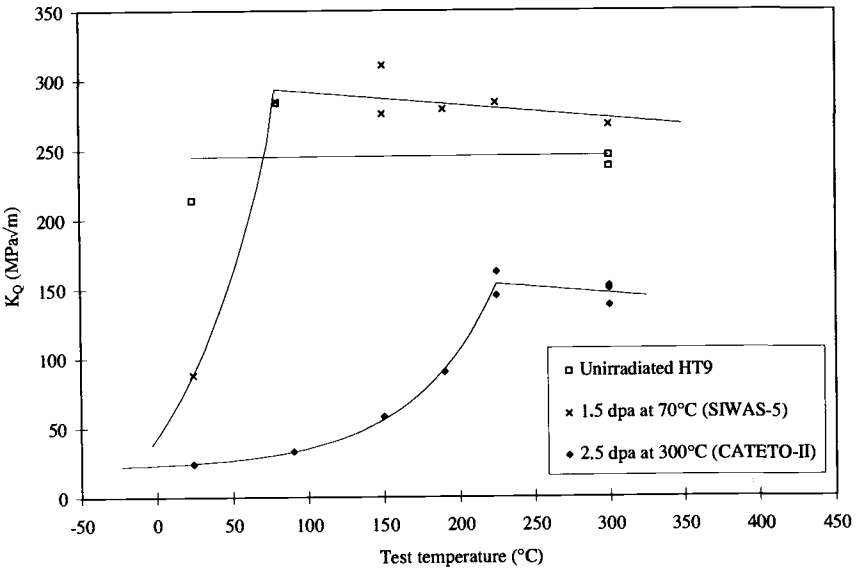


Figure 7 - *Fracture toughness transition curves of HT9*

All unirradiated materials show upper shelf ductile tearing behavior for the test temperature range of RT up to 300°C. The ductile to brittle transition is below RT. A shift in ductile to brittle transition temperature has not been determined in this study. The fracture toughness results of HT9 material are shown in Fig. 7. It must be mentioned that the upper shelf ductile tearing behavior of the HT9 material (Fig. 7) is not adequately described by the 4 experiments that have been performed. Irradiation to 1.5 dpa at 70°C results in brittle fracture and hence low K_Q toughness values at RT. At temperatures of 80°C and higher, the material shows ductile tearing behavior. The upper shelf toughness values are considered to be identical to the unirradiated ones. Irradiation to 2.5 dpa at 300°C results in linear-elastic and transitional behavior up to about 200°C. Upper shelf behavior is observed at temperatures above 200°C, but at a considerably lower level than the unirradiated (and 70°C irradiated) material. Irradiation of MANET-II material at 70°C and 300°C shifts the transition temperature to values above RT, see Fig. 8. The material irradiated at 70°C starts to behave in a ductile tearing mode above temperatures of 150°C. When the temperature is increased, the recovery of the damage structure results in a gradual increase in toughness. The

toughness values reach the unirradiated ones at a test temperature of 300°C. The material irradiated at 300°C shows a slightly larger shift. (Data points have been removed for clarity.) A recovery of the unirradiated behavior is not observed contrary to the 70°C irradiated material. The upper shelf toughness is reached at temperatures above 200°C. The values are even below 100 MPa$\sqrt{m}$ and decrease with increase in temperature. The two Mod.9%Cr steel heats behave identically in the unirradiated and irradiated condition.

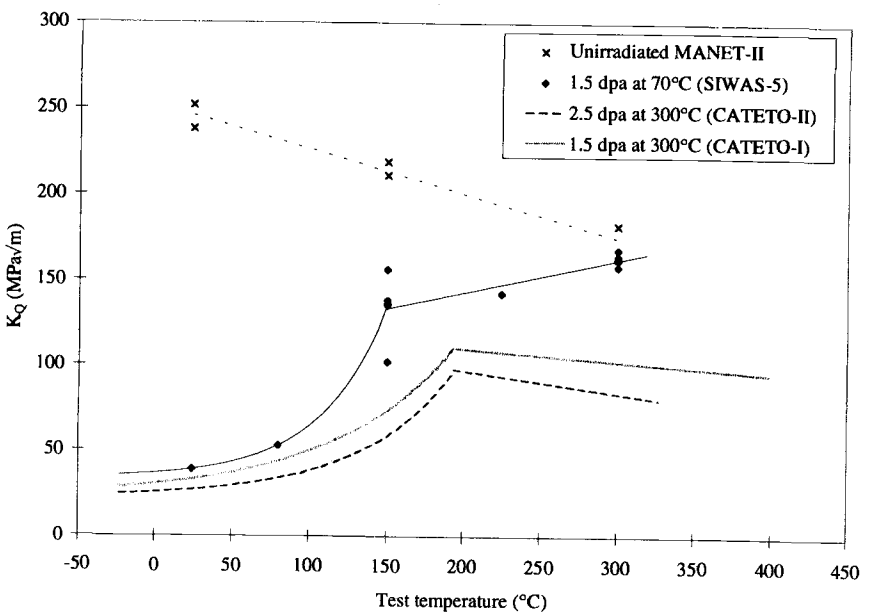


Figure 8 - *Fracture toughness transition curves of MANET-II*

The shift in transition temperature is identical for material irradiated at 70°C and 300°C (Fig. 9). The toughness of the material irradiated at 300°C decreases gradually with test temperature after the upper shelf has been reached at about 80°C. The material irradiated at 70°C has a plateau toughness of about 240 MPa$\sqrt{m}$ between 80°C and 200°C. The damage structure starts to recover at temperatures above 200°C. The toughness of unirradiated material has almost been reached at a test temperature of 300°C. The behavior of irradiated 9%Cr steels and 10-12%Cr steels is compared in Fig. 10. The 9%Cr steels Mod.9%Cr have much higher toughness values after irradiation to 2.5 dpa at 300°C than those of 10-12%Cr steels. The transition temperature of Mod.9%Cr steel is about 50°C (at 100 MPa$\sqrt{m}$), whereas the 10-12%Cr steels have transition temperatures of about 200°C. The upper shelf toughness is 200-250 MPa$\sqrt{m}$ higher than those of the 10-12%Cr steels. Some preliminary data on NF616 and HCM12A are shown in this figure as well. These materials show brittle fracture at RT after irradiation at both 70°C and 300°C.

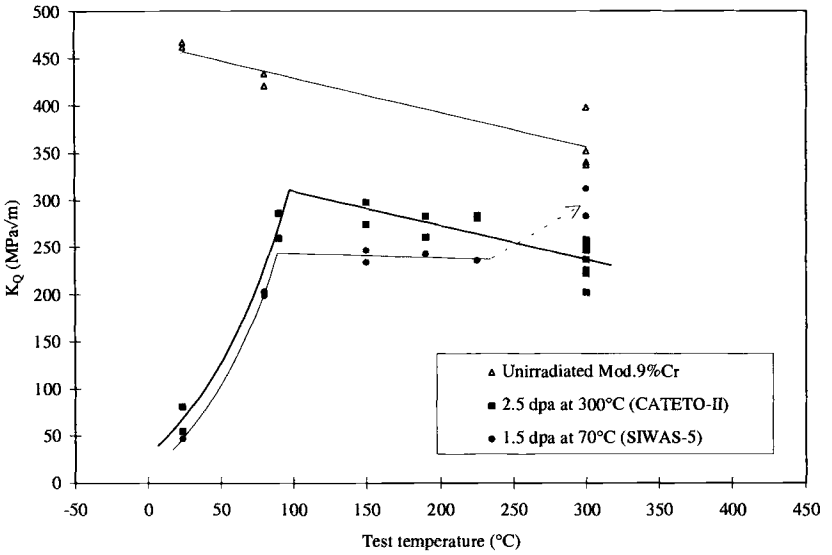


Figure 9 - *Fracture toughness transition curves of Mod.9%Cr steel*

Irradiated NF616 has toughness values that are much lower than observed for the Mod.9%Cr steels. This is again similar to what was observed in the Charpy impact experiments. The NF616 material shows brittle fracture at RT in unirradiated condition. This reflects the hard initial condition of the unirradiated NF616 material. The HCM12A material has properties that are similar to HT9 after irradiation and tested at 350°C.

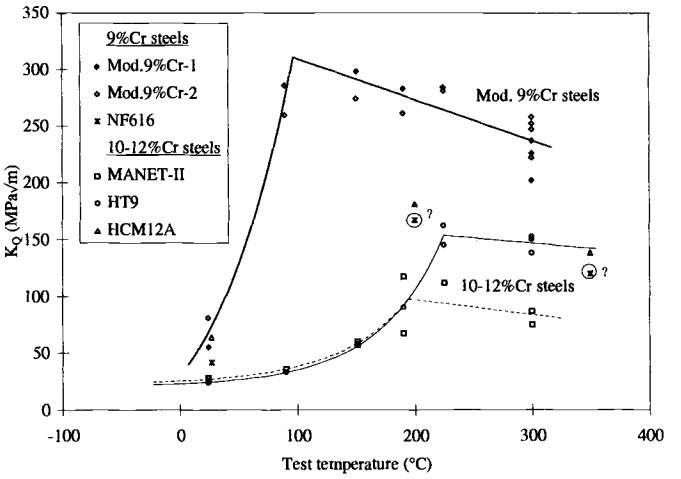


Figure 10 - *Static fracture toughness curves of FM steels irradiated to 2.5 dpa at 300°C*

Conclusions

The results on the six different ferritic-martensitic steels show that:

1. The 9%Cr and 10-12%Cr steels show severe hardening and ductility reduction at RT after neutron irradiation at a temperature of 70°C, but strength, ductility and toughness gradually recover with increase in test temperature.
2. The 9%Cr and 10-12%Cr steels show severe hardening and embrittlement at RT after irradiation at 300°C. Similar temperature trends are observed as for unirradiated material, but recovery with increase in temperature is not observed below 400°C.
3. The 9%Cr steels show less hardening and loss in ductility than the 10-12%Cr steels. The radiation damage of the 10-12%Cr steels seems to anneal out at higher temperatures than the 9%Cr steels.
4. The reduction of area and 0.2% yield stress correlate well with the upper-shelf energy and ductile-to-brittle transition temperature, respectively, both for the unirradiated and irradiated condition.
5. The fracture toughness of 9%Cr steels is more resistant to irradiation at 300°C than the fracture toughness of 10-12%Cr steels. The 9%Cr steel NF616 is the exception: unirradiated NF616 shows brittle fracture at RT.

Acknowledgment

We wish to thank Mr. Ohgami of Nippon Steel Corporation for supplying NF616 material and Mr. Ohgami of Sumitomo Metal Industries for supplying HCM12A material. We wish to thank Dr. D.R. Harries for consultancy.

References

[1] D. Gilbon et al, "Behavior and Microstructure of Ferritic Steels Irradiated in Phénix Reactor," *Effects of Radiation on Materials: 14th International Symposium, ASTM STP 1046,* 1989, pp. 5-34.

[2] A. Alamo et al, "Irradiation Effects on Base Metal and Welds of 9Cr-1Mo (EM10) Martensitic Steel," *Effects of Radiation on Materials: 17th International Symposium, ASTM STP 1270,* 1996, pp. 761-774.

[3] Y. Dai, "Martensitic/Ferritic Steels as Container Materials for Liquid Mercury Target of ESS," *Proceedings of the International Workshop on the Technology and Thermal-hydraulics of Heavy Liquid Metals,* Schruns (Austria), June 1996, pp. 6.27-6.39.

[4] A. G. Ioltukhovsky et al, "Metallurgical Aspects of Possibilities of 9-12%Chromium Steel Application as a Structural Material for First Wall and Blanket of Fusion Reactors," *Proceedings of the 7th International Conference on Fusion Reactor Materials,* Journal of Nucl. Mat., Vol. 233-237, October 1996, pp 299-304.

[5] D. S. Gelles, "Microstructural Examination of Commercial ferritic Alloys at 200 dpa," *Proceedings of the 7th International Conference on Fusion Reactor Materials,* Journal of Nucl. Mat., Vol. 233-237, October 1996, pp 289-292.

[6] J. J. Kai and R. L. Klueh, "Microstructural Analysis of Neutron-irradiated Martensitic Steels," Journal of Nucl. Mat. Vol. 230 (2), June 1996, pp 116-123.

[7] R. L. Klueh et al, "Microstructure-Mechanical Properties Correlation of Irradiated Conventional and Reduced-Activation Martensitic Steels," Journal of Nucl. Mat. 225 (1995) pp 175-186.

[8] ESIS Procedure for determining the Fracture Behaviour of Materials, ESIS P2-91.

[9] R. L. Klueh and D. J. Alexander, "Embrittlement of 9Cr-1MoVNb and 12Cr-1MoVW steels Irradiated in HFIR," Journal of Nucl. Mat. 187 (1992) pp 60-69.

[10] E. V. van Osch et al, "Mechanical Properties of RA Martensitic Steel F82H after 2.5 dpa, 300°C irradiation," *to be published in Effects of Radiation on Materials: 19th International Symposium, ASTM STP 1366.*

[11] E. I. Materna-Morris, "Mechanical Properties and Microstructure of HFR-Irradiated Ferritic/Martensitic Low-Activation Alloys," *to be published in Effects of Radiation on Materials: 19th International Symposium, ASTM STP 1366.*

Low Activation Ferritic/Martensitic Alloys

Edeltraud I. Materna-Morris,[1] Michael Rieth,[1] and Karl Ehrlich[2]

Mechanical Properties and Microstructure of HFR-Irradiated Ferritic/Martensitic Low-Activation Alloys

Reference: Materna-Morris, E. I., Rieth, M., and Ehrlich, K., **"Mechanical Properties and Microstructure of HFR-Irradiated Ferritic/Martensitic Low-Activation Alloys,"** *Effects of Radiation on Materials: 19th International Symposium, ASTM STP 1366*, M. L. Hamilton, A. S. Kumar, S. T. Rosinski, and M. L. Grossbeck, Eds., American Society for Testing and Materials, West Conshohocken, PA, 2000.

Abstract: Within the framework of the European Fusion Technology Programme, a series of ferritic/martensitic developmental alloys have been investigated after irradiation in the HFR (Petten, Netherlands). These new 7-10%CrWVTa alloys have been optimized towards long-term activation and the properties are compared with the conventional 9-12% CrMoVNb steels. The comparison contains two alloys from FZK (OPTIFER - type), the commonly investigated IEA alloy F82H and an ORNL - 9Cr2WVTa material. The irradiation was carried out in the temperature range of 250 - 450 °C up to an accumulated dose of 0.8 dpa.

The mechanical properties of the unirradiated and irradiated specimens were determined by tensile and impact tests. Radiation hardening, shift in DBTT to higher temperatures and partially a reduction of upper shelf energy were observed. Selected samples have been investigated by means of metallographic, SEM and TEM methods. The microstructures developed during neutron irradiation showed irradiation-induced precipitates, dislocation loops and He bubbles or small voids. These microstructures contribute to the observed irradiation-induced hardening and the changes of the fracture mode from transgranular to intergranular fractures.

Keywords: Martensitic steel, chromium steel, low activation alloys, impact tests, tensile tests, fracture analysis, microstructure, He bubbles, loops, strengthening, transmission electron microscopy, scanning electron microscopy.

Introduction

The martensitic 9 - 12% CrMoVNb steels have advantageous properties like sufficient high-temperature strength, corrosion resistance and a good thermophysical

[1] Research Scientists and [2] Professor, Dr., Department Head, Forschungszentrum Karlsruhe, Institut für Materialforschung, Postfach 3640, D-76021 Karlsruhe, Germany.

Copyright© 2000 by ASTM International www.astm.org

behavior. In nuclear technology these materials have been used as wrapper and cladding for fuel elements in Fast Breeder Reactors. These materials have been exposed to neutron fluences well above 100 dpa, in the typical Fast Breeder Reactor temperature range of 380 - 630 °C, there were negligible shifts of the DBTT (ductile to brittle transition temperature) or reduction of the USE (upper shelf energy). The material was not very sensitive to He-induced high temperature embrittlement or void formation [1]. These 9-12% CrMoVNb steels have another advantage. They are much less activated after neutron irradiation than, for example, the austenitic Cr-Ni-alloys. However, a critical effect of low temperature irradiation-induced hardening and embrittlement occurs. This negative observation was that in the fusion-relevant temperature range of 250 - 400 °C these materials exhibit a remarkable shift of DBTT towards higher temperatures. This behavior occurs at moderate neutron fluences of only few dpa. However, it was also shown that the effect can be reduced by chemical modifications, for example, by operating with Cr-contents in the range of 9%.

For the low-activation properties the overall analysis showed that elements like Cr, V, Ta and Si as well as B and Ti can be used further without restrictions. Whereas the elements Mo, Ni and Nb have to be eliminated to very low concentrations. But these are important elements, because Mo acts as matrix hardener and Nb as a carbide forming element to control the prior austenitic grain size. For the alloys, the following proposals were made by our and other laboratories: Mo has to be substituted by W and the grain size stabilizer Nb by Ta or Ti. But further impurity elements like Ag, Eu, Tb, Ho and Bi have very low concentration limits of much less than 1 ppm. This was the basis for further variations in the chemical compositions of these types of steels and further irradiation programs.

At the Forschungszentrum Karlsruhe, Institut für Materialforschung I, different alloys have been developed based on the experience with martensitic steels. These alloys are called OPTIFER in the European Long-Term-Program for Fusion Technology and they are investigated together with a Japanese and an ORNL batch. These new OPTIFER alloys on the basis of the 7 - 10% CrWVTa have an improved fracture toughness and DBTT and approximately comparable tensile and creep rupture strengths that are approximately comparable with those of martensitic 9 - 12% CrMoVNb steels [2-7].

The results of mechanical tests and structural investigations illustrate the changes of the material properties in dependence of the changes of the alloying elements. Particular attention was given to the contents of boron and the production of helium as well as to other radiation-induced microstructural changes. For separation of the temperature and irradiation effects a comparative program with unirradiated samples was designed.

Experimental Procedure

Materials

All investigated steels had the structure of a quenched and tempered martensite. The chemical compositions are given in Table 1. The OPTIFER alloys were developed by the FZK [1-6]. Their carbon contents were low and the nitrogen was strongly reduced to

achieve a low DBTT. The steel F82H was provided by JAERI/Japan and the steel ORNL 3791 from ORNL, USA. The MANET II as a conventional 10%CrMoVNb steel was added to this series due to its former extensive investigations as a material for Fusion Reactor components.

Table 1 – *Chemical compositions of the alloys*

	MANET II	OPTIFER Ia	OPTIFER II	F82H	ORNL 3791
Cr	9.94	9.3	9.5	7.73	8.9
C	0.1	0.10	0.125	0.092	0.11
N	0.023	0.0155	0.0159	0.0027	0.0215
Mn	0.79	0.50	0.49	0.083	0.44
P	<0.006	0.0046	0.0043	0.003	0.015
S	<0.007	0.005	0.002	0.003	0.008
V	0.22	0.26	0.28	0.189	0.23
B	0.007	0.0061	0.0059	0.003	<0.001
Si	0.14	0.06	0.038	0.09	0.21
Ni	0.66	0.005	0.005	0.032	<0.01
Mo	0.59	0.005	0.005	0.0053	0.01
Al	<0.2	0.008	0.008	0.01	0.017
Co	<0.2			0.0024	0.012
Cu	<0.01	0.035	0.007	0.0059	0.03
Nb	0.14	0.009	0.009	0.0057	
Zr	0.034				<0.001
Ti				0.0104	<0.01
W		0.96	0.006	2.06	2.01
Ta		0.066	0.018	0.018	0.06
Ge			1.2		
Ce		<0.001	<0.001		
Fe	bal	bal	bal	bal	bal

The heat treatments have been optimized for the different alloys to achieve a fine grain size and optimized mechanical properties. Table 2 summarizes the heat treatments, the grain size of the former austenitic grain and the hardness.

Table 2 – Heat treatments, grain size and hardness of the alloys

Heat	Heat treatment	ASTM-grain size	Hardness HV 0.4
OPTIFER Ia	1075 °C 30 min + 780 °C 2 h	6.5	199
OPTIFER II	950 °C 2 h + 780 °C 2 h	7.5	206
F82H	1040 °C 30 min + 750 °C 2 h	6.5	227
ORNL 3791	1050 °C 30 min + 750 °C 2 h	8.5	245
MANET II	965 °C 2h + 1075 °C 30 min + 750 °C 2 h	7.5	274

Specimen Preparation

The Charpy subsize specimens (4 mm x 3 mm x 27 mm) were produced parallel to the rolling direction (L-T) of the material plates. The circular tensile samples were also taken parallel to the rolling direction. They had a diameter of 3 mm and a gauge length of 18 mm. The MANET II and ORNL 3791 alloys were not included in the tensile program.

Irradiation

The irradiation was performed at the HFR (High Flux Reactor) in Petten, Netherlands. A special wrapper, with irradiation capsules accommodating the tensile and impact specimens, was inserted into the reactor core. The radiation was set to 250, 300, 350, 400 and 450 °C, respectively. The temperatures were controlled by changing the gas mixture (helium and neon) in the gas gaps surrounding the samples. The irradiation was carried out in 95 FPD (Full Power Days) up to a dose of 0.8 dpa.

Post-irradiation Tests and Examinations

The impact tests were performed in an instrumented facility which was installed in the Hot Cells. For each experiment the force-vs.-deflection curve was recorded and the impact energy was determined by integration. This quantity was plotted against the test temperature and from this the characteristic values of USE and DBTT were derived. DBTT is determined by USE/2. The test temperatures were between -120 and 500 °C. The results have been compared with an unirradiated series of samples subjected to the heat treatments shown in Table 2; without any further annealing.

The tensile samples were also tested in the Hot Cells. The tests were performed on a static mechanical tensile testing machine with a strain rate of 1% min^{-1}. The unirradiated samples have also been tested at RT (Room Temperature). Further unirradiated tensile samples have been tempered for 95 days, i.e. to the FPD of the reactor insert, at 300 and 450 °C and have been tested at 300 and 450 °C, too. The irradiated samples were tested at their irradiation temperatures of 250, 300, 350, 400 and 450 °C.

The fracture zones of the impact specimens were cut off and studied by means of SEM (Scanning Electron Microscopy) and the chemical analysis was performed by EDX (energy dispersive x-ray analysis). For the microstructural investigations TEM (Transmission Electron Microscopy) and EDX methods were used to examine the unirradiated and irradiated materials. The TEM samples (Ø = 3 mm) were prepared by the TENUPOL technique. The electrolyte used was an aged methanol sulfuric acid (80 vol.%. methanol and 20 vol.% sulfuric acid). The 3 mm samples were strongly ferromagnetic. It was necessary to minimize their mass with the view to reduce the astigmatism in the TEM. With a 1 mm Ø-punch the thinned area around the hole was punched out. Using a special 1 mm TEM holder, or between a Cu-sandwich grid, the samples have been investigated. The contents of carbides in the unirradiated material was determined by chemical extraction. The solution was picric acid in ethanol. The extraction could be weighted, analyzed by X-ray diffraction and EDX.

Results

Impact Tests

For every material the impact energy vs. test temperature was determined. The DBTT values are given in Table 3 [8-9]. The highest irradiation effect was observed at the irradiation temperature of 250 °C. In Figure 1, the graph of the ΔDBTT ($DBTT_{unirradiated}$ - $DBTT_{irradiated}$) presents the reduction of the DBTT due to the irradiation and radiation temperatures. Another value characterizing the ductility of a material is the USE. These results are outlined in Table 4. The loss of USE ($USE_{unirradiated}$ - $USE_{irradiated}$) is shown in Figure 2 as a function of irradiation.

Table 3 – DBTTs of the investigated alloys in [°C]

Heat	Unirra-diated	irrad. at 250 °C	irrad. at 300 °C	irrad. at 350 °C	irrad. at 400 °C	irrad. at 450 °C
OPTIFER IA	-80	25	10	-50	-45	-60
OPTIFER II	-70	25	35	20	15	-10
F82H	-70	-5	-25	-50	-40	-60
ORNL 3791	-80	-55	-45	-60	-40	-25
MANET II	-45	100	70	25	-20	-30

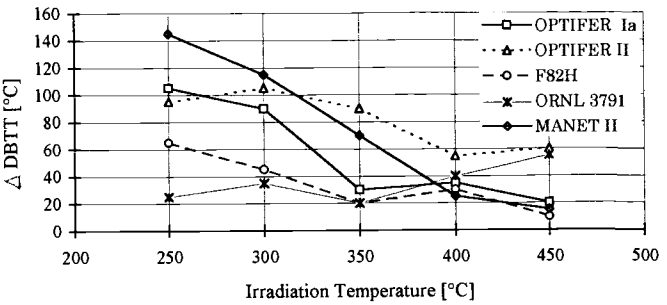


Figure 1 – ΔDBTT depending on the irradiation temperature

Table 4 – USEs of the investigated alloys in [Joule]

Heat	unirra-diated	irrad. at 250 °C	irrad. at 300 °C	irrad. at 350 °C	irrad. at 400 °C	irrad. at 450 °C
OPTIFER IA	9.3	9.4	9.2	9.2	10.0	9.7
OPTIFER II	9.8	8.1	7.9	8.3	8.0	9.2
F82H	10.7	10.1	10.4	10.5	10.4	10.2
ORNL 3791	9.2	8.3	8.4	8.7	8.4	8.3
MANET II	7.3	5.1	5.5	5.5	7.2	7.3

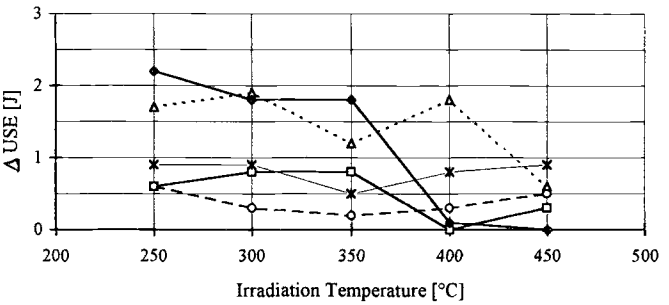
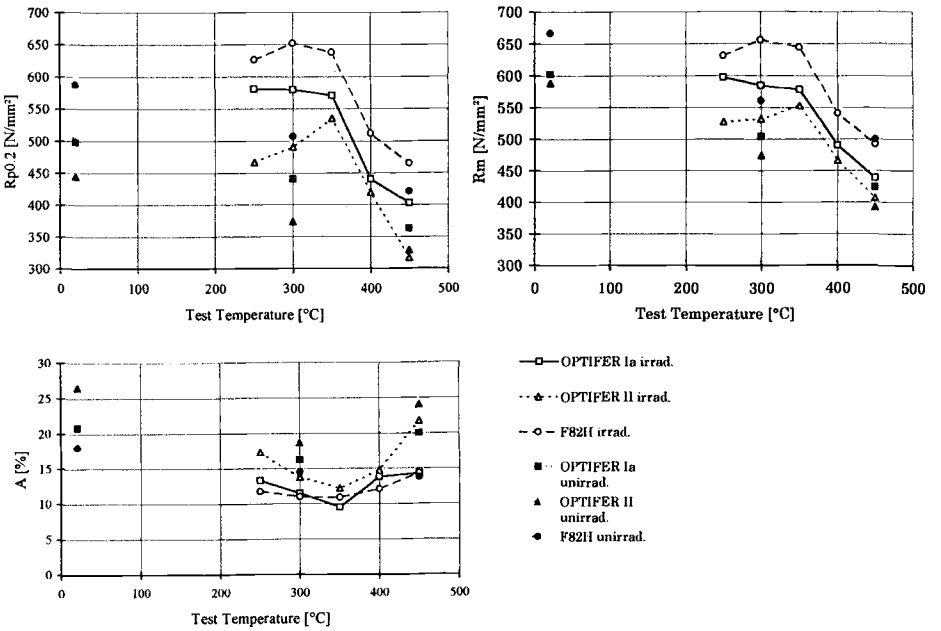


Figure 2 – ΔUSE depending on the irradiation temperature

Tensile Tests

The results of the yield strength ($R_{p0.2}$), tensile strength (R_m) and the total elongation (A) are plotted vs. the test temperature which corresponds to the irradiation temperature; Figure 3. The unirradiated tensile samples showed a decrease in yield and tensile strength with increasing test temperature. The irradiated samples of F82H and

Figure 3 – Tensile properties



OPTIFER Ia demonstrated constant yield strength and tensile strength values up to 350 °C. The steel F82H reaches the highest strength level. The data of OPTIFER II showed a moderate increase up to 350 °C and then, like the other alloys a decrease depending on the temperature down to values near those of the unirradiated material.

Fracture Surface Analysis

The fracture surfaces and the microstructure of the unirradiated and irradiated impact samples at 250 and 450 °C have been investigated systematically. The fracture analysis was carried out on samples of the range of ductile to brittle transition or upper shelf. These are the samples which were strongly influenced by the irradiation, especially at the lower irradiation temperature of 250 °C.

In the unirradiated samples, the fractures in the range of DBTT showed a ductile initial fracture surface. The rims, on the left and right side of the fracture, are shear lips. In the center, the fracture showed a typical martensitic mixed mode, the crystalline spot; transgranular, with cleavage areas and in between ductile dimples in the abrupt drops; Figure 4A. The fractures of the upper shelves were completely ductile and the surfaces are covered with transgranular dimple formations; Figure 4B. Although the unirradiated low-activation alloys have nearly the same DBTTs, the topography of the fractures was slightly different. The unirradiated OPTIFER Ia samples of the USE had very flat and

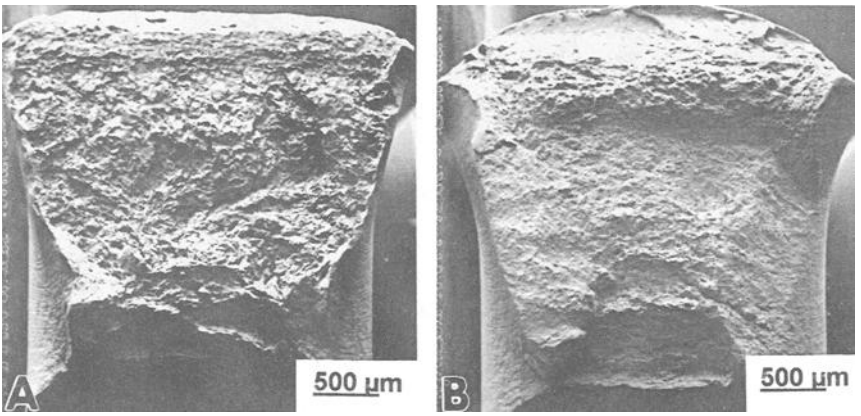


Figure 4 – Fracture surfaces of OPTIFER Ia, 0 dpa:
A) Range of DBTT (T_{test} = -80 °C)
B) Range of USE (T_{test} = -60 °C)

large dimples in the center of the fracture; Figure 5A. But in the range of DBTT the cleavage areas of the fracture are larger. They correspond in the size with the pior austenitic grains; Figure 5B. The ductile fracture surface of OPTIFER II (USE, T_{test} = 26 °C) was rougher in the topography than in OPTIFER Ia (Figure 6A), but the cleavage areas had about half the diameter compared with the lath package sizes; Figure 6B.

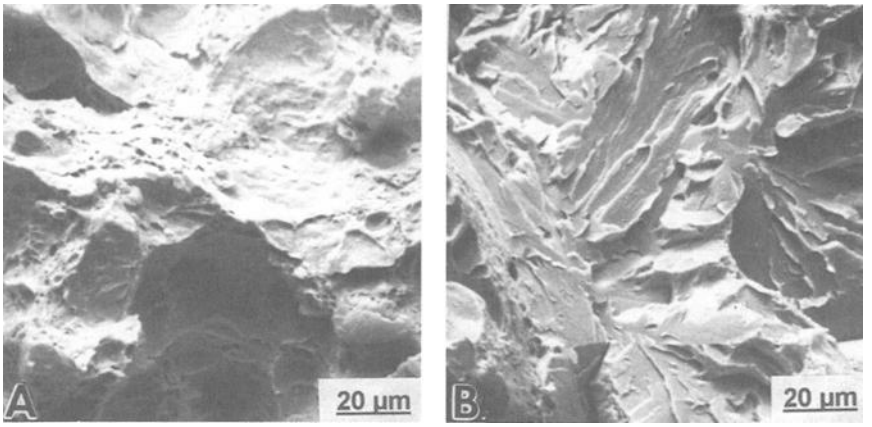


Figure 5 – Fracture surfaces of OPTIFER Ia, 0 dpa:
A) Dimple formation (T_{test} = -60 °C)
B) Cleavage formation (T_{test} = -80 °C)

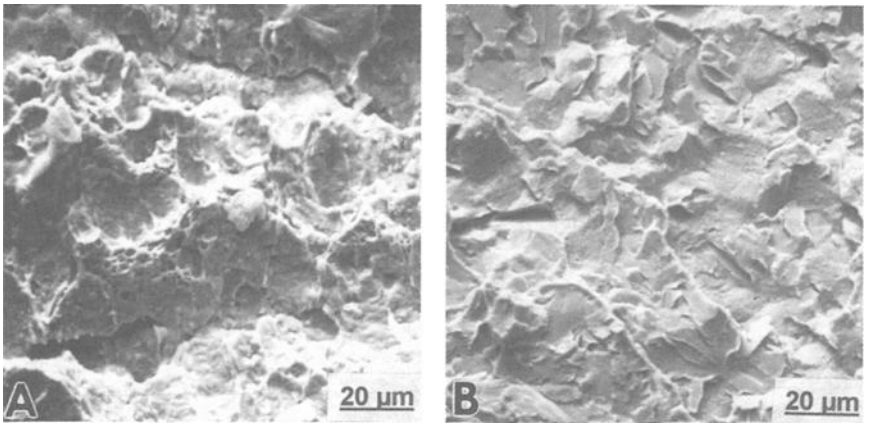


Figure 6 – Fracture surfaces of OPTIFER II, 0 dpa:
A) Dimple formation (T_{test} = 26 °C)
B) Cleavage formation (T_{test} = -60 °C)

After the irradiation at 250 °C of OPTIFER Ia, structures of grain surfaces became visible between the dimples. At the irradiation temperature of 450 °C, T_{test} = -60 °C, this effect was stronger and a clear mixed mode of inter- and transgranular brittle fracture could be seen in the range of DBTT; Figure 7A. In OPTIFER II a similar development could be observed, but again in a much finer structure; Figure 7B. The measurements of the cleavage and intergranular areas are comparable again to the package size of the laths.

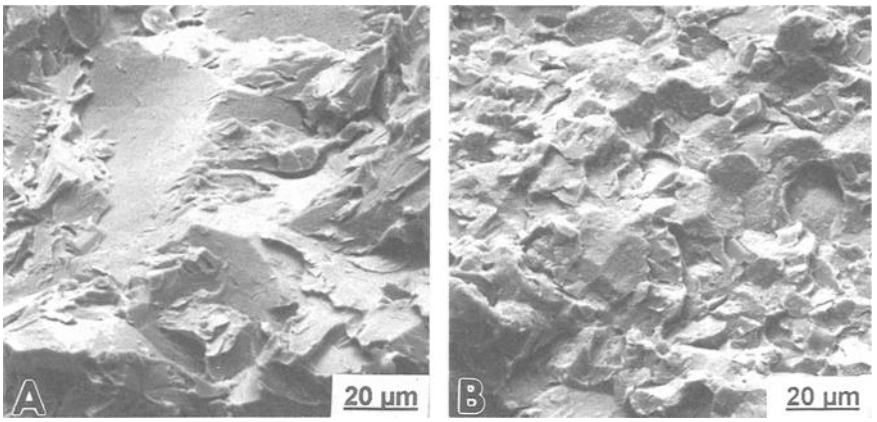


Figure 7 – Fracture surfaces in the range of DBTT, T_{irrad} = 450 °C, 0.8 dpa:
A) OPTIFER Ia (T_{test} = -60 °C)
B) OPTIFER II (T_{test} = -20 °C)

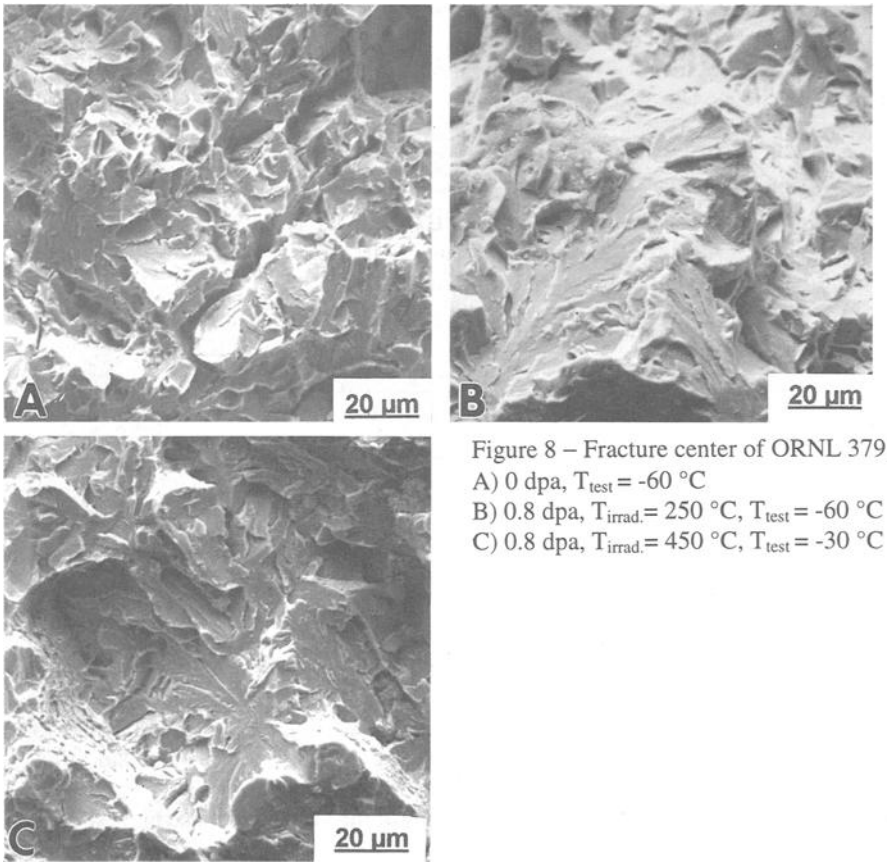


Figure 8 – Fracture center of ORNL 3791:
A) 0 dpa, T_{test} = -60 °C
B) 0.8 dpa, $T_{irrad.}$ = 250 °C, T_{test} = -60 °C
C) 0.8 dpa, $T_{irrad.}$ = 450 °C, T_{test} = -30 °C

The samples of F82H always have, under all material conditions, a transgranular cleavage or dimple fracture. On the ductile fracture surfaces of ORNL 3791, there was no difference between the unirradiated and irradiated material. In the brittle fractures of the unirradiated material, in the range of the DBTT, intergranular areas could be found. The cracks in the material pass the prior austenitic grain boundaries, Figure 8A. But after the irradiation at 250 °C the fracture mode changed to transgranular cleavage fracture; Figure 8B. After the irradiation at 450 °C, the typical martensitic mixed mode of cleavage areas and deep drops with dimples could be observed; Figure 8C. The fracture behavior of MANET II could be compared with the behavior of OPTIFER II under both unirradiated and irradiated conditions.

Microstructure

In the metallographic cuts no significant change could be observed in the etched structures for the different alloys and material conditions. Only by means of hardness measurements a small increase of hardness after the irradiation at 250 °C could be determined in all samples. After the irradiation at 450 °C the materials showed a small tendency to soften; Table 5. The hardness of the irradiated samples has been compared with the unirradiated hardness values.

Thin foils have been investigated in the TEM in order to determine the microstructure and the irradiation effects. In the unirradiated state the typical lath structures, lath packages and the prior austenitic grains of these martensitic steels could be seen. The lath boundaries were decorated with the $M_{23}C_6$ precipitates($(Cr,Fe,V)_{23}C_6$). The precipitation concentrations were between 2.0 and 2.5 wt.%. Depending on the different alloying elements further primary carbides could be detected, e.g. TaC (OPTIFER Ia and II, F82H), WC (OPTIFER Ia), or Zr(C,N) (MANET II). In the $M_{23}C_6$ precipitates in the lath boundaries of the W-alloyed heats, W could also be found in $(Cr,Fe,V, W)_{23}C_6$. This microstructure did not change during irradiation up to 450 °C.

Table 5 – Δ Hardness after irradiation at 250 and 450 °C.

Heat	Δ Hardness 250 °C	Δ Hardness 450 °C
OPTIFER Ia	31	-1
OPTIFER II	26	-8
F82H	18	-9
ORNL 3791	15	-11
MANET II	53	-2

But in the matrix of the irradiated materials, in between the lath boundaries, He-bubbles, dislocation loops and α`-precipitates could be found. These irradiation induced phenomena have been recorded quantitatively in all materials, irradiated at 250 and 450 °C; Tables 6-7. The highest concentration of bubbles (3.8×10^{18} cm^{-3}) and dislocation loops could be identified in OPTIFER II after the irradiation at 250 °C; Figures 9A,B. The bubbles were concentrated in the dislocations of the lath matrix. The highest con-

centration of the coherent α' precipitates (∅ 2 nm) was determined in OPTIFER Ia; Figure 10. In the F82H and ORNL 3791 alloys, it was difficult to detect these He bubbles. The data in Tables 6 and 7 are the highest concentrations in e.g. one or two laths; large areas are without bubbles.

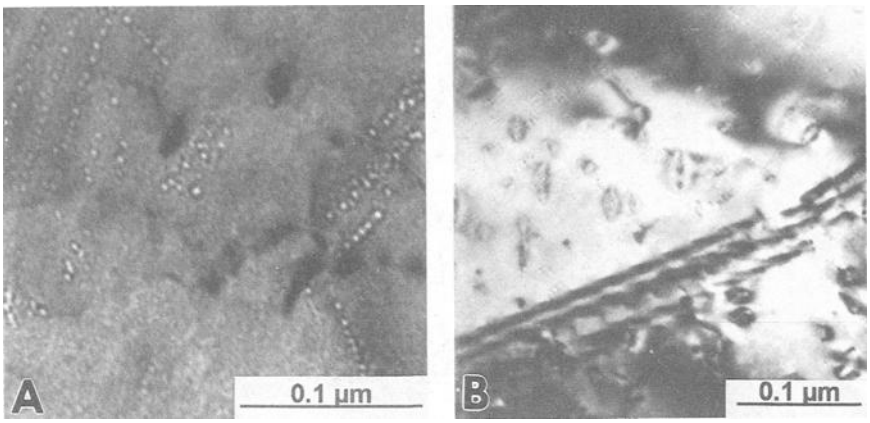


Figure 9 – Microstructure of OPTIFER II, 0.8 dpa, $T_{irrad.}$ = 250 °C:
A) He bubbles
B) Dislocation loops

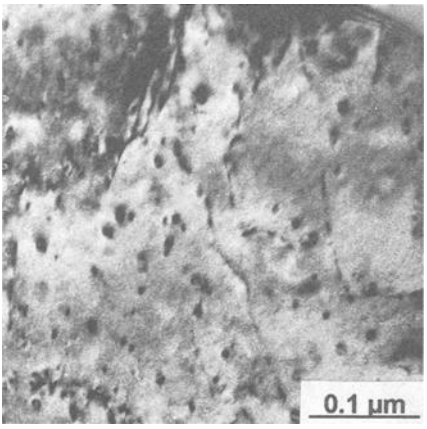


Figure 10 – Microstructure of OPTIFER Ia, 0.8 dpa, $T_{irrad.}$ = 250 °C:
Coherent α precipitates.

At the higher irradiation temperature of 450 °C, the dislocation loops and the very fine coherent α precipitates could not be detected, except in the matrix of the F82H. In

Table 6 – Quantitative analysis of the irradiation effects at 250 °C.

Heat	He bubbles size [nm]	He bubbles density [cm^{-3}]	He bubbles location	Density of loops [cm^{-3}]	Density of α` [cm^{-3}]
OPTIFER Ia	2	1.5×10^{16}	D, H	5.9×10^{15}	1.0×10^{16}
OPTIFER II	3	3.8×10^{18}	D	2.6×10^{17}	2.1×10^{15}
F82H	1.5	1.4×10^{17}*	H, S, P	1.9×10^{16}	7.5×10^{15}
ORNL 3791	2	1.1×10^{15}*	D, P	1.0×10^{15}	3.5×10^{10}
MANET II	2	3.6×10^{16}	D, S, P	1.4×10^{15}	3.8×10^{15}

D = Dislocations, S = Sub-grain boundaries, P = Precipitates, H = Homogeneously distributed, * = Maximum concentration

Table 7 – Quantitative analysis of the irradiation effects at 450 °C.

Heat	He-bubbles size [nm]	He-bubbles density [cm^{-3}]	He-bubbles location	Density of loops [cm^{-3}]	Density of α` [cm^{-3}]
OPTIFER Ia	2	5.7×10^{15}	D, S, P	-	-
OPTIFER II	6	1.2×10^{15}	D, S	-	-
F82H	3	3.7×10^{16}*	H, D	-	1.9×10^{16}
ORNL 3791	3	4.6×10^{15}*	D	-	-
MANET II	4	1.1×10^{16}	D, P	-	-

D = Dislocations, S = Sub-grain boundaries, P = Precipitates, H = Homogeneously distributed, * = Maximum concentration

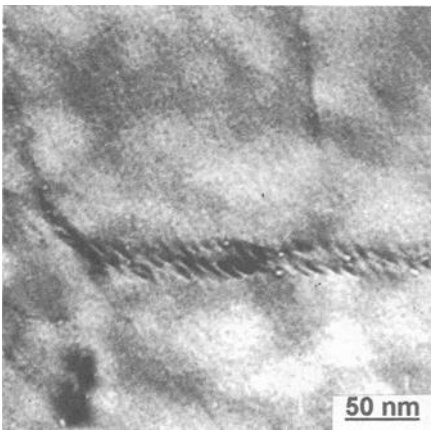


Figure 11 – Microstructure of OPTIFER Ia, 0.8 dpa, $T_{irrad.}$ = 450 °C: He bubbles in the sub grain boundaries.

this material a high density of fine precipitates (1.9 x 10^{16} cm^{-3}) has been observed. Some Fe_2W (Laves phase) could be found in the prior austenitic grain boundaries, but this phase was induced by thermal treatment. In all materials recovery with the formation of sub-grains could be determined. The observed He bubbles were fixed in the sub-grain boundaries and dislocations, as can be seen in Figure 11, an example of OPTIFER Ia.

Discussion

It is an important task to reveal the reason for the embrittlement of martensitic steels under lower irradiation temperatures. These results give more information about the irradiation behavior of 8-9% Cr steels, especially the low-activation variants. An important aspect is the content of helium in these materials; Table 8. But not only the He bubbles contribute to the strengthening of the material. Dislocation loops and α' precipitates also induce irradiation hardening by forming barriers for dislocations. Remarkable is the fact that at this low irradiation temperature of 250 °C, the three irradiation-induced defects in the material matrix - He-bubbles, dislocation loops and α precipitates appear always in all materials.

Table 8 – Calculated helium content after complete ^{10}B burn-up irradiation temperature and the Δ-values of the mechanical properties after $T_{irrad.}$ = 250 °C.

	OPTIFER Ia	OPTIFER II	F82H	ORNL 3791	MANET II
max. He	60 appm	60 appm	<20 appm	<10 appm	70 appm
ΔDBTT	105	95	65	25	145
$\Delta R_{p0.2}$	83	22	39	-	-
ΔR_m	-7	-62	-35	-	-
ΔA	-7.5	-9.2	-6.2	-	-

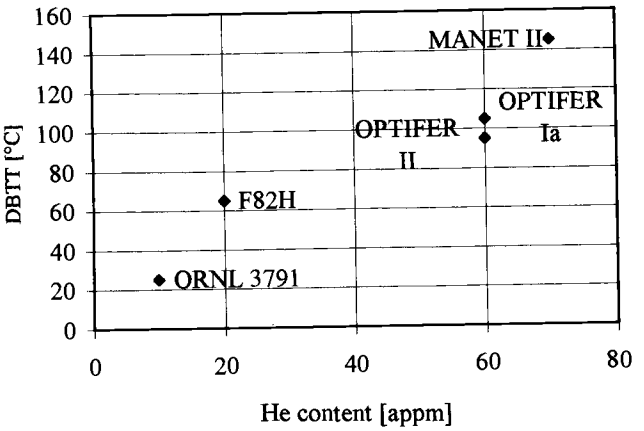


Figure 12 – The DBTT shift depending on the He content.

In Figure 12 the relationship between ΔDBTT and the calculated He content is shown. The shift in DBTT can be compared with the results of other authors [10], but the low-activation alloys show a more moderate ΔDBTT/He-content behavior, perhaps due to the lower Cr contents. The shift of the tensile properties is also indicated in Table 8. These values do not show a clear dependence on the He content or ΔDBTT. Certainly, the influence of the microstructure and the fracture development are of importance.

An important point is to find out the distribution of the boron in the material. The alloys, F82H and ORNL 3791, with the lower He content showed an inhomogeneous distribution of He bubbles. The main reason probably is the coarse distribution of the borides in the material [11]. In MANET II and the OPTIFER alloys there was a high density of He bubbles due to higher contents of boron. In previously investigated alloys, Cr-Fe-borides could be found at the triple points of the lath package boundaries. But the helium is not only produced by boron; other elements and their reactions with the neutrons contribute to this gas formation.

In any case, it was observed that higher quantities of irradiation-induced defects cause higher strengthening in the steel matrix. The highest hardness differences could be found in the alloys MANET II and OPTIFER Ia and II with the highest defect rate. In these alloys matrix strengthening was observed. The fracture modes were transcrystalline. But at a higher irradiation temperature, 450 °C, the boundaries lost their strength during the recovery of the matrix, which encouraged the mixed fracture mode, in the cleavage fracture with about 1/3 intercrystalline proportions. Interestingly, the F82H alloy had a similar behavior. The fine irradiation-induced precipitates in the matrix perhaps influence the properties of the material. In the ORNL 3791 alloy there was the opposite behavior. The grain boundaries strengthened during the irradiation, the material got softer and at the irradiation temperature of 450 °C, the fracture mode was like in the unirradiated state, which was seen in MANET II or the OPTIFER alloys. This material has not such a strong tendency to intergranular fractures during lower irradiation temperatures. Perhaps the higher Si content improves this material behavior. Si will not influence the carbide formation. In a solid solution it can contribute to the strengthening of the matrix [12]. During the irradiation, the Si could diffuse out of the matrix and could agglomerate. Softening of the matrix occurred.

The data presented are very encouraging and support the further development of these martensitic steels with low-activation properties for fusion reactors. All these results were combined with the experience of other laboratories to design an other alloy which is called EUROFER.

References

[1] Materna-Morris, E., Petersen, C., Rieth, M., Romer, O., Schirra, M., and Ehrlich, K., "Mechanical Properties and Microstructure of a High-Dose Irradiated Martensitic 10%Cr-Steel," *Euromat 96*, 1996, Bournemouth, UK.

[2] Ehrlich, K., Kelzenberg, S., Röhrig, H.D., Schäfer, L., Schirra, M., *Proc. of ICFRM-6, Stresa, Italy, 27.9.-1.10.93,* J. of Nucl. Mat., 212-215 (1994) 678-683.

[3] Ehrlich, K., "Die Entwicklung niedrigaktivierender ferritisch-martensitischer Stähle für Fusionsreaktoren" (The Development of low-activating F/M steels for fusion reactors), Report FZ-Nachrichten, Jahrg. 29 1/97.

[4] Ehrlich, K., Harries, D.R., Möslang, A., Characterization and Assessment of Ferritic/Martensitic Steels, Report FZKA 5626, Feb. 1997

[5] Schirra, M., Ehrlich, K., Heger, S., Hernandez, M.T., Lapena, J., Report FZKA 5624, Nov.1995.

[6] Daum, E., Ehrlich, K., Schirra, M., Proc. of Second Milestone Meeting: Development of Ferritic/Martensitic Steels, Report FZKA 5848, June 1997.

[7] Materna-Morris, E., "Mechanical Strength of Martensitic 10%-Cr-Steel After Low-Dose Irradiation in HFR," *Fusion Technology 1994*, 1281-1284.

[8] Rieth, M., Daffener, B., Ries, H., Romer, O., "Bestrahlungsprogramm MANITU: Ergebnisse der Voruntersuchungen und der Kerbschlagbiegeversuche mit den unbestrahlten Werkstoffen," Report FZKA 5550, April 1995.

[9] Rieth, M., Daffener, B., Ries, H., Romer, O., "Bestrahlungsprogramm MANITU: Ergebnisse der Voruntersuchungen und der Kerbschlagbiegeversuche mit den 0,8 dpa bestrahlten Werkstoffen der ersten Bestrahlungsphase," Report FZKA 5619, April 1995.

[10] Gelles, D.S., Hankin, G.L., Hamilton, M.L., "A Reassessment of the Effects of Helium on Charpy Impact Properties of Ferritic/Martensitic Steels," to be published.

[11] Kumar, A., Garner, F.A., "Transmutation-Induced Deposition Profiles in Halos Surrounding Spherical Precipitates," *Radiation Effects*, 1984, Vol. 82, 61-72.

[12] Irvine, K.J., Pickering, F.B., "High-strength 12% chromium steels," The Metallurgical Evolution of Stainless Steels, ed. by F.B.Pickering, ASM, 1979.

Emile van Osch,[1] Marc Horsten,[1] Gene E. Lucas,[2] and G. R. Odette[3]

Mechanical Properties of Four 7-9%Cr Reduced Activation Martensitic Steels after 2.5 dpa, 300°C Irradiation[4]

Reference: van Osch, E., Horsten, M., Lucas, G. E., and Odette, G. R., **"Mechanical Properties of Four 7-9%Cr Reduced Activation Martensitic Steels after 2.5 dpa, 300°C Irradiation,"** *Effects of Radiation on Materials: 19th International Symposium, ASTM STP 1366,* M. L. Hamilton, A. S. Kumar, S. T. Rosinski, and M. L. Grossbeck, Eds., American Society for Testing and Materials, West Conshohocken, PA, 2000.

Abstract: Reduced Activation Ferritic/Martensitic alloys are being developed for application in future thermonuclear fusion reactors. The behavior of the reduced activation martensitic steel F82H-mod was compared with small amounts of related alloys JLF-1, JLF-1B and ORNL-9Cr2WVTa, following irradiation in the High Flux Reactor (HFR) in Petten. Tensile, KLST-type Charpy impact and CT fracture toughness mechanical properties specimens, were neutron irradiated to a dose level of 2-3 dpa at 300°C. Results of post irradiation tensile, miniaturized charpy impact, and static fracture toughness tests are presented and interpreted in terms of irradiation hardening and irradiation induced shift of ductile to brittle transition temperature (DBTT) and reduction of upper shelf energy (USE). The observed irradiation hardening (140 – 170 MPa at 300°C) is moderate, whereas the observed radiation induced shift in DBTT is approximately 150°C for KLST-type impact test specimens for F82H. Similar observations are made for the static fracture toughness tests. For JLF-1B the irradiation hardening is one third higher than for JLF-1, and shift in DBTT for JLF-1B is almost 70% larger than for JLF-1. The difference is attributed to the tenfold larger boron content prior to irradiation.

Keywords: neutron irradiation, ferritic-martensitic 7-9%Cr steels, low activation, tensile properties, fracture toughness, Charpy impact behavior, embrittlement, hardening, ductility

[1]Materials scientists, NRG (former ECN), PO Box 25, 1755 ZG Petten, Netherlands.
[2]Professor, Dept. of Mech. and Environm. Engineering and Dept. of Chemical Engineering, University of California Santa Barbara, Santa Barbara, CA 93106.
[3]Professor, Dept. of Mech. and Environm. Engineering and Dept. of Materials, University of California Santa Barbara, Santa Barbara, CA 93106.
[4]The work reported is carried out and funded in the framework of the European Fusion Technology Program, and in the framework of the UCSB Program, funded by US-DOE.

Copyright© 2000 by ASTM International www.astm.org

Introduction

Reduced Activation Ferritic/Martensitic alloys are being developed for application in future thermonuclear fusion reactors by various partners in the fusion community. One of the major issues of these ferritic/martensitic alloys is the low temperature irradiation embrittlement. The irradiation behavior of the reduced activation martensitic steel F82H-mod (IEA heat), together with small amounts of other related alloys, such as JLF-1, JLF-1B or ORNL-9Cr2WVTa, was investigated by irradiation experiments in the High Flux Reactor (HFR) in Petten. Mechanical test specimens, such as tensile, KLST-type Charpy impact specimens and CT-specimens, were neutron irradiated to a dose level of 2-3 dpa at a temperature of 300°C.

Materials and Specimens

Materials

The materials studied are F82H, 7.5 and 15 mm plate from heat #9741 (also known as IEA Heat), and small amounts of JLF-1, JLF-1B, and ORNL-9Cr2WVTa. The chemical compositions are in Table 1. Details on the final heat treatment are given in Table 2. A common denominator of RAFM steels is the substitution of highly activating elements used in conventional ferritic/martensitic steels, e.g. molybdenum and niobium, with low or reduced activation elements such as tungsten, vanadium and tantalum.

JLF-1 and JLF-1B were produced in identical processes, and intended to obtain materials with virtually identical microstructure, essentially differing only in boron content. JLF-1B has a tenfold larger boron content than JLF-1. These alloys are used to study the effect of boron on hardening and embrittlement. Boron is a helium generating element, when irradiated with thermal neutrons. This is often used to generate fusion relevant helium concentrations in the steels, simulating the large amounts of helium generated by 14 MeV reactions in a thermonuclear fusion spectrum.

The structure of the steels is fully tempered martensitic. The temper treatment of all materials is aimed to obtain good toughness properties and keep sufficient tensile strength.

Specimens

Three types of specimens were used; cylindrical tensile specimens with a gage length of 20 mm and a diameter of 4 mm, miniaturized Charpy impact specimens KLST-type, and finally compact tension (CT) specimens of thickness of 10 mm. Drawings of each specimen type are presented in Fig. 1a to 1c. Tensile specimens were taken in the L orientation, CT and KLST specimens were taken in the L-T orientation, all with respect to the rolling direction.

Table 1 - *Chemical composition of materials*

Element	F82H-mod IEA heat 9741	JLF-1	JLF-1B	ORNL-9Cr2WVTa heat 3791
C	0.09	0.10	0.10	0.11
Si	0.11	0.05	0.04	0.21
Mn	0.16	0.45	0.46	0.44
P	0.002	<0.005	<0.005	0.015
S	0.002	0.0026	0.0027	0.008
Cr	7.71	8.88	8.87	8.9
Ni	0.02	-	-	<0.01
Mo	0.003	-	-	0.01
N	0.006	0.0215	0.0218	0.0215
Cu	0.01	-	-	0.03
Co	0.005	-	-	0.012
Ta	0.02	0.090	0.090	0.06
B	0.0002	0.0002	0.0022	<0.001
Ti	0.01	-	-	<0.01
Nb	0.0001	-	-	-
V	0.16	0.2	0.19	0.23
Al	0.003	-	-	0.017
W	1.95	1.95	1.94	2.01
Fe	bal.	bal.	bal.	bal.

Table 2 - *The final heat treatment, hardness and grain size of the FM steels*

	F82H-mod heat 9741	JLF-1	JLF-1B	ORNL-9Cr2WVTa
Normalizing	1040°C/38min	1050°C/1h	1050°C/1h	1050°C/0.5h
Tempering	750°C/60min	780°C/1h	780°C/1h	750°C/1h
Hardness (HV5)	204	207	204	n.a.
Grain size (μm)	75	27±6	32±4	n.a.

n.a. not available

Irradiation Experiments

The specimens were irradiated in the HFR reactor in Petten. The irradiation capsules were of the type CHARIOT and ILAS, both targeted at a neutron dose level of 2.5 dpa at an irradiation temperature of 300°C. These capsules were instrumented with thermocouples for temperature monitoring and control, and with neutron monitor sets to determine accurately the accumulated dose and fluence profile over the capsule. The temperature of the capsule was controlled by adjusting the helium-neon cooling medium mixture. The axial temperature profile could be controlled by adjusting the

vertical position of the experiment in the HFR core. A summary of irradiation conditions is given in Table 3, details can be found in [1,2].

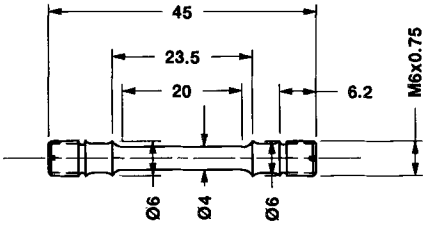


Figure 1a - *Tensile test specimen*

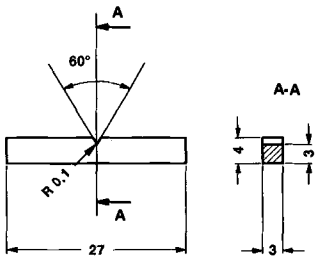


Figure 1b – *Miniaturized Charpy impact specimen*

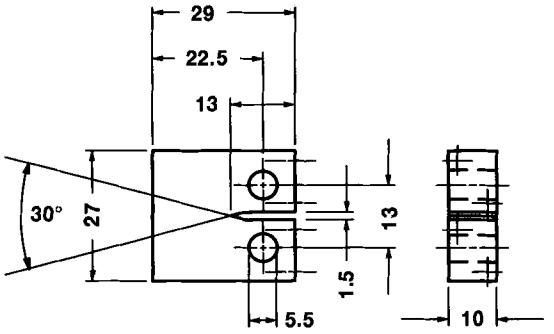


Figure 1c - *CT-10 Compact tension specimen*

The actual temperatures are indicated as ranges and are time-average values for the different locations within the experiment. The temperature averages are determined either from direct temperature measurements on the samples or by calculation on basis of measured specimen holder (drum) temperatures.

The displacement per atom dose was calculated from the neutron fluences, as derived from the activity measurement of the neutron fluence monitors contained in each experiment. The actual chemical composition of the sample materials as well as the irradiation history is taken in account to calculate the dpa-level.

Table 3 - *Overview of irradiation experiments*

Experiment	Specimen type	T_{irr} range (°C)	Dose (dpa)	Calculated helium content (appm)			
				F82H	JLF-1	JLF-1B	ORNL
ILAS-4	Tensile	325 – 335	2.4 - 3.0	2.7	2.8	23	<11
CHARIOT-2	CT-10mm, KLST	280 – 320	2.2 – 3.0	2.7	2.8	23	-

The formation of helium by transmutation reactions, in particular of boron, was also calculated with these neutron fluences (Table 3). As helium presumably plays an important role in the embrittlement behavior of the RAFM steels, and as boron is the largest contributor to the formation of helium for RAFM steels when irradiated in thermal and mixed spectrum reactors, the accuracy of the boron content is therefor of direct importance for the accuracy of helium content calculation. In past programs, investigating austenitic stainless steels, checks have been made with actual helium content measurements. The accuracy of the correspondence of the helium content and the content in boron and nickel was found to be satisfactory. For the current class of RAFM steels, who have very low boron contents, the accuracy of the boron content determination may be insufficient to determine the helium concentration by calculation alone, and should be checked by actual helium measurements.

The helium contents as stated in Table 3 are generated for 75% by the transmutation of ^{10}B in the case of F82H, JLF-1 and ORNL, and for 97% in the case of JLF-1B.

Mechanical Testing

Tensile Testing

The tensile experiments were performed on an electro-mechanical testing machine installed in the ECN Hot Cell Laboratory. The testing assembly was equipped with a 10 kN dynamic load cell and a two zone furnace. The tensile tests were performed with a constant actuator movement, resulting in a strain rate of $5x10^{-4}$ s^{-1}. From the load-displacement curves strength data at specific plastic strain intervals were calculated. The 0.2% Yield Strength (0.2YS), the Ultimate Tensile Strength (UTS), Uniform Elongation (UE) and Total Elongation (TE) will be used here for presentation of results and discussion.

Charpy Impact Testing

Impact testing was performed on a instrumented and automated miniaturized impact tester, with a potential energy of 50 J and an impact speed of 3.85 m/s. Impact specimens can be tested automatically, at temperatures in the range of –150 to +450°C. The results are presented in terms of impact energy. The impact energies are used to plot transition curves from which the ductile to brittle transition temperature (DBTT) and upper shelf energy (USE) for the material can be determined.

Fracture Toughness Testing

The post-irradiation fracture resistance experiments were performed on a servo-hydraulic testing machine, installed in a hot-cell. The test procedure is based on the ESIS P2-91 recommendation of the European Group on Fracture (EGF) for the single specimen J-resistance determination technique [3]. The load-line displacement is measured by

means of a strain-averaging system with two LVDTs. A separate direct current potential drop (DCPD) system is used for crack monitoring. The tests were performed in a two-zone furnace, in air environment after a temperature stabilization period of 30 minutes. Side-grooving after fatigue pre-cracking, as recommended in the ESIS procedure, is not performed with 10 mm CT specimens. The plane-sided specimens were fatigue pre-cracked at room temperature after irradiation. Automatic load shedding was applied for the K-controlled fatigue pre-cracking. Fatigue pre-cracking was done at 10 Hz with an R ratio of 0.1. The specimens that showed ductile tearing were heat-tinted after testing and then fractured by means of post test fatigue cracking at room temperature. The final DCPD crack length measurement is calibrated with the final crack length as measured on both fracture surfaces (weighted nine points averaging method).

In the brittle regime and in the transition regime, the K_Q is calculated according to ESIS-P2, which is practically identical to the ASTM E399 K_{1c} procedure. Because of the test specimens size, the K_Q can not be promoted to K_{1c}. In the ductile regime, the J-toughness is based on the ESIS-P2 approximation of J allowing for crack growth. The procedure differs from ASTM 1737 in the slope of the blunting line, which is used to determine the estimate of the initiation of stable crack propagation. This, in general, gives a somewhat lower value for the initiation toughness J_{02BL} than J_Q in the ASTM case. The material parameters used in this procedure are given in Table 4. The engineering estimate for onset of stable crack propagation J_{02bl} is subsequently converted to K-toughness by simple calculation.

Table 4 – *Material properties used in the FTT evaluation, unirradiated and 2.5 dpa 300°C irradiated F82H-mod, 15 mm plate*

	Unirradiated		2.5 dpa 300°C irradiated					
	24°C	325°C	24°C	50°C	80°C	100°C	150°C	325°C
0.2YS (MPa)	507	453	714	700	687	679	666	622
UTS (MPa)	629	520	762	742	724	714	694	640
E (GPa)	216	192	216	214	211	210	206	192
ν (-)	0.30	0.30	0.30	0.30	0.30	0.30	0.30	0.30

Results

Tensile Properties

Tensile tests were carried out in the range from room temperature to 550°C. The 0.2% yield stress, ultimate tensile strength and total and uniform elongation, for both unirradiated and irradiated specimens, are plotted as a function of test temperature in Figs 2-4. The results for F82H are in Fig 2, for both JLF-1 and JLF-1B in Fig 3, and finally the results for ORNL-9Cr2WVTa in Fig 4.

Irradiation hardening is observed for all four materials, and amounts to approximately 140 - 170 MPa at 300°C and 150 – 210 MPa at room temperature. F82H shows the most hardening, 170 MPa (Fig 2), and JLF-1 the least, 140 MPa (Fig 3). The

irradiation hardening is summarized in Table 5, for both room temperature and 300°C test temperatures. Further, the ductility was reduced by irradiation, approximately by 2.3-3.4 % for TE and 1.2-2.4 % for UE, tested at 300°C. The uniform elongation after irradiation remains above or just below 1% for all materials and all test temperatures. A limited amount of strain hardening capacity is still present after irradiation. F82H shows a minimum uniform elongation of 0.5 - 1% in the range of 200 to 500°C test temperatures. At test temperatures above 500°C, very little difference remains between the unirradiated and irradiated material; most of the irradiation hardening and loss of ductility was recovered at 550°C.

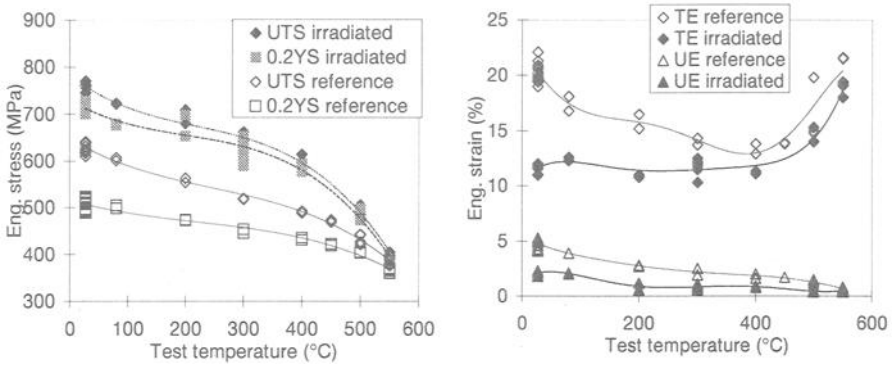


Figure 2 – *Tensile properties of IEA F82H,heat 9741, before and after 2.5 dpa 300°C irradiation; (a) yield stress and ultimate strength, and (b) total and uniform elongation*

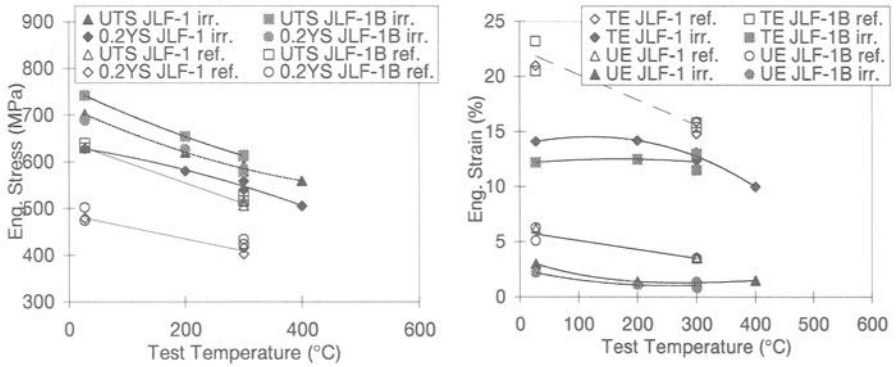


Figure 3 – *Tensile properties of IEA JLF-1 and JLF-1B, before and after 2.5 dpa 300°C irradiation; (a) yield stress and ultimate strength, and (b) total and uniform elongation*

In the unirradiated condition, JLF-1 and JLF-1B have almost identical tensile properties. After irradiation, and tested at room temperature, JLF-1B shows significantly more hardening than JLF-1; 200 versus150 MPa. The loss of ductility is also more

pronounced for JLF-1B than for JLF-1. At 300°C test temperature, the differences are much smaller (Fig 3). The uniform elongation remains above 1% in the temperature range up to 400°C.

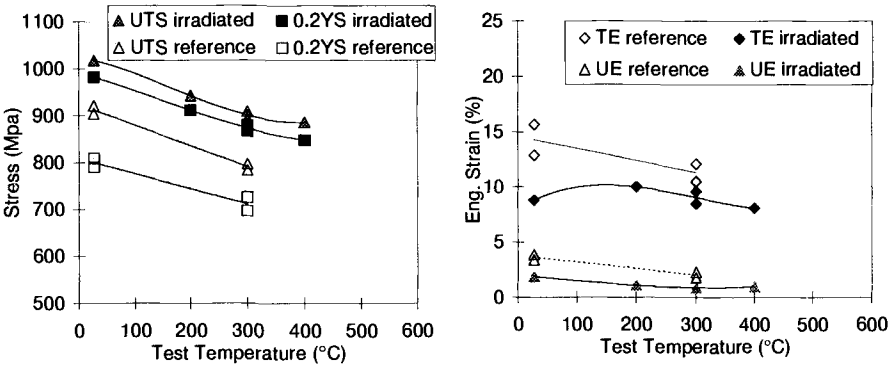


Figure 4 – *Tensile properties of ORNL-9Cr2WVTa, before and after 2.5 dpa 300°C irradiation; (a) yield stress and ultimate strength and (b) total and uniform elongation*

A remarkable point is the high strength of the ORNL steel, both in unirradiated and irradiated condition, (Fig 4). The ductility of this steel is lower than the other three steels. The uniform elongation after irradiation is minimally approximately 1%. The data for the unirradiated material correspond fairly well with properties measured by ORNL [4]. The reason for the higher tensile strength of this alloy is yet unresolved.

Table 5 - *Overview of irradiation hardening and loss of ductility*

	Tested at 27°C		Tested at 300°C	
	ΔYS (MPa)	ΔTE (%)	ΔYS (MPa)	ΔTE (%)
F82H	207	8.7	169	2.3
JLF-1	149	6.9	140	2.6
JLF-1B	200	9.6	153	2.3
ORNL	182	5.5	162	2.1

Miniaturized Charpy Impact Results

The Charpy impact test results are presented for both unirradiated and 2.5 dpa 300°C irradiated F82H-mod in Fig. 5. The results for JLF-1 and JLF-1B are in Fig. 6. The ORNL RAFM steel was not impact tested. The DBTT for unirradiated F82H lies around –95°C, whereas after irradiation, the DBTT has shifted to +55°C, an irradiation induced shift of approximately 150°C. The DBTT of JLF-1 and JLF-1B in the unirradiated condition differ slightly; –112 and –100°C respectively. After irradiation the DBTT for JLF-1 lies at –25°C, a shift of approx. 90°C, whereas the DBTT for JLF-1B

after irradiation is around +50°C, a shift of 150°C. The irradiation induced shift for JLF-1B is 60°C (66%) larger than for JLF-1.

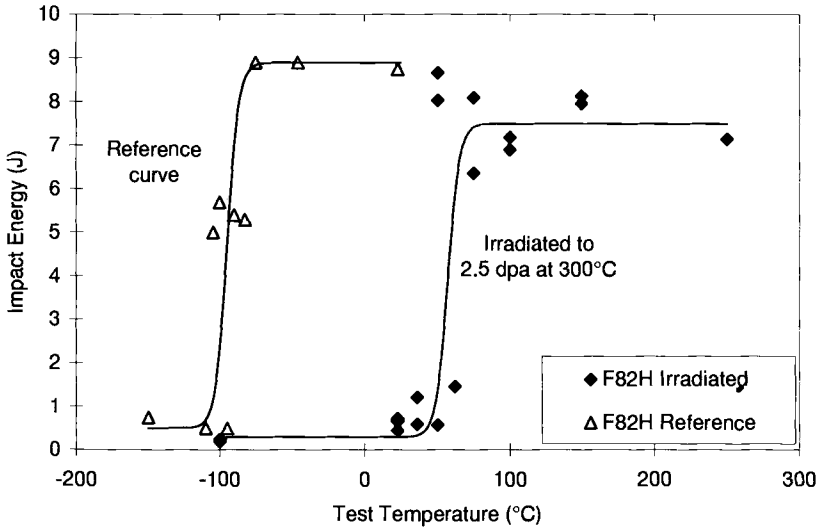


Figure 5 - *Miniaturized Charpy (KLST) impact transition curves for unirradiated and 2.5 dpa 300°C irradiated F82H, IEA heat 9741*

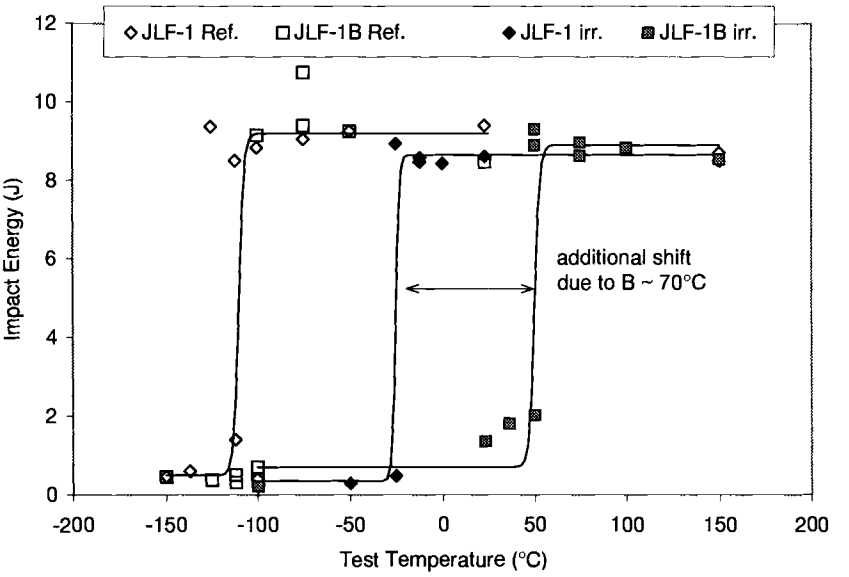


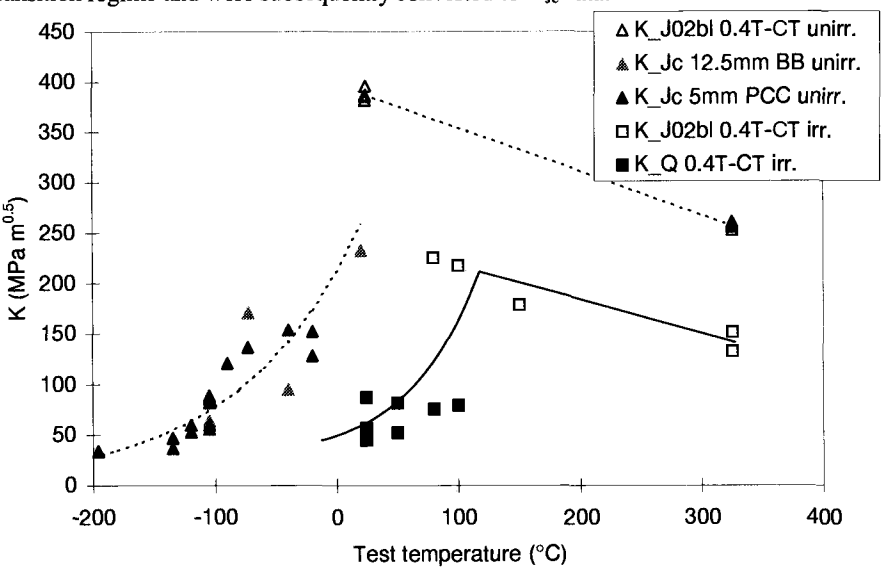
Figure 6 - *Miniaturized Charpy (KLST) impact transition curves for unirradiated and 2.5 dpa 300°C irradiated JLF-1 and JLF-1B*

The upper shelf energy (USE) of F82H is 8.9 J, after irradiation it is approximately 7.5 J, with a relatively large scatter. Hence, the reduction of USE is approximately 1.4 J for F82H. For both JLF-1 and JLF-1B, the USE is 9.2 J in the unirradiated condition. After irradiation, the USE is for both just a little lower, 0.6 and 0.3 J respectively.

It should be noted that for almost all upper shelf tests (unirradiated and irradiated, F82H and JLF-1, JLF-1B), the specimens were not broken by the impact.

Fracture Toughness Behavior

The results of the fracture toughness tests, carried out at ECN and at UCSB are plotted in Fig.7 as a function of test temperature. Only F82H data were available. The datapoints are designated with K_{Jc}, K_Q, and K_{J02bl}, indicating by subscript the nature of the datapoint. K_{J02bl} is determined according to the ESIS procedure in the ductile regime, K_Q is determined according to the ESIS procedure for the brittle regime, and K_{Jc} is determined according to the ASTM procedure in the transition regime. The K_{Jc} data were supplied by UCSB, the K_Q, and K_{J02bl} data by ECN. The UCSB data were produced with unirradiated 5 mm precracked charpies (PCC) and 12.5 mm bend bars (BB). The ECN data, were produced with 10 mm thick CT specimens, or 0.4T-CT. All 0.4T-CT tests showed either complete ductile tearing or cleavage fracture. No cases with noticeable crack extension before cleavage fracture were found. The tests with cleavage fracture were treated as brittle regime data in the K_Q calculation. The ductile regime data were treated to obtain J_{02bl} according to the ESIS standard. The J_{02bl} was subsequently converted to K_{J02bl}. The PCC and BB specimens were tested to obtain J_c data in the transition regime and were subsequently converted to K_{Jc} data.



The transition curve thus obtained with K_Q and K_{J02bl}, is qualitative transition curve, not a firm quantitative transition curve of one specific toughness parameter. The unirradiated F82H is fully ductile for the 0.4T-CT's from 325°C down to room temperature. The 5 mm PCC's and 12.5 mmBB's yield a DBTT (in terms of $T_{K=100}$) of approximately -70°C. After irradiation, the 0.4T-CT show brittle behavior up to 100°C, the DBTT is in the range of +80 to +100°C. The combination of these data indicates a shift in DBTT of approximately 160°C. The reduction of upper shelf energy by irradiation is found to be approximately 125 $MPam^{0.5}$.

Discussion

The four alloys are similar, but differ in a few aspects. Firstly, the chemical compositions are somewhat different (Table 1). F82H has low(est) chromium, manganese, nitrogen and tantalum contents, the ORNL RAFM steel has high(est) silicon, phosphorus and sulfur contents and intermediate tantalum, whereas the JLF-1 and JF-1B have low(est) silicon and high(est) tantalum. Finally, JLF-1B has highest boron content. The heat treatments are also similar but differences exist (Table 2). Hardness of F82H and JLF-1,1B are similar, whereas the grain size of F82H is significantly larger than that of JLF-1, 1B (ORNL not available). F82H was produced on industrial scale, the other alloys were produced on laboratory scale. The specimens were irradiated at the same time in the same irradiation capsules.

Irradiation Hardening and Loss of Ductility

The tensile data (Fig 2,3,4 and Table 5), show that the irradiation hardening and loss of ductility behavior of the four alloys is approximately similar at 300°C. All show intermediate hardening in the range of 140-170 MPa, which is relatively low compared to results obtained with conventional 9Cr-steels [5]. More significant differences occur when tested at room temperature (Fig. 8). JLF-1B shows 50 MPa (33%) more irradiation hardening than JLF-1. A similar difference is present for the loss of ductility. The originally tenfold larger boron content of JLF-1B, transmuted by irradiation to helium (and lithium), seems to be the cause of an additional hardening and loss of ductility. At irradiation temperature however, this difference is not as pronounced.

Irradiation Hardening and DBTT shift for KLST specimens

The DBTT for F82H, JLF-1 and JLF-1B do not differ strongly in the unirradiated state (Fig 5,6 and Table 6). After irradiation however, the JLF-1 DBTT has shifted by 90°C, whereas JLF-1B DBTT has shifted by 150°C, approx. 66% more than JLF-1. This does suggest that the originally tenfold higher boron content, yielding tenfold higher helium content, does seriously affect the DBTT in irradiated state. F82H shows a shift similar to the high shift of JLF-1B, whereas the original boron content is low and similar to that of JLF-1, not to JLF-1B. Evidently, boron, or helium, is not the only factor affecting the embrittlement. One of the reasons for the difference between F82H and JLF-

1 can be the larger grain size of F82H. The irradiation hardening of F82H and JLF-1B is similar at room temperature. The USE of JLF-1 is reduced slightly more than the USE of JLF-1B (Fig 6). It seems as is if the higher hardening gives JLF-1B a slightly higher USE after irradiation. F82H does shows a much more pronounced degradation of the USE.

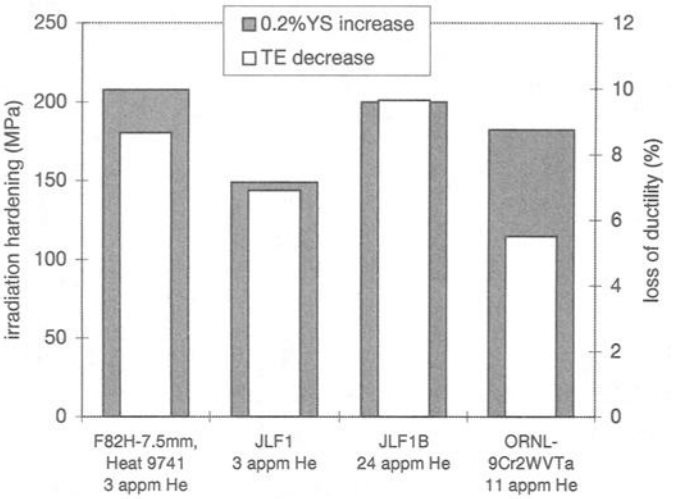


Figure 8 - *Hardening and loss of ductility at 24°C after 2.5 dpa 300°C irradiation*

Based on these comparisons, JLF-1 would be the best radiation resistant of the three RAFM alloys investigated here (ORNL excluded because of lack of data). The DBTT-shift is by far smallest for JLF-1, and its USE is only marginally affected. F82H might be called the worst of the three, given that the boron content was low, comparable to JLF-1, but showing an embrittlement behavior similar to the high boron content JLF-1B. A further disadvantage of F82H is the larger reduction of USE.

Table 6 - *Overview of (shift in) DBTT and (reduction of) USE of F82H, JLF-1, and JLF-1B (KLST impact tests)*

	Unirradiated		after 2.5 dpa 300°C		Change	
	DBTT (°C)	USE (J)	DBTT (°C)	USE (J)	ΔDBTT (°C)	ΔUSE (J)
F82H	-95	8.9	+55	7.5	+150	-1.4
JLF-1	-115	9.2	-25	8.6	+90	-0.6
JLF-1B	-100	9.2	+50	8.9	+150	-0.3

Static Fracture Toughness Tests

The qualitatively determined irradiation induced shift of DBTT of F82H in static fracture toughness tests corresponds fairly well to the value found for KLST impact tests,

both being approximately 150 to 160°C (Fig 5,7). The reduction of USE however, is much larger for the static fracture toughness tests than for impact tests; i.e. a 16% reduction for KLST impact and 45% for CT-10mm fracture toughness tests (Table 7). This suggests that considering the toughness degradation in terms of DBTT-shift or transition behavior alone is not sufficient. The USE apparently has a tendency to reduce to fairly low levels by irradiation (especially at higher test temperatures, Fig 7), possibly introducing toughness related complications even in the ductile regime. Evidently, one of the first priorities in developing RAFM steels is to avoid brittle behavior after irradiation, but consideration should be given to the ductile regime as well.

Table 7 – *Comparison of USE at 100°C before and after irradiation for impact tests and static fracture toughness tests of F82H.*

	USE unirr.	USE irradiated	ΔUSE	Relative ΔUSE
KLST impact test (J)	8.9	7.5	-1.4	-16%
CT fracture toughness ($MPam^{0.5}$)	350	225	-125	-45%

Summary and Conclusions

Mechanical test specimens of four reduced activation alloys F82H-mod, JLF-1, JLF-1B and ORNL-9Cr2WVTa have been irradiated up to 2.5 dpa at 300°C. The observed irradiation hardening is largest for F82H and lowest for JLF-1. A small amount of strain hardening capacity remains for all four alloys after irradiation.

The radiation induced shift in DBTT for F82H is approximately 150 to 160°C, in miniaturized Charpy impact tests and static fracture toughness experiments. The upper shelf energy for static fracture toughness tests is almost halved after irradiation. The observed shift in DBTT and amount of irradiation hardening is fairly large, at least larger than expectations based on experience with the pre-IEA heat of F82H. However, the hardening and shift in DBTT is smaller than observed for many other (RA)FM alloys studied in fusion and fission programs.

JLF-1B, identical to JLF-1 but containing about ten times more boron before irradiation, behaves similarly to JLF-1 in the unirradiated condition. After irradiation however, the amount of helium generated in JLF-1B is significantly higher, causing a 60°C larger shift in DBTT for miniaturized Charpy impact tests, and 50 MPa higher irradiation hardening than JLF-1. Evidently, the tenfold larger helium content generated during irradiation is suspected to play an important role.

Comparing irradiation hardening and embrittlement of F82H, JLF-1 and JLF-1B, indicates JLF-1 as being the best radiation resistant of the three, and F82H slightly worse than JLF-1B because of larger USE reduction.

Acknowledgment

The authors wish to thank the following persons and institutions for the kind supply of materials: dr. A. Hishinuma, JAERI, for IEA heat F82H; drs A. Kohyama and Y.Kohno, University of Tokyo, for JLF-1 and JLF-1B; and dr. R.L Klueh, ORNL, for supply of ORNL-9Cr2WVTa.

References

[1] D.J. Ketema, Neutron metrology in the HFR, Experiment ILAS-4, ECN-I-98-028, 1998.

[2] J.H. Baard, Neutron Metrology in the HFR, Experiment CHARIOT-2, ECN-I-98-025, 1999.

[4] R.L. Klueh, Metals and Ceramics Division, ORNL, personal communications April 1995 and May 1999.

[3] ESIS Procedure for determining the Fracture Behaviour of Materials, ESIS P2-91.

[5] M.G.Horsten et al., "Irradiation Behavior of Ferritic-Martensitic 9-12%Cr Steels," to be published in Effects of Radiation on Materials: 19th International Symposium, ASTM STP 1366.

Akihiko Kimura,[1] Taro Morimura,[2] Ryuta Kasada,[1] Hideki Matsui,[2] Akira Hasegawa,[3] and Katsunori Abe[3]

Evaluation of Ductile-Brittle Transition Behavior of Helium-implanted Reduced Activation 9Cr-2W Martensitic Steel by Small Punch Tests

---

Reference: Kimura, A., Morimura, T., Kasada, R., Matsui, H., Hasegawa, A., and Abe, K., **"Evaluation of Ductile-Brittle Transition Behavior of Helium-implanted Reduced Activation 9Cr-2W Matensitic Steel by Small Punch Tests,"** *Effects of Radiation on Materials: 19th International Symposium, ASTM STP 1366,* M. L. Hamilton, A. S. Kumar, S. T. Rosinski, and M. L. Grossbeck, Eds., American Society for Testing and Materials, West Conshohocken, PA, 2000.

Abstract: Helium implantation was performed by cyclotron with a beam of 36MeV-α particles at temperature below 429 K using a beam energy degrader to obtain homogeneous distribution of helium in a reduced activation 9Cr-2W martensitic steel up to a concentration of 120 at.ppm. The ductile-brittle transition temperature (DBTT) was evaluated by small punch (SP) tests in which the disk specimens of 3 mm diameter with 0.22 mm thickness were deformed by bulge mode. The shift in the DBTT (SP-ΔDBTT) and the increase in Vickers hardness (ΔH_v) caused by helium implantation were measured to be 26 K and 67 kg/mm^2, respectively, which were estimated to be 65 K of standard CVN-ΔDBTT and 104 MPa of increase in the yield stress ($\Delta\sigma_y$) from empirical relationships between them. The enhancement of irradiation hardening by helium was never recognized and no change in the fracture mode at low temperatures was observed by the helium implantation. It is considered that the shift in the DBTT is mainly associated with irradiation hardening by displacement damage.

Keywords: He implantation, small punch test, ductile-brittle transition temperature

---

[1]Professor and Graduate Student, IAE, Kyoto University, Gokasho, Uji, Kyoto 611-0011, Japan.
[2]Professor and Graduate Student, IMR, Tohoku University, Sendai 980-77, Japan.
[3]Associate Professor and Professor, respectively, Tohoku University, Aramaki, Aoba, Sendai 980-77, Japan.

Copyright© 2000 by ASTM International www.astm.org

Introduction

Helium-induced embrittlement is one of the critical issues of fusion structural materials in which several thousands at.ppm of helium is estimated to be generated during reactor operation. It is well known that a small amount of helium enhances irradiation embrittlement of austenitic steels [*1-3*] and some vanadium alloys [*4,5*] in the tests at relatively high temperatures accompanied by the change in the fracture mode from transgranular to intergarnular cracking. Microstructural observations revealed that many bubbles, which were considered to be helium bubbles, existed at grain boundaries, indicating that the helium atoms in the matrix of these materials diffused to form bubbles at grain boundaries during irradiation and/or testing at a high temperature. In contrast, it was reported that the martensitic steels were highly resistant to helium bubble-induced grain boundary embrittlement [*6-8*] at high temperatures. High resistance to the bubble formation in the martensitic steels is attributed to trapping of helium atoms and point defects in the martensitic structure or at dislocations, lath boundaries and carbides present at high density, which prevent the helium atoms from segregating to form helium bubbles at grain boundaries [*9*].

Ductile-brittle transition behavior is characteristic of body centered cubic metals such as martensitic steels, and irradiation hardening usually results in an increase in the DBTT. It is expected that the trapped helium atoms in the martensitic structure would enhance irradiation hardening of the matrix and resultantly shift in DBTT to high temperature. As for the effects of helium on the ductile-brittle transition behavior of the martensitic steels, several studies have been conducted relating to the effects of transmutation helium. Isotope-tailoring experiments on helium effects utilizing nuclear transmutation helium from nickel [*10-12*] and boron [*13*] showed that the addition of nickel or boron caused severe irradiation embrittlement in the martensitic steels, and the enhanced embrittlement, which was usually accompanied by severe irradiation hardening, was attributed to the helium transmuted from nickel or boron. It is, however, not clear that the transmutation helium in itself really induces low temperature embrittlement, since the addition of boron or nickel results in the change in the martensitic structure and post-irradiation precipitation morphology which are considered to be accompanied by the change in mechanical properties of the steel [*14*]. Thus, in the isotope-tailoring experiments especially for BCC steels, the effect of addition of Ni and/or B in itself should be taken into account in the discussion of radiation effects on the steel.

Helium implantation technique is more effective to evaluate directly helium effects in itself and many investigations have been performed for the martensitic steels, although

the helium/dpa ratio is usually very larger than the ratio expected for fusion environment. Since the range of the implantation is usually smaller than 0.5mm, the experiments have been often limited to microstructural observation, hardness measurement and tensile test with thin specimens. Lindau et al.[*15*] investigated the effects of implanted helium on the ductile-brittle transition behavior of F82H using 3 x 4 mm CVN specimens, although the range of helium implantation was less than a half of the specimen thickness, and showed that helium increased the DBTT of F82H. However, the detail of irradiation temperature control was unclear.

In this study, the effect of helium implantation on the ductile-brittle transition behavior of martensitic steel has been investigated by means of small punch test technique. Also, irradiation hardening and its annealing behavior are compared with that after neutron irradiation.

Experimental

The material used is the JLM-1 reduced-activation 9%Cr martensitic steel of which the chemical composition is shown in Table 1 with the heat treatment conditions.

Table 1 - *Chemical Composition of JLM-1*

	C	Si	Mn	P	S	Cr	W	V	Ta	Ti	B
wt.%	0.1	0.042	0.53	0.002	0.0014	9.03	2.06	0.26	0.051	0.021	0.0032

Normalized at 1323K for 30min and then tempered at 1033K for 30min, followed by air cooling.

Sheets of 0.23mm thickness were cut from a steel plate by multi-wire saw following mechanical polishing by sand paper (#800), and ten of the specimens were punched into disks, which measure 3mm diameter and 0.22mm thick. All of the specimens were fixed by molten indium on the specimen holder shown in Fig.1 and simultaneously implanted with a beam of 36MeV-α particles, whose range was estimated to be 0.23mm, by cyclotron implantation at Tohoku

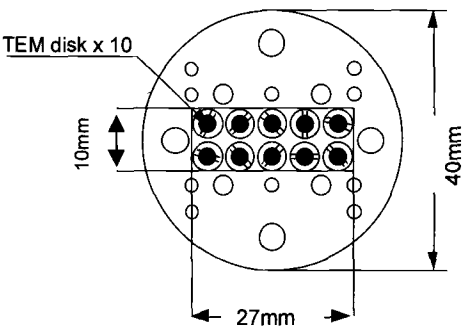


Fig.1- *Specimen holder for He implantation*

University. An energy degrader was used to implant helium into the specimens homogeneously, and the total helium concentration and displacement damage was estimated to be 120at.ppm and 0.048dpa, respectively. The implantation temperature was monitored by two thermocouples located on one of the specimens and the holder surface. The specimen temperature during the implantation was too unstable to be measured accurately, although the temperature of the holder was stable and measured to be lower than 333K. After the implantation, there was no features indicating that the indium paste melted during the implantation. This clearly indicates that the specimen temperature during the implantation was lower than 429K.

Following the implantation, small punch (SP) tests were carried out at temperatures between 77K and 293K. Test temperature was measured by a thermocouple in contact with the lower die. Figure 2 shows the schematic view of SP test method and a typical example of the load-deflection curve with the definition of SP properties, such as SP fracture energy and so on. The SP-DBTT was obtained by measuring the SP-fracture energy, which was defined as the total area below the SP load-deflection curve, at various test temperatures. A 3mm diameter of disk was grasped by dies at along its peripheral edge and deformed by bulge deformation mode in a cold bath of which the temperature was controlled within a error of ±1K. The displacement rate was 0.2 mm/min. After the SP tests, fracture surfaces were observed by scanning electron microscopy (SEM). The microstructure was examined by transmission electron microscopy (TEM). Micro-Vickers hardness tests and positron life time measurements were performed on a specimen in the as-irradiated condition and after post-irradiation annealing.

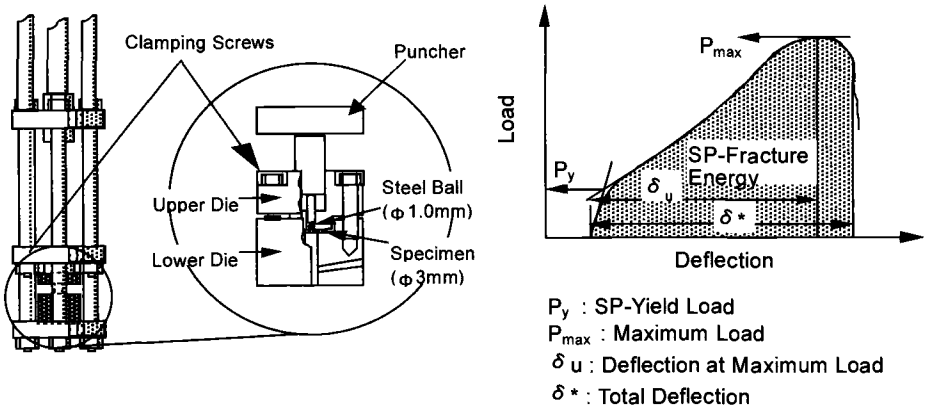


Fig. 2- *Schematic diagram of dies for SP tests and the definition of SP properties.*

Results

1. Micro-Vickers hardness measurement

The results of micro-Vickers hardness measurements of both surfaces of a helium-implanted specimen are shown in Fig. 3. Each data point is the average value of five measurements. As clearly shown in the H_v-distance relationship diagram, helium implantation resulted in an increase in the hardness of the martensitic steel and the irradiation hardening appears to be maximum at the center of the specimen. The average implantation-induced hardening (ΔH_v) at the irradiation surface and the reverse side of the specimen is 67 and 52 kg/mm^2, respectively, indicating that almost homogeneous irradiation and/or helium implantation was performed on the specimens.

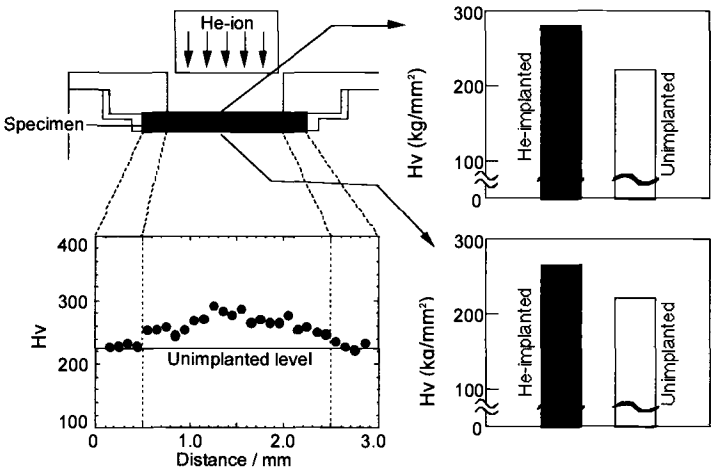


Fig. 3- *Micro-Vickers hardness of both the specimen surfaces before and after He Implantation.*

2. Small Punch Tests

The load-deflection curves of unimplanted and implanted specimens at various test temperatures are shown in Fig.4. No significant effects of implantation is recognized in the load-deflection curves at temperatures between RT and around 110 K. This indicates that the implanted 120 at.ppm He has no influence on the ductile shear rupture of the steel. Below 100 K, however, the load-deflection curves are markedly influenced

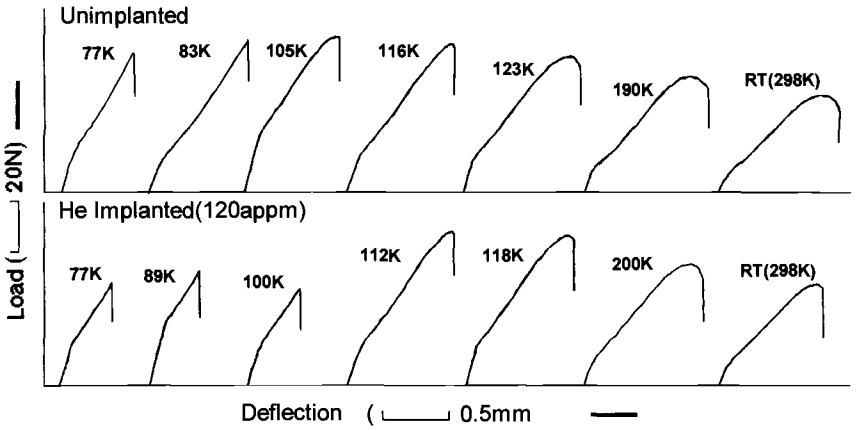


Fig. 4 - *Load-displacement curves of JLM-1 steel unimplanted (top) and helium-implanted (bottom). Effects of the He implantation are only observed when the test temperature is lower than 110K.*

by the implantation. In helium-implanted specimens, the maximum loads at temperatures below 110 K are almost the same, suggesting that the load corresponds to the fracture load in the lower-shelf energy temperature region. In unimplanted specimens, however, the maximum load still appears to decrease with decreasing temperature, which is because the transition from ductile to brittle is not complete yet even at 77 K. Figure 5 shows the dependence of SP properties on test temperature; a) SP-yield load, P_Y, is increased by the implantation at all the test temperatures, and the amount of the hardening seems to be independent of test temperature, b) The deflection at maximum load, δ_U is remarkably reduced by the implantation below 100K, c) Maximum load increases with decreasing temperature from room temperature to 110K and 80K for implanted and unimplanted specimen, respectively, and then appears to decrease with decreasing test temperature in umimplanted specimens, while they are almost the same in the implanted specimen, where the maximum load is considered to correspond to SP-fracture load, d) Almost the same feature is observed for the behavior of total deflection, δ^*, with that of δ_U. Generally, a transition is observed in the temperature dependence of SP properties in the helium-implanted specimen, while the transition seems to be still incomplete in unimplanted specimens. The dependence of SP fracture energy on test temperature is shown in Fig. 6 with the fracture surfaces of implanted specimens. The diagram of SP

fracture energy versus test temperature indicates that the ductile to brittle transition occurs at a low temperature in both the specimens with and without implantation, although again the transition in unimplanted specimens is still incomplete. The brittle fracture mode of the helium-implanted specimen is cleavage, which is the same as that of the unimplanted specimen. There is no indication of grain boundary embrittlement even at low temperatures after the helium implantation to 120 at.ppm. The SP-DBTT, which is defined to be the temperature where the fracture energy is the average value (0.18J) of the maximum and lower-shelf energy, is evaluated to be 81 K and 107 K for unimplanted and implanted JLM-1 steel, respectively; the implantation increases the SP-DBTT by 26K. Figure 7 shows the relation between the DBTTs obtained by utilizing standard-size CVN specimen and SP specimen for a variety of ferritic steels, indicating that there is a linear relationship between them and represented by the following empirical equation;

$$\Delta DBTT\ (Std\text{-}CVN) = 2.5 \times \Delta DBTT(SP) \qquad (1)$$

From equation (1), the shift in DBTT using standard size CVN specimens is estimated to be 65 K.

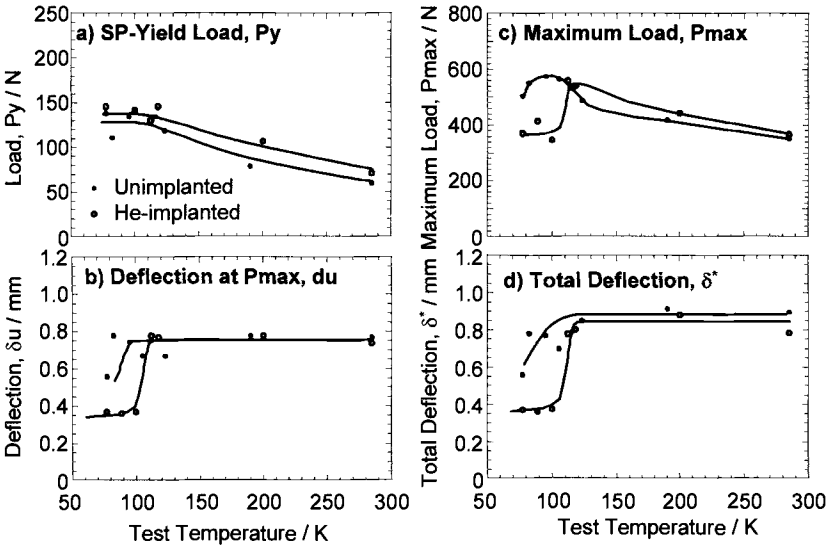
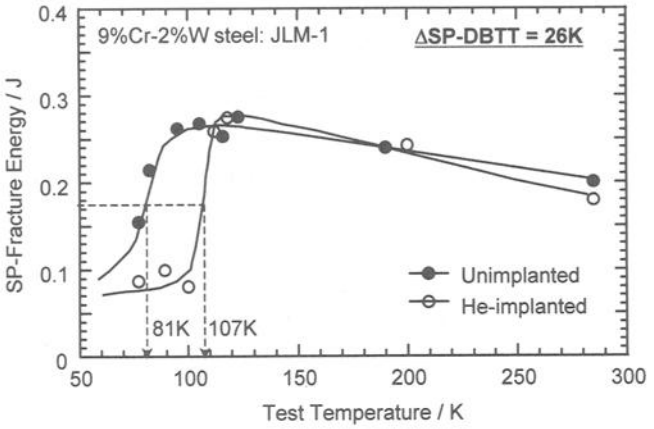


Fig. 5 - *Effects of He implantation on a) SP-yield load, b) SP-deflection at maximum load, c) SP-maximum load and d) SP-total deflection at various temperature. At temperatures above 110K, no effect of He implantation is observed, while below 110K He implantation resulted in the changes in the SP properties.*



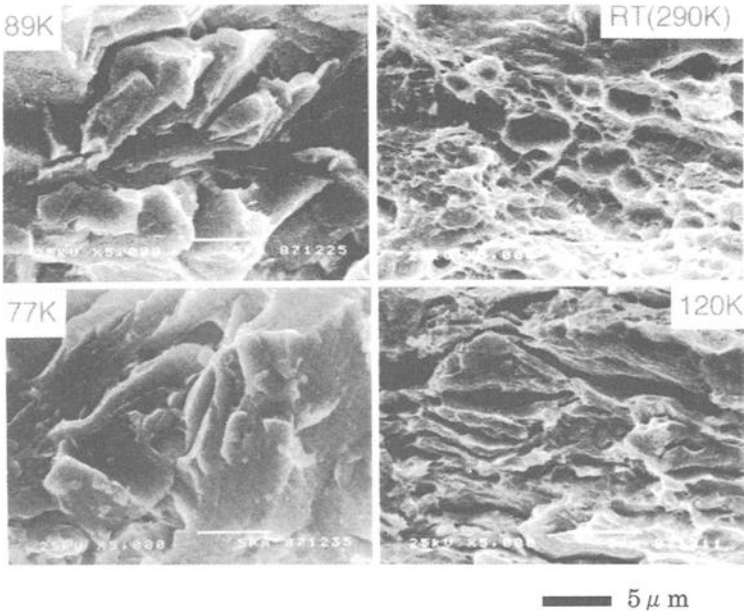


Fig. 6 - *Dependence of SP-fracture energy on test temperature and fracture surfaces of He implanted JLM-1; Ductile brittle transition is observed at around 110K below which the fracture mode is brittle cleavage, while it is ductile shear rupture above it. No intergranular fracture is observed even in the specimen fractured at 77K.*

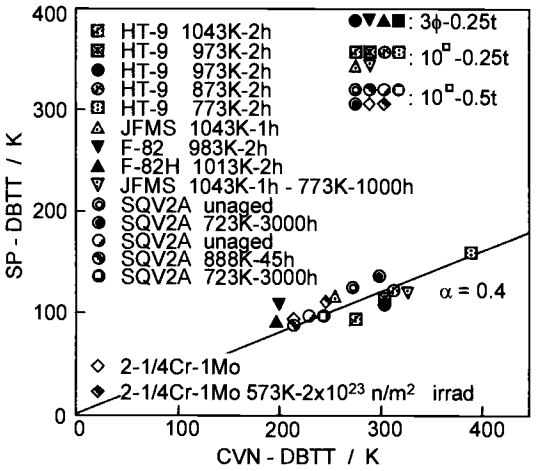


Fig. 7 – *The relation between the DBTTs obtained by utilizing standard size CVN specimen and SP specimen for a variety of ferritic steels.*

3. TEM observation and positron life time measurements

Microstructural examinations were performed by TEM for both the specimens with and without He implantation, but no difference in the microstructure was found between them. In order to get information of vacancy type defect clustering in helium-implanted steel, positron life time measurements were carried out for the helium-implanted specimen and a neutron-irradiated specimens. The results of a two-component analysis of positron annihilation spectra are summarized in Table 2. The longer life time component of the helium-implanted specimen is much smaller than that of the neutron-irradiated specimen, indicating that the size of the vacancy cluster is reduced by the helium implantation. It is considered that implanted helium suppresses the vacancy clustering by means of trapping a vacancy (V) to form a V-He complexes below 429 K.

Table 2- *Positron annihilation data*

Facility	Irr. Dose (dpa)	Irr. Temp. (°C)	τ_1 (ps)	τ_2(ps)	I_2 (%)
Cyclotron*	0.048	160	112	231	82
JMTR	0.05	220	172	432	16

* 120at.ppm of helium was implanted

4. Post-implantation annealing experiments

To make clear the characteristics of the defect clusters causing irradiation hardening of the helium-implanted steel, the recovery behavior of the hardening during isochronal annealing (1 hr) was investigated in comparison with that of neutron irradiated specimen in JMTR at 493 K (Fig. 8). Since the irradiation condition is different; helium implantation was performed at a lower temperature and up to higher dose than neutron irradiation, the increase in the irradiation hardening is larger in He implanted specimen. It is clear that the recovery of irradiation hardening of helium-implanted specimen is significantly retarded in comparison with that of neutron-irradiated specimen, suggesting that helium suppresses the annealing out of the defect clusters, such as the dislocation loops which cause the hardening. Another possibility is that helium bubbles are formed during annealing above 673K and contribute the hardening. More details of microstructural evolution during annealing will be reported elsewhere.

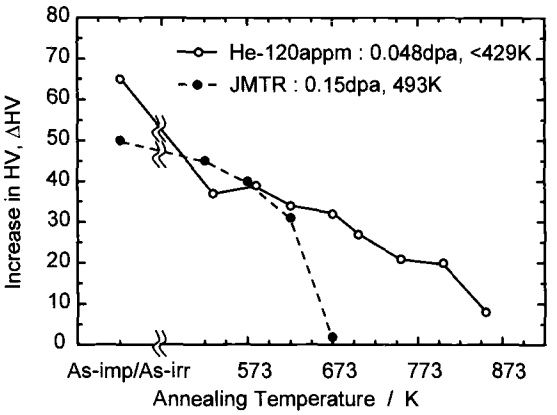


Fig. 8- *Annealing behavior of irradiation hardening*

Discussion

Effects of helium on the ductile-brittle transition behavior

The shift in the DBTT caused by helium implantation is considered to be due to the following:

1) The reduction of intergranular fracture stress caused by the formation of helium bubbles at the grain boundaries,

2) The reduction of cleavage fracture stress caused by helium trapped at carbides and/or dislocation cores,

3) The formation of defect clusters and helium enhances dislocation pinning.

Since intergranular fracture was never observed in the helium-implanted specimen, even in the lower-shelf energy temperature region, the first mechanism can be rejected. The

martensitic structure contains a lot of trapping sites for helium and point defects that can prevent helium cavities from being formed at grain boundaries. There is the possibility that the trapped helium induces the reduction of cleavage fracture stress. The maximum load in Fig.5 (c) gives information on fracture stress; the maximum load at temperatures of the lower-shelf region correspond to the cleavage fracture load as indicated in the load-deflection curves (Fig.4). Unfortunately, the fracture load of the unimplanted specimen was not measured in this experiment, because the SP-DBTT of an unimplanted specimen seems to be lower than 77K, which was the lowest temperature available in this work. The apparatus for SP tests at temperatures below 77K is now under construction. As for the last mechanism, the focus is placed on the role of helium on the hardening.

In order to estimate the irradiation hardening as an increase in tensile yield stress, the correlation between micro-Vickers hardness and yield stress in neutron irradiated reduced-activation martensitic steel was investigated. Figure 9 shows a linear relationship between them in 9%Cr-2%W steels;

$$\sigma_y \text{ (MPa)} = 1.54 \times H_V \text{ (kg/mm}^2\text{)} + 213 \qquad (2)$$

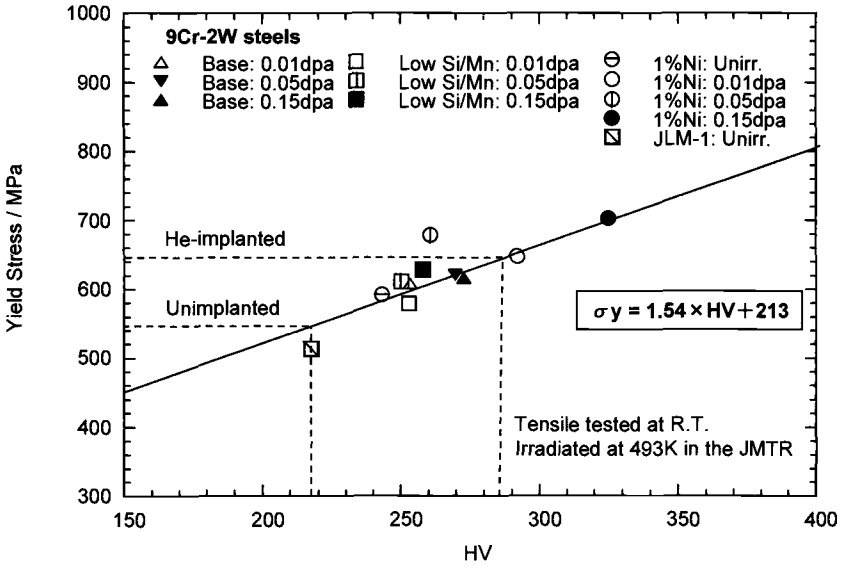


Fig. 9- *A linear relationship between σ_y and H_V in neutron irradiated 9Cr-2W steels. Specimens were neutron irradiated in JMTR at 473K and tensile tests were carried out at room temperature.*

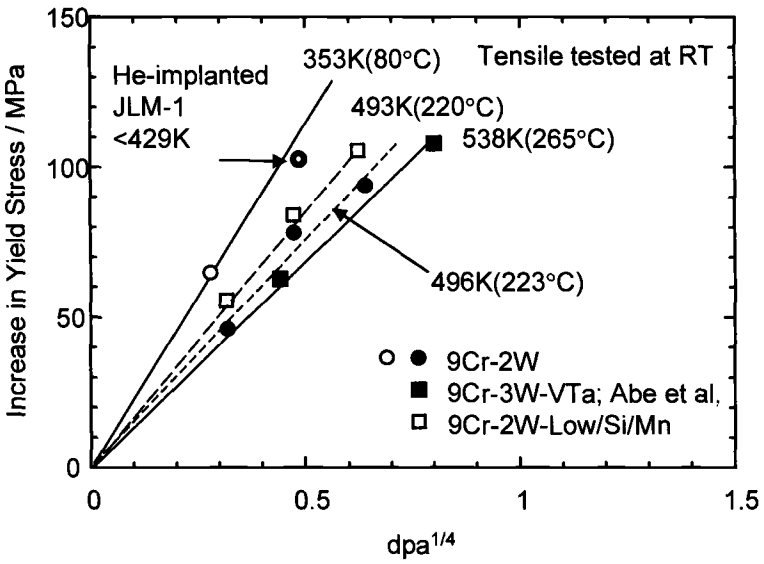


Fig. 10 - *Dependence of $\Delta\sigma_y$ of 9Cr-2W steels on irradiation dose, which follows 1/4 power of dpa. The slop seems to depend on irradiation temperature.*

The increase in tensile yield stress caused by helium implantation is estimated to be 104MPa from the empirical equation (2). In order to investigate the effects of helium on the irradiation hardening, the amount of the hardening in helium-implanted steel is compared with that of neutron irradiated steels. Although the chemical compositions of minor elements of the steels are somewhat different, the dose dependence of the irradiation hardening of all the steels, as shown in Fig. 10, seems to follow the 1/4 power law as previously reported [*16,17*]. The slope of the linear relationship between $\Delta\sigma_y$ and $(dpa)^{1/4}$ depends on the irradiation temperature; the slope increases with decreasing irradiation temperature. The $\Delta\sigma_y$ of helium-implanted steel is also plotted in the figure, indicating that the data point of $\Delta\sigma_y$ of the helium-implanted steel is located at the very position expected from the dose and temperature dependence of neutron irradiated steels, that is, the irradiation hardening of helium-implanted steel is easily interpreted in terms of displacement damage. Thus, it is considered that the 120at.ppm of helium does not enhance irradiation hardening and consequently that the shift in the SP-DBTT is due to irradiation hardening caused by displacement damage.

Finally, it is obvious that no helium effect was recognized in the reduced-activation 9Cr-2W martensitic steel implanted with 120at.ppm of helium; no

enhancement of the hardening and embrittlement. It is very likely that in the martensitic structure, the density of trapping sites, such as dislocations, lath boundaries and carbide/matrix interfaces, is high enough to distribute 120at.ppm of helium homogeneously. The helium effects investigated in this work is only for the case that the helium implantation was performed at below 429K, where helium atoms are considered to be immobile. It is noteworthy that the annealing-induced hardening was only observed above 673K, where the irradiation results in the softening without helium implantation, and helium bubble formation during post-implantation annealing of the steel containing 120 at.ppm of He appears to cause no significant hardening.

Effects of nickel addition

Although the isotope-tailoring experiment is one of the powerful experimental method to simulate the helium effects in fusion environment, there are some issues to be taken into account for the case of the nickel isotope-tailoring. It is expected that the addition of nickel in itself significantly changes the precipitation morphology of the martensitic steels and probably changes the susceptibility to irradiation embrittlement. One of the authors reported that in the JFMS steel, which contains 0.6wt.%Ni, a high density of nickel-silicides were induced by neutron irradiation [18]. More recently, it was also shown that only nickel added martensitic steel suffered a large irradiation hardening at the irradiation temperatures below 443K [19,20]; more than 400MPa of huge irradiation hardening was observed when the 9Cr-2W martensitic steel with 1%Ni addition was irradiated in JMTR at 443 K only to a dose of 0.15dpa. The temperature history during the reactor shut down should be taken into account for the discussion of irradiation embrittlement.

Defect clusters

According to previous work on irradiation hardening of reduced-activation of 9Cr-2W martensitic steels, factors controlling irradiation hardening include:
1) interstitial-type dislocation loops,
2) irradiation-induced precipitates, and
3) microvoids.
Since no changes in the microstructure was recognized between steels with and without helium implantation in this work, the factor controlling the hardening is quite obscure. Positron life time measurements give us information of vacancy clustering behavior,

namely size and number of voids. Although there is a significant difference in the longer life time components between the specimens irradiated in JMTR and implanted with helium, the irradiation hardening is not significantly changed between the specimens, suggesting that the contribution of microvoids to irradiation hardening is not substantial.

Post-implantation annealing experiments revealed that the recovery of irradiation hardening in helium-implanted steel was retarded in comparison with that in neutron-irradiated steel. Since the irradiation hardening is considered to be due to the small dislocation loops invisible by TEM, helium is expected to make dislocation loops be thermally stable. It is possible that this dislocation pinning effect of helium may suppress the dislocation recovery at high temperature and reduce creep deformation. It is also possible that the remaining hardening in helium-implanted specimen is considered to be due to helium bubbles formed during the annealing above 623K. More details of microstructural evolution during post-implantation annealing will be reported elsewhere.

Conclusion

The effect of helium implantation at 429 K up to 120at.ppm on the ductile-brittle transition behavior of reduced activation 9Cr-2W martensitic steel (JLM-1 steel) was investigated. The helium implantation resulted in a shift in SP-DBTT to higher temperature and an increase in the micro-Vickers hardness. These implantation effects were interpreted in terms of irradiation hardening caused by displacement damages without any enhancement by helium. The martensitic structure, which consists of a number of dislocations, lath boundaries and carbides, contains a high density of trapping sites for helium atoms and prevent helium atoms from segregating at any crack nucleation sites. It is expected that the helium embrittlement, whether it is transgranular or intergranular, will not occur until the helium generation overcomes the capacity of trapping sites for helium.

Acknowledgements:

The authors express their sincere thanks to graduate students in Dept. of Quantum Engineering, Tohoku University, for conditioning specimens for helium implantation. They are also grateful to Cyclotron Center, Tohoku University, for helium implantation and to Oarai Branch, Institute for Materials Research, Tohoku University, for facilitating post-implantation experiments. This work is partly supported by Japan-US collaborative JUPITER program.

References:

[1] Schroeder, H., and Batfalsky, P. J., "The Dependence of the High Temperature Mechanical Properties of Austenitic Stainless Steels on Implanted Helium," *Journal of Nuclear Materials*, vol. 117, 1983, pp. 287-294.

[2] Trinkaus, H., "Modeling of Helium Effects in Metals: High Temperature Embrittlement, " *Journal of Nuclear Materials*, vols. 133&134, 1985, pp. 105-112.

[3] Schroeder, H., "High Temperature Helium Embrittlement in Austenitic Stainless Steels-Correlations between Microstructure and Mechanical Properties," *Journal of Nuclear Materials*, vols. 155-157, pt. B, 1988, pp. 1032-1037.

[4] Braski, D. N., and Ramey, D. W., "A Modified Tritium Trick Technique for Doping Vanadium Alloys with Helium," *Effects Radiation on Materials, ASTM STP 870*, 1985, pp. 1211.

[5] Satou, M., Koide, H., Hasegawa, A. , Abe, K., Kayano, H., and Matsui, H., "Tensile Behavior of Helium Charged V-Ti-Cr-Si Type Alloys," *Journal of Nuclear Materials*, vols. 233-237, 1996, pp. 447.

[6] Stamm, U., and Schroeder, H., "The Influence of Helium on the High Temperature Mechanical Properties of DIN 1.4914 Martensitic Steel," *Journal of Nuclear Materials*, vols. 155-157, 1988, pp. 1059-1063.

[7] Möslang, A., and Preininger, D., "Effect of Helium Implantation on the Mechanical Properties and the Microstructure of the Martensitic 12%Cr-Steel 1.4914," *Journal of Nuclear Materials*, vols. 155-157, 1988, pp. 1064-1068.

[8] Hasegawa, A., Shiraishi, H., "Helium Implantation Effects on Low Activation 9Cr Martensitic Steels," *Journal of Nuclear Materials*, vols. 191-194, 1992, pp. 910-914.

[9] Ayrault, G., "Cavity Formation during Single- and Dual-Ion Irradiation in a 9Cr-1Mo Ferritic Alloy," *Journal of Nuclear Materials*, vol. 114, (1983) pp. 34-39.

[10] Klueh, R. L., and Vitek, J. M., "Fluence and Helium Effects on the Tensile Properties of Ferritic Steels at Low Temperatures," *Journal of Nuclear Materials*, vol. 161, 1989, pp. 13-20.

[11] Klueh, R. L., and Alexander, D. J., "Impact Behavior of 9Cr-1MoVNb and 12Cr-1MoVW Steels Irradiated in HFIR," *Journal of Nuclear Materials*, vols. 179-181, 1991, pp. 733-736.

[12] Klueh, R. L., and Maziasz, P.J., "Effect of Irradiation in HFIR on Tensile Properties of Cr-Mo Steels," *Journal of Nuclear Materials*, vol. 187, 1992, pp. 43-54.

[13] Rieth, M., Dafferner, B., and Rohrig, H. D., "Embrittlement Behavior of Different International Low Activation Alloys after Neutron Irradiation", *Journal of Nuclear Materials*, vols. 258-263, 1998, pp. 1147.

[14] Heinisch, H. L., "Effects of the Neutron Spectrum on Mechanical Property Changes in Low Dose Irradiation," *Journal of Nuclear Materials*, vol. 155-157, 1988, pp. 121.

[15] Lindau, R., Möslang, A., Preininger, D., Rieth, M., and Rohrig, H. D., "Influence of Helium on Impact Properties of Reduced-Activation Ferritic/Martensitic Cr Steels," *ICFRM-8*, (1997).

[16] Leslie, W.C., The Physical Metallurgy of Steels, McGraw-Hill Series in Mat. Sci & Eng., 1982, pp. 269-300.

[17] Abe, F. , Narui, M., and Kayano, H., "Effect of Neutron Irradiation on Yield Stress and Ductility of Reduced-Activation Martensitic 9Cr-WVTa Steels," *Materials Transactions, JIM*, vol. 34, No. 11, 1993, pp. 1053.

[18] Kimura, A., Gelles, D. S., Kohyama, A., and Puigh, R. J., "Dimensional Changes and Microstructure of In-Pile Crept Ferritc-Martensitic Steel," *Materials Transactions, JIM*, vol. 34, No. 11, 1993, pp. 1075.

[19] Kasada, R., Kimura, A., Matsui, H., and Narui, M., "Enhancement of Irradiation Hardening by Nickel Addition in the Reduced-Activation 9Cr-2W Martensitic Steel," *Journal of Nuclear Materials*, vols. 258-263, 1998, pp. 1199-1203.

[20] Kasada, R., Morimura, T., Matsui, H., Narui M. and Kimura, A. "Two-Step Recovery Process of Irradiation Hardening in 1%Ni Doped 9%Cr-2%W Martensitic Steel," *Effects of Radiation on Materials, ASTM STP 1366,* M. L. Hamilton, A. S. Kumar, S. T. Rosinski and M. L. Grossbeck, Eds., American Society for Testing and Materials, West Conshohocken, PA, 1999.

Irradiation Creep and the Creep-Swelling Relationship

Victor S. Neustroev[1] and Valentin K. Shamardin[1]

Irradiation Creep of Austenitic Steels Irradiated Up to High Damage Dose

Reference: Neustroev, V. S. and Shamardin, V. K., **"Irradiation Creep of Austenitic Steels Irradiated Up to High Damage Dose,"** *Effects of Radiation on Materials: 19th International Symposium, ASTM STP 1366*, M. L. Hamilton, A. S. Kumar, S. T. Rosinski, and M. L. Grossbeck, Eds., American Society for Testing and Materials, West Conshohocken, PA, 2000.

Abstract: The irradiation-induced creep and swelling of annealed 16Cr-15Ni-3Mo-Nb stainless steels with different contents of carbon and boron in BOR-60 at 420°C have been investigated to exposures of 100 dpa. Swelling depends on carbon content and boron. The creep rate directly depends on stress and instantaneous swelling rate. The creep-swelling coupling coefficient of austenitic steels does not appear to be very sensitive to microaddition.

Keywords: irradiation-induced creep, swelling, austenitic steels, neutron irradiation, fast reactors

Introduction

Most investigations of irradiation-induced creep on steels and its interrelation with swelling have been performed with gas-pressurized tubes made of non-stabilized or titanium-stabilized Type AISI 316, AISI 304L, PCA austenitic steels [1-4, 8-12, 14, 15]. All efforts of our investigators were focused on the study of creep in niobium-stabilized austenitic steels [5-7, 13, 16, 17].

The present work highlights the analysis of creep and its interrelation with swelling of 16Cr-15Ni-3Mo-Nb austenitic steels specified by carbon and boron content irradiated up to high neutron fluences in the BOR-60 reactor.

Experimental details

This gas-pressurized tube experiment was conducted in Row 6 of the BOR-60 reactor. The rate of damage dose varied along the specimen length from 3 to 6×10^{-7} dpa/sec. During 11 years of irradiation the maximum neutron fluence was 21.8×10^{26} m^{-2} E>0.1 MeV (100 dpa). Each tube was 200 mm long, 6.0 or 6.9 mm inner diameter and 0.3 or 0.4 mm thick. The experiment used seven values of stress varying from 0 to 320 MPa at irradiation temperature -420 °C. During reloading the tubes were taken out of the reactor to measure their deformation. The analysis of deformation kinetics against dose of gas-pressurized specimens was carried out on the basis of 16Cr-15Ni-3Mo-Nb-B steel (Table).

The final heat treatment of all steels was vacuum austenization at 1100 °C. In measurement of diameter the error was ± 0.007 mm. Some results of steel investigation at lower neuron fluence were given in earlier works [13, 16].

[1]Leading research scientist & Head of laboratory, respectively, Research Institute of Atomic Reactors, Dimitrovgrad, Ulyanovsk region, 433510, Russia.

Copyright© 2000 by ASTM International www.astm.org

Table - *Chemical Composition of Annealed Austenitic Steel, Mass %*

Type	C	Cr	Ni	Mn	Mo	Si	Nb	P	S	B
0.046C-16Cr-15Ni-3Mo-Nb	0.046	15.8	15.3	0.54	2.8	0.43	0.6	0.012	0.009	-
0.06C-16Cr-15Ni-3Mo-Nb-B	0.06	15.6	15.0	0.65	2.6	0.36	0.84	0.01	0.010	0.006
0.006C-16Cr-15Ni-3Mo-Nb	0.006	15.5	15.2	0.5	2.5	0.32	0.65	0.008	0.006	-

Experimental Results

Figures 1 and 2 show the dependence of maximum complete deformation in 0.046C-16Cr-15Ni-3Mo-Nb and 0.006C-16Cr-15Ni-3Mo-Nb steels on fast neutron fluence and stress. In this case the maximum complete deformation is responsible for irradiation swelling and creep. As a rule, the deformation dependence of steels on neutron fluence is linear. The deformation creep of steel specimens irradiated up to neutron fluence of $21.8*10^{26}$ m^{-2} (E>0.1 MeV) at 420 °C does not practically depend on carbon content. Creep-stress dependence was shown to have some anomaly along with usual deformation increasing with growing of stress. There was observed some decreasing of the creep deformation with increasing stress in the intermediate range (100-150 MPa) at 140 MPa for type 0.046C-16Cr-15Ni-3Mo-Nb and at 120 MPa for type 0.006C-16Cr-15Ni-3Mo-Nb, respectively (Fig. 2).

The creep-stress dependence on fluence for three steels different in carbon and boron content are presented in Fig. 3. The deformation of boron-containing steel 0.06C-16Cr-15Ni-3Mo-Nb-B is considerably less than that of two steels (0.046C-16Cr-15Ni-3Mo-Nb and 0.006C-16Cr-15Ni-3Mo-Nb) available the different carbon content.

The swelling-fluence dependence was also obtained for three steels when studying the specimens without stress (Fig. 4). The rate of swelling for specimen without stress at temperature 420 °C is following:

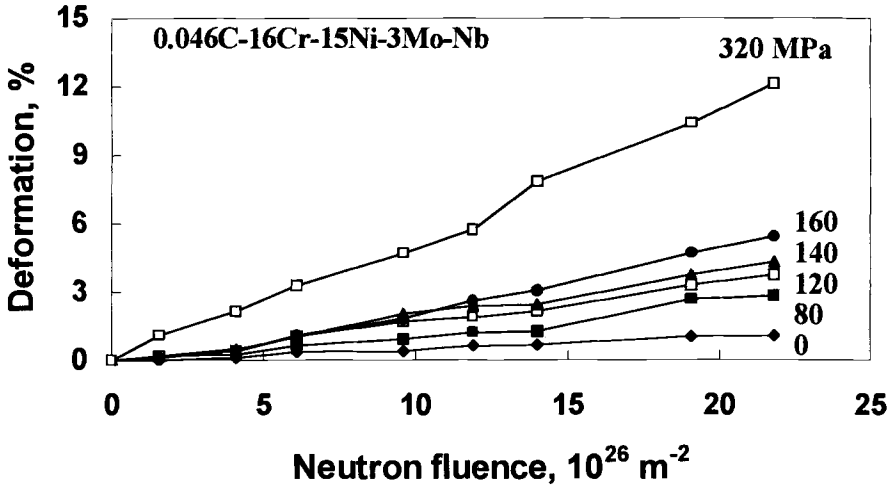
0.012 %/dpa (Type 0.06C-16Cr-15Ni-3Mo-Nb-B),
0.034 %/dpa (Type 0.046C-16Cr-15Ni-3Mo-Nb),
0.052 %/dpa (Type 0.006C-16Cr-15Ni-3Mo-Nb).

Discussion

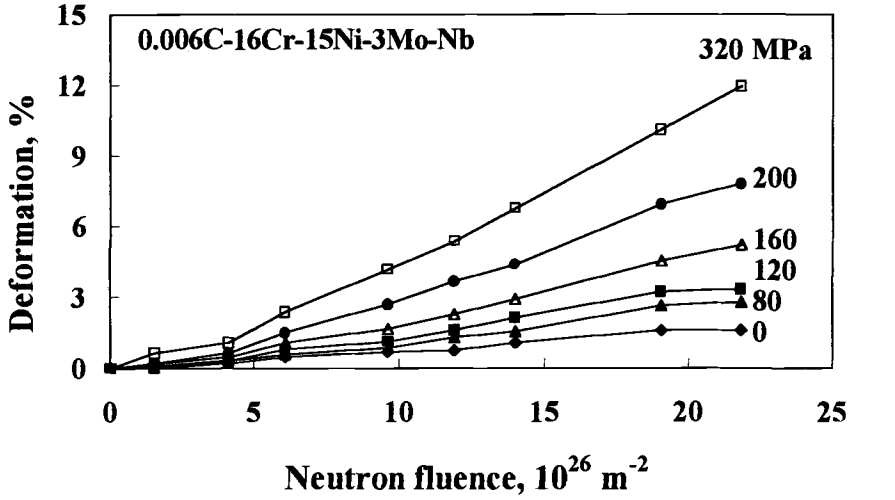
In study of irradiation-induced creep in the temperature range of swelling, the deformation of pressurized specimens is usually defined by an equation of the form [1-4, 8-12, 16]

$$\varepsilon/\sigma = B(\sigma) = B_o + D_x S, \qquad (1)$$

where ε - unsteady state (current) creep,
σ - effective stress ($\sigma=\sqrt{3}/2\ \sigma_o$),
$B(\sigma)$ -unsteady state (current) creep coefficient,
B_0 - swelling undependent creep coefficient,
D - pair coefficient of swelling and creep correlation,
S - current swelling rate.

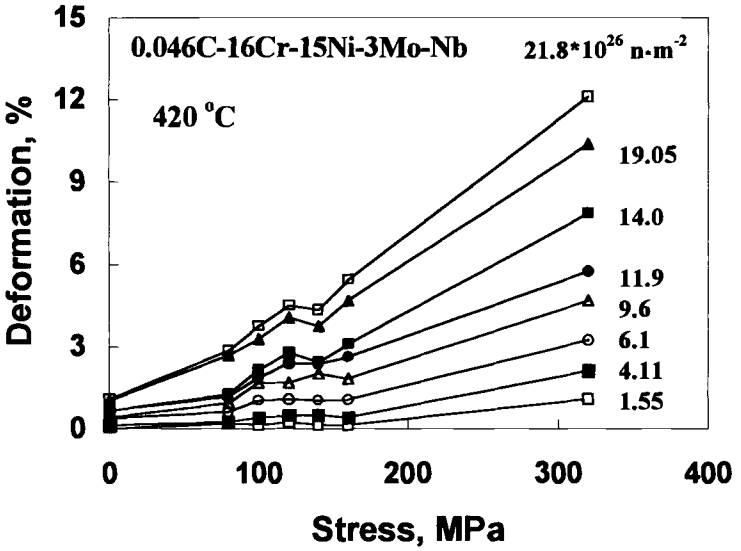


a

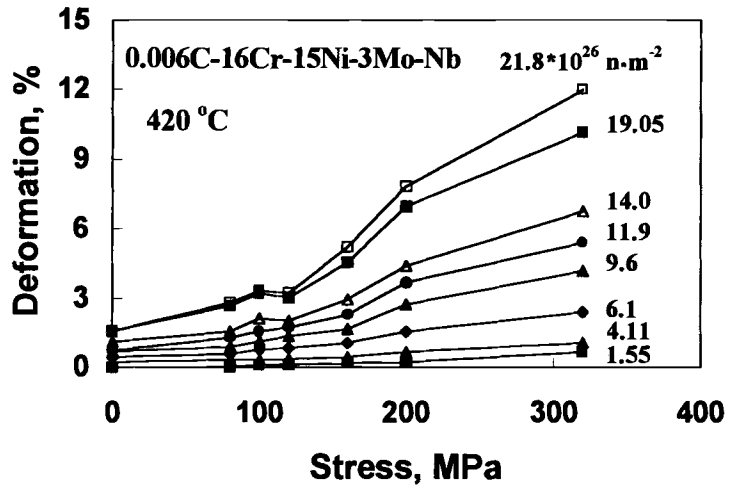


b

FIG. 1 - *Creep deformation on austenized steels 0.046C-16Cr-15Ni-3Mo-Nb (a) and 0.006C-16Cr-15Ni-3Mo-Nb (b) as a function of fast neutron fluence.*



a



b

FIG. 2 - *Creep deformation on austenized steels 0.046C-16Cr-15Ni-3Mo-Nb (a) and 0.006C-16Cr-15Ni-3Mo-Nb (b) as a function of stress, irradiated in BOR-60 reactors.*

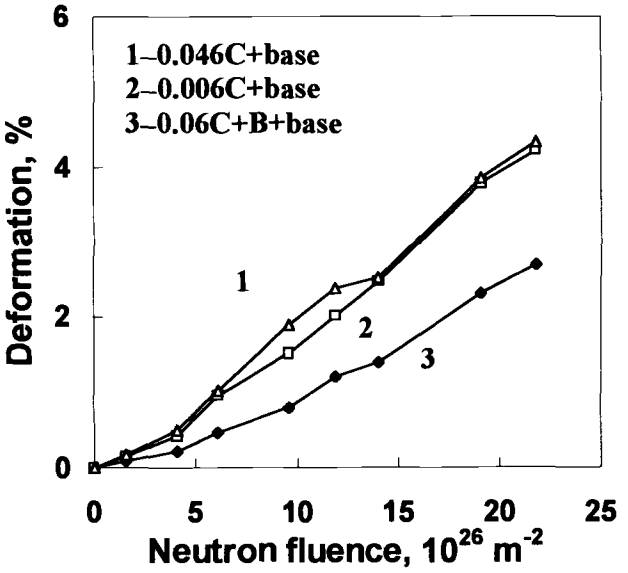


FIG. 3 - *Creep deformation of austenized steels on the base of 16Cr-15Ni-3Mo-Nb as a function of fast neutron fluence (stress 140 MPa).*

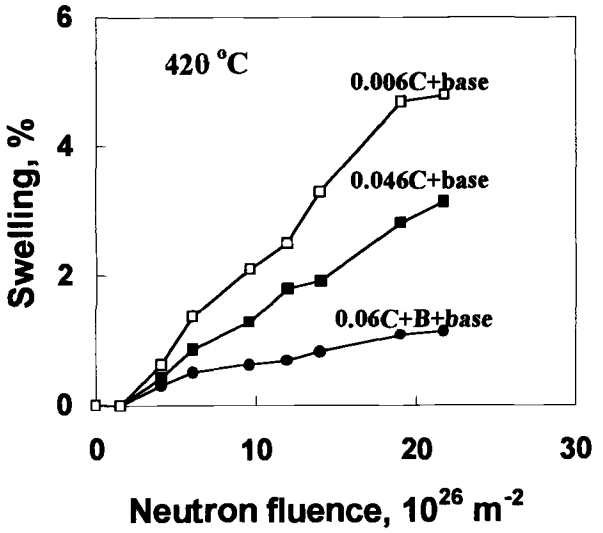


FIG. 4 - *Swelling of austenized steels on the base of 16Cr-15Ni-3Mo-Nb as a function of fast neutron fluence.*

The results of creep for the austenitic stainless steels showed that the creep process is defined by the equation (1) available poorly changed coefficients B_o and D in spite of complex character of variation in the current creep coefficient with fluence [8,14]. For example, the coefficient B_o is equal to about 1×10^{-6} $(MPa\times dpa)^{-1}$ for the austenitic stainless steels, while the coefficient D is changing in the interval $(0.6\text{-}1.0)\times10^{-2}$ MPa^{-1}.

The measurement of creep deformation on steels allowed to plot the creep modulus as a function of fluence (Fig. 5 - 6). One can see that the averaged modulus value is equal to about 1×10^{-6} $(MPa\times dpa)^{-1}$ at zero fluence and the range of stress from 80 to 160 MPa for all three steels. However at neutron fluence 1.55×10^{26} m^{-2} when the swelling rate is still equal to zero, the creep modulus B_o for the different steels is equal to:

0.06C-16Cr-15Ni-3Mo-Nb-B: 1.0×10^{-6} $(MPa\times dpa)^{-1}$ (at 136 MPa),
0.046C-16Cr-15Ni-3Mo-Nb: 1.7×10^{-6} $(MPa\times dpa)^{-1}$ (at 80-160 MPa),
0.006C-16Cr-15Ni-3Mo-Nb: 1.4×10^{-6} $(MPa\times dpa)^{-1}$ (at 80-160 MPa).

Particular emphasis should be placed upon the dependence of creep modulus of 0.046C-16Cr-15Ni-3Mo-Nb steel on neutron fluence in the beginning part (Fig.7) of irradiation in different reactors. At the first moment of irradiation the creep modulus is rather high in steels irradiated in the BOR - 60 reactor at the high stress value 320 MPa. At other stresses (80-250 MPa) at the first moment of irradiation in the SM reacror (from 3 to 140×10^{-9} dpa/s) the creep modulus decreases [17]. With increasing fluence the modulus decreases, reaching the values specific to other stresses. The low values of initial yield stress for steel free of boron and high relative stress result in high creep modulus in the beginning of irradiation. At high stress there is observed a fast rebuilding of dislocation structure, sharp increase of dislocation concentration and material strengthening. Above the neutron fluence of 9×10^{26} m^{-2} the characteristics of strength became similar in specimens with the different stress and for this reason the modulus of creep take the closely spaced values.

The obtained results of the creep modulus allow us to determine the coefficients of pair correlation of swelling and creep D. For investigated steels it became equal to:

0.06C-16Cr-15Ni-3Mo-Nb-B: 1.02×10^{-2} MPa^{-1} (136 MPa)
0.046C-16Cr-15Ni-3Mo-Nb: 0.47×10^{-2} MPa^{-1} (140 MPa)
and 0.65×10^{-2} MPa^{-1} (80-160 MPa),
0.006C-16Cr-15Ni-3Mo-Nb: 0.33×10^{-2} MPa^{-1} (140 MPa)
and 0.44×10^{-2} MPa^{-1} (80-160 MPa).

It is possible that the D depends on the swelling rate. The less the swelling rate, the more the modulus D. The values of coefficients B_o and D obtained for BOR-60 reactor irradiated steels on the basis of 16Cr-15Ni-3Mo-Nb with different carbon and boron content $(0.33\text{-}1.02)\times10^{-2}$ MPa^{-1} were seen to be in well agreement with the coefficients determined for Type AISI 316, AISI 304L, PCA austenitic steels in the various structural compositions [8-12, 14, 15].

Conclusion

On the beginning stage of specimens irradiation with high stress and low initial strength it was observed the abnormal increasing of the creep modulus depend on the content of carbon and boron.

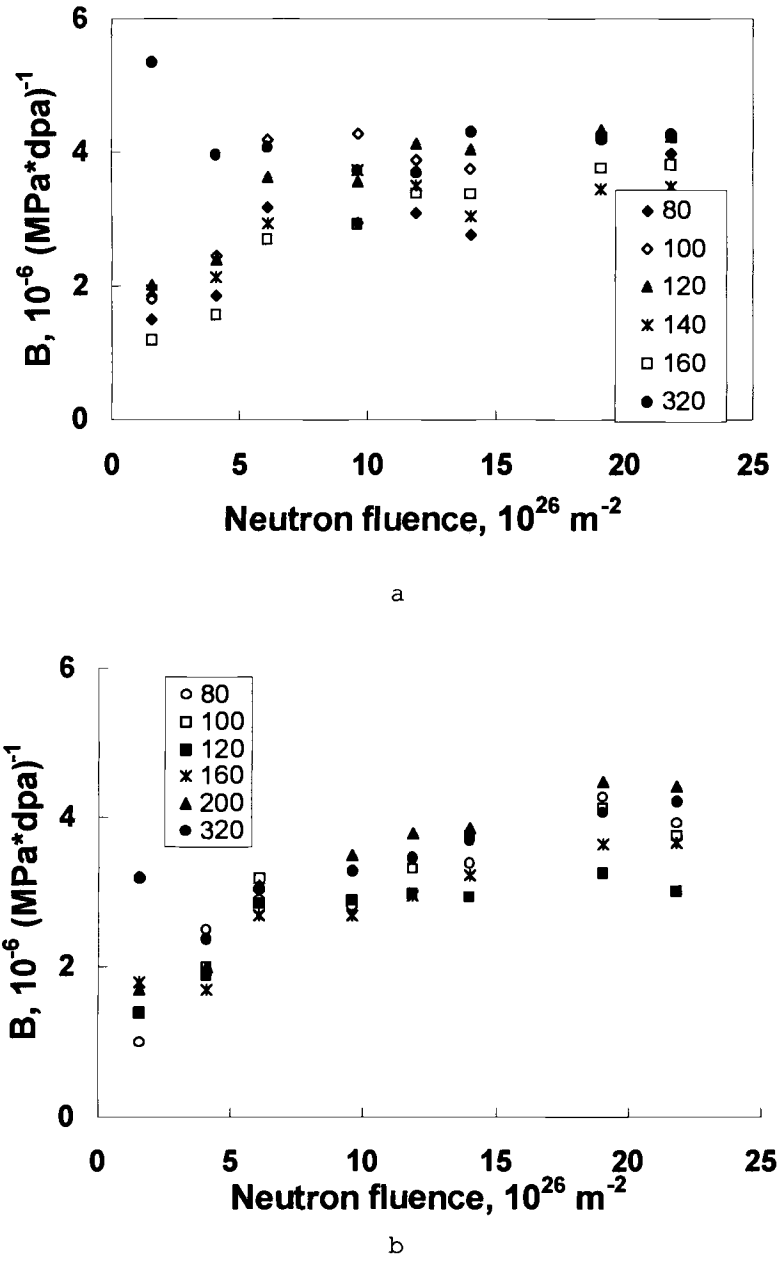


FIG. 5 - *Creep modulus of austenized steels 0.046C-16Cr-15Ni-3Mo-Nb (a) and 0.006C-16Cr-15Ni-3Mo-Nb (b) as a function of fast neutron fluence at different stresses.*

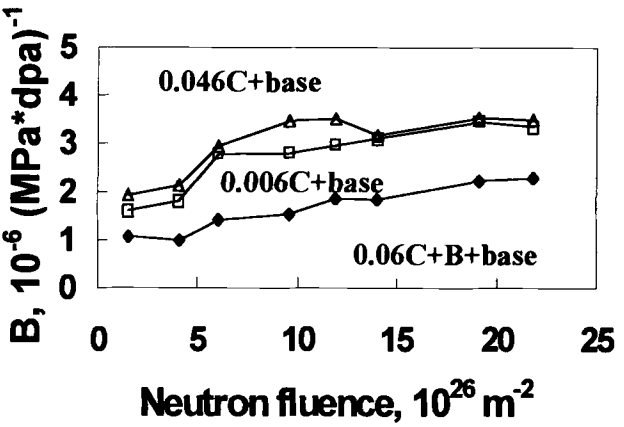


FIG. 6 - *Creep modulus of austenized steels on the base of 16Cr-15Ni-3Mo-Nb different with carbon and boron content as a function of fast neutrons at 140 Mpa.*

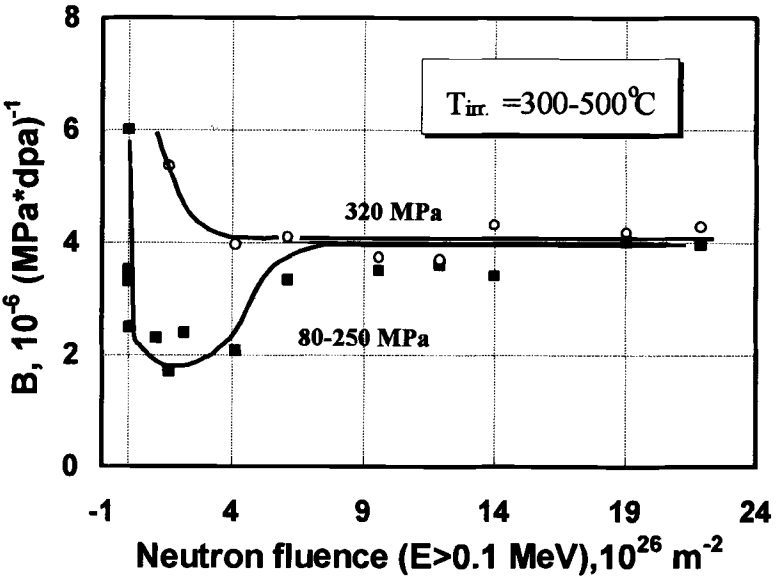


FIG. 7 - *Creep modulus of austenized steels 0.046C-16Cr-15Ni-3Mo-Nb as a function of fast neutron fluence at various stresses irradiated in different reactors.*

The swelling rate of pressurized specimens on the basis of 16Cr -15Ni -3Mo-Nb steel was decreasing with increasing the carbon and boron content under irradiation up to fluence 21.8×10^{26} m^{-2} (E>0.1 MeV) at temperature 420 °C.

The rate of irradiation creep on investigated steels was rather exactly defined by the equation (1) at the values of B_0 and D coefficients 1×10^{-6} $(MPa \times dpa)^{-1}$ and $(0.3\text{-}1.02) \times 10^{-2}$ MPa^{-1}, respectively. The coefficients are in well agreement with similar coefficients of other austenitic steels.

References

[1] Ehrlich K., "Irradiation Creep and Interrelation with Swelling in Austenitic Stainless Steels," *Journal of Nuclear Materials*, Vol.100, 1981, pp.149-153.

[2] Foster, J.P., Wolfer, W.G., Biancheria, A. and Boltax, A., *Proceedings European Conference on Irradiation Embrittlement and Creep in Fuel Cladding and Core Components*, London, 1972, p.273.

[3] Bergmann, H.J., Haas, D. and Herschbach, K., *Proceedings International Conference on Radiation Effects in Breeder Reactor Structural Materials*, Scottsdale, AZ, 1977, p.241.

[4] Straalsund, J., "Irradiation Creep in Breeder Reactor Materials," *Proceedings International Conference on Radiation Effects in Breeder Reactor Structural Materials*, Scottsdale, AZ, 1977, p.191.

[5] Krasnoselov, V.A., Kolesnikov, A.N., Prokhorov, V.I. et al. "Experimental Study of Irradiation Creep of Austenitic Stainless Steels," *Preprint RIAR - 16(469)*, Dimitrovgrad, 1981, 28 p.

[6] Tsykanov, V.A., Reshetnikov, F.G., Shamardin, V.K. i dr. "Radiatsyonnye Issledovaniya Konstruktsionnyh Materialov, Obluchehhyh v Reaktore BOR-60," *Voprocy atomnoy nauki i texniki. Ser.:Atomnoe materialovedenie*, Vol.1(18), 1985, pp. 45-53.

[7] Shamardin, V.K., Neustroev, V.S., Golovanov, V.N. et al "Irradiation Creep and Swelling of 16Cr-15Ni-3Mo-Nb and Its Modification 16Cr-15Ni-3Mo-Nb-B Steel," *Effects of Radiation on Materials: 14th International Symposium (Volume 2), ASTM STP 1046*, N.H.Packan, R.E.Stoller and A.S.Kumar, Eds., American Society for Testing and Materials, Philadelphia, 1990, pp. 753-765.

[8] Garner, F.A., Porter, D.L. and Makenas, B.J., *Journal of Nuclear Materials*, 1987, Vol.148, p.279.

[9] Garner, F.A. and Porter, D.L., *Journal of Nuclear Materials*, 1988, Vol.155-157, p.1006.

[10] Porter, D.L. and Garner, F.A., *Journal of Nuclear Materials*, 1988, Vol.159, p.114..

[11] Garner, F.A., Porter, D.L. and Hudman, G.D. *Radiation Material Science (Proceedings of the International Conference on Radiation Material Science, Alushta, SU)*, Vol.1, Kharkov, 1990, p.68.

[12] Garner, F.A., and Puigh, P.J. *Proceedings International Conference on Radiation Effects in Breader Reactor Structural Materials*, Scottsdale, AZ 1977, p.75.

[13] Neustroev, V.S., Shamardin, V.K., Ohzigov, L.S. "Vlijanie Naprjahzenija na Radiatsionnuyu Polzuchest i Raspukhanie Stali Tipa 16Cr-15Ni-3Mo-Nb," *Voprosy atomnoy nauki i tekhniki. Ser.:FRP i RM*, Vol. 1(52), 1990, pp.20-25.

[14] Porter, D.L., Wood, E.L. and Garner, F.A. "Influence of Thermomechanical Treatment and Environmental History on Creep, Swelling and Embrittlement of AISI 316 at 400 °C and 130 dpa," *Effects of Radiation on Materials: 14th International Symposium, ASTM STP 1046, (Volume2)*, N.H.Packan, R.E.Stoller, and A.S.Kumar, Eds., American Society for Testing and Materials, Philadelphia, 1990, pp. 551-569.

[15] K.Herschbach, W.Schneider and H.J.Bergmann "Swelling and In-Pile Creep Behavior of Some 15Cr15NiTi Stainless Steel in the Temperature Range 400 to 600 °C," ibid [14], pp.570-587.

[16] Neustroev, V.S., Shamardin, V.K. "Radiation Creep and Swelling of Austenitic 16Cr-15Ni-3Mo-Nb Steel Irradiated in the Reactor BOR-60 at 350 and 420 °C," *Effects of Radiation on Materials: 16th International Symposium, ASTM STP 1175*, A.S.Kumur, R.K.Nanstad, and E.A.Little, Eds., American Society for Testing and Materials, Philadelphia, 1993, pp.816-823.

[17] Neustroev, V.S., Shamardin, V.K. "Interrilation Between Radiation Effects in Irradiated Austenitic Steel," *Proceedings of the 5th Russia Conference on Reactor Material Science, (Dimitrovgrad, 8-12 September 1997)*, Dimitrovgrad, 1998, Vol. 2, Part 1, pp. 270-282.

M. B. Toloczko[1] and F. A. Garner[1]

Reanalysis of Swelling and Irradiation Creep Data on 316 Type Stainless Steels Irradiated in the FFTF and Phénix Fast Reactors

Reference: Toloczko, M. B. and Garner, F. A., **"Reanalysis of Swelling and Irradiation Creep Data on 316 Type Stainless Steels Irradiated in the FFTF and Phénix Fast Reactors,"** *Effects of Radiation on Materials: 19th International Symposium, ASTM STP 1366,* M. L. Hamilton, A. S. Kumar, S. T. Rosinski, and M. L. Grossbeck, Eds., American Society for Testing and Materials, West Conshohocken, PA, 2000.

Abstract: In comparing results of irradiation creep experiments conducted by researchers in France and those by researchers at Pacific Northwest National Laboratory in the United States, quite different values for the creep-swelling coupling coefficient were reported. The differing coefficients complicated the understanding of the growing data base on irradiation creep. However, upon careful consideration, the French and US results showed key differences in experimental technique and analysis. The French and US irradiation creep experiments were conducted with several important differences that were initially thought to be of little consequence. One difference was related to whether stress-free swelling or stress-enhanced swelling was measured and used in calculating the creep strains. Inspection of irradiation creep results published by the French also showed their technique for extracting the creep-swelling coupling coefficient was different than that used by the present authors. In an effort to better understand the origin of the differing creep coefficients, data from the French and US experiments was reanalyzed taking into account these differences. In performing this reanalysis, completely consistent results were obtained.

Keywords: austenitic steels, irradiation creep, swelling, creep coefficients

Background

One of the most successful methods for studying irradiation creep has been the pressurized tube technique. In this technique, a thin-walled tube is capped at both ends with one cap containing a tiny hole which is used to pressurize the tube. After pressurization with an inert gas, the hole is welded closed with a laser [1]. Away from the end caps, the stress state in the tube wall is nearly biaxial, with the axial stress equal to half the hoop stress. For pure deviatoric creep strain, i.e. no swelling, the stresses remain nearly constant because the pressure drop due to an increase in the tube volume is

[1] Graduate student and Senior Staff Scientist respectively, Pacific Northwest National Laboratory, Richland, WA 99352.

Copyright© 2000 by ASTM International www.astm.org

compensated almost exactly by thinning of the tube wall [2]. Creep strains are estimated from changes in the outer wall diameter of a pressurized tube.

Several research groups, including those in France and those at Pacific Northwest National Laboratory (PNNL) in the United States, have used pressurized tubes to study irradiation creep [2-14]. In most cases, the data have been analyzed in the context of the well-known $\dot{\bar{\varepsilon}}/\bar{\sigma} = B_0 + D\dot{S}$ creep equation. $\dot{\bar{\varepsilon}}$ is the effective (and thus deviatoric) creep rate. The creep compliance, B_0, is a constant which represents the stress-normalized creep rate in absence of swelling. D is the creep-swelling coupling coefficient and represents a contribution to the (deviatoric) creep rate which occurs when the material swells. This equation has been popular because it is founded on simple microstructural based creep models [15]. Several creep models lead to the same equation [15].

In recent years, it has become obvious that these models inadequately represent the contribution to creep that occurs when void swelling occurs [2, 15-18]. The reason is due, in part, to the models not accounting for stress-enhanced swelling. More importantly, the models fail to predict "creep cessation" as defined by Garner and coworkers [17], and thus, the models are somehow inadequate in one or more as yet unidentified ways. The creep equation, nevertheless, continues to be used, partly because it allows comparison with data already examined using this equation, and partly because a suitable replacement does not yet exist.

Creep Coefficient Calculations

Selected US Irradiation Creep Studies

Extraction of the creep coefficients from the experimental data can be done in several ways, with the method often dictated by the amount of creep and swelling data available. For pressurized tube creep studies performed by the present authors, swelling is measured from the diameter change of a stress-free tube irradiated side-by-side with a group of stressed tubes, each having a different stress. The effect of stress on swelling is usually ignored in this method, and the swelling in the stressed tubes is assumed to be equal to the swelling in the stress-free tube. Creep strain is calculated by subtracting the "linear" swelling strain of the stress-free tube from the total diametral strain of a stressed tube. This outer wall deviatoric hoop strain is converted to a midwall (i.e. average) deviatoric hoop strain using a multiplicative factor of the order of 1. The multiplicative factor varies with tube wall thickness and tube diameter. Typical plots for stress-free volumetric swelling and midwall creep strains are shown in Figure 1, which shows previously unpublished data on a 20% cold-worked titanium-modified 316 stainless steel (D9 Heat 83508) that was irradiated in the Fast Flux Test Facility (FFTF) at ~400°C to about 65 dpa.

Using the type of data shown in Figure 1, swelling rates and creep rates are often calculated by finding the slope of a straight line between data points. The creep equation

$$B = \frac{\dot{\bar{\varepsilon}}}{\bar{\sigma}} = B_0 + D\dot{S} \qquad (1)$$

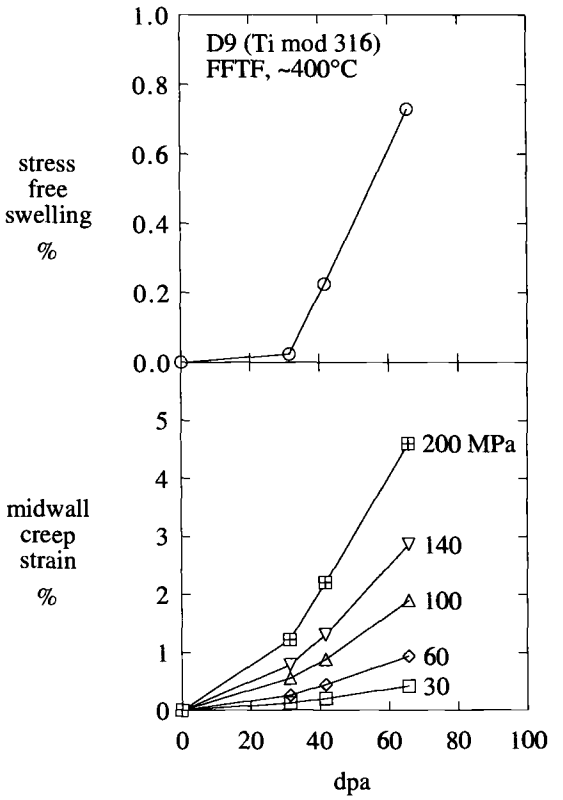


Figure 1 -- *Volumetric stress-free swelling and midwall creep strains calculated from diameter change measurements of pressurized tubes irradiated in FFTF. Stresses indicated are hoop stresses.*

is used to calculate the creep coefficients from the midwall strain and the hoop stress. Since there are two unknowns (B_o and D), the creep coefficients cannot be calculated from a single irradiation interval. If empirical parametric equations are used to describe creep and swelling, the creep coefficients may be derived using a least squares curve fitting procedure [3]. Since the $\dot{\bar{\varepsilon}}/\bar{\sigma} = B_o + D\dot{S}$ creep model only adequately represents irradiation creep over a narrow range of conditions where the swelling rate is much less than 1%/dpa and the effect of stress on swelling is small, curve fitting has only limited application. More insight into the nature of swelling and creep is gained when the creep coefficients are calculated by using a simple "two equations for two unknowns" method. Based on the following notation

$$B_i = B_o + D\dot{S}_i \tag{2}$$

where "i" refers to the ith irradiation interval, B_o was found from

$$B_o = \frac{B_i\dot{S}_j - B_j\dot{S}_i}{\dot{S}_j - \dot{S}_i}. \tag{3}$$

Likewise, D was calculated from

$$D = \frac{B_j - B_i}{\dot{S}_j - \dot{S}_i}. \tag{4}$$

Often, little if any swelling occurs in stainless steels during the first irradiation cycle, and B_o is found from

$$B_o = B_1, \tag{5}$$

and for any of the subsequent irradiation cycles, D may be found from

$$D_i = \frac{B_i - B_o}{\dot{S}_i} \tag{6}$$

where $i > 1$. In this latter method, D is calculated for each interval on the curve except the first. This process is applied to each stressed tube in a tube-set. If materials exactly obeyed the $B_o + D\dot{S}$ creep equation where D is defined to be a constant, then each D_i would be identical. In general, D is not a constant and has been observed to fall with increasing swelling rate, and thus materials do not strictly obey the $B_o + D\dot{S}$ creep equation.

B_o and D can be expressed graphically by plotting $\dot{S}_i$ versus B_i ($4\dot{\varepsilon}_{m,i}/3\sigma_h$). The result, as shown in Figure 2a for the Ti-modified 316 SS from Figure 1, is a set of straight lines with y-axis intercept equal to B_o and slope equal to D. There is a separate line for each D_i. Shown in Figure 2b are the D_i coefficients (slopes of lines in Figure 2a) plotted versus swelling rate. In this plot, it can be more easily seen that D varies from ~1-2x10^{-2} MPa^{-1}, and that D increases with increasing stress. The increase in D with stress is thought to be a consequence of stress-enhanced swelling being masked by the swelling estimate technique used in creep experiment where only stress-free swelling was measured.

Selected French Irradiation Creep Studies

A group of French researchers have also used pressurized tubes to study irradiation creep [7-9]. However, their experiments were conducted in a somewhat different manner. Pressurized tubes were welded together end-to-end to form a long pin with the dimensions of a fuel pin†. Groups of these pins were irradiated together to form a complete irradiation experiment. Several redundant sets of tubes (the exact redundancy

† Personal communication between F.A. Garner and J.-L. Séran.

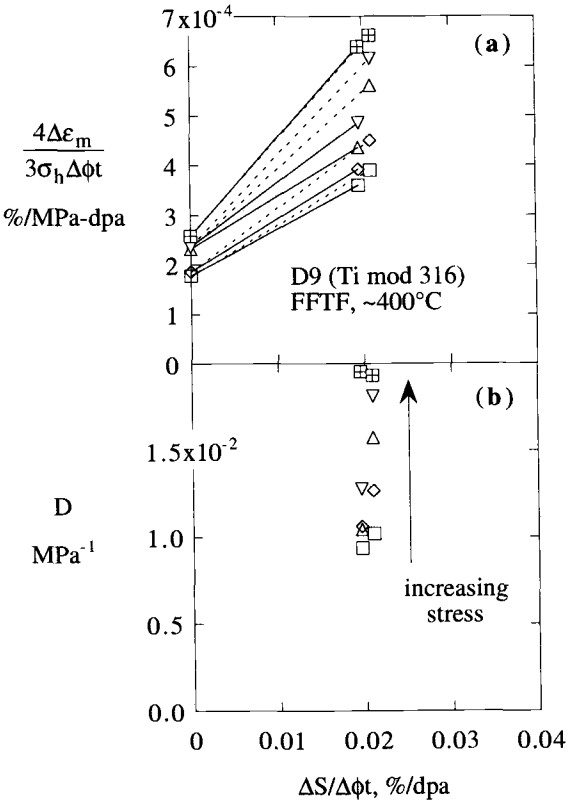


Figure 2 -- *a) The creep compliance, $4\Delta\varepsilon_m/3\sigma_h\Delta\phi t$, plotted versus the swelling rate for a Ti-modified 316 SS irradiated in FFTF at ~400°C. The y-axis intercept is B_o and the slope of a line is D. Solid lines represent the first irradiation interval while dotted lines represent the second irradiation interval. Plot symbols are defined in Figure 1. b) Derived values of D versus swelling rate for the same material. In this treatment, D ranges from ~1-2x10^{-2} MPa^{-1} and increases with increasing stress. The dependence on stress is thought to be a consequence of the swelling estimate technique used in this experiment.*

is unknown to the current authors) with a range of stresses were irradiated at each target irradiation temperature. The arrangement of stress levels along a pin, the irradiation temperature profile along a pin, and dose rate profile along a pin were not available to the current authors, however, so it is unclear if side-by-side irradiations were performed. In the French experiments, swelling of the stressed tubes was directly measured by density measurement. This technique requires that the measured tube be sacrificed. Because of the redundancy in tube-sets at each target temperature, swelling data at several fluences could be obtained. Such experiments have been enormously valuable as they have shown

conclusively that stress enhanced swelling is real and significant in austenitic stainless steels at moderate irradiation temperatures. Earlier work had suggested that stress-enhanced swelling was largely confined to higher irradiation temperatures [19].

The French researchers used a method similar to that described in the previous section to plot the creep coefficients. Some of their results, reproduced from a study of cold-worked Ti-modified 316 SS, are shown in Figure 3 [7]. Examination of the plots showed the creep compliance, B_o, to be 1-1.5x10^{-6} %/MPa-dpa which is similar to that typically observed in 316 SS and Ti-modified 316 SS [3, 5, 14]. From the slope of the line fit to the data points in Figure 3b, the creep-swelling coupling coefficient, D, was found to be ~0.15x10^{-2} MPa^{-1}. This value was much lower than previously observed values of ~0.5-1.0x10^{-2} MPa^{-1} by the authors of this paper and has stimulated much discussion on the possible origins of the discrepancy.

Reanalysis

French Irradiation Creep Studies

In an effort to understand the origin of the discrepancy, the analysis focused initially on the French research. Because their experiments were run differently from the U.S. experiments presented here, swelling and creep rates were measured as average values over all irradiation intervals up to the measurement rather than over each individual irradiation interval. Thus, the average swelling rate was calculated from

$$\dot{S}_i = \frac{S_i}{\phi t} \tag{7}$$

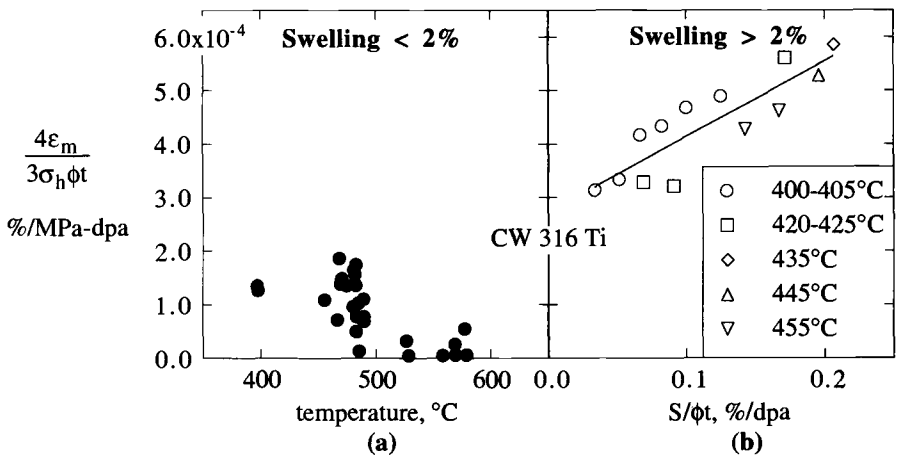


Figure 3 -- *Stress normalized creep rate plotted versus temperature for swelling < 2% and plotted versus average swelling rate for swelling > 2% [7]. Based on these data, B_0 is ~1.25x10^{-6} MPa^{-1} dpa^{-1} for temperatures less than 460°C, and D is ~0.15x10^{-2} MPa^{-1}.*

where in this instance, S_i is the total swelling of the sacrificed tube, and ϕt is the dose the tube received at the time of the swelling measurement. Because of the very large swelling incubation period that often occurs in Ti-modified austenitic steels, this technique invariably results in an underestimate of both the swelling and creep rates once swelling has begun.

A closer examination of their experimental analysis also revealed that the French had been analyzing their data in a manner slightly different than that described in the previous section. The French had assumed that beyond a certain amount of swelling, here assumed to be 2%, the $D\dot{S}$ contribution to irradiation creep was much greater than the B_o contribution. As a result, D was estimated from the equation

$$D_i = \frac{B_i}{\dot{S}_i} \tag{8}$$

Based on this approach, the French took D to be the slope of the line depicted in Figure 3b. In examining this approach and their experimental results, it was determined that B_o was still making a significant contribution to irradiation creep when swelling was greater than 2%. After recognizing the importance of the difference in data analysis between the present authors and the French researchers, the French data in Figure 3b were replotted based on the equation

$$D_i = \frac{B_i - B_o}{\dot{S}_i}. \tag{9}$$

To plot the results with this equation, a value for B_o was required, and this value was chosen from Figure 3a. Recalling that the creep data in Figure 3b were derived at temperatures less than 460°C, a corresponding average B_o was selected from the data in Figure 3a for temperatures also less than 460°C. This B_o value was found to be 1.25×10^{-6} MPa^{-1} dpa^{-1}. The resulting plot using Equation 9 is shown in Figure 4a. As before, the slope of a line represents D, but here the values range from 0.6×10^{-2} to 0.2×10^{-2} MPa^{-1}. The decreasing values of D are a result of the now well known phenomenon of creep cessation [17] and stress enhanced swelling [10, 19-21]. The fall in D with increasing swelling rate is shown in Figure 4b where D is plotted versus $S/\phi t$.

US Irradiation Creep Studies

The fall in D can be observed in the French data because creep and swelling in the stressed tubes were separated by measuring the true swelling in the stressed tubes rather than estimating the swelling using stress-free tubes as done in the US experiments. In an effort to compare US and French results on an equivalent basis, an analytical method was developed to estimate stress enhanced swelling in stressed tubes where the swelling has not been directly measured [2]. The method is based on the assumption that for reasonably low stresses, irradiation creep is linearly proportional to the applied stress. In many of the irradiation creep data sets analyzed by the present authors, irradiation creep was observed to be non-linear with stress at low stresses. Its was concluded that this non-linearity was due to stress-enhanced swelling which could not be subtracted from the

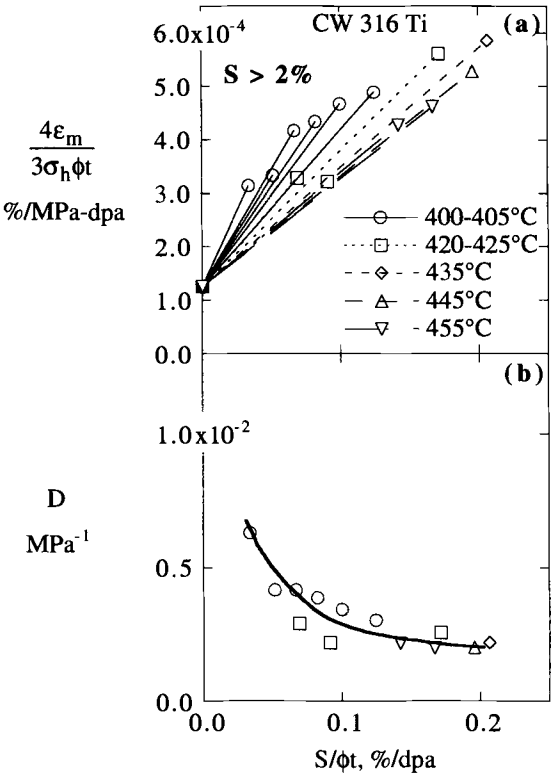


Figure 4 -- *a) Replot of results from Figure 3. B_0 was determined from Figure 3a for irradiation temperatures less than 460°C. Here, D ranges from $0.6x10^{-2}$ to $0.2x10^{-2}$ MPa^{-1}. b) Derived values of D versus S/φt for the data in a).*

total strains of a stressed tube using the US technique. By assuming a linear relationship between the irradiation creep rate and stress, stress-enhanced swelling could be deduced and removed from the total strains by using the lowest stress tube as a reference point. For further details, see [2].

For comparison with the Ti-modified 316 SS studied by the French, the US Ti-modified 316 SS shown in Figures 1 and 2 was reexamined using this method for estimating stress enhanced swelling. The results where then plotted using the same method used to replot the French data. The results are shown in Figure 5. The behavior of B and D versus $\dot{S}$ is very similar to that observed in the French irradiation creep data sets.

Once the origin of the apparent discrepancy in creep coefficients was recognized, it then became apparent that many other apparently divergent facets of irradiation creep behavior could be reconciled. For instance, in the PNNL studies, D was found to be independent of all variables except the swelling rate, while in the French studies, D

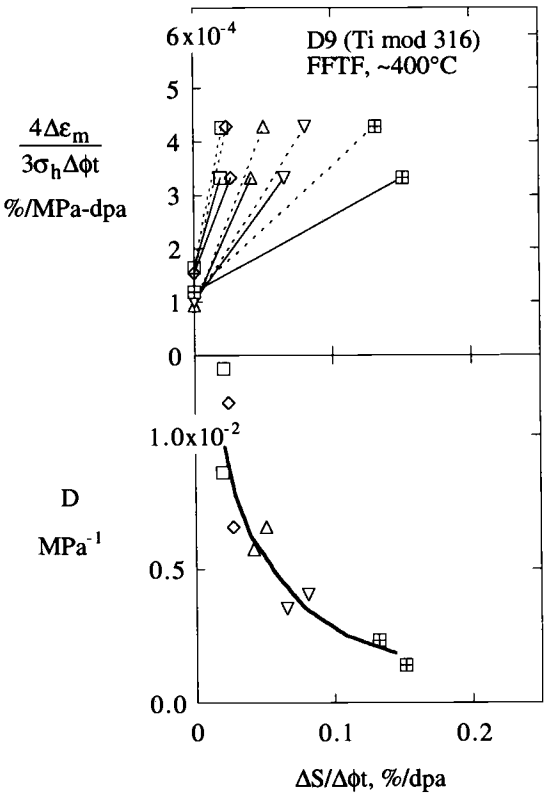


Figure 5 -- *The creep compliance, $4\Delta\varepsilon_m/3\sigma_h\Delta\phi t$, and D plotted versus* S *for 20% CW D9 pressurized tubes irradiated in FFTF at ~400°C. Solid lines represent the first irradiation interval while the dotted lines represent the second irradiation interval. Plot symbols are defined in Figure 1.*

initially appeared to be dependent on thermomechanical starting state, irradiation temperature, and alloy composition. In reality, these variables affected only the swelling and thereby the derived D coefficient. These and other consequences of creep cessation and the creep-swelling relationship are covered in detail by Garner in Ref. [16].

Conclusions

Pressurized tubes constructed from a Ti-modified 316 SS were irradiated by French researchers while other pressurized tubes constructed from another Ti-modified 316 SS were irradiated by the present authors under irradiation conditions similar to that of the French experiment. Initial comparison of the French and US results suggested that the wo Ti-modified 316 SS alloys had different creep-swelling coupling coefficients.

However, key differences in experimental technique and analysis were identified when the French and US results were compared more closely. It was observed that the French had been calculating the creep-swelling coupling coefficient, D, without accounting for B_o in their calculations. This resulted in an artificially low estimate of D. US irradiation creep experiments performed at Pacific Northwest National Laboratory have traditionally been limited by access to only stress-free swelling data which resulted in an artificially high estimate of D. In compensating for the differences in these two experiments, it was found that values for D obtained from French and US irradiation creep experiments were in remarkably good agreement. In demonstrating that the creep data from French and US studies are consistent, this study has brought together two apparently inconsistent parts of the irradiation creep data base.

Before reanalysis, both these experiments suggested that D was a constant, but after reanalysis, these data sets now, in fact, support the proposal that D is not a constant and instead, falls with increasing swelling rate. This result suggests that the entire irradiation creep database may support the proposal the D is not a constant.

In effect, comparison of the two experiments has improved the interpretation of both experiments and has also enhanced our perception of the relationship between void swelling and irradiation creep.

References

[1] Gilbert, E.R., and Chin, B.A., "In-Reactor Creep Measurements", *Nuclear Technology*, Vol. 52, Feb. 1981, pp. 273-283.

[2] Toloczko, M. B., and Garner, F. A., "Relationship Between Swelling and Irradiation Creep in Cold-Worked PCA Stainless Steel Irradiated to ~178 dpa at ~400°C", *Journal of Nuclear Materials*, Vols. 212-215, 1994, pp. 509-513.

[3] Toloczko, M.B., Garner, F.A., and Eiholzer, C.R., "Determination of the Creep Compliance and Creep-Swelling Coupling Coefficient for Neutron Irradiated Titanium-Modified Stainless Steels at ~400°C", *Journal of Nuclear Materials*, Vols. 191-194, 1992, pp. 803-807.

[4] Garner, F.A., Hamilton, M.L., Eiholzer, C.R., Toloczko, M.B., and Kumar, A.S., "Influence of Cold Work on the Irradiation Creep and Creep Rupture of Titanium Modified Austenitic Stainless Steel", *Effects of Radiation on Materials: 16th International Symposium*, ASTM STP 1175, A.S. Kumar, D.S. Gelles, R.K. Nanstad, and E.A. Little, Eds., American Society for Testing and Materials, Philadelphia, PA, 1994, pp. 696-713.

[5] Grossbeck, M.L., Mansur, L.K., and Tanaka, M.P., "Irradiation Creep in Austenitic Stainless Steels at 60 to 400°C with a Fusion Reactor Helium to dpa Ratio", *Effects of Irradiation on Materials: 14th International Symposium (Volume II)*, ASTM STP 1046, N.H. Packan, R.E. Stoller, and A.S. Kumar, Eds., American Society for Testing and Materials, Philadelphia, PA, 1990, pp. 537-550.

[6] Gilbert, E.R., and Blackburn, L.D., "Creep Deformation of 20 Percent Cold-Worked Type 316 Stainless Steel", *Journal of Engineering Materials and Technology*, Vol. 99, April 1977, pp. 168-180.

[7] Séran, J.-L., Touron, H., Maillard, A., Dubuisson, P., Hugot, J. P., Le Boulbin, E., Blanchard, P., and Pelletier, M., "The Swelling Behavior of Titanium-Stabilized Austenitic Steels Used as Structural Materials for Fissile Subassemblies in Phénix", *Effects of Radiation on Materials: 14th International Symposium (Volume II)*, ASTM STP 1046, N.H. Packan, R.E. Stoller, and A.S. Kumar, Eds., American Society for Testing and Materials, Philadelphia, PA, 1990, pp. 739-752.

[8] Maillard, A., Touron, H. Séran, J.-L., and Chalony, A., "Swelling and Irradiation Creep of Neutron-Irradiated 316Ti and 15-15Ti Steels", *Effects of Radiation on Materials: 16th International Symposium*, ASTM STP 1175, A.S. Kumar, D.S. Gelles, R.K. Nanstad, and E.A. Little, Eds., American Society for Testing and Materials, Philadelphia, PA, 1994, pp. 824-837.

[9] Dubuisson, P., Maillard, A., Delalande, C., Gilbon, D., and Séran, J.-L., "The Effect of Phosphorous on the Radiation-Induced Microstructure of Stabilized Austenitic Stainless Steels", *Effects of Radiation on Materials: 15th International Symposium*, ASTM STP 1125, R.E. Stoller, A.S. Kumar, and D.S. Gelles, Eds., American Society for Testing and Materials, Philadelphia, PA, 1992, pp. 995-1014.

[10] Herschbach, K., Schneider, W., and Ehrlich, K., "Effects of Minor Alloying Elements upon Swelling and In-Pile Creep in Model Plain Fe-15Cr-15Ni Stainless Steels and in Commercial DIN 1.4970 Alloys", *Journal of Nuclear Materials*, Vol. 203, 1993, pp. 233-248.

[11] Herschbach, K., Schneider, W., and Bergmann, H.-J., "Swelling and In-Pile Creep Behavior of Some 15Cr15NiTi Stainless Steels in the Temperature Range 400 to 600°C", *Effects of Radiation on Materials:14th International Symposium (Volume II)*, ASTM STP 1046, N.H. Packan, R.E. Stoller, and A.S. Kumar, Eds., American Society for Testing and Materials, Philadelphia, PA, 1990, pp. 570-587.

[12] Kohyama, A., Kohno, Y., Asakura, K., Yoshino, M., Namba, C., and Eiholzer, C.R., "Irradiation Creep in Low-Activation Ferritic Steels in FFTF/MOTA", *Journal of Nuclear Materials*, Vols. 212-215, 1994, pp. 751-754.

[13] Shibahara, I., Ukai, S., Onose, S., and Shikakura, S., "Irradiation Performance of Modified 316 Stainless Steel for Monju Fuel", *Journal of Nuclear Materials*, Vol. 204, 1993, pp. 131-140.

[14] Neustroev, V.S., and Shamardin, V.K., "Radiation Creep and Swelling of Austenitic 16Cr-15Ni-3Mo-Nb Steels Irradiated in the Reactor BOR-60 at 350 and 420°C", *Effects of Radiation on Materials: 16th International Symposium*, ASTM STP 1175, A.S. Kumar, D.S. Gelles, R.K. Nanstad, and E.A. Little, Eds., American Society for Testing and Materials, Philadelphia, PA, 1994, pp. 816-823.

[15] Matthews, J.R., and Finnis, M.W., "Irradiation Creep Models – An Overview", *Journal of Nuclear Materials*, Vol. 159, 1988, pp. 257-285.

[16] Garner, F.A., "Irradiation Performance of Cladding and Structural Steels in Liquid Metal Reactors", *Materials Science and Technology, a Comprehensive Treatment*, Ch. 6, Vol. 10A, Part 1, R.W. Cahn, P. Haasen, and E.J. Kramer, Eds., VCH Verlagsgesellschaft mbH, 1994, pp. 419-543.

[17] Garner, F.A., Porter, D.L., Makenas, B.J., "A Third Stage of Irradiation Creep Involving its Cessation at High Neutron Exposures", *Journal of Nuclear Materials*, Vol. 148, 1987, pp. 279-287.

[18] Garner, F.A., and Toloczko, M.B., "Irradiation Creep of 316 Stainless Steel Irradiated in FFTF", in this conference.

[19] Garner, F.A, Gilbert, E.R., and Porter, D.L., "Stress-Enhanced Swelling of Metals During Irradiation", *Effects of Radiation on Materials: 10th Conference*, ASTM STP 725, D. Kramer, H.R. Brager, and J.S. Perrin, Eds., American Society for Testing and Materials, Philadelphia, PA, 1981, pp. 680-697.

[20] Toloczko, M.B., Garner, F.A., and Eiholzer, C.R., "Irradiation Creep and Swelling of the US Fusion Heats of HT9 and 9Cr-1Mo to 208 dpa at ~400°C", *Journal of Nuclear Materials*, Vols. 212-215, 1994, pp. 604-607.

[21] Lauritzen, T., Vaidyanathan, S., Bell, W.L, and Yang, W.J.S., "Irradiation-Induced Swelling in AISI 316 Steel: Effect of Tensile and Compressive Stresses", *Radiation-Induced Changes in Microstructure: 13th International Symposium, (Part I)*, ASTM STP 955, F.A. Garner, N.H. Packan, and A.S. Kumar, Eds., American Society for Testing and Materials, Philadelphia, PA, 1987, pp. 101-113.

F. A. Garner,[1] M. B. Toloczko,[2] and R. J. Puigh[3]

The Relationship Between Swelling and Irradiation Creep in 20% Cold-Worked 316 Stainless Steel

Reference: Garner, F. A., Toloczko, M. B., and Puigh, R. J., **"The Relationship Between Swelling and Irradiation Creep in 20% Cold-Worked 316 Stainless Steel,"** *Effects of Radiation on Materials: 19th International Symposium, ASTM STP 1366,* M. L. Hamilton, A. S. Kumar, S. T. Rosinski, and M. L. Grossbeck, Eds., American Society for Testing and Materials, West Conshohocken, PA, 2000.

Abstract: The relationship between swelling and irradiation creep was investigated using eight sets of pressurized tubes, representing two heats of 20% cold-worked 316 stainless steel irradiated at either 550°C, 575°C, 600°C, and 670°C in the FFTF-MOTA to doses of 79-84 dpa. After reaching these exposures, the tubes were clearly being affected by the "creep cessation" phenomenon. Many of the tubes had already reached the previously observed maximum strain rate of 0.33%/dpa characteristic of creep cessation. Fortuitous failure of fourteen tubes allowed the separation of creep and swelling strains in the creep cessation regime, showing that the maximum strain rate limitation was reached long before the maximum swelling rate of 1%/dpa was reached. Thus, the creep contribution was declining as the swelling rate increased throughout the irradiation.

Keywords: stainless steels, neutron irradiation, swelling, irradiation creep

Introduction

In a series of earlier papers by the authors, it has been shown that void swelling and irradiation creep of austenitic and ferritic/martensitic stainless steels are intimately connected phenomena rather than independently operating processes [1-18]. A summary of the major insights on the two related phenomena developed from these reports and those of other researchers is presented in ref. [19].

Of particular interest is the role of irradiation-induced swelling to first accelerate irradiation creep at the onset of void growth, but then to throttle back the creep rate as the swelling rate grows larger. This late-term decrease in creep rate has been designated "creep cessation" or "creep disappearance" by Garner and coworkers [2-4].

Creep cessation has a number of interesting manifestations. In terms of the $B = B_o + DS$ creep model, creep cessation is manifested as a drop in the creep-swelling coupling coefficient, D, with swelling rate. Second, for stresses where dislocation climb is the dominant creep mechanism, the maximum total linear deformation rate (creep plus swelling)

[1] Senior Staff Scientist, Pacific Northwest National Laboratory, Richland, WA 99352.
[2] Graduate Student, Washington State University, Pullman, WA 99163.
[3] Manager, Fluor Daniel Northwest Inc., Richland, WA 99352.

Copyright© 2000 by ASTM International www.astm.org

does not exceed 0.33%/dpa, and once reached it is unresponsive to further increases in stress. The reason for this behavior is not yet fully understood. Finally, the stress-enhancement of void swelling is somehow involved in the interaction between swelling and creep, such that its operation tends to compensate for the decline in the creep-swelling coupling coefficient, D. If stress-enhancement of swelling is neglected in the separation of strains when calculating the D-coefficient, the D-coefficient appears to be a constant at ~0.6×10^{-2} MPa^{-1}, regardless of the stress-free swelling behavior [12].

Toloczko and Garner address the effect of stress-enhancement on swelling and its impact on the determination of the D-coefficient in a companion paper at this conference [20], and show that the apparent difference between reported D-coefficients of French and U.S. researchers is a direct result of differences in the data generation with respect to the role of stress-enhancement of swelling and also in the extraction of the D-coefficient from the data.

Another facet of the creep cessation concept under investigation is the exact partitioning of swelling and creep strains when the maximum total strain rate of 0.33%/dpa has been attained. Since fully isotropic swelling at the maximum swelling rate of 1%/dpa [21-24] would yield a 0.33%/dpa strain rate, does this imply that creep has fully disappeared when the total strain rate of 0.33%/dpa is first attained, and that only swelling is operating thereafter?

To address the issues of stress-enhanced swelling and separation of strains at 0.33%/dpa, the following experiment was performed involving pressurized tubes constructed from cold-worked AISI 316 stainless steel irradiated in the Materials Open Test Assembly (MOTA). These tubes were selected because they had reached strain rates where creep

Table 1--*Composition, in weight percent, of the two 316 type stainless steels.*

Element	Core 1	Core 4
carbon	0.047	0.056
manganese	1.77	1.53
silicon	0.57	0.54
phosphorous	0.004	0.002
sulfur	0.006	0.005
chromium	17.4	17.7
nickel	13.7	13.7
molybdenum	2.34	2.82
copper	0.01	0.02
boron	0.0005	0.0005
cobalt	0.005	0.01
aluminum	0.005	0.01
vanadium	0.02	0.01
niobium	0.005	0.01
tantalum	0.015	0.01
arsenic	0.005	0.005
nitrogen	0.004	0.002
oxygen	0.002	0.002

Table 2--*Hoop stress levels of pressurized tubes studied in this experiment.*

Temperature °C	Heat	Hoop Stress MPa
550	Core-1	0, 35, 70 ,117, 163, 233
	Core-4	same
575	Core-1	0, 16, 31, 63, 104, 146
	Core-4	same
600	Core-1	0, 15, 30, 61, 101
	Core-4	0, 15, 30, 61
670	Core-1	0, 5, 15, 31, 62
	Core-4	0, 5, 15, 31

cessation was thought to be a dominant factor in their behavior. Some of these tubes had developed pin-hole leaks and therefore lost gas pressure during the experiment, which allowed observation of the subsequent stress-free swelling in previously stressed tubes.

Experimental Details

Two heats of 20% cold-worked AISI 316 stainless steel, designated FFTF Core-1 and Core-4 steels, were used to construct 28.2 mm long gas-pressurized tubes with outer and inner diameters of 4.57 and 4.17 mm, respectively. The pressurized tube construction technique is described in ref. [25]. Tubes were pressurized at room temperature, and since helium was used as the fill gas, it was possible to assume ideal gas behavior in calculating the gas pressure at the irradiation temperature.

The compositions of the two heats are presented in Table 1. These tubes were irradiated in MOTAs 1A, 1B, and 1C at the hoop stress levels shown in Table 2. During irradiation, the temperature was actively controlled within ±5°C, and the tubes were in contact with sodium coolant. The exposures reached at the end of the third and final irradiation interval were 80 dpa at 550 and 575°C, 84 dpa at 600°C, and 79 dpa at 670°C .

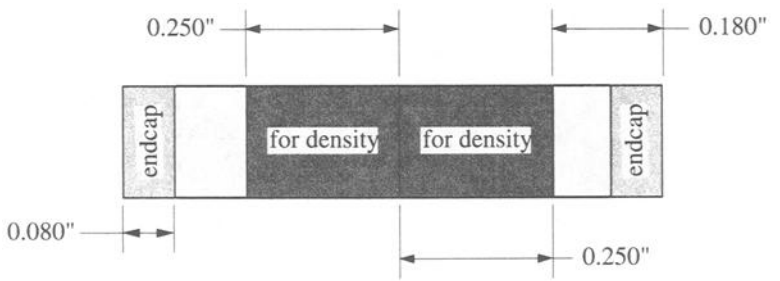


Figure 1--*Location of tube segments cut from Core-1 tubes irradiated to 80 dpa at 550°C and to 84 dpa at 670°C. The tube segments were used to perform stress-enhanced swelling measurements.*

The diameter changes were measured with a non-contacting laser technique accurate to within ±10 μm as described in ref. [26]. After each irradiation interval, the tube diameters were measured, the specimens were placed into fresh canisters, and finally, the tubes were returned to a new MOTA for continued irradiation.

At the end of the third irradiation interval, the Core-1 tubes irradiated at 550°C and 670°C were each sectioned into four pieces as shown in Figure 1. Swelling was determined from the two middle sections using an immersion density technique.

Results

As shown in Figures 2 and 3, a large fraction of the tubes developed strain rates of 0.33%/dpa before the experiment was terminated. This guarantees that creep cessation was well in progress. Most importantly, however, fourteen of the tubes had lost gas pressure during irradiation but were returned for further irradiation in the now stress-free condition. In all cases, the failed tubes were those at the highest stress levels. Figures 2 and 3 both show a decrease in the diametral strain rate after failure of a tube and that the post-failure strain rate is slightly greater than the strain rate of the respective stress-free tube.

The stress-enhanced swelling estimated from density measurements are shown in Table 3. Some variation in swelling between the two measured sections of each tube was observed, but the variation was not large relative to the absolute values. At both 550 and 670°C, there is a clear enhancement of swelling at higher stresses. As shown in Figure 4a, stress-free swelling estimated from diameter change was 13.7% at 80 dpa, while it was 16.0% when estimated from density measurements. Figure 4b shows that in those tubes which did not fail, the enhancement of swelling may be linear with stress. The assumed stress-enhanced swelling behavior at lower doses is shown in Figure 4c. These values were estimated by taking the ratio of stress-enhanced swelling at 80 dpa to the stress-free swelling calculated from diameter measurements at 80 dpa, and then this ratio was applied to stress-free swelling calculated from diameter measurements at lower doses.

Table 3--*Measured swelling of tube sections.*

Temperature °C	Hoop Stress MPa	Dose to Failure	Total Dose	Swelling %
550	0	---	80	15.42, 16.59
	35	---	80	15.03, 15.75
	70	---	80	17.37, 17.90
	117	---	80	19.78, 20.77
	163	37	80	18.77, 18.64
	233	24	37	3.54, 3.46
670	0	---	79	1.42, 1.29
	5	---	79	1.39, 1.14
	15	~42	79	1.86, 2.22
	31	~27	79	2.54, 3.29
	62	<27	42	2.61, 1.35

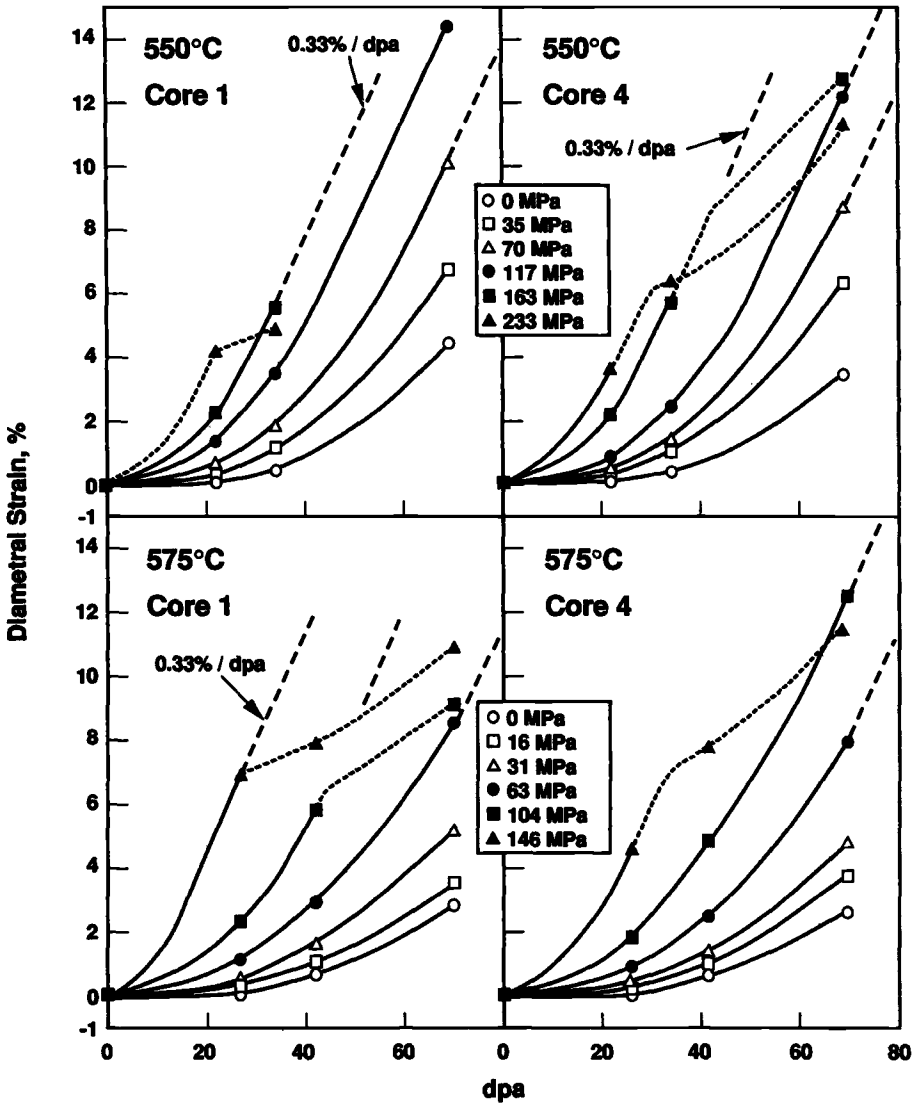


Figure 2--*Diametral strains induced by swelling and irradiation creep in two heats of 20% cold-worked 316 stainless steel tubes irradiated in FFTF-MOTA at 550 and 575°C.*

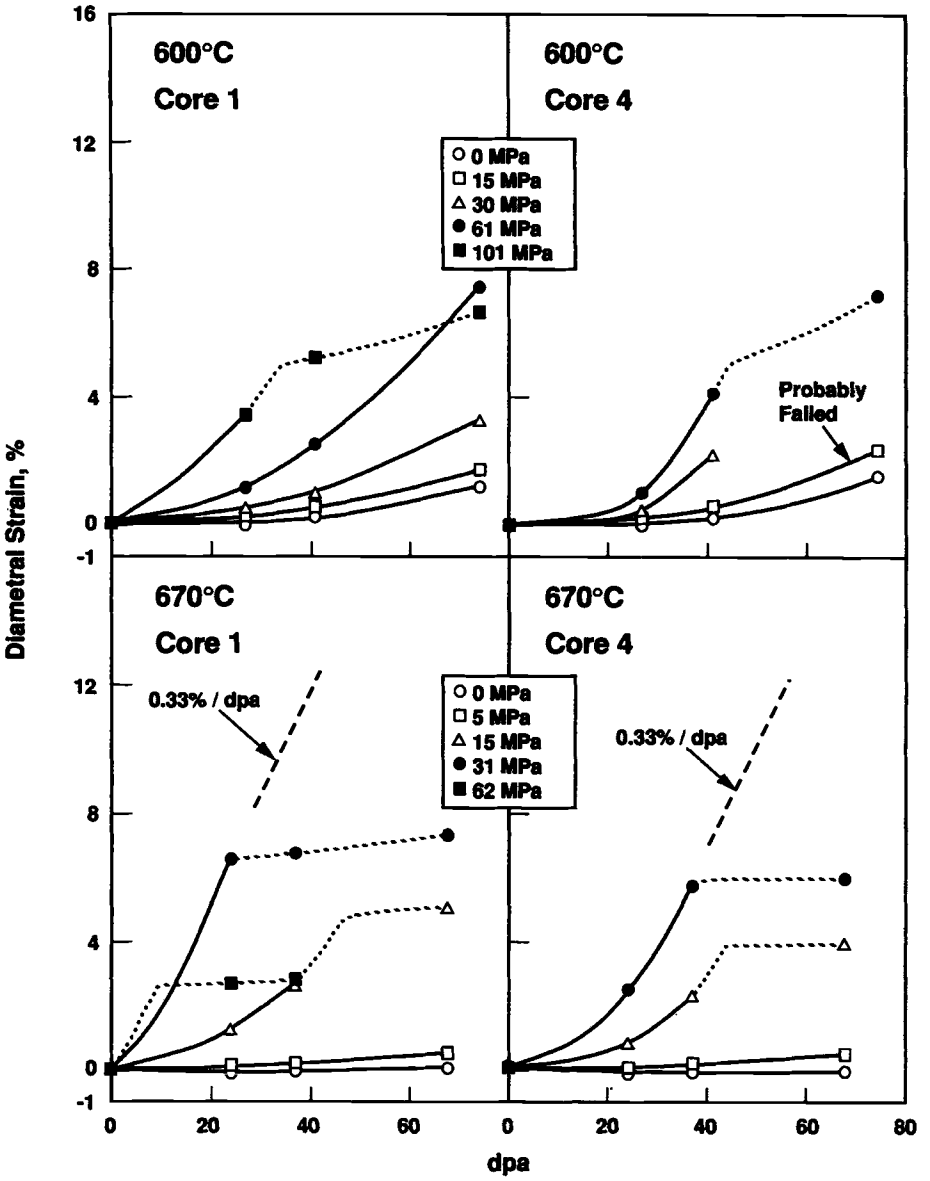


Figure 3--*Diametral strains induced by swelling and irradiation creep in two heats of 20% cold-worked 316 stainless steel tubes irradiated in FFTF-MOTA at 600 and 670°C.*

Table 4--*Diametral strains and linear swelling from density of 670°C Core-1 tubes showing that attainment of 0.33%/dpa diametral strain rate does not require a 1%/dpa swelling rate or even a significant amount of swelling.*

Temperature °C	Hoop Stress MPa	Dose to Failure	Total Dose	Diametral Strain %	Avg. Linear Swelling %
670	0	---	79	0.074	0.45
	5	---	79	0.495	0.42
	15	~42	79	5.084	0.68
	31	~27	79	7.333	0.96
	62	<27	42	2.773	0.66

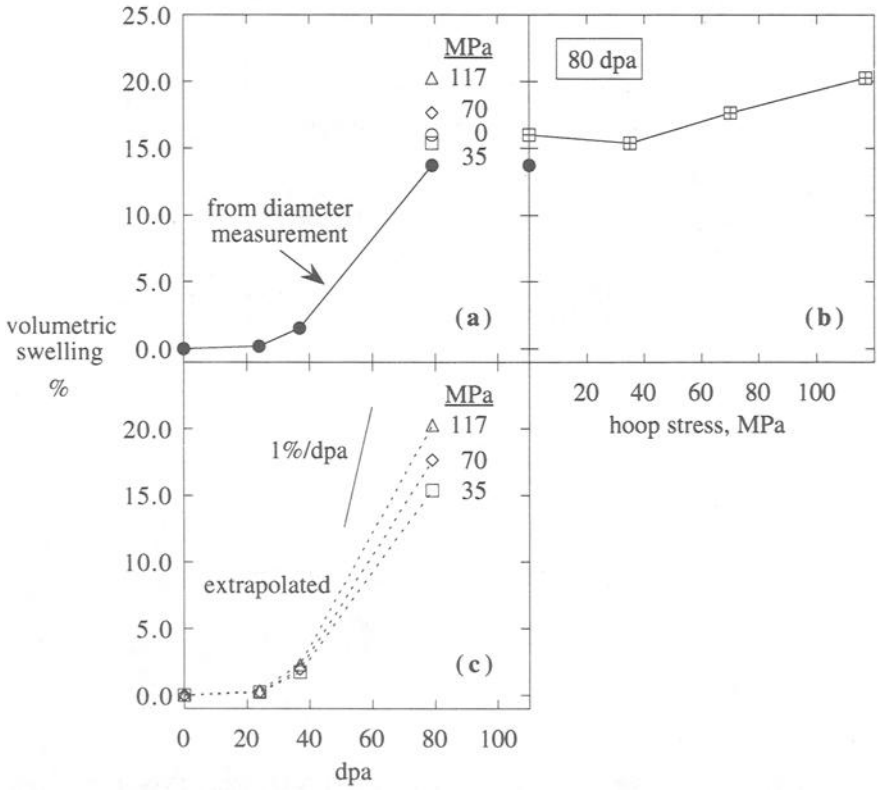


Figure 4--*Measured swelling of the 550°C irradiated Core-1 tube segments. Stresses shown are hoop stresses. Note there is some small difference between the density measurement and diameter change measurement for the stress-free swelling. Figure 4c shows the assumed swelling behavior at doses less than 80 dpa.*

Discussion

The data shown in Figures 2 and 3 clearly show that, with the exception of the tubes irradiated at 670°C, significant amounts of swelling were achieved in the absence of stress in the tube-sets. In the stressed tubes that failed during irradiation, the post-failure diametral strains rates are similar to that of the stress-free tubes at the same neutron fluence, suggesting that prior to failure, both creep and swelling were contributing to the strain of the tubes that had reached a diametral strain rate of 0.33%/dpa. Explicit proof that both creep and swelling may be simultaneously contributing to strain at the strain rate limit of 0.33%/dpa can be seen by comparing the 670°C diametral strain data and density data. Of the five Core-1 tubes irradiated at 670°C, three appeared to have reached or nearly reached 0.33%/dpa diametral

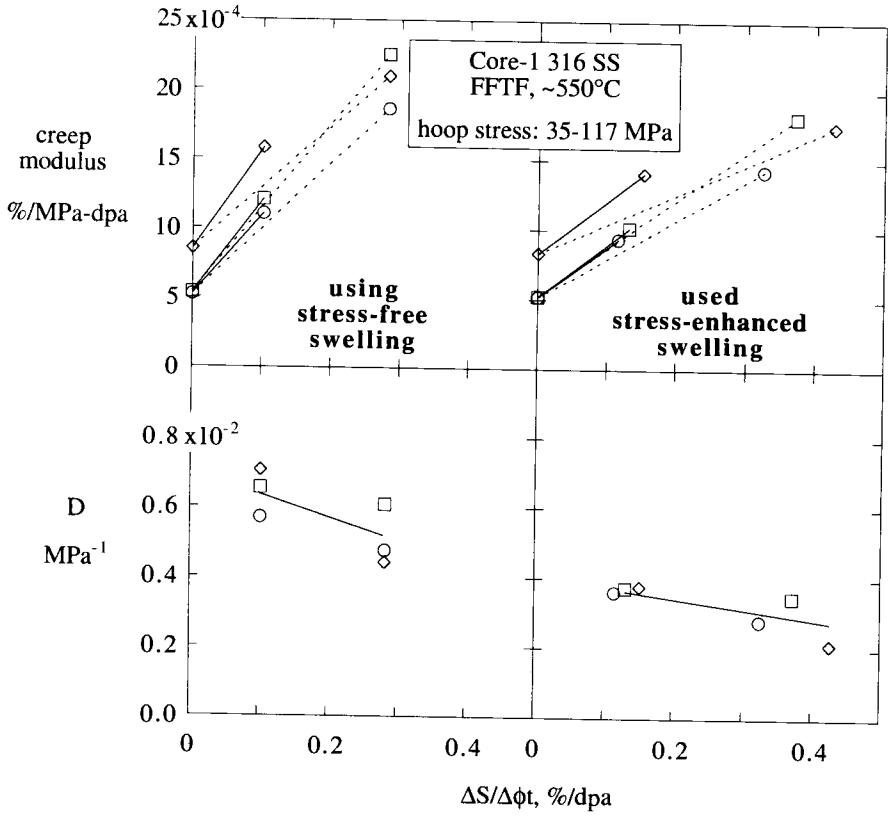


Figure 5--*Creep modulus and creep-swelling coupling coefficient plotted versus $\Delta S/\Delta\phi t$ for pressurized tubes irradiated at 550°C. Stress-free swelling was used to calculate the creep strains for the plots on the left and stress-enhanced swelling was used for the plots on the right.*

strain rate and then failed. If only swelling were contributing to the 0.33%/dpa diametral strain rate prior to failure, then the swelling values estimated from density would have been only slightly less than the swelling values estimated from the diametral strains assuming the diametrai strains were due mainly to swelling. Table 4 shows that instead, the swelling was only a small contribution to the total strains.

Focusing on the 550°C Core-1 tubes, it was possible to extract creep coefficients using both the stress-free swelling and the actual swelling. In both cases, the creep-swelling coupling coefficient, D, fell as the swelling rate increased as shown in Figure 5. When stress-enhanced swelling was included, D fell even further as observed in other previous work [8,12,20].

The above conclusion, concerning the interplay between creep and swelling was reached independently by the Russian researchers, Karaulov and Shkolnik in 1990, when they showed that the creep modulus of two Russian stainless steels saturated long before the swelling rate reached the 1%/dpa level, as shown in Figure 6 [27]. These researchers referred to the creep cessation process as "creep damping".

Conclusions

When irradiation creep occurs under high stress levels in a swelling-prone steel, the total deformation rate rapidly approaches its maximum value of 0.33%/dpa, even though swelling has barely begun. As swelling increases in rate, the creep rate was observed to decline, such that the 0.33%/dpa maximum deformation rate was preserved.

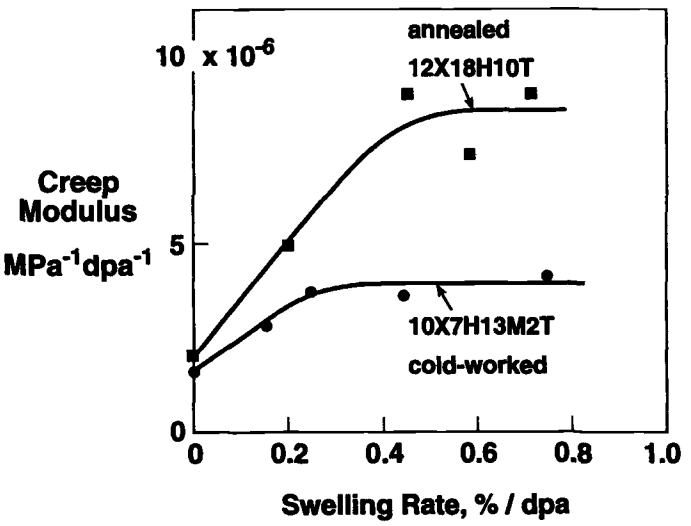


Figure 6--*Influence of the swelling rate on the creep modulus of several Russian stainless steels, illustrating the phenomenon of "creep damping" [27].*

References

[1] Garner, F.A, Gilbert, E.R., and Porter, D.L., "Stress-Enhanced Swelling of Metals During Irradiation", *Effects of Radiation on Materials: 10th Conference*, ASTM STP 725, D. Kramer, H.R. Brager, and J.S. Perrin, Eds., American Society for Testing and Materials, Philadelphia, 1981, pp. 680-697.

[2] Garner, F.A., Porter, D.L., Makenas, B.J., "A Third Stage of Irradiation Creep Involving its Cessation at High Neutron Exposures", *Journal of Nuclear Materials*, Vol. 148, 1987, pp. 279-287.

[3] Garner, F.A., and Porter, D.L., "Irradiation Creep and Swelling of AISI 316 to Exposures of 130 dpa at 385-400°C", *Journal of Nuclear Materials*, Vols. 155-157, 1988, pp. 1006-1013.

[4] Porter, D.L., and Garner, F.A., "Irradiation Creep and Embrittlement Behavior of AISI 316 Stainless Steel at Very High Neutron Exposures", *Journal of Nuclear Materials*, Vol. 159, 1988, pp. 114-121.

[5] Garner, F.A., and Puigh, R.J., "Irradiation Creep and Swelling of the Fusion Heats of PCA, HT9, and 9Cr-1Mo Irradiated to Very High Neutron Fluence", *Journal of Nuclear Materials*, Vols. 179-181, 1991, pp. 577-580.

[6] Porter, D.L., Hudman, G.D., and Garner, F.A., "Irradiation Creep and Swelling of Annealed Type 304L Stainless Steel at ~390°C and High Neutron Fluence", *Journal of Nuclear Materials*, Vols. 179-181, 1991, pp. 581-584.

[7] Porter, D.L., and Garner, F.A., "Swelling of AISI Type 304L Stainless Steel in Response to Simultaneous Variations in Stress and Displacement Rate", *Effects of Radiation on Materials: 12th International Symposium*, ASTM STP 870, F.A. Garner and J.S. Perrin, Eds., American Society for Testing and Materials, Philadelphia, 1985, pp. 212-220.

[8] Porter, D.L., and Garner, F.A., "Cessation of Irradiation Creep in AISI 316 Concurrent with High Levels of Swelling", *Influence of Radiation on Material Properties: 13th International Symposium (Part II)*, ASTM STP 956, F.A. Garner, C.H. Henager Jr., and N. Igata, Eds., American Society for Testing and Materials, Philadelphia, 1987, pp. 11-21.

[9] Porter, D.L., Wood, E.L., and Garner, F.A., "Influence of Thermomechanical Treatment and Environmental History of Creep, Swelling, and Embrittlement of AISI 316 at 400°C and 130 dpa", *Effects of Radiation on Materials: 14th International Symposium (Volume II)*, ASTM STP 1046, N.H. Packan, R.E. Stoller, and A.S. Kumar, Eds., American Society for Testing and Materials, Philadelphia, 1990, pp. 551-569.

[10] Puigh, R.J., and Garner, F.A., "Irradiation Creep Behavior of the Fusion Heats of HT9 and Modified 9Cr-1Mo Steels", *Effects of Radiation on Materials: 14th International Symposium (Volume II)*, ASTM STP 1046, N.H. Packan, R.E. Stoller, and A.S. Kumar, Eds., American Society for Testing and Materials, Philadelphia, 1990, pp. 527-536.

[11] Toloczko, M.B., Garner, F.A., and Eiholzer, C.R., "Irradiation Creep and Swelling of the US Fusion Heats of HT9 and 9Cr-1Mo to 208 dpa at ~400°C", *Journal of Nuclear Materials*, Vols. 212-215, 1994, pp. 604-607.

[12] Toloczko, M. B., and Garner, F. A., "Relationship Between Swelling and Irradiation Creep in Cold-Worked PCA Stainless Steel irradiated to ~178 dpa at ~400°C", *Journal of Nuclear Materials*, Vols. 212-215, 1994, pp. 509-513.

[13] Toloczko, M.B., Garner, F.A., and Eiholzer, C.R., "Determination of the Creep Compliance and Creep-Swelling Coupling Coefficient for Neutron Irradiated Titanium-Modified Stainless Steels at ~400°C", *Journal of Nuclear Materials*, Vols. 191-194, 1992, pp. 803-807.

[14] Garner, F.A., Hamilton, M.L., Eiholzer, C.R., Toloczko, M.B., and Kumar, A.S., "Influence of Cold Work on the Irradiation Creep and Creep Rupture of Titanium Modified Austenitic Stainless Steel", *Effects of Radiation on Materials: 16th International Symposium*, ASTM STP 1175, A.S. Kumar, D.S. Gelles, R.K. Nanstad, and E.A. Little, Eds., American Society for Testing and Materials, Philadelphia, 1994, pp. 696-713.

[15] Toloczko, M. B. and Garner, F. A., "Variability of Irradiation Creep and Swelling of HT9 Irradiated to High Neutron Fluence at 400-600°C", *Effects of Radiation on Materials: 18th International Symposium,* ASTM STP 1325, R. K. Nanstad, M. L. Hamilton, F. A. Garner, and A. S. Kumar, Eds., American Society for Testing and Materials, 1999, pp. 765-779.

[16] Garner, F. A., Toloczko, M. B., Munro, B., Adaway, S., and Standring, J., "Comparison of Irradiation Creep and Swelling of an Austenitic Alloy Irradiated in FFTF and PFR", *Effects of Radiation on Materials: 18th International Symposium,* ASTM STP 1325, R. K. Nanstad, M. L. Hamilton, F. A. Garner, and A. S. Kumar, Eds., American Society for Testing and Materials, 1999, pp. 713-724.

[17] Toloczko, M.B., Garner, F.A., Standring, J., Munro, B., and Adaway, S., "Flux and Composition Dependence of Irradiation Creep of Austenitic Alloys Irradiated in PFR at ~420°C", *Journal of Nuclear Materials*, Vols. 258-263, 1998, pp. 1606-1612.

[18] Toloczko, M.B., Garner, F.A., and Eiholzer, C.R., "Irradiation Creep of Various Ferritic Alloys Irradiated at ~400°C in the PFR and FFTF Reactors", *Journal of Nuclear Materials*, Vols. 258-263, 1998, pp. 1163-1166.

[19] Garner, F.A. in Chapter 6 of *Materials Science and Technology, a Comprehensive Treatment*, Vol. 10A, Part 1, R.W. Cahn, P. Haasen, and E.J. Kramer, Eds., VCH Verlagsgesellschaft mbH, pp. 419-543.

[20] Toloczko, M.B. and Garner, F.A., "Reanalysis of Swelling and Irradiation Creep data on 316 Type Stainless Steels Irradiated in the FFTF and Phénix Fast Reactors", *Effects of Radiation on Materials: 19th International Symposium*, ASTM-STP 1366, M.L. Hamilton, A.S. Kumar, S.T. Rosinski, and M.L. Grossbeck, Eds., American Society for Testing and Materials, 1999, this publication.

[21] Garner, F.A., "Recent Insights on the Swelling and Creep of Irradiated Austenitic Alloys", *Journal of Nuclear Materials*, Vols. 122 & 123, 1984, pp. 459-471.

[22] Garner, F.A., and Brager, H.R., "Swelling of Austenitic Iron-Nickel-Chromium Ternary Alloys During Fast Neutron Irradiation", *Effects of Radiation on Materials: 12th International Symposium*, ASTM STP 870, F.A. Garner and J.S. Perrin, Eds., American Society for Testing and Materials, Philadelphia, 1985, pp. 187-201.

[23] Garner, F.A., and Kumar, A.S., "The Influence of Both Major and Minor Element Composition on Void Swelling in Austenitic Steels", *Radiation-Induced Changes in Microstructure: 13th International Symposium (Part I)*, ASTM STP 955, F.A. Garner, N.H. Packan, and A.S. Kumar, Eds., American Society for Testing and Materials, Philadelphia, 1987, pp. 289-314.

[24] Garner, F.A., and Gelles, D.S., "Neutron-Induced Swelling of Commercial Alloys at Very High Exposures", *Effects of Radiation on Materials: 14th International Symposium (Volume II)*, ASTM STP 1046, N.H. Packan, R.E. Stoller, and A.S. Kumar, Eds., American Society for Testing and Materials, Philadelphia, 1990, pp. 673-683.

[25] Gilbert, E.R., and Chin, B.A., "In-Reactor Creep Measurements", *Nuclear Technology*, Vol. 52, Feb. 1981, pp. 273-283.

[26] Gilbert, E. R., and Chin, B. A., "Irradiated Materials Measurement Technology", *Effects of Radiation on Materials, 10th Conference*, ASTM STP 725, American Society for Testing and Materials, 1981, pp. 665-679.

[27] Karaulov, V.N., Shkolnik, T.G., "Study of the Swelling and Radiation Creep Process in Structural Materials of BN-350 Subassembly Wrappers on the Basis of Wrapper Shape Change Data", *International Conference on Radiation Materials Studies*, Alushta, Ukraine, May 22-25, 1990, in Russian.

S. I. Porollo,[1] A. N. Vorobjev,[1] Yu. V. Konobeev,[1] N. I. Budylkin,[2]
E. G. Mironova,[2] and F. A. Garner [3]

Irradiation Creep and Stress-Affected Swelling in Austenitic Stainless Steel 16Cr-15Ni-3Mo-Nb-B Irradiated in the BN-350 Reactor

Reference: Porollo, S. I., Vorobjev, A. N., Konobeev, Y. V., Budylkin, N. I., Mironova, E. G., and Garner, F. A., **"Irradiation Creep and Stress-Affected Swelling in Austenitic Stainless Steel 16Cr-15Ni-3Mo-Nb-B Irradiated in the BN-350 Reactor,"** *Effects of Radiation on Materials: 19th International Symposium, ASTM STP 1366,* M. L. Hamilton, A. S. Kumar, S. T. Rosinski, and M. L. Grossbeck, Eds., American Society for Testing and Materials, West Conshohocken, PA, 2000.

Abstract: Irradiation creep and void swelling are important damage processes for stainless steels when subjected to neutron irradiation at elevated temperatures. To date, most published data of this type have been derived from steels prepared by various Western nations and Japan. This paper describes the results of an experiment involving irradiation of gas-pressurized tubes constructed from Russian niobium-stabilized austenitic steel EP-172 of type 16Cr-15Ni-3Mo-Nb doped with boron. The tubes were irradiated in the low-enrichment zone of the BN-350 fast reactor to three doses of 20, 45 and 60 dpa at temperatures in the range of 480-520°C.

It was shown that the swelling of 16Cr-15Ni-3Mo-Nb stainless steels can vary strongly with minor changes in composition. Whereas EI-847 swelled easily, boron addition and other minor changes to produce EI-172 yielded a significant reduction in swelling. In both alloys, however, the swelling increased linearly with applied stress and the irradiation creep coefficients were very similar. Applied stresses influence the void number density, but not the void size or dislocation density.

Keywords: irradiation creep, swelling, neutron irradiation, stainless steel

Introduction

The study of irradiation creep and swelling in austenitic stainless steels is of interest for an assessment of the structural materials performance in fast reactor cores, fusion reactor components, as well as of internals in PWRs and VVERs. Earlier, in Ref. [*1*], some results

[1]Head of Laboratory, Senior Scientist and Head of Division, respectively, State Scientific Center of Russian Federation, The Institute of Physics and Power Engineering, Bondarenko Sq.1, Obninsk 249020, Kaluga Region, Russia.

[2]Senior scientist and Scientific worker, respectively, State Scientific Center of Russian Federation, The Research Institute of Nonorganic Materials, Rogova Street 5a, Moscow 123060, Russia.

[3]Senior Staff Scientist, Pacific Northwest National Laboratory, Richland, WA, U.S.A.

Copyright© 2000 by ASTM International www.astm.org

were presented on the study of irradiation creep and swelling in EI-847 of type 16Cr-15Ni-3Mo-Nb austenitic stainless steel irradiated as creep tubes in the fast reactor BN-350 (Kazakhstan) to 20 and 60 dpa at irradiation temperatures of 480 and 520°C, respectively. It was shown that both the irradiation creep rate and swelling in the steel increase with increasing hoop stress. The dependence of swelling on stress also contributed to a decrease in the value of the creep-swelling coupling coefficient D characterized as "creep disappearance," as defined by Garner and coworkers [*2*].

In the present paper, data on irradiation creep and swelling in type 16Cr-15Ni-3Mo-Nb-B (EP-172) austenitic stainless steel are reported. The composition of the steel differs from the composition of the 16Cr-15Ni-3Mo-Nb (EI-847) steel investigated in Ref. [*1*], primarily by the deliberate addition of boron, but there are also potentially significant but small differences in Mn, Nb, C and Si. Both steels were irradiated side-by-side at identical conditions. The compositions of the two steels are shown in Table 1.

Table 1 - *The Chemical Composition of the Steels, in wt.%*

	Cr	Ni	Mo	Mn	Nb	Si	C	B	S	P	N
EI-847	15.74	15.32	2.95	0.78	0.54	0.29	0.05	0.001	0.009	0.011	0.035
EP-172	16.05	14.90	2.75	0.37	0.72	0.16	0.09	0.009	0.009	0.009	0.046

Experimental Details

Creep tubes of 6.9 mm in outer diameter and of 0.4 mm in wall thickness were fabricated from EP-172 austenitic stainless steel. The final treatment of the tubes involved annealing at 1040°C for 5 s and subsequent cooling in air. Pressurization was accomplished with 99.998% argon gas. The gas pressure was measured at room temperature and ideal gas behavior assumed at the irradiation temperature. The design of the creep tubes, irradiation conditions and methods of measurement have been described in detail in Ref. [*1*]. Hoop stress levels of 0, 98 and 196 MPa were used, calculated using the thin-wall tube approximation. The tubes are illustrated in Fig. 1 and were contained in three perforated cylindrical baskets placed in an experimental assembly in BN-350. They were irradiated in contact with the sodium coolant at different positions with respect to the core midplane. Fig. 2 shows the location of creep tubes in the assembly (levels #3, #10 and #15) and also the normalized fluence and temperature profiles.

The target dpa levels and irradiation temperatures were: 60 dpa/480°C at level #3, 45 dpa/500°C at level #10, and 20 dpa/520°C at level #15. Before measurements, the outer surfaces of the irradiated tubes was cleaned with a 50/50 solution of ethyl alcohol and water. The diameters were measured with an accuracy of 10 μm at the tube middle by a directly contacting method.

After puncturing the tubes and measuring of the gas pressure, the end caps of the tubes were removed, leaving a section of 50 mm length. The density of the steel was measured by an immersion technique for this 50 mm section. For microscopy investigations

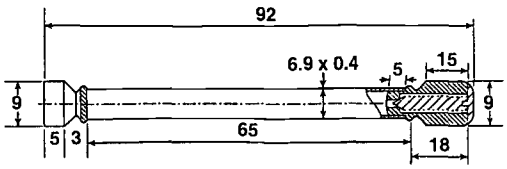


Figure 1 - *Argon-pressurized creep tubes irradiated in the BN-350 reactor.*

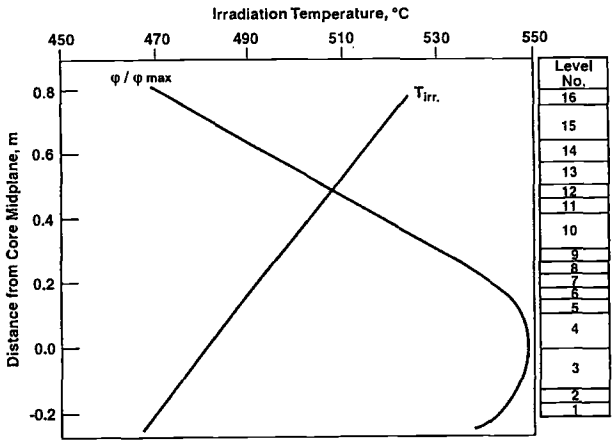


Figure 2 - *Axial profiles of irradiation temperature and normalized neutron fluence (E > 0.1 MeV) for the experimental assembly in the BN-350 fast reactor.*

rings of 4 mm width were machined from the tubes and then standard microscopy specimens were prepared by punching and electropolishing. Microscopy was performed on a JEOL 100 CX electron microscope at an accelerating voltage of 100 keV.

Results

None of the creep tubes failed during irradiation. The argon pressure measured after puncturing of the tubes was always very close to the calculated value. In Fig. 3 the diametral strain as a function of the hoop stress is shown for the three dpa levels. Fig. 4 shows the dependence of swelling on the hoop stress in 16Cr-15Ni-3Mo-Nb-B steel irradiated to 60 dpa at 480°C, measured by three different methods. No measurements of swelling in creep tubes irradiated to 20 and 45 dpa were made by either immersion density or electron microscopy. For these tubes the contribution of irradiation creep was

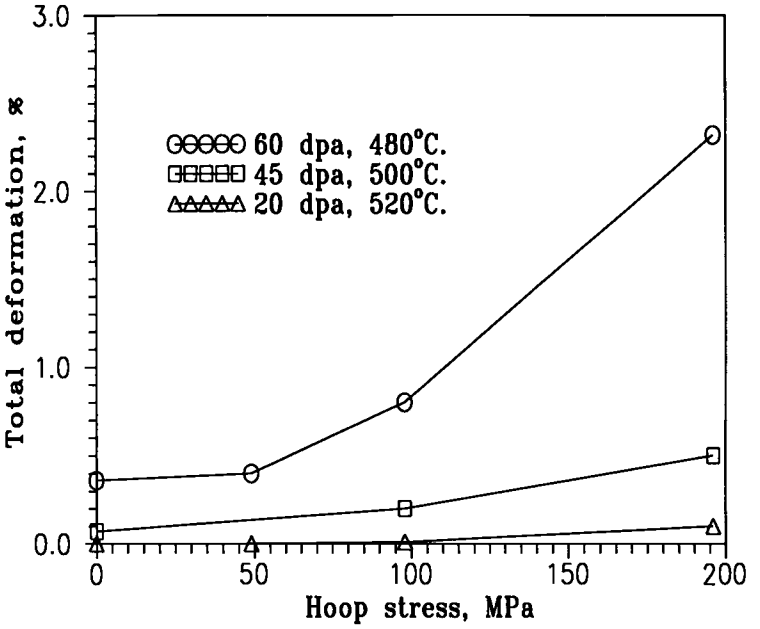


Figure 3 - *Measured diametral strains of the creep tubes versus hoop stress.*

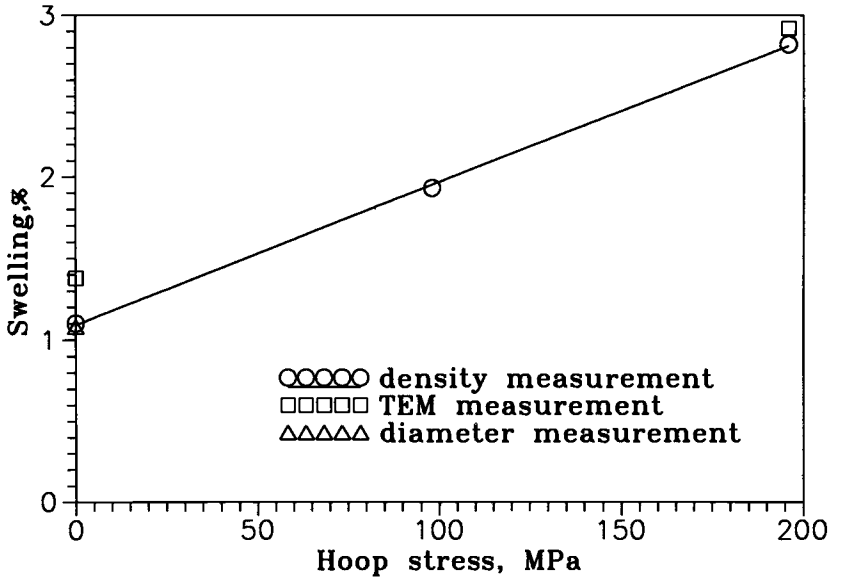


Figure 4 - *Void swelling in solution treated 16Cr-15Ni-3Mo-Nb-B (EP-172) austenitic stainless steel as a function of hoop stress at 480 °C and 60 dpa.*

determined by subtracting the diametral strains for stress-free tubes from the diametral strain of stressed creep tubes, thereby ignoring the possibility of an increase of swelling with increasing applied stress. At these lower fluences the total strains were small, and the consequences of this assumption are not considered to be very large. Most significantly, the strains were not linear with stress, as is often observed in such experiments [7]. The dependence of irradiation creep on hoop stress is shown in Fig. 5 at 20, 45 and 60 dpa.

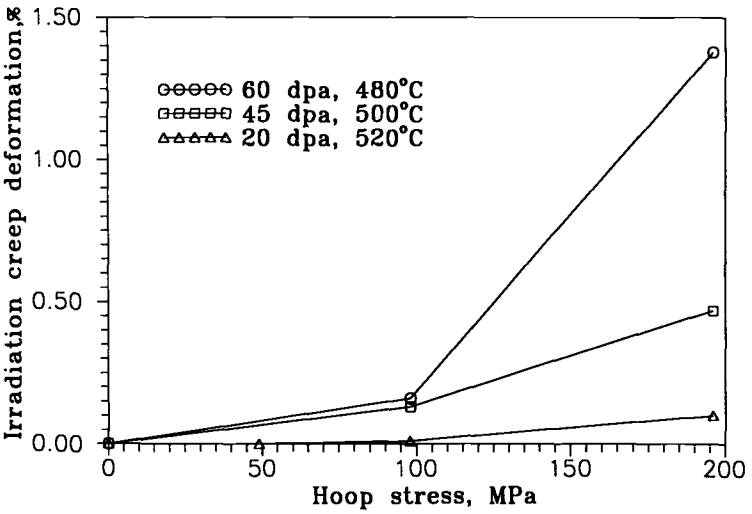


Figure 5 - *Irradiation creep strains in the solution treated 16Cr-15Ni-3Mo-Nb-B (EP-172) austenitic stainless steel as a function of hoop stress. The values at 20 and 45 dpa may contain some influence of stress-affected swelling.*

The study of the microstructure in the 16Cr-15Ni-3Mo-Nb-B steel was conducted for specimens produced from tubes irradiated at 480°C to 60 dpa at hoop stresses of 0 and 196 MPa. The swelling level measured by electron microscopy was 1.1 and 2.8% at 0 and 196 MPa, respectively (Fig. 4). Such an effect of stress on swelling was found to arise from an increase of the void concentration (from 1.6×10^{14} to 3.2×10^{14} cm^{-3}) with the mean void diameter essentially constant (52.4 nm at zero hoop stress and 52.8 nm at 196 MPa). In addition to voids, finely dispersed precipitates of Nb(C,N) were observed throughout the microstructure of the irradiated steel. In addition, a smaller density of large size G-phase precipitates were found, usually attached to voids (Fig. 6). Within the limits of measurement accuracy, both the mean size and concentration of precipitates did not appear to depend on the stress level. The dislocation structure of the irradiated steel was composed of dislocation segments and Frank dislocation loops (Fig. 6). The total dislocation density was approximately the same in specimens irradiated at hoop stresses of both 0 and 196 MPa, falling in the range $4 - 5 \times 10^{10}$ cm^{-2}.

Discussion

First of all, it should be noted that the boron additions to the 16Cr-15Ni-3Mo-Nb austenitic stainless steel, as well as the other small elemental variations resulted in a difference in the swelling of more than one order of magnitude. After neutron irradiation in stress-free condition the swelling in the 16Cr-15Ni-3Mo-Nb-B steel was in the range of 1.1 - 1.4%, whereas the swelling in 16Cr-15Ni-3Mo-Nb steel exceeded 20% at identical irradiation conditions, as shown in Figs. 4 and 7, respectively. Nevertheless, the swelling in both of the steels was linear with hoop stress.

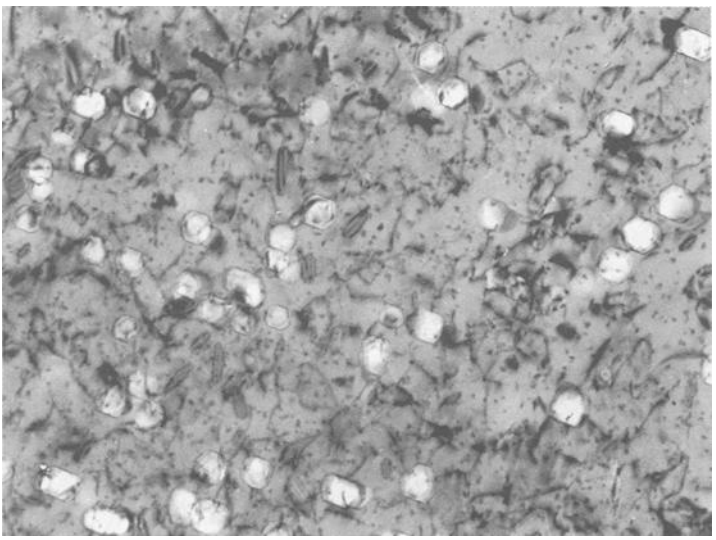


Figure 6 - *The microstructure of the 16Cr-15Ni-3Mo-Nb-B steel irradiated to 60 dpa at 480 °C and 196 MPa.*

When fitting the swelling data versus hoop stress σ_h:

$$S(\sigma_h) = S_o(1 + A\sigma_h), \quad (1)$$

where S_o is the stress-free swelling, one finds that A = 7.9 x 10^{-3} MPa^{-1}. This value of A is close to values obtained in other studies (see, for example [*3-6*]).

In contrast to the swelling, as seen in Fig. 4, irradiation creep as a function of applied stress appears to deviate from a linear dependence. The deviation becomes more pronounced with increasing dose. An increase of irradiation creep is observed at hoop stresses above 100 MPa. Such behavior is in disagreement with the data of Ref. [*1*], according to which diametral strains and irradiation creep in these tubes were found to be linear with stress.

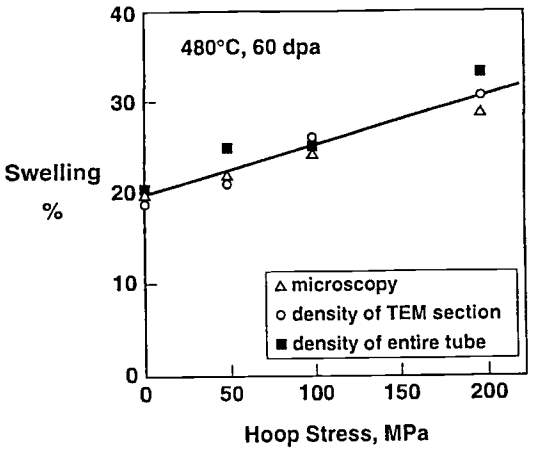


Figure 7 - *Swelling of EI-847 measured by three methods in tubes irradiated at ~480 °C to 60 dpa [1].*

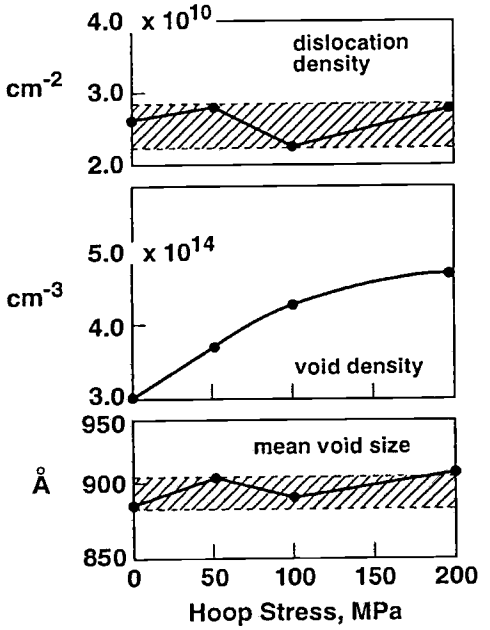


Figure 8 - *Microstructural data obtained by microscopy of EI-847 specimens irradiated at ~480 °C to 60 dpa [1].*

The data derived in the present study do not allow us to accurately determine the coefficients B_O and D employed in the standard irradiation creep equation:

$$B = \frac{\bar{\dot{\varepsilon}}}{\sigma} = B_o + D\dot{S}, \qquad (2)$$

where $\bar{\dot{\varepsilon}} / \bar{\sigma}$ is the ratio of the effective strain and effective stress, B_O is the creep modulus, independent of swelling, D is the creep-swelling coupling coefficient, and $\dot{S}$ is the swelling rate. However, with some assumptions it is possible to estimate these coefficients. Assuming that the swelling rate in creep tubes irradiated at 520°C to 20 dpa is very low and can be ignored, one finds at the hoop stress of 196 MPa that $B_O = 0.34 \times 10^{-6}$ (MPa dpa)$^{-1}$. This is lower than the usual value of ~1 x 10^{-6} MPa^{-1} dpa^{-1} and implies that some densification-induced negative strains have occurred, probably due to precipitation of niobium carbides. If we assume that the coefficient B_O is only slightly dependent on irradiation temperature and dose, this value of B_O can be used to determine the value of D at 45 and 60 dpa from eq. (1). At 196 MPa the values of D thus obtained are 6.5 x 10^{-3} MPa^{-1} and 2.5 x 10^{-3} MPa^{-1} for 45 and 60 dpa, respectively. It should be noted in the calculations of D at 45 dpa and at the hoop stress of 196 MPa that the swelling of the steel was taken to be equal to three times the diametral strain for the creep tube irradiated at zero stress. If we account for the dependence of swelling on stress, the value of D decreases slightly. From the estimates obtained one may conclude that the value of D decreases with increasing swelling level. The latter result is in agreement with data of Ref.[*1*] and other works by Garner and coworkers, which show the decrease of the coefficient D with increasing void swelling rate.

Two important observations were made in the present work when investigating the microstructure of the irradiated steel. First, applied stresses lead to increasing void number density, while their effect on void growth is very low. Second, the total dislocation density doesn't depend on stress. These observations are in good agreement with results of the microstructural investigation for neutron irradiated 16Cr-15Ni-3Mo-Nb stainless steel [*1*].

Conclusions

It was shown that the swelling of 16Cr-15Ni-3Mo-Nb stainless steels can vary strongly with minor changes in composition. Whereas EI-847 swelled easily, boron addition and other minor changes to produce EI-172 yielded a significant reduction in swelling. In both alloys, however, the swelling increased linearly with applied stress and the irradiation creep coefficients were very similar. Applied stresses influence the void number density, but not the void size or dislocation density.

References

[1] Vorobjev, A.N., Budylkin, N.I., Mironova, E.G., Porollo, S.I., Konobeev, Yu.V. and Garner F.A., "Irradiation Creep and Stress-Enhanced Swelling of Fe-16Cr-15Ni-Nb Austenitic Steel in BN-350", *Journal of Nuclear Materials,* Vols. 258-263, 1998, pp. 1618-1622.

[2] Garner, F.A., Porter, D.I., and Makenas, B.J., "A Third Stage of Irradiation Creep Involving its Cessation at High Neutron Exposures", *Journal of Nuclear Materials*, Vol. 148, 1987, pp. 279-287.

[3] Bates, J.F., and Gilbert E.R., "Experimental Evidence for Stress-Enhanced Swelling", *Journal of Nuclear Materials*, Vol. 59, 1975, p. 95.

[4] Porter, D.L., Takata, M.L., and Wood, E.L., "Direct Evidence for Stress-Enhanced Swelling in Type 316 SS", *Journal of Nuclear Materials*, Vol. 116, 1983, p. 272.

[5] Bates, J.F., and Gilbert, E.R.,"Stress Effect on Swelling in 316 SS", *Journal of Nuclear Materials*, Vol. 71, 1978, p. 286.

[6] Ehrlich K., "Irradiation Creep and Interrelation with Swelling in Austenitic Stainless Steels", *Journal of Nuclear Materials*, Vol.100, 1981, p. 149.

[7] Garner, F.A., "Irradiation Performance of Cladding and Structural Steels in Liquid Metal Reactors", in Nuclear Materials Science and Technology: A Comprehensive Treatment, Ch. 6, Vol. 10A, VCH Verlagsgesellschaft mbH, Weinheim, 1994, pp. 419-543.

Andrey D. Lopuga[1] and Yury S. Pyatiletov[1]

Effects of Impurity on Radiation Creep Rate of the Interstitial Solid Solutions

Reference: Lopuga, A. D. and Pyatiletov, Y. S., **"Effects of Impurity on Radiation Creep Rate of the Interstitial Solid Solutions,"** *Effects of Radiation on Materials: 19th International Symposium, ASTM STP 1366,* M. L. Hamilton, A. S. Kumar, S. T. Rosinski, and M. L. Grossbeck, Eds., American Society for Testing and Materials, West Conshohocken, PA, 2000.

Abstract: The numerical self-concerted calculation of the radiation creep rate of the interstitial solid solutions was carried out with allowance for main effects of impurity on creep rate: formation of impurity atmosphere around dislocations and voids; generation of the fixed and mobile impurity atom-intrinsic point defect complexes.

Keywords: interstitial atom; vacancy; impurity atmosphere; radiation creep

Introduction

It is well known that impurities in the irradiated metals can essentially modify the physical-mechanical properties, in particular, the radiation-induced deformation rate [*1*]. There are various effects of impurities on swelling and creep rate [*2*]. The following effects are of great importance for the interstitial solid solutions. At first, the impurity atoms can trap interstitials and vacancies, forming with them stable fixed complexes as additional recombination centers for intrinsic point defects (IPDs) and reducing the radiation-induced deformation rate. Secondly, segregation of impurities on the sinks (dislocations, voids etc.) can change point defect capture efficiencies, with which the deformation rate is straight connected. Thirdly, impurities can form with IPDs complexes characterized by high mobility. For interstitials and vacancies, the additional migration channel to sinks in structure of such complexes is opened. That results in the modification of diffusion fluxes as a whole and, therefore to the modification of the deformation rate.

In order to research the effects of impurities on the deformation rate of the interstitial solid solutions under irradiation, it is necessary to construct a theoretical model of the radiation creep, which apparently takes into account all above-mentioned effects. In the present paper such simplified model is proposed. Using this model, the physical values determining the creep rate are numerically calculated.

[1]Research scientist and professor, respectively, Institute of Nuclear Physics, Almaty, 480082, Kazahkstan.

Copyright© 2000 by ASTM International www.astm.org

Radiation Creep Model

Let the dislocation system contained in a specimen be rectilinear and have density ρ_d and Burgers vector b. Due to induced dislocation preference [*3, 4*] the external stresses result in that the dislocations glide down to the stop on obstacles. If shift stress is sufficiently large the dislocation overcomes by force some number of barriers, including assemblages of the radiation point defects and moves in the glide plane on the distance L, which depends on the distribution of barriers, their strength, and also on magnitude of external stress. As applied stress is less than critical shift stress, the dislocation is not capable to overcome all barriers, therefore, gone the distance L, it is fixed on them in some stable configuration. Under irradiation it climbs these barriers leaving in other glide plane and again glides on the distance L. Further described process multiply repeats. As a result, the specimen is deformed, and in general as gliding and climbing of dislocations contributes.

We designate by λ a mean size of barriers. If the mobile impurity atom-IPD complexes are available, the creep rate is defined by

$$\begin{aligned}\dot{\varepsilon} &= \frac{L}{3\lambda}\rho_d \Omega(I_I + I_{iI} - I_V - I_{iV}) \\ &= \frac{L}{3\lambda}\rho_d (Z_I D_I C_I^0 + Z_{iI} D_{iI} C_{iI}^0 - Z_v D_V C_V^0 - Z_{iv} D_{iv} C_{iV}^0),\end{aligned} \tag{1}$$

where I_β and $I_{i\beta}$ are a number of interstitials (β=I), vacancies (β=V), complexes the impurity atom-interstitial ($i\beta$=iI) and the impurity atom-vacancy ($i\beta$= iV), adsorbed by dislocation per unit length and unit time; Z_β and $Z_{i\beta}$ are capture efficiencies for point defects β and complexes $i\beta$: $Z_\beta = \Omega I_\beta / D_\beta C^0{}_\beta$, $Z_{i\beta} = \Omega I_{i\beta} / D_{i\beta} C^0{}_{i\beta}$; D_β and $D_{i\beta}$ are diffusivities of point defects β and complexes $i\beta$; $C^0{}_\beta$ and $C^0{}_{i\beta}$ are their atomic concentrations on half of distance between the sinks; Ω is atomic volume.

Numerical Calculation of Creep Rate

As is seen from the formula (1), the creep rate is determined by fluxes of the intrinsic point defects and the mobile complexes on the dislocation. These fluxes could be found by the numerical method, if the steady-state distributions of the mobile point defects around of sinks were known. The steady-state distributions can be obtained to solve the system of diffusion equations for IPDs and complexes the impurity atom-IPD with allowance for the mutual interaction of the point defects and the interaction with elastic fields of sinks. For solving this problem the various approximations and models are used. They are discussed in the paper [*5*]. From which follows, that three models are applied more often: 1) the model of the absorbing medium; 2) the model of periodic distribution of sinks; 3) the hybrid model as the combination two previous ones. The model of absorbing medium is considered most successful. However, for its usage it is necessary to set boundary conditions on indefinitely large distance from the chosen sink. For this reason, such model cannot be used for numerical calculation, when a settlement grid with the final-size cells should be set. For this reason we use hybrid model, according to

which dislocation places in centre of the cylindrical cell; in space inside the cell voids are considered uniformly "smeared"; outside the cell the crystal represents as similar absorbing medium with uniformly "smeared" both dislocation and voids.

In general when with IPD and the mobile impurity atom-interstitial and impurity atom-vacancy mobile complexes are considered, for calculation of steady-state concentration of these point defects in the cell around of dislocation we will write down following diffusion equations:

$$D_V\nabla^2 C_V + \frac{D_V}{k_b T}(\nabla C_V \nabla E_V^{(d)} + C_V \nabla^2 E_V^{(d)}) + G - D_V k_V^{(h)2} C_V - \alpha C_V C_I + \gamma_{iV} C_{iV} - \\ - \mu_I C_V C_{iI} - \kappa_V C_V (C_i - C_{iI} - C_{iV}) = 0; \quad (2)$$

$$D_I\nabla^2 C_I + \frac{D_I}{k_b T}(\nabla C_I \nabla E_I^{(d)} + C_I \nabla^2 E_I^{(d)}) + G - D_I k_I^{(h)2} C_I - \alpha C_V C_I + \gamma_{iI} C_{iI} - \\ - \mu_V C_I C_{iV} - \kappa_I C_I (C_i - C_{iI} - C_{iV}) = 0; \quad (3)$$

$$D_{iV}\nabla^2 C_{iV} + \frac{D_{iV}}{k_b T}(\nabla C_{iV} \nabla E_{iV}^{(d)} + C_{iV} \nabla^2 E_{iV}^{(d)}) - D_{iV} k_{iV}^{(h)2} C_{iV} - \alpha' C_{iV} C_{iI} - \\ - \gamma_{iV} C_{iV} - \mu_V C_I C_{iV} + \kappa_V C_V (C_i - C_{iI} - C_{iV}) = 0; \quad (4)$$

$$D_{iI}\nabla^2 C_{iI} + \frac{D_{iI}}{k_b T}(\nabla C_{iI} \nabla E_{iI}^{(d)} + C_{iI} \nabla^2 E_{iI}^{(d)}) - D_{iI} k_{iI}^{(h)2} C_{iI} - \alpha' C_{iV} C_{iI} - \\ - \gamma_{iI} C_{iI} - \mu_I C_V C_{iI} + \kappa_I C_I (C_i - C_{iI} - C_{iV}) = 0; \quad (5)$$

where C_i is impurity concentration in impurity atmosphere; $E_\beta^{(d)}$ and $E_{i\beta}^{(d)}$ are energies of elastic interaction for point defects β and complexes $i\beta$ with the dislocation, surrounded the impurity atmosphere; $k_\beta^{(h)2}$ and $k_{i\beta}^{(h)2}$ are void capture strengths for the point defects β and the complexes $i\beta$ respectively; α is mutual recombination coefficient for interstitial atoms and vacancies; α' is mutual recombination coefficient for complexes iI and iV; μ_β is recombination coefficient for free point defects β with complexes contained point defect of the opposite type; κ_β is coefficient of capture of the defects β by impurity atoms; $\gamma_{i\beta}$ is inverse to average life-time of a defect in the complex $i\beta$. These coefficients are set by the following formulas:

$$\alpha = \frac{\omega \nu_D}{\Omega}\exp(-E_I^m / k_b T); \quad (6)$$

$$\alpha' = \frac{\omega \nu_D}{\Omega}\exp(-E_{iI}^m / k_b T); \quad (7)$$

$$\mu_I = 4\pi r_I D_V / \Omega; \quad (8)$$

$$\mu_V = 4\pi r_V D_I / \Omega; \quad (9)$$

$$\kappa_\beta = 4\pi r_{i\beta} D_\beta / \Omega; \quad (10)$$

$$\gamma_{i\beta} = \frac{D_\beta}{b_0^2}\exp(E_{i\beta}^b / k_b T); \quad (11)$$

$$k_{\beta}^{(h)2} = Y_{\beta} 4\pi r_h N_h; \qquad k_{i\beta}^{(h)2} = Y_{i\beta} 4\pi r_h N_h; \tag{12}$$

where ν_D is Debye frequency; r_β is radius of volume, in which defect recombines with opposite point defect; $r_{i\beta}$ is radius of capture of point defect by the impurity atom; b_0 is size near interatomic distance; $E^b_{i\beta}$ is binding energy of the complex $i\beta$; E^m_I is migration energy of interstitial atom; Y_β and $Y_{i\beta}$ are void efficiencies for point defects β and the complexes $i\beta$ respectively; r_h is average radius of voids.

In order to solve the differential equation system (2)-(5), it is necessary to set boundary conditions. According to the results of computer simulation, the radiuses of zones of spontaneous capture by dislocation for vacancies r^0_{dV} and interstitial atoms r^0_{dI} differ from each other $r^0_{dI} > r^0_{dV}$, and IPD, getting in the own zones of capture, have positive binding energy with dislocation $E^b_{d\beta}$. Therefore we will consider that at $r=r^0_{d\beta}$ the concentration of IPDs β is equal to zero:

$$C_\beta(r^0_{d\beta})=0. \tag{13}$$

As $E^b_{d\beta}$ is more large than the binding energy of the complex the impurity atom-IPD, on boundary of capture zones (at $r=r^0_{d\beta}$) complexes $i\beta$ decay, and IPDs leave on dislocation, and impurity atoms come back in the bulk. Therefore the boundary conditions for complexes at $r=r^0_{d\beta}$ will look as follows:

$$C_{i\beta}(r^0_{d\beta})=0. \tag{14}$$

On external boundary of the cell (at $r = R_d$, where R_d is average half distance between dislocation) the concentration C^0_β and $C^0_{i\beta}$ are determined from the equation system of balance for concentration of point defects β and $i\beta$ in absorbing medium with uniformly "smeared" dislocations and voids and characterised by the sink strengths:

$$k_{\beta}^2 = k_{\beta}^{(h)2} + k_{\beta}^{(d)2}; \qquad k_{i\beta}^2 = k_{i\beta}^{(h)2} + k_{i\beta}^{(d)2}; \tag{15}$$

where $k^{(d)2}_\beta$ and $k^{(d)2}_{i\beta}$ are dislocation strength for defects β and complexes $i\beta$ respectively:

$$k^{(d)2}_\beta = Z_\beta \rho_d; \qquad k^{(d)2}_{i\beta} = Z_{i\beta} \rho_d. \tag{16}$$

These equations are from (2)-(5), in which spatial derivatives are equal to zero, $k^{(h)2}_\beta$ and $k^{(h)2}_{i\beta}$ are replaced on k^2_β and $k^2_{i\beta}$ respectively, and C_t is done on C^0_i:

$$G - D_V k_V^2 C_V^0 - \alpha C_V^0 C_I^0 + \gamma_{iV} C_{iV}^0 - \mu_I C_V^0 C_{iI}^0 - \kappa_V C_V^0 (C_i^0 - C_{iI}^0 - C_{iV}^0) = 0; \tag{17}$$

$$G - D_I k_I^2 C_I^0 - \alpha C_I^0 C_V^0 + \gamma_{iI} C_{iI}^0 - \mu_V C_I^0 C_{iV}^0 - \kappa_I C_I^0 (C_i^0 - C_{iI}^0 - C_{iV}^0) = 0; \tag{18}$$

$$D_{iV} k_{iV}^2 C_{iV}^0 - \alpha' C_{iV}^0 C_{iI}^0 + \gamma_{iV} C_{iV}^0 - \mu_V C_I^0 C_{iV}^0 - \kappa_V C_V^0 (C_i^0 - C_{iI}^0 - C_{iV}^0) = 0; \tag{19}$$

$$D_{iI} k_{iI}^2 C_{iI}^0 - \alpha' C_{iV}^0 C_{iI}^0 + \gamma_{iI} C_{iI}^0 - \mu_I C_V^0 C_{iI}^0 - \kappa_I C_I^0 (C_i^0 - C_{iI}^0 - C_{iV}^0) = 0; \tag{20}$$

The non-linear equation system (17)-(20) is solved numerically by an iterative method. In result we determine boundary conditions on external boundary:

$$C_{\beta}(R_d)=C^0_{\beta}; \qquad C_{i\beta}(R_d)=C^0_{i\beta} \tag{21}$$

and, hence, one can begin to solve the equation system (2)-(5).

Results

Impurity Atmospheres

We shall consider b.c.c.-crystal, in which the interstitial solutes with a mean concentration C_i^0 are distributed. In crystal the rectilinear edge dislocation is created, which length considerably exceeds an average distance between impurity atoms. Let us connect with it coordinate system (x, y, z), considering, that the line of the dislocation lies along axes z, the Burgers vector is directed on axis x, and xz is gliding plane (Figure 1). Impurity atoms around a dislocation form an impurity atmosphere. Taking into account, that the mutual interaction of impurity atoms provides an ordered disposition of atoms, we shall consider, that all impurity atoms are in middles of edges of the lattice and fill in $C_i^0 N$ from the available N octahedral positions. Thus, impurity dipoles will be oriented in a direction z ', which corresponds to the axis < 001 > b.c.c.-lattice. Then impurity dipole orientation is determined by two angles: θ is angle between axis z and axis of dipole; φ is angle between an axis x and projection of the dipole on a plane xz. The numerical parameters necessary for calculation are taken for carbon martensite (Table 1) [6].

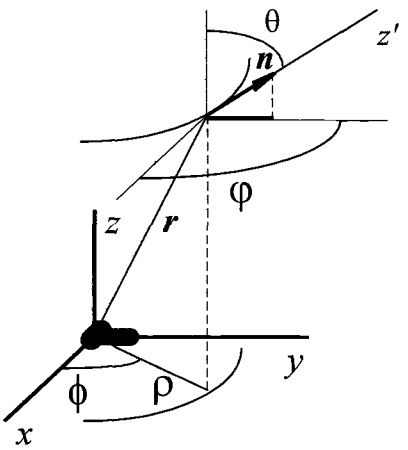


Figure 1 – *Orientation of the Impurity Dipole.*

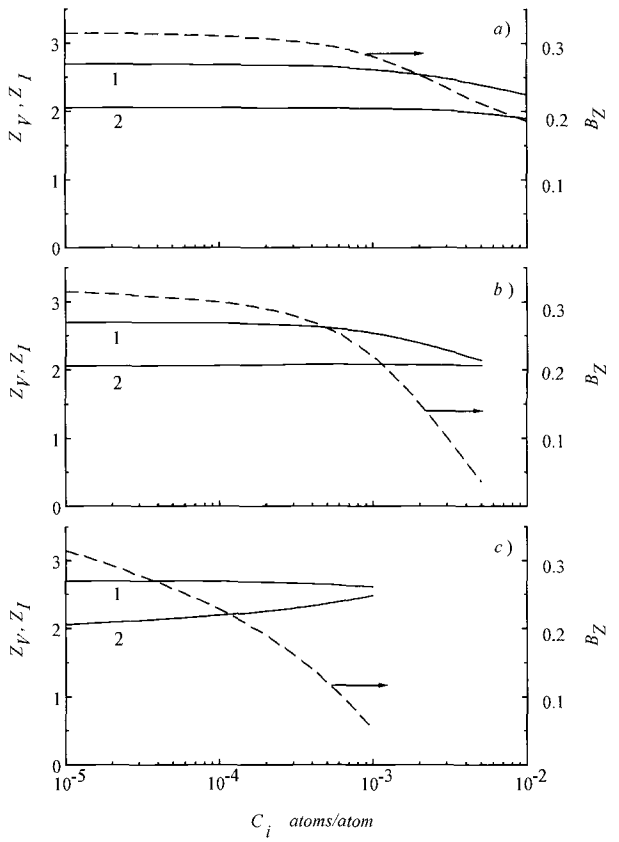


Figure 2 - *Dependencies of Capture Efficiencies for Interstitials (1) and Vacancies (2) and Bias (Dash Curve) on Impurity Concentration for Various Dislocation Systems: a) the Impurity Dipole is Along the Dislocation Line; b) 1/2 [111], ($\bar{1}\bar{1}2$); c) 1/2 [111], ($\bar{1}10$).*

On (Figure 2) the dependencies of Z_β and B are represented on the impurity concentration C_i^0 for various dislocation systems. With increase of impurity concentration for all systems B monotonically decreases, but for impurity dipoles oriented not along the dislocation line B decreases considerably more strong. For the glide system with Burgers vector 1/2 [111] and glide plane ($\bar{1}\ \bar{1}\ 2$) the bias B is equal zero at $C_i^0=6\cdot10^3$, and for the system 1/2 [111], ($\bar{1}\ 10$) already at $C_i^0=2\cdot10^3$.

On (Figure 3) dependencies of relative creep rate $\varepsilon / \varepsilon_0$ (ε_0 is creep rate at $C_i^0=0$ *atoms/atom* and $\theta=0^0$) on impurity concentration for various glide systems are shown. Impurity atmosphere around the dislocation with Burgers vector 1/2 < 111 > and glide plane {112} more strong reduce creep rate, with increase of impurity concentration, than atmosphere around the dislocation with Burgers vector 1/2 < 111 > and glide plane {110} at orientations of impurity dipoles along the direction [001].

Table 1 -- *Calculating Parameters*

Parameter	Symbol	Value
Vacancy migration energy (eV)	E^m_V	1.3
Interstitial migration energy (eV)	E^m_I	0.3
Vacancy diffusion coefficient pre-exponential (m^2/sec)	D^0_V	$0.58 \cdot 10^{-4}$
Interstitial diffusion coefficient pre-exponential (m^2/sec)	D^0_I	10^{-7}
Atomic volume (m^3)	Ω	$1.2 \cdot 10^{-29}$
Vacancy relaxation volume	$\Delta V_V/\Omega$	-0.5
Interstitial relaxation volume	$\Delta V_I/\Omega$	1.1
Burgers vector (m)	b	$2.48 \cdot 10^{-10}$
Shear modulus (MPa)	μ	$8 \cdot 10^4$
Poisson's ratio	ν	0.3
Dislocation density (m^{-2})	ρ_d	$3 \cdot 10^{14}$
Mean void radius (m)	r_h	10^{-8}
Void density (m^{-3})	ρ_h	10^{20}
Defect production rate (dpa/sec)	G	10^{-6}

Impurity Traps

Impurity traps are centers of the recombination of IPD and hence influence to steady-state distribution of interstitials and vacancies in the specimen, and consequent on magnitudes Z_β and C^0_β, defining the radiation creep rate. As the complexes the impurity

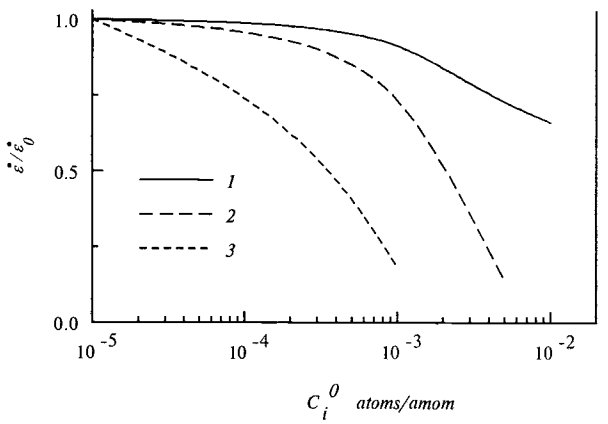


Figure 3 - *Dependencies of Relative Creep Rate on Impurity Concentration for Various Dislocation Systems: 1) the Impurity Dipole is Along the Dislocation Line; 2) 1/2 [111], ($\bar{1}\bar{1}2$); 3) 1/2 [111], ($\bar{1}10$).*

atom-IPD are fixed, in the formula (1) fluxes of mobile complexes are equal to zero. To calculate the steady-state concentration of IPD around the dislocation with allowance for such complexes, in equations (2)-(5) it is necessary to put $D_{i\beta}=0$ and $\alpha'=0$. The boundary conditions for IPD are set by the formulas (13), (21a), and the concentration of IPD on the external boundary of the settlement cell is determined from equations (17)-(20), in which it is necessary also to put $D_{i\beta}=0$, $\alpha'=0$.

As a result of carried out calculations it was established that the account of the recombination of IPD on impurity traps results in two effects: at first, the concentration of free IPD is reduced and, accordingly, there is distinct from zero the concentration of complexes the impurity atom-vacancy, secondly, the curve gradient $C_\beta(r)$ on the sink surface decreases, *i.e.* the relative fluxes of interstitials and vacancies on sinks decrease.

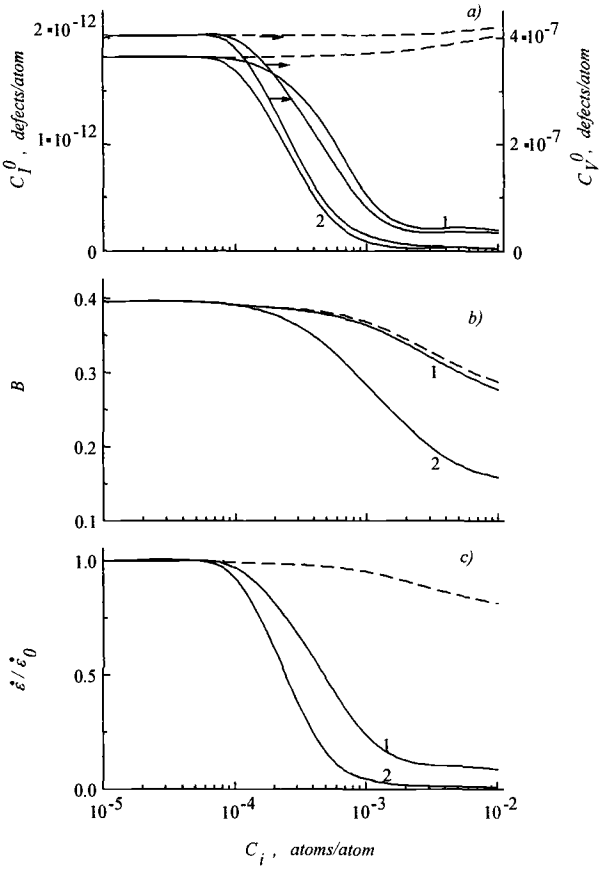


Figure 4 - *Dependencies of Stationary Concentration of Interstitials and Vacancies (a), Bias (b) and Relative Creep Rate (c) on Impurity Concentration: E_{iV}^b = 0,3 eV (1), E_{iV}^b = 0,5 eV (2) and without Impurity Trapping (Dash Curve).*

And these both effects are amplified with magnification of E_{iV}^b and C^0_i. On (Figure 4) the dependencies of concentrations IPD C_I^0 and C_V^0, immediately included in the formula for the creep rate (1), on impurity concentration is represented. As it is seen from (Figure 4*a*) $C_I^0(C^0_i)$ and $C_V^0(C^0_i)$ behave identically, sharply decreasing at magnification C^0_i from 10^{-4} up to 10^{-3}. And the effect will increase with magnification E_{iV}^b. On (Figure 4*b*) the dependence of bias B on C^0_i, is represented. From this figure it is followed that B as well monotonically decreases with magnification C^0_i, but not so strongly, as C_β^0. At last, on (Figure 4*c*) are indicated dependence of the relative creep rate $\dot{\varepsilon}/\dot{\varepsilon}_0$ on impurity concentration C^0_i at E_{iV}^b=*1,3* and *0,5eV*. On the same figure the dependence $\dot{\varepsilon}/\dot{\varepsilon}_0$ on C^0_i, found without impurity trapping (dashed line) is indicated. From comparison of solid lines with dashed one it is may see, that at account of impurity trapping the creep rate decreases with growth C^0_i considerably more strong, than without their account, and the effect will increase with magnification E_{iV}^b.

From comparison of (Figures 4a and 4в) it follows the decrease of concentration of free IPD at the expense of degree of vacancies by impurity traps and recombination on them IPD influences on the creep rate more strong, than modification of concentration profiles near to sinks, defining magnitude of parameters Z_β and B.

Mobile Complexes

Calculations have shown that the account of mobility of the impurity atom-IPD complexes results in two main effects: at first, the concentration of IPD on comparison with the concentration for case of fixed complexes increases; secondly, fluxes of mobile complexes on sinks and the gradient for $C_\beta(r)$ on sink surface is increased, that is the fluxes of IPD on sinks increase. The indicated effects amplify with magnification of mobility of complexes.

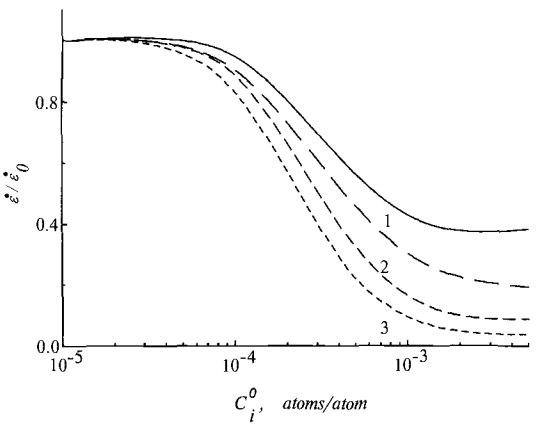


Figure 5 - *Dependencies of Relative Creep Rate on Impurity Concentration: All Complexes are Mobile (Solid Line); Impurity Atom - Vacancy Complexes (Dashed Line 1) are Mobile Only; Impurity Atom - Interstitial Complexes (Dashed Line 2) are Mobile Only; All Complexes are Immobile (Dashed Line 3).*

For revealing direct effect of mobile complexes on the creep rate, the fluxes on the dislocation of all mobile components were calculated. Calculations of these fluxes on impurity concentration for $E_{iV}^m = 1,6eV$, $E_{iI}^m = 0,3eV$ have shown, that with increases C_i^0 the fluxes of IPD on the dislocation $I_I^{(d)}$ and $I_V^{(d)}$ decrease, whereas the fluxes of complexes $I_{iI}^{(d)}$ and $I_{iV}^{(d)}$ are increased. The creep rate is determined by differences of fluxes $I_I^{(d)}$-$I_V^{(d)}$ and $I_{iI}^{(d)}$-$I_{iV}^{(d)}$ therefore, at low impurity concentration the IPD fluxes is mainly contributed to magnitude $\dot{\varepsilon}$, and with increase C_i^0 the significance of IPD fluxes in structure of complexes increases. From this it is possible to assume, that at account of mobility of complexes the creep rate will be higher, than in case, when the complexes are fixed. It is confirmed by calculations of dependence of the creep rate on impurity concentration, which results are represented on (Figure 5) (solid line). For comparison the dependence $\dot{\varepsilon} / \dot{\varepsilon}_0$ on C_i^0 for fixed complexes (dashed line 3) is indicated.

To study as each complex (*iI* or *iV*) influence on the creep rate separately, the calculation of $\dot{\varepsilon} / \dot{\varepsilon}_0$ for two cases was carried out. In first case only mobile complexes *iI* (dashed curve 2 on (Figure 5)) was considered, and the migration energy of complexes was accepted to equal to the migration energy of interstitials, *i.e.* the complexes were maximum mobile. In second case only complexes *iV* (dashed curve 1 on (Figure 5)) were mobile, and the migration energy of complexes was taken rather large ($E_{iV}^m = 1,6eV$), i.e. the complexes *iV* have little mobility. Nevertheless, in the second case the curve of dependence $\dot{\varepsilon} / \dot{\varepsilon}_0$ on C_i^0 deviates from the curve 3, corresponding situation with fixed complexes *iI* and *iV*, more strong, than in first one, and places closer to the curve 1. From above it follows that the mobile complexes the impurity atom-vacancy influence on the creep rate stronger, than complexes the impurity atom-interstitial.

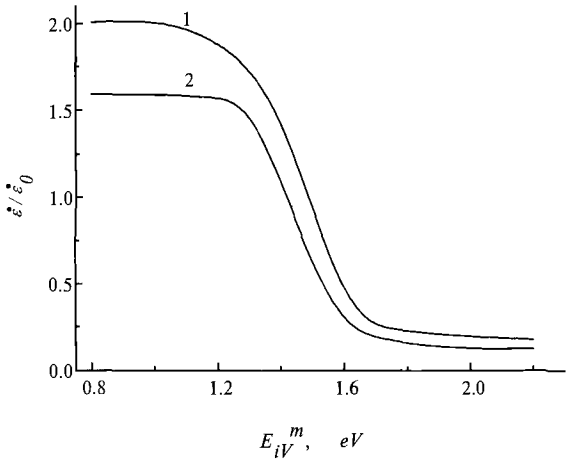


Figure 6 - *Dependence of Relative Creep Rate on Migration Energy of Impurity Atom – Vacancy Complexes: Impurity Atom - Interstitial Complexes are Mobile ($E_{iI}^m = 0,3$ eV, Curve 1) and Immobile (Curve 2).*

For quantitative confirmation of made conclusion the dependence $\varepsilon / \dot{\varepsilon}_0$ on migration energy of the impurity atom-vacancy complexes E_{iV}^m (Figure 6) is calculate. Two situations are considered: the complexes *iI* are fixed (curve 2) and they are as much as possible mobile ($E_{iI}^m=0,3eV$, curve 1). Thus, the curves 1 and 2 limit area with all possible values of migration energy of complexes *iI* and *iV*. From (Figure 6) it is seen, that at large values E_{iV}^m the creep rate is close to that for a material with fixed complexes. At magnification of mobility of complexes *iV*, when the value E_{iV}^m comes about the migration energy of free vacancies E_V^m, the creep rate becomes higher, than for the pure material. It is explained to that the part of IPD migrates on dislocations and voids in structure of complexes, the interaction energy for that with sinks is higher, than for IPD, and, therefore, the dislocation bias is higher.

Conclusion

The following main conclusions may be made:

- dipole orientation essential affects creep rate;
- the decreases of concentration of intrinsic point defects due to recombination at impurity traps affects the creep rate stronger than change of bias;
- the mobile impurity atom-vacancy complexes effects the creep rate stronger than the impurity atom-interstitial complexes;
- when mobility of complexes are about mobility of free point defects, the creep rate becomes higher than for the pure material.

References

[1] Williams, T.M., "The Effect of Solute Carbon on Void Swelling and Low Dose Dislocation Structures in Type 316 Austenitic Stainless Steel Irradiated with 46,5 MeV Ni6 + Ions," *Journal of Nuclear Materials*, Vol. 88, 1980, pp. 217-225.

[2] Mansur, L.K. and Yoo, M.H., "The Effects of Impurity Trapping on Irradiation-Induced Swelling and Creep," *Journal of Nuclear Materials*, Vol.74, No. 2, 1978, pp. 228-241.

[3] Pyatiletov, Yu.S. and Edemskyi, N.I., "Influence of Impurity Atmospheres Around Dislocations and Voids on Swelling and Radiation Creep Rate of the Interstitial Solid Solutions," *Technical Journal*, Vol. 62, No. 11, 1992, pp. 89-95.

[4] Heald, P.T. and Speight, M.V., "Point Defect Behaviour in Irradiated Materials," *Acta Met.*, Vol. 23, No. 11, 1975, pp.1389-1399.

[5] Brailsford, A.D. and Bullough, R., "The Theory of Sink Strengths," *Phil. Trans. Roy. Soc. London*, A302, No. 1465, 1981, pp. 87-137.

[6] Pyatiletov, Yu. S., Kislisin, S.B., and Edemskyi, N.I., "Theoretical Study of Defect Formation Processes in Metals," *Radiation Effects and Defects in Solids*, Vol. 25, 1993, pp. 224-237.

Yury V. Konobeev,[1] Valery A. Pechenkin,[1] and Frank A. Garner[2]

On the Role of Internal Stresses in Void Denuded Zone Formation Under HVEM-Irradiation of Metals and Alloys Preconditioned by Reactor Exposure

Reference: Konobeev, Y. V., Pechenkin, V. A., and Garner, F. A., **"On the Role of Internal Stresses in Void Denuded Zone Formation Under HVEM-Irradiation of Metals and Alloys Preconditioned by Reactor Exposure,"** *Effects of Radiation on Materials: 19th International Symposium, ASTM STP 1366,* M. L. Hamilton, A. S. Kumar, S. T. Rosinski, and M. L. Grossbeck, Eds., American Society for Testing and Materials, West Conshohocken, PA, 2000.

Abstract: Irradiation of thin metallic foils in a High Voltage Electron Microscope (HVEM) has been widely used for investigating void swelling. One of the observations in HVEM experiments is the formation of void denuded zones in foils prepared from metals and alloys preconditioned by neutron irradiation. Under electron irradiation, pre-existing voids shrink in regions near foil surfaces. Such a shrinkage is thought to occur without any transfer of vacancies to other voids and is proposed to be related to the interstitial flux exceeding the vacancy flux into near-surface voids. In the present paper internal stresses arising due to non-uniform swelling under conditions of HVEM irradiation are taken into consideration. It is demonstrated that by assuming the presence of sufficiently large stress gradients within the foil one can explain the origin of the void shrinkage in near-surface zones and also explain why a swelling enhancement is often observed on the boundary of the voided zone.

Keywords: swelling, void denuded zone, electron irradiation, thin foils, internal stresses, neutron preconditioning, stainless steel

Introduction

Irradiation of thin foils in a High Voltage Electron Microscope (HVEM) has been widely used as a rapid and convenient method of investigating the mechanisms and parametric dependencies of the void swelling phenomenon in metals and alloys. It is known that the electrons of ~1 MeV energy do not produce displacement cascades typical of irradiation with fast neutrons and self-ions. This feature of electron irradiation is thought to cause a high efficiency of electrons in producing freely migrating point defects, vacancies and interstitials [1,3,4], and as a result yield higher swelling rates as compared with those observed during neutron or ion irradiations. For instance, Laidler et al.[*1*] observed that in annealed Type 316 stainless steel irradiated to 26 dpa with 1 MeV electrons in a HVEM at 680°C, the void volume fraction reached 68%, which corresponds to a swelling level of

[1] Head of Division and Head of Laboratory, respectively, State Scientific Center of Russian Federation, Institute of Physics and Power Engineering, Obninsk, Russia.

[2] Senior Staff Scientist, Pacific Northwest National Laboratory, Richland, WA, USA.

Copyright© 2000 by ASTM International www.astm.org

210 %. At these irradiation conditions the steady-state rate of swelling increase is ~3%/dpa, significantly larger than the 1%/dpa rate universally observed in fission neutron irradiations of austenitic stainless steels [*2*].

Another important observation in HVEM experiments is the formation of void denuded zones in foils prepared from pure metals (Ni [*3*], Cu [*4*]) and stainless steels both in unirradiated foils [*5*] and foils previously irradiated with neutrons to a relatively high damage dose [*6*]. Prior to HVEM irradiation, the void layer in neutron-irradiated specimens comprises the entire foil thickness exposed by electropolishing. After electron irradiation the regions near foil surfaces become denuded of voids even as the central region experiences void growth to high levels [*3,4,6*]. The shrinkage of near-surface voids appears to occur without any transfer of vacancies to other voids [*6*]. Such a behavior of near-surface void loss is thought to be related to the flux of interstitials exceeding the flux of vacancies into the voids.

Another manifestation of the void disappearance phenomenon near foil surfaces has been observed in foils, which have not been previously irradiated with neutrons. In such foils the denuded zones form naturally, but voids on the boundary of the denuded zone eventually grow to some large size that causes them to suddenly shrink and disappear when their diameter carries them beyond the original denuded zone boundary [*7,8*].

Furthermore, the depth distribution of voids across an electron irradiated surface shows that both the void densities and the swelling peak just outside each denuded zone, as demonstrated by both Buswell [*9*] and Garner [*10*]. Even more interestingly, the two near-surface peaks in swelling are usually not equal in height but are larger near one surface than the other. Garner has interpreted such distributions to result from stress gradients that develop as the result of differential swelling, noting that the stress distribution is modified when the foil buckles in response to large swelling [*10*]. Stereoscopic examination of small electron-irradiated area frequently shows such buckling and once buckling occurs, both the stress and the swelling distributions become asymmetrical.

There are many sources of spatial and time-dependent stresses in both unirradiated and especially irradiated foils that can lead to buckling. The foil is not comprised of two parallel surfaces but is a wedge-shaped foil of narrow angle attached to a larger volume of material with highly irregular cross section. There are locally varying internal stresses resulting from preparation of the original specimen as well as irregularities arising from both the polishing and the clamping forces on the TEM disk.

The electron beam induces strong radial gradients and temperature and thereby in stress. During irradiation there are also periodic interruptions in the beam-induced temperature gradients as the experiment is interrupted to take micrographs at the much lower and more uniform electron intensities required for photography. As the beam is turned on or off, or is spread out and refocused, there are large transients in temperature and thereby stress distribution. Irradiations are also usually conducted near the foil edge, leading to a radially asymmetrical distribution in temperature and stress about the irradiated area.

There is also a strong possibility that there is a temperature gradient across the foil thickness, due to the different net radiative heat fluxes from the two surfaces. These arise from the different local mass and temperatures of microscope components above and below the specimen holder. This possibility is supported by the fact that in any given

microscope, most of the foils are observed to buckle preferentially in one direction.

Once the instability is initiated and the foil buckles, the situation is self-propagating. The buckling is not an abrupt, mechanically unstable process, however, but rather a slow and progressive deformation process whose rate is driven by the rates of swelling and irradiation creep.

If we ignore most of the smaller stress contributions discussed above, both the void swelling in the interior of the foil and the behavior of voids in near-surface regions can still be strongly affected by internal stresses arising only from non-uniform swelling and irradiation creep.

The objective of this paper is to demonstrate that assuming the existence of sufficiently large gradients of internal stress in irradiated foils allows us to explain the void shrinkage near foil surfaces in specimens preconditioned by neutron irradiation, as well as some features of the enhancement of swelling and its distribution across the foil interior.

Sources of Major Internal Stresses in Foils

The major sources of internal stress in a foil under HVEM-irradiation are the radial temperature gradient, the mechanical interaction between the void bearing layer and the surrounding matrix, a non-uniform distribution of voids and dislocations in radial and perpendicular directions, as discussed in [*10*], and possibly also surface layers of compounds formed due to adsorption of oxygen, nitrogen and especially beam-deposited carbon.

A nearly Gaussian radial profile of the electron flux in a HVEM (the electron beam radius δR ranges usually from one to several μm) causing radial temperature and dose rate gradients that lead to non-uniform swelling. Also, the swelling is non-uniform along the incident electron beam direction (this direction is chosen below as the z-coordinate axis). It is well known that void denuded zones on the order of 100 nm in width form in metals and alloys under HVEM-irradiation [*5*]; i.e. a swelling gradient arises in the z-axis direction. This phenomenon is usually explained in terms of strongly reduced nucleation of voids due to low point defect concentrations near foil surfaces which act as point defect sinks. However, according to Refs. [*3,4,6*] such void denuded regions also develop in foils prepared from bulk specimens of metal and alloys preconditioned in a neutron environment. Prior to electron irradiation, the void bearing layer comprises the entire foil thickness exposed by electropolishing. Under HVEM irradiation, the uniformly distributed voids of relatively large diameters shrink quickly in the regions near the foil surfaces. The denuding effect begins immediately and ceases before a dose of 1-5 dpa is accumulated. Since the rate of thermally activated void shrinkage is usually negligible at HVEM irradiation conditions, such a denudation can only be rationalized if we assume that the diffusion flux of interstitials into the voids exceeds the flux of vacancies. Such a difference of point defect fluxes can be induced by non-uniform internal stresses in a foil under electron irradiation. It is known that there is a tendency for the vacancy flux to be directed toward compressive regions of a material and, vice versa, for the interstitial flux to be directed to regions of tension.

The picture of internal stress development appears to be rather complicated and dependent on the starting microstructure of a material. From the beginning of electron irradiation, due to heating by the non-uniform focused electron beam [*11,12*], compressive

thermal stresses arise in the cylindrical damage zone. The swelling in this zone leads to the appearance of additional compressive stresses due to mechanical interaction between the zone and surrounding material, in which the dose rate is negligible [*10*]. Both the swelling and swelling-induced stresses are non-uniform in both the r and z-directions. The radial swelling gradient is determined by the radial profile of electron flux and by the accompanying temperature gradient. Along the electron beam direction the swelling gradient is caused, in particular, by the point defect concentration profiles. Near the foil surfaces the concentrations are less than those of the bulk are since the surfaces are defect sinks.

With increasing swelling, the swelling-induced stresses may increase strongly and irradiation creep begins to play an increasing role in determining the local stress level. Eventually, the radial component of the swelling rate will be compensated by the irradiation creep rate. In this case the total strain of the irradiated region in z-direction will be determined only by the swelling. When buckling occurs this will lead to the appearance of additional tensile stresses in near-surface regions.

Analytical Treatment

In the approach developed below, a stress gradient along z-axis gives rise to a drift of point defects. As a result, additional point defect fluxes arise with the vacancy flux directed toward the central compressed foil zone and the interstitial flux to the foil surface. Under some conditions, the interstitial flux into voids in near-surface regions will exceed the vacancy flux so that the voids near foil surfaces will shrink under electron irradiation. Moreover, as it will be shown below, in the foil interior regions the swelling rate may increase up substantially if the second z-derivatives of the stress tensor become sufficiently large.

Under electron irradiation the mean vacancy concentration C_v and interstitial concentration C_i can be found from the following equations:

$$\nabla j_\alpha = G - k_\alpha^2 D_\alpha C_\alpha, \quad \alpha = v, i \tag{1}$$

where G are the dose rate, and k_α^2 the total sink strength for point defect α. The sink strengths k_α^2 will be taken below as follows: $k_v^2 = D + L$, $k_i^2 = k_v^2 + BL$, where $D=4\pi\langle r_v\rangle N_v$ ($\langle r_v\rangle$ is the mean void radius, N_v is the void number density), L is the total dislocation length per unit volume, and B is the dislocation bias factor. According to Ref. [*13*] the point defect flux j_α is given as

$$j_\alpha = -\nabla (D_\alpha C_\alpha) - \beta D_\alpha C_\alpha \nabla E^s_\alpha, \tag{2}$$

where $\beta = 1/kT$, k is the Boltzmann constant, T the absolute temperature, D_α the diffusion coefficient, and E^s_α is the change in the free energy ("interaction energy", see [*13*]) of the saddle-point configuration of the point defect in a strained crystal.

Considering vacancies and interstitials to be spherical inclusions, let us take into account only the size interaction in the interaction energy E^s_α

$$E^s_\alpha = -V_\alpha \sigma_{ii}, \tag{3}$$

where V_α is the point defect relaxation volume, which is the difference between the volume of the point defect and the atomic volume Ω. The value σ_o in eq. (3) is equal to $\sigma_o = \sigma_{ii}/3 = K\varepsilon_{ii}$, where K is the bulk modulus, ε_{ij} the elastic strain tensor [*13*].

For simplicity, the dependence of dose rate on the r and z coordinates will be ignored in the electron irradiated zone. In addition, it will be assumed that the value σ_o depends only on z ($0 \le z \le d$, where d is the foil thickness). At z=0 and z=d the point defect concentrations are taken to be zero. It will be assumed also, that voids themselves are not biased toward interstitial absorption. In this case, at any foil point the time derivatives of both the voidage $\Delta V/V$ and the void radius r_v are proportional to the difference $D_v C_v - D_i C_i$:

$$\frac{dr_v}{dt} = \frac{D_v C_v - D_i C_i}{r_v}, \tag{4}$$

$$\frac{d}{dt}\Delta V/V = D(D_v C_v - D_i C_i). \tag{5}$$

In the stress-free case the solution of eqs. (1)-(2) can be easily obtained and has the following form:

$$D_\alpha C_\alpha = \frac{G}{k_\alpha^2}(1 - g(k_\alpha z)), \tag{6}$$

where

$$g(k_\alpha z) = \frac{\sinh(k_\alpha d - k_\alpha z) + \sinh(k_\alpha z)}{\sinh(k_\alpha d)} = \frac{\cosh(k_\alpha z - k_\alpha d/2)}{\cosh(k_\alpha d/2)}. \tag{7}$$

Since the ratio $(k_i^2 - k_v^2)/k_v^2$ is proportional to the bias factor B and, consequently is small in the stress-free case, the difference $D_vC_v - D_iC_i$ can be obtained from eqs. (6)-(7) using a linear bias factor approximation:

$$F_o(x) = \frac{D_v C_v - D_i C_i}{\frac{G(k_i^2 - k_v^2)}{k_v^4}} = \frac{1}{4}[4 - g(x)(4 + x_o \tanh(x_o/2)) - (x_o - 2x)f(x)], \tag{8}$$

where the function g(x) is given by eq.(6) with $x = k_v z$, $x_o = k_v d$, and f(x)=dg(x)/dx.

The function $F_o(x)$ yields zero at $x = 0$ and $x = x_o$, but $F_o(x) = 1$ at $x \rangle\rangle 1$.

Void Denuded Zone Formation in a Neutron Preconditioned Material

As was mentioned above, internal stresses arise in a foil from the very beginning of electron irradiation, the stress field being determined by the differential swelling and depending on radiation time. The stress field and its evolution in the electron irradiated zone is not known at the present. One can assume that to doses lower than ~1 dpa the compression stress reaches some high level, and then ceases to increase significantly due to the action of irradiation creep.

To demonstrate a possible influence of stresses on the void behavior in a foil under

electron irradiation, two different stress profiles will be tried. One of them corresponds to an initial stage of void denuded zone formation. For this stage, the sink strengths of voids and dislocations in a neutron preconditioned material can be taken to be equal to the initial values ($k_\alpha^2=k_{\alpha o}^2$) and the stress profile to be proportional to the swelling rate so that

$$\sigma_o(x) = -\sigma_o F_o(x), \tag{9}$$

where σ_o is the absolute value of $\sigma_{ii}/3$, the function $F_o(x)$ is given by eq. (8), and $x=k_{vo}z$ and $x_o=k_{vo}d$.

For the stress profile given by eq.(9) one can solve analytically the equations (1) - (2) using the linear bias factor approximation. The normalized difference $D_vC_v - D_iC_i$ is:

$$F(x) = \frac{D_vC_v - D_iC_i}{\frac{G(k_i^2 - k_v^2)}{k_v^4}} = F_o(x) + A F_1(x), \tag{10}$$

where

$$A = \beta(V_i - V_v)\sigma_o k_{vo}^2/(k_{i0}^2 - k_{vo}^2), \tag{11}$$

$$F_1(x) = \frac{1}{3}\left[1 - \tanh^2\left(\frac{x_o}{2}\right) + g(x)\left(\frac{3x_o}{4}\tanh\left(\frac{x_o}{2}\right) - 1 - \tanh^2\left(\frac{x_o}{2}\right)\right) + 2f^2(x) - f(x)\frac{3}{2}\left(x - \frac{x_o}{2}\right)\right]. \tag{12}$$

One can be convinced that at sufficiently large values of x_o and A the function $F(x)$ at $0<x<0.8$ and $x_o-0.8<x<x_o$ is negative, and consequently, voids must shrink in these zones. At larger distances from foil surfaces this function becomes positive and goes through two maximums, approaching the function $F_o(x)$ in the central region of the foil. The maximum values of $F(x)$ depend linearly on A-parameter.

The second stress profile was chosen to reproduce the void behavior at the end of void denuded zone formation. This profile was taken in the following form:

$$\sigma_o(x) = \sigma_o(1/b_1 - g(bx)/b), \tag{13}$$

where b and b_1 are fitting parameters. Since in eqs. (1)-(2) only derivatives of the stress profile determine the solution, the fitting parameter b_1 can be taken so as to require that the stresses not exceed the amplitude σ_o in the foil.

In the case of constant sink strengths one can obtain an analytical solution of eqs. (1)-(2) with the stress distribution given by eq. (13). But due to disappearance of voids and, possibly, nucleation and growth of interstitial loops near foil surfaces, the sink strengths of voids and dislocations become dependent on the z-coordinate. Therefore, one has to solve eqs. (1)-(2) numerically in this case. The results of calculating the difference $D_vC_v - D_iC_i$ on the basis of eqs. (1)-(2), (9) and (13) are given below.

Results of Calculations

For these calculations experimental data have been used from an HVEM experiment [*6*] involving 1 MeV electron irradiation at 535°C at a dose rate G=1.07 x 10^{-3} dpa/s of annealed type AISI 304 austenitic stainless steel that was previously irradiated in the EBR-II fast reactor at 412°C to ≈70 dpa. The neutron irradiation had resulted in swelling of 11.2 %, a mean void diameter $< d_v >$ of 26.8 nm, and a void number density N_v of 9.7 x 10^{21} m^{-3}. Prior to electron irradiation, voids were distributed uniformly in the foil of thickness d=9000A. The void sink strength for the starting microstructure was equal to D =1.6 x 10^{15} m^{-2}. Unfortunately, data on the dislocation sink strength are not available from Ref.[*6*] and for these calculations it was taken as L=4 x 10^{14} m^{-2}. Such a choice is thought to be reasonable since in Ref. [*14*] for solution treated Type 304 stainless steel irradiated in EBR-II at 427°C to ≈65 dpa it was found that L= 3.4 x 10^{14} m^{-2}, $< d_v >$=20.0 nm, N_v= 8.7 x 10^{21} m^{-3}. Thus, the initial total sink strength is $k_{vo}^2 = D+L$=2 x 10^{15} m^{-2} and $x_o=k_{vo}d=40$. The mean voidage rate of approximately 0.16 %/dpa and the combination of sink strengths for point defects, $DL/(D+L)^2$ = 0.16 result in a bias factor value B of 1% for neutron preconditioned steel, and in the ratio $(k_{io}^2 - k_{vo}^2)/k_{vo}^2 = BL/(D+L)$ of 2 x 10^{-3}. Under HVEM-irradiation to 1 dpa, void denuded zones of d_1=100 ±5 nm in width formed at 535°C [*6*]. This width corresponds to $x_{dz}=k_{vo}d_1$=4.44; i.e. the denuding depth exceeds the mean free path $1/k_{vo}$ of the point defects by factor of 4.44. Obviously, the irradiation temperature of 535°C in the HVEM-experiment (≈0.48 T_m, T_m=1,672 K) is too low for void shrinkage from annealing (according to Ref. [*15*], the required temperature for annealing the voids of 22-23 nm diameter in AISI 304 stainless steel is ≈704°C=0.58 T_m).

From data on the dose dependence of voidage given in Ref.[*6*] one can estimate that the voidage rate reaches the level of ≈2.9 %/dpa to electron dose of 1 dpa, that is 18 times higher than the mean voidage rate of 0.16 %/dpa under neutron irradiation. The point defect relaxation volumes were taken to be equal to ones found for nickel in Ref.[*16*]: V_i=1.8Ω, V_v= - 0.2Ω with the atomic volume Ω of 11.5 x 10^{-30} m^3 for the steel.

The results of calculating the function $F(x)$ for the stress distribution given by eq. (9) are shown as curve 2 in Fig.1. Since this function is symmetrical in respect of the foil center, only one half of full curve is shown in Fig.1, i.e. for x ranging from 0 to 20. It is seen that this function is negative in the interval $0 \le x \le 0.8$. Consequently, voids should shrink in this region. Behind this region there is a well expressed maximum, and then the function $F(x)$ tends toward unity at the foil center.

The absolute value of F_{min} in the region of voids shrinkage must be sufficiently large in order to cause voids of 26.8 nm in diameter to disappear in the near-surface zones during the time Δt, corresponding to an electron dose $G\Delta t \approx 1$ dpa [*6*]. As a rough estimate, taking the difference $D_vC_v - D_iC_i$ to be constant and negative in the near-surface zones, from eq.(4) one calculates that this difference should be equal to - $<d_v>^2 G/8$, and, consequently, $F_{min} = - < d_v >^2 k_v^4 /8(k_t^2 - k_v^2)$.. For the parameters chosen above, one finds the quantity F_{min} = - 0.9/B=90. Both the minimum and maximum values of the function $F(x)$ depend almost linearly on the parameter A, which is related to stress amplitude σ_o as follows: $A=0.01\sigma_o/B$, where σ_o is in units of MPa. In contrast, the width of denudation is practically insensitive to the A-parameter. All curves in Fig.1 were obtained taking A = 1,600. The

corresponding stress amplitude equals $\sigma_o = |\sigma_{ii}/3| = 1{,}600$ MPa., which is probably the highest value of σ_0 that one can justify (see «Discussion» section). One can see in the case of the stress distribution given by eq. (9) that both the minimum value of $F(x)$ (F_{min}=-34.7) and the denuded depth (x_{dz}=0.8) are in disagreement with experimental data.

Curves 3 and 4 in Fig.1 show the function $F(x)$, calculated for the stress distribution given by eq. (13) with b=0.01. In the calculation the depth distribution of void sink strength $D(x)$ at dose of 1 dpa was taken in the following form:

$$D(x) = D(1 - g(b_2 k_{vo} z)), \tag{14}$$

where $b_2 = 1/x_{dz} = 0.225$.

The magnitudes of the parameters b and b_1 in eq. (13) were varied to get the void denuded zone width of 100 nm (x_{dz}=4.44) and also about 18-fold voidage rate enhancement in the central foil region under HVEM-irradiation. No success was achieved with the dislocation sink strength L equal to the starting value. This is due to presence of a hump of the function $F(x)$ just behind the zone of void shrinkage. This hump prevents broadening of the region where the function is negative. A noticeable broadening was obtained only in the case when the dislocation sink strength decreases up to L at the foil center with increasing the distance from foil surfaces. Such a decrease implies that the nucleation and growth of interstitial dislocation loops occurs in near-surface foil regions simultaneously with void denuded zone formation. Curves 3 and 4 were obtained for the following depth distribution of $L(x)$:

$$L(x) = L + L_1 \frac{\cosh(b_2 x - b_2 x_o/2) - 1}{\cosh(b_2 x_o/2) - 1}, \tag{15}$$

where L_1 is the dislocation sink strength at foil surfaces, $x = k_{vo} z$.

The calculation results are very sensitive to the magnitude of L_1. As seen from Fig.1, the curves 3 and 4 have no maximum for the parameters chosen, the function $F(x)$ is on the level of 16-18 in the central foil region. It should be emphasized that such a result was obtained for the bias factor value of 1%, i.e. neglecting possible cascade efficiency effects.

With b=0.01, both the requirements of internal stresses not exceeding the amplitude σ_0 over all of the irradiated zone and of the need to obtain a 16 to 18th-fold enhancement of the swelling rate in the void bearing layer leaves little room for a choice of the parameter b_1. This parameter was taken as $b_1 = b/(1-b)$. In this case both the tension stress at the foil surface and the compression stress at the foil center are equal to σ_o. The voidage rate enhancement is due to the second x-derivative of stress distribution being nearly constant in the case of b-magnitudes as small as 0.01. It should be noted that by changing slightly the stress distribution given by eq. (13) it is possible to shift the minimum position to larger x without a significant change of both the minimum and maximum values of the $F(x)$ function. However, in the present work no attempt has been made in such a direction.

Discussion

A number of questions should be answered in order for the results obtained above to

be considered as meaningful.

The most important question is the value of σ_o taken above for calculations. To address the question let us take into account that the electron irradiated zone of the foil is under compression. According to the elasticity theory, in a fully-dense cylinder loaded by an outer pressure, the non-diagonal components of the stress tensor are zero, with diagonal components being related to each other as follows: $\sigma_{rr} = \sigma_{\varphi\varphi} = (1/2\nu)\sigma_{zz}$ where ν is the Poisson's ratio. Therefore, the effective stress is $\sigma_{eff} = (1-2\nu)\sigma_{rr}$ and $\sigma_{ii} = 2(1+\nu)\sigma_{rr}$. Then it follows that $\sigma_o = \sigma_{ii}/3 = \sigma_{eff}\, 2(1+\nu)/3(1-2\nu)$. For estimation, taking into account the complex stress condition of the material one can put σ_{eff} to be equal to the tensile yield strength prior to electron irradiation. According to experimental data referenced by Garner [*17*], the yield strength of annealed 316 stainless steel reaches about 700-800 MPa after neutron irradiation at 410-420°C to 70 dpa. Assuming the yield strength in type 304 stainless steel being close to this value at the same irradiation conditions, at $\nu = 0.3$ one finds that σ_o = 1,520-1,730 MPa. The value $\sigma_o = \sigma_{ii}/3$ of 1,600 MPa falls in this range. So, this value of σ_o seems to be meaningful. But, more accurate estimations are needed because of the finite width of the foils used in HVEM experiments.

The next question is the electron dose needed to establish the stress field shown in eqs.(9) and (13) with $\sigma_o = \sigma_{ii}/3$ = 1,600 MPa. Since compression strains in the irradiated zone of the foil are caused by swelling, one has $\varepsilon_{ii} = \Delta V/V$. From the elasticity theory it follows that $\sigma_o = K\varepsilon_{ii} = K(\Delta V/V)$. Using the well known relationship $K = E/3(1-2\nu)$ between the bulk modulus and Young modulus E, and taking E =155 GPa at 535°C for stainless steels 304 and 316, one finds that $\Delta V/V$ must be of 1.2% in order to get the value of σ_o as high as 1,600 MPa. According to experimental data of Ref. [*6*], at 535°C and low electron doses the mean voidage rate in the neutron preconditioned 304 steel is approximately 3 %/dpa. Therefore, compression stresses may reach the level of 1,600 MPa already at dose of only $\approx$ 0.4 dpa. That is less than the dose of 1 dpa needed for the void denuded zone formation [*6*].

The third question is the existence of long-range stress fields like that given by eq. (13). To answer this question it is necessary to model self-consistently the simultaneous evolution of swelling and internal stress field in a foil under electron irradiation. For this purpose one needs realistic equations describing the nucleation of both voids and dislocation loops. No attempts have been undertaken so far in such a direction. But, one can imagine that at sufficiently high swelling levels the radial strain rate due to swelling at the central part of electron irradiated thin foil will be compensated by irradiation creep. In this case all the strain will occur in the direction perpendicular to foil surfaces. As a result, buckling will develop that may give rise to increase of tension stresses in near surface zones of the foil.

The fourth question is the irradiation creep may prevent reaching the very high stress amplitude of 1 600 MPa needed for explanation of both the void denuded zone width of 100 nm and the swelling rate enhancement by factor of 18. One can think that already at low doses the diametral strain rate $\dot{S}/3$ in electron irradiated zone due to swelling will be compensated by irradiation creep rate. It is known that the following relationship exists between the effective irradiation creep strain rate $\dot{\varepsilon}_{eff}$ and the stress-free swelling rate $\dot{S}_o$:

$\dot{\varepsilon}_{eff} = B_o G + D_o \dot{S}_o$, where σ_{eff} is the effective stress, B_o is the creep compliance, D_o is the creep-swelling coupling coefficient, $\dot{S}_o$ is the stress-free swelling rate [*14,15,16*]. For a fully-dense cylinder loaded by external pressure one has $\dot{\varepsilon}_{eff} = \dot{\varepsilon}_{rr}$ and $\sigma_o = \sigma_{eff}\, 2(1+\nu)/3(1-2\nu) \approx 2\sigma_{eff}$. At a sufficiently high swelling rate the creep compliance B_o can be neglected. By equating $\dot{S}/3$ to $\dot{\varepsilon}_{eff} = \sigma_{eff} D_o S_o$ one finds that

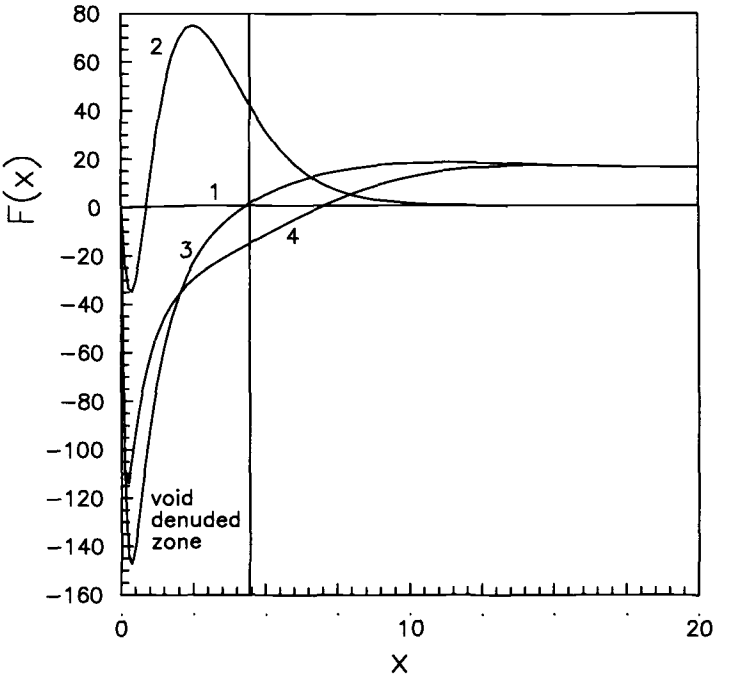


Figure 1 - *Calculated profiles of normalized void growth rate in a foil under HVEM-irradiation: 1- no stress case, 2 - eq. (9), 3 and 4 - eq. (13) at* $L_1 = 4 \times 10^{15}\ m^{-2}$ *and* $L_1 = 7.6 \times 10^{15}\ m^{-2}$, *respectively.*

$\sigma_o \approx 2\dot{S}/3D_o\dot{S}_o$. As it was shown above, the ratio $\dot{S}/\dot{S}_o$ may reach the value of 18 at foil midplane. Taking $D_o = 6 \times 10^{-3}$ MPa^{-1} [*14*] one obtains $\sigma_o \approx 2\,000$ MPa that is higher than the stress amplitude of 1,600 MPa taken in calculations. Moreover, experimental data give evidence (see, for example, Ref. [*20*]) on a decrease of D_o-value with increasing the swelling rate ("creep disappearance" at high dpa, as defined by Garner and coworkers [*17,21*]). The swelling rate of the annealed AISI 304 in the HVEM-experiment [*6*] exceeded 1%/dpa from the very beginning of electron irradiation. Lower values of D_o will result in more high stress amplitude.

In this work the bias factor B is considered to be identical for neutron and electron

irradiations. In principle, under cascade forming irradiation the bias factor value may be less by a factor of 0.5 to 0.1 as compared to one under 1 MeV electron irradiation due to a low efficiency of cascade in producing the freely migrating point defects. However, as it follows from calculations, the function $F(x)$ varies as ~1/B for an arbitrary depth distribution of stress, and, consequently, the difference D_vC_v - D_iC_i is independent of B-magnitude. Thus, the results of the present work do not allow us to elucidate a possible separate role of displacement cascades in production and accumulation of point defects.

The formation of void denuded zones at grain boundaries is a well-known feature of the microstructure of metals and alloys irradiated with neutrons and ions. One can expect that internal stresses caused by non-uniform void swelling play a substantial role in the void denudation at grain boundaries. But, usually the grain size is much larger than the thickness of foils used in HVEM experiments. In this case the stress distribution in the interior of grains should be more uniform and the profile of the difference D_vC_v-D_iC_i will resemble curve 2 in Fig.1. Probably, the maximum of this difference at the edge of the denuded zone is the cause of the enhanced voidage reported in many papers on the microstructure of neutron and ion irradiated metals and alloys.

Only swelling-induced stresses in the direction perpendicular to foil surfaces have been considered in the present paper. However, the possible contribution of dose rate gradients in the direction perpendicular to the incident electron flux on swelling enhancement can not be excluded. The necessary condition is that sufficiently large swelling in the central part of the foil will induce high enough compressive stresses imposed by the material surrounding the irradiated zone. It should be emphasized that effects of internal stresses mentioned above have been demonstrated ignoring a possible role of gradients of total point defect sink strength that may be developed under non-uniform swelling conditions. For a more accurate prediction of the void evolution under HVEM-irradiation it is necessary to model self-consistently the void swelling and stress field development in an electron irradiated foil as well as to take into account the possible role of irradiation creep.

Swelling-induced stresses also have been shown to play an essential role in ion irradiated materials resulting in such features as a swelling rate increase at some doses, anisotropic swelling leading to formation of a "step" on the target surface, spreading the depth of void formation and so on, as discussed by Garner and coworkers [*18,19*].

From the results of the present work it follows that the depth distribution of dislocation sinks for point defects probably affects strongly denuded zone formation during HVEM irradiations. If the interstitial flux exceeds the flux of vacancies into point defect sinks in near-surface foil regions, loop nucleation and growth should be enhanced in these regions. It seems to be important to verify experimentally such a prediction.

Conclusions

From the treatment given above one can conclude that gradients of internal stresses arising in foils due to non-uniform swelling under electron irradiation can significantly affect the void behavior and its distribution. First of all, an additional separation of point defect fluxes occurs near foil surface zones that results in the shrinkage of voids and the development of void denuded layers in metals and alloys preconditioned by neutron irradiation. In the case where internal stresses spread deeply into the foil one can expect an

enhancement of void swelling rate in the central electron irradiated zone. This enhancement will be in addition to any enhancement of the swelling rate arising from the greater survivability of point defects thought to be characteristic of electron-induced displacements.

References

[1] Laidler, J.J., Mastel, B., and Garner, F.A., "Swelling in Electron-Irradiated Type 316 Stainless Steel", *Properties of Reactor Structural Alloys After Neutron or Particle Irradiation, ASTM STP 570*, American Society for Testing and Materials, 1975, pp. 415-468.

[2] Garner, F.A., "Recent Insights on the Swelling and Creep of Irradiated Austenitic Alloys", *Journal of Nuclear Materials*, vol. 122-123, 1984, pp. 454-471.

[3] Harbottle, J.E., "The Influence of HVEM Irradiation on Neutron Induced Voids in Nickel", *Voids Formed by Irradiation of Reactor Materials, Proceedings of the B.N.E.S. European Conference*, S.E.Pugh, M.H.Loretto and D.I.R.Norris, Eds., Reading University, 1971, pp. 293-300.

[4] Makin, M.J.," The Production of Voids in Copper by Electron Irradiation in a 1 MV Electron Microscope", *Voids Formed by Irradiation of Reactor Materials, Proceedings of the B.N.E.S. European Conference*, S.E.Pugh, M.H.Loretto and D.I.R.Norris, Eds., Reading University, 1971. pp. 269-274.

[5] Garner, F.A. and Thomas, L.E., "Production of Voids in Stainless Steel by High Voltage Electrons", *Effects of Radiation on Substructure and Mechanical Properties of Metals and Alloys, ASTM STP 529*, American Society for Testing and Materials, 1973, pp. 303-325.

[6] Garner, F.A., Laidler, J.J., Mastel, B., and Thomas, L.E., "Influence of High Voltage Electron Microscope Irradiation on Neutron-Produced Microstructures in Stainless Steel", *Properties of Reactor Structural Alloys After Neutron or Particle Irradiation, ASTM STP 570*, American Society for Testing and Materials, 1975, pp. 433-448.

[7] Garner, F.A. and Laidler, J.J., "Review of Neutron and Charged Particle Intercorrelation Programs", *Proceedings of the Workshop on Correlation of Neutron and Charged Particle Damage, CONF-760673,* Oak Ridge, TN, June 8-10, 1977, pp. 177-239.

[8] Laidler, J.J., Garner, F.A., and Thomas, L.E., "Simulation Experiments with the High Voltage Electron Microscope", *Radiation Damage in Metals,* N.L. Peterson and S.D. Harkness, Eds., American Society of Metals, 1976, pp. 194-226.

[9] Buswell, J.T., "An Examination of the Distribution of Voids in Electron Irradiated Foils", *CECB Report RD/B/N3171,* October 1974.

[10] Garner, F.A., "Evidence of Stress-Affected Swelling in HVEM Irradiations", *Alloy Development Program Quarterly Technical Report, Oct.-Dec. 1975, TC-160-7*, Hanford Engineering Development Laboratory, pp. 101-123.

[11] Fisher, S.B., "On the Temperature Rise in Electron Irradiated Foils", *Radiation Effects*, vol. 5, 1970, pp. 239-243.

[12] Garner, F.A., Thomas, L.E., and Gelles, D.S., "Beam-Induced Temperature Changes in HVEM Irradiations", *Symposium on Experimental Methods for Charged Particle Irradiations, CONF-750947*, Gatlinburg, TN, Sept. 30, 1975, pp. 52-81.

[13] Wolfer, W.G., and Ashkin, M., "Diffusion of Vacancies and Interstitials to Edge Dislocations", *Journal of Applied Physics*, Vol. 47, No.3, 1976, pp. 791-800.

[14] Michel, D.J., and Smith, H. H., "Fatigue Behavior and Microstructure of Neutron Irradiated Thin Section Type 304 Stainless Steel at Elevated Temperatures", *Properties of Reactor Structural Alloys After Neutron or Particle Irradiation, ASTM STP 570*, American Society for Testing and Materials, 1975, pp. 156-170.

[15] Holmes, J.J., Robbins, R. E., Brimhall, J.L., and Mastel, B., "Elevated Temperature Irradiation Hardening in Austenitic Stainless Steel", *Acta Metallurgica,* , Vol. 16, 1968, p. 955.

[16] Bender, O. and Ehrhart, P., "Self-Interstitial Atoms, Vacancies and Their Agglomerates in Electron-Irradiated Nickel Investigated by Diffuse Scattering of X - Rays", *Journal of Physics. F: Metal Physics*, Vol. 13, 1983, No. 5.

[17] Garner, F.A., "Chapter 6, Irradiation Performance of Cladding and Structural Steels in Liquid Metal Reactors", in Vol. 10A, *Nuclear Materials, Materials Science and Technology: A Comprehensive Treatment*, VCH Publishers, 1994, pp. 419-534.

[18] Garner, F.A., Wire, G. L., and Gilbert, E. R., "Stress Effects in Ion Bombardment Studies", *Radiation Effects and Tritium Technology for Fusion Reactors, CONF-750989,* 1976, pp. 474-490.

[19] Wolfer, W.G. and Garner, F.A., "Swelling-Induced Stresses in Ion-Bombarded Surfaces: Effects of Crystalline Orientation, *Journal of Nuclear Materials,* Vols. 85-86, 1979, pp. 583-584.

[20] Garner, F. A., Toloczko, M. B., and Puigh, R. J., "The Relationship Between Swelling and Irradiation Creep in 20% Cold-Worked 316 Stainless Steel", *Effects of Radiation on Materials, 19th International Symposium, ASTM STP 1366,* M. L. Hamilton, A. S. Kumar, S. T. Rosinski and M. L. Grossbeck, Eds.,

American Society for Testing and Materials, West Conshohocken, PA, 1999.

[21] Toloczko, M. B. and Garner, F.A., "Relationship between Swelling and Irradiation Creep in Cold-Worked PCA Stainless Steel Irradiated to ~178 dpa at ~400°C", *Journal of Nuclear Materials*, Vols. 212-215, 1994, pp. 509- 513.

Y. Murase,[1] J. Nagakawa,[1] N. Yamamoto,[1] and Y. Fukuzawa[1]

Creep-Fatigue Response of 20% CW 316 SS Under Irradiation at 60°C

Reference: Murase, Y., Nagakawa, J., Yamamoto, N., and Fukuzawa, Y., **"Creep-Fatigue Response of 20% CW 316 SS Under Irradiation at 60°C,"** *Effects of Radiation on Materials: 19th International Symposium, ASTM STP 1366,* M. L. Hamilton, A. S. Kumar, S. T. Rosinski, and M. L. Grossbeck, Eds., American Society for Testing and Materials, West Conshohocken, PA, 2000.

Abstract: An in-beam creep-fatigue testing machine for a miniaturized specimen was developed at National Research Institute for Metals to investigate the synergistic effects of stressing and irradiation damage on the mechanical properties of materials. The loading and displacement measuring system of the machine is outlined in this paper. An in-beam creep-fatigue experiment was carried out with 17 MeV protons for 20% cold-worked 316 stainless steel at 60°C. The specimen size was $4 \times 10 \times 0.15$ mm in gauge with fatigue crack starter notch introduced at the edge. Creep-fatigue (ramp with hold) tests were carried out in stress control (536.4 MPa, 12 s ↔ 236.4 MPa, 1 s; rate = 50 MPa/s). Simple fatigue tests without holding time were also performed in the same condition. Although the lifetime of simple fatigue was substantially prolonged under irradiation, the prolongation was not so much in the creep-fatigue. The holding during irradiation appeared to play some role in reducing the lifetime.

Keywords: analytical instruments and methods, radiation effects, proton irradiation, mechanical properties, creep-fatigue, austenitic steels

Introduction

Structural materials in the fusion core will receive various loadings such as thermal and magnetic stress. At the same time, they will be subjected to the atomic displacement damage caused by high-energy neutrons. It is, therefore, important to understand the synergistic effect of stressing and irradiation damage on the lifetime of material in order to evaluate its feasibility for fusion reactor application. The nature of the stress is basically cyclic with holding periods, reflecting the thermal cycling due to periodic fueling/maintenance and steady burning periods, even in the advanced Tokamak fusion reactors with extended burn.

It is now recognized that the material response to loading is significantly modified under irradiation [1-3]. Plastic deformation under irradiation is much enhanced and shows very weak stress-dependence, almost linear, and this leads to a very significant stress relaxation [4, 5]. Furthermore, when the temperature is so low that only interstitial

[1] Researcher, subgroup leader, senior researcher, and senior researcher, respectively, 2nd subgroup, 2nd group, National Research Institute for Metals, 1-2-1 Sengen, Tsukuba, Ibaraki 305-0047, Japan.

Copyright© 2000 by ASTM International www.astm.org

atoms can migrate, the transient state of point defect distribution is enhanced during irradiation and lasts for a prolonged period. This transient in point defect kinetics may induce very significant radiation-induced deformation, sometimes larger than that at high temperatures [3, 6]. Thus, the radiation-induced deformation can affect the material life even at lower temperatures. Since the actual loading condition in the reactor core region is a combination of cyclic and constant loads, in-beam creep-fatigue experimentation is essential to evaluate the feasibility of the materials for fusion reactor core application.

In this paper, the development of an in-beam creep-fatigue testing machine using a miniaturized specimen is outlined. The in-beam creep-fatigue tests were carried out for a miniaturized specimen of the 20% cold-worked 316 stainless steel under 17 MeV proton irradiation at 60°C. The testing temperature of 60°C is critical because significant radiation-induced deformation is expected even in the low irradiation damage levels as mentioned above [3, 6]. Simple fatigue tests without holding were also performed at the same condition in order to examine the effect of holding during irradiation.

Creep-Fatigue Testing Machine

Loading Train

A creep-fatigue testing machine for a miniaturized specimen requires [7];

(1) very high load/displacement resolution,
(2) slow displacement rate but very precise control,
(3) high machine stiffness but very low inertia,
(4) exclusion of vibration noise from the oil pneumatic system.

These requirements lead to an adoption of the electro-mechanical actuator system with a direct-drive digital servomotor and a ball-screw type non-rotation drive system with extremely small back rush as shown in Fig. 1. Photo-electronic components like optical encoders are avoided because of deterioration by neutrons and γ-rays during irradiation. Instead a resolver, an electromagnetic rotation sensor, is used to control the direct-drive digital servomotor. Since the specimen is very small and rather thin, attaching type extensometers cannot be used. Instead, two LVDT's (Schaevitz 005MHR) with a very high resolution ($\pm$ 0.01 μm) are installed at the driving shaft. This high resolution LVDT inevitably has a very small measurement range ($\pm$ 125 μm). To overcome this point, solenoids of the two LVDT's are driven by servomotors and switched over to one another automatically so that a very wide displacement range (10 mm) can be covered. These straining and strain measuring components shown in Fig. 1 are installed below a bottom flange plate of the irradiation chamber. The components installed above the flange plate is shown in Fig. 2. The pulling rods are made of Super-Invar alloy which has an extremely low thermal expansion coefficient, two orders of magnitude lower than that of stainless steel below 150°C. The specimen temperature is controlled through the combination of beam heating, an infrared gold image heater and helium gas jet. The helium circulation system is equipped with a specially designed electric heater and a flow controlling valve. The specimen temperature is monitored by an infrared pyrometer at temperatures ranging from 200 to 600°C and by thermocouples at temperatures below 200°C. The infrared pyrometer is a glass-fiber type, which has a lens component and a

sensor/amplifier assembly separated from each other by a flexible 2-meter glass-fiber cable to prevent the latter from irradiation damage.

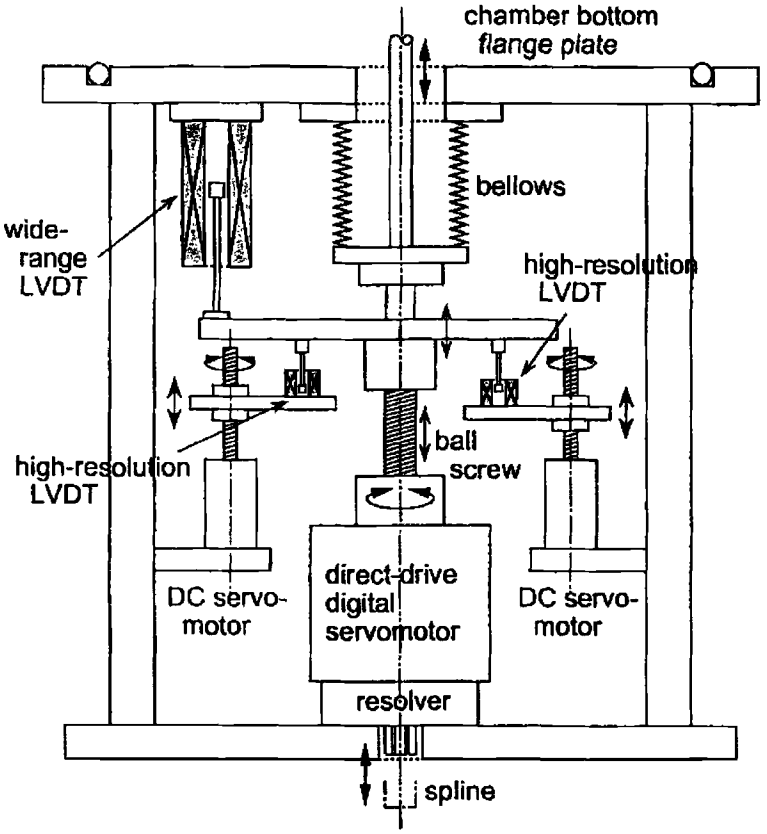


Figure 1 - *Drive and Measuring System of Loading Train*

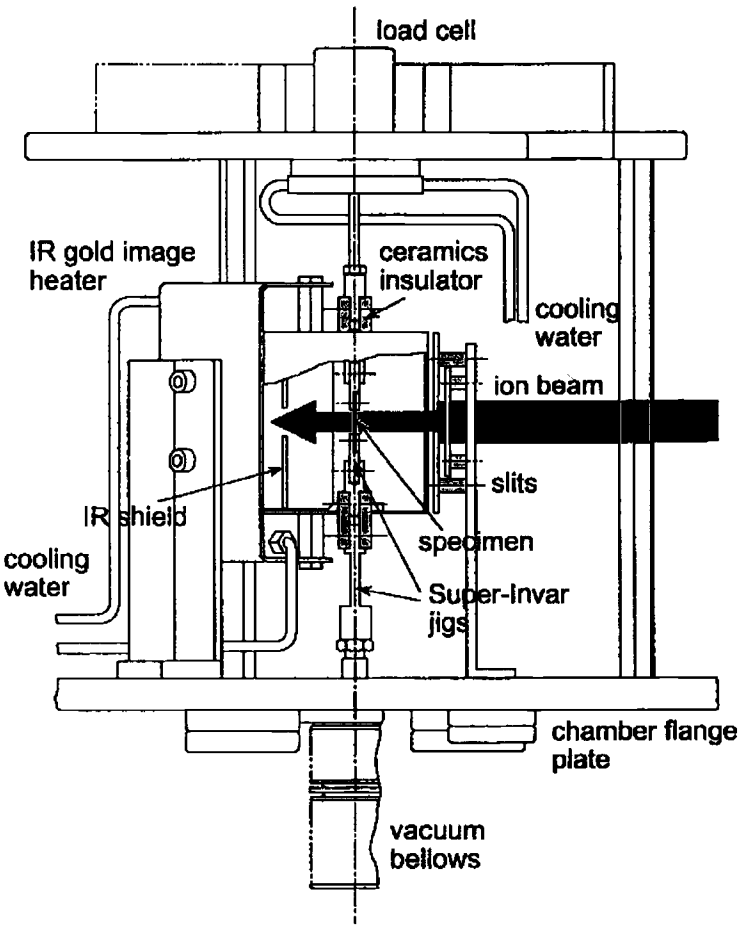


Figure 2 - *Loading Train above Chamber Flange Plate*

Irradiation Chamber

The chamber which houses the loading train for in-beam experiments is connected to the beam line of the National Research Institute for Metals (NRIM) compact cyclotron facility. The cyclotron produces 4.25 and 17 MeV protons, 10 MeV deuterons, 20 MeV He-4 ions and 26 MeV He-3 ions. Charged particles listed above are available for the in-beam creep-fatigue experiments. The irradiation chamber consists of the following

components in the downstream direction of the beam as schematically shown in Fig. 3;
(1) thin Al foil (50 μm thick) and beam aperture at the chamber entrance
(2) movable Faraday cup, coming down to the beam position,
(3) beam profile monitor,
(4) beam slits (four independent plates, isolated from each other),
(5) specimen (installed with incident beam angle of 45° to the surface)
(6) thin Al foil and main Faraday cup specially designed for the helium atmosphere.

It is difficult to measure the ion beam current in a gaseous atmosphere. The main Faraday cup has a rather unique structure with He-cooled Al foil which keeps the inside vacuum to exclude the gas effect and to ensure the correct beam current measurement. The operation of the loading train and beam monitoring system can be carried out at the control room of the cyclotron facility, which is connected to the irradiation room by 60 m wiring.

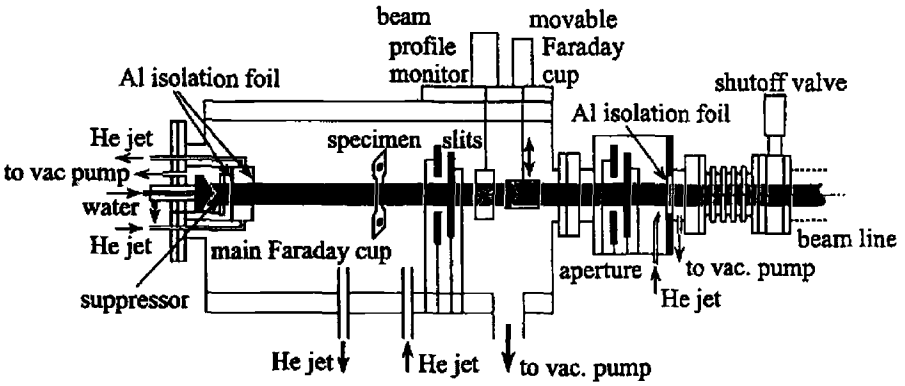


Figure 3 - *Beam Monitoring System of the Irradiation Chamber*

Testing Modes

Various testing modes are available in the present loading train such as;
(1) simple tensile test with constant strain or stress rate, including creep and stress relaxation,
(2) simple fatigue test in strain or stress control with sinusoidal or triangular wave,
(3) creep-fatigue (ramp with hold) test in strain or stress control,
(4) creep-fatigue (ramp with hold) test in strain control with stress hold or stress control with strain hold.

The effective setting load range is from 0.1 to 200 kg in stress control, and from 0.001 to 25 mm in strain control. The maximum loading rate is 3.33 kg/s in stress-controlled mode, and 200 mm/min in strain-controlled mode. In sinusoidal wave mode, maximum loading frequency is 1.0 Hz.

Experimental Procedure

The creep-fatigue and fatigue tests were carried out for a standard type of commercial 316 stainless steel in both in-beam and off-beam conditions. The chemical composition of the alloy is given in Table 1. Cold-rolled sheets of the alloy with a thickness of 0.19 mm were annealed for 30 min at 1223 K. The grain size was controlled to be less than 10 μm in order for mechanical properties to approximate those of truly polycrystalline material [8]. The annealed sheets were further rolled to 20% reduction in thickness to produce the cold-worked (CW) sheets. The CW sheets were punched out into specimens of type shown in Fig. 4. The specimen consists of a gauge section of $4 \times 10 \times 0.15$ mm in dimension and the shoulders to be clamped by bolts. A fatigue crack starter notch was introduced into the gauge from the edge to 0.60 mm in length by means of spark erosion, as presented in Fig. 4. The notch was 0.12 mm wide with an end radius of 0.06 mm. Fig. 5 shows the depth dependence of displacement damage rate calculated by the TRIM-91 code for the 316 stainless steel under 17 MeV proton irradiation with incident angle of 45°. As shown in Fig. 5, the specimen with a thickness of 150 μm ensures the variation of atomic displacement rate less than 15% between the two surfaces. In the present in-beam experiment, atomic displacement rate was adopted to be 1×10^{-7} dpa/s in the middle area of the specimen thickness. The specimen was cooled by a helium gas jet in order to compensate the beam heating. The irradiation temperature was controlled at 60 ± 3°C by adjusting the helium gas flow to about 60 m/s. The temperature of the helium gas jet was 24°C for in-beam condition, and the helium gas was warmed by an electric heater to keep the specimen temperature at 60°C in off-beam condition. Since the infrared pyrometer cannot be used for such low temperatures, the specimen temperature was monitored by two pairs of thermocouples attached directly to the gauge by spot welding. The two attaching points were upper and lower away from the expected crack propagation path by 2 mm, so that the spot welding would not affect the creep-fatigue process. The distribution of incident beam intensity in the gauge section was arranged uniformly with addressing the beam profile monitor located in front of the specimen. The difference of temperature between upper and lower thermocouples was within 3°C during the present experiment.

Table 1 - *Chemical composition of 316 stainless steel used (wt. %)*

C	Ni	Cr	Mn	Mo	Si	P	S	Fe
0.06	10.30	16.79	1.17	2.16	0.68	0.027	0.001	balance

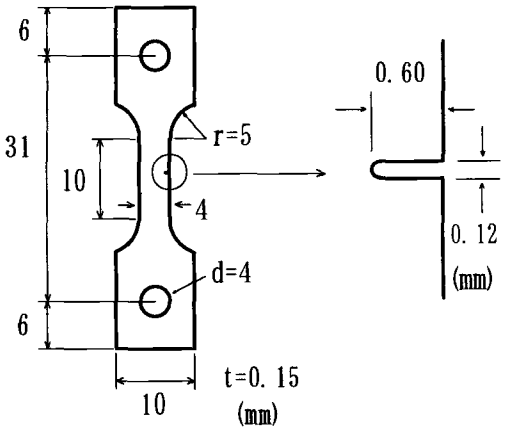


Figure 4 - *Dimensions of the Notched Specimen for the Fatigue and Creep-Fatigue Experiments*

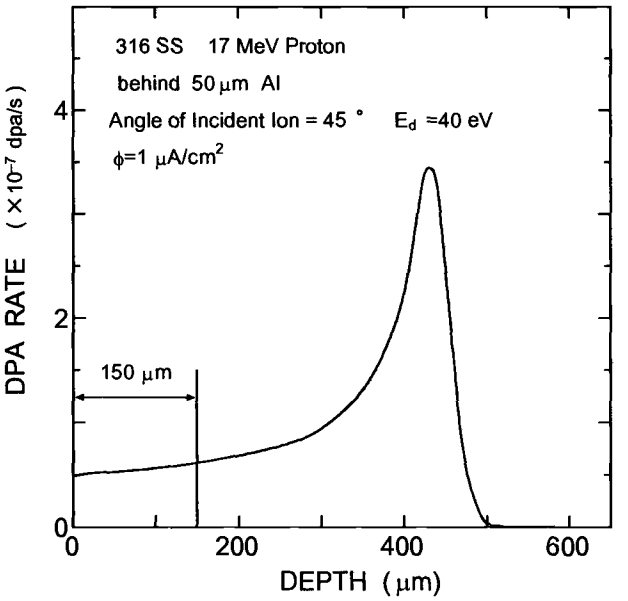


Figure 5 - *Depth Dependence of Displacement Damage Rate in 316 SS Irradiated with 17 MeV Protons*

The testing mode of the machine was ramp with hold in stress control. Since the 0.2% off-set yield stress was 700 MPa at 60°C for the specimen without notch, the stress at the notched ligament in gauge should be lower than 700 MPa in order for linear elastic fracture mechanics to be applicable [9]. Therefore, the maximum applied stress away from the notch was selected to be 536.4 MPa, corresponding to 90% of the yield stress at the notched ligament. The minimum applied stress and loading rate was 236.4 MPa and 50 MPa/s, respectively. The holding time was 12 s at 536.4 MPa and 1 s at 236.4 MPa for the creep-fatigue tests.

Results and Discussion

The relative displacement in the gauge section at the maximum stress (536.4 MPa) was plotted with the number of cycles for the creep-fatigue and fatigue experiments at 60°C, as shown in Fig. 6. The relative displacement is the actual displacement minus the displacement at the maximum stress in the first cycle. The total amount of dpa was 0.018 and 0.023 dpa for the in-beam fatigue and creep-fatigue, respectively. In off-beam condition, the number of cycle to fracture (N_f) was similar in both creep-fatigue and fatigue experiments (Fig. 6). This indicates that the holding in creep-fatigue has no significant effect on the fatigue process in unirradiated condition at 60°C. Material lifetime was substantially prolonged under irradiation in fatigue experiments, whereas the prolongation of creep-fatigue was not so much as that of fatigue (Fig. 6).

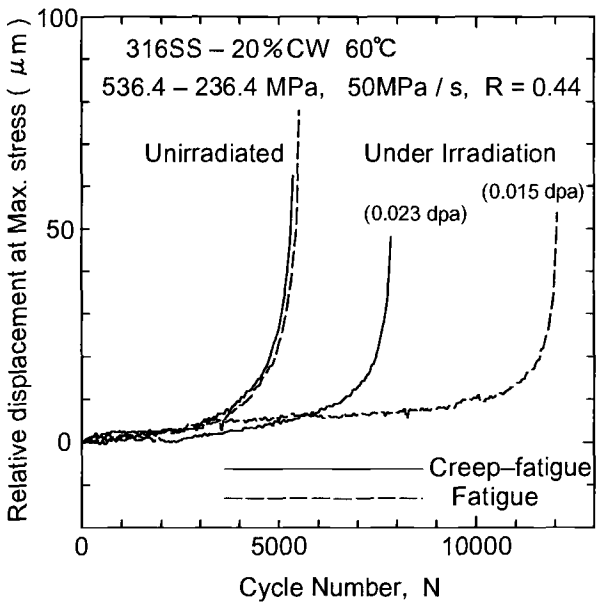


Figure 6 - *Effect of Irradiation on Lifetime in Fatigue and Creep-Fatigue Experiments*

Fig. 7 presents the results of the scanning electron microscope (SEM) observation on the fracture surface of fatigue specimens with and without irradiation. Although the crack surface appeared to be rougher in off-beam fatigue specimen, no major difference in fatigue mode was observed between the two specimens. Ductile striation was detectable in the crack surface for both in-beam and off-beam fatigue specimens. Fig. 8 shows the variation of the striation spacing with the distance from the notch tip. The crack length was 855 and 630 μm for in-beam and off-beam fatigue specimens, respectively. Since the striation spacing was smaller in the in-beam specimen at the same distance from notch tip, the crack growth rate is suggested to be lower under irradiation.

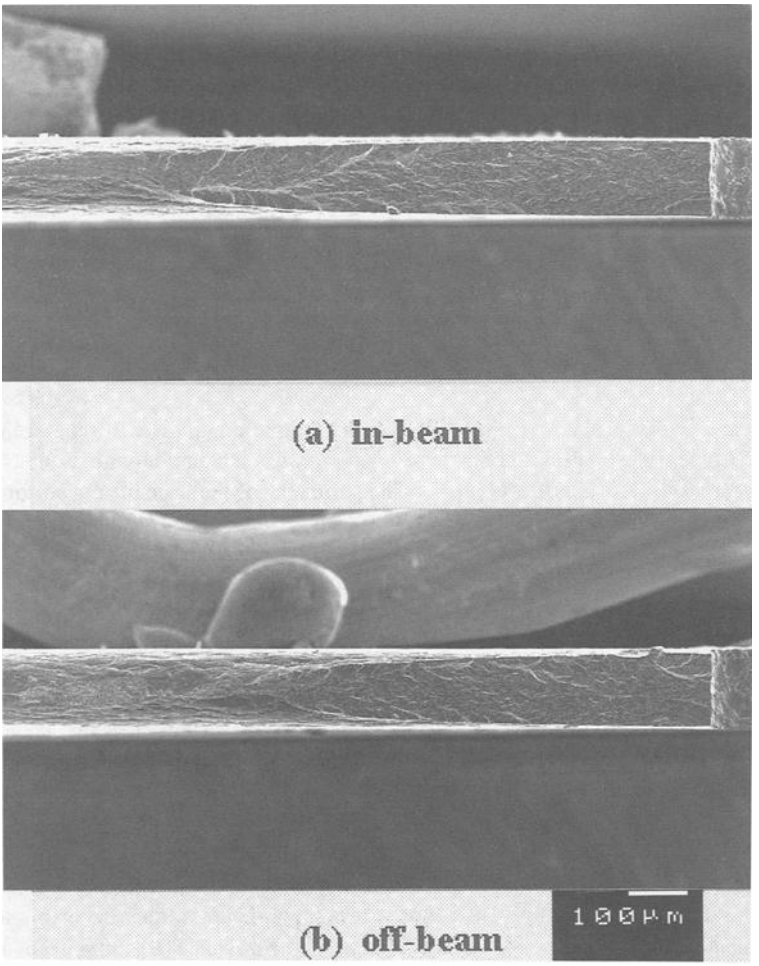


Figure 7 - *Fracture Surface of In-beam and Off-beam Fatigue Specimens*

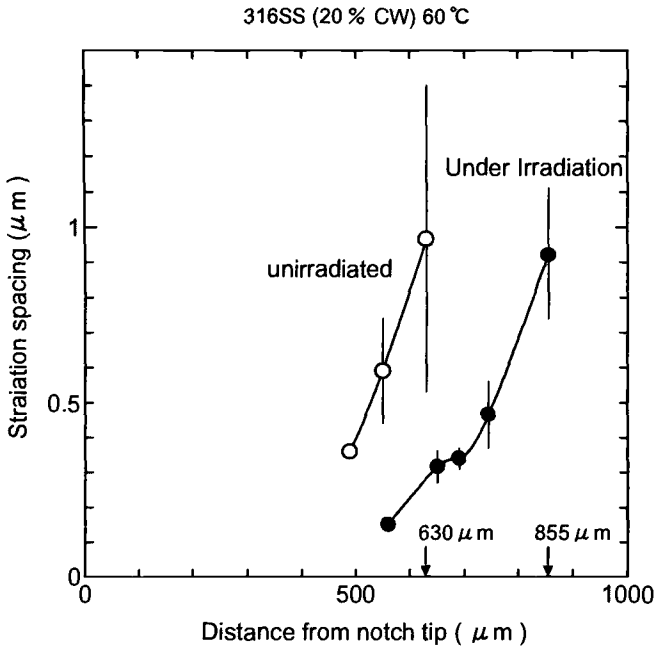


Figure 8 - *Variation of Striation Spacing with Distance from Notch Tip*

Fenici and Suolang have recently reported the fatigue crack growth on a solution-annealed AISI type 316 stainless steel under 20 MeV proton irradiation with a dpa rate of 6×10^{-7} dpa/s at 100, 200 and 300°C [10]. The geometry of the specimen used for their experiments was very similar to that of the present experiments. The loading mode was a sinusoidal wave with 1 Hz frequency in stress control of 186 - 190 MPa at a load ratio of 0.1. The experimental results revealed a longer fatigue lifetime and a slight decrease of fatigue crack growth rate under irradiation. An examination of the fracture surface was also carried out by using SEM. Since the facets and slip steps were not clearly recognized in the in-beam fatigue specimen, it was suggested that the radiation-induced defects blocked the dislocation glide and crystallographic planer slip. They have pointed out that the higher resistance to fatigue fracture under irradiation was attributed to the irradiation hardening by defect agglomerates produced by displacements at low fluences and low temperatures [10].

In the present experiments, the lifetime of fatigue was substantially prolonged under irradiation (Fig. 6). Fig. 8 shows the smaller striation spacing in the crack surface of the in-beam fatigue specimen at the same distance from notch tip, indicating a decrease of crack growth rate under irradiation. It is noted that the in-beam fatigue behaviors are in good agreement with the results reported by Fenici and Suolang [10], in spite of some major differences in experimental conditions such as loading mode and material processing. Since no major differences in the fatigue mode were observed in the crack surfaces

between in-beam and off-beam fatigue specimens, the effect of irradiation on the fatigue process was not clarified in the present experiments.

In the creep-fatigue tests, the prolongation of N_f under irradiation was not so substantial as fatigue (Fig. 6). The N_f of in-beam creep-fatigue was much smaller than that of in-beam fatigue, whereas N_f was similar in both fatigue and creep-fatigue in off-beam condition. This indicates that the holding during irradiation plays some role in reducing lifetime of creep-fatigue. Fatigue crack initiation is a plastic deformation process, in which the dislocation motion represents the principle contribution. The radiation-induced defects was considered to block the dislocation glide and delay the fatigue process [10]. However at lower temperature and at early stage of irradiation, the dislocation climb was reported to be enhanced by preferable absorption of the radiation-induced interstitials at dislocations [6]. Therefore, the enhanced dislocation climb which leads to the low-temperature irradiation creep would cancel out the effect of irradiation hardening on crack initiation in fatigue process. The holding of the in-beam creep-fatigue may be influenced by the low-temperature irradiation creep to promote the fatigue process at early stage of irradiation.

Thus, some essential difference in material response between with and without irradiation was recognized in both fatigue and creep-fatigue experiments. Further investigation utilizing the machine is under way to contribute to the understanding of the creep-fatigue response of fusion reactor materials.

Summary

An in-beam creep-fatigue testing machine for a miniaturized specimen has been developed to investigate the synergistic effects of irradiation and cyclic stress with holding on the mechanical properties of fusion reactor core materials. The loading and displacement measuring system of the machine was outlined in this paper. Fatigue and creep-fatigue responses of 20% cold-worked 316 stainless steel were examined under 17 MeV proton irradiation at 60°C. The lifetime of fatigue was substantially prolonged under irradiation, although the prolongation was not so much in the creep-fatigue. The radiation-induced defects was considered to block the dislocation glide and delay the fatigue process. On the other hand, the irradiation creep may reduce the effect of irradiation hardening on crack initiation in fatigue process. More experiments and quantitative analyses are definitely needed to understand the irradiation effect on the creep-fatigue life for fusion reactor core materials.

References

[1] Matthews, J. R. and Finnis, M. W., "Irradiation Creep Models - An Overview," *Journal of Nuclear Materials*, Vol. 159, 1988, pp. 257-285.

[2] Grossbeck, M. L., Ehrlich, K. and Wassilew, C., "An Assessment of Tensile, Irradiation Creep, Creep Rupture, and Fatigue Behavior in Austenitic Stainless Steels with Emphasis on Spectral Effects," *Journal of Nuclear Materials*, Vol. 174, 1990, pp. 264-281.

[3] Nagakawa, J., Yamamoto, N. and Shiraishi, H., "Computer Simulation of Early-Stage Irradiation Creep," *Journal of Nuclear Materials*, Vol. 179-181, 1991, pp. 986-989.

[4] Nagakawa. J., "Calculation of Radiation-Induced Creep and Stress Relaxation," *Journal of Nuclear Materials*, Vol. 225, 1995, pp. 1-7.

[5] Nagakawa, J., "Calculation of Radiation-Induced Stress Relaxation," *Journal of Nuclear Materials*, Vol. 212-215, 1994, pp. 541-545.

[6] Grossbeck, M. L. and Mansur, L. K., "Low-Temperature Irradiation Creep of Fusion Reactor Structural Materials," *Journal of Nuclear Materials*, Vol. 179-181, 1991, pp. 130-134.

[7] Nagakawa, J., Murase, Y. and Yamamoto, N, "Development of In-Beam Creep-Fatigue Machine," The Proceeding of IEA/JUPITER Joint Symposium on Small Specimen Test Technologies for Fusion Research, Miyagi, JAPAN, 1996, in press.

[8] Miyazaki, S., Shibata, K. and Fujita, H., "Effect of Specimen Thickness on Mechanical Properties of Polycrystalline Aggregates with Various Grain Sizes," *Acta Metallurgica*, Vol. 27, 1979, pp. 855-862.

[9] Rickerby, D. G. and Fenici, P., "Fatigue Crack Growth in Thin Section Type 316 Stainless Steel," *Engineering Fracture Mechanics*, Vol. 19, 1984, pp. 585-599.

[10] Fenici, P. and Suolang, Shi, "Fatigue Crack Growth in 316 Type Stainless Steel at Temperatures and Displacement Damage Rates Representative for The First Wall Loading," *Journal of Nuclear Materials*, Vol. 191-194, 1992, pp. 1408-1412.

Emil S. Aitkhozhin,[1] Yury S. Pyatiletov,[1] and Eugene V. Chumakov[1]

In-Reactor Creep Regularities of Copper

Reference: Aitkhozhin, E. S., Pyatiletov, Y. S., and Chumakov, E. V., **"In-Reactor Creep Regularities of Copper,"** *Effects of Radiation on Materials: 19th International Symposium, ASTM STP 1366,* M. L. Hamilton, A. S. Kumar, S. T. Rosinski, and M. L. Grossbeck, Eds., American Society for Testing and Materials, West Conshohocken, PA, 2000.

Abstract: The systematic research of in-reactor creep regularities for different purity polycrystalline copper and elaboration of the related theoretical model are discussed. The stress and temperature dependence of the in-reactor and thermal creep rates of pure copper and temperature dependence of the in-reactor and thermal creep rates of technical copper have been analyzed. It is shown that for each of the materials studied there is a temperature region where an abnormal reduction of the creep rate with increasing temperature takes place. A creep model based on dislocations sliding and thermoactivation overcoming of barriers by them is suggested. It is shown that the model well describes the conduct peculiarities of the in-reactor and thermal creep rates of copper in different temperature-strength conditions. The reasons for the abnormal temperature dependence of the creep rate in the intermediate temperature region are discussed.

Keywords: creep, yield stress, irradiation, dislocation, copper

Introduction

Because of today's higher demands on the physical-mechanical properties of metal materials used for reactor construction, there is great interest in development of reactor metal alloys with high radiation resistance, durability and sufficient plasticity. When elaborating the materials a problem of choice of optimal defect structure and chemical element composition arises. It was well know that a defect structure formed by the preliminary processing of samples and an addition of an even small amount of dissolved elements may cause a strong change in the physical-mechanical properties. Therefore, the efforts of many researchers are directed to revealing the mechanisms of the influence of point and extended defects of the crystal lattice on the course of physical processes in irradiated materials. Although there are no authentic answers for a lot of questions, the understanding of a number of the basic aspects of the discussed problem has been reached. In particular, different channels of the impurities,

[1]Group leader, deputy director and senior scientist, respectively, Institute of Nuclear Physics, National Nuclear Center, Almaty, 480082, Republic of Kazakstan.

Copyright© 2000 by ASTM International www.astm.org

dislocations and other defects' influence on the radiation and thermal creep rate have been revealed and discussed [*1-3*]. It is shown that in principle it is possible to get desirable changes of creep rate by the modifying the type and concentration of impurities and dislocation structure. However, in order to do purposeful practical steps in this direction it is necessary, first, to carry out systematic experimental research of the deformation and endurance characteristics on a well investigated model metal materials with controlled defects structure and element composition, and, second, to have an advanced quantitative theory of the related physical processes.

The article is devoted to such researches. We have carried out systematic research of the polycrystalline copper in-reactor creep regularities in the temperature range 0.31-0.51 of the melting temperature T_m [*4-7*]. In the first part the results of experimental studies of the stress and temperature dependencies of the pure copper in-reactor and thermal creep rates and the temperature dependence of the technical copper in-reactor and thermal creep rates are presented. In the second part the theoretical model on the basis of which the experimentally observed regularities of the in-reactor and thermal creep of copper are explained is described. The discussion of the results of the work is given in the last part.

Experimental Technique

As an object of the study copper of purity 99.99% and 99.95% were used. Planar specimens of 20×4×0.5 mm^3 dimensions were cut from a rolled sheet and subsequently annealed to obtain the necessary microstructure. The creep characterization were performed under uniaxial tension. The strain constancy was provided by a special load arrangement with the control of the specimen section change during the deformation.

The in-reactor and laboratory tests for copper creep characterization were carried out at identical remote-control installations which consist of in-reactor testing machine and control panel. The in-reactor testing machine allows to test three specimens simultaneously. It includes an electromechanical power block, strain gauge and force sensor as well as an replaceable ampoule with specimens and heater. The control of the specimen deformation, strain and temperature during the test were performed by devices placed in the remote-control panel. Table 1 gives the technical characteristics of the installation.

Table 1 - *Technical Characteristics of the Installation for a Creep Test*

Measuring parameters	Value
Axial tensile force, N	20...350
Accuracy of tensile force control, %	± 1
Maximum linear displacement, mm	20
Accuracy of linear displacement control, μm	± 3
Range of the test temperature, °C	293...873
Accuracy of temperature measure, %	± 0.5
Accuracy of temperature control, %	± 1

The in-reactor testing machine with the specimen-contained ampoule were situated in one of the experimental channels of the WWR-K reactor and irradiated. Most of the specimens heating was performed by the radiation field of the reactor. Further precise heating proceeded by a special electrical heater using temperature control device. An average heating rate was 10...15°C/min. The temperature was measured by a chromel-alumel thermocouple. The in-reactor test duration was up to 500 hours and sometimes more. The laboratory tests for thermal creep were carried out using an identical installation.

Experimental Results

Copper of Purity 99.99%

Before tests the samples were annealed at 1023 K for 1 h to do an average grain size equal 50 μm. In-reactor tests were carried out in channels of the WWR-K reactor at the neutron flux density of $1.4 \cdot 10^{16}$ $n \cdot m^{-2} \cdot s^{-1}$ ($2.5 \cdot 10^{15}$ $n/m^{-2} \cdot s^{-1}$, E>0.1MeV) in the temperature range of 473...693 K at a constant stress of 40 MPa and in the stress range of 30...57 MPa at the constant temperature of 523 K. The laboratory tests were performed in the temperature range of 473...703 K at the constant stress of 40 MPa and in the stress range of 23...69 MPa at 523 K. The temperature and deformation of samples were measured with an accuracy of 2% and 1%, respectively.

The stress dependencies of the in-reactor ($\dot{\varepsilon}_R$) and thermal ($\dot{\varepsilon}_T$) creep rates of copper in the semi-logarithmic coordinates are given in Fig. 1. It is seen that the dependencies are linear. So $\dot{\varepsilon}_R$ and $\dot{\varepsilon}_T$ depend on the stress exponentially.

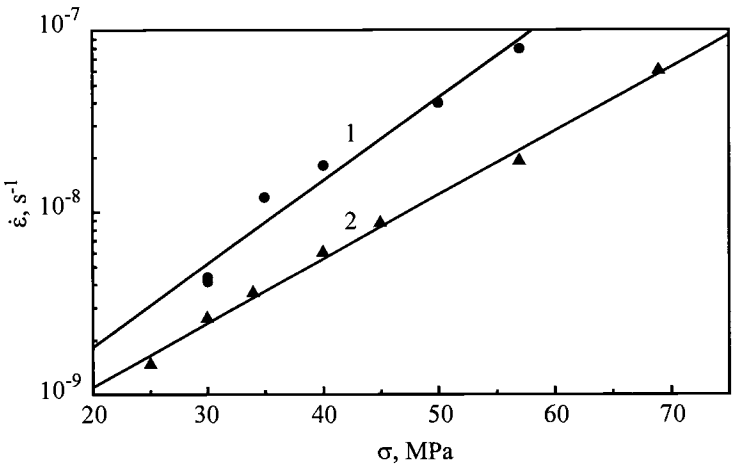


Figure 1 - *Stress dependencies of the in-reactor (1) and thermal (2) creep rates of the pure copper. Points are experimental data. Lines are the data calculated by using formula (10).*

Fig. 2 shows the semi-logarithmic dependencies of $\dot{\varepsilon}_R$ and $\dot{\varepsilon}_T$ upon the homologous inverse temperature. The curves have two inflections. So one can divide

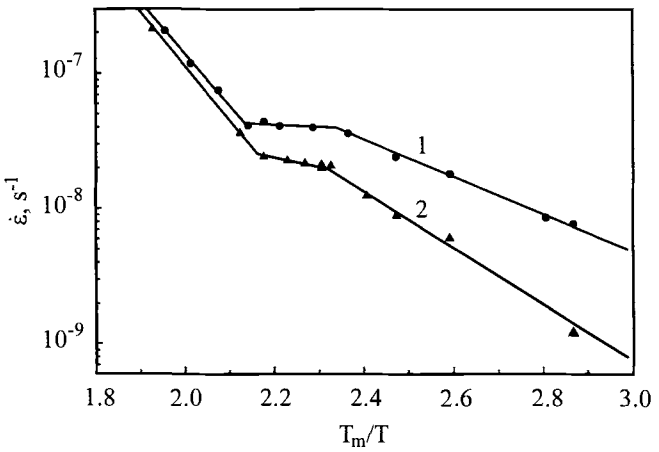


Figure 2 - *Temperature dependencies of the in-reactor (1) and thermal (2) creep rates of the pure copper. Points are experimental data. Lines are the predictions calculated using formula (10).*

the studied temperature range into three regions: the low temperature region A below 0.42 T_m, the medial temperature region B of 0.42...0.47 T_m and the high temperature region C above 0.47 T_m which differ considerably from each other by a value of radiation effect. The radiation effect is the largest in the region A where at 473 K the ratio of $\dot{\varepsilon}_R$ to $\dot{\varepsilon}_T$ is equal 6.4 whereas in the region C the ratio is only 1.4. In the regions A and C the creep rate dependence is close to the exponential one. In the region B the $\dot{\varepsilon}_R$ and $\dot{\varepsilon}_T$ values are comparable and do not significantly depend on the temperature.

Copper of Purity 99.95%

The specimens were annealed at 1023 K for 1h. Both in-reactor tests in the temperature range of 433...613 K and laboratory tests in the 423...643 K range were carried out at the constant stress of 50 MPa. Fig.3 shows the temperature dependencies of $\dot{\varepsilon}_R$ and $\dot{\varepsilon}_T$ of 99.95% copper. Here three characteristic temperature regions are also observed. Those are the low temperature region below 0.36 T_m, the medial temperature region of 0.36...0.41 T_m and the high temperature region above 0.41 T_m. In both low and high temperature regions the deformation behavior for copper of purity 99.95% and 99.99% is identical. However in the intermediate temperature region $\dot{\varepsilon}_R$ of technical copper sharply decreases with increasing of test temperature from 0.37 to 0.41 T_m. Apparently the phenomena is due to a larger content of impurities in technical copper (99.95%), mainly of iron and zinc, in comparison with pure copper.

The considered experimental results require a theoretical confirmation, which is given in the next sections.

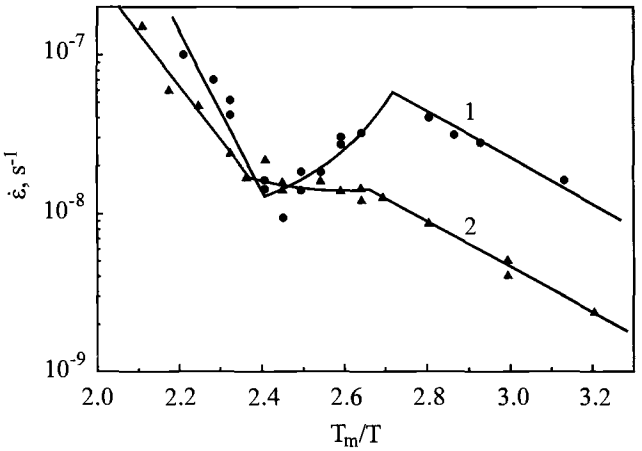


Figure 3 - *Temperature dependencies of the in-reactor (1) and thermal (2) creep rates of technical copper. Points are experimental data. Lines are the predictions calculated using formula (10).*

The Dislocation Model of Creep

Let us consider a model metal sample having a cubic lattice with edge dislocations of density ρ_n. We will assume that the sample is situated in neutron radiation field of neutron flux density G and stretched along an axis x_i of the laboratory Dekart coordinate system. The stress in this system has the single nonzero component $\sigma'_{11} = \sigma$. The stress tensor components in the C-coordinate system $x_1;x_2;x_3$ related to the <100>, <010>, <001> crystallographic directions of the sample are expressed through σ_{11} as follows:

$$\sigma_{kl} = S_{k1} S_{l1} \sigma'_{11}, \qquad (1)$$

where matrix elements S_{j1} are the direction cosines between x_j (j=1,2,3) and the tension axis x'_1. We will assume that the dislocations contained in the sample are rectilinear and aligned along the x_j axises with the same direction of the related Burgers's vectors. So the dislocations are divided into three groups with the densities $\rho_n^{(j)}$ equal to 1/3 of a total dislocation density ρ_n. The shift components of the stress tensor σ_{kl} ($k \neq l$) (let's mark them as τ_{kl}) will cause the dislocation sliding. The dislocations with Burgers's vectors directed along x_k and located within the planes which are normal to x_l will glide along x_k until stopped by obstacles provided by forest dislocations and defects of crystal lattice.

At high enough shift stresses τ_{kl} the dislocation overcomes by a force through an amount of barriers, then glides in the sliding plain on a distance L and turns out in the vicinity of barrier in some stable configuration. The distance L depends on the arrangement and strength of barriers as well as from the magnitude of applied stress. Then the dislocation overcomes again the barriers due to the thermal activation or

climb and glides on the distance L. Further the described process repeats many times and leads to the deformation of the sample.

The process of the barriers overcoming by dislocation after stopping in stable configuration is the one which controls the deformation rate in the course of dislocation gliding. Therefore the mean velocity of dislocations at the stress τ_{kl} in the direction x_k is expressed as

$$V(\tau_{kl}) = \frac{L(\tau_{kl})}{t}, \tag{2}$$

where t is the time of barriers overcoming by dislocation.

We consider here the case of low dose radiation when the rate of dislocation climb is low. Therefore the overcoming of barriers proceeds due to the thermal activation and t may be expressed as

$$t = \nu^{-1} \exp\left(\frac{U}{kT}\right). \tag{3}$$

Here ν denotes the vibration frequency of a dislocation segment pinned by its ends at the obstacles and is equal to $\nu = \nu_D/l$, where ν_D is Debay's frequency; l is the segment length; U is the activation energy of the barriers overcoming by the dislocation.

The density of the dislocations which moves along x_k direction is equal to 1/6 of ρ_n. Therefore the contribution of the dislocations into the creep rate may be written as

$$\dot{\varepsilon}_{kl} = \frac{1}{6} b \rho_n V(\tau_{kl}) \tag{4}$$

The components of a strain tensor are transformed in the same way as the components of the stress tensor, when it turns from one coordinate system to another. Thus the creep rate $\dot{\varepsilon}'_{11}$ along the axis of external tension is calculated as a sum of contributions of all the components $\dot{\varepsilon}_{kl}$

$$\dot{\varepsilon}'_{11} = S_{kl} S_{ll} \varepsilon_{kl} \tag{5}$$

Let's take the x'_1 axis direction in the first quadrant of the C-coordinate system (it does not limit the generality of conclusions) and let's define it through the angles ϑ and φ of a spherical coordinate system connected with the C-system. As a result we obtain the following expression for the creep rate:

$$\dot{\varepsilon}'_{11} \equiv \dot{\varepsilon} = \frac{1}{3} b \rho_n \Big[V(\tau_{12}) \sin^2 \vartheta \sin\varphi \cos\varphi + V(\tau_{13}) \sin\vartheta \cos\vartheta \cos\varphi + V(\tau_{23}) \sin\vartheta \cos\vartheta \sin\varphi \Big], \tag{6}$$

where in accordance with the formula (1) all the components τ_{ij} are expressed through applied tension stress σ.

To simplify formula (6) we will use a circumstance that dislocations of different orientations give equal contribution into $\dot{\varepsilon}'$ in case when the most symmetrical direction of the load axis <111> is chosen. Thus according to (1) all the shift

components of stress are equal to $\sigma/3 \equiv \tau$. As a result the expression in square brackets of (6) which we mark as $v(\sigma,\vartheta,\varphi)$ is changed on 2V. Introducing a designation

$$\xi = \frac{v(\sigma,\vartheta,\varphi)}{V(\tau)}, \tag{7}$$

and taking into the account (2) and (3) one can finally derive from (6) the expression

$$\dot{\varepsilon} = \frac{1}{3} b \rho_n L v \xi \exp\left(-\frac{U}{kT}\right) \tag{8}$$

where the parameter ξ varies from zero for x_j' coinciding with one of the x_j to some value slightly more than one.

To do quantitative calculations by using the formula (8) it is necessary to know the value of the activation energy U and to have an algorithm of calculation of L. The exact analytical calculation of L in case of a random distribution of defects of different types is practically impossible. Therefore for calculation of L the computer simulation of dislocation movement through the network of random obstacles [*8*] by the methods offered in [*9*] is used.

The determination of the dependence of activation energy upon the stress is very important. The question has been discussed in scientific literature for a long time [*10-13*] but to final conclusion the researchers did not come yet. Different authors offered some variants of the dependence of U from τ. Zhurkov [*10*] and his followers [*11*] used the formula $U = U_0 - \gamma\tau$ where U_0 is the activation energy at $\tau=0$ (for metals U_0 is close to sublimation energy), γ is a structure-sensitive coefficient. According to Fridel's approach [*12*] the formula should have the following form: $U=U_0-\alpha\tau^{2/3}$ where α is a coefficient. Recently [*13*] the dependence $U=U_0[1-(\tau/\tau_0)^p]^q$ was suggested. Here τ_0 is a critical shift stress for T = 0 K, p and q are numerical coefficients. The last formula for U is the most preferable. However it is also idealized in the sense that does not take into account real defect structure at nonzero temperature that is considerably different from the structure at T = 0 K.

Therefore in view of told the formula must be changed by replacing τ_0 to the yield stress σ_{02} at nonzero temperatures. Thus Zhurkov's formula for U will be transformed to the form

$$U = U_0\left(1 - \beta\frac{\tau}{\sigma_{02}}\right), \tag{9}$$

where β is a numerical factor.

Introducing a designation $\varepsilon_0 = \frac{1}{3} b \rho_n v \xi L(\tau)$ and taking into the account (9) one can receive from (8) a calculation formula which is convenient for analysis

$$\varepsilon = \varepsilon_0 \exp\left(-\frac{U_0}{kT} + \frac{U_0\beta}{kT}\frac{\sigma}{\sigma_{02}}\right). \tag{10}$$

Thus one and the same formula (10) will be used for the calculation of both in-reactor creep rate at low dose radiation and thermal creep rate. The role of the radiation is

reduced to change of evolution of defect structure at tests on creep that should influence on values of $\dot{\varepsilon}_0, \sigma_{02}, U_0, \rho$ and consequently on $\dot{\varepsilon}$.

The Dislocation Model Application for Describing of Creep Regularities of Copper

Before beginning the analysis of the pure and technical copper creep rate dependencies upon temperature and stress which are presented above let's take into account that yield stress σ_{02} included into the formula (10) is also dependent on temperature. For this reason there was a necessity of determination of dependence σ_{02} (T) for both materials investigated here. The corresponding measurements were carried out at an initial stage of samples loading in each experiment on creep when the curves "stress-deformation" were actually registered down to an output on a working stress σ more than σ_{02}. From these curves the values of σ_{02} at different temperatures were determined and the graphs of dependence of σ_{02} from T_m/T were constructed. The results of the measurements are given in Fig. 4 and Fig. 5. It is seen that in temperature

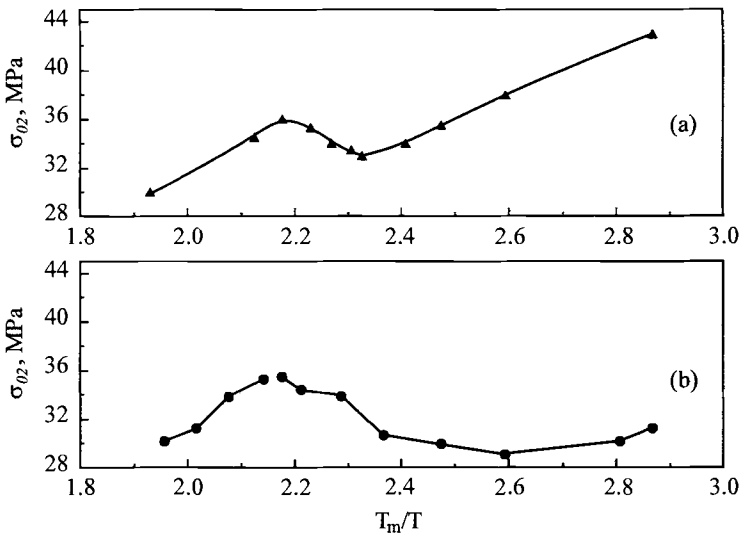


Figure 4 - *The temperature dependence of the yield stress for non-irradiated (a) and irradiated (b) pure copper samples.*

regions in which the abnormal reduction of an inclination of a curve $\lg \dot{\varepsilon}(T_m / T)$ (region B in Fig. 2 and Fig. 3) is observed the yield stress abnormally increases with growth of temperature.

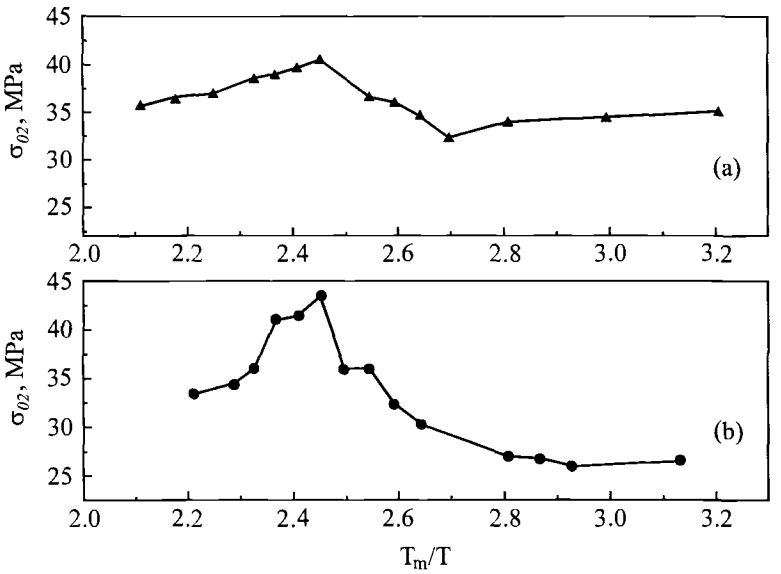


Figure 5 - *The temperature dependence of the yield stress for non-irradiated (a) and irradiated (b) technical copper samples.*

Table 2 - *Calculated Parameters Defining the Creep Rates of Pure and Technical Copper*

Material	Type of test	Temperature region	U_o, eV	β	$\dot{\varepsilon}_0$, s^{-1}
pure copper (99.99%)	in-reactor	A	0.535	0.256	$4.50 \cdot 10^{-5}$
		B	0.774	0.265	$1.10 \cdot 10^{-3}$
		C	0.840	0.179	$8.10 \cdot 10^{-3}$
	laboratory	A	0.504	0.270	$1.50 \cdot 10^{-5}$
		B	0.495	0.256	$1.76 \cdot 10^{-5}$
		C	0.800	0.226	$1.55 \cdot 10^{-3}$
technical copper (99.95%)	in-reactor	A	0.550	0.180	$2.45 \cdot 10^{-4}$
		B	0.514	0.318	$9.68 \cdot 10^{-6}$
		C	0.542	0.183	$6.10 \cdot 10^{-5}$
	laboratory	A	0.507	0.228	$3.04 \cdot 10^{-5}$
		B	0.643	0.209	$3.25 \cdot 10^{-4}$
		C	0.950	0.233	$1.30 \cdot 10^{-2}$

Knowing that σ_{02} is changing with temperature one can analyze the dependencies $\dot{\varepsilon}(\sigma)$ and $\dot{\varepsilon}(T)$ given in Fig. 1 - Fig. 3 on the basis of the formula (10). In accordance with (10) the creep rate $\dot{\varepsilon}$ is a complex function of the temperature and depends upon the stress exponentially. It includes three parameters $\dot{\varepsilon}_0$; U_0; β the values of which are

dependent on material's type and its defect structure. These parameters may be found at the analysis of experimental curves in Fig. 1 - Fig. 3 by using the formula (10) and each of temperature region (A, B, C) in Fig. 2 and Fig. 3 is characterized by the set of values of parameters (see Table 2). The calculated curves $\dot{\varepsilon}(\sigma)$ and $\dot{\varepsilon}(T)$ received by using the formula (10) with use of the data from Table 2 and values of σ_{02} determined from graphs in Fig. 4 are given in Fig. 1 - Fig. 3 (solid lines). It is seen in the figures that the formula (10) satisfactorily describes experimental dependencies $\dot{\varepsilon}(\sigma)$ and $\dot{\varepsilon}(T)$ including the abnormal behavior of the creep rate in the region B of intermediate temperature.

Discussion of Results

The observed anomaly of the temperature dependence of the copper creep rate and yield stress in the region B (in Fig. 2 - Fig. 4) are connected probably with the effect of defect structure reconstruction which caused by the dynamic deformation aging, i.e. the formation of impurities atmosphere around dislocations. As a result the material's strengthening is expressed in an increase of the yield stress σ_{02} and a delay of the creep rate $\dot{\varepsilon}$ growth with increasing temperature is observed. The comparison of curves $\dot{\varepsilon}(\sigma)$ and $\dot{\varepsilon}(T)$ for pure copper with the same curves for technical copper shows that the effect is greater for the "dirtiest" sample, i.e. for sample with a larger content of impurities.

It is supposed in the dislocation model of copper creep, elaborated in the work, that the low dose in-reactor radiation does not essentially affect the mechanism of deformation. The model describes well the regularities of the in-reactor and thermal creep rates dependencies upon the temperature and stress change. In particular it describes the exponential dependence of $\dot{\varepsilon}$ upon the stress and the dependence of $\dot{\varepsilon}(T)$ in the whole studied temperature range including the region B of intermediate temperatures where the abnormal behavior of $\dot{\varepsilon}(T)$ is observed. The quantitative differences of the in-reactor and thermal creep rates of the same samples tested in different conditions (in the reactor and out of the reactor) are explained by the different character of evolution of defect structure which causes the different values of σ_{02} and parameters $\dot{\varepsilon}_0$; U_0; β determining the values of $\dot{\varepsilon}_R$ and $\dot{\varepsilon}_T$.

It follows from Table 2 that the activation energy U_0 of overcoming of barriers by dislocations is close to 1 eV that in accordance with [*14, 15*] is caused by barriers of weak and intermediate strength. The barriers consist of impurities, their tiny conglomerations and "forest" dislocation which are known as barriers for sliding dislocations in the accepted dislocation model of creep.

At last, the experimental data presented in Fig. 2- Fig. 4 show that in the temperature region B where the abnormal decreasing of $\dot{\varepsilon}$ with temperature takes place the behavior of the endurance characteristic is also abnormal: the yield stress in the A and C regions is changed as usual, i.e. is decreased with temperature, while in the region B the value of σ_{02} is increased with temperature. Such correlative behavior of $\dot{\varepsilon}(T)$ and $\sigma_{02}(T)$ indicates that there is a certain interrelation between $\dot{\varepsilon}$ and σ_{02}. It is obvious that this question demands more detailed research. Therefore it will be studied separately in one of our future works.

References

[1] Mansur, L. K., and Yoo, M. H., "The Effects of Impurity Trapping on Irradiation-Induced Swelling and Creep", *Journal of Nuclear Materials*, Vol. 77, No. 2, 1978, pp. 228-241.

[2] Wiedersich, H. M., and Even, S. R., "Solute Effects on Radiation-Induced Creep and Growth", *Journal of Nuclear Materials*, Vol. 90, No. 1-3, 1980, pp. 157-168.

[3] Ibragimov, Sh. Sh., Kirsanov, V. V. and Pyatiletov, Yu. S., *Radiation Damage of Metals and Alloys*. - Moskwa : Energoatomizdat, 1985. - 242p.

[4] Ibragimov, Sh. Sh., Aitkhozhin, E. S., and Pyatiletov, Yu. S., "Radiation-Induced Creep of Aluminum and Copper", *Influence of Radiation on Material Properties: 13th Int. Symp. (Part II), ASTM STP 956*, F.A.Garner, C.H.Henager, Jr., and N.Igata, Eds., ASTM, Philadelphia, 1987, pp. 5-10.

[5] Aitkhozhin, E. S., Ibragimov, Sh. Sh., and Chumakov, E. V., "The Temperature Dependence of the In-Reactor Creep for Copper and Aluminum", *Atomnaya Energiya*, Vol. 69, 1990, pp. 142-145.

[6] Aitkhozhin, E. S., Aristov, P. A., Ibragimov, Sh. Sh., and Chumakov, E. V., "Influence of Impurities and Grain Size on the Policrystal Copper during a Reactor Irradiation", *Atomnaya Energiya*, Vol. 70, 1991, pp. 110-111.

[7] Aitkhozhin, E. S., and Chumakov, E. V., "Radiation-Induced Creep of Copper, Aluminum and their Alloys", *Journal of Nuclear Materials*, Vol. 233-237, 1996, pp. 537-541.

[8] Kirsanov, V. V., Pyatiletov, Yu. S., and Tyupkina, O. G., "Irradiation Creep Due to Dislocation Glide", *Physica status solidi (a)*, Vol. 64, 1981, pp. 735-740.

[9] Foreman, J. E., and Makin, M. J., "Dislocation Movement through Random Obstacles", *Philosophical Magazine*, Vol. 14, 1966, pp. 911-924.

[10] Zhurkov, S. N., "Problems of Solid State Strength", *Vestnik Academii Nauk SSSR*, No. 11, 1957, pp. 78-82.

[11] Regel, V. R., Slutsker, A.I., and Tomashevsky, E.E., *Kinetic Nature of Solid State Strength*. - Moskwa: Nauka, 1974.- 560p.

[12] Friedel, J., *Dislocations*.-Moskwa: Mir, 1967.- 645p.

[13] Frost, J. and Eshby, M. F., *Deformation - Mechanism Maps*. - Chelyabinsk, 1989. - 328 p.

[14] Bement, A. L., "Irradiation Effects on Structural Materials. I. Radiation Hardening", *Review of Roumanian Physics*, Vol. 17, No. 3, 1972, pp. 360-380.

[15] Ibragimov, Sh. Sh., Pyatiletov, Yu. S. and Tjupkina, O. G., "About Creep Models of Irradiated Metals", *Pis'ma v Zhurnal Tekhnicheskoy Fiziki*, Vol. 11, 1985, pp.1458-1461.

Austenitic Alloys— Irradiation-Induced Swelling, Segregation and Microstructure

T. R. Allen,[1] J. T. Busby,[2] J. Gan,[2] E. A. Kenik,[3] and G. S. Was[2]

The Correlation Between Swelling and Radiation-Induced Segregation in Iron-Chromium-Nickel Alloys

Reference: Allen, T. R., Busby, J. T., Gan, J., Kenik, E. A., and Was, G. S., **"The Correlation Between Swelling and Radiation-Induced Segregation in Iron-Chromium-Nickel Alloys,"** *Effects of Radiation on Materials: 19th International Symposium, ASTM STP 1366,* M. L. Hamilton, A. S. Kumar, S. T. Rosinski, and M. L. Grossbeck, Eds., American Society for Testing and Materials, West Conshohocken, PA, 2000.

Abstract: The magnitudes of both void swelling and radiation-induced segregation (RIS) in austenitic iron-chromium-nickel alloys are dependent on bulk alloy composition. In this work, the resistance to swelling from major element segregation is estimated and alloys with greater nickel enrichment and fast-developing segregation profiles are shown to be less prone to swelling. In austenitic iron-chromium-nickel alloys, the total swelling depends on the duration of the transient swelling period that precedes steady-state swelling. A longer transient swelling period leads to less overall swelling for the same irradiation dose. The duration of this transient period depends on the void nucleation rate which is determined directly by the average vacancy diffusivity and indirectly by the magnitude of the segregation to the void surface. Alloys with faster vacancy diffusion have a slower void nucleation rate, a longer transient swelling period, and less swelling. Radiation-induced segregation affects swelling by decreasing the vacancy flux to the void. Because the diffusivity of nickel via the vacancy flux is slow relative to chromium, nickel enriches and chromium depletes at void surfaces during irradiation in all austenitic iron-chromium-nickel alloys. This local composition change reduces the subsequent vacancy flux to the voids, increasing the bulk point defect recombination rate, reducing the bulk vacancy concentration, which further reduces the nucleation rate and swelling. Alloys that display the greatest amount of nickel enrichment and chromium depletion are found to be most resistant to void swelling, as predicted from both void nucleation and void growth considerations.

Keywords: void swelling, radiation-induced segregation, austenitic steels

[1] Argonne National Laboratory-West, PO Box 2528, Idaho Falls, ID 83403-2528.
[2] Department of Nuclear Engineering and Radiological Sciences, University of Michigan, Ann Arbor, MI 48109.
[3] Metals and Ceramics Division, Oak Ridge National Laboratory, Oak Ridge, TN 37831.

Copyright© 2000 by ASTM International www.astm.org

Introduction

Void swelling in austenitic alloys can cause unacceptable dimensional changes in reactor structural materials. After void swelling was discovered in irradiated austenitic stainless steels [1], many studies were undertaken to determine not only the magnitude of the swelling problem but also the variables that influenced swelling (A comprehensive review of void swelling was recently written by Garner [2].) One of the major factors that has been shown to affect void swelling is the bulk composition of the structural component. A relationship between swelling and bulk composition of iron-chromium-nickel alloys irradiated using heavy ion irradiations was initially discovered by Johnston et al. [3]. At 675°C and 140 dpa, for an alloy series with constant chromium and varying nickel concentration, swelling decreased strongly with increasing bulk nickel concentration. For example, for alloys with 15 wt% chromium, the swelling decreased from 120% for an alloy with 15 wt% nickel to around 1% for an alloy with 45 wt% nickel. The swelling reached a minimum at intermediate nickel concentration (between 45 and 60 wt%). At higher nickel concentrations, the swelling increased slowly with increasing nickel concentration. For an alloy series with constant nickel and varying chromium concentration, swelling increased with increasing bulk chromium concentration. Studies of iron-chromium-nickel alloys irradiated with neutrons to low fluence showed similar trends in void swelling as a function of bulk alloy composition [4-6]. Garner showed that the dependence of swelling on bulk composition occurs in the transient regime that precedes steady-state swelling [7]. Following the transient period, the rate of swelling in austenitic alloys reaches a constant rate of about 1%/dpa. Alloys with a longer transient swelling regime will have less total swelling at a given neutron exposure.

Esmailzadeh and Kumar [8], Garner and Wolfer [9], and Coghlan and Garner [10, 11], evaluating a model set forth by Garner, proposed that the major compositional dependence of swelling is caused by the compositional dependence of the effective vacancy diffusion coefficient. Those alloys with faster vacancy diffusion have a slower void nucleation rate (due to the smaller bulk vacancy concentration), a longer transient swelling period, and less swelling. However, the analysis was incomplete in two ways. First, the original analysis used the compositional dependence of self-diffusion coefficients measured at 1200°C and assumed that the relative diffusion coefficients could be extrapolated down to radiation temperatures. Second, the original analysis did not account for the fact that as voids started to grow, they would develop segregation at the surface and that this segregation must slow the rate of void growth. Without a detailed understanding of radiation-induced segregation (RIS) in iron-chromium-nickel alloys, these two limitations in the theory could not be tested at the time. Later treatments by Garner and co-workers addressed some features of these two deficiencies [12-14], not only for iron, chromium, and nickel, but also for silicon and phosphorous, which strongly influence the diffusivities of iron, chromium, and nickel.

Detailed studies of RIS in iron-chromium-nickel alloys have recently been completed which allow a more complete understanding of the effect of bulk composition on swelling. Radiation-induced segregation is the non-equilibrium segregation that occurs at grain boundaries and other defect sinks such as dislocation loops and voids during irradiation of an alloy at high temperature (30 to 50 percent of the melting temperature) [17]. In irradiated iron-chromium-nickel alloys, nickel enriches and chromium depletes at defect sinks. Iron either enriches or depletes depending on the bulk alloy composition. Marwick noted that RIS of the slow-diffusing nickel to void surfaces in iron-chromium-nickel alloys could reduce the rate of void growth by reducing the arrival rate of vacancies to the void surface [18]. Marwick postulated that differences in diffusion rates between different iron-chromium-nickel alloys might explain the differences in swelling behavior. Since swelling measurements have shown that swelling reaches a steady state of 1%/dpa, any effect of segregation on swelling during void growth must occur during the transient phase of void swelling.

This work explores the relationship between RIS, swelling behavior, and bulk composition. A recent analysis of RIS in seven different iron-chromium-nickel alloys indicated that grain boundary segregation is driven primarily by the interaction between elements and the vacancy flux [19,20]. For each bulk composition, the rate at which chromium, nickel, and iron diffuse via the vacancy flux differs. Therefore, changes in bulk composition alter the amount of segregation at any defect sink, including a void. This segregation causes a resistance to void swelling which changes as a function of bulk alloy composition. Those alloys with the greatest segregation will be shown below to also be the alloys that begin to swell the latest.

Theory

Changing the bulk composition affects void swelling in two ways. First, altering the bulk composition changes the overall rate of vacancy diffusion and thus the concentration of point defects. As an example, as bulk nickel concentration increases, the absolute diffusion rate of all species via the vacancy flux increases. This decreases the steady-state vacancy concentration and reduces the void nucleation rate. Altering the bulk composition can also change the relative diffusion rates and thus the amount of RIS. These compositional gradients in the vicinity of the defect sinks affect the rate at which defects migrate to the sinks. In iron-chromium-nickel alloys, chromium diffuses more rapidly via a vacancy mechanism than does iron or nickel, and therefore depletes at grain boundaries. Nickel diffuses more slowly via a vacancy mechanism than does iron or chromium and therefore enriches at grain boundaries. The enrichment of the slow-diffusing nickel and depletion of the fast-diffusing chromium at a defect sink reduces the flux of vacancies to the sink. The reduced vacancy flux caused by RIS should affect the rate of swelling in iron-chromium-nickel alloys.

A detailed description of RIS in concentrated alloys is provided by Perks [21]. The flux of vacancies to a void is given by:

$$J_V = N\left[-D_V \nabla C_V + C_V \alpha\left(d_{CrV}\nabla C_{Cr} + d_{FeV}\nabla C_{Fe} + d_{NiV}\nabla C_{Ni}\right)\right], \quad (1)$$

where D_v is the diffusion coefficient of vacancies, C_v is the vacancy concentration, α is the thermodynamic factor, C_j is the concentration of the jth (j=Fe, Cr, Ni) atom, and d_{jv} is the diffusivity of the jth atom. The term $-D_V \nabla C_V$ is the flux of vacancies from the bulk to the defect sink caused by the gradient in the vacancy concentration. The term $C_V \alpha\left(d_{AV}\nabla C_A + d_{BV}\nabla C_B + d_{CV}\nabla C_C\right)$ is the flux of vacancies away from the defect sink due to gradients in the atom concentrations (vacancy back diffusion). In a ternary iron-chromium-nickel alloy:

$$C_{Cr} + C_{Fe} + C_{Ni} = 1, \quad (2a)$$

or

$$\nabla C_{Fe} = -\nabla C_{Cr} - \nabla C_{Ni}. \quad (2b)$$

Substituting (2b) into (1) and simplifying gives

$$J_V = N C_V \nabla C_V \left[\frac{-D_V}{C_V} + \alpha\left[\frac{(d_{CrV} - d_{FeV})\nabla C_{Cr}}{\nabla C_V} + \frac{(d_{NiV} - d_{FeV})\nabla C_{Ni}}{\nabla C_V}\right]\right]. \quad (3)$$

Void growth depends on the flux of vacancies to the void (the magnitude of which is dependent on the vacancy diffusion coefficient D_v), and the back-diffusion of vacancies from the void (the magnitude of which is determined by $\alpha\left[\frac{(d_{CrV} - d_{FeV})\nabla C_{Cr}}{\nabla C_V} + \frac{(d_{NiV} - d_{FeV})\nabla C_{Ni}}{\nabla C_V}\right]$). Those alloys with a smaller flux of vacancies to the void and a greater back diffusion away from the void will take less time to develop a steady-state segregation profile. Additionally, greater back diffusion occurs in systems with steeper segregation profiles. Therefore, those alloys with a smaller flux of vacancies to the void and a greater back diffusion away from the void quickly and significantly reduce the subsequent vacancy flux to the void. The reduced flux to the void increases the bulk point defect recombination rate, reducing the bulk vacancy concentration and the void nucleation rate. The net effect is to further reduce the void nucleation rate, increase the length of the transient swelling regime, and reduce the total flux.

The forward and back-diffusion vacancy flux terms can be analyzed further. The bulk vacancy concentration is related to the vacancy diffusion coefficient by [22]:

$$C_v \propto \left(\frac{1}{D_v}\right)^{1/2} \tag{4}$$

The flux of vacancies to the boundary therefore depends on $D_v^{3/2}$, with the diffusion coefficient for vacancies given by:

$$D_v = d_{CrV}C_{Cr} + d_{FeV}C_{Cr} + d_{NiV}C_{Cr}. \tag{5}$$

The diffusivity of the jth atom via vacancies is given by:

$$d_{jv} = d_0^j \exp\left(\frac{-E_{vm}^j}{kT}\right), \tag{6}$$

where d_0 is the pre-exponential factor and E_{vm}^j is the migration energy via vacancies.

The back-diffusion of vacancies away from the void depends on the magnitude of the difference in the diffusivities of chromium and iron $(d_{CrV} - d_{FeV})$ and on the magnitude of the difference in the diffusivities of nickel and iron $(d_{NiV} - d_{FeV})$. It also depends on the ratio of the chromium gradient to the vacancy gradient $\frac{\nabla C_{Cr}}{\nabla C_V}$ and the ratio of the nickel gradient to the vacancy gradient $\frac{\nabla C_{Ni}}{\nabla C_V}$.

The magnitude of the term

$$\frac{(d_{CrV} - d_{FeV})\nabla C_{Cr}}{\nabla C_V} + \frac{(d_{NiV} - d_{FeV})\nabla C_{Ni}}{\nabla C_V}, \tag{7}$$

determines the resistance to void swelling due to back diffusion. The gradient ratios ($\frac{\nabla C_{Cr}}{\nabla C_V}$ and $\frac{\nabla C_{Ni}}{\nabla C_V}$) can be estimated from the steady-state solution to the equations describing RIS. The equations describing RIS have been solved by Wiedersich et al. [23] to obtain the relationship between an atom gradient and the vacancy gradient at *steady state* for a binary alloy. The ratio of these two gradients at steady state has been termed the determinant (M) by Watanabe et al. [24]. For a binary alloy, the determinant for atom A is:

$$M_A = \frac{\nabla C_A}{\nabla C_v} = \frac{C_A C_B d_{Ai} d_{Bi}}{\alpha(d_{Bi}C_B D_A + d_{Ai}C_A D_B)}\left(\frac{d_{Av}}{d_{Ai}} - \frac{d_{Bv}}{d_{Bi}}\right). \tag{8}$$

If the term $\left(\frac{d_{Av}}{d_{Ai}} - \frac{d_{Bv}}{d_{Bi}}\right)$ is positive, the gradient of atom A is in the same direction as the vacancy gradient and atom A would deplete. Watanabe et al. [24] derived an expression for the determinant in a ternary alloy. The determinant for atom j (where j is Fe, Cr, or Ni in a ternary alloy) is:

$$M_j = \frac{\nabla C_j}{\nabla C_v} = \frac{\frac{d_{jv}C_j}{D_j}\sum_{k\neq j}\frac{d_{ki}C_k}{D_k} - \frac{d_{ji}C_j}{D_j}\sum_{k\neq j}\frac{d_{kv}C_k}{D_k}}{\alpha\sum_k \frac{d_{ki}C_k}{D_k}}. \quad (9)$$

If the determinant for the jth atom is positive, then the jth atom depletes during irradiation. Although the determinants ($\frac{\nabla C_{Cr}}{\nabla C_V}$ and $\frac{\nabla C_{Ni}}{\nabla C_V}$) are a steady-state solution, the resistance to swelling from back diffusion throughout the irradiation can be estimated using the determinants.

Since atom diffusivities and vacancy diffusion coefficients vary significantly from iron-base to nickel-base alloys, the flux terms are more easily compared by normalizing them to the nickel diffusivity. Carrying out this normalization, equation 3 becomes:

$$J_V = Nd_{NiV}C_V\nabla C_V\left[\frac{-\left(D_V/d_{NiV}\right)}{C_V} + \alpha\left[\frac{(d_{CrV}-d_{FeV})}{d_{NiV}}\frac{\nabla C_{Cr}}{\nabla C_V} + \frac{(d_{NiV}-d_{FeV})}{d_{NiV}}\frac{\nabla C_{Ni}}{\nabla C_V}\right]\right]. \quad (10)$$

Since the vacancy concentration is proportional to $D_v^{-1/2}$, the magnitude of the forward diffusion term can be defined as:

$$\left(D_V/d_{NiV}\right)^{3/2} \equiv \text{FDM}. \quad (11)$$

Recall that references 8-10 showed that the void nucleation rate was dependent on the average diffusivity of vacancies. The FDM is therefore also a measure of the void nucleation rate without consideration of segregation.

The magnitude of the back diffusion term can be defined as:

$$\alpha\left[\frac{(d_{CrV}-d_{FeV})}{d_{NiV}}\frac{\nabla C_{Cr}}{\nabla C_V} + \frac{(d_{NiV}-d_{FeV})}{d_{NiV}}\frac{\nabla C_{Ni}}{\nabla C_V}\right] \equiv \text{BDM}. \quad (12)$$

The ratio $\frac{FDM}{BDM}$ is an indication of the propensity to swell. The larger $\frac{FDM}{BDM}$, the more likely an alloy of given composition will begin to swell. The propensity to swell could also be defined as the difference FDM-BDM. Either formulation is sufficient. In this work, the ratio $\frac{FDM}{BDM}$ will be used to define the propensity to swell.

To calculate the FDM and BDM for a given alloy, the diffusivities must be known *at the temperatures at which swelling and RIS occur*. Using the diffusivities and steady-state determinants obtained from RIS measurements, the FDM and BDM for different iron-chromium-nickel alloys can be calculated. The trends in the ratio $\frac{FDM}{BDM}$ as a function of alloy composition can be compared to the trends in void swelling as a function of composition to show that the reduction in swelling corresponds directly to the magnitude of the vacancy flux in these alloys.

Comparison of Swelling Data to Swelling Resistance from Segregation

The largest set of RIS data for iron-chromium-nickel alloys has been generated using proton irradiations [19,20,26-32]. Seven different iron-base alloys (Fe-16Cr-24Ni, Fe-20Cr-24Ni, Fe-24Cr-24Ni, Fe-24Cr-19Ni, Fe-20Cr-9Ni, Ni-18Cr-9Fe, and Ni-18Cr) were irradiated at five different temperatures (200°C-600°C at 100°C intervals), to five different doses (0.1, 0.3, 0.5, 1.0, and 3.0 dpa). Grain boundary compositions were measured using both Auger electron spectroscopy (AES) and scanning transmission electron microscopy with energy dispersive x-ray spectroscopy (STEM/EDS), resulting in over 1,100 grain boundary composition measurements.

Table 1. *Vacancy diffusivities determined from segregation measurements.*

Alloy	d_{vm}^{Cr}/d_{vm}^{Ni}	d_{vm}^{Fe}/d_{vm}^{Ni}	E_{vm}^{Cr}	E_{vm}^{Fe}	E_{vm}^{Ni}
Fe-16Cr-24Ni	2.54	1.68	1.32	1.305	1.30
Fe-20Cr-24Ni	2.48	1.60	1.32	1.305	1.30
Fe-24Cr-24Ni	2.39	1.47	1.32	1.305	1.30
Fe-24Cr-19Cr	2.32	1.34	1.32	1.305	1.30
Fe-20Cr-9Ni	2.31	1.28	1.32	1.305	1.30
Ni-18Cr-9Fe	2.54	1.67	0.83	0.815	0.80
Ni-18Cr	2.54	--------	1.07	--------	1.04

From the grain boundary composition measurements, the diffusivities of iron, chromium, and nickel were determined for each alloy. The diffusivities, which are input to the RIS model calculations, were determined by changing the diffusivities (model inputs) until the model best fit the measured data [26,27]. These "best-fit" diffusivities follow the trends of self-diffusion coefficients for all of the alloys involved, indicating that preferential coupling with the vacancy flux was probably the primary mechanism of RIS in these alloys. The pre-exponential factors and vacancy migration energies that best predicted the measured segregation are listed in (Table 1). The fit of the data was better for the iron-base alloys so the uncertainty in the diffusivities of the nickel-base alloys is greater. The pre-exponential factors for iron-base alloys in Table 1 match those from the self-diffusion work of Rothman [33] and are the same as those used in references [8-10] to explain the effect of bulk composition on void nucleation rate. Therefore, the effect of bulk composition on void nucleation rate predicted by Esmailzadeh and Kumar using high-temperature self-diffusion measurements holds true at radiation temperatures. The effect of RIS on void swelling will now be examined.

The ratio $\frac{FDM}{BDM}$ was calculated using equations 11-12 at two temperatures (510°C and 675°C) where published swelling measurements as a function of composition are available. The calculations assumed that the interstitial diffusivities were equal for chromium, iron, and nickel [30]. As described, void swelling should be inhibited in those alloys where the ratio $\frac{FDM}{BDM}$ is a minimum. Figure 1 plots the measured void swelling and $\frac{FDM}{BDM}$ at 675°C for Fe-xCr-(19-29)Ni alloys where the chromium concentration x varies from 8 to 31 at%. Figure 2 plots the measured void swelling and $\frac{FDM}{BDM}$ at 510°C for Fe-xCr-(19-24)Ni alloys where the chromium concentration x varies from 8 to 31 at%. For both irradiation temperatures, the mean swelling and the $\frac{FDM}{BDM}$ (propensity to swell) increase as bulk chromium concentration increases.

The relationship between swelling and back diffusion can also be examined in constant chromium alloys. Figure 3 plots the measured void swelling and calculated $\frac{FDM}{BDM}$ at 675°C for Fe-(16-24)Cr-xNi alloys where the nickel concentration x varies from 14 to 33 at%. Figure 4 plots the measured void swelling and calculated $\frac{FDM}{BDM}$ at 510°C for Fe-(16-24)Cr-xNi alloys where the nickel concentration x varies from 14 to 34 at%. The swelling in iron-base alloys decreases as bulk nickel concentration increases. At both temperatures, the ratio $\frac{FDM}{BDM}$ follows the trends of the swelling as bulk nickel concentration changes. The only instance in which the ratio $\frac{FDM}{BDM}$ does not follow the trends in swelling is for the Ni-15Cr alloy irradiated at 510°C. In all other cases, reduction in swelling correlates with swelling resistance segregation.

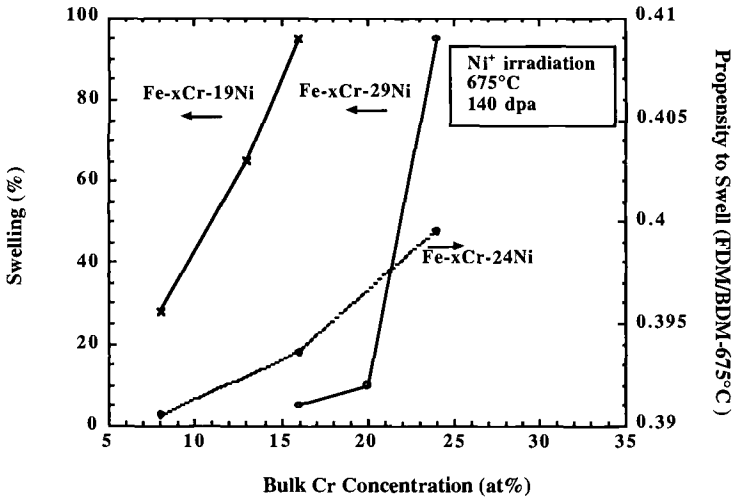


Figure 1. *Comparison of swelling with swelling resistance for 675°C Ni-ion irradiations. Constant nickel varying chromium alloys. Swelling measurements from [3].*

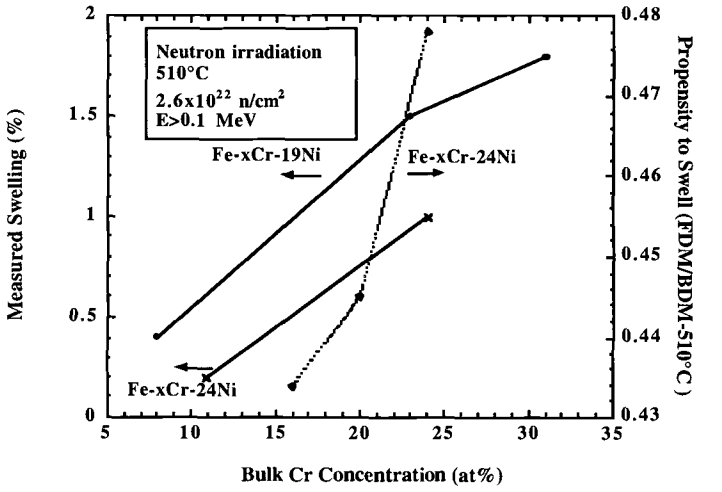


Figure 2. *Comparison of swelling with swelling resistance for 510°C neutron irradiations. Constant nickel varying chromium alloys. Swelling measurements from [5].*

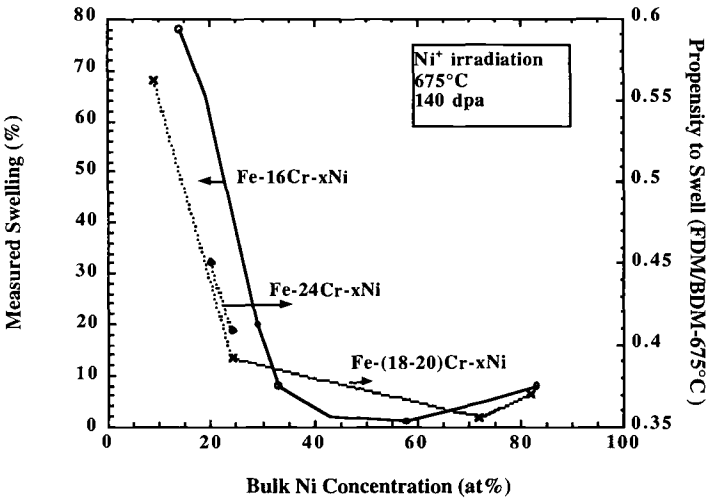


Figure 3. *Comparison of swelling with swelling resistance for 675°C Ni-ion irradiations. Constant chromium, varying nickel alloys. Swelling measurements from [3].*

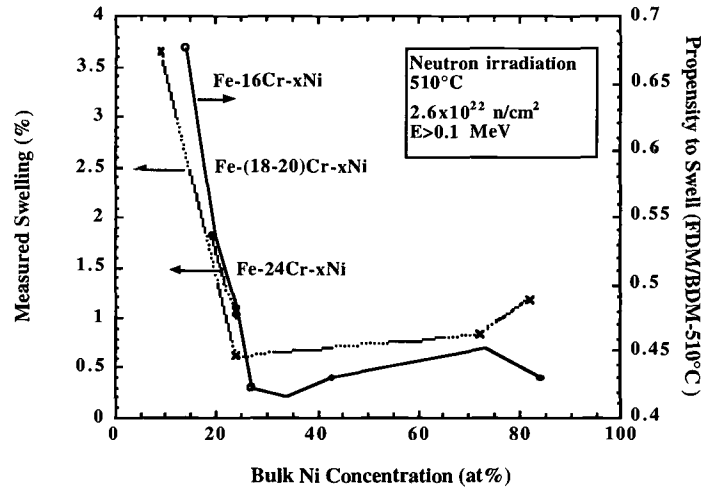


Figure 4. *Comparison of swelling with swelling resistance for 510°C neutron irradiations. Constant chromium, varying nickel alloys. Swelling measurements from [5].*

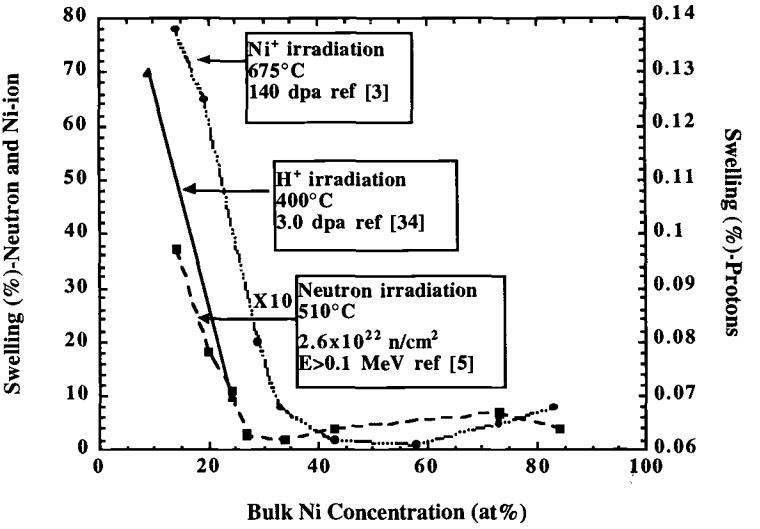


Figure 5. *Swelling as a function of bulk composition is similar for alloys irradiated with protons, neutrons and Ni+ ions.*

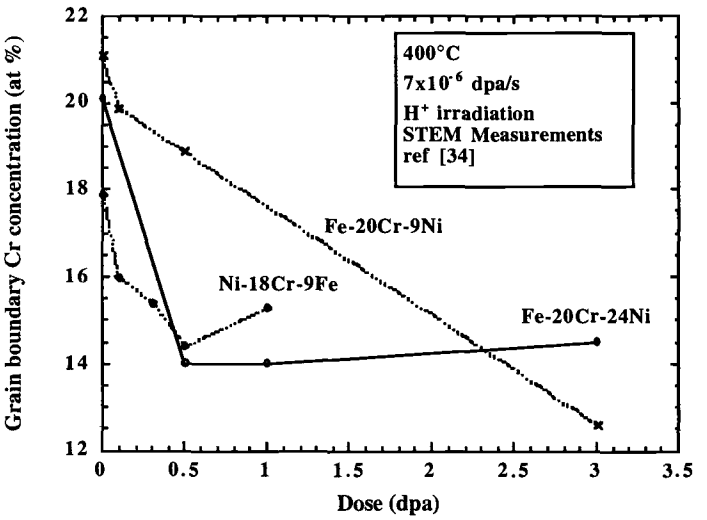


Figure 6. *Dose dependence of segregation as a function of alloy composition for Fe-(18-20)Cr-xNi alloys (x=9, 24, 72)*

For the proton-irradiated alloys from which segregation measurements were taken, bulk swelling was not measured, but the swelling was calculated from the measured void size and density [34]. Figure 5 plots the calculated swelling as a function of composition for alloys irradiated with protons, neutrons, and nickel-ions. The trends in swelling are the same for all three irradiating particles. Therefore, the diffusion mechanisms are not strongly affected by the identity of the irradiating particle.

As previously discussed, alloys that take the longest to reach steady-state segregation should also swell the most because of their shorter incubation period. Measurements of RIS have shown that the time required for the grain boundary composition to reach steady-state differs with bulk nickel concentration [34]. Figure 6 shows the grain boundary chromium concentrations for Fe-20Cr-9Ni, Fe-20Cr-24Ni, and Ni-18Cr-9Fe irradiated with protons at 400°C to various doses. While Fe-20Cr-24Ni and Ni-18Cr-9Fe reach a relatively stable concentration by around 1 dpa, the grain boundary composition in Fe-20Cr-9Ni is still changing between 1 and 3 dpa. The time to steady-state segregation in the Fe-20Cr-9Ni alloy is longer than in Fe-20Cr-24Ni and Ni-18Cr-9Fe. For the iron-base alloys, increasing bulk nickel concentration decreases the time to reach steady-state segregation and decreases the amount of swelling.

The effective vacancy diffusion coefficient is also smaller in Fe-20Cr-9Ni than Fe-20Cr-24Ni. Therefore, the void nucleation rate is faster in Fe-20Cr-9Ni which also contributes to the shorter duration of the transient swelling period and greater swelling. For constant chromium, varying nickel alloys, swelling is reduced as the bulk nickel concentration increases because the void nucleation rate decreases, enhanced by the steep segregation profiles. The effect of bulk composition on segregation and swelling is demonstrated in Figure 7. For 20 at% chromium alloys, as the nickel concentration increases, the swelling decreases and the average diffusivity increases as does the ratio of the chromium to nickel diffusivities. The increase in average diffusivity leads to decreases in the void nucleation rate and decreased swelling. The increase in the ratio of the chromium to nickel diffusivities leads to greater segregation and less swelling. Figure 8 summarizes the effect of bulk composition and vacancy diffusivity on void nucleation, segregation, and void swelling.

While there appears to be very strong evidence that the inverse Kirkendall-induced segregation and the composition-dependence of the effective vacancy diffusivity can explain most of the composition dependence of swelling, there are other contributing factors which add to the complexity of swelling. Wolfer, Garner, and Thomas [14] demonstrated that back-diffusion terms would also be expressed in the interstitial flux. Additionally, Hoyt and Garner [15, 16] showed that to explain the full composition dependence of swelling, it was necessary to add the composition effects on dislocation biases for vacancies and interstitials as well as this bias on void nucleation. In all cases, however, it appears that the primary effect of composition lies in the effect on vacancy diffusion.

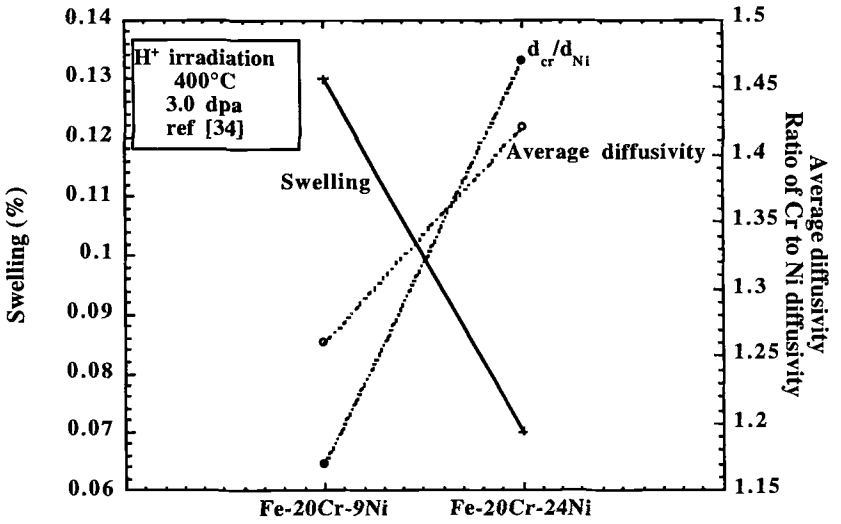


Figure 7. *Swelling as a function of nickel concentration for proton irradiated alloys. As average diffusivity and the ratio of chromium to nickel diffusivity increase, swelling decreases.*

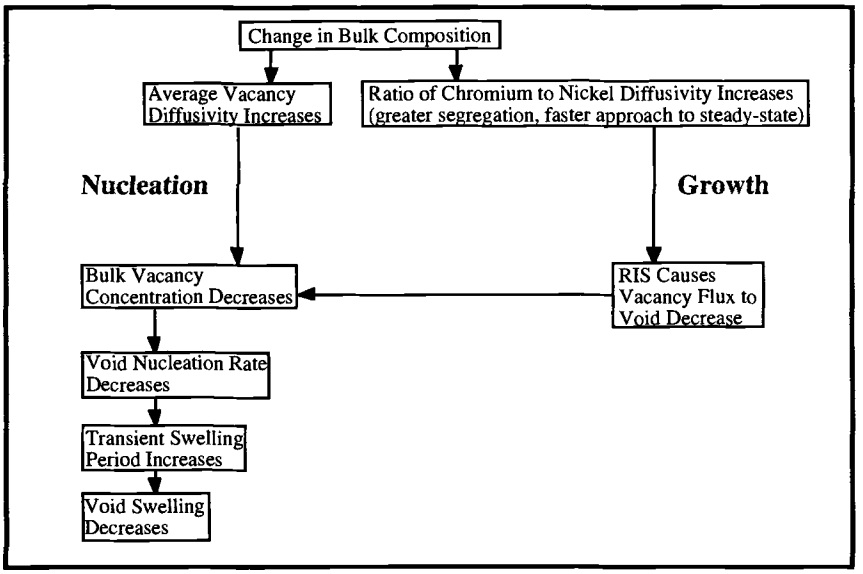


Figure 8. *The relationship between bulk composition, radiation-induced segregation and void swelling*

Conclusion

The degree of both swelling and RIS in austenitic iron-chromium-nickel alloys varies with bulk alloy composition. Resistance to void swelling in iron- and nickel-base alloys changes with bulk vacancy diffusivity and the degree of major element segregation. The resistance to void swelling from segregation can be estimated by calculating the magnitude of the vacancy diffusion to the void using the diffusivities determined from RIS measurements. Enrichment of nickel and depletion of chromium reduces the vacancy flux to voids, decreasing the void nucleation rate, and limiting the magnitude of void growth. The swelling is greater in alloys in which the RIS profiles are slow to develop. These conclusions hold true for iron-base alloys with both constant chromium, varying nickel and constant nickel, varying chromium. Alloys with greater nickel enrichment and chromium depletion are less prone to swelling.

Acknowledgments

The authors gratefully acknowledge R. D. Carter, J. M. Cookson, D. Damcott , and J. Gan for their insight and assistance. Thanks go out to S. M. Bruemmer at Pacific Northwest National Laboratory for his support. This research was supported by the U.S. Department of Energy under grant DE-FG02-93ER-12310 and by the Associated Western Universities-Northwest under U.S. Department of Energy grant DE-FG02-89ER-7552. Support was also provided by the Materials Sciences Branch, Office of Basic Energy Sciences, under contract DE-AC06-76LO1830, through Pacific Northwest National Laboratory. Research was partially supported by the Division of Materials Sciences, U. S. Department of Energy under contract DE-AC05-96OR00033 with Lockheed Martin Energy Research Corp., and through the SHaRE Program under contract DE-AC05-76OR00033 with Oak Ridge Associated Universities. Work was also supported under contract W-31-109-Eng-38 with the Department of Energy.

References

[1] Cawthorne, C. and Fulton, J. E., *Nature*, Vol. 216, 1967 p. 515.

[2] Garner, F. A., *Irradiation Performance of Cladding and Structural Steels in Liquid Metal Reactors, in Materials Science and Technology, A Comprehensive Treatment, Vol 10A Nuclear Materials*, Eds., R. W. Cahn, P. Haasen, and E. J. Kramer, (VCH Weinheim, 1994).

[3] Johnston, W. G., Rosolowski, J. H., Turkalo, A. M., and Lauritzen, T., *J. Nucl. Mater.* Vol. 54, 1974, p. 24.

[4] Watkin, J. S., *Irradiation Effects on the Microstructure and Properties of Metals, STP 611, Philadelphia: ASTM*, 1976 pp.270-283.

[5] Bates, J. F. and Johnston, W. G., *Proc. Int. Conf. Radiation Effects in Breeder Reactor Structural Materials*, Scottsdale, New York: The Metallurgical Society of AIME, 1977 pp. 625-644.

[6] Bates, J. F. and Powell, R. W., *J. Nucl. Mater.* Vol. 102, 1981, p. 200.

[7] Garner, F. A., *J. Nucl. Mater.* Vol. 122-123, 1984, p. 459.

[8] Esmailzadeh, B. and Kumar, A. S., *Effects of Radiation on Materials: Twelfth International Symposium, STP 870*, F. A. Garner and J. S. Perrin, Eds., American Society for Testing and Materials, Philadelphia, 1985, pp. 139.

[9] Garner, F. A. and Wolfer, W. G., *J. Nucl. Mater.* Vol. 102, 1981, p. 143.

[10] Garner, F. A. and Wolfer, W. G., *J. Nucl. Mater.*, Vol. 122, 1984, p. 201.

[11] Coghlan, W. A. and Garner, F. A., *Radiation-Induced Changes in Microstructure: 13th International Symposium (Part I), ASTM STP 955*, F. A. Garner, N. H. Packan, and A. S. Kumar, Eds., American Society for Testing and Materials, Philadelphia, 1987, pp. 315-329.

[12] Garner, F. A. and Kumar, A. S., *Radiation-Induced Changes in Microstructure: 13th International Symposium (Part I), ASTM STP 955*, F. A. Garner, N. H. Packan, and A. S. Kumar, Eds., American Society for Testing and Materials, Philadelphia, 1987, pp. 289-314.

[13] Esmailzadeh, B., Kumar, A. S., and Garner, F. A., *J. Nucl. Mater.* Vol. 133&134, 1985, p. 590.

[14] Wolfer, W. G., Garner, F. A., and Thomas, L. E., *Radiation-Induced Changes in Microstructure: 11th International Symposium, ASTM STP 782*, H. R. Brager and J. S. Perrin, Eds., American Society for Testing and Materials, 1982, pp. 1023-1041

[15] Hoyt, J. J. and Garner, F. A., *J. Nucl. Mater.* Vol. 179-181, 1991, p. 1096.

[16] Hoyt, J. J. and Garner, F. A., Fusion Reactor Materials Semiannual Progress Report, DOE/ER-0313-9, pp. 81-86, 1992.

[17] Okamoto, P. R. and Rehn, L. E., *J. Nucl. Mater.* Vol. 83, 1979, p.2.

[18] Marwick, A. D., *J. Phys. F.: Metal Phys.* Vol. 8, 1978, p. 1849.

[19] Allen, T. R., Was, G. S., and Kenik, E. A., *J. Nucl. Mater.* Vol. 244, 1997, p. 278..

[20] Allen, T. R. and Was, G. S., in *Proceedings of the MRS Fall Meeting Symposium B: Microstructure of Irradiated Materials*, (Mater. Res. Soc. Proc. 439, Pittsburgh, PA, 1997), p. 539.

[21] Perks, J.M., Marwick, A.D., and English, C.A., "A computer code to calculate radiation-induced segregation in concentrated ternary alloys," AERE R 12121 June 1986.

[22] Sizmann, R., *J. Nucl. Mater.* Vol. 69&70, 1968, p. 386.

[23] Wiedersich, H., Okamoto, P. R., and Lam, N. Q., *J. Nucl.. Mater.* Vol. 83, 1979, p. 98.

[24] Watanabe, S. and Takahashi, H., *J. Nucl. Mater.* Vol. 208, 1994, p. 191.

[25] Busby, J., Allen, T. R., Was, G. S., and Kenik, E. A. in *Proceedings of the MRS Fall Meeting Symposium B: Microstructure of Irradiated Materials*, (Mater. Res. Soc. Proc. 439, Pittsburgh, PA, 1997), p. 563.

[26] Allen, T. R., Damcott, D. L., Was, G. S., and Kenik, E. A., *Proceedings of the Seventh International Symposium on Environmental Degradation of Materials in Nuclear Power Systems-Water Reactors*, August 1995, Breckenridge, Colorado. p. 997.

[27] Allen, T. R. and Was, G. S., *Proceedings of the 1994 MRS Fall Meeting: Symposium Y: Microstructure of Irradiated Materials.*, Eds. I. M. Robertson, L. E. Rehn, S. J. Zinkle, W. J. Phythian (Mater. Res. Soc. Proc. 373, Pittsburgh, PA, 1995) p. 101.

[28] Allen, T. R. and Was, G. S., *J. Nucl. Mater.* Vol. 244, 1997, p. 278.

[29] Allen, T. R. and Was, G. S., *Effects of Radiation on Materials: 18th International Symposium, ASTM STP 1325*, R. K. Nanstad, M. L. Hamilton, F. A. Garner, and A. S. Kumar, Eds., American Society for Testing and Materials, 1997.

[30] Allen, T. R. and Was, G. S., *Acta Met.* Vol. 46, 1998, p. 3679.

[31] Allen, T. R., Busby, J. T., Was, G. S., and Kenik, E. A., *J. Nucl. Mater.* Vol. 255, 1998, p. 44.

[32] Damcott, D. L., Allen, T. R., and Was, G. S., *J. Nucl. Mater.*, Vol. 225, 1995,p. 97.

[33] Rothman, S.J., Nowicki, L.J., and Murch, G.E., *Journal of Physics F:Metal Physics* Vol. 10, 1980, p. 383.

[34] Busby, J.T., Allen, T.R., Gan, J., Kenik, E.A., and Was, G.S., *Proceedings of Eighth International Symposium on Environmental Degradation of Materials in Nuclear Power Systems - Water Reactors*, Aug. 10-14, 1997, Amelia Island Fl.

S. Ohnuki,[1] S. Yamashita,[2] H. Takahashi,[1] and T. Kato[3]

Effect of IVa and Va Elements on Void Formation in Neutron-Irradiated 316 Stainless Steels

Reference: Ohnuki, S., Yamashita, S., Takahashi, H., and Kato, T., **"Effect of IVa and Va Elements on Void Formation in Neutron-Irradiated 316 Stainless Steels,"** *Effects of Radiation on Materials: 19th International Symposium, ASTM STP 1366,* M. L. Hamilton, A. S. Kumar, S. T. Rosinski, and M. L. Grossbeck, Eds., American Society for Testing and Materials, West Conshohocken, PA, 2000.

Abstract: In a previous electron irradiation study it was shown that additions of elements from the IVa and Va columns of the periodic table to 316L stainless steel could have a pronounced effect on its swelling resistance. The results suggested that vacancy binding was the main operative mechanism, increasing in strength with increasing size factor. In the current experiment these same alloys were irradiated with fast neutrons, but the influence of the size factor does not appear to be the only important mechanism. Whereas essentially precipitation was limited during electron irradiation, substantial precipitation occurred during neutron irradiation at lower displacement rates, overshadowing the effect of size factor on swelling. The addition of Hf and especially Zr, however, was particularly effective in suppressing swelling in both the electron and neutron cases, although the suppression mechanism in the neutron case appears to be a combination of both size effect and precipitation to alter the sink structure.

Keywords: 316 stainless steel, void formation, neutron irradiation, swelling suppression, solute addition, size effect

Introduction

To improve the void swelling resistance of austenitic stainless steels, many approaches such as cold-working, thermal treatments and solute addition have been employed, as reviewed in ref. [1]. Solute additions have been used to alter the phase stability of the steel and also to serve as trapping sites for radiation-induced point defects. Whatever the influence of the solutes, it appears that their action is exerted only in the transient regime of swelling, with a post-transient swelling rate of ~1%/dpa eventually

[1] Professors, Hokkaido University, Sapporo, 060-8278, Japan.
[2] Graduate Student, Hokkaido University, Sapporo, 060-8278, Japan.
[3] Senior Engineer, Hitachi Works, Hitachi Ltd., Hitachi, 317-8511, Japan.

Copyright© 2000 by ASTM International www.astm.org

established [1,2]. Therefore, the factors which determine the transient regime are of most interest for experimental studies.

One approach that has not previously received sufficient attention is the systematic addition of over-size elements to bind with vacancies, thereby retarding both radiation-induced segregation and void nucleation. Most previous work in this area was performed with charged particle irradiations [3-6]. In one previous study in this current experimental series, it was shown that addition of elements from columns IVa and Va of the periodic table could have a pronounced effect on the swelling of low-carbon 316 stainless steel [6], as shown in Figure 1. Note that the addition of 0.3 at % of Zr or Hf were particularly effective in suppressing swelling during electron irradiation.

In this previous study [6-8], Kato and coworkers added 0.3 at % of six oversize elements expected to have some potential for binding with vacancies and self-interstitials. To ensure that size effects alone were being studied, they used a low carbon steel, as shown in Table 1, to ensure that the added solutes did not form carbides, but instead remained in solution. Since Si and P are also known to exert strong effects on void nucleation [1,9], these elements were also kept to very low levels to avoid synergistic or competitive effects that would obscure the action of the oversize elements.

It is well known, however, that there are significant differences between neutron-induced and charged particle-induced swelling, arising primarily from the much higher atomic displacement rate in charged particle studies, and also to the unavoidable strong influence of specimen surfaces in electron and ion irradiation experiments. Therefore the relative swelling of alloys shown in Figure 1 must be confirmed during neutron irradiation, which of course is the actual environment of practical interest.

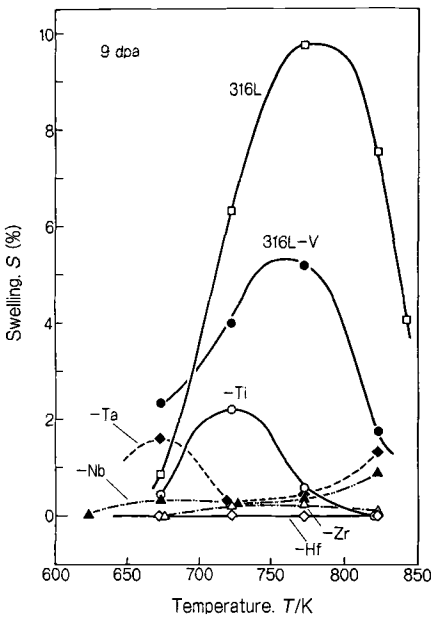


Figure 1. *Void swelling in the alloys irradiated with electrons to 9 dpa.*

Experimental Procedure

As detailed in Table 1, six 316L austenitic stainless steels containing very low levels of common interstitial elements were produced, each with 0.3 at % of oversized elements. A phosphorus-modified alloy was also included. With the base 316L alloy, therefore, a total of eight alloys were prepared for both electron and neutron irradiation, as described in ref. 6. The final specimen form was that of a 3 mm diameter, 0.25 mm thick microscopy disk annealed at 1150 C for 30 minutes. Four-digit identification codes were applied by laser engraving after annealing.

The volume size factor (in %) of the added solutes were previously determined by X-ray diffraction for these alloys to be: IVa elements, Ti, 37.3; Zr, 156.2; Hf, 193.1; Va elements, V, 9.97; Nb, 62.5 and Ta, 78.6 [6].

Neutron irradiation was performed in the Fast Test Flux Facility (FFTF) under active ($\pm$5 C) temperature control in the Materials Open Test Assembly in FFTF cycle 12. There were three separate irradiation canisters at 425, 520 and 600 C with dose levels of 30, 32, and 35 dpa, respectively. Microscopy examination was performed at 200 keV, after conventional twin-jet electro-polishing.

Table 1. *Chemical composition of 316L-X alloys (mass %).*

Material	C	P	S	Ni	Cr	Mo	N	O	
316L	0.003	0.002	0 003	13.9	17.7	2.2	0 0020	0 0131	
Material	C	P	S	Ni	Cr	Mo	N	O	Additive
316L-Ti	0.003	0 003	0.003	13.7	17.0	2.2	0.0019	0.0082	0.30Ti
316L-Zr	0.003	0 002	0 003	13.9	16.7	2.3	0.0079	0 0067	0.78Zr
316L-Hf	0.005	0.002	0.002	13.8	16.6	2.2	0.0034	0.0033	0.90Hf
316L-V	0 004	0 003	0 003	13.9	16.9	2.2	0.0018	0.0187	0.28V
316L-Nb	0.010	0.003	0 003	13.8	17.3	2.2	0 0025	0 0094	0 49Nb
316L-Ta	0.009	0.002	0 003	13.8	16.9	2.2	0 0028	0 0132	0 74Ta

Results

General Microstructure

Figure 2 shows typical microstructures observed at relatively low magnification and near-Bragg conditions for all eight alloys irradiated to 35 dpa at 520 C. All of observed areas include a grain boundary. In general, large amounts of dislocations and precipitates were developed in the alloy matrix. Migrated grain boundaries and relatively large precipitates were also observed in almost all alloys, with the exception of the alloys with Zr and Hf. In these cases, only fine precipitates were found. All microstructures are summarized in Table 2, where the indications are as follows: V; void, D; dislocation, P; precipitate, F-P; fine precipitate, L-P; large precipitate.

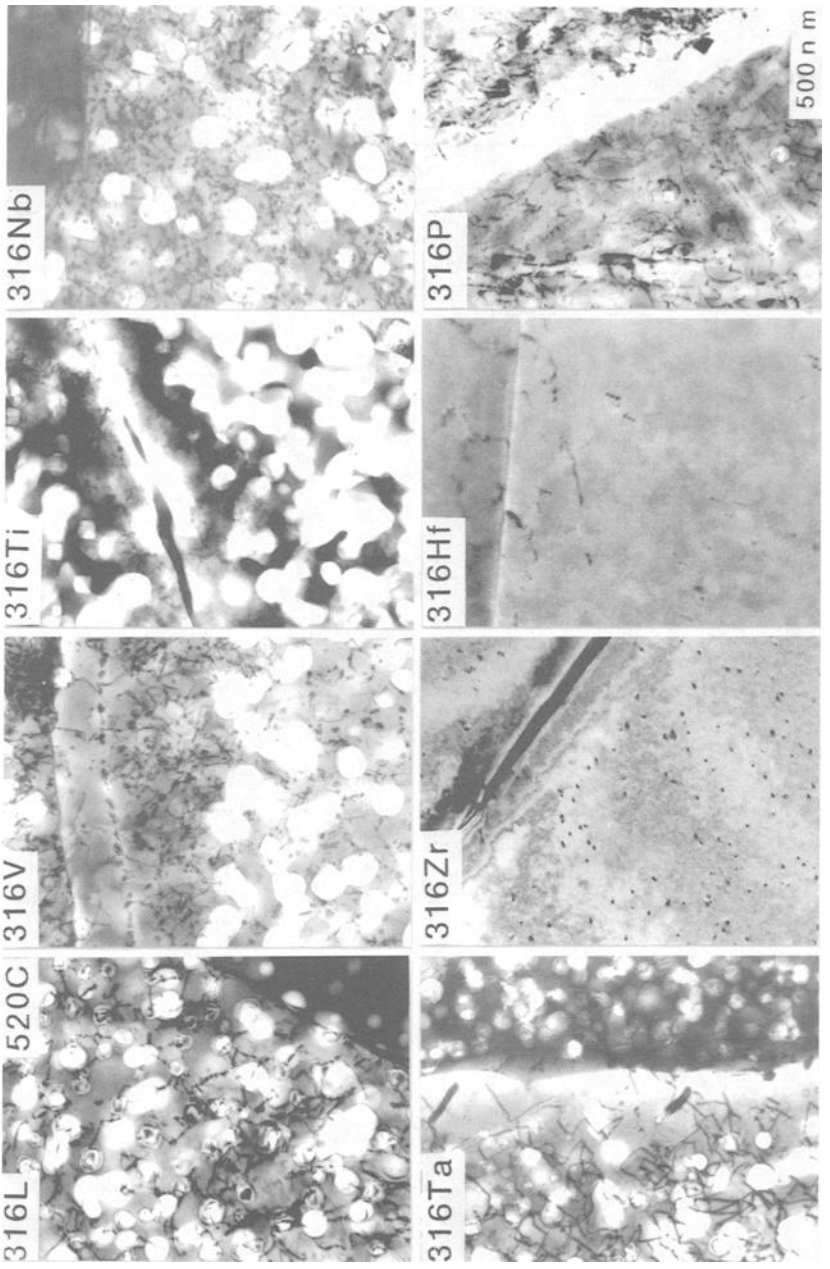


Figure 2. *Typical microstructures developed in the alloys irradiated by neutrons to 35 dpa at 520 C (Low magnification and near-Bragg condition).*

Table 2. *Typical microstructures in the alloys irradiated by neutrons to 30-35 dpa.*

	425 C	520 C	600 C
316L	V, D, P	V, D, P	V, D, P
316L-V	V, D, P	V, D, P	V, D, P
316L-Ti	V, D, P	V, D, P	V, D, P
316L-Nb	V, D, P	V, D, P	V, D, P
316L-Ta	V, D	V, D, P	V, D, P
316L-Zr	V, D	D, F-P	D, F-P
316L-Hf	V, D	D, F- P	D, F- P
316L-P	V, D	V, D, L- P	D, L- P

Void Structure

Figure 3 shows typical microstructures attained at 425 C. At this temperature, void formation is clearly observed in all alloys except those containing Zr, Hf, and P.

Figure 4 shows microstructures attained at 520 C. At this temperature large voids were developed in most alloys and some precipitates associated with voids were observed. In case of the P alloy, small amounts of voids were located on the edges of Fe_2P precipitates. In the case of the Zr and Hf alloys, void formation was completely suppressed, and fine precipitates were observed.

Figure 5 shows typical microstructures for the alloys irradiated at 600 C. At this temperature, the voids in most alloys had very large sizes and lower number density, with the void size often exceeding the specimen thickness. Long thin precipitates were observed in the P alloy, however, and fine, plate-like precipitates were developed in the Zr and Hf alloys, where the precipitates are assumed to be coherent in nature. In the Zr and Hf alloys, the void formation was suppressed completely, and no other secondary defect clusters were observed.

Figure 6 shows the temperature dependence of void swelling measured from microstructural observation. Most of the alloys that exhibited void formation had a maximum at 520 C. From the behavior of swelling, alloys can be categorized into three groups: 316L and 316Ta were at a relatively high swelling level. Alloys with V, Nb, Ti showed medium level of swelling. The alloys with Zr, Hf, and P swelled at a very low level or the swelling was completely suppressed.

Discussion

Role of Size Factor in Void Swelling

Figure 7 shows a comparison of swelling data as a function of volume size factor for electron and neutron irradiation. In the case of electron irradiation, the swelling

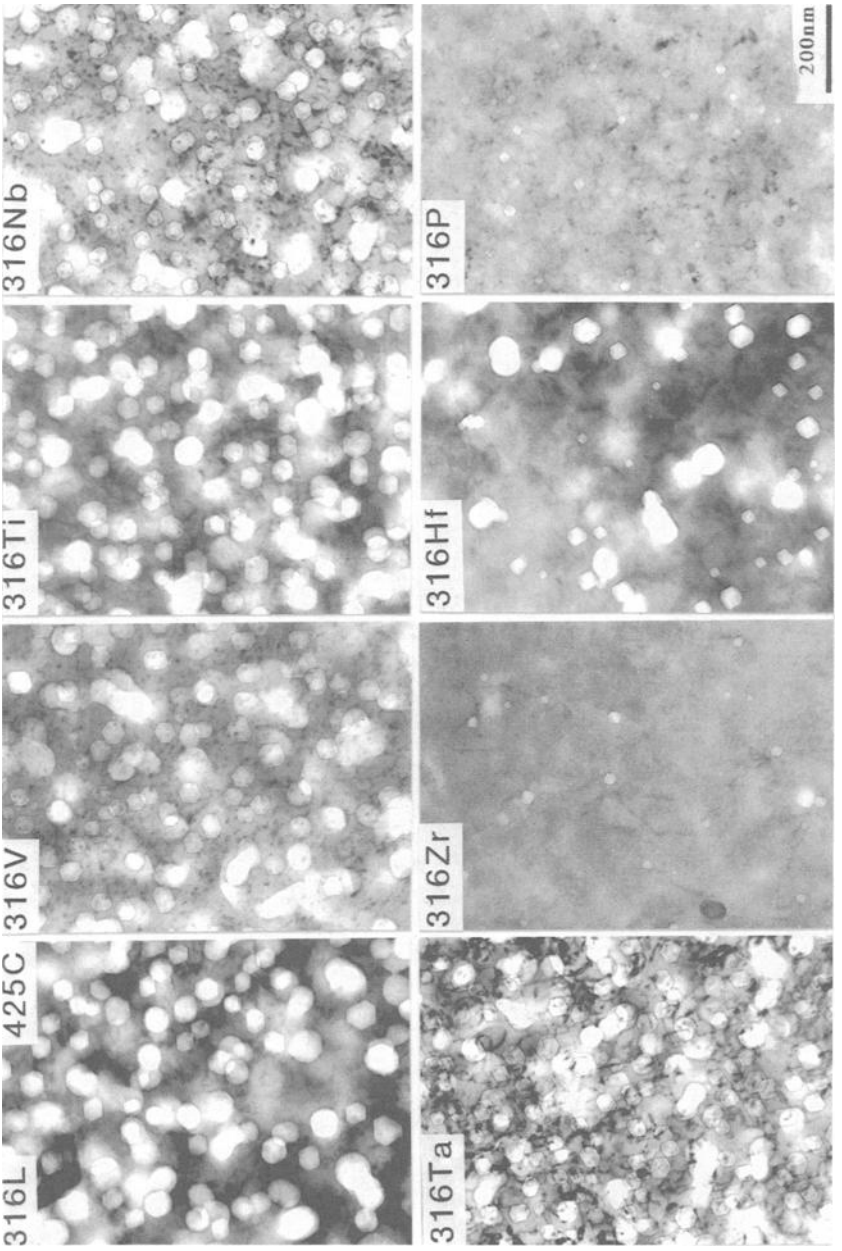


Figure 3. *Void and dislocation structures developed in the alloys irradiated by neutrons to 35 dpa at 425 C.*

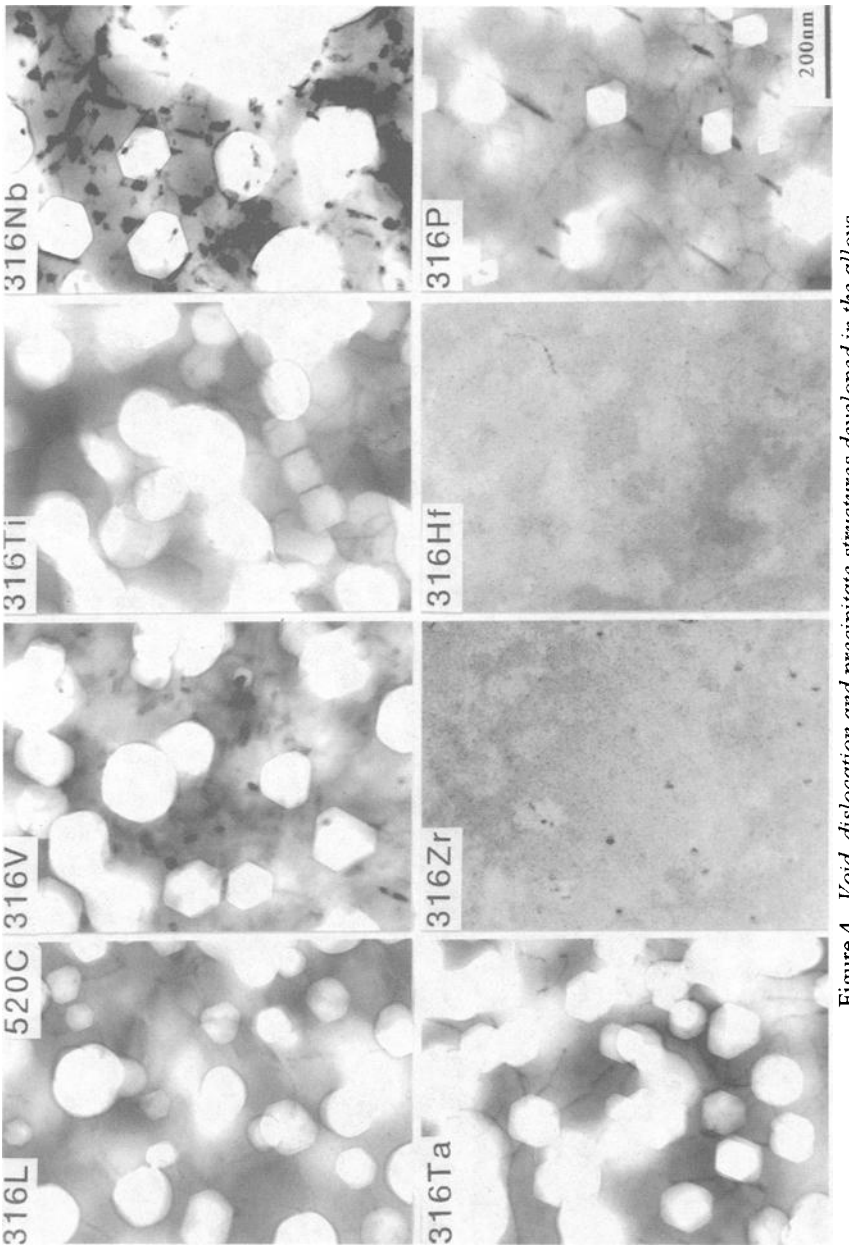


Figure 4. *Void, dislocation and precipitate structures developed in the alloys irradiated by neutrons to 35 dpa at 520 C.*

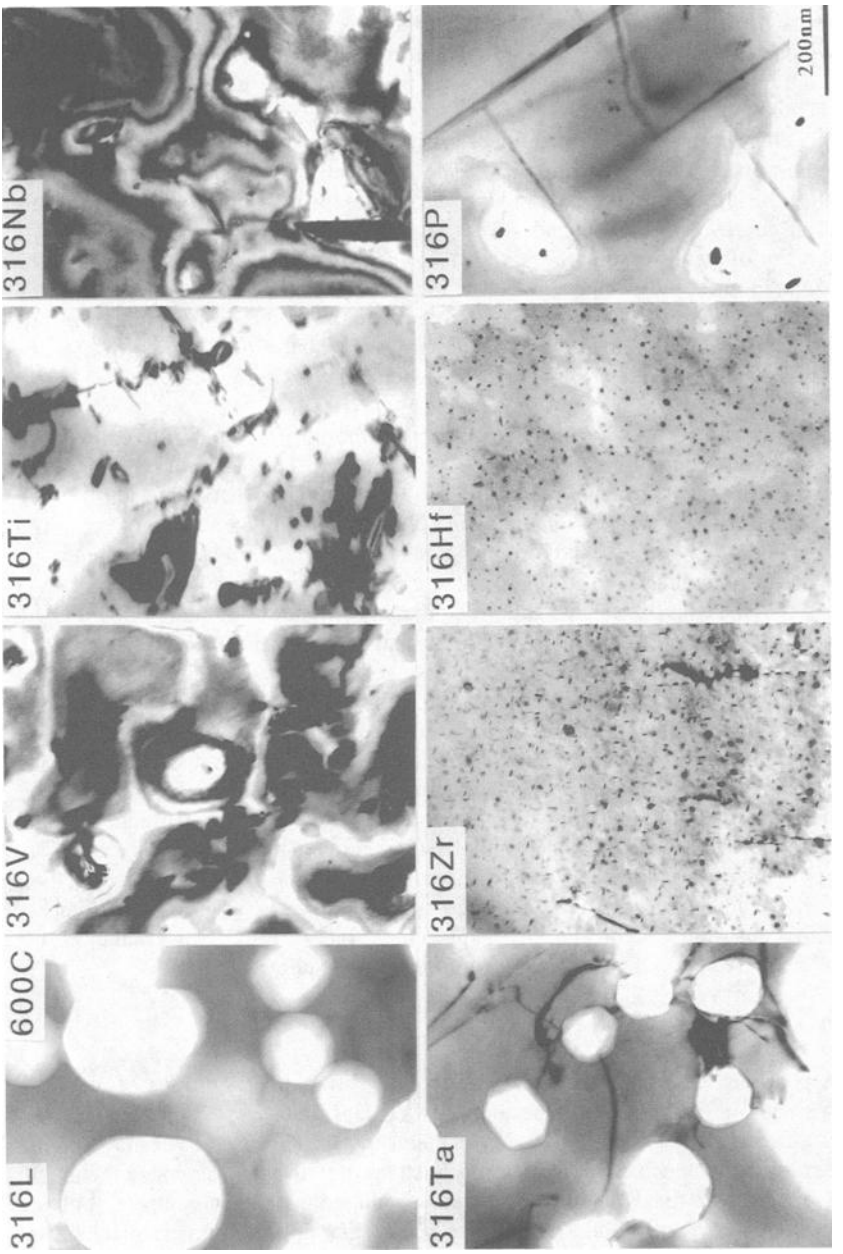


Figure 5. *Void and precipitate structures developed in the alloys irradiated by neutrons to 35 dpa at 600 C.*

decreased with an increase of the size factor, and the strong role of the size factor was observed at each irradiation temperature. Especially, the Zr and Hf alloys showed no swelling, which agrees with the results of the neutron irradiation. In the case of neutron irradiation, the relationship with size factor is not as clear as was observed for electrons, perhaps except at 600 C.

In the electron-irradiation experiment a strong interaction between vacancies and over-sized solute atoms was confirmed [6]. The actual migration energies of vacancies increased with the alloying addition, which were measured from loop growth experiments. The migration energy was 1.1 eV and 1.21-1.25 eV for 316L and the Ti or Nb alloys, respectively. For other alloys, the migration energy could not be measured because of the difficulty of the loop formation during electron irradiation. From the behavior of vacancy migration energy, however, the vacancy trapping mechanism should be acting. In this experiment, the Zr and Hf alloys contain no significant dislocation structure after the neutron irradiation, which suggests a strong recombination-dominated condition for irradiation defects.

There was no evidence of the precipitation in the un-irradiated alloys after heat treatment, as shown by X-ray diffraction and conventional TEM observation. This is due primarily to the low content of interstitial elements (C; 0.003-0.010%, N; 0.02-0.07%) Under such conditions, almost all of the added elements can remain in solution. The complete void suppression by Zr and Hf during neutron irradiation was accompanied by formation of fine precipitates. The precipitates were coherent, of small size, and high number density. It is suggested that the precipitation is radiation-induced, possibly by segregation to defect clusters. Such precipitates may act as possible recombination centers for point defects. A possible mechanism of the strong swelling suppression developed in the neutron irradiated Zr and Hf alloys might therefore include both mechanisms; strong trapping for vacancies and defect recombination at fine precipitates.

Most importantly, such precipitation on a large scale was not observed in the electron-irradiated alloys. It means that the precipitation must be enhanced strongly during neutron irradiation in long term, such as 6000 hrs. Therefore, size effects were the predominant effect at the higher displacement rate characteristic of electron irradiation. At the lower displacement rates attained in the current neutron irradiation, precipitation obviously can be intensified, changing both the matrix composition, and the sink density for point defect absorption. Thus, at low displacement rate or long term irradiation, the influence of size effects can be overshadowed in most of the alloys studied.

Conclusion

In a previous electron irradiation study it was shown that additions of elements from the IVa and Va columns of the periodic table to 316L stainless steel could have a pronounced effect on its swelling resistance. The results suggested that vacancy binding was the most operative mechanism, increasing in strength with increasing size factor. In the current experiment these same alloys were irradiated with fast neutrons, but the influence of the size factor does not appear to be the only important mechanism. Whereas essentially precipitation was limited during electron irradiation, substantial precipitation occurred during neutron irradiation at lower displacement rates, overshadowing the effect of size factor on swelling. The addition of Hf and especially Zr,

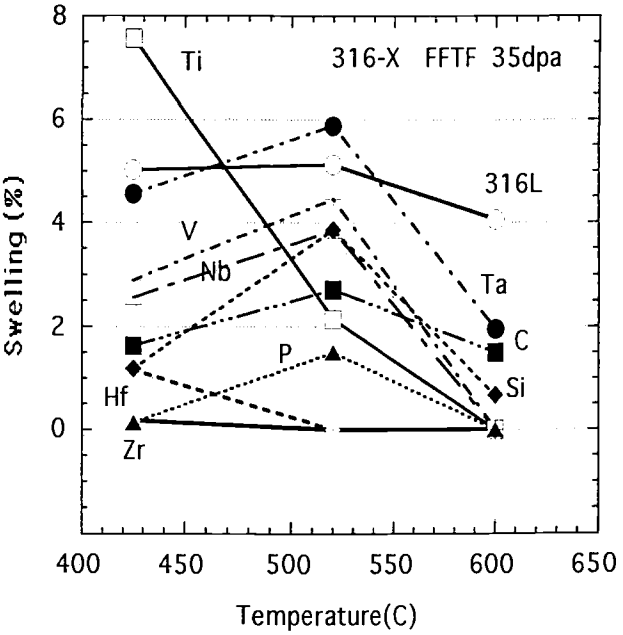


Figure 6. *Void swelling as a function of temperature.*

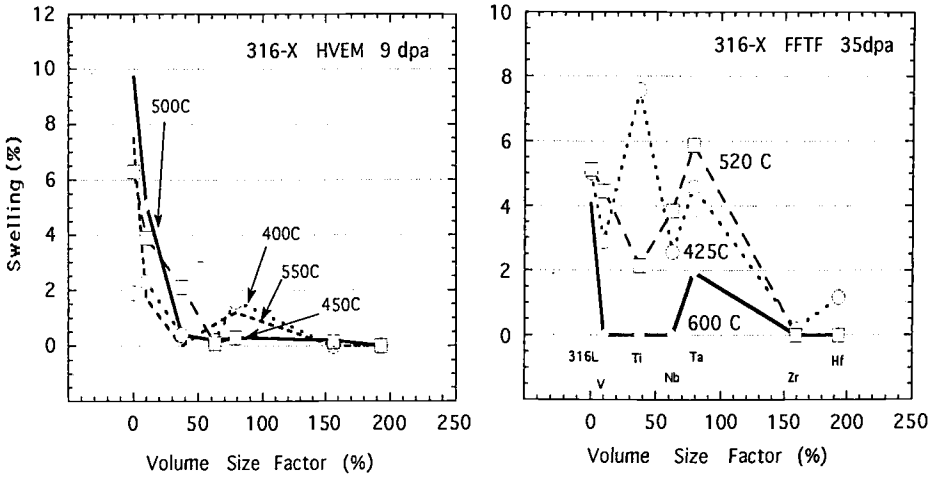


Figure 7. *Relationship observed between void swelling and volume size factor for electron and neutron irradiation.*

however, was particularly effective in suppressing swelling in both the electron and neutron case, although the suppression mechanism in the neutron case appears to be a combination of both size effect and precipitation to alter the sink structure.

Acknowledgement

This work was supported by Monbusho/US DOE collaboration on fusion reactor materials, FFTF/MOTA and JUPITER programs.

References

1. Garner, F. A., "Nuclear Materials", *Materials Science and Technology: A Comprehensive Treatment,* VCH publishers, Weinheim, Germany, Chapter 6 of Vol. 10A 1994, pp. 419-543.

2. Garner, F. A., *Journal of Nuclear Materials*, Vol. 122-123, 1984, 459-471.

3. Bates, J. F. and Johnston, W. G., *Proceedings AIME International Conference on Radiation Effects in Breeder Reactor Structural Materials*, June 1977, pp. 625-644.

4. Gessel, G. R., and Rowcliffe, A. F., *Proceedings AIME International Conference on Radiation Effects in Breeder Reactor Structural Materials*, June 1977, pp. 431-477.

5. Watanabe, H. , Muroga, T. and Yoshida, N. , *Journal of Nuclear Materials,* Vol. 239, 1996, 95-98.

6. Kato, T. , Takahashi, H., and Izumiya, M., *Materials Transaction of Japan Institute of Metals*, Vol. 32, 1991, 921-930.

7. Kato, T. , Takahashi, H., and Izumiya, M., *Journal of Nuclear Materials,* Vol. 189, 1992, 167-174.

8. Kato, T. , Takahashi, H., and Izumiya, M., *Transaction of Japan Institute of Atomic Energy*, Vol. 34, 1992, 889-899.

9. Garner, F. A., Laukritzen, T. and Mitchell, M. A., " *Effect of Radiation on Material, 19th International Symposium, ASTM ST 1175,* American Society for Testing and Materials, West Conshohocken, PA, 1993, pp. 803-815.

F. A. Garner[1] and C. A. Black[2]

The Question of Saturation of Void Swelling in Fe-Cr-Ni Austenitic Alloys

Reference: Garner, F. A. and Black, C. A., **"The Question of Saturation of Void Swelling in Fe-Cr-Ni Austenitic Alloys,"** *Effects of Radiation on Materials: 19th International Symposium, ASTM STP 1366,* M. L. Hamilton, A. S. Kumar, S. T. Rosinski, and M. L. Grossbeck, Eds., American Society for Testing and Materials, West Conshohocken, PA, 2000.

Abstract: Whereas in earlier publications it appeared that a possible saturation of neutron-induced void swelling might be developing at temperatures of 400 and 427°C in annealed Fe-Cr-Ni model alloys in a manner that was dependent on composition, data obtained at higher neutron exposures in EBR-II have led to the conclusion that such an expectation was erroneous. At all temperatures in the range 400-650°C, the neutron-induced swelling eventually reaches ~1%/dpa and continues to very high swelling levels thereafter without any hint of saturation.

Keywords: Fe-Cr-Ni austenitic alloys, void swelling, neutron irradiation, saturation

Introduction

In the early 1970's when neutron-induced void swelling in austenitic stainless steels was first being studied, it was often argued that such a process must be inherently self-limiting, and should lead to saturation, hopefully at some low enough swelling level to avoid any large impact on design and operation of fast reactors. This expectation was progressively disappointed as each data set was produced at higher levels of neutron exposure, always showing increased levels of swelling.

Although theories were developed showing the possible circumstances under which saturation should occur (see review by Mansur [*1*]), and saturation was indeed shown to occur in pure nickel [*2*], swelling levels approaching 100% without a hint of saturation were reached in a number of typical stainless steels at high neutron exposure [*3-5*]. In general, all steels eventually swelled at ~1%/dpa. If saturation was to eventually occur, it would be at swelling levels much too high to be of engineering relevance.

In one particular and very comprehensive series of irradiation experiments conducted in EBR-II on model Fe-Cr-Ni ternary alloys by Garner and coworkers, however, it appeared that after having swelled at ~1%/dpa, saturation was beginning to

[1] Senior Staff Scientist, Pacific Northwest National Laboratory, P.O. Box 999, MSIN P8-15, Richland, WA.

[2] Product Engineer, Wyman-Gorden Investment Casting, Carson City, NV.

Copyright© 2000 by ASTM International www.astm.org

occur in a rather systematic manner at lower irradiation temperatures, increasing in level as the nickel content decreased [6,7]. Figure 1 shows the tendency toward saturation as observed at 427°C. Similar behavior was not observed for temperatures above 480°C. To address this possibility that true saturation might actually occur, many of these specimens were returned to EBR-II for further irradiation. A number of years passed, however, before the density of these specimens was measured and the data analyzed.

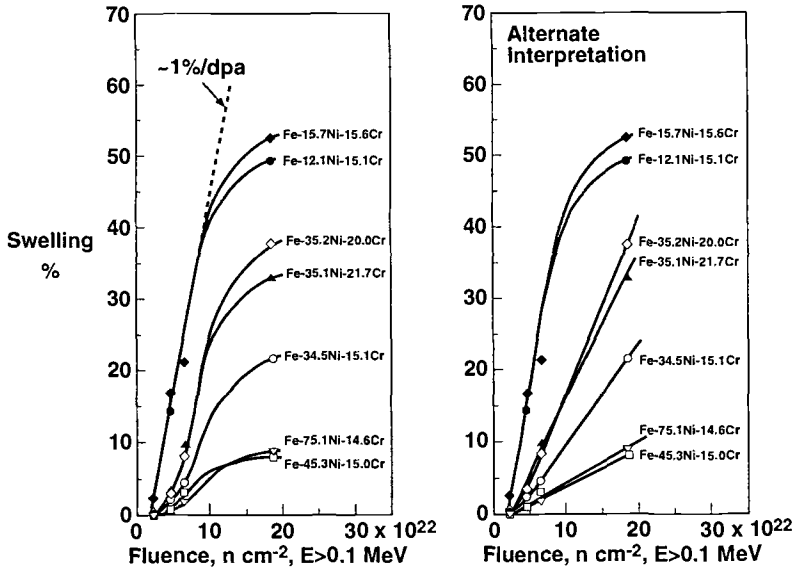


Figure 1 - *Two possible interpretations of previously published swelling data at 427 °C for simple ternary alloys irradiated in EBR-II, showing either a tendency toward saturation or a reduction in swelling rate as the nickel content increased or the chromium content decreased [6,7].*

Experimental Details

Fourteen iron-nickel-chromium ternary alloys and one binary alloy (85Ni-15Cr) were irradiated in the AA-VII experiment in Experimental Breeder Reactor-II (EBR-II) in the form of 3 mm diameter disks used for transmission electron microscopy. The specimens were irradiated in perforated stainless steel packets to allow contact with reactor sodium. The compositions of these alloys are given in Table 1. They were irradiated without active temperature control at eight target temperatures between 400 and 650°C in a series of capsules to exposures as large as 25.4 x 10^{22} n/cm^2 (E>0.1 MeV) or approximately 130 displacements per atom (dpa) using the standard NRT model. At the end of each irradiation exposure level a set of capsules were removed and the specimens measured while other capsules continued to higher exposure.

In most cases, two identical specimens were irradiated side-by-side. Each pair of specimens were engraved with a unique identification code that specifies the packet, and thereby the temperature and neutron exposure, and also the alloy identity. The radiation-

induced density changes were measured using an automated immersion density technique. In the majority of cases, the swelling of each member of the pair was identical within the system measurement error (±0.16% change in density). Whenever the swelling varied more than 0.2% between members of the pair, the two values were reported separately. Otherwise they were simply averaged.

Table 1 - *Compositions of the Simple Iron-Nickel-Chromium Alloys.*

Designation	Fe	Ni	Cr	C	O	N
E18	Bal[a]	12.1	15.1	0.005	0.016	0.0024
E90	Bal	15.7	15.6	0.013	...	...
E39	Bal	20.3	7.5	0.004	0.016	0.0014
E26	Bal	20.1	11.8	0.002	0.016	0.0019
E19	Bal	19.4	14.9	0.003	0.018	0.0015
E27	Bal	24.7	10.2	<0.001	0.012	0.0017
E20	Bal	24.4	14.9	0.003	0.017	0.0017
E21	Bal	29.6	15.3	0.004	0.017	0.0020
E37	Bal	35.5	7.5	0.002	0.016	0.0013
E22	Bal	34.5	15.1	0.003	0.017	0.0021
E38	Bal	35.2	20.0	0.004	0.017	0.0010
E25	Bal	35.1	21.7	0.004	0.015	0.0020
E23	Bal	45.3	15.0	0.002	0.014	0.0017
E24	Bal	75.1	14.6	0.001	0.0077	0.0011
E36	...	84.9	15.1	0.002	0.0064	0.0010

[a]Bal = balance.

Table 2 - *Neutron Exposures Reached in this Experiment.*

	Neutron fluence (E>0.1)*				
°C	previous	new	total	dpa/10^{22} n cm^{-2}	dpa
454	7.1	2.1	9.2	4.9	45.1
482	17.4	2.6	20.0	5.05	101.0
538	20.4	3.2	23.6	5.14	121.3
650	21.9	3.4	25.3	5.16	130.6
593	22.0	3.4	25.4	5.17	131.3
510	11.2	3.3	14.5	5.13	74.4
427	9.5	2.8	12.3	5.08	62.5
400	7.4	2.2	9.6	4.75	45.6

*The relative positions in this table reflect the loading of the subcapsules from the top down. Note the large flux gradients at the core ends.

Results

The specimens at different compositions are irradiated as sets for each combination of irradiation conditions. Therefore the best one-variable presentation is to present the data derived from each capsule. All specimens in a given capsule were subjected to exactly the same irradiation history, and vary only in composition.

The swelling data from six irradiation capsules are shown in Figure 2 as a function of nickel content at 15% Cr. Not all of the specimens were retrieved and measured at the two other temperatures, but where available, the data are shown in Figure 3. Similar comparisons are made in Figures 4 and 5 as a function of chromium content.

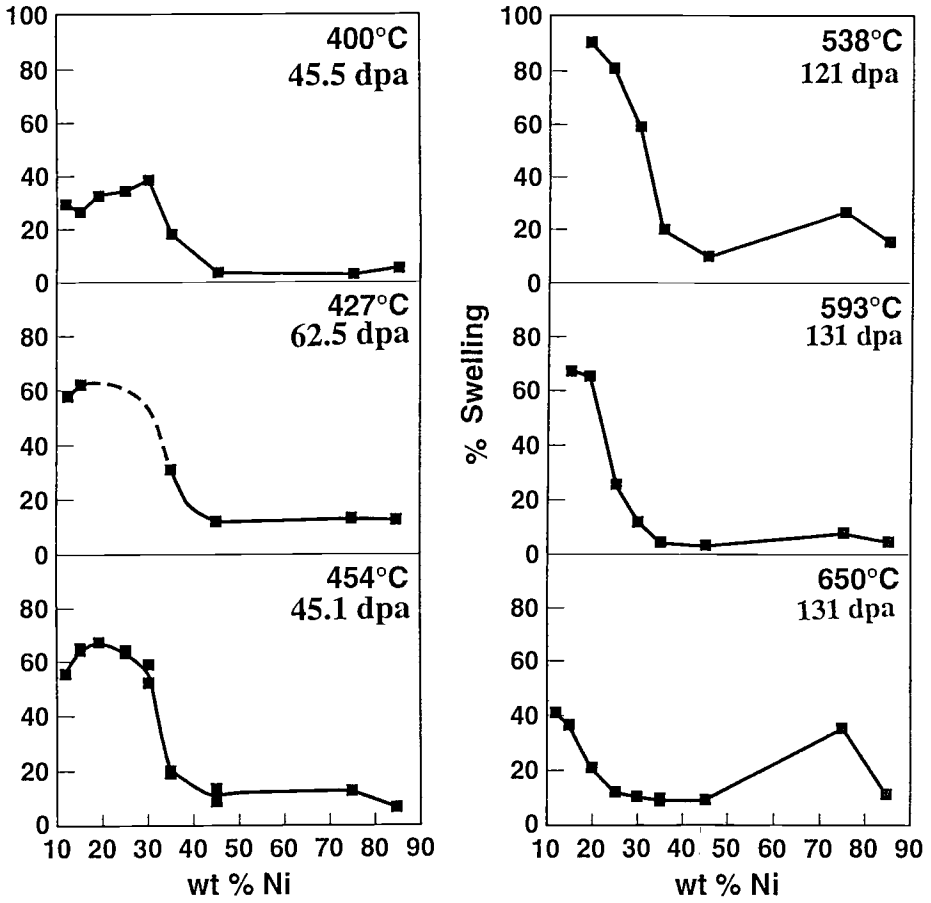


Figure 2 - *Swelling of Fe-15Cr-XNi alloys observed in EBR-II at six irradiation temperatures. Note the ~90% swelling reached at 538 °C.*

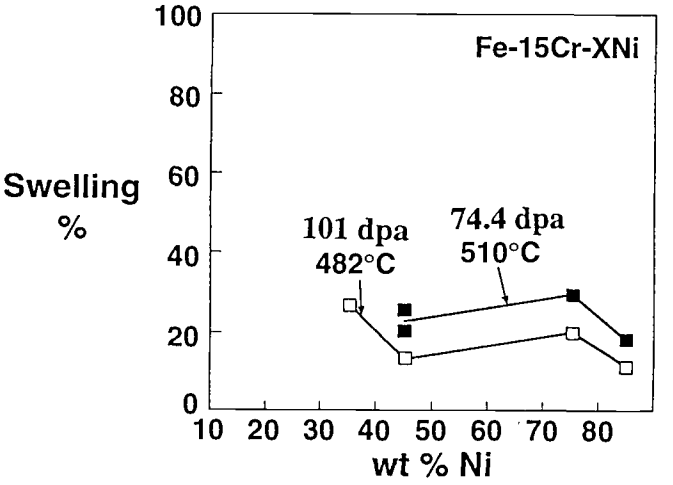


Figure 3 - *Incomplete sets of swelling data on Fe-15Cr-XNi alloys observed at two other irradiation temperatures.*

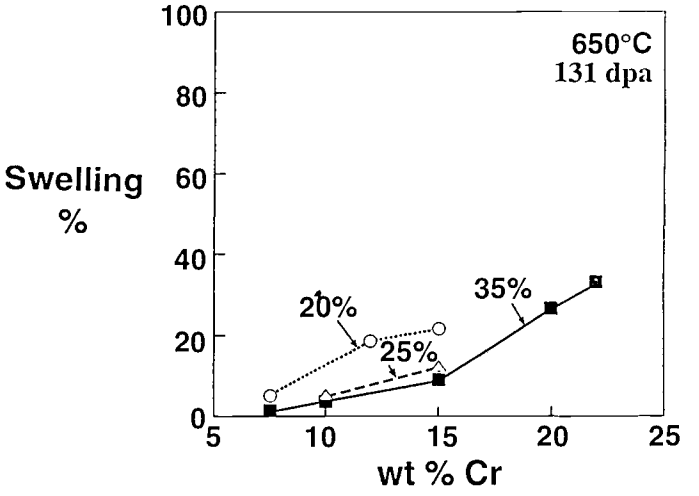


Figure 4 - *Swelling of Fe-Cr-Ni alloys in EBR-II as a function of both chromium and nickel content at 650 °C.*

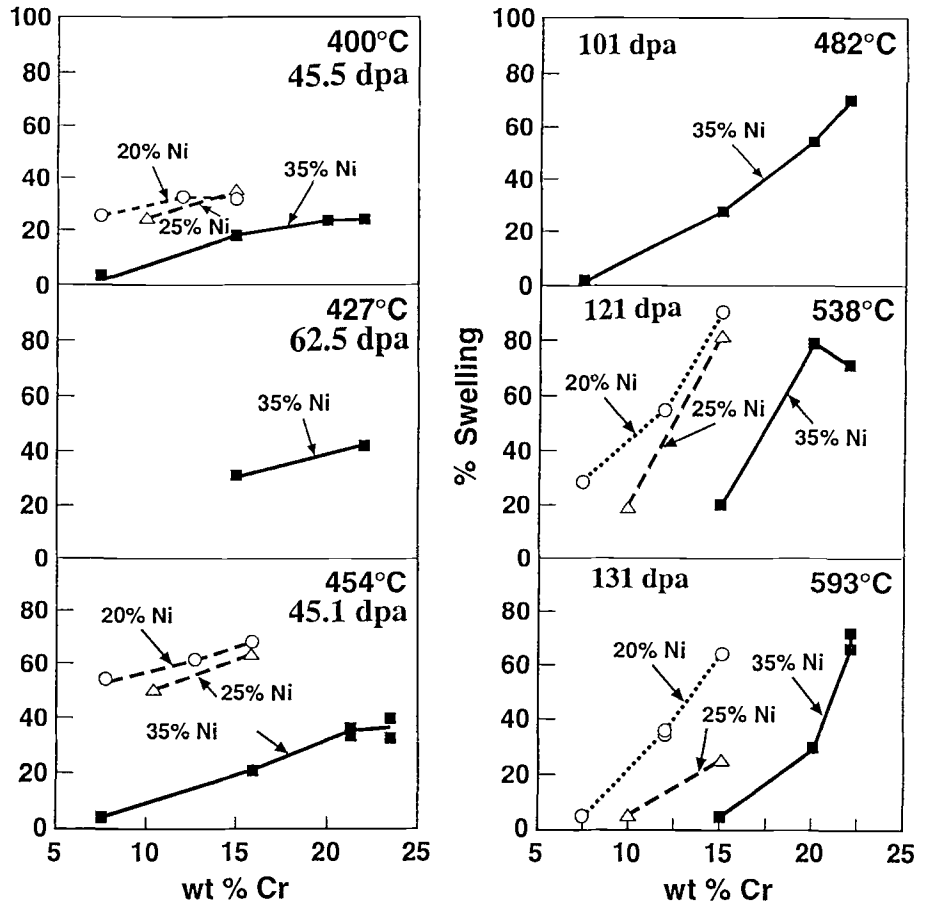


Figure 5 - *Swelling of Fe-Cr-Ni alloys as a function of both chromium and nickel content at six temperatures. No data are available at 510 °C.*

The most startling result comes when the data at 427°C are plotted as a function of neutron fluence to assess the possibility of saturation. Note in Figure 6 that after appearing to develop saturation, the swelling rate in the latest irradiation sequence returns to the characteristic 1%/dpa. When similar compilations for temperatures above 427°C are plotted, the anticipated 1%/dpa is still maintained without the saturation-like detour taken at 427°C, as shown in Figure 7.

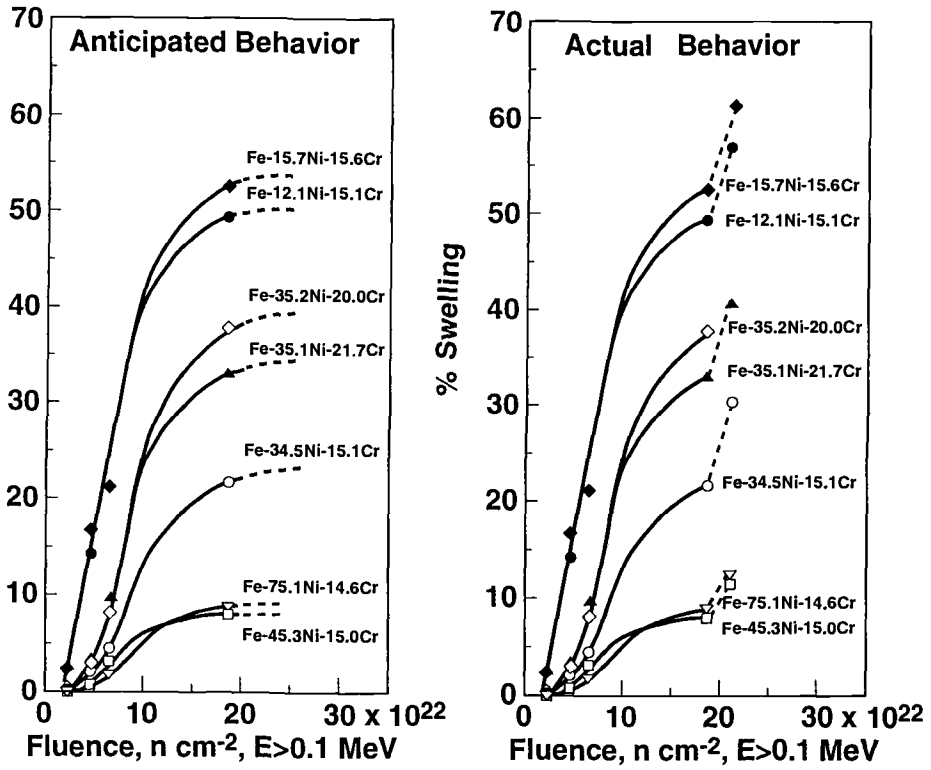


Figure 6 - *Comparison of anticipated behavior vs. actually observed behavior, indicating that swelling at ~1%/dpa had occurred over the last irradiation interval.*

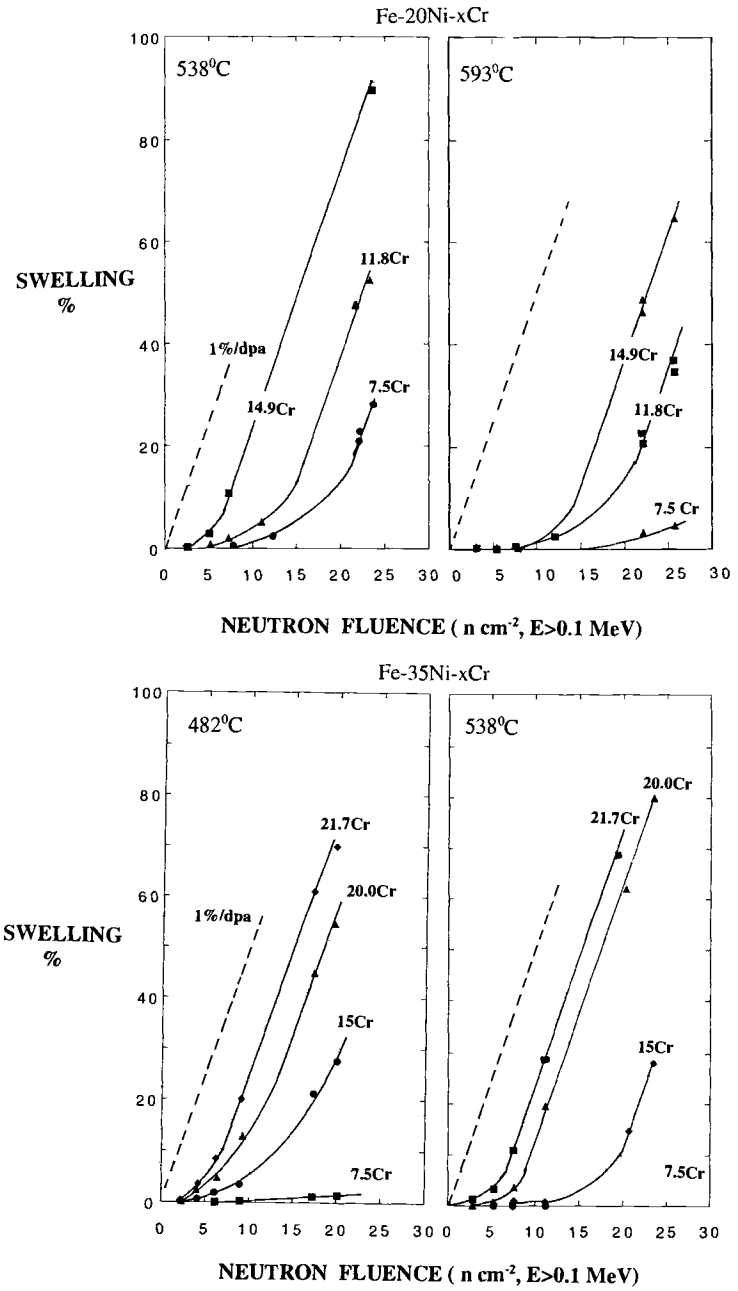


Figure 7 - *Swelling at various compositions and temperatures above 427 °C, showing continued swelling at ~1%/dpa to very high levels.*

Discussion

There is obviously some problem with the 400 and 427°C data that is not reflected in the >427°C data. A careful check of the specimen handling records indicates that a decision was made to divide the pairs of specimens in the two lower temperature capsules from one of the previous discharges and return one-half of each pair to continued irradiation, while the other half was sent for density measurement. Thus, the specimen identification codes were no longer a unique description of the irradiation exposure. The previously reported density changes [*6,7*] were erroneously assigned the neutron exposure of the higher dose specimens. The swelling data at 400 and 427°C were simply misplotted. As shown in Figure 8, saturation was not occurring earlier and is not now occurring at 427°C.

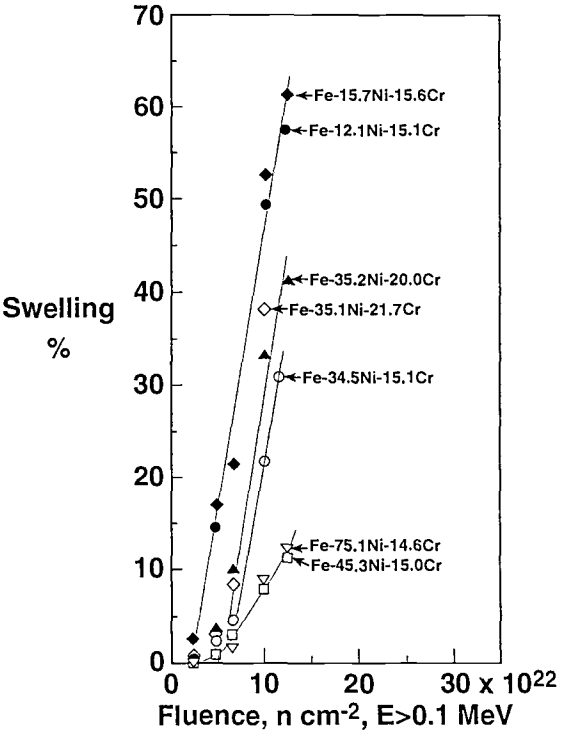


Figure 8 - *Swelling data at 427 °C plotted with corrected exposure levels, showing no tendency toward saturation.*

When considering the data in Figures 2-5, it appears that the trends observed in earlier[*6,7*] and more recent [*8*] experiments are confirmed in this higher exposure experiment. The dependence of swelling on nickel content involves a plateau or peak at low nickel levels, followed by a steep decline at intermediate nickel levels and then a

lower plateau at the highest nickel levels, although at higher irradiation temperatures swelling tends to again increase slowly with nickel content.

This nonmonotonic behavior is not observed in the dependence of swelling on chromium content, however. Swelling increases with chromium content at all nickel levels, in agreement with the results of earlier studies at lower exposure [*6,7*].

It is known from this and previous studies that the dependence of both chromium and nickel is manifested only in the duration of the incubation regime of swelling, and not the steady-state swelling rate. The latter is a remarkably constant quantity at ~1%/dpa, regardless of composition, starting state or irradiation conditions over a wide range of temperatures and dpa rates.

Conclusions

Swelling of neutron-irradiated model Fe-Cr-Ni austenitic alloys is dependent on the alloy composition and irradiation temperature, but such dependencies are expressed only in the duration of the transient regime of swelling. Eventually, the steady-state swelling becomes ~1%/dpa for all cases. To swelling levels approaching 100% there is no evidence that saturation of swelling will occur for any set of conditions studied.

Acknowledgements

This research was supported by the US Department of Energy, Office of Fusion Energy, under Contract DE-AC06-76RLO 1830.

References

[1] Mansur, L. K., "Theory of Transitions in Dose Dependence of Radiation Effects in Structural Alloys", in *Journal of Nuclear Materials*, Vol. 206, 1993, pp. 306-323.

[2] Stubbins, J. F., and Garner, F. A., "Saturation of Swelling in Neutron Irradiated Pure Nickel and Its Dependence on Temperature and Starting Dislocation Microstructure," in *Effects of Radiation on Materials, 17th International Symposium, ASTM STP 1270,* D. S. Gelles, R. K. Nanstad, A. S. Kumar, and E. A. Little, Eds., American Society for Testing and Materials, 1996, pp. 1038-1046.

[3] Gelles, D. S., "Swelling in Several Commercial Alloys Irradiated to Very High Neutron Fluence," in *Journal of Nuclear Materials*, Vols. 122 and 123, 1984, pp. 207-213.

[4] Garner, F. A., and Gelles, D. S., "Neutron-Induced Swelling of Commercial Alloys at Very High Exposures," in *Effects of Radiation on Materials, 14th International Symposium (Volume II), ASTM STP 1046,* N. H. Packan, R. E. Stoller, and A. S. Kumar, Eds., American Society for Testing and Materials, 1990, pp. 673-683.

[5] Garner, F. A., in Chapter 6 of *Materials Science and Technology, a Comprehensive*

Treatment, Vol. 10A, Part 1, R. W. Cahn, P. Haasen, and E. J. Kramer, Eds., VCH Verlagsgesellschaft mbH, 1994, pp. 419-543.

[6] Garner, F. A., and Brager, H. R., "Swelling of Austenitic Iron-Nickel-Chromium Ternary Alloys During Fast Neutron Irradiation," in *Effects of Radiation on Materials, Twelfth International Symposium, ASTM STP 870,* F. A. Garner and J. S. Perrin, Eds., American Society for Testing and Materials, 1985, pp. 187-201.

[7] Garner, F. A., and Kumar, A. S., "The Influence of Both Major and Minor Element Composition on Void Swelling in Austenitic Steels," in *Radiation-Induced Changes in Microstructure, 13th International Symposium (Part I), ASTM STP 955,* F. A. Garner, N. H. Packan, and A. S. Kumar, Eds., American Society for Testing and Materials, 1987, pp. 289-314.

[8] Garner, F. A., Black, C. A., and Edwards, D. J., "Factors Which Control the Swelling of Fe-Cr-Ni Ternary Austenitic Alloys," in *Journal of Nuclear Materials,* Vol. 245, 1997, pp. 124-130.

Ralph Hübner[1] and Karl Ehrlich[2]

Influence of Minor Alloying Elements and Stress on Microstructural Evolution and Void Swelling of Austenitic Steels Under Neutron Irradiation

Reference: Hübner, R. and Ehrlich, K., **"Influence of Minor Alloying Elements and Stress on Microstructural Evolution and Void Swelling of Austenitic Steels Under Neutron Irradiation,"** *Effects of Radiation on Materials: 19th International Symposium, ASTM STP 1366,* M. L. Hamilton, A. S. Kumar, S. T. Rosinski, and M. L. Grossbeck, Eds., American Society for Testing and Materials, West Conshohocken, PA, 2000.

Abstract: A pressurized tube experiment was carried out in the British Prototype Fast Reactor (PFR) at Dounreay, U.K. in order to determine swelling and stress-induced swelling of four heats of the commercial German austenitic steel DIN 1.4970, with different contents of the minor alloying elements Si, Ti and Ti/C ratio. The maximum doses achieved are 106 dpa_{NRT} at 420°C, 81 dpa_{NRT} at 500°C and 61 dpa_{NRT} at 600°C. The hoop stresses of the pressurized tubes were 0, 60 and 120 MPa at all irradiation temperatures. TEM-examinations have been carried out to determine the influence of the minor alloying elements and the stress on the void swelling and the microstructural evolution. All alloys exhibited the highest swelling values at 420°C and no swelling at 600°C. The measurements show the large effect of the minor alloying elements upon swelling and in-pile creep. The maximum swelling suppression is achieved by a high Si-content and an understoichiometric Ti/C ratio (understabilization). The analysis of the microstructural evolution shows that the swelling resistance is correlated to the formation and stability of very fine γ'-precipitates. For the alloy with the highest swelling resistance these precipitates can be found up to 106 dpa_{NRT} at 420°C, whereas they dissolve in the course of irradiation for the alloys with lower swelling resistance.

The estimates of the stress-induced swelling using the Soderberg theorem and the length measurements are compared with immersion density measurements and results of void structure analysis by TEM. All methods yield the same order of magnitude for the stress-induced linear swelling.

Keywords: neutron irradiation, swelling, stress-induced swelling, austenitic alloy, DIN 1.4970, silicon, titanium, pressurized tube experiment, microstructure

[1]Dr., Research Scientist, Forschungszentrum Karlsruhe, Institute for Materials Research (IMF I), P.O. Box 3640, D-76021 Karlsruhe, Germany.

[2]Professor Dr., Department Head, Forschungszentrum Karlsruhe, Institute for Materials Research (IMF I), P.O. Box 3640, D-76021 Karlsruhe, Germany.

Copyright© 2000 by ASTM International www.astm.org

Introduction

The irradiation program PFR-M2 was started to study the influence of minor alloying elements and thermo-mechanical treatment on swelling and in-pile creep of austenitic alloys. The limitation of these effects is important to achieve a high burn-up of Fast Breeder fuel elements. First results of the intermediate measurements have been presented previously [*1-3*]. These results showed a strong effect of the Si- and Ti-content on swelling and as a result of a creep-swelling coupling also on the in-pile creep. After the irradiation, examinations of the microstructure have started to reveal the basic mechanisms which influence swelling. The results of four lots of the German austenitic steel DIN 1.4970 will be presented in the following sections.

Experimental Procedure

Materials

Four different lots of the titanium-stabilized 15Cr15Ni-austenitic steel DIN 1.4970 have been irradiated. The chemical composition of these alloys is given in Table 1. They can be characterized as follows. The B-lot is a low silicon bearing melt whereas the I-, K- and L-lot are made from high silicon bearing melts. The K- and the L-lot are made from the same melt and differ only by a slightly different solution annealing temperature. In addition the I-lot has a lower Ti-content which results in an understabilized condition.

Cladding material was made out of these alloys with an outer diameter D_0 of 6 mm and a wall thickness of 0.38 mm. From this material pressurized tubes were made with a cladding section of 25.5 mm. The total length L_0 of the finished tubes amounts to 28.5 mm including the endplugs, which were resistance-welded to the sections. Argon was used as the filling gas instead of helium gas normally employed in order to achieve a greater weight loss in case of blow out. Therefore an eventual pressure loss can be easily revealed by determining the weight of the samples. The filling pressures at room temperature were chosen to yield three different hoop stresses σ at the irradiation temperature, namely 0, 60 and 120 MPa.

Table 1 - *Composition of the DIN 1.4970 lots (wt%)*[1]

Alloy	C	Si	Mn	Cr	Ni	Mo	Ti
B-lot	0.083	0.42	1.60	14.92	14.73	1.19	0.47
K-lot	0.086	0.99	1.60	15.06	14.86	1.46	0.49
L-lot	0.086	0.96	1.64	15.15	14.90	1.46	0.50
I-lot	0.089	1.01	1.16	15.15	15.00	1.45	0.31

[1] Thermo-mechanical treatment: 1100°C SA + 20% CW, except L-lot: 1120°C SA + 20% CW

Irradiation and Macroscopic Measurements

The tubes were irradiated in the British Prototype Fast Reactor (PFR) at Dounreay at three different irradiation temperatures of nominally 420, 500 and 600°C. At certain intervals the samples were withdrawn from the reactor for inspections and measurements. The maximum achieved doses were 106 dpa_{NRT} at 420°C (4 intermediate measurements),

81 dpa_{NRT} at 500°C and 61 dpa_{NRT} at 600°C (3 intermediate measurements in each case). The dose is calculated according to the standard NRT-model. The diameter D and length L of the tubes were measured with a 2σ accuracy of $\pm$ 2 μm. Because of technical reasons no length measurements could be done after the last irradiation campaigns. Additionally the weight of the tubes was determined to reveal an eventual pressure loss through very fine cracks, which are not easily detected during normal handling in the hot cells. No pressure loss was observed for the samples presented here. After irradiation, immersion density measurements were performed on some samples. The density change $\Delta\rho/\rho_0<0$ is determined with an absolute measurement error of $\pm$ 0.4 %. The volume swelling can be obtained from the density change by the following formula. The approximation is valid for small swelling levels only.

$$\frac{\Delta V}{V_0} = \frac{-\Delta\rho/\rho_0}{1+\Delta\rho/\rho_0} \cong -\frac{\Delta\rho}{\rho_0} \tag{1}$$

The following quantities can be derived by the one-dimensional length and diameter changes ($\Delta L = L - L_0$, $\Delta D = D - D_0$). For unpressurized tubes both the length and diameter changes yield the stress-free linear swelling, which amounts to one third of the volume swelling $\Delta V/V_0$, providing small swelling levels:

$$\begin{aligned}\varepsilon_s(\sigma=0) &= \Delta D/D_0(\sigma=0) = \Delta L/L_0(\sigma=0)\\ &= \tfrac{1}{3}\Delta V/V_0\end{aligned} \tag{2}$$

According to the Soderberg theorem [*4,5*] the length changes $\Delta L/L_0$ originate solely from swelling as long as no other effects like texture effects occur. Therefore, in the case of a pressurized tubes, the length changes yield the total linear swelling which is the sum of stress-free and stress-induced linear swelling. However the heat-affected zone and the endplugs, for technical reasons all fabricated from the same material, distort the length increase. Because of this, the length and the diameter changes differ significantly [*1*]. For that reason the stress-induced linear swelling is defined as the difference between the length changes of a pressurized and an unpressurized sample:

$$\varepsilon_s(\sigma) = \Delta L/L_0(\sigma) - \Delta L/L_0(\sigma=0) \tag{3}$$

This method hopefully eliminates the influence of the endplugs and the heat-affected zone, which are assumed to be the same for both pressurized and unpressurized samples.

Microstructure

Microstructural examinations have been performed on irradiated samples of the B-, I- and K-lot. The transmission electron microscopy (TEM) was conducted using a Philips EM 400 TEM operating at 100 kV. After cutting the tubes in pieces, the samples were electropolished down to 200 μm. Thin foils with a diameter of 3 mm were prepared by electropolishing in a twin jet device (Struers Tenupol 3).

The void swelling was determined by the void size distribution and the number density. Microstructural evolution has been studied by the usual techniques of microdiffraction and bright- and dark-field imaging.

Results of Macroscopic Measurements

Swelling of DIN 1.4970

Temperature Dependence - The influence of the irradiation temperature on the swelling behavior can be seen in Figure 1, which presents the diameter change of stress-free samples of the B-lot as a function of the dose for the three temperatures. The other alloys show a similar temperature dependence. The highest swelling occurs at 420°C. Because of this high swelling the samples of the B-lot have been withdrawn before the final measurement. With rising temperature the swelling decreases because of an increase of the incubation dose and a reduced swelling rate. At 600°C no swelling can be detected for any of the alloys.

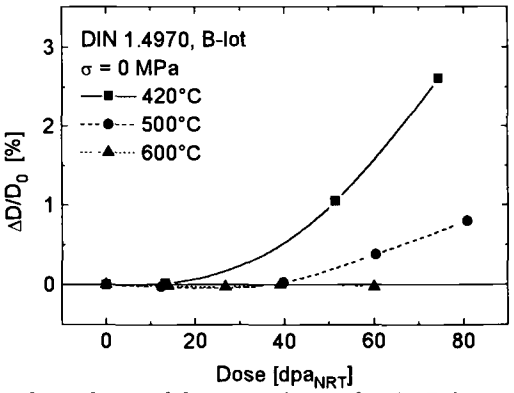


Figure 1 - *Dose dependence of diameter change for the B-lot at different irradiation temperatures*

Lot Dependence - The differences between the four alloys can be seen in Figures 2 and 3. The negative values of $\Delta D/D_0$ during the transient are due to the shrinkage of the material in the beginning of the irradiation. This effect is usually explained by the recovery of the density decrease due to cold working and by the evolution or precipitates [6]. Figure 2 shows the dose dependence of the stress-free linear swelling of the four alloys at 420°C. The higher Si-content of the K- and L-lot reduces the swelling significantly because of a longer incubation period. The slight difference in solution annealing temperature between the K- and the L-lot has no influence on swelling. The additional reduction of the Ti-content has no influence on the incubation dose, but improves the swelling resistance of the I-lot by reducing the swelling rate. The comparison of the linear swelling rate at $\Delta D/D_0 \cong 1.5$ % yields that the B-, K- and L-lot have a very similar linear swelling rate of 0.07 %/dpa_{NRT}, whereas the I-lot has a lower swelling rate of 0.04 %/dpa_{NRT}.

Figure 3 shows the stress-free linear swelling of the three alloys as a function of dose at 500°C. Like at 420°C the B-lot exhibits the highest swelling, followed by the K- and L-lot, which behave identically. The best swelling resistance has the I-lot. In contrast to 420°C all alloys have a similar incubation period. The differences of the swelling resistance is only due to the different linear swelling rates which vary between 0.02 %/dpa_{NRT} for the B-lot and 0.007 %/dpa_{NRT} for the I-lot.

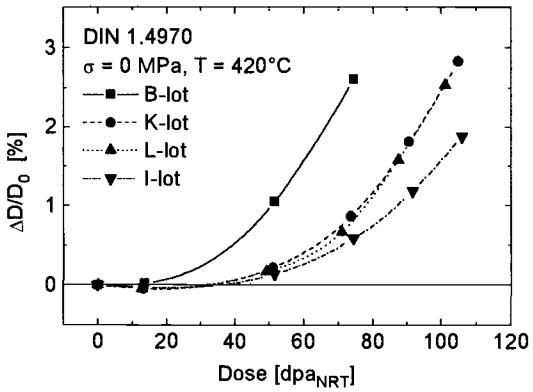


Figure 2 - *Comparison of the dose dependence of diameter change for all lots at 420°C*

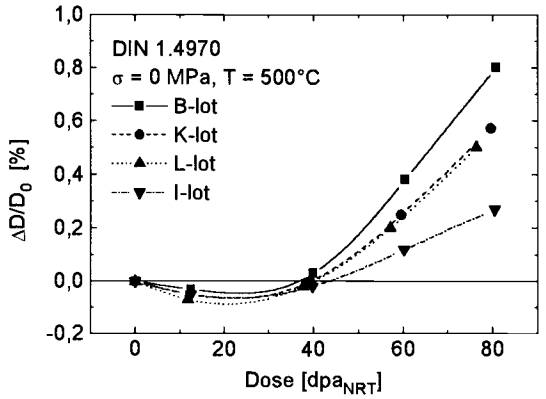


Figure 3 - *Comparison of the dose dependence of diameter change for all lots at 500°C*

Stress-induced Swelling

The results of the length measurements to determine stress-induced swelling at intermediate doses have already been presented [*2*]. They can be summarized as follows: Stress-induced swelling is found in all lots of DIN 1.4970. The ranking according to the swelling resistance is preserved (Figure 4a). This means that the B-lot shows the highest swelling and the I-lot the lowest swelling. Astonishing is the difference of stress-induced swelling between the K- and the L-lot, which differ only in a slightly different solution annealing temperature and show no difference in stress-free swelling and in-pile creep. Figure 4b shows a linear stress dependence of the stress-induced swelling.

After the irradiation, immersion density measurements were performed on some samples. These results presented in Table 2 show the effect of stress on swelling. All stressed samples show a greater density change than the unstressed ones. To compare the results of the different methods the linear swelling is assumed as one third of the density change. The stress-induced swelling is then the difference of the linear swelling of a stressed and an unstressed sample. The results for the K-lot are plotted in Figure 4c. The agreement is similar for the other lots.

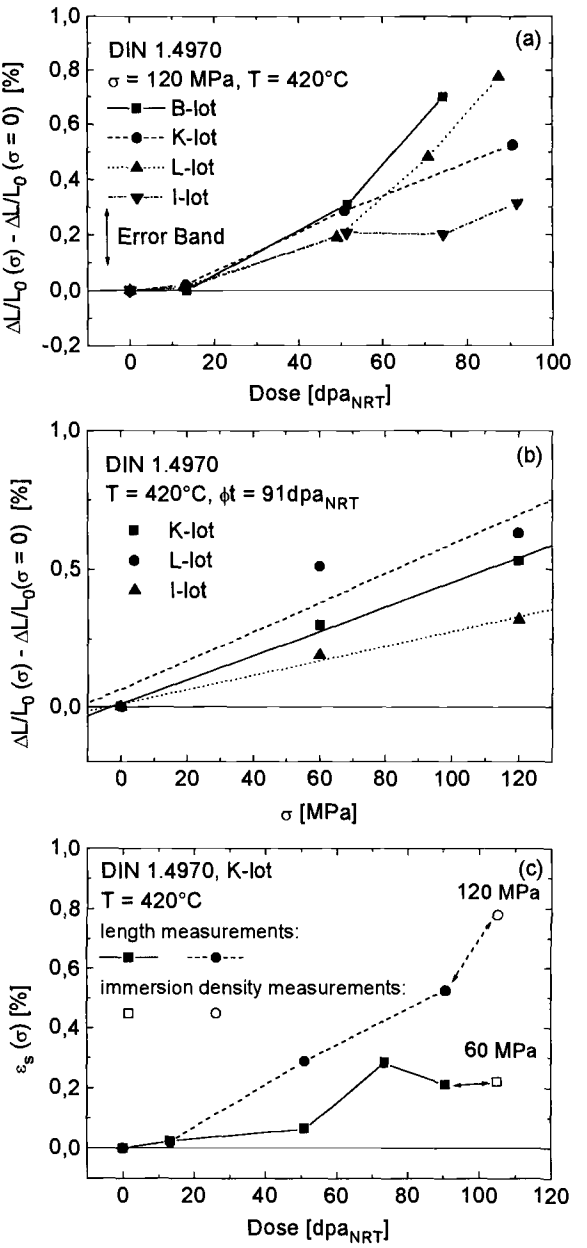


Figure 4 - *Stress-induced swelling: (a) Dose dependence at 420°C and σ = 120 MPa for all lots, (b) Stress dependence at 420°C and 91 dpa$_{NRT}$, (c) Comparison of length and immersion density measurements at 420°C for K-lot*

Two approaches are usually used to describe the effect of stress on swelling. The stress is assumed either to reduce the incubation dose or to increase the steady state swelling rate [7]. Assuming a linear stress dependence, these effects can be described mathematically as follows ($\Delta V/V_0$: volume swelling, σ_{hy}: hydrostatic stress), after the swelling rate has reached the steady state swelling rate [8]:

$$\Delta V/V_0(\sigma_{hy}) = \Delta V/V_0(\sigma_{hy} = 0) \times (1 + A \times \sigma_{hy}) \quad (4)$$

$$\Delta V/V_0(\sigma_{hy}) = \Delta V/V_0(\sigma_{hy} = 0) + B \times \sigma_{hy} \quad (5)$$

The experimental data can be described with both equations. Because of the data scatter, no distinction can be made which equation fits the data better. The average values of the constants determined for 420°C in the dose range of 50 - 105 dpa_{NRT} are:

B-lot:	$A = 4.5 \pm 1 \times 10^{-3}$ MPa^{-1}	$B = 2.7 \pm 1 \times 10^{-4}$ MPa^{-1}
I-lot:	$A = 4 \pm 2 \times 10^{-3}$ MPa^{-1}	$B = 1.5 \pm 2 \times 10^{-4}$ MPa^{-1}
K-lot:	$A = 6 \pm 3 \times 10^{-3}$ MPa^{-1}	$B = 3 \pm 1 \times 10^{-4}$ MPa^{-1}
L-lot	$A = 9 \pm 1.5 \times 10^{-3}$ MPa^{-1}	$B = 3.5 \pm 2 \times 10^{-4}$ MPa^{-1}

Table 2 - *Results of void structure analysis and immersion density measurement.*

Sample	T [°C]	σ [MPa]	ϕt [dpa_{NRT}]	c [10^{15} cm^{-3}]	d [nm]	ΔV/V [%]	$-\Delta\rho/\rho_0$ [%]
B-lot							
B15	420	0	74	7.9	26	8.0	8.1
B31	500	0	81	0.29	50	2.2	2.0
B46	600	0	60	---	---	0	-0.3
I-lot							
I14	420	0	106	5.6	24.9	5.6	5.9
I08	420	60	106	4.7	27.2	6.2	6.7
I04	420	120	105	5.5	27.0	7.1	6.9
K-lot							
K80	420	0	36	0.26	16.1	0.07	-0.3
K84	420	120	55	1.2	20.0	0.6	0.4
K23	420	0	105	5.8	27.2	7.7	9.4
K10	420	60	106	6.3	28.0	9.2	10.0
K04	420	120	105	6.2	28.9	10.5	11.3

Microstructural Evolution

Void Structure

The void structure was determined with the TEM after irradiation. The results on the average void concentration c and the average void diameter d for the different samples are presented in Table 2:

Temperature Dependence - The results of the stress-free B-lot samples B15, B31 and B46 show that at 500°C the average diameter is two times that at 420°C but the void concentration is only 4 % of that at 420°C. At 600°C no voids have been observed. Figure 5 presents TEM-micrographs of these samples.

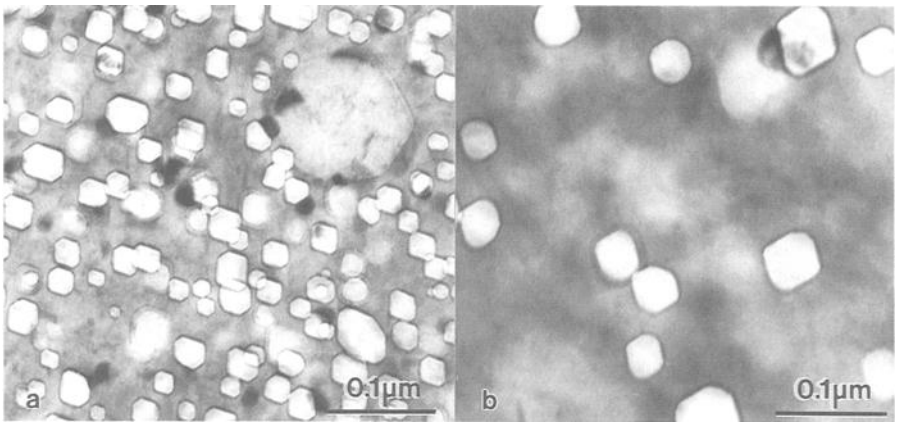


Figure 5 - *Void microstructures in B-lot samples (a) B15 irradiated at 420°C and 74 dpa_{NRT} (b) B31 irradiated at 500°C and 81 dpa_{NRT}*

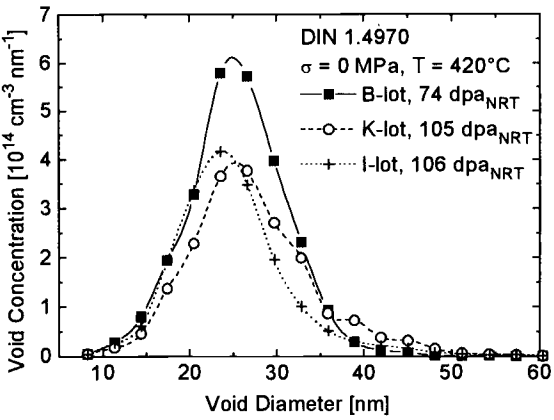


Figure 6 - *Void concentration per 3 nm size increment as a function of void diameter for three DIN 1.4970 lots at 420°C.*

Stress Dependence - The results of the I-lot samples I14, I08 and I04 and the K-lot samples K23, K10 and K04 confirm the existence of stress-induced swelling at 420°C. The volume swelling determined by the void size distribution and the void concentration is always higher for the pressurized samples. However, the influence of the stress on the average void diameter and the void concentration is not straightforward. For the I-lot the void concentration of the pressurized samples is reduced or similar to that of the unpressurized sample. The average void diameter is higher for the pressurized samples but is independent of the amount of stress. For the K-lot the void concentration is increased slightly but without influence of the amount of stress. The average void diameter is also increased with a higher increase for the higher stress. Taking into account the great uncer-

tainty in determining the void concentration because of the uncertainty of the sample thickness, the stress results first of all in higher void diameter.

Lot Dependence - The differences in the void structure of the three examined lots can be seen in Figure 6. The analysis of the data is complicated by the different doses of the samples. But the comparison of the K-lot sample K23 and the I-lot sample I14 shows that the lower swelling strain of the I-lot is due to the smaller average void diameter, whereas both samples show nearly the same void concentration. The B-lot sample B15 which has a similar amount of swelling as the K-lot sample has a much higher void concentration and a similar average void diameter. Comparing these results with Figure 2, it can be stated that the lot with the lowest incubation period has the highest void concentration, despite the lower final dose. Besides the two lots with the same incubation period have also similar void concentrations. From these two lots, the one with the lower swelling rate exhibits the smaller average void diameter.

Precipitates

Common to all samples is the existence of primary TiC-precipitates. They have a fcc-structure with a lattice parameter a $\cong$ 4.3 Å. Their morphology is spherical with slight facetting and a diameter of 150 - 300 nm.

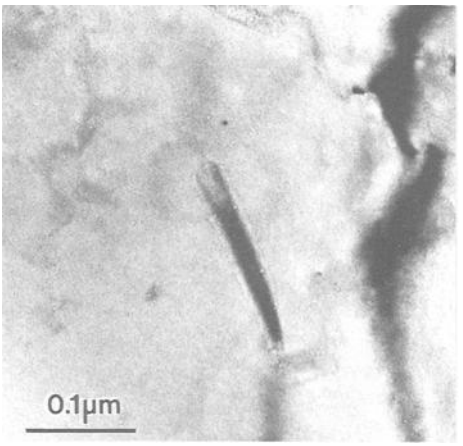


Figure 7 - Secondary *TiC-precipitate found in B46 irradiated at 600°C and 61 dpa_{NRT}.*

Temperature Dependence - The analysis of the three B-lot samples yields that at 420°C a high density of small intragranular precipitates is found. They have a fcc-structure with a lattice parameter a = 10.65 ± 0.1 Å. Therefore they are assumed as $M_{23}C_6$ [*9*]. Most of them are associated with voids (Figure 5a). At 500°C only a few intragranular precipitates can be found, which are again identified as $M_{23}C_6$. They are like the voids larger than at 420°C and also associated with the voids (Figure 5b). At 600°C no more $M_{23}C_6$ can be found. There are a lot of secondary MC particles (fcc-structure, a = 4.3 ± 0.05 Å). They show two distinct morphologies. Some are oval with a size of ~70 x 150 - 200 nm. The others are rod-shaped with a size of ~30 x 200 nm. Small He-bubbles can be found on the matrix-precipitate interface (Figure 7). Similar TiC-precipitates have been found in solution annealed and aged DIN 1.4970 [*10*]. This effect was explained with the

hindered nucleation due to the low dislocation density. This might explain also the formation of rod-shaped TiC in this case, because the dislocation density is rather low ($0.8 \pm 0.3 \times 10^{10}$ cm^{-2}), when determined after the irradiation.

Only $M_{23}C_6$ precipitates have been found on the grain boundaries at all temperatures. The density decreases with increasing temperature. At 420°C the grain boundaries are covered with a high density of precipitates whereas at 600°C the grain boundaries are very straight and no precipitates can be found on them. At 500°C the density of the precipitates on the grain boundaries is rather inhomogeneous.

Dose Dependence - The evolution of the precipitate structure for the K-lot shows that even at 36 dpa_{NRT} a measurable amount of intragranular $M_{23}C_6$ precipitates exist with a diameter of 20 - 30 nm (Figure 8a). Most of these precipitates are not associated with voids. In addition very fine γ'-precipitates (cubic-structure, $a = 3.52 \pm 0.03$ Å) with a diameter of 10 - 20 nm are found in a high density (Figure 8b). The K-lot sample with a dose of 55 dpa_{NRT} was loaded with a hoop stress of 120 MPa. This might cause the observed inhomogeneous precipitate density. But similar to the 36 dpa_{NRT} sample only $M_{23}C_6$ and γ'-precipitates can be found in the grains. At 105 dpa_{NRT} the situation has changed significantly. No longer can γ' be detected. The density of the $M_{23}C_6$-precipitates is higher than at 36 and 55 dpa_{NRT} and the precipitates are larger (up to 100 nm in diameter). Additionally smaller intragranular precipitates are found with a fcc-structure and a lattice parameter $a = 11.15 \pm 0.1$ Å. They are identified as G-phase ($Ni_{16}Si_7Ti_6$) [9].

All samples show a high density of $M_{23}C_6$ precipitates on the grain boundaries. At 105 dpa_{NRT} also some G-phase can be found on the grain boundaries.

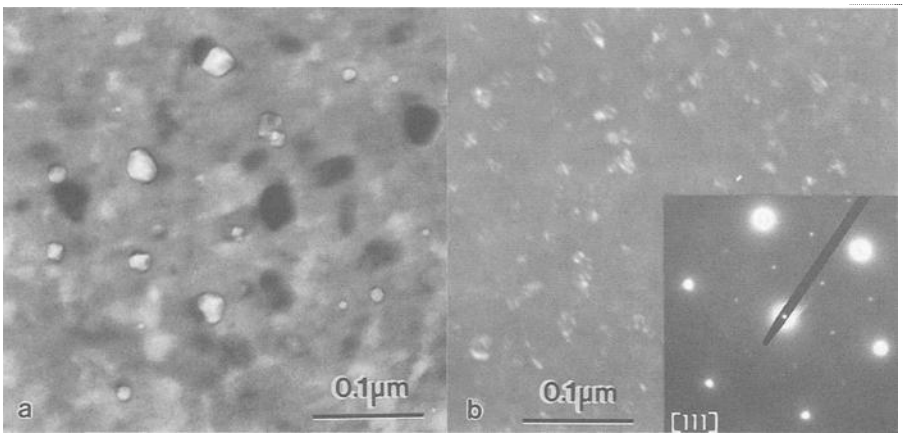


Figure 8 - *Microstructure of the K-lot sample irradiated at 420°C and 36 dpa_{NRT} (a) Voids and $M_{23}C_6$ precipitates (b) γ' (Darkfield image)*

Lot Dependence - The comparison of the samples with the highest doses yields that the samples of the B- and the K-lot have a high density of intragranular $M_{23}C_6$-precipitates, which are often associated with voids. For the B-lot sample these are the only intragranular precipitates (Figure 5a). The K-lot sample has in addition some smaller G-phase precipitates which might be formed out of the very fine γ'-precipitates found at

lower doses (Figure 9a). The I-lot sample has also a high density of intragranular $M_{23}C_6$ (Figure 9b). In addition very weak reflections of γ' precipitates have been found in the diffraction patterns.

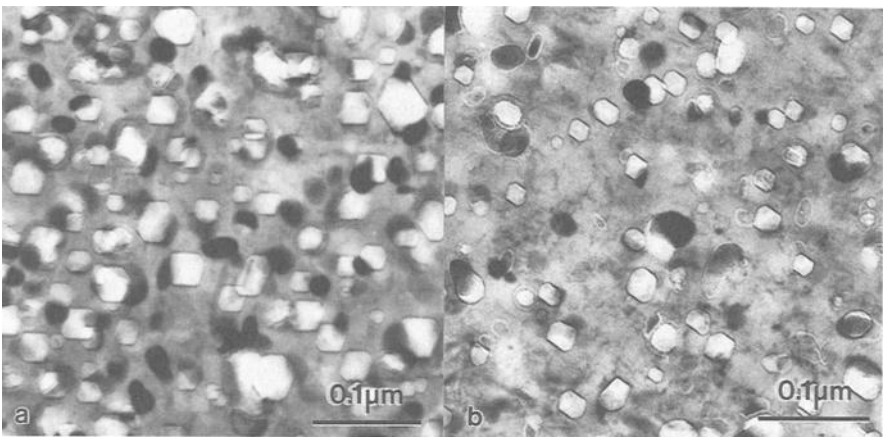


Figure 9 - *Microstructure of samples irradiated at 420°C and 105 dpa_{NRT}. (a) K23 with voids and G-phase (b) I14 with voids and $M_{23}C_6$*

Discussion

The starting point of this work was the idea that the presence of fast diffusing elements like silicon suppresses void formation [*11*]. This effect is usually explained by the enhancement of the vacancy mobility by the fast diffusing solute atoms. This is analogous to an increase in temperature which reduces also void swelling (Figure 1). In both cases the vacancy supersaturation is reduced and therefore the void nucleation rate [*12, 13*]. The beneficial effect of silicon on void swelling has been widely confirmed since that time for a broad range of austenitic steels over the whole temperature range where swelling occurs [*14-16*]. The stabilization with titanium also reduces swelling in austenitic steels [*17-19*]. A simulation experiments with 48MeV Ni ions yielded a minimum of swelling at 0.25 % Ti at 575°C for a Fe-15Cr-15Ni model alloy [*20*]. The influence of the Si-content on swelling is constrained to the extension of the incubation dose. After the swelling has started, the steady state swelling rate is independent on the Si-content [*6*]. The onset of swelling is often accompanied by the evolution of Si-rich precipitates like γ' (Ni_3Si) or G-phase ($Ni_{16}Si_7Ti_6$) [*21, 22*]. The evolution of these precipitates at point defect sinks can be explained by the inverse Kirkendall-effect and the interstitial drag of undersized solutes [*22*]. Since these precipitates reduce the content of Si in the matrix, their evolution is seen to be disadvantageous for swelling resistance. On the other hand, if these precipitates are very fine, they have a very large matrix-precipitate interface which acts as a point defect sink and enhances the point defect recombination which reduces again the vacancy supersaturation [*23*].

With these results in mind, the swelling behavior of the different lots of DIN 1.4970 at 420°C can be understood as follows. The reference lot B starts swelling around 20 - 40 dpa_{NRT} with a maximum linear swelling rate of 0.07 %/dpa_{NRT}. The increase of the Si-

content up to 1 % for the K-lot results in a extension of the incubation period of 25 dpa_{NRT} (Figure 2). At 36 dpa_{NRT} when first voids can be detected by TEM also a high content of very fine γ'-precipitates can be observed. These precipitates cannot be found at 105 dpa_{NRT}. Instead G-phase precipitates are found, which have a morphology similar to the $M_{23}C_6$-precipitates found in the B-lot sample at 74 dpa_{NRT} and are coarser than the γ'. The reduction of the Ti-content from 0.5 to 0.3 % for the I-lot has no influence on the incubation dose but the linear swelling rate is reduced to 0.04 %/dpa_{NRT} (Figure 2). For this lot some γ'-precipitates can be found still at 105 dpa_{NRT}. Probably the Ti-content is too low for a conversion into the Ti-containing G-phase. Therefore it can be concluded that the Si in the matrix hinders void nucleation until the precipitation of γ' reduces the Si-content below a certain amount. The higher the Si-content the longer is the incubation period. After the void swelling has started, the void growth and therefore the swelling rate is determined by the morphology of the precipitates. Very fine γ'-precipitates enhance the point defect recombination, which reduces the vacancy supersaturation and slow down the void growth. This is in accordance with the results of the void structure (Figure 6). The increase of the Si-content leads to a reduced void concentration. This void concentration is the same for the K- and I-lot at 105 dpa_{NRT}. These lots differ only in the average void diameter which is smaller for the I-lot with the reduced Ti-content.

The effect of stress-induced swelling has been found in many alloys at different temperatures and thermo-mechanical treatments [*24*]. Two approaches are usually used to describe the effect of stress on swelling. The stress is assumed either to reduce the incubation dose or to increase the steady state swelling rate [*7*]. The reduction of the incubation dose corresponds to accelerated void nucleation and would lead to a higher void concentration. The increased steady state swelling rate is related to an accelerated void growth and would lead to a bigger average void diameter [*8*]. Both effects have already been found. A higher void concentration was found in solution annealed AISI 316 at 500°C [*25*] and in cold worked AISI 316 at 400°C [*26*]. A bigger void diameter was detected in cold worked DIN 1.4981 at 480°C [*8*] and in cold worked AISI 316 at 550°C [*26*].

The post irradiation results of immersion density measurements and TEM-Analysis (Table 2) of the different lots of DIN 1.4970 confirm the results of the length measurements published earlier [*2*]. This means that the amount of stress-induced linear swelling is about 0.3 - 0.8 % at 100 dpa_{NRT} and a hoop stress of 120 MPa (Figure 4a). The differences between the lots are not as great as they are in stress-free swelling, but the ranking of the different lots is preserved. The analysis of the stress dependence of the stress induced swelling yields no difference between the mechanisms of reduced incubation dose and increased steady state swelling rate. The values found for the constants A and B are in the same order of magnitude as reported for other austenitic stainless steels [*27*]. The analysis of the void structure of the K-lot and the I-lot yields in both cases an increased average void diameter. The increase is about 5 - 10 % at 105 dpa_{NRT} and 120 MPa. The analysis of the void concentration is hindered by the high measurement error due to the uncertain sample thickness. But the tendency is that it remains constant for the I-lot and that it increases with increasing stress for the K-lot. Therefore these results speak in favor of the effect of accelerated void growth, whereas an additional contribution by accelerated void nucleation cannot be ruled out at least for the K-lot.

Conclusion

The results of this pressurized tube experiment on different lots of the austenitic steel DIN 1.4970 can be summarized as follows.

Stress-free swelling can be reduced significantly by the proper choice of the content of minor alloying elements silicon and titanium. Increasing the Si-content extends the incubation dose at 420°C, which is limited by the precipitation of Si-rich γ'. The reduction of the Ti-content prevents the evolution of G-phase and stabilizes the γ'-precipitates, which act as point defect sinks and slow down the void growth.

The determination of the stress-induced swelling by length measurements according to the Soderberg theorem is confirmed by the immersion density measurements and the TEM-analysis. The results of the TEM-analysis on average void diameter and void concentration support the accelerated void growth as the cause for stress-induced swelling.

References

[1] Herschbach, K., Schneider, W., and Bergmann, H.-J., *Effects of Radiation on Materials: 14th International Symposium ASTM STP 1046*, N. H. Packan, R. E. Stoller, and A. S. Kumar, Eds., American Society for Testing and Materials, 1990, Vol. 2, pp. 570-587

[2] Herschbach, K., Schneider, W., and Ehrlich, K., *Journal of Nuclear Materials*, Vol. 203, 1993, pp. 233-248

[3] Hübner, R., and Ehrlich, K., Proceedings Jahrestagung Kerntechnik '98 (Kerntechnische Gesellschaft e.V., München 1998), pp. 737-740

[4] Soderberg, C. R., *Transactions of the American Society for Mechanical Engineers*, Vol. 63, 1941, pp. 737-748

[5] Norton, F. H., and Soderberg, C. R., *Transactions of the American Society for Mechanical Engineers*, Vol. 64, 1942, pp. 769-777

[6] Garner, F. A., in *Nuclear Materials, Materials Science and Technology, A Comprehensive Treatment*, Vol 10A, (VCH Weinheim 1994), pp. 419-543

[7] Garner, F. A., Gilbert, E. R., and Porter, D. L., *Effects of Radiation on Materials: 10th Conference, ASTM STP 725*, D. Kramer, H. R. Brager, and J. S. Perrin, Eds., American Society for Testing and Materials, 1981, pp. 680-697

[8] Herschbach, K., Schneider, W., and Ehrlich, K., *Journal of Nuclear Materials*, Vol. 101, 1981, pp. 326-335

[9] Yang, W. J. S., *Radiation-Induced Changes in Microstructure, 13th International Symposium (Part I) ASTM STP 955*, F. A. Garner, N. H. Packan, and A. S. Kumar, Eds., American Society for Testing and Materials, 1987, pp. 628-646

[10] Schneider, W., Wassilew, C., and Ehrlich, K., *Zeitschrift für Metallkunde*, Bd. 77, 1986, pp. 611-619

[11] Venker, H., Ehrlich, K., *Journal of Nuclear Materials*, Vol. 60, 1976, pp. 347-349

[12] Wiedersich, H., *Radiation Effects*, Vol. 12, 1972, pp. 111-125

[13] Garner, F. A., and Wolfer, W. G., *Journal of Nuclear Materials*, Vol. 102, 1981, pp. 143-150

[14] Seran, J. L., Lévy, V., Dubuisson, P., Gilbon., D., Maillard, A., Fissolo, A., Touron, H., Cauvin, R., and LeBoulbin, E., *Effects of Radiation on Materials, 15th International Symposium, ASTM STP 1125*, R. E. Stoller, A. S. Kumar, and D. S. Gelles, Eds., American Society for Testing and Materials, 1992, pp. 1209-1233

[15] Maillard, A., Touron, H., Seran, J. L., and Chalony, A., *Effects of Radiation on Materials, 16th International Symposium, ASTM STP 1175*, A. S. Kumar, D. S. Gelles, R. K. Nanstad, and E. A. Little, Eds., American Society for Testing and Materials, 1993, pp. 824-837

[16] Garner, F. A., Lauritzen, T., and Mitchell, M. A., *Effects of Radiation on Materials, 16th International Symposium, ASTM STP 1175*, A. S. Kumar, D. S. Gelles, R. K. Nanstad, and E. A. Little, Eds., American Society for Testing and Materials, 1993, pp. 803-815

[17] Garner, F. A., Brager, H.R., and Puigh, R.J., *Journal of Nuclear Materials*, Vols. 133&134, 1985, pp. 535-539

[18] Seran, J. L., Touron, H., Maillard, A., Dubuisson, P., Hugot, J. P., LeBoulbin, E., Blanchard, P., and Pelletier, M., *Effects of Radiation on Materials: 14th International Symposium ASTM STP 1046*, N. H. Packan, R. E. Stoller, and A. S. Kumar, Eds., American Society for Testing and Materials, 1990, Vol. 2, pp. 739-752

[19] Sekimura, N., and Ishino, S., *Journal of Nuclear Materials*, Vols. 179-181, 1991, pp. 542-545

[20] Ehrlich, K., and Vaidya, W. V., Proceedings Jahrestagung Kerntechnik (Kerntechnische Gesellschaft e.V., Mannheim 1982), pp. 465-468

[21] Brager, H. R., and Garner, F. A., *Journal of Nuclear Materials*, Vol. 73, 1978, pp. 9-19

[22] Maziasz, P. J., *Journal of Nuclear Materials*, Vol. 169, 1989, pp. 95-115

[23] Maziasz, P. J., *Journal of Nuclear Materials*, Vol. 205, 1993, pp. 118-145

[24] Hassan, M. H., Blanchard, J. P., and Kulcinski, G. L., University of Wisconsin Fusion Technology Report UWFDM-901, May 1992, Madison WI

[25] Brager, H. R., Garner, F. A., and Guthrie, G. L., *Journal of Nuclear Materials*, Vol. 66, 1977, pp. 301-321

[26] Porter, D. L., Takata, M. L., and Wood, E. L., *Journal of Nuclear Materials*, Vol. 116, 1983, pp. 272-276

[27] Ehrlich, K., *Journal of Nuclear Materials*, Vol. 100, 1981, pp. 149-166

V. S. Neustroev,[1] V. K. Shamardin,[1] Z. E. Ostrovsky,[1] A. M. Pecherin,[1]
and F. A. Garner[2]

Temperature-Shift of Void Swelling Observed in Annealed Fe-18Cr-10Ni-Ti Stainless Steel Irradiated in the Reflector Region of BOR-60

Reference: Neustroev, V. S., Shamardin, V. K., Ostrovsky, Z. E., Pecherin, A. M., and Garner, F. A., **"Temperature-Shift of Void Swelling Observed in Annealed Fe-18Cr-10Ni-Ti Stainless Steel Irradiated in the Reflector Region of BOR-60,"** *Effects of Radiation on Materials: 19th International Symposium, ASTM STP 1366,* M. L. Hamilton, A. S. Kumar, S. T. Rosinski, and M. L. Grossbeck, Eds., American Society for Testing and Materials, West Conshohocken, PA, 2000.

Abstract: Evidence has been provided to support the "temperature-shift" concept of swelling. The swelling of annealed X18H10T stainless steel in the BOR-60 fast reactor at PWR-relevant dpa rates was found to be higher than predicted by a swelling equation developed from data obtained at dpa rates almost an order of magnitude higher. These data were derived from identical hexagonal wrappers irradiated in both in-core and reflector positions. Based on these results, irradiation in PWRs would yield higher swelling to lower temperatures than would occur in core regions of fast reactors.

Keywords: stainless steels, swelling, pressurized water reactors, fast reactors

Introduction

In a series of recent papers by Garner and coworkers, it was proposed that some long-lived austenitic components of the baffle-former assemblies of pressurized water reactors (PWRs) might experience significant levels of void swelling toward the end of their target lifetimes. As a consequence these components might also develop embrittlement via a well-known mechanism associated with void formation at relatively low irradiation temperatures [*1-4*]. Some aspects of these predictions have been supported by recently published data derived from various irradiations conducted in three reactors located in Russia and Kazakhstan [*3-7*]. Those data showed that voids formed at lower-than-expected temperatures and dpa levels when the displacement rate was typical of PWRs, a finding that supports the operation of the well-known "temperature-shift" of swelling, wherein the temperature regime of swelling shifts with changes in displacement

[1] Leading Research Scientist, Head of Laboratory, Senior Research Scientist, Senior Research Scientist, respectively, Research Institute of Atomic Reactors, Dimitrovgrad, Russia.

[2] Senior Staff Scientist, Pacific Northwest National Laboratory, Richland, WA USA.

Copyright© 2000 by ASTM International www.astm.org

rate, as demonstrated in Figure 1. Note that the swelling rate is thought to be temperature-dependent in this concept, and at a given temperature will change as a function of dpa rate. At low PWR-relevant temperatures and dpa rates, the temperature-shift leads to an increase in swelling when compared to that obtained at higher displacement rates characteristic of fast reactors.

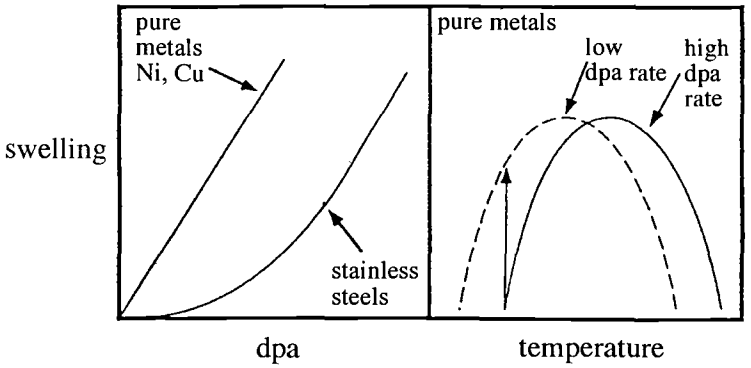


Figure 1 - *"Temperature-shift" concept as applied to void swelling in simple one-component metals and possibly also to more complicated alloys that exhibit a large transient or incubation regime of swelling.*

The temperature-shift has been demonstrated conclusively to be ~50°C per order of magnitude change in displacement rate, but only for pure metals such as copper and nickel, as demonstrated in Figure 2 [*8*]. These metals have very small incubation periods before the onset of high swelling, but the swelling of austenitic stainless steels is known to involve relatively large incubation periods of 10-70 dpa prior to the onset of swelling at high rates [*9*]. These incubation or transient periods are sometimes observed to be dependent on displacement rate, as shown in Figure 3. This effect might be called a "transient-shift". In stainless steels at relatively low swelling levels, it is anticipated that the transient shift will probably be the more important shift. This is the area of flux effects that is our primary current interest.

As shown in Figure 4, data from the EBR-II fast reactor demonstrate that the swelling of annealed 304 stainless steel indeed increases in the 380-400°C range as the dpa rate decreases, but these data are inconclusive with respect to the relative roles of transient-shift and temperature-shift [*10,11*]. In another more extensive experiment on this same steel, the influence of both neutron flux and applied stresses were interpreted in terms of transient shifts [*11*].

In the current study, evidence for the temperature-shift was sought by making comparisons between swelling obtained on identical hexagonal wrapper components irradiated in-core and one irradiated in the reflector region of the BOR-60 fast reactor. BOR-60 has a flux-spectra environment typical of an enriched UO_2-fueled fast reactor. With a mean in-core neutron energy of 0.45 MeV, its spectrum is closer to that of the

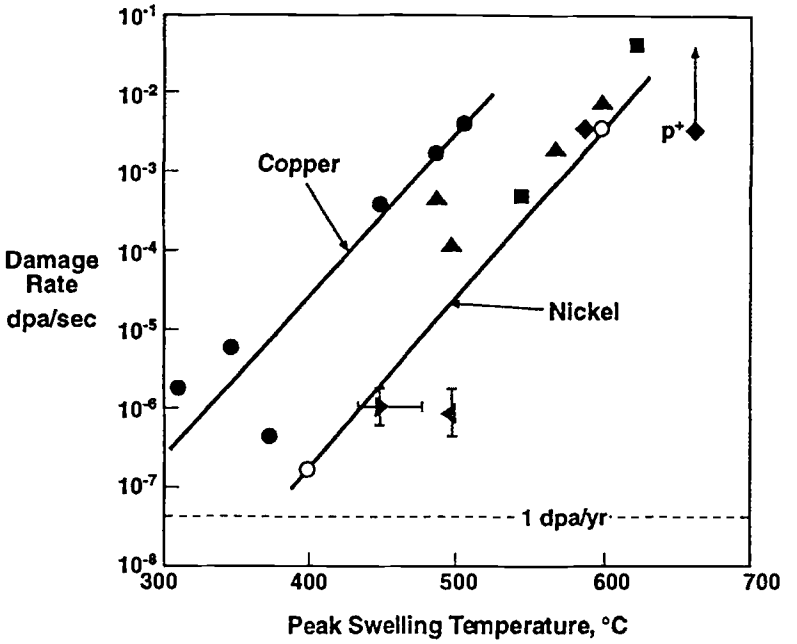


Figure 2 - *Data supporting a temperature-shift of swelling in pure copper and pure nickel, compiled by Packan and coworkers [8].*

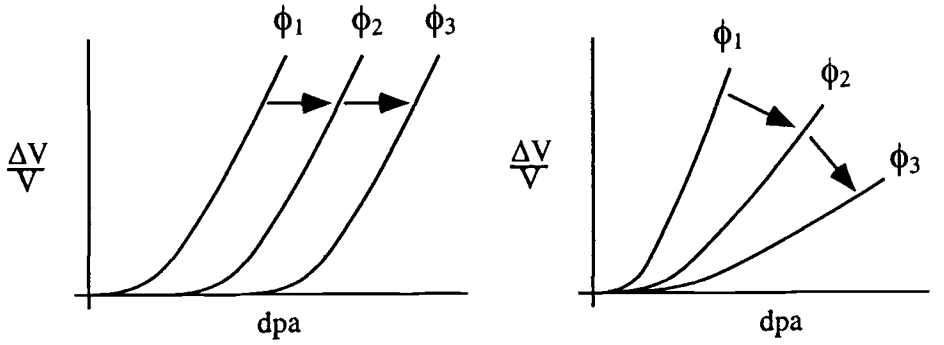


Figure 3 - *Two possible effects of changes in neutron flux or dpa rate on void swelling. Hereafter, these are called the "transient-shift" and the "temperature-shift", respectively. Note that it is assumed that* $\phi_1 < \phi_2 < \phi_3$.

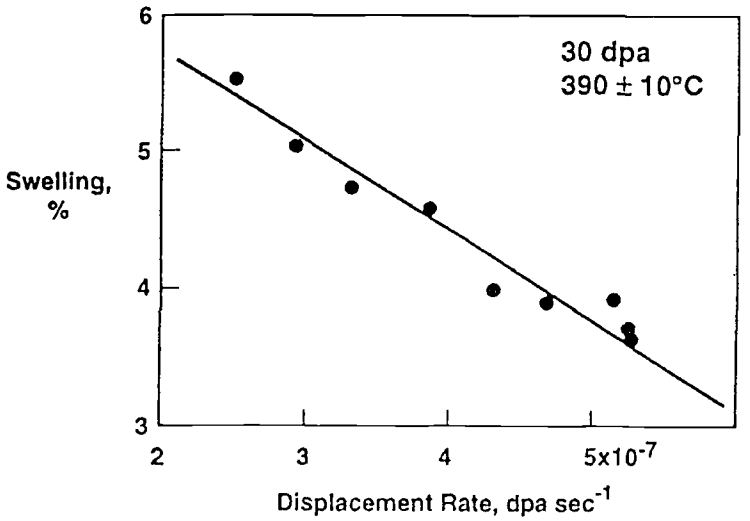


Figure 4 - *Effect of displacement rate on the swelling of AISI 304L stainless steel observed in the EBR-II fast reactor [10].*

Fast Flux Test Facility (FFTF) than that of the metal-fueled EBR-II reactor. The spectrum in the reflector is softer with a mean energy of ~0.35 MeV.

The hexagonal wrappers were constructed from a standard austenitic Fe-18Cr-10Ni-Ti steel (12X18H10T) in the annealed condition, which is extensively used in the countries of the former Soviet Union for a variety of reactors. It is analogous to AISI 321. In similar Western PWR applications the equivalent steel would be AISI 304.

The swelling of this material in fast-reactor wrappers has been extensively studied in Russia. Swelling profiles determined by immersion density along the wrapper axial direction typically exhibit a bell-shaped form, with only the amplitude of the maximum swelling and its position exhibiting any differences. The authors of ref. 12 provide a mathematical dependence describing the swelling of this steel to be $S[\%] = 0.55\ [dpa + 0.1T\ (°C) - 67]\ \exp\ [-29 \times 10^{-5}\ (T-485)^2]$, where the displacement rates varied from ~0.4-1.4 x 10^{-6} dpa/sec.

Figure 5 shows typical in-core data in the range 460-500°C and dpa rates of 9-14 x 10^{-7} dpa/sec. Figure 6 shows swelling predictions by this equation over a range of temperatures and dpa rates. Note that swelling predicted by this equation does not extend below ~350°C.

Experimental Details

A hexagonal wrapper designated E-26 was removed from Row 8 of the BOR-60 fast reactor. The wrapper had been in this position throughout its residence, reaching a maximum neutron fluence of 17.0 x 10^{26} n m^{-2} (E>0.1 MeV), corresponding to a maximum damage dose of 62 dpa, as defined by the standard NRT model. The maximum dpa rate was 2.5 x 10^{-7} dpa/sec. The temperatures were determined primarily

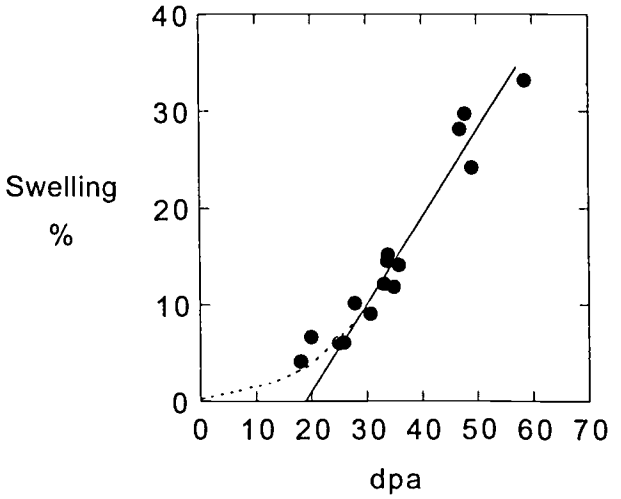


Figure 5 - *Swelling response of the annealed X18H10T steel observed in the in-core region of the BOR-60 fast reactor at 460-500 °C.*

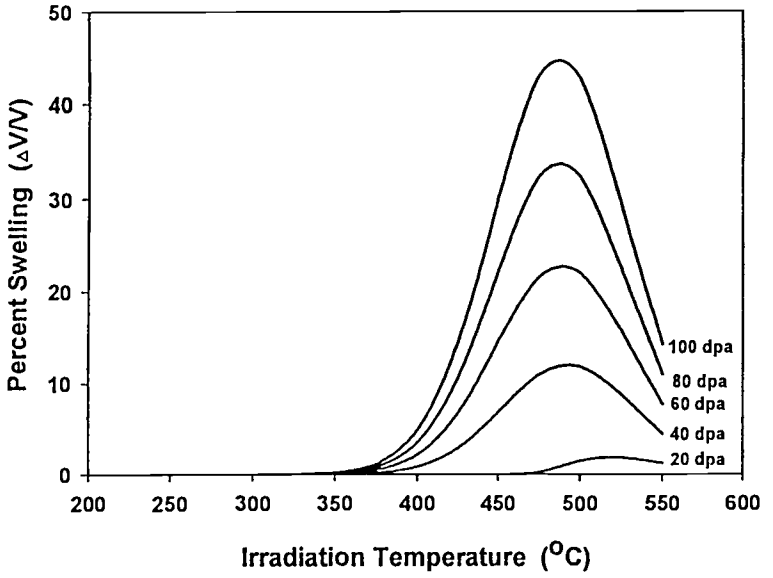


Figure 6 - *Predictions of the swelling behavior of annealed X18H10T steel based on in-core data [12].*

by the local temperature of the sodium coolant, and varied somewhat over the component lifetime due to build-up of plutonium in the depleted UO_2 fuel used in the reflector region. In general, reflector subassemblies run at lower temperatures compared to those located in-core.

Sections were removed from the component at three elevations, as measured with respect to the center plane of the reactor. These were Z = -225 mm (39 dpa), Z = 0 mm (62 dpa) and Z = +225 mm (39 dpa) and the swelling was measured by electron microscopy. The time-averaged temperature ranges were calculated for each position, and were 330-340°C, 360-370°C, and 380-395°C, respectively.

Results

The microscopy data and irradiation conditions are shown in Table 1 and the void microstructures are shown in Figure 7. The ~10^{16} cm^{-3} void densities observed are characteristic of densities usually observed in this temperature range. Figure 8 shows a comparison of the measured swelling with the predictions of the in-core swelling equation at the appropriate temperatures and dpa levels.

Note that at the Z = 0 position that the 62 dpa curve would have to be "shifted" downward in temperature by 37°C to coincide with the measured swelling of this reflector wrapper. The dpa rate for this position is ~18% of that of the core center rate. The dpa rate falls quickly away in the axial direction from the Z = 0 position, yielding an apparent shift of 65°C in the below-center position and 53°C in the above-center position. The dpa rate at these positions is ~9% of that of the core center rate.

Discussion

The values of 37-65°C "shift" are relatively crude measurements of the "temperature-shift", but are consistent with the ~50°C shift per order of magnitude change in dpa rate derived by Packan and coworkers. These data therefore provide some support for the concept of a temperature-shift and allow the possibility that any particular stainless steel may swell more at a given temperature and dpa level when the displacement rate is low compared to PWR-relevant values. Such a shift also implies that swelling will extend to lower temperatures in a PWR. Note that in Figure 6 that no swelling would have been predicted by the design equation at 39 dpa and 330-340°C, yet 1.4% swelling was found in this experiment.

It can not be stated with certainty, however, that the increased swelling was caused only by a temperature-shift. A transient-shift might also contribute or perhaps even dominate the swelling response. From these data alone, no firm conclusion can be drawn concerning the relative contributions of the two shifts.

The second most significant finding is that significant swelling occurred at 330-340°C, which is contrary to conventional wisdom that swelling does not occur at these temperatures. However, recent data at both high and low dpa rates on this steel and another Russian stainless steel show that swelling does occur over this temperature range [3-7]. It appears that conventional wisdom on this point was developed primarily in fast reactors with relatively high inlet coolant temperatures (365-375°C), thereby leading to an incorrect perception.

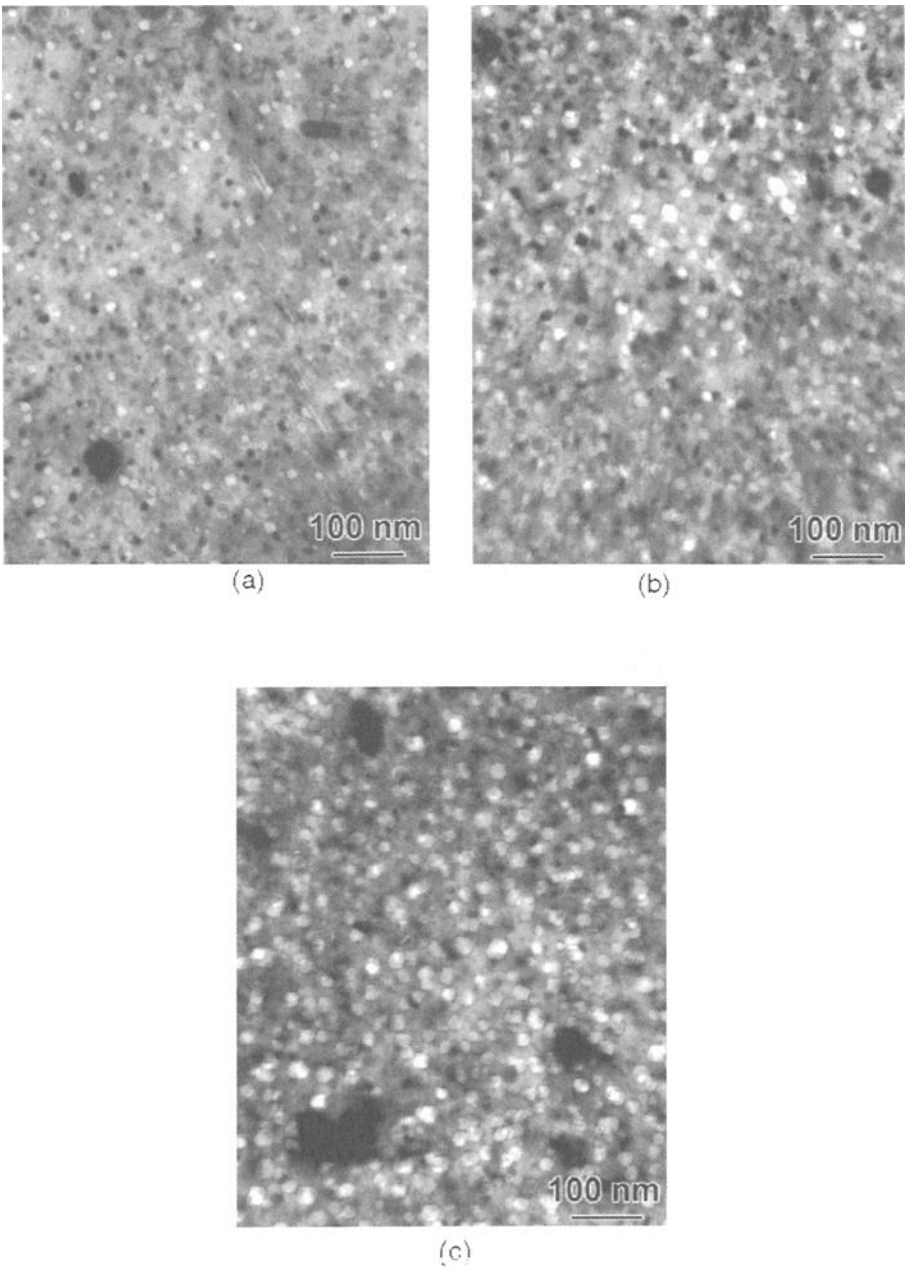


Figure 7 - *Void microstructure observed in assembly E-26 at (a) -225 mm (b) 0 mm, and (c) +225 mm from the component center.*

Table 1 - *Swelling Observed in Three Positions of the Reflector Assembly E-26*

distance from center	peak dpa rate x 10^{-7} sec^{-1}	peak dose dpa	average temperature °C	mean void size, nm	density 10^{15}, cm^{-3}	swelling, %
-225	1.3	39	330-340	11.0	15.5	1.4
0	2.5	62	360-370	16.2	10.9	3.1
+225	1.3	39	380-395	18.4	14.6	6.0

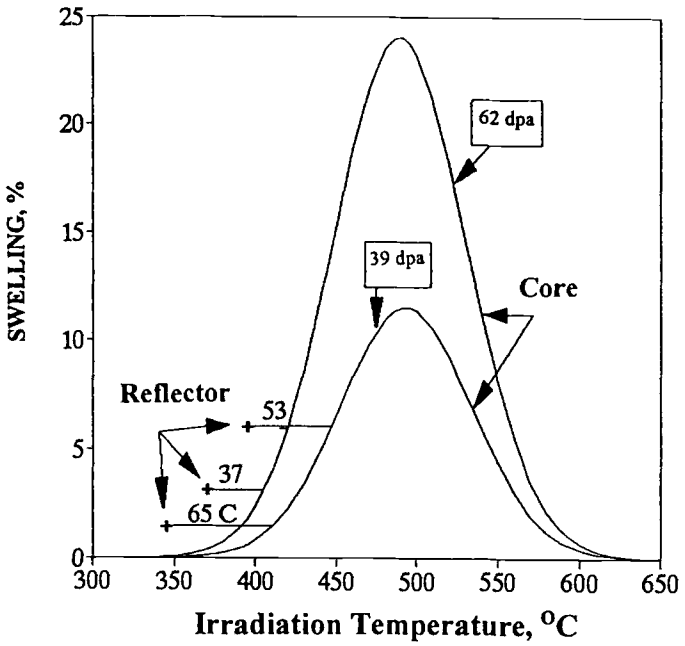


Figure 8 - *Comparison of measured swelling of E-26 specimens with in-core predictions, showing the magnitude of shifts of the high-flux prediction required to match the low-flux measurements.*

References

1. Garner, F. A., Greenwood, L. R., and Harrod, D. L., *Sixth International Symposium on Environmental Degradation of Materials in Nuclear Power Systems - Water Reactors, The Minerals, Metals, and Materials Society, 1993*, pp. 783-790.

2. Garner, F. A., *Transactions of the American Nuclear Society*, 71, (1994) pp. 190-191.

3. Garner, F. A., and Toloczko, M. B., *Journal of Nuclear Materials*, 251 (1997) 252-261.

4. Garner, F. A., Toloczko, M. B., Porollo, S. I., Vorobjev, A. N., Dvoriashin, A. M., and Konobeev, Yu. V., *Eighth International Symposium on Environmental Degradation of Materials in Nuclear Power Systems - Water Reactors, August 10-14, 1997, Amelia Island, Florida, 1997*, pp. 829-845.

5. Porollo, S. I., Vorobjev, A. N., Konobeev, Yu. V., Dvoriashin, A. M., and Garner, F. A., *Proc. Inter. Symp. on "Contributions of Materials Investigation to the Resolution of Problems Encountered in Pressurized Water Reactors," 14-18 Sept. 1998, Fontevraud, France,* pp. 271-280.

6. Garner, F. A., Porollo, S. I., Vorobjev, A. N., Konobeev, Yu. V., Dvoriashin, A. M., Krigan, V. M., Budylkin, N. I., and Mironova, E. G., *Proc. Inter. Symp. on "Contributions of Materials Investigation to the Resolution of Problems Encountered in Pressurized Water Reactors," 14-18 Sept. 1998, Fontevraud, France,* pp. 249-260.

7. Garner, F. A., Porollo, S. I., Vorobjev, A. N., Konobeev, Yu. V., Dvoriashin, A. M., and Krigan, V. M., "Void-Induced Swelling and Embrittlement in the Russian EI-847 Stainless Steel at PWR-Relevant End-of-Life Conditions," these proceedings.

8. Packan, N. F., Farrell, K., and Steigler, J. O., *Journal of Nuclear Materials*, 78 (1978) 143-155.

9. Garner, F. A., "Irradiation Performance Cladding and Structural Steels in Liquid Metal Reactors," *Materials Science and Technology: A Comprehensive Treatment*, Volume 10A, VCH Publishers, 1994, pp. 419-543.

10. Porter, D. L., and Hudman, G. L., *Transactions of American Nuclear Society*, 1980, pp. 230-231.

11. Porter, D. L., and Garner, F. A., in *Effects of Radiation on Materials: Twelfth Inter. Symp., ASTM STP 870*, 1985, pp. 212-220; also *Journal of Nuclear Materials*, 179-181 (1991) 581-584.

12. Votinov, S. N., Prokhorov, V. I., and Ostrovsky, Z. E., "Irradiated Stainless Steels," M. Nauki, 1987 (in Russian).

Colin C. Goodwin,[1] Roy G. Faulkner,[1] John C. Walmsley,[2*] and Paul Spellward[2]

The Effect of Molybdenum on the Grain Boundary Segregation of Chromium Exhibited by Austenitic Stainless Steels after Neutron Irradiation in a BWR

Reference: Goodwin, C. C., Faulkner, R. G., Walmsley, J. C., and Spellward, P., **"The Effect of Molybdenum on the Grain Boundary Segregation of Chromium Exhibited by Austenitic Stainless Steels after Neutron Irradiation in a BWR,"** *Effects of Radiation on Materials: 19th International Symposium, ASTM STP 1366,* M. L. Hamilton, A. S. Kumar, S. T. Rosinski, and M. L. Grossbeck, Eds., American Society for Testing and Materials, West Conshohocken, PA, 2000.

Abstract: Analytical investigations employing field-emission gun scanning transmission electron microscopy (FEGSTEM) have indicated that the degree of chromium depletion at grain boundaries is less pronounced in AISI type-316 when compared to type-304 stainless steel after neutron irradiation in Boiling Water Reactor (BWR) conditions to a fluence of 10^{26} n.m^{-2} (E > 1 MeV). An explanation of this observation is proposed, which is based on the non-equilibrium segregation (NES) theory of grain boundary segregation. NES model predictions for the radiation-induced segregation of chromium and molybdenum in an austenitic matrix are presented together for the first time. The predicted segregation profiles are compared with the FEGSTEM data, whilst the predicted trends as a function of neutron dose are discussed in terms of possible microstructural evolution in a BWR environment. In particular it will be demonstrated how, according to NES theory, the binding of molybdenum to self-interstitial atoms (SIAs) will take precedence over chromium. In turn, the subsequent migration of molybdenum-SIA "complexes" retard the migration of chromium away from the grain boundary, thus moderating the magnitude of radiation-induced chromium depletion.

Keywords: grain boundaries, chromium depletion, radiation-induced segregation, austenitic alloys, neutron irradiation, point defect-solute complexes

[1] Research assistant & Professor of Physical Metallurgy respectively, Power & Aerospace Materials Research Group, Institute of Polymer Technology & Materials Engineering, Loughborough University, LOUGHBOROUGH, Leicestershire, LE11 3TU, UK.

[2] Electron Optics Unit, Nuclear Facilities Branch, BNFL Magnox Generation, Berkeley Centre, BERKELEY, Gloucestershire, GL13 9PB, UK.

* Currently at: Applied Physics, SINTEF Materialteknologi, 7034 Trondheim, Norway.

Copyright© 2000 by ASTM International www.astm.org

The depletion of chromium at grain boundaries has been identified as a major contributor to the irradiation-assisted stress corrosion cracking (IASCC) of austenitic stainless steels in water-cooled reactor systems [*1,2*]. Such depletion is a consequence of radiation-induced segregation (RIS), which may be considered as being the "net effect" of a number of different mechanisms [*3-5*]. There has been a continuing effort aimed at measuring grain boundary segregation with the aim of establishing possible correlations with susceptibility to IASCC. In particular, a method to control the degree of chromium depletion would be of major benefit to the operators of water-cooled reactor systems.

There have been numerous analytical studies of grain boundaries in austenitic stainless steels employing field-emission gun scanning transmission electron microscopy (FEGSTEM) [*6-13*]. Some of these studies have highlighted possibly significant influences of particular solute additions on the moderation of chromium depletion [*7,12,13*]. Such work will be discussed in more detail later. What needs to be emphasised however, is that microchemical measurements made during FEGSTEM analyses, such as those made utilising energy dispersive X-ray spectroscopy (EDXS) for example, may only, at best, provide an underestimation of the actual segregated state of a given grain boundary. This is due to a number of factors including initial grain boundary misalignment to the electron beam and subsequent beam broadening as the beam passes through the thin foil specimen. Both effects result in X-ray generation from regions other than the grain boundary, thus diluting the actual chemical composition. Suitable care is thus needed when interpreting analytical data in terms of what is actually occurring.

A number of theoretical appraisals of grain boundary segregation have been forwarded [*14-17*]. When assessing the segregated state of a grain boundary however, we must not forget that the segregation we are able to observe is dependent both upon the thermal history and any irradiation environment to which the material has been subjected. In other words, a number of different segregation mechanisms may have exerted an influence, be they induced by thermal or irradiation processes. The segregated state of the grain boundary prior to irradiation has previously been demonstrated to be crucial to the understanding of the segregation exhibited by a grain boundary after irradiation [*18,19*]. At this stage of the discussion, a brief summary of the possible solute segregation mechanisms may be of benefit (the discussion will also apply equally to the case of impurity atom segregation).

Equilibrium segregation (ES) [*14*] tends to become prominent at elevated temperatures with the kinetics of the mechanism being determined by solute diffusion. The driving force for ES is the release of strain energy associated with placing a misfitting solute atom at interfaces in the matrix such as grain boundaries. Therefore ES effectively describes the affinity between a given solute atom and a grain boundary. Non-equilibrium segregation (NES) [*15,20*] results from the presence of non-equilibrium concentrations of point defects within the matrix, i.e. vacancies and self-interstitial atoms (SIAs), which need to be relieved if equilibrium is to be reinstated. Grain boundaries act as sinks by absorbing the point defects thus relieving any associated strains and consequently, concentration gradients are established between the grain and its boundary, which provide the necessary driving force for point defect migration to the boundary. In turn, the point defects may interact with solute elements to form freely migrating complexes. It is these mobile complexes that may contribute to the transport of the solute

atom [*3*], which will be discussed in more detail later. It is worth highlighting the fact the NES mechanisms by themselves only describe solute migration and not their subsequent affinity with the grain boundary itself.

By far the most widely-accepted RIS model is based on the inverse-Kirkendall (IK) effect [*3*]. The IK model assumes that the observed segregation in iron-nickel-chromium ternary alloys is solely the result of differences in the flux of vacancies together with the major alloy elements [*16,17*]. An alternative approach is the non-equilibrium segregation (NES) theory, which models those mechanisms dependent upon the formation of point defect complexes [*15,20*]. The ability to predict trends in segregational behaviour resulting from thermal processing and irradiation, provides a valuable insight into materials selection for designers of nuclear power systems. In light of the above, it is desirable for any discussion relating to grain boundary segregation to cater for multiple mechanisms. The various segregation models presented in the literature are thus somewhat limited, since they tend to concentrate only on a single mechanism. Regardless of this observation, our knowledge of grain boundary segregation has been greatly enhanced by the results of such theoretical appraisals of the phenomenon.

The validity of a given model is assessed by comparing its predictions to the available data from experimental investigations of appropriate material. It therefore seems appropriate to first present some recent FEGSTEM-EDXS results from grain boundaries in solution treated and subsequently neutron-irradiated AISI type-304 and type-316 austenitic stainless steels. Such results will highlight the complexity of the phenomenon of grain boundary segregation in these technological steels. Predictions will then be presented for the RIS of chromium and molybdenum in an austenitic matrix as made by the NES theory model. The discussion will then assess the validity of the NES model in terms of the available experimental data.

Observed Segregation Of Chromium And Molybdenum

Previous work [*11-13*] has reported the results of FEGSTEM-EDXS analyses of type-304 and type-316 austenitic stainless steels after solution treatment and subsequent neutron irradiation in a BWR at 288°C to a neutron fluence of 10^{25} n.m^{-2} (E > 1 MeV) and 10^{26} n.m^{-2} (E > 1 MeV). A summary of these findings is given (Table 1). The corresponding dose was calculated using the method forwarded by Mansur [*21*] together with the standard NRT approximation [*22*] for the damage energy. Measured segregation profiles across the grain boundary are reproduced (Figure 1), which depict the evolution of the concentration profiles in each material for chromium, molybdenum and phosphorus.

It can be seen (Figure 1) that neutron irradiation has a profound effect on the composition exhibited by grain boundaries. For example, both chromium and molybdenum were initially enriched at grain boundaries after solution treatment, whilst neutron irradiation results in the gradual depletion of both these elements. This point serves to stress the importance of the pre-service segregation exhibited by the boundary. It should be noted therefore that such radiation-induced depletion must be the result of the migration of these elements away from the boundary. Note also that phosphorus retains a

Table 1-- *Summary of FEGSTEM-EDXS analyses of grain boundaries in type-304 and type-316 austenitic stainless steels [11-13].*

	Fe	Ni	Cr	Mo	P	Si
304 MB	Balance	8.5	18.3	0.37	0.03	0.65
316 MB	Balance	12.2	16.7	2.58	0.02	0.59
304 ST	63.2	8.0	24.0	1.6	0.4	0.7
316 ST	48.3	8.2	21.1	19.9	0.7	0.5
304 0.3 dpa	56.6	14.1	21.4	2.0	2.9	3.0
316 0.3 dpa	54.2	15.1	18.9	6.8	1.4	2.8
304 3.0 dpa	65.7	14.4	15.5	0.5	0.7	3.3
316 3.0 dpa	58.2	22.4	13.4	2.5	0.7	2.9

MB denotes bulk concentrations measured by chemical analysis. ST denotes solution treated condition and represents the average of 10 grain boundaries. The irradiation conditions were for subsequent neutron irradiation in a BWR and represent the average of 4 grain boundaries. All measurements given in wt.%.

degree of enrichment after neutron irradiation to the higher dose, although its peak concentration at the grain boundary appears to occur at some intermediate dose.

A closer inspection of the FEGSTEM data (Table 1) reveals some interesting trends in the segregational behaviour of chromium in the presence of molybdenum. For example, in the type-316 stainless steel, chromium and molybdenum become depleted at the grain boundary to levels of 13.4 and 2.5 wt.% respectively. What is particularly interesting is that the magnitude of chromium depletion represents a change of about 7.7 wt.% when compared to the solution treated condition, whilst the change in molybdenum concentration is over 17 wt.%. This effect becomes even more noticeable when the respective bulk concentrations are taken into account: the ratio of the change in segregated-to-bulk concentrations are approximately 0.5 and 6.7 for chromium and molybdenum respectively. The magnitude of molybdenum depletion is therefore roughly 14 times greater than that for chromium.

As far as the type-304 is concerned, we find that the similar change of chromium and molybdenum concentrations are about 8.5 and 1.1 wt.% respectively. When compared to their respective bulk concentrations, we find that the ratio of change-in-segregated to bulk concentrations work out to be roughly 0.5 and 2.8 for chromium and molybdenum respectively. Therefore the molybdenum becomes depleted at the grain boundary in type-304 to a magnitude greater than that for chromium by a factor of almost 6 times. So even though the chromium profiles change more dramatically in type-304, i.e. when the molybdenum concentration is relatively low, when the bulk concentrations are taken into account it is still, as before, molybdenum which exhibits the greater degree of depletion. This would appear to be a significant trend. In essence, this would tend to suggest that molybdenum is a more dominant segregant when compared to chromium.

Before we look at the predictions of grain boundary segregation, a further trend would appear to become apparent when the individual grain boundary analyses are compared. Such a comparison is given (Figure 2), which depicts each of the measured

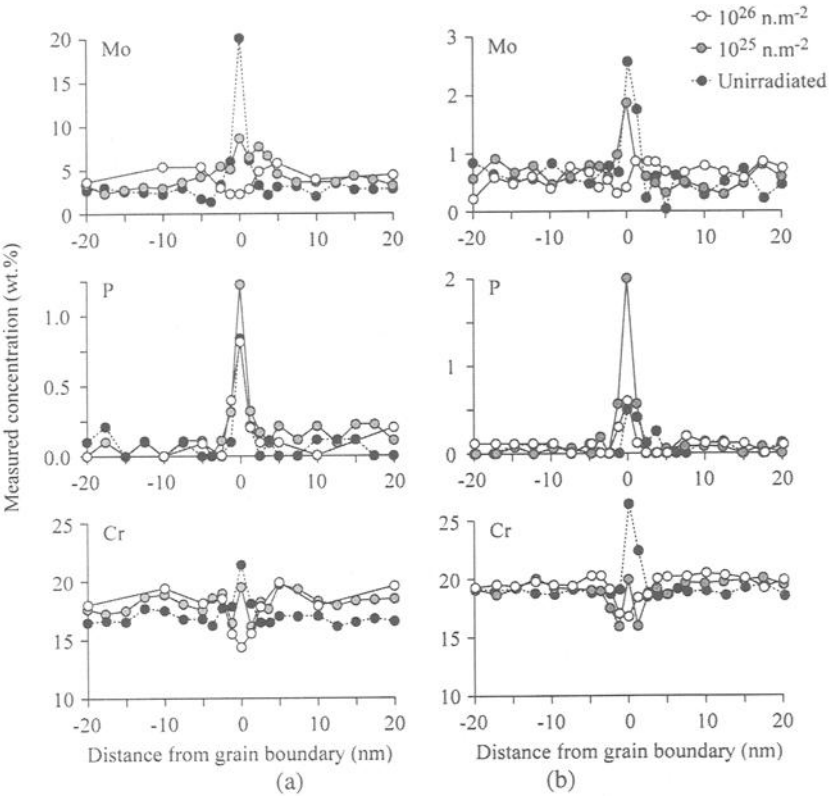


Figure 1--*Typical FEGSTEM-EDXS grain boundary composition profiles for molybdenum, phosphorus and chromium after various treatments in: (a) type-316; (b) type-304.*

grain boundary concentrations of chromium, molybdenum and phosphorus in the type-316 steel. The trend is perhaps easiest to see in the solution treated material (Figure 2a) whereby the concentration of molybdenum appears to correlate with that of phosphorus: a relatively high molybdenum concentration appears to be accompanied with a relatively high phosphorus concentration and vice versa. Only the measurements taken at boundary number 9 would appear to contravene this trend. Similarly for the intermediate (Figure 2b) and high dose material (Figure 2c), in each instance the molybdenum and phosphorus concentrations rise and fall together. In all cases there does not appear to be any significant correlation with the concentration of chromium at the grain boundary. Admittedly, the scatter in the results reflects the relatively small number of data, yet the trend does appear to be consistent. However, archive data may be rescrutinised in an effort to verify the trend. The reason we would want to do this is to attempt to establish

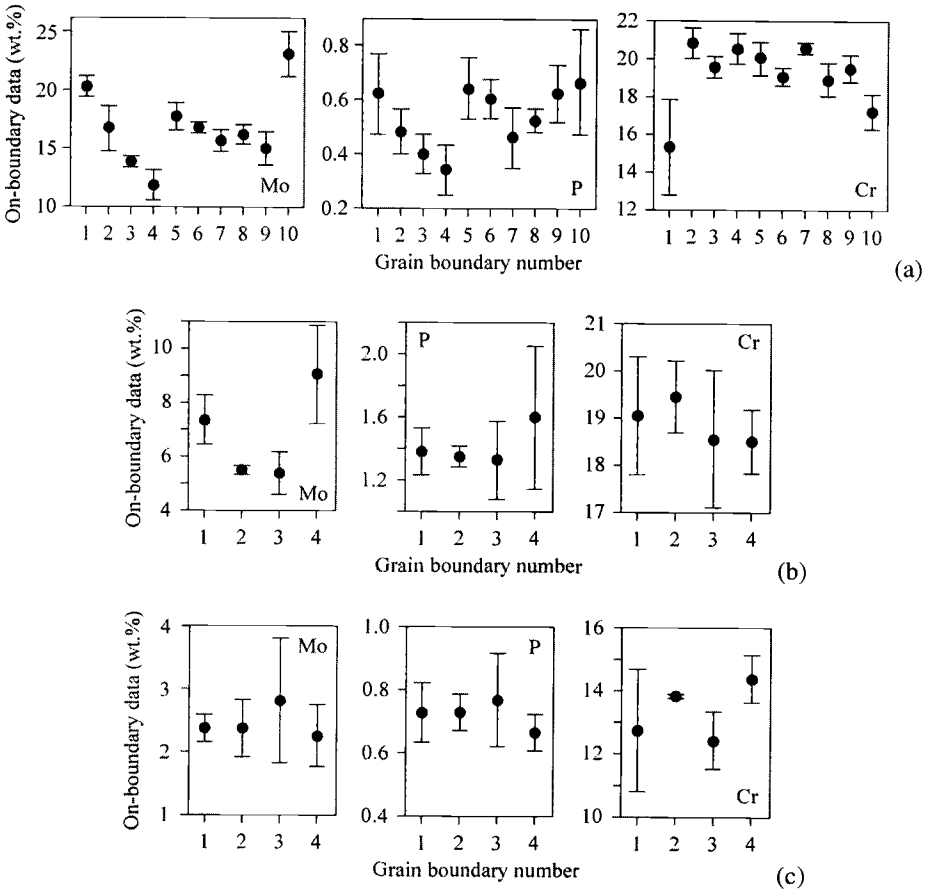


Figure 2--*FEGSTEM-EDXS grain boundary composition measurements for molybdenum, phosphorus and chromium in type-316 after: (a) solution treatment; (b) neutron irradiation to 0.3 dpa; (c) neutron irradiation to 3 dpa. Error bars represent ± σ (the standard deviation of 3 measurements taken at a given boundary).*

some knowledge of interactions between given solute elements at the grain boundary itself. This will be expanded upon later. In the meantime it should be noted that the trend, if it exists, is characteristic of the alloy and not a feature of the environment.

We can perhaps assume that in the relative absence of molybdenum, the degree of chromium depletion at grain boundaries is greater. If it is the intention to limit the degree of chromium depletion at grain boundaries then, based on the above results and subsequent observations, the addition of molybdenum would therefore appear to exert a

beneficial influence on this process. Clearly, at this stage of the discussion, it would be interesting to see if any mathematical model could explain these findings.

Predicted Segregation Of Chromium And Molybdenum

The predictions to be presented are those of the NES theory as employed at Loughborough University. Details of the RIS model have been presented elsewhere [*5*]. Here we will concentrate only upon the predictions themselves and how the results may be interpreted. For the purpose of the discussion, it should be noted that the predictions of RIS relate only to the effect of SIA-solute atom complexes and therefore do not include any prior segregation nor beam broadening. Furthermore, the predicted RIS of a given element is made in isolation from the possible influences of other solute elements. Key data [*5,23-25*] for the RIS model predictions are given (Table 2). Predicted segregation profiles away from the grain boundary are given (Figure 3) after neutron doses of 0.3 and 3.0 dpa for: (a) chromium; (b) molybdenum. Additional predictions indicate predicted trends in grain boundary RIS as a function of the irradiation environment (Figure 4). The irradiation temperature dependence is presented (Figure 4a) together with the neutron dose dependence (Figure 4b) for both chromium and molybdenum. In these figures the segregation ratio is defined as the segregated over the bulk concentration.

Table 2--*Key data employed by NES theory model predictions for the RIS of chromium and molybdenum in an austenitic matrix.*

Parameter	Units	Cr	Mo	
Complex binding energy	eV	-0.01	-0.26	[*23*]
Activation energy for solute diffusion	eV	2.27	2.57	[*24*]
Activation energy for complex migration	eV	2.26	2.31	[*5*]
Pre-exponent for solute diffusion	$m^2.s^{-1}$	1.2×10^{-7}	6.8×10^{-6}	[*24*]
Pre-exponent for complex diffusion	$m^2.s^{-1}$	1×10^{-4}	1×10^{-4}	[*25*]

Discussion

It can be seen from the RIS model predictions that there would appear to a clear driving force for both chromium and molybdenum to migrate away from the grain boundary during neutron irradiation. This is perhaps not surprising since it has been demonstrated previously that the NES theory is able to successfully describe the transition between the thermally-induced enrichment of chromium at grain boundaries in austenitic alloys, to its radiation-induced depletion [*18,19*]. It would now be beneficial to assess the

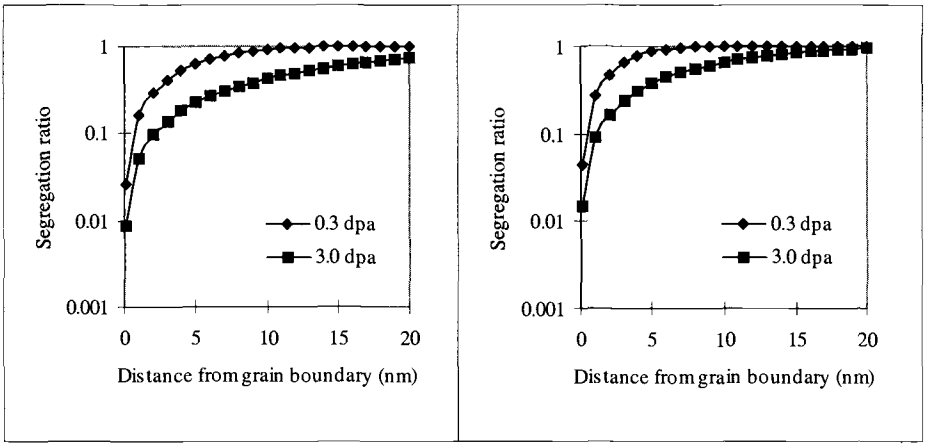


Figure 3--*Grain boundary RIS profiles in an austenitic matrix as predicted by the NES theory: (a) chromium; (b) molybdenum. Irradiation temperature = 290 °C; dose rate = 10^{-8} dpa.s^{-1}; dislocation density = 10^{14} .m^{-2}; grain size 50 μm.*

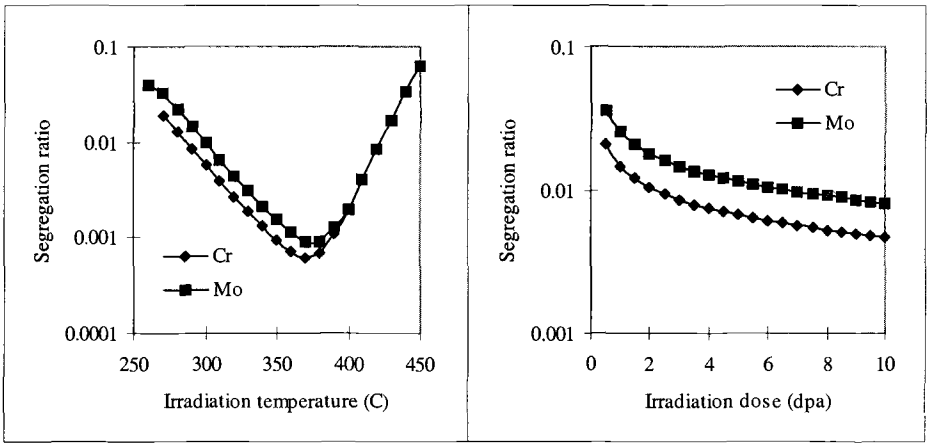


Figure 4--*Grain boundary RIS of chromium and molybdenum in an austenitic matrix as predicted by the NES theory: (a) irradiation temperature dependence (dose = 3.0 dpa); (b) irradiation dose dependence (temperature = 290 °C). Dose rate = 10^{-8} dpa.s^{-1}; dislocation density = 10^{14} .m^{-2}; grain size 50 μm.*

above predictions for the RIS of chromium and molybdenum in terms of the experimental data, in an effort to explain the trends highlighted (Figure 1) and discussed previously.

The predicted RIS profiles (Figure 3) are of the order of nanometers wide and would therefore appear to provide a reasonable picture of the effect of the SIA-solute atom complexes. Whilst the predicted widths of the profiles are somewhat wider at 3 dpa than the measured profiles (Figure 1), the prediction does not take into account the thermally-induced enrichment of these elements after quenching from solution treatment. Naturally this would have a significant effect on the segregational state of the grain boundary. In essence therefore, and to re-emphasise the point made previously, from these predictions it can be assumed that there is much incentive for chromium and molybdenum to migrate away from the vicinity of the grain boundary.

The predicted irradiation temperature dependence of grain boundary RIS (Figure 4a) clearly shows that, in the temperature range of interest, the degree of depletion of chromium is greater than that for molybdenum. At higher temperatures however, i.e. above about 390°C, the predicted RIS is the same for both elements. This reflects the fact that the thermodynamic aspect of the RIS mechanism becomes small when compared to the kinetics of the process. Since this effect only becomes apparent at temperatures very much greater than those of interest to this study, we need not concern ourselves with this matter. What is interesting about the predictions is that they highlight that chromium would tend to become depleted to a greater extent than molybdenum at temperatures lower than about 350°C, i.e. those temperatures relevant to water-cooled reactor systems.

This trend is again clearly evident in the predicted dose dependence of RIS (Figure 4b), which also indicates that continued irradiation would lead to a further depletion of chromium and molybdenum at grain boundaries. Considering the discussion to date however, the greater predicted degree of chromium depletion may seem initially to be somewhat surprising, since this would obviously appear to be contrary to the assumption made previously that molybdenum was the dominant segregant when compared to chromium. However, an inspection of the data employed (Table 2) may provide an explanation.

To explain it should be noted that the proposed mechanism for solute migration due to interactions with SIAs involves two stages [5]: (i) complex formation; (ii) complex dissociation. The binding energy for molybdenum within this complex configuration is larger than that for chromium. It thus seems reasonable to assume that molybdenum would dominate over chromium in the competition to form such complexes. This may explain why molybdenum is the dominant segregant, but it does not yet explain the predictions made whereby for equivalent conditions, the degree of molybdenum depletion is less. To explain this the diffusion data needs to be compared, which indicates that the molybdenum complex would be less mobile than the equivalent chromium complex. So in isolation from the influence of the other element, chromium would deplete more in a given time than molybdenum. However, the presence of molybdenum inhibits the segregation of chromium since it dominates when interacting with a SIA, even though the resultant migration is slower than when compared to chromium. This now could explain why the presence of molybdenum would appear to inhibit the degree of chromium depletion: the migration of molybdenum due to interactions with SIAs takes precedence over similar interactions for chromium.

It would appear that the role of phosphorus remains somewhat unclear. The retention of its thermally-induced enrichment after neutron irradiation would perhaps imply that a different segregation mechanism is in effect when compared to the RIS of chromium and molybdenum. In addition, there would also appear to be a saturation of phosphorus at the grain boundary, which was highlighted by the results of the intermediate dose material. It may be the case that the magnitude of phosphorus enrichment becomes so great at the grain boundary that the supply of this element from the grain centre becomes exhausted. This would presumably result in the back-diffusion of phosphorus away from the boundary, in an attempt to equilibrate the system.

One possible explanation for the role of phosphorus can be found in the work of Guttmann et al. [*26*], who demonstrated that there is no, or very little, driving force for chromium or molybdenum to migrate to grain boundaries in α-iron. Whilst dealing specifically with ES in ferritic matrices, the findings of the study can be used to shed some light on the situation for austenitic matrices. It is assumed that this is not unreasonable, since the McLean model of ES [*14*] indicates no significant effect for either chromium or molybdenum in an austenitic matrix at the temperatures of interest [*5*]. Significantly, the Gibbsian free energy for both these elements are very low. Consequently, there is no incentive for chromium or molybdenum to remain at the boundary *a priori*, even if NES processes result in the migration of these elements to the grain boundary after quenching from the solution treatment temperature. Guttmann et al. [*26*] went on to demonstrate how it was the presence of other elements at the grain boundary, such as phosphorus, which caused the enrichment of chromium and molybdenum to be maintained. This effect was attributed to the fact that phosphorus possessed a strong affinity for the grain boundary and an affinity with either the chromium or molybdenum atoms. Significantly, this affinity was reported to be stronger between phosphorus and molybdenum than that between phosphorus and chromium. If we assume that the situation at the grain boundary in a ferritic matrix is not so different from a boundary in an austenitic matrix, then this observation could explain why the grain boundary concentrations of molybdenum and phosphorus were so interconnected, as shown previously (Figure 2).

What has to be remembered is that the above predictions have been made to describe the effect of one mechanism of segregation in isolation from the influence of others. More importantly, the predictions do not cater for interactions between the various atomic species either during the segregation process or in the plane of the grain boundary. Both these points are significant when one considers the work of Guttmann et al. [*26*]. Whilst site competition at the grain boundary has been incorporated into the NES theory [*27,28*], the work was concerned with the effect of carbon on the RIS of phosphorus in ferritic steels. The situation for the case of the austenitic alloys under scrutiny here is somewhat different, since the site competition would appear to exist between chromium and molybdenum and a segregated phosphorus atom. Consequently, more thought needs to be applied before a similar extension to the RIS predictions presented previously can be made.

Given that it is the IK model that has currently enjoyed the highest prominence in the literature to date, it is necessary to consider predictions made by this model in light of the above discussion. In such work it is assumed that the RIS of chromium in technological alloys can be considered to be much like the RIS observed in model iron-

nickel-chromium alloys. Whilst this simplification is not unreasonable, questions need to be asked regarding the assumptions made in the literature that the IK predictions by themselves, adequately describe the actual segregation taking place in technological alloys. From the analytical results presented here and the corresponding discussion forwarded, it seems that this cannot be the case because the IK model is currently incapable of incorporating the effects of elements such as molybdenum and phosphorus in addition to iron-nickel-chromium.[1] What the IK model does provide however, is a much valued insight to the effect of solute diffusion in the presence of point defect concentration gradients about the grain boundary for concentrated alloy situations. The most logical approach to the theoretical investigation of this phenomenon therefore, would be to analyse the predictions made by different models, and thus different mechanisms, in an effort to ascertain how the mechanisms may inter-relate. Only with such a holistic approach are we likely to truly understand the phenomenon at hand.

Another aspect of the IK model is of particular significance: the role of SIA is neglected. This is because when incorporated, the corresponding predictions indicate a much greater degree of chromium depletion.[2] Considering the point that in the NES theory, the negative binding energy is interpreted as meaning the complex disassociates instantaneously [*18,19*], the migration of the SIA-solute "complexes" can effectively be considered as being a SIA-driven IK effect. This aspect is significant because in essence, the IK and NES models are predicting the same thing: there is much incentive for chromium to migrate away from the grain boundary.

Recent developments to the IK model have investigated the effect of prior thermal enrichment on the RIS of chromium [*29*]. Whilst no direct predictions may be forwarded by the IK model, the assumption that an additional mechanism plays a vital role prior to RIS enabled a more complete discussion to be forwarded. In essence, this particular work demonstrated the synergistic advantages of a more broad-minded theoretical appraisal of the phenomenon at hand. Clearly a similar approach to modelling grain boundary segregation in technological alloys should be employed in future literature for the mutual benefit of the radiation damage community.

To this end, it is hoped that the current study has highlighted a number of important issues that should be pursued. In particular, it should not be forgotten that the driving force for chromium and molybdenum to remain in the vicinity of the grain boundary, may appear to be solely dependent upon the presence of other elements such as phosphorus. Clearly then, more attention should be paid to interactions between the various atomic species at the grain boundary itself. The moderating effect of molybdenum on the chromium depletion has highlighted one possible avenue of research, which could provide a possible understanding of the problems associated with IASCC. Particular solute additions provide a potentially fertile source of information, especially when one considers the work of Kato et al. [*7*], who demonstrated that additions of zirconium and hafnium successfully maintained the chromium concentration at the grain boundary in electron irradiated type-316L. An intimate understanding of why this is so, would naturally provide a significant step towards a mechanistic understanding of IASCC.

---

1 Was, G. S., private communication, 1997.

2 Allen, T. R., private discussion at the ASTM meeting in Hyannis, 1996.

Summary

The RIS exhibited by technological alloys in water-cooled reactor systems is an extremely complex phenomenon and can be considered in more general terms as being the "net effect" of all possible mechanisms of segregation. Analytical measurements of such segregation at grain boundaries employing FEGSTEM-EDXS, provide a measurement of the actual segregation taking place. Care must be exercised when interpreting these data in terms of what occurs on the atomic scale, since the measurement includes data from regions other than the grain boundary. It has been demonstrated that the NES theory is able to provide a reasonable discussion pertaining to the phenomenon of grain boundary segregation in austenitic stainless steels. Predictions made by the RIS model were shown to be illustrative of equivalent experimental data for chromium and molybdenum. In addition, and perhaps more fundamentally, the discussion stemming from the NES predictions provides a perhaps more complete description of the processes at work during RIS.

Acknowledgments

The work was funded by BNFL Magnox Generation. The authors would like to thank Mr. Richard J. Scowen and Mr. John M. Stump, BNFL Magnox Generation, for their care and patience whilst obtaining the FEGSTEM data. CCG would like to thank: Mr. Anders Jenssen, ABB Atom, for permission to present previously unpublished analytical data; Dr. Stan B. Fisher, BNFL, for instigating the project; Dr. Song Shenhua and Mr. Duncan Meade, I.P.T.M.E., for stimulating discussion and generally stolid assistance.

References

[*1*] Nelson, J. L. and Andresen, P. L., "Review of current research and understanding of irradiation-assisted stress corrosion cracking," *Fifth International Symposium on Environmental Degradation of Materials in Nuclear Reactor Systems - Water Reactors*, E. P. Simonen and D. Dubicciotti Eds., American Nuclear Society, La Grange Park, IL, 1992, pp. 10-26.

[*2*] Kenik, E. A., Jones, R. H. and Bell, G. E. C., "Irradiation-assisted stress corrosion cracking," *Journal of Nuclear Materials*, Vol. 212-215, 1994, pp. 52-59.

[*3*] Rehn, L. E. and Okamoto, P. R., "Non-equilibrium segregation in irradiated alloys," *Phase Transformations During Irradiation*, F. V. Nolfi Jnr., Ed., Applied Science Publishers, Barking, 1983, pp. 247-290.

[4] English, C. A., Murphy, S. M. and Perks, J. M., "Radiation-induced segregation in metals," *Journal of the Chemistry Society Faraday Transactions*, 1990, pp. 1263-1271.

[5] Goodwin, C. C., The mathematical modelling of grain boundary segregation in austenitic alloys," Ph.D. thesis, Loughborough University, 1998.

[6] Asano, K., Fukuya, K., Nakata, K. and Kodama, M., "Changes in grain boundary composition induced by neutron irradiation on austenitic stainless steels," *Fifth International Symposium on Environmental Degradation of Materials in Nuclear Reactor Systems - Water Reactors*, E. P. Simonen and D. Dubicciotti Eds., American Nuclear Society, La Grange Park, IL, 1992, pp. 838-846.

[7] Kato, T., Takahashi, H. and Izumia, M., "Grain boundary segregation under electron irradiation in austenitic steels modified with oversized elements," *Journal of Nuclear Materials*, Vol. 189, 1992, pp. 167-174.

[8] Jacobs, A. J., Wozadlo, G. P., Okada, T., Kawano, S., Nakata, K., Kasahara, S. and Suzuki, S., "The correlation of grain boundary composition in irradiated stainless steel with IASCC resistance," *Sixth International Symposium on Environmental Degradation of Materials in Nuclear Reactor Systems - Water Reactors*, R. E. Gold and E. P. Simonen Eds., The Minerals Metals & Materials Society, Warrendale, PA, 1993, pp. 597-606.

[9] Cookson, J. M., Damcott, D. L., Was, G. S. and Andresen, P. L., "The role of microchemical and microstructural effects in the IASCC of high purity austenitic stainless steels," *Sixth International Symposium on Environmental Degradation of Materials in Nuclear Reactor Systems - Water Reactors*, R. E. Gold and E. P. Simonen Eds., The Minerals Metals & Materials Society, Warrendale, PA, 1993, pp. 573-581.

[10] Bruemmer, S. M., Charlot, L. A. and Simonen, E. P., "Measurement and modeling of radiation-induced grain boundary segregation in austenitic stainless steels," *Seventh International Symposium on Environmental Degradation of Materials in Nuclear Reactor Systems - Water Reactors*, A. R. McIlree and S. M. Bruemmer Eds., National Association of Corrosion Engineers, Houston, 1995, pp. 971-984.

[11] Walmsley, J., Spellward, P., Fisher, S. B. and Jenssen, A., "Microchemical characterisation of grain boundaries in irradiated steels," *Seventh International Symposium on Environmental Degradation of Materials in Nuclear Reactor Systems - Water Reactors*, A. R. McIlree and S. M. Bruemmer Eds., National Association of Corrosion Engineers, Houston, 1995, pp. 985-995.

[12] Jenssen, A., Ljungberg, L. G., Walmsley, J. and Fisher, S., "The importance of

molybdenum on irradiation assisted stress corrosion cracking in austenitic stainless steels," *Corrosion 96: The NACE International Annual Composition and Exposition*, National Association of Corrosion Engineers, Houston, 1996, paper 101.

[*13*] Jenssen, A., Ljungberg, L. G., Walmsley, J. and Fisher, S. B., "The importance of molybdenum on irradiation assisted stress corrosion cracking in austenitic stainless steels," *Corrosion*, Vol. 54, No. 1, 1998, pp. 48-60.

[*14*] McLean, D., *Grain Boundaries in Metals*, Oxford University Press, London, 1957, pp. 116-149.

[*15*] Faulkner, R. G., Song, S. and Flewitt, P. E. J., "A model describing neutron irradiation-induced segregation to grain boundaries in dilute alloys," *Metallurgical and Materials Transactions A*, Vol. 27A, 1996, pp. 3381-3390.

[*16*] Simonen, E. P. and Bruemmer, S. M., "Lattice defect / grain boundary interactions relating to IASCC," *Journal of Nuclear Materials*, Vol. 239, 1996, pp. 185-193.

[*17*] Allen, T. R. and Was, G. S., "Modeling radiation-induced segregation in austenitic Fe-Cr-Ni alloys," *Effects of Radiation on Materials: 18th International Symposium, ASTM STP 1325*, R. K. Nanstad, M. L. Hamilton, F. A. Garner and A. S. Kumar, Eds., American Society for Testing and Materials, Philadelphia, 1997, submitted.

[*18*] Goodwin, C. C., Faulkner, R. G. and Fisher, S. B., "Radiation and thermally-induced grain boundary segregation of chromium in austenitic alloys," *Interface Science and Materials Interconnection: Proceedings of JIMIS-8*, The Japan Institute of Metals, 1996, pp. 571-574.

[*19*] Goodwin, C. C., Faulkner, R. G. and Fisher, S. B., "The modelling of combined radiation-induced and thermal non-equilibrium segregation of chromium in neutron-irradiated austenitic stainless steels," *Effects of Radiation on Materials: 18th International Symposium, ASTM STP 1325*, R. K. Nanstad, M. L. Hamilton, F. A. Garner and A. S. Kumar, Eds., American Society for Testing and Materials, Philadelphia, 1997, submitted.

[*20*] Jiang, H. and Faulkner, R. G., "Modelling of grain boundary segregation, precipitation and precipitate-free zones of high strength aluminium alloys - I. The model," *Acta Materialia*, Vol. 44, 1996, pp. 1857-1864.

[*21*] Mansur L. K., "Mechanisms and kinetics of radiation effects in metals," *Kinetics of Nonhomogeneous Processes*, J. R. Freeman Ed., John Wiley & Sons, New York, 1987 pp. 399-404.

[*22*] Norgett, M. J., Robinson, M. T. and Torrens, I. M., "A proposed method of calculating displacement dose rates," *Nuclear Engineering and Design*, Vol. 33, 1975, pp. 50-54.

[23] Faulkner, R. G., Song, S. and Flewitt, P. E. J., "Determination of impurity-point defect binding energies in alloys," *Materials Science and Technology*, Vol. 12, 1996, pp. 904-910.

[24] *Smithells Metals Reference Book*, E. A. Brandes and G. B. Brook Eds., Butterworth-Heinemann, Oxford, 1992, pp. **13**-70-102.

[25] Lam, N. Q., Kumar, A. and Weidersich, H., "Kinetics of radiation-induced segregation in ternary alloys," *Effects of Radiation on Materials: 11th International Symposium, ASTM STP 782*, H. R. Brager and J. S. Perrin, Eds., American Society for Testing and Materials, Philadelphia, 1982, pp. 985-1007.

[26] Guttmann, M., Dumoulin, P. and Wayman, M., "The thermodynamics of interactive co-segregation of phosphorus and alloying elements in iron and temper-brittle steels," *Metallurgical Transactions A*, Vol. 13A, 1982, pp. 1693-1711.

[27] Faulkner, R. G., Song, S., Flewitt, P. E. J., Victoria, M. and Marmy, P., "Grain boundary segregation under neutron irradiation in dilute alloys," *Journal of Nuclear Materials*, Vol. 255, 1998, pp. 189-209.

[28] Meade, D., Faulkner, R. G. and Ellis, D., "Radiation induced grain boundary segregation of phosphorus in ASME SA533B ferritic pressure vessel steel," *Effects of Radiation on Materials: 19th International Symposium, ASTM STP 1366*, M. L. Hamilton, A. S. Kumar, S. T. Rosinski and M. L. Grossbeck Eds., American Society for Testing and Materials, West Conshohocken, PA, 1999, submitted.

[29] Simonen, E. P. and Bruemmer, S. M., "Thermally induced grain boundary composition and effects on radiation-induced segregation," *Eighth International Symposium on Environmental Degradation of Materials in Nuclear Reactor Systems - Water Reactors*, Vol. 2, American Nuclear Society, La Grange Park, IL., 1997, pp. 751-757.

Jean Henry,[1] Alain Barbu,[2] and Ahn Hardouin-Duparc[2]

Microstructure Modeling of a 316L Stainless Steel Irradiated with Electrons

Reference: Henry, J., Barbu, A., and Hardouin-Duparc, A., **"Microstructure Modeling of a 316L Stainless Steel Irradiated with Electrons,"** *Effects of Radiation on Materials: 19th International Symposium, ASTM STP 1366,* M. L. Hamilton, A. S. Kumar, S. T. Rosinski, and M. L. Grossbeck, Eds., American Society for Testing and Materials, West Conshohocken, PA, 2000.

Abstract: The work presented here is a first step in an effort to develop a rate theory model useful for the prediction of microstructural evolution of austenitic stainless steels in typical irradiation conditions for PWR core internals. An important difficulty associated with this type of model is the lack of well known material parameters (apparent defect migration energies, bias factors, etc.), which depend on the composition of the alloy and on the presence of impurities. The approach adopted here consists in finding an adequate set of parameters which results in a good agreement between model predictions and microstructural data after irradiating a 316L stainless steel at different temperatures in a 1 MeV electron microscope. Model results can then be compared with microstructural data corresponding to different irradiation conditions. We have chosen here to perform irradiations at low damage rate using 3 MeV electrons, which is a simpler case compared for example with neutron irradiations. We have found that calculated and measured densities of interstitial loops are in good agreement if a small fraction of the generated defects is considered to be in the form of di-interstitials, in accordance with molecular dynamics results. In the future, we intend to modify the model for the case of neutron irradiations. The same procedure as implemented here for the choice of material parameters (i.e., 1 MeV electron irradiations) will be carried out for different types of austenitic stainless steels. Model predictions will then be compared with microstructural observations obtained after irradiations of the steels up to different doses in an experimental reactor.

Keywords: 316L stainless steel, rate theory model, electron irradiation, microstructural evolution, dislocation loop

[1]CEA-CEREM, Service de Recherches Métallurgiques Appliquées, 91 191 Gif-sur-Yvette, France.

[2]CEA, Laboratoire des Solides Irradiés, Ecole Polytechnique, 91 128 Palaiseau, France.

Copyright© 2000 by ASTM International www.astm.org

Introduction

Radiation hardening due to the nucleation and growth of small dislocation loops is known to play an important role in the degradation of the mechanical properties of the core internals in the Pressurized Water Reactors (PWR) (see for instance [*1*]). The French Electricity Utility, EdF, seeks to extend the operation time of the PWR to at least 40 years, which would lead to the exposure of the core internals to a high irradiation damage and raises the question of their lifetime. Modeling the microstructural evolution of austenitic steels under relevant irradiation conditions for the PWR would be an useful tool to answer this question, in addition to experimental data obtained through irradiations in experimental reactors.

A first step towards this goal is described here, which consists of modeling using rate theory the microstructural evolution of a type 316L austenitic steel under electron irradiation. Indeed, electron irradiation is a simpler case compared with ion or neutron irradiation since only isolated defects are created (Frenkel Pairs). Therefore, any attempt to model the microstructural evolution of irradiated steels should at least be able to account well for the case of electron irradiation.

The parameters of the model have been adjusted to fit experimental data obtained after irradiation at high flux in a 1 MeV electron microscope. Model predictions have then be compared with microstructural observations after irradiations at low flux using a 3 MeV Van de Graaff electron accelerator.

In the following, we will first present the experimental data for the two type of irradiations, followed by the description of the model and the comparison of data and model predictions.

Material and Experimental Procedure

The material used for the irradiations is an industrial 316L type steel which has a typical composition of the steel used for the bolts of core internals in the French PWR (Table 1). The material was supplied to us by EdF.

Table1-*Composition of the 316L Steel (Weight %)*

C	Cr	Ni	Mn	Si	S	Mo	P	N
0.031	16.8	10.3	1.6	0.37	0.011	2.04	0.027	0.043

Two 0.5 mm thick discs of this material were sliced from a 30 mm diameter extruded rod, which had been annealed for 10 min at 1050 °C. One disc was electropolished and subsequently irradiated with 3 MeV electrons delivered by the Van de Graaff accelerator at CEA-Grenoble. The irradiation was performed under 4 10^4 Pa He pressure in order to avoid surface contamination and to assure good heat transfer. The sample surface

opposite to the surface exposed to the electron beam (rear surface) is in contact with a copper furnace. The temperature was measured on both surfaces using Chromel-Alumel thermocouples, which are made of a Chromel wire and an Alumel wire point welded on the surface. The wire diameter is very small (4 10^{-2} mm) in order to minimise the heat generated in the thermocouple due to energy losses by the electrons. During the irradiation, the surface temperature was monitored and kept constant within a ± 15 °C margin. In order to perform the irradiation over a long period (about 3 weeks), the accelerator operates in an automatic mode and the parameters which control the beam are regulated. In case of a machine breakdown, the accelerator starts automatically up again and the previous irradiation conditions are restored.

Following irradiation, mechanical polishing was performed on the rear surface of the disc down to a thickness of about 100 μm. For such a low thickness, the temperature gradient during irradiation is negligible and the electron energy can be considered constant. Discs of 3 mm were then punched out of the 100 μm thin foil and electrolitically jet-polished in a 10% $HClO_3$, 20% C_4H_9-O-C_2H_4OH and 70% C_2H_5OH solution at 30V and 15 °C, in order to obtain samples suitable for observations by Transmission Electron Microscopy (TEM). They were performed using a CM30 Philipps microscope operated at 300 kV or a JEM 2010F microscope (200 kV).

From the second 0.5 mm thick disc, TEM samples were prepared according to the procedure described above, before being irradiated using the 1MeV electron microscope of CEA-Saclay. The irradiations were carried out using a double-tilt heating specimen holder. The vacuum in the vicinity of the specimen is kept during irradiation experiments to a value lower than 5 10^{-8} Torr. The temperature, which varies by less then 3 °C during an experiment, is measured with a thermocouple welded on the cradle of the specimen holder. In the irradiated region of the sample, the temperature is higher then the value given by the thermocouple. However, previous measurements based on the observation of the order-disorder transition in Ni_3Fe and Ni_2Cr have shown that the temperature increase is smaller than 10 °C.

Experimental Results

Irradiation with the 3 MeV Van de Graaff Accelerator

An irradiation with the Van de Graaff accelerator at CEA-Grenoble was carried out with an average current density on the irradiated zone (20x5 mm^2) of 39 μA/cm^2. Given the displacement cross-section of 100b, this current density results in the displacement rate of 2.45 10^{-8} dpa/s. The irradiation was performed up to a dose of 5.5 10^{-2} dpa, which corresponds to a total experiment time of about 624 h. The irradiated surface temperature was 350 ± 15 °C.

Observations by TEM (Figure 1) show that the microstructure of the irradiated steel consists of a high density of very small black dots.

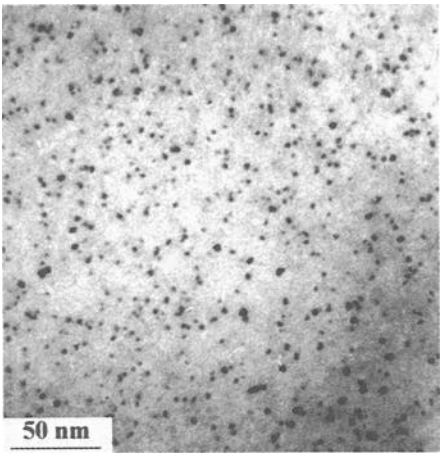


Figure 1-*Microstructure after irradiation at low damage rate (350 °C, 5.5 10^{-2} dpa).*

We did not attempt to analyse the nature of these objects, but given the irradiation conditions (electrons, low damage rate), the black dots are most probably small faulted interstitial loops. Imaging was performed after tilting the sample in order to have a [110] zone axis parallel to the electron beam [2].

The loop number density was determined by counting the number of objects and measuring the foil thickness using the convergent beam technique. The density measurements were performed for 4 different areas of two TEM samples. An estimation of the average loop size was obtained by measuring the size of about 70 black dots. The results are given in Table 2.

Table 2-*Measured Average Size and Number Density of Black Dots*

density, cm^{-3}	diameter, nm
$(3.3 \pm 0.7)\ 10^{16}$	3.3 ± 0.8

Irradiations with the 1 MeV Transmission Electron Microscope

The purpose of the irradiations performed in the 1 MeV Transmission Electron Microscope of CEA-Saclay, was to measure the evolution with temperature of

i) the growth rate of dislocation loops created by irradiation.

ii) the saturation density of dislocation loops.

However, it was found that at high temperature (450-600 °C), the growing loops develop an very irregular, often dendritic shape. This makes growth kinetics measurements very difficult to perform. They were thus abandoned.

The saturation density measurements were carried out in the following way: after inserting the specimen-holder in the microscope, the specimen cradle is heated in order to reach the lowest temperature at which we intend to irradiate the sample. During the heating up time, the beam is blanked so as not to nucleate loops at low temperature. Once thermal stability is obtained, a suitable grain is selected. In particular, the selected zone should not be "bent", but should have a wedge shape. The reason for this requirement is detailed below. The sample is then slightly shifted so that the electron beam passes entirely through the hole in the sample. This allows the beam intensity to be adjusted without irradiating the specimen. Intensity adjustment is performed by varying the excitation of the second condenser lens to obtain the desired current value, measured on the fluorescent screen of known efficacy. For all experiments, we have used a current density of $8\ 10^{18}$ e/cm^2 which corresponds to a displacement rate of $3.2\ 10^{-4}$ dpa/s. The selected zone is shifted back again under the beam in order to start the irradiation which is followed on a video-camera. The irradiation is performed until we judge that the density of objects has become constant. In practice, the irradiation time was around ten to fifteen minutes. The sample is then heated again to reach the next temperature at which we want to measure the saturation density of loops. The irradiation is performed preferably in the same grain if it is large enough.

After irradiation, TEM observations are carried out to determine the density of dislocation loops. This is done in a following way : first, the sample is tilted in the microscope so that two beam diffraction conditions are obtained in the irradiated zone, with a diffraction vector g of the type g={111}. For such diffraction conditions, a wedge-shaped grain exhibits thickness fringes, as shown in Figure 2a. Each fringe connects regions of same thickness and two successive bright or dark fringes correspond to a thickness increase equal to the extinction distance ξ_g (ξ_{111}= 40 nm at 200 kV). A second micrograph of the irradiated zone is then recorded after tilting slightly the specimen in order to obtain a positive deviation from the exact Bragg angle (kinematical diffraction conditions). On this micrograph it is possible to count the number of loops per surface unit in each region of equal thickness corresponding to the fringes in Figure 2a.

The saturation loop density D_{sat} is given by the relation:

$$D_{surf} = D_{sat}(e - 2Z_d) \tag{1}$$

where

D_{surf} = number of loops per surface unit
Z_d = thickness of the defect depleted zone
e = thickness of the irradiated region

If we then plot D_{surf} as a function of e, we obtain the value of D_{sat} and Z_d for the temperature at which the irradiation has been carried out.

In fact, we had some difficulties in implementing the procedure described above. Indeed, it turned out that the steel supplied by EdF had a rather fine grain microstructure (grain size of 40 μm). As a result, the irradiations could not be performed at all temperatures in a single grain.

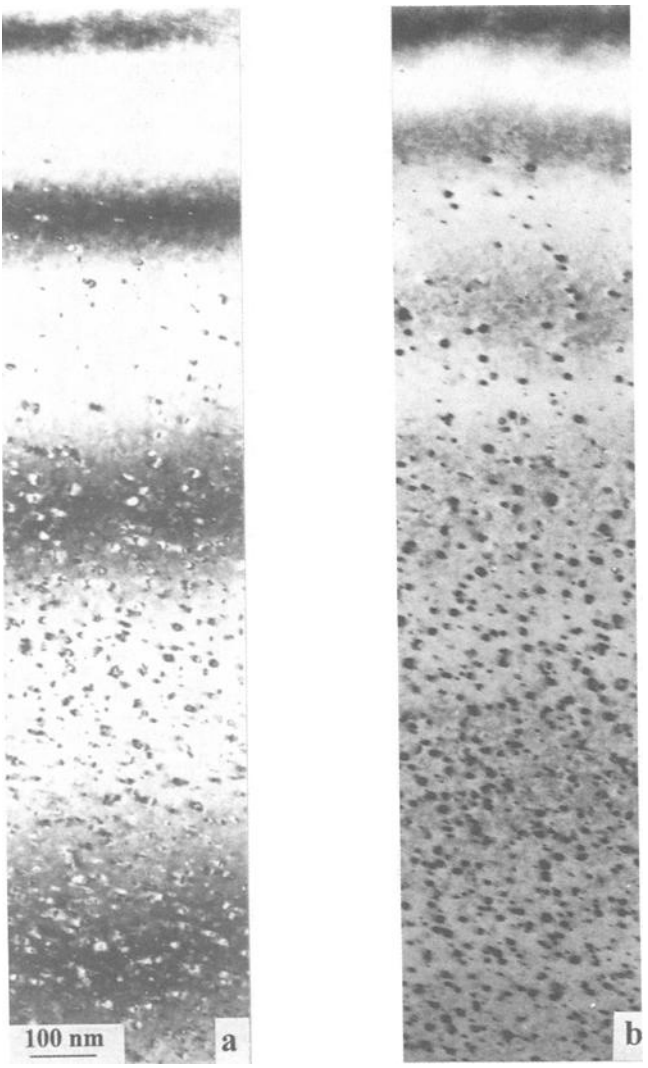


Figure 2-*Irradiated region (346 °C) imaged in two beam conditions (a) and kinematical diffraction conditions (b).*

Furthermore, probably due to the fine microstructure, it was very difficult to find wedge-shaped regions in the TEM samples, and most of the grains where the irradiations were carried out turned out to be slightly bent. This led to a rather high error bar on the thickness measurements. It was therefore not possible to determine experimental values for the effective migration energy and the diffusivity prefactor. However, the experimental results were compared with the model predictions for the chosen set of input parameters.

The experimental results concerning the saturation densities of interstitial loops are plotted in Figure 3. Figure 4 features the irradiation microstructure observed at different temperatures.

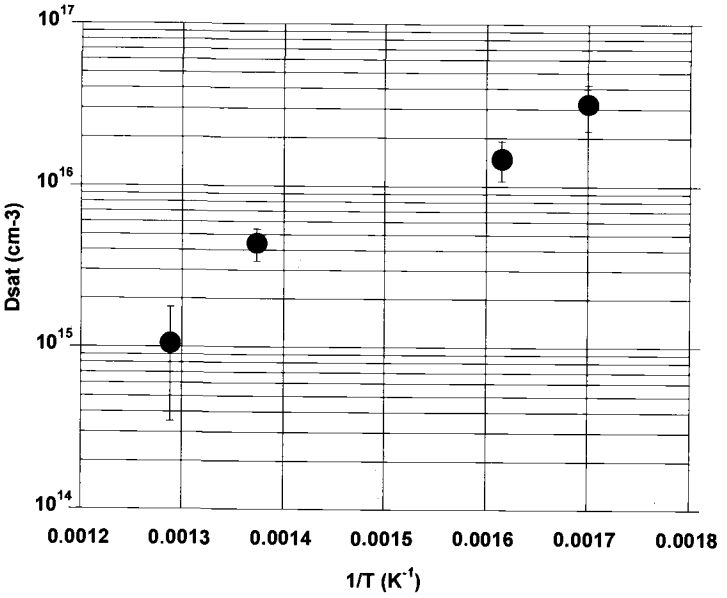


Figure 3-*Saturation densities of interstitial loops.*

Description of the Model

In the past, various authors have used the rate theory to model the microstructural evolution of irradiated metallic alloys [3-6]. In this type of modelling, the evolution with time of the concentration C_n of defect (interstitial or vacancy) clusters consisting of n point defects is described by a chemical reaction rate equation of the following general form:

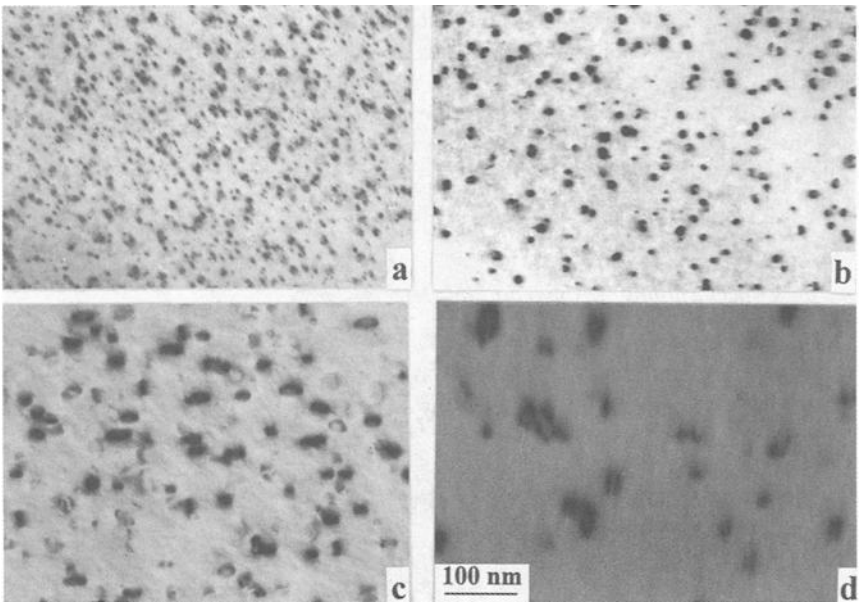


Figure 4-*The microstructure at different irradiation temperatures (a : 315 °C, b : 346 °C, c : 455 °C, d : 503 °C)*

$$\frac{dC_n(t)}{dt} = a_{n+1}C_{n+1}(t) + b_nC_n(t) + c_{n-1}C_{n-1}(t) \qquad (2)$$

The time evolution of the cluster size distribution is obtained through the resolution of a system of $n_{max}=N_i+N_j$ such equations, where N_i (respectively N_j) is the maximum size for interstitial (respectively vacancy) clusters. In fact, in the early works, the maximum size n_{max} was either kept to a low value [3] or the system of discrete equations was replaced by a system of N continuous equations, with N small with respect to n_{max}. Different methods were used to reduce the number of equations. For instance in [8,9], the defect clusters are grouped in a limited number of size classes characterised by their mean cluster size. In [10], the authors replaced the discrete equations by a set of Fokker-Planck type continuous equations which describe the evolution of the density of probability C(x,t) in the space of the number of defects x contained in the cluster.

More recently, a model was developed [5,11] which uses equation (2) for interstitial clusters up to a size of $n_{max}= 4$; for larger sizes, the interstitial clusters are considered to be faulted loops. The loop size distribution is divided into a histogram and the evolution of the number of loops in each size class is given by a growth equation.

With the computers available today, it is possible to perform discrete clustering calculations up to cluster sizes of a few hundreds (as done for example in [6]) even with a simple microcomputer. However, the cluster size which corresponds to maximum loop

sizes typically observed in irradiated austenitic steels is of the order of 10^4. This is why the model presented here, which is essentially inspired by the models mentioned above and was originally developed for the case of ferritic steels [7], is a "mixed" model: up to a size of a few tens, discrete equations are used, while for larger sizes, Fokker-Plank type equations describe the evolution of the size distribution.

The rate equations are given below. For clarity purposes, the discrete equations have been divided into three groups.

Equations for Concentrations of Isolated Point Defects

$$\frac{dC_{1,i}}{dt} = \frac{G}{V_{at}} - R_{iv}(D_i + D_v)C_{1,i}C_{1,v} - K_i^2(C_{1,i} - C_i^e)D_i$$
$$-\sum_{n=2}^{Ni}\beta_{n,i}^i D_i C_{1,i} C_{n,i} + \sum_{n=2}^{3}\alpha_{n,i}^i D_i C_{n,i} - \sum_{n=2}^{Nv}\beta_{n,v}^i D_i C_{1,i} C_{n,v} \qquad (3)$$
$$-2\beta_{1,i}^i D_i C_{1,i} C_{1,i} + \beta_{2,i}^v D_v C_{1,v} C_{2,i} + \alpha_{2,i}^i D_i C_{2,i}$$

$$\frac{dC_{1,v}}{dt} = \frac{G}{V_{at}} - R_{iv}(D_i + D_v)C_{1,i}C_{1,v} - K_i^2(C_{1,v} - C_v^e)D_v$$
$$-\sum_{n=2}^{Nv}(\beta_{n,v}^v C_{1,v} - \alpha_{n,v}^v)D_v C_{n,v} + \sum_{n=2}^{Ni}(\beta_{n,i}^v C_{1,v} - \alpha_{n,i}^v)D_v C_{n,i} \qquad (4)$$
$$-2\beta_{1,v}^v D_v C_{1,v} C_{1,v} + \beta_{2,v}^i D_i C_{1,i} C_{2,v} + \alpha_{2,v}^v D_v C_{2,v}$$

where

$C_{n,j}$ = concentration of clusters containing n defects of type j (j=i for interstitials, j=v for vacancies)
G = point defect generation rate
R_{iv} = recombination coefficient
K_j^2 = coefficient of elimination of j-type defects on dislocations and free surfaces
C_j^e = equilibrium concentration of point defects of type j
V_{at} = atomic volume
N_j = maximum number of defects contained in a cluster of type j
D_j = diffusion coefficient for defects of type j
$\alpha_{n,j'}^j$ = emission coefficient of a defect of type j by a cluster containing n defects of type j'
$\beta_{n,j'}^j$ = absorption coefficient of a defect of type j by a cluster containing n defects of type j'

Although implicit in the equations (3) and (4), it must be pointed out that only isolated point defect are considered to be mobile.

Evolution of the Populations of Interstitial or Vacancy Cluster Containing n defects, with n≥4

$$\frac{dC_{n,i}}{dt} = (\beta^{i}_{n-1,i} D_i C_{1,i} + \alpha^{v}_{n-1,i} D_v) C_{n-1,i} + \beta^{v}_{n+1,i} D_v C_{1,v} C_{n+1,i} - (\alpha^{v}_{n,i} D_v + \beta^{v}_{n,i} D_v C_{1,v} + \beta^{i}_{n,i} D_i C_{1,i}) C_{n,i} \quad (5)$$

$$\frac{dC_{n,v}}{dt} = \beta^{v}_{n-1,v} D_v C_{1,v} C_{n-1,v} + (\beta^{i}_{n+1,v} D_i C_{1,i} + \alpha^{v}_{n+1,v} D_v) C_{n+1,v} - (\alpha^{v}_{n,v} D_v + \beta^{v}_{n,v} D_v C_{1,v} + \beta^{i}_{n,i} D_i C_{1,i}) C_{n,v} \quad (6)$$

Evolution of the Populations of Interstitial or Vacancy Cluster Containing n Defects, with 2≤n<4

$$\frac{dC_{2,i}}{dt} = (\beta^{i}_{1,i} D_i C_{1,i} + \alpha^{v}_{1,i} D_v) C_{1,i} + (\beta^{v}_{3,i} D_v C_{1,v} + \alpha^{i}_{3,i} D_i) C_{3,i} - (\alpha^{i}_{2,i} D_i + \alpha^{v}_{2,i} D_v + \beta^{v}_{2,i} D_v C_{1,v} + \beta^{i}_{2,i} D_i C_{1,i}) C_{2,i} \quad (7)$$

$$\frac{dC_{3,i}}{dt} = (\beta^{i}_{2,i} D_i C_{1,i} + \alpha^{v}_{2,i} D_v) C_{2,i} + \beta^{v}_{4,i} D_v C_{1,v} C_{4,i} - (\alpha^{i}_{3,i} D_i + \alpha^{v}_{3,i} D_v + \beta^{v}_{3,i} D_v C_{1,v} + \beta^{i}_{3,i} D_i C_{1,i}) C_{3,i} \quad (8)$$

Equations (7) and (8) differ from equation (5) because the terms which correspond to the dissociation of bi and tri-interstitials are included. For larger interstitial clusters, we consider that the dissociation does not take place. As regards the evolution of $C_{2,v}$ and $C_{3,v}$, they are given by equation (6).

Evolution of the Concentrations of Large Size Interstitial Clusters (n greater than 20)

As was mentioned above, it is not possible to use only discrete equations if one wants that the maximum cluster size be of the same order of magnitude as maximum loop sizes observed experimentally. Therefore, above a given interstitial cluster size (n=20), discrete equations are replaced by continuous equations relative to the evolution of a probability density $C_i(x,t)$, where x is a continuous variable corresponding to the number of defects contained in the cluster. The continuous equations are obtained by a

development to the second order of equations (5) and (6), which yields the following Fokker-Planck type equations :

$$\frac{dC_i(x,t)}{dt} = -\frac{\partial}{\partial x}\left[f(x)C_i(x,t)\right] + \frac{\partial^2}{\partial x^2}\left[d(x)C_i(x,t)\right] \tag{9}$$

with

$$f(x) = \alpha^v_{x,i} D_i + \beta^i_{x,i} D_i C_{1,i} - \beta^v_{x,i} D_v C_{1,v} \tag{10}$$

$$d(x) = \frac{1}{2}(\alpha^v_{x,i} D_i + \beta^i_{x,i} D_i C_{1,i} + \beta^v_{x,i} D_v C_{1,v}) \tag{11}$$

The use of two types of equations raises the question of the appropriate boundary conditions. It was found necessary [7] that the first step in the space of cluster sizes (continuous description) be equal to the step corresponding to the discrete equations, i.e. 1. Therefore, in order to reach large cluster sizes, the increment Δx_n between successive points in the size space where $C_i(x,t)$ is calculated has to increase with n. The following expression was chosen [12] :

$$x_n = x_{n-1} + \frac{x_{n-1}}{N_i} \tag{12}$$

where N_i is the number of discrete equations.

It is well known from experimental observations that under electron irradiation, the loops which grow to large sizes are always interstitial loops. Therefore the continuous equations were not used in the case of vacancy clusters, for which we set the maximum size to n=100. For the interstitial clusters, calculations were performed with 250 continuous equations.

Expressions for the Coefficients in the Rate Equations

Recombination Coefficient R_{iv} -It is calculated according to the expression: $R_{iv} = 4\pi r_{iv}$ where r_{iv} is the recombination radius. With a recombination volume equal to 100 V_{at} [13], one obtains:
$r_{il} \approx 1.81a \approx 0.65nm$ where a is the lattice parameter.

Coefficient of Elimination on Dislocations and Free Surfaces K_j^2 - This parameter describes the sink strength of the dislocations present before irradiation and of the free surfaces (for the case of irradiation in the electron microscope) or the grain boundaries in the case of the bulk irradiation with the Van de Graaff accelerator. We make the assumption that the absorption rate of point defects by each sink is independant of the presence of other sinks. This hypothesis is valid as long as the density of sinks remains low [14]. The contributions of the two types of sinks can then be added, which yields:

$$K_j^2 = (\frac{k_s}{d^2}) + \rho_d Z_j^d \tag{13}$$

where

ρ_d: dislocation density. This parameter is considered to be invariant during irradiation.
k_s, d: in the case of thin foils for irradiations in the high voltage transmission microscope, k_s equals 12 and d corresponds to the average thickness of the irradiated zones. In the case of the irradiation with bulk samples in the Van de Graff accelerator, d corresponds to the average grain size and k_s equals 24 [15].
Z_j^d : dislocation bias factor for point defects of type j. We have set the dislocation bias factor for interstitials and vacancies to 1.1 and 1 respectively.
C_j^e : equilibrium concentration for the defects of type j.

$$C_j^e = exp\left(\frac{-E_j^f}{kT}\right) \tag{14}$$

where E_j^f is the formation energy of j-type point defects.

Absorption and Elimination Coefficients of the Defect Clusters- The absorption ($\beta_{n,j'}^j$) and emission ($\alpha_{n,j'}^j$) coefficients are calculated according to:

$$\beta_{n,j'}^j = 2\pi r_{n,j'} Z_{n,j'}^j \tag{15}$$

$$\alpha_{n,j'}^j = 2\pi r_{n,j'} Z_{n,j'}^j C_{j,e}(r_n, j') \tag{16}$$

where

$Z_{n,j'}^j$ is the bias factor which characterises the interaction between a cluster of type j', containing n defects and a defect of type j. For energy reasons, interstitial clusters can only grow in a two-dimensional way. Here, for n>3, interstitial clusters are treated as small faulted dislocation loops. Furthermore we assume that the bias factors for both types of defects are independent of the loop size and have the same value as in the case of straight dislocation lines.

As for vacancy clusters, we assume that they adopt a disc shape and that crystal planes above and below the disc do not collapse to form a dislocation loop. In such case, to a very good approximation, there is no interaction between a cluster and a point defect, either vacancy or interstitial. Therefore, $Z_{n,v}^v = Z_{n,v}^i = 1$

$r_{n,j'}$ is the radius of the cluster j', treated as a dislocation loops. Hence $r_{n,i} = r_{n,v} = \sqrt{\frac{nV_{at}}{\pi b_l}}$

where b_l is the Burgers vector of a dislocation loop.

$C_{j,e}(r_n, j')$ is the concentration of point defects of type j which are in equilibrium with a loop of type j' and radius r_n. For interstitial clusters with n>3 we have used the expression given in [16]:

$$C_{v,e}(r_n, i) = C_v^e \exp\left(-\frac{(\gamma_{sf} + f_{el}(r_n))b_l^2}{kT}\right) \quad (17)$$

where γ_{sf} is the stacking fault energy and $f_{el}(r_n)$ is the elastic energy of the loop, given by:

$$f_{el}(n) = \frac{\mu b_l^2}{4\pi(1-\nu)(r_n + b_l)} ln\left(\frac{r_n + b_l}{b_l}\right) \quad (18)$$

where μ is the shear modulus and ν is Poisson's ratio. For vacancy clusters, we do not take into account any size dependence ($C_{v,e}(r_n, v) = C_v^e$).

Given the values for the interstitial and vacancy formation energies (respectively around 5 and 1.6 eV), only vacancies can be emitted by the loops. However, a very small interstitial cluster can thermally dissociate and emit interstitials. These two points have been taken into account in equations (3) to (8). The possibility of thermal dissociation of interstitial clusters is considered only for di and tri interstitials. Furthermore, for very small clusters, the concepts of elastic energy of the loop or stacking fault energy are no longer relevant. In this case, $C_{j,e}(n, j)$ is given by:

$$C_{j,e}(n, j) = exp\left(-\frac{E_{n,j}^b}{kT}\right) \quad (19)$$

where $E_{n,j}^b$ is the binding energy of the cluster. This expression is used for di and tri-interstitials as well as for di-vacancies.

Comparison of Model Predictions and Experimental Data

Choice of Model Parameters

As pointed out in [5], the choice of model parameters is an important problem when using a rate theory model to predict microstructural evolution under irradiation. Various parameters such as bias factors, binding energies of clusters etc., can not be measured experimentally. For other parameters, only experimental values for pure metals or alloys of controlled purity have been measured. This is the case for instance for interstitial and vacancy migration energies. Moreover, apparent values for such parameters in austenitic stainless steels are known to be sensitive to alloy composition and to the presence of impurities [17, 18].

The approach adopted here for the choice of model parameters is the following: we have tried to find a set of input parameters which give a satisfactory agreement between model predictions and experimental results (mainly the measurements of saturation densities of interstitial loops) obtained after irradiations at high damage rate in the 1 MeV electron microscope. The chosen values for all model parameters are listed in Table 3 and we will comment on the key parameters in the following.

According to a simplified analytical model [19], the interstitial migration energy E_i^m determines the slope of the curve $\ln(D_{sat})$ as a function of 1/T. As first input parameter we took E_i^m=0.85 eV, which is a value used in [6,11] and in good agreement with our data. Furthermore, this choice agrees rather well with the resistivity measurements carried out in ternary FeNiCr alloys of various compositions [18].

Table 3-*Input Parameters*

Parameter	Value
Vacancy migration energy E_v^m	1.1 eV
Interstitial migration energy E_i^m	0.85 eV
Vacancy formation energy E_v^f	1.6 eV
Interstitial formation energy E_i^f	5 eV
Di-interstitial binding energy $E_{2,i}^b$	1.5 eV
Tri-interstitial binding energy $E_{3,i}^b$	10 eV
Di-vacancy binding energy $E_{2,v}^b$	0.3 eV
Interstitial diffusivity pre-exponential D_i^0	2.5 cm^2/s
Vacancy diffusivity pre-exponential D_v^0	1 10^{-6} cm^2/s
Loop/interstitial bias Z_i^l	1.1
Dislocation/interstitial bias Z_i^d	1.1
Recombination radius r_{iv}	0.65 nm
Stacking fault energy γ_{sf}	20 10^{-3} J/m^2
Foil thickness (irradiations at high damage rate)	250 nm
Grain size	40 μm
Dislocation density ρ_d	10^8 cm^{-2}

These authors have also determined an experimental value for the vacancy migration energy in such alloys, which they found to be independent of alloy composition. We have chosen as input parameter their experimental value, i.e. E_v^m=1.1 eV. The loop/interstitial bias factor Z_i^l was set to 1.1, which is a value well within the range of values used by other authors for this parameter. The above parameters having been set, the value of the interstitial diffusivity prefactor was chosen in order to obtain a satisfactory agreement with the loop densities measurements. We used a rather low value for the vacancy diffusivity prefactor. This was required in order to obtain reasonable computed loop sizes compared with our experimental observations. However, the agreement is still not perfect. For example, at 345 °C, the mean loop

diameter after 10 min irradiation is about 17 nm, whereas the computed value is 37 nm. This could be improved by decreasing either Z_i^I and/or D_v^0.

As concerns the di and tri-interstitial binding energies, we have first used very high values (10 eV). In practice, such a choice implies that thermal dissociation of bi and tri-interstitials is impossible at all temperatures. In Figure 5, we can see that, given the experimental error bars, model results with no dissociation do not totally agree with the experimental data at the highest temperature. With a value of $E_{2,I}^b$=1.5 eV and $E_{3,I}^b$ kept at 10 eV, the agreement is improved. With $E_{2,I}^b$=1.2 eV, the computed density at 503 °C is too low (2.5 10^{14}cm^{-3}).

In order to illustrate the results given by the model, we have drawn in Figure 6 different distributions of interstitial loops concentrations. They all correspond to the same irradiation time, but to different temperatures.

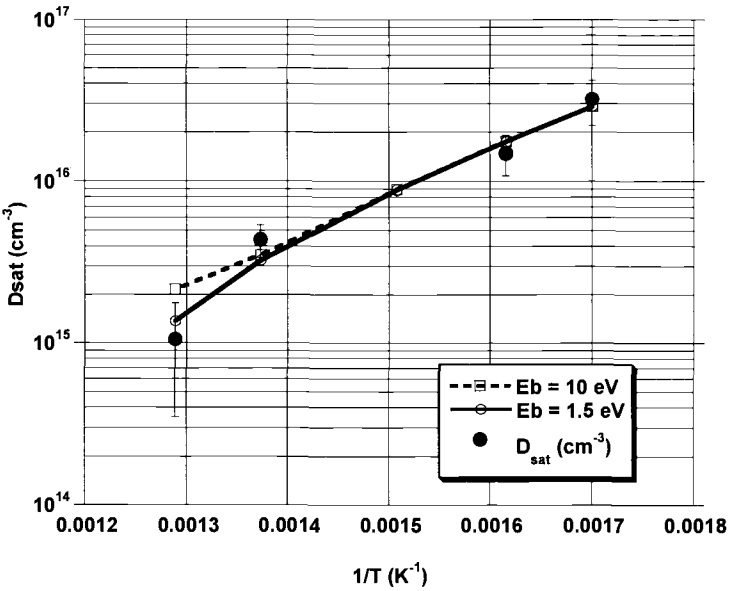


Figure 5-*Comparison between experimental data and computed saturation densities of interstitial loops. The dashed line corresponds to the case where no dissociation occurs and the continuous line is relative to a di-interstitial binding energy of 1.5 eV.*

Comparison of Model Predictions with Experimental Data at Low Damage Rate

As was shown in Figure 5 above, the chosen set of values for the model parameters results in a satisfactory agreement between computed saturation densities of interstitial loops and experimental data measured after irradiations at high damage rate. We want

now to compare model predictions and TEM microstructural observations performed on the 316L steel irradiated at low damage rate in the 3 MeV electron accelerator. Figure 7 presents the calculated distribution of loops concentrations which correspond to the total irradiation time (624h). Table 4 gives the associated values for the total loop density and mean loop size.

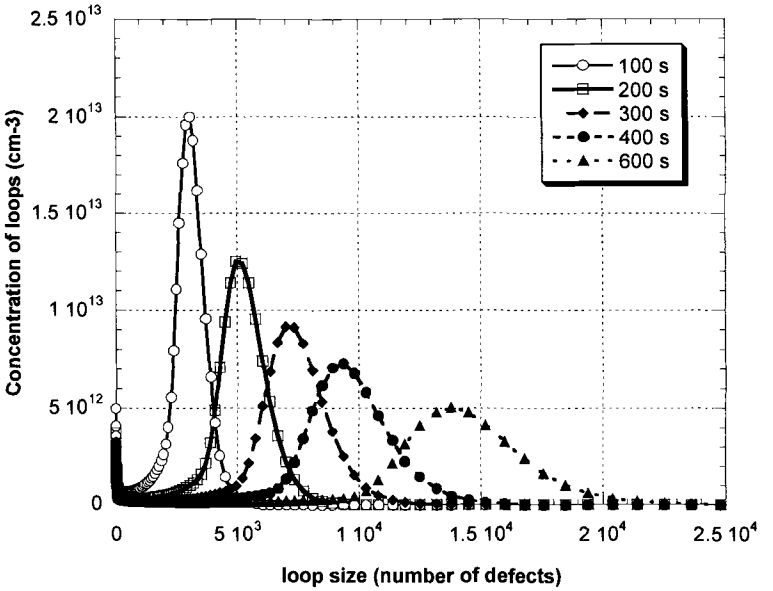


Figure 6-*Distributions of loop concentrations at 315 °C and different irradiation times.*

Table 4-*Computed Loop Density and Mean Diameter (3 MeV Electrons)*

density, cm^{-3}	size, nm
$1.9\ 10^{14}$	274

Comparison with experimental data (Table 2) shows that the computed density is two orders of magnitude lower than the experimental one and that the value given by the model for the average loop size is far too large. What can be the reason for this discrepancy between model results and experimental observations?

A plausible answer is related to the primary damage created by 3 MeV electrons. For such particles, the maximum transferred energy to target atoms is about 450 eV. Molecular dynamics simulations show that a fraction of the defects created in a few hundreds eV cascade in iron at 600 K clusters as di or tri-interstitials [20]. Such in-cascade clustering will result in a higher density of loops compared with the situation

where all defects are created as isolated Frenkel pairs. We have therefore slightly modified the model to take into account in cascade clustering. In the modified version, a fraction ε of the created defects is in the form of di-interstitials. Table 5 show that a value of $\varepsilon=4\ 10^{-4}$ results in a good agreement between the computed loop density and the experimental data. This value of ε is perfectly reasonable according to the molecular dynamics results. The agreement in the case of the mean loop size, although much better than previously, is still not very good, but could be improved as suggested above for the case of 1 MeV electron irradiations.

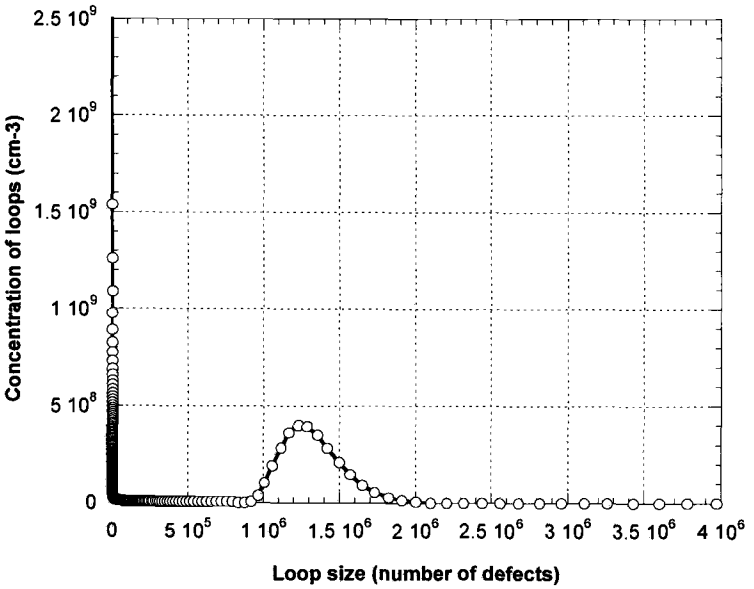


Figure 7-*Computed distribution of loop concentrations (3 MeV electrons).*

Table 5-*Loop Density and Mean Diameter Calculated with the Modified Model* ($\varepsilon = 4\ 10^{-4}$)

density, cm^{-3}	size, nm
$3.4\ 10^{16}$	18

Concerning the shape of the distribution of loop concentrations, we have to point out that the peak which is always present in the case of ε=0 has disappeared. The distribution now takes the form of a continuously decreasing function as shown in Figure 8. However, it is difficult to determine the shape of the experimental size

distribution of clusters from the TEM micrographs due to the fact that many loops have most probably a size which is below the resolution limit for imaging of such objects (about 1-1.5 nm).

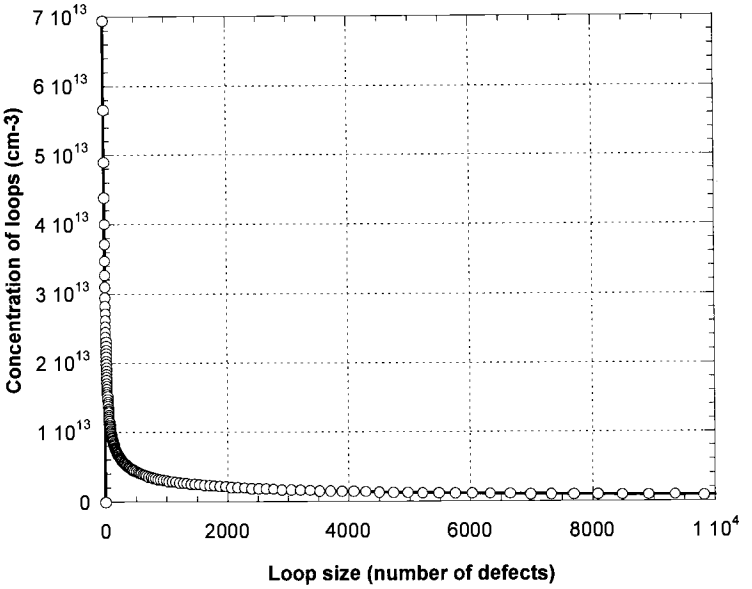


Figure 8-*Computed distribution of loop concentrations, modified model ($\varepsilon = 4\ 10^{-4}$).*

Summary and Conclusion

We have presented a rate theory model which describes the time evolution of vacancy and interstitial clusters in austenitic stainless steels under electron irradiation. The model combines discrete equations up to a given cluster size and continuous equations for larger interstitial clusters. A set of input parameters was found which gives a satisfactory agreement between calculated and measured interstitial clusters densities in the case of irradiations of a 316L stainless steel at high damage rate and different temperatures in a 1 MeV transmission electron microscope. Model predictions were then compared with microstructural observations of the steel irradiated at low damage rate with 3 MeV electrons. The agreement is poor if it is assumed in the model that all the created defects are Frenkel pairs. The model was slightly modified in order to include the creation of a small fraction of the defects in the form of di-interstitials, as suggested by molecular dynamics results. In this case a much better agreement is found.

It would be interesting to compare model predictions and microstructural data after irradiation at low flux with 1 MeV electrons, which generate only isolated defects. Furthermore, we intend to modify the model to take into account in-cascade clustering

for the case of neutron irradiation. Several austenitic stainless steels (304, 316LN, Ti-mod. 316) are currently being irradiated in an experimental reactor at 330 °C up to different doses, starting at 1 dpa. Different sets of model parameters will be determined for the various steels using 1 MeV electron irradiations as performed in this work, before comparing model results and experimental data.

References

[1] Cauvin, R., Goltrant, O., Rouillon, I., *Proceedings of the Third International Symposium on the Contribution of Materials Investigations to the Resolution of Problems Encountered in Pressurized Water Reactors* , SFEN, Fontevraud, 1994, pp. 54-65.

[2] Bench, M.W., Tappin, D.K. and Robertson, I.M., *Philosophical Magazine Letters*, Vol. 66, 1992, pp. 39-45.

[3] Johnson, R.A., *Journal of Nuclear Materials*, Vol. 83, 1978, p. 77.

[4] Ghoniem, N.M. and Cho, D.D., *Physica Statu Solidi (a)*, Vol. 54, 1979, p. 171.

[5] Stoller, R.E. and Odette, G.R., *Radiation Induced Changes in Microstructure: 13th International Symposium, ASTM STP 955*, F.A. Garner, N.H. Packan and A.S. Kumar, Eds., American Society for Testing and Materials, Philadelphia, 1987, pp. 371-392.

[6] Katoh, Y., Muroga, T., Kohyama, A., Stoller, R.E. and Namba,C., *Journal of Nuclear Materials,* Vol. 233-237, 1996, pp. 1022-1028.

[7] Hardouin Duparc, T.H.A., Thesis, Université d'Orsay, 1997.

[8] Kiritani, M., *Journal of the Physics Society*, Vol. 35, 1973, p. 95.

[9] Hayns, M.R., *Journal of Nuclear Materials*, Vol. 59, 1976, p. 175.

[10] Wolfer W.G., Mansur, C.K. and Sprague, *Radiation Effects in Breeder Reactor Structural Materials*, M. Bleiber, Ed., American Institute of Metallurgical Engineers, New York, 1977, p. 841.

[11] Stoller, R.E., *Journal of Nuclear Materials*, Vol. 244, 1997, pp. 195-204.

[12] Hayns, M.R., *Journal of Nuclear Materials*, Vol. 59, 1976, p. 1.

[13] Duensing, G., Hemmerich, H., Sassin, W. and Schilling, W., *International Conference on Vacancies and Interstitials in Metals*, North Holland Publ., Jülich, 1968, p.246.

[14] Barbu, A. and Martin, G., *Solid State Phenomena*, Vol. 30-31, 1993, p. 179.

[15] Heald, T.T. and Harbottle, J.E., *Journal of Nuclear Materials*, Vol. 67, 1977, p. 229.

[16] Bullough, R., Eyre, B.L. and Krishan, K., *Proceedings of the Royal Society*, Vol. A 346, 1975, p.81.

[17] Housseau, N. and Pelissier, J., *Journal of Nuclear Materials*, Vol. 119, 1983, pp. 317-325.

[18] Benkaddour, A., Dimitrov, C. and Dimitrov, O., *Journal of Nuclear Materials*, Vol. 217, 1994, pp. 118-126.

[19] Brown, L.M., Kelly, A. and Mayer, R.M., *Philosophical Magazine,* Vol. 19, 1969, p. 721.

[20] Phythian, W.J., Stoller, R.E., Foreman, A.J.E., Calder, A.F. and Bacon, D.J., *Journal of Nuclear Materials*, Vol. 223, 1995, pp. 245-261.

Qiu Xu,[1] Toshimasa Yoshiie,[1] and Michio Iseki[2]

Effects of Damage Rate on Formation of Voids and Dislocation Loops in Metals

Reference: Xu, Q., Yoshiie, T., and Iseki, M., **"Effects of Damage Rate on Formation of Voids and Dislocation Loops in Metals,"** *Effects of Radiation on Materials: 19th International Symposium ASTM STP 1366*, M. L. Hamilton, A. S. Kumar, S. T. Rosinski, and M. L. Grossbeck, Eds., American Society for Testing and Materials, West Conshohocken, PA, 2000.

Abstract: Effects of damage rate on the formation of voids and interstitial type dislocation loops in pure metals, such as Au, Cu, Ni, Fe and V, and alloys of Ni and V, were investigated. The specimens were irradiated at the Kyoto University Reactor (KUR) with improved temperature control. The dose rates of neutron irradiation were 4.4×10^{15} n/m^{2}s (E > 0.1 MeV) and 3.9×10^{17} n/m^{2}s (E > 0.1 MeV) at 573 K. By the total dose of about 7×10^{21} n/m^2 (E > 0.1 MeV), the loop density increased with increasing dose rate, whereas the growth behavior of microvoids depended on the dose rate and irradiated materials. In Cu, Fe and V, the concentration and the size of microvoids increased with increasing dose rate. In Au, the difference of microvoid formation between two dose rates was small. While in Ni, Ni-Cu and Ni-Ge, the size of microvoids increased with decreasing dose rate. The behaviors of formation of microvoids and dislocation loops were analyzed by the rate theory. It was clarified that the microvoid formation strongly relates to the mobility of vacancies. The calculation also showed that the nucleation of dislocation loops increases with increasing dose rate.

Keywords: neutron irradiation, damage rate, positron annihilation, vacancy clusters, gold, copper, nickel and vanadium

Introduction

For the development of nuclear materials, material irradiation experiments are usually performed with higher dose rate than that employed in power reactors. Dose rate effects on the microstructural evolution have been studied experimentally by using neutrons, heavy ions and electrons [1-5]. Some results show that the peak swelling temperature increases with increasing dose rate [1, 2], this phenomenon can be explained theoretically [6]. In these studies, however, the effect of dose rate on forma-

[1]Research Associate and Professor, respectively, Research Reactor Institute, Kyoto University, Kumatori-cho, Osaka-fu, 590-0494, Japan.
[2]Associate Professor, Faculty of Engineering, Nagoya University, Nagoya, Aichi 464-0814, Japan.

Copyright© 2000 by ASTM International www.astm.org

tion of defect clusters in the initial stage of irradiation has not been clarified. To understand the mechanism of microstructural evolution during irradiation, it is necessary to know the process of nucleation and growth of void and dislocation loops. In the present work, dose rate dependence of cluster formation in pure metals and alloys under the beginning of irradiation and the effect of additional element on it were investigated.

The irradiation temperature is also an important factor to dominate the microstructural evolution. In most of neutron irradiation experiments so far, however, the irradiation temperature, especially during the start-up and shutdown period, has not been controlled strictly. Recent studies showed that the temperature variation during the irradiation influences microstructural evolution [7-9]. In this study, the irradiation was carried out in the same reactor KUR with two facilities named Hydraulic Conveyer (Hyd) and Slant Exposure Tube (Sl) under well-controlled temperature by using an electric heater. The difference of neutron intensity was two orders of magnitude. As an example, Fig. 1 shows the primary knock-on atom (PKA) energy spectra for copper calculated by SPECTER code [10] in the Hyd and low temperature loop facility (LTL). The positron of Hyd is the center of reactor core, and those of Slant Exposure Tube (Sl) and LTL are symmetrical with respect to Hyd. So we consider the neutron spectra of Sl and LTL are almost the same. Although the neutron spectrum of Hyd is harder a little than that of LTL, the difference of PKA energy spectra was taken into account by using the damage rate. Another of characteristic of present work was that the start of irradiation was after reactor start-up, and the stop of irradiation was before reactor shutdown, the neutron flux was almost constant during the irradiation.

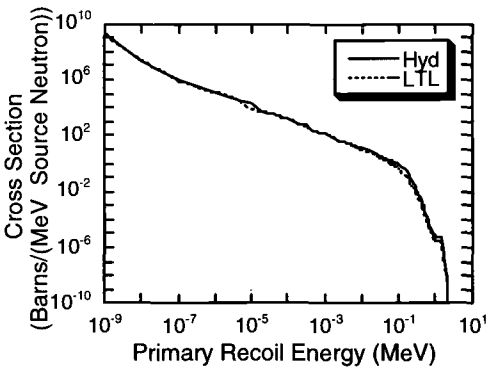


Figure 1 -- Primary knock-on atom energy spectra for copper calculated by SPECTER code. Copper was irradiated by Hydraulic Conveyer (Hyd) and low temperature loop facility (LTL) of KUR.

Experimental Procedure

Pure metals of Au, Cu, Ni, Fe, V, and V alloys of V-10Ti, V-20Ti, and Ni alloys

were tested in this study. In Ni alloys, 2at. % solute atoms of Si (-5.81%), Cu (+7.18%), Ge (+14.76%) and Sn (+74.08%) were added respectively to investigate the effect of volume size factor on the microstructural evolution. The values in parentheses are volume size factors, which are the ratio of difference of volume size between additional element and solvent element to the volume size of solvent element [11]. These specimens were irradiated in Hyd ($3.9x10^{17}$ n/m^{2}s (E > 0.1 MeV),*$6.4x10^{-8}$ dpa/s for Cu) and Sl ($4.4x10^{15}$ n/m^{2}s (E > 0.1 MeV), $6.0x10^{-10}$ dpa/s for Cu) of KUR at 573 K. The dose rate of former was about 100 times higher than that of latter. The total dose of irradiation in Hyd and Sl was $7.0x10^{21}$ n/m^2 (E > 0.1 MeV, 0.0012 dpa for Cu), and $6.3x10^{21}$ n/m^2 (E > 0.1MeV, 0.00087 dpa for Cu), and irradiation time was 5 and 400 hours, respectively. Specimens were sealed in a small specimen holder and a heater

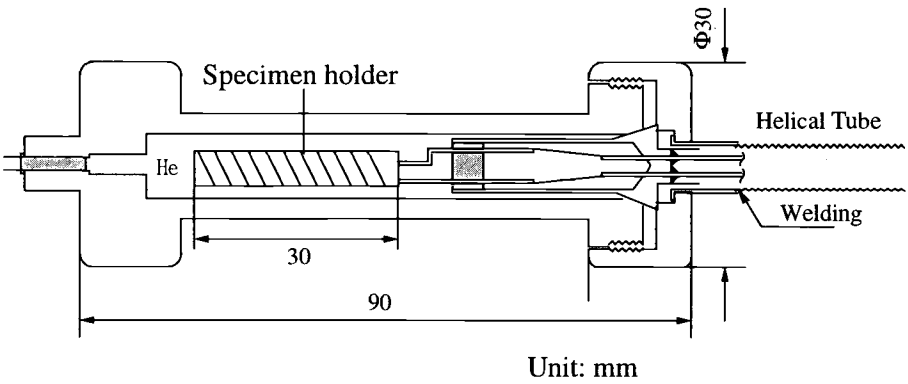


Figure 2 -- Schematic Drawing of the KUR Irradiation Capsule.

was wound directly on the holder, which was in an aluminum capsule as shown in Fig. 2. The temperature of the specimen holder, which was controlled within ±5 K during irradiation, measured by a thermocouple. Capsule was inserted to reactor after the reactor star-up, and pulled out of reactor before reactor shutdown. The temperature of specimens was increased to 573 K before irradiation and decreased to room temperature after irradiation.

After irradiation, positron lifetime measurement and electron microscopy observation were carried out. Positron lifetime was measured at room temperature by using a positron lifetime spectrometer with a time resolution of 190 psec. ^{22}Na (0.7MBq) was used as a positron source, which was sealed with Mylar film (5 μm in thickness).

Results

Pure Metals

Fig. 3 shows the typical positron lifetime spectra for Cu before and after irradiation by using the Hydraulic Conveyer and the Slant Exposure Tube. After irradiation, the lifetime spectrum became broad due to the formation of vacancy clusters.

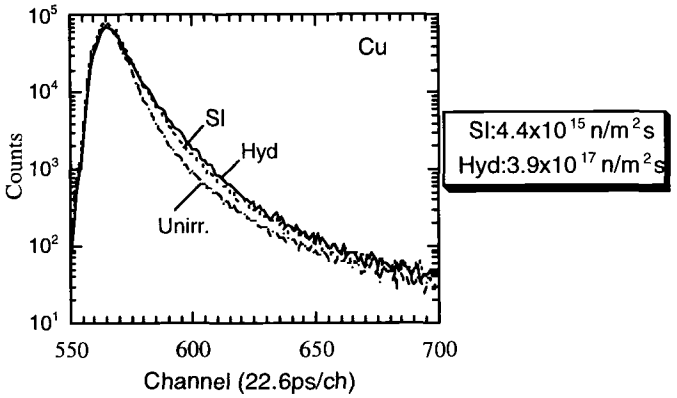


Figure 3 -- Typical positron lifetime spectra for Cu before and after irradiation by the Hydraulic Conveyer ($3.9x10^{17}$ n/m^2s) and the Slant Exposure Tube ($4.4x10^{15}$ n/m^2s).

Positron lifetimes were analyzed by the computer programs Resolution [12] and Positronfit Extended [13, 14] after subtracting the source-background. The results for pure metals are summarized in Table 1. τ_m is the positron mean lifetime resulting from single-component analysis of measured lifetime spectra. In order to see the change of the lifetime in more detail, the two-lifetime-component analysis was also made. The lifetime spectra for the irradiated specimens are well decomposed into two discrete components. The shorter lifetime τ_1 mainly comes from free positron in the matrix, and the longer lifetime τ_2 results from positrons trapped at defects. The lifetimes and the intensity are related to the size and the density of microvoids, respec-

Table 1 -- Positron Annihilation Lifetime of Pure Metals

Conditions / Samples	Unirr.	Hydraulic Conveyer					Slant Exposure Tube				
	τ_m	τ_m	τ_1	I_1	τ_2	I_2	τ_m	τ_1	I_1	τ_2	I_2
Cu	108	166	140	87	345	13	137	127	95	334	5
Fe	106	138	107	83	253	17	125	112	92	237	8
V	127	159	121	82	325	18	130	124	97	313	3
Au	120	154	133	90	362	10	149	131	92	386	8
Ni	106	155	126	83	283	17	146	111	86	368	14

Units of lifetime τ and intensity I are psec and %, respectively.

tively. After irradiation, the lifetime spectra of irradiated specimens indicate that the longer lifetime components τ_2 are between 199 psec and 386 psec, which show the existence of microvoids.

The positron lifetime of pure metals can be divided into three groups. In the first group (Cu, Fe, V), the lifetime τ_2 and its intensity increased with increasing dose rate. In the second group (Au), the difference of lifetime τ_2 and its intensity between the two dose rates was small. In the third group (Ni), in contrast to the first group, the lifetime τ_2 increased with decreasing dose rate, although the difference of its intensity was small.

Figs. 4 and 5 show the dark-field weak-beam images of microstructures formed in Cu and Ni. The main defect clusters observed were stacking fault tetrahedra (SFT) in Cu, and interstitial type dislocation loops in Ni. Fig. 6 shows the number density of SFT in Cu and dislocation loops in Ni. The densities of SFT and loops formed in the irradiation with high dose rate were 7 times and 5 times higher than that in the irradiation with low dose rate, respectively.

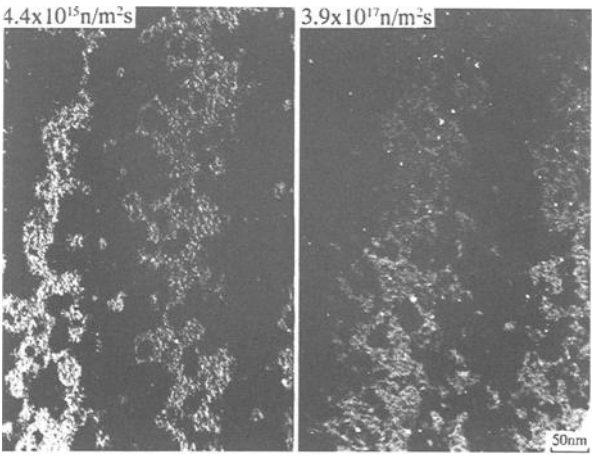


Figure 4 -- Dark-field weak-beam images of SFT formed in Cu irradiated with two different dose rates.

Ni Alloys

Table 2 lists the positron lifetime of Ni alloys. To understand the effect of additional minor elements, the positron lifetimes of pure Ni are also shown in the table. In Ni-Si alloy, the longer lifetime components τ_2, which were smaller than those in Ni, increased with increasing dose rate. Just the same as the lifetime τ_2 in Ni, however,

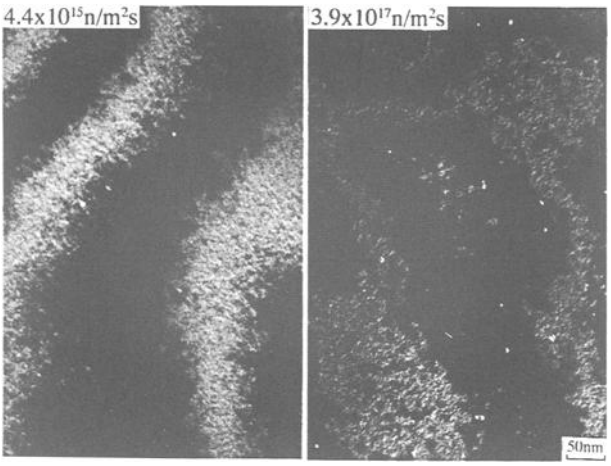


Figure 5 -- Dark-filed weak-beam images of dislocation loops formed in Ni irradiated with two different dose rates.

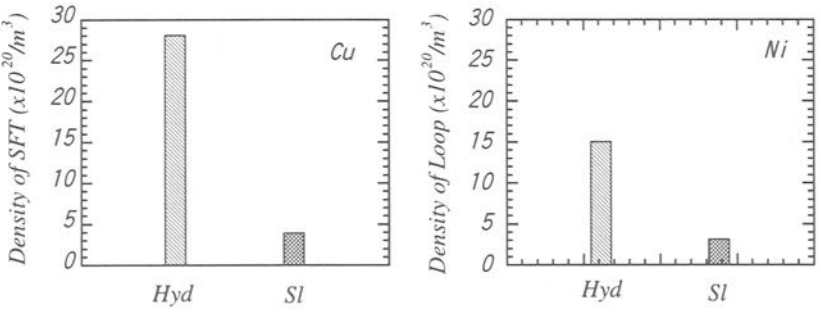


Figure 6 -- Changes in the number density of SFT in Cu and dislocation loops in Ni. The specimens were irradiated in the Hydraulic Conveyer (Hyd) and Slant Exposure Tube (Sl) of KUR

the lifetime τ_2 in Ni-Cu and Ni-Ge alloys decreased with increasing dose rate. In Ni-Sn alloy, the lifetime spectra were not decomposed into two components, since the density of microvoids was very low. The nucleation of microvoids was suppressed strongly by addition of Sn or Si.

Table 2 -- Positron Annihilation Lifetime of Ni Alloys

Conditions / Samples	Unirr.	Hydraulic Conveyer					Slant Exposure Tube				
	τ_m	τ_m	τ_1	I_1	τ_2	I_2	τ_m	τ_1	I_1	τ_2	I_2
Ni-Si	108	131	105	56	227	44	119	102	74	199	26
Ni	106	155	126	83	283	17	146	111	86	368	14
Ni-Cu	107	129	106	74	243	26	124	101	78	260	22
Ni-Ge	107	143	108	66	292	34	118	108	92	328	8
Ni-Sn	109	132	—	—	—	—	127	—	—	—	—

Units of lifetime τ and intensity I are psec and %, respectively.

V Alloys

The positron lifetimes in V alloys are shown in Table 3, in which the data of pure V are also included. In comparison to pure V, the lifetime τ_2 decreased in V-10Ti irradiated with high dose rate. Two-lifetime-component analysis of measured lifetime spectra could not be carried out in V-10Ti irradiated with low dose rate, because the density of microvoids was too low to detect. With increasing the amount of Ti, the formation of microvoids was suppressed, and two-lifetime-component decomposition was impossible in both irradiation.

Table 3 -- Positron Annihilation Lifetime of V Alloys

Conditions / Samples	Unirr.	Hydraulic Conveyer					Slant Exposure Tube				
	τ_m	τ_m	τ_1	I_1	τ_2	I_2	τ_m	τ_1	I_1	τ_2	I_2
V	127	159	121	82	325	18	130	124	97	313	3
V-10Ti	142	155	141	82	206	18	149	—	—	—	—
V-20Ti	150	163	—	—	—	—	157	—	—	—	—

Units of lifetime τ and intensity I are psec and %, respectively.

Discussion

Model Description

The experimental results show that the density and the size of microvoid depend

not only on dose rate but also on the materials. In order to investigate qualitatively the effects of dose rate on the growth of microvoid, the simulations were carried using the rate theory. The effects of cascade damage were not considered in this study since even the microvoids were formed by cascade damage, the growth of them was caused by absorbing vacancies. The assumptions used in the calculation are following:
(1) Displacement occurs in the form of Frenkel pairs and the defect production is homogeneous in space and in time.
(2) Mobile defects are single interstitials and vacancies.
(3) Di-interstitials are stable enough to be the nuclei of interstitial clusters.
The equations for concentrations of interstitials (C_I), vacancies (C_V) and interstitial type dislocation loops (C_L) are given by

$$dC_I/dt = P(1-C_V)(1-Z_{IV}C_V) - Z_{IV}(M_I+M_V)C_IC_V - 2Z_{II}M_IC_I^2 - Z_{LI}M_I(C_{LI}C_L)^{1/2}C_I - Z_{SI}M_IC_{SI}C_I \quad (1)$$

$$dC_V/dt = P(1-C_V)(1-Z_{IV}C_V) - Z_{IV}(M_I+M_V)C_IC_V - Z_{LV}M_V(C_{LI}C_L)^{1/2}C_V - Z_{SV}M_VC_{SV}C_V \quad (2)$$

$$dC_L/dt = Z_{II}M_IC_I^2 \quad (3)$$

where P is the point defect generation rate, Z_{ij} the number of sites for the reactions between the defects of i and j types or between the sink of i and defects of j, C_{SI} and C_{SV} the sink concentrations for interstitials and vacancies, respectively. C_{LI} is the concentration of interstitials incorporated in the loops. Point defect mobilities M_I and M_V are expressed by $\nu \exp(-E_m^I/kT)$ and $\nu \exp(-E_m^V/kT)$, where ν is an attempt frequency, k Boltzman constant, T the absolute temperature, E_m^I and E_m^V are migration energy of interstitials and vacancies, respectively.

The reaction processes of point defects have been made in many metals and alloys irradiated with electrons by utilizing a high voltage electron microscope (HVEM). The experimental results can be explained very well by numerical calculation by using the rate theory [15, 16]. By referring to the parameters of pure metals [17, 18], in the present calculations, the number of reaction sites Z_{II}, Z_{IV}, Z_{LI}, Z_{SI} and Z_{SV} were set to be 10, 100, 10, 1, 1, respectively. The production rates of point defect using the Hydraulic Conveyer and the Slant Exposure Tube are 6.4×10^{-8} and 6.0×10^{-10} dpa/s, the irradiation temperature 573 K.

Effect of Vacancy Mobility

Fig. 7 shows the change of interstitial and vacancy concentration as a function of irradiation time at 573 K. Here, the migration energy of interstitials is 0.15 eV, and the migration energies of vacancies are 0.7, 0.9 and 1.2 eV, which correspond to vacancy

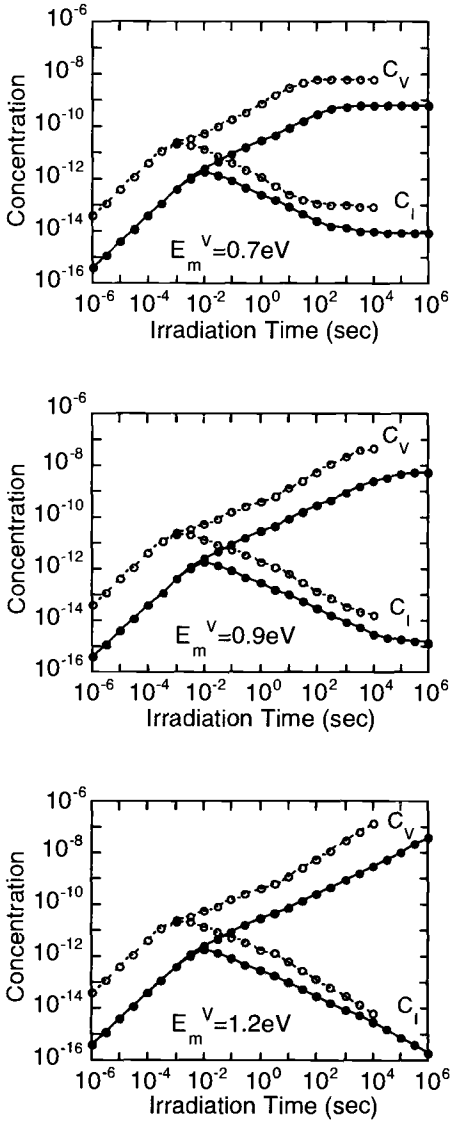


Figure 7 -- Changes in vacancy and interstitial concentration as a function of irradiation time at 573 K under the dose rates of $6.4x10^{-8}$ dpa/s (○) and $6.0x10^{-10}$ dpa/s (●).

migration energies of Cu, Au and Ni, respectively. The concentrations of interstitials and vacancies in the irradiation with the dose rate of 6.4×10^{-8} dpa/s are higher than that in the irradiation with the dose rate of 6.0×10^{-10} dpa/s. The irradiation dose needed for interstitial and vacancy concentration to reach their saturation values increases with increasing dose rate. The concentration of interstitials and vacancies influences the nucleation and growth of defect clusters. The arrival rate of interstitials and vacancies to defect clusters is proportional to their migration efficiency defined as $M_I C_I$ for interstitial and $M_V C_V$ for vacancy. The behavior of defect clusters depends on the difference between $M_I C_I$ and $M_V C_V$. For example, if $M_I C_I$ is larger than $M_V C_V$, the nucleation and the growth of interstitial clusters are promoted, while those of vacancy clusters are suppressed. Fig. 8 shows the change of migration efficiencies $M_I C_I$ and $M_V C_V$ as a function of irradiation time. The migration efficiency $M_I C_I$ is larger than $M_V C_V$ in the initial stage of irradiation, and it becomes equal to $M_V C_V$ with increasing irradiation time. The required irradiation time when the migration efficiency $M_I C_I$ is equal to $M_V C_V$ becomes short with decreasing the migration energy of vacancies. In addition to this, the total dose needed for $M_I C_I$ to equal $M_V C_V$ with high dose rate is higher than that with low dose rate, because more interstitials recombine with vacancies during the irradiation with high dose rate.

As the results of calculations, in Cu, the migration efficiency $M_I C_I$ is equal to $M_V C_V$ after 10^3 sec in the irradiation with high dose rate and 10^4 sec in the irradiation with low dose rate, the nucleation of interstitial and vacancy clusters is not suppressed in both irradiation. The densities of interstitial and vacancy clusters are higher in the irradiation with high dose rate than those in the irradiation with low dose rate, since the concentration of point defects is high in the former. In Ni, however, the migration energy of vacancies is larger than that in Cu. The migration efficiency $M_I C_I$ is higher than $M_V C_V$ in both irradiation, and the difference between $M_I C_I$ and $M_V C_V$ is large in the irradiation with high dose rate. In this case, the nucleation and the growth of vacancy clusters are suppressed strongly. Consequently, the density and the size of vacancy clusters in the irradiation with low dose rate are higher and larger than those in the irradiation with high dose rate. If the formation of precipitates relates to the diffusion of vacancies, they are also promoted with low dose rate [19]. In contrast to the behavior of vacancy clusters, the density of interstitial clusters increases with increasing the dose rate. The microvoid formation in Au, Fe and V can be understood by the same analysis.

Effect of Alloy Elements

In Ni alloys, no strong interaction was observed between the interstitials and the oversize atoms of Cu and Ge [20]. The formation of vacancy clusters in these alloys is similar to that in pure Ni. However, undersize atom of Si and large oversize atom of Sn interact with both interstitials and vacancies [20, 21]. The recombination of interstitial and vacancy increases by addition of Si or Sn, and the formation of vacancy clusters is suppressed.

The gaseous impurities in V or V alloys, such as O and N, play an important role in the swelling and embrittlement [22, 23]. Since these impurities also interact with Ti, the formation of microvoids is suppressed by addition of Ti in V alloys.

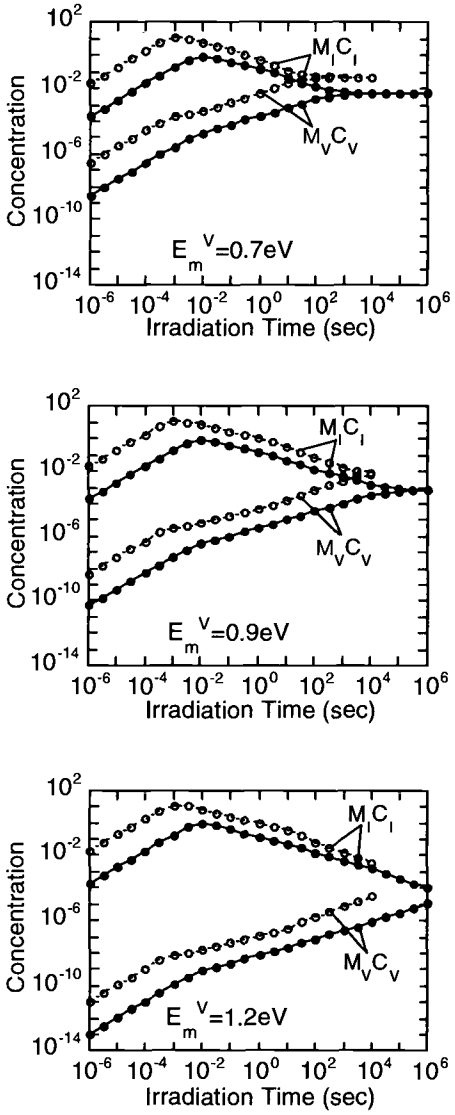


Figure 8 -- Changes in migration efficiencies M_IC_I and M_VC_V as a function of irradiation time at 573 K under the dose rates of $6.4x10^{-8}$ dpa/s (○) and $6.0x10^{-10}$ dpa/s (●).

Conclusion

In order to understand the effects of damage rate on the formation of voids and interstitial type dislocation loops, several pure metals and alloys were irradiated with two dose rates by changing neutron intensity in two orders of magnitude. The formation of dislocation loops is promoted by increasing dose rate, while the formation of microvoids depends on the dose rate and materials. The nucleation of vacancy clusters increases with increasing the dose rate when the concentration of interstitials and vacancies are in their steady state; on the other hand, the nucleation of vacancy clusters decreases with increasing the dose rate when the concentration of interstitials and vacancies are before their steady state.

Acknowledgments

This study was partly supported by the Grants-in-Aid sponsored by Ministry of Education, Science, Sports and Culture (Monbusho) of Japan.

References

[1] Packan, N. H., Farrell, K., and Stiegler, J. O., "Correlation of Neutron and Heavy-ion Damage," *Journal of Nuclear Materials*, Vol. 78, 1978, pp. 143-155.

[2] Glowinski, L., Fiche, C., and Lott. M., "Study of the Formation of Voids in Copper Irradiated with 500 KeV Cu^+ Ions " *Journal of Nuclear Materials*, Vol. 47, 1973, pp. 295-310.

[3] Muroga, T., Watanabe, H., Araki, K., and Yoshida, N., "Fission-Fusion Correlation of Void Swelling in Pure Nickel," *Journal of Nuclear Materials*, Vol. 155-157, 1988, pp. 1290-1295.

[4] Muroga, T., Watanabe, H., and Yoshida, N., "Correlation of Fast Neutron, Fusion Neutron and Electron Irradiations Based on the Dislocation Loop Density," *Journal of Nuclear Materials*, Vol. 174, 1990, pp. 282-288.

[5] Woo, C. H., Sigh, B. N., and Semenov, A. A., "Recent Advances in the Understanding of Damage Production and its Consequences on Void Swelling, Irradiation Creep and Growth," *Journal of Nuclear Materials*, Vol. 239, 1996, pp. 7-23.

[6] Mansur, L. K., "Correlation of Neutron and Heavy- Ion Damage," *Journal of Nuclear Materials*, Vol. 78, 1996, pp. 156-160.

[7] Kiritani, M., "The Need for Improved Temperature Control during Reactor Irradiation," *Journal of Nuclear Materials*, Vol. 160, 1988, pp. 135-141.

[8] Kiritani, M., Yoshiie, T., Kojima, S., Satoh, Y., and Hamada, K., "Fission-Fusion Correlation by Fission Reactor Irradiation with Improved Control, "

Journal of Nuclear Materials, Vol. 174, 1990, pp. 327-351.

[9] Yoshida, N., Xu, Q., Watanabe, H., Miyamoto, Y., and Muroga, T., "Effect of Cyclic Temperature Change on Microstructural Evolution in Austenitic Stainless Steel under Fission Neutron Irradiation," *Journal of Nuclear Materials*, Vol. 212-215, 1994, pp. 471-475.

[10] Greenwood, L. R., and Simither, R. K., "Specter: Neutron Damage Calculations for Materials Irradiations,", Argonne National Laboratory, *ANL/FPP/TM-97*, 1985.

[11] King, H. W., "Quantitative Size-Factors for Metallic Solid Solutions,"*Journal of Materials Science*, Vol. 1, 1966, pp. 79-90.

[12] Kirkegaard, P., Eldrup, M., Morgensen. O. E., and Pedersen, N., "Program System for Analyzing Positron Lifetime Spectra and Angular Correlation Curves," *Comput. Phys. Commun.*, Vol. 23, 1981, pp. 307-335.

[13] Kirkegaard, P., and Eldrup, M., "A Versatile Program for Analyzing Positron Lifetime Spectra," *Comput. Phys. Commun.*, Vol. 3, 1972, pp. 240-55.

[14] Kirkegaard, P., and Eldrup, M., "Positronfit Extended: A New Version of A Program for Analyzing Positron Lifetime Spectra," *Comput. Phys. Commun.*, Vol. 7, 1974, pp. 401-409.

[15] Kiritani, M., and Hiroshi, T., "Dynamic Studies of Defect Mobility Using High Voltage Electron Microscopy," *Journal of Nuclear Materials*, Vol. 69-70, 1978, pp. 277-309.

[16] Watanabe, H., Aoki, A., Murakami, H., Muroga, T., and Yoshida, N., "Effects of Phosphorus on Defect Behavior, Solute Segregation and Void Swelling in Electron Irradiated Fe-Cr-Ni Alloys," *Journal of Nuclear Materials*, Vol. 155-157, 1988, pp. 815-822.

[17] Yoshida, N., and Kiritani, M., "Point Defect Clusters in Electron-Irradiated Gold," *Journal of the Physical Society of Japan*, Vol. 35, 1973, pp. 1418-1429.

[18] Kiritani, M., Yoshida, N., Takata, H., and Maehara, Y., "Growth of Interstitial Type Dislocation Loops and Vacancy Mobility in Electron Irradiated Metals," *Journal of the Physical Society of Japan*, Vol. 38, 1975, pp. 1677-1686.

[19] Yanagita, S., Xu, Q., Yoshiie, T., and Ino, H., "Neutron Irradiation Rate Dependence of Damage Structure in Fe-Cu Model Alloy," *Effects of Radiation on Materials, 19th International Symposium, ASTM STP 1366*, M. L. Hamilton, A. S. Kumar, S. T.Rosinski and M. L. Grossbeck, Eds., American Society for Testing and Materials, 1999 (These proceedings).

[20] Hamada, K., Kojima, S., Ogasawara, Y., Yoshiie, T., and Kiritani, M., "Role of Solute Atoms on Microstructural Evolution in Neutron Irradiation Nickel,", *Journal of Nuclear Materials*, Vol. 212-215, 1994, pp. 270-274.

[21] Piller, R. C., and Marwick, A. D., "Radiation-Enhanced Diffusion and Segregation in Ni and Ni (Si) Alloy: The Effects of Point-Defect Trapping,", *Journal of Nuclear Materials*, Vol. 83, 1979, pp. 42-47.

[22] Matsui, H., Fukumoto, K., Smith, D. L., Chung, H. M., Witzenburg, W., and Votinov, S. N., "Status of Vanadium Alloys for Fusion Reactors," *Journal of Nuclear Materials*, Vol. 233-137, 1996, pp. 92-99.

[23] Ryazanov, A. I., Manichev, V. M., and Witzenburg, W., "Influence of Helium and Impurities on the Tensile Properties of Irradiated Vanadium Alloys," *Journal of Nuclear Materials*, Vol. 227, 1996, pp. 304-311.

S. I. Porollo,[1] Yu. V. Konobeev,[1] A. S. Kruglov,[1] Yu. M. Pevchikh,[1] and F. A. Garner[2]

Stress-Affected Dislocation Development of Stainless Steel During Neutron Irradiation

Reference: Porollo, S. I., Konobeev, Y. V., Kruglov, A. S., Pevchikh, Y. M., and Garner, F. A., **"Stress-Affected Dislocation Development of Stainless Steel During Neutron Irradiation,"** *Effects of Radiation on Materials: 19th International Symposium, ASTM STP 1366,* M. L. Hamilton, A. S. Kumar, S. T. Rosinski, and M. L. Grossbeck, Eds., American Society for Testing and Materials, West Conshohocken, PA, 2000.

Abstract: When stainless steels are irradiated at 530°C with neutrons to ~0.2 dpa at stresses above the yield stress, the evolution of dislocation microstructure is very different from that which occurs when stresses are held below the yield stress. The dislocation network that forms is more uniform and crystallographically-oriented than the cell structure that forms in the absence of irradiation. Small defect clusters form instead of Frank loops, but their density decreases with the applied stress level.

Whereas network dislocations, defect clusters and Frank loops evolving at lower stress levels primarily communicate indirectly through their competition for point defects, stress-induced glide of dislocations is strongly activated above the yield strength and there is a strong, direct physical interaction between dislocations and loops that changes the nature of the saturation state of both components.

Keywords: stainless steel, dislocations, neutron irradiation

Background

It is well-known that neutron irradiation of stainless steels while under stress leads to a microstructure composed of network dislocations, Frank loops and voids that is strongly dependent on the applied stress state, as reviewed in reference 1. However, the majority of data on stress-affected dislocation and void evolution were generated in experiments where the applied stress did not exceed the yield stress of the steel. This limitation on data availability reflects in general the engineering necessity to avoid both inadvertent plastic strains and also significant amounts of thermal creep under all conceivable normal operating conditions. In effect, why generate data for unanticipated

[1] Head of Hot Laboratory, Head of Nuclear Materials Division, Leading Investigator, Leading Developer, respectively, Institute of Physics and Power Engineering, Obninsk, Russian Federation.

[2] Senior Staff Scientist, Pacific Northwest National Laboratory, Richland, WA USA.

Copyright© 2000 by ASTM International www.astm.org

or undesired conditions?

However, from the scientific viewpoint, it is very useful to study irradiation creep at stress levels above the yield point. The information gained may also be useful for predicting behavior during off-normal conditions of reactor operation.

This paper explores the microstructural development of stainless steels at higher applied stress levels. Some portions of this work have been published in Russian earlier [2].

Experimental Details

The steel employed was 0X16H15M3b in the annealed condition, with composition in wt% of Fe-(15-16)Ni-(15-16.5)Cr-(2.7-3.2)Mo-(0.4-0.8)Mn-(0.3-0.6)Si-0.9Nb-(0.04-0.05C)-(<0.02)P. The specimens prepared for microscopy were machined from various portions of 0.4-0.5 mm thick tensile specimens after in-pile creep testing in the BR-10 fast reactor. The specimens were irradiated at a radial distance of 43 cm in the core midplane, where the damage rate is 3.34 dpa per 10^{22} n cm^{-2} (E>0.1 MeV). The test apparatus and test procedures are described in detail in reference 3.

The irradiation conditions were 530°C, with tensile stress levels of 0, 24 and 30 Kg/mm^2 (0, 235, 294 MPa) and 5.8 x 10^{20} n cm^{-2} (E>0.1 MeV) at a neutron flux density of ~1 x 10^{14} n cm^{-2} s^{-1}. This dose corresponds to ~0.19 dpa. Reference specimens were also subjected to an out-of-pile creep test at the same stress levels and temperature. Electron microscopy was conducted at 100 KeV using standard procedures.

Results

As shown in Table 1 and Figure 1 the microstructural components are primarily network dislocations and small black-spot clusters on the order of 20-30 Å (2-3 nm) diameter. Nb(C,N) precipitates were also formed. Although the displacement dose was rather low, there was a total lack of the larger dislocation loops normally observed in stainless steel at this temperature, as can be confirmed in the micrographs shown in Figures 2-6. The presence of large dislocation segments implies that some loops must have formed and unfaulted earlier, however.

The cluster density fell with increasing stress and the network dislocation density increased with stress, as shown in Figure 1. There was no apparent effect of the radiation on the network dislocation density, however. The density was essentially the same for both the radiation creep and thermal creep tests.

The most significant microstructural difference lay in the orientation and distribution of the network dislocations. The stressed but unirradiated specimens exhibit the typical tangled cell structure observed in thermal creep tests, with the dislocation density rising with increasing stress level. The irradiated specimens exhibit a much more regular distribution of dislocations, however, with relatively straight dislocation segments aligned on {111} slip planes.

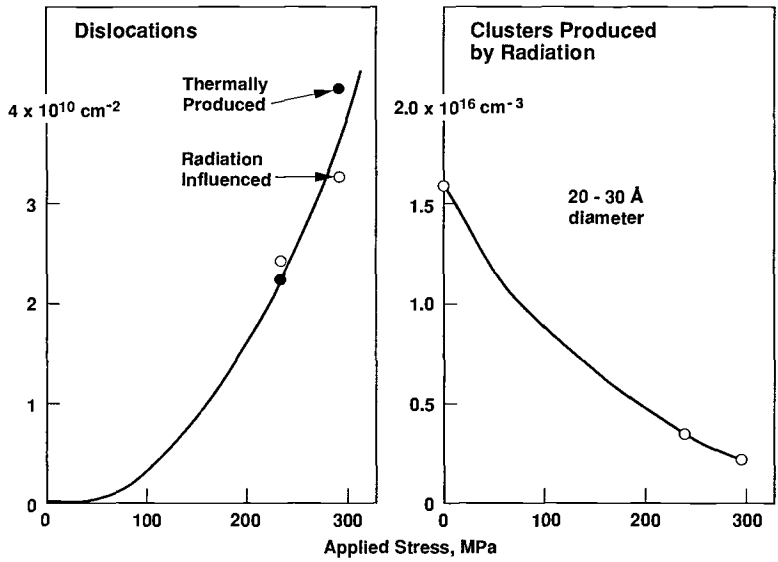


Figure 1 - *Influence of radiation and stress on the evolution of dislocation microstructure in 0X16H15M3b at 530 °C and 5.8 x 10^{20} n/cm^2 (E>0.1 MeV).*

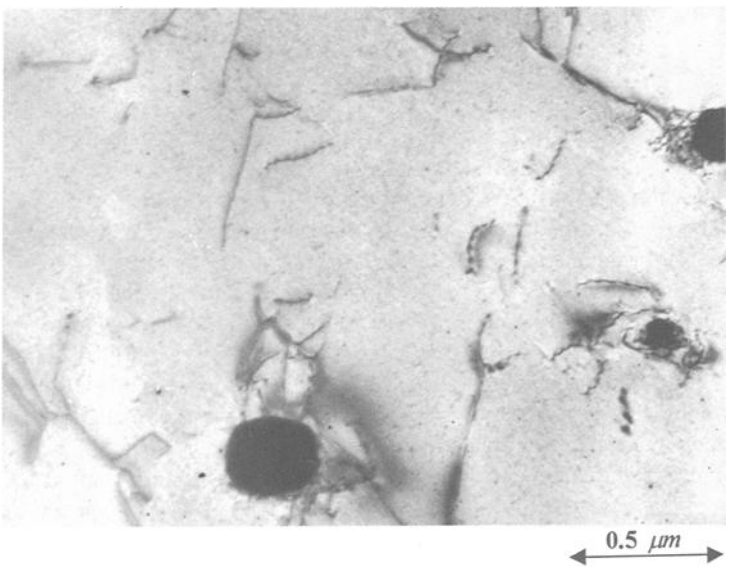


Figure 2 - *Microstructure formed during irradiation but without stress, showing a low density of dislocations, black spot clusters and some large Nb (C,N) precipitates.*

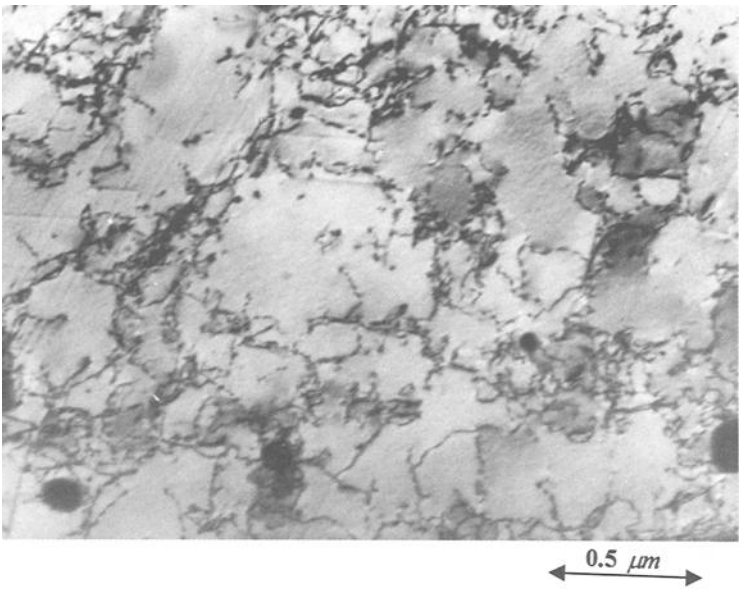


Figure 3 - *Microstructure formed in the absence of irradiation at a uniaxial stress of 24 Kg/mm^2, showing initial stage of dislocation cell formation.*

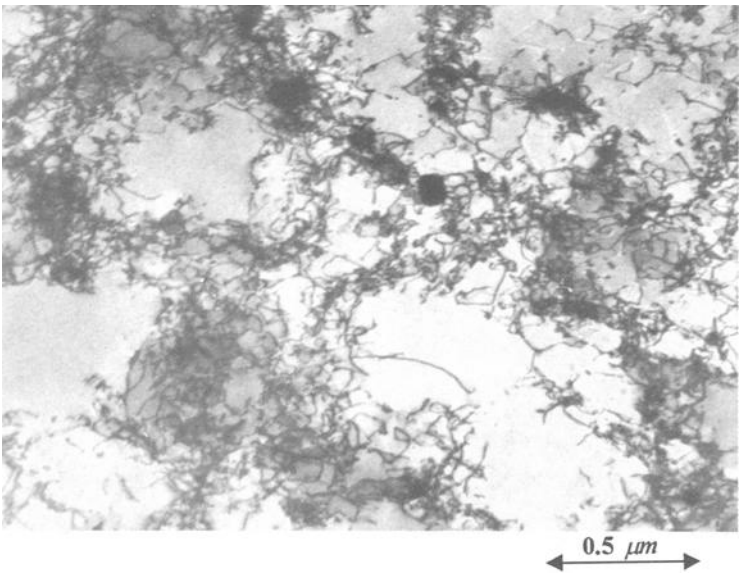


Figure 4 - *Microstructure formed in the absence of irradiation at a uniaxial stress of 30 Kg/mm^2, showing advanced stage of dislocation cell formation.*

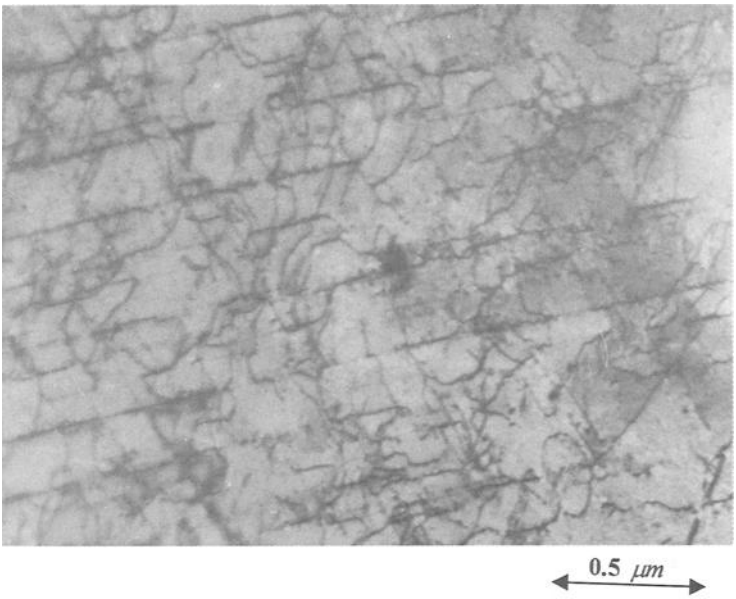


Figure 5 - *Microstructure formed during irradiation at 24 Kg/mm^2, showing alignment of dislocations with a more uniform distribution.*

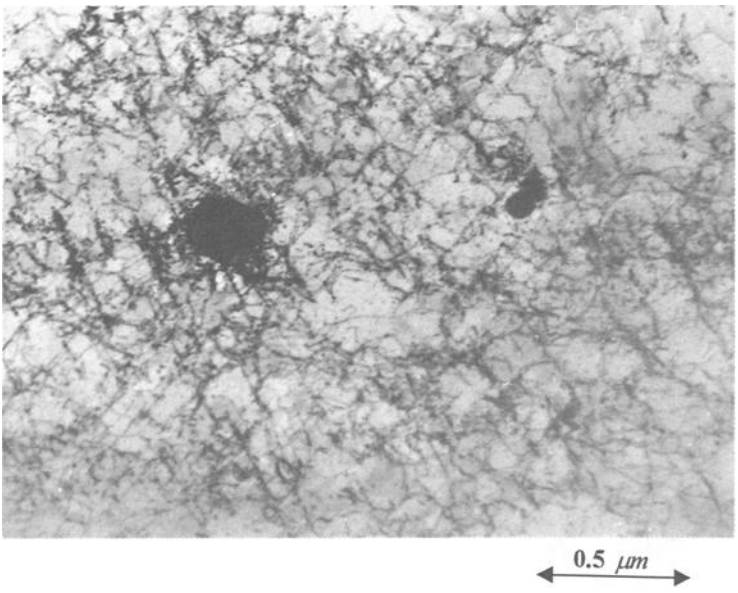


Figure 6 - *Microstructure formed during irradiation at 30 Kg/mm^2, showing highly aligned distribution of dislocations.*

Table 1 - *Microstructural Development Arising from Applied Stress and Irradiation*

Stress, Kg/mm^2*	Fluence E>0.1 MeV	Dislocation Density, cm^{-2}	Cluster Density, cm^{-3}	Cluster Diameter, Å
0	0	5×10^8	0	0
0	5.8×10^{20}	6×10^8	16×10^{15}	20-30
24	0	2.3×10^{10}	0	0
30	0	4.2×10^{10}	0	0
24	5.8×10^{20}	2.4×10^{10}	3.6×10^{15}	20-30
30	5.8×10^{20}	3.3×10^{10}	2.4×10^{15}	20-30

*24 and 30 Kg/mm^2 are 235, 294 MPa, respectively.

Discussion

Several conclusions can be drawn from this study. First, the total number of network dislocations observed in these specimens is primarily due to the stress level and not the irradiation. Irradiation only affects their alignment and distribution. The density does not exceed the mid -10^{10} cm^{-2} saturation level that usually occurs in both stressed and unstressed specimens during irradiation [*1,4*].

Second, the small clusters formed by irradiation are either directly removed by moving dislocations or by the stronger competition for point defects as dislocations increase in density. Finally, the presence of moving network dislocations precludes the formation and the long-term survival of larger Frank loops.

On the basis of these data alone, one might suspect that the quoted irradiation temperature was possibly incorrect, and that this might account for the lack of Frank loops. However, in reviewing a series of published and original data, Loguntsev and coworkers came to the same conclusion concerning stress-affected dislocation evolution [*5*]. They found that if the stress is below the yield stress Frank loops are formed during irradiation. Above the yield stress, however, Frank loops are not formed and dislocation networks and cells of varying perfection form instead.

Third, it appears that very little displacement dose is required to generate the crystallographically oriented arrays of dislocations. This implies that radiation significantly accelerates the movement of dislocations.

Grabova and coworkers [*6*] also conducted irradiations on stainless steels at stresses above the yield stress. They deduced the dislocation density from x-ray line broadening measurements of irradiated specimens. They noted that while the dislocation density in thermal creep tests was dependent on both stress level and temperature, the temperature dependence disappeared with irradiation, as shown in Figure 7. Note that

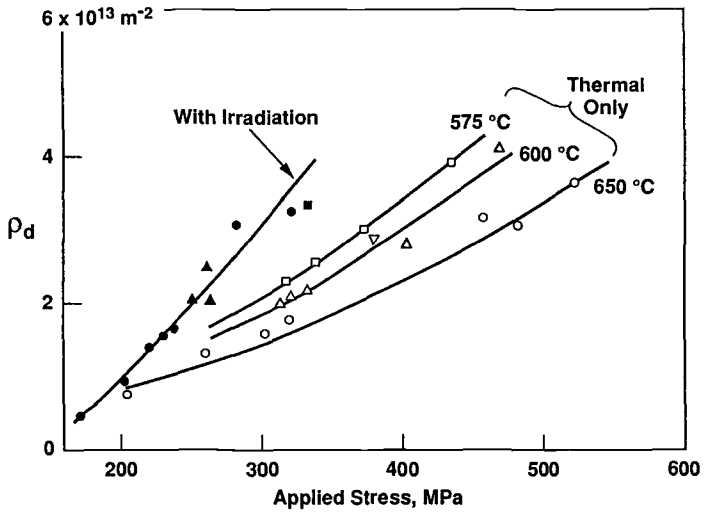


Figure 7 - *Effect of radiation and temperature on dislocation density during thermal creep of annealed 03Kh20N45M4BCh stainless steel [6]. Note the independence of temperature during irradiation.*

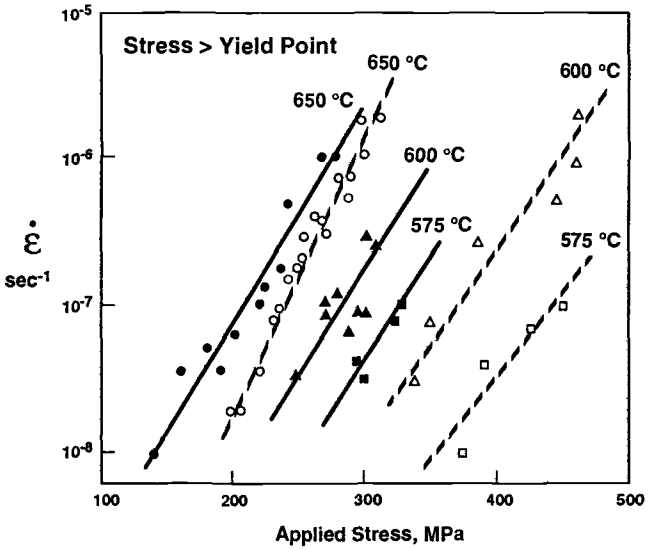


Figure 8 - *Effect of radiation and temperature on the thermal creep rate of 03Kh20N45M4BCh stainless steel, showing that the radiation-induced acceleration of the creep rate is greatest at lower temperatures. Dotted lines are thermal creep only. Solid lines are radiation-enhanced creep in SM-2 (575, 600 °C) and RBT (650 °C) reactors [6].*

Grabova's results show that the densities approach the radiation-induced densities as the temperature falls in the range 650 to 575°C. Thus the current results showing no difference in dislocation density between thermal and irradiation creep studies at 530°C are probably compatible with the results of Grabova.

Grabova also noted that there was an increase in dislocation velocity and the resultant creep rate (Figure 8) with irradiation, but there was no change in obstacle character, probably indicating that the dislocation's primary obstacle was another dislocation. Drawing from the current results, this suggests that the dislocation distribution is not as important as the dislocation density in determining the creep rate.

From the current studies and those of Loguntsev's and Grabova's groups, the following mechanisms appear to be operating. In the absence of radiation, stresses above the yield stress activate dislocation sources and produce high densities of dislocations whose movement is impeded by other dislocations. Local inhomogeneities in obstacle distribution lead to cell formation which reinforces the inhomogeneity. Radiation provides large fluxes of point defects that allow dislocations to easily climb over obstacles and glide to the next obstacle. This reduces the inhomogeneity and also allows straighter dislocation segments to develop. While the velocity of an individual dislocation may increase with irradiation, the overall density is limited by irradiation temperature only. It is thought to be particularly significant that the highest dislocation densities observed are no larger than that known as the saturation level for both stressed and unstressed material during irradiation.

The small clusters that form are either swept up by moving dislocations or are reduced by the competition of network dislocations for point defects, lowering the supersaturations necessary for cluster nucleation.

The current data may cast some light on stress-affected swelling data published earlier by Bates and Gilbert [*7*], and confirmed later by Shamardin and coworkers [*8*]. Void swelling at a given dose and temperature usually increases linearly with applied stress until the yield stress is exceeded, and then the swelling drops. The net effect of stress is only exerted on the incubation period, however, and not on the steady-state swelling rate [*9,10*]. Since both dislocation loops and network dislocations are normally cited to influence the nucleation of voids, it is not surprising that the absence of Frank loops at stress levels above the yield may somewhat delay the onset of accelerated swelling.

Acknowledgements

This work has been sponsored by the Civilian Research and Development Foundation under Grant RE2-123.

References

[1] Garner, F. A. and Gelles, D. S., *Journal of Nuclear Materials,* Vol. 159, 1988, pp. 286-309.

[2] Porollo, S. I., Shcherbak, V. I., Dmitriyev, V. D., Kruglov, A. S., and Pevchikh, Yu. M., *Fiz. Metal. Metalloved.*, Vol. 49, 1980, pp. 1302-1304.

[3] Bulkanov, M. G., Kruglov, A. S., and Pevchikh, Yu, M., Vapr. atomnoy nauki I tekniki, ser. Radiatsionnoye Materialovedeniye, Metodika I technika oblucheniya, Vol. 2, 1977, pp. 3-6.

[4] Garner, F. A., *Journal of Nuclear Materials,* Vol. 205, 1993, pp. 98-117.

[5] Logunstsev, Ye. N., Safonov, V. A., Tyumentsev, S. N., Kozlov A. V., and Nalesnik, V. M., *Fiz. Metal. Metalloved.*, Vol. 57, 1984, pp. 802-807.

[6] Grabova, R. B., Goncharenko, Yu. D., Gorbatov, V. K., Kosenkov, V. M., Losev, N. P., Rogozyanov, A. Ya., and Samsonov, B. V., *Fiz. Metal. Metalloved.*, Vol. 61, 1986, pp. 1164-1169.

[7] Bates, J. F., and Gilbert, E. R., *Journal of Nuclear Materials,* Vol. 59, 1975, p. 96; also Vol. 71, 1978, p. 286.

[8] Sharmardin, V. K., Golovanov, V. N., Povstyanko, A. V., Neustroev, V. S., Bibilashvili, Yu. K., Golovnin, I. S., Kalashnik, G. V., and Romaneev, V. V., in *Effects of Radiation on Materials, 14th Inter. Symp. (Vol. II), ASTM STP 1046,* N. H. Packan, R. E. Stoller, and A. S. Kumar, Eds., American Society for Testing and Materials, 1990, pp. 753-765.

[9] Garner, F. A., Gilbert, E. R., and Porter, D. L., "Stress-Enhanced Swelling of Metals During Irradiation," *Effects of Radiation on Materials, 10th Conference, ASTM STP 725,* D. Kramer, H. R. Brager, and J. S. Perrin, Eds., American Society for Testing and Materials, 1981, pp. 680-697.

[10] Garner, F. A. in Chapter 6 of *Materials Science and Technology, A Comprehensive Treatment*, Vol. 10A, Part 1, R. W. Cahn, P. Haasen, and E. J. Kramer, Eds., VCH Verlagsgesellschaft mbH, pp. 419-543.

H. Watanabe[1] and F. A. Garner[2]

Influence of Silicon or Titanium on the Microstructural Evolution of Fe-Cr-35Ni Alloys Irradiated with Neutrons or Self-Ions

Reference: Watanabe, H. and Garner, F. A., **"Influence of Silicon or Titanium on the Microstructural Evolution of Fe-Cr-35Ni Alloys Irradiated with Neutrons or Self-Ions,"** *Effects of Radiation on Materials: 19th International Symposium, ASTM STP 1366,* M. L. Hamilton, A. S. Kumar, S. T. Rosinski, and M. L. Grossbeck, Eds., American Society for Testing and Materials, West Conshohocken, PA, 2000.

Abstract: A series of Fe-Cr-35Ni alloys was irradiated to doses ranging from 12 to 36 dpa with fast neutrons at 375-600°C and to 59-117 dpa at 675°C with Ni^+ ions. The primary purpose of this study was to examine the effect of silicon and titanium on both microstructural evolution and the tendency of Fe-Cr-35Ni alloys to spinodally decompose during irradiation. As expected, the addition of these solutes suppresses void swelling and alters the microstructural evolution. They do not appear, however, to suppress the tendency toward spinodal-like decomposition, but only to change somewhat the microstructural consequences of the decomposition.

Keywords: stainless steel, neutron irradiation, ion irradiation, spinodal-like decomposition, microstructural evolution, silicon, titanium

Introduction

The radiation-induced alteration of the microstructure of metals and alloys is well known for its ability to modify their mechanical properties and also to cause large changes in dimension. The more pronounced of these modifications are those processes leading to void swelling, irradiation creep, and embrittlement. A very large amount of research has been directed toward the study of these phenomena and their potential mitigation [*1*].

One of the major approaches used in mitigation of these problems has been the addition of solute elements known to alter microstructural evolution and sometimes to suppress void swelling, especially by adding silicon, phosphorus and titanium. The current authors have previously concentrated on the effect of these elements in a variety of studies involving either neutron or charged particle irradiation, as reviewed elsewhere

[1]Professor, Research Institute for Applied Mechanics, Kyushu University, Kasuga, Fukuoka, Japan.

[2]Senior Staff Scientist, Pacific Northwest National Laboratory, P.O. Box 999, MSIN P8-15, Richland, WA 99352, USA.

Copyright© 2000 by ASTM International www.astm.org

[*2*]. These studies have focused on both simple model Fe-Cr-Ni austenitic alloys and on more complex commercial austenitic steels.

Some of the studies conducted by Garner and coworkers on irradiated ternary Fe-Cr-Ni austenitic alloys showed several unusual features when the nickel content was near 35 weight percent. Not only was the void swelling induced by irradiation in these Invar-like alloys often at a minimum at this concentration, but prior to the onset of void swelling, the alloy was often found to decompose in a spinodal-like fashion [*3-10*]. This decomposition was manifested as periodic oscillations in composition, with iron and chromium behaving as one specie and nickel as the other specie. The oscillation period increased strongly with increasing temperature but appeared to be relatively insensitive to the dpa rate.

Associated with this decomposition was a decrease in density, pronounced hardening that could not be related to microstructure, and a tendency toward selective electropolishing that produces modulated patterns of foil thickness or sometimes forms crystallographic and periodic arrays of "worm-holes" through the foil. Shamardin and coworkers have shown that the hardening and selective electropolishing also occurred in a more complex solute-modified alloy [*10*].

The current study represents an opportunity to study the interaction of two important solutes with the spinodal-like decomposition process. It focuses on two simple Fe-Cr-35Ni alloys and the corresponding quaternary alloys involving additions of 0.7 weight percent of either silicon or titanium. In one case, three alloys based on Fe-15Cr-35Ni were irradiated side by side in the FFTF fast reactor at four temperatures between 375 to 600°C to doses ranging from 12 to 36 dpa. In a second case, some of these same alloys, along with a Fe-30Cr-35Ni series, were irradiated using 5 MeV Ni^+ ions at 675°C to doses ranging from 59 to 117 dpa. These specimens were part of a larger study by W. G. Johnston and coworkers to study the compositional dependence of void swelling [*13-15*]. All alloys in both the neutron and ion irradiations were in the annealed condition.

Experimental Details

The neutron-irradiated specimens were irradiated in the Materials Open Test Assembly (MOTA) in the Fast Flux Test Facility with active temperature control to ±5°C. The specimens were standard 3 mm diameter microscopy disks contained in perforated stainless steel packets that allowed contact with the sodium coolant. The irradiation conditions reached in FFTF-MOTA were 12.3 dpa at 375°C, 35.8 dpa at 430°C, 36.3 dpa at 520°C and 33.2 dpa at 600°C. After irradiation the swelling of the specimens were determined by an immersion density technique known to be accurate to ±0.2% change in density.

The ion-irradiated specimens were irradiated at ~10^{-2} dpa/sec many years ago by W.G. Johnston and coworkers of General Electric Company to 59 and 117 dpa at 675°C. They were thinned, examined only cursorily by electron microscopy, but never fully investigated. These specimens were supplied by Johnston to F.A. Garner and examined by H. Watanabe.

In both irradiation series the Fe-15Cr-35Ni alloys were identical, as prepared by Johnston, with the composition given in Table 1. The ion irradiation series also contained specimens of Johnston's Fe-30Cr-35Ni alloys, as shown in Table 2. Also

presented in Table 2 are step height data which was measured by Johnston and can be used to estimate the swelling at the peak dose depth [*13*].

All alloys were annealed 1010°C for 10 minutes and water quenched. The ion-bombarded specimens were pre-implanted with 15 appm helium. Electron microscopy at 200 KeV was employed to study the microstructure of both types of specimens.

In previous studies [*3-9*] several methods were used to identify the presence of spinodal-like decomposition. The earliest method was the use of energy-dispersive X-ray traces. Later methods involved the observation of densification without concurrent second-phase formation, and most importantly, the development of selective electropolishing of the foil surfaces, sometimes leading to periodic perforations (designated as "worm-holes") through the foil. Another method that might be used would be the periodic formation and spacing of new microstructural components when solutes such as Si and Ti are added. All of these methods were employed in the current study.

Table 1 - *Composition in wt% of Alloys Used in this Study*

Alloy Number	Cr	Ni	Si	Ti	C*	N	O	H
7	15.0	35.0	-	-	0.01	0.001	0.0066	0.0006
9	30.0	35.0	-	-	0.022	0.013	0.0090	0.008
109	15.0	35.0	0.7	-	-	-	-	-
110	15.0	35.0	-	0.7	-	-	-	-
111	30.0	35.0	0.7	-	-	-	-	-
112	30.0	35.0	-	0.7	-	-	-	-

*Residual elements were measured only for ternary alloys and not quaternary alloys.

Table 2 - *Description of Ion-Bombarded Specimens*

Alloy	dpa	Temperature, °C	Step height, Å
Fe-15Cr-35Ni	59*	675	<100⊕
Fe-15Cr-35Ni-0.7Si	117*	675	<200
Fe-15Cr-35Ni-0.7Ti	117	675	<100
Fe-30Cr-35Ni-0.7Si	117	675	<200
Fe-30Cr-35Ni-0.7Ti	117	675	1020

*Johnston originally reported these numbers as 72 and 144 dpa, using a 33 eV displacement threshold [*14*] rather than the later accepted value of 40 eV.

⊕100 Å was considered by Johnston to be the lowest resolvable step-height. 60Å of step height is expected for each percent of swelling a the peak displacement position [*13*].

Results: FFTF Irradiation

As shown in Table 3, the swelling of Fe-15Cr-35Ni at 375°C and 12.3 dpa was 0.9%, while at 430-600°C and 33-36 dpa the swelling was in the range 1.5-1.9%, indicating that a faster average rate of swelling was probably occurring at 375°C than at 430-600°C.

Table 3 - *Swelling Measured by Immersion Density in Fe-15Cr-35Ni Alloys after Irradiation in FFTF-MOTA*

Temperature, °C	Dose, dpa	Solute content, wt.%	Swelling, %
375	12.3	0.0	0.91
		0.7Si	0.21
		0.7Ti	-0.24
430	35.8	0.0	1.51
		0.7Si	1.16
		0.7Ti	0.04
520	36.3	0.0	1.65
		0.7Si	0.28
		0.7Ti	0.12
600	33.2	0.0	1.88
		0.7Si	0.28
		0.7Ti	-0.04

The effect of silicon to reduce swelling was observed at all temperatures, while the effect of titanium was even stronger. At 375°C titanium actually caused a significant densification of 0.24%, indicating either that spinodal-like decomposition or a phase instability had occurred.

Figure 1 shows that a very high dislocation typical of low temperatures was observed at 375°C and 12.3 dpa. Voids were not observed in either the silicon-doped or titanium-doped alloys, indicating that the measured density changes must have been associated with phase changes or spinodal-like decomposition. Indeed, the Ni_3Si γ' phase was observed in the silicon-doped alloy. The voids observed in the undoped alloy at 375°C were on the order of 10 nm in diameter.

Figure 2 shows that a high dislocation density was still retained at 430°C and 35.8 dpa in all alloys. In the undoped alloy the voids were ~22 nm in diameter. In the silicon-doped alloy the voids were a little larger at ~30 nm and coexisted with Ni_3Si γ' precipitates. There was a much lower low void density in the titanium-doped alloy.

Figure 3 shows that the dislocation density is lower at 520°C and 36.3 dpa, and the voids were larger at ~60 nm in the undoped alloy. In the silicon-doped alloy the voids were very small in size at ~5 nm diameter with concurrent formation of Ni_3Si, with clear evidence that the specimen has spinodally decomposed, as shown in Figure 4. Spinodal-like decomposition was also observed in the 0.7Ti specimen, but no voids were

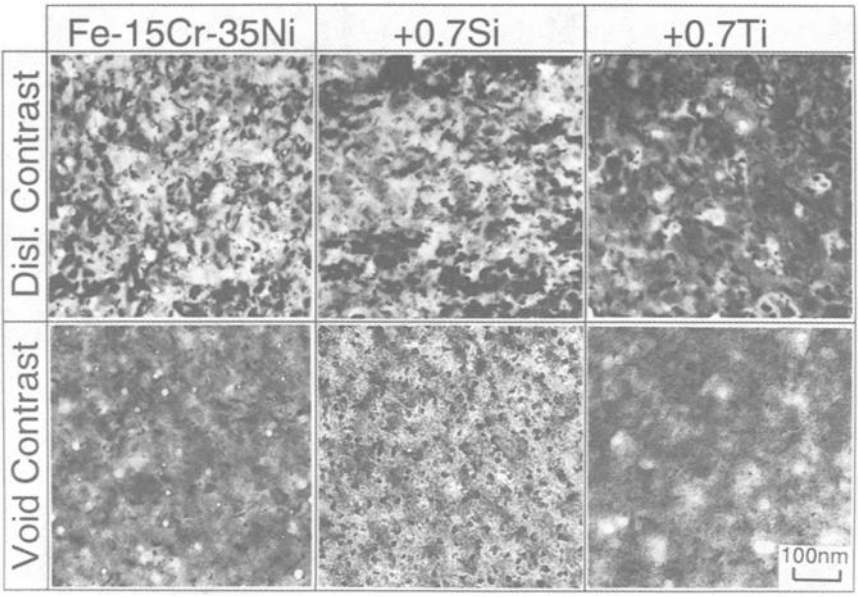


Figure 1 - *Microstructures observed at 375 °C and 12.3 dpa in FFTF. Small dark features are γ′ precipitates.*

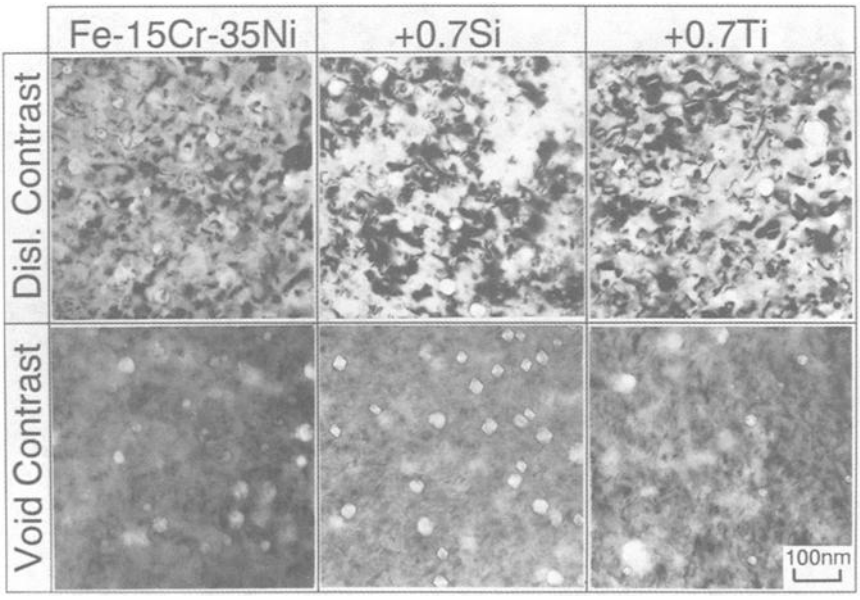


Figure 2 - *Microstructures observed at 430 °C and 35.8 dpa in FFTF.*

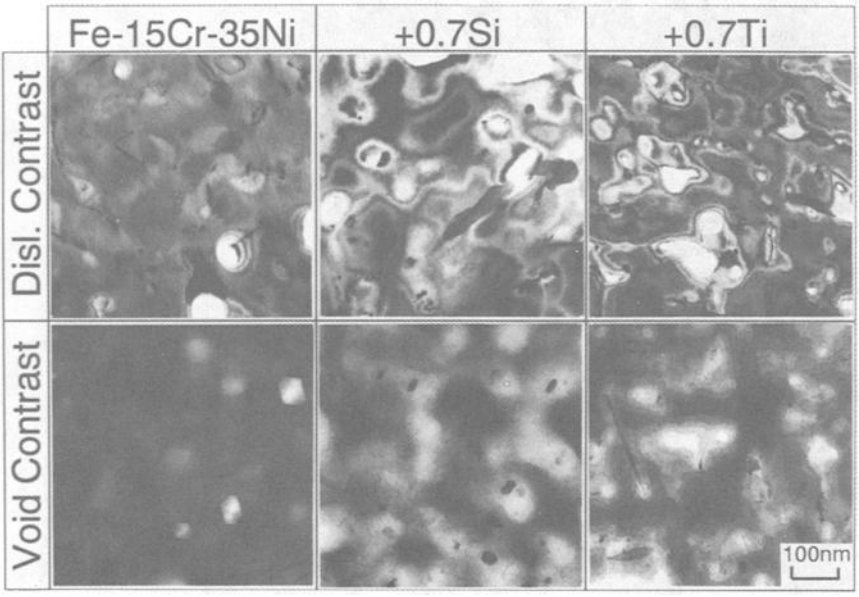


Figure 3 - *Microstructures observed at 520 °C and 36.3 dpa in FFTF.*

observed. Figure 5 shows that the most convincing evidence of spinodal-like decomposition arises from the highly crystallographic nature of the electropolishing to produce a very regular perforation pattern. There also appears to be an array of platelet-type precipitates on a very fine scale.

Figure 6 shows a characteristically low dislocation density at 600°C and 33.2 dpa, with large voids at ~60 nm diameter in the undoped alloy. No voids or Ni_3Si γ' were observed in the silicon-doped specimen. Some very small voids were seen to be attached to dislocation loops in the titanium-doped alloy.

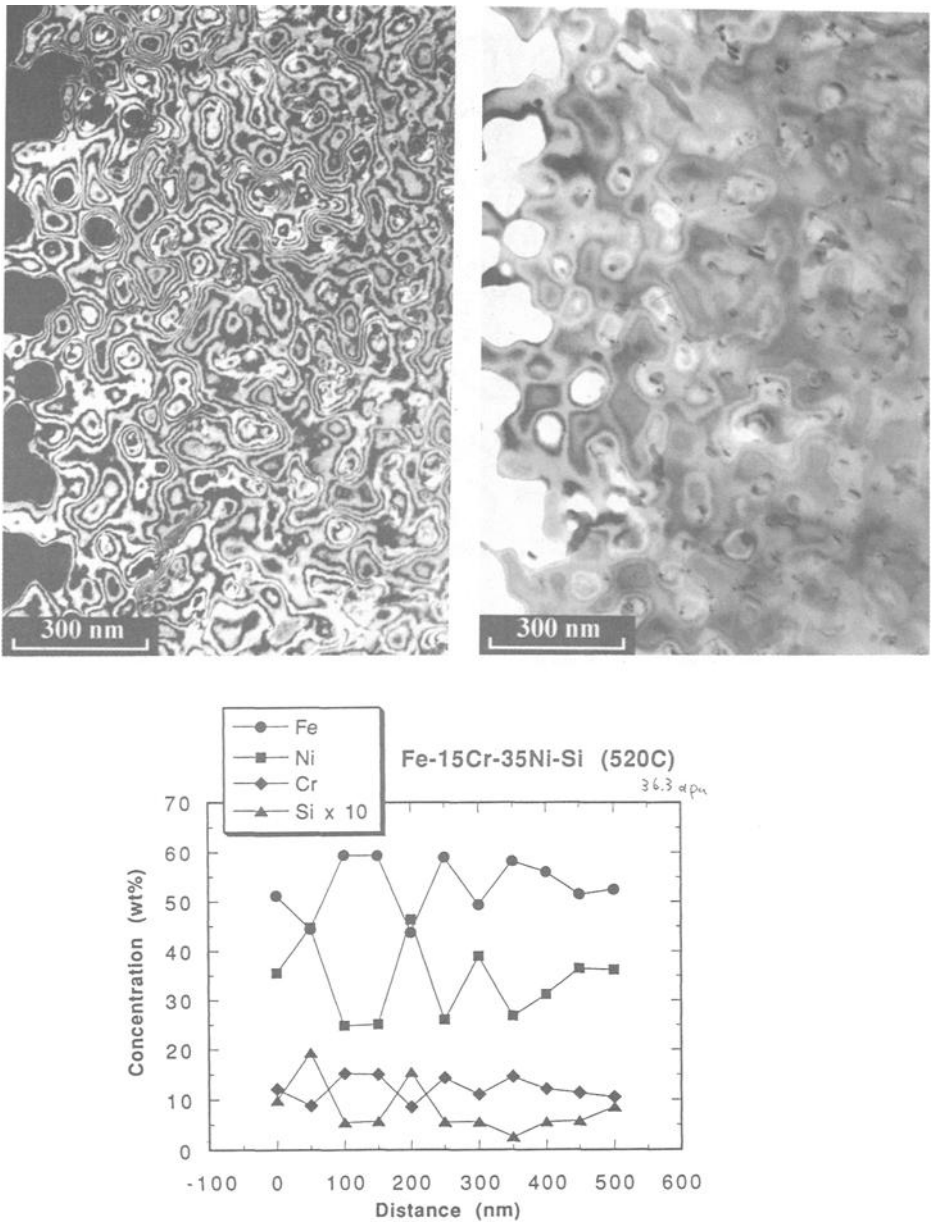


Figure 4 - *(top) Transmission electron micrographs showing irregular polishing of Fe-15Cr-35Ni-0.7Si after irradiation at 520 °C with neutrons to 36.3 dpa. (bottom) EDX compositional profiles showing Ni and Si behaving as one specie and Fe and Cr as another specie.*

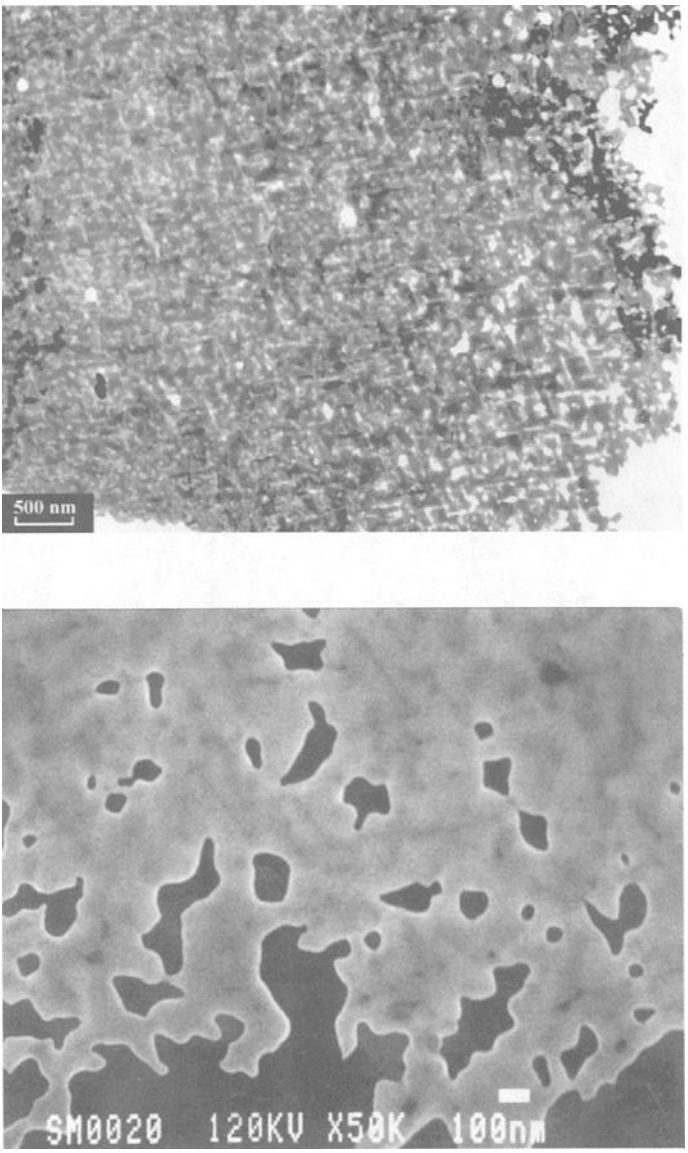


Figure 5 - *top) Electron micrograph showing selective electropolishing along <110> directions of Fe-15Cr-35Ni-0.7Ti after 36.3 dpa irradiation with neutrons at 520 °C; bottom) Scanning image of another area of the surface of the foil shown in top figure.*

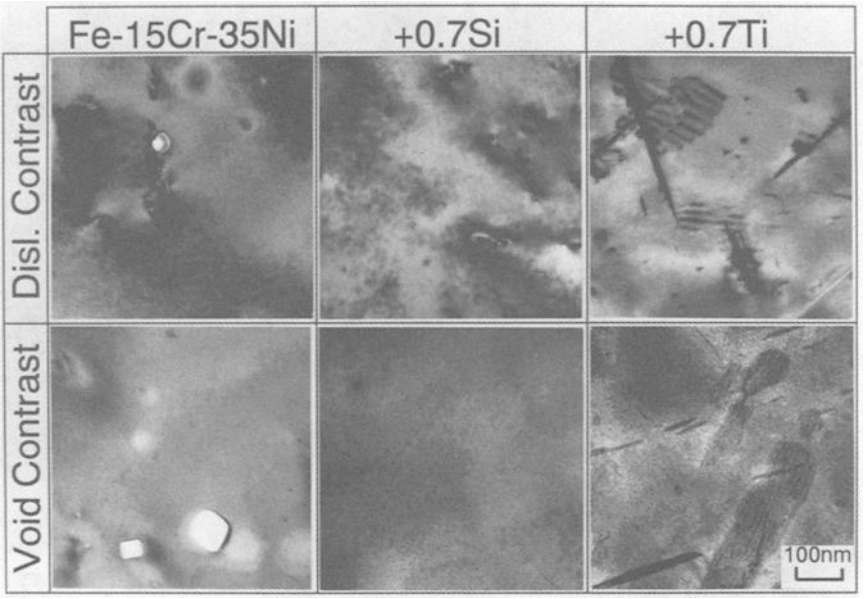


Figure 6 - *Microstructures observed at 600 °C and 33.2 dpa in FFTF.*

Results: Ion Bombardment

Figure 7 shows that large voids have formed in the Fe-15Cr-35Ni already by 59 dpa at 675°C. Silicon addition suppresses void nucleation substantially even at 117 dpa, as does titanium, although the void density is a little higher in the titanium-doped alloy.

There is no easily observed evidence of spinodal decomposition in any of these specimens if one observes only on a very local level. If, however, one observes on a very large scale, as shown in Figure 8, the characteristic preferential thinning of the foil can be observed, showing that a compositional oscillation period of ~2μm is involved. Similar large wavelengths have been observed in earlier studies of Fe-Cr-35Ni alloys and are not a random polishing artifact.

Figure 9 shows that at 144 dpa and 675°C the void density in the Fe-15Cr-35Ni alloy is still very low, with swelling effectively suppressed. When the chromium level is increased to 30%, however, both the silicon-doped and titanium-doped alloys increase strongly in swelling, especially in the titanium-doped alloy. Evidence of spinodal-like decomposition was not observed in any of the Fe-30Cr-35Ni specimens.

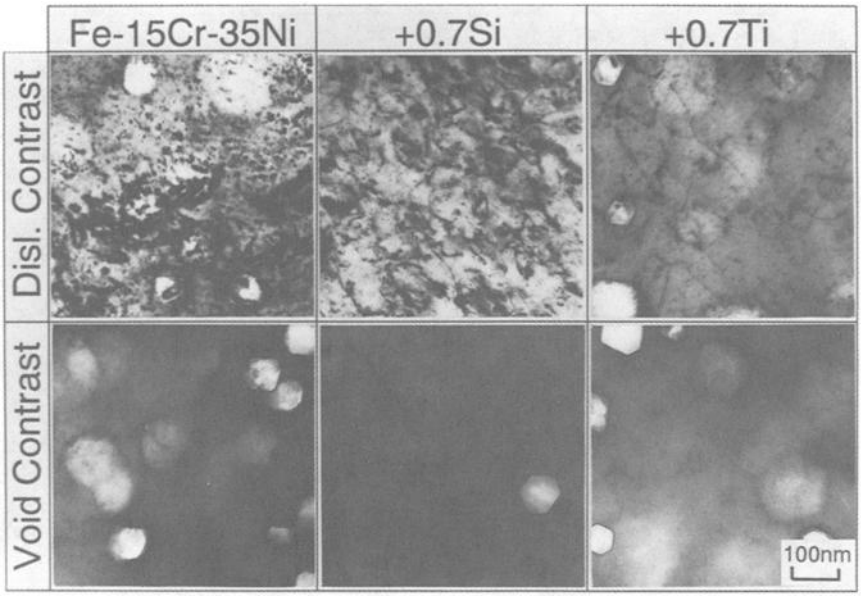


Figure 7 - *Microstructures observed at 675 °C for Fe-15Cr-35Ni at 59 dpa and the silicon and titanium-doped variants at 117 dpa after ion bombardment.*

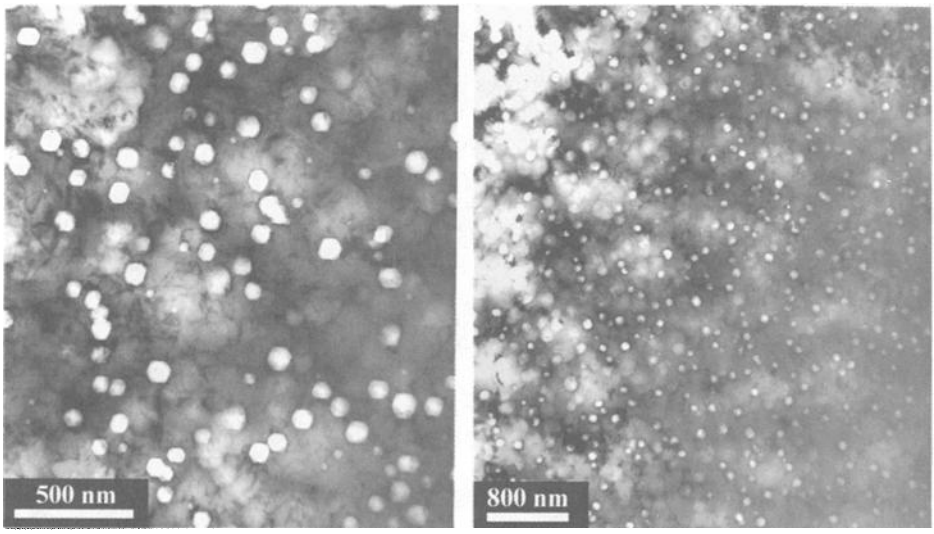


Figure 8 - *Transmission electron micrographs of Fe-15Cr-35Ni after irradiation to 59 dpa at 675 °C with 5 MeV Ni+ ions. The major notable features are the voids inside the foil and the large lighter contrast areas. This latter feature results from low nickel areas produced by spinodal-like decomposition that were then selectively thinned during electropolishing.*

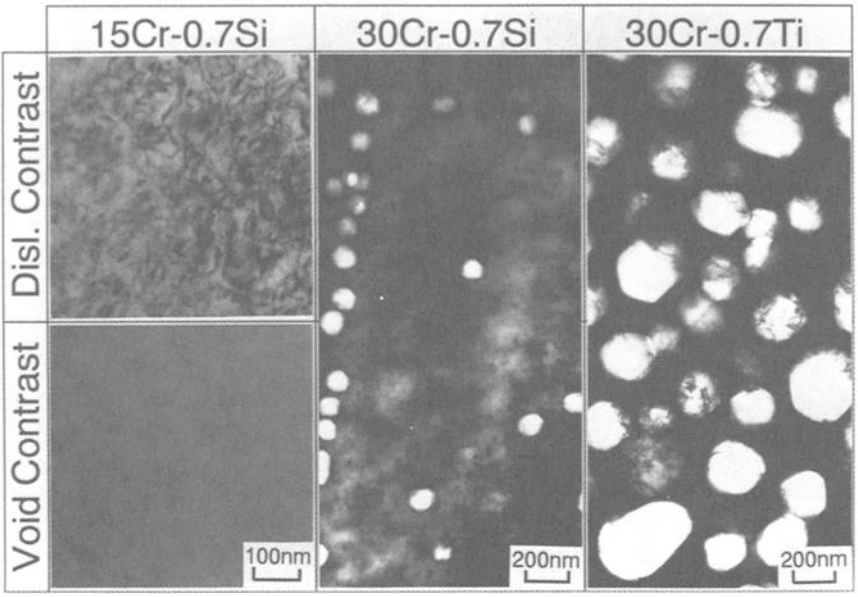


Figure 9 - *Microstructures observed at 675 °C for the silicon-doped alloys at 15 and 30% Cr, and the titanium-doped alloy at 30% Cr, all at 117 dpa.*

Discussion and Conclusions

In earlier papers it was shown that large amounts of silicon addition suppressed the swelling of Fe-15Cr-Ni alloys at all nickel levels studied [*2,11*]. This study confirms the generality of this observation for Fe-Cr-35Ni ternary alloys and demonstrates that titanium additions also suppress swelling. When the chromium level increases to 30%, however, the swelling of the Ti-doped alloy can still be very large, as shown in Figure 9. Note in Table 2 that Johnston and coworkers measured a step-height of 1020Å in Fe-30Cr-35Ni-0.7Ti, which at 60Å/% swelling implies a swelling of ~17% at the peak swelling position.

Evidence was provided in this study showing that spinodal-like decomposition occurred in two conditions in this study. First, it was found in Fe-15Cr-35Ni after 5.0 MeV Ni+ ion irradiation at 675°C to 59 dpa, but on a very large scale. The ~2μm period is consistent with the ~1μm period observed earlier at 593°C, 38 dpa neutron [*5*] and 625°C, 117 dpa ion [*6*], reflecting the strong dependence of the spinodal-like decomposition process on irradiation temperature.

The absence of visible spinodal-like decomposition at 30% Cr in the ion-bombarded specimens is not surprising. It has been shown that the spinodal state is not stable and can not compete with the surface segregation of nickel at high swelling levels [*10*].

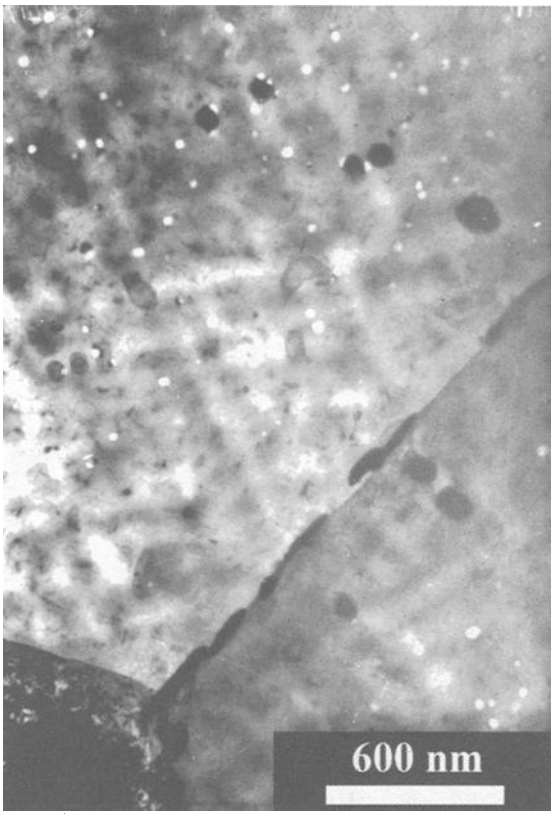


Figure 10 - *Previously unpublished micrograph by V. S. Neustroev, showing selective electropolishing of a complex alloy with ~35% nickel after irradiation to 53 dpa at 430 °C in the BOR-60 fast reactor [12].*

Similar decomposition was also observed at 520°C and 36 dpa in both the silicon and titanium-modified versions of Fe-15Cr-35Ni. It is not surprising that such decomposition led to formation of the Ni_3Si γ' phase in the silicon-doped alloy. Since this phase was also observed at 430°C and 36 dpa, it is possible that decomposition was in progress there also, but was not resolved due to the expected smaller oscillation period at 430°C. Earlier studies have shown that the oscillation period is on of 0.2 μm at ~510°C [*5,9*] and at 430°C is therefore is probably below the resolution limit by both EDS and selective electropolishing methods. A similar conclusion was reached in an earlier study where spinodal-like hardening could be measured at 450°C and 12.5 dpa after irradiation in EBR-II but no other supporting microstructural or microchemical evidence could be seen.

The absence of neutron-induced Ni_3Si γ' formation at 375°C, 12.3 dpa and 600°C, 33.2 dpa is also not surprising. Nor is its absence at 675°C and 117 dpa in the ion-bombarded specimens surprising. This phase is known to inhabit an intermediate

range of temperatures and to shift upwards in temperature with increasing displacement rate [*2*].

The nature of the micro-oscillations observed in Fe-15Cr-35Ni-0.7Ti is difficult to determine from the limited evidence available in this study, primarily due to the strong preferential attack of the foil during electropolishing. It appears, however, that the strong tendency of Invar-like alloys at ~35% Ni to decompose spinodally persists in spite of solute addition. This conclusion is further supported by the observation that spinodal-like hardening was observed by Shamardin and coworkers in Fe-14.6Cr-35.6Ni-2.8Mo-1.8Mn-0.31Si-0.05C steel with small additions of B, Y, Zr and P after neutron irradiation in the BOR-60 fast reactor at ≥400°C [*12*]. Even more importantly, the steel exhibited the selective electropolishing characteristics of spinodal-like decompositions, as shown in Figure 10.

Acknowledgments

The authors thank W. G. Johnston who supplied the ion-bombarded specimens and step height measurements prior to his retirement. This research work is supported by Monbusho, the Japanese Ministry of Education, Science, and Culture and the US Department of Energy through the FFTF/MOTA collaboration and JUPITER programs.

References

[1] Garner, F. A., "Irradiation Performance of Cladding and Structural Steels in Liquid Metal Reactors," in Chapter 6 of *Materials Science and Technology, a Comprehensive Treatment*, Vol. 10A, Part 1, R. W. Cahn, P. Haasen, and E. J. Kramer, Eds., VCH Verlagsgesellschaft mbH, 1994, pp. 419-543.

[2] Garner, F. A., Lauritzen, T., and Mitchell, M. A., "The Complex Action of Major Solutes on Radiation-Induced Swelling of Fe-Cr-Ni Austenitic Alloys," *Effects of Radiation on Materials: 16th International Symposium, ASTM STP 1175*, A. S. Kumar, D. S. Gelles, R. K. Nanstad, and E. A. Little, Eds., American Society for Testing and Materials, 1993, pp. 803-815.

[3] Brager, H. R., and Garner, F. A., "The Origin of the Large Resistance to Void Swelling Observed in Fe-35.5Ni-7.5Cr," in *Optimizing Materials for Nuclear Applications*, F. A. Garner, D. S. Gelles, and F. W. Wiffen, Eds., The Metallurgical Society, 1985, pp. 141-166.

[4] Garner, F. A., Brager, H. R., Dodd, R. A., and Lauritzen, T., "Ion-Induced Spinodal -Like Decomposition of Fe-Ni-Cr Invar Alloys," in *Nuclear Instruments and Methods in Physics Research B16*, 1986, pp. 224-250.

[5] Garner, F. A., Brager, H. R., and McCarthy, J. M., "Neutron-Induced Spinodal-Like Decomposition of Fe-Ni and Fe-Ni-Cr Alloys," in *Radiation-Induced Changes in*

Microstructure, 13th International Symposium (Part 1) ASTM STP 955, F. A. Garner, N. H. Packan, and A. S. Kumar, Eds., American Society for Testing and Materials, 1987, pp. 775-787.

[6] Dodd, R. A., Garner, F. A., Kai, J.-J., Lauritzen, T., and Johnston, W. G., "Spinodal -Like Decomposition and Swelling Induced by Ion Irradiation in Simple Fe-Ni and Fe-Ni-Cr Alloys," ibid., pp. 788-804.

[7] Garner, F. A. and McCarthy, J. M., "Spinodal-Like Decomposition of Fe-Ni and Fe-Ni-Cr "Invar" Alloys During Neutron or Ion Irradiation," in *Physical Metallurgy of Controlled Expansion Invar-Type Alloys*, K. C. Russell and D. F. Smith, Eds., The Minerals, Metals and Materials Society, 1990, pp. 187-206.

[8] Garner, F. A, McCarthy, J. M., Russell, K. C., and Hoyt, J. J., "Spinodal-Like Decomposition of Fe-35Ni and Fe-Cr-35Ni Alloys During Irradiation of Thermal Aging," in *Journal of Nuclear Materials,* Vol. 205, 1993, pp. 411-425.

[9] Brager, H. R., Garner, F. A., and Hamilton, M. L., "The Influence of Composition on Microstructural Evolution and Mechanical Properties of Irradiated Fe-Cr-Ni Ternaries," in *Journal of Nuclear Materials,* Vols. 133-134, 1985, pp. 594-598.

[10] Garner, F. A., Watanabe, H., Russell, K. C., McCarthy, J. M., Dodd, R. A., and Hoyt, J. J., "Irradiation-Induced Spinodal-Like Decomposition of Fe-35Ni and Fe-Cr-35Ni Alloys," in *The Invar Effect, A Centennial Symposium, Oct. 7-8, 1996, TMS,* pp. 117-136.

[11] Garner, F. A. and Kumar, A. S., "The Influence of Both Major and Minor Element Composition on Void Swelling in Austenitic Steels," in *Radiation-Induced Changes in Microstructure, 13th International Symposium (Part I), ASTM STP 955,* F. A. Garner, N. H. Packan, and A. S. Kumar, Eds., American Society for Testing and Materials, 1987, pp. 289-314.

[12] Shamardin, V. K., Neustroev, V. S., Povstyanko, A. V., Bulanova, T. M., Ostrovsky, Z. E., Kuznetzov, A. A., Kursevitch, I. P., and Nikolaey, V. A., "Swelling, Mechanical Properties and Structure of Austenitic High-Nickel Alloy Irradiated in a Fast Reactor," in *Effects of Radiation on Materials, 17th International Symposium, ASTM STP 1270,* D. S. Gelles, R. K. Nanstad, A. S. Kumar, and E. A. Little, Eds., American Society for Tesing and Materials, 1996, pp. 842-857.

[13] Johnston, W. G., Rosolowski, J. H., Turkalo, A. M., and Lauritzen, T., *Journal of Nuclear Materials* Vol. 47, 1973, p. 155.

[14] Johnston, W. G., Lauritzen, T., Rosolowski, J. H., and Turkalo, A. M., "The Effect of Metallurgical Variables on Void Swelling," in *Radiation Damage in Metals,* N. L. Peterson and S. D. Harkness, American Society for Metals, 1976, pp. 227-266.

[15] Bates, J. F. and Johnston, W. G., "Effects of Alloy Composition on Void Swelling," in *Radiation Effects in Breeder Reactor Structural Materials,* M. L. Bleiberg and J. W. Bennett, Eds., The Metallurgical Society of AIME, 1977, pp. 625-644.

F. A. Garner,[1] S. I. Porollo,[2] A. N. Vorobjev,[2] Yu. V. Konobeev,[2] A. M. Dvoriashin,[2] V. M. Krigan,[2] N. I. Budylkin,[3] and E. G. Mironova[3]

Void-Induced Swelling and Embrittlement in the Russian EI-847 Stainless Steel at PWR-Relevant End-of-Life Conditions

---

Reference: Garner, F. A., Porollo, S. I., Vorobjev, A. N., Konobeev, Y. V., Dvoriashin, A. M., Krigan, V. M., Budylkin, N. I., and Mironova, E. G., **"Void-Induced Swelling and Embrittlement in the Russian EI-847 Stainless Steel at PWR-Relevant End-of-Life Conditions,"** *Effects of Radiation on Materials: 19th International Symposium, ASTM STP 1366*, M. L. Hamilton, A. S. Kumar, S. T. Rosinski, and M. L. Grossbeck, Eds., American Society for Testing and Materials, West Conshohocken, PA, 2000.

Abstract: Void swelling has been proposed to eventually reach significant levels in some austenitic internals at PWR end-of-life conditions. A prevailing perception based on previously published data from fast reactors is that swelling will never reach significant levels at temperatures in the 330-372°C range, even at the 80-90 dpa level anticipated in PWR baffle-former components after 40 years of operation. Fast reactor data are presented in this paper that show that this perception is incorrect, at least for a niobium-stabilized 16Cr-15Ni steel used in Russian reactors for applications where 316 would be used in Western reactors. As a result of the large swelling levels reached in some cases, the steel becomes very brittle, as expected from fast reactor experience.

Keywords: stainless steels, void swelling, embrittlement, PWRs, neutron irradiation

Introduction

In several recent papers, it has been proposed that significant amounts of void swelling and associated void-induced embrittlement may develop in the near-core austenitic components of pressurized water reactors (PWRs), especially toward the

---

[1] Senior Staff Scientist, Pacific Northwest National Laboratory, Richland, WA, USA
[2] Head of Hot Laboratory, Lead Scientist, Head of Nuclear Materials Division, Leading Scientist and Senior Scientist, respectively, Institute of Physics and Power Engineering, Obninsk, Russian Federation.
[3] Leading Scientist, Senior Scientist, Bochvar's Institute of Nonorganic Materials, Moscow, Russian Federation.

Copyright© 2000 by ASTM International www.astm.org

end-of-life condition where atomic displacement levels of 80-90 dpa will be attained in the 304 and 316 steels used in the baffle-former assemblies [*1,2*]. Swelling is predicted to arise from the combined action of atomic displacement, gamma-heating of thick components to raise the temperatures, large levels of helium and possibly hydrogen generated by transmutation, and finally, the dependence of swelling on displacement rate, characterized by the "temperature-shift" phenomenon. Research on the temperature shift is presented in a companion paper [*3*]. The "temperature-shift" would cause the temperature regime of swelling to move to lower temperatures relative to that observed in fast reactors.

Data are now becoming available to support the possibility at PWR-relevant displacement rates of "larger-than-expected" void swelling levels at "lower-than-expected" irradiation temperatures and at "lower-than-expected" dpa levels [*4,5*], but in general, the dpa levels attained to date in these studies are rather low compared to 80-90 dpa.

The "expectations" of swelling are based on extensive irradiation experience attained from fast reactor irradiation at dpa rates significantly higher than that of PWRs [*6*]. Most of these data were generated in the "second generation" of fast reactors where the inlet coolant temperature was on the order of 365-375°C. Therefore no data are available from these reactors at temperatures below 365°C. In the "first generation" of fast reactors, however, the inlet temperatures were on the order of 270-320°C, allowing the possibility of exploring void swelling over the full range of PWR-relevant temperatures.

In both generations, however, the strong gradients in neutron flux near the bottom of the cores did not allow dpa levels relevant to PWR end-of-life conditions to be reached without exceeding swelling limits in the core center region. As a consequence, fast reactor data at >50 dpa have not been attained at PWR-relevant temperatures of 330-372°C, reinforcing the expectation that there is no significant amount of swelling over this temperature range. This perception is now known to be incorrect, at least for one stainless steel.

In the current study, it has been found that in the 70-80 dpa range significant amounts of void swelling can be reached at PWR-relevant temperatures in a steel commonly used in the construction of various reactor types in the countries of the former Soviet Union. The steel is EI-847, a niobium-stabilized 16Cr-15Ni austenitic steel used for applications where AISI 316 stainless steel would be employed in PWR's of the Western design type. Some preliminary results have been presented in earlier papers [*4,5,7*].

Experimental Details

The EI-847 steel was irradiated in both the solution-treated and cold-worked condition. Composition and treatments of these two steels are shown in Table 1. The specimens were in the form of relatively long, argon-pressurized, thin-walled creep tubes, with hoop stress levels ranging from 0 to 196 MPa. The dimensions of these tubes are shown in Figure 1.

The tubes were irradiated in a special test subassembly in the BN-350 fast reactor located at Aktau, Kazakhstan. This subassembly is similar to fuel driver assemblies used in BN-350, but the central fuel pins were replaced by an extractable

container 30 mm in diameter. Cylindrical baskets of 27 mm diameter containing seven creep tubes each were placed in the extractable container. All surfaces of the baskets had perforations to allow the reactor sodium coolant to flow over the tubes. The inlet coolant temperature for this reactor is ~285°C.

Table 1 - *Composition of EI-847 Steels in wt%*

	C	Si	Mn	S	P	Cr
S.T.*	0.050	0.29	0.78	0.009	0.011	15.74
C.W.†	0.060	0.20	0.73	0.004	0.012	15.61
	Ni	Mo	Nb	B	N	
S.T.	15.32	2.95	0.54	0.001	0.035	
C.W.	14.90	2.96	0.59	0.001	0.022	

*Solution treated 1040°C/3 min, grain size 12 μm.
†Solution treated 1040°C/3 min, 18 ± 2% cold-work, grain size 10-15 μm.

The test subassembly was irradiated 14,400 hours over the period 12/03/86 to 11/10/89 in the low-enrichment zone of BN-350. The irradiation was conducted in two segments with a transfer into a second subassembly at 4/03/88. The temperatures of the tubes were determined by calculations involving the known coolant flow and the heat production of surrounding fuel pins, and are thought to be accurate to ~10°C or less over the lifetime of the experiment.

Two groups of specimens were irradiated. As shown in Table 2 the first group contained solution-treated tubes which had average temperatures from top to bottom of 324 to 350°C and dose levels of 65-78 dpa, respectively. The temperatures fall slowly during irradiation. The second group contained CW tubes ranging from 350-385°C and 78-85 dpa. At the center of these tubes the conditions were 73 dpa, 335°C, and 82 dpa, 365°C for the solution-treated and cold-worked tubes,

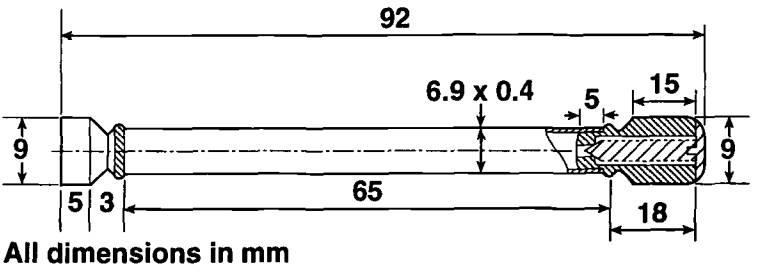


Figure 1 - *Argon-pressurized creep tubes irradiated in BN-350.*

Table 2 - *Irradiation Conditions of the Pressurized Portion of the Tubes*

Steel	Position	Dose, dpa*	Temperature, °C		
			beginning	mid-life	end-of-life
EI-847 ST basket #5	bottom	65.0	331	324	320
	middle	**72.8****	345	**335**	328
	top	78.1	362	350	340
EI-847 CW basket #6	bottom	78.1	362	350	340
	middle	**82.4**	378	**365**	355
	top	85.2	395	385	370

*Calculated using the standard NRT model
**Underline indicates nominal values

respectively. These conditions will be the ones quoted as the nominal conditions in the following sections when referring to the various tube sets. More specific dpa and temperature assignments will be employed for smaller specimens cut from these tubes.

Upon disassembly of the baskets all tubes, except those in the stress-free condition, were found to have lost pressure, with most having failed in a very brittle manner without any obvious physical insult having been experienced during disassembly. Some of the stressed tubes were reduced to fragments. Many of the tubes were also bent toward one or both ends, having elongated enough to interact with the ends of the basket. Such elongation is known to arise only from swelling and not from irradiation creep. Both failure and bending can be seen in Figure 2. Only the stress-free tubes appeared to be free of failure.

Although it was difficult to measure diameter changes and density on such broken tubes, it became obvious, where measurements could be made, that diameter changes as large as 5.4% on the annealed tubes and 7.6% on the cold-worked tubes had occurred, indicating that substantial combined creep and swelling strains had occurred.

The central 50 mm section of the unbroken tubes was mechanically removed and weighed by an immersion density technique. Rings of 4 mm length were cut from the 50 mm segment. Some 4 mm rings were also subjected to immersion density measurement, and some 4 mm rings were then used to punch 3 mm diameter microscopy disks, followed by transmission electron microscopy. Some of the 2 mm rings were subjected to a ring-tensile test described elsewhere [*8*].

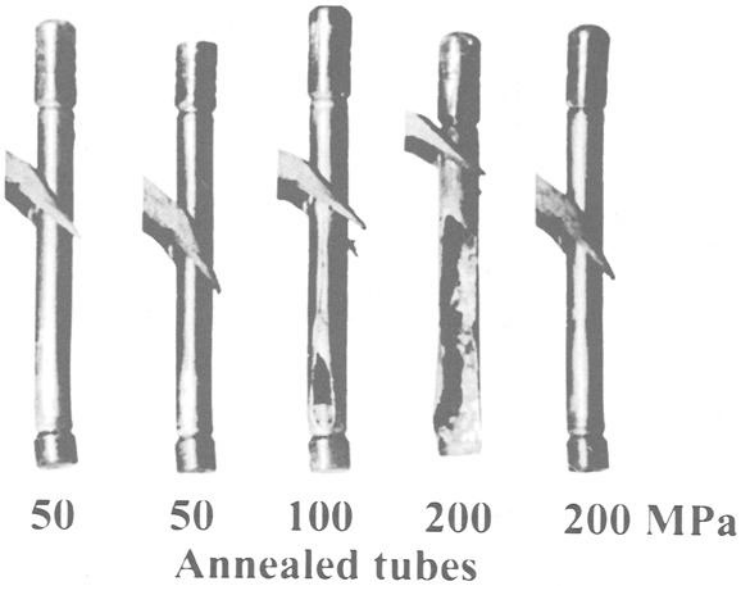


Figure 2a - *Post-irradiation condition of EI-847 tubes at 335°C showing swelling-induced fracture and bending in 92 mm creep tubes. Hoop stresses are shown.*

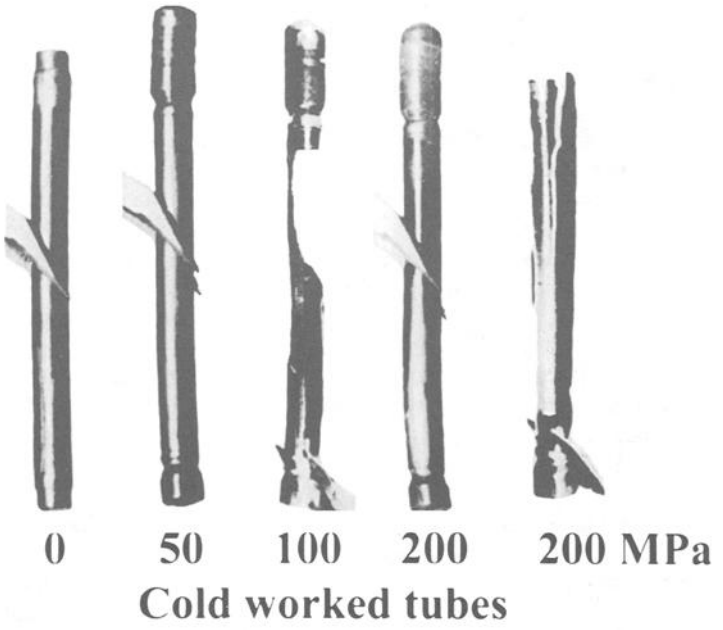


Figure 2b - *Post-irradiation condition of EI-847 tubes at 365°C showing swelling-induced fracture and bending.*

Results

Examination of these tubes is still in progress. Some early results were first presented in ref. 4 for the 20% cold work tube irradiated to 82 dpa at 365°C with a hoop stress of 100 MPa, with microscopy showing swelling of ~14%. Fracture surfaces were also examined by scanning microscopy. These surfaces indicated a strong role of swelling in the failure mechanism. In this second paper are reported the first data derived from the stress-free tubes.

The swelling measured by immersion density of the 50 mm central section of each stress-free tube was 2.9% for the solution-treated tube and 15.4% for the cold-worked tube. Since the solution-treated tube was irradiated closer to the bottom of the core, they had a larger axial gradient in dpa rate and thereby a larger variation in swelling along its length, ranging from ~0.1% near its bottom to ~6% at its top end, as shown in Table 3. The swelling along the cold-worked tube ranged from ~12% to ~16%, reflecting the smaller gradient in dpa rate along its length.

Table 3 - *Compilation of Microscopy Data on Void Swelling of Stress-free Tubes*

	#	Z	dpa	T, °C	$\overline{D}$, nm	σ_v, cm^{-3}	S, %	comments
ST	1	-7.5	74.0	341	17.4	4.7	1.9	two areas
				341	16.5	6.4	2.3	
ST	2	-7.5	74.0	341	25.1	4.4	6.0	two areas
				341	23.8	4.5	5.2	
ST	3	-2.5	75.0	342	26.0	3.8	6.2	mean value of measurements on four specimens
ST	4	-47.5	68.0	330	13.7	4.9	1.0	two areas
					15.5	5.0	1.7	
ST	5	-47.5	68.0	330	9.7	1.2	0.1	single area
ST	6	-43.0	69.3	331	11.8	0.7	0.1	single area
CW	7	-2.5	83.2	372	31.5	5.7	16.2	two areas
					33.5	4.9	15.4	
CW	8	-4.5	83.0	371	33.0	6.0	18.7	single area
CW	9	-43.5	80.0	358	28.5	7.2	13.7	two areas
					29.5	6.3	13.9	

Z = distance from top of tube, T = temperature, $\overline{D}$ = mean void diameter, σ_v = void density in units of 10^{15}, S = swelling

Inspection of the data in Table 3 shows that the local swelling can vary across a given specimen and even more strongly between specimens taken from different positions on a given ring. Such variability is common in stainless steels and is known to occur most strongly near the onset of swelling, and to become less pronounced at higher dpa and higher swelling levels. A typical void microstructure is shown in Figure 3 for the solution-treated condition at 342°C and 75 dpa. As shown in Figure 4 the swelling incubation period for solution-treated EI-847 in the range 330-342°C appears to be somewhat greater than 60 dpa. For the cold-worked condition, the limited data now available at 358-372°C imply that the incubation period is also ~60 dpa.

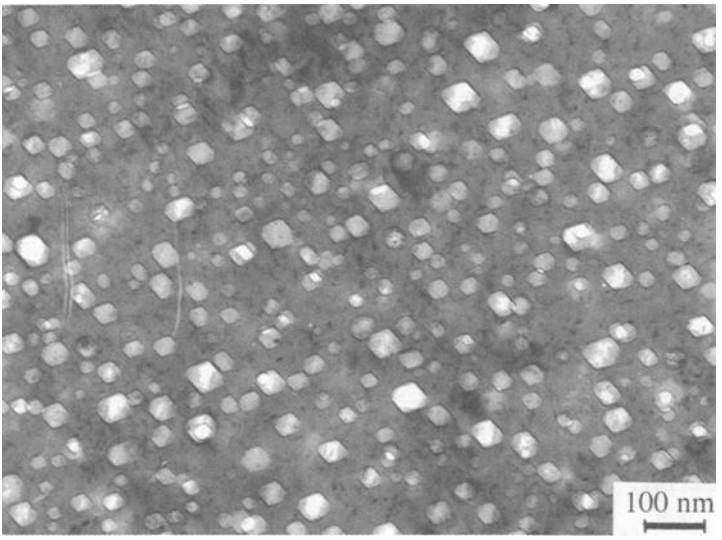


Figure 3 - *Microstructure of solution-treated EI-847 after irradiation at 342°C and 75 dpa in the absence of applied stress. The swelling level is 6.2%.*

It is also well-known that the maximum swelling rate of all austenitic steels is ~1%/dpa over a wide range of material and environmental conditions [6]. Note that the swelling rates in Figure 4 may be approaching this value. It is important to realize, however, that dpa variations in these data arise from variations in dpa rate along the tube.

Using the ring tensile method, mechanical property tests are now in progress at an initial deformation rate of 1.4×10^{-3} per second, with testing proceeding at room temperature. Using a solution-treated ring at 67 dpa and 327°C, the material had a yield strength of 723 MPa, an ultimate strength of 797 MPa, with uniform and total elongation equal at 3.2%. Swelling was estimated at ~1% in this specimen based on measured swelling of adjacent specimens.

After annealing of an adjacent specimen for one hour at 800°C, the yield and ultimate strengths dropped to 640 and 717 MPa, and the uniform and total elongation increased somewhat to 14.5 and 17.5%, yielding only minor improvement.

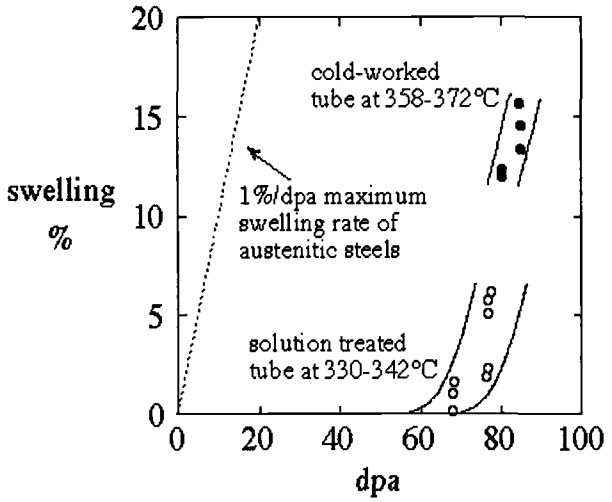


Figure 4 - *Stress-free swelling behavior observed in this experimental series, showing large incubation doses required to observe accelerated swelling. The maximum swelling rate of 1%/dpa for all austenitic steels is shown for comparison. Note that dpa variations arise from differences in dpa rate along the tube.*

In the testing of four cold-worked specimens the yield and ultimate strengths at ~83 dpa and 376°C were all in the range 40-71 MPa only, with 0% uniform and total elongation, indicating severe embrittlement. Annealing two similar specimens at 800°C for one hour partially restored the strength to the 600 MPa range, but failed to restore the ductility, which remained in the 0-0.2% range.

Discussion and Conclusions

Swelling in solution-treated EI-847 in the range 330-342°C appears to begin at incubation doses above ~60 dpa, an exposure range not explored previously in this temperature range. The rate of swelling thereafter is very large and may be approaching the maximum rate of ~1%/dpa observed in all stainless steels over a wide range of temperature. The post-incubation swelling of cold-worked EI-847 in the range 358-372°C is also very large, with an incubation period on the order of 60 dpa. It must be noted, however, that these swelling results were obtained at dpa rates about an order of magnitude higher than expected in PWR baffle plates. Based on temperature- shift considerations, one might expect higher swelling at PWR-relevant dpa rates [*1,3*].

The mechanical property tests show that the microstructural development associated with ~1% swelling still allows significant ductility. Swelling of ~15%

leads to extreme embrittlement and zero ductility, however. According to the work of several groups [9-11], such behavior is to be expected above ~10% swelling for temperatures less than ~425°C.

The implication of these results for PWR applications is that the possibility exists that beyond 60 dpa, stainless steels may be prone to an accelerated swelling behavior at temperatures previously thought not to be conducive to void swelling. Based on the experience of the fast reactor program, if one stainless steel exhibits this type of behavior, all stainless steels will eventually do the same. This Russian steel might be expected to begin swelling somewhat earlier than 304 stainless based on its Nb and Si levels, but somewhat later based on its higher Ni level [6]. Without data for comparison, however, a prediction of relative swelling behavior for 304 stainless can not be made at this time.

Acknowledgements

The US Department of Energy, Office of Basic Energy Sciences supported this work under Contract DE-AC06-76RLO 1830.

References

[1] Garner, F. A., Greenwood, L. R., and Harrod, D. L., " Potential High Fluence Response of Pressure Vessel Internals Constructed from Austenitic Stainless Steels", *Sixth International Symposium on Environmental Degradation of Materials in Nuclear Power Systems - Water Reactors*, The Minerals, Metals, and Materials Society, 1993, pp. 783-790.

[2] Garner, F. A, "Materials Issues Involving Austenitic Pressure Vessel Internals Arising from Void Swelling and Irradiation Creep", *Transactions of the American Nuclear Society*, Vol. 71, (1994) pp. 190-191.

[3] Neustroev, V. S., Shamardin, V. K., Ostrovsky, Z. E., Pecherin, A. M., and Garner, F. A., "Temperature Shift of Swelling Observed in Annealed Fe-18Cr-10Ni-Ti Stainless Steel Irradiated in the Reflector Region of BOR-60", these proceedings.

[4] Garner, F. A. and Toloczko, M. B., "Irradiation Creep and Void Swelling of Austenitic Stainless Steels at Low Displacement Rates in Light Water Energy Systems", *Journal of Nuclear Materials*, Vol. 251 (1997) pp. 252-261.

[5] Garner, F. A., Toloczko, M. B., Porollo, S. I., Vorobjev, A. N., Dvoriashin, A. M., and Konobeev, Yu. V., "Potential Irradiation Creep and Void Swelling of Stainless Steels in PWR Internals", Eighth International Symposium on Environmental Degradation of Materials in Nuclear Power Systems - Water Reactors, August 10-14, 1997, Amelia Island, Florida, *1997*, pp. 839-845.

[6] Garner, F. A., "Irradiation Performance of Cladding and Structural Steels in Liquid Metal Reactors", *Materials Science and Technology: A Comprehensive*

Treatment, Volume 10A, VCH Publishers, 1994, pp. 419-543.

[7] Porollo, S. I., Vorobjev, A. N., Konobeev, Yu. V., Dvoriashin, A. M., Krigan, V. M., Budylkin, N. I., Mironova, E. G., and Garner, F. A., "Swelling and Void-Induced Embrittlement of Austenitic Stainless Steel Irradiated to 73-82 dpa at 335-365°C", *Journal of Nuclear Materials,* Vols. 258-263, (1988) pp. 1613-1617.

[8] Porollo, S. I., Vorobjev, A. N., Konobeev, Yu. V., and Garner, F. A., in preparation.

[9] Hamilton, M. L., Huang, F. -H., Yang, W. J. S., and Garner, F. A., "Mechanical Properties and Fracture Behavior of 20% Cold-Worked 316 Stainless Steel Irradiated to Very High Neutron Exposures", in *Influence of Radiation on Materials Properties: 13th International Symposium, Part II, ASTM STP 956,* F. A. Garner, C. H. Henager, Jr., and N. Igata, Eds., American Society for Testing and Materials, 1987, pp. 245-270.

[10] Fissolo, A., Cauvin, R., Hugot, J. P., and Levy, V., "Influence of Swelling on Irradiated CW Titanium Modified 316 Embrittlement", in *Effects of Radiation on Materials: 14th International Symposium, Vol. II, ASTM STP 1046,* N. H. Packan, R. E. Stoller and A. S. Kumar, Eds., American Society for Testing and Materials, Philadelphia, 1990, pp. 700-713.

[11] Neustroev, V. S. and Shamardin, V. K., *Atomnaya Energiya,* Vol. 71 (1991), pp. 345-348.

D. L. Porter,[1] F. A. Garner,[2] and G. M. Bond[3]

Interaction of Void-Induced Phase Instability and Subsequent Void Growth in AISI 304 Stainless Steel

Reference: Porter, D. L., Garner, F. A., and Bond, G. M., **"Interaction of Void-Induced Phase Instability and Subsequent Void Growth in AISI 304 Stainless Steel,"** *Effects of Radiation on Materials: 19th International Symposium, ASTM STP 1366,* M. L. Hamilton, A. S. Kumar, S. T. Rosinski, and M. L. Grossbeck, Eds., American Society for Testing and Materials, West Conshohocken, PA, 2000.

Abstract: There are two types of radiation-induced phase instabilities that AISI 304 is prone to develop at temperatures in the 400-550°C range at dpa rates typical of fast reactors, and there is some concern that these instabilities may shift to lower temperatures (≤400°C) at lower dpa rates typical of pressurized water reactors.

One of these instabilities, the void-induced $\gamma \rightarrow \alpha$ transformation, is investigated in this study at dpa rates typical of both types of reactors. The mode of nickel segregation shifts somewhat at PWR-relevant conditions, but the $\gamma \rightarrow \alpha$ transformation has not yet been observed in the range 380-400°C for swelling levels less than 2%.

Keywords: AISI 304, AISI 304L, void swelling, embrittlement, ferrite, displacement rate

Introduction

The possibility has recently been raised that AISI 304 and 316 stainless steels will exhibit void swelling to significant levels in some internal components of Pressurized Water Reactors (PWRs) as a consequence of very high neutron exposures (80-90 dpa) and the action of the "temperature shift" to increase swelling at PWR-relevant displacement rates of $\leq 10^{-7}$ dpa sec^{-1} and temperatures on the order of 300-400°C [*1-8*]. The "temperature-shift" is the observed movement in the temperature regime of swelling in response to significant changes in displacement rate during irradiation [*9,10*].

It is well known, however, that other phenomena such as radiation-induced segregation also are susceptible to temperature shift effects [*11*]. One segregation phenomenon of particular interest is the severe embrittlement observed during room temperature deformation after swelling levels of ~10% have been exceeded for

[1] Senior Metallurgical Engineer, Argonne National Laboratory-West, Idaho Falls, ID USA.
[2] Senior Staff Scientist, Pacific Northwest National Laboratory, Richland, WA USA.
[3] Associate Professor, New Mexico Institute of Mining and Technology, Socorro, NM USA.

Copyright© 2000 by ASTM International www.astm.org

irradiations conducted at ~400°C in fast reactor cores [*12,13*]. This failure mechanism has been shown to arise from a combination of stress concentration between voids, nickel segregation to voids surfaces, and precipitation of nickel-rich phases. The resultant lower nickel concentration of the alloy matrix predisposes the alloy to form very high densities of ϵ-martensite platelets during low temperature deformation. These platelets strongly strengthen the matrix but also provide a path for crack propagation as the stress concentration at the crack tip transforms the ϵ-martensite to the very brittle α-martensite. ϵ-martensite formation is enhanced by the tendency of the stacking fault energy to fall strongly both with lower nickel content and decreased temperature. This is important because ϵ-martensite is essentially a stacking fault in the fcc matrix.

The foregoing raises the possibility that PWR baffle-former components constructed of AISI 304 or 316 stainless steels might become very brittle toward the end of their target 40-year operation lifetime. If swelling and nickel segregation are both shifted to lower temperatures during irradiation at PWR-relevant displacement rates, then the possibility of void-induced embrittlement may be higher than that observed in fast reactors where the displacement rates are on the order of $\geq 1 \times 10^{-6}$ dpa sec^{-1}. There is some limited evidence to show that AISI 304L increases in swelling as the dpa rate declines [*14-16*].

There is another phase instability to which AISI 304L is uniquely prone to develop at somewhat higher temperatures during irradiation in fast reactor cores. At ~500°C, segregation of nickel occurs at void surfaces at an even stronger rate and results in extensive transformation of the austenite matrix to ferrite, with austenite retained only on void surfaces. If this process is also subject to a temperature shift, then this represents another embrittlement mechanism that must be addressed for end-of-life PWR operation.

This paper explores this latter potential embrittlement mechanism. Some portions of the work relevant to fast reactor operation were published earlier [*17,18*].

Experimental Details

Annealed AISI 304L irradiated to doses of ≤50 dpa in the form of unstressed creep capsules in EBR-II were sectioned to produce a number of specimens in the range 400-550°C. The composition of the steel is Fe-18.3Cr-9.26Ni-0.02Mo-1.37Mn-0.62Si-0.03C with small amounts of P(0.01), Ti(0.02), Cu(0.074), Co(0.05) and S(0.007), all in weight percent. Magnetic examination had earlier suggested the formation of significant amounts of α-ferrite.

Electrolytic dissolution of the matrix was used to extract $M_{23}(C,Si)_6$ precipitates from a wide range of temperature/fluence combinations. Other potential phases such as α-ferrite and γ' dissolve. The $M_{23}(C,Si)_6$ precipitates were identified in the alloy matrix by electron microscopy. Atomic absorption analysis was used to determine the relative amounts of Fe, Ni and Cr in the precipitates. Electron microscopy at 100 KeV was also performed on several specimens at ~500°C to investigate the formation of massive ferrite transformation of the alloy matrix. The swelling levels for transformed specimens ranged from ~3 to 17%, as measured by immersion density [*17*].

A separate study now in progress involves the microscopy examination of annealed AISI 304 (not low carbon) stainless steel reflector components irradiated at

lower dpa rates. The composition of this steel is Fe-18.7Cr-9.1Ni-0.01Mo-1.5Mn-0.6Si-0.06C-0.03P-0.02Co-0.05N, in weight percent.

Results

Figure 1 shows that the time dependence of irradiation-induced $M_{23}(C,Si)_6$ precipitation is relatively insensitive to irradiation temperature in range 415-525 °C. Figure 2, however, shows that the nickel content of the precipitates rises strongly as the temperature decreases.

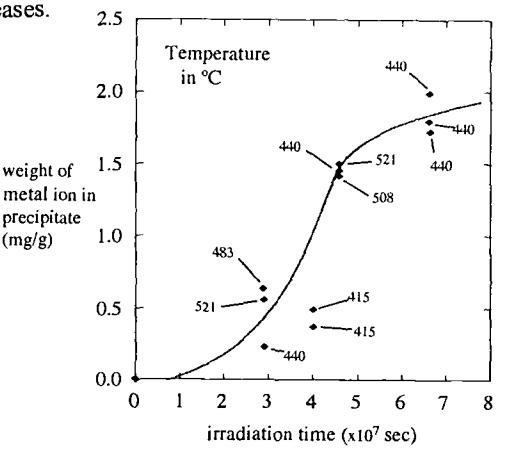


Figure 1 - *Development of irradiation-induced precipitation in annealed 304L stainless steel, showing a relative insensitivity of total precipitate volume to irradiation temperature.*

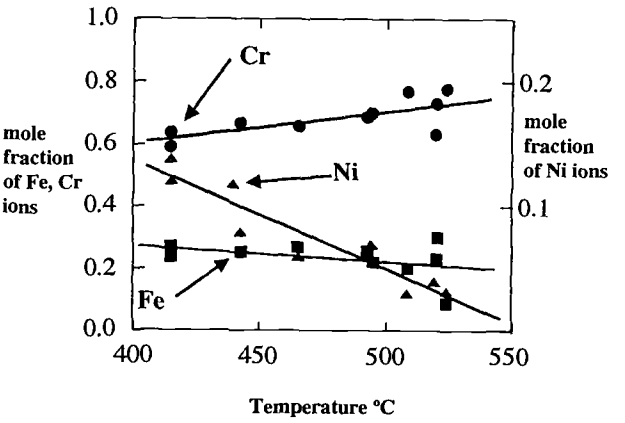


Figure 2 - *Dependence on irradiation temperature of metal ion composition in $M_{23}(C,Si)_6$ precipitates extracted from annealed 304L stainless steel over a wide range of neutron fluences.*

At these displacement rates the swelling in these specimens at ~400°C has not yet approached the 10% level so the void-induced embrittlement by martensite phenomenon has not yet surfaced. Most of the nickel segregation at lower temperature is concentrated in the $M_{23}(C,Si)_6$ precipitates, while at higher temperatures precipitate-related segregation of nickel is lower and segregation to void surfaces is proportionally more important.

Figure 3 shows that at ~500°C and ~18 dpa a partially transformed state has been reached where a large ferrite region is growing at the expense of a remaining austenite regions. The transformation interface induces heavy faulting in the austenite just ahead of the interface, probably as a consequence of the strains induced by the larger volume occupied by the less-dense α-ferrite phase. Note also that austenite shells are retained around the voids, reflecting the higher nickel content on their surfaces.

The series of micrographs in Figure 4 shows that in a completely transformed region the matrix is essentially all α-ferrite with the γ-phase retained only as shells on the void surfaces.

Since bcc structures are thought to be inherently lower swelling than fcc structures, such a void-driven process should be self-limiting, in that the void-swelling rate should strongly decline once the transformation is complete. This possibility was checked by measuring the void density and sizes in a number of completely transformed and untransformed areas of two different specimens.

As shown in Figure 5, the swelling within the γ regions is larger than that of the α regions, with the latter always having slightly lower mean void sizes. In the two cases shown, the swelling in the γ regions is 39-46% higher than that of adjacent α regions. While such data are not totally conclusive, they are consistent with a cessation or strong reduction in void growth rate after the $\gamma \rightarrow \alpha$ transformation.

To investigate the possibility that a temperature-shift in both void swelling and the $\gamma \rightarrow \alpha$ transformation might occur, specimens of annealed AISI 304 irradiated at lower PWR-relevant dpa rates are being examined by electron microscopy. These specimens are being extracted from unfueled hexagonal reflector elements which typically reach temperatures of only 370-420°C. Some early results are presented in this paper.

As shown in Figures 6 and 7, void swelling indeed occurs under these conditions and is accompanied by precipitates identified as $M_{23}(C,Si)_6$. The swelling at the specified dpa levels is larger than that expected for comparable in-core irradiations at higher dpa rates, but has not yet exceeded 2% under any conditions studied. The most significant feature is the absence of α-ferrite, although there is no guarantee that it will not form at higher neutron exposures and swelling levels.

The higher level of carbon in the reflector elements compared to that of the 304L capsule should promote and increase the formation of nickel-rich $M_{23}(C,Si)_6$ precipitates at these lower temperatures, and may actually encourage an earlier onset of the $\gamma \rightarrow \alpha$ transformation, but more data are required to investigate this possibility. The role of higher carbon levels to stabilize against the $\gamma \rightarrow \alpha$ transformation may mitigate the transformation, however, and the issue requires further investigation.

Conclusions

At temperatures near 500°C and at dpa rates on the order of 1×10^{-6} dpa/sec, a void-induced segregation of nickel in AISI 304L leads to a $\gamma \rightarrow \alpha$ transformation of the

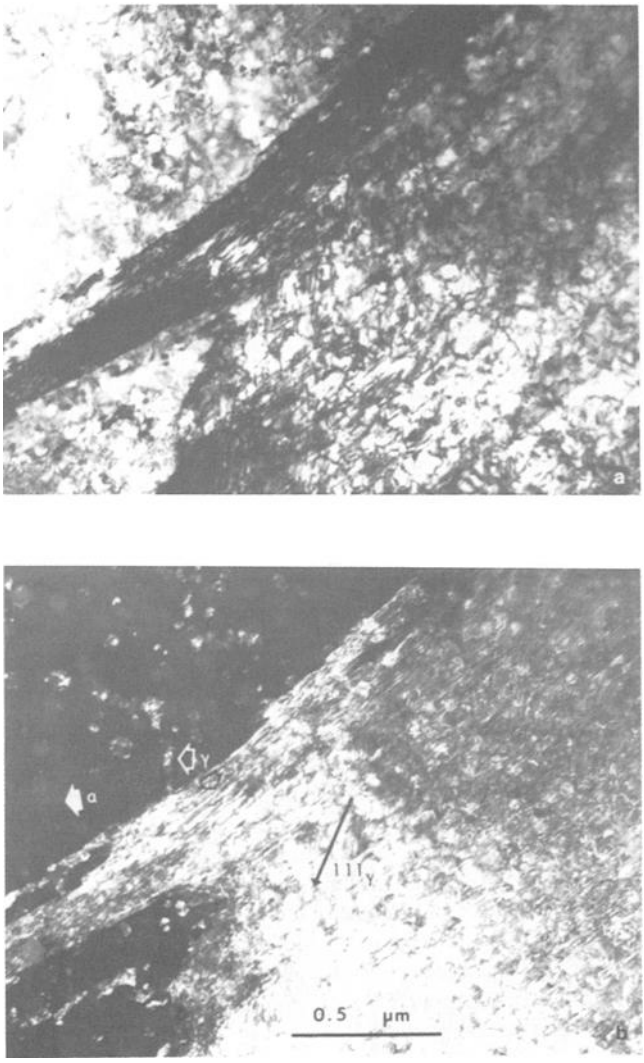


Figure 3 - *Bright-field and dark-field micrographs showing a $\gamma \rightarrow \alpha$ transformation interface advancing from left to right, inducing large amounts of faulting in the γ phase and leaving in its wake austenite only as shells on voids. This specimen was extracted from annealed 304L irradiated at ~399 °C and 3.5 x 10^{22} n cm^{-2} (E>0.1 MeV) or ~17.5 dpa.*

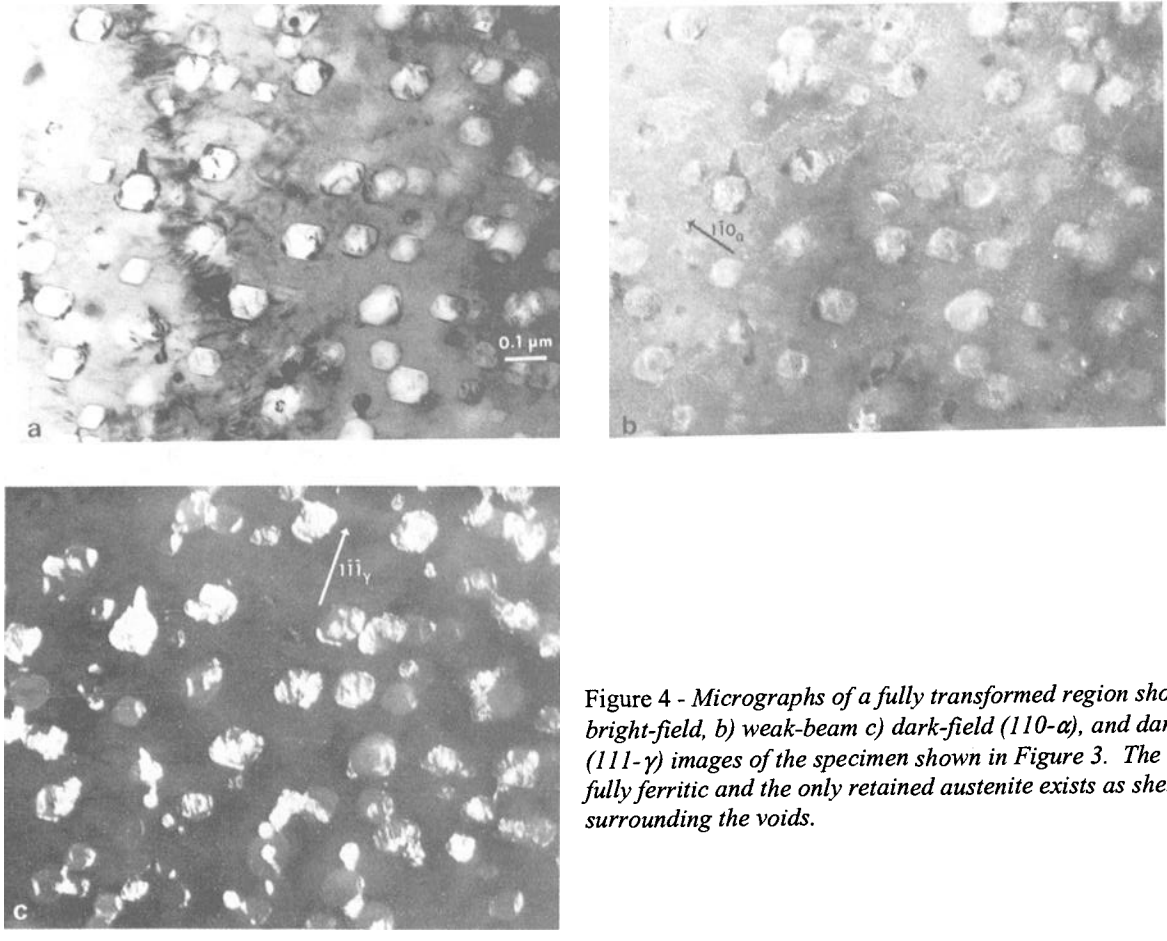


Figure 4 - *Micrographs of a fully transformed region showing a) bright-field, b) weak-beam c) dark-field (110-α), and dark-field (111-γ) images of the specimen shown in Figure 3. The matrix is fully ferritic and the only retained austenite exists as shells surrounding the voids.*

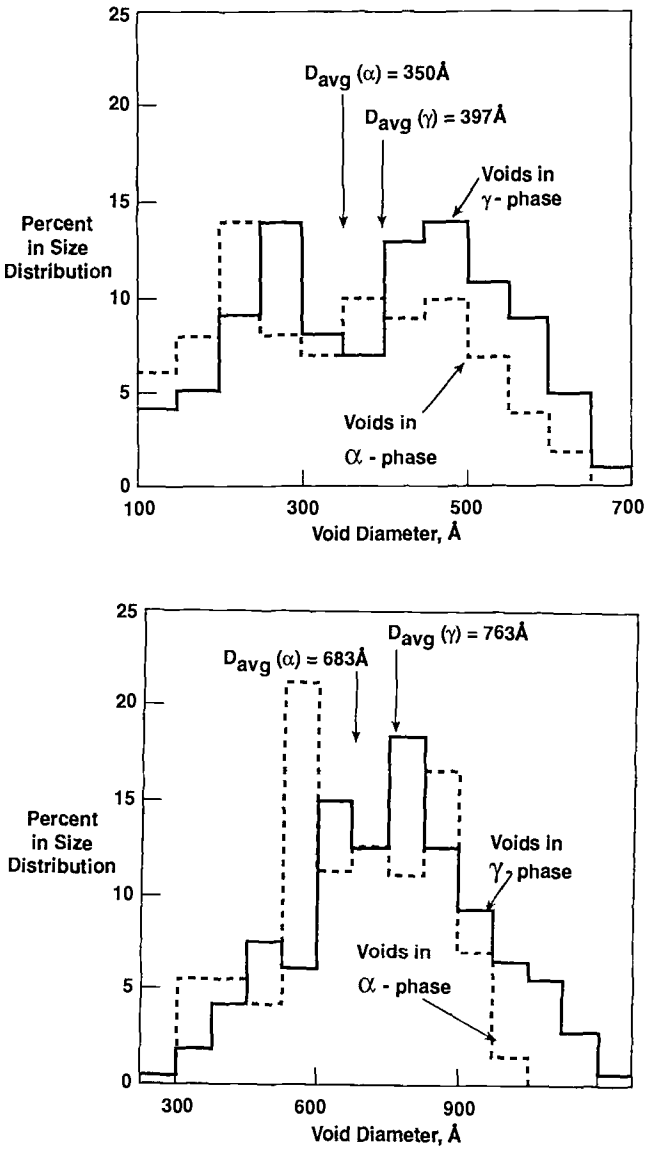


Figure 5 - *Void size distributions measured in both transformed and untransformed regions of annealed AISI 304 at 499 °C and 17.5 dpa (top), and at 518 and 33 dpa (bottom). The void sizes in transformed regions are smaller, and the total swelling is less than in untransformed regions. The ratio of swelling in γ-regions compared to α-regions is 1.46 and 1.39 respectively.*

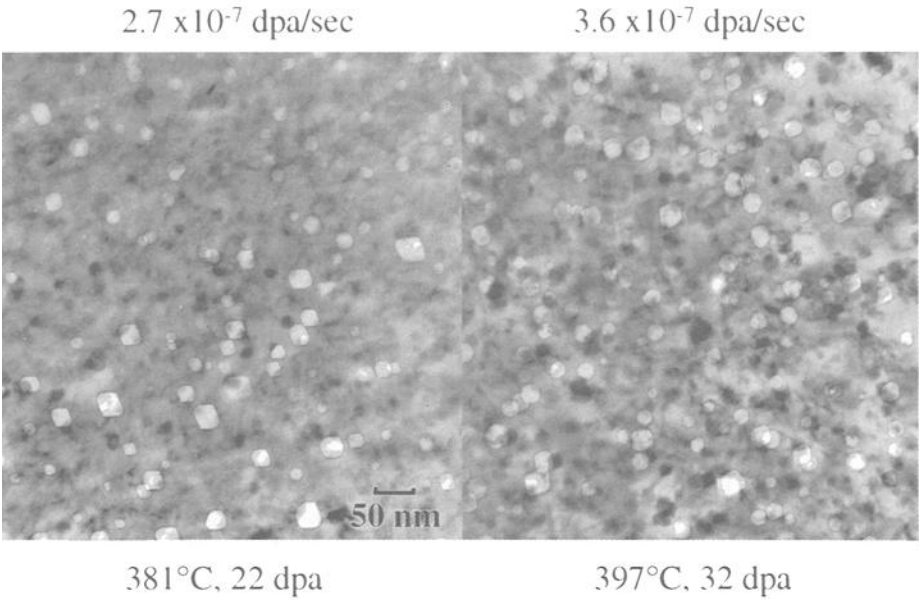


Figure 6 - *Void swelling observed in annealed AISI 304 at lower dpa rates, with swelling at ≤2%, $M_{23}(C,Si)_6$ precipitation, and the absence of ferrite formation.*

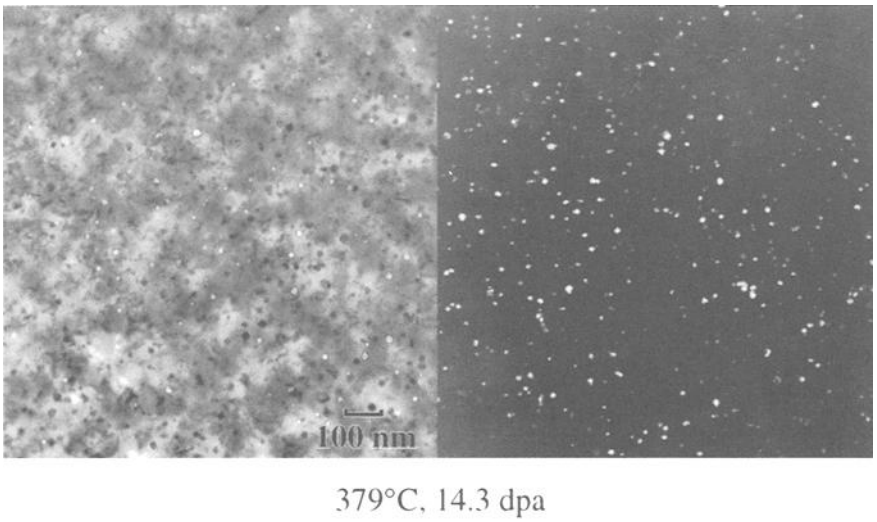


Figure 7 - *Bright-field and dark-field images showing concurrent growth of void swelling and $M_{23}(C,Si)_6$ precipitates at a dpa rate of 1.7×10^{-7} dpa sec^{-1}.*

alloy matrix, leaving austenite only as shells on void surfaces. Void swelling appears to be strongly reduced in rate in transformed areas, indicating that at least the swelling may be self-limiting under such circumstances.

At lower temperatures (~400°C) ferrite formation has not yet been observed and the major nickel-segregation mechanism shifts towards the formation of Ni-rich $M_{23}(C,Si)_6$ precipitates, although it is expected that this precipitation process saturates and segregation to void surfaces will eventually become larger.

The possibility still exists, however, that as the dpa rate is reduced to levels comparable to those of PWRs, void swelling, nickel segregation and the $\gamma \rightarrow \alpha$ transformation will shift to lower PWR-relevant temperatures. In annealed 304 stainless steel in the 380-400°C range this has not yet been observed to happen for dpa rates on the order of $\leq 3 \times 10^{-7}$ dpa sec^{-1} and swelling levels of $\leq 2\%$.

Acknowledgements

The US Department of Energy supported this work under Contract DE-AC06-76RLO 1830.

References

[1] Garner, F. A., Greenwood, L. R., and Harrod, D. L., *Sixth International Symposium on Environmental Degradation of Materials in Nuclear Power Systems - Water Reactors, The Minerals, Metals, and Materials Society, 1993*, pp. 783-790.

[2] Garner, F. A., Transactions of the American Nuclear Society, Vol. 71, 1994, pp. 190-191.

[3] Garner, F. A. and Toloczko, M. B., *Journal of Nuclear Materials*, Vol. 251, 1997, pp. 252-261.

[4] Garner, F. A., Toloczko, M. B., Porollo, S. I., Vorobjev, A. N., Dvoriashin, A. M., and Konobeev, Yu. V., *Eighth International Symposium on Environmental Degradation of Materials in Nuclear Power Systems - Water Reactors, August 10-14, 1997, Amelia Island Florida, 1997*, pp. 829-845.

[5] Porollo, S. I., Vorobjev, A. N., Konobeev, Yu. V., Dvoriashin, A. M., and Garner, F. A., *Proc. Inter. Symp. on "Contributions of Materials Investigation to the Resolution of Problems Encountered in Pressurized Water Reactors," 14-18 Sept. 1998, Fontevraud, France*, pp. 271-280.

[6] Garner, F. A., Porollo, S. I., Vorobjev, A. N., Konobeev, Yu. V., Dvoriashin, A. M., Krigan, V. M., Budylkin, N. I., and Mironova, E. G., *Proc. Inter. Symp. on "Contributions of Materials Investigation to the Resolution of Problems Encountered in Pressurized Water Reactors," 14-18 Sept. 1998, Fontevraud, France*, pp. 249-260.

[7] Garner, F. A., Porollo, S. I., Vorobjev, A. N., Konobeev, Yu. V., Dvoriashin, A. M., and Krigan, V. M., these proceedings.

[8] Neustroev, V. S., Shamardin, V. K., Ostrovsky, Z. E., Pecherin, A. M., and Garner, F. A., these proceedings.

[9] Packan, N. F., Farrell, K., and Steigler, J. O., *Journal of Nuclear Materials,* Vol. 78, 1978, pp. 143-155.

[10] Mansur, L. K., "Theory of Transitions in Dose Dependence of Radiation Effects in Structural Alloys", in *Journal of Nuclear Materials,* Vol. 206, 1993, pp. 306-323.

[11] Simonen, E. P., and Bruemmer, S. M., "Lattice Defect/Grain Boundary Interactions Related to IASCC," in *Journal of Nuclear Materials,* Vol. 239, 1996, pp, 185-193.

[12] Hamilton, M. L., Huang, F. -H., Yang, W. J. S., and Garner, F. A., "Mechanical Properties and Fracture Behavior of 20% Cold-Worked 316 Stainless Steel Irradiated to Very High Neutron Exposures," in *Influence of Radiation on Material Properties, 13th International Symposium, Part II, ASTM STP 956,* F. A. Garner, C. H. Henager, Jr., and N. Igata, Eds., American Society for Testing and Materials, 1987, pp. 245-270.

[13] Garner, F. A., "Irradiation Performance Cladding and Structural Steels in Liquid Metal Reactors," in *Materials Science and Technology, A Comprehensive Treatment*, Vol. 10A, VCH Publishers, 1994, pp. 419-543.

[14] Porter, D. L. and Hudman, G. L., Trans. ANS, 1980, pp. 230-231.

[15] Porter, D. L. and Garner, F. A., "Swelling of AISI Type 304L Stainless Steel in Response to Simultaneous Variations in Stress and Displacement Rate," in *Effects of Radiation on Materials, Twelfth International Symposium, ASTM STP 870,* F. A. Garner and J. S. Perrin, Eds., American Society for Testing and Materials, 1985, pp. 212-220.

[16] Porter, D. L., Hudman, G. D., and Garner, F. A., "Irradiation Creep and Swelling of Annealed Type 304L Stainless Steel at ~390°C and High Neutron Fluence," in *Journal of Nuclear Materials,* Vols. 179-181, 1991, pp. 581-584.

[17] Porter, D. L., "Ferrite Formation in Neutron-Irradiated Type 304L Stainless Steel," in *Journal of Nuclear Materials,* Vol. 79, 1979, pp. 406-411.

[18] Porter, D. L., and Wood, E. L., "In-Reactor Precipitation and Ferritic Transformation in Neutron-Irradiated Stainless Steels," in *Journal of Nuclear Materials,* Vol. 83, 1979, pp. 90-97.

Wolfgang Schüle[1]

On the Formation of α-Ferrite in Stainless Steel Alloys

Reference: Schüle, W., **"On the Formation of α-Ferrite in Stainless Steel Alloys,"** *Effects of Radiation on Materials: 19th International Symposium, ASTM STP 1366,* M. L. Hamilton, A. S. Kumar, S. T. Rosinski, and M. L. Grossbeck, Eds., American Society for Testing and Materials, West Conshohocken, PA, 2000.

Abstract: Results of investigations on the microstructure of nickel-containing and of manganese-containing stainless steel alloys by means of the electrical resistivity are reported. These investigations were completed by X-ray diffractometry, by measurements of the magnetic response and of the stored energy. The investigations were performed on AMCR- and 316-type materials and on model stainless steel alloys varying slightly in the composition of the main components of the alloys and the concentrations of the additions.

The following phases were identified: α-ferrite, γ-austenite, α'-martensite, $\alpha'_{def.}$-martensite, ε-martensite, $\varepsilon_{def.}$-martensite, α-Mn and σ-phase. Small amounts of α-ferrite, α-Mn and σ-phase in stainless steel alloys cause brittleness.

It was found that α-ferrite is always formed when nucleation sites, e.g. α'-martensite and dislocations, are provided. α-ferrite is readily formed by annealing at e.g. 356°C and is dissolved again after annealing for one month at the same temperature, when the nucleation sites are dissolved or recovered.

During irradiation with high energy particles α-ferrite is formed below about 600°C in AMCR- and 316-type stainless steel alloys. The amount of α-ferrite formed at 100°C is so large that many of the stainless steel specimens broke before a dose of 0.11 dpa was obtained.

These findings require a modification of the phase diagrams of stainless steel alloys.

Keywords: phase diagrams of stainless steel alloys, radiation, α-ferrite, α'-martensite, α-Mn-and ε-phase, nucleation, ductility, radiation-induced microstructure

[1] Professor, Institut für Angewandte Physik der Johann Wolfgang Goethe-Universität Frankfurt, Robert Mayer Straße 2-4, D-60325 Frankfurt, Germany. Corresponding address: Via Bosco 23, I-21038 Leggiuno (Va), Italy.

Copyright© 2000 by ASTM International www.astm.org

Introduction

Iron-chromium-nickel alloys have been extensively investigated in many different laboratories all over the world during the last century. Many different properties were developed for certain applications varying the type of additions and the concentration of these additions, and the thermo-mechanical treatments. The influence of many elements added simultaneously to iron-chromium-nickel alloys on many different properties were investigated and the respective phase diagrams were prepared. An impression on the variety of the results can be obtained from steel factory catalogues, in which often more than four hundred steels for different purposes and applications are listed. The complexity of the problems and the complexity of the constitution of the steel alloys due to the formation of α-ferrite can be obtained from the Handbook of Stainless Steels [1].

Studies on the kinetics of the formation and dissolution of the various possible phases in stainless steel alloys show that the mobility of the component atoms in stainless steel alloys is very similar to the mobilities of atoms in nickel [2]. However, some phases, e.g. α-ferrite, are only formed if nucleation sites are provided. This means that they are often formed in a very sluggish way, when no nucleation sites are present, but that they are dissolved readily in that temperature range in which they are not stable. However, α-ferrite is a very brittle phase causing a decrease in volume, when it is formed. Many 316- and AMCR-type stainless steel specimens broke before they obtained an irradiation dose of 0.11 dpa irradiating at 100°C [3].

From the many possible candidate materials for applications in nuclear reactors only very few mainly commercially available 316-type stainless steel materials have been investigated during the last forty years. It was found that the compositions of the many phases and compounds present in stainless steel alloys change during irradiation with high energy particles and also new phases are formed [4-6]. However, phase diagrams of stainless steel alloys valid during irradiation with high energy particles were not obtained during the last forty years by varying the main elements and the type and concentration of the additions systematically. There is no known reason for most of the many elements added to stainless steel alloys used in nuclear applications. Fortunately, all the many phases present in stainless steel materials do not limit their use in nuclear applications, except titanium. The formation of titanium carbide is connected with a huge increase in volume and causes a decrease in ductility so that e.g. the tubes of the heat exchanger in a German nuclear power reactor broke after two years of service. The tubes were not even exposed to radiation during that time but the tube temperature of 200°C was sufficiently high that titanium carbide is formed in the two years of service [3].

Stainless steel alloys, which contain manganese instead of nickel, have been investigated during the last twenty years, especially with respect to their possible application in nuclear reactors. The phase diagram of these stainless steel alloys was hardly known for temperatures below about 600°C. Extensive studies on this phase diagram also below 600°C were reported recently [7,8]. A sectional view of the phase diagram for 600°C is shown in Fig. 1. The γ-phase field is very narrow and is much smaller than that of the nickel-containing stainless steel alloys.

Adjacent to the single γ-phase field is the two-phase field containing γ-austenite and α-Mn-phase. The α-Mn-phase is ductile, if it does not contain chromium and is very brittle, if it contains about 20% chromium. This phase is always formed readily and hardly any incubation time was observed for its formation. It should be mentioned that the phase diagrams of iron-chromium-manganese and also the two element iron-manganese phase diagram are often not reported correctly in the literature [1,9]. Fortunately, the α-Mn-phase is not formed in AMCR-type materials with or without high energy particle irradiation, if these materials contain less than about 12% chromium, i.e. the phase boundary does not depend on temperature.

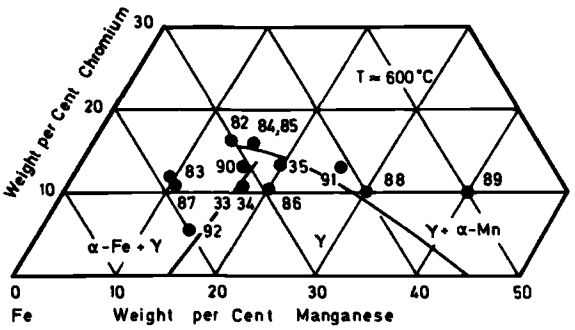


Figure 1 - *The α-Fe+γ⇔γ- and the γ⇔γ+α-Mn-phase boundaries for iron-manganese-chromium alloys are shown for temperature T ≈ 600°C. After references [7] and [8].*

The α-ferrite phase is a very brittle phase both in nickel- and in manganese-containing steels. The volume change connected with the formation of this phase changes the external dimensions of the materials dramatically, i.e. the shape of the materials changes completely when this phase is formed during annealing. The formation of this phase decreases the volume by which the materials shrink. This phase is also formed during irradiation with an applied stress [6,10]. During an irradiation in a low flux position of the High Flux Reactor at Petten, The Netherlands, many stainless steel samples of the AMCR-type materials and also of 316L-type materials broke at an irradiation temperature of 100°C before an irradiation dose of only 0.11 dpa was obtained [3].

Many different phases and compounds have been identified in 316-type stainless steel alloys [4,5] during the last twenty years. It was further found that all these phases become enriched in nickel during irradiation, but that, however, these phases were not enriched in silicon, if silicon was present, and that instead, e.g. Ni-Si-precipitates were formed. Also the carbides were not enriched in nickel and silicon during irradiation. The influence of all these phases on e.g. the mechanical properties is not fully understood and the influence of many of the phases formed during irradiation with high energy particles on e.g. the mechanical behavior or on the corrosion resistance is not known. However, the nickel content of the γ-phase must increase during irradiation with respect to solution annealed materials.

Many of the types of phases, which are found in 316-type stainless steel alloys, may also be present in manganese-containing stainless steel alloys. However,

investigations on these possible phases were not performed on AMCR-type materials so far.

We will report in the present work especially on the formation of α-ferrite in AMCR-type and in 316-type materials especially during irradiation with high energy particles. We will show that nucleation sites must be provided so that α-ferrite is formed in these materials. Suggestions on the course of the $\alpha+\gamma \Leftrightarrow \gamma$-phase boundaries in the two alloys are made.

Experiments

Materials

The materials investigated in the present work were obtained from Creusot-Loire (France) and from Vakuum Schmelze Hanau (Germany). The compositions of the various alloys investigated in the present work are listed in Table 1.

Table 1 - *The composition of stainless steel alloys in wt% investigated in the present work is listed. The balance is iron.*

Alloy	C [wt%]	Cr [wt%]	Mn [wt%]	Ni [wt%]	Mo [wt%]	W [wt%]	Si [wt%]	Ti [ppm]	V [wt%]
AMCR 0033	0.105	10.12	17.50	<0.10	<0.060	-	0.55	-	<0.02
AMCR 0035	0.029	14.09	19.88	0.265	0.060	-	0.63	-	-
316L	0.022	17.44	1.81	12.34	2.3	-	0.45	-	-
81/5283	0.005	11.40	6.85	4.20	-	-	-	-	-
81/5282	0.003	16.95	-	12.10	-	-	-	-	-
81/5284	0.004	18.00	5.10	10.50	-	-	-	-	-
81/5286	0.004	10.20	19.95	-	-	-	-	-	-
1S5P	0.31	12.37	10.62	0.23	0.023	1.42	0.17	<10	0.645
1E3	0.08	17.8	11.0	2.08	0.041	2.02	0.30	<10	0.74
D3	0.26	10.24	16.92	0.13	0.026	2.04	0.50	<20	0.036
1C4P	0.10	13.14	18.00	2.14	0.037	1.92	0.20	<10	0.021
1A1T	0.10	13.5	11.3	2.04	0.031	1.42	0.2	<10	0.63

The AMCR-type materials were obtained in the solution-annealed state in huge plates having a cross section of about 15 cm x 3 cm and a length of about 300 cm or in rods having a diameter of about 2.5 cm. Small pieces were cut from these plates and cold-worked to foils having a thickness of about 0.2 mm with many intermediate annealings at high temperatures. The detailed treatments of the materials prior to the investigation including the final degree of cold-work are mentioned in the text.

In the present work results of investigations obtained by various electrical resistivity techniques are reported. These techniques are described in references [7] and [8].

The annealing treatments of the materials were performed in an argon atmosphere containing 5% hydrogen and under vacuum (<10^{-4} torr). The evaporation of manganese in some of the investigated materials was noticed when annealing at temperatures higher than 800°C under vacuum (<10^{-4} torr).

Results and Discussion

It is well known that nucleation is a preliminary stage for the formation of precipitates in an alloy. This means that an alloy can remain single phase even though the thermal equilibrium would consist of two phases when nucleation sites are not provided. In reality the matter is much more complicated, because precipitates may also be formed, if nucleation sites are provided, when the precipitates are not stable in thermal equilibrium. In such cases, however, if the nucleation sites are used up, no new precipitates are formed and the already existing precipitates will dissolve.

Nucleation for α-ferrite formation in stainless steel alloys is provided by i) dislocations, ii) applied stresses iii) dislocations and applied stresses, iv) α'-martensite, v) α'-martensite and dislocations, vi) $\varepsilon_{def.}$-martensite and vii) $\varepsilon_{def.}$-martensite and applied stresses.

Diffusion rates are often enhanced by many orders of magnitudes during irradiation with high energy particles with respect to thermal diffusion rates for the same temperature. Thus the rate of change of the geometrical arrangement of component atoms in an alloy during irradiation, i.e. the microstructural evolution, is much faster during irradiation with high energy particles than that due to thermal diffusion. For the formation of radiation-induced structures nucleation is also necessary as it is without irradiation. However, radiation can cause nucleation itself and enhance the formation of radiation-induced microstructures.

Only vacancy type defects can rearrange the geometrical distribution of component atoms in experiments performed without irradiation. During irradiation with high energy particles interstitials can also often change sites with the component atoms of an alloy and thus contribute to diffusion. Interstitials are often much more mobile than vacancies. Thus radiation-enhanced diffusion due to interstitials is often orders of magnitude larger than that due to vacancies only [11]. The rate of formation of radiation-induced structures is usually especially large, when one component element of the alloy is undersized, e.g. beryllium in copper, or silicon in nickel, or silicon in stainless steel alloys. The correlation factor for interstitialcy diffusion is f_{1V}=0.783 in a self-diffusion experiment [2]. But the correlation factor for interstitialcy diffusion of silicon in nickel may achieve values of several thousands or a silicon-interstitial remains a silicon interstitial till it becomes precipitated.

In the following we mainly present results on the formation of α-ferrite in nickel- and in manganese-containing stainless steel alloys with and without irradiation and on the rule of nucleation for the formation of this phase.

We will mainly report results obtained by measuring the electrical resistivity or the electrical resistance as a function of the annealing temperature. The electrical resistivity is often very sensitive to any microstructural change occurring during or after a thermomechanical treatment. However, the electrical resistivity is a non-specific property for microstructural

variations. Therefore almost all microstructural variations observed in the present work were determined by means of X-ray diffraction spectroscopy (XRD). In addition highly sensitive calorimetric and magnetic response measurements were performed. In the present work only resistivity data are reported and reference is made to results of investigations obtained by other means [7,8].

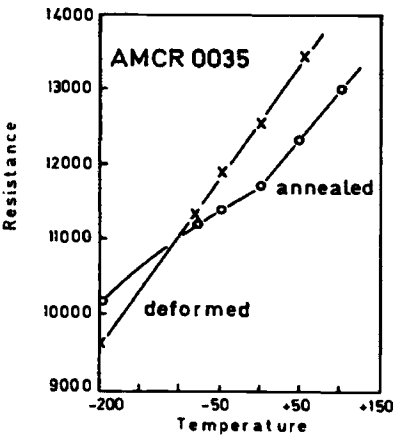


Figure 2 - *The electrical resistivity is plotted versus the measuring temperature for a specimen first annealed at 1000°C in an argon atmosphere containing 10% hydrogen and then 41% cold worked. After references [7] and [8].*

There is a further peculiarity of the electrical resistivity in stainless steel alloys varying from alloy to alloy. The electrical resistance of an annealed and of a cold-worked material, namely of alloy AMCR 0035, is plotted versus the measuring temperature in Fig. 2. The electrical resistance of a cold worked specimen of AMCR 0035 is smaller than that of an annealed specimen, if the measuring temperature is below about -100°C. However, the electrical resistance of a deformed specimen is larger than that of an annealed specimen, if it is measured above about -100°C.

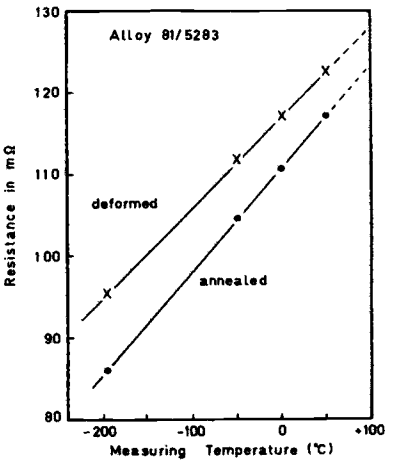


Fig. 3 - *The electrical resistance of a cold worked and of an annealed specimen is plotted versus the measuring temperature. The specimen was 18% cold worked prior to annealing and was annealed in an argon atmosphere containing 5% hydrogen. After references [7] and [8].*

The electrical resistance of annealed and of cold worked alloy 81/5283 is plotted versus the temperature in Fig. 3. The resistance of a cold worked specimen is always larger than that of an annealed specimen in the temperature range between -200 and +100°C. However, the two curves extrapolated to high temperatures intersect at about 440°C. This means that the resistivity of an annealed sample is larger than that of a cold worked specimen for temperatures higher than about 440°C.

This means that the formation of α-ferrite in alloy 81/5283 causes a decrease of the electrical resistivity, if measured below about 440°C, and the dissolution of this phase also causes a decrease, if measured above 440°C.

On the Formation of α-Ferrite in Alloy 81/5283 (77.55 Fe, 11.40 Cr, 4.20Ni, and 6.85 Mn)

The change of the electrical resistance and the derivative of this quantity with respect to the temperature is plotted for increasing and decreasing temperature in Fig. 4 [7,8]. The sample was about 20% cold worked prior to annealing. It is seen that the electrical resistance decreases with increasing temperature first in two stages at about 400 and 450°C and then again in two stages at 590 and 620°C.

On cooling the electrical resistance decreases in a steady way from 1000°C to about 150°C and increases beyond this temperature. It is evident that α'-martensite is formed below 150°C without diffusion of component atoms. Results of XRD-measurements show that even all γ-austenite is transformed into α'-martensite at ambient temperature.

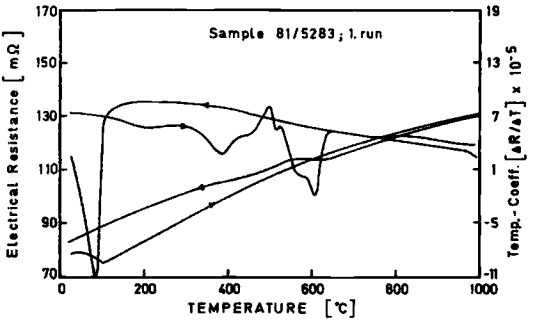


Fig. 4 - *The electrical resistivity and the temperature coefficient of a previously about 20% cold worked specimen of alloy 81/5283 is plotted for increasing and decreasing temperature (1. run). The anneals were performed in argon with 5% hydrogen.*

The electrical resistivity of a deformed specimen is always larger than the electrical resistivity of an annealed specimen, when the measurements are performed below 440°C (Fig. 3). However, there is a temperature, which is obtained by extrapolating the two curves to high temperatures, at which the electrical resistivities of an annealed and of a cold worked specimen are equally large and above which the electrical resistivity of a deformed specimen is smaller than that of an annealed specimen.

Therefore, we can explain the features reported in Fig. 4. The microstructure formed during heating between 300 and 450°C causes a decrease of the electrical resistivity and the dissolution of this microstructure in the temperature range between 450 and 650°C also causes a decrease in the electrical resistivity.

Almost the same variation of the electrical resistivity is obtained during a second heating till 1000°C and a subsequent cooling down to ambient temperature as was found after plastic deformation (Fig. 5 (2.run)).

During heating α-ferrite and γ-austenite is formed between 300 and 450°C and the α-ferrite dissolves between 450 and 650°C (Figs. 4 and 5). Above 650°C the specimen consists only of γ-austenite. This phase is maintained during cooling till about 150°C. At ambient temperature all γ-austenite is transformed into mainly α'-martensite and into some ε-martensite as derived from X-ray diffraction and from measurements of the magnetic response and the stored energy. This means that α-ferrite is not formed during cooling from 1000°C because nucleation sites are necessary for this phase to form. If nucleation sites are provided, e.g. α'-martensite, which is obtained on cooling alloy 81/5283 below 150°, the α-ferrite and γ-austenite is formed during subsequent heating above that temperature above which the component atoms are sufficiently mobile.

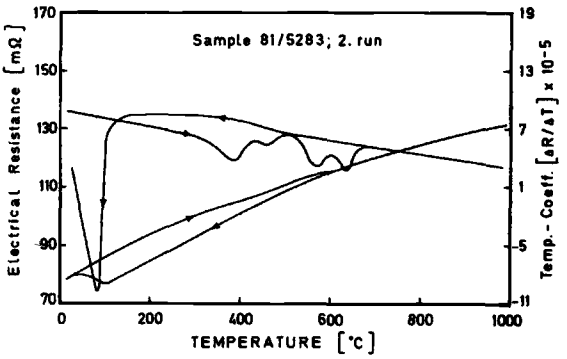


Figure 5 - *The electrical resistivity and the temperature coefficient of an annealed specimen of alloy 81/5283 is plotted for increasing and decreasing temperature (2. run). The anneals were performed in argon with 5% hydrogen.*

During annealing of cold worked alloy 81/5283 α-ferrite and γ-austenite is formed. Dislocations and α'-martensite are formed by cold work prior to annealing and thus in a cold worked alloy 81/5283 dislocations and α'-martensite are present acting as nucleation sites during annealing.

The formation of α-ferrite and γ-austenite occurs in two steps between 300 and 450°C and also the transformation of α-ferrite and γ-austenite into γ-austenite between 450 and 650°C occurs in two steps (Figs. 4 and 5). The kinetics of these transformations are not very clear. It is imaginable that the jump number necessary for the formation of γ-austenite from α'-martensite is much smaller than that necessary for the formation of α-ferrite. The two step kinetics between 450 and 650°C, in which temperature range α-ferrite and γ-austenite transform into γ-austenite, is also not very clear. Whether some remaining α'-martensite transforms into γ-austenite and α-ferrite into γ-austenite, or

whether the rates of formation of γ-austenite from α-ferrite and from γ-austenite are distinct, is not clear.

The variation of the electrical resistivity after 20% cold work is plotted versus the annealing temperature in Fig. 6. The electrical resistivity decreases between about 400 and 600°C due to the formation of γ-austenite and α-ferrite from α'-martensite. Then with further increasing temperature the electrical resistivity increases due to the transformation of α-ferrite and γ-austenite into γ-austenite. On cooling the electrical resistivity decreases somewhat between 1000 and 650°C and drops rapidly between 650 and 600°C. On cooling in this temperature region α-ferrite is formed, and at first we assumed erroneously that the γ⇔γ+α-phase boundary would be at 650°C or slightly below this temperature [7,8].

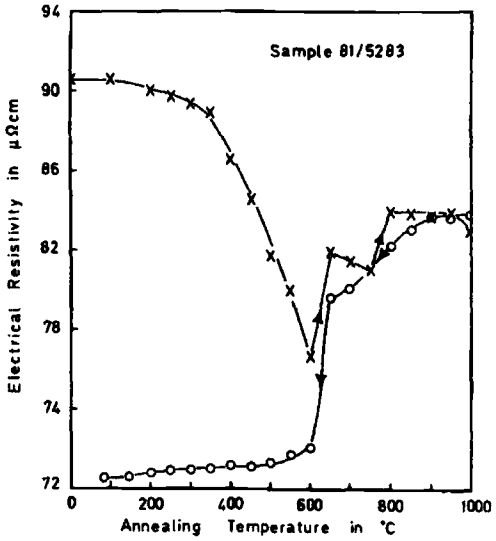


Figure 6 - *The change of the electrical resistivity of a 20% cold worked specimen of alloy 81/5283 is plotted for increasing and decreasing temperature. The specimen was kept for 30 min. at each indicated temperature before it was cooled and put into liquid nitrogen (-196°C) to measure the electrical resistivity. The specimen was annealed in argon with 5% hydrogen.*

No α-ferrite is formed during cooling alloy 81/5283 very slowly from 1000° down to ambient temperature (Figs. 4 and 5). We found that α-ferrite in alloy 81/5283 is only formed when nucleation sites are provided; either α'-martensite or dislocations introduced by cold work. Thus α-ferrite is formed in an annealed specimen only because nucleation sited are provided. They are formed, because measuring the electrical resistivity always at the temperature of liquid nitrogen (-196°C) α'-martensite is formed, acting during subsequent annealing as nucleation sites (Fig. 6).

If this conclusion is correct then α-ferrite is always formed above that temperature, above which the component atoms are sufficiently mobile that microstructural changes can occur in laboratory time scales. We found α-ferrite in cold worked alloy 81/5283 after one day's annealing at 356°C. After an anneal of about one month all α-ferrite formed previously was dissolved again and only γ-austenite was present. Simultaneously with the formation of γ-austenite the nucleation sites, namely

α'-martensite and dislocations, were transformed or recovered, so that no new α-ferrite was formed any more during annealing at 356°C.

Therefore the phase diagram of the stainless steel alloys has to be revised. The γ⇔γ-α-phase boundary for the iron-chromium-manganese alloy shown in Fig. 7 is only very approximately drawn. It is not evident that this phase boundary is independent of temperature. We only know that α-ferrite of alloy 81/5283 is transformed into γ-austenite by annealing at 356°C and that thus only γ-austenite is stable in thermal equilibrium at this temperature.

The results obtained for the iron-chromium-nickel alloy 81/5282 are almost identical with that of alloy 81/5283. We conclude that the γ⇔γ-α-phase boundary must be almost identical for both types of stainless steel alloys. However, the γ⇔γ-α-phase boundary for iron-chromium-nickel alloys known from the literature [1] is completely different from that shown in Fig. 7. We believe that α-ferrite formation can be observed at almost any temperature as long as nucleation sites are provided, i.e. also at temperatures, at which α-ferrite is not stable, leading to an erroneous interpretation of experimental results concerning the course of the γ⇔γ-α-phase boundary [1]. We like to add that we previously made similar mistakes evaluating our data especially with respect to the course of the γ⇔γ-α-phase boundary [7,8].

The γ⇔γ+α-Mn phase boundary is not shown in Fig. 7, because a similar phase boundary does not exist in the iron-chromium-nickel phase diagram. It is well known that the γ-phase field is very extended in the iron-chromium-nickel alloys. However, the γ⇔γ+α-Mn phase boundary for the iron-chromium-manganese alloy is shown in Fig. 1 for about 600°. It results that the γ-phase field is very narrow in the iron-chromium-manganese alloys depending on the chromium content. For iron-chromium-manganese alloys containing about 14%Cr the γ⇔γ+α-Mn phase boundary is at 20%Mn (Fig. 7).

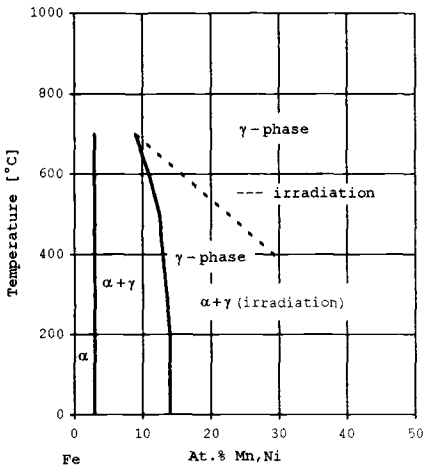


Figure 7 - *The γ⇔γ+α-phase boundary and the α⇔γ+α-phase boundary for the iron-chromium-manganese and iron-chromium-nickel phase diagrams are shown for a chromium content of about 12%. The dashed curve is the γ⇔γ+α-phase boundary valid during irradiation with high energy particles.*

The dashed line shown in Fig. 7 corresponds to the $\gamma \Leftrightarrow \gamma+\alpha$-phase boundary valid during irradiation with high energy particles. This means that α-ferrite is formed when irradiating below the $\gamma \Leftrightarrow \gamma+\alpha$-phase boundary temperature and this $\gamma \Leftrightarrow \gamma+\alpha$-phase boundary is valid for nickel and manganese-containing stainless steel alloys. The amount of α-ferrite formed increases with decreasing irradiation temperature and the amount of α-ferrite formed when irradiating at 100°C is so large that specimens of both materials break before they obtained an irradiation dose of 0.11 dpa [3,6,10].

Alloy 81/5282 and Alloy 316L

In the discussion of the experimental results we did not pay attention to alloys with certain additions and alloys which consists only or mainly of the component atoms. Alloy 81/5282 consists mainly of the component atoms, namely of iron, chromium, and nickel, and has as its only addition carbon, the content of which is very similar to the content of carbon of the European reference steel 316L (Table 1). The composition of the European reference steel 316L is very similar to the American steels US-316 and US-PCA [10]. Both US-steels have slightly larger carbon contents than the European reference steel 316L and the US-PCA steel contains in addition about 0.3%Ti. In the following we will discuss the features of the "pure" and the modified 316 stainless steel alloys.

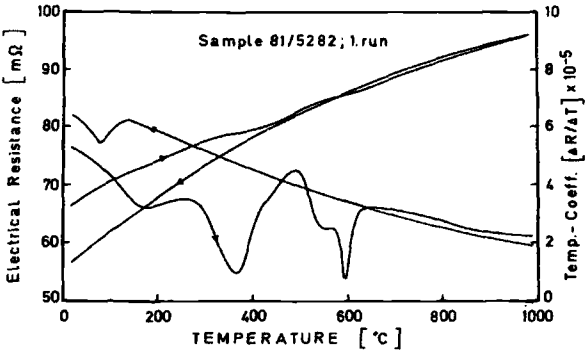


Figure 8 - *The electrical resistivity and the temperature coefficient of an annealed specimen of alloy 81/5282 is plotted for increasing and decreasing temperature (1. run). The degree of cold work prior to annealing was 37.5%. The anneals were performed in argon with 5% hydrogen.*

The following phases were found after a 37.5% cold work in alloy 81/5282, which is considered a "pure" 316L stainless steel: α'-martensite, γ-austenite, and a small amount of $\varepsilon_{def.}$-martensite. During a subsequent anneal $\varepsilon_{def.}$-martensite is transformed into γ-austenite at about 200°C, and α-ferrite and γ-austenite is formed at 350°. At about 550°C α'-martensite is transformed into γ-austenite. With further increasing annealing temperature α-ferrite is dissolved into γ-austenite (Fig. 8). During cooling no phase transition can be recognized in the entire temperature range. However, below 150°C some γ-austenite transforms into α'-martensite. Therefore on reannealing this alloy some α-ferrite is formed again, because α'-martensite acts as nucleation sites for α-ferrite formation (Fig. 9).

In alloy 316L none of the phases, which were detected on cold working alloy 81/5282, were found. Also during cooling from 1000°C to ambient temperature no α'-martensite is obtained. Thus on reheating alloy 316L no microstructural change could be detected during a 2nd annealing by measurements of the electrical resistivity. The additions in 316L apparently have the effect that no α'-martensite is formed during cooling to ambient temperature or to -196°C, which can act as nucleation sites for the formation of α-ferrite.

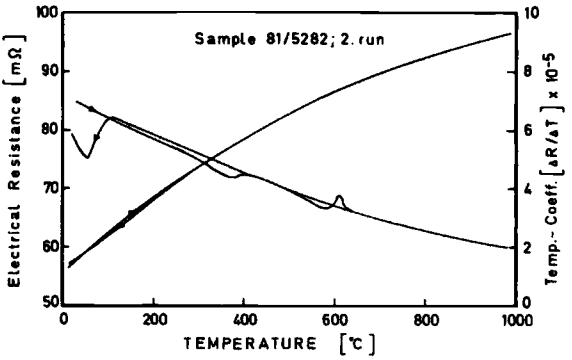


Figure 9 - *The electrical resistivity and the temperature coefficient of an annealed specimen of alloy 81/5282 is plotted for increasing and decreasing temperature (2. run). The anneals were performed in argon with 5% hydrogen.*

If alloy 81/5282 is 37.5% cold worked then the electrical resistivity decreases in three steps during a subsequent anneal (Fig. 10) indicating the three types of microstructural changes described previously (Fig. 8). During cooling the electrical resistivity decreases between 1000 and 600°C due to the formation of α-ferrite, which is formed during heating, because α'-martensite is always formed when measuring the electrical resistivity at -196°C.

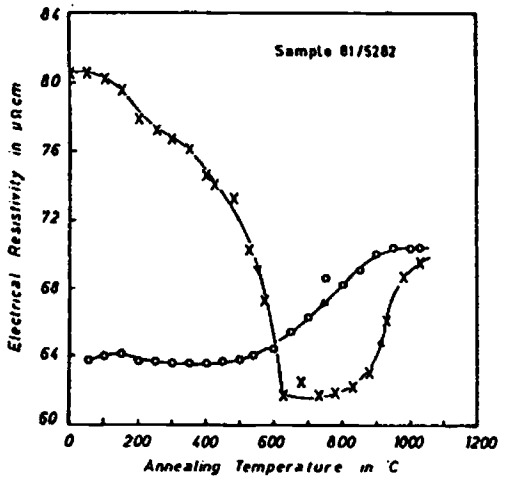


Figure 10 - *The change of the electrical resistivity is plotted versus increasing and decreasing temperature. The specimen was kept for 30 min. at each indicated temperature before it was cooled and put into liquid nitrogen (-196°C) to measure the electrical resistivity. The anneals were performed in vacuum (<10^{-4} torr).*

The change of the electrical resistivity of alloy 316L after 10% cold work is plotted versus the annealing temperature in Fig. 11. The total change of the electrical resistivity is very small, namely only 3.9% in contrast to more than 30% found for alloy 81/5282 (Fig. 10). We found only γ-austenite after cold work in 316L by XRD-measurements and none of the other phases found in alloy 81/5282 could be detected.

The electrical resistivity decreases in three or even four steps during annealing (Fig. 11). These decreases can be attributed to the annihilation of point defects namely to interstitials at about 250°C, and to vacancies at about 400°C. It is not clear whether only the annihilation of these defects causes the observed decreases of the electrical resistivity or whether these point defects are also able to rearrange the geometrical distribution of the component atoms through their migration. This rearrangement of the component atoms can also cause a change of the electrical resistivity of the materials. The decrease of the electrical resistivity at 600 and at 700°C is again attributed to the formation of microstructural changes due to the migration of vacancies in thermal equilibrium, e.g. recovery of work hardening and/or to the formation or dissolution of phases or compounds.

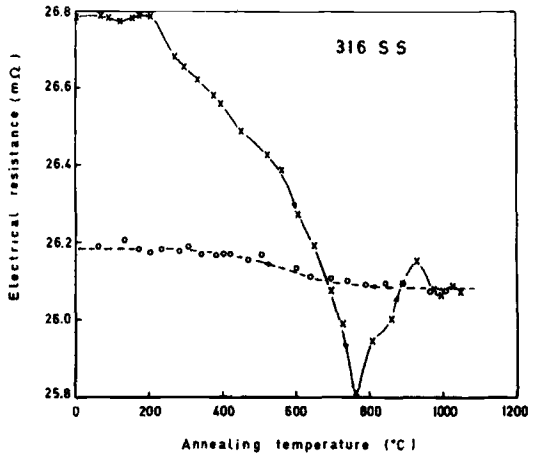


Figure 11 - *The change of the electrical resistivity is plotted versus increasing and decreasing temperature. The specimen was kept for 30 min. at each indicated temperature before it was cooled and put into liquid nitrogen (-196°C) to measure the electrical resistivity. The anneals were performed in vacuum ($<10^{-4}$ torr).*

This means that the additions in the 316L material have the effect of suppressing the formation of α'-martensite, of ε-martensite, and of $\varepsilon_{def.}$-martensite by cold work at ambient temperature and/or by cooling down to -196°C. Consequently α-ferrite is not formed during annealing in a 316L alloy, because no nucleation sites are present. Also dislocations, which often provide nucleation sites in many different stainless steel materials, do not act as nucleation sites in 316L materials. However, if alloy 316L is irradiated α-ferrite is readily formed. The formation of this phase is connected with a decrease in volume, i.e. a densification of the material. The α-ferrite is so brittle that the materials often do not withstand irradiation doses of 0.1 dpa if the irradiation is performed at low temperatures, e.g. at 100°C [3,6,10].

The α'-martensite and $\varepsilon_{def.}$-martensite phases are obtained by cold work in alloy 316L, if the cold work is performed much below ambient temperature [1]. Then α-ferrite is formed during a subsequent annealing causing brittleness of the material.

On the Formation of α-Ferrite during Irradiation in AMCR 0033, US 316, and US-PCA

A systematic study of neutron irradiation creep on various stainless steel alloys, mainly on AMCR 0033, US 316, and US PCA, has been reported during the last decade [3,6,10]. A negative creep elongation was found at the beginning of an irradiation mainly of 20% cold worked materials. The results obtained for US 316 are shown in Fig. 12. It is evident that the length of a material increases due to irradiation creep and that consequently the observed negative creep elongation must be attributed to the formation of precipitates during irradiation, which causes a decrease in volume of the material [6].

It was shown [6] that the negative creep elongation is connected with the formation of α-ferrite. The α-ferrite is very brittle and even small amounts of this phase when precipitated in γ-austenite cause fracture. Many of the AMCR- and 316-type materials broke during irradiation at +100°C before they obtained a neutron irradiation dose of 0.1 dpa [3].

We have shown previously that no α-ferrite is formed in cold worked 316-type materials during a subsequent annealing in contrast to the findings in AMCR-type alloys. However, α-ferrite is formed in a very similar way in AMCR- and 316-type materials during irradiation with high energy particles [6]. It is very important to notice that irradiation causes nucleation for α-ferrite formation in all investigated 316-type materials. The formation of α-ferrite in commercially 316-type materials is obtained without irradiation only after cold work at very low temperatures [12].

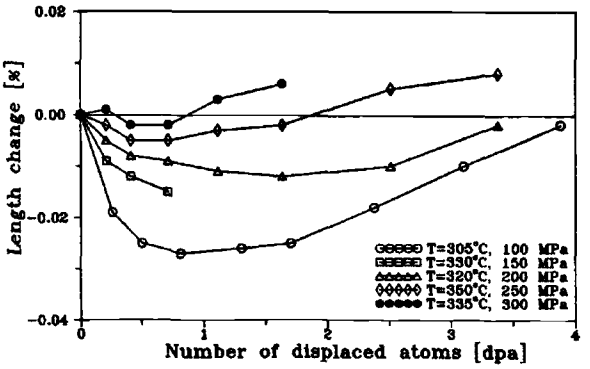


Figure 12 - *The changes in length of five samples of US 316 are plotted versus the number of displaced atoms. The irradiation temperatures and the respective applied stresses are listed in the figure. The samples were 20% cold worked prior to irradiation (after reference [6]).*

It is very simple to describe the features of α-ferrite formation during irradiation in the stainless steel alloys. The rate of formation of α-ferrite during irradiation decreases with decreasing irradiation temperature. The amount of α-ferrite formed during irradiation increases with decreasing irradiation temperature and with decreasing applied stress. This means that α-ferrite is readily formed for negative applied stresses. The main amount of α-ferrite is formed after an irradiation dose of about 1 dpa for an irradiation temperature of about 320°C. However, the thermal equilibrium state has very probably not yet been obtained for irradiation doses of about 4 dpa (Fig. 12).

Deriving the characteristic irradiation temperature below which α-ferrite is formed on irradiating with high energy particles from the results of the investigations of irradiation creep is very complicated. The various features which were observed in the AMCR- and 316-type alloys are not fully understood and therefore various explanations are possible [6]. Many experiments were repeated several times and sometimes different results were obtained even though we tried to apply the same experimental conditions concerning the preparation of the materials and the irradiation.

A negative length change during irradiation is observed at 420°C for an applied stress of 130 MPa [6]. This is the highest temperature at which we performed irradiation experiments on cold worked materials. This means that the characteristic temperature, below which α-ferrite is formed during irradiation, must be much higher than 420°C. We believe that the characteristic temperature below which α-ferrite is formed during irradiation is below about 600°C (Fig. 7).

Alloy 1C4P (0.10C, 13.14Cr, 18.00Mn, 2.14Ni, 0.037Mo, 1.92W, 0.20Si, 0.021V, and traces of Ti)

The change of the electrical resistivity of alloy 1C4P after 33.3% cold work for increasing and decreasing annealing temperature is shown in Figs. 13 and 14. The electrical resistivity was measured in liquid nitrogen (-196°C) and in an oil bath at +50°C.

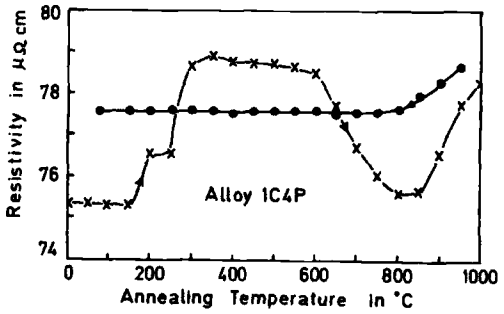


Figure 13 - *The change of the electrical resistivity is plotted versus increasing and decreasing temperature. The specimen was kept for 30 min. at each indicated temperature before it was cooled and put into liquid nitrogen (-196°C) to measure the electrical resistivity. The annealings were performed in vacuum (<10^{-4} torr).*

The electrical resistivity increases in two steps between 150 and 200°C and between 200 and 300°C, and remains almost constant between 300 and 600°C. Then the electrical resistivity decreases till about 800°C and increases again till 1000°C (Fig. 13). If the electrical resistivity of the same specimen is measured at +50°C then the electrical resistivity decreases between 150 and 300°C (Fig. 14). The two steps which can be recognized on measuring in liquid nitrogen can hardly be recognized when measuring at +50°C. We assume that the two steps correspond to two different types of microstructural changes occurring during annealing between 150 and 300°C and causing an increase in the electrical resistivity, if measured at -196°C, and a decrease of the electrical resistivity, if measured at +50°C.

The composition of alloy 1C4P is very similar to that of alloy AMCR 0035, which was investigated very thoroughly, measuring the magnetic and the calorimetric response [7,8]. The main phases developing in this alloy during various thermo-

mechanical treatments were determined by XRD-measurements. In analogy to the findings in this alloy we believe that after cold work of an annealed specimen γ-austenite, $\varepsilon_{def.}$-martensite, and α'-martensite are present. During subsequent annealing the $\varepsilon_{def.}$-martensite transforms into the γ-austenite in the temperature range between 150 and 300°C. The $\varepsilon_{def.}$-martensite apparently decreases the electrical resistivity, if measured at -196°C, and increases the electrical resistivity, if measured at +50°C with respect to the γ-austenite.

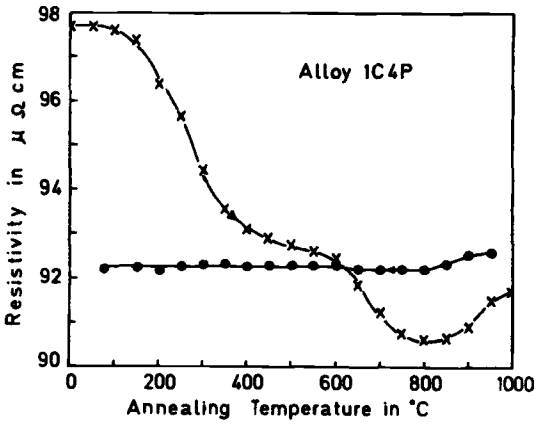


Figure 14 - *The change of the electrical resistivity is plotted versus increasing and decreasing temperature. The specimen was kept for 30 min. at each indicated temperature before it was cooled and put into an oil bath of +50°C to measure the electrical resistivity. The annealings were performed in vacuum (<10^{-4} torr).*

The variation of the electrical resistivity in two steps between 150°C and 300°C, which can be recognized on measuring at -196°C, is not observed in alloy AMCR 0035. However, the peak temperature for the recovery of the $\varepsilon_{def.}$-martensite phase depends on the degree of cold work prior to annealing and thus we believe that the two-step recovery in alloy 1C4P is due to the recovery of two types of $\varepsilon_{def.}$-martensite formed during plastic deformation.

A smaller amount of α'-martensite phase, which is also formed during plastic deformation prior to annealing in AMCR 0035, transforms into α-ferrite and γ-austenite by diffusion at about 400°C. This phase transition is only recognized on measuring the magnetic response and the lattice parameters. We believe that the same phase transition also occurs in alloy 1C4P during annealing between 300 and 600°C, which can not be made out on measuring the electrical resistivity alone (Figs. 3 and 14).

The recovery of work hardening, the dissolution of the α-ferrite, and the formation and dissolution of the α-Man-phase is recognized in AMCR 0035 type alloys by annealing between 600 and 1000°C.

During cooling the resistivity decreases slightly between 950°C and 800°C in alloy 1C4P. Hardly any change of the electrical resistivity is found in AMCR 0035 on cooling in the same temperature region. However, the formation and dissolution of α-Mn is observed in AMCR 0035 at about 650°C [8] by measuring the electrical resistivity at-temperature. Thus we believe that on cooling of alloy 1C4P a small amount of α-Mn is formed.

However, and this is important, there is no variation of the electrical resistivity below 700°C, which indicates a formation or a dissolution of a phase below 700°C, i.e. the γ-austenite is the main phase of alloy 1C4P between ambient temperature and 700°C (Figs. 13 and 14). If the electrical resistivity is measured at -196°C then ε-martensite is formed in a reversible way below about 0°C and on heating alloy 1C4P ε-martensite does not cause nucleation of any phase. Dislocations and α'-martensite, which are present after cold work in alloy 1C4P, act as nucleation sites for the formation of α-ferrite.

Alloy D3 (0.26C, 10.24Cr, 16.92Mn, 0.13Ni, 0.026Mo, 2.04W, 0.50Si, 0.036V, and traces of Ti)

The variation of the electrical resistivity after a cold work of 28.6% with increasing and decreasing annealing temperature is shown in Figs. 15 and 16 for two measuring temperatures, namely for -196°C and +50°C.

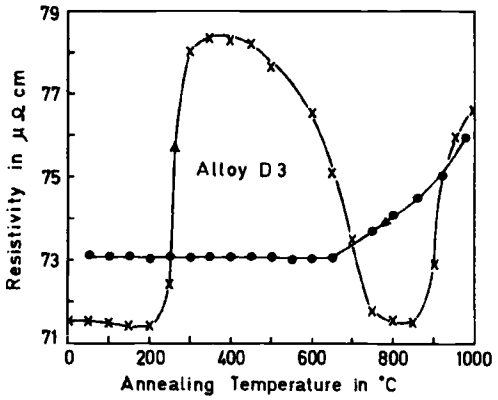


Figure 15 - *The change of the electrical resistivity is plotted versus increasing and decreasing temperature. The specimen was kept for 30 min. at each indicated temperature before it was cooled and put into liquid nitrogen (-196°C) to measure the electrical resistivity. The annealings were performed in vacuum (<10^{-4} torr).*

The results obtained are very similar to the results obtained for alloy 1C4P, for AMCR 0033 and AMCR 0034 [8]. The electrical resistivity increases between 200 and 300°C, if measured at the temperature of liquid nitrogen, and decreases, if measured at +50°C, when $\varepsilon_{def.}$-martensite dissolves.

The trend of the electrical resistivity for annealing temperatures higher than 400°C is very similar for both measuring temperatures (Figs. 15 and 16). The α'-martensite, which is formed during cold work prior to annealing, acts as nucleation sites for the formation of α-ferrite between 400 and 800°C by decreasing the electrical resistivity for both measuring temperatures. The dissolution of α-ferrite is observed in the temperature range between 800 and 1000°C. On cooling the electrical resistivity decreases slightly for both measuring temperatures between 1000 and 650°C (Figs. 15 and 16). Perhaps some α'-martensite is formed on cooling the materials to -196°C for

the measurement of the electrical resistivity. α'-martensite acts as nucleation sites for the formation of α-ferrite during annealing.

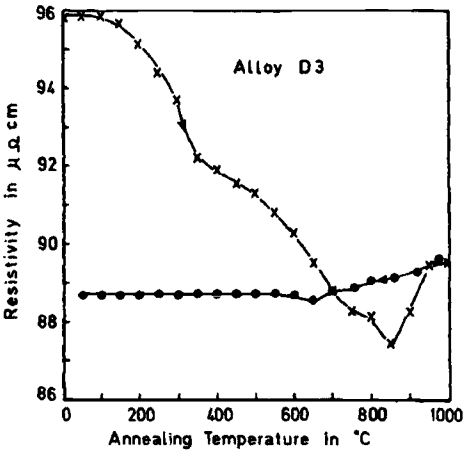


Figure 16 - *The change of the electrical resistivity is plotted versus increasing and decreasing temperature. The specimen was kept for 30 min. at each indicated temperature before it was cooled and put into a +50°C oil bath to measure the electrical resistivity. The annealings were performed in vacuum (<10^{-4} torr).*

Alloy 1A1T (0.10C, 13.5Cr, 11.3Mn, 2.04Ni, 0.031Mo, 1.42W, 0.2Si, 0.63V, and traces of Ti)

The specimen was annealed several times in an atmosphere of argon with 15% hydrogen for one hour at 1000°C and cold worked. The final degree of cold work prior to annealing was 25%. The change of the electrical resistivity with increasing and decreasing temperature is plotted in Figs. 17 and 18.

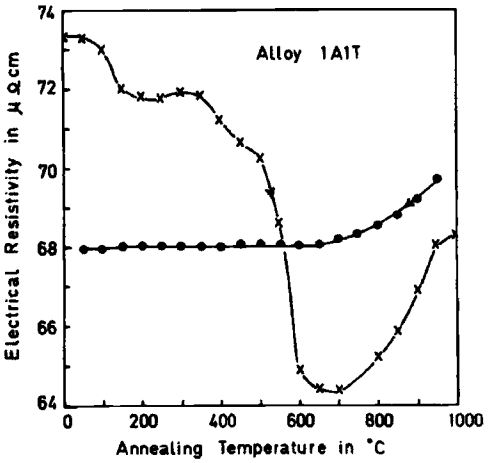


Figure 17 - *The change of the electrical resistivity is plotted versus increasing and decreasing temperature. The specimen was kept for 30 min. at each indicated temperature before it was cooled and put into liquid nitrogen (-196°C) to measure the electrical resistivity. The annealings were performed in vacuum (<10^{-4} torr).*

It can be recognized that the changes of the electrical resistivity for the two measuring temperatures are very similar. Thus the electrical resistivity of a deformed specimen must always be larger than that of an annealed specimen in the temperature range between -196 and +50°C. A similar feature was found for alloy 81/5283 (Fig. 3), the composition of which is very similar to that of alloy 1A1T (Table 1).

The decrease of the electrical resistivity between 100 and 200°C, which is pronounced when measuring the electrical resistivity at -196°C (Fig. 17) is attributed to the transformation of $\varepsilon_{def.}$-martensite into γ-austenite.

The decrease of the electrical resistivity between 350 and 500°C and between 500 and 600°C (Figs. 17 and 18) is attributed to the formation of 1) α-ferrite from γ-austenite and of 2) α-ferrite and γ-austenite from α'-martensite, respectively (or vice versa). It is concluded from the increase of the electrical resistivity between 0 and 1000°C that the amount of α-ferrite formed decreases with increasing annealing temperature between 750 and 1000°.

The decrease of the electrical resistivity between 1000 and 700°C is attributed to the formation of α-ferrite, the amount of which is very small and does not increase with further decreasing temperature.

The behavior of the electrical resistivity with increasing and decreasing temperature is very similar for alloy 1A1T and alloy 81/5283 (Figs. 17 and 18, and Fig. 6). Thus the features of both alloys must be very similar and the interpretation of the results obtained for alloy 1A1T must be analogous.

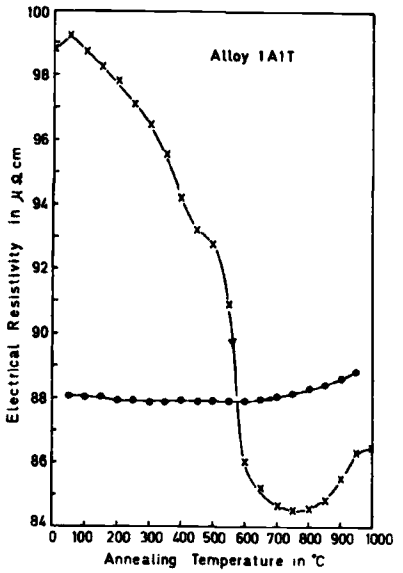


Figure 18 - *The change of the electrical resistivity is plotted versus increasing and decreasing temperature. The specimen was kept for 30 min. at each indicated temperature before it was cooled and put into a +50°C oil bath to measure the electrical resistivity. The anneals were performed in vacuum (<10^{-4} torr).*

The α-ferrite phase is formed during annealing of a cold worked specimen, because nucleation sites, i.e. dislocations and α'-martensite, are present. However, in the

thermal equilibrium state the alloy 1A1T consists of only γ-austenite at least for temperatures higher than about 200°C. During cooling α-ferrite is also formed, because α'-martensite is always formed on measuring the electrical resistivity after each anneal at -196°C and α'-martensite always acts as nucleation sites for the formation of γ-austenite during a subsequent anneal. The decrease of the electrical resistivity of alloy 1A1T (Figs. 17 and 18) is much smaller than the corresponding decrease in alloy 81/5283 (Fig. 6). Probably the amount of α'-martensite formed during the measurement of the electrical resistivity at -196°C is much smaller in alloy 1A1T than in alloy 81/5183 (Fig. 6). Thus, the amount of α-ferrite which is formed during subsequent annealing is much smaller in alloy 1A1T than in alloy 81/5183.

Alloy 1E3 (17.8 Cr, 11.0 Mn, 2 Ni, and 2 W)

The composition of alloy 1E3 is very similar to the composition of alloy 81/5182 and of alloy 81/5184 (Table 1). These latter two alloys have been investigated very extensively [7,8] and the results obtained can be used for the interpretation of the data obtained for alloy 1E3.

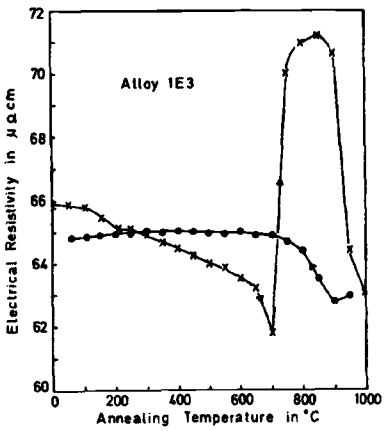


Figure 19 - *The change of the electrical resistivity is plotted versus increasing and decreasing temperature. The specimen was kept for 30 min. at each indicated temperature before it was cooled and put into liquid nitrogen (-196°C) to measure the electrical resistivity. The annealings were performed in vacuum (<10^{-4} torr).*

The sample of alloy 1E3 was 61% cold worked prior to annealing. We assume that the sample contained the same phases prior to annealing as alloy 81/5182 and alloy 81/5184, namely α'-martensite, γ-austenite, $\varepsilon_{def.}$-martensite, and α-Mn. On heating the electrical resistivity decreases in three steps; namely between 100 and 200°C, between 200 and 550°C, and finally between 650 and 700°C for both measuring temperatures (Figs. 19 and 20).

We assume further in analogy to the results obtained for the other two alloys that in the first temperature region $\varepsilon_{def.}$-martensite transforms into γ-austenite, and in the second and in the third temperature region α'-martensite transforms into γ-austenite of

different composition. The α-Mn-phase is formed in the temperature region between 700 and 850°C and is dissolved again between 850 and 1000°C.

An increase of the electrical resistivity is observed on cooling the specimen between 950 and 700°C (Figs. 19 and 20) and then the electrical resistivity decreases slightly between 700°C and ambient temperature. The increase of the electrical resistivity is attributed to the formation of α-Mn and the decrease of the electrical resistivity to the formation of α-ferrite. If alloy 1E3 is annealed at 700°C then it is so brittle that it can not be cold worked at all. During annealing at 700°C so much α-Mn-phase is formed that the material becomes so brittle that it can be broken simply by hand.

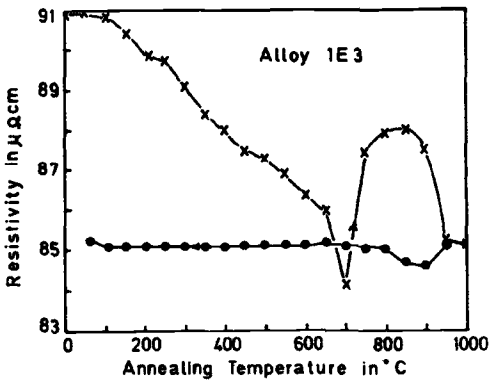


Figure 20 - *The change of the electrical resistivity is plotted versus increasing and decreasing temperature. The specimen was kept for 30 min. at each indicated temperature before it was cooled and put into a +50°C oil bath to measure the electrical resistivity. The annealings were performed in vacuum (<10^{-4} torr).*

Alloy 1S5P (12.3 Cr, 10.6 Mn, 0.23 Ni, and 1.4 W)

The composition of alloy 1S5P is very similar to that of alloy 81/5283. The features of alloy 1S5P are also very similar to those of alloy 81/5283, which were described earlier in this work.

The electrical resistivity of a deformed specimen of alloy 81/5283 is always larger than the electrical resistivity of an annealed specimen for measuring temperatures smaller than 450°C (Fig. 3). We believe that this feature, valid for alloy 81/5283, is also valid for alloy 1S5P. However, the various microstructural changes occurring during annealing of a deformed specimen can cause a decrease and also an increase of the electrical resistivity so that one or the other process can be better investigated by measuring the electrical resistivity at +50°C and not at -196°C.

The electrical resistivity decreases in three steps after a 46% cold work, if the measurements are performed at +50°C, namely between 150 and 200°C, between 300 and 400°C, and between 500 and 650°C (Fig. 22).

We assume that ε_{def}-martensite is transformed into γ-austenite between 150 and 200°C and that α'-martensite is transformed into α-ferrite and γ-austenite between 300 and 400 and between 400 and 650°C. These three temperature regions can not be

recognized, if the electrical resistivity is measured at the temperature of liquid nitrogen (Fig. 21).

The electrical resistivity increases with further increasing temperature between 650 and 1000°C, in which temperature region more and more α-ferrite is transformed into γ-austenite.

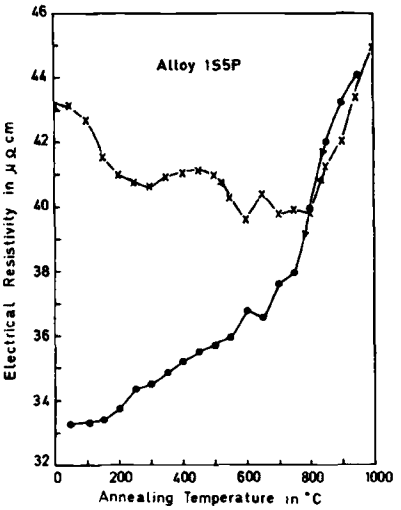


Figure 21 - *The change of the electrical resistivity is plotted versus increasing and decreasing temperature. The specimen was kept for 30 min. The specimen was kept for 30 min. at each indicated temperature before it was cooled and put into liquid nitrogen (-196°C) to measure the electrical resistivity. The annealings were performed in vacuum (<10^{-4} torr).*

The electrical resistivity decreases very strongly between 1000° and about 600° (Fig. 21) and decreases still with further decreasing temperature till about 200°C, if the measurements are performed at -196°C. This decrease in the electrical resistivity is attributed to the formation of α-ferrite. It is important to keep in mind that the mobilities of the component atoms in stainless steel alloys at 200°C are still so high that the rates of microstructural changes are high enough at 200°C that they can be measured by means of the electrical resistivity.

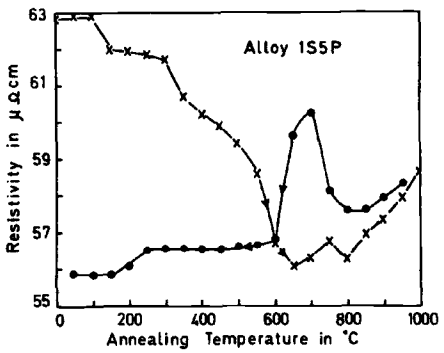


Figure 22 - *The change of the electrical resistivity is plotted versus increasing and decreasing temperature. The specimen was kept for 30 min. at each indicated temperature before it was cooled and put into an oil bath of +50°C to measure the electrical resistivity. The annealings were performed in vacuum (<10^{-4} torr).*

The variation of the electrical resistivity measured at +50°C is very strange (Fig. 22) with respect to the data obtained at -196°C. The electrical resistivity increases between 800 and 700°C and then decreases between 700 and 600°C. We believe that this feature is connected with the formation of α-ferrite and the increase of the concentration of nickel in the γ-austenite. Both microstructural changes may result in an increase of both the electrical resistivity and the temperature coefficient of the electrical resistivity when the measurements are performed at +50°C.

Conclusions

Many different phases are formed in solution-annealed nickel and manganese-containing stainless steel alloys during various thermo-mechanical treatments and by irradiation with high energy particles. The following phases were identified and considered in the present work: α-ferrite, γ-austenite, α'-martensite, $\alpha'_{def.}$-martensite, ε-martensite, $\varepsilon_{def.}$-martensite, α-Mn and σ-phase. The σ-phase is only present in nickel-containing and the α-Mn-phase is only present in manganese-containing stainless steel alloys. Both phases are very brittle and steel alloys containing these phases can not be cold-worked. The α-Mn-phase is formed readily in AMCR-type materials below about 600°C, if these materials contain more than about 12%Cr. Only traces of the σ-phase were found in 316-type stainless steel alloys.

For the formation of α-ferrite in nickel and in manganese containing stainless steel alloys nucleation is required. α'-martensite and dislocations act as nucleation sites for the formation of α-ferrite. α'-martensite and dislocations are formed in AMCR-type materials by cold work. α'-martensite is also formed in these alloys by cooling below the martensite temperature, which is $T_M \approx 200$°C for a manganese-containing stainless steel alloy with a manganese content of 11% and decreases with further increasing content of manganese. In 316-type stainless steel alloys α'-martensite is only formed during cold work at very low temperatures. Thus α-ferrite is not observed during annealing of cold worked commercial 316-type materials. However, in "pure" 316-type steels, which contain only iron, chromium, and nickel, and which contain in addition only small amounts of carbon (Table 1), α'-martensite is formed by cooling below about 150°C and by cold work at ambient temperature. Thus α-ferrite is formed during annealing in these alloys, because α'-martensite and/or dislocations are formed by simple treatments. The additions in the commercially available 316-type stainless steels hinder the formation of α'-martensite.

However, α-ferrite is formed readily in AMCR- and in 316-type materials, regardless of the additions, when these materials are irradiated with high energy particles. This means that α-ferrite is formed in both in "pure" 316- and in commercially available 316-type stainless steel alloys. α-ferrite is a very brittle microstructure, which is formed during irradiation below an irradiation temperature of about 600°C (Fig. 7). So much α-ferrite is formed at an irradiation temperature of about 100°C that the materials break under stress before they have received an irradiation dose of 0.11 dpa.

Further work on the constitution of 316-type alloys is necessary with and without irradiation with high energy particles to optimize the alloy from a metallurgical point of

view. A suggestion is to study "pure" 316-type materials and to vary the chromium and the nickel content, i.e. to decrease the chromium and to increase the nickel content. Small additions of carbon very probably increase the mechanical resistance of the stainless steel alloys satisfactorily. The service temperature of 316-type stainless steel alloys in an radiation environment should not be smaller than T = 340°C.

Acknowledgement

The experimental part of this work was performed at the Institute of Advanced Materials of the Joint Research Centers at Ispra (Va), Italy, and at Petten, The Netherlands. The author is especially grateful to Ch. Burgos, Peru, for the preparation of the graphics.

References

[1] Peckner D. and Bernstein I. M. , eds., Handbook of Stainless Steels, Mc Graw-Hill Book Company, New York, 1977

[2] Schüle W., *Proceedings of the 19th International Symposium on Effects of Radiation on Materials*, ASTM STP 1366, M. L. Hamilton, A. S. Kumar, S. T. Rosinski, and M. L. Grossbeck, Eds., American Society for Testing and Materials, West Conshohocken, PA, 1999.

[3] Hausen H. and Schüle W., *Proceedings of the 18th International Symposium on the Effects of Radiation on Materials*, ASTM STP 1325, R. K. Nanstad, M. L. Hamilton, F. A. Garner, and A. S. Kumar, Eds., Hyannis, Mass., USA, June 22-26, 1996, American Society for Testing and Materials, West Conshohocken, PA, 1999, pp. 742-764.

[4] Garner F. A., "Irradiation Performance of Cladding and Structural Steels in Liquid Metal Reactors", Materials Science Technology, R. W. Cahn, P. Haasen, and E. J. Kramer, Eds., Nuclear Materials, B. R. T. Frost, Ed., Part I, Vol. 10A, 1994, pp. 419-543.

[5] Holland J. R., Mansur L. K., and Potter D. I., Eds., "Phase Stability During Irradiation", Proceedings of the Fall Meeting of the Metallurgical Society of AIME, Pittsburgh, Pennsylvania, USA, October 5-9, 1980.

[6] Hausen H. and Schüle W., *Proceedings of the 18th International Symposium on the Effects of Radiation on Materials*, ASTM STP 1325, R. K. Nanstad, M. L. Hamilton, F. A. Garner, and A. S. Kumar, Eds., Hyannis, Mass., USA, June 22-26, 1996, American Society for Testing and Materials, West Conshohocken, PA, 1999, pp. 830-849.

[7] Schüle W. and Lang E., *Proceedings of the 15th International Symposium on Effects of Radiation on Materials*, ASTM STP 1125, R. E. Stoller, A. S. Kumar, and D. S. Gelles, Eds., Nashville, Tenn., USA, June 19-21, 1990, American Society for Testing and Materials, Philadelphia, 1992, pp. 945-957.

[8] Schüle W., Lang E., and Panzarasa A., "Study of Phase Transformations in Fe-Mn-Cr-Alloys", Report EUR 11756 EN, 1988.

[9] Hansen M. and Anderko K., "Constitution of Binary Alloys", McGraw-Hill Book Company, Inc., New York, Toronto, and London, 1958.

[10] Schüle W. and Hausen H., "Sixth International Conference on Fusion Reactor Materials", (ICFRM-6), Stresa, Lago Maggiore, Italy, September 27 - October 1, 1993, D. G. Rickerby, H. Stamm, K. Ehrlich, and M. Victoria, Eds., Journal of Nuclear Materials, Vols. 212-215, 1994, pp. 388-392.

[11] Gieb M., Heieck J., and Schüle W., *Proceedings of the 17th International Symposium on the Effects of Radiation on Materials*, Sun Valley, Idaho, USA, June 20-23, 1994, D. S. Gelles, R. K. Nanstad, A. S. Kumar, and E. A. Little, Eds., Journal of Nuclear Materials, Vol. 225, 1995, pp. 85-96.

[12] T. Angel, "Journal of the Iron and Steel Institute London", London, Great Britain, Vol. 177, 1954, p. 165.

S. Watanabe,[1] N. Sakaguchi,[2] H. Takahashi[2] and S. Ohnuki[1]

A Composite Model for Segregation and Microstructural Evolution Under Electron Irradiation

Reference: Watanabe, S., Sakaguchi, N., Takahashi, H., and Ohnuki, S., **"A Composite Model for Segregation and Microstructural Evolution Under Electron Irradiation,"** *Effects of Radiation on Materials: 19th International Symposium, ASTM STP 1366,* M. L. Hamilton, A. S. Kumar, S. T. Rosinski, and M. L. Grossbeck, Eds., American Society for Testing and Materials, West Conshohocken, PA, 2000.

Abstract: We have investigated radiation-induced segregation (RIS) near a grain boundary in an austenitic stainless steel under electron irradiation taking into account the simultaneous evolution of faulted dislocation loops and network dislocations by a composite model. It has been found that dislocation free zones (DLFZ) formed in the vicinity of the grain boundary by the irradiation, and we carried out direct observation of the DLFZ formation by in-situ irradiation in a high-voltage electron microscope (HVEM). Prediction of temperature and dose dependence of DLFZ formation agreed with experimental results. The inter-relationship between RIS and DLFZ formation near a grain boundary has been substantially clarified. RIS and DLFZ were understood considering point defect and solute flow associated with the excess defect to the grain boundary.

Keywords: radiation-induced segregation, grain boundary, austenitic stainless steel, electron irradiation, dislocation, defect free zone, nonequilibrium phenomena

Introduction

Austenitic stainless steel has been considered as a first-wall material in near-term fusion experimental reactors [1,2], primarily because there exists a large database of irradiated properties for this material and because of its reliability as a nuclear material. Although irradiation with energetic particles generates numerous microscopic and non-equilibrium phenomena which influence the macroscopic material properties, a prediction of the response of the materials to the reactor conditions is not yet completed even with the use of the most recent experiments and computational models [3,4].

Important radiation-induced phenomena include radiation-induced segregation (RIS), radiation-enhanced diffusion, radiation-induced precipitation, radiation-induced grain boundary segregation and radiation-induced amorphization. These radiation-induced phenomena are known to be closely related to the point defects

[1] Associate Professor and Professor, respectively, Department of Materials Science, Faculty of Engineering, Hokkaido University, Sapporo, Japan, 060.

[2] Graduate Student and Professor, respectively, Center for Advanced Research of Energy Technology, Hokkaido University, Sapporo, Japan, 060.

Copyright© 2000 by ASTM International www.astm.org

introduced due to collision between high energy particles and atoms in an alloy. A grain boundary is the one of places where such complex phenomena occur since it is a strong point defect sink. Among these phenomena, RIS near grain boundaries is known to cause a significant degradation in physical, chemical and mechanical properties [5,6] in austenitic stainless steels. To thoroughly understand the phenomenon one needs to develop a composite model to predict various microstructural and microchemical concurrent changes. It is thus of great importance to investigate retardation of radiation-induced solute redistribution [7-9], viz. RIS, and also behavior of simultaneous microstructural evolution under irradiation.

In the present study, we investigated the solute segregation and simultaneous evolution of extended defects of faulted dislocation loops and network dislocations in an Fe-Cr-Ni alloy during irradiation by computer simulation. The calculation was conducted by solving the coupled rate equations for the solute and point defect concentrations. Simultaneously, the evolution of the faulted dislocation loops and network dislocations at and near a grain boundary was predicted. The authors then predict dislocation free zone (DLFZ) formation near a grain boundary with Ni enrichment and Cr depletion at the boundary generated by RIS.

The prediction was tested and compared with the results of the electron irradiation experiment with a high-voltage electron microscope at 1MV. RIS and DLFZ will be discussed considering point defects flow and solute flow driven by nonequilibrium concentration of defects to the boundary. The interrelationship between the solute segregation and the heterogeneous formation of the dislocations near the grain boundary will be clarified.

Experimental Method

Specimens of an Fe-Cr-Ni alloy containing 20.1Ni, 15.2Cr and, as impurities, 0.003C and 0.0011N(in wt.%) were used. After heat treatment at 1323K for 60mins and electro-polishing, the thin TEM specimens were irradiated with 1MeV electrons at various temperatures using a HVEM (H-1300) at Hokkaido University. The mean damage rate was $1x10^{-3}$dpa s^{-1}. The temperatures and doses were in the ranges of 523~623K and 1~10dpa, respectively. After irradiation, we carried out ion-thinning of the TEM specimens with an ion-milling instrument (GATAN: DuoMill Model 600) for a few minutes, in order to get rid of surface regions of a few hundred nano-meters,. The chemical composition was then measured using a conventional analytical 200keV transmission electron microscope (JEOL-2000FX) equipped with an energy dispersive X-ray analyzer (EDS).

The Model and Calculation Method

The calculation was performed to evaluate the rate equations for solvent atom (Fe), solute atoms (Cr and Ni) and point defects (vacancy and interstitial) concentrations for various irradiation conditions. We also treated the nucleation process of interstitial-type faulted dislocation loops by clustering of single-interstitials and the evolution of the loops and network dislocations on the basis of rate theory [10-14].

In the calculation, we also considered the spatial resolution in the EDS analysis with a finite-size probe, by means of averaging the calculated concentration profile by the formula of the normalized two dimensional Gaussian average for the one dimensional concentration profile [15]. The probe radius used in averaging was 10nm for a conventional TEM and for a 200nm-thick stainless steel sample. The last technique is necessary for simulating the actual profile data obtained by TEM-EDS analysis.

Modeling of RIS

The approach is to solve the coupled diffusion equations for vacancies, interstitials, solvent and solute atoms to provide the terms which couple the defect and atom fluxes. We dealt with the inverse-Kirkendall flux by taking account of interstitial diffusions which is well known as mixed-dumbbell mechanism as well as vacancy diffusion [13].

The continuity equations we used for the quantities of interest are

$$\frac{\partial C_k}{\partial t} = -\nabla \cdot \mathbf{J}_k \qquad (k \text{ denotes solvent Fe, solute Cr and Ni}) \tag{1}$$

$$\frac{\partial C_v}{\partial t} = -\nabla \cdot \mathbf{J}_v + \eta G_{dpa} - K_{vi} C_v C_i - S_v D_v \left(C_v - C_v^0\right) \tag{2}$$

$$\frac{\partial C_i}{\partial t} = -\nabla \cdot \mathbf{J}_i + \eta G_{dpa} - K_{vi} C_v C_i - S_i D_i C_i - 2K_{ii} C_i^2 \tag{3}$$

where C_k is the concentration of k-atoms, C_v and C_i are the concentration of vacancies and interstitials, C^o_V is the equilibrium vacancy concentration at a given temperature, J_k is the flux of k-atoms, J_v and J_i are the flux of vacancy and interstitials, η is the damage efficiency (1 in the case of electron irradiation), G_{dpa} is the generation rate of point defects by irradiation, K_{vi} is the recombination rate of point defects, D_v and D_i are the diffusivity of vacancies and interstitials, and K_{ii} is the clustering rate of single interstitials to di-interstitials which are the nuclei for the dislocation loops.

The internal sink strength for vacancies and interstitials, $S_{v,i}$, is of the form

$$S_{v,i} = 2\pi r_l Z^l_{v,i} C_l / \Omega + Z^n_{v,i} \rho_n \quad , \tag{4}$$

where r_l is the mean radius of faulted dislocation loops, C_l is the concentration of the loops, Ω is the atomic volume, ρ_n is the density of network dislocations, $Z_{v,i}{}^l$ is the bias factor of faulted dislocation loops and $Z_{v,i}{}^n$, the bias factors for network dislocations for vacancies and interstitials, respectively.

The rate equations (1)-(3) with S in eqn. (4) were evaluated as a function of the one dimensional coordinate perpendicular to the grain boundary and of irradiation time. In the calculation, we dealt with the simultaneous evolution of both faulted dislocation loops and network dislocations as follows.

Modeling of Faulted Dislocation Loops

In the present model, we deal with the evolution of the faulted dislocation loops by treating a multisize-class description of the loop population [10,11]. The loop size is divided up into a number of size classes, and the time constant for the growth of

is divided up into a number of size classes, and the time constant for the growth of size class between radii r_l^j and r_l^{j+1} is

$$\frac{1}{K_i^j} = \int_{r_l^j}^{r_l^{j+1}} \left\{ \frac{2\pi}{b_l \ln(r_o / r_c)} \left[Z_i^l D_i C_i - Z_v^l D_v (C_v - C_v^l) \right] \right\}^{-1} dr \quad , \qquad (5)$$

where the integration corresponds to the loop radial growth velocity. b_l is the Burgers vector of the faulted loop. r_0 and r_c are an average inter-dislocation distance and capture radius for point defects, respectively. (In the present study we used $r_0 = 2b_l$ and $r_c = (\pi\rho_n)^{-0.5}$ [11].) The concentration of loops in the j-th size class (C_l^j) is then governed by the following equation

$$\frac{\partial C_l^j}{\partial t} = \left(1 - P_{unf}^{j-1}\right) K_l^{j-1} C_l^{j-1} - K_l^j C_l^j \quad , \qquad (6)$$

where P_{unf}^j is the probability of unfaulting from the faulted loop to the network dislocation while the loop grows with radii r_l^j and r_l^{j+1}, depending on the loop size [14]. The loop size distribution between the nucleus of the loop and the maximum loop radius is divided into a histogram that preserves the essential features of the distribution.

Modeling of Network Dislocation

The model for the evolution of the dislocation structure includes three components, one of which is solely due to the irradiation and two of which are thermal. The irradiation component is the generation term caused by unfaulting from the faulted loops to the network dislocations. The thermal components are a high-temperature climb source term (Bardeen-Herring sources) and a thermal annihilation term caused by stress-assisted directional diffusion of vacancies. Models of this type have been developed for the study of creep processes [12]. Network dislocations can be recovered by climb and glide processes to annihilate. The present model assumes that climb is the rate controlling process. The rate equation describing such an evolution of the dislocation network is

$$\frac{\partial \rho_n}{\partial t} = \frac{2\pi}{\Omega} \sum_j P_{unf}^j r_l^j C_l^j + K_{BH} \rho_n - A \rho_n^2 \quad , \qquad (7)$$

where the first term is generation by unfaulting mechanism, K_{BH} is the generation rate from Bardeen-Herring sources, and A is the annihilation rate by recovery process [13].

Results and Discussion

The present model takes account of both RIS and dislocation evolution simultaneously. The effect of each phenomenon on the other is of interest because the local composition changes by RIS may influence the defect clustering. Additionally, the internal sink strength of the faulted dislocation loops and the network dislocations is an important factor for RIS. In this section, we discuss the inter-relationship between RIS and heterogeneous dislocation formation near a grain boundary.

Table1 *The main parameters used in the present study*

Parameter	Notation	Value
Vacancy jump frequency via Fe	$\upsilon_{v\text{-Fe}}$	$2.5\text{x}10^{13}\text{s}^{-1}$
Vacancy jump frequency via Cr	$\upsilon_{v\text{-Cr}}$	$3.5\text{x}10^{13}\text{s}^{-1}$
Vacancy jump frequency via Ni	$\upsilon_{v\text{-Ni}}$	$1.5\text{x}10^{13}\text{s}^{-1}$
Vacancy migration energy	E_m^v	1.05eV
Interstitial jump frequency via Fe	υ_i	$2.5\text{x}10^{12}\text{s}^{-1}$
Fe-interstitial migration energy	$E_{\text{Fe-}i}^m$	0.3eV
Cr-interstitial migration energy	$E_{\text{Cr-}i}^m$	0.3eV
Ni-interstitial migration energy	$E_{\text{Ni-}i}^m$	0.15eV
Ni-interstitial binding energy	$E_{\text{Ni-}i}^b$	0.75eV
Vacancy formation enthalpy	H_v^f	1.9eV
Vacancy formation entropy	S_v^f	$5k_B$
Lattice constant	a_0	0.358nm
Faulted loop bias for vacancy	Z_v^l	1.0
Faulted loop bias for interstitial	Z_i^l	1.5
Network dislocation bias for vacancy	Z_v^n	1.0
Network dislocation bias for interstitial	Z_i^n	1.25
Initial dislocation density	ρ_0	$1\text{x}10^{10}\text{m}^{-2}$

Radiation-Induced Segregation

We show typical theoretical and experimental results on RIS near a grain boundary in an Fe-15Cr-20Ni alloy after 1MV HVEM electron irradiation in Fig. 1. The damage rate, irradiation dose and temperature were $1\text{x}10^{-3}$dpa s^{-1}, up to 1dpa and, Fig.1 (a) 523, (b)573 and (c)623K, respectively. Ni enrichment and Cr depletion took place at the grain boundary. There is good agreement between theoretical and experimental results. Also shown is that local minima of the Ni and maxima of the Cr exist in the vicinity of the grain boundary. This is because of diffusion of Ni atoms toward the grain boundary or Cr atoms diffusion away from the grain boundary. The amount of solute segregation at the grain boundary increases as the dose increases and the region of segregation is also enlarged. The RIS shows rapid increase up to about 1dpa and then gradually increases as dose increases. The temperature that the maximum RIS occurs is about 700K or more; thus the all temperatures (a) to (c) in Fig.1 are lower than the RIS maximum temperature. In these temperature regions RIS increases as the temperature increases. Moreover, the segregation region (width) increases as the temperature increases because of thermal diffusion enhancement.

Heterogeneous Dislocation: DLFZ Formation

The distribution of faulted dislocation loops and network dislocations near a grain boundary is shown in Fig. 2, assuming electron irradiation to 1dpa at $1\text{x}10^{-3}$dpa

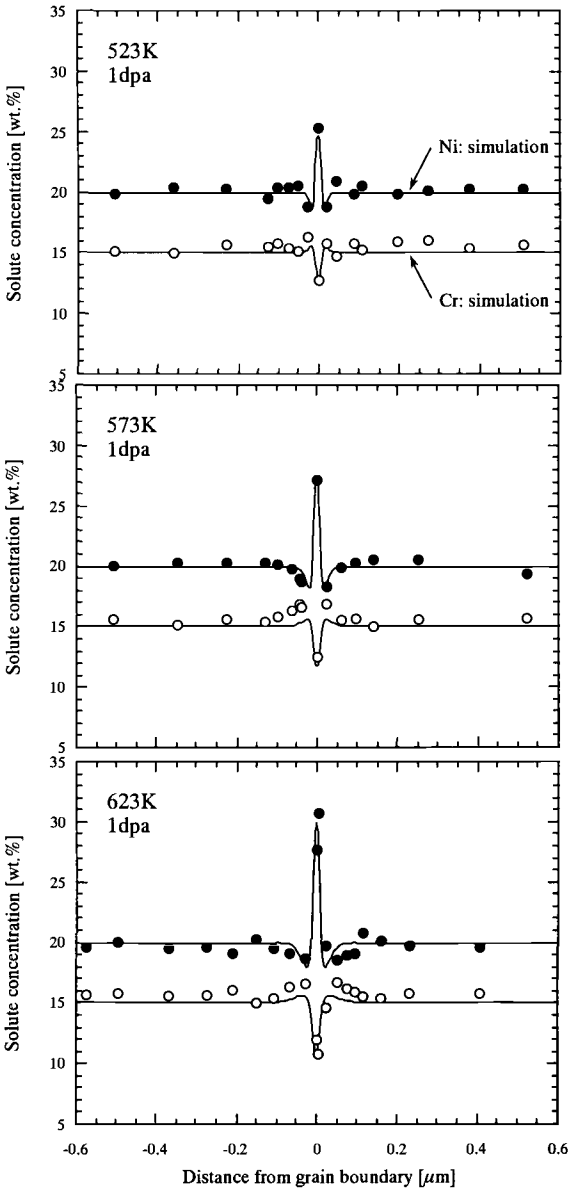


FIG 1—Solute concentration profiles near a grain boundary in Fe-15wt.%Cr-20wt.%Ni alloy after electron irradiation to 1dpa at (a)523K, (b)573K and (c)623K. Calculation results are shown by solid curves.

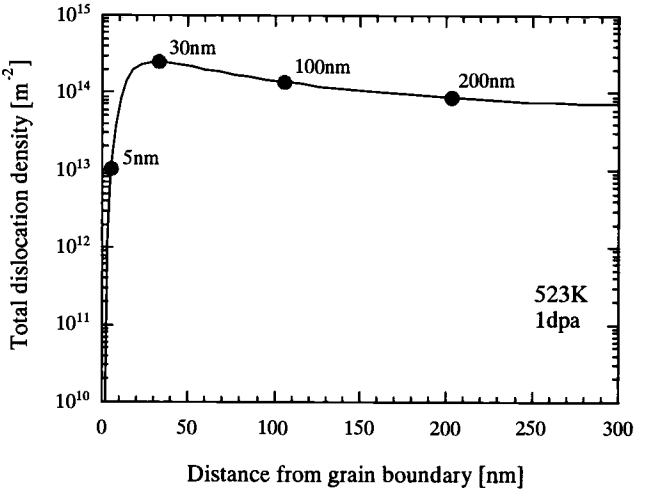


FIG 2—*Dislocation density distribution near a grain boundary after irradiation at 523K, 1dpa.*

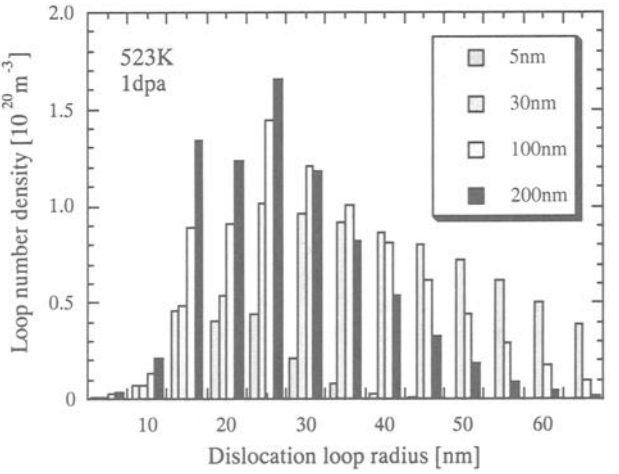


FIG 3 —*The loop size distribution at each position from the grain boundary after irradiation to 1dpa at 523K.*

s^{-1} and at 573K. Fig. 3 shows loop size distributions at several positions from the grain boundary. It can be seen from Fig. 2 and 3 that many large loops exist at a distance from grain boundary and there is a region of fewer dislocations in the vicinity of the grain boundary of the width about 30nm. The region is a denuded zone for dislocations and we defined this region as *dislocation-free zone* (DLFZ)[16]. We have actually observed DLFZ formation as in Fig. 4, about 20-50nm at both sides of a grain boundary during HVEM irradiation. Frank type faulted interstitial loops with Burgers vector of $(a/3)<111>$, the black dots in the photograph, were seen. Loops are expected to contain many Ni atoms since Ni is the undersized atom. Although invisible in Fig.4, we have observed a few void-like clusters in the interior of the grain. DLFZ width becomes larger as the temperature increases. However, it starts shrinking when irradiated to more than 1dpa.

Interrelationship between RIS and DLFZ formation

The formation of DLFZ is thought to occur because of the diffusion of point defects towards a grain boundary sink. The lack of supersaturated point defects near the grain boundary suppresses the defect clustering and thus DLFZ formation occurs there. Also the diffusion of point defects induces the solute composition changes near the grain boundary by inverse-Kirkendall segregation. It is thus essential to understand the interrelationship between RIS and DLFZ formation near the grain boundary. Here, we introduce characteristic widths of RIS and DLFZ formation. We showed in Fig. 5 the definitions of RIS width (W_{RIS}) and DLFZ width (W_{DLFZ}). In the figure, W_{RIS} indicates the nodal point of concentration profiles, for example, local minima of Ni concentration. W_{RIS} directly corresponds to W_{DLFZ} through the diffusional behavior of the point defects introduced by the irradiation. In Fig. 6, we plotted W_{RIS} and W_{DLFZ} after irradiation to 1dpa between 473K and 673K. The widths of both RIS and DLFZ enlarge with temperature increase, showing a linear relationship between the RIS width and the DLFZ width. The theoretical line shows a rather larger slope than the experimental one, since EDS probe size consideration is not taken into account in the prediction. The true RIS width should be narrowed at lower temperatures and the slope will thus be larger than the experimental. However the both lines show the linearity. This linear relationship implies that the both RIS and DLFZ phenomena are governed by the same thermally enhanced process, most probably, solute atom diffusion linked with the point defects flow towards the grain boundary.

A schematic illustration showing DLFZ formation is in Fig.7. In the vicinity of a grain boundary, nucleation of the faulted dislocation loops does not occur because the point defect diffusion towards the grain boundary should be the dominant process in the DLFZ region. If one of the point defects was unbalanced, secondary defects like loops or voids would have formed. After accumulation of extra defects is completed, further segregation is suppressed and dominant defect flow stops, and then the DLFZ starts shrink. In the present experiment the dose level of about 1 dpa is the critical value. The same arguments hold at higher temperature and at lower temperature. If only interstitials are mobile at lower temperature, then a DLFZ will not appear and loops homogeneously form. At high temperature where vacancy can

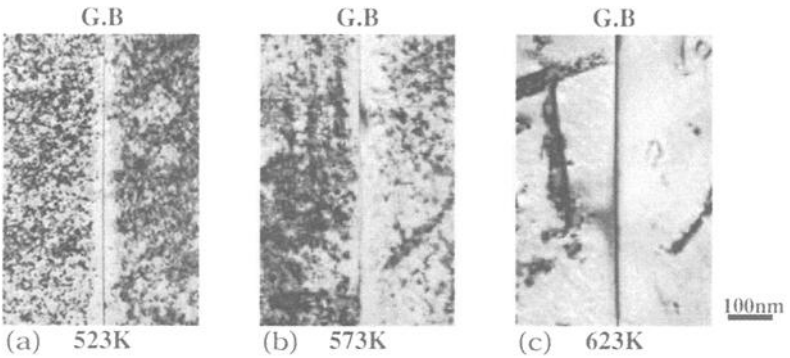


FIG 4—*Formation of DLFZ near a grain boundary in Fe-15wt.%Cr-20wt.%Ni alloy by means of in-situ TEM observation at irradiation to 1dpa at (a)523K, (b) 573K and (c) 623K.*

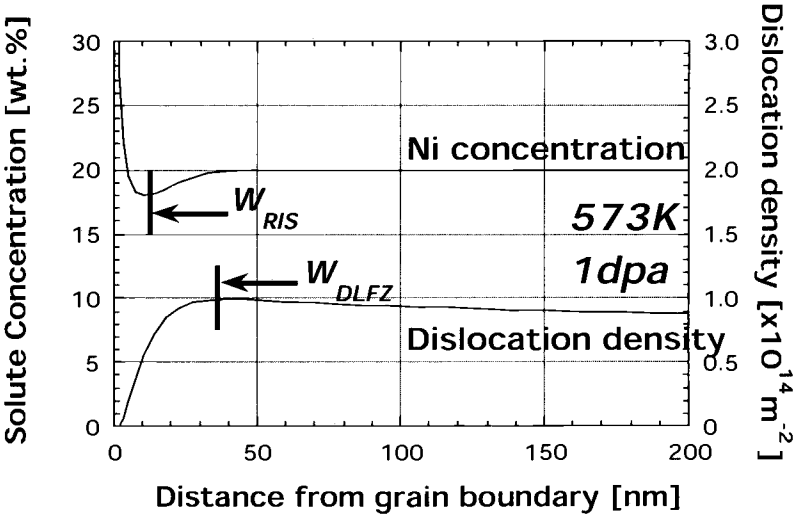


FIG 5—*Definition of width of RIS (W_{RIS}) and width of DLFZ (W_{DLFZ}). W_{RIS} indicates the nodal points of the solute concentration profiles. (Simulation)*

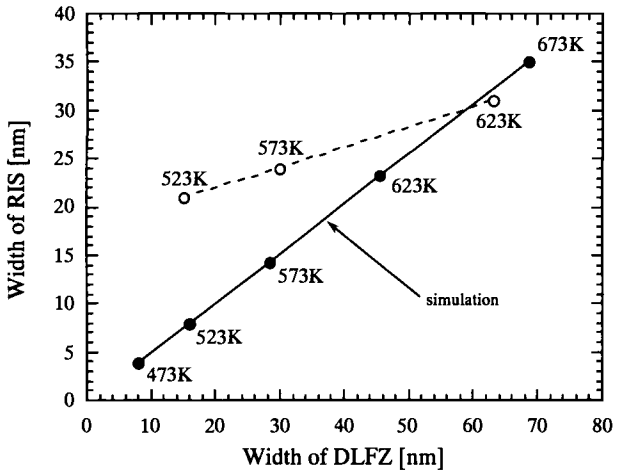


FIG 6—*Experimentally (broken lines) obtained dependence of W_{RIS} and W_{DLFZ} after irradiation to 1dpa at each temperature. Solid line is theoretically predicted one (without EDS probe size consideration).*

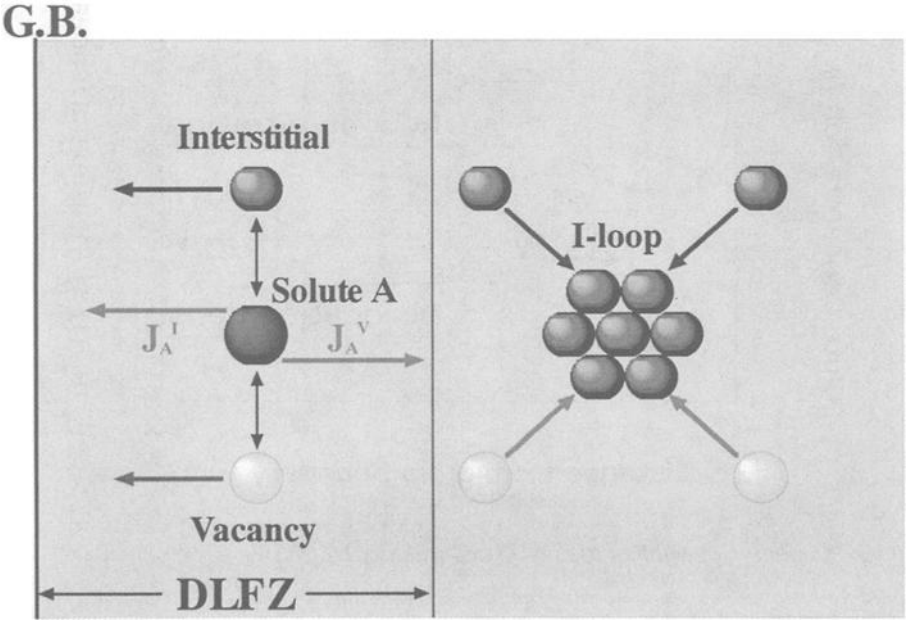


FIG 7—*Schematic diagram of DLFZ formation under irradiation.*

move freely loops form. Hence the DLFZ formation should occur to a maximum extent at an intermediate temperature region.

In Fig. 8, we show an Arrhenius plot of both W_{DLFZ} after irradiation to 1dpa and radiation-enhanced solute diffusivity:

$$D^{irr} = d_v C_v + d_i C_i \ , \qquad (8)$$

where d's are (intrinsic) diffusivities for point defects and C's are concentrations of these defects under a irradiation condition. In the figure, circles denote experimental results after HVEM electron irradiation at the same conditions as the calculation. The value of the activation energy (theory: 0.3 eV; experimental: 0.4 eV) obtained by DLFZ width measurement is a half of the activation energy for solute diffusion under irradiation (0.6 eV) which must be evaluated in terms of eqn.(8). (Notice that the interstitial migration energy via Ni is about 0.15 eV, while 0.3eV via Cr, and the energy for vacancy is 1.05 eV.) This is because, from the linearity in Fig.6, we have:

$$W_{DLF} \propto W_{RIS} \propto \textit{Diffusion length} \propto (D^{irr})^{0.5} \propto exp(-E^{irr}/2kT) \qquad (9)$$

where k, T are the Boltzmann constant and temperature, respectively. E^{irr} is the solute migration energy (most probably Ni's). It indicates that we can obtain diffusional information on solute atoms under irradiation through a DLFZ observation.

Although not mentioned in the above the radiation-induced phenomena near a grain boundary depends on the grain boundary, because the boundary nature influences the defect sink efficiency. Such effects also need to be considered but will be reported somewhere else. In the present study all the grain boundaries were however random grain boundaries with a sigma value (> 19).

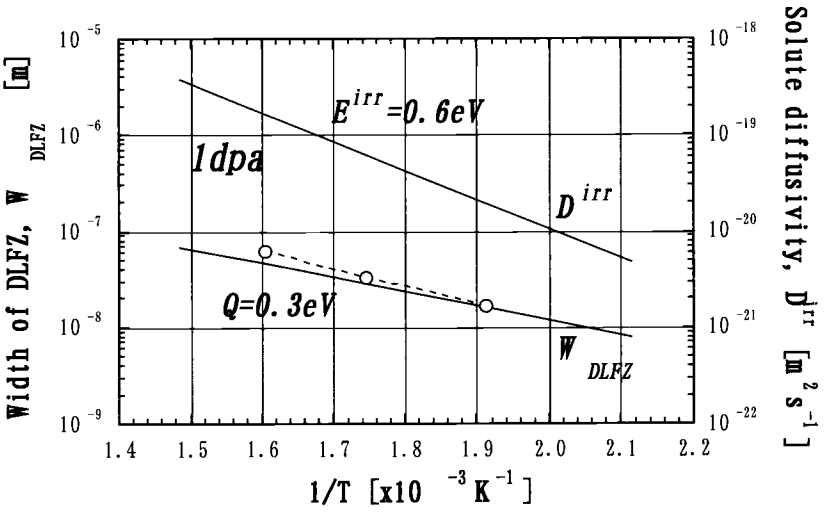


FIG 8—*Arrhenius plot of W_{DLFZ} and D^{irr} after irradiation to 1dpa. Circles show experimental results using HVEM at the same conditions with simulation.*

Conclusion

We have investigated both the solute redistribution and heterogeneous dislocation formation in an Fe-Cr-Ni alloy during irradiation in the vicinity of a grain boundary in an Fe-Cr-Ni alloy on the basis of computer simulation and HVEM irradiation experiments. The present calculation was conducted by solving the coupled rate equations for the solute and point defect concentrations and, simultaneously, for the evolution of the faulted dislocation loops and network dislocations. Ni enrichment and Cr depletion took place at a grain boundary during irradiation. We have clarified the formation of DLFZ in the vicinity of the grain boundary. The influence of internal sink evolution on RIS is complicated by the formation of DLFZ near the grain boundary. We have also clarified the interrelationship between RIS and DLFZ formation. It indicates that DLFZ formation is controlled by solute diffusional process via point defects diffusion near the grain boundary, so the activation energy obtained by a DLFZ width measurement is a half of the value of the solute diffusivity under irradiation.

References

[1] Gross, H., Fuchs, H. P., Lippert, H. J. and Dambeitz, W., *Nuclear Engineering Design* 108(1988)433.

[2] Hanien, H. and Aho-Mantila, I., *Proceedings of 3rd International Symposium on Environmental Degradation of Materials in Nuclear Power System - Water Reactors*, eds. G.J. Thsis and J.R. Weeks (The Metallurgical Society of AIME, Warrendal, PA, 1988)p. 77.

[3] Stoller, R.E., *Journal of Nuclear Materials* 174(1990)289.

[4] Stoller, R.E., Maziasz, P.J., Rowcliffe, A.F. and Tanaka, M.P., *Journal of Nuclear Matererials* 155(1988)1328.

[5] Bates, J.F., Powell, R.W. and Gilbert, E.R., *Proc. 10th Conf. on Effects of Radiation on Materials, ASTM STP 725*, eds. D. Kramer, H.R. Brager and J.S. perrin (American Society for Testing and Materials, Philadelphia, PA 1980)p. 713.

[6] Simonen, E.P and Bruemmer, S.M., *Corrosion `93*, No. 93615(1993).

[7] Johnson, R.A. and Lam, N.Q., *Physical Review B*13(1976)4364.

[8] Okamoto, P.R. and Rehn, L.E., *Journal of Nuclear Materials* 83(1979)2.

[9] Watanabe, S. and Takahashi, H., *Journal of Nuclear Materials* 208 (1994)191.

[10] Stoller, R.E. and Odette, G.R., *Proceedings of 13th Conf. of Radiation Induced Changes in Microstructure, ASTM STP 955*, eds. Garner, F.A., Packan, N.H. and Kumar, G.R. (American Society for Testing and Materials, Philadelphia, PA 1987)p. 371.

[11] Stoller, R.E., *Metal. Trans. A*, 21(1990)1829.

[12] Glasgow, B.B. and Wolfer, W.G., *Proc. of 12th Conf. of Effects on Radiation on Materials, ASTM STP 870*, eds. Garner, F.A. and Perrin, J.S. (American Society for Testing and Materials, Philadelphia, PA 1985)p. 453.

[13] Yacout, A.M., Lam, N.Q. and Stubbins, J.F., *Nuclear Instrument and*

*Method B*42(1989)49.
[14] Katoh, Y., Doctoral Thesis, Tokyo University, 1995, in Japanese.
[15] Watanabe, S., Sakaguchi N., Hashimoto N., and Takahashi, H., *Journal of Nuclear Materials* 224(1995)158.
[16] Watanabe, S., Sakaguchi, N., Mochizuki, S. and Takahashi, H., *Philosophical Magazine Letters* 74(1996)351.

Irradiated Structural Alloys—Welding

Chin-An Wang,[1] Howard C. Wikle, III,[2] Martin L. Grossbeck,[3] and Bryan A. Chin[4]

Stress-Modified Welding of Neutron Irradiated Steels

Reference: Wang, C. A., Wikle, III, H. C., Grossbeck, M. L., and Chin, B. A., **"Stress-Modified Welding of Neutron Irradiated Steels,"** *Effects of Radiation on Materials: 19th International Symposium, ASTM STP 1366,* M. L. Hamilton, A. S. Kumar, S. T. Rosinski, and M. L. Grossbeck, Eds., American Society for Testing and Materials, West Conshohocken, PA, 2000.

Abstract: Catastrophic centerline fractures in the fusion zone have been observed in neutron irradiated steels after welding using the conventional gas tungsten arc (GTA) welding process. Specimens of type 316 stainless steel, Prime Candidate Alloy (PCA) and Sandvik HT-9 were obtained from a capsule irradiated at 200°C in the Oak Ridge Research Reactor. Severe fusion zone cracking was observed in type 316 stainless steel (up to 75 appm He) and PCA alloy (up to 86 appm He) after GTA welding. No cracking was observed in HT-9 steel with up to 2.5 appm He concentrations. The application of a compressive stress during GTA welding eliminated fusion zone cracking in both 316SS and PCA. The results indicate that the stress-modified welding technique may be used to suppress and control helium-induced cracking during repair welding of irradiated materials.

Keywords: neutron irradiated steels, stress-modified welding, weld cracking, helium

Introduction

Changes in material composition and microstructure of the components of irradiated structures will cause the deterioration of the mechanical properties resulting in premature failure. The repair and replacement of the degraded components will be necessary throughout the lifetime of a reactor. Welding will be one of principle methods used to make the necessary repairs on these structures.

[1]Former Graduate Research Assistant, Materials Engineering, Auburn University, Auburn, AL 36849.
[2]Graduate Research Assistant, Materials Engineering, Auburn University, Auburn, AL 36849.
[3]Research Staff Member, Oak Ridge National Laboratory, Oak Ridge, TN 37831.
[4]Professor and Chairman, Materials Engineering, Auburn University, Auburn, AL 36849.

Copyright© 2000 by ASTM International www.astm.org

The repair of irradiated structures using fusion welding will be difficult due to the presence of entrapped helium. Helium is generated by the reactions between thermal neutrons and alloying constituents in the metal, primarily with nickel and boron. Helium concentrations as high as 100 appm are not totally unexpected in the first wall and blanket materials of a tokamak fusion reactor. Due to its extreme low solubility in metals, helium will diffuse and agglomerate to form helium bubbles after being trapped at point defects, dislocations, and grain boundaries. It is known that the degradation of irradiated materials at elevated temperature is partially exacerbated by the presence of helium. At high temperature, helium bubbles have been shown to grow rapidly along grain boundaries under the influence of both temperature and stress [1-2]. This situation is found typically in autogenous welding upon cooling. Internal tensile stresses are generated due to the volume contraction upon solidification and subsequent thermal contraction in the solid state.

Previous attempts to join irradiated materials using GTA and GMA welding processes have shown varying degrees of success [3-6]. Hall et al. [3] observed intergranular cracking in the heat affected zone (HAZ) of a small fraction of welds during GTA welding of thin wall type 304 stainless steel tubing which was irradiated in the Experimental Breeder Reactor-II (EBR-II). In these materials, helium concentrations were estimated to be between 3 to 15 appm. Atkin [4] GTA welded 20% cold-worked 316 stainless steel, irradiated in EBR-II, in an unconstrained condition. Helium concentrations in these steels were estimated to be in the range of 4 to 25 appm. Bend tested samples from these welds indicated that welds were sound and free of cracks. At Savannah River Laboratory [5,6] attempts have been made to repair stress corrosion cracks in irradiated type 304 stainless steel in C-reactor and R-reactor containing different levels of helium. In steel containing 0.8 appm helium with intrinsic constraint, successful welds were made. However, later attempts to repair similar material at a level of 1 to 3 appm helium were unsuccessful.

A stress modified welding technique has been investigated [7-10] to eliminate the catastrophic cracking that occurs during fusion welding of helium bearing materials. A compressive stress, up to 75% of the yield stress of the material, applied during the welding process has been effective in eliminating both HAZ and FZ cracking in helium doped specimens. In earlier work, helium doping through tritium charge and decay was used to isolate the effects of helium on weld cracking from that of displacement damage due to neutron irradiation. The helium distribution after doping was concentrated along the grain boundaries of the material thus representing a much worse case than expected in neutron irradiated specimens. The work presented here extends the investigation of this welding technique to neutron irradiated specimens.

Experimental Procedures

Test specimens irradiated at 200°C in the Oak Ridge Research Reactor (ORR) in capsule ORR-MFE-6J were salvaged from a terminated program to study crack growth mechanisms. These materials included type 316 stainless steel with 20% cold-work, Prime Candidate Alloy (PCA) with 25% cold-work and tempered HT-9 steel. Helium concentrations in these neutron irradiated materials were calculated from the Ni content

and based upon the average damage gradients for type 316 stainless steel in the ORR-MFE-6J experiment [11]. The radioactivity level was measured to be 0.3 Ci, mainly ^{60}Co, for 316 stainless steel.

A dimensional drawing of the recovered crack growth specimens is shown in Figure 1. These neutron irradiated specimens were welded in a radiation hot cell using both standard (unstressed) and stress modified gas tungsten arc welding. A compressive welding stage similar to the one previously used with the helium doped steels [7] was used to perform the welding. The GTA welding parameters used are given in Table 1. If weld cracking was observed, the length of the crack was measured as well as the total length of the weld to calculate the percentage of cracking.

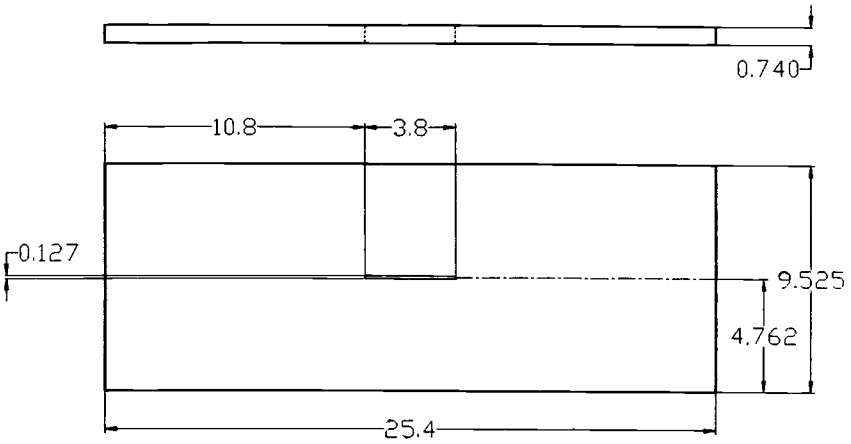


Figure 1. *Recovered crack growth specimen. All dimensions in mm.*

Table 1. *Parameters used for welding of neutron irradiated materials.*

Voltage	14 V DC
Current	
Type 316SS, PCA	22 A
HT-9	24 A
Torch Speed	3.2 mm/s
Gas Flow	1.57×10^{-4} m^3/s
Tungsten Electrode	1.6 mm dia 2% thoriated

Results and Discussion

The results from hot cell welding of the neutron irradiated materials are given in Table 2. Photographs of the welded materials are shown in Figures 2-4. Fusion zone

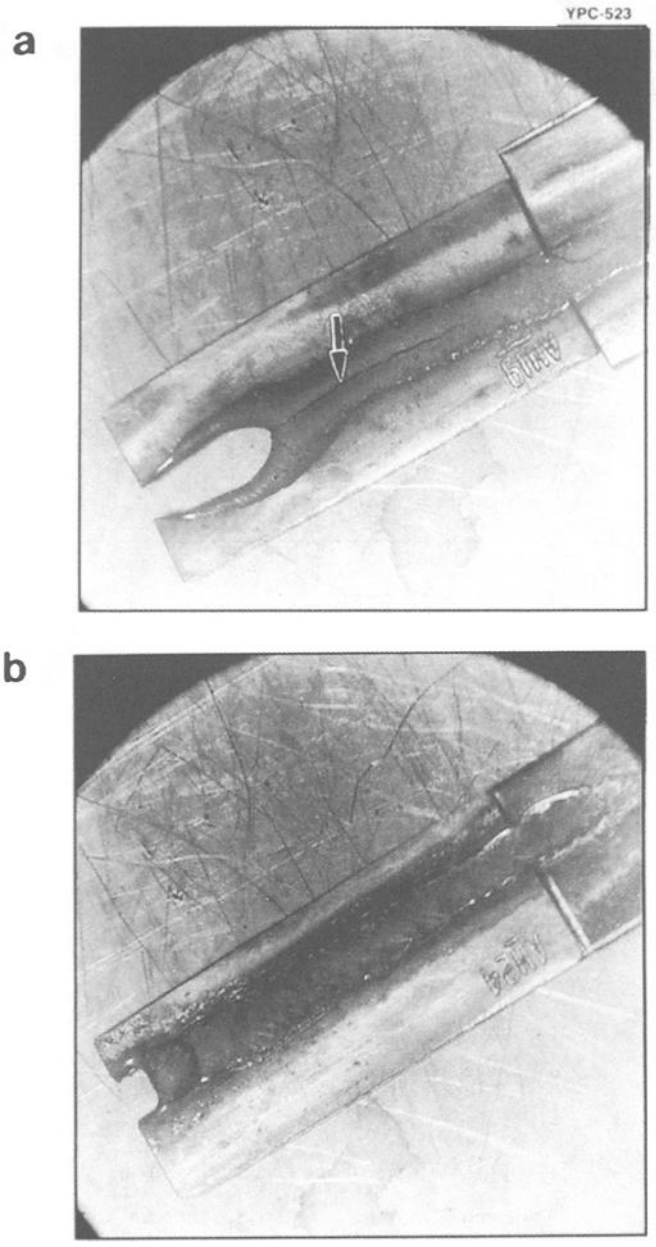


Figure 2. *Photographs of welds of irradiated type 316 stainless steel using (a) standard welding process (unstressed) - fusion zone cracking indicated by arrow (b) stress-modified welding process, 55 MPa - no cracking.*

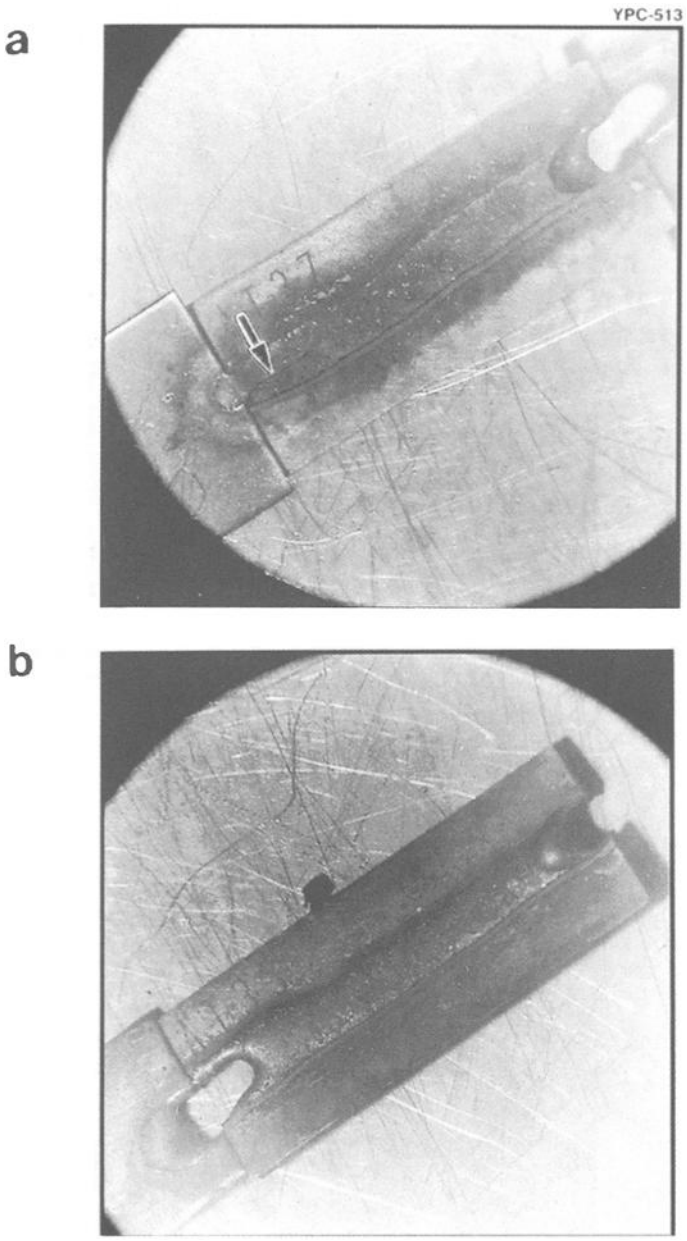


Figure 3. *Photographs of welds of irradiated PCA alloy (a) standard welding process (unstressed) - fusion zone cracking indicated by arrow (b) stress-modified welding process, 165 MPa - no cracking.*

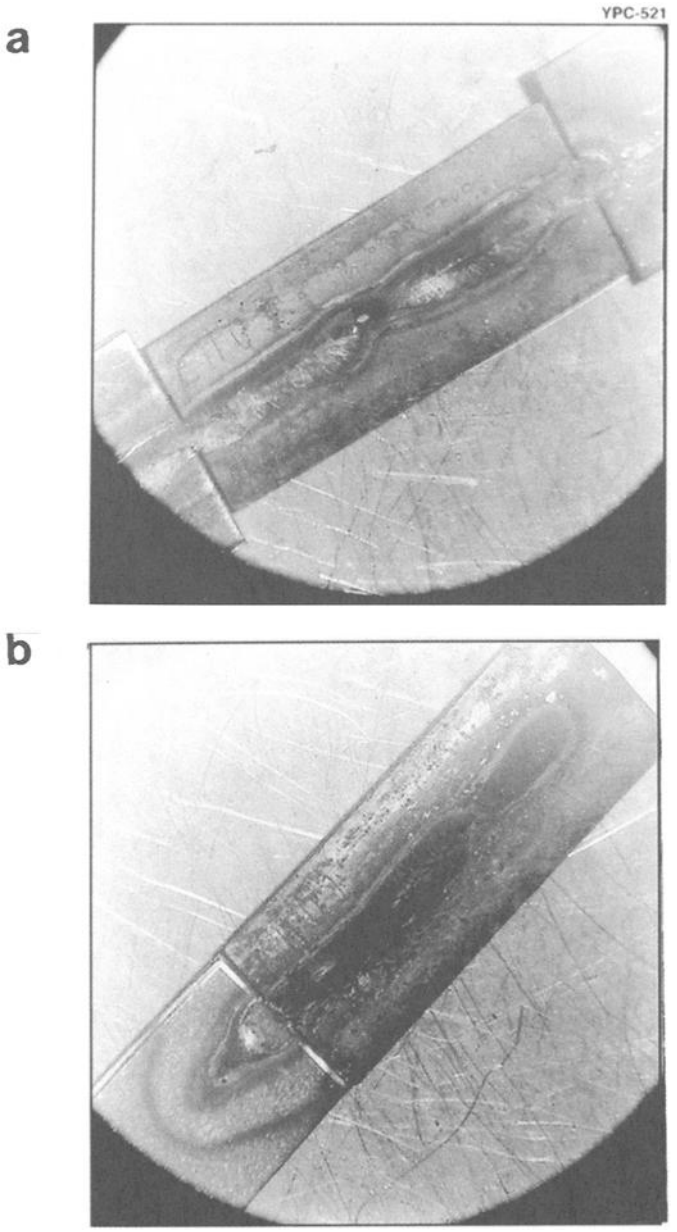


Figure 4. *Photographs of welds of irradiated HT-9 steel (a) standard welding process (unstressed) - fusion zone cracking indicated by arrow (b) stress-modified welding process, 165 MPa - no cracking.*

cracking was observed in both type 316 stainless steel and PCA alloy with no compressive stress applied during welding. PCA welds were more resistant to fusion zone cracking, 18% cracking of the total weld length, as compared to 68% cracking in type 316 stainless steel. Severe fusion zone cracking was eliminated in both materials with a compressive stress as low as 55 MPa applied during welding for the 316 stainless steel. No cracking was observed in the irradiated HT-9 steel with up to 2.5 appm helium. Preliminary examinations showed no macroscopic HAZ cracking in any of the alloys. More detailed examination is necessary to evaluate the weld integrity in the heat-affected zone.

The results of welding ORR irradiated materials are consistent with the results of welding tritium-charged materials. Type 316 stainless steel has shown the worst cracking resistance in both irradiated and tritiated conditions. The results from welding irradiated PCA are somewhat unexpected though. The formation of MC precipitates during thermal treatment prior to irradiation is expected to hinder void growth. However, the MC precipitates were found to be unstable, and all were dissolved after irradiation at 200°C in the ORR [12]. While HT-9 steel exhibited the greatest resistance to helium induced cracking among these steels, it also had the lowest helium concentration. It is expected however, that voids and helium bubbles are trapped by the subgrain lath structure of the HT-9 steel.

Table 2. *Test matrix of specimens from ORR-MFE-6J.*

ID	Alloy	Condition	dpa	He appm	Compressive Stress	Result
AH-19	316SS	20% CW	6.9	74.6	none	68% FZ Cracking
AH-20	316SS	20% CW	6.9	74.6	none	Bad Weld
AH-24	316SS	20% CW	6.9	75.2	55 MPa	No Macroscopic Cracking
AH-25	316SS	20% CW	6.8	75.2	110 MPa	No Macroscopic Cracking
AH-17	316SS	20% CW	6.8	72.7	165 MPa	No Macroscopic Cracking
AH-37	PCA	25% CW	6.3	81.1	none	18% FZ Cracking
AH-33	PCA	25% CW	6.6	86.6	165 MPa	No Macroscopic Cracking
EH-03	HT-9	Tempered	5.6	2.2	none	No Macroscopic Cracking
EH-01	HT-9	Martensite	6.0	2.5	165 MPa	No Macroscopic Cracking

Conclusions

Specimens of 316 stainless steel, PCA and HT-9 irradiated at 200°C in the ORR were welded in both a standard (unstressed) and a stress-modified manner. Severe fusion zone cracking was observed in 316 stainless steel and PCA welded in the standard

manner. Using the stress modified welding technique, fusion zone cracking in the 316 stainless steel and PCA alloy was eliminated. No fusion cracking was observed in HT-9 using either the standard or stress modified welding technique. The results of stress-modified welding of neutron irradiated specimens were consistent with previous work with tritiated specimens.

Acknowledgments

Research sponsored by the Office of Fusion Energy Sciences, U.S. Department of Energy, under contract DE-AC05-840R21400 and grant DE-FG05-91ER54134 with the Martin Marietta Energy System, Inc. and Auburn University.

References

[1] Speight, M. V. and Harris, J. E., "The Kinetics of Stress-Induced Growth of Grain Boundary Voids," *Metal Science Journal*, Vol. 1, 1967, pp. 83-85.

[2] Barnes, R. S., "Embrittlement of Stainless Steel and Nickel-Based Alloys at High Temperature Induced by Neutron Irradiation," *Nature*, Vol. 206, 1965, pp. 1307-1310.

[3] Hall, M. M., Jr., Hins, A. G., Summers, J. R. and Walker, D. E., "Fusion Welding of Irradiated AISI 304L Stainless Steel Tubing," *Weldment: Physical Metallurgy and Failure Phenomena, Proceedings of the Fifth Bolton Landing Conference*, August 1978, pp. 365-378.

[4] Atkin, S. D., "Weld Bend Tests on Irradiated, 20% Coldwork 316 Stainless Steel," ADIP Semiannual Progress Report, September 30, 1981, DOE/ER-0045/7, U.S. DOE, Office of Fusion Energy, pp. 110-117.

[5] Kanne, W. K., Angerman, C. L. and Eberhard, B. J., "Weldability of Tritium-Charged 304L Stainless Steel," DP-1740, E. I. du Pont de Nemours & Co., Savannah River Laboratory, Aiken, SC, February 1987.

[6] Kanne, W. R., Jr., "Remote Reactor Repair: GTA Weld Cracking Caused by Entrapped Helium," *Welding Journal*, 67(8) 1988, pp. 33-39.

[7] Lin, H. T., Goods, S. H., Grossbeck, M. L. and Chin, B. A., "Helium-Induced Degradation in the Weldability of an Austenitic Stainless Steel," *Effects of Radiation on Materials: 14th International Symposium, Volume I, ASTM STP 1046*, N. H. Packan, R. E. Stoller, and A. S. Kumar, Eds., American Society for Testing and Materials, West Conshohocken, PA, 1989, pp. 301-314.

[8] Wang, C. -A., Grossbeck, M. L. and Chin, B. A., "Technique to Eliminate Helium Induced Weld Cracking in Stainless Steels," *Effects of Radiation on Materials,*

16th International Symposium, ASTM STP 1175, A. S. Kumar, D. S. Gelles, R. K. Nansted and E. A. Little, Eds., American Society for Testing and Materials, West Conshohocken, PA, 1994, pp. 779-788.

[9] Wang, C. -A., Grossbeck, M. L., Potluri, N. B. and Chin, B. A., "Welding of Irradiated Stainless Steel," *Journal of Nuclear Materials*, Vol. 233-236, 1996, pp. 213-217.

[10] Wang, C. -A., Grossbeck, M. L., Aglan, H. and Chin, B. A., "The Effect of an Applied Stress on the Welding of Irradiated Steels," *Journal of Nuclear Materials*, Vol. 239, 1996, pp. 85-89.

[11] Greenwood, L. R. and Steidl, D. V., "Neutron Dosimetry and Damage Calculations for the ORR-MFE6J Experiment," DOE/ER-0313/8, U.S. DOE, Office of Fusion Energy pp. 34-39.

[12] Maziasz, P. J., "Temperature Dependence of the Dislocation Microstructure of PCA Austenititc Stainless Steel Irradiated in ORR Spectrally-Tailored Experiments," *Journal of Nuclear Materials*, Vol. 191-194, 1992, pp. 701-705.

Kyoichi Asano,[1] Ryoei Katsura,[2] Shohei Kawano,[3] and Masato Koshiishi[4]

Thick Plate Welding of Irradiated Stainless Steel

Reference: Asano, K., Katsura, R., Kawano, S., and Koshiishi, M., **"Thick Plate Welding of Irradiated Stainless Steel,"** *Effects of Radiation on Materials: 19th International Symposium, ASTM STP 1366*, M. L. Hamilton, A. S. Kumar, S. T. Rosinski, and M. L. Grossbeck, Eds., American Society for Testing and Materials, West Conshohocken, PA, 2000.

Abstract: Recent welding tests using either neutron irradiated or tritium charged material have shown that there was a good chance of success when there was no repeated heat cycle during welding, e.g., stringer bead welding, single pass laser welding, etc. However, the replacement/repair of the actual load carrying components often requires thick plate welding which can only be realized with multi-layer welding. In the present study, 20-mm-thick grooved plate of type 304 stainless steel was irradiated and then butt-welded by multi-layer welding. The weld heat input used was 1.0 and 2.0 MJ/m, which required 28 and 14 passes to fill up the groove. The samples were irradiated to 2.5×10^{21}~ 1.8×10^{23} n/m^2 (E>1MeV), which resulted in 0.1~1.6 appm of helium being produced. A conventional gas tungsten arc welding procedure was employed. The welded joints were subjected to the tensile test, side bend test, root bend test and cross-sectional metallography. The samples containing as much as 0.14 appm of helium passed all the tests; the mechanical properties fulfilled the standard requirement for the unirradiated base metal. At 0.6 appmHe and 1.0 MJ/m heat input, the welded joint showed sufficient strength, however, tiny intergranular cracking was observed in the HAZ where repetitive thermal cycles operated.

Keywords: irradiated stainless steel, weldability test, multi-layer welding, mechanical properties, welded joint, helium bubbles

Introduction

Austenitic stainless steels containing nickel as a major alloying element and a trace of boron generate helium atoms when irradiated by thermal neutrons via the following transmutation reactions:

^{58}Ni(n, gamma)^{59}Ni(n, alpha)^{56}Fe, ^{10}B(n, alpha)^{7}Li

[1] Materials Engineering Group, Tokyo Electric Power Co. Inc., Yokohama 230-8510, Japan.

[2] Nippon Nuclear Fuel Development Co. Ltd., Ooarai-machi, Ibaraki 311-1313, Japan.

[3] Power & Industrial Systems R&D Center, Toshiba Corporation, Yokohama 235-8523, Japan.

[4] Hitachi Works, Hitachi Limited, Hitachi 317-8511, Japan.

Copyright© 2000 by ASTM International www.astm.org

These helium atoms are thought to be held in solution in the temperature range of light water reactor (LWR) operation, nominally around 560 K, since their mobility in the austenite matrix is negligibly small. However, when helium-containing material is exposed to very high temperature, the motion of the helium atoms will be much enhanced, and a certain portion of the helium atoms will diffuse into grain boundaries and precipitate as bubbles. This process can be followed by intergranular cracking in the case of welding where the effect of tensile stresses produced by solidification shrinkage exists. [1-4]

The authors have previously shown [1] that the liability to cracking by welding irradiated steel depends largely on the weld heat input as well as on the helium content of the material. With a low heat input welding, a heavily irradiated material containing more than 100 atomic parts per million of helium (appmHe) could be welded free of penetrant test (PT) indication. For a material containing 8 appmHe, welding with heat input greater than 1 MJ/m caused significant surface cracking while no cracking occurred with heat input less than 0.5 MJ/m. Also shown in that work is that those regions which experience repeated thermal cycles during welding are liable to crack. Even if the material condition–helium content–and welding condition–e.g. heat input–suggested the soundness of the weld, a possibility of cracking remains in such regions as the crater treatment region of a stringer bead, or the terminating region of a circumferential weld where the bead overlaps the start of the bead.

These findings show that there are difficulties while undertaking repair welding of irradiated components. As the heat input becomes higher, the allowable maximum helium content will be lower, which means the extent of weldable component fluence will be limited; this is contrary to the needs to use higher heat input welding from the viewpoint of work efficiency. The occurrence of cracking is likely in regions subjected to thermal cycling; however, welding of thick components requires multi-layer welding where the heat affected zone of a preceding pass will inevitably experience another thermal cycle by the welding of the following pass. A weldability assessment including both those aspects is much needed before implementing welding of the actual components.

In this work, type 304 austenitic stainless steel thick plate was irradiated and welded by multi-layer welding at high heat input in a very practical manner. The weldability was assessed by conventional tensile tests and bending tests of the joint. The helium content of the material was determined, at which there was little concern for the soundness of the joint.

Experimental Details

Materials and Sample Preparation

The chemical compositions of the materials used are shown in Table 1. The type 304 stainless steel plate was obtained as a hot rolled 20 mm thick plate. The plate was mill-annealed at 1373 K for 72 s and water quenched. The filler wire was of type 308L and was 1.2 mm in diameter.

Figure 1 schematically shows the geometry of the specimens. Specimens were cut out from the plate and double U grooved with a 60° bevel angle machined on one side.

Table 1—*Chemical Composition of the Materials in Weight Percent*

	C	Si	Mn	P	S	Cr	Ni	N	Co	B
SUS304	0.05	0.61	1.02	0.002	0.004	18.30	8.51	0.06	0.02	0.00075
Y308L	0.017	0.30	1.90	0.020	0.001	19.94	9.82	0.04	0.19	-

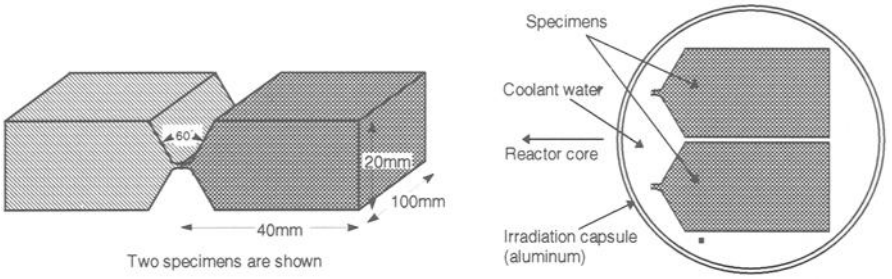


Figure 1—*Geometry of the specimen and configuration during irradiation.*

Two of these specimens will be used in the following weldability test. The width of the specimen, 40 mm, was chosen to be accommodated in the irradiation capsule as shown in the figure.

Irradiation

The Japan Material Test Reactor (JMTR) of Japan Atomic Energy Research Institute (JAERI) was employed for neutron irradiation of the specimens. The 'leaky' capsule was used to place the specimens in position. This capsule was open to 323 K (nominal) coolant water, and the specimens were directly in contact with the coolant water. Three irradiation holes in the reflector region were selected to vary the thermal neutron fluence from 1×10^{23} n/m^2 to 1×10^{24} n/m^2. Specimens were piled up to six levels in each capsule and each level contained two specimens as shown in Figure 1. Each set of two specimens was used to make up a weld joint. Samples were set in the capsule such that the root face of the groove looked toward the reactor core. The specimens were irradiated at ambient temperature without temperature measurement. Although the

Table 2—*Irradiation Conditions*

Weld joint ID	L11	L12	L21	L22	M11	M12	M21	H11	H21
ϕt_{fast} ($\times10^{22}$ n/m^2)	0.30	0.31	0.25	0.30	3.6	3.8	2.9	18	15
$\phi t_{thermal}$($\times10^{22}$ n/m^2)	10	11	9	10	48	52	39	140	110
He (appm)	0.13	0.14	0.11	0.14	0.53	0.63	0.48	1.6	1.4

Specimens were in contact with reactor coolant water (323K) and irradiated at ambient temperature.

specimen was thick, the estimated specimen temperatures, considering gamma heating, were lower than 473 K because of the relatively low gamma flux at the irradiation position.

The neutron fluence and measured helium content are shown in Table 2 for each weld joint. The irradiation period was 2.1×10^6 seconds (24 days). The neutron fluence was calibrated to the measurement of dosimeters consisting of iron, copper and cobalt. Four sets of dosimeters were attached to each capsule. To determine the helium content of the specimens, a total of twelve samples of the same heat was obtained after irradiation and analyzed in accordance with the procedure in the reference. [5]

Welding Procedure

To assure the practicality of the test results, conventional gas tungsten arc welding (GTAW) was applied. The heat input to the material was set to be 1.0 and 2.0 MJ/m which is the lower and higher heat input, respectively, employed in the actual welding. Table 3 shows the welding conditions for each heat input level. In all the welding tests, the welding position was flat; argon cover gas was supplied from the welding torch; the root gap was zero, no weld tab was used, and no weaving action was applied to the torch. A welding jig was used to restrain angular distortion. This jig was made of copper, and served also as a heat sink to facilitate keeping the interpass temperature below 363 K.

The root pass welding fully penetrated the root face. The occurrence of weld defects on the root pass was examined in selected joints by the dye penetrant test (PT) on both sides. The remaining passes were built up with the cross-sectional sequence illustrated in the insets of Figure 11. The set of specimens and jig were reversed several times to minimize the overall angular distortion. The buildup sequence shows this reversing action. The number of passes required to buildup the groove was 28 and 14, respectively, for heat input of 1.0 and 2.0 MJ/m. Figure 2 shows the welding test set-up in the hot-cell.

After the completion of welding, each joint was checked for weld defects by remote visual inspection using a charge coupled device (CCD) camera and by PT. Specimens for post-weld test were then machined from the joint. Figure 3 schematically shows the dimensions of the specimens for mechanical tests: welded joint tensile test, side bend test

Table 3—*Welding Conditions*

Nominal heat input	Low : 1.0 MJ/m		High : 2.0 MJ/cm	
	Root pass	Fill passes	Root pass	Fill passes
Average welding current (A)(peak/base)	190/145	190/145	230/160	240/180
Average arc voltage (V)	9.8	10	11.9	11.6
Welding speed (mm/s)	1.63	1.77	1.17	1.22
Wire feed speed (mm/s)	8.3	8.3	8.3	16.7
Heat input (MJ/m)	1.01	1.01	1.99	2.00
Overall number of passes	28		14	

The buildup sequence is shown in the inset of Figures 11. Interpass temperature was kept below 363 K.

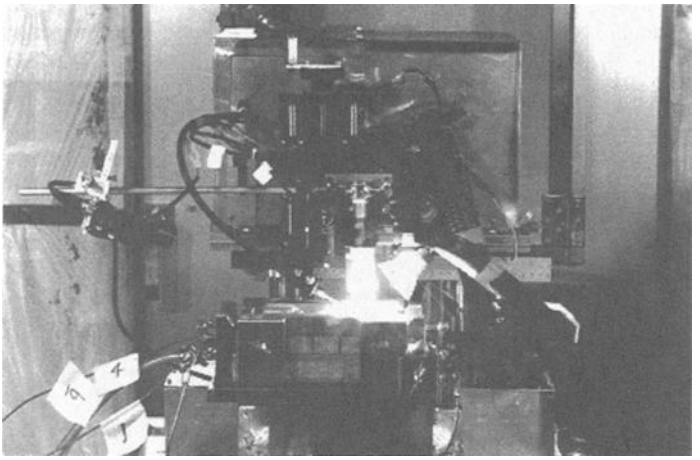


Figure 2—*Welding test set-up in the hot-cell.*

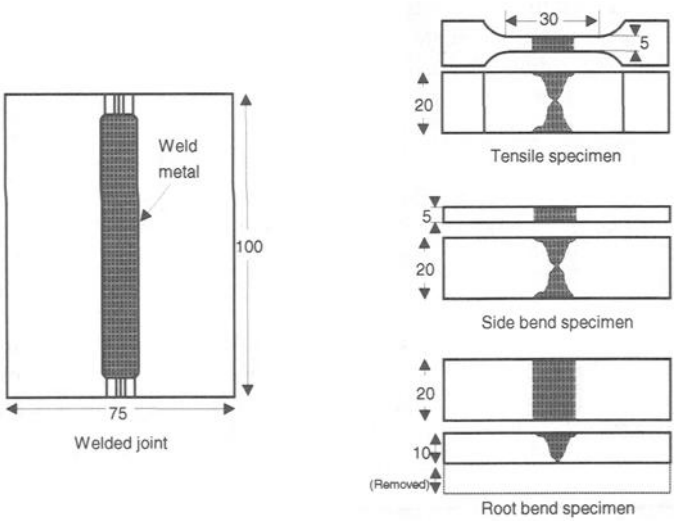


Figure 3—*Post-welding test specimens.*

and root bend test. The cross section of the tensile specimen was 20 mm (i.e. plate thickness) in height, 5 mm in width, and the gauge length was 30 mm. The side bend specimen was 5 mm in thickness. The thickness of the root bend specimen was reduced to 10 mm, half the plate thickness, to place the root pass on the bending surface.

Welded Joint Test

Tensile Test—Only those joints for which the absence of weld defects could be

expected were tested. When indications of defects were identified by PT either on the root pass or on the completed surface, the joint tests, including other bending tests, were not performed. After the tensile test, the fractured surface was examined using a scanning electron microscope (SEM).

Side Bend Test—Side bend tests were performed in accordance with the procedure given in the Japan Industrial Standard (JIS) Methods of bend test for butt welded joint (Z 3122-1990). The radius of curvature of the plunger was 10 mm, which was two times the thickness of the sample. The width of the weld metal did not exceed 20 mm so that the whole weld metal and HAZ were subjected to tensile strain. The bent surface was examined both by CCD camera observation and by PT.

Root Bend Test—Root bend tests also followed the same procedure as side bend tests except that minor modifications had to be made on the bending die to meet the short length of the specimen. The plunger had a 20-mm radius of curvature.

Figure 4 shows the bend test set-up in the hot-cell.

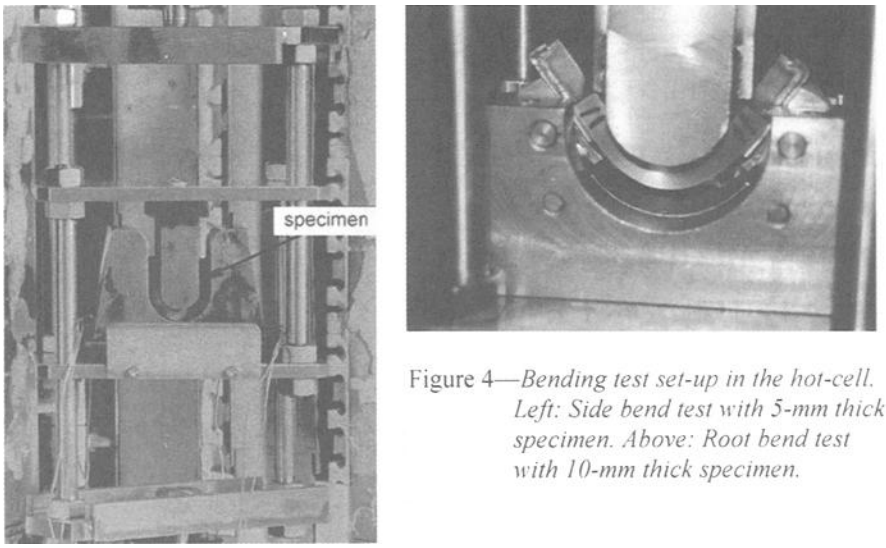


Figure 4—*Bending test set-up in the hot-cell. Left: Side bend test with 5-mm thick specimen. Above: Root bend test with 10-mm thick specimen.*

Results

Welding and Penetrant Test Results

Table 4 summarizes all the experimental results.

The root passes of six joints were welded for the first run. Their weld IDs in Table 4 were L11, L21, M11, M21, H11 and H21. These joints were subjected to root pass PT, and flaw indications appeared in M21, H11 and H21. Figure 5 is an example of indications observed in H11. Those indications appeared along the HAZ of the penetrated bead on the backside as illustrated in the figure. No indication was identified on the welding side, or in the weld metal.

Table 4—*List of Weldability Test Results*

Weld ID	L11	L12	L21	L22	M11	M12	M21	H11	H21
He content (appm)	0.13	0.14	0.11	0.14	0.53	0.63	0.48	1.6	1.4
Heat input (MJ/m)	1.0	1.0	2.0	2.0	1.0	1.0	2.0	1.0	2.0
Root pass PT indication	N.D.	-	N.D.	-	N.D.	-	yes‡	yes‡	yes‡
As completed PT indication	N.D.	N.D.	N.D.	N.D.	N.D.	N.D.	N.D.	N.D.	N.D.
Weld defect †	N.D.	N.D.	N.D.	N.D.	N.D.	N.D.	N.D.	N.D.	N.D.
Joint tensile test									
U.T.S. (MPa) ††	650	699	627	684	653	570	-	-	-
Elongation (%) †††	65.9	65.0	64.0	65.7	57.7	29.5	-	-	-
Position of fracture	WM	WM	WM	WM	HAZ	HAZ	-	-	-
Side bend test									
Number of PT indications	0	0	0	0	1	4	-	-	-
Total length of crack(mm)	-	-	-	-	0.83	4.3‡‡	-	-	-
Root bend test									
Number of PT indications	0	0	0	0	0	0	-	-	-
Cross-sectional Metallography	-	done	-	done	-	done	-	-	-

N.D. : Not detected. - Not done or not measured. WM : weld metal. HAZ : heat affected zone.
† . Presence of surface defects was examined by a CCD camera. †† : Ultimate tensile strength.
††† : Elongation was given as crosshead displacement / gauge length of 30 mm including the weld.
‡ : Indication was found in the HAZ on the backside. ‡‡ : Maximum length of single crack was 1.4 mm.

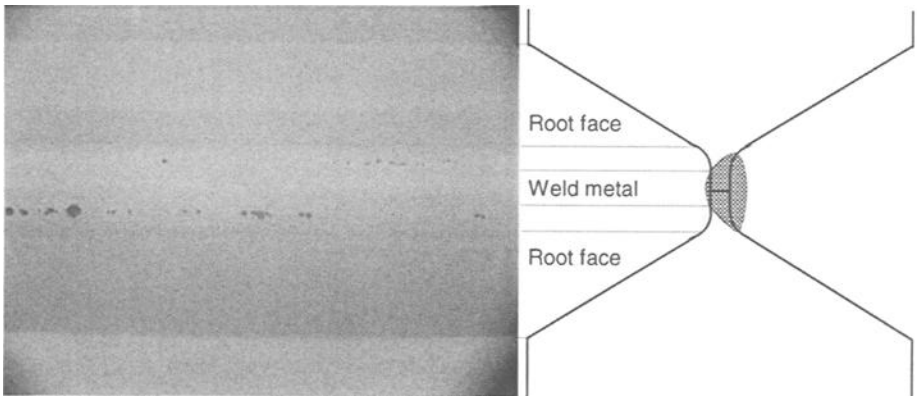


Figure 5—*Flaw indications detected by dye penetrant test along the HAZ on the backside in H11.*

The root pass of the remaining three joints, L12, L22 and M12, were welded for the second run. No root pass PT was performed considering the soundness of the joints L11, L21 and M11.

All nine joints were subsequently welded using the welding conditions for fill passes shown in Table 2. The completed joints were then examined and no flaw indications were observed in any joints including M21, H11 and H21. An example of the appearance of the root pass (backside displaying the penetrated bead) and the completed joint is shown in Figure 6 for M21.

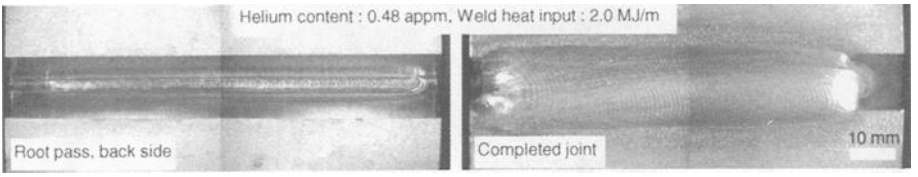


Figure 6—*Appearance of welded joint M21.*

Joint Tensile Test

Those welded joints which PT detected no flaw indication were subjected to a joint tensile test. Figure 7 shows the stress-strain relations. The ultimate tensile strength (UTS) and elongation at fracture are also given in Table 4. The requirement for tensile properties of the welded joint in the welding procedure test is that the UTS must exceed that specified for base metal: in the case of SUS304, the UTS must be greater than 520 MPa. All six joints satisfied this criterion. The elongation requirement for SUS304 base metal is 40% and M12 fell short of this criterion; however, this is not mandatory.

Figure 8 shows the appearance of fractured specimens. It is clear that the specimens failed in the weld metal in low-helium-containing specimens, L11, L21. Other two low-helium specimens, L12 and L22, also failed in the weld metal in a very similar way. Medium-helium-content specimens, M11 and M12, failed differently; M11 failed both in

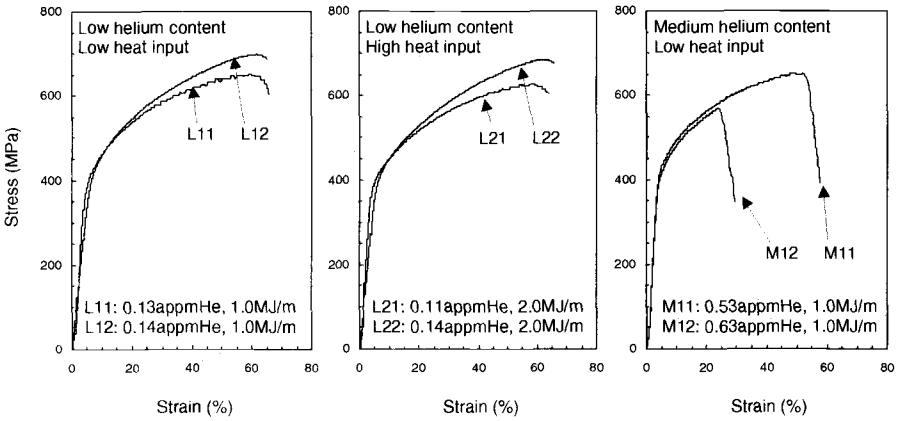


Figure 7 —*Stress-strain curve in tensile tests. Strain is given as crosshead displacement divided by gauge length of 30 mm including the weld.*

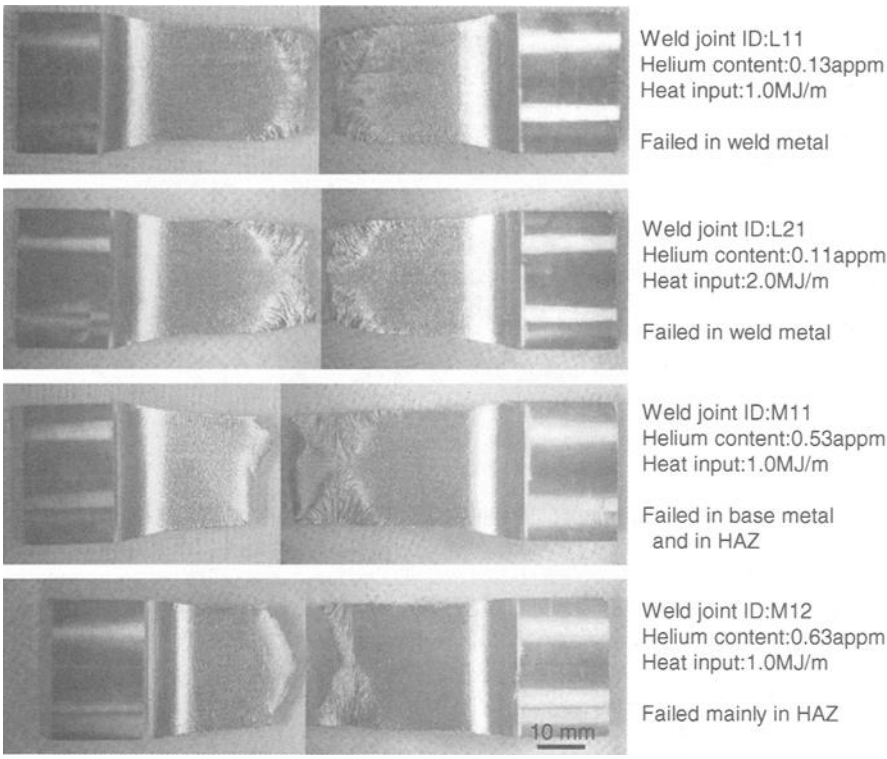


Figure 8—*The appearance of tensile tested specimens.*

the base metal and in the HAZ; M21 failed mainly in the HAZ. Note that there was some extent of reduction of area in all specimens.

The entire fractured surface of joint L11, Figure 9(a), which failed in the weld metal, was covered with ductile dimples. Figure 9(b) shows the fractograph for joint M12 in which nearly 90% consisted of intergranular fracture. Figure 9(c) shows the detail. In the near-surface areas in Figure 9(b), were located the regions covered with ductile dimples as shown in Figure 9(d). The dimple fracture observed in L11 was almost of the same one as Figure 9(d).

Side Bend Test and Root Bend Test

Figure 10 shows examples of bend tested specimens and bent surface examination by PT. Figures 10 (a) and (b) show the side bend test result for M12 in which the severest flaw indications were detected. Note that the detected flaws were found neither in the root region nor on the surfaces, but in the HAZ of one to two passes below the surface. This position of flaw was the same in M11 in which only a small indication was identified. Other L-series specimens containing less helium were bent without formation of

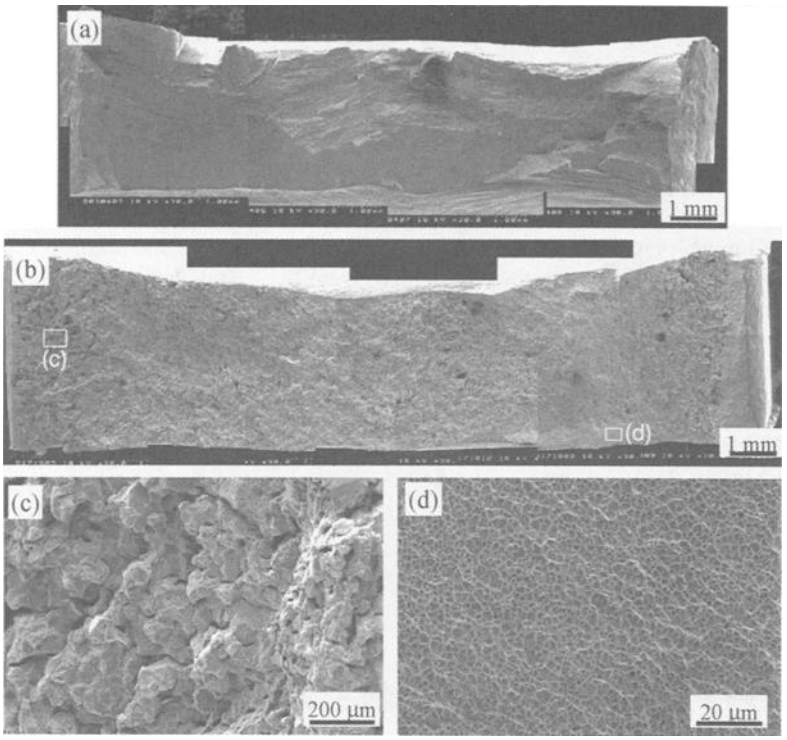


Figure 9—*Examples of fractured surface after the tensile test. (a) Surface of L11 was entirely covered with ductile dimples. (b) Surface of M12 consisted mainly of intergranular facets as shown in (c) and only a limited portion failed with ductility (d).*

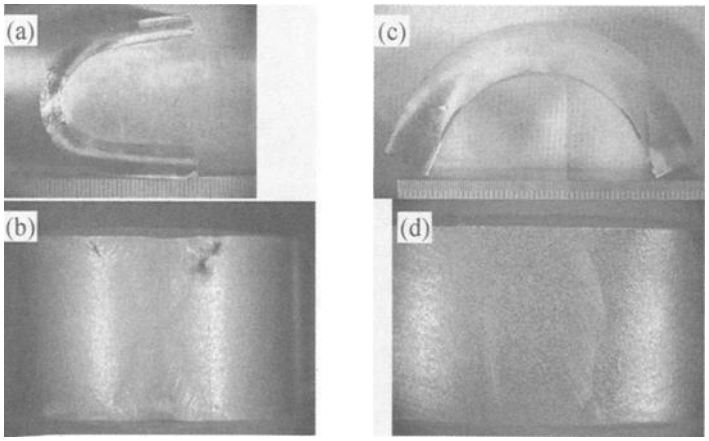


Figure 10 —*Examples of the bend tested specimens. (a), (b) Side bend test on M12. (c), (d) Root bend test on L12.*

detectable flaws. Figures 10 (c) and (d) show the root bend test result for L12. In all root bend tests, no flaw indication was observed.

Cross-sectional Metallography

Three welded joints, L12, L22, M12, were further examined by metallography. Figures 11 (a) and (b) show the macrographs for M12 and L22, which were welded at 1.0 and 2.0 MJ/m heat input, respectively. No large cracking was observed at this magnification. Figure 12 shows the micrographs from M12. The observed area is shown in the illustration. Intergranular fissures can be seen in Figure 12 (b, c) in the HAZ, within about 200 μm from the fusion line. The area shown in (b, c) corresponded to that area where flaws were observed in Figure 10 (b). In the root pass region and weld toe region, Figures (a) and (d, e), respectively, no fissure was observed.

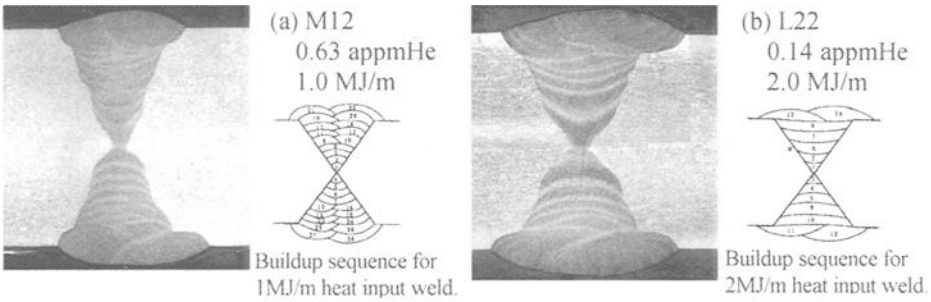


Figure 11 —*Macrographic examination of the cross sections of the welded joint.*

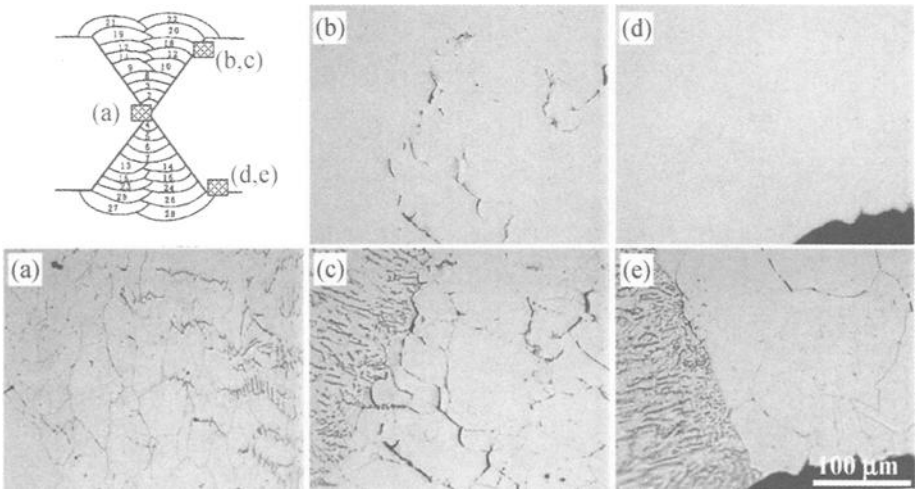


Figure 12 —*Micrographic features of the cross sections of the welded joint M12. (b) and (d) are in non-etched condition of the same area as (c) and (e), respectively.*

Discussion

Threshold Weldable Helium Content

In this work, no flaw indication by PT was detected in the completed joint and the UTS of the welded joint exceeded the standard requirement for unirradiated base metal in all six specimens that were subjected to the mechanical property tests. Furthermore, the fracture surfaces of the four low helium content joints contained no HAZ intergranular failure that is the prime concern for welding irradiated materials. No apparent fissure was observed either by bending test or by metallography. From these experimental results, it can reasonably be concluded that irradiated stainless steel containing no more than 0.14 appm of helium is weldable by GTAW with as much as 2.0 MJ/m weld heat input.

In the higher helium content material, such as in M11 (0.53 appmHe) and M12 (0.63 appmHe), the embedded tiny intergranular fissures were identified by side bend test and by metallography in the HAZ somewhat below the surface. The intergranular fracture, although ductile in nature as described in the following section, was also observed in these joints, which indicated that helium effects were taking place. The ratio of intergranular failure in the fracture surface was larger in M12 than in M11. The flaw indications that appeared in side bend tests were also severer in M12 than in M11. It can be pointed out that these differences might be attributed to the difference in helium content of these two joints, although the difference was not very large. This suggested

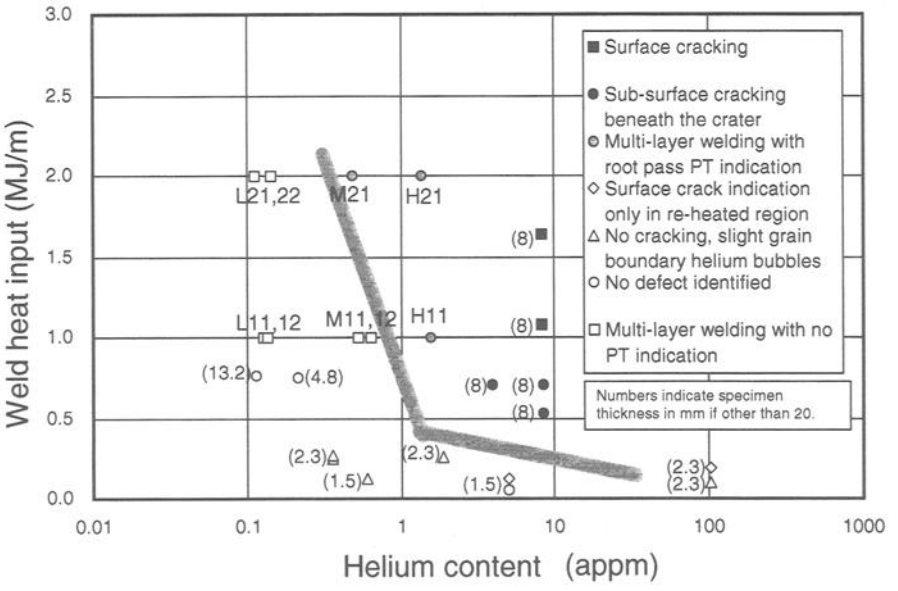


Figure 13 —*The dependence of the severity of weld defects on the helium content of the materials and weld heat input.*

that 0.5 appmHe was a threshold weldable helium content for welding with 1.0 MJ/m heat input. At this helium level, however, welding the joint M21 (0.48 appmHe) at 2.0MJ/m heat input resulted in a weld defect being produced on the root pass. By considering these results at two levels of heat input, it can be concluded that the weldability depends largely on the welding conditions at around 0.5 appmHe.

Figure 13 shows the severity of the weld defects observed both in the present study and in the previous work of the authors [1] in relation to the helium content of the tested materials and weld heat input. The region below the thick line is estimated to represent the nominal conditions where sound welding using conventional GTAW is probable.

The Mode of Fracture

Among the six tensile tested joints, the mode of fracture in the four lower helium content joints was ductile dimple fracture in the weld metal, while that in the other two medium helium content joints was a mixture of intergranular fracture and ductile fracture mainly in the HAZ. In M12 (0.63 appmHe), the fractured surface was almost dominated by intergranular failure as shown in Figure 9 (c). In M11 (0.53 appmHe), the intergranular failure covered about a half of the fractured surface, and the remaining region, mainly the middle of the thickness, was covered with transgranular ductile dimples. Most of the facets in these intergranular-fractured surfaces were also covered with ductile dimples; this feature reproduced well the observations reported in the previous work of the authors. [1] Figure 14 (a) shows the magnified view of the tensile tested joint specimen fabricated by welding a 0.6 appmHe, 1.5-mm-thick thin wall tube circumferentially. The UTS and fracture elongation of this joint exceeded the requirement for unirradiated base metal. The observed ductile dimples which covered the entire intergranular facets indicated that this characteristic feature was produced during the tensile test and it can be clearly distinguished from the intergranular facets decorated with smooth dimples as shown in Figure 14 (b), which was believed to have formed just by

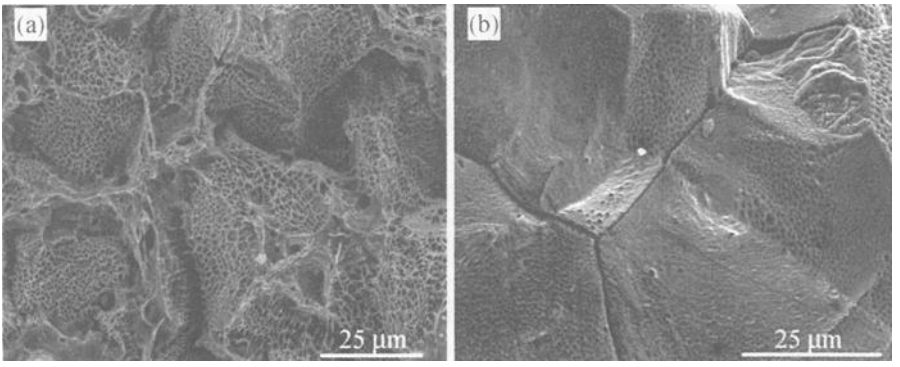


Figure 14 —*Differences in the intergranular failure morphology observed in the welded 1.5-mm-thick thin wall tube. (a) 0.6 appmHe containing specimen after the tensile test. (b) Failed in as-welded condition in 5 appmHe containing specimen.*

welding. The formation of this ductile dimple fracture on the grain boundary facets suggested the existence of helium bubbles by the diffusion of helium during welding to the grain boundaries. However, the strength of the grain boundaries seemed little degraded if no fissure was formed in the as-welded condition by considering that the joints had sufficient strength and ductility such as shown in Figure 7.

Effects of Thermal Cycling

In the welding of irradiated stainless steel, it has recently been recognized that those regions which experience repeated thermal cycles are liable to crack. [1,6] On the contrary, if the irradiated material be subjected to only one thermal cycle, as often encountered in the stringer bead welding of thin plate reported in the literature [7], no cracking will be introduced even if the materials contain a fairly high content of helium. In the present study, no weld defect was identified on the completed surface as shown in Figures 12 (d) and (e), probably because this region experienced a severe thermal cycle only once during the welding of the cover pass. Again in the root pass region that was strongly deformed by weld shrinkage during the follow-on pass welding as shown in Figure 12 (a), no fissure was observed. In the first four layers of both sides, each layer was welded with a single pass and this probably imposed a less severe thermal cycle to the HAZ of the preceding pass, including the root pass, thus not promoting the formation of fissures.

The intergranular fissures in the HAZ, which has been a critical concern in the welding of irradiated materials, were observed in Figures 12(b) and (c) by metallography. The fissures were also identified by PT in Figure 10 (b) in the symmetrical locations. These locations are supposed to have experienced the repetitive thermal cycles: the area shown in Figure 12 (b) and (c) were under the thermal cycling by welding passes 18, 20 and 22 depicted in Figure 12.

From these observations, it can be concluded that the possibility to obtain sound weld joints will be increased by designing the buildup sequence so as to avoid thermal cycling from the multiple weld passes.

Conclusions

The weldability of neutron irradiated type 304 stainless steel thick plate containing 0.11 to 1.6 appm of helium was examined by a conventional GTA welding procedure at 1.0 and 2.0 MJ/m weld heat input with special consideration on the applicability to the actual component. From this study, it can be concluded that:

1. Irradiated stainless steel containing as much as 0.14 appm of helium welded at a heat input of no more than 2.0 MJ/m is readily weldable with little concern for the strength of the joint and defect production.
2. The integrity of the welded joint made of materials containing about 0.5 appm of helium was dependent on the welding conditions.
3. Intergranular fissures, if they occurred, were observed in locations where the effect of thermal cycling may have operated. This suggested the potential improvement in the weldability of a given material by properly considering the buildup sequence.

Acknowledgments

The co-sponsorship of this work by other boiling water reactor owners of Japan, Tohoku Electric Power Co. Inc., Chubu Electric Power Co. Inc., Hokuriku Electric Power Co. Inc., The Chugoku Electric Power Co. Inc. and The Japan Atomic Power Company, is gratefully acknowledged.

References

[1] Asano, K., Nishimura, S., Saito, Y., H. Sakamoto, Yamada, Y., Kato, T. and Hashimoto, T., "Weldability of neutron irradiated austenitic stainless steels", *Journal of Nuclear Materials*, Vol.264, 1998, p.1. Also presented in *Eighth International Conference on Fusion Reactor Materials, ICFRM-8*, October 26-31, 1997, Sendai, Japan.

[2] Maloney, J. P., Baker, D., Kennedy, W. R., Day, W. A., McClain, J. B., Fraser, W. G., McKenney, D. H., Huxford, H. R., Meyer, C. A., Kehr, K. E., Mittelberg, R. F. and Walls, J. E., "Repair of a Nuclear Reactor Vessel", AEC R&D report, Savannah River Laboratory, DP-1199 (1969).

[3] Birchenall, A. K., presented in *TMS-AIME Symposium on Welding of Helium-Containing Metals*, Indianapolis, IN, USA, Oct. 3, 1989, DP-MS-89-41.

[4] Lin, H. T., Grossbeck, M. L. and Chin, B. A., *The Metallurgical Transactions A*, Vol.V21A, 1990, p.2585.

[5] Farrar, H. and Oliver, B. M., *Journal of Vacuum Science and Technology*, Vol.A4, 1986, p.1740.

[6] Kanne, W. R., Jr., Bruck, G. J., Madeyski, A., Lohmeier, D. A., Louthan, M. R., Jr., Rankin, D. T., Shogan, R. P., Lessmann, G. G. and Franco-Ferreira, E. A., *Proceedings of 5th International Symposium on Environmental Degradation of Materials in Nuclear Power Systems - Water Reactors*, Monterey, CA, USA, Aug. 1991, p.390 (The American Nuclear Society).

[7] Atkin, S. D., *ADIP Quarterly progress report*, DOE/ER-0045/7, 1981, p.110.

A. Kohyama,[1] T. Hirose,[2] T. Suzuki,[2] M. Narui,[3] and Y. Katoh[4]

Cracks in TIG Welded, Neutron-Irradiated 304 Stainless Steel

Reference: Kohyama, A., Hirose, T., Suzuki, T., Narui, M., and Katoh, Y., **"Cracks in TIG Welded, Neutron-Irradiated 304 Stainless Steel,"** *Effects of Radiation on Materials: 19th International Symposium, ASTM STP 1366,* M. L. Hamilton, A. S. Kumar, S. T. Rosinski, and M. L. Grossbeck, Eds., American Society for Testing and Materials, West Conshohocken, PA, 2000.

Abstract: In fission and fusion reactor applications, properties of welds and welded joints are key factors that limit component service conditions including their lifetime. Therefore, the availability of reliable repair welding techniques is strongly required in order to reduce the cost of electricity. One of the most difficult and unique characteristics, which repair welding has to overcome, is the radiation damaged microstructure including nuclear transformed gaseous atoms, such as helium from the (n, α) and hydrogen from the (n, p) reaction. There have been many attempts to investigate weldability of heavily neutron-damaged materials for establishing criteria for the repair welding process. The objective of this research is to clarify the mechanisms of weld cracking, especially for heat affected zone cracking in heavily neutron irradiated stainless steels.

Keywords: stainless steel, weld, heat affected zone, cracks, neutron irradiation

[1] Professor and [4]Asociate professor, Institute of Advanced Energy, Kyoto University, Gokasho, Uji, Kyoto 611-0011, Japan.

[2] Graduate student, Graduate School of Energy Science, Kyoto University, Yoshida-Honmachi, Sakyo-ku, Kyoto 606-8501.

[3] Assistant Researcher, Oarai Branch, Institute for Materials Research, Tohoku University, Oarai, Higashi-Ibaraki-Gun, Ibaraki 311-1313, Japan.

Copyright© 2000 by ASTM International www.astm.org

Introduction

As one of the important technologies for maintenance and repair of fission and fusion reactors, welding techniques have been extensively studied in recent decades. Due to the technological difficulties of repair welding of irradiated components, current fission reactor operators prefer, in general, replacement of damaged components. However, repair by replacement of components has many disadvantages, such as, an increase of radioactive wastes, long lead-time and long process-time for replacement, all of which have a strong impact on cost. Applications of welding techniques in repair and maintenance are becoming an attractive alternative to replacement schemes. Thus the emphasis seen in the R & D of welding irradiated materials, the objectives of these research programs is to produce sound-welded joints in materials with pre-existing neutron damage. The difficulty to produce sound-welded joints arises from (1) helium and hydrogen from (n, α)[*1*] and (n, p) reactions and (2) damage microstructure from displacement damage. Heating during the welding process induces nucleation and growth of He bubbles along grain boundaries [*2*], which makes it easy to initiate weld cracks in weld metals and/or heat affected zones (HAZs). There have been many attempts to investigate these issues [*3,4*], but to date they have been unsuccessful to quantitatively define the limiting conditions of repair welding.

The objectives of this work are to clarify the mechanisms of weld cracking, and to establish a measure to evaluate crack susceptibility, especially for HAZ cracking in neutron irradiated stainless steels (SUS304). In order to carry out this study, the mini-sized Varestraint (variable restraint) testing method was developed.

Experimental procedure

Specimen

The specimens used were plates of SUS304. The chemical composition of SUS 304 is shown in Table 1. The specimens were cut from plates 20mm in thickness. The plate thickness was reduced to 2 mm by a milling machine. The size of the specimens tested was $100 \times 25 \times 2$ mm. The specimens were neutron irradiated in the Japan

Materials Test Reactor (JMTR) of the JAERI Oarai Establishment, to three neutron fluences. Table 2 shows neutron fluence and He contents of the neutron irradiated specimens.

Table 1 – *Chemical composition of SUS304 (mass%)*

C	Si	Mn	P	S	Cr	Ni	N	Al	Co
0.05	0.6	1.03	0.002	0.004	18.3	8	0.06	0.01	0.02

Table 2 – *The neutron fluence for specimens*

Specimen Type	Fast neutron (E>1.0MeV)	Thermal neutron	He content
A	$1.0 \times 10^{23} n/m^2$	$1.2 \times 10^{24} n/m^2$	1.5appm
B	$2.0 \times 10^{22} n/m^2$	$4.0 \times 10^{23} n/m^2$	0.5appm
C	$1.5 \times 10^{21} n/m^2$	$1.4 \times 10^{21} n/m^2$	0.13appm

Varestraint test[*5*]

In order to evaluate the weld crack susceptibility, the Varestraint test was introduced. The Varestraint test was originally designed by Savage et al. [*5*], as a means to evaluate weld crack susceptibility, for example, weld metal cracks, HAZ (heat affected zone) cracks, and etc. It was necessary to develop the test machine for remote operation in a hot laboratory, because the specimens used in this work were radioactive. Therefore a mini-sized Varestraint test machine was designed and fabricated [*6*].

The specific feature of the mini-sized Varestraint test machine was its use for neutron irradiated specimens with induced radioactivity. Therefore, the following features were considered in designing the machine.

(1) Operation in a radiation environment utilizing radioactive specimens.
(2) Easy operation in a glovebox or hotcell where indirect specimen handling processes, such as magic hand handling, etc., are to be applied.

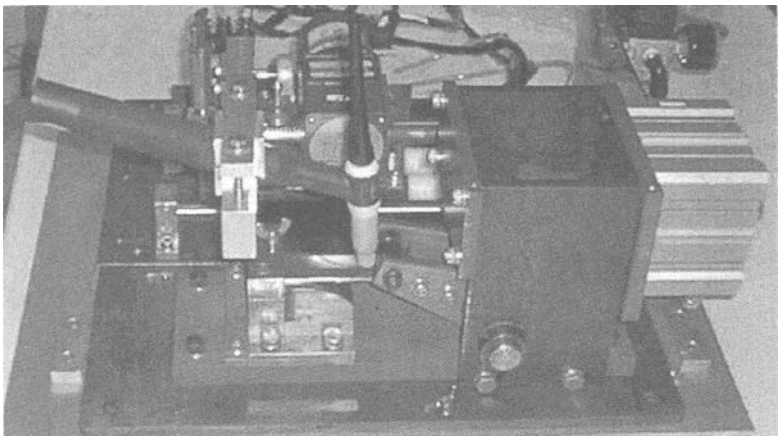


Figure 1 – *Mini-sized Varestraint test machine*

(3) Applicable to small or mini-sized specimens which requires modification of the bending die shape.

System miniaturization, remote operation capability, easy specimen placement and easy maintainability of the machine were major design objectives. The most difficult part was to simplify the mechanism of the rapid specimen bending procedure where a pneumatic system is used. To control the whole test procedure, sequential control by simple relay circuits was used. Figure 1 shows the mini-sized Varestraint test machine.

Figure 2 shows the principle of the Varestraint test. To start the Varestraint test, a specimen is placed in the Varestraint test machine. The welding method applied here is TIG welding. Welding was performed at 10VDC/90A and 8.9VDC/60A at a travel speed of 5mm/s, under a protective argon atmosphere. The heat input values were calculated to be 1.8kJ/cm, 1.2kJ/cm, respectively. The bead-on plate by TIG welding was done for about 35mm and followed by a rapid bending of the specimen and a simultaneous arc stop. The restraint strain was controlled by the curvature of the bending die. The precise surface strain of the specimen was also measured by strain gauges. The nominal surface stain (ε) induced by the Varestraint test is as follows.

$$\varepsilon\,(\%) = \{(t/2)/(R+t/2)\} \times 100 \cong (t/2R) \times 100 \qquad (1)$$

where

t = specimen thickness

R = radius of curvature of the bending die

In this work, the surface strains applied were 1.5%, 2% and 4% where 4% strain was applied only for the unirradiated specimens.

For optical microscopy and SEM, the welded specimens with uniform surface strain were cut into small pieces. The specimens were embedded in resin to be mechanically polished followed by etching with aqua regia (nitrohydrochloric acid) for optical microscopy. For TEM observation, the small pieces were sliced into thin plates and electropolished (twinjet technique) in a solution of 80% methanol with 20% sulfuric acid at 0°C.

Results and discussions

Temperature distribution along fusion line[7]

The temperature distribution along the fusion line, when the restraint stress is applied to a specimen was measured by thermography and was also predicted by the finite element method using the ABAQUS code. In the Varestraint test sequence, the

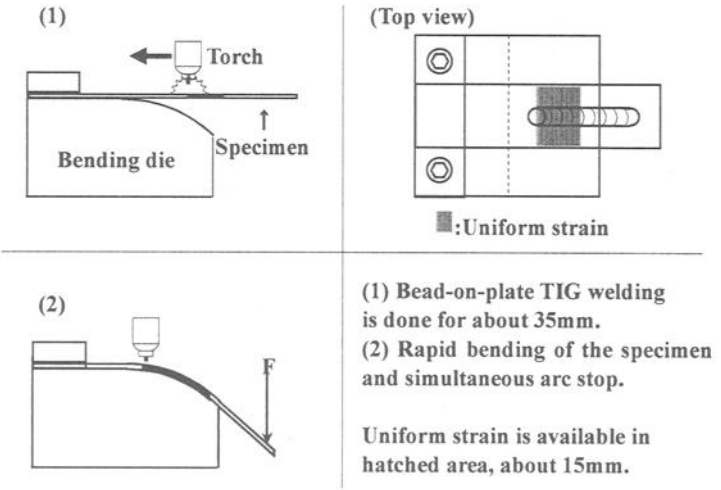


Figure 2 – *The schematic of the Varestraint test*

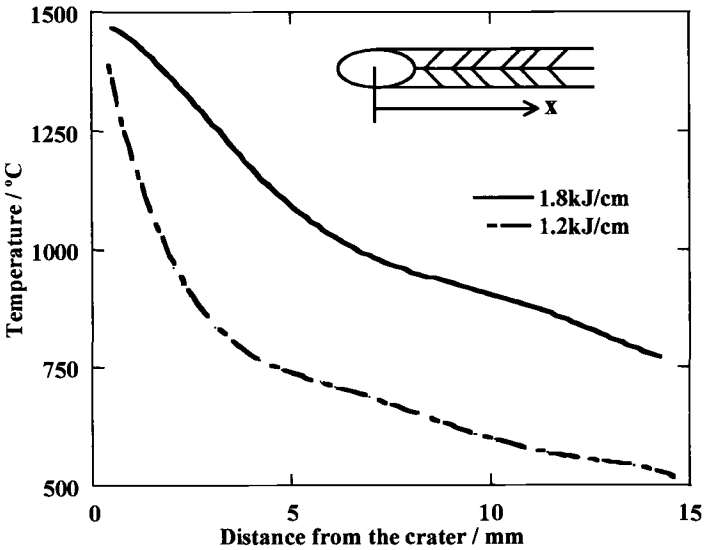


Figure 3 – *Temperature distribution along the weld fusion line*

restraining stress is applied to the specimen before the arc is stopped. Figure 3 shows temperature distribution along the fusion boundary.

Observation of HAZ cracks

At the beginning of this experiment, Varestraint tests for unirradiated specimens were carried out. For the case of unirradiated specimens even after polishing, cracks were not observed for surface strains as large as 4%. Even for the case of irradiated specimens, HAZ cracks were barely observed by video-microscopic observation with magnification of 175 x. By the precise observation of the surface of tested specimens by SEM, as shown in Figure 4 for example, no cracks were observed in the weld metal. Many HAZ cracks (intergranular cracks) were observed in the black areas, which were oxidized when the cracks initiated at high temperature.

In order to observe the cracks more precisely, Optical microscopic observations were carried out. Figure 5 is the typical optical micrograph of the polished surface of irradiated specimen after deformation.

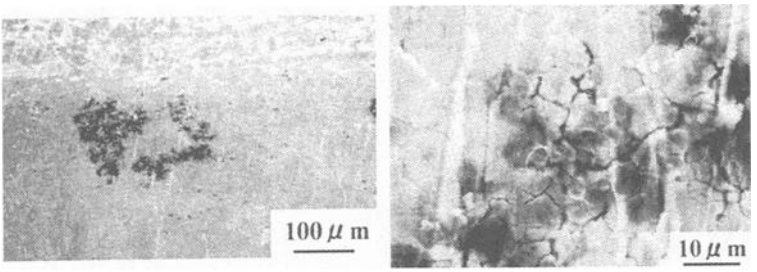


Figure 4 – *HAZ cracks observed by SEM*
He content: 1.5appm, Heat input: 1.8kJ/cm, Surface strain: 2.0%

HAZ cracks seen by surface observation are distributed within a certain distance from the fusion line with the peak distribution at distance Δl (shown in Figure 5). There are many other crack-like images over the surface, but they are identified by higher magnification observation to be parts of over-etched grain boundaries. In the case of higher heat input, HAZ cracks had wider distributions. The distance of peak crack distribution, Δl, became larger with increasing heat input. Although the change of Δl along the welding direction was small, with increasing distance from the center of crater, Δl slightly decreased. To interpret the HAZ crack distribution, the effect of residual stress distribution is studied where the direction of residual stress concerned is the one parallel to the welding direction. Figure 6 is a schematic illustration of crack distribution and residual stress distribution. The dashed line shows the position where the shear component of residual stress is the largest. HAZ cracks are considered to have a peak

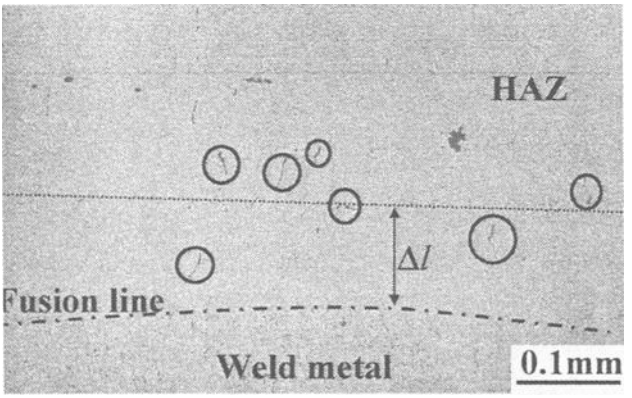


Figure 5 – *Optical micrograph showing HAZ cracks distribution (marked by circles)*
He content: 1.5appm, Heat input: 1.8kJ/cm, Surface strain: 2.0%

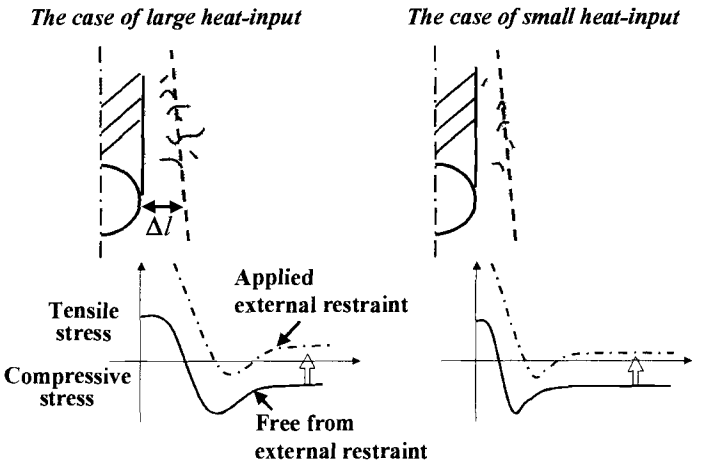


Figure 6 – *Schematic expression for the distribution of residual stress*

distribution along this line. Therefore, in case of large heat input, HAZ cracks form further from the fusion line. In order to study the combined effect of residual stress and external restraint quantitatively, a detailed thermal stress analysis is required.

According to TEM observation, bubbles were not observed in either the matrix or on grain boundaries. Other studies [*7-9*] reported that the radius of He bubbles induced by post-irradiation heat treatment was about 20nm. In the case, the He content was about 1000appm. It was 10^3 times larger than that of this work. In the current work visible bubbles were not detected. However, it was considered that invisible He might induce some grain boundary degradation.

Crack susceptibility

In this study, the heat input, external restraint, surface temperature during specimen bending and He concentrations were measured quantitatively. To evaluate crack susceptibility, a new parameter, P_{cs}, was defined as follows.

$$P_{cs} = (X_1 + X_2 + \bullet\bullet\bullet + X_n) / W \qquad (2)$$

where

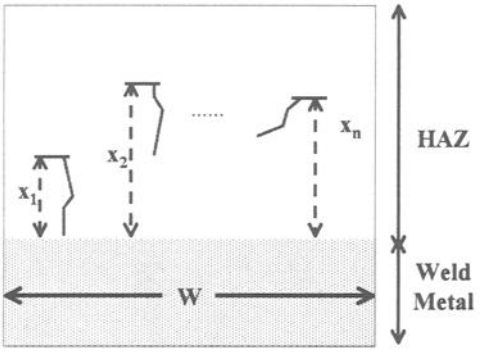


Figure 7 – *Definition of the original crack susceptibility*

Xn = The distance from the fusion boundary to the far end of cracks
W = The width of the observed region

As mentioned above, temperature varied strongly over a small area. In order to investigate the relationship between crack susceptibility and temperature precisely, the parameter P_{cs} was proposed. Figure 7 defines schematically the crack susceptibility. In this work, the crack length means the distance from the fusion line to the far end of cracks. The far end of HAZ cracks is the end of cracks. This is based on the fact, as previously mentioned, that most of the cracks are propagated to the fusion line and the crack length observed at the surface of the specimen has no special meaning.

Figure 8 shows the effect of neutron fluence and He content on the parameter P_{cs} [*10*]. Two effects are simultaneously involved, these are the displacement damage and the transmutation damage where the former produces radiation embrittlement and the latter degrades the strength of grain boundaries [*11,12*]. Because the cracks were the HAZ cracks neighboring the fusion line, it may be appropriate to assume that the effect of radiation hardening is not the most important factor. The larger the He content, the more the HAZ was crack susceptible. When the He content was reduced to 0.13appm, no cracks were observed.

Figure 9 shows the effect of external restraint on the crack susceptibility. The parameter P_{cs} was sensitive to external restraint (surface strain). For the case of the specimen 2.0% applied surface strain, the susceptibility reached almost 1. However, in the case of 1.5%, the susceptibility was less than 0.2. This may indicate an effectiveness of reducing induced strain by welding as a means of preventing crack formation.

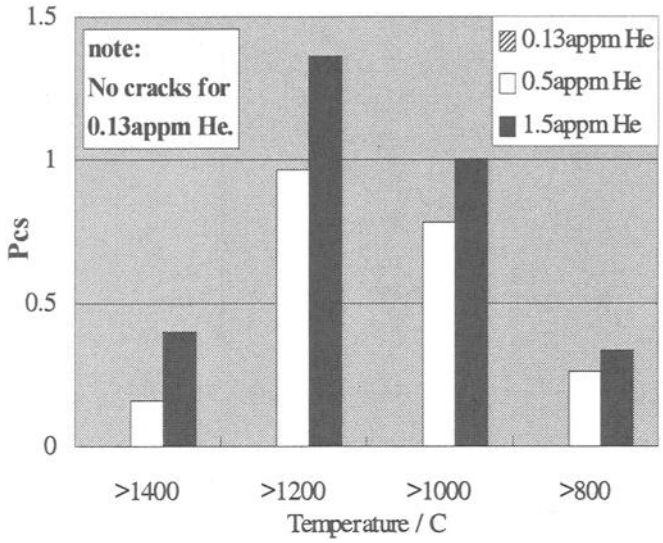


Figure 8 – *He content dependence of crack susceptibility*
Heat input: 1.8kJ/cm, Surface strain: 2.0%

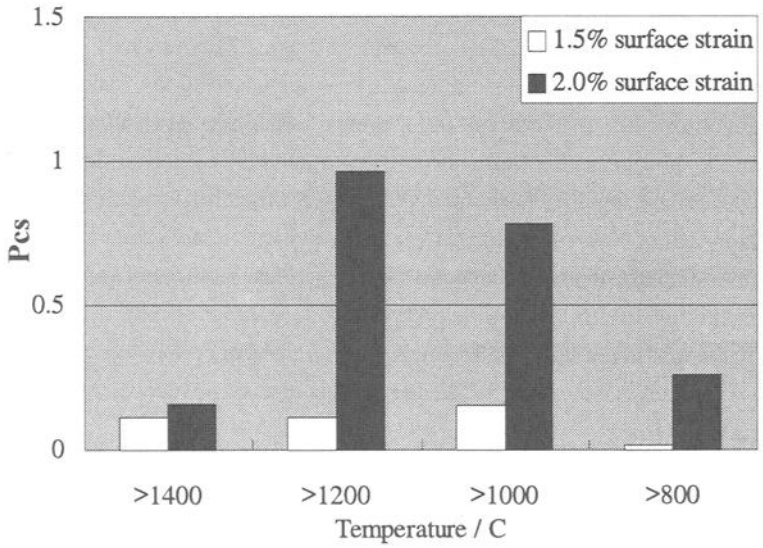


Figure 9 – *Surface strain dependence of the susceptibility*
He content: 0.5appm, Heat input: 1.8kJ/cm

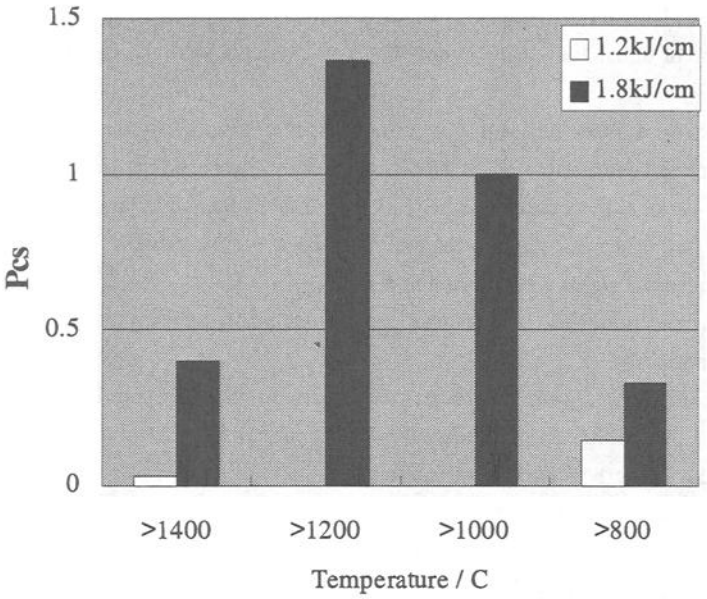


Figure 10 – *Heat input dependence of the crack susceptibility*
He content: 1.5appm, Surface strain: 2.0%

Figure 10 shows the effect of the heat-input value on the susceptibility. The susceptibility was very sensitive to heat-input. For the specimen given 1.2kJ/cm heat-input, HAZ cracks were seldom observed. The maximum susceptibility was less than 0.15. This is another indication that an appropriate welding condition may lead to reduce cracking.

The present study keeps open the question about the possibility that even under the very low He contents, lower than 0.13appm, HAZ cracking by welding may be taking place, however.

Conclusions

(1) To evaluate the weld crack susceptibility for neutron irradiated stainless steels, a mini-sized Varestraint (variable restraint) test machine for hot laboratory operation was designed and fabricated. It was operated both in and out of a hot cell at Oarai Branch,

IMR, Tohoku University, using TIG welding method.

(2) For the case of unirradiated specimens, HAZ cracks were seldom observed even after polishing.

(3) HAZ cracks were observed even in specimens with relatively low He content.

(4) A difference in the distribution of HAZ cracks was observed. For higher heat inputs and higher strains, the cracks reached far from the fusion boundary. For lower heat inputs and lower strains, the cracks gathered near the fusion line. This difference is caused by residual stress and external restraint.

(5) Larger He concentrations, larger surface strain and higer heat inputs increased HAZ crack susceptibility

(6) No visible He bubbles were observed in the specimen with 0.5appm He, 1.5% surface strain and 1.2kJ/cm heat input. However, it was considered that invisible He bubbles degraded the strength of grain boundaries.

(7) The reduction of surface strain and appropriate choice of welding condition and heat-input might reduce HAZ cracking. Designing of the weld joints and controlling the heat-input may solve the problem of welding cracks.

Acknowledgement

The authors would like to express their sincere appreciation to Prof. E. Murakawa and Dr. H. Serizawa of JWRI, Osaka University, Dr. K. Asano of TEPCO, Dr. M. Hashimoto of Hitachi Co. Ltd. Prof. A. Kimura of IAE, Kyoto University and Dr. T. Shibayama of CARET, Hokkaido University for their help in many aspects to this work. This work was partly conducted at the Irradiation Experimental Facility, Institute for Materials Research, Tohoku University. The technical support by members of this facility is greatly appreciated.

References

[1] Garner, F. R. and Greenwood, L. R., "Neutron Irradiation Effects in Fusion or Spallation Structural Materials: Some Recent Insights Related to Neutron Spectra," *Radiation Effects & Defects in Solids*. Vol.144, 1998, pp.251-286.

[2] Wang, C.A., Grossbeck, M.L. and Chin, B.A., "Threshold Helium Concentration Tequired to Initiate Cracking During Welding of Irradiated Stainless Steel," *Journal of Nuclear Materials*. Vol.25, 1995, pp.59-68.

[3] Tsuchiya, K., Kawamura, H. and Oyamada, R., "Reweldability Test of Irradiated SS316 by the TIG Welding Method," *Journal of Nuclear Materials*, Vol.233-236, 1996, pp.218-223.

[4] Hall, M. M., Jr., Hins, A. G., Summers, J. R. and Walker, D. E., Weldments, Physical Metallurgy and Failure Phenomena, Proc. 5th Bolton Landing Conf., Aug. 1978, General Electric Co., Schenectady, NY, 1979, pp.365.

[5] Savage W.F. and Lundin C.D., "Application of the Varestraint Technique to the Study of Weldability," *Welding Journal*, Vol.45, 1966, pp.497-503.

[6] Suzuki, T., Kohyama, A., Hirose, T. and Narui, M., "Evaluation of Weld Crack Susceptibility for Neutron Irradiated Stainless Steels," 1997, ICFRM-8 to be published.

[7] Foulds, J. R., "Thermal History of HT-9 Weldment Heat-Affected Zones During Welding" *Journal of Nuclear Materials*, Vol.141-143, 1986, pp. 434-438.

[8] Y. Ishiyama, Y., Kodama, M, Yokota, N., Asano, K., Kato, T. and Fukuya, K., "Post-irradiation Annealing Effects on Microstructure and Helium Bubbles in Neutron Irradiated Type 304 Stainless Steels," *Journal of Nuclear Materials*, Vol.239, 1996, pp.90-94.

[9] Kanne, W. R., Jr., Chandler, G. T., Nelson, D. Z. and Franco-Ferreira, E. A., "Welding irradiated stainless steel," *Journal of Nuclear Materials*, Vol.225, 1995, pp.69-75.

[10] Wang, C. A., Grossbeck, M. L., and Chin, B. A., "Technique to Eliminate Helium Induced Weld Cracking in Stainless Steels" *Effects of Radiation on Materials: 16th International Symposium, ASTM STP 1175*, Arvind S. Kumar, David S. Delles, Randy K. Nanstad, and Edward A. Little, Editors, American Society for

Testing and Materials, Philadelphia, 1993, pp. 779-788.

[11] Grossbeck, M. L., and Chin, B. A., "Helium-Induced Weld Degradation of HT-9 Steel" *Effects of Radiation on Materials: 16th International Symposium, ASTM STP 1175*, Arvind S. Kumar, David S. Delles, Randy K. Nanstad, and Edward A. Little, Editors, American Society for Testing and Materials, Philadelphia, 1993, pp. 789-802.

[12] Lin, H. T., Goods, S. H., Grossbeck, M. L., and Chin, B. A., "Helium-Induced Degradation in the Weldability of an Austenitic Stainless Steel" *Effects of Radiation on Materials: 14th International Symposium, ASTM STP 1046,* N. H. Packan, R. E. Stoller, and A. S. Kumar, Editors, American Society for Testing and Materials, Philadelphia, 1989, pp. 301-314

Tsuneyuki Hashimoto[1] and Masahito Mochizuki[2]

Modeling of Helium Bubble Formation During Welding of Irradiated Stainless Steels

Reference: Hashimoto, T. and Mochizuki, M., **"Modeling of Helium Bubble Formation During Welding of Irradiated Stainless Steels,"** *Effects of Radiation on Materials: 19th International Symposium, ASTM STP 1366,* M. L. Hamilton, A. S. Kumar, S. T. Rosinski, and M. L. Grossbeck, Eds., American Society for Testing and Materials, West Conshohocken, PA, 2000.

Abstract: Helium atoms are generated in neutron-irradiated stainless steels. In order to predict the post-irradiation weldability, a model is presented to calculate helium bubble formation along grain boundaries during welding of helium containing stainless steels. It calculates helium diffusion toward the grain boundary, bubble nucleation, coalescence and growth at the grain boundary, using the temperature and stress changes during welding. Annealing experiments of helium implanted stainless steels at constant temperatures are analyzed first to examine the bubble formation without tensile stresses. Good agreement with measurements is obtained for the bubble density and the average radius. Then, bubble formations are calculated for a bead-on-tube welding test on a neutron-irradiated stainless steel. Good correlation is confirmed between bubble formation calculations and the crack formation observed in the welding test.

Keywords: irradiated stainless steel, welding, helium bubble, computer modeling

Introduction

Austenitic stainless steels are used as the internal structural materials in nuclear reactors. They contain nickel and boron, which produce helium atoms under neutron irradiation via transmutation reactions. The experience of welding to repair an irradiated component in a military reactor [*1*] and subsequent analyses revealed that the presence of helium is one of the important issues in determining the post-irradiation weldability. Welding tests have been performed using helium bearing stainless steels prepared with the tritium trick technique [*2-6*], and neutron irradiation [*7-11*]. These

[1]Senior Researcher, Hitachi Research Laboratory, Hitachi Ltd., 7-1-1 Omika-cho, Hitachi, Ibaraki 319-1292, Japan.

[2]Researcher, Mechanical Engineering Research Laboratory, Hitachi Ltd., 502 Kandatsu-cho, Tsuchiura, Ibaraki 300-0013, Japan. Present address: Osaka University, 2-1 Yamadaoka, Suita, Osaka, 565-0871, Japan.

Copyright© 2000 by ASTM International www.astm.org

studies showed that the susceptibility to weld cracking depended on helium content, as well as on factors such as welding method, heat input, specimen shape and size. Degradation in weldability and subsequent cracking typically occurred in the heat-affected zone (HAZ). Metallographic examination showed that the cracking was intergranular, and at high magnification, the grain boundary (GB) facet was found to be decorated with small dimples. These observations indicated that He bubbles formed along the GB were responsible for the intergranular cracking.

A model has been proposed by Lin et al. [2] to analyze the growth kinetics of GB helium bubbles. The growth kinetics is divided into three sequential time regimes, then the model calculates bubble radius when an average spacing between bubbles is provided. The average spacing or bubble number density, however, is not determined from the model, because modeling of the bubble nucleation process is not included there.

This paper presents an improved model to calculate both the nucleation and growth of helium bubbles at the GB during welding. The following sections describe the basic model and calculations for annealing at constant temperatures and for bead-on-tube welding with transient temperature and stress changes.

Basic Model

Assumptions and Approximations

Helium atoms are produced by neutron reactions with alloy constituents of stainless steels. Although its solubility in metals is very low, helium accumulates at pre-existing or radiation-induced defects. Since no voids have been observed by transmission electron microscopy (TEM) in stainless steels irradiated under boiling water reactor (BWR) temperature conditions, helium atoms are thought to be trapped at vacancies, invisible microvoids, dislocations, dislocation loops, and so on. For simplicity, the proposed model assumes an initial condition in which helium atoms are piled up in the matrix, in the form of a vacancy-helium complex (V-He), namely a vacancy containing one helium atom.

As is discussed later (see Eq. 11), helium gas pressure in a bubble is calculated using the Carnahan-Starling equation of state (CS-EOS) for a hard sphere system [*12*]. Applying this EOS and the vacancy absorption rate equation (Eq. 10) to a vacancy, the followings are derived. (a) A vacancy can hold up to two helium atoms. (b) The gas pressure is insufficient for V-He to grow by absorbing another vacancy. (c) V-2He, a vacancy containing two helium atoms, has sufficient gas pressure to grow by absorbing another vacancy. Therefore, V-2He is assumed to be the nucleus of a bubble.

Bubble growth induced by tensile stresses is calculated using a Hull-Rimmer type growth rate equation (Eq. 10), similar to the model of Lin et al. [2]. Since the equation is derived on the assumption of equally sized bubbles, an average radius approximation is adopted here, instead of considering the distribution of the bubble radii.

Equations

This model consists of two major parts; bubble formation at the GB and helium atom diffusion in the matrix. The bubble formation model calculates bubble nucleation,

coalescence, and growth at the GB. The helium diffusion model calculates helium flow toward the GB. The effect of a helium trap due to bubble formation in the matrix is also considered in the diffusion model.

Bubble Formation at GB-Concentration of GB bubbles (N) in the unit of atomic fraction is determined from the nucleation and coalescence.

$$\frac{dN}{dt} = \left(\frac{dN}{dt}\right)_{nucl} + \left(\frac{dN}{dt}\right)_{coal} \tag{1}$$

Subscripts 'nucl' and 'coal' mean nucleation and coalescence, respectively. Since V-2He has been assumed to be a bubble nucleus, the nucleation rate is given as the reaction rate of V-He and a helium atom. The concentration of helium atoms at the GB (N_{He}) is determined by their flow into the GB, trapping and release by a vacancy, bubble nucleation, and absorption by bubbles. The concentration of V-He at GB (N_{HeV}) is calculated similarly.

$$\left(\frac{dN}{dt}\right)_{nucl} = f_1^{GB}(K_{He}^{GB} + K_{HeV}^{GB})N_{He}N_{HeV} \tag{2}$$

$$\begin{aligned}\frac{dN_{He}}{dt} = {} & \frac{F}{N_0\delta} - f_1^{GB}K_{He}^{GB}N_{He}C_V^e + f_1^{GB}KR_{HeV}^{GB}N_{HeV} \\ & - f_1^{GB}(K_{He}^{GB} + K_{HeV}^{GB})N_{He}N_{HeV} - f_r^{GB}(K_{He}^{GB} + K_N^{GB}(r))N_{He}N\varepsilon\end{aligned} \tag{3}$$

$$\begin{aligned}\frac{dN_{HeV}}{dt} = {} & f_1^{GB}K_{He}^{GB}N_{He}C_V^e - f_1^{GB}KR_{HeV}^{GB}N_{HeV} \\ & - f_1^{GB}(K_{He}^{GB} + K_{HeV}^{GB})N_{He}N_{HeV} - f_r^{GB}(K_{HeV}^{GB} + K_N^{GB}(r))N_{HeV}N\end{aligned} \tag{4}$$

$$C_V^e = \exp(S_V^F / k)\cdot\exp(-E_V^F / kT) \tag{5}$$

where

f = geometrical factor of the reaction
K, and KR = reaction rate coefficients
C_V^e = thermal vacancy concentration
F = helium atom flow rate into GB
N_0 = atomic density
δ = GB thickness
S_V^F = vacancy formation entropy
E_V^F = vacancy formation energy
k = Boltzmann's constant
T = temperature

Subscripts 'He', 'HeV' and 'N' mean, respectively, helium atom, V-He and bubble. Superscript 'GB' is used if it is necessary to indicate clearly that the quantity is defined at the GB. Reaction rate coefficients are related to diffusion coefficients (D), and are

given as follows.

$$K_{He}^{GB} = D_{He}^{GB} / b^2$$
$$K_{HeV}^{GB} = D_{HeV}^{GB} / b^2 \qquad (6)$$
$$KR_{HeV}^{GB} = K_{He}^{GB} \cdot \exp\left(-E_{HeV}^{b} / kT\right)$$

where

b = lattice constant
$E_{HeV}{}^{b}$ = binding energy between a vacancy and a helium atom

Considering that a larger bubble moves more slowly, the reaction rate coefficient of a bubble is set to be radius-dependent, as is shown in Eq.7. The radius dependent expression, the first term in the right-hand side of Eq. 7, is derived from the Brownian migration of the center-of-mass of a bubble with a vacancy and an atom on its surface. The major dependence, r^{-4}, is the same as the one given by Gruber [*13*]. Although this expression is derived for big bubbles whose radius (r) is much larger than the vacancy radius (r_V), it is also applied to smaller ones. If this coefficient exceeds the reaction rate coefficient of V-He, $K_{HeV}{}^{GB}$, $K_{HeV}{}^{GB}$ is used instead, so as to avoid the inconsistency that a small bubble migrates more easily than a vacancy.

$$K_N^{GB}(r) = \min\left[D_N^{GB}((r_V / r)^4 + (r_V/r)^6) / (2b^2), \quad K_{HeV}^{GB}\right] \qquad (7)$$

ε in the fifth term of the right-hand side of Eq. 3 is the number of helium atoms per bubble to be absorbed by the bubbles and it is calculated by the following equation.

$$\varepsilon = (r / r_{He})^3 - m \qquad (8)$$

where

r_{He} = helium atom radius
m = number of helium atoms contained in a bubble

In case ε >1, ε is set to 1, because only one helium atom is absorbed in the reaction between a bubble and a vacancy. The bubble coalescence rate is given as the reaction rate between two bubbles.

$$\left(\frac{dN}{dt}\right)_{coal} = -f_{coal}^{GB} K_N^{GB}(r) N^2 \qquad (9)$$

Average radius of a bubble (r) is calculated from the following equations.

$$\frac{dr}{dt} = \left(\frac{dr}{dt}\right)_{nucl} + \left(\frac{dr}{dt}\right)_{HeV} + \left(\frac{dr}{dt}\right)_{coal} + \left(\frac{dr}{dt}\right)_{gr}$$

$$\left(\frac{dr}{dt}\right)_{nucl} = \frac{r_V^3 - r^3}{3r^2 N} \cdot \left(\frac{dN}{dt}\right)_{nucl}$$

$$\left(\frac{dr}{dt}\right)_{HeV} = \frac{r_V^3}{3r^2} \cdot f_r^{GB}(K_{HeV}^{GB} + K_N^{GB}(r))N_{HeV}$$

$$\left(\frac{dr}{dt}\right)_{coal} = -\frac{r}{3N} \cdot \left(\frac{dN}{dt}\right)_{coal} \tag{10}$$

$$\left(\frac{dr}{dt}\right)_{gr} = \begin{cases} \dfrac{\delta \Omega D_V^{GB} C_V^e \left\{1 - \exp\left[-(p - 2\gamma / r + \sigma)\Omega / kT\right]\right\}}{2r^2} & (\sigma \le 0) \\ \dfrac{2\pi \delta \Omega D_{gb} (\sigma + p - 2\gamma / r)}{r\, kT} \cdot N^{1/2} (N_0 \delta)^{1/2} & (\sigma > 0) \end{cases}$$

where

r_V = vacancy radius
Ω = atomic volume
D_V^{GB} = vacancy diffusion coefficient at GB
D_{gb} = self-diffusion coefficient at GB
p = gas pressure
γ = surface free energy
σ = tensile stress perpendicular to GB

The first term is the decrease in the average radius due to the nucleation of a bubble of radius r_V. The second one is the growth caused by the absorption of a V-He. The third term denotes the radius increase arising from the coalescence of two bubbles. The last one is the growth rate of the individual bubble. Similar to the model by Lin et al.[2], the GB bubble is assumed to grow by absorbing thermal vacancies when the stresses are compressive ($\sigma \leq 0$), and to grow by tensile stresses when shrinkage stresses are applied ($\sigma > 0$). The Hull-Rimmer equation [*14*] is used for the tensile-stress-induced growth. Average spacing used in the Hull-Rimmer equation is replaced here with the bubble density.

Gas pressure is calculated using CS-EOS for a hard sphere system [*12*].

$$\frac{pV}{mkT} = \frac{1 + y + y^2 - y^3}{(1 - y)^3}$$

$$y = \frac{\pi d^3}{6} \cdot \frac{m}{V} \tag{11}$$

$$V = \frac{4}{3}\pi r^3$$

$$d = 0.2556(0.9937 - 0.041168\ln(T/10.22))$$

where

V = bubble volume
d = helium atom diameter in the unit of nm

The number of helium atoms in a bubble (m) is determined from the conservation of helium atoms.

$$\frac{d(Nm)}{dt} = \frac{F}{N_0\delta} - \frac{dN_{He}}{dt} - \frac{dN_{HeV}}{dt} \tag{12}$$

N, N_{He}, and N_{HeV} in the above equations are calculated in units of atomic fraction. If necessary, they are converted into areal density, m^{-2}, by multiplying by $N_0\delta$.

Helium Diffusion in the Matrix-Helium can reside in the matrix either on an interstitial site or a lattice site [*15*]. Since helium on a lattice site is identical to V-He, concentrations of the interstitial helium and V-He (C_{He} and C_{HeV}, respectively) are calculated in the diffusion model.

$$\frac{\partial C_{He}}{\partial t} = -\nabla J_{He} - f_1^{mtx} K_{He}^{mtx} C_{He} C_V^e + f_1^{mtx} KR_{HeV}^{mtx} C_{HeV} - f_T^{mtx} K_{He}^{mtx} C_{He} C_T + f_T^{mtx} KR_{THe}^{mtx} C_{THe} \tag{13}$$

$$\frac{\partial C_{HeV}}{\partial t} = -\nabla J_{HeV} + f_1^{mtx} K_{He}^{mtx} C_{He} C_V^e - f_1^{mtx} KR_{HeV}^{mtx} C_{HeV} - f_T^{mtx} K_{HeV}^{mtx} C_{HeV} C_T + f_T^{mtx} KR_{THeV}^{mtx} C_{THeV} \tag{14}$$

$$J_{He} = -D_{He}^{mtx} \nabla C_{He}$$

$$J_{HeV} = -D_{HeV}^{mtx} C_V^e \nabla C_{HeV}$$

$$KR_{THe}^{mtx} = K_{He}^{mtx} \cdot \exp\left(-E_{THe}^b / kT\right)$$

$$KR_{THeV}^{mtx} = K_{HeV}^{mtx} \cdot \exp\left(-E_{THeV}^b / kT\right)$$

$$\frac{dC_{THe}}{dt} = f_T^{mtx} K_{He}^{mtx} C_{He} C_T - f_T^{mtx} KR_{THe}^{mtx} C_{THe} \tag{15}$$

$$\frac{dC_{THeV}}{dt} = f_T^{mtx} K_{HeV}^{mtx} C_{HeV} C_T - f_T^{mtx} KR_{THeV}^{mtx} C_{THeV} \tag{16}$$

$$C_T = C_T^o - C_{THe} - C_{THeV} \tag{17}$$

Superscript 'mtx' is used to show explicitly that the quantities are defined for the matrix. Two types of mechanisms, a dissociative mechanism and a vacancy mechanism, are possible for the helium diffusion [*15*]. Equation 13 represents the dissociative

mechanism, in which a helium atom jumps from V-He into an interstitial position, and migrates as an interstitial atom until it is trapped again by a vacancy. The first term in the right-hand side is diffusion of interstitial helium. The second one is trapping by a vacancy, and the third is release from V-He. The fourth and fifth terms are trapping and release from a trapping site. Each trapping site is defined to trap either a helium or a V-He. C_T is the concentration of the vacant trapping site, and C_{THe} is the concentration of the sites which have trapped a helium atom, namely it is equal to the concentration of helium trapped at the sites. Equation 14 describes the diffusion via normal vacancy mechanism, in which helium on a lattice site migrates through the position exchange with a vacancy.

C_T^0 is the total concentration of the trapping site. As is explained next, this is introduced to include the suppression of helium flow toward GB caused by bubble formation in the matrix. Hence, C_T^0 is varied with time in accordance with the matrix bubble formation.

Concentrations in Eqs. 13-17 are calculated as atomic fraction, and they can be converted into volume density, m^{-3}, by multiplying by N_0.

Bubble Formation in the Matrix-Helium bubbles will also be formed in the matrix during welding. They suppress helium flow toward the GB, and consequently, reduce the GB bubble formation. Although bubble formation would vary as a function of distance from the GB, a one point approximation is adopted in this model to account for the restraint of helium flow. Equations for matrix bubbles can be obtained by replacing the superscript 'GB' by 'mtx', though some modifications are needed. The first term in Eqs. 3 and 12, $F/N_0\delta$ is unnecessary for matrix bubbles. Bubble growth rate by absorbing thermal vacancies (Eq. 10), is substituted by the following equation, because matrix bubble growth is three-dimensional, while that of GB bubbles is two-dimensional.

$$\left(\frac{dr^{mtx}}{dt}\right)_{gr} = \frac{D_V^{mtx} C_V^e \left\{1 - \exp\left[-(p^{mtx} - 2\gamma / r^{mtx} + \sigma)\Omega / kT\right]\right\}}{r^{mtx}} \quad (\sigma \le 0) \tag{18}$$

The Hull-Rimmer equation is not applicable to stress-induced growth of matrix bubbles, because it was derived for the bubbles on a plane. Therefore, stress-induced growth during the cooling period is not calculated for matrix bubbles in this model. This does not affect the results, because the diffusion calculation indicates that helium flow into the GB ceases during the heatup period, regardless of the bubble radius in the cooling period.

Connection of the Bubble Formation and Helium Diffusion Calculations- GB bubble formation and diffusion calculations described above are connected to each other through the following relationships.

$$F = -(J_{He} + J_{HeV})_{x=0} \cdot N_0 \tag{19}$$

$$(C_{He})_{x=0} = N_{He} \tag{20}$$

$$(C_{HeV})_{x=0} = N_{HeV} \tag{21}$$

$$C_T^0 = N^{mtx}\, m^{mtx} \tag{22}$$

Equation 19 means that helium flow into the GB is given by the diffusion flux. N_0 is multiplied so that the dimensions of F become $m^{-2}s^{-1}$. Equations 20 and 21 denote that the boundary conditions for the diffusion equations are determined from the helium or V-He concentration at the GB. Equation 22 represents the helium flow suppression due to the matrix bubbles, by setting the concentration of trapping sites as equal to the total number of helium atoms that can be contained in matrix bubbles.

Analysis of Annealing Experiments

Annealing experiments are analyzed in this section to examine the bubble formation under shrinkage-stress free situations. Details of the experiments will be presented elsewhere [*16*], so only experimental conditions are briefly summarized here. Type 304 stainless steel specimens (C: 0.06 wt%), 3mm in diameter and 0.16mm thick are solution annealed at 1323 K for 30 minutes. They are irradiated, simultaneously, with Ni^{3+} and He^+ ions at 573K. Ni ion energy is 4MeV, producing ~5 dpa (displacement per atom) at the damage peak of ~700 nm depth. He ions are irradiated at 400 keV so that the helium implantation peak is the same depth as the Ni damage peak. Helium concentration at the peak is varied from 8 appm (atomic parts per million) to 500 appm. After ion irradiation, specimens are annealed at constant temperatures between 673 and 1273 K for 30 minutes. Helium bubble formation is examined with a TEM at the damage peak depth.

Table 1 - *Major Parameter Values Used in the Calculations*

Parameter	Value
D_V^{mtx}	5.0×10^{-5} exp (-1.3 eV／kT) (m^2/s)
D_{He}^{mtx}	6.6×10^{-7} exp (-0.2 eV／kT) (m^2/s)
D_{HeV}^{mtx}	5.0×10^{-5} exp (-1.3 eV／kT) (m^2/s)
$D_n^{mtx}(r)$	5.0×10^{-2} exp (-2.6 eV／kT) $\times((r_V/r)^4+(r_V/r)^6)/2$ (m^2/s)
D_V^{GB}	5.0×10^{-5} exp (-1.3 eV／kT) (m^2/s)
D_{He}^{GB}	6.6×10^{-7} exp (-0.1 eV／kT) (m^2/s)
D_{HeV}^{GB}	5.0×10^{-5} exp (-1.3 eV／kT) (m^2/s)
$D_n^{GB}(r)$	1.5 exp (-2.6 eV／kT) $\times((r_V/r)^4+(r_V/r)^6)/2$ (m^2/s)
E^b_{HeV}	2.2 (eV)
S^F_V	5k
E^F_V	1.9 (eV)
δ	4×10^{-10} (m)
γ	1 (J/m^2)
Ω	1.2×10^{-29} (m^3)
N_0	8.5×10^{28} (m^{-3})
b	3.63×10^{-10} (m)

Calculations are performed for the cases in which 500 appm helium specimens are annealed at 973, 1073 and 1173 K. Grain radius is set to 50 μm, and one-dimensional diffusion calculations are performed in the radial direction. As was stated earlier, helium is assumed to be located on the lattice site, namely to be in the form of V-He, prior to welding. Major parameter values used in the calculations are summarized in Table 1. The same diffusion coefficients are used for a vacancy at the GB and in the matrix. Diffusion coefficients of V-He are also set to be equal to those of a vacancy. Helium atoms are assumed to migrate faster at the GB than in the matrix by setting a smaller migration energy at the GB. Diffusion coefficients of the bubble have a radius dependent form as is given in Eq.7. The same activation energy is assumed for GB and matrix bubble migration, and it is varied to fit the temperature dependence observed in the experiments. Pre-exponential factors are adjusted from the measured bubble densities.

Figure 1 shows the calculated changes of bubble density and average radius during the 1173 K annealing. Bubble density, both at the GB and in the matrix, peaks in a very short time, then decreases due to coalescence. Bubble radius, on the other hand, increases with time, and reaches ~7 nm after 30 min. annealing. Table 2 compares the calculations and measurements. Agreement is satisfactory.

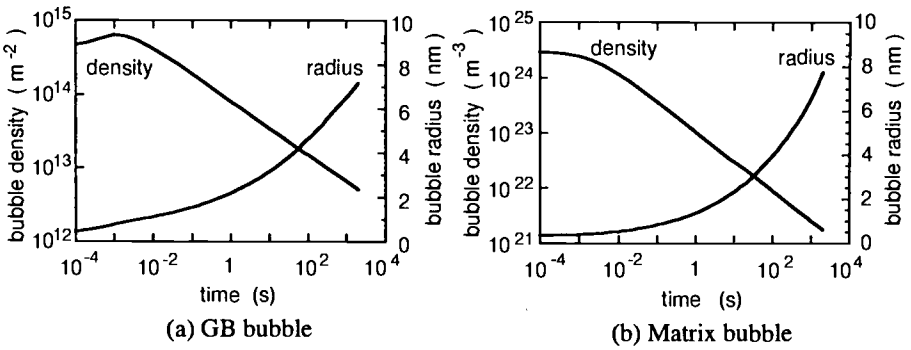


Figure 1- *Calculated bubble density and radius during 1173K annealing.*

Analysis of the Welding Tests of Neutron-Irradiated Stainless Steel

Welding tests have been performed using neutron-irradiated stainless steels [*9-11*]. Various shapes and sizes of specimens, such as plates with 8 mm thickness, tubes with 1.5-2.3 mm thickness, and so on, were tested using gas tungsten arc welding (GTAW) or YAG laser welding techniques. Among these tests, circumferential GTAW on a tube [*9*] is selected for analysis. The specimen is a type 304 stainless steel tube with outer diameter of 17.3 mm and 2.3 mm thickness. It was irradiated in a BWR core up to 1.4 $\times 10^{26}$ n/m^2 (>1 MeV). Helium content was measured as 103 appm. One pass circumferential GTAW was performed with 550 W at a travel speed of 2.7 mm/s

Table 2 - *Comparison with Annealing Experiments*

			Calculation	Measurement
1173 K	matrix	density (m^{-3})	2.8×10^{21}	4.5×10^{21}
	bubble	av. radius (nm)	6.7	8.3
	GB	density (m^{-2})	5.2×10^{12}	4×10^{12}
	bubble	av. radius (nm)	7.1	9.9
1073 K	matrix	density (m^{-3})	9.3×10^{21}	1.4×10^{22}
	bubble	av. radius (nm)	3.6	3.0
	GB	density (m^{-2})	6.9×10^{12}	–
	bubble	av. radius (nm)	4.1	–
973 K	matrix	density (m^{-3})	4.6×10^{22}	8.6×10^{22}
	bubble	av. radius (nm)	1.8	1.4
	GB	density (m^{-2})	1.1×10^{13}	–
	bubble	av. radius (nm)	2.2	2.3

(0.2 kJ/mm), under which full penetration welding was produced. Argon was used as the shielding gas. At the start and end of the welding, there was an overlap region. In the subsequent liquid penetrant test on the outer surface, dye indications were detected only in the overlapped region, but not in the one pass region. Cross sectional metallurgical examination, however, revealed that intergranular cracks were generated at the HAZ on the inner surface, even in the one pass region. This case is selected for the calculations, because various situations occur in one specimen.

Calculations are performed at 180° and 70° cross sections (see Figure 2). The former is for the one pass region, where no cracking is detected on the outer surface, while cracking is observed on the inner surface. The latter is for the overlapped region, where cracking is found on the outer surface, as well as on the inner surface.

Two-dimensional thermal elastic-plastic analysis is carried out, using ABAQUS, to obtain temperature and stress changes at each cross section. Temperature and three stress components are picked up at points 0.1 mm away from the fusion line on the inner and outer surfaces. This distance is chosen because cracking has been observed to occur in this region by metallurgical examinations [9]. Then, helium bubble growth at GB is evaluated for each stress component. Figure 3 shows the temperature and stress changes. Only the stress component that produced the largest bubble growth, stress parallel to the weld bead, is shown. In the 180° cross section, temperature changes are identical at inner and outer surfaces. Similarly, when cooling begins, compressive stresses become tensile stresses at both surfaces. Tensile stress after that, however, changes differently: it continues to increase to the level of 120 MPa at the inner surface, while it peaks near 50 MPa, then decreases at the outer surface. The figure also shows how the 70° cross section undergoes the thermal cycle twice, due to the overlap.

Figure 4 shows the calculated GB bubble density and average radius for the three cases. The same parameters as listed in Table 1 are used. The self-diffusion coefficient at the GB in Eq. 10, D_{gb}, is taken as $3.5\times10^{-7}\exp(-1.0\ eV/kT)$. Helium atoms begin to flow into the GB when temperature exceeds ~ 500℃, and bubble density

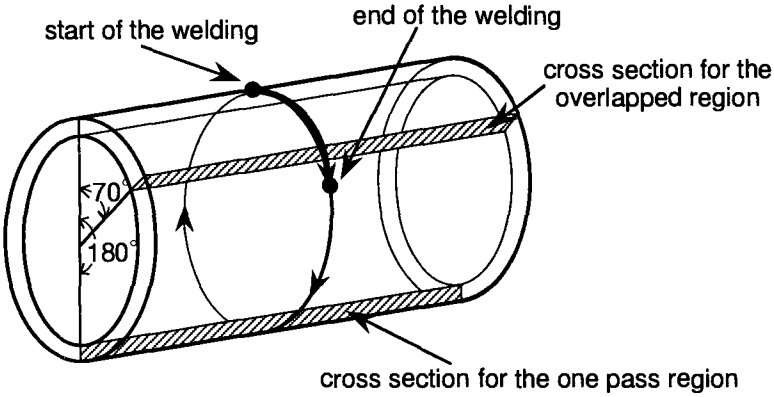
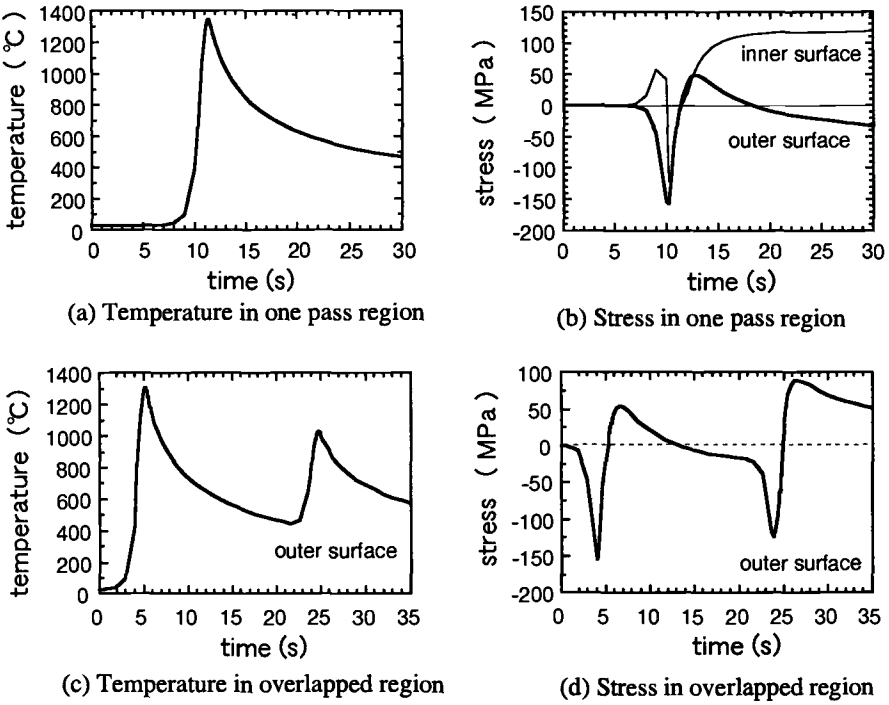


Figure 2- *Schematic of the cross sections to analyze the bead-on-tube welding test.*



(a) Temperature in one pass region

(b) Stress in one pass region

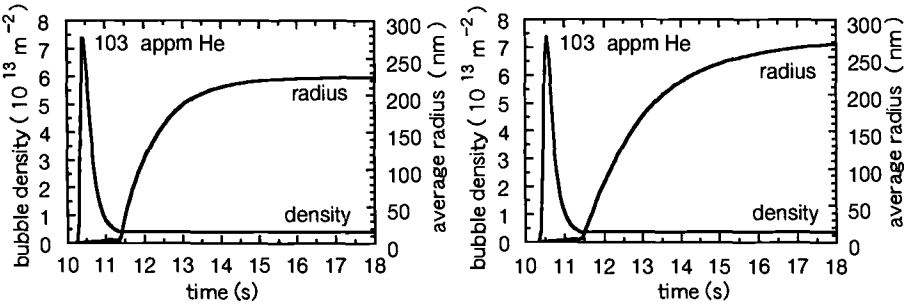
(c) Temperature in overlapped region

(d) Stress in overlapped region

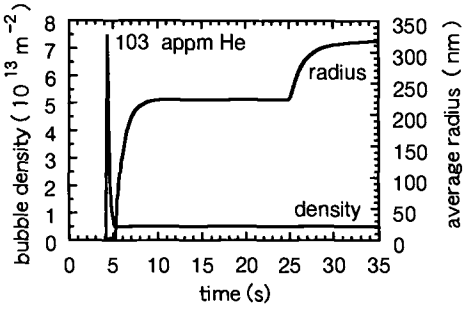
Figure 3- *Temperature and stress changes at points 0.1 mm away from the fusion line during circumferential bead-on-tube welding.*

starts to increase. In early stages of the heatup period, during which temperature is not high enough for the bubble to grow by absorbing sufficient vacancies, more helium atoms flow into the GB than the existing bubbles can absorb. Consequently, nucleation proceeds and bubble density increases rapidly, though coalescence occurs simultaneously. When bubbles become larger due to coalescence and vacancy absorption at higher temperatures late in the heatup period, more helium can be taken into the bubbles, nucleation slows down, and bubble density decreases because coalescence continues to take place. Since larger bubbles migrate more slowly (Eq. 7), coalescence also slows down gradually, and consequently, bubble density becomes constant at the level of 4.1×10^{12} m^{-2} near the end of the heatup period. The average bubble radius still remains below 10 nm at the end of the heatup period, but it starts to increase quickly when tensile stress is generated in the cooling period. Stress-induced bubble growth is dominant at high temperatures, because of the temperature dependent factor D_{gb}/T in the growth rate equation (Eq. 10). At the outer surface in the one pass region, in the 180° cross section, the average radius saturates at ~ 220 nm, due to the decrease in tensile stress and temperature. Since the bubble density, 4.1×10^{12} m^{-2}, corresponds to the average spacing of ~490 nm, this result indicates that GB bubbles remain isolated in this case. At the inner surface, on the other hand, bubbles continue to grow because of higher tensile stress, though the growth rate slows down with the decrease in temperature. In this case, the radius exceeds half of the average spacing, that means adjacent bubbles contact each other during the growth to generate cracks at the GB. At the outer surface in the overlapped region, the 70° cross section, the same behavior as in the one pass region is seen during the first thermal cycle. The radius begins to increase again in the second thermal cycle, and then surpasses a cracking threshold. Bubbles might shrink during the heatup period of the second thermal cycle due to the compressive stress at high temperatures. Actually, Eq. 10 gives a negative growth rate because the gas pressure of the grown bubbles has become quite low. In this calculation, however, the growth rate during this period is set to be 0. Since bubble density and radius measurements are not available for these tests, direct comparison cannot be performed, but the calculated results correspond well to the crack behavior observed in the welding tests.

Figure 5 shows how the GB bubble density depends on the helium content. Temperature and stress changes at the outer surface in the one pass region are used. Two cases, considering and neglecting bubble formation in the matrix, are presented. When neglecting the matrix bubble formation, the GB bubble density increases with helium content with a power of ~2/3. This dependence becomes much weaker, especially in the high helium content region, when matrix bubble formation is considered. Therefore, matrix bubble formation is an important issue even for short term nucleation during welding, as well as the long nucleation in annealing.



(a) Outer surface in one pass region (b) Inner surface in one pass region



(c) Outer surface in overlapped region

Figure 4- *GB bubble density and average radius for circumferential bead-on-tube welding.*

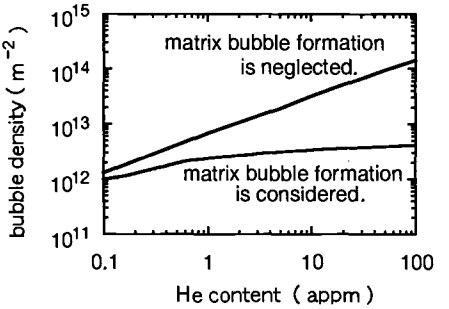


Figure 5- *Helium content dependence of GB bubble density. Temperature and stress at the outer surface in one pass region are used.*

Summary

A model has been presented to calculate the formation of GB helium bubbles during welding. Temperature and stress changes are used to calculate helium diffusion toward the GB, GB bubble nucleation and coalescence, and bubble growth by absorbing thermal vacancies or by tensile stress. Bubble formation in the matrix is also considered in a simplified way. Bubble density and average radius in annealing experiments were calculated to examine the bubble formation under an unstressed condition, and satisfactory agreement with the measurements was obtained. Bead-on-tube welding tests using a neutron irradiated stainless steel was analyzed, and a good correlation was confirmed between the bubble calculations and crack behavior observed in the welding test.

References

[1] Kanne, Jr., W. R., *Welding Journal*, Vol. 67, August 1988, pp.33-39.

[2] Lin, H. T., Grossbeck, M. L. and Chin, B. A., *Metallurgical Transactions*, Vol. 21A, 1990, pp. 2585-2596.

[3] Goods, S. H. and Yang, N. Y. C., *Metallurgical Transactions*, Vol. 23A, 1992, pp. 1021-1032.

[4] Franco-Ferreira, E. A. and Kanne, Jr., W. R., *Welding Journal*, Vol. 43, 1992 February, pp. 43-51.

[5] Wang, C. A., Grossbeck, M. L. and Chin, B. A., *Effects of Radiation on Materials: 16th International Symposium, ASTM STP 1175*, A. S. Kumar et al. Eds., American Society for Testing and Materials, Philadelphia, PA, 1993, pp. 779-788.

[6] Wang, C. A., Grossbeck, M. L. and Chin, B. A., *Journal of Nuclear Materials*, Vol. 225, 1995, pp. 59-68.

[7] Kanne, Jr., W. R., Chandler, G. T., Nelson, D. Z., and Franco-Ferreira, E. A., *Journal of Nuclear Materials*, Vol. 225, 1995, pp. 69-75.

[8] Watanabe, K., Jitsukawa, S., Hamada, S., Kodaira, T., and Hishinuma, A., *Fusion Engineering and Design*, Vol. 31, 1996, pp. 9-15.

[9] Asano, K., Nishimura, S., Saito, Y., Sakamoto, H., Yamada, Y., Kato, T., and Hashimoto, T., *Journal of Nuclear Materials*, Vol. 264, 1999, pp. 1-9.

[10] Nishimura, S., Katsura, R., Saito, Y., Kono, W, Takahashi, H., Koshiishi, M., Kato, T., and Asano, K., *Journal of Nuclear Materials*, Vol. 258-263, 1998, pp. 2002-2007.

[11] Asano, K., Katsura, R. Kawano, S., and Koshiishi, M., *Effects of Radiation on Materials: 19th International Symposium, ASTM STP 1366*, M. L. Hamilton et al. Eds., American Society for Testing and Materials, Philadelphia, PA, 1999.

[12] Brearley, I. R. and MacInnes, D. A., *Journal of Nuclear Materials*, Vol. 95, 1980, pp. 239-252.

[13] Gruber, E. E., *Journal of Applied Physics*, Vol. 38, 1967, pp. 243-250.

[14] Hull, D. and Rimmer, D. E., *Philosophical Magazine*, Vol. 4, 1959, pp. 673-687.

[15] Schilling, W., *Point Defects and Defect Interactions in Metals: Proceedings of Yamada Conference V*, , J. Takamura et al. Eds., University of Tokyo Press, 1982, pp. 303-308.

[16] Hashimoto, T., manuscript in preparation.

Kunihiko Tsuchiya,[1] Masaru Nakamichi,[1] and Hiroshi Kawamura[1]

Effect of Neutron Irradiation on Mechanical Properties of Cu-Alloy/SS316 Joints

Reference : Tsuchiya, K., Nakamichi, M., and Kawamura, H., **"Effect of Neutron Irradiation on Mechanical Properties of Cu-Alloy/SS316 Joints,"** *Effects of Radiation on Materials: 19th International Symposium, ASTM STP 1366,* M. L. Hamilton, A. S. Kumar, S. T. Rosinski, and M. L. Grossbeck, Eds., American Society for Testing and Materials, West Conshohocken, PA, 2000.

Abstract : The effects of neutron irradiation on tensile properties of the Cu alloys to type 316 stainless steel (SS316) joints fabricated by friction welding method were examined. Additionally, irradiation tests of Al_2O_3-dispersed copper alloy (Al-15), oxygen free copper (OF-Cu) and SS316 were conducted. The Al-15/SS316 and OF-Cu/SS316 joints were irradiated in the Japan Materials Testing Reactor (JMTR), and tension tests and metallographical observation of these joints have been performed as the post irradiation examination (PIE). In the tension tests of Al-15/SS316 and OF-Cu/SS316 joints, all irradiated specimens fractured at the copper sides. In the tension tests at 293K, tensile strength of the Al-15/SS316 joints irradiated at 693K was equal to that of the base metal (Al-15) irradiated in the same condition. On the other hand, tensile strength of Al-15/SS316 joints was smaller than that of Al-15 in the tension tests at the same temperature as each irradiation temperature. In this study, useful data of the irradiated Al-15/SS316 and OF-Cu/SS316 joints fabricated by friction welding method were obtained to design fusion reactors.

Keywords : fusion reactor, heat sink material, Al_2O_3-dispersed copper alloy, oxygen free copper, friction welding method, neutron irradiation, PIE

[1] Research engineer, research engineer and principal scientist, respectively, Blanket Irradiation and Analysis Laboratory, Oarai Research Establishment, Japan Atomic Energy Research Institute, Narita-cho, Oarai-machi, Higashi-Ibaraki-gun, Ibaraki-ken 311-1394, Japan.

Copyright© 2000 by ASTM International www.astm.org

Copper-based alloys have been considered as possible candidate materials for first wall, limiter and divertor for fusion reactors [*1-2*]. Particularly, Al_2O_3-dispersed copper alloys are attractive candidates and exhibit the best combination of swelling resistance, retention of strength, and electrical conductivity of any copper alloy [*3-4*]. The deformation resistance of Al_2O_3-dispersed copper alloys is higher than that of oxygen free copper (OF-Cu) and zirconium copper alloys. Therefore, the change in the yield strength of Al_2O_3-dispersed copper alloys due to high temperature exposure is minimal in comparison with those of OF-Cu and zirconium copper alloys [*5*].

Recently, development of joining technology for Al_2O_3-dispersed copper alloy and type 316 austenitic stainless steel (SS316) has been investigated for diffusion bonding, brazing, roll bonding, explosive bonding, and hot isostatic pressing (HIP) [*6-7*]. On the other hand, friction welding is one of the most popular welding method for tube joint of different materials [*8-9*]. This welding method has been applied to joints of Al_2O_3-dispersed copper alloy to SS316 [*10*].

In the present study, joint of Al_2O_3-dispersed copper alloy to SS316 and OF-Cu to SS316 was examined by friction welding method. The mechanical properties on these Cu-alloy/SS316 joints and the base metals were evaluated after neutron irradiation.

Experimental Method

Materials and Condition of Friction Welding

Al_2O_3-dispersed copper, Al-15 with alumina contents of ~0.30 wt%, was used in this study. This copper alloy was fabricated by OMG Americas, formerly SCM Metal Products. Oxygen free copper (OF-Cu) manufactured by Daido Steel Co. Ltd. was prepared as well. The chemical compositions and mechanical properties of Al-15 and OF-Cu are shown in Table 1. The dimension of Al-15 and OF-Cu rods used for friction welding was ϕ25mm×82mm.

The chemical composition and mechanical properties of SS316 are shown in Table 2. The dimension of SS316 rod used for friction welding was ϕ25mm×152mm.

A brake-typed friction welding machine was employed throughout. Therefore, the welding conditions, i.e. friction pressure, friction time, upset pressure and upset time, were decided by preliminary fabrication tests since these conditions influence mechanical properties of the joints. The burr of the joints produced during welding was removed by the lathe. These joints were examined by liquid penetrant test and macro-defects of joint interface were detected. As the main result of preliminary fabrication tests, cracks in joint interface were observed on Al-15/SS316 joints when the upset pressure was more than 160 MPa. On the other hand, tension test was carried out at room temperature using specimens satisfying the liquid penetrant test. Maximum

Table 1—*Chemical Compositions and Mechanical Properties of Al-15 and OF-Cu*

Material	Chemical composition (%)				Mechanical properties	
	Cu	Al_2O_3	Fe	Ni	T.S.[1] (MPa)	Hardness (H_v)
OF-Cu	99.99	-	-	-	294	74.3
Al-15	Bal.	0.27	0.01	0.01	393	111

[1] Tensile strength at room temperature

Table 2—*Chemical Composition and Mechanical Properties of SS316*

Material	Chemical composition (%)				Mechanical properties	
	Fe Mo	Cr Si	Ni Cu	Mn Co	T.S.[1] (MPa)	Hardness (H_{RB})
SS316	Bal. 2.50	17.60 0.63	12.37 0.02	1.60 0.02	562	74.5

[1] Tensile strength at room temperature

Table 3—*Conditions of Friction Welding for Al-15/SS316 and OF-Cu/SS316 Joints*

Joints	Friction pressure (MPa)	Upset pressure (MPa)	Friction time (s)	Upset time (s)
OF-Cu/SS316	49.0	147	0.5	7
Al-15/SS316	73.5	147	0.5	7

Rotating Speed : 2000rpm

rupture strength of 435 MPa was obtained when the friction and upset pressures were 49 MPa and 147 MPa, respectively. From the results, the optimum conditions of friction welding were obtained for each material as shown in Table 3.

Neutron Irradiation and Post Irradiation Examination (PIE)

The specimens for neutron irradiation tests were made of Al-15/SS316 and OF-Cu/SS316 joints fabricated in each optimum condition. The shape of irradiation test specimens (tension test) is shown in Figure 1. Neutron irradiation of these joints has been carried out in the Japan Materials Testing Reactor (JMTR). Additionally, neutron irradiation of the base metals, i.e. Al-15, OF-Cu and SS316 has been also carried out in the same condition. The fast neutron fluence (>1MeV) was between 6.5×10^{20} and 1.0×10^{21} n/cm^2 which corresponds to a displacement damage rate of 0.9-1.5 dpa, and the irradiation temperatures were 563K, 598K, 693K and 773K. The irradiation condition of specimens is shown in Table 4. After neutron irradiation, tension tests and metallographical observations of the Al-15/SS316 and OF-Cu/SS316 joints have been

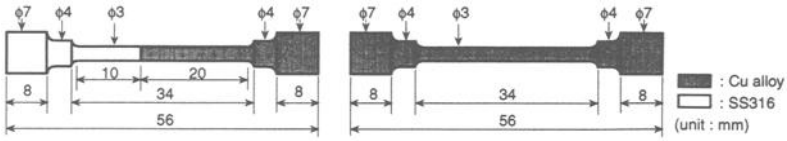


Figure 1—*Shape of Irradiation Test Specimens (tension test)*

Table 4—*Irradiation Condition of Specimens*

Irr. Temperature (E>1MeV) (K)	Materials	Neutron Fluence (N/cm^2)
563	Al-15/SS316	1.0×10^{21}
	Al-15	9.4×10^{20}
	SS316	1.0×10^{21}
598	Al-15/SS316	8.1×10^{20}
	OF-Cu/SS316	6.5×10^{20}
	Al-15	6.5×10^{20}
	OF-Cu	6.5×10^{20}
	SS316	6.5×10^{20}
693	Al-15/SS316	9.7×10^{20}
	OF-Cu/SS316	9.3×10^{20}
	Al-15	9.3×10^{20}
	OF-Cu	9.3×10^{20}
	SS316	9.3×10^{20}
773	Al-15/SS316	9.3×10^{20}
	OF-Cu/SS316	9.4×10^{20}
	Al-15	9.4×10^{20}
	OF-Cu	9.4×10^{20}
	SS316	9.4×10^{20}

performed. The tension tests were carried out in vacuum at 293K and at the same temperature as each irradiation temperature. A crosshead speed was 0.1 mm/min before the elastic region, and was 1 mm/min past this region. The fracture surfaces were observed by a scanning electron microscopy (SEM) after the tension tests.

Experimental Results

Characterization of Al-15/SS316 and OF-Cu/SS316 Joints without Neutron Irradiation

The tension tests were carried out at room temperature. OF-Cu/SS316 joints by friction welding fractured at the part of base metal (OF-Cu). The tensile strength of OF-Cu/SS316 joint was 242 MPa and was similar to the strength of OF-Cu. On the other

hand, the tensile strength of Al-15/SS316 joint was 423 MPa. Though Al-15/SS316 joint fractured at the part of base metal (Al-15), the tensile strength was smaller than that of base metal.

Hardness of the cross section of Al-15/SS316 and OF-Cu/SS316 joints was measured at the center (Line B) and at the point 7 mm (Line A) apart from the center. Hardness distributions in Al-15/SS316 and OF-Cu/SS316 joints are shown in Figure 2. In Figure 2, hardness of Al-15 was lower than that of base metal in the vicinity of the joint interface and increased gradually with the distance from the joint interface to 500 μm. Beyond 500 μm, hardness of Al-15 was constant and equal to that of base metal. It can be considered that there is a significant effect of heat generated during friction welding. Hardness of OF-Cu near the interface was higher than that of base metal and decreased gradually with the distance from the joint interface to 200 μm. Hardness of SS316 was always constant and equal to that of base metal (SS316). In Line B of Figure 2, hardness of Al-15 and OF-Cu was constant and equal to that of each base metal. Hardness of SS316 was higher than that of base metal in the vicinity of the joint interface and this hardness decreased with the distance from joint interface to 200 μm. Beyond 200 μm, hardness of SS316 was constant and equal to that of base metal.

Qualitative analysis with EPMA was carried out for the observation of element

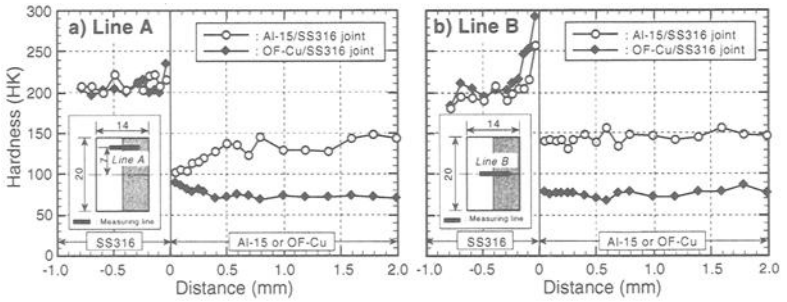


Figure 2—*Hardness Distribution across Cu-Alloy/SS316 Joints*

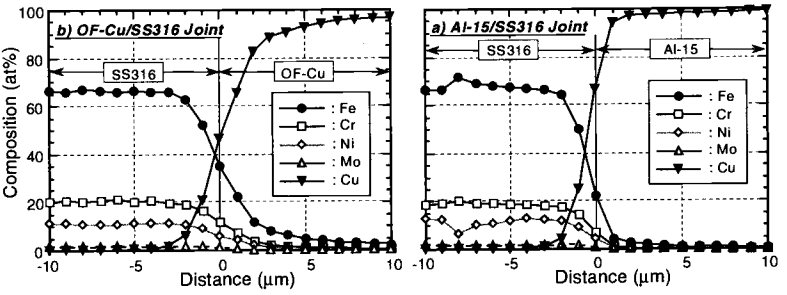


Figure 3—*Line Profiles of Fe, Cr, Ni, Mo and Cu on Cu-Alloy/SS316 Joints*

distribution in the vicinity of Al-15/SS316 and OF-Cu joints. Line profiles of Fe, Cr, Ni, Mo and Cu on Al-15/SS316 and OF-Cu/SS316 joints are shown in Figure 3. In Figure 3, the intermetallic layer of Al-15/SS316 joints was about 5 μm thick. The composition of each element changed at the joints interface, and the layer of an intermetallic compound was very narrow at Al-15/SS316 joints. On the other hand, the intermetallic layer of OF-Cu/SS316 joints was about 12 μm thick. The composition of each element was changed in the vicinity of the joint except with Fe and Cu. The compositions of Fe and Cu changed gradually in OF-Cu side, respectively.

Characterization of Al-15/SS316 and OF-Cu/SS316 Joints with Neutron Irradiation

Tension tests of Al-15/SS316 joints, OF-Cu/SS316 joints, Al-15, OF-Cu and SS316 were carried out at room temperature (293K) and at the same temperature as each irradiation temperature. Results of tension tests are shown in Table 5. In the tension tests of Al-15/SS316 and OF-Cu/SS316 joints, all irradiated joints fractured at copper alloy side.

In the results of tension tests at the same temperature as each irradiation temperature (high temperature tests), the irradiated OF-Cu/SS316 joints fractured at OF-Cu side, and tensile strength of OF-Cu/SS316 joint was similar to those of OF-Cu at each temperature. Tensile strength of OF-Cu/SS316 joint was less than 100 MPa at the same temperature as each irradiation temperature and decreased with increasing temperature. Reduction of OF-Cu/SS316 joint and OF-Cu was almost constant with temperature.

In the results of tension tests at 293K, the tensile properties of OF-Cu except on reduction were almost constant. Yield strength and tensile strength were 69±14 MPa and 206±4 MPa, respectively. These values were smaller than those of the un-irradiated OF-Cu. From these results, it is considered that no effect of neutron irradiation on mechanical properties appeared and the annealing affected the change of mechanical properties of the irradiated OF-Cu. In the high temperature tests, tensile strength and yield strength of irradiated OF-Cu decreased with increasing temperature.

In the results of tension tests at the same temperature as each irradiation temperature (high temperature tests), tensile strength of Al-15/SS316 joints was smaller than that of Al-15 at each temperature. The fracture occurred on the Al-15 side before 5 mm from joint interface. Tensile strength of Al-15/SS316 joints decreased with increasing temperature and was softened at each temperature. For example, tensile strength of the Al-15/SS316 joints irradiated at 693K was 76 MPa. Reduction of area was smaller than that of Al-15. In the high temperature tests, tensile strength decreased with increasing temperature.

Yield strength and tensile strength of Al-15 decreased with increasing irradiation temperature in the tensile tests at 293K. Reduction of area of Al-15 were almost

Table 5—*Results of Tension Tests on Al-15/SS316 and OF-Cu/SS316 Joints after Neutron Irradiation*

Material	Irr. Temp. (K)	Test Temp. (K)	Y.S. [1] (MPa)	T.S. [2] (MPa)	El. [3] (%)	Re. [4] (%)
OF-Cu/SS316	598	598	—	98	—	13.2
	693	693	—	76	—	12.9
	773	293	—	211	—	52.6
		773	—	58	—	14.2
OF-Cu	598	293	75	206	72.0	76.3
		598	54	100	15.0	10.9
	693	293	53	202	73.0	60.0
		693	36	70	13.5	8.5
	773	293	78	210	78.0	90.1
		773	37	60	17.0	11.6
Al-15/SS316	563	293	—	446	—	14.7
		563	—	185	—	4.9
	598	293	—	382	—	34.5
		598	—	137	—	7.9
	693	293	—	395	—	17.3
		693	—	76	—	11.0
	773	293	—	383	—	13.7
		773	—	46	—	4.4
Al-15	563	293	462	476	7.5	56.4
		563	237	255	14.0	57.1
	598	293	382	426	14.5	56.2
		598	176	214	17.5	14.7
	693	293	341	408	23.5	54.5
		693	124	153	20.0	21.2
	773	293	334	400	20.5	66.6
		773	95	119	17.0	14.7
SS316	563	293	728	796	41.0	63.1
		563	561	610	23.0	56.9
	598	293	556	741	35.5	64.7
		598	336	541	34.5	69.6
	693	293	359	648	86.0	87.6
		693	239	488	53.0	68.8
	773	293	314	616	81.0	81.1
		773	232	469	47.5	62.7

[1] Yield Strength, [2] Tensile Strength, [3] Elongation, [4] Reduction

constant with irradiation temperature. In the high temperature tests, yield strength and tensile strength decreased with increasing temperature. However, elongation increased with increasing temperature.

The SEM micrographs of the fracture surfaces of irradiated OF-Cu, OF-Cu/SS316 joint, Al-15 and Al-15/SS316 joint after tension tests are shown in Figure 4. Fracture surface of OF-Cu/SS316 joint was similar to that of OF-Cu. The specimens irradiated at 595K or higher exhibited both intergranular fracture and transgranular fracture over the entire cross section. On the other hand, fracture surfaces of Al-15/SS316 joint and Al-15 differed from each other. Fracture surface of Al-15 exhibited transgranular fracture, but large necking was observed. However, fracture surface of Al-15/SS316 joint was more brittle and exhibited dimpled transgranular fracture.

Discussion

Both pure copper and Al_2O_3-dispersed copper alloy are significantly hardened by neutron irradiation at low temperature. A large amount of radiation hardening observed at irradiation temperatures below 443K is known to be due to small defect clusters. Additionally, neutron spectrum affects yield strength of copper at low temperature. However, tensile strength of these copper alloys became comparable or inferior to

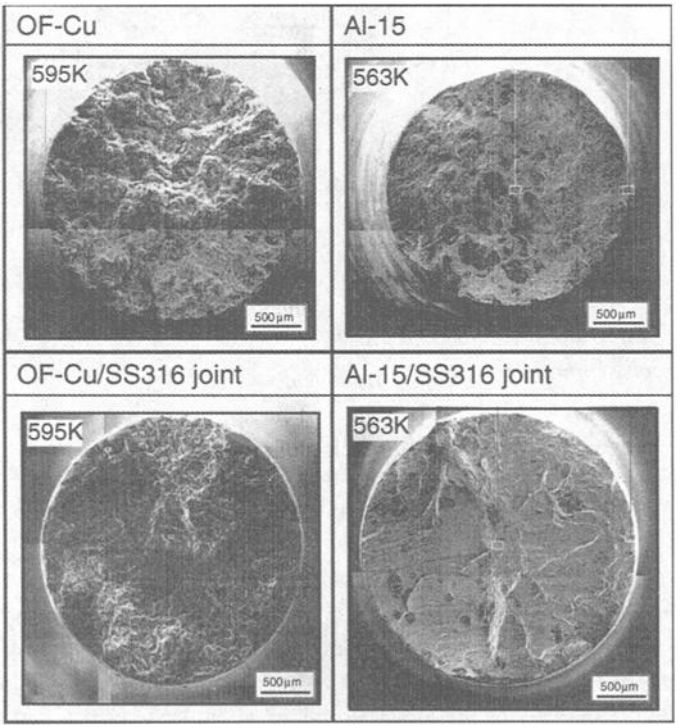


Figure 4 — *SEM Micrographs of the Fracture Surfaces of Irradiated OF-Cu, OF-Cu/SS316 Joint, Al-15 and Al-15/SS316 Joint after Tension Tests.*

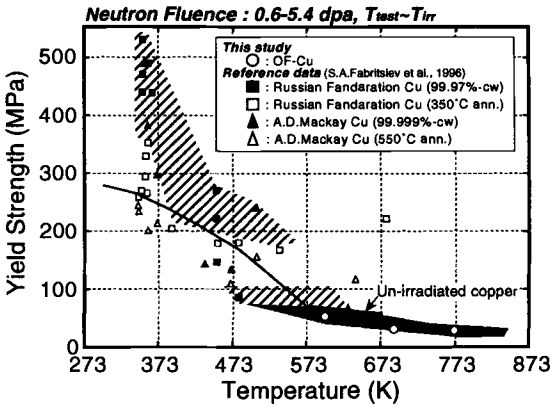


Figure 5 — *Effect of Irradiation Temperature on the Yield Strength of Pure Coppers*

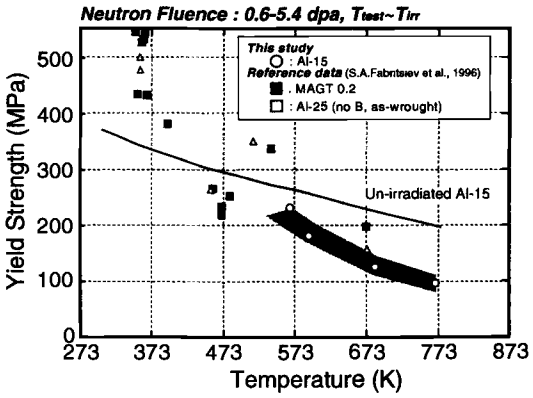


Figure 6—*Effect of Irradiation Temperature on the Yield Strength of Al_2O_3-dispersed Copper Alloys*

un-irradiated values for the irradiation temperature above 473K. Irradiation of copper alloys at temperatures above ~443K produces rapid decrease in defect cluster density with increasing temperature, and the hardening and embrittlement effects become small [*11-12*].

Effect of irradiation temperature on the yield strength of pure copper is shown in Figure 5. In the results of tension tests at the same temperature as each irradiation temperature, no effect of neutron irradiation on yield strength appeared and the annealing affected the change of yield strength of OF-Cu. As to OF-Cu/SS316 joints, the mechanical properties of the joints also show a similar tendency and no effect of neutron irradiation. The tensile properties of irradiated OF-Cu/SS316 joints will be

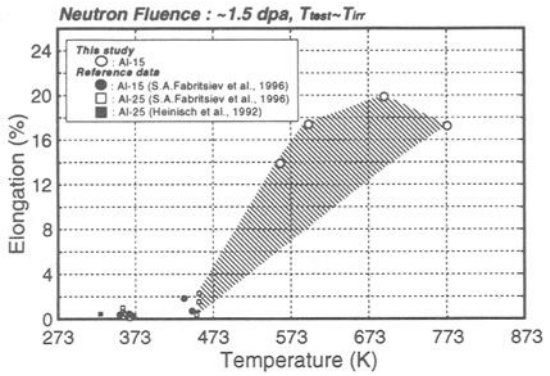


Figure 7—*Effect of Irradiation Temperature on the Elongation of Al_2O_3-dispersed Copper Alloys*

predicted from these results though tensile properties of these joints should be obtained at low irradiation temperatures.

The effect of irradiation temperature on the yield strength of Al_2O_3-dispersed copper alloy is shown in Figure 6. Effect of irradiation temperature on the elongation of Al_2O_3-dispersed copper alloy is also shown in Figure 7. From Figure 6, yield strength of irradiated Al-15 was inferior to that of un-irradiated Al-15. Elongation of irradiated Al-15 was larger than the un-irradiated values and was similar to that of irradiated OF-Cu. The neutron irradiation and/or annealing affected yield strength of Al-15. However, metallographic structure of irradiated Al-15 was similar to that of un-irradiated Al-15. As observed by Edwards et al. [*13*], several α-Al_2O_3 inclusions were present inside the dimples in the un-irradiated Al_2O_3-dispersed copper alloys, but they were no longer visible after irradiation. This microstructural evoluation will change mechanical properties. As to Al-15/SS316 joint, the tensile strength of Al-15/SS316 joints was smaller than that of Al-15 at the same temperature as each irradiation temperature. It seems that welding temperature also affected the change of tensile strength. Therefore, mechanical properties of irradiated Al-15/SS316 joints could not be estimated only from the results of the irradiated Al-15.

Mechanical properties including fatigue properties of copper alloys to austenitic stainless steel joints should be obtained at low irradiation temperature.

Conclusion

The friction welding technique of different materials has been developed, and tensile properties of friction welded OF-Cu/SS316 and Al-15/SS316 have been investigated with neutron irradiation.

1) The optimum conditions for friction welding of OF-Cu/SS316 and Al-15/SS316 joints were obtained and characteristics of their joints were evaluated without neutron irradiation. Especially, OF-Cu/SS316 and Al-15/SS316 joints fractured at each base metal (copper side). The composition of each element was changed at the joints interface and the layer of an intermetallic compound was very narrow at joints.
2) The irradiated OF-Cu/SS316 joints fractured at OF-Cu side, and tensile properties of OF-Cu/SS316 joint were similar to those of OF-Cu at each irradiation temperature. No effect of neutron irradiation on tensile properties appeared and the annealing affected the change of tensile properties of OF-Cu/SS316 joint and OF-Cu. Fracture surface of OF-Cu/SS316 joint was similar to that of OF-Cu and these irradiated joints exhibited both intergranular fracture and transgranular fracture over the entire cross section.
3) In the results of tensile tests at the same temperature as each irradiation temperature, the irradiated Al-15/SS316 joints fractured at the Al-15 side, but tensile strength of Al-15/SS316 joints was smaller than that of Al-15 at each irradiation temperature. Fracture surface of Al-15/SS316 joints was more brittle and exhibited dimpled transgranular fracture.

From these results, tensile properties of OF-Cu/SS316 and Al-15/SS316 joints irradiated at high irradiation temperature were obtained. In the future, irradiation tests below 523K will be performed with these joints for the application of cooling tubes of fusion blanket.

Acknowledgments

We would like to acknowledge the support of the hot laboratory staffs of the JMTR for the post irradiation examinations (PIEs).

REFERENCES

[1] Harling, O. K., Yu, G. P., Grant, N. J., and Meyer, J.E., "Application of High Strength Copper Alloys for a Fusion Reactor First Wall," *Journal of Nuclear Materials*, 103&104, 1981, pp. 127-132.

[2] Butterworth, G. J., "Transmutation and Activation Effects in High-Conductivity Copper Alloys Exposed to a First Wall Fusion Neutron Flux," *Journal of Nuclear Materials*, 135, 1985, pp. 160-172.

[3] Grant, N.J., Harling, O.K., Kohse, G., Megusar, J., and Lee, T., "The Potential for Iron and Copper Based Rapidly Solidified Alloys as Fusion Reactor Materials," *Journal of Nuclear Materials*, 141&143, 1986, pp. 427-433.

[4] Livak, R. J., Frost, H.M., Zocco, T. G., Kennedy, J. C., and Hobbs, L. W., "Promising Copper Alloys for High Heat Load Applications in Neutron Environments," *Journal of Nuclear Materials*, 141&143, 1986, pp. 160-162.

[5] Butterworth, G. J., and Forty, C. B. A., "A Survey of the Properties of Copper Alloys for Use as Fusion Reactor Materials," *Journal of Nuclear Materials*, 189, 1992, pp.237-276.

[6] Nishi, H., Muto, Y., and Araki, T., "Tests of Solid State Diffusion Bonding of Alumina Dispersion Strengthened Copper to 316 Stainless Steel," NGEGAL, vol.36, 1994, pp. 432.

[7] Nishi, H., and Araki, T., "Low Cycle Fatigue Strength of Diffusion Bonded Joints of Alumina Dispersion Strengthened Copper to 316 Stainless Steel," JAERI-Research 94-035, 1994.

[8] Kikuchi, T., and Kawamura, H., "Development of Niobium Alloy/Stainless Steel Joints by Friction Welding (1)," JAERI-M 88-150, 1988.

[9] Tsuchiya, K., Kawamura, H., and Kikuchi, T., "Characterization of Nb-1%Zr/SS304 Joints Fabricated by friction Welding," *Interface Science and Materials Interconnection*, Proceedings of JIMIS-8, the Japan Institute of Metals, 1996, pp. 455-458.

[10] Tsuchiya, K., Kawamura, H., and Saito, M., "Mechanical Properties of Al_2O_3-dispersed Copper and SS316 Joints Fabricated by Friction Welding," *Fusion Technology*, 1994, pp. 447-450.

[11] Zinkle, S. J., Horsewell, A., Singh, B. N., and Sommer, W. F., "Defect Microstructure in Copper Alloys Irradiated with 750 MeV Proton," *Journal of Nuclear Materials*, 212&215, 1994, pp. 132-138.

[12] Fabritsiev, S. A., Pokrovsky, A. S., Zinkle, S. J., and Edwards, D. J., "Low-temperature Radiation Embrittlement of Copper Alloys," *Journal of Nuclear Materials*, 233&237, 1996, pp. 513-518.

[13] Edwards, D. J., Garner, F. A., Newkirk, J. W., and Nadkarni, A., "Neutron-induced Microstructural Alteration of GlidCop^{TM} Alloys at ~415°C and High Neutron Exposure," *Journal of Nuclear Materials*, 212&215, 1994, pp. 1313-1317.

Experimental Techniques and Facilities

M. L. Hamilton,[1] F. A. Garner,[1] G. L. Hankin,[2] R. G. Faulkner,[2] and M. B. Toloczko[3]

Neutron-Induced Evolution of Mechanical Properties of 20% Cold-Worked 316 Stainless Steel as Observed in Both Miniature Tensile and TEM Shear Punch Specimens

Reference: Hamilton, M. L., Garner, F. A., Hankin, G. L., Faulkner, R. G., and Toloczko, M. B., **"Neutron-Induced Evolution of Mechanical Properties of 20% Cold-Worked 316 Stainless Steel as Observed in Both Miniature Tensile and TEM Shear Punch Specimens,"** *Effects of Radiation on Materials: 19th International Symposium, ASTM STP 1366,* M. L. Hamilton, A. S. Kumar, S. T. Rosinski, and M. L. Grossbeck, Eds., American Society for Testing and Materials, West Conshohocken, PA, 2000.

Abstract: Three heats of 20% cold worked 316 stainless steel were irradiated in the Materials Open Test Assembly of the Fast Flux Test Facility producing data at three or four irradiation increments to doses ranging from 12 to 88 dpa. There were five irradiation temperatures ranging from 400 to 730°C. The specimens were in two forms, standard TEM microscopy disks and miniature tensile specimens, irradiated side by side. The tensile specimens were tested at room temperature, and the TEM disks were subjected to a shear punch test, also at room temperature. Both methods yielded very similar results, showing that the mechanical properties of these steels quickly approached and then maintained saturation levels of yield strength. The saturation levels were only slightly dependent on heat identity, but were strongly dependent on irradiation temperature. Ductility decreased with increasing exposure, however.

It was shown that the tensile and shear punch data can be well-correlated with simple expressions that reflect the differences in stress state and physical constraints of the two techniques. This allows the application of the shear punch technique to situations where steep neutron flux or gamma heating gradients, insufficient irradiated material or insufficient reactor volume prevent the use of even small tensile specimens.

Keywords: 316 stainless steel, neutron irradiation, tensile properties, shear punch

[1]Senior Scientist, Senior Staff Scientist, respectively, Pacific Northwest National Laboratory, Richland, WA 99352, USA.

[2]Graduate Student, Professor, respectively, I.P.T.M.E., Loughborough University, Leicestershire, LE11 3UT, UK.

[3]Washington State University, Pullman, WA 99163, USA.

Copyright© 2000 by ASTM International www.astm.org

Introduction

The generation of material response data in irradiation environments is often complicated by steep flux gradients, the lack of sufficiently large irradiation volumes in test reactors, the high levels of induced radioactivity, and also by the large gamma heating rates found in some reactor types. This problem has led to the development of miniature specimen test techniques and also to the generation of property-property correlations, where some properties of engineering relevance are predicted from other types of more easily obtained property data. Several symposia have been held to address this rapidly developing technological area [*1-4*].

While many property-property correlations and size effects studies have been conducted on unirradiated materials, the real challenge lies in the validation and application of these techniques using irradiated materials. Two test types currently receiving attention at this laboratory are the "minitensile" specimen test and the shear punch test, with the latter conducted on 3 mm diameter transmission electron microscopy (TEM) disks.

The very small minitensile specimens and the horizontal test frame used in these studies are shown in Figures 1 and 2. These very small specimens have been employed previously in a wide variety of studies on irradiated materials as summarized in ref. 5. With careful preparation of these small specimens valid results can be obtained [*6*].

The use of even smaller (3 mm diameter by 0.25 mm thickness) microscopy disks in shear punch tests was initially used to study unirradiated materials [*7-11*], but recently the emphasis has shifted to irradiated materials [*12-14*]. Of particular current importance is the development of correlations between tensile and shear punch data to allow valid estimates of tensile properties when only microscopy disks are available. An example of such an application is the recent study of the influence of both helium production levels and nickel content on the radiation-induced behavior of ferritic alloys [*15*]. Other studies involving light water reactor specimens and spallation neutron specimens are also in progress.

The successful development of tensile-shear punch correlations for irradiated materials requires that both types of specimens be irradiated side-by-side to avoid the inevitable differences in reactor history that occur in the absence of specimen proximity. Also important for correlation development is that a wide range of irradiation-produced microstructures be tested in a given study. In the materials discussed in this paper, these conditions are well met.

Experimental Details

Three different heats (designated Al, A61, CN13) of 20% cold-worked 316 stainless steel were irradiated in Fast Flux Test Facility (FFTF) at five temperatures between 400 and 730°C to doses ranging from 12 to 88 dpa. The compositions of these heats are shown in Table 1. The miniature tensile and microscopy disks were irradiated side-by-side in perforated stainless steel subcapsules in contact with flowing sodium in

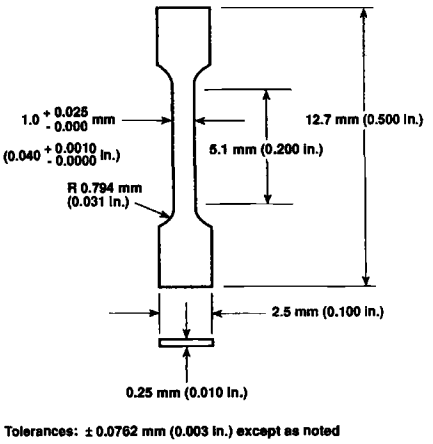


Figure 1 - *Dimensions of the miniature tension specimen.*

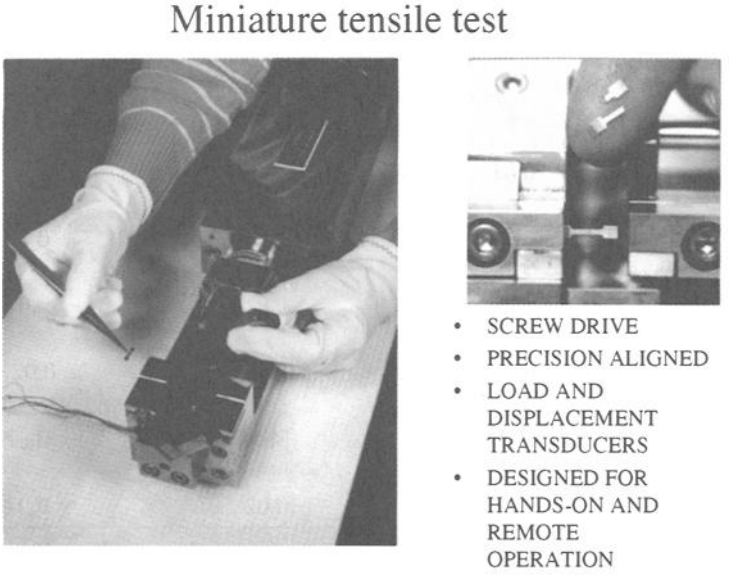


Figure 2 - *Horizontal test frame and miniature tension specimens employed in this study.*

Table 1 - *Composition (wt.%) of Three Heats of Steel Used in this Study*

	A1[1]	A61[1]	CN13[2]
Carbon	0.05	0.02	0.04
Manganese	1.99	1.77	1.38
Silicon	0.62	0.38	0.69
Phosphorus	0.016	0.017	0.020
Sulfur	0.018	0.019	0.024
Chromium	15.73	15.75	15.26
Nickel	13.77	13.60	12.48
Molybdenum	2.45	2.49	2.05
Cobalt	0.07	0.07	0.01
Titanium	0.012	0.010	0.002
Niobium	0.02	0.02	0.01
Tantalum	0.01	0.01	0.01
Aluminum	0.032	0.034	0.023
Iron	Base	Base	Base
Copper	0.02	0.02	0.02

(1) 40% CW +1150°C/15 min +20% CW
(2) 40% CW +1030°C/30 min +20% CW

the Materials Open Test Assembly (MOTA), with active temperature control within any one irradiation segment to ±5°C. The target temperature sometimes varied a little (≤10°C) from irradiation segment to segment, however.

The mechanical test techniques are described in refs. 5 and 13. All tests were conducted at room temperature. In addition, specimens of another heat of unirradiated AISI 316 with four cold-work levels between 0 and 75% were tested using both techniques. Density change measurements were performed on a selected set of microscopy specimens prior to testing to ascertain how much void swelling had occurred.

Results

Figure 3 shows typical stress-strain curves for the tensile specimens, showing that irradiation at lower temperatures and higher dpa levels increases the yield strength and reduces the ductility of the steel. The yield strength of the steel was found to saturate after 10-20 dpa at a level that is a strong function of irradiation temperature, as shown in Figure 4. Both the starting yield strength and saturation yield strengths were dependent on the heat identity, however. Note that the alloy softened during irradiation at temperatures above 471°C.

As shown in Figure 5, the effective shear yield strengths exhibited all of the same features although numerically the effective shear yield strengths were roughly a factor of two lower, resulting from the difference in stress state of the two specimen types. Note in Figure 6 that the specimens covered a wide range (<0 to 8%) of swelling levels. Figure 7 presents the results of mechanical tests on the unirradiated specimens.

As can be seen in Figure 8, the tensile-shear punch correlations derived for yield and ultimate strength are exceptionally good, with either correlation represented by a straight line fit to all data regardless of heat identity, irradiation condition and associated microstructure, or even the presence or absence of irradiation.

A similar correlation for uniform elongation is shown in Figure 9 for both AISI 316 and another experimental series discussed in the next section. Each correlation is linear but with an offset in shear strength designated by τ_o, determined by a least square fitting analysis. Such offsets appear to be a very general feature of the shear punch test, but vary with the material [*12-14*]. The origin of the offset is now under investigation.

It is important to note that τ_o could be determined only from the unirradiated material at various cold-work levels. This is particularly useful when TEM disks in the irradiated condition are available, but tensile specimens are not available in the irradiated condition.

Discussion and Conclusions

The tendency of the yield strength of AISI 316 to reach a saturation state dependent on the irradiation temperature is consistent with the behavior observed in larger specimens of 20% cold worked AISI 316 irradiated in the EBR-II fast reactor [*16*]. It is not surprising that the shear yield stress also follows the same behavior.

The slope of 2.0, while close to the least-squares fit, is not necessarily the "best

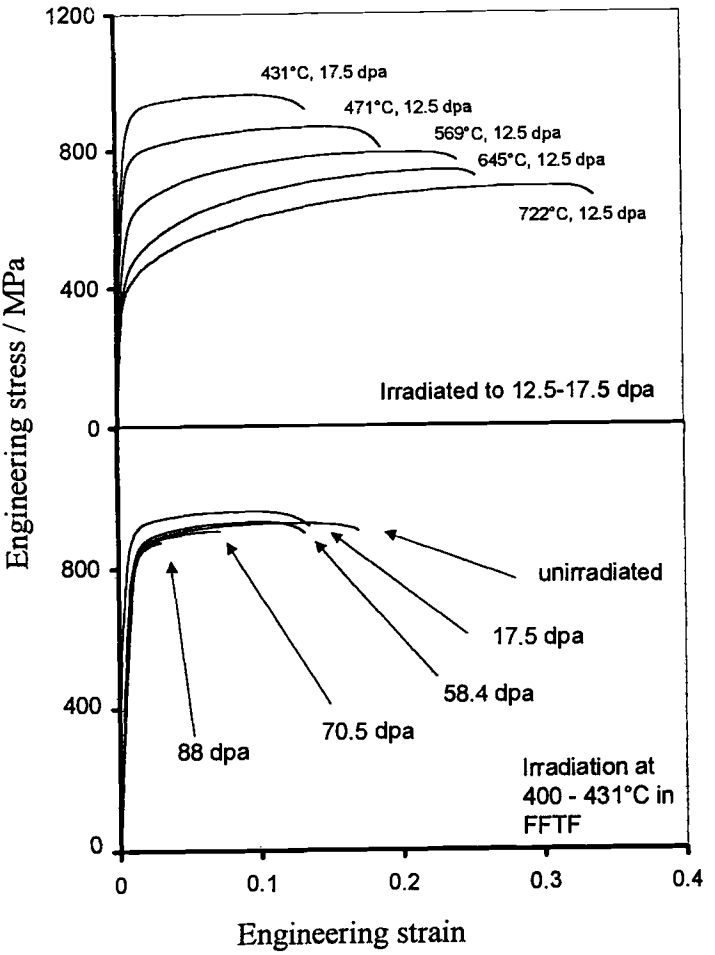


Figure 3 - *(top) Typical stress strain curves at room temperature derived from tensile specimens of the CN-13 heat irradiated in the first segment of the FFTF-MOTA experiment, showing primarily the effect of irradiation temperature.*

(bottom) Typical stress-strain curves derived from tensile specimens of the CN-13 heat irradiated at 400-430 °C in the FFTF-MOTA over four irradiation segments, showing the influence of dpa level in reducing the ductility. Within any one irradiation increment, the temperature was constant within ±5 °C, but varied somewhat from segment-to-segment.

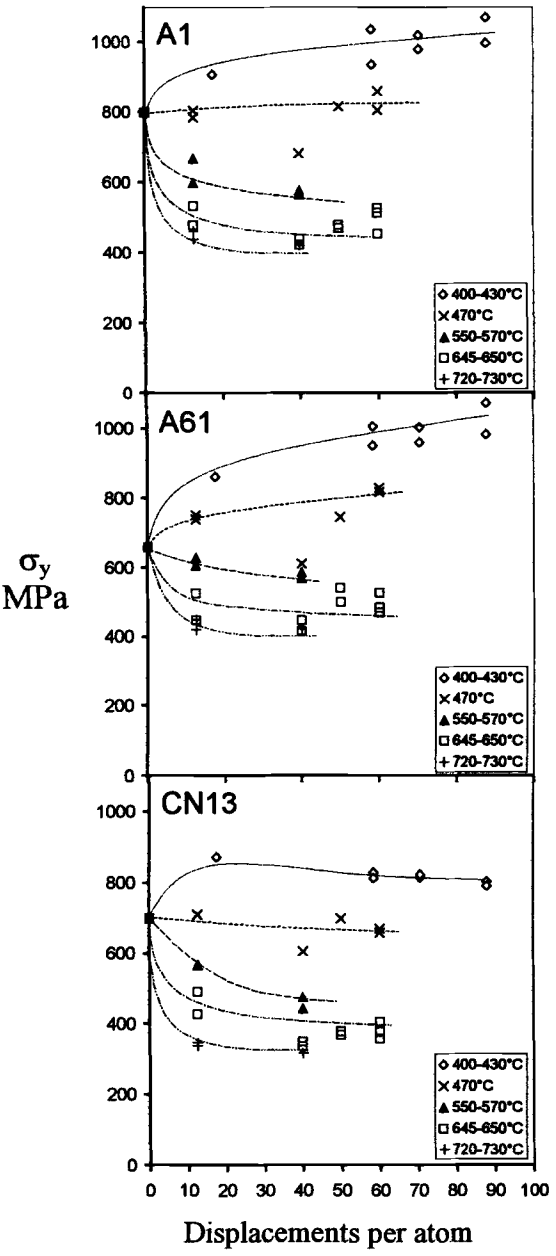


Figure 4 - *The influence of heat identity, irradiation temperature and dpa level on the evolution of tensile yield stress at room temperature of the three heats of 20% cold worked 316 stainless steel.*

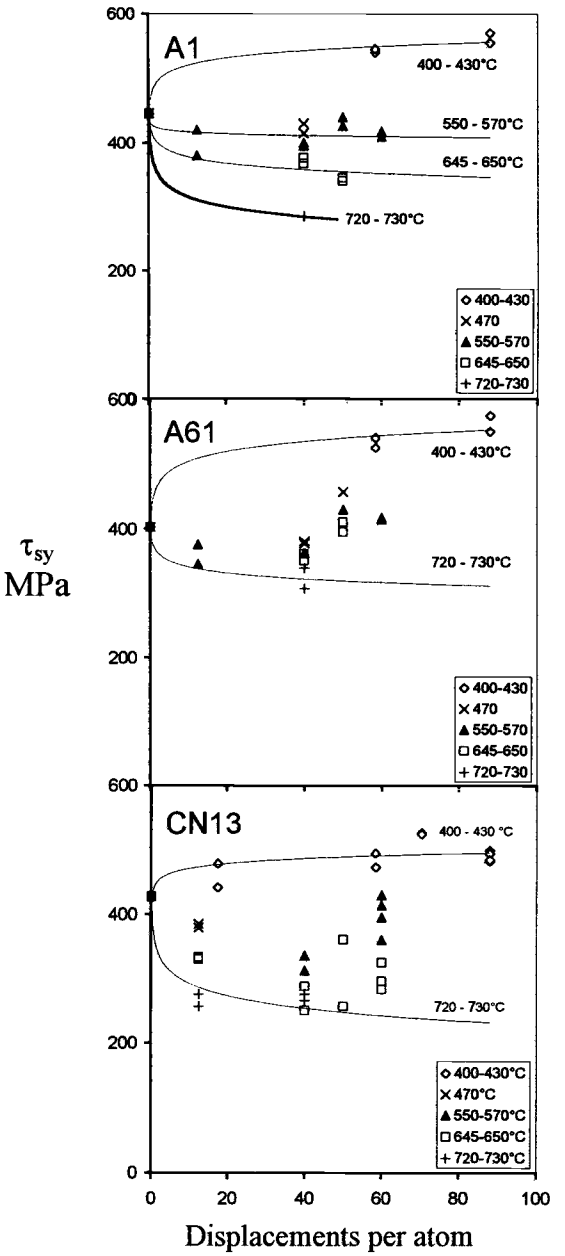


Figure 5 - *The influence of heat identity, irradiation temperature and dpa level on the evolution of shear yield stress at room temperature of the three heats of 20% cold worked 316 stainless steel.*

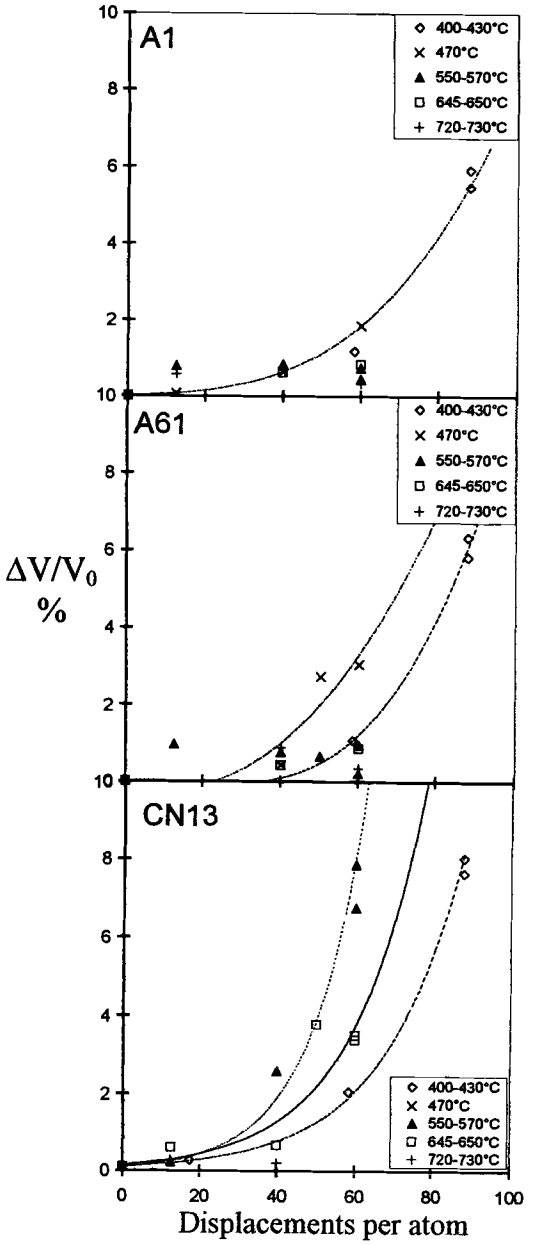


Figure 6 - *Swelling of AISI 316, as measured by an immersion density technique, showing that a wide range of swelling levels and sometimes a slight densification were obtained in this experiment.*

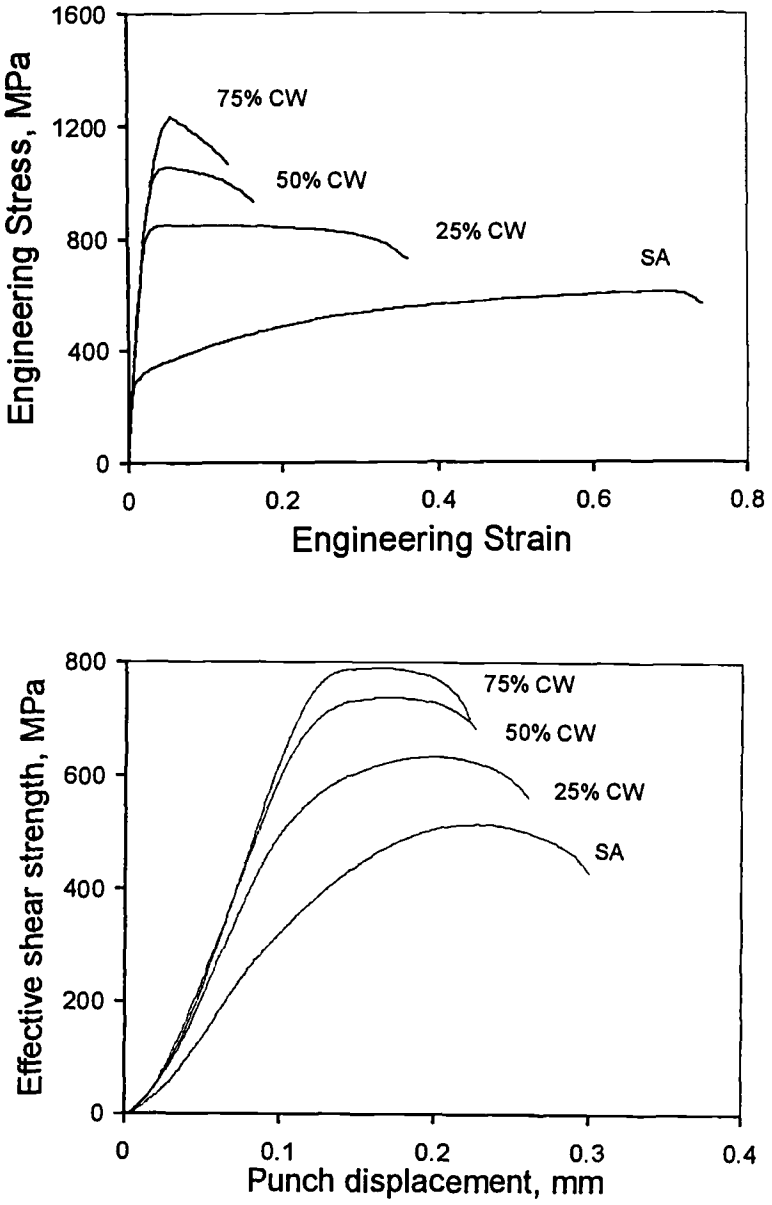


Figure 7 - *Tensile and shear punch stress-strain curves observed at room temperature in unirradiated 316 stainless steel, heat CN13, at various cold-work levels.*

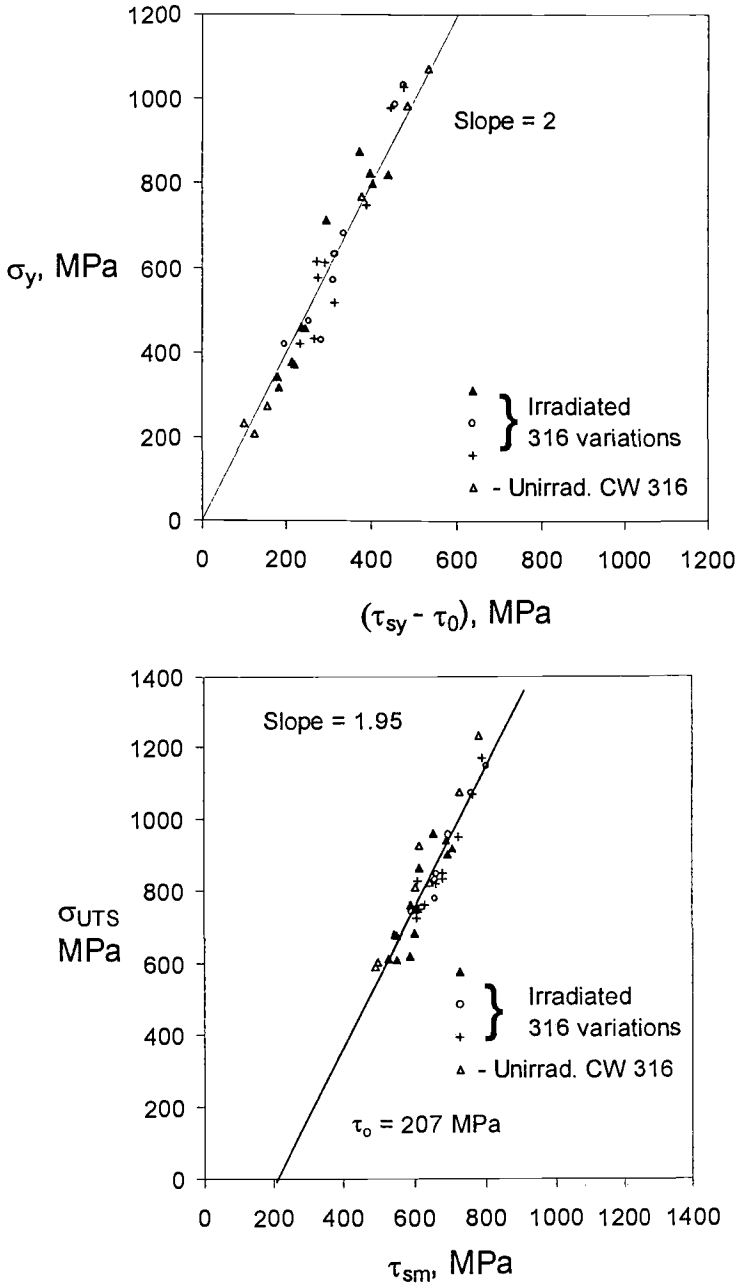


Figure 8 - *(top) Correlation observed between yield strengths obtained from tensile and shear punch tests of AISI 316. (bottom) Correlation observed between ultimate tensile strengths obtained from tensile and shear punch tests of AISI 316.*

fit" to the 316 SS data. In an effort to derive a simple and consistent correlation between tensile yield and effective shear yield data for a variety of alloys, it was decided that the data would be fit to a master slope set equal to 2.0. The value of 2.0 fits between the minimum and maximum slopes observed for yield strength correlations between tensile and shear punch tests previously conducted using a variety of unirradiated and irradiated alloys [*9,14*]. However, it was noted by Lucas [*7*] that for a state of pure shear, a yield strength correlation between a tensile test and a shearing test ought to have a slope of 1.73. The deviation from the ideal slope of 1.73 suggests that a state of pure shear does not exist during a shear punch test. The nature of the true stress state is currently under investigation.

Very similar results were obtained in a companion tensile-shear punch study [*13,14*] conducted on a series of model Fe-Cr-Ni austenitic alloys in the ^{59}Ni isotopic doping experiments on helium effects summarized in ref. 17. This experiment involved the side-by-side irradiation of specimens with greatly different He/dpa ratios. The results of the tensile-shear punch correlations are shown in Figures 9 and 10. The only significant difference observed in tensile-shear punch correlations developed for the ^{59}Ni series relative to that of AISI 316 was that the offset was somewhat smaller, possibly reflecting the relative softness of these alloys compared to that of AISI 316. Note that the "unforced" slopes of the lines in Figure 10 are very close to 2.0.

When the results of the ^{59}Ni and AISI 316 series are combined, it is obvious that the mechanical property measurements obtained from both miniature tensile specimens and TEM shear punch tests are very consistent, and that the derived property-property

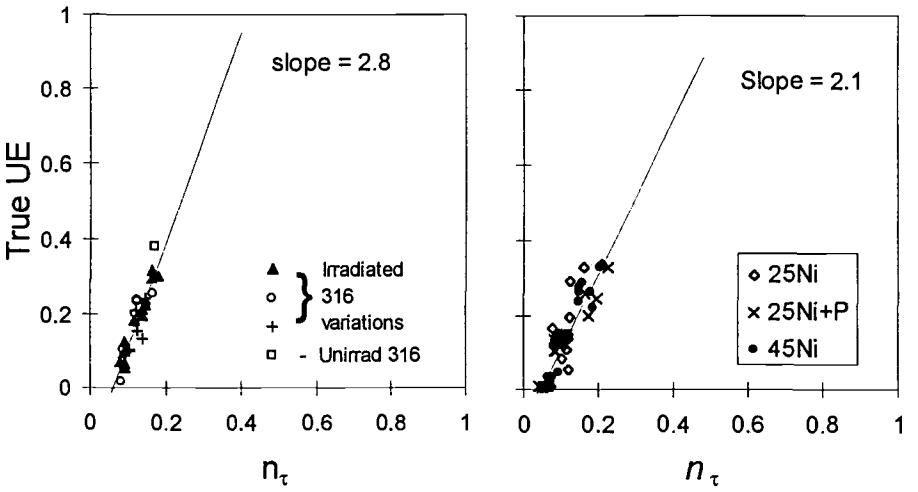


Figure 9 - *Correlations observed between tensile true uniform elongation and the strain hardening exponent derived from the shear punch test on AISI 316 (top) and Fe-15Cr-Ni isotopically-tailored specimens [14].*

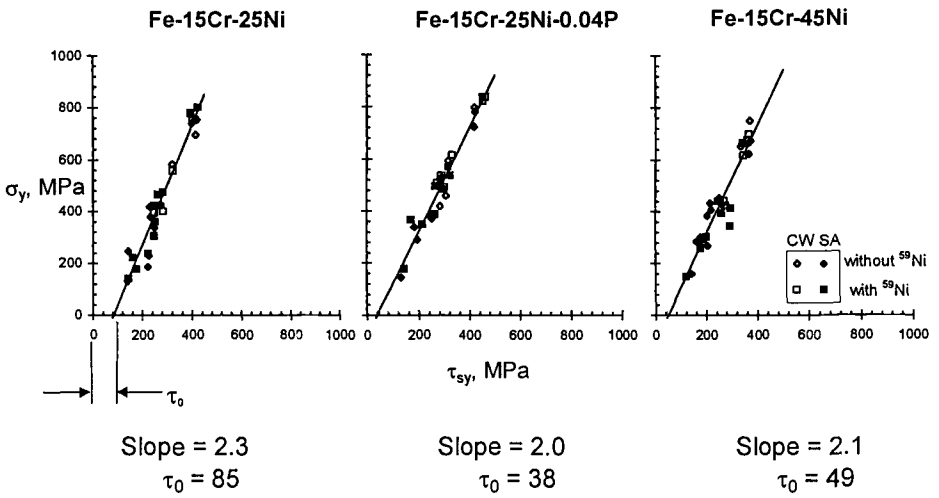


Figure 10 - *Correlations observed between yield strengths obtained from tensile and shear punch tests of three Fe-Cr-Ni isotopically tailored alloys in both annealed and cold-worked starting states. Alloy doped with ^{59}Ni have much higher He/dpa ratios and somewhat different microstructures compared to undoped alloys [14].*

correlation describing their relationship is independent of composition and starting state, temperature, dose and dose rate, helium to dpa ratio and details of irradiation history, including the absence of irradiation.

Thus, the tensile-shear punch correlation is effectively independent of starting state and irradiation condition over a very wide range of microstructures whether they be induced either by thermal-mechanical treatment and/or irradiation. This independence allows the prediction of tensile properties from highly radioactivated material, using the smallest amount of material, as long as a TEM disk can be produced from the irradiated materials.

Another important result of this study is that the intercept τ_0 can be determined for a given material using only unirradiated variations in cold-work level. Thus, predictions can be made for tensile properties when only TEM disks have been irradiated, as long as archive specimens at several cold-work levels are also available.

References

[1] *The Use of Small-Scale Specimens for Testing Irradiated Material, ASTM STP 888*, W. R. Corwin and G. E. Lucas, Eds., American Society for Testing and Materials, Philadelphia, 1986.

[2] *Small Specimen Test Techniques Applied to Nuclear Reactor Vessel Thermal Annealing and Plant Life Extension, ASTM STP 1204*, W. R. Corwin, F. M. Haggag, and W. L. Server, Eds., American Society for Testing and Materials, Philadelphia, 1993.

[3] *Miniaturized Specimens for Testing of Irradiated Materials*, P. Jung and H. Ullmaier, Eds., Forschungszentrum Jülich GmbH, 1995.

[4] *Miniaturized Specimens for Testing of Irradiated Materials, IEA International Symposium, Feb. 1996, Miyagi, Japan*, in press.

[5] Garner, F. A., Hamilton, M. L., Heinisch, H. L. and Kumar, A. S., "Application of Miniature Tension Specimens to Studies of Radiation Damage in Metals," *Small Specimen Test Techniques Applied to Nuclear Reactor Vessel Thermal Annealing and Plant Life Extension, ASTM STP 1204*, W. R. Corwin, F. M. Haggag, and W. L. Server, Eds., American Society for Testing and Materials, Philadelphia, 1993, pp. 336-355.

[6] Hamilton, M. L., Blotter, M. A., and Edwards, D. J., "Evaluation of Miniature Tension Specimens Fabrication Techniques and Performance," *Small Specimen Test Techniques Applied to Nuclear Reactor Vessel Thermal Annealing and Plant Life Extension, ASTM STP 1204*, W. R. Corwin, F. M. Haggag, and W. L. Server, Eds., American Society for Testing and Materials, Philadelphia, 1993, pp. 368-385.

[7] Lucas, G. E., Odette, G. R., and Sheckherd, J. W., *The Use of Small-Scale Specimens for Testing Irradiated Material, ASTM STP 888*, W. R. Corwin and G. E. Lucas, Eds., American Society for Testing and Materials, Philadelphia, 1986, pp. 112-140.

[8] Lucas, G. E., Sheckherd, J. W., Odette, G. R., and Panchandeeswaran, S., *Journal of Nuclear Materials* 122-123 (1984) 429.

[9] Hamilton, M. L., Toloczko, M. B., and Lucas, G. E., "Recent Progress in Shear Punch Testing," *Miniaturized Specimens for Testing of Irradiated Materials*, P. Jung and H. Ullmaier, Eds., Forschungszentrum Jülich GmbH, 1995, pp. 46-58.

[10] Toloczko, M. B., Hamilton, M. L., and Lucas, G. E., "Ductility Correlations Between Shear Punch and Uniaxial Tensile Test Data," *Miniaturized Specimens for Testing of Irradiated Materials, IEA International Symposium, Feb. 1996, Miyagi, Japan*, in press.

[11] Toloczko, M. B., Lucas, G. E., Odette, G. R., Stoller, R. E., and Hamilton, M. L., "An Investigation of Microstructures and Yield Strengths in Irradiated Stainless Steels Using Small Specimen Techniques," *Effects of Radiation on Materials: 17th*

Intern. Symp., ASTM STP 1270, D. S. Gelles, R. K. Nanstad, A. S. Kumar and E. A. Little, Eds., American Society for Testing and Materials, 1996, pp. 902-918.

[12] Hamilton, M. L., Toloczko, M. B., Edwards, D. J., Sommer, W. F., Borden, M. J., Dunlap, J. A., Stubbins, J. F., and Lucas, G. E., "Correlation Between Shear Punch and Tensile Data for Neutron-Irradiated Aluminum Alloys," *Effects of Radiation on Materials: 17th Intern. Symp., ASTM STP 1270*, D. S. Gelles, R. K. Nanstad, A. S. Kumar and E. A. Little, Eds., American Society for Testing and Materials, 1996, pp. 1057-1067.

[13] Hankin, G. L., Toloczko, M. B., Hamilton, M. L., and Faulkner, R. G., "Validation of the Shear Punch-Tensile Correlation Technique Using Irradiated Materials," *Journal of Nuclear Materials*, 258-263 (1998) pp.1651-1656.

[14] Hankin, G. L., Toloczko, M. B., Hamilton, M. L., Garner, F. A., and Faulkner, R. G., "Shear Punch Testing of ^{59}Ni Isotopically-Doped Model Austenitic Alloys After Irradiation in FFTF at Different He/dpa Ratios," *Journal of Nuclear Materials*, 258-263 (1998) pp. 1657-1663.

[15] Gelles, D. S., Hankin, G. L., Hamilton, M. L., "A Reassessment of the Effects of Helium on Charpy Impact Properties of Ferritic/Martensitic Steels," *Journal of Nuclear Materials*, 258-263 (1998) pp. 1216-1221.

[16] Garner, F. A., Hamilton, M. L., Panayotou, N. F., and Johnson, G. D., *Journal of Nuclear Materials*, 103-104 (1981) pp. 803-808.

[17] Garner, F. A., Hamilton, M. L., Greenwood, L. R., Stubbins, J. F., and Oliver, B. M., "Isotopic Tailoring with ^{59}Ni to Study Helium Generation Rates and Their Effect on Tensile Properties of Neutron-Irradiated Fe-Cr-Ni Alloys," *Effects of Radiation on Materials: 16th International Symposium, ASTM STP 1175*, A. S. Kumar, D. S. Gelles, R. K. Nanstad, and E. A. Little, Eds., American Society for Testing and Materials, Philadelphia, 1993, pp. 921-939.

G. L. Hankin,[1] M. B. Toloczko,[2] K. I. Johnson,[3] M. A. Khaleel,[3] M. L. Hamilton,[3] F. A. Garner,[3] R. W. Davies,[3] and R. G. Faulkner[1]

An Investigation into the Origin and Nature of the Slope and x-axis Intercept of the Shear Punch-Tensile Yield Strength Correlation using Finite Element Analysis

Reference: Hankin, G. L., Toloczko, M. B., Johnson, K. I., Khaleel, M. A., Hamilton, M. L., Garner, F. A., Davies, R. W., and Faulkner, R. G., **"An Investigation into the Origin and Nature of the Slope and x-axis Intercept of the Shear Punch-Tensile Yield Strength Correlation using Finite Element Analysis,"** *Effects of Radiation on Materials: 19th International Symposium, ASTM STP 1366,* M. L. Hamilton, A. S. Kumar, S. T. Rosinski, and M. L. Grossbeck, Eds., American Society for Testing and Materials, West Conshohocken, PA, 2000.

Abstract: Recent studies have shown that for a variety of unirradiated and irradiated materials, a slope of ~2 is obtained for a correlation between yield in a shear punch test and yield in a uniaxial tensile test. Application of the von Mises yield criterion would predict a slope of $\sqrt{3}$. A finite element model (FEM) of the shear punch test was developed to aid in understanding the experimentally obtained slope of ~2. FEM simulations of the shear punch test were conducted using stress-strain data from uniaxial tensile tests on 316 stainless steel in four initial cold-work conditions. A correlation was developed between the FEM-evaluated effective shear yield strength and the experimentally-evaluated uniaxial yield strength. The slope from this correlation was found to be nearly the same as for the slope from the correlation between the experimentally-evaluated effective shear yield strength and the experimentally-evaluated uniaxial yield strength. The finite element model showed that stresses other than pure shear exist in a specimen during a shear punch test, and these other stresses may explain why the slope of the experimental yield strength correlation is different than $\sqrt{3}$.

Keywords: small specimen testing, 316 stainless steel, neutron irradiation, tensile properties, shear punch test, property-property correlation.

[1]Graduate Student and Professor, respectively, I.P.T.M.E., Loughborough University, Leicestershire, LE11 3UT, UK.

[2]Graduate Student, Washington State University, Pullman, WA 99163, USA.

[3]Senior research engineer, Staff engineer, Senior staff scientist, Senior staff scientist, and Development engineer, respectively, Pacific Northwest National Laboratory, Richland, WA 99352, USA.

Copyright© 2000 by ASTM International www.astm.org

Introduction

A number of shear punch experiments have been completed to develop empirical relationships between mechanical properties obtained from uniaxial tensile tests and mechanical properties from the shear punch test [1-8]. The shear punch-tensile correlations for strength and ductility have been shown to be independent of small variations in material composition, thermomechanical starting state, irradiation temperature, dose, dose rate, helium-to-dpa ratio, and the details of irradiation history [7, 8]. It was shown in these studies that a correlation derived from unirradiated materials is applicable to irradiated materials.

The shear punch test (SPT) is essentially a blanking operation in which a 1 mm diameter punch is driven at a constant rate of 0.127 mm/min. (0.005 in./min.) through a TEM-sized disk (nominally 0.25 mm thick and 2.8 mm in diameter). The disk is constrained along both its upper and lower surfaces in a test fixture which also guides the punch. The load on the punch is measured as a function of specimen displacement which is taken to be equivalent to the crosshead displacement [3]. The yield load in the punch test is recorded as the deviation from linear elastic behaviour rather than an offset value. The effective shear yield strength (τ_{sy}) and maximum shear strength (τ_{sm}) are evaluated from the yield and maximum loads respectively, by the following equation [4]:

$$\tau_{sy,sm} = \frac{P_{sy,\,sm}}{(2\pi rt)}, \tag{1}$$

where $P_{sy,\,sm}$ is the yield or maximum load, r is the average of the bore and punch radii, and t is the specimen thickness.

When the pairs (τ_{sy}, σ_y) or (τ_{sm}, σ_m) are plotted, the data fall on a straight line. Fig. 1 shows such a correlation between the uniaxial yield strength and the effective shear yield strength for 316 stainless steel (SS) in a variety of cold-work conditions and irradiation hardened conditions. A linear regression is performed to obtain the constants m and τ_0:

$$\sigma_{y,UTS} = m(\tau_{sy,sm} - \tau_0). \tag{2}$$

Fig. 1 shows a recently constructed yield strength correlation that was derived from shear punch and miniature tensile tests on three variations of a 20% CW 316 stainless steel [7, 8]. It is typical of yield strength correlations developed for other materials, with a characteristic slope and x-axis intercept. The τ_0 offset parameter is thought to be associated with the shear punch test and not the tensile test. τ_0 was originally assumed to arise from punch-die-specimen friction [1], and m and τ_0 appear to be somewhat material-dependent [4]. In the most recent study [8], however, it has been shown that many alloy groups exhibit the same slope of around 2.0-2.3, with the offset parameter still appearing to be material-dependent. Table 1 summarises the slopes and

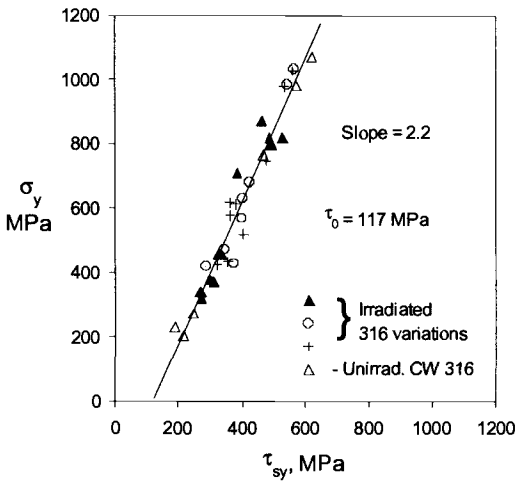


FIG. 1 -- *Shear punch-tensile correlation for yield strength that was constructed from shear punch and miniature tensile tests on three variations of irradiated 20% CW 316 SS and four cold-work levels of unirradiated 316 stainless steel, after Hankin et al. [8].*

offsets of recent yield strength correlations constructed from experimental data on a number of austenitic stainless steel alloys, including a correlation constructed from the four cold-work levels of AISI 316 stainless steel that were used for the FEM analysis in this work.

TABLE 1 -- *Summary of the yield strength correlation coefficients in recent studies [8].*

Materials	Number of data points	Slope	τ_o offset, MPa	Range of tensile yield strengths MPa
Fe-12Cr-25Ni [a]	33 [d]	2.3	85	131 - 801
Fe-12Cr-25Ni-0.04P [a]	29 [d]	2.0	38	145 - 837
Fe-12Cr-45Ni [a]	29 [d]	2.1	49	151 - 750
316 variations [b]	36 [d]	2.2	117	206 - 1069
CW 316 SS [c]	4	2.1	108	275 - 1100

a) 3 irradiation temperatures up to 52 dpa, from CW and SA starting states, with and without enhanced helium generation, plus unirradiated controls

b) 3 alloys with 5 irradiation temperatures up to 88 dpa starting from a 20% CW starting state, with unirradiated controls, plus 4 unirradiated cold- work conditions of AISI 316 stainless steel

c) Four individual cold-work conditions of AISI 316 stainless steel (unirradiated)

d) Each data point on a correlation represents a different material condition and is the average of 2-3 shear punch tests and 1 or 2 tensile tests.

In preliminary studies on the yield correlation, Lucas [2] noted that the regression coefficient or slope in a tensile-shear punch correlation for yield data from a variety of materials when combined was close to $\sqrt{3} = 1.73$. This is the ratio of pure shear yield stress to uniaxial yield stress when using the von Mises effective stress, i.e., $\sigma_y = \sqrt{3}\tau_{sy}$. This result would be expected if the tensile test specimen experiences pure uniaxial tension (which is a reasonable assumption) and if the process zone of a SPT specimen experiences a state of pure shear. These assumptions would lead to an idealised correlation, whose regression has a slope of $\sqrt{3}$ and passes through the origin. As can be seen from Table 1, however, this idealised correlation does not match the experimentally determined correlation coefficients for austenitic stainless steel alloys. As has been previously shown [3], additional stresses are likely to exist in the deformation zone of the shear punch specimen. These stresses arise from compression, stretching, and bending, and the stresses should be considered in the application of the yield criterion. If these additional stresses are inserted into the von Mises yield criterion for the state of stress during the shear punch test, the ratio of uniaxial tensile yield stress to effective shear yield stress will be greater than $\sqrt{3}$. This provides a rationale to explain the experimentally observed yield correlation slopes of 2.0-2.3.

It is the intention of the current work to further investigate the origin and nature of the slope and τ_o offset for the yield strength correlation. A finite element model (FEM) of the shear punch test was constructed to evaluate the effective shear yield strength so that a correlation could be constructed between the FEM-evaluated effective shear yield strength and the experimentally-evaluated uniaxial yield strength. This correlation was compared to the correlation between the experimentally-evaluated effective shear yield strength and the experimentally-evaluated uniaxial yield strength.

Experimental Details

Four cold-work levels (solution annealed, 25, 50 and 75% cold-work) of a 316 stainless steel were used to construct shear punch specimens and miniature tensile specimens. Four shear punch tests and two miniature tensile tests were conducted on specimens of each of the four cold-worked conditions [8, 9]. This data were used to generate a correlation between effective shear yield strength and uniaxial yield strength. The stress-strain data from the miniature tensile tests was also used to define the material properties required by the FEM program.

A finite element model was constructed using MARC code in 2 dimensions. The model was axisymmetric about a centreline through the middle of the punch. This reduces the complexity of the model, and hence the processing time required for completing an analysis. A schematic of the model is shown in Fig. 2. There are 50 elements across the thickness of the specimen that are graded in the radial direction (*r*-axis in Fig. 2) to give nearly square elements in the deformation zone and larger elements near the centre and outer radius of the disk. Since the focus of the study was to investigate the nature of the yield stress correlation, the model was only run just slightly beyond yield. Examination of partially tested shear punch specimens has shown that in

this range of deformation, the specimen is still entirely intact [3]. Therefore, no criterion for crack formation was added to the finite element model. Fig. 3 shows plots of true stress versus true plastic strain curves for the 316 SS uniaxial tensile test data that were required by the finite element program.

The finite element model was constructed so that the geometry of the specimen, punch and die, including all corner radii, could be changed, and the material properties of the specimen could also be changed. The die and punch were modelled as being rigid, and the contacting surfaces were modelled with friction acting upon them.

The finite element model was run for each of the four material conditions using the punch and specimen geometry from the actual shear punch testing. Using a shadowgraph apparatus, the corner radius of the punch was determined to be approximately 0.010 mm, and the corner radius of the fixture bore was assumed to be the same as the corner radius of the punch. Just as in the experimental setting, the load on the punch was measured as a function of punch displacement, and the effective shear yield strength was taken to be the deviation from linearity of the load-displacement trace generated by the FEM program.

Results and Discussion

The standard deviations in the experimentally measured effective shear strength and uniaxial yield strength of the controls were of the order of 15 MPa and 8 MPa respectively. The experimental shear punch test curves show the same trends as the tensile tests in terms of the increase in effective shear yield and shear maximum strengths with increasing cold work. The load-displacement traces generated by the finite element model of the shear punch test are shown with the corresponding real shear punch test

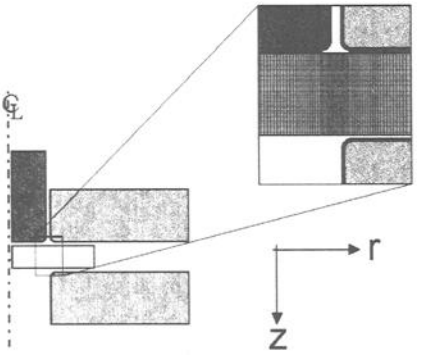


FIG. 2 -- *Schematic diagram of a 2D, axisymmetric finite element model of the shear punch test.*

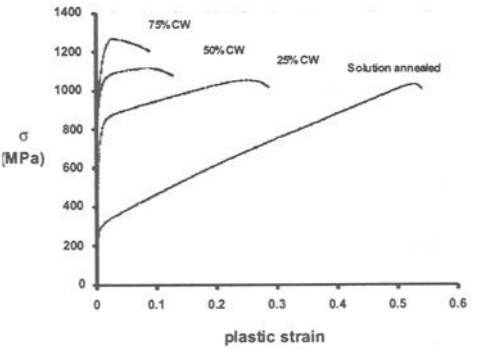


FIG. 3 -- *Uniaxial true stress versus true plastic strain traces required by the finite element model to simulate the shear punch test of the 316 stainless steel variants.*

traces in Figs. 4a and 4b, respectively (note the expanded x-axis scale in Fig. 4a relative to Fig. 4b). The finite element model was run to a point just beyond the effective shear yield strength. The loading curve generated by the finite element model is quite stiff when compared to the experimental results, despite machine and test rig compliance having been removed from the experimental results. The authors have not had an opportunity to investigate this deviation from the observed experimental shear punch test behaviour, and its impact is therefore unknown.

The correlation that was developed from the FEM-evaluated effective shear yield strength and the experimentally determined uniaxial yield strength is shown in Fig. 5 together with the experimentally determined yield strength correlation. The slopes of the two correlations are approximately equal, but the FEM-tensile correlation passes through the origin. The fact that the τ_0 offset is not observed in the FEM-tensile correlation suggests that there is either some systematic error involved in determining the effective shear yield strength experimentally, or that the finite element model may be deficient in some way.

Figs. 6-8 show the development of the plastic zone in the region of the specimen between the punch and die for the solution annealed 316 stainless steel material. The stress contours show the intensity of the von Mises stress within the specimen. A scale has been chosen such that stresses exceeding the level at which plastic strain occurs (~260 MPa) are shown in dark grey colours. The load-displacement curve in each figure shows the point during the FEM simulation that corresponds to the contour plot. Fig. 6 shows that localised plastic yielding is occurring in the region near the punch and die. Fig. 7 shows the extent of plastic zone at the point where the effective shear yield strength was determined. As can be seen, plastic deformation is occurring in a region that is wider than the clearance region of the punch and die. Fig. 8 shows the model run

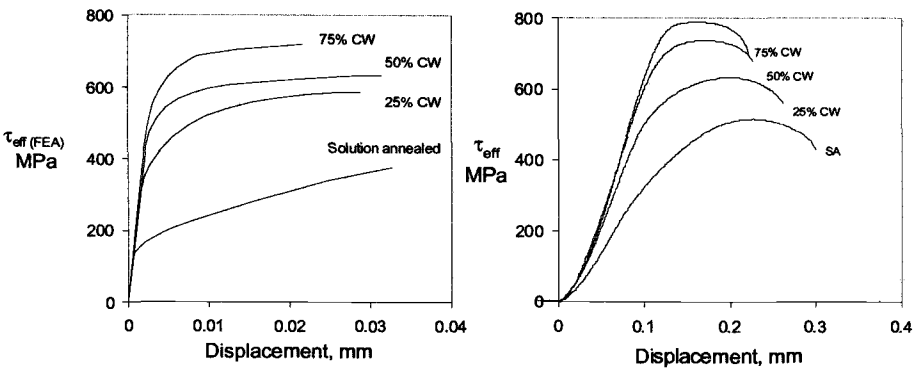


FIG. 4 -- *(a) Effective shear strength versus punch displacement as evaluated for four thermomechanical-starting conditions of 316 stainless steel by a finite element model of the shear punch test. (b) Experimentally derived shear punch traces for the same materials.*

to a point beyond yield. In real shear punch tests, cupping of the slug is observed with the degree of cupping increasing for softer materials. This cupping behaviour is the result of a bending moment arising during a shear punch test. No such cupping is shown in Fig. 8, in part because the FEM has been run to just slightly beyond the effective shear yield stress where the overall deformation of the specimen is quite small, and in part because the illustration only shows the portion of the specimen in the immediate vicinity of the deformation zone. However, the deformation at the top-right and bottom-left of the deformation zone in Fig. 8 indicates a bending moment has formed.

Fig. 9 shows the magnitude of the major contributing stress components sampled across a line AA' that spans the plastic zone shown in Fig. 7. The shear component τ_{rz} reaches a maximum at the centre of the deformation zone, and the component σ_{zz} reaches a maximum compressive value on either side of the deformation zone. Within the clearance region, the von Mises stress is mostly a function of these two stress components. While each stress component varies significantly across the deformation zone, the von Mises stress is remarkably constant across the process zone.

The effect of friction between the punch face and the specimen was systematically studied. Since the punch is modelled as a rigid component, the area of contact between the punch face and the specimen is determined by the elastic and plastic deformation which occurs in the specimen as it is loaded. When different values of friction were used in the FEM runs for the solution annealed material, no significant difference in the FEM-evaluated effective shear yield strength was observed. Fig. 10 shows two runs of the model for the solution annealed 316 stainless steel material condition, one with the coefficient of friction set to zero and the other with the coefficient of friction set to 0.204.

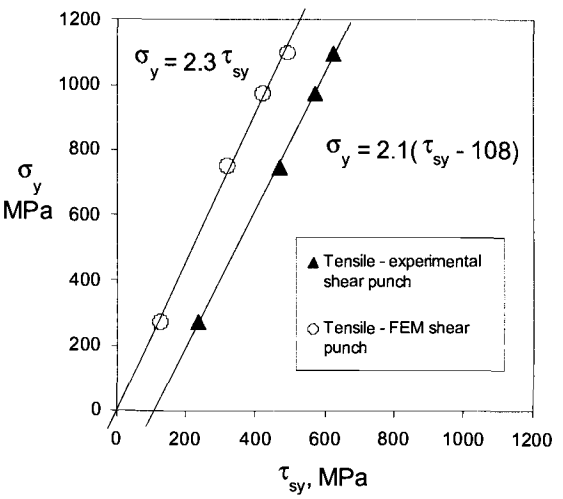


FIG. 5 -- *Tensile-shear punch and tensile-FEM evaluated correlation for yield strength for unirradiated 316 stainless steel in four thermomechanical starting conditions.*

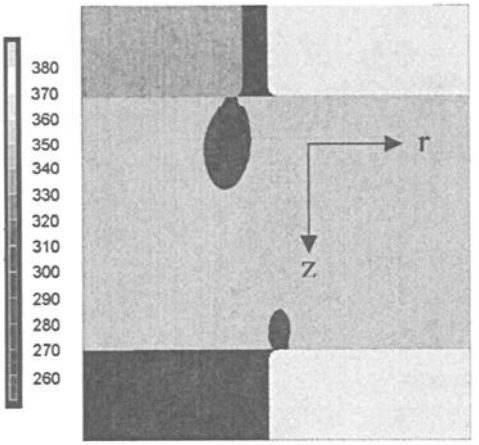


FIG. 6 -- *Stress contours in the SA 316 SS shear punch specimen as calculated by the finite element model. Only stresses greater than the yield stress are shown. Here, local plastic strain is observed before the point perceived to be the effective shear yield strength.*

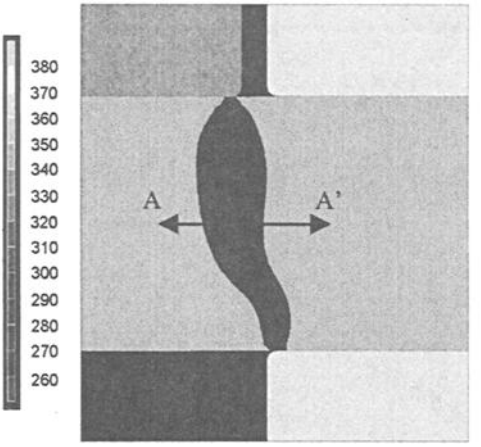


FIG. 7 -- *Finite element model showing the extent of plastic deformation at the point perceived to be the effective shear yield strength in SA 316 stainless steel.*

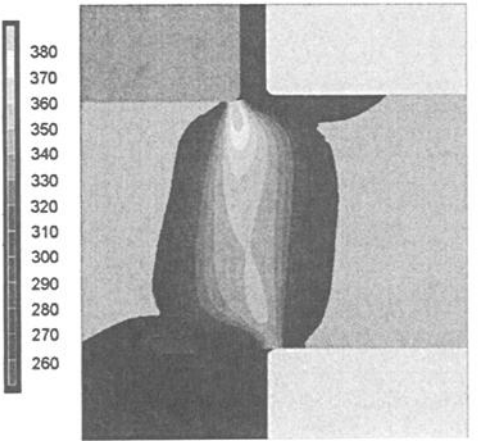


FIG. 8 -- *Finite element model showing the extent of plastic deformation at a point beyond the effective shear yield strength in SA 316 stainless steel. The deformation region has become wider, and there is evidence that bending is occurring in the specimen along the face of the upper die and adjacent to the lower die.*

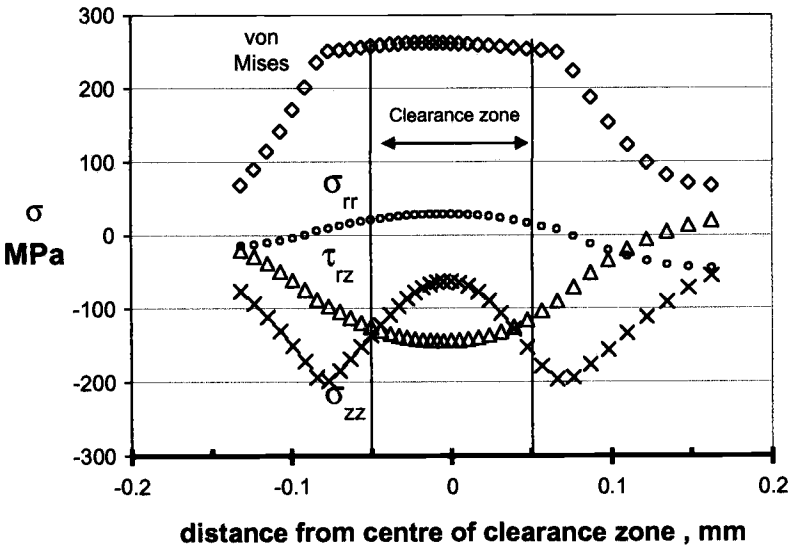


FIG. 9 -- *Stress components along a line AA' that spans the clearance zone of the FEM shear punch test specimen in FIG. 7. The specimen is loaded to the point perceived to be the effective shear yield strength.*

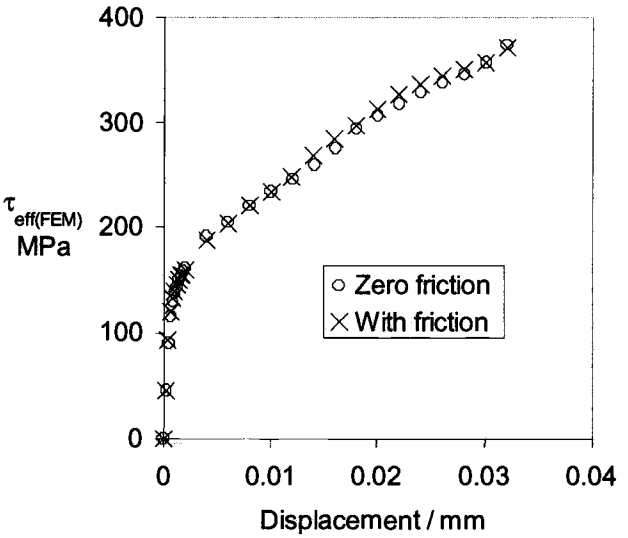


FIG. 10 -- *The effect of different frictional coefficients (μ=0.0 and μ=0.204) on the effective shear strength as determined by a finite element model of the shear punch test using the material properties of solution annealed 316 stainless steel.*

The same value for effective shear yield strength would be chosen for either trace, which implies that friction has no effect on the effective shear yield strength, and is therefore not responsible for the τ_0 offset in the yield strength correlation.

Variation of the punch and die radius as well as the size of the clearance region was also systematically studied. Variation of these parameters within the experimentally observed range of values had little effect on the FEM-calculated effective shear yield strength.

Conclusions

The finite element model provides insight into some of the features of the tensile-shear punch correlation. The model confirmed that a stress state more complex than that of simple shear does exist in the deformation zone of a shear punch specimen during a test, and these additional stresses are responsible for the slope being larger than the predicted value of $\sqrt{3}$ in the correlation between the FEM-derived effective shear yield strength and the experimentally-determined yield strength. It seems reasonable to conclude that a similar stress state exists in a TEM disk during an actual shear punch test.

The effect of friction during a shear punch test was also investigated using the finite element model of the shear punch test. It was observed that in the range of reasonable values for the coefficient of friction between the punch face and the specimen, there was a negligible effect of friction on the behaviour of the finite element model.

The τ_0 offset is an inherent characteristic of the shear punch test, but its origin was not resolved with this particular finite element model.

References

1. Lucas, G.E., "The Development of Small Specimen Mechanical Test Techniques," *Journal of Nuclear Materials*, Vol. 117, 1983, p. 327.

2. Lucas, G.E., Sheckherd, J.W., Odette, G.R. and Panchandeeswaran, S., "Shear Punch Tests for Mechanical Property Measurements in TEM Disc-Sized Specimens," *Journal of Nuclear Materials*, Vols. 122-123, 1984, p. 429.

3. Lucas, G.E., Odette, G.R. and Sheckherd, J.W., "Shear Punch and Microhardness Tests for Strength and Ductility Measurements," *The Use of Small Scale Specimens for Testing Irradiated Material, ASTM STP 888*, 1986, p. 112.

4. Hamilton, M.L., Toloczko, M.B., Lucas, G.E., "Recent Progress in Shear Punch Testing," *Miniaturized Specimens for Testing of Irradiated Materials*, Hans Ullmaier and Peter Jung, Eds., Forschungszentrum Jülich GmbH, January, 1995, p. 46.

5. Toloczko, M.B., Hamilton, M.L., Lucas, G.E., "Ductility Correlations Between Shear Punch and Uniaxial Tensile Data," *Proceedings of the Workshop on*

Miniaturised Specimens for Testing of Irradiated Materials IEA International Symposium, March 13-16, 1996 Japan, in press.

6. Toloczko, M.B., Lucas, G.E. Odette, G.R., Stoller, R.E. and Hamilton, M.L., "An Investigation of Microstructures and Yield Strengths in Irradiated Austenitic Stainless Steels using Small Specimen Techniques," *17th Symposium on the Effects of Radiation on Materials, ASTM-STP 1270*, David S. Gelles, Randy K. Nanstad, Arvind S. Kumar and Edward A. Little, Eds., 1996, p. 902.

7. Hankin, G.L. Hamilton, M.L., Garner, F.A. and Faulkner, R.G., "Shear Punch Testing of ^{59}Ni Isotopically Doped Model Austenitic Alloys after Irradiation in FFTF at Different He/dpa," *Journal of Nuclear Materials,* Vols. 258-263, 1998, pp. 1657-1663.

8. Hankin, G.L., Toloczko, M.B., Hamilton, M.L. and Faulkner, R.G., "Validation of the Shear Punch-Tensile Correlation Technique using Irradiated Materials," *Journal of Nuclear Materials,* Vols. 258-263, 1998, pp. 1651-1656.

9. Hamilton, M. L., Garner, F. A., Hankin, G. L., Faulkner, R. G., and Toloczko, M. B., "Neutron-Induced Evolution of Mechanical Properties of 20% Cold Worked 316 as Observed in Both Miniature Tensile and TEM Shear Punch Specimens", *Effects of Radiation on Materials: 19th International Symposium, ASTM STP 1366*, M. L. Hamilton, A. S. Kumar, S. T. Rosinski and M. L. Grossbeck, Eds., American Society for Testing and Materials, 1999, in press.

Salem Miloudi,[1] Stéphanie Jumel,[2] Philippe Pareige,[3] Jean-François Coste,[4] and Jean-Claude Van Duysen[5]

Thermoelectric Power: A Nondestructive Method for Monitoring Irradiation Effects in Ferritic Steels

Reference: Miloudi, S., Jumel, S., Pareige, P., Coste, J. F., and Van Duysen, J. C., **"Thermoelectric Power: A Nondestructive Method for Monitoring Irradiation Effects in Ferritic Steels,"** *Effects of Radiation on Materials: 19th International Symposium, ASTM STP 1366,* M. L. Hamilton, A. S. Kumar, S. T. Rosinski, and M. L. Grossbeck, Eds., American Society for Testing and Materials, West Conshohocken, PA, 2000.

Abstract: We try to develop nondestructive methods to monitor the effects of neutron irradiation in ferritic alloys. In this paper we report results obtained with a method based on thermoelectric power (TEP). This method is already used to monitor the thermal aging of duplex stainless steels.

It is shown that the measurement of the thermoelectric power allows the monitoring of the effects of i) electron irradiations on Fe-Cu model alloys, and ii) neutron irradiations on industrial pressure vessel steels. The recovery of these irradiation effects during thermal annealing can also be followed with the proposed method.

On the basis of the results obtained on Fe-Cu alloys, we propose a law to determine the limit of copper solubility in α iron at temperatures below 600°C.

Keywords: pressure vessel steel, irradiation, nondestructive method, thermoelectric power.

[1] PhD student, Electricité de France, Département Etude des Matériaux - Site des Renardières - Ecuelles 77818 Moret sur Loing CEDEX, France.

[2] PhD student, Electricité de France, Département Etude des Matériaux - Site des Renardières - Ecuelles 77818 Moret sur Loing CEDEX, France.

[3] Research Scientist, Groupe de Métallurgie Physique, UMR CNRS 6634, Université-INSA de Rouen, 76821 Mont Saint Aignan CEDEX, France.

[4] Research Scientist, Electricité de France, Département Etude des Matériaux - Site des Renardières - Ecuelles 77818 Moret sur Loing CEDEX, France.

[5] Head of Department, Electricité de France, Département Etude des Matériaux - Site des Renardières - Ecuelles 77818 Moret sur Loing CEDEX, France, also Professor, Laboratoire de Métallurgie Physique, Université de Lille I, Bât C6, 59655 Villeneuve d'Ascq, France.

Copyright© 2000 by ASTM International www.astm.org

Introduction

Neutron irradiation induces an evolution of the mechanical properties of nuclear reactor pressure vessel steels [1,2]. For the steels in service, this evolution is determined from forecasting formulas or mechanical testing in the framework of the surveillance program of the considered vessel.

In the case of steels used for laboratory studies (after irradiation in test reactors for example), these two methods can also be used but it could be useful to complement them by other techniques easy to apply. In this context, we attempt to develop non-destructive methods to monitor the effects of neutron irradiation on pressure vessel steels. Presently, several tracks are being considered.

This paper reports results obtained with a method based on the thermoelectric power (TEP) [3], which is a method already used to monitor the thermal aging of duplex stainless steels [4].

After reviewing the principle of the TEP measurement and showing that it can be used to determine the free copper content in α iron, this paper presents two applications of the proposed method:

- First, we used it to monitor the irradiation effects in a simple case: a Fe-0.2wt%Cu model alloy irradiated with electrons. We also looked at the possibility to use the method to follow the recovery of the electron-induced damage during thermal annealing.
- Secondly, we applied the TEP method to monitor the effects of neutron irradiations in an industrial pressure vessel steel. We also tried to follow the recovery of these effects during thermal annealing.

The Thermoelectric Power

Figure 1 shows the principle of the apparatus designed for TEP measurements. It is made of two blocks of iron maintained at temperatures T and T+ΔT, respectively. A flat specimen is pressed onto these blocks so as to ensure a good thermal electrical contact. In response to ΔT, a low voltage ΔV provided by the Seebeck effect can be measured between the two blocks [5,6].

ΔS (μV/K) is the relative TEP of the studied alloy with respect to the iron of the blocks. At the mean temperature T+ΔT/2, it is given by :

$$\Delta S = \frac{\Delta V}{\Delta T} \qquad (1)$$

In our case, the chosen temperatures were T = 15 $\pm$ 0.1°C and ΔT = 10 $\pm$ 0.1°C. The average accuracy on ΔS was estimated to $\pm$ 0.05 μV/K [3]. Thus, the absolute TEP of the alloy is given by: S = S(Fe) + ΔS, where S(Fe) is the absolute TEP of the iron of the blocks.

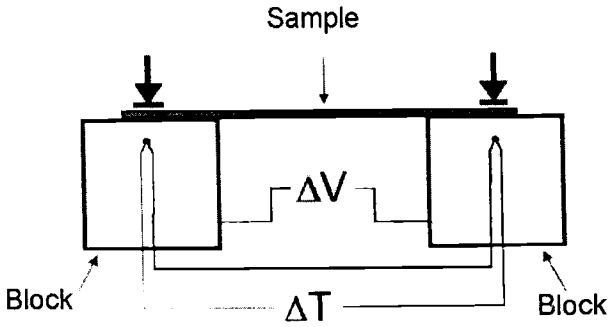


Figure 1 - *Schematic drawing of the apparatus used for the TEP measurements*

The absolute TEP of an alloy can also be expressed by [5]:

$$S = S_d + S_g \qquad (2)$$

S_d is the diffusion thermopower; it is the part of the TEP associated with the diffusion of electrons by a random distribution of scattering centres in thermal equilibrium. S_d varies quasi linearly with the absolute temperature and is the predominant part of S at high temperature.

S_g is the phonon-drag thermopower; it depends on the interaction of the crystal phonons with the diffusion centres of the lattice. Its variation with temperature is not linear and is the predominant part of S at low temperature (70 K).

We finally have to mention that TEP is a function of the amount of elements in solid solution. Their influence depends upon the measurement temperature [5,6]. At room temperature, this influence is considered as large.

Experimental Procedure

Application to Model Alloys

The study on the model alloys was carried out with pure iron and the following Fe-Cu alloys (made from the former): Fe-0.1wt%Cu, Fe-0.2wt%Cu, Fe-0.3wt%Cu and Fe-0.6wt%Cu. These materials were prepared at the DRFMC/SPMM Laboratories of the CEA Grenoble.

For the pure iron, platelets (20x5x0.5mm) were cut from the ingot in the raw casting state. For the binary alloys, samples (2.7 mm thick) were taken from the cast ingots. These samples were cold worked with a thickness reduction ratio on the order of 20-25%, and finally underwent the heat treatments shown in Table 1. The last heat treatment (2 h at 800°C) was followed by an accelerated gas cooling in order to maintain the copper in solid solution. At the end of the manufacturing process,

rectangular platelets (20x5x0.5mm) were cut from each alloy and their copper content was determined by atom probe analysis. The results are shown in Table 1; it can be noticed that the actual contents are slightly different from the target values.

Finally, each platelet underwent a mechanical grinding with 600 and 800 grit papers.

Table 1 - *Chemical compositions and thermo-mechanical heat treatments for pure iron and binary alloys used to determine the relationship between TEP measurement and free copper content.*

Sample	Copper content determined by atom probe analysis (wt%)	Cold work ratio (%)	Heat treatment
Fe_{pure}	Pure iron	0	Raw casting
Fe-0.1Cu	0.08 ± 0.01	20-25	Hfc, 2h 800°C + Agc
Fe-0.2Cu	0.17 ± 0.01	20-25	Hfc, 20min 900°C + Foc 2h 800°C + Agc
Fe-0.3Cu	0.32 ± 0.03	20-25	Hfc, 20min 825°C + Foc 2h 800°C + Agc
Fe-0.6Cu	0.63 ± 0.05	20-25	Hfc, 20min 825°C + Foc 2h 800°C + Agc

Hfc: Heated furnace charging. Foc: Furnace-off cooling (0.3°C). Agc: Accelerated gas cooling (20-25°C/s).

Determination of a Relationship $Cu_{free} = f$ (TEP) for Fe-Cu Alloys - To verify that at room temperature, the TEP of ferritic alloys depends strongly on the elements in solid solution, we tried to establish a relationship between the free copper content $[Cu]_{free}$ and the TEP for such alloys. The TEP measurements were carried out on the platelets prepared from the pure iron and the four Fe-Cu alloys [3].

Monitoring of Electron Irradiation Effects on a Fe-Cu Alloy - Electron irradiations were carried out at 290°C on Fe-0.2wt%Cu platelets in a 3 MeV Van de Graaf accelerator [3]. The platelets were irradiated with fluences of 0.1, 0.5, 1, 1.2, 2, 4, 6 or 10 10^{19} e.cm^{-2}. Previous studies [3,7,8-12] have shown that these irradiations induce the formation of copper precipitates, copper-vacancy complexes (about four vacancies with a copper atom), clusters of point defects as well as a decrease of the copper content in solid solution.

For each fluence, TEP and hardness measurements were carried out on the irradiated surface of the platelet after a mechanical grinding with 600 and 800 grit

papers. Hardness measurements were performed with a RZD-D0 Leitz hardness tester using a load of 200 g applied for 15 s.

Monitoring of the Recovery of an Electron-Irradiated Fe-Cu Alloy during Thermal Annealing - In order to assess the interest of the TEP method to monitor the recovery of irradiation damage, annealing treatments were carried out on Fe-0.2wt%Cu platelets electron-irradiated with a fluence of 2 10^{19} e.cm^{-2} [4]. These treatments were performed at 455, 482, 515 or 575°C for times ranging up to 2000 hours (one platelet for each treatment).

After each treatment, the platelet was mechanically ground with 600 and 800 grit papers on the irradiated surface, then hardness and TEP measurements were carried out on it.

Application to a Neutron-Irradiated Pressure Vessel Steel

Monitoring the Neutron Irradiation Effects on a Pressure Vessel Steel - The steel used in this study was the base metal of the C shell of the CHOOZ A reactor pressure vessel [2,13]. The chemical composition of this steel is given in Table 2.

The samples were platelets (20x10x1mm) taken from irradiated and non-irradiated Charpy specimens of the surveillance program of the reactor. For the irradiated specimens, the irradiation temperature was 265°C and the average fluences were: 0.4, 3.3, 9, 13.6 and 14.6 10^{19} n.cm^{-2} (E> 1MeV). In previous studies [3,7,10,11,13-15] it was observed or deduced that such irradiations induced the formation of clusters of solute atoms (Cu, Si, Mn, Ni), copper-vacancy complexes, clusters of point defects as well as an evolution of the chemical composition of the solid solution of the steel (mainly a decrease of the copper content).

TEP and hardness measurements were carried out on each platelet [3].

Table 2 - *Chemical composition of the base metal of the C shell of CHOOZ A reactor pressure vessel.*

C	S	P	Si	Cr	Mo	Mn	Ni	V	Cu
0.16	0.005	0.012	0.32	0.16	0.39	1.26	0.57	0.02	0.09

Monitoring the Recovery of a Neutron-Irradiated Pressure Vessel Steel during Thermal Annealing - In order to determine if the TEP-based method can be used to monitor the recovery of a neutron-irradiated pressure vessel, annealing treatments of 2, 20 or 100 hours at 450°C were carried out on the platelets irradiated with fluences of 0.4, 3, 8.4 or 15 10^{19} n.cm^{-2} (E> 1 MeV). After each treatment, the platelet was mechanically ground with 600 and 800 grit papers, then hardness and TEP measurements were carried out on it [3].

To assess the influence of the annealing temperature on the evolution of the TEP during annealing, additional treatments of 2, 20 or 100 hours at 265°C, 300°C or

350°C were performed on the platelets irradiated with a fluence of 15 10^{19} n.cm^{-2} (E>1 MeV). After each treatment, the platelet was mechanically ground with 600 and 800 grit papers, then TEP measurements were carried out on it [3].

Results

Application to Model Alloys

Determination of a Relationship $Cu_{free} = f(TEP)$ for Fe-Cu Alloys - The results of the TEP measurements carried out on the five materials studied (Fe, Fe-0.1wt%Cu, Fe-0.2wt%Cu, Fe-0.3wt%Cu and Fe-0.6wt%Cu) are shown in Figure 2 versus the free copper contents measured with the atom probe.

In the range of the studied copper concentrations (between 0 and 0.6wt%), it can be noticed that there is a linear relationship between the TEP and the copper content in solid solution:

$$[Cu]^{free}_{wt\%} = 0.43 - 0.14TEP \qquad (3)$$

This result confirms that at room temperature, the chemical composition of the solid solution has a strong influence on the TEP of ferritic alloys. According to the average accuracy on the TEP values (± 0.05 µV/K) and on the copper contents in the five considered alloys, the accuracy on the copper contents given by equation is about ±0.02%.

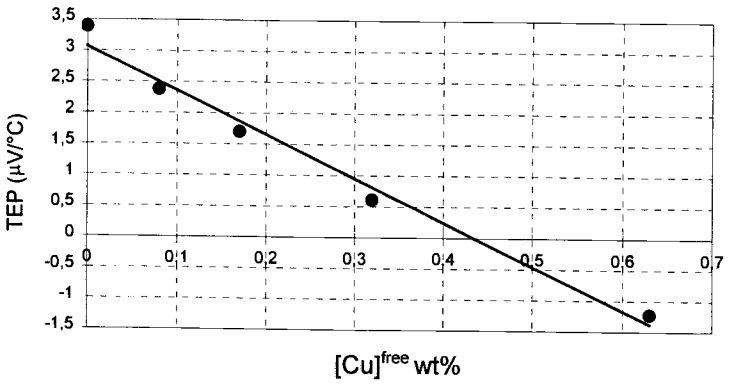


Figure 2 - *Relationship between the free copper content and the TEP of ferritic Fe-Cu alloys.*

Monitoring of Electron Irradiation Effects on a Fe-Cu Alloy - Figure 3 shows the hardness and TEP evolutions of the Fe-0.2wt%Cu alloy versus the square root of the electron fluence. It appears that the two graphs have similar shapes and that they tend

towards a plateau for fluences higher than 4.10^{19}e.cm^{-2}. It therefore seems possible to monitor the effect of electron irradiations by TEP measurements.

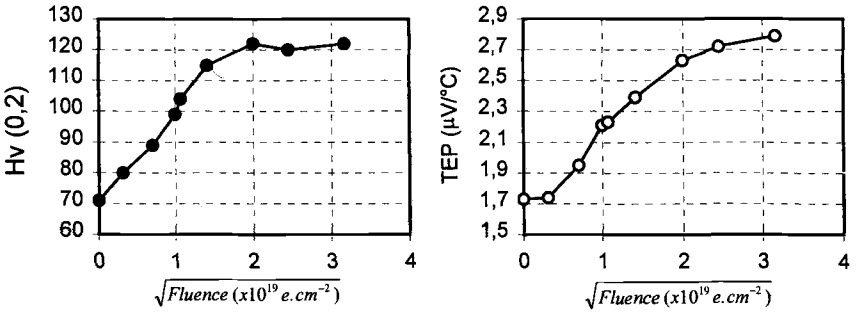


Figure 3 - *Evolution of hardness and TEP of a Fe-0.2wt%Cu alloy after electron-irradiations at 290°C.*

From Figure 3 and equation (3), it is possible to determine the evolution of the free copper in the Fe-0.2wt%Cu alloy during the electron irradiations. This evolution is given in Figure 4 which shows that the copper content does not change significantly until the fluence reaches 0.1 10^{19}e.cm^{-2}, then the copper content decreases rapidly and finally reaches a plateau corresponding to 0.04wt%.

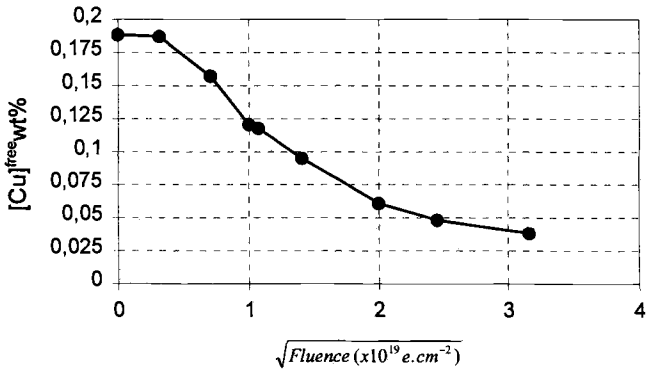


Figure 4 - *Evolution of the free copper in a Fe-0.2wt%Cu after electron irradiations at 290°C.*

In order to determine whether the free copper contents deduced via TEP measurements and equation (3) are correct or not, additional analyses were carried out by atom probe. They were performed on samples (rods) cut from Fe-0.2%Cu platelets in the non-irradiated state or after electron irradiations with fluences of 2 or 10 10^{19} e.cm^{-2}

The comparison of the free copper contents determined by the two techniques is shown in Table 3. The results are in good agreement, which reveals that in this case the TEP evolution is mainly controlled by the copper depletion of the solid solution. Thus, the copper precipitates induced by the electron irradiation have a weak influence on the TEP of the Fe-Cu alloy.

Table 3 - *Free copper content in Fe-0.2wt%Cu alloys unirradiated or irradiated with electrons, comparison of results obtained by TEP measurements and atom probe analyses.*

Fluence ($x10^{19}e.cm^{-2}$)	Copper content in solid solution determined by	
	TEP (wt%)	Atomic Probe (wt%)
0	0,19 ± 0,02	0,19 ± 0,01
2	0,09 ± 0,02	0,12 ± 0,01
10	0,04 ± 0,02	0,04 ± 0,01

Monitoring of the Recovery of an Electron-Irradiated Fe-Cu Alloy during Thermal Annealing - TEP and hardness measurements were carried out on an electron-irradiated Fe-0.2wt%Cu alloy (fluence of 2 10^{19} $e.cm^{-2}$) after annealing treatments at 455, 482, 515 or 575°C. The results are given versus the annealing time in Figure 5.

At each temperature, the hardness and TEP exhibit the same evolution with the annealing time. Therefore, on the basis of TEP measurements, it seems possible to monitor the recovery of electron-irradiated Fe-Cu alloys annealed at temperatures higher than the irradiation temperature.

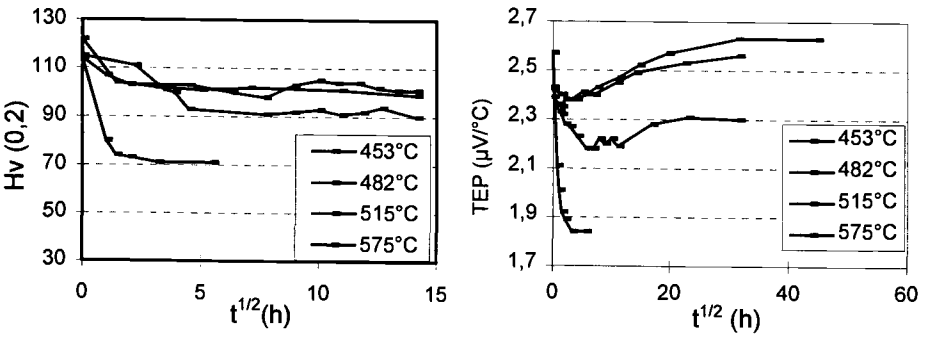


Figure 5 - *Evolution of the hardness and TEP of an electron-irradiated Fe-0.2wt%Cu during annealing treatments.*

As above, the evolution of the copper content in the solid solution during the

annealing treatments was determined from equation (3) and the TEP measurements. The results are shown in Figure 6.

- At 575°C, the free copper content increases rapidly and seems to stabilize at a value of approximately 0.17wt%, which is almost the nominal copper content of the alloy.
- At 515°C, the free copper content increases slower. For the longest annealing time, it seems to tend towards a value of 0.11wt% via a transit at a maximum value of 0.12wt% after about 90 hours of annealing.
- At 482 and 455°C, the free copper content decreases during annealing, which indicates a thermal copper precipitation. The free copper content tends towards 0.07 and 0.06wt%, respectively, after a 1000 hour holding time.

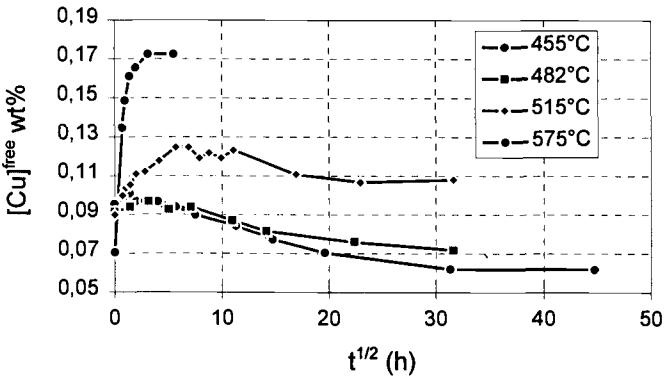


Figure 6 - *Evolution of the free copper content in an electron-irradiated Fe-0.2wt%Cu during annealing treatments.*

Application to the Limit of Copper Solubility in Iron - The limit of copper solubility in α iron is poorly known at temperatures below 600°C. It is possible to assess this solubility from the free copper contents we have determined in the electron-irradiated Fe-0.2%Cu alloy after annealing treatments. Indeed, at each annealing temperature (575, 515, 482 and 455°C), the free copper content tends over time towards a value (Figure 5) that can be considered as the solubility limit (C_e) of copper in iron at the considered temperature.

Figure 7 shows the evolution of the Naperien logarithm of C_e (in wt%) versus the inverse of the temperature T (in Kelvin). Two results determined elsewhere [16,17] at 650°C and 550°C are also shown in this figure. It can be noticed that all results are coherent. In the range of temperature under consideration, the copper solubility evolves with the temperature according to the following equation:

$$\text{Ln}\,(Ce/100) = 0.184 - 5560 / T \qquad (4)$$

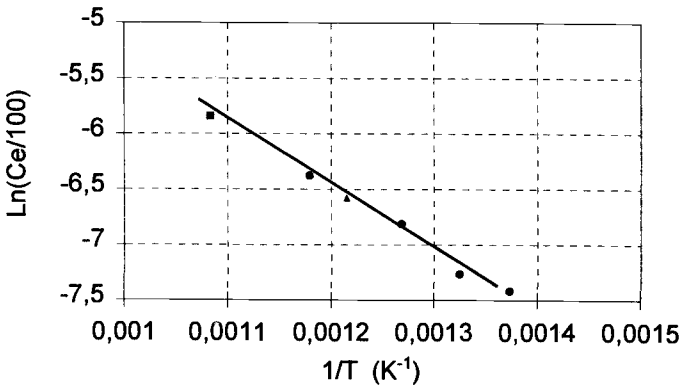


Figure 7 - *Limit of copper solubility in iron*

Application to Neutron-Irradiated Pressure Vessel Steel

Monitoring the Effects of Neutron Irradiation on a Pressure Vessel Steel - The results of the TEP and hardness measurements carried out on the neutron-irradiated base metal of CHOOZ A (fluences: 0.45, 3.1, 8.5, 15.2 10^{19} n.cm^{-2}) are shown in Figure 8.

A significant increase in TEP with the fluence is observed (+1.55 μV/°C for the highest fluence). It can also be noticed that the TEP and hardness evolutions with the fluence are very similar. Based on this correlation, it seems possible to monitor the effects of neutron irradiation on pressure vessel steels by TEP measurements.

For such an industrial steel, it is yet difficult to determine which part of the neutron-induced damage is at the origin of the evolution of the TEP during irradiation.

Monitoring the Recovery of a Neutron-Irradiated Pressure Vessel Steel during Thermal Annealing

• *Annealing at 450°C - Effect of the Fluence*: As a first step, a non-irradiated platelet was annealed at 450°C with different holding times. For each of them, a TEP measurement was carried out on the platelet. After 500 hours in temperature, no change in the TEP value was noticed, which demonstrates the structural stability of the steel at this temperature. Thus, the TEP evolution measured on the irradiated steel during annealing at 450°C will only be imputed to the recovery of the irradiation-induced damage.

Figure 9 shows the results of TEP and hardness measurements carried out on the platelets irradiated with fluences of 0.45, 3.1, 8.5 or 15.2 10^{19}n.cm^{-2} and annealed at 450°C for 2, 20 or 100 hours. During the annealing, the TEP of the irradiated alloy decreases and reaches its initial value by about 100 hours, whatever the fluence. The

graphs obtained are similar to those describing the recovery of the hardness.

Therefore, at 450°C it seems possible to use the TEP measurement in order to monitor the recovery of neutron-irradiated pressure vessel steel during annealing treatment.

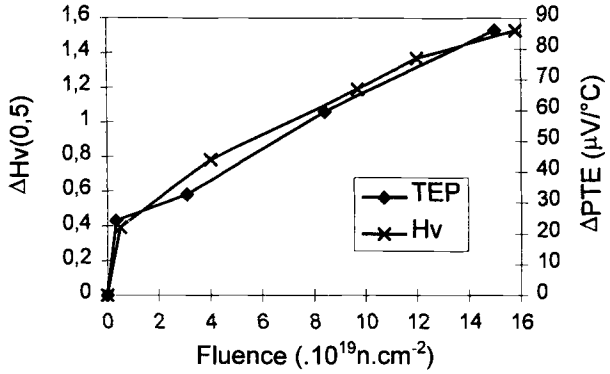


Figure 8 - *Evolution of hardness and TEP with the fluence for the base metal of the C shell of the CHOOZ A reactor vessel.*

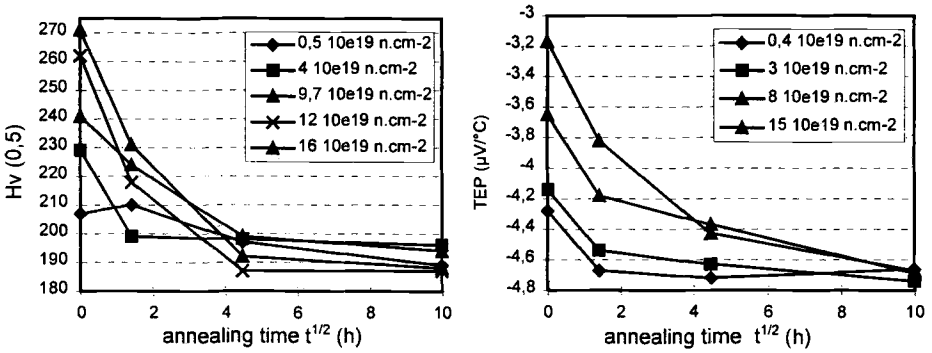


Figure 9 - *Base metal of the C shell of the CHOOZ A reactor vessel : evolution of hardness and TEP during annealing at 450°C - influence of the fluence on the recovery.*

• *Annealing at 265°C, 300°C and 350°C - Effect of the Temperature:* Figure 10 shows the evolution of TEP during annealing at 265°C, 350°C, 400°C or 450°C for platelets irradiated with fluence in the order of 15 10^{19} n.cm^{-2}.

At 265°C, 300°C and 350°C, the TEP value decreases slightly with the holding time in temperature. This decrease becomes more important at higher temperatures.

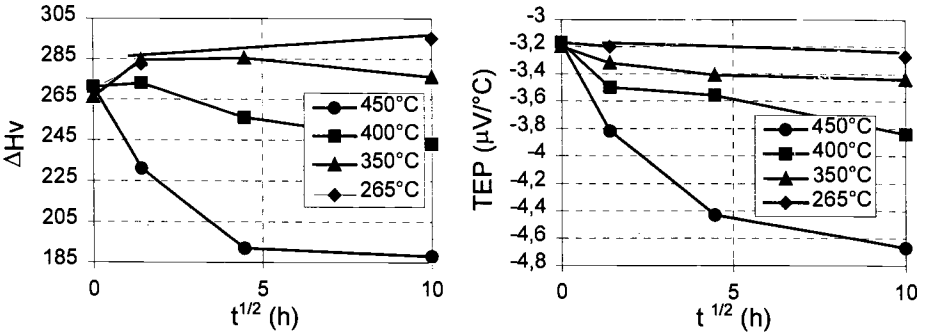


Figure 10 : *Base metal of the C shell of the CHOOZ A reactor vessel irradiated with a fluence of 15 10^{19} n.cm^{-2}: evolution of TEP during annealing - influence of the annealing temperature on the recovery.*

Conclusion

It has been shown that the measurements of the thermoelectric power (TEP) allows both the monitoring of the effects of electron irradiations in model Fe-Cu alloys and the monitoring of neutron irradiations on industrial pressure vessel steels. The recovery of these irradiation effects during annealing treatments can also be followed with the proposed method.

On the basis of the results obtained on Fe-Cu alloys, it was possible to propose a law to determine the limit of copper solubility in iron at temperatures below 600°C.

References

[1] Brillaud, C., Hedin, F., "In-Service Evaluation of French Pressurized Water Reactor Steel," Effects of Radiation on Materials: ASTM STP 1125, Stoller R.E., Kumar A.S., Gelles D.S., Eds ASTM, Philadelphia, 1992, 23-49.

[2] Brillaud C., "Centrale de Chooz - Cuve de Réacteur ; Surveillance de la Tenue du Matériau à l'Irradiation - Synthèse des Résultats acquis à ce Jour," Technical Report EDF-SCMI D.5004/BRD/R 88.07, Electricité de France, 1998.

[3] Miloudi, S. , "Etude du Dommage d'Irradiation dans les Aciers de Cuve des Réacteurs à Eau Pressurisée," Doctoral Thesis, Université Paris XI, Octobre 1997.

[4] Leborgne, J. M., "Appareil de mesure locale du pouvoir thermoélectrique,

application au contôle du vieillissement thermique des aciers inoxydables austénoferritiques moulés des réacteurs à eau pressurisée," Doctoral Thesis, INSA de Lyon, 1996.

[5] Borelli, R., Merle, P., Adenis, D., "Seebeck Effect Study of Precipitation," Light Metals 1989, Ed. Paul G.Campbell, The Minerals, Metals and Materials Society, 1988.

[6] Borelli, R., "Applications des mesures de pouvoir thermoelectrique à l'étude des alliages metalliques," Mémoires Scientifiques, Revue Métallurgie, 1979.

[7] Pareige, P., "Etude à la Sonde Atomique de l'Evolution Structurale sous Irradiation d'Alliages Ferritiques FeCu et d'Aciers de Cuve de Réacteurs Nucléaires," Doctoral Thesis, University of Rouen, 1994.

[8] Mathon, M.H., "Etude de la Précipitation et des Mécanismes Microscopiques de Durcissement sous Irradiation dans les Alliages Ferritiques Dilués," Doctoral Thesis, University of Orsay, 1994.

[9] Akamatsu, M., "Evolution Structurale d'Alliages Ferritiques sous Irradiation," Doctoral Thesis, Université Paris XI, Octobre 1994.

[10] Auger, P., Pareige, P., Akamatsu, M., Van Duysen, J.C., "Microstructural Characterisation of Atom Clusters in Irradiated Pressure Vessel Steels and Model Alloys," Journal of Nuclear Materials, 211, 1994, pp. 194-201.

[11] Miloudi, S., Van Duysen, J.C., "Study of the Mechanisms of Solute-Clustering in Pressure Vessel Steels," Seventh International Symposium on Environmental Degradation of Materials in Nuclear Power Systems-Water Reactor, Breckenridge (Colorado), August 7-10, 1995, p.1179.

[12] Akamatsu, M., Van Duysen, J.C., Pareige, P., Auger, P., "Experimental Evidences of Several Contributions to the Radiation Damage in Ferritic Alloys," Effects of Radiation on Materials, American Society for Testing and Materials, 1995.

[13] Van Duysen, J.C., Bourgoin, J., Janot, C., Penisson, J.M., "Evolution of the Microstructure of PWR Pressure Vessel Steels from the CHOOZ A Reactor Surveillance Program after Long-Term Irradiations," ASTM STP 1125, Stoller R.E., Kumar A.S., Gelles D.S., Eds ASTM, Philadelphia, 1992, pp. 117.

[14] Van Duysen, J.C., Bourgoin, J., Moser, P., Janot, C., "Study by Positrons Annihilation of Neutron Damage in a PWR Pressure Vessel Steel after a 13-year Irradiation in the CHOOZ A Reactor Surveillance Program," AIEA

Specialist's Meeting on "Radiation Embrittlement of Nuclear Reactor Pressure Vessel Steels", Baltonfüned, Hungary, ASTM-STP 1170, 1990.

[15] Pareige, P., Van Duysen, J.C., Auger, P., Appl. Surf. Sci. 67, 1993, p.342.

[16] Salje, G., J. Appl. Phys., 48, 1977, P. 1833.

[17] Kenway-Jackson, A. J., Mace, J., Thomas, R. N., Phythian, Technical Report AEA-RS 4411, AEA Technology, Harwell, UK, 1993.

Josef Mittendorfer[1]

Design of a Dedicated Electron Beam Facility for Material Treatment

Reference: Mittendorfer, J., **"Design of a Dedicated Electron Beam Facility for Material Treatment,"** *Effects of Radiation on Materials: 19th International Symposium, ASTM STP 1366,* M. L. Hamilton, A. S. Kumar, S. T. Rosinski, and M. L. Grossbeck, Eds., American Society for Testing and Materials, West Conshohocken, PA, 2000.

Abstract: Electron beam has been applied as source of ionizing radiation in a wide field of applications. Sterilization, decontamination, treatment of materials for cross-linking, curing, and polymerization have been carried at an industrial scale.
Interest in material treatment with accelerated electrons increased significantly over the last years. Especially industrial strength electron accelerators with energies up to 10 MeV make it possible to process with increased penetration depth, and offer new opportunities in electron curing of polymer matrix composites (PMC) and cross-linking.

10 MeV accelerators are currently used mostly in contract facilities such as sterilization of medical devices and material treatment. Therefore these facilities are not optimized for material processing tasks and thus less efficient and versatile.

In this paper requirements and design guidelines for a dedicated material processing facility are discussed.

Keywords: Electron beam irradiation, electron beam facility, linear accelerator

[1] Consultant, Mediscan GmbH, Bad Haller Straße 34, A-4550 Kremsmünster, Austria.

Copyright© 2000 by ASTM International www.astm.org

Building Blocks of an Electron Beam Facility

The main modules of an electron beam facility are:

a) Electron Accelerator
b) Material Handling
c) Facility and Process Control
d) Quality Assurance

Requirements and design guidelines are discussed in the following sections.

Electron Accelerator

An electron beam accelerator is used to deposit a dose of ionizing radiation to the product. The choice of radiation (high energy electrons, low energy electrons or Bremsstrahlung-Gammas), depends on the application and effect looking for.

For semiconductors only the electron dose is of major concern, whereas in applications like polymerization come along with any form of ionizing radiation [*1*]. In this paper only high energy electron accelerators with nominal energy up to 10 MeV are discussed. With these machines it is possible to cure thick layers and treat products in their original shipping container.

Industrial accelerators can be divided into two categories:

- pulse power machines
- continuous power machines.

In pulse power linear accelerators, electrons are introduced in short bursts, with a pulse length in the order of tenth microseconds, and with a frequency of several hundred pulses per second.

The average beam current is calculated by averaging the pulse peak current.

$$I = RR. \int_0^{1/RR} i(t)dt = RR.i_{\max}.PW$$

where

i_{max} Peak Pulse Current
RR Pulse Repetition Rate
PW Pulse Length

The product of average beam current and the electron energy determines the average beam power, which is usually in the range of 15 to 150 kW.

Continuous power accelerator deliver a constant beam current. While the average dose may be the same, the dose rate in the millisecond level is much higher in the case of pulsed linear accelerators.

The dose range for material processing is huge compared to sterilization of medical devices. The doses can be in the range of hundreds of kilogray as in the case of Teflon degradation, down to hundreds of grays for certain semiconductor application.

The huge dose range is a big challenge for the accelerator design. To vary the dose delivered by a linear accelerator many parameters can be tuned, such as:

- Processing speed of the product in the beam
- Increasing the scan width
- Lowering the beam current
- Reducing the pulse width
- Lowering of the pulse repetition rate

The first two parameters are easy to change in an industrial process, but the other parameters require more effort and cannot be changed easily by design. Especially the lowering of the pulse rate can be critical for some machine types. Interlocks have to be set to avoid a damage of the machine.

The dose rate determines the amount of radiation energy delivered to the product mass per second and is an important parameter for the polymerization process. It is affected by the above mentioned parameters.

The maximum dimension of the target area, determines the desired scan width. In the case of industrial polymer irradiation scan horns from 60 cm to several meters are used.

The beam direction can be vertical, where the products are irradiated from top to down, or horizontal where the products are irradiated from the side.
Newer designs can have double scan possibilities, with two scan horns and a kicker magnet. Beam splitting also can be used at a pulse per pulse level.

The useful range of electron treatment is determined by the primary energy and the density of the material. The useful range r of electrons is commonly estimated by [*2*]

$$r = \frac{E}{3 \cdot \rho}$$

Where E is the initial electron energy in MeV and ρ is the density in g per cm^3. For a density of 1.5 gcm^{-3} and 10 MeV this leads to a range of about 2.2 cm.

If this range of treatment is not sufficient, it may be further extended by x-ray conversion using a high-Z target. Problems arise with the low conversion ratio to bremsstrahlung, reflection to the scan horn and heat removal (about 75 % of the primary energy) from the target. Neutron production has to be carefully evaluated and accounted for in the radiation protection plan.

Material Handling

The material handling system has to accomplish a couple of tasks:

- Fast delivery of the product into the irradiation vault
- Controlled movement through the scanned beam with maximum beam utilization
- Optional turning of the product for double- or multi-sided irradiation
- Fast delivery to the unloading station

The design of the material handling is determined by the type of product, whether there are bulky single parts or items packed in cardboard boxes.

For boxes horizontal beams are favorable, since simple and efficient turning units can be designed. To deliver very high doses with a medium power accelerator, a multi-pass-feature of the material handling system is desirable. In such a system the operator determines the number of passes through the beam. The irradiation process is then performed fully automatic.

When roller conveyors are to be used, easily transportable fixtures to which the products are attached are needed. Their materials and design has to be carefully evaluated for radiation degradation and beam interference.

Facility

In the design of the irradiation vault a principal decision has to be made: do the dimensions of the products allow a transport through a maze or are doors or removable parts in the shielding necessary ?

Keeping in mind the dimension of a concrete primary shielding of 3 to 4 meters, the costs for radiation protection doors are very high. But for a full scale electron beam facility dedicated to material processing easy access for bulky items and a large chamber volume are inevitable.

Industrial electron beam processing is a challenging enterprise. A technically complex process has to be handled with high efficiency to meet the cost and throughput expectations of the industry.

A fully computerized factory control system which interfaces and controls the accelerator, material handling, safety and facility subsystems with minimal operator interference is very desirable and inevitable from the economic point of view. Wrapping the irradiation process with a state-of–the-art process control is crucial but within the scope of existing technologies.
Remote servicing and trouble shooting via the Internet is a feature which can be easily applied to electron beam facilities.

Quality Assurance

Highly developed standards and regulations [*3*] are applicable for the radiation sterilization of medical devices and contract radiation sterilization companies are very well prepared to meet them.

Among these procedures are the recording of critical machine parameters, a dosimetry system traceable to a national standard, and validated, well maintained software.

Applying these standards to the industrial irradiation of polymers can be valuable since they may be a criteria for clients when choosing a contract facility or even necessary to cope with the quality policy of the client.

To keep the costs of quality assurance acceptable, test and measurements have to be fully automated with minimal operator inference. A factory data base system, where all facility data are accumulated, is crucial for an effective and lean data and document management. A local area network or intranet solutions help to cut costs and transfer information between divisions.

Conclusion

Keeping in mind the diversity of industrial applications of electron irradiation, an universal design scheme is outlined. Evaluating the application, required dose, dose rate, and product dimension, the principal building blocks may be optimized and constructed as interchangeable modules in the design process.

However the use of state-of-the-art process control techniques and the adoption of procedures and standards developed for quality assurance in the medical device industry are crucial in any facility design. This will enhance the usage of industrial electron beam irradiation even more attractive for the industry.

Acknowledgement

The author would like to thank the Mediscan team for valuable discussions. Work supported in part by the Austrian "Forschungsförderungsfond der Gewerblichen Wirtschaft"

References

[1] Zyball, A., "Crosslinking of Plastics by Means of Ionising Radiation – Industrial Use," BGS Beta-Gamma-Service , D-51647 Wiehl, Germany

[2] Woods, R.J. and Pikaev, A.K., "Applied Radiation Chemistry," A Wiley-Interscience Publication, 1994

[3] ISO 11137, "Sterilization of Health Care Products – Requirements for Validation and Routine Control - Radiation Sterilization," International Organization for Standardization, Geneve, Switzerland, 1995

Beryllium and Ceramics

David S. Gelles,[1] Mario Dalle Donne,[2] Hiroshi Kawamura,[3] Somei Ohnuki,[4] and Francesco Scaffidi-Argentina[2]

Microstructural Examination of Irradiated Beryllium Pebbles

Reference: Gelles, D. S., Dalle Donne, M., Kawamura, H., Ohnuki, S., and Scaffidi-Argentina, F., **"Microstructural Examination of Irradiated Beryllium Pebbles,"** *Effects of Radiation on Materials: 19th International Symposium, ASTM STP 1366,* M. L. Hamilton, A. S. Kumar, S. T. Rosinski, and M. L. Grossbeck, Eds., American Society for Testing and Materials, West Conshohocken, PA, 2000.

Abstract: Commercially available beryllium pebbles have been irradiated to approximately $4x10^{22}$ n/cm^2 (E > 0.1 MeV) at 380°C in the EBR-II. Microstructural examination has now been performed on pebbles 3 mm in diameter manufactured by Brush Wellman, USA and contained in that experiment. This paper describes optical, scanning electron and transmission electron microscopy of these pebbles. It was found that the major effect of irradiation was formation of small, highly non-equiaxed bubbles. The bubbles were thin disk shapes lying on the basal plane.

Keywords: Beryllium, microstructure, bubbles, neutron irradiation

Introduction

Beryllium pebbles are being considered in fusion reactor blanket designs for the neutron multiplier [1,2]. The blanket is intended to provide a source of available tritium fuel. The solid breeder blanket design is based on tritium transmutation from lithium. However, in order to optimize tritium production, it is found necessary to use beryllium as a neutron multiplier such that beryllium constitutes as much as 75% of the blanket volume. Examples are the European "Helium Cooled Pebble Bed Blanket" and the International Thermonuclear Experimental Reactor [2]. Several

[1]Staff Engineer, Structural Materials Research, Battelle Pacific Northwest National Laboratory,* Richland, WA 99352.
[2]Forschungszentrum Karlsruhe, INR, D-76021 Karlsruhe, Germany.
[3]JMTR, Oarai Establishment, JAERI, Oarai-machi, Kbaraki-ken 311-13, Japan.
[4]Hokkaido University, Sapporo 060, Japan.
*Operated for the U.S. Department of Energy by Battelle Memorial Institute under Contract DE-AC06-76RLO 1830.

Copyright© 2000 by ASTM International www.astm.org

forms of inexpensive beryllium pebbles are commercially available that would be useful for a solid breeder blanket design, but little is known about these forms in response to fast neutron irradiation.

A large number of beryllium specimens have been irradiated in joint US DOE Office of Fusion Energy Sciences/Monbusho experiments in the Experimental Breeder Reactor II (EBR-II) in Idaho Falls, ID and the Fast Flux Test Facility (FFTF) in Hanford, WA. Due to lack of funding, most of those specimens have never been tested, but DOE and Monbusho still retain an interest in the results. With the increased difficulty for performing irradiation experiments, due in part to the shut down of FFTF and EBR-II and other reactors worldwide, these specimens are becoming very valuable. The German fusion materials development program centered at Forschungszentrum Karlsruhe INR has been concentrating efforts on design of a fusion blanket, using beryllium pellets, an inexpensive intermediate product in the production of high grade beryllium, as a neutron multiplier. An EBR-II test, called COBRA-1A, included four beryllium pebble product forms, and thereby provides fast neutron irradiated materials for postirradiation testing. Therefore, Forschungszentrum Karlsruhe INR has concluded that it is efficient use of their available funds to invest in the testing of some of these specimens. A part of that program is intended to characterize beryllium pebbles irradiated in the COBRA-1A experiment, including density change measurement, microstructural examination, helium and tritium release response on heating and neutronic analysis. Other parts include efforts to estimate and measure helium and tritium production and release, and to make available other beryllium specimens irradiated in the FFTF [3-4]. This report is intended to describe the microstructures of the 3 mm pebbles, including optical, scanning electron and transmission electron microscopy examinations and a companion paper in this proceedings describes helium production estimation and production and release measurements. The 3 mm pebbles were chosen for the present work because they could be most easily processed into the standard geometry used for transmission electron microscopy (TEM): 3mm TEM disks.

Experimental Procedure

EBR-II

Details concerning the COBRA-1A irradiation vehicle and associated dosimetry are provided in Reference [4]. The vehicle included two beryllium containing capsules, canisters C03 and DO3 with beryllium in several product forms: 1 mm pebbles, 3 mm pebbles, 5 mm pebbles, 7.6 mm diameter x 20 mm right cylinders and 7.7 mm diameter x 6 mm right cylinders. (The cylinders were of two densities, 100% and 97% and were used for other purposes [5]). Pebbles were from two sources, Brush Wellman in all sizes and Nippon Gaishi Co. (NGK) at 1 mm. This report only describes results for the 3 mm pebbles from Brush Wellman contained in the C03 canister. Details for the 3 mm pebbles, as supplied by the manufacturer are provided in Table 1.

About 75 3 mm pebbles were irradiated. Because reactor neutron flux varied as a function of vertical position, minor differences in dose developed for the 3 mm

Table 1. *Pebble details*

Type	Supplier & Batch #	Size	Major Impurities	Minor Impurities (in ppm)
3 mm	Brush Wellman 826-64-3	3 mm -6 +7 mesh	0.020 wt% BeO 0.038 % C 0.013 % O_2	2400 Mg, 375 Al, 370 Fe, 250 Si, 105 Zr, 90 Mn, 85 Cr, 85 Zn, 75 Ti, 65 Ni, etc.

pebbles in C03. Accumulated fluences were estimated based on capsule position and information in reference [2], giving a mean of 4.31×10^{22} n/cm^2 (E > 0.1 MeV). The operating temperature was estimated as 379°C and is therefore described as 380°C in the remainder of this report.

Experimental Results

Optical Microscopy (OM) and Scanning Electron Microscopy (SEM)

In order to gain an understanding of pebble to pebble conformity and determine surface degradation due to irradiation, several specimens were selected for optical examination and one pebble of each of the irradiated and unirradiated conditions was then examined by SEM. Figures 1 and 2 provide optical microscopy examples; in each case a pebble is shown from different directions, first in focus at the diameter and then on the top surface. Both figures demonstrate that beryllium pebbles vary significantly in size and many contain surface irregularities, including depressions and seams.

The results of SEM examination are provided as stereo pairs in Figures 3 and 4. The unirradiated specimen was #3 shown in Figure 1 and the irradiated specimen was #6 shown in Figure 2. Tilt between stereo pairs was 7° so that quantitative depth measurements can be obtained for surface features of interest. Comparisons between Figures 3 and 4 reveal that both specimens contain two types of shallow surface depressions, on the order of 100 μm in diameter and on the order of 5 μm in diameter, and specimen #6 has many particles adhered to the surface. The adhered particles are assumed to be dust and dirt accumulated during handling, and therefore both samples contain similar features. Evidence for fine surface porosity due to irradiation was not found.

Swelling in 3 mm pebbles

Four irradiated pebbles from the C03 capsule were selected for density measurement and compared with four unirradiated specimens. Specimens were weighed in air and in water at least three times, until reasonable consistency was obtained because imperfect wetting and air bubble adherence were found to be problems. The results of the measurements are listed in Table 2 so that the density

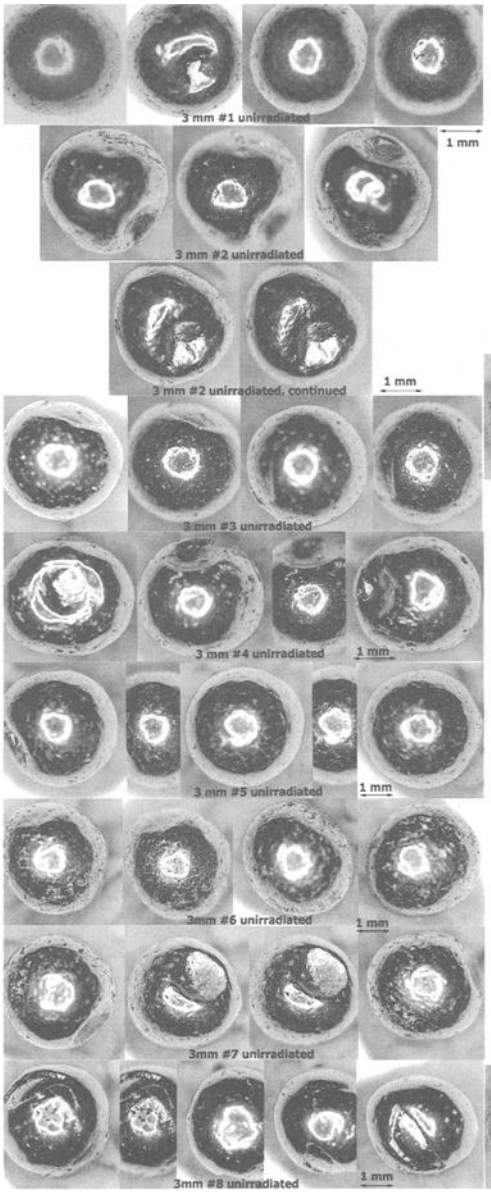


Figure 1. *Optical photomicrographs of unirradiated beryllium pebbles showing several views at different focus of each pebble.*

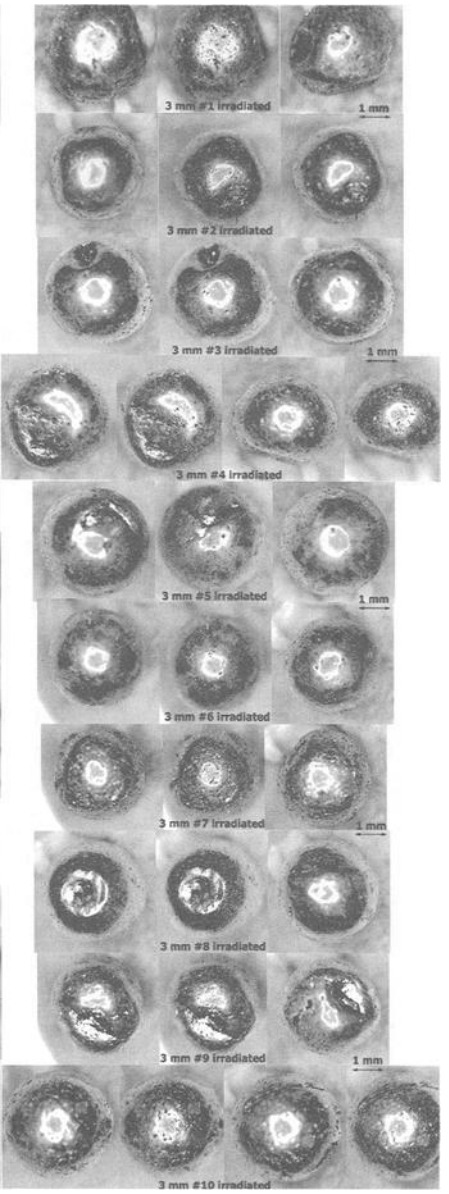


Figure 2. *Optical photomicrographs of irradiated beryllium pebbles shown similarly.*

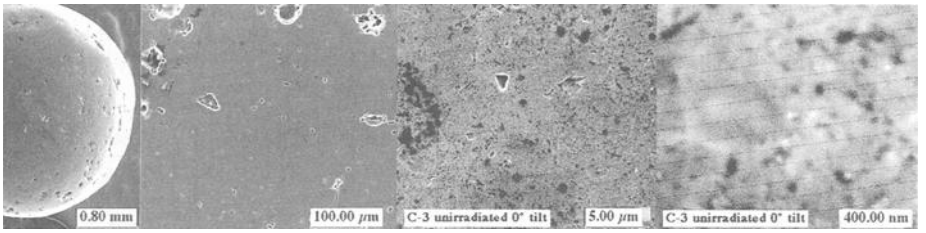


Figure 3. *SEM photomicrographs of unirradiated 3 mm beryllium pebble #3 showing the surface features at increasing magnification.*

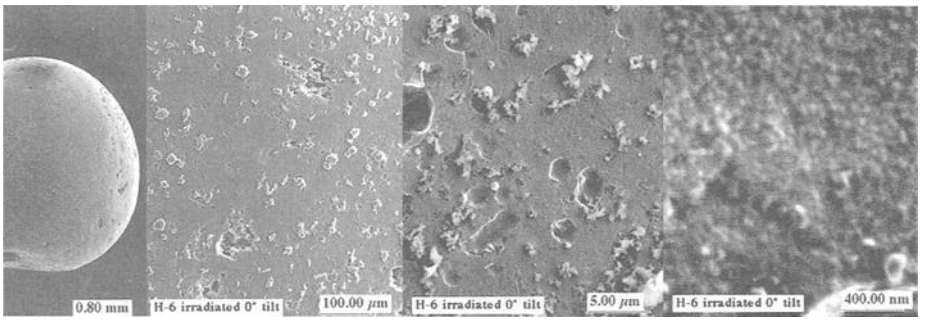


Figure 4. *SEM photomicrographs of irradiated 3 mm beryllium pebble #6 showing the surface features at increasing magnification.*

following irradiation (V) was found to be 1.79474 $\pm$ 0.01130 and the unirradiated density (V_0) was 1.80969 $\pm$ 0.03370. The resultant swelling $(V-V_0)/V_0$ was 1.45%, of the same magnitude as the uncertainty for the unirradiated density (1.86%) but larger than the uncertainty for the irradiated density (0.6%). The large uncertainties may either be due to the surface conditions (bubble adherence) or variations in impurity concentrations within the pebbles. However, given the larger scatter in the unirradiated samples, the latter cause is more likely.

Transmission Electron Microscopy (TEM)

Several 3 mm pebbles were ground to disks approximately 0.12 mm thick and thinned by electropolishing in a solution of 75 parts nitric acid, 15 parts sulfuric acid, 15 parts hydrochloric acid in 750 parts ethylene glycol at 9 to 13 V with the solution cooled to -20°C. Pitting presumed to be due to internal flaws was found to be a problem, but suitably thin areas were obtained in several specimens prepared for examination following brief repolishing of pitted specimens. Two unirradiated specimens (#4, #8) and two irradiated specimens (#1, #7) were thinned and polished providing one good specimen #1 and one poor specimen #4 with #7 providing sufficient thin area to confirm observations on specimen #4.

Examinations revealed several noteworthy features. In the irradiated specimens, grain size was found to be large, with a low dislocation density but

Table 2 *Density measurements for 3 mm pebbles.*

Sample	Condition	Density g/cm^2	Standard Deviation
1	380°C, 4.31x10^{22} n/cm^2	1.78818	± 0.02987
2	"	1.8114	± 0.0096
3	"	1.79206	± 0.02958
4	"	1.7873	± 0.02691
5	unirradiated	1.83124	± 0.02032
6	"	1.77046	± 0.01331
7	"	1.8435	± 0.0152
8	"	1.79354	± 0.00661

containing many small features tentatively identified as bubbles lying as plate-like features on the basal plane. Several examples were also found of large regions as big as 5 μm in diameter with amorphous diffraction patterns. Such regions were found to be rich in Si, Al, Mg and Mn, indicating that impurities were non-uniformly distributed and that the impure regions became amorphous due to irradiation. In comparison, the dislocation density was greater in the unirradiated condition, with evidence of subgrain development. Also, a region containing impurity was found. Therefore, irradiation is found to reduce the dislocation density significantly, to form a fine distribution of unusually shaped bubbles and to amorphize large regions of impurity.

Examples of the structure found prior to irradiation are shown in Figure 5. Figure 5a shows a region at low magnification, with several subgrains clearly defined, and with an elliptical region near the top believed to be a region of impurity. The dislocation structure is shown in dark field in Figure 5b. The dislocation density within grains is low, but subgrain boundaries are quite well defined.

Examples of the structure found following irradiation are shown in Figures 6, 7, and 8. The dislocation structure is shown in Figure 6a showing a region in bright field and Figure 6b, another region in dislocation dark field contrast. the bright field image demonstrates a loose tangle of dislocations, whereas the dark field image also shows a high density of smaller features in weaker contrast. Previously, these weaker features had been identified as c-type dislocation loops [3]. However, when the foil was tilted to bring these weaker features edge-on, they were found to image as cavities. A sequence is provided in Figure 7 using void contrast showing these features edge-on in (a), tilted off 7° in (b) and tilted off 12° in (c). Figure 7d provides the unusual situation where the features are shown in strong contrast with the features tilted edge-on and demonstrates that the features are probably internally stressed. It can therefore be concluded that the weaker features are probably unusually shaped helium bubbles, the planar surfaces of which can be imaged weakly

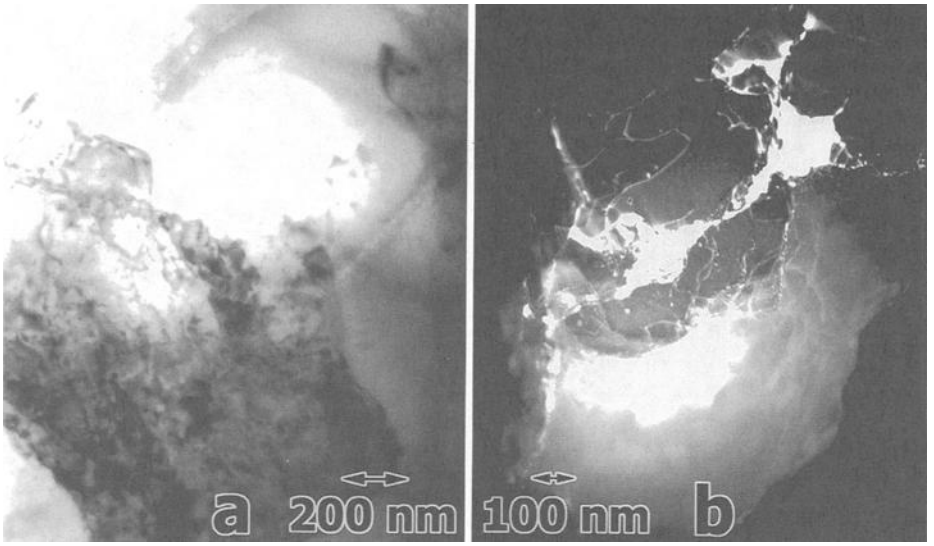


Figure 5. *Microstructures in an unirradiated 3 mm beryllium pebble showing a) a region containing subgrain structure and a large region of impurity and b)* $\vec{g}=11\bar{2}0$ *dislocation dark field contrast.*

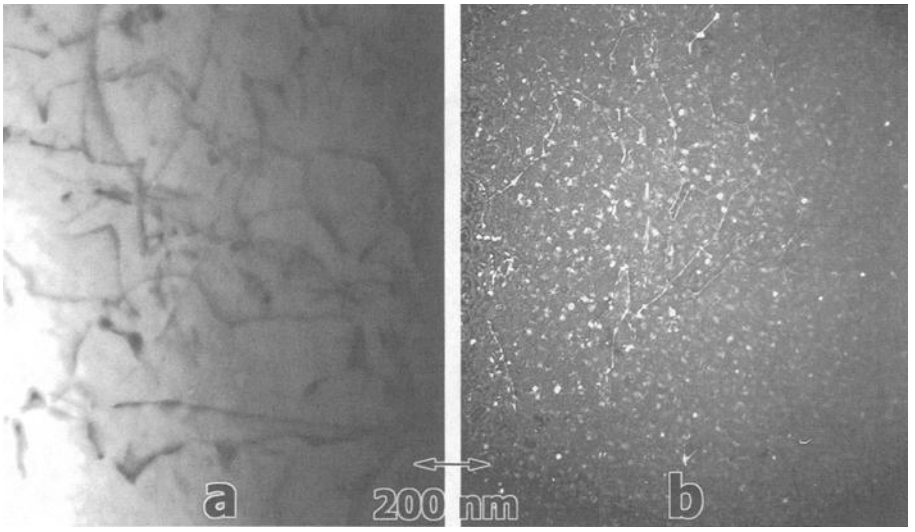


Figure 6. *Microstructures in an irradiated 3 mm beryllium pebble showing the dislocation structure in bright field* $\vec{g}=11\bar{2}0$ *contrast in a) and dark field* $\vec{g}=0002$ *contrast in b).*

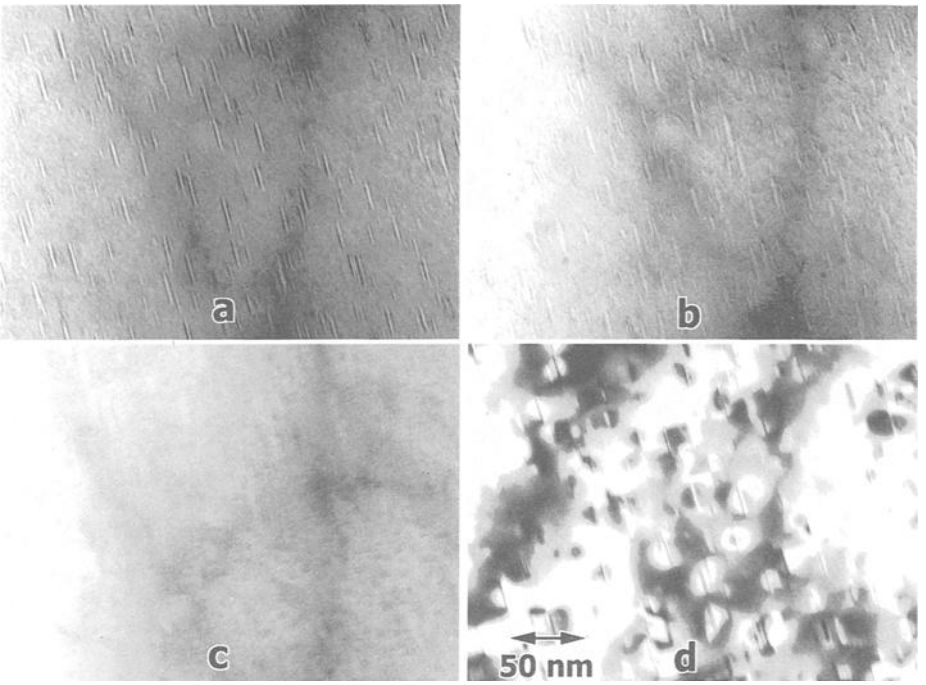


Figure 7. *Gas bubbles in an irradiated 3 mm beryllium pebble tilted parallel to the basal plane so that the cavities are edge-on in a), tilted off 7° in b), tilted a further 5° in c) and shown edge-on in strong multibeam contrast in d).*

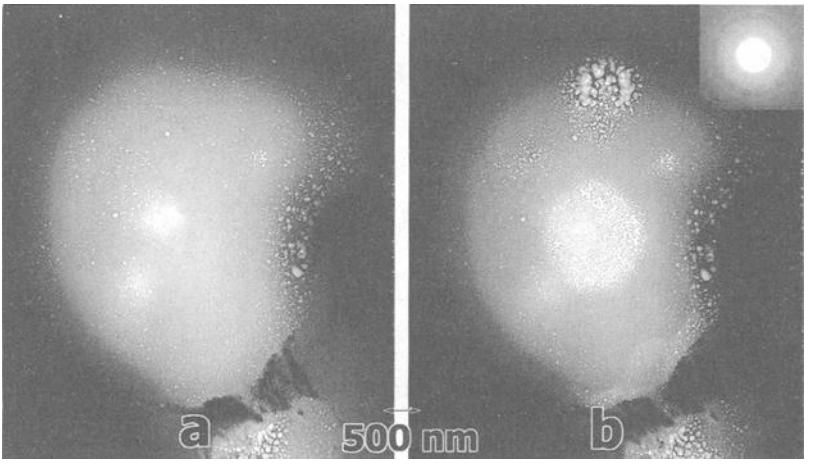


Figure 8. *A low magnification example of amorphous regions in an irradiated 3 mm beryllium pebble early a) and late b) in the examination showing that electron beam damage occurs.*

in dislocation contrast. Figure 8 at low magnification shows an area containing two amorphous regions of impurity taken early and late during examination. The amorphous region is found to be damaged by the electron beam, allowing blistering and crystallization, with more beam damage apparent later during examination. An example of an amorphous diffraction pattern is inset.

Discussion

Effects of Irradiation on Microstructure

It was previously assumed that irradiation would cause microporosity, and c-type loop formation. The added complexity of neutron damage near pebble surfaces was expected to enhance transmutation possibly leading to enhanced surface microporosity. The present SEM examination appears to indicate that surface roughening due to irradiation is negligible to resolutions on the order of 100 nm. TEM did not provide microstructural information regarding cavitation at grain boundaries, but it now appears that swelling in the form of helium bubbles takes on an unusual highly non-equiaxed geometry of thin platelets on the basal plane. Bubbles are approximately 25 nm in diameter and 4 nm in thickness. These features had not been identified previously as bubbles, perhaps because the helium levels were lower, estimated at 80 appm helium following irradiation at 400°C to 8 dpa ($1.8x10^{22}$ n/cm^2) below core in FFTF. In the present experiment, the fluence was approximately $4.3x10^{22}$ n/cm^2 below core in EBR-II, a similar reactor, and therefore the helium level is expected to be about 3 times larger, and is estimated at 3000 appm. It can be noted that the earlier experiment produced significantly coarser damage structure, possibly because the irradiation temperature was higher. Careful review of the earlier micrographs shows examples of contrast similar to that found in the present experiment. An example is provided in Figure 9, which shows a view of the basal plane edge-on, similar to that shown in Figure 7a but with higher strain contrast approaching that in Figure 7d. The differences in interpretation may be compatible if it is possible that c-type loops accumulate gases such as helium and tritium, eventually becoming highly anisotropic bubbles. Figure 9 therefore represents a lower level of helium present in the bubble than for the condition in Figure 7. It can be noted that work by Chernikov and co-workers on 15 KeV He ion irradiation of beryllium at 700K did not show similar bubble features. Instead bubbles were much larger, with faceted sides and apparently without the large aspect ratio [7].

The bubbles were measured to provide diameter, number density and an estimate of swelling. It was found that the bubbles ranged in diameter from 5 to 25 nm, with a mean diameter of 11.9 nm at a number density of $2.0x10^{16}$ cm^{-3}. If one were to assume spherical voids with these diameters, this corresponded to 2.5% swelling, but as the bubble shape was flattened, with an aspect ratio for thickness to diameter of about 4/25 or .16, the actual swelling can be estimated at about 0.4 of the spherical value or about 1%. Therefore, the measured density change of 1.45% appears to be largely due to the development of internal bubbles estimated at 1% swelling.

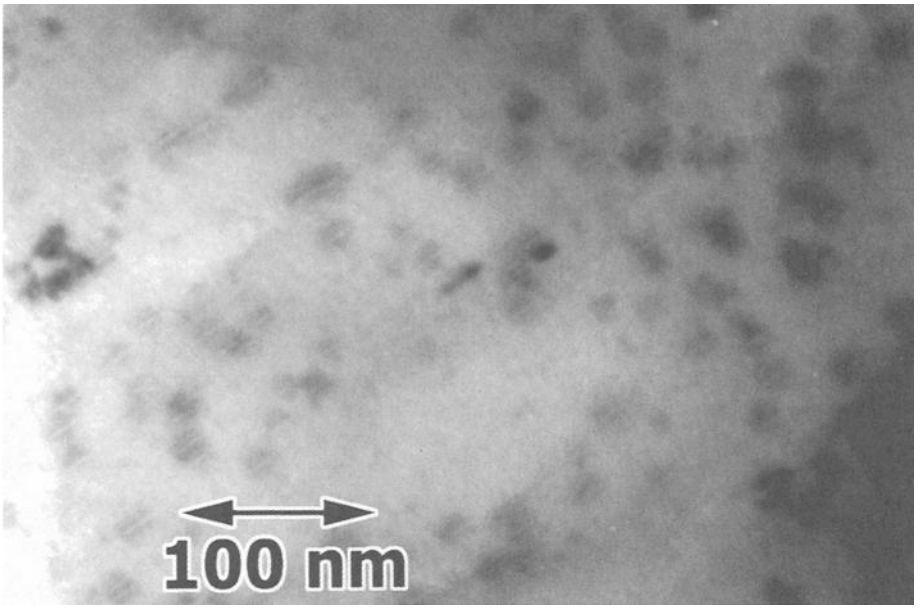


Figure 9. *Evidence for cavity formation in beryllium irradiated to 1.8x10^{22} n/cm^2 at 400°C.*

Swelling may also originate from the transformation of impurity regions from a crystalline to an amorphous phase. It is difficult to estimate the volume fraction of impurity regions or to estimate the resultant swelling due to phase transformation, so the magnitude of the swelling change cannot be estimated at this time.

If much of the helium and tritium is bound in bubbles, then release of these gases from heated specimens can be expected to occur only after bubble coarsening and therefore will be observed mainly at higher temperatures. This may explain helium and tritium release response that was observed on heating such that helium and tritium were released under almost identical conditions [3,5,8], and is in agreement with observed fracture surface features after heat treatment [8]. Examination of heated specimens may allow verification of such a prediction.

Conclusions

Beryllium pebbles, a byproduct in the production of high purity beryllium, are being considered as the neutron multiplier in the a fusion blanket design. 3 mm pebbles have been examined following irradiation in EBR-II to 4.31x10^{22} n/cm^2 at 380°C in order to determine effects of radiation on microstructure. It is found the major consequences of irradiation are amorphization of impurity slags and formation of helium bubbles. The bubbles are unusually shaped thin platelets oriented on basal planes and account for much of the 1.45% swelling found following irradiation. It is

anticipated that such bubbles form by segregation of helium to c-type loops.

References

[1] Dalle Donne, M., Harries, D. R., Kalinin, G., Mattas R., and Mori, S., Journal of Nuclear Materials, Vol. 212-215, 1994, pp. 69-79.

[2] Dalle Donne, M., Goraieb, A., Piazza, G., and Sordon, G., in *Proceedings of the Third Intenational Workshop on Beryllium Technology for Fusion,* JAERI-Conf 98-001, 1998, pp. 17-24.

[3] Gelles, D. S., Greenwood, L. R., Oliver, B. M., Baldwin, D. L., Ermi, R. M., and Tsai, H., "Post-Irradiation Examination of Beryllium" Battelle Pacific Northwest National Laboratory internal report for Project 26919, PNNL-SA-29550, copies available from the authors. For summary, see Dalle Donne, M., Baldwin, D. L., Gelles, D. S., Greenwood, L. R., Kawamura, H., Oliver, B. M., and Scaffidi-Argentina, F., IBID Reference [2], pp. 296-303.

[4] Greenwood, L. R., Oliver, B. M., Gelles, D. S., Baldwin, D. L., "Measurement and Calculation of Helium Generation in Beryllium Pebbles Irradiated In EBR-II," this proceedings.

[5] Anderl, R. A., Longhurst, G. R., Oates, M. A., and Pawelko, R. J., IBID Reference [2], pp. 307-315.

[6] Gelles, D. S., and Heinisch, H. L., Journal of Nuclear Materials, Vol. 191-4 1992, pp. 194-198.

[7] Chernikov, V. N., Ullmaier, H., and Zakharov, A. P., Journal of Nuclear Materials, Vol. 258-63 1998, pp. 694-699.

[8] Baldwin, D. L., Slagle, O. D., and Gelles, D. S., Journal of Nuclear Materials, Vol. 179-81 1991, pp. 329-334.

L. R. Greenwood,[1] B. M. Oliver,[1] D. S. Gelles,[1] D. L. Baldwin,[1]
M. Dalle Donne,[2] H. Kawamura,[3] and F. Scaffidi-Argentina[2]

Measurement and Calculation of Helium Generation in Beryllium Pebbles Irradiated in EBR-II

Reference: Greenwood, L. R., Oliver, B. M., Gelles, D. S., Baldwin, D. L., Dalle Donne, M., Kawamura, H., and Scaffidi-Argentina, F., **"Measurement and Calculation of Helium Generation in Beryllium Pebbles Irradiated in EBR-II,"** *Effects of Radiation on Materials: 19th International Symposium, ASTM STP 1366,* M. L. Hamilton, A. S. Kumar, S. T. Rosinski, and M. L. Grossbeck, Eds., American Society for Testing and Materials, West Conshohocken, PA, 2000.

Abstract: Beryllium pebbles are being evaluated for their potential use as a neutron multiplier in fusion power reactors. Commercially available pebbles were irradiated in the Experimental Breeder Reactor II to study property changes and gas production. Helium production rates from fast neutron irradiation are significantly higher in beryllium than in other metals due to the low neutron energy threshold and large (n,2n)2α nuclear cross section. Furthermore, the $^{9}Be(n,\alpha)^{6}He(\beta)$ reaction breeds ^{6}Li, which has a high thermal neutron cross section for producing helium and tritium. Calculations of helium and tritium production were performed based on neutron dosimetry measurements.

Stepped-anneal and total helium release measurements were conducted on single and multiple beryllium pebbles, from two different suppliers, Brush Wellman and Nippon Gashi Co.-Japan. The measurements were conducted to determine the total helium content for comparison with predictions, and to determine the helium release characteristics as a function of time and temperature. These data are required for fusion reactor design. Sequential helium analyses were conducted over a temperature range from 500°C to 1100°C in approximately 100°C steps. Observed helium release in both beryllium lots was nonlinear with time at each temperature interval, with each step being characterized by a rapid initial release rate, followed by a gradual slowing of the rate over time. Fractional helium release as a function of temperature was observed to be substantially different for the two lots.

Comparisons of the measured and calculated total helium production in the beryllium agree within ±5%. This agreement validates our understanding of the reaction mechanisms, nuclear cross sections, and neutron dosimetry results, thereby demonstrating that we can confidently predict helium generation and release characteristics for the design of fusion reactors.

Keywords: helium measurements, helium release, beryllium

[1] Pacific Northwest National Laboratory, P. O. Box 999, Richland, WA 99352, USA.
[2] Forschungszentrum Karsruhe INR, Postfach 3540, D-76021 Karlsruhe, Germany.
[3] JMTR, Oarai Establishment, JAERI Oarai-machi, Higashi Ibaraki-gun, Ibaraki-ken 311-13, Japan.

Copyright© 2000 by ASTM International www.astm.org

Introduction

Beryllium pebbles are being considered for the neutron multiplier medium in the European Fusion Technology Program Helium Cooled Pebble Bed (HCPB) Blanket. That design is also being considered for testing in ITER. The pebbles to be used are an inexpensive form of beryllium produced in an intermediate step of the production of higher purity beryllium. The opportunity to obtain helium release measurements from prototypic fast neutron irradiated pebbles became possible after pebbles were irradiated in the US/DOE Office of Fusion Energy/MONBUSHO COBRA 1A2 experiment in EBR-II. Details of the beryllium pebbles and postirradiation examination *[1,2,3]* and the irradiation in EBR-II *[4]* are published separately.

Gas Production Calculations

The COBRA subassembly X516 was irradiated in core position 2B1 from November 26, 1992 to September 26, 1994 for a total of 337.26 effective full power days at 62.5 Mwt. Beryllium specimens were irradiated in two different locations including subcapsule C03, spanning –5.8 to –15.5 cm with respect to core centerline in capsule B390, and subcapsule D03, spanning –6.2 to –15.9 cm in capsule B391. Reactor dosimetry capsules were located above and below both the C03 and the D03 subcapsules. A full report of the neutron dosimetry results has been previously published *[5]*. For the present calculations, there were three measurements of the neutron fluence spectrum, which cover the elevations of the beryllium capsules. Neutron flux gradient measurements were conducted in the various subcapsules that were located at the same elevations in the reactor. These gradient data indicate that the neutron fluences were virtually identical for the two beryllium assemblies C03 and D03. Hence, the gas production calculations as a function of reactor elevation are the same for both assemblies.

The production of tritium and ^{4}He from beryllium is dependent on the following nuclear reactions:

$$^9\text{Be}(n,\alpha)^6\text{Li};\ ^9\text{Be}(n,2n)2\alpha;\ ^9\text{Be}(n,d)2\alpha;\ \text{Li}(n,\alpha)t;\ ^9\text{Be}(n,t)^7\text{Li}$$

At short irradiation times, only the direct Be reactions are important. However, as ^{6}Li grows in, this reaction can become an increasingly important source of both helium and tritium due to the very high thermal neutron cross section. Two other nuclear processes must also be considered, mainly the decay of tritium to ^{3}He and the ^{3}He(n,p)t reaction which has a very high thermal neutron cross section for converting ^{3}He back into tritium. Neutron cross sections for these reactions were taken from the ENDF/B-V Gas Production File 533 *[6]*. This file was specially constructed to sum all sources of a particular gaseous species such as helium. The file thus lists neutron cross section data for the ^{9}Be(n,helium) reaction, and this reaction was used to determine the direct production of helium from beryllium. Reaction rates calculated from the dosimetry-adjusted neutron spectra at the three elevations spanning the beryllium materials are listed in Table 1.

The reaction rates listed in Table 1 are given at the full reactor power of 62.5 MWt. Since tritium decays during irradiation and the resultant ^{3}He can burn back to tritium, it is important to consider the reactor power history for the COBRA-1A2

irradiation. For these calculations, the reaction rates were time-averaged over the entire 669-day irradiation history.

Table 1- *Reaction rates in beryllium for COBRA-1A2 (62.5 MWt)*

	Reaction Rate (atom/atom·day)		
Reaction	-3.0 cm	-16.0 cm	-28.7 cm
^{9}Be(n,helium)	1.22E-5	7.74E-6	1.39E-6
^{9}Be(n,α)^{6}Li	2.16E-6	1.51E-6	3.11E-7
^{9}Be(n,t)^{7}Li	1.37E-10	8.85E-11	1.34E-11
^{6}Li(n,α)t	1.80E-4	1.79E-4	2.06E-4
^{3}He(n,p)t	1.02E-3	1.02E-3	1.17E-3

The calculations were performed using a Fortran program to numerically integrate the production and burnup of each nuclear species on a daily basis over the 669-day irradiation period. The net ^{4}He and tritium values are shown as a function of elevation in the reactor in Figure 1. It is important to note that the net production of both ^{4}He and tritium vary strongly with the elevation in the reactor. The trendlines for the calculated values for each reaction are described by polynomials, as shown on Figure 1. These equations can thus be used to determine the gas production at any height within the C03 and D03 assembly.

The calculations for the production of ^{4}He and tritium assume that both species remain trapped in the beryllium close to the point of generation. Although this is a good assumption for helium, the tritium may be subject to significant diffusion and possible loss from the beryllium at the irradiation temperatures of 388°C and 395°C for the C03 and D03 subcapsules, respectively. Consequently, comparisons of these calculations with measured tritium evolution from the beryllium must consider the possible diffusion and loss from the subcapsules. It is also important to note that the calculated values at the end of irradiation time, September 26, 1994, must be corrected for decay after irradiation. Tritium decays with a half-life of 12.32 years, which amounts to 5.5% per year.

The elevations of the 1, 3, and 5 mm beryllium pebbles were determined using the radiographs shown in Figure 2. The resultant elevation ranges were then used to calculate the ^{4}He and ^{3}H expected for each type of pebble in each capsule. There were no 3 mm pebbles in D03. For the 1 mm pebbles, the calculated values are given at the estimated center of the pebble. For the 3 and 5 mm pebbles, values are given at the top and bottom of the elevation ranges. It was not possible to determine the exact elevation of each 3 and 5 mm pebble; therefore, a range of values is given. Tables 2 and 3 summarize our best estimates of the ^{4}He and ^{3}H concentrations in each type of Be pebble decayed to May 1, 1997, to correspond with the time of the He^{3} measurements presented later in this paper.

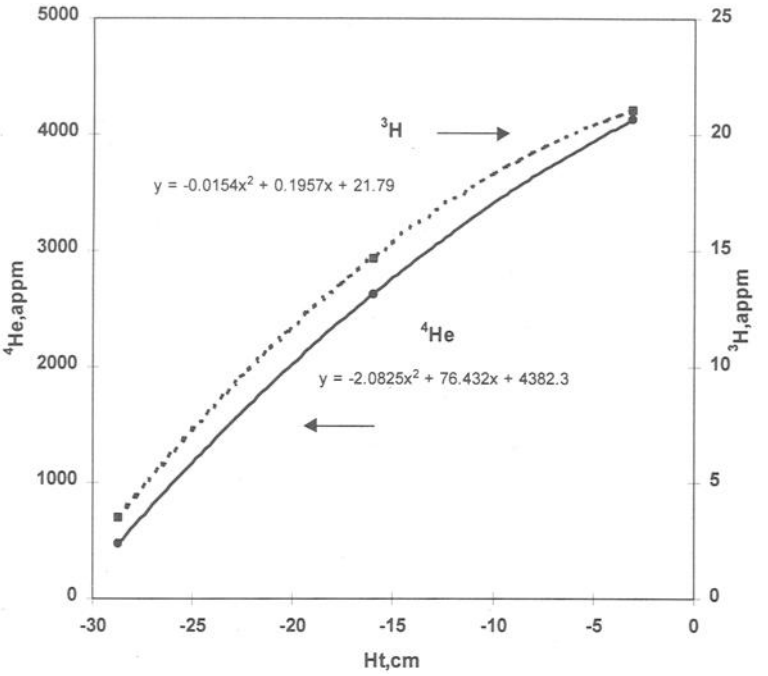


Figure 1- *Production of ^{4}He and ^{3}H as a function of reactor elevation*

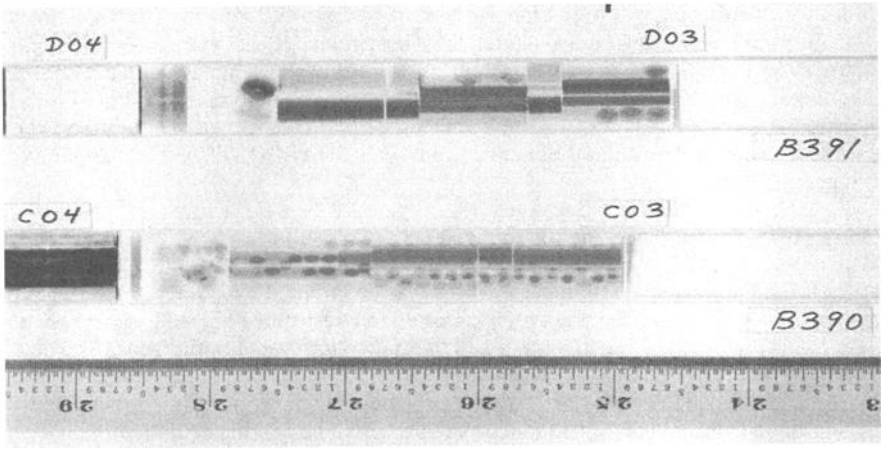


Figure 2- *Radiograph of Be capsules in COBRA-1A2*

Table 2- *Calculations for Be pebbles in position C03 of COBRA-1A2 at 5/1/97*

Be Pebble	Ht,cm	^{4}He,appm	^{3}H,appm	Fast Fluence > 1 MeV x10^{22} n/cm^2	Fast Fluence >0.1 MeV x10^{22} n/cm^2	Be dpa
1 mm	-15.3	2723	13.1	1.35	5.04	29.0
3 mm	-15.2	2734	13.2	1.35	5.05	29.0
3 mm	-8.4	3595	16.5	1.60	5.70	32.3
5 mm	-8.4	3595	16.5	1.60	5.70	32.3
5 mm	-7.1	3733	17.0	1.63	5.78	32.7

Table 3- *Calculations for Be pebbles in position D03 of COBRA-1A2 at 5/1/97*

Be Pebble	Ht,cm	^{4}He,appm	^{3}H,appm	Fast Fluence > 1 MeV x10^{22} n/cm^2	Fast Fluence >0.1 MeV x10^{22} n/cm^2	Be dpa
1 mm	-15.7	2662	12.9	1.32	4.98	28.7
5 mm	-15.7	2662	12.9	1.32	4.98	28.7
5 mm	-11.7	3205	15.0	1.50	5.44	31.0

Helium Analysis Samples

Several groups of beryllium pebbles were analyzed for the present study. In an initial analysis series, two pebbles were analyzed using a stepped-anneal process to determine the helium release characteristics as a function of both time and temperature. These analyses were followed by rapid vaporization to determine any remaining helium. Two other samples were analyzed by rapid vaporization alone to determine total helium content. For each pair of samples, one was from the "C03" assembly, and the other from the "D03" assembly. The C03 pebbles were fabricated by Brush Wellman. The D03 pebbles were fabricated by NGK - Japan.

In a second analysis series, a total of 30 beryllium pebbles were analyzed using the stepped-anneal process in two separate sets. Fifteen of the samples were from the C03 assembly, and fifteen were from the D03 assembly. Prior to analysis, the mass of each pebble or group of pebbles was determined using a microbalance with calibration traceable to National Institute of Standards and Technology (NIST). Mass uncertainty is estimated to be ±0.001 mg.

Helium Release Measurements (First Series)

The helium released from each pebble was determined by isotope-dilution gas mass spectrometry during heating or vaporization in a resistance-heated graphite crucible in one of the mass spectrometer system's high-temperature vacuum furnaces.*[7]* The absolute amount of ^{4}He released was measured relative to a known quantity of added ^{3}He "spike". The ^{3}He spikes were obtained by expanding and partitioning a known quantity of gas through a succession of calibrated volumes.*[8]* The mass spectrometer was calibrated for mass sensitivity during each series of runs by analyzing known mixtures of ^{3}He and ^{4}He.

For two of the samples, multiple sequential analyses were conducted while the temperature of the sample crucible was increased in approximately 100°C increments,

starting at 500°C and increasing to a maximum of 1100°C. For this procedure, a ^{3}He spike was first added to the furnace. While still at room temperature (~25°C), a known small fraction (~0.04%), or aliquot of the sample gas was then taken from the furnace to determine the absolute amount of ^{4}He initially present in the furnace. This analysis was done to determine the starting background ^{4}He level. The crucible was then heated to 500°C, and additional aliquots taken for ^{4}He analysis. Each temperature was held until some leveling off of the ^{4}He was observed, at which point the temperature was raised to the next temperature. The time period between each analysis was varied from a minimum of about 5 minutes to a maximum of about 30 minutes depending on the observed ^{4}He release rate at each temperature. Crucible temperature was measured using a standard chromel-alumel thermocouple in direct contact with the crucible.

All measured helium levels were corrected for background helium buildup in the analysis furnace as a function of time. These background helium levels were determined by separate "control" analyses conducted immediately before or after the sample runs. Background ^{4}He levels generally rise linearly with time due largely to diffusion of helium from the atmosphere through the Pyrex furnace top. Background ^{4}He levels were in the range of 10^{12} to 10^{13} atoms over the 6 to 7 hour time period for each analysis series. Uncertainty in the ^{4}He background is estimated to be approximately 10^{12} atoms. Background ^{3}He levels remained in the 10^{12} atom range, and were negligible compared to the added ^{3}He spike (~10^{16} atoms).

Following the time/temperature measurements, the two pebbles were relocated, in their original crucibles, to different locations in the same furnace for subsequent vaporization analysis along with the other two beryllium samples analyzed as part of the present effort. For the vaporization runs, both ^{3}He and ^{4}He were determined in each sample. This was done by analyzing a first aliquot of the gas released during vaporization prior to the addition of the ^{3}He spike. Because only a small fraction of the gas was taken from the furnace for each analysis, this procedure did not adversely affect the accuracy of the final measured ^{4}He value.

Helium Release Results (First Series)

The results of the helium release measurements for the first analysis series are shown graphically in Figures 3 and 4. Temperature increase for each interval took approximately 1 minute. Indicated uncertainties in the temperature data are the standard deviations in the observed temperature variations over the temperature interval. Table 4 gives the total helium released after vaporization of the four beryllium pebbles. Results are listed as total atoms of ^{3}He and ^{4}He, and as concentrations, again in atomic parts per million (appm, 10^{-6} atom fraction) with respect to the total number of beryllium atoms in each sample. Conversion from total helium to helium concentration was based on a calculated value of 6.682×10^{22} atoms per gram assuming pure beryllium. Also shown in Table 4 are the end results for Be-C03-1 and Be-D03-1 from the helium release measurements, and the combined helium release for these two samples from both measurements.

Absolute uncertainty (1σ) in the individual helium analysis results, determined from the cumulative uncertainties in the sample mass, isotope ratio measurement, spike size, and helium background subtractions, is estimated to be approximately 1% combined with 10^{12} atoms in quadrature. For the lowest measured helium levels, therefore, the uncertainty of 10^{12} atoms is the dominant term. For helium levels above about 10^{14} atoms, the uncertainty is approximately 1%.

Discussion of Total Helium Release Measurements

Observed helium release from both pebbles was nonlinear with time at each temperature level. As is evident in Figures 3 and 4, both pebbles showed definite "steps" in the helium release at each temperature, with each step being characterized by a rather rapid initial release rate, followed by a gradual slowing of the rate over time. Except for Sample Be-C03-1 at 1000 °C, none of the release steps showed saturation over the 1 to 2 hour time periods the temperatures were held.

Helium release as a fraction of the total helium in the sample was markedly different for the C03 and D03 material. Sample Be-C03-1 released virtually all of its helium after approximately 30 minutes at 1000 °C. Sample Be-D03-1, on the other hand, released only about 62% of its helium even after about 1 hour at 1100 °C. Absolute helium release was correspondingly lower for Be-D03-1 at each temperature level. As indicated earlier, the C03 beryllium material was fabricated by Brush Wellman, whereas the D03 material was fabricated by NGK - Japan. The different helium release characteristics suggests some material differences in the two beryllium lots. However, additional analyses would be required to verify any material effects. Information currently available on these materials is summarized in reference 1.

Total helium release after vaporization for all four pebbles are given in Table 4. In terms of helium concentration, the totals for Be-C03-1 and -2 are 2724 and 2941 appm, with an average value of 2833 appm. The corresponding totals for Be-D03-1 and -2 are 2459 and 2574 appm, with an average value of 2517 appm. In both cases, the total ^{4}He for the combined heating+vaporization runs is lower than that for the separate vaporization runs alone. This variation amounts to 8% for Be-Co3-1, and 5% for Be-D03-1. Some of this variation may be due to radial gradients in the two irradiation assemblies, although this was not anticipated to be larger than perhaps 5%. Predicted helium concentrations in the C03 and D03 beryllium are 2723 and 2662 appm, respectively. Mean calculated to experimental ratios (C/E's) are 1.04 for Be-C03 and 0.95 for Be-D03. Helium-3 levels measured during the vaporization runs were 2.80 appm for Be-C03-2, and 2.62 appm for Be-C03-2. Predicted ^{3}He levels, assuming no tritium loss during or after irradiation, are slightly lower at 2.55 and 2.50 appm, suggesting somewhat higher levels of tritium in the beryllium than calculated.

Table 4- *Total Helium Release Measurements and Comparison with Calculations*

		Measured Helium (appm)[a]			Measured ^{4}He (total) (appm)			
	Mass	^{3}He	^{4}He					
Sample	(mg)	Vaporized	Heated	Vaporized	Total[b]	Mean	Predicted	C/E
Be-C03-1	1.419	0.3	2722	1.8	2724	**2833**	**2723**	**0.96**
Be-C03-2	1.633	2.8	--	2941	2941	**±153**		
Be-D03-1	1.472	1.2	1519	940	2459	**2517**	**2662**	**1.06**
Be-D03-2	1.206	2.6	--	2574	2574	**±81**		

[a]Helium concentration in atomic parts per million (10^{-6} atom fraction) with respect to the total number of beryllium atoms in the sample.
[b]Total ^{4}He (heated + vaporized).

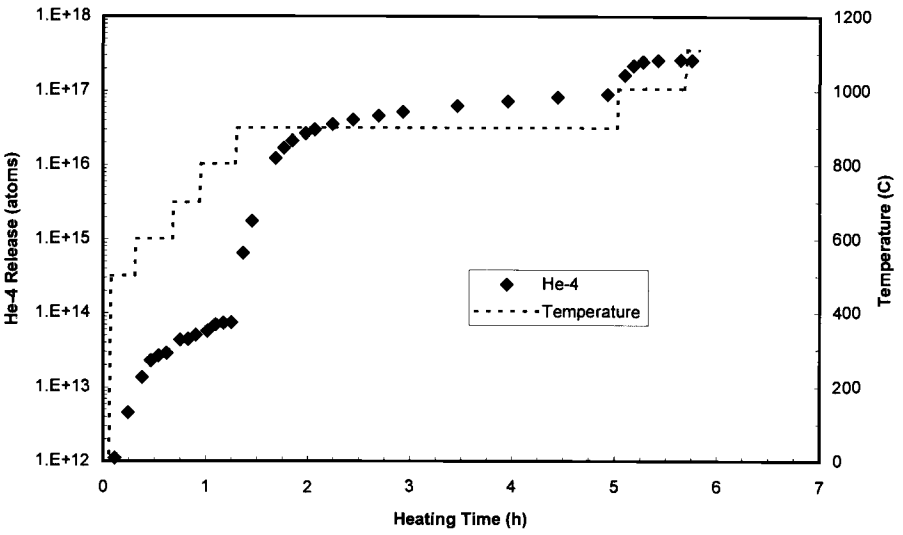


Figure 3- *Helium Release from Sample Be-C03-1*

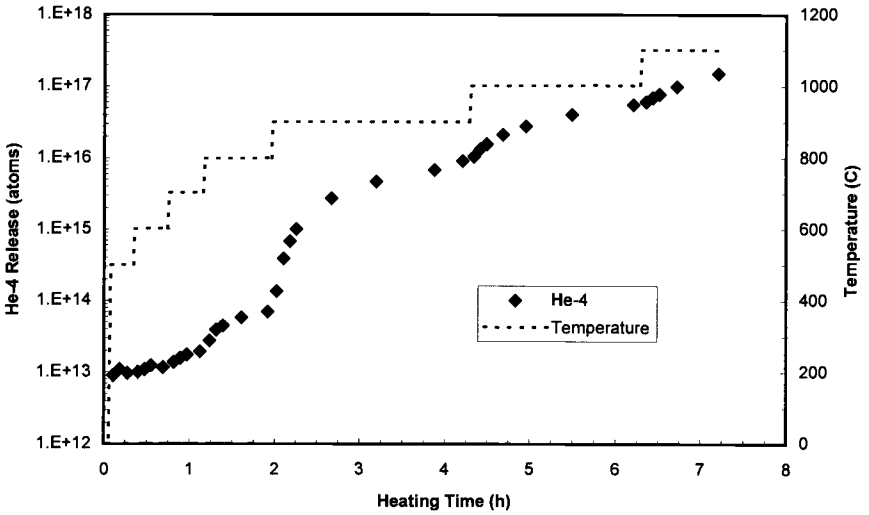


Figure 4- *Helium Release from Sample Be-D03-1*

Helium Release Measurements (Second Series)

In the second analysis series, stepped-anneal helium release measurements were conducted on two sets of fifteen beryllium pebbles. The purpose of the measurements was to determine the helium release characteristics of the beryllium using larger sample sizes and longer anneal times relative to the total release measurements presented above for the first series. Sequential helium analyses were conducted over a narrower temperature range from approximately 800°C to 1100°C in 100°C increments, but with longer anneal time periods. To accommodate the longer anneal times, a temperature controller and associated circuitry were added to the experimental setup.

Each temperature was held for a minimum of ~24 hours, or until a leveling off of the ^{4}He was observed. The time period between each measurement was varied from a minimum of about 5 minutes to a maximum of about 2 hours depending on the observed ^{4}He release rate at each temperature.

The fifteen beryllium pebbles were loaded into the central section of one of the system's standard 3/16" (0.48 cm) diameter graphite crucibles. To accommodate the pebbles, the central coaxial hole in the crucible was enlarged to 0.094" (0.24 cm) diameter. Small graphite plugs were placed at each end of the hole to position the samples as close as possible to the middle of the crucible. A diagram of the setup, showing a section of the high temperature furnace used, is shown in Figure 5. Crucible temperature was measured using a standard K-type (chromel-alumel) thermocouple inserted into the side of the crucible. As indicated in the figure, this thermocouple was also used in conjunction with a separate temperature readout and controller circuit to maintain a constant temperature in the crucible for each temperature step, and to allow for unattended operation.

Because of the relatively long periods of time the furnace remained isolated, it was necessary to pump out the furnace at regular intervals (usually about 24 hours) in order to keep offgas pressure in the furnace to below about 500 microns (67 Pa). Immediately after pumpout, a new ^{3}He spike was added to the furnace, and the measurements continued. Pumpout times were chosen to coincide with periods of slower helium release, usually near the end of each anneal period. Small corrections were made to the total helium release data to account for helium release during the pumpout (about 3 minutes).

As was done for the first series, the measured helium levels were corrected for background helium buildup in the analysis furnace as a function of time. Background ^{4}He levels were in the range of 10^{12} to 10^{13} atoms. Uncertainty in the ^{4}He background is estimated to be ~10^{12} atoms. Background ^{3}He levels remained in the 10^{12} atom range, and were negligible compared to the added ^{3}He spike of ~10^{16} atoms.

Stepped-Anneal Helium Release Results

The results of the helium release measurements for the groups of fifteen beryllium pebbles are shown graphically in Figures 6 and 7. Temperature increase for each interval took approximately 1 minute. In Figures 6 and 7, the top figure shows the cumulative helium release in atoms, and the bottom figure shows the calculated helium release rate in atoms/second.

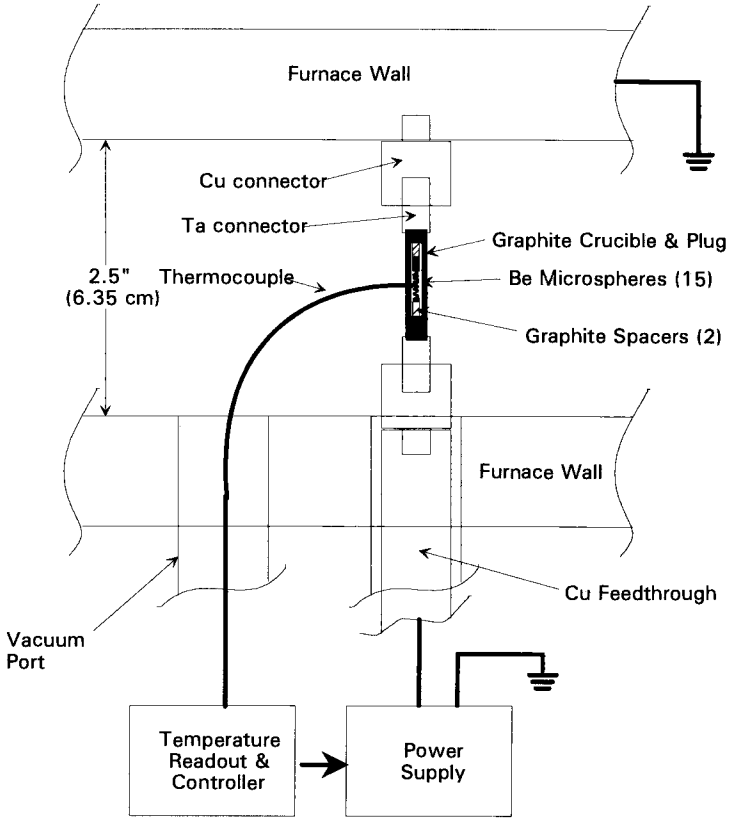


Figure 5- *Diagram of Sample Crucible and Temperature Control*

Discussion of Stepped-Anneal Helium Results

Consistent with the results obtained in the first series for single Be-C03 and Be-D03 pebbles, helium release from both sets of fifteen pebbles was nonlinear with time at each temperature level. Both samples showed definite "steps" in the helium release at each temperature, with each step being generally characterized by an initial release rate, followed by a slowing of the rate over time. The one exception to the above behavior was the initial helium release in Sample Be-C03 at the first temperature step of 774 °C. Here, the release rate initially rises, then falls, then rises again and continues to rise slowly over the remaining anneal period.

Observed helium release from Sample Be-C03 showed a leveling off at the 890°C temperature step. Additional increases to 1028°C and 1132°C, showed very little extra helium release (<2%). Sample Be-D03, on the other hand, showed a leveling off only at the highest step of 1100°C. Final measured ^{4}He concentrations were 2276 appm for Be-C03 and 2312 appm for Be-D03.

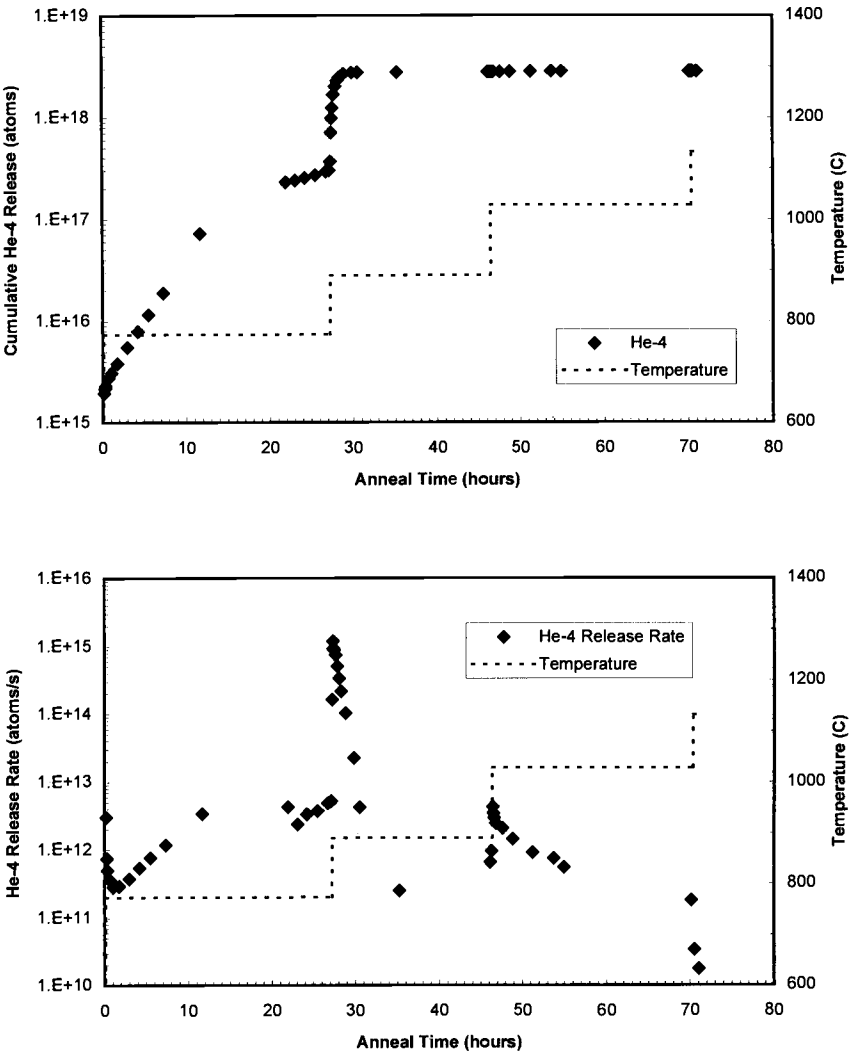


Figure 6- *Cumulative Helium Release and Release Rate from Sample C03*

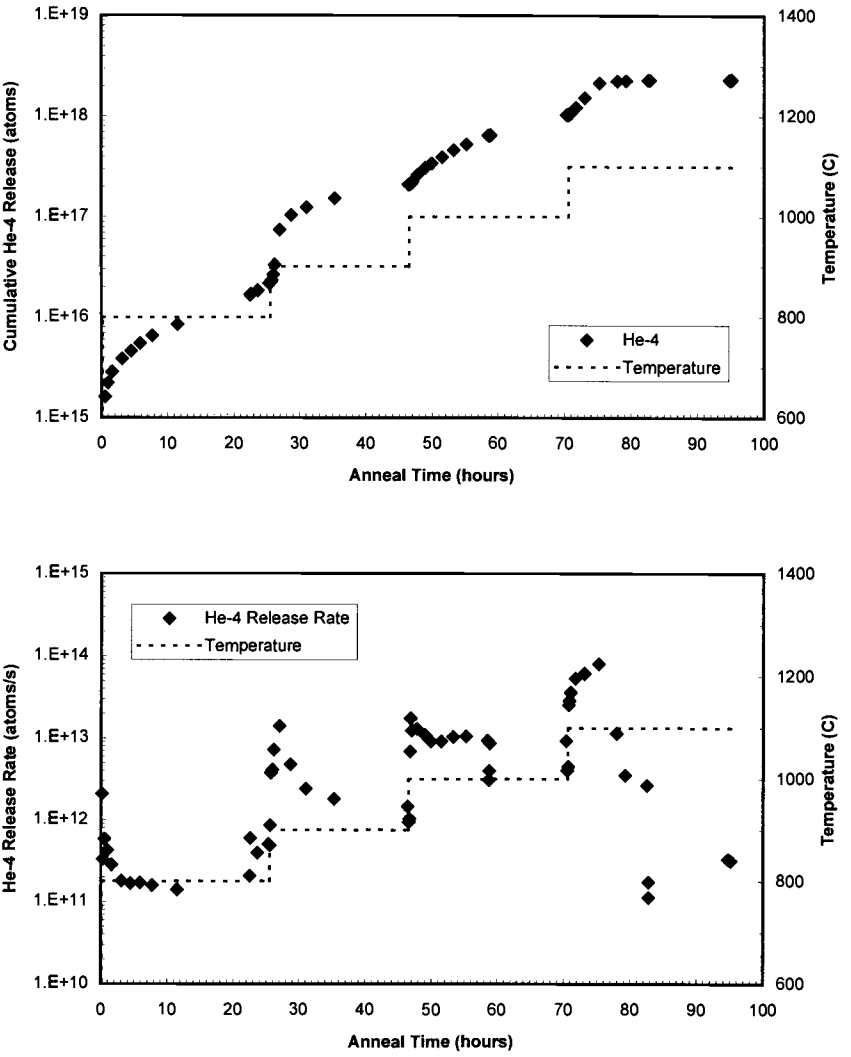


Figure 7- *Cumulative Helium Release and Release Rate from Sample D03*

The above trend of lower temperature helium release in the C03 material is consistent with that observed for the single pebble, and further supports the conclusion of differences in the helium release characteristics of the two material lots. None of the lower temperature steps showed any leveling off of the helium release, even with increased anneal times of at least 24 hours. The initial measurements had anneal times of only 1 to 2 hours.

Based on the average helium concentrations measured in the first series for the C03 and D03 beryllium (2833 appm for Be-C03-1, and 2517 appm for Be-D03-1), the values observed here represent ~80 % and ~92 % of the total "expected" helium concentrations. These percentages are in contrast to the initial results which showed virtually complete helium release from Be-C03-1 at 1000 °C, but only about 62 % release in Be-D03-1 at 1100 °C.

Acknowledgments

The beryllium specimens were provided by H. Kawamura of JAERI as part of the US/DOE Office of Fusion Energy/MONBUSHO Fusion Materials Program. The helium measurements and calculations were funded by Forschungszentrum Karlsruhe under the direction of Prof. M. Dalle Donne.

References

[1] Gelles, D. S., Dalle Donne, M., Kawamura, H., Scaffidi-Argentina, F.,Microstructural Exmination of Irradiated Beryllium Pebbles, 19th International Symposium on *Effects of Radiation on Materials, ASTM STP 1336,* M. L. Hamilton, A. S. Kumar, S. T. Rosinski, and M. L. Grossbeck, Eds., American Society for Testing and Materials, 1999.

[2] Gelles, D.S., Greenwood, L.R., Oliver, B.M., Baldwin, D.L., Ermi, R.M., Tsai, H., Post Irradiation Examination of Beryllium, *Battelle Project Report 26919 (1997).*

[3] Baldwin, D.L., *Fusion Materials Semiannual Progress Report, DOE/ER-0313/23 (1998) 267.*

[4] Hamilton, M.L., Ermi, R.M., and Eiholzer, C.R., *Fusion Reactor Materials,DOE/ER-0313/14* (1993)3.

[5] Greenwood, L.R., *Fusion Materials Semiannual Progress Report, DOE/ER-0313/23* (1998) 317.

[6] *ENDF/B-V Gas Production File 533*, National Nuclear Data Center, Brookhaven National Laboratory.

[7] Farrar, H., and Oliver, B.M., *Journal of Vaccuum Science and Technology* A4 (1986) 1740.

[8] Oliver, B.M., Bradley, J.G., and Farrar, H., *Geochimica Cosmochim*ica *Acta* 48 (1984) 1759.

Masaru Nakamichi[1] and Hiroshi Kawamura[1]

In-situ Electrical Resistivity Measurement of $MgO \cdot Al_2O_3$ Coating under Neutron Irradiation

Reference: Nakamichi, M. and Kawamura, H., **"In-situ Electrical Resistivity Measurement of $MgO \cdot Al_2O_3$ Coating under Neutron Irradiation,"** *Effects of Radiation on Materials: 19th International Symposium, ASTM STP 1366,* M. L. Hamilton, A. S. Kumar, S. T. Rosinski, and M. L. Grossbeck, Eds., American Society for Testing and Materials, West Conshohocken, PA, 2000.

Abstract: Ceramic coatings on the surface of structural materials such as 316SS have been considered for electrical insulators and tritium permeation barriers in fusion reactor designs. $MgO \cdot Al_2O_3$ is one of the most promising materials as a coating material from a point of high electrical resistivity and so on. In this report, the electrical resistivity of a $MgO \cdot Al_2O_3$ coating on 316SS was investigated under neutron irradiation with the JMTR (Japan Materials Testing Reactor) by in-situ electrical resistivity measurement. The specimen was irradiated at 360°C in a He atmosphere. Radiation Induced Conductivity (RIC) was observed at the beginning of reactor. The electrical resistivity of the coating before neutron irradiation decreased from $1 \times 10^{11} \Omega \cdot cm$ to $2 \times 10^{8} \Omega \cdot cm$ with increase reactor power. The electrical resistivity of the coating under neutron irradiation decreased again from $2 \times 10^{8} \Omega \cdot cm$ to $5 \times 10^{4} \Omega \cdot cm$ above $1 \times 10^{19} n/cm^2$ (En>1 MeV). It did not recover up to unirradiated level. The electrical resistivity of the coating after neutron irradiation was about $2 \times 10^{6} \Omega \cdot cm$. It was clear that Radiation Induced Electrical Degradation (RIED) in the $MgO \cdot Al_2O_3$ coating was recognized above a fluence of about $1 \times 10^{20} n/cm^2$ (En>1MeV).

Keywords: fusion reactor, neutron irradiation, electrical insulator, $MgO \cdot Al_2O_3$, electrical resistivity, RIC, RIED, in-situ measurement

1. Introduction

In fusion reactor designs, ceramic coatings on the surface of structural materials such as 316SS have been considered for electrical insulators and tritium permeation barriers. Ceramic coating materials such as $MgO \cdot Al_2O_3$ [*1*], Y_2O_3 [*2-7*], Al_2O_3 [*8-13*], AlN [*13*], CaO [*14*], TiN and TiC [*15*] have previously been studied, with emphasis on fabrication and properties. On the other hand, in general industrial fields, ceramic and metal coatings are useful for heat resisting coating and anti-corrosion coating. In particular, plasma spraying coating is used widely, because this method is able to apply various materials as a coating and to make thick coatings. $MgO \cdot Al_2O_3$ was selected as a coating, because it was one of the most promising materials as a coating from a point of high electrical resistivity, etc.

In this study, in-situ electrical resistivity of a $MgO \cdot Al_2O_3$ coating on 316SS was investigated under neutron irradiation with the JMTR.

[1]Japan Atomic Energy Research Institute, Oarai Research Establishment, Oarai-machi, Higashi Ibaraki-gun, Ibaraki-ken 311-1394, Japan.

Copyright© 2000 by ASTM International www.astm.org

2. Experimental

Specimen

The fabrication process for $MgO•Al_2O_3$ coating on the surface of 316SS developed by the authors [*1*] is shown in Figure 1.

We have developed new ceramic coating technique, which is combined plasma spraying method, metallic undercoating and chemical densified process [*1*] (see Figure 1). In the case of ceramic coating on the austenitic stainless steel (316SS) by the plasma spraying method, it has been observed that crack formation in the coating and a peeling of the coating occur due to the difference in thermal expansion between the coating layer and the substrate. In order to prevent these problems, a buffer layer of ferritic stainless steel (410SS) was coated as undercoating on 316SS substrate by the plasma spraying before $MgO•Al_2O_3$ coating. 410SS has an intermediate thermal expansion coefficient between 316SS and $MgO•Al_2O_3$. Plasma sprayed coating usually include many pores. They were successfully filled by the chemically densification method, where the coated specimen was immersed in $Y(NO_3)_3$ solution and fired at 500 °C.

Some properties were investigated in relation to some parameters for fabrication. First of all, the number of densification treatments was investigated by the hardness test in the cross section of the $MgO•Al_2O_3$ coating. From the results of the hardness test on the cross section of $MgO•Al_2O_3$ coating layer, 9 repetitions of the densification processes were decided. And from the results of the verification test of open pore in the $MgO•Al_2O_3$ coating, open pore could be enclosed by densification treatment. Second, on the basis of the results on the thermal shock test of undercoating performed by two plasma spraying methods (the atmospheric plasma spraying method and the vacuum plasma spraying method) and two kinds of 410SS powders with different particle sizes (10-45 μm and 10-75 μm), the fabrication condition was selected. Finally, the relation between undercoating condition and thermal shock resistivity of the $MgO•Al_2O_3$ coating layer was investigated. From the results of the thermal shock test, it was obvious that the thermal shock resistivity of $MgO•Al_2O_3$ coatings could be improved on 410SS undercoating fabricated by the vacuum plasma spraying method with 10-45 μm 410SS particle size. The $MgO•Al_2O_3$ coating (100μm thickness) with 410SS undercoating (150μm thickness) on the surface of 316SS was sound after 30 cycles of the thermal shock test at 500, 600 and 700°C which was performed by water quenching from each temperature.

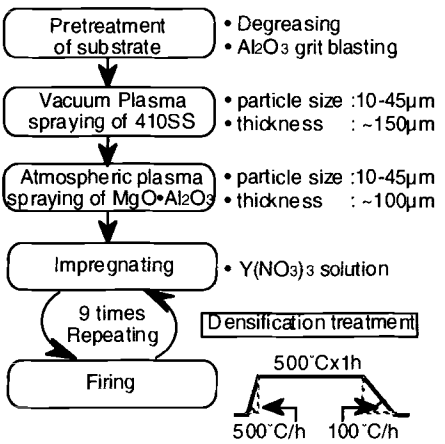


Figure 1 - *Fabrication process of the $MgO•Al_2O_3$ coating*

The shape of specimen used for the electrical resistivity measurement under neutron irradiation is shown in Figure 2. The dimension of 316SS substrate was ϕ15x1.5 mm. The surface of the substrate degreased by methyl alcohol and blasted by Al_2O_3 grit to improve the adhesion between the 316SS substrate and the 410SS undercoating. The undercoating was conducted about 150 μm thick by the vacuum plasma spraying method. The particle size of 410SS (Fe-12wt%Cr) was in the range from 10 μm to 45 μm. The spraying conditions of 410SS are shown in Table 1. The $MgO \cdot Al_2O_3$ (purity : 98.9 wt%, particle size : 10-45 μm) was coated about 100μm thick by the atmospheric plasma spraying method. The spraying conditions of $MgO \cdot Al_2O_3$ are shown in Table 2. The $MgO \cdot Al_2O_3$ coating was densified by impregnation with $Y(NO_3)_3$ solution and fired for one hour at 500 °C in air to fill up open pores and cracks. The rate of heating and cooling were 500 °C/h and 100 °C/h, respectively. Furthermore, this densification treatment was repeated 9 times.

The guard electrode and the center electrode were formed by Ag paste on the surface of $MgO \cdot Al_2O_3$ coating. The outer diameter and inner diameter (D_2) of the Ag guard electrode were 13 and 9 mm, respectively. The diameter of the Ag center electrode (D_1) was 5 mm. The Ag paste was heated at 150°C for 20min in air.

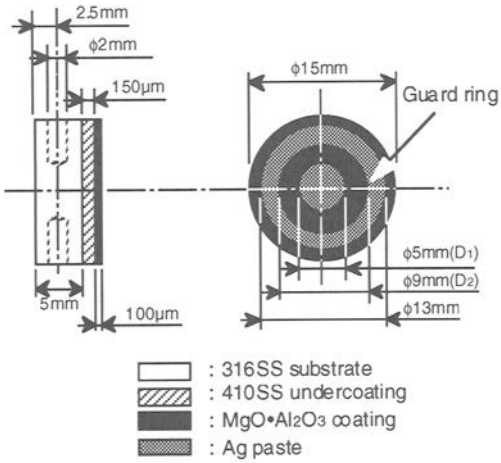


Figure 2 - *The shape of 316SS with $MgO \cdot Al_2O_3$ coating specimen*

Table 1 - *Spraying conditions of 410SS by the vacuum plasma spraying method*

Spraying apparatus	: PLASMA-TECHNIK AG A-2000V
Particle size	: 10-45 μm
Plasma gases	
Ar	: 7.5×10^{-4} m^3/s
H_2	: 1.3×10^{-4} m^3/s
Plasma current	: 685 A
Plasma voltage	: 64 V
Spray distance	: 275 mm
Pressure in chamber	: 5.9 kPa

Table 2 - *Spraying conditions of $MgO{\bullet}Al_2O_3$ by the atmospheric plasma spraying method*

Spraying apparatus	: PLASMA-TECHNIK AG A-3000S
Particle size	: 10-45 μm
Plasma gases	
Ar	: 6.7×10^{-4} m^3/s
H_2	: 2.2×10^{-4} m^3/s
Plasma current	: 630 A
Plasma voltage	: 74 V
Spray distance	: 120 mm

In-situ Measurement

The electrical resistivity of the $MgO{\bullet}Al_2O_3$ coating under neutron irradiation in the JMTR was measured in-situ with a three-electrode guard-ring configuration of Ag electrodes as shown in Figure 3.

The equations for electrical resistivity are as follows;

$$\rho = \frac{A}{d} R \qquad (1)$$

$$A = \frac{\pi (D_1 + g)^2}{4} \qquad (2)$$

$$g = \frac{D_2 - D_1}{2} \qquad (3)$$

where

ρ : Electrical resistivity ($\Omega{\bullet}$cm),
R : Resistance (Ω),
A : Effective cross section of electrode (cm^2),
g : Gap between guard and center electrode (cm),
d : Thickness of coating (cm),
D_1 : Center electrode diameter (cm),
D_2 : Guard electrode inner diameter (cm).

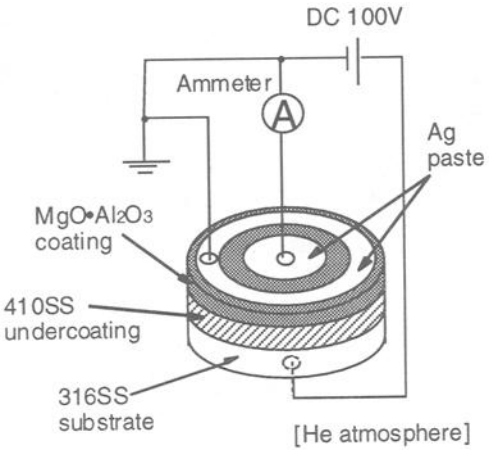


Figure 3 - *The measurement method of electrical resistivity with a three-electrode guard-ring configuration*

The inner capsule configuration for neutron irradiation is shown in Figure 4. Mineral insulated cable was used for electrical signal measurements and sintered Al_2O_3 (purity : 99 wt%) was used as the specimen holder. DC 100V was applied between a center electrode and substrate to measure electrical resistivity of the coating layer. The specimen was irradiated at 360 °C in He atmosphere in JMTR K-5 position. The thermal neutron flux (En<0.6826eV) and the fast neutron flux (En>1MeV) were about $2x10^{14}$ and $5x10^{13}$ n/cm^2/s, respectively. The specimen was irradiated for two cycles of the JMTR operation. One JMTR cycle corresponds to about 25 days of operation. The thermal neutron fluence and the fast neutron fluence were about $9x10^{20}$ and about $2x10^{20}$ n/cm^2, respectively.

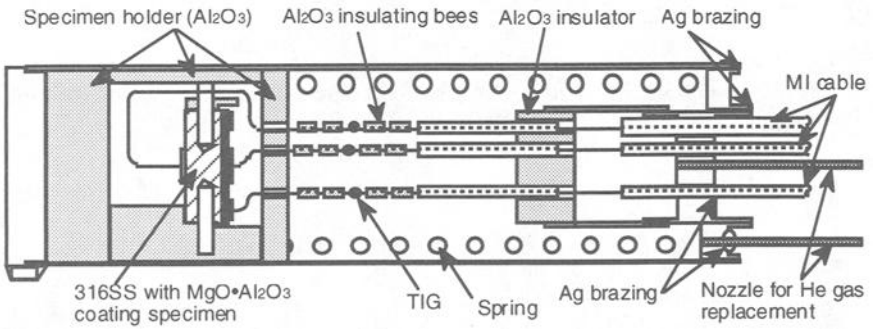


Figure 4 - *Inner capsule configuration for neutron irradiation*

3. Results and Discussion

The results of electrical resistivity measurement with and without neutron irradiation are shown in Figure 5. The electrical resistivity of $MgO \cdot Al_2O_3$ coating decreased with increasing reactor power at power-up. This phenomenon was named as Radiation Induced Conductivity (RIC). This decrease of electrical resistivity of ceramic insulators under irradiation was understood to correspond to the photo-conductivity of the semiconductor [7]. The valence electrons in the insulator are excited by the ionization effect of the radiation and jump from the valence band to the conduction band. These excited electrons give rise to the decrease of electrical resistivity.

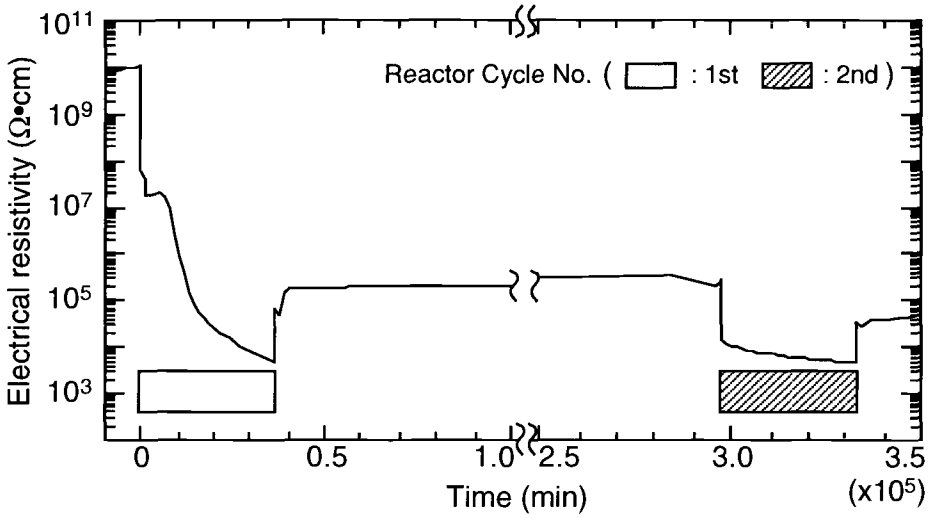


Figure 5 - *The result of electrical resistivity measurement with and without neutron irradiation*

The result of the electrical resistivity measurement at reactor power-up in log-log plot is shown in Figure 6. RIC is described as below [8-11] :

$$RIC = K \times P^{\delta} \qquad (4)$$

where

RIC : Radiation induced conductivity,
K : Constant of proportionality
P : Reactor power,
δ : Constant.

Parameters K and δ are constant strongly depending on materials (δ is usually equal to 0.5-1.0) [12]. Shikama evaluated the electrical properties of single crystal alumina under neutron irradiation at the JMTR [9-11] and found that δ was in the range of 1.0-1.2. Noda evaluated the electrical properties of single crystal alumina under 14MeV neutron

irradiation with the Fusion Neutronics Source (FNS) [*11*]. The magnitude of δ was found to be in the range of 0.90-0.96. The electrical properties of Y_2O_3 coating by plasma spray method with densification treatment under neutron irradiation had evaluated at the JMTR [*6*] and δ of Y_2O_3 coating was in the range of 0.76-0.86. With regard to RIC in the $MgO{\bullet}Al_2O_3$ coating, it was found that the magnitude of δ was about 0.70 at reactor power-up.

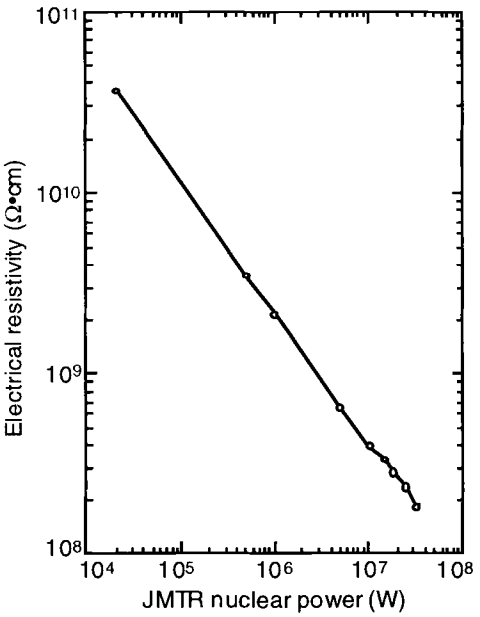


Figure 6 - *The results of electrical resistivity measurements at the 1st reactor power-up period*

The electrical resistivity of the $MgO{\bullet}Al_2O_3$ coating before the 1st cycle was about $1x10^{11}$ Ω•cm. The electrical resistivity of the coating under neutron irradiation decreased from $2x10^{8}$Ω•cm to $5x10^{4}$Ω•cm up to about $1x10^{20}$n/cm^2(>1MeV). The electrical resistivity of the coating after the 1st and the 2nd cycle did not recover up to that of unirradiated one.

RIED in $MgO{\bullet}Al_2O_3$ coating was recognized above about $1x10^{19}$n/cm^2 (En>1MeV). The result of electrical resistivity degradation under neutron irradiation is shown in Figure 7. The electrical resistivity of $MgO{\bullet}Al_2O_3$ coating layer under neutron irradiation was constant up to 3 RFPD (Reactor Full Power Days) (Φ^* : $2x10^{19}$n/cm^2 (En>1MeV)). With regard to Al_2O_3, Hodgson reported that RIED took place at about 10^{-5} dpa and about 10^{5-6} Gy ionization dose by electron irradiation [*8*]. And Shikama reported that RIED of Al_2O_3 took place at about 10^{-2} dpa and about 10^{9} Gy ionization dose by neutron irradiation with the JMTR [*10*]. In this neutron irradiation test, RIED of $MgO{\bullet}Al_2O_3$ coating took place at about 10^{-2} dpa and about $8x10^{8}$ Gy ionization dose, and has some similarities to the phenomenon observed by Shikama.

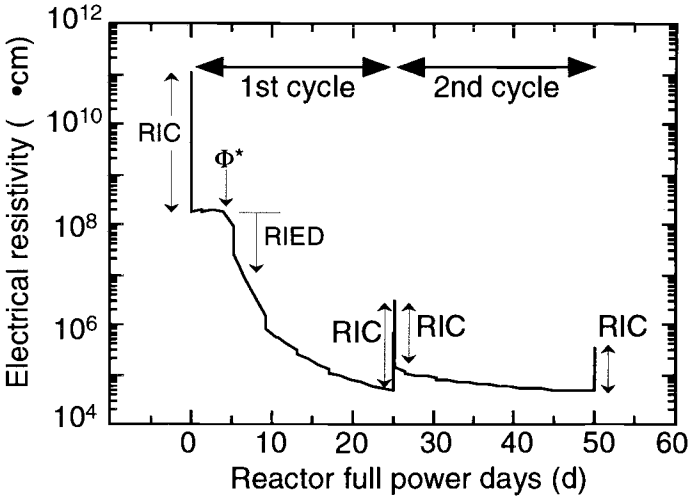


Figure 7 - *The result of electrical resistivity degradation under neutron irradiation*

4. Summary

RIC on $MgO{\bullet}Al_2O_3$ coating was recognized at each the JMTR power up. RIC on $MgO{\bullet}Al_2O_3$ coating is described by the following relation :

$$RIC = K \times P^{\delta}$$

$(\delta : 0.70).$

It was clear that the constant δ for the $MgO{\bullet}Al_2O_3$ coating was about 0.70 under fission neutron irradiation.

RIED of $MgO{\bullet}Al_2O_3$ coating layer took place at about 10^{-2} dpa and about $8x10^8$ Gy ionization dose.

References

[1] M.Nakamichi, H.Kawamura, K.Miyajima, Y.Harada and R.Oyamada, Trial fabrication and preliminary characterization of $MgO{\bullet}Al_2O_3$ coating, J. Nucl. Mater. 233-237 (1996) 1427

[2] M.Nakamichi, H.Kawamura, K.Miyajima, Y.Harada and M.Saito, Trial fabrication and preliminary characterization of Y_2O_3 film as electrical insulator in liquid metal blanket, Fusion Technol. 2 (1994) 1217

[3] M.Nakamichi, H.Kawamura and R.Oyamada, Trial fabrication and preliminary characterization of electrical insulator for liquid metal system, JAERI-Tech 95-009 (1995)

[4] M.Nakamichi, H.Kawamura, R.Oyamada, K.Miyajima and Y.Harada, Trial fabrication of Y_2O_3 coating on 316SS, Thermal Spraying 2 (1995) 1027

[5] M.Nakamichi, H.Kawamura, R.Oyamada, K.Miyajima and Y.Harada, Effect of undercoating on properties of Y_2O_3 coating, Thermal Spraying 2 (1995) 815
[6] M.Nakamichi and H.Kawamura, Characterization of Y_2O_3 coating under neutron irradiation, J. Nucl. Mater., to be published
[7] T.Terai, T.Yoneoka, H.Tanaka, A.Suzuki, S.Tanaka, M.Nakamichi, H.Kawamura, K.Miyajima and Y.Harada, Compatibility of yttria (Y_2O_3) with liquid lithium, J. Nucl. Mater. 233-237 (1996) 1421
[8] E.R.Hodgson, Radiation-enhanced electrical breakdown in fusion insulators, J. Nucl. Mater., 179-181 (1991) 383
[9] T.Shikama, Study of dynamic radiation effects in ceramics using fission reactors, Materia Japan, 33 (11) (1994) 1363
[10] T.Shikama, M.Narui, H.Kayano, T.Sagawa and Y.Endo, Dynamic radiation effects on electrical properties of ceramic insulators, Mater. Trans., JIM, 34 (11) (1993) 1143
[11] T.Shikama, M.Narui, Y.Endo, A.Ochiai and H.Kayano, Study of radiation induced conductivity by ac-method in a fission reactor, J. Nucl. Mater., 191-194 (1992) 544
[12] K.Noda, T.Nakazawa, Y.Oyama, D.Yamaki and Y.Ikeda, Electrical resistivity of ceramic insulators under irradiation using 14MeV neutrons, J. Nucl. Mater., 233-237 (1996) 1289
[13] S.Malang and R.Mattas, Comparison of lithium and the eutectic lead-lithium alloy, two candidate liquid metal breeder materials for self-cooled blankets, Fusion Engi. Des., 27 (1995) 399
[14] J.-H.Park and T.F.Kassner, CaO insulator coatings and self-healing of defects on V-Cr-Ti alloys in liquid lithium system, J. Nucl. Mater., 233-237 (1996) 476
[15] A.Perujo and K.S.Forcey, Tritium permeation barriers for fusion technology, Fusion Engi. Des., 28 (1995) 252

Vladimir A. Stepanov,[1] Petr A. Stepanov,[1] Vyacheslav M. Chernov,[1]
Aleksey V. Golovinov,[2] and Lyudmila M. Kryukova[2]

Effect of Ionizing and Displacive Components of Irradiation on the Structural Transformations in Pyrolitic Boron Nitride Ceramics

Reference: Stepanov, V. A., Stepanov, P. A., Chernov, V. M., Golovinov, A. V., and Kryukova, L. M., **"Effect of Ionizing and Displacive Components of Irradiation on the Structural Transformations in Pyrolitic Boron Nitride Ceramics,"** *Effects of Radiation on Materials: 19th International Symposium, ASTM STP 1366,* M. L. Hamilton, A. S. Kumar, S. T. Rosinski, and M. L. Grossbeck, Eds., American Society for Testing and Materials, West Conshohocken, PA, 2000.

Abstract: The structure of pyrolitic boron nitride (BN) samples assembled to a package and irradiated with protons has been studied with Raman spectroscopy and X-ray diffraction. Shift and change of shape of X-ray bands and change of Raman band shape have been found to correlate with the calculated values of energy losses along the proton track. Ionizing constituent of irradiation is responsible for a change of the state of grain boundaries and partial recrystallization of pyrolitic BN. Displacive constituent of irradiation is responsible for stacking fault formation in the grains. A mechanism of the effect of ionizing constituent of irradiation has been introduced, where energy release on grain boundaries and break of chemical bonds on the boundaries result in partial recrystallization of the material. According to this mechanism the recrystallization is much more feasible in pre-irradiated materials.

Keywords: radiation-induced structural transformations, pyrolitic boron nitride, Raman spectroscopy, X-ray diffraction.

Introduction

An important problem of radiation material science for dielectrics is concerned with mechanisms of effect of ionizing and damaging (displacive) constituents of irradiation on the structural changes. Separation of contributions from various radiation effects is necessary to compare testing results and predict behavior of materials in various radiation facilities. However, mechanisms of effect of the ionizing and displacive constituents have not been studied comprehensively yet. Experimental separation of contributions of various irradiation constituents is possible when materials are irradiated with high energy particles. In this case, the displacive constituent of irradiation reveals itself at the particle track ends; whereas for the most of track regions, the ionization is predominant.

[1]Head of laboratory, research scientist and professor, respectively, SSC RF – Institute of Physics and Power Engineering, 249020 Obninsk, Russia.
[2]Research scientists, Moscow Steel and Alloys Institute, 117936 Moscow, Russia.

Copyright© 2000 by ASTM International www.astm.org

Structural changes in proton-irradiated samples of pyrolytic boron nitride (BN) have been investigated in regions of ion tracks.

The pyrolytic BN has been chosen because of the prospects for using this material in irradiation facilities, on the one hand, and on the other, its peculiar microstructure [*1*]; changes of the latter make possible to conclude concerning the actual features of radiation-induced structural changes.

Pyrolytic BN is a fine crystal material with a characteristic structural hierarchy. Aggregates of up to 2000 nm size consist of grains of 120-180 nm size with wide boundaries. There is a network of small (20-40 nm size) cells inside and narrow low angle boundaries.

Structure of pyrolytic BN after proton irradiation

A package of 8 thin (60 μm) samples of pyrolytic BN was irradiated in air with 7 MeV protons (flux $2.5 \cdot 10^{12}$ $cm^{-2}s^{-1}$, dose $5.2 \cdot 10^{15}$ cm^{-2}), their projection ranges in the material being ~350 μm. The Raman spectra with the band of the high frequency vibration E_{2g} and X-ray diffraction at the angles ranging from 25 to 70° have been measured for each sample.

The Raman spectra for BN samples from the irradiated package are shown in (Figure 1). With a similar position of maximum (1365-1367 cm^{-1}), on increasing sample number (along the proton track) the gradual decrease of Raman band width is observed, whereas considerable increase takes place for sample 6 corresponding to the projected range of protons. The decrease of Raman band width as compared to the initial value is also observed for sample 7.

(Figure 2) shows the X-ray diffraction for samples from irradiated package. From the sample 2 to the sample 5, widths of X-ray diffraction bands (100), (101) and (102) decrease as compared with initial samples. X-ray pattern of the sample 7 placed just after the area of proton projected range is characterized by wider diffraction bands compared to the spectrum of the sample 5; however, these bands appears to be narrower than those of the unirradiated sample.

A notable shift of the band (002) to higher angles is found for the sample 5 with in respect to the sample 2 (Figure 3). Positions of the band (002) correspond to 29.990 and 30.213 degrees (in 2θ), respectively. A "shoulder" is observed at the high angle edge of diffraction bands (002) and (004).

The "improved" structure of the first five samples from the package after proton irradiation revealed in the narrowing the Raman and X-ray bands can be associated with re-crystallization under irradiation. Indeed, a notable decrease of the width of diffraction bands (100), (101) and (102) is explained by the increase of the range of coherent scattering, and, consequently, by the increase of grain size and decrease of the boundary density. It was shown [*2*] that diffraction bands of pyrolytic BN (002) and (004) are complicated and consist of several narrow bands corresponding to the iso-structural phases with different inter-plane distances. Radiation exposure followed by a thermal treatment can change the contents of these phases, resulting in a change of shape and shifts of bands (002) and (004). The appearance of "shoulder" at the high angle edge of diffraction band (004) and high angle shift of band (002) of boron nitride irradiated with protons indicate the increase of content of phases with smaller inter-plane distances.

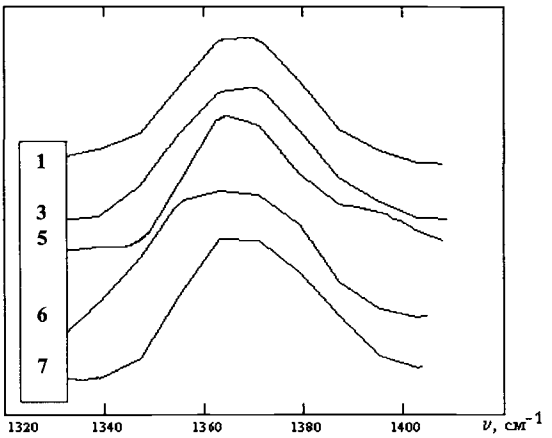


Figure 1 - *Raman spectra of BN from proton-irradiated package*
1 – Sample N1 (track part 0-60 μm), 3 – sample N3 (120-180 μm), 5 – sample N 5 (240-300 μm), 6 – sample N 6 (300-360 μm), 7 – sample N 7.

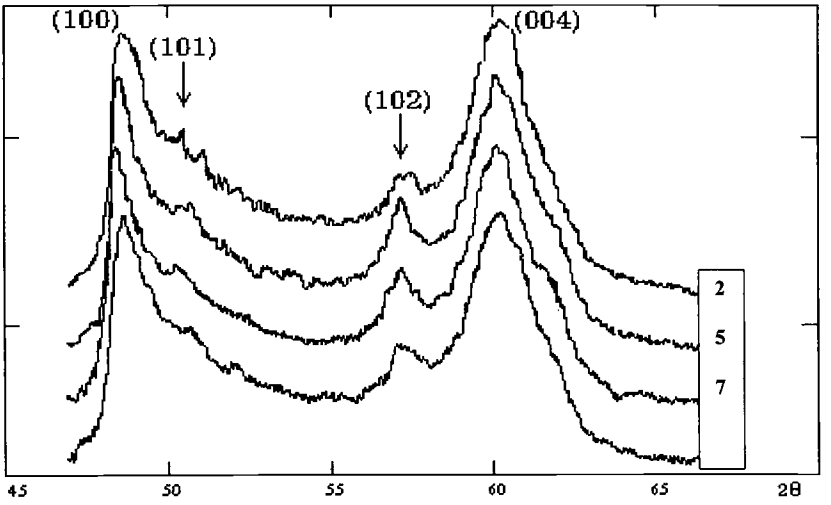


Figure 2 - *X-ray diagram (K_α - Co radiation) of BN samples from proton-irradiated package*
2 – Sample N2 (track part 60-120 μm); 5 – sample N 5 (240-300 μm); 7 – sample N 7; bottom curve is for initial sample.

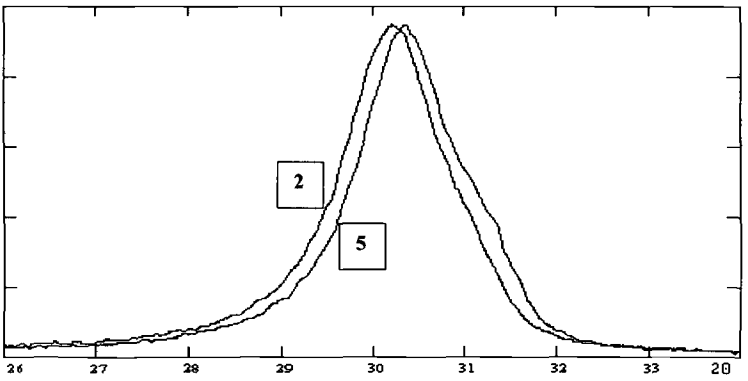


Figure 3 - *X-ray band shape (002) of BN samples from proton-irradiated package. (K_α - Fe radiation)*
2 – sample N2 (track part 60-120 μm), 5 – sample N 5 (240-300 μm).

The Raman band shapes also depend on the total number and the state of inter-crystallite boundaries in the material. The shape of Raman band of high frequency vibrations E_{2g} in BN based materials is determined by superposition of vibration frequencies shifted relative to the principle vibration frequency [*3*]. The shifts of principal frequency are caused by local vibrations at the boundaries associated with impurities (hydrogen, halogen ions) or with the change of force constants of atomic bonds at the boundaries. İf local vibrations of atoms (at the boundary) with the frequency ω_1 differs from the eigen value ω_0, the decrease of the vibration amplitude s_1 at frequency ω_1 with the increase of the atom number n (corresponding to the distance from the boundary) is described by the following equation [*4*]:

$$s_1=s_0\{(1-\varepsilon)/(1+\varepsilon)\}^n, \quad (1)$$

where
$1-\varepsilon = (\omega_0/\omega_1)^2$
s_0 = amplitude of the principle vibration

Widening Raman band up to 25 cm^{-1} (Figure 1) associated with local vibrations at the boundaries can be caused by the change of the vibration frequency in the 5 nm neighbourhood of the BN grain surfaces. With the grain size of 30-60 nm, up to 30% of atoms involve into vibrations with the frequencies differing from ω_0. The decrease of Raman band width is the result of a decrease in the portion of atoms with «shifted» frequencies of vibrations, or a decrease of the number of boundaries in the material.

Separation of effects of ionizing and damaging constituents of radiation

Calculation of ionizing and collision-related losses of protons in BN (TRIM-90 code) gives a possibility to compare the values of ionizing and damaging constituents of proton irradiation with the results on Raman spectroscopy and X-ray diffractometry. In (Figure 4) this comparison is given for the Raman band half width. Raman band width is decreased with the increase of ionizing constituent. The decrease of Raman band width vs. the initial state revealed itself also in regions beyond those of proton track where they are subjected to the ionizing effect of bremsstrahlung radiation only. Thus, re-crystallization processes are associated with the ionizing effect of radiation.

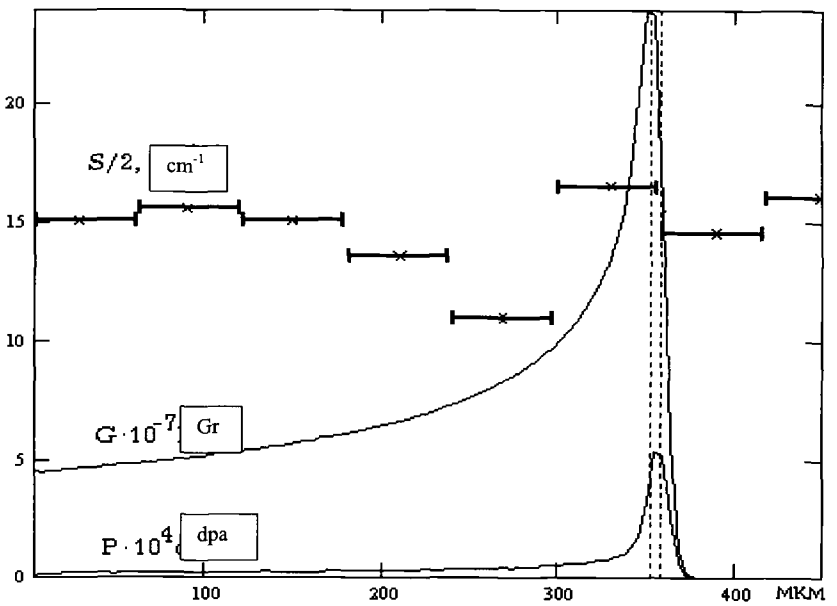


Figure 4 - *Dependence of the Raman band half width (S/2) on the distance from the surface of the package faced to proton beam as compared to calculated dependencies of the ionization losses (G) and atom shifts (P). Dashed line – the region of proton projection range.*

On increasing the displacive constituent of radiation, the Raman band widens significantly (Figure 4). The widening is associated with radiation defect production in the grain bulk and near the boundaries. In this case, the asymmetric widening of Raman band with predomination in low frequency range (spectrum 4, Figure 1) indicates the formation of certain defects, which are similar to displacements of basic hexagonal planes in crystal structure of BN [*3*].

We have managed to observe partial re-crystallization in pyrolytic BN after reactor irradiation up to a dose of 10^{20} n/cm^2 (E>0.1 MeV) in the course of transmission electron

microscopy (heating in the microscope column did not exceed 100-150°). After reactor irradiation, the material retained its initial large grains with a certain decrease of boundary contrast. In several grains the internal network of small cells was absent. In the regions where the network remained, the re-crystallization was easily stimulated by 120 keV electron irradiation (flux $6 \cdot 10^{15}$ $cm^{-2}s^{-1}$) directly in the microscope column. Electron irradiation with 5-20 s exposure (depending on local thickness) resulted in a disappearance of low angle boundaries between small cells, the large grains remaining stable. Re-crystallization in non-irradiated boron nitride occurs at temperature exceeding 1300°C.

Relaxation of radiation-induced charge carriers at the boundaries may cause the decrease of grain boundary density under irradiation. Due to electron- hole relaxation at the boundaries, energy of 4-6 eV is released (band gap). This can result in breaking chemical bonds and stimulate the diffusion of atoms.

Probability of atomic jumps under non-equilibrium conditions can be estimated, according to [*5*], with the help of equation

$$\nu = \nu_0 \cdot n \cdot \tau \qquad (2)$$

where

ν_0 = frequency of atomic vibrations in the equilibrium ($4 \cdot 10^{13}$ s^{-1} for BN)
n = number of the transfers of energy exceeding the diffusion barrier for atoms, per time unit
τ = characteristic time of thermalization of atomic vibrations ($10^{-11} - 10^{-12}$ s)

In the steady state, the rate of electron and hole production is equal to relaxation rate. The production rate (10^{20} $cm^{-3}s^{-1}$) is estimated with the help of the values of dose rates and band gap. The electron-hole relaxation mainly occurs at grain boundaries. Taking into account the grain size in pyrolytic BN being about of 20-40 nm, portion of atoms at boundaries is up to 10% of the total number (mean density 10^{22} cm^{-3}), and magnitude of n is about 10^{-2} s^{-1}, which, according to Eq.2, corresponds to the magnitude of probability (ν) of radiation-stimulated diffusion jumps of atoms at the boundaries equal to $4 \cdot (1\text{-}10^{-1})$ s^{-1}.

The effective diffusion temperature at the similar values of transfer probability is about 1450-1540 K. This temperature corresponds to the temperature of re-crystallization in BN based material.

The introduced mechanism for radiation-induced selective acceleration of diffusion at grain boundaries can be assumed to occur in different ceramics. In the study [*6*], possible types of radiation defects are reviewed in ceramics based on Al_2O_3, $MgAl_2O_4$, MgO, etc. Electron microscopy of irradiated materials has shown that the structural damage and defect clusters are observed primarily near the grain boundaries.

Conclusions

1. Investigation on the structure of thin samples of pyrolytic boron nitride from proton irradiated package (proton energy 7 MeV, flux $2.5 \cdot 10^{12}$ $cm^{-2}s^{-1}$, dose $5.2 \cdot 10^{15}$ cm^{-2}) have been carried out with Raman spectroscopy and X-ray methods.

2. The shifts and width change of X-ray bands and change of Raman band shapes have been found to correlate with the calculated losses for ionization and displacements in the different regions along the proton track (TRIM code).
3. The ionizing constituent of radiation is responsible for a partial re-crystallization of pyrolytic BN according to the mechanism of selective stimulation of diffusion at the grain boundaries. This is manifested in the narrowing the Raman band, the X-ray diffraction bands becoming sharper and shifted. A considerable decrease of the threshold for re-crystallization has been found in reactor materials irradiated with a dose up to 10^{20} n/cm^{-2}.
4. The displacive constituent of irradiation (at the end of proton track) is responsible for defect formation in crystal structure, that is displacements of basic hexagonal planes in crystal structure of BN, which cause an asymmetric widening of Raman bands.

References

[1] Buzhinskij, O.I., Lopatin, V.V. and Sharupin, B.N., "Application of pyrolytic boron nitride in fusion devices," Journal of Nuclear Materials, 173, 1990, pp. 179-184.

[2] Plaksin, O.A., Stepanov, V.A., Stepanov, P.A. et al. "Structural transformation and properties deterioration of in Dielectric materials under Irradiation," Plasma Devices and Operations, V.4, 1996, pp. 325-335.

[3] Stepanov, V.A., Stepanov. P.A., Optika i spektroskopia. 78, N3, 1995, pp. 431-435 (in Russian).

[4] Madelung, O. Festkorpertheorie III., Springer-Verlag., Berlin Heidelberg New York., 1972.

[5] Stepanov V.A. "Kinetic of processes at laser resonance action", Laser Surface Microprocessing, V.I.Konov, B.S.Luk'yanchuk and I. Boyd, Ed., Proc. SPIE 1352, 1990, pp. 208-209.

[6] Hobbs, L.W., Clinard, F.W., Zinkle, S.J. and Ewing, R.C."Radiation effects in ceramics," Journal of Nuclear Materials, V.216, 1994., p.291.

Other Materials

Farhad Tavassoli,[1] Helen Burlet,[2] Andres Lind,[3] Bachu N. Singh,[4] SeppoTähtinen,[5] and Emile van Osch [6]

Effect Of Irradiation On Structural Materials In Fusion Reactors

Reference: Tavassoli, F., Burlet, H., Lind, A., Singh, B. N., Tähtinen, S., and van Osch, E., **"Effect of Irradiation on Structural Materials in Fusion Reactors,"** *Effects of Radiation on Materials: 19th International Symposium, ASTM STP 1366,* M. L. Hamilton, A. S. Kumar, S. T. Rosinski, and M. L. Grossbeck, Eds., American Society for Testing and Materials, West Conshohocken, PA, 2000.

Abstract: The ITER R&D program on the structural design criteria includes the effects of irradiation on material's properties. The work has started with the design rules for stainless steels at low temperatures (< 350°C) and at moderate irradiation doses (3 - 10 dpa), where degradation of ductility and toughness are of primary concern. It is now extended to copper alloys and multi-layer components, as well as to rules for high temperature properties. A similar work has also been initiated on ferritic / martensitic steels for the future Demonstration reactor, where the operating temperature range is 250-550°C and anticipated irradiation doses are well over 70 dpa.

This paper presents an overview of the above work. It details some of the recent irradiation data obtained for stainless steel type 316LN, precipitation strengthened CuCrZr alloy, oxide dispersion strengthened Cu-Al25 alloy, and commercial and low activation grades of 7-10%Cr ferritic / martensitic steels. Since most of the fusion in-vessel components have to be fabricated using advanced manufacturing techniques, e.g. high temperature isostatic pressing (HIP) of steel/copper/beryllium layers in ITER primary modules, the paper also analyzes effects of such processes on the materials properties and design data.

Keywords: iter, demo, stainless steel, ferritic steel, martensitic steel, copper alloy, 316LN, IG, F82H, CuCrZr, Cu-Al25, tensile, impact, fracture, small specimen, hip, multilayer, code, design

[1] CEA-CEREM, CEA/Saclay, 91191 Gif sur Yvette CEDEX, France.
[2] CEA-CEREM, CEA/Grenoble, 17 rue des Martyres, 38054 Grenoble CEDEX 9, France.
[3] Studsvik Material AB, 611 82 NYKÖPING, Sweden.
[4] Materials Research Dept., Riso National Laboratory, DK-4000 Roskilde, Denmark.
[5] VTT Manufacturing Technology, Materials and Structural Integrity, P.O. Box, 1704, FIN-03044 VTT, Finland.
[6] Netherlands Energy Research Foundation ECN, P.O. Box 1, NL-1755 ZG Petten, The Netherlands.

Copyright© 2000 by ASTM International www.astm.org

Introduction

Most of the internal structures of fission and the present fusion reactors have been fabricated with austenitic stainless steels. These steels are very ductile and, therefore, the design rules (ASME/US, RCC-MR/France, MITI/Japan, PP/RF) [1-4] do not treat their ductility or fracture toughness as a limiting parameter. However, recent studies have shown that these steels are also prone to low temperature irradiation embrittlement [5] and, therefore, their eventual embrittlement has to be incorporated in design rules. This is the situation found in the International Thermonuclear Experimental Reactor (ITER), where the operating temperature is below 350°C [6] and irradiation doses are low to moderate.

The future fusion demonstration reactor (DEMO) will operate over a wider temperature range and in an environment similar to a liquid metal or a gas cooled fission reactor [7]. The structural material for DEMO will most likely be a ferritic / martensitic steel with an operating temperature range of 250-550°C and an irradiation dose of over 70 dpa [8]. Here, modifications to the design rules at both low and high temperatures would be needed.

In this context, the fusion community has taken the lead in extending the fission design rules to cover the effects of irradiation on structural materials [9]. The work has started with the rules for Type 316LN stainless steel, i.e. the reference structural material in ITER (T< 350°C and neutron doses 10 to 30 dpa). It is currently being extended to copper alloys and copper to stainless steel joints, where low and high temperature properties of copper alloys are involved. In parallel, similar work is being initiated on ferritic/martensitic (F/M) steels under the fusion technology's long term program [10].

It is important to note that most of these rules are equally valid for fission reactors. The operating conditions of ITER (temperature and cooling medium) are very similar to those of light water reactors. Those of the DEMO, as stated hereabove, are similar to the liquid metal fast breeder or high temperature gas cooled reactors. In addition, most of the experimental data used for deriving these rules come from experiments performed in fission reactors [11]. Nevertheless, when these rules are applied to fusion reactors, they have to take into account possible changes that may occur in the materials properties as a result of the advanced fabrication techniques needed to construct several in-vessel components (e.g. stainless steel / copper alloy / beryllium multilayer parts in ITER first wall) or exposure to fast neutrons (14 MeV) and a higher helium to dpa ratio.

Materials

Four types of materials are discussed. Their chemical compositions are given in Table 1.

1) Stainless Steel

Type 316LN-IG (Iter Grade) is the reference structural material in ITER. It is specified in the solution annealed and quenched condition with conventional fusion

welding techniques for joining most sections [5]. Advanced manufacturing techniques envisaged for this steel are mainly solid and powder high temperature isostatic pressing (HIP), [12]. Both of these techniques require heating the steel to high temperatures (1050-1150°C) and maintaining it for 1 to several hours under an isostatic pressure (100 to 150 MPa).

Table 1 - *Chemical compositions (wt.%) of the five materials discussed in this paper.*

wt. %	316LN-IG	9Cr-Mo	F82H	CuCrZr-IG	Cu-Al25
C	0.015-0.030	0.080-0.120	0.08-0.12		
Mn	1.6-2.0	0.30-0.50	0.05-0.20		
Si	< 0.50	0.20-0.50	0.05-0.20	(0.011)	
P	< 0.025	≤ 0.020	≤ 0.01	≤ 0.04	2 ppm
S	0.005-0.01	≤ 0.010	≤ 0.01	(0.0023)	10 ppm
Cr	17.0-18.0	8.00-9.00	7.5-8.5	0.65-0.80	
Ni	12.0-12.5	≤0.20	≤ 0.02		
Mo	2.30-2.70	0.85-1.05	1.8 <W <2.2		
Al		<0.040	≤ 0.1		0.25
Fe	bal.	bal.	bal.	(0.010)	22 ppm
Nb or Ta	Nb+Ta+Ti < 0.15	0.06<Nb<0.10	0.01<Ta<0.06		
Ti			0.004-0.012		
V		0.17-0.25	0.15-0.25		
Cu	< 0.3	≤ 0.10	≤ 0.05	bal.	
Zr				0.07-0.15	
O2			≤ 0.01	(0.0020)	0.22
B	< 0.0020		≤ 0.001		0.025
Co	< 0.25 [1]		≤ 0.01	(0.06)	
N_2	0.060-0.080	0.030-0.070	≤ 0.02		

2) Precipitation Hardened Copper Alloy

The conventional thermo-mechanical treatment for CuCrZr consists of a solution anneal treatment (950-1020°C for 20-30 minutes), followed by quenching then heavy cold working (≈ 40-80%) followed by aging (2 to 4 hours at 450-500°C). The advanced manufacturing technique envisaged for this alloy also involves HIPing [12]. A solid block of CuCrZr alloy is HIPed onto a solid or pre-compacted powder block of steel, most likely with an intermediate layer between the two metals. The HIP assembly is heated to a temperature near the conventional annealing temperature (> 850°C) and then cooled down. Since the cooling rate after HIP is slower than the usual quench and the possibility of cold working HIPed components before the final aging is unlikely, the ITER specification for CuCrZr must be modified accordingly [11].

3) Dispersion Strengthened Copper Alloy

The reference manufacturing process for DS-Copper (Cu-Al25) involves several steps [13], but the final product is delivered in the form of cross rolled plates (stress

relieved at 980°C for 1 h). The advanced manufacturing technique envisaged for DS-copper is HIPing the solid copper plate onto steel [12]. Unlike CuCrZr, DS-copper is less sensitive to high temperature exposures and is expected to maintain its initial properties after HIPing.

4) Ferritic / Martensitic (F/M) Steels

a) Conventional ferritic / martensitic steels - Modified 9Cr-1Mo steel [10] is widely used in the steam generators of conventional power plants and probably will be retained for the next generation of fast breeder reactors. It is also assumed for preliminary DEMO design calculations [14].

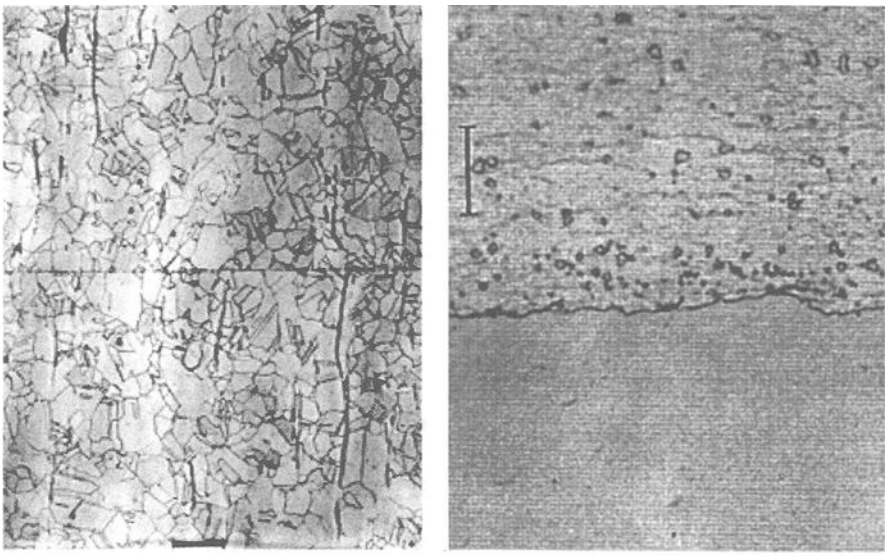
b) Low activation ferritic / martensitic steels - These steels are similar to the Modified 9Cr-1Mo steel, but have molybdenum and niobium replaced with the equivalent low activation elements (W and V) with high activation residual elements reduced to as low as possible. F82H is a steel presently investigated under an IEA sponsored collaborative program, Table 1. It was fabricated and supplied to the other parties by Japan [15]. Europe has also developed several low activation grades. Eurofer steel is the latest grade. It has a Cr content close to the Modified 9Cr steel but a lower W (1%) than F82H, in order to decrease neutron absorption losses. The thermo-mechanical treatments specified for all low activation alloys are optimised to improve resistance to low temperature irradiation embrittlement.

Manufacturing Processes

In addition to the conventional techniques, High temperature Isostatic Pressing (HIPing) is envisaged for manufacturing or joining of several components in ITER and DEMO. The initial state of the material (powder or solid) may vary according to the particular component.

Excellent results have been obtained from solid to solid joining of stainless steel onto stainless steel and stainless steel onto copper alloys, Fig. 1 [16], with the joint properties often approaching those of the parent metal. The main disadvantage of this method is its cost and possible grain growth. Indeed, due to long exposures at high temperatures, significant grain growth may occur in stainless steel (Fig. 1a).

Powder technique offers better flexibility and reduced cost. Its main disadvantages are control of oxygen content and final product dimensions. Here also excellent results have been obtained. Figure 2 shows microstructure of a joint taken from a large scale ITER module (1250 x 650 x 250 mm) fabricated by PowderMet [17] and examined at NFR/Sweden [18]. The HIP temperature is 1085°C, pressure 110 MPa and time 4 h. The problem of grain growth is less important in powder HIP products, as the powder particle surface acts as a barrier to grain growth. It remains of concern, nevertheless, for solid inserts that are placed inside the powder before HIP (Fig. 2). Since the copper alloys have a low tap density and a high mismatch in physical and mechanical properties with steel, they are usually HIPed in solid form onto the steel.



a) SS/SS joint, scale = 200 μm b) Cu/SS joint, scale = 20 μm

Figure 1 - *Photomicrographs of solid-solid HIP bonded joints a) 316L(N)-IG steel to 316L(N)-IG steel (HIP conditions: 1100°C - 2h - 100 MPa, Grain Size No= 3-4), and b) Cu-Al25-IG (top) to 316L(N)-IG (HIP conditions: 920°C - 3h - 120 MPa). The joint in both cases runs horizontally in the middle of photo.*

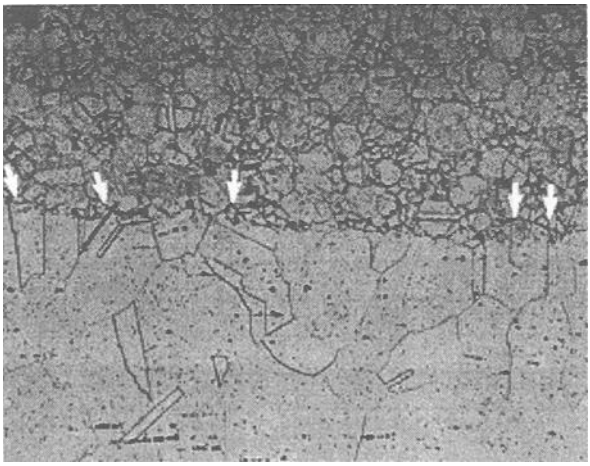


Figure 2 - *Microstructure of the interface between stainless steel powder (above) and solid stainless steel tube inserts (below). Arrows show grain growth penetrating inside powder matrix (distance between first and third from left = 300 μm).*

Results

In order to limit the length of the paper, presentation of results will be mainly limited to low temperature properties relevant to ITER.

Tensile Properties

At low irradiation temperatures (test temperature equal to irradiation temperature), all five alloys exhibit an increase in yield and tensile strength and a reduction in ductility with increasing irradiation dose. A saturation in property changes is observed at higher dose levels [19, 20].

Stainless steel shows the best resistance to low temperature irradiation embrittlement of the five alloys, Fig. 3 [20] [7]. The two copper alloys, despite having a face centered cubic (fcc) microstructure, show already at 0.3 dpa a significant reduction in ductility [19]. The level of embrittlement in the copper alloys varies with the irradiation / test temperature, but in general DS-copper is more sensitive to irradiation embrittlement than CuCrZr. In addition, an exposure of a few hours at 300°C (envisaged as a bake-out treatment) can restore most of the initial ductility of CuCrZr while embrittlement of DS-Copper remains more persistent. The behavior of ferritic/martensitic steels is more complicated than that of the fcc materials due to a shift in ductile to brittle transition temperature and will be discussed in the next section.

At higher irradiation temperatures, hardening in all four materials is reduced or eliminated. The temperature at which the transition from low temperature behavior to high temperature behavior occurs varies for each type of material. For copper alloys it is in the range of 200°C to 300°C and for steels in the range of 350°C to 500°C.

Impact Toughness

These tests are often used as a simple method during acceptance tests to control the quality of initial material or to predict the evolution of materials properties during service. They are also extensively used in the ITER program for testing the performance of HIP joints.

In F/M steels, impact toughness values have a broader significance and hence these tests have been an integral part of the R&D program. Figure 4 shows an example of the results that have helped to establish the current compositions of F/M alloys for DEMO at around 7-10% Cr [21] and Figure 5 gives an example of the data obtained for F82H.

---

[7] Notice that stainless steel shows a higher ductility at room temperature than at about 325°C, where maximum hardening and embrittlement is observed.

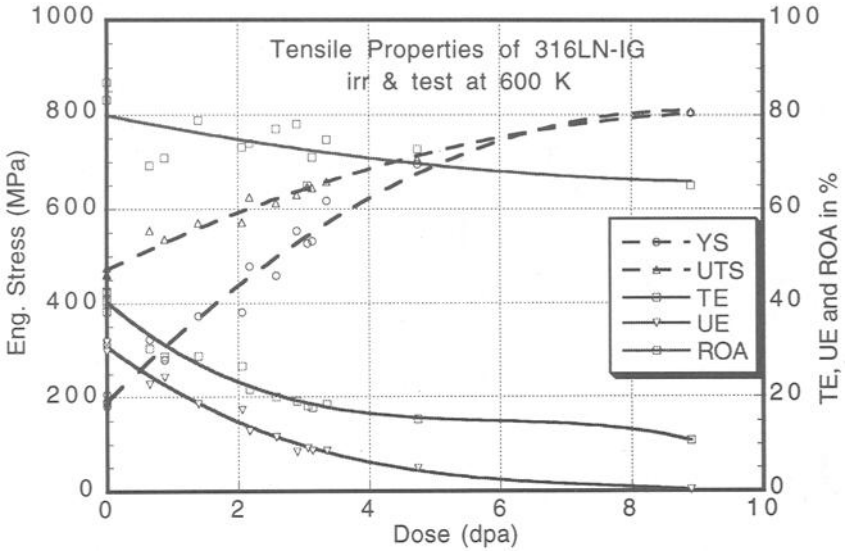


Figure 3 - *Evolution of tensile properties of Type 316LN-IG versus irradiation dose at 600K. Uniform elongation values at strain to necking are only slightly above the max. load values shown in figure, except at 9 dpa where they are relatively higher (0.5%).*

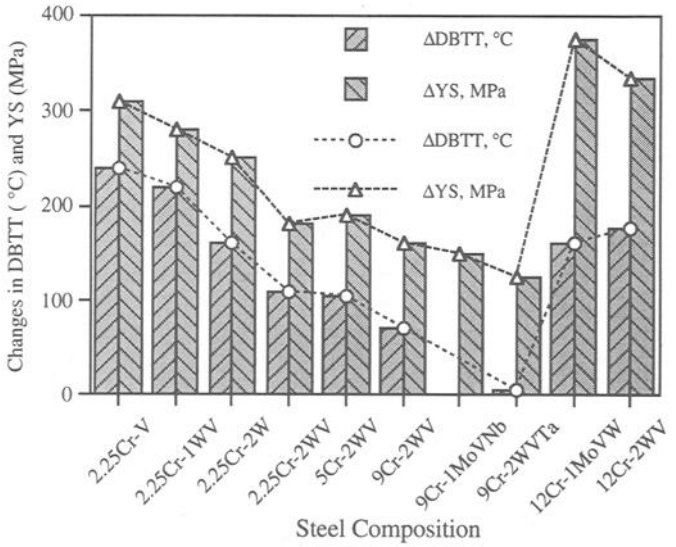


Figure 4 - *Effect of steel composition on the shift in ductile-to-brittle transition temperature (ΔDBTT) of ferritic/martensitic steels after 7 dpa at 365°C.*

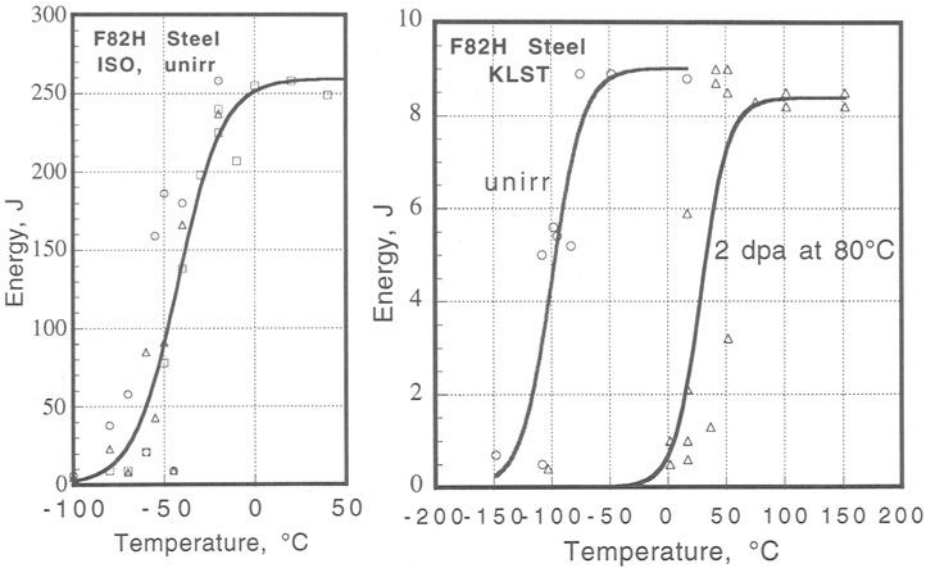


Figure 5 - *Impact toughness of ferritic/martensitic steels before (unirr) and after irradiation (irr) for ISO and KLST specimens* [8].

Fracture Toughness

a) Stainless steel - The results obtained *(J 0.2% offset blunting line)* from tests performed on irradiated 316LN-IG stainless steel and its welded joints have been encouraging, Figure 6. J-integral values remain adequate at least up to 2 dpa [22]. The tests also confirm that the initial peak observed during tension tests is not a true uniform elongation and that the material conserves a reasonable amount of work hardening.

b) Copper alloys - Copper alloys and in particular Cu-Al25, show lower fracture toughness values than 316LN-IG steel [23, 24] and their toughness decreases with increasing test temperature, Figure 7. In the case of Cu-Al25, values as low as 7 kJ/m^2 are recorded in the unirradiated condition at at 300°C. These values are even lower in the irradiated condition or in the short transverse orientation. The reason for such a marked reduction in toughness of DS-Cu with increasing temperature is not yet known. Thermal creep of the copper matrix is probably one of the reasons, as the material is sensitive to strain rate.

c) Ferritic / Martensitic steels - Both conventional and low activation grades of F/M steels have a ductile to brittle transition temperature (DBTT) well below room temperature, often less than –50°C, Figure 5. Their fracture toughness in the ductile region is high and exceeds 200 kJ/m^2 ($J_{0.2BL}$). However, when irradiated at T < ≈ 300°C, their DBTT exceeds room temperature [21]. One of the main objectives of the current fusion R&D program has been to lower the critical temperature at which embrittlement

[8] ISO = standard 10*10*55 mm specimen, KLST = small 4*3*27 mm specimen

occurs to less than 250°C, or if not possible, to limit the extent of the embrittlement in the range of 250-300°C [9].

This goal has been partially achieved and the latest results show that through optimisation of compositions and heat treatments, the DBTT of irradiated materials can be kept below or around room temperature [21]. There are, nevertheless, three reservations. One is that these results are obtained after few dpa and for DEMO data at 70 dpa and higher are needed. Second, the present data do not include or adequately cover the He/dpa ratio expected in fusion reactors. Increasing the He/dpa ratio may shift the DBTT to higher temperatures. Third, the fine tuning of compositions and heat treatments may not hold for HIPed products.

Joint Properties

The available data base for conventional 316LN-IG welds is relatively good and allows reliable statistical analyses. Besides, the trends observed for these joints are similar to those of the parent 316LN-IG metal and at high doses the ductilities of base and weld metals are similar.

In contrast, the data base for copper alloys and ferritic / martensitic steels is still sparse. In ITER most of the joints are HIPed joints and hence, significant effort has been devoted to development, testing, inspection and qualification of these joints.

HIP bounded SS/Cu joints have shown excellent resistance, with failures after tension or fracture toughness testing often located in the copper alloy [18, 19, 23, 24]. However, finite element analyses have shown that standard tests may not reveal the true resistance of the joint. Indeed, higher stresses are developed in the copper alloy side and the crack propagates in a zone adjacent to the joint. Figure 8 shows an example of such an analysis. A cylindrical specimen is cut from a SS/Cu HIP joint (upper half Cu, lower half SS) and then a circular notch is machined around its center (HIP joint). The analysis is performed along different orientations [24]. However, limited available experimental data, show that during creep or creep-fatigue, failure occurs at the joint.

Discussion

The following discussion is centered on two aspects: a) tensile properties and b) small specimen testing.

a) Tensile Properties - Since the ductility of stainless steel is severely reduced after irradiation at low temperatures, a new structural design criterion is needed to supplement the present ones. In ITER this is done by placing a maximum limit on local plastic strain that can be tolerated [9].

---

[9] These materials are well known for their irradiation resistance at higher temperatures.

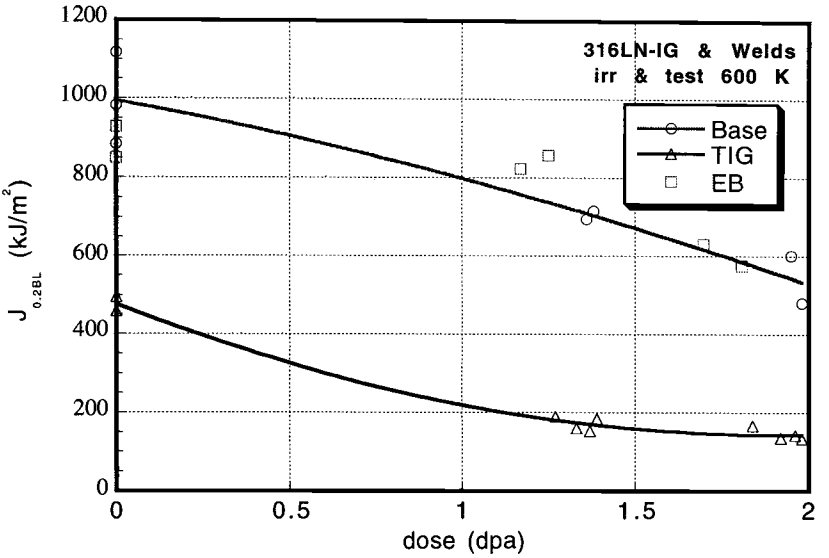


Fig. 6 - *Fracture toughness of 316LN-IG (European Reference Heats I and II) and weld metals (Tungsten Inert Gas and Electron Beam) versus irradiation dose at 600 K.*

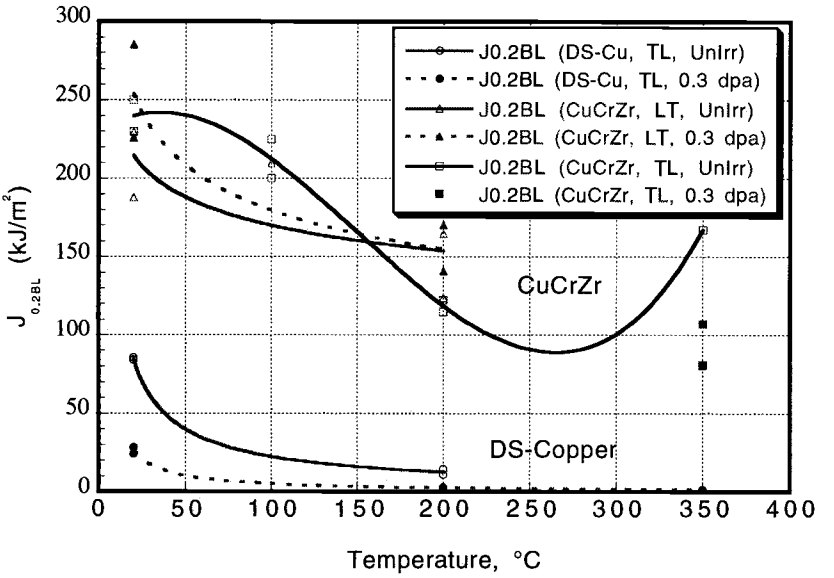


Figure 7 - *Fracture toughness of Cu-Al25 and CuCrZr alloys versus test temperature. Specimen orientation, with respect to the rolling direction, is identified by two letters, 1st letter indicates loading axis and 2nd letter notch direction (e.g. LT).*

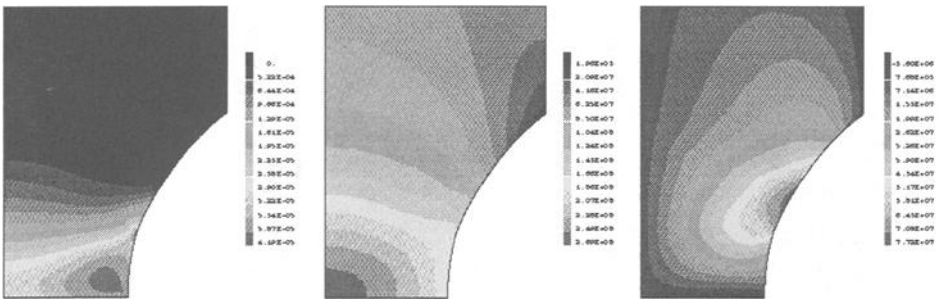


Figure 8 - *Contour maps at rupture on the DS-Cu side of a cylindrical SS/Cu specimen: cumulated plastic strain (left), axial stress σ_{zz} (middle), and shear stress σ_{rz}, (right). Figures shown represent the upper right hand quarter of an axial cross section, where the HIPed joint is situated at the bottom and the specimen head at top.*

If elastic-plastic analyses are performed, it must be demonstrated that the specified load-controlled and strain-controlled loadings do not cause damage due to plastic flow localization (including necking). That is, after calculating the mechanical and thermal loads, the significant mean plastic strain resulting from these loads $(\tilde{\varepsilon}_m)_{pl}$ at all times must satisfy the following limit:

$$(\tilde{\varepsilon}_m)_{pl} \leq \frac{\varepsilon_u(\theta_m, \phi t)}{2} \qquad (1)$$

where

ε_u = the minimum uniform elongation[10] for the thickness-averaged temperature and fluence.

θ_m = mean temperature

ϕ = neutron flux

t = irradiation time

Likewise, to prevent immediate local fracture due to exhaustion of ductility at all times during the life of the component subjected to all loadings for which Criteria Level A is specified, significant local plastic strain $(\tilde{\varepsilon})_{pl}$ must always satisfy:

---

10 Often a peak in stress of irradiated fcc materials is observed just after the elastic region. The material may or may not show subsequent strain hardening. By definition, the true uniform elongation is calculated at the point where necking occurs, i.e. the "strain to necking" criterion.

$$\left(\tilde{\varepsilon}\right)_{pl} \leq \frac{\varepsilon_{tr}(\theta_m, \phi t)}{TF} \qquad (2)$$

where

ε_{tr} = minimum true strain at rupture, for the temperature and fluence of the point under consideration,

TF = Triaxiality factor

Material's data needed are therefore the minimum true strain to rupture and the minimum uniform elongation. The minimum true strain at rupture (ε_{tr}) is determined using the minimum per cent reduction in area at rupture (%RA) by the following formula:

$$\varepsilon_{tr} = \ln\left(\frac{100}{100 - \%RA}\right) \qquad (3)$$

where

% RA = per cent reduction in area at rupture

In cases where the minimum percent reduction in area is not known, the total elongation at rupture (ε_t) can be taken as a lower bound of ε_{tr}. In cases where the total elongation at rupture (ε_t) is not known, the uniform elongation (ε_u) can be taken as a lower bound of ε_t.

In general terms, for each material a correlation between ε, temperature, and dose is needed. In simple terms, the lower ε_u value admitted is roughly about 0.5%.

In cases where the uniform elongation ε_u is lower to 0.2%, the S_y value is taken equal to S_u value (minimum specified yield and ultimate stress values).

b) Specimen size effect - Small or miniaturized specimen testing[11] will be inevitable in the long term fusion program. This is due to the fact that the volume available in an intense neutron source or other high dose facilities will be limited. In preparation for such transition, one has to test the validity of small or miniaturized specimen testing methods and when applicable establish a correlation between standard and small specimen size results.

A series of tests have been performed in the European Union [26, 27] on ferritic/martensitic steels. The results are used to verify the validity of the master curve approach [28]. Figure 8 shows a set of such results for F82H steel . In this figure, the specimen types and sizes tested are: 25 mm Compact Tension (CT) specimens, 10 x 10 x 55 mm Charpy-V three point bend (3PB) specimens, 5 x 10 x 55 mm sub-size Charpy

[11] It is worth noting that the term DBTT is vague and could define a wide range of temperature. Furthermore, DBTT usually varies with the specimen size.

3PB specimens, 5 x 5 x 27 mm miniature 3PB specimens and 3 x 4 x 27 mm KLST 3PB specimens. Specimens are pre-cracked to produce a/W=0.5 in 3PB specimens and a/W=0.6 in CT specimens, and then side grooved. In this figure, T_o defines a transition temperature at which the mean fracture toughness, corresponding to a 25 mm thick specimen, is 100 MPa$\sqrt{m}$ and K_o is 108 MPa$\sqrt{m}$. K_{jc} is calculated from

$$K_{jc} = \sqrt{J_c E} \qquad (4)$$

where:

J_c = J integral of $J_{elastic} + J_{plastic}$ and E = plain strain elastic modulus.

The uncorrected results show the expected trend of increasing fracture toughness as specimen size decreases from CT to smaller specimens. When the results are corrected for the statistical size effects, the results of CT and 10 x 10 x 55 mm 3PB specimens fall within the same scatter band. Reasonable correlations are also obtained for smaller size specimens, but occasionally the latter fall outside the scatter band. Local material heterogeneity or loss of constraint may explain these deviations.

Conclusions

- Austenitic stainless steels, ferritic / martensitic steels and copper alloys are prone to irradiation embrittlement at low temperatures.
- The level of embrittlement varies according to the type of material and is more pronounced in oxide dispersion hardened Cu-Al25 alloy where the initial toughness is already low.
- Advanced manufacturing techniques such as HIPing can produce good quality similar and disimilar joints (SS/SS, SS/Cu, and SS/Cu/Be), but particular attention should be paid to testing of such joints as simple tests may not reveal their true resistance.
- Additional design rules are proposed to guard against irradiation embrittlement of austenitic stainless steels by placing a limit on local plastic strains that can be tolerated.

Acknowledgment

The authors would like to acknowledge the following points:
The current understanding of the materials and joints behavior for application in ITER and beyond is the result of contributions from all four home teams (EU, Japan, RF and USA) and the ITER Joint Central Team.
Technical and financial backing of the European Commission and the NET Team, as well as their own respective laboratories.

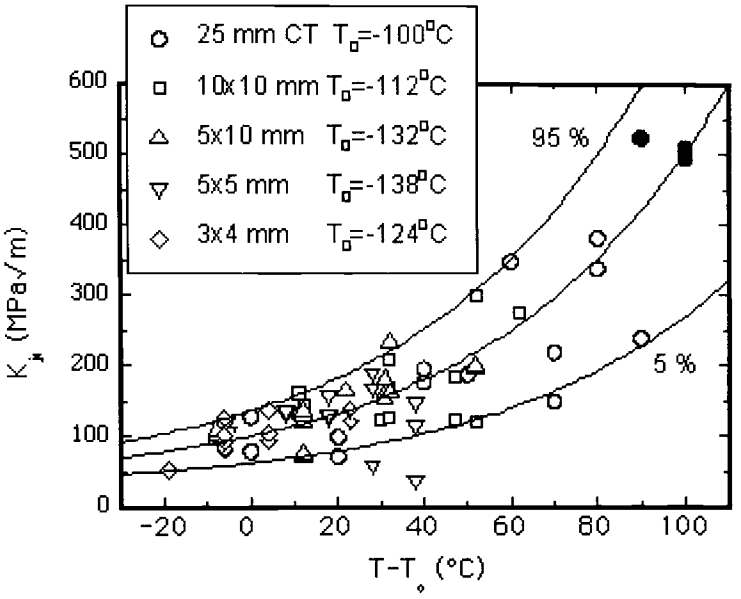


Figure 8 - *Specimen size effect on fracture toughness of unirradiated F82H steel.*

References

[1] ASME Boiler and Pressure Vessel Code, Section III, Case N47-14, (Class I Components in Elevated Temperature service.), pg. 105, New York, American Society of Mechanical Engineers, 1978.

[2] RCC-MR "Règles de Conception et de Construction des Matériels Mécaniques des Ilots Nucléaires RNR.," Tomes, I et II, AFCEN, édition 1993.

[3] MITI, Japanese code for the Monju reactor

[4] PNAE G-7-008-89 "Rules on NPP Equipment and Pipeline Design and Safe Operation," Russian Federation, 1989

[5] Tavassoli, A-A. F., "Assessment of Austenitic Stainless Steels", *Fusion Engineering and Design* , 29, 1995, pp. 371-390.

[6] Dänner, W., Ioki, K., Lorenzetto, P., Cardella, A., Kalinin, G., Santoro, R.T., Gohar, Y., Mattas, R., Strebkov, Y., Takatsu, H., Tavassoli, A-A. F., Batistoni, P., Heller, M., Vieider, G., Vallone, C., Rodgers, E. and Ferrari, M. "The ITER L-4 Blanket Project", 16th IAEA Fusion Energy Conf., Montreal, Canada, Oct. 7-11, 1996

[7] Giancarli, L., "Status of the European Breeding Blanket Technology," 19th Symposium on Fusion Technology, Lisbon, Portugal, Sept. 16-20, 1996

[8] van der Schaaf, B., Ehrlich, K., Fenici, P., Tavassoli, A-A.F. and Victoria, M., "European Structural Materials Development for Fusion Applications", IAEA Meeting, Culham, UK. 1998

[9] "ITER Interim Structural Design Criteria", prepared by ITER Partners, edition 6, August 1997, ITER JWS, San Diego, USA.
[10] Wareing, J. W. and Tavassoli, A-A. F., "Assessment of Martensitic Steels for Advanced Fusion Reactors", Session E08: Advanced Reactor Concepts, Structural Mechanics In Reactor Technology (SMIRT-13), Porte Alegre, 13-18 August 95.
[11] ITER Materials Properties Handbook, prepared by the ITER partners, Package 3, August 1997, ITER JWS, San Diego, USA.
[12] Tavassoli, A. A. F., "Overview of Advanced Techniques for Fabrication and Testing of ITER Multilayer Plasma Facing Walls", 4th International Symposium of Fusion Nuclear Technology, Tokyo, April 6-11, 97.
[13] Solomon, R., Troxell, J.D. and Nadkarni, A.V., "Glidcop Al-25 IG0 Plates - Current Database of Unirradiated Tensile Properties" 4th International Symposium of Fusion Nuclear Technology, Tokyo, April 6-11, 97, MR-P11.
[14] Vella, G., Aiello1, G., Fütterer, M. A., Giancarli, L., Oliveri, E. and Tavassoli, A-A. F., "Water-cooled Pb-17Li Test Blanket Module for ITER: Impact of the Structural Material Grade on the Neutronic Responses" ICFRM-8, 26-31 Oct 97, Sendai, Japan.
[15] Hishinuma, A., Kohyama, A., Klueh, R.L., Gelles, D.S., Dietz, W. and Ehrlich, K., "Current status and future R&D for reduced - activation ferritic/martensitic steels", ICFRM-8, Sendai, Japan. Paper OI-1.
[16] Burlet, H., Marini, B. and Le Marois, G., "ITER Task 214, Unirradiated Tensile Properties of 31LN HIP Joints", EU HT/JCT review Meeting on ITER Materials and Joining Tech. Tasks, Nov. 19-20, 1997, RISO, Denmark.
[17] ITER Primary Module Demonstrator, PowderMet, Sweden.
[18] Lind, A., "Copper Powder / Stainless Steel HIP Joining Techniques", M-97/41, 1997, Studsvik , Sweden.
[19] Edwards, D. J., Singh, B. N., Toft, O. and K. Morita, "Effect of bonding and bakeout thermal cycles on the properties of copper alloys irradiated at 100°C", Poster P-2B-047 ICFRM-8, 26-31 Oct 97, Sendai, Japan.
[20] van Osch, E.V., Horsten, M.G. and de Vries, M.I., "Irradiation Testing of 316LN-IG austenitic stainless steel for ITER", paper S20-016, ICFRM-8, 26-31 Oct 97, Sendai, Japan.
[21] Proceedings of the IEA Working Group Meeting on Reduced Activation Ferritic / Martensitic Steels, JAERI HQ, Tokyo, Japan, Nov. 3-4, 1997.
[22] van Osch, E.V., "Effects of Neutron Irradiation on the Mechanical Properties of Austenitic Stainless Steel Type 316L(N), ITER L4 WP 1.2.2/3 (T214)", ECN-C-97-014, ECN, Petten, The Netherlands.
[23] Tähtinen, S., "Crack Growth Properties of Unirradiated and Irradiated CuAl25 IG0 and CuCrZr Alloys and HIP Joints with 316LN IG0 steel", EU HT/JCT review Meeting on ITER Materials and Joining Tech. Tasks, Nov. 19-20, 1997, RISO, Denmark.
[24] Burlet, H., Bucci, P., and Chu, I., "ITER DPI Task 212b, Fracture Testing of Cu Alloys/316LN SS Joint Interface", CEA/CEREM/DEM 97/77, CEA-CEREM, CEA/Grenoble, France.
[26] Nevalainen, M., Wallin, K., Planman, T., Valo, M. and Tähtinen, S., "Statistical fracture toughness determination with various small specimen types made of F82H-

modified steel", IEA/Jupiter symposium on small specimen test technologies for fusion research, March 13-16, 1966, Tougatta Onsen, Miagi, Japan.

[27] van Osch, E., "Effects of neutron irradiation on the mechanical properties of martensitic stainless steels", in ECN - Netherland annual Progress Report 1996 on Fusion Technology Tasks by J. G. van der Laan, ECN-C-97-014, pp. 53-61, ECN, Petten, The Netherlands.

[28] Wallin, K., "Validity of small specimen fracture toughness estimates neglecting constraint corrections", Constraints effects in fracture theory: Theory and Applications, ASTM STP 144, M. Kirk and A. Backer, Eds., American Society for testing and Materials, Philadelphia, USA, 1995, pp. 519-537.

B. M. Oliver,[1] M. L. Hamilton,[1] F. A. Garner,[1] W. F. Sommer,[2]
S. A. Maloy,[2] and P. D. Ferguson[2]

Helium/Hydrogen Measurements in High-Energy Proton-Irradiated Tungsten

Reference: Oliver, B. M., Hamilton, M. L., Garner, F. A., Sommer, W. F., Maloy, S. A., and Ferguson, P. D., **"Helium/Hydrogen Measurements in High-Energy Proton-Irradiated Tungsten,"** *Effects of Radiation on Materials: 19th International Symposium, ASTM STP 1366,* M. L. Hamilton, A. S. Kumar, S. T. Rosinski, and M. L. Grossbeck, Eds., American Society for Testing and Materials, West Conshohocken, PA, 2000.

Abstract: To provide structural material design data for the Accelerator Production of Tritium (APT) project, a 1 mA, 800 MeV proton beam at the Los Alamos Neutron Science Center (LANSCE) was used to irradiate a large number of metal samples, including a tungsten target similar to that being considered as the neutron source for the tritium production. The maximum proton fluence to the tungsten target was ~10^{21} protons/cm^2. An unavoidable byproduct of spallation reactions is the formation of large amounts of hydrogen and helium. Postulated off normal conditions for APT would result in target temperatures approaching 1200°C. The use of tungsten target rods clad with Alloy 718 raises concerns as to the amount and rate of release of these gases under such off normal conditions, with the major concern being pressurization and possible failure of the cladding. To address these issues, portions of the LANSCE tungsten rods were heated to temperatures up to 1200°C, and the time-dependent evolution of helium and hydrogen gas was measured.

Stepped-anneal and total helium/hydrogen measurements were conducted at Pacific Northwest National Laboratory (PNNL) on multiple samples of the tungsten material. Helium measurements were conducted using a high-sensitivity magnetic-sector isotope-dilution helium analysis system. Stepped-anneal measurements were conducted at temperatures from 25°C to 1600°C in ~100°C steps. Total helium measurements were conducted by rapid vaporization after completion of the stepped-anneal process, and are compared with Monte Carlo calculations performed at Los Alamos National Laboratory (LANL) using the LAHET code system.

Hydrogen measurements were conducted between 750°C and 1200°C using a high-temperature furnace that had been extensively modified for the application. Hydrogen detection was accomplished by periodic sampling of the furnace gas using a separate quadrupole analyzer. Hydrogen measurements are also compared with LANL calculations.

Keywords: helium measurements, hydrogen measurements, Accelerator Production of Tritium (APT), hydrogen release, helium release, tungsten targets, Alloy 718

[1] Pacific Northwest National Laboratory, P.O. Box 999, Richland, Washington 99352, USA.

[2] Los Alamos National Laboratory, Los Alamos, NM 87545, USA.

Copyright© 2000 by ASTM International www.astm.org

Introduction

The Accelerator Production of Tritium (APT) project *[1]* has been proposed as a solution to the national need for tritium. In the APT design, high-energy protons will impinge on a tungsten target producing high-energy spallation neutrons. These neutrons will in turn be multiplied using a lead blanket, then thermalized using water. Tritium production will occur through capture of the thermalized neutrons by ^{3}He gas. One key technical issue that must be addressed by APT is radiation damage to materials in the mixed high-energy proton and neutron environment. To address this issue, a materials irradiation program *[2]* using the 800-MeV proton accelerator at the Los Alamos Neutron Science Center (LANSCE) has been initiated. To simulate the tungsten neutron source in the APT target, a series of tungsten rods was included in the LANSCE materials irradiation assembly.

While reviewing postulated off normal conditions for the APT target, the question of gas buildup inside the Alloy 718 clad tungsten rods was raised. Spallation reactions typically result in copious amounts of helium and hydrogen being produced in the target material. If enough gas is produced and released from the target material, and then trapped at the tungsten/cladding interface, this gas could result in the failure of the target cladding due to a pressure build-up. For the materials irradiation at LANSCE, sufficient room was allowed to accommodate any released gas. However, for the APT target design, this option is not satisfactory. The tungsten rods in the LANSCE materials irradiation were used to address two important questions: (1) Is the produced gas released from the target material and at what rate? (2) how accurately can gas production be predicted for the APT target?

Tungsten Analysis Samples

Five tungsten samples were prepared at Los Alamos National Laboratory (LANL) for the helium and hydrogen measurements. Each sample was in the form of a thin disk cut from a 3.18 mm diameter tungsten target rod that had been irradiated with 800 MeV protons to a fluence of about 10^{21} /cm^2. As the rods were highly radioactive, sample preparation was done in a hot cell. Extensive radiometric analysis was conducted on the samples to provide flux and gradient data for the model calculations discussed below.

Helium Measurements

Helium Analysis System

Helium analyses were conducted by mass spectrometry at Pacific Northwest National Laboratory (PNNL). Details on the mass spectrometry system have been presented elsewhere *[3,4]*. Helium contents were determined by heating and/or vaporizing each sample in a resistance-heated crucible in one of the mass spectrometer system's high-temperature vacuum furnaces. Helium values were determined either by direct measurements of the mass spectrometer helium signal, or by an isotope-dilution technique where the released helium is compared with a known quantity of added ^{3}He "spike". The helium spikes were obtained by expanding and partitioning known quantities of gas through a succession of calibrated volumes*[3]*. The mass spectrometer was calibrated for mass sensitivity during each series of runs by analyzing known mixtures of

^{3}He and ^{4}He. Reproducibility of the analysis system for samples with known homogeneous helium content is ~0.5%. Absolute accuracy is better than 1%.

Stepped-Anneal and Total Helium Measurements

For the helium measurements, small specimens were cut from each tungsten disk using small diagonal wire cutters. Two of these specimens were then analyzed for both stepped-anneal helium release and then later for total helium by rapid vaporization. The mass of each analyzed specimen was determined using a microbalance with calibration traceable to the National Institute of Standards and Technology (NIST). Mass uncertainty is conservatively estimated to be ±0.002 mg.

For the stepped-anneal helium release measurements, the specimens were individually loaded into the central section of a 0.48 cm diameter graphite crucible. Small graphite plugs were placed at each end of the hole to position the samples as close as possible to the middle of the crucible. A diagram of the setup, showing a section of the high temperature furnace is shown in Figure 1.

The initial system design used a thermocouple to measure the crucible temperature. Because of voltage isolation problems encountered with the thermocouple, however, crucible temperature was ultimately measured using an optical pyrometer. Temperature values below the usable range of the pyrometer (<750°C) were determined by applying a linear correction to the thermocouple data based on earlier thermocouple/pyrometer intercomparisons. The temperature for sample W-2 ranged from 25°C to 1600°C in ~133°C increments. Temperature for sample W-3 ranged from 25°C to 1200°C in ~100°C increments. Except for the final temperature step, each step was held for a period of 10 minutes, with helium measurements being made at the approximate midpoint of each interval. For the final (highest) temperature, multiple measurements were taken in approximately 5-minute intervals. The time to reach equilibrium for each temperature was approximately 1 minute. Temperature uncertainty is estimated to be ±50°C. As both ^{3}He and ^{4}He were expected in the samples, no ^{3}He spike was used.

Results of the stepped-anneal measurements are shown graphically in Figures 2 and 3. Helium results are plotted in atomic parts per million (appm), based on a calculated value of 0.328×10^{22} atoms per gram for tungsten. Helium levels were corrected for background helium buildup in the analysis furnace as a function of time, obtained from separate "control" analyses conducted immediately after the sample runs. Background levels increased approximately linearly with time for both helium isotopes, and were in the range of 10^{12} atoms for ^{3}He and 10^{13} atoms for ^{4}He. He-4 background was from diffusion from the atmosphere through the glass furnace top and through the double o-ring top seal. He-3 background was much smaller, likely coming from surface desorption from the furnace walls from previous analyses. The estimated uncertainty in the stepped-anneal results is $\pm 10^{12}$ atoms (±0.1 appm), and is dominated by variability in the helium background.

For sample W-2, helium release is first observed at a temperature of ~800°C. From 800°C up to the final temperature of ~1600°C, the incremental helium release is approximately the same for each temperature step, although there is some indication of a slowly increasing release rate up to ~1400°C. At the final temperature of 1600°C, a total of five measurements were made, and these data show a leveling off of the gas release at a value of ~1.4 appm. Similar trends were observed for sample W-3, with the ^{4}He release tending asymptotically to ~1.0 appm at the highest temperature of ~1200°C. For this second sample, however, there is little evidence for an increasing helium release rate with

temperature (above ~800°C). The ^{3}He release for both specimens was at or below the detection limit of the analysis system (~10^{12} atoms) for the particular setup used in these tests. Variability in the helium release curves is due largely to variability in the subtracted helium background as discussed above.

Following the stepped-anneal measurements, the two tungsten specimens were relocated, in their original crucibles, to different positions in the same furnace for subsequent vaporization analysis. For these measurements, the residual helium contained in the specimens was determined using the isotope-dilution method. Prior to the addition of the spike, however, a first aliquot of the sample gas was taken for a determination of the helium isotopic ratio in the sample itself.

Total helium measurements in the two samples after vaporization are given in Table 1. Total helium measured was 752 appm for W-2 and 713 appm for W-3, with an average of 733 ± 28 (1σ) appm. The ^{4}He/^{3}He isotopic ratio observed in the two specimens was 13.9 and 13.7, respectively, with an average value of 13.8 ± 0.1 (1σ). Background levels for the total helium measurements were negligible compared with the atoms measured. The absolute uncertainty (1σ) in the helium contents is estimated to be approximately 1% to 2%.

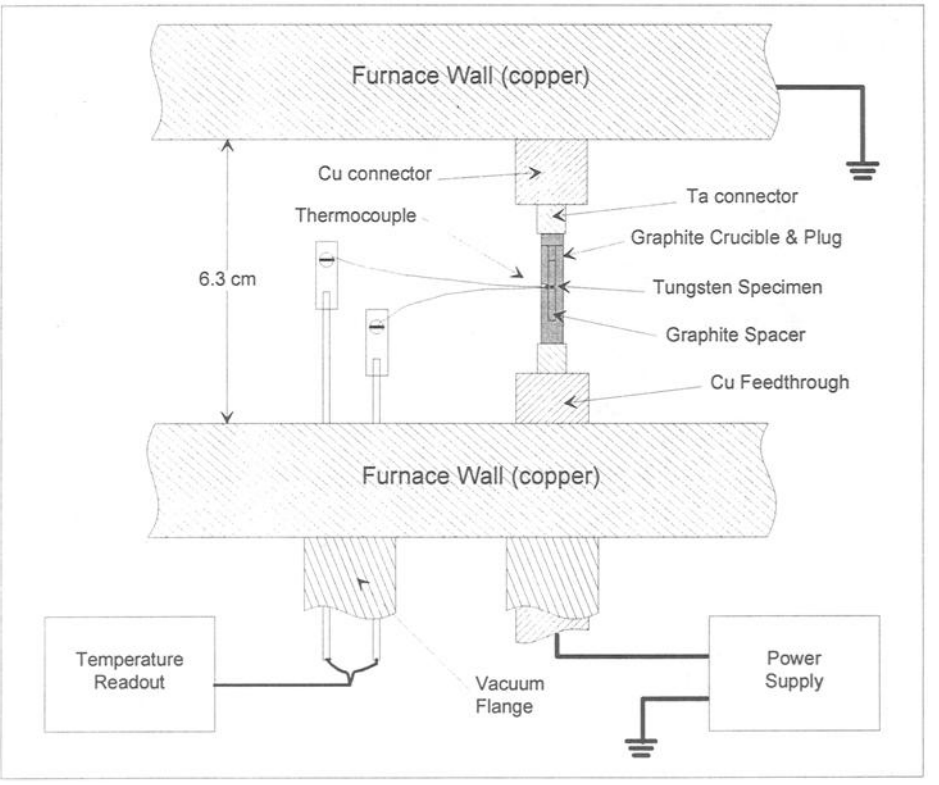


Figure 1 - *Stepped-Anneal Helium Release Setup*

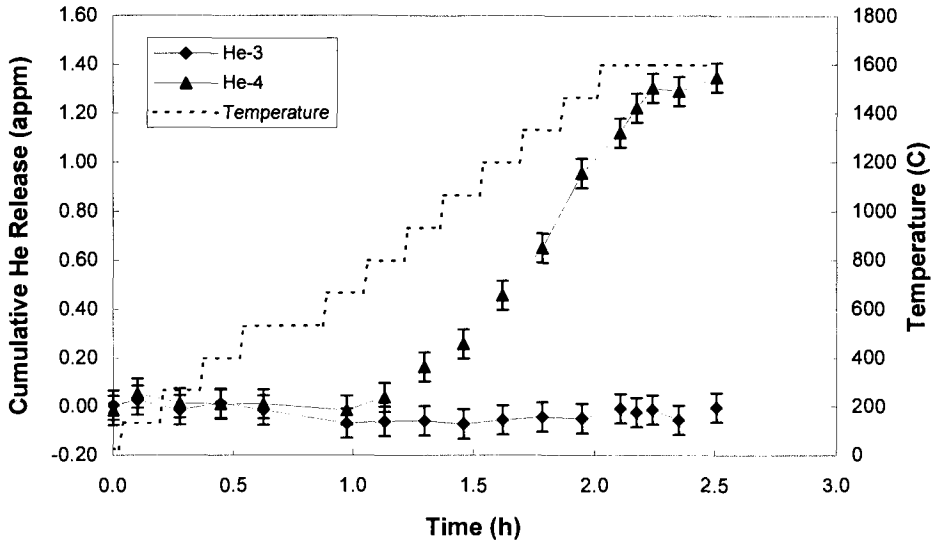


Figure 2 - *Helium Release in Sample W-2*

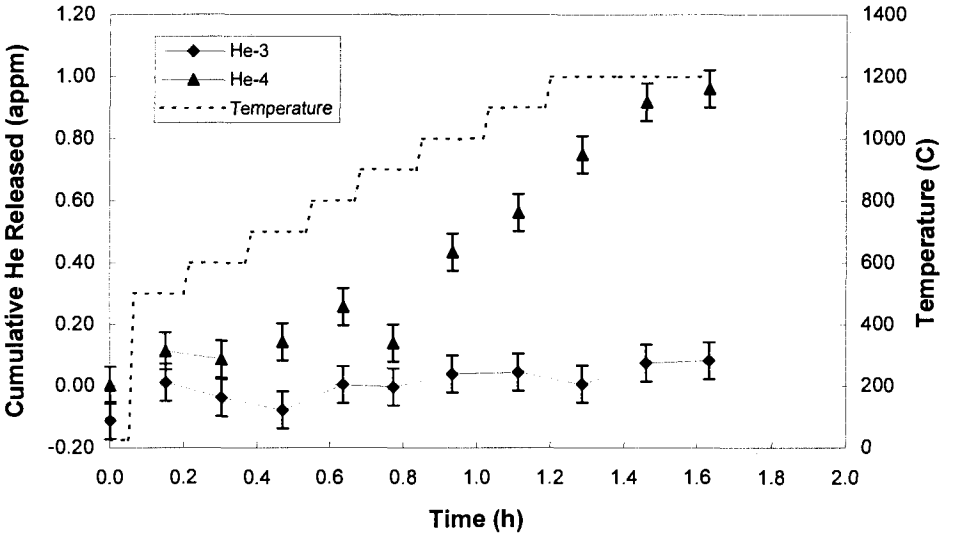


Figure 3 - *Helium Release in Sample W-3*

Table 1 – *Residual Helium Contents in APT Tungsten*

Sample	Material	Specimen Mass[a] (mg)	Measured Helium (10^{14} atoms) ^{3}He	^{4}He	Total	Helium Concentration (appm)[b]
W-2	Tungsten	5.373	8.88	123.4	132.3	752
W-3	Tungsten	3.606	5.74	78.50	84.24	713
					Average:	733 ± 28

[a]Mass uncertainty is ±0.002 mg.
[b]Helium concentration in atomic parts per million (10^{-6} atom fraction) with respect to the total number of atoms in the specimen.

As can be seen from Figures 2 and 3, and Table 1, helium release from the tungsten during the initial stepped-anneal tests was small compared to the total helium inventory. For W-2, the total ^{4}He released at 1600°C was only ~0.2% of the total ^{4}He. Similarly, for W-3, the ^{4}He released by 1200°C was only ~0.1% of the total.

Hydrogen Measurements

Hydrogen Analysis System

Hydrogen measurements were accomplished using one of the analysis furnaces attached to the helium analysis system that had been extensively modified for the task. A schematic diagram of the hydrogen analysis setup is shown in Figure 4. As with the total helium measurements discussed earlier, the hydrogen measurements used an isotope-dilution method with an added ^{4}He spike. Hydrogen and helium ratios were determined using a separate quadrupole detector attached to the helium analysis system. A liquid nitrogen-cooled U-trap was employed in the quadrupole analysis volume to reduce condensable background gas buildup. The magnetic sector instrument used for the helium measurements was not employed due to the integral use of hydrogen getters in the helium system. These getters could be bypassed by use of the quadrupole detector, but still allowed the use of other system vacuum lines and the helium spikes.

The analysis furnace consisted of a boron nitride crucible heated by a resistance-heated tungsten filament inside a water-cooled copper enclosure. The crucible temperature over the range of 750°C to 1200°C was determined using an optical pyrometer. The temperature uncertainty is estimated to be ±50°C. The inside surface of the copper was partially plated with a gold evaporation layer to minimize hydrogen uptake by the furnace walls that had been observed during initial system testing.

For analysis, the sample was placed in the upper stainless steel section of the furnace, and after a suitable pumping period to minimize the hydrogen background, was mechanically dropped into the heated furnace for analysis. Just prior to dropping the sample, the furnace was isolated from its vacuum pump, and the ^{4}He spike was added to the enclosure. After approximately one minute, a sample of the furnace gas was taken by expanding and then trapping the gas between two valves on the analysis line. This sample was then expanded into the quadrupole analyzer volume, which at this point was also isolated from its vacuum pump. This sampling process was repeated, allowing multiple determinations of the helium/hydrogen ratio. A control run was conducted immediately

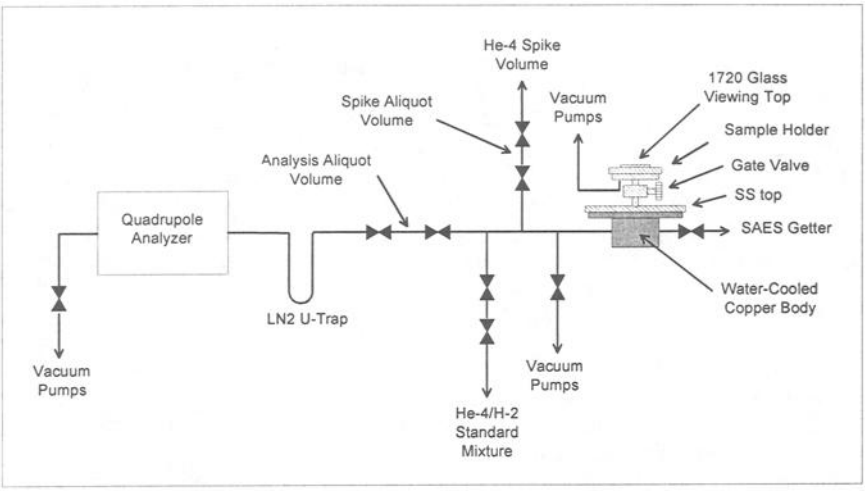


Figure 4 - *Schematic Diagram of Hydrogen Analysis System*

prior to the sample analysis. Calibration of the quadrupole for each sample run was accomplished using a hydrogen/helium standard mixture attached to the analysis furnace.

Hydrogen Release From Tungsten

Hydrogen measurements were conducted on two of the irradiated tungsten samples from the original group of five samples prepared at LANL, and on two unirradiated samples from the same material lot. Both of the unirradiated and one of the irradiated samples were analyzed at a single temperature of ~1200°C, which is the postulated off normal scenario for the APT project. The second irradiated sample was analyzed sequentially at four different temperatures, starting at ~750°C and increasing in ~150°C steps up to ~1200°C. The results of the hydrogen measurements are given in Table 2.

Measured hydrogen releases for the unirradiated materials were 32 ± 43 and 228 ± 19 appm, for an average of 130 appm. For the irradiated tungsten sample analyzed at a single temperature of 1200°C, the observed hydrogen release was 2110 ± 140 appm. In each case, the second of the two numbers are the 1-sigma values for the distribution of three or four replicate measurements. For the second irradiated sample, W-1, the observed releases at 750°, 900°, and 1050°C, showed continuing cumulative hydrogen release during the replicate measurements. The values in the last two columns of Table 2 give the range (first and last) of values measured over the ~8 minute analysis time period. At the 1200°C step, however, all four replicate measurements gave essentially no additional hydrogen above system background (i.e., <100 appm). This suggests that the hydrogen had all been released from the sample, and that this release occurred in the five to six minute time period following the 1050°C measurements while the sample was still at temperature. The last row in the table, therefore, gives an estimate of total hydrogen in sample W-1, based on the total heating time (~16 min), and the rate of hydrogen released (in appm/min) at each temperature step. This estimated range assumes that all the

hydrogen was released from the tungsten, since there was no additional release observed at the 1200°C step.

Hydrogen release values for sample W-1 are also shown graphically in Figure 5. The dotted lines in the figure represent a linear extrapolation of the observed hydrogen release for each temperature for the five to six minute period that the sample was still at temperature following each set of replicate measurements. Hydrogen release rates at 750°, 900°, and 1050°C were ~60, 50, and 140 appm/min, respectively. Hydrogen release values in Figure 5 for the 1200°C step are plotted at the highest estimated total release value of ~3800 appm, however, it was not possible from the available data to determine at what point in the 1050°C step the hydrogen stopped being released.

Uncertainty in the hydrogen measurements is conservatively estimated at ±50%, due largely to two factors; 1) hydrogen background, and 2) hydrogen uptake by the furnace components and/or walls. Hydrogen background generally ranged from about 10^{16} to 10^{17} atoms over the time period of the analyses resulting in signal-to-background ratios from about 1.2 to 4. Hydrogen uptake was observed in the system during system testing. Performing an in-situ gold plating of the furnace interior resulted in a significant reduction in the uptake, from maximum values of ~99% down to ~50%. This uptake is accounted for by applying a correction factor based on the C/M ratio observed for the internal helium/hydrogen standard mixture. This correction also accounts for sensitivity differences in the quadrupole analyzer for helium and hydrogen. Since the amount of hydrogen in the standard mixture is generally larger than measured in the tungsten samples, however, some uncertainty in the accuracy of this correction remains.

Table 2 - *Hydrogen Release in APT Tungsten*

Sample	Material	Sample Mass[a] (mg)	Analysis Temperature (°C)	Measured Hydrogen 10^{16} atoms	Measured Hydrogen (appm)
W-Blk-1	Tungsten control	48.8	1200	0.5	30
W-Blk-4	Tungsten control	87.2	1200	6.5	230
W-4	Irr. Tungsten	22.8	1200	160	2100
W-1	Irr. Tungsten	11.7	750	0.8 – 1.6	220 – 410
"	"	"	900	0.5 – 1.5	140 - 390
"	"	"	1050	0.1 – 2.8	15 - 720
"	"	"	1200	<0.1	<100
	Estimated total hydrogen release for Sample W-1:				2400 - 3800

[a]Mass uncertainty is ±0.01 mg.

[b]Hydrogen concentration in atomic parts per million (10^{-6} atom fraction) with respect to the total number of atoms in the sample.

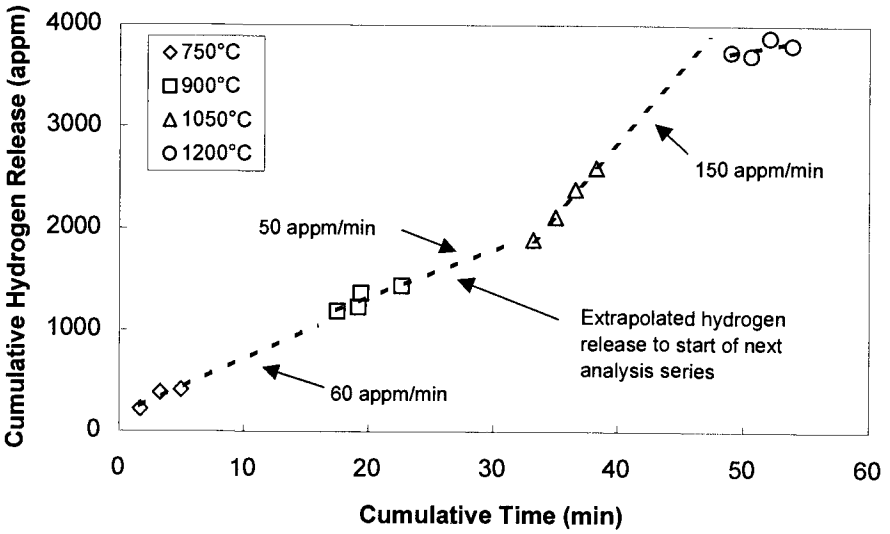


Figure 5 – *Hydrogen Release From Irradiated Tungsten at Temperatures Between 750°C and 1200°C*

LAHET Calculations of Helium and Hydrogen Content

A detailed Monte Carlo model of the APT materials irradiation has been completed at LANL using the LAHET Code System (LCS) *[5]*. The LCS is the neutronic tool used for the design of APT and the estimation of radiation damage parameters, such as DPA and gas production. Because the proton energy spectrum and beam profile vary throughout the APT target/blanket (starting typically at 1.6 GeV), the measurement presented is prototypic for only one region of the target system. However, using the measurement as a calibration for the LCS will provide some insight into the accuracy of gas production predictions throughout the APT target/blanket.

Figure 6 shows an elevation view of the Monte Carlo model with the location of the tungsten rods indicated. The incident 800-MeV proton beam first travels through a proton beam entry window (Alloy 718) and is then incident on four tubes loaded with materials samples of varying composition. The inclusion of these elements in the Monte Carlo model is critical due to energy loss and beam divergence resulting from the elements. Additional elements, such as the furnaces near the tungsten samples and the materials samples downstream (in the direction of the proton beam) from the tungsten samples, insure that the neutron return from surrounding structures is modeled correctly. The model and tallies used also insure a direct comparison with the experiment because what was actually measured was not the helium or hydrogen production, but rather the helium or hydrogen atoms that slowed down and stopped in the samples and did not diffuse out of the samples. The LCS does not account for the diffusion of hydrogen and helium during irradiation and no attempt was made to correct the calculations for diffusion out of the samples during irradiation. While diffusion was not expected to be a

problem with the helium comparison, the possibility of significant hydrogen diffusion out of the sample was identified as a possible error for the comparison.

Calculations of the helium and hydrogen production were carried out using versions 2.70 and 2.83 of the LCS. While LCS version 2.83 is the standard for APT, most of the previous comparisons with gas measurements were completed with LCS 2.70 or equivalent programs*[6]*. Because the measured results are related to the total number of helium and hydrogen atoms that are stopped in the sample volume and not necessarily the production rate in the sample, the tally option used was IOPT=14 with charged particle transport turned on in LAHET (this is not the default LAHET option). The LCS default level density model was used with a pre-equilibrium model following the intranuclear cascade (not the LCS default). The results are summarized in Table 3 with a comparison to the average measured values. Statistical errors in the LCS calculations were less than 3%. With the statistical error as a guideline, the LCS versions appear to have roughly the same accuracy with regards to predicting helium and hydrogen concentration in the samples in the center of the proton beam (i.e., where gas production is dominated by the primary 800-MeV proton beam). Other irradiation geometries (e.g., where secondary, lower-energy particles produce more of the helium) may lead to larger differences between the two versions of LCS. Although the statistical errors in the LAHET calculations are small, overall uncertainty is expected to be about 50% for the prediction of radionuclides in general. This uncertainty estimate is based primarily upon the work of Ullmann, et al.*[7]*, who measured radioactive spallation products from tungsten and lead targets. The variation of predictive capabilities is large and seems, to some extent, to be a function of the target material *[6,7]*.

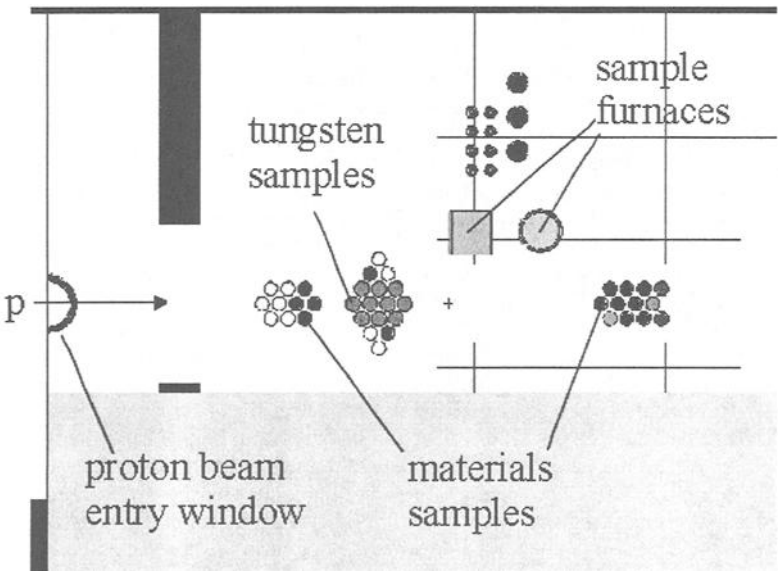


Figure 6 - *Monte Carlo Model of the APT Materials Irradiation*

Table 3 - *Comparison of LCS Calculations With Measured Helium and Hydrogen Concentrations*

LAHET Version	Gas Concentrations (appm)					
	Helium			Hydrogen		
	Measured	Calculated	C/M[a]	Measured[b]	Calculated	C/M[a]
2.70	734	710	0.97	~2600	4950	1.90
2.83	734	760	1.04	~2600	4980	1.92

[a]Calculated-to-measured ratio.
[b]Average of measured values for W-2 and W-3 (~2100 appm and ~3100 appm).

Discussion and Conclusions

Helium release from two irradiated tungsten samples during stepped-anneal tests was small compared to the total residual helium inventory measured in the same samples. At 1200°C, which is the postulated off normal temperature for the APT project, the total helium release for one sample was only ~0.1%. At 1600°C, the total helium release in a second sample was only slightly higher at ~0.2%. Helium release was first observed at about 800°C. One sample showed some evidence for an increasing helium release with temperature between 800°C and 1400°C. At the highest temperatures reached, where multiple helium analyses were conducted, both samples showed evidence of a leveling off in the helium release, suggesting a helium release mechanism other than simple diffusion. Helium-3 release for both samples was at or below the detection limit of the analysis system (~10^{12} atoms) for the particular setup used in these tests. Given the low quantities of helium release at 1200°C, it is unlikely that this release will result in any pressure buildup at the target/cladding interface of a production target.

Total helium concentrations measured in the two irradiated tungsten samples had an average value of 733 ± 28 (1σ) appm, with sample W-2 being slightly higher. Review of the radiometric data from the irradiated samples would suggest that Samples W-2 through W-4 would be expected to have about the same gas production, with Sample W-1 being somewhat higher. Comparison with LAHET calculations gives C/M values of 0.97 and 1.04 depending on the version of LAHET used. This is excellent agreement, however, in view of the estimated 50% uncertainty in the LAHET values, this close agreement is likely fortuitous. Absolute uncertainty (1σ) in the helium contents is estimated to be approximately 1% to 2%.

Hydrogen measurements conducted on two unirradiated samples of as-received tungsten material showed a low hydrogen impurity content of less than about 100 appm. Analyses of two irradiated samples, one at 1200°C, and the other sequentially from 750°C to 1200°C gave total hydrogen contents ranging from approximately 2100 up to possibly 3800 appm. The stepped temperature measurements showed hydrogen release from the tungsten at the three lower temperatures of 750°C, 900°C, and 1050°C, with the highest observed release rate (~140 appm/min) occurring at the 1050°C step. No additional hydrogen release was observed at 1200°C, suggesting that all the hydrogen had been removed from the sample at some point during the heating at 1050°C.

Both analyses suggested complete hydrogen release from the tungsten at temperatures of 1200° (or lower), within a few minutes, and suggest diffusion controlled release. Whether or not this released hydrogen will result in a pressure buildup at the

target/cladding interface of a production target depends largely on whether or not any gaps exist between the tungsten and the cladding. If no gap exists, then the hydrogen will likely diffuse through the Alloy 718 at a rate equal to its release from the tungsten. If a gap exists, however, the hydrogen will likely recombine to form molecular H_2, and release through the cladding may be slow.

Comparison of the hydrogen values with LAHET calculations gives C/M values of 1.90 and 1.92, again depending on the version of LAHET used. Some of the discrepancy between the calculated and measured values is undoubtedly the result of the combined uncertainties in both the measurements and the calculations (about 50% each). In addition, there was expected to be some diffusion of hydrogen out of the tungsten during the irradiation which would result in measured values being lower than calculated.

Within the respective uncertainties of the gas measurements and calculations, several observations can be made:

- Significant levels of helium and hydrogen were measured in the irradiated tungsten target material. Hydrogen levels in unirradiated material were less than ~100 appm. Although not measured, helium levels are expected to be negligible in the unirradiated tungsten.
- Helium release at the postulated off normal temperature of 1200°C is small at about 0.1 to 0.2% of the total generated helium. Helium release first occurs at ~800°C, and the release rate does not change significantly with temperature. Multiple helium measurements conducted at 1200°C and 1600°C showed a leveling off of the helium release with time, suggesting release mechanisms other than simple diffusion.
- Given the small levels of helium released, helium gas buildup should not contribute significantly to any pressure buildup at the target/cladding interface of a production target.
- Hydrogen release was seen to occur at the lowest temperature of 750°C employed in the present analyses, with the highest observed release rate occurring at the 1050°C step, suggesting diffusion controlled release.
- The measurements suggest that complete release of generated hydrogen occurs within a few minutes at a temperature of 1200°C. Whether or not this released hydrogen will contribute to a pressure buildup at the target/cladding interface will depend on whether there is a gap at the interface.
- LAHET calculations of gas generation in the target tungsten agreed reasonably with measurements within estimated uncertainties.

Acknowledgements

This work was supported by the U.S. Department of Energy under the Accelerator Production of Tritium Program at Los Alamos National Laboratory.

References

[1] APT ^{3}He Target/Blanket Topical Report, Los Alamos National Laboratory Report LA-CP-94-27, rev. 1, 1994.

[2] Maloy, S. A. and Sommer, W. F., "Spallation Source Materials Test Program", *Proceedings of the Topical Meeting on Nuclear Applications of Accelerator Technology*, Albuquerque, NM, November 16-20, 1997, pp. 58-61.

[3] Farrar, H. IV and Oliver, B. M., "A Mass Spectrometer System to Determine Very Low Levels of Helium in Small Solid and Liquid Samples," *Journal of Vacuum Science and Technology - A*, Vol. 4, 1986, pp. 1740-1741.

[4] Oliver, B. M., Bradley, J. G., and Farrar, H. IV, "Helium Concentration in the Earth's Lower Atmosphere," *Geochimica et Cosmochimica Acta*, Vol. 48, 1984, pp. 1759-1767.

[5] Prael, R. E. and Lichtenstein, H., "User Guide to LCS: The LAHET Code System," Los Alamos National Laboratory Report LA-UR-89-3014, September 1989.

[6] Green, S. L., et al., "Production of Helium by Medium Energy Protons", *Journal of Nuclear Materials*, Vol. 155-157, 1988, pp. 1350-1353.

[7] Ullmann, J. L., et al., APT Radionuclide Production Experiment Technical Report, LA-UR-95-3327, September 1995.

Vitalii D. Parkhomenko,[1] Sergei F. Dubinin,[1] Sergei G. Teploukhov,[1] and Boris N. Goshchitskii[1]

Amorphization of Solids Irradiated by Fast Neutrons

Reference: Parkhomenko, V. D., Dubinin, S. F., Teploukhov, S. G., and Goshchitskii, B. N., **"Amorphization of Solids Irradiated by Fast Neutrons,"** *Effects of Radiation on Materials: 19th International Symposium, ASTM STP 1366,* M. L. Hamilton, A. S. Kumar, S. T. Rosinski, and M. L. Grossbeck, Eds., American Society for Testing and Materials, West Conshohocken, PA, 2000.

Abstract: The diffraction patterns of amorphous solids produced by both a conventional technique and fast neutron irradiation were systematized. The diffraction patterns of the substances of these classes differ essentially. It was first ever shown that neutron radiation modified solids belong to the group of amrophous substances of a distortion type.

Keywords: neutron irradiation, atomic displacement cascade, long- and short-range atomic order, amorphous state, X-ray and neutron diffraction

Introduction

The early papers on the amorphization of solids by fast neutrons were published a little more than fifteen years ago [*1,2*]. There, the ferrogarnet $Y_3Fe_5O_{12}$ and intermetallics V_2Zr were transformed into an amorphous state after irradiation by the fast neutrons, fluence $F \sim 2 \times 10^{24}\ m^{-2}$. Later, several more types of substances were amorphized with fast neutrons in nuclear reactors [*3-5*].

Table 1– *Scattering Vectors of Diffraction Peaks in Neutron Diffraction Patterns of Solids Amorphized under Fast Neutron Irradiation.*

Substance	*Initial phase*	k_1, $Å^{-1}$	k_2, $Å^{-1}$	k_3, $Å^{-1}$
V_2Zr [*2*]	C15	2.5	3.6	4.2
Mo_3Si [*3*]	A15	2.9	4.5	
$Gd_3Ga_5O_{12}$ [*4*]	Garnet	2.2	3.8	
$Ti_{49}Ni_{51}$	B2	1.9	3.0	3.5

[1]Head of group, research scientist, research scientist, professor, respectively, Institute for Metal Physics, Ural Division Russian Academy of Sciences, Kovalevskoi Str.18, 620219, Ekaterinburg, Russia.

Copyright© 2000 by ASTM International www.astm.org

In Figures 1b and 1c the X-ray and neutron diffraction patterns of the single crystal $Ti_{49}Ni_{51}$ after irradiation ($F_n=2.5\times10^{24}$ m^{-2}, $E_n\geq0.1$ Mev, $T_{irr}=340K$) are given as an example of such a type. The scattering vectors k_i $(i=1,2,3)$ corresponding to maximum intensities of diffraction peaks from Figure1c are presented in Table 1; the experimental values of k_i for some other amorphous substances of this class are also included.

It can be seen from Table1 that k_i-values for various substances differ essentially. This fact testifies that the positional short-range order varies in irradiated materials.

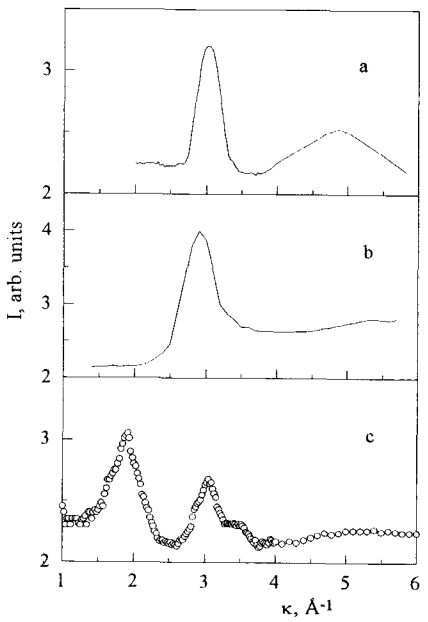


Figure 1 – *Diffraction Patterns of Amorphous Titanium Nickelide:*
a – X-ray diffraction pattern of $Ni_{40}Ti_{60}$, amorphized by rapid quenching from the melt [6];
b – X-ray diffraction pattern of $Ti_{49}Ni_{51}$ single crystal amorphized by fast neutron irradiation;
c – neutron diffraction pattern of $Ti_{49}Ni_{51}$ single crystal amorphized by fast neutron irradiation.

The peculiarity of the diffraction patterns considered is clearly revealed when they are compared with diffraction patterns of amorphous substances produced by the rapid quenching from a liquid phase and which are well known from the literature [6-8]. It is illustrated by the X-ray pattern (Fig.1a) of $Ti_{40}Ni_{60}$ [6] amorphized by the above technique.

Diffraction peaks in Figure 1a correspond to the scattering vector

$$k_1 \cong 3\ \text{Å}^{-1},\quad k_2 \cong 5\ \text{Å}^{-1}. \quad (1)$$

As it follows from Figure1 an experimental situation essentially depends on a method used to produce amorphous substances.

It is known, that values k_i are universal for amorphous materials produced by the quenching from liquid state. It can be proved by the data from Table 2.

At present the diffraction patterns of classical amorphous substances are quite reliably interpreted. Their universality was found to be mostly due to the similarity of short-range atomic orders of these materials in amorphous and liquid phases [7].

It is exactly the lack of universality in the scattering patterns of the solids amorphized with fast neutrons (see Table 1) that constitutes their peculiarity. This work aimed to determine the structure state specificity of amorphous materials of this class.

With this object in view a single crystal of the binary alloy with a simple cubic lattice β-$Ti_{49}Ni_{51}$ was chosen. The structure state of irradiated titanium nickelide were studied by the X-ray and the thermal neutron diffraction; and the data on point defects

Table 2 – *The Scattering Vectors of Diffraction Peaks in the Diffraction Pattern of the Substances Amorphized by Quenching from a Liquid Phase.*

Substance	*Initial Phase*	k_1, $Å^{-1}$	k_2, $Å^{-1}$
NiTi [6]	B2	3	5
Fe [7]	A2	3	5
NiNb [8]	R	3	5

were obtained from electrical resistivity measurements. Detailed information on samples and methodology can be found in [*9*].

Experimental Results and Discussion

We must focus on the most significant peculiarity of titanium nickelide amorphized under fast neutron irradiation. It consists in the recovery not only of the initial crystal structure but also the degree of perfection of a single crystal sample after annealing of the irradiated alloy.[2] In Figure 2, the intensities (110) of structural reflex are shown in the neutron diffraction pattern of $Ti_{49}Ni_{51}$ before irradiation, and annealed after irradiation. It is an important fact since it means that a positional short order of the amorphous phase (***AP***) produced by fast neutrons is directly related to the crystal phase (***CP***) of the unirradiated sample. In other words, a structural transformation to the amorphous phase proceeds under fast neutron irradiation according to the direct scheme

$$CP \Rightarrow AP \qquad (2)$$

and does not follow the sequence

$$CP \Rightarrow LP \Rightarrow AP \qquad (3)$$

as is the case of quenching from the liquid phase (***LP***).

Now we can compare a neutron scattering pattern of titanium nickelide in an amorphous state after irradiation with that of unirradiated polycrystalline $Ti_{49}Ni_{51}$.

The required data are present in Figures 3a and 3b, respectively. The diffraction peaks angular positions nearly coincide with the (100), (110) and (111) reflections of the initial ***B2*** phase. The first and the third peaks in Figure 3a, as well as the (100) and (111) reflections in Figure 3b are superstructural. The origin of this super structure is related to keeping the chemical short order in the amorphous phase of titanium nickelide. The intensities of superstructural diffusion peaks are proportional to the squared difference of atomic scattering factors of nickelide and titanium - $(f_{Ni} - f_{Ti})^2$. Then in the case of neutron diffraction the super structure would be well observed,

[2] In our opinion, a convertibility of a titanium nickelide single crystal macrostructure fully eliminates the statement that the diffusion scattering pattern in Figures 1b, 1c is a result of nanostructure formation in the irradiated alloy.

since scattering nuclear amplitudes of *Ni* and *Ti* have different signs; it is not detectable in X-ray diffraction, because their atomic factors have the same signs and close values. This agreed well with the experimental results. Thus, only one diffusion peak in Figures 1b and 1ccorresponding to $k = 2.9 Å^{-1}$ characterizes a positional short-range order in the irradiated $Ti_{49}Ni_{51}$. There are two peaks for the amorphous alloy produced by quenching from the liquid phase. This constitutes one more peculiarity of amorphous $Ti_{49}Ni_{51}$ produced by fast neutrons. A diffraction peak absence in the range $k > 3 Å^{-1}$ in Figure 1b testifies to a compact positional short range order, i.e. the atomic distribution in the radiation-modified alloy is more uniform.

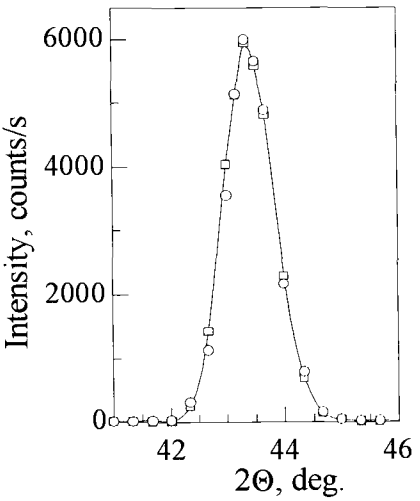


Figure 2 – *Neutron Diffraction Patterns Peak (110) Single Crystal* $Ti_{49}Ni_{51}$

○ – *before irradiation;*

□ – *after irradiation and after annealing*

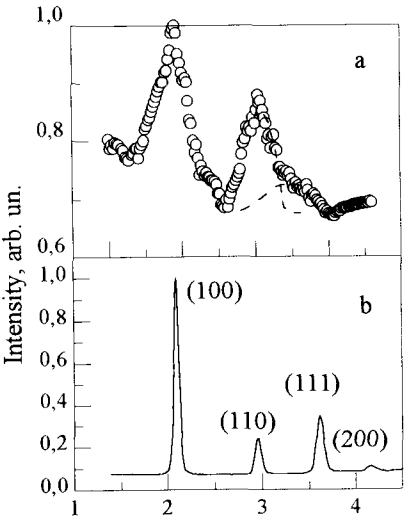


Figure 3 – *Neutron Diffraction Pattern*

a – irradiated single crystal $Ti_{49}Ni_{51}$

b – unirradiated powder

Now we need to consider the radial distribution of atoms in such an alloy. For isotropic systems the reduced function for the radial distribution has the form [*10*]:

$$g(r) - 1 = \frac{\Omega}{N} 2\pi^2 r \int [I(k) - 1] \, Sin\,(kr)\, k\, dk \qquad (4)$$

The function $g(r)$ is proportional to the average number of atoms in a layer between two spheres of radii r and $r+dr$. The value of N/Ω in (4) is equal to a mean density of atoms in an amorphous alloy. $I(k)$ is the structural factor, which represents

an experimental diffraction pattern with the deduction of the known corrections. The results of the calculation performed are presented as a solid curve in Figure 4. In this curve the density modulation of atoms are quickly damping with the increasing r, and $g(r)$ is becoming equal to its mean value in the region $r > 6$ Å. For a comparison, the function for titanium nickelide [6] quenched from the melt is designated by a dash line. One can see that modulations of the dash curve reach the value of $r \sim 10$Å; i.e., a short-range order in a classical amorphous substance is more extended.

In Figure 4 there is one more noteworthy difference in the two functions. It is more vivid in the structure of the second modulation $g(r)$, which comprises two peaks [6].

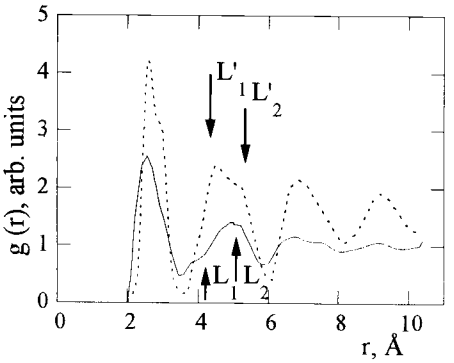


Figure 4 – *Radial Distribution Atom Functions of Amorphized TiNi*

---------- *quenched from the melt* [6];

——— *irradiated by fast neutrons*

Their positions are designated as L_1 and L_2 in the solid curve and L'_1 and L'_2 in the dash line. It is reasonable that these peaks values can be considered as proportional to the occupational numbers of the crystal lattice, by the type of which a short- range order is realized in a specified amorphous substance. In the case under consideration a comparison, should be made with the typical atomic distance of a *BCC* lattice; and in the analysis of the $g(r)$ (designated by dashes) function, the atomic distance of close packed lattices, e.g. *FCC*, should be used.

The occupational numbers for *BCC* and *FCC* lattices are given in Figures 5a and 5b, respectively. Atomic distances and occupational numbers form the peaks of the correlation functions under the analysis; they are designated by the same symbols there. Their correlation qualitatively explains the values of the corresponding peaks in Figure 4.

Thus, preliminary conclusions can be made with respect to the structure of titanium nickelide amorphized by fast neutrons:

- its short-range positional order corresponds to the initial *B2* phase, opposite to a close packed crystal structure of the amorphous alloys produced by the traditional technique;
- a chemical short range order is retained in an amorphous phase;
- a short range order of radiation modified titanium nickelide is more compact.

Earlier it was shown [11], that radiation defects cause amorphization, since they initiate a chaotic displacement of atoms from their sites in an original cubic lattice. We consider in more details the qualitative titanium nickelide amorphization model.

In the case under study here, radiation damage proceeds according to the scheme:

$$n^0 \Rightarrow PKA \Rightarrow ADC \qquad (5)$$

where:

n^0 = a fast neutron;
PKA = a primary atom knocked out from a crystal lattice;
ADC = an atom displacement cascade.

An atom displacement cascade is created by a ***PKA*** in a crystal. The values of sections of separate reactions (5) are discussed in detail in [*12*].

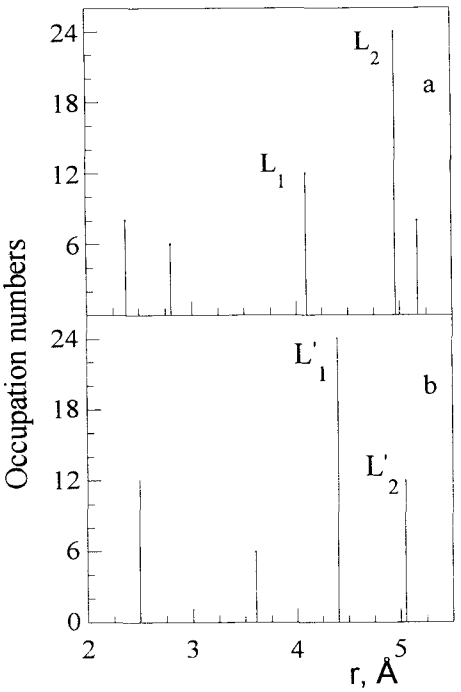


Figure 5 – *Occupation Numbers Nearest Coordination Spheres*
a – BCC lattice; b – FCC lattice

According to the experimental data [*11*] one should assume an amorphous phase to be formed in the after-path of ***ADC*** in the massive $Ti_{49}Ni_{51}$. Then the mean volume, ***V***, of an amorphous cluster is to be determined. Its relation to an amorphous phase fraction in a sample follows the expression [*13*]:

$$C = 1 - exp(-VN\sigma F), \quad (6)$$

where:
C = the amorphous volume fraction of a sample;
N, σ, F = the known parameters [*11*].

Assuming that a form of a cluster is spherical, we calculated its diameter to be equal to ~***70 Å***. Thus, in a massive specimen separate particles of amorphous materials have a rather small size under neutron irradiation.

As is known [*12*], a ***PKA*** "produces" an ***ADC*** with the energy of several tens of ***KeV***. It is suggested that the structure state of the ***ADC*** in its initial state corresponds to the structure of a substance in a liquid phase. Since the time of ***ADC*** relaxation is very short ($\tau \approx 10^{-11} \div 10^{-10}$ s [*12*]) then a positional disorder, close to a liquid phase structure, might be expected in the crystal volume, through which the ***ADC*** has just passed. However, the real experiment does not follow such a simple physical scheme.

Actually, there exists the types of multicomponent solids (not to mention pure metals) which cannot be amorphized with fast neutrons even at ***80K*** (for example, spinels [*14*] and ***FeNiCr*** alloys [*15*]) but only atomic disordering is observed.

In order to have a realistic picture of radiation effects one should take into account that the microvolume of an ***ADC*** is small and the crystal lattice surrounding it must be an obstacle for its amorphization at the relaxation stage. Within the framework of our

model, a recovery of atomic periodicity in the *ADC* microvolume may be hindered by an atomic replacement and point defects if they cause a large local deformation of crystal and their quantity exceeds a certain critical level [*11*].

Unfortunately, it is very difficult to determine correctly an amplitude of displacements of atoms and a concentration of point defects from neutron diffraction experiments, therefore we calculated and estimated these values from indirect data.

A point[3] defect can be viewed as a center producing near-by atomic displacements. For calculation purposes a medium around a point defect is considered to be an isotropic elastic continuum. For this model, an atom, being at the distance r from a defect, moves radially and this displacement is equal to [*16*]:

$$U = c/r^2, \qquad (7)$$

where c is a constant, describing "a force" of a defect. Since vacancies in the irradiated alloy exist in a wide temperature range, we shall take into account only this type of point defect in the following analysis. In the case of vacancies, atomic displacements are directed inside and a constant value is $c = 0.033v$, where v is an atomic volume. The calculated values of U_v for $r = 2\text{Å}$ and 5 Å are 0.1Å and 0.01Å, respectively. Hence, a zone of local distortion by the vacancy is a sphere of radius not more than 5Å.

Most probably, the distortions around the atomic substitutional defects – U_{as} are thought to proceed by the same scheme. Here, the distortions occur from a 10% difference in atomic sizes of *Ni* and *Ti*.

According to our estimations, the maximum amplitude of atomic distortions (with respect to their ideal positions in the lattice *B2*) in the volume damaged by an *ADC* does not exceed the following sum $U = U_v + U_{as} < 0.2\text{Å}$.

The role of atomic substitution in the titanium nickelide amorphization mechanism is far beyond its contribution to the total amount of atomic displacements. It seems to be necessary since a disordered alloy may accumulate a higher concentration of point defects than an ordered one.

Assume that $U_v \approx U_{as}$. The critical number of vacancies, n, necessary for the amorphization of the *ADC* microvolume, can be estimated by the formula $n = V/2w$, where w is the volume of the zone distorted by a single vacancy. The value n obtained was equal to approximately 150. That constitutes $\sim 1\%$ of the total number of atoms in the atomic displacement cascade.

In our opinion, the values of U and n are physically reasonable. However, for the amorphization model to be more realistic, direct and reliable methods of its determination are required.

---

[3] Opposite to crystalline solids, defects in amorphous metals should not be treated as local deviation from an ideal structure. In the latter a defect is the volume, where atomic density substantially deviates from its mean value. For example, there are negative (n-type) and positive (p-type) fluctuations of atomic density. These two types of amorphous structure defects correspond to vacancies and interstitials in crystalline solids. With all those remarks in mind we shall keep using the terminology of point defects for simplicity of presentation.

Conclusion

In this work a model for amorphous titanium nickelide produced by fast neutron irradiation was discussed. This model, based on amorphization of the distortion type, is opposite to a classical one, based on a liquid state substance.

The centers of atomic displacements in a crystal are radiation defects, namely, substitutional defects (the sizes of ***Ti*** and ***Ni*** differ by ***10 %***) and point defects (most probably, these are vacancies). A definite quantity of radiation defects to initiate a rather strong distortion of a crystal lattice is necessary for the amorphization effect to exist in the metal alloy in a wide temperature range. We estimated the maximum amplitude of atomic displacement in the modified $Ti_{49}Ni_{51}$ as ~*7 %* of the initial lattice parameter and a critical vacancy concentration of ~*1 %*. It is quite natural that packing of atoms and typical distances in such amorphous phase should not differ significantly from those parameters in an initial crystal. It is exactly the reason for the recovery of the macroscopic structure in the $Ti_{49}Ni_{51}$ single crystal after the annealing of the amorphous phase in the irradiated sample.

The suggested model of the amorphization of solids by fast neutrons needs numerous try-outs and, herewith, further experiments on single crystal samples Unfortunately, from the above mentioned works [*1-4*] only the experiment on the ***Ga-Gd*** garnet single crystal was fulfilled [*4*]. As a result of annealing of the irradiated ***Ga-Gd***, the latter was classified as an amorphous structure of a distortion type because the macroscopic structure of the single crystal sample was recovered.

Acknowledgment

This work was performed with a funding from: State Scientific-Technical Research Program (Neutron Investigation of Matter, Project 96-104); Russian Foundation for Fundamental Research (Projects 98-02-16166 and 98-02-17341) ; The Program of State Support for Leading Research Schools (Project 96-15-96515).

References

[1] Chukalkin, Yu., Stirts, V., and Goshchitskii, B., *Physica Status Solidi (a),* 1983, Vol. 79, p. 361.

[2] Arkhipov, V., Voronin, V., and Goshchitskii, B., *Physica Status Solidi (a),* 1984, Vol. 63, p. K59.

[3] Arkhipov, V., Voronin, V., and Goshchitskii, B., *Fizika Metallov i Metallovedenie* (rus.), 1987, Vol., p. 748.

[4] Chukalkin, Yu., Stirts, V., *Physica Status Solidi (a),* 1994, Vol., 144, p. .9.

[5] Dubinin, S., Teploukhov, S., and Parkhomenko, V., *The Physics of Metals and Metallography,* 1996, Vol., 82, pp. 297-300.

[6] Schwarz, R., Petrich, R., and Saw, C., *Journal of Non-Crystalline Solids*, 1985, Vol., 76, p. 281.

[7] Grant, W., *Journal of Nuclear Instruments and Methods*, 1981, Vol., 182, p. 809.

[8] Koch, C., Cavin, O., *Applied Physics Letters*, 1983, Vol., 43, p.1017.

[9] Dubinin, S., Parkhomenko, V., Teploukhov, S., and Karkin, A., *The Physics of Metal and Metallography*, 1997, Vol., 83, p.p. 656-660.

[10] Handrih, K., Kobe, S., *Amorphe Ferro- und Ferrimagnetika*, Akademie-Verlag, Berlin, 1980, p. 34.

[11] Dubinin, S., Parkhomenko, V., Teploukhov, S., *The Physics of Metal and Metallography*, 1998, Vol., 85, p.p. 332-335.

[12] Kirsanov, V., *EVM-eksperiment v Atomnom Materialovedenii* (rus), Energoatomizdat, Moskva, 1990, p.302.

[13] Beyagoub, A., Thome, L., *Physical Review*, 1988, Vol., 38, p.10205

[14] Parkhomenko, V., Dubinin, S., Goshchitskii, B., et al., *Physica Status Solidi (a)*, 1976, Vol., 38, p. 57.

[15] Dubinin, S., Vologin, V., Kinev, E., et al., *Fizika Metallov i Metallovedenie* (rus), *1994*, Vol., 77, p. 63.

[16] Dines, G., Vineyard, G., *Radiation Effects in Solids*, Interscience Publishers, Inc. New York, 1957, p.126.

Sergey F. Dubinin,[1] Vitaliy D. Parkhomenko,[1] and Sergey G. Teploukhov[1]

Effects of Fast Neutron Irradiation at 80K on Titanium Nickelide

Reference: Dubinin, S. F., Parkhomenko, V. D., and Teploukhov, S. G., **"Effects of Fast Neutron Irradiation at 80K on Titanium Nickelide,"** *Effects of Radiation on Materials: 19th International Symposium, ASTM STP 1366,* M. L. Hamilton, A. S. Kumar, S. T. Rosinski, and M. L. Grossbeck, Eds., American Society for Testing and Materials, West Conshohocken, PA, 2000.

Abstract: The structural state of a $Ti_{49}Ni_{51}$ single crystal irradiated by fast neutrons at 80K was investigated by the neutron diffraction method. It was found that a relatively low fluence amorphized 40% of sample volume. It was shown that the existence of a critical concentration of point defects provides the stability of positional atom disorder in $Ti_{49}Ni_{51}$ low temperature irradiation damages of titanium nickelide can be well explained within the Gibbon statistical scheme.

Keywords: titanium nickelide, single crystal, irradiathion, fast neutron, amorphous, atomic disordering, damage.

Introduction

The irradiation damage of a $Ti_{49}Ni_{51}$ single crystal irradiated by fast neutrons at a relatively high temperature (T_{irr} = 340K) has been investigated by Dubinin et al., *[1]*. It was shown that the alloy irradiated with low fluences, $\Phi < 10^{24}m^{-2}$ (energy - $E > 0.1$Mev and flux - $F = 10^{18}m^{-2}$), underwent an atomic disordering mostly, with its amorphization becoming noticeable at $\Phi > 10^{24}m^{-2}$.

Usually the irradiation damages in solids are discussed according to the Thompson scheme [*2*]:

$$n^{\circ} \Rightarrow PKA \Rightarrow ACC, \qquad (1)$$

where

n° - a fast neutron

PKA - primary knocked atom

ACC - atomic collision cascade produced by a *PKA*.

Individual reaction cross sections involved in (1) are discussed in detail in [*2*].

Experimental data on the volume fraction of amorphous and disordered phases at high temperature irradiation were compared with those calculated using the Gibbon statistical model [*3*]. A good agreement was obtained with the assumption that the disordering proceeded in each *ACC*, while the amorphization took place in the zone of

[1] Research Scientists, Institute for Metal Physics, Ural Division, Russian Academy of Scients, Kovalevskoi Str. 18, 620219, Ekaterinburg, GSP - 170, Russia.

Copyright© 2000 by ASTM International www.astm.org

overlapping of, at least, two *ACCs*. In other words, only the microzones with quite a high concentration of point defects can be amorphized; such a concentration under high temperature irradiation can be obtained only overlapping of, at least, two *ACCs*. In other words, only the microzones with quite a high concentration of point defects can be amorphased, such an irradiation temperature decrease. The verification of this hypothesis is the objective of the present work.

Experimental

The object of the investigation was a titanium nickelide $Ti_{49}Ni_{51}$ single crystal of the same chemical composition as in article Dubinin et al., [*1*]. A detailed information on samples can be found in [*4*].

The irradiation of the samples with fast neutrons fluence of $\Phi = 1.5 \times 10^{23} m^{-2}$ ($F = 6 \times 10^{17} m^{-2}$; $E > 0.1$Mev) at the temperature of 80K was conducted in a special channel ILTICI inserted into a nuclear reactor core [*5*]. The irradiated samples were removed from the ILTICI to a storage-cryostat for two months to reduce the absorbed gamma dose rate. After that, with no heating, they were placed into various cryostats for measurements.

An information on point defects in irradiated crystals was obtained by measuring the electrical resistance. For this purpose the samples were placed into a helium cryostat at 1.7K. Then they were warmed up and the temperature dependence of the electrical resistance was measured. After heating to 150K the sample was annealed by 25K steps for 20 minutes. After each step of keeping at a given temperature the sample was cooled again and the temperature dependence of electrical resistance was measured as well.

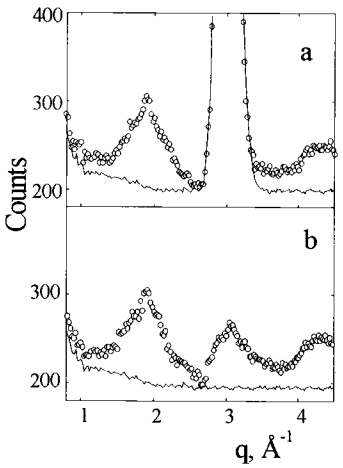


Figure 1- *Neutron diffraction patterns for $Ti_{49}Ni_{51}$ single crystal scanned along directions:* a - *[100] B2-phase;* b - *general type.* - - - - *before and* o - *after irradiation.*

The high temperature irradiation of the samples was performed in an ordinary channel ($\Phi = 2.9 \times 10^{23} m^{-2}$, $T_{irr} = 340$K, $F = 10^{18} m^{-2}$, $E > 0.1$Mev).

The structural state of $Ti_{49}Ni_{51}$ was studied by the neutron diffraction method using $\lambda = 1.57$ Å^{-1} which described in [*1*].

Results and Discussion

First of all it is necessary to notice that no martensite transformation occurred in $Ti_{49}Ni_{51}$ after irradiation to $\Phi = 1.5 \times 10^{23} m^{-2}$ at 80K. The results on the electrical resistance of modified $Ti_{49}Ni_{51}$ obtained for the range of 1.7K-350K testified to that. Further it will be proved that the temperature dependence of ρ has no anomalies typical for martensite transformation as in paper [*6*].

Now, the effect, which is of most interest for

the present work, will be distinguished. It is the partial amorphization of starting titanium nickelide single crystal under low temperature irradiation. The typical diffraction patterns at 140K are shown in figs.1a and 1b. The patterns correspond to a [110]B2 direction and a general type direction, respectively. Both the strong Bragg peak (110)B2 (fig.1a, q = 3Å^{-1}) and diffusion reflexes, which intensities are independent of the sample orientation in a scattering plane are present in the diffraction patterns. Angular positions of diffusion peaks in fig.1b correspond to the amorphous phase [*1*]. Thus, the structural state of modified $Ti_{49}Ni_{51}$ is a mixture of amorphous and crystalline B2 phases. It will be underlined here that the amorphous phase is virtually absent in the crystal under high temperature irradiation to $\Phi = 2.9 \times 10^{23} m^{-2}$.

A quantitative analysis of phases in the irradiated $Ti_{49}Ni_{51}$ with the use of neutron diffraction method can be carried out using the intensities of structural and superstructural Bragg reflexes measured before and after recovery annealing the alloy. As an example, squares and circles in fig.2 designate structural (110) and superstructrural reflections (111), measured before and after the recovery annealing of the irradiated alloy respectively,. In fig. 2 relative intensities of these reflexes are presented. Such a representation of intensities *J(hkl)* allows to use very simple formulas for determination of structural parameters.

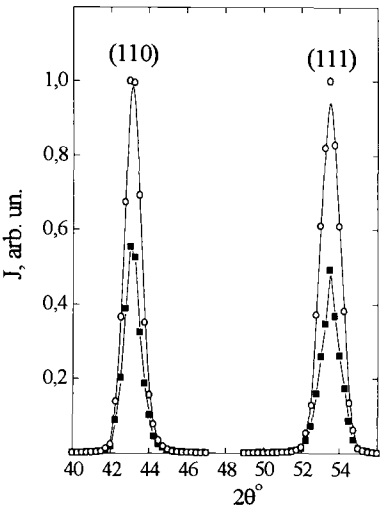


Figure 2- *Neutron diffraction patterns of $Ti_{49}Ni_{51}$ single crystal:*■*-sample irradiated at 80K;* o *-sample annealed after irradiation at 620K.*

$$C = 1 - J_{110}; \; V = 1 - C - J_{111}, \quad (2)$$

where

C and V = the fractions volume of amorphous phase and completely disordered crystal phase, respectively.

Substituting the experimental data (designated by solid squares in fig.2) into eq. (2) one obtains following magnitude of the parameters:

$$C = 0.42; \qquad V = 0.08 \quad .(3)$$

Since the amount of the disordered cubic phase is very small, both the amorphous and ordered B2 -phases are present in $Ti_{49}Ni_{51}$ alloy after irradiation at low temperature

In order to represent the specificity's of low temperature irradiation damages we compare the experimental values (3) with those calculated by the Gibbon model. According to this model the analytical expression of the volume portion of an amorphous phase has the form:

$$C = \sum_{k=0}^{n-1} (\beta\Phi)^k / k! \times exp(-\beta\Phi) \qquad (4)$$

where

Φ = fast neutron fluence
β = a kinetic parameter, characterizing a damaged area, which is created by an individual *ACC*
n = a number of the overlapping *ACC*s.

The results of the calculation of C for the low temperature irradiation for two β-values are given in two upper lines of the table1. In the third line the values of n, β, C and Φ are given for high temperature irradiation. As it seen from the table1,

Table 1-Calculated Values for Amorphous Phase in the Irradiated $Ti_{49}Ni_{51}$

T_{irr}, K	n	β,m^2	Φ,m^{-2}	C
80	1	1.8×10^{-24}	1.5×10^{23}	0.24
80	1	3.7×10^{-24}	1.5×10^{23}	0.42
340	2	1.8×10^{-24}	2.9×10^{23}	0.07

an agreement with the low temperature experimental data is reached at the $n = 1$ and $\beta = 3.7 \times 10^{-24}$ m^2. With results obtained one can make the following conclusions:

1. The parameter β, which is proportional to the volume of *ACC* [*3*], increases more than 2 times. At low temperatures such an increase can be attributed to the increase of the chain length of focused collision sequences and to the decrease of annihilating point defect number, [*2*].
2. The parameter n becomes minimal. This means that for reaching the point defect concentration essential for the amorphization $Ti_{49}Ni_{51}$ under high temperature irradiation it is necessary to verlapping, temperature irradiation such a condition is realized within an isolated cascade.

On the existence of such a critical point defect concentration one can be conclude from the results of the isochronical annealing of titanium nickelide irradiated at 80K. Under the isochronal annealing the following values have been measured: the volume fraction of the crystalline phase, the long range order degree in the crystalline phase and the change of the point defects concentration. Let us discuss these experiments in a consistent manner.

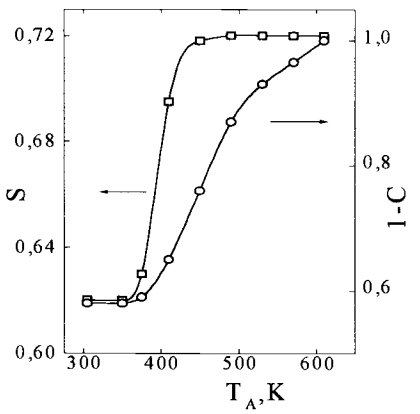


Figure 3 - *Volume fraction – (o) and atomic long order – (■) crystalline phase irradiated $Ti_{49}Ni_{51}$ vs temperature of isochronal annealing*

In fig. 3 open circles stand for the volume fraction of crystalline phase measured under the isochronal annealing at T_{an} > 300K The duration of each temperature stage was 20 minutes. Then a sample was cooled to 300K and intensities of the structural reflex (110) were measured. As it follows from this figure, the amorphous phase beginsto anneal at 375K and recovery stops at 600K, i.e. proceeds in a wide temperature range.

The results on the long range order recovery in the crystalline phase S are in a close relation to data on the annealing of the amorphous phase. Such results are shown as light squares in Fig. 3. It should be recovery in the crystalline phase S are in a close relation to data on the annealing of the amorphous phase. Such results are shown as light squares in Fig. 3. It should be noted that S and 1 - C were measured at the same temperature. The long range order was determined by neutron diffraction with respect to the intensities of superstructural (111) and structural (110) reflexes. It is seen from the be noted that S and 1 - C were measured at the same temperature. The long range order was determined by neutron diffraction with respect to the intensities of superstructural (111) and structural (110) reflexes. It is seen from the figure that the order degree and the crystal phase volume recovery begins at the same temperature. After words that point the solid and dashed curves have different temperature runs. Such a behavior can be explained as follows. The constant value of the parameter S = 0.72 in the temperature range 450K < T_{an} < 600K testifies that the crystal phase, which recovers at the amorphous phase annealing, has the starting value of the long range order (S of unirradiated sample = 0.72). A steep increase of S in the temperature range 375K < T_{an} < 450K is due to annealing the small volume fraction of the disordered crystal phase formed under irradiation (3).

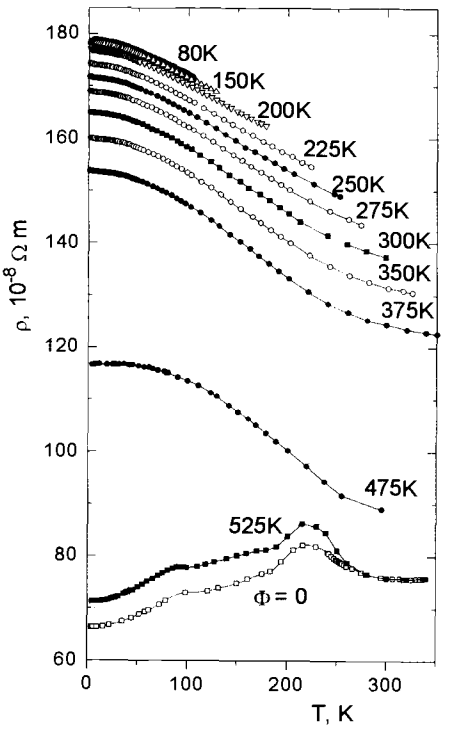


Figure 4 - Temperature dependencies resistivity irradiated $Ti_{49}Ni_{51}$ after isochronous (20 min.) annealing. Φ =0, before irradiation.

The results shown in Fig. 3 and high temperature irradiation data testify that the atomic disordering $Ti_{49}Ni_{51}$ solely is insufficient for an alloy amorphization, though this condition seems to be necessary. The necessity of atomic disordering for $Ti_{49}Ni_{51}$ amorphization to occur, probably, is related to the fact that at the same temperature a much higher concentration of point defects can be reached in the disordered alloy than in the ordered one.

We believe that the amorphization occurs only in the case when the point defect concentration in the ACC zone reaches a certain value. Therefore, there is a sense to the date on electrical resistance measured in modified titanium nickelide. The temperature dependence of the electrical resistance for different isochronical annealing temperatures is shown in Fig.4. The absolute value of resistance decreases with T_{an} increase and the temperature run keeps stable within the range 80K <T_{an} <375K.This is justified by Fig. 5

plotted in the coordinates $\rho_{100K} - \rho_0$ and T_{an}. The data shown prove that the electrical resistance of irradiated $Ti_{49}Ni_{51}$ obeys the Mattisen rule:

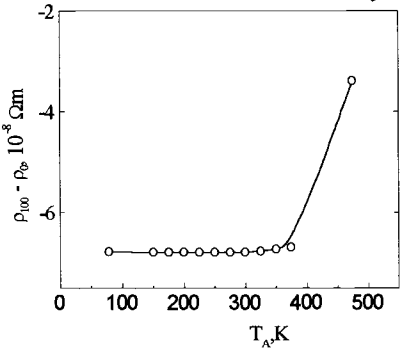


Figure 5 -*The difference of resistivity at 100K and residual resistivity for irradiated $Ti_{49}Ni_{51}$ vs isochronous annealing temperature.*

$$\rho = \rho_0 + \rho(T), \qquad (5)$$

where

ρ_0 = the temperature-independent electrical resistance determined by the point defect concentration.

In fig.5 one can see a strong increase of the value $\rho_{100} - \rho_0$ at above $T_{an} \cong 375K$. Obviously, this temperatures corresponds to the recovery stage of the parameters *1-C* and *S*, fig.3. At the range beginning of annealing the value ρ_0 is $154\times10^{-8}\Omega m$. This threshold value of ρ_0 is evidence of the existence of a critical point - defect concentration that provides the stability of the atomic disorder in the damaged *CAC* microzone.

Acknowledgment

The authors are thank full to Dr. A.E. Kar'kin for his assistance in measuring the electrical resistance and also for helpful discussions of the results of the present work.

This work was performed with the financial support from: The Governmental Scientific -Technical Program "Neutron Studies of Substance", Project 96 – 104; Russian Foundation of Fundamental Research, Project 98-02-17341, 98-02-16166; The Governmental Support for Leading Research Schools in RF", Project 96 -15- 96515.

References

[1] Dubinin S., Teploukhov S., Parkhomenko V., "Structural State of Titanium Nickelide Irradiated with Fast Neutrons", *Fizika Metallov i Metallovedenie*, 1996, Vol. 82, No.1, pp.136- 141.

[2] Thompson M. Defects and Radiation Damage in Metals, Cambridge, 1969, p.367.

[3] Gibbjns J.F., "Ion Implantation in Semiconductors. Part 2. Damage Production and Annealing ", *Proc. IEEE*, 1972, Vol. 60, No.9, pp. 1062-1096.

[4] Dubinin S., Parkhomenko V., Teploukhov S., Karkin A., "Negative Temperature coefficient of Resistivity and Structure of Radiation-modified Titanium Nickelide" , *Fizika Metallov i Metallovedenie*, 1997, Vol.83, No.1, pp. 125- 131.

[5] Parkhomenko V., Goshchitskkii B., Dubinin S., "Condensation-type Channel for Low-temperature Irradiation", *Atomnaja Energija*, 1974, Vol.36, No.1, pp.62-64.

[6] Khachin V., Pushin V., Kondratev V. Titanium Nickelide, Moscow, Nauka, pp. 35-41.

Ferenc Gillemot,[1] László Gillemot,[1] and Gábor Uri[2]

Irradiation Aging of Aluminum Alloys

Reference: Gillemot, F., Gillemot, L., and Uri, G., **"Irradiation Aging of Aluminum Alloys,"** *Effects of Radiation on Materials: 19th International Symposium, ASTM STP 1366,* M. L. Hamilton, A. S. Kumar, S. T. Rosinski, and M. L. Grossbeck, Eds., American Society for Testing and Materials, West Conshohocken, PA, 2000.

Abstract: In Hungary the VVRSZM-5 research reactor went into operation in 1959 and was operated continuously until 1986 without any failure. In 1986 the reactor was shut down for reconstruction. Since then the primary and secondary cooling circuits were dismantled and replaced. Many of these components were made from precipitation hardened aluminum alloy SZAV-1 similar in composition to AA6005 alloy. To increase knowledge about the aging of the mechanically loaded components few dismantled parts of the reactor were tested or samples were cut and stored for testing.

In the meantime a new aluminum alloy for production of the main components of the reconstructed reactor has been developed and tested. This alloy, R-AlMg2.5 was produced on a clean aluminum base, and its weldment was carefully tested before usage. Sample heats of the SZAV-1 alloy (material of the dismantled reactor) and its weldments were irradiated together with the new R-AlMg2.5 (similar to AA5252) alloy and the properties of the materials compared. The results of the laboratory test series show a good correlation with the data obtained on the out-of-service material and weldments.

The results shows that high dose irradiation (~10^{24}-10^{26} n/m^2) fast neutron fluence, (E>1MeV) does not decrease the mechanical properties of the R-AlMg2.5 alloy and its weldments, while the toughness of the SZAV-1 weldments is reduced.

The reconstructed reactor (called VVRSZM-10) had also a surveillance testing program, and surveillance results are verify the application of the irradiation resistant R-AlMg2.5 alloy.

Keywords: research reactor, aluminum alloys, irradiation ageing, mechanical properties, surveillance

Introduction

The VVRSZM-5 research reactor was dismantled after 27 years of safe operation . One of the reasons was that the available manufacturer's documentation was insufficient for

[1] Senior research associate, Atomic Energy Research Institute, H-1525 Bp. P.O.B. 49.
[2] Research associate, Atomic Energy Research Institute, H-1525 Bp. P.O.B. 49.

Copyright© 2000 by ASTM International www.astm.org

evaluation of the aging and of the remaining lifetime. At the same time it was decided to change the type of aluminum alloy used for the new reactor tank and primary circuit, and increase the reactor power up to 10 MW. The mechanical properties of the heat affected zone (HAZ) of the originally used age hardened SZAV-1 type alloy were different from that of the base material. This relatively mild zone can absorb the service loads, therefore low-cycle fatigue may occurs here in case of frequent stops and restarts. The R-AlMg2.5 alloy has been selected for the reconstructed reactor in order to avoid this phenomenon. This alloy is strain hardenable, and used in annealed condition, which means that its heat affected zone regains the original mechanical properties some months after the welding. The previously used alloy SZAV-1 is an AlMgSi1 type material that gains the maximum tensile properties after heat treatment. The R-A1Mg2.5 material was produced on a 99.99% clean aluminum base, and a similarly clean Mg metal was used for alloying it to avoid long-half life isotope production during service.

The mechanical properties of the new alloy were carefully checked and compared with the properties of the previously used SZAV-1. For this comparison a research heat of SZAV-1 and materials obtained from the dismantled reactor tank were used. The comparison was performed in as received and irradiated state too. For further evaluation of the mechanical properties of the R-AlMg2.5 alloy in aged condition surveillance specimens were irradiated in the reconstructed reactor for a period of 3 years and subsequently tested. The results are summarized in this paper.

Aging of VVRSZM-5 tank

The sketch of the reactor tank's cross section is shown in Figure 1. The reactor tank and parts of the primary circuit were made from SZAV-1 aluminum alloy. The average chemical composition of the SZAV-1 alloy is given in Table 1. The pumps, heat exchangers and the remaining part of the pipes were produced from stainless steel.

The diameter of the tank is 2300 mm, the average wall thickness is 20 mm. Inside the main vessel a smaller (1100 mm diameter) tank is placed for locating the core. It is a very safe design, because in case of leakage of the main vessel, this inside tank can withhold enough water for cooling the fuel elements. The diameter of the core is 600 mm the height is 700 mm. Enriched uranium oxide fuel elements are used. The 70 mm thick grid plate holds the fuel elements. Table 2 shows typical neutron irradiation level at different parts of the reactor after 27 years of operation.

Table 1 - *Chemical composition of the SZAV-1 type aluminum alloy*

Fe%	Si%	Mg%	Zn%	Ti%	Cu%	Mn%	Ni%
0.085	0.81	0.48	0.011	0.004	0.0058	0.0026	0.001

Table 2 - *Neutron fluence values in the VVRSZM-5 reactor after 27 operational years. (Calculated by SABINE 3 code)*

Fluence [n/m^2]	Reactor wall	Horizontal neutron channel	Thermal column	Vertical neutron channel
E>0.1MeV	$1.9*10^{21}$	$3.5*10^{21}$	$5.9*10^{24}$	$2.8*10^{26}$
E>1MeV	$1.2*10^{21}$	$1.1*10^{21}$	$2.0*10^{24}$	$1.6*10^{26}$
Total	$6.1*10^{21}$	$1.1*10^{22}$	$1.4*10^{26}$	$1.4*10^{27}$

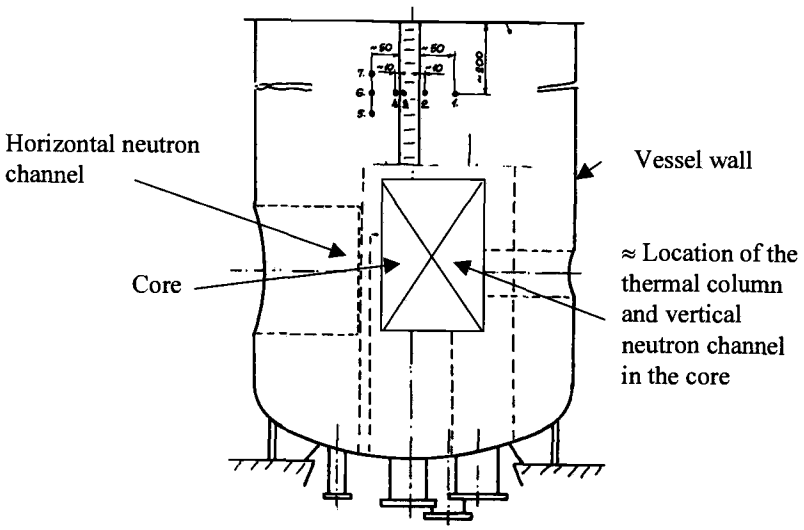


Figure 1 - *VVRSZM pressure vessel*

During the dismantling some of the main components were hardness tested. Since the main vessel was dismantled and stored in one piece and filled with water, no specimens were cut from any location that could decrease of the integrity of the vessel. Specimens for destructive mechanical testing were cut only from the inside structural elements like vertical channel pipes, grids etc. The results of the hardness and mechanical tests are given in Tables 3-4. The high increase in the hardness of the vessel bottom and nozzle welds were caused by low-cycle fatigue at the joints of the main coolant pipes and the vessel bottom.

Although the hardness increased largely, no cracks were observed. Furthermore, there was no corrosion damage on the surface. The SZAV-1 alloy tank has not reached the end of its safe lifetime, although it was operated mostly with 5 MW power instead of the 2 MW designed originally, and the design lifetime has been extended by 30 %.

Table 3 - *Summary of the in site hardness testing of the SZAV materials (HB scale)*

Location	Base material	HAZ	Weld
Vessel wall	32	48	51
Vessel bottom	67	-	53
Outlet nozzle	59	44	53
Degas pipe nozzle	30	30	40
Inlet nozzle	61	62	47

The ductility of the SZAV-1 alloy was reduced by neutron irradiation and by low-cycle fatigue, but the remaining toughness of the vessel still satisfied even the most exaggerated safety requirement.

Table 4 - *Summary of the average mechanical properties measured on the samples cut from the inside components of the dismantled reactor*

Component	Distance from the core middle [mm]	Fluence (E>1MeV) [n/m^2]	Hardness average [HV10]	S_u [MPa]	S_y [MPa]	Elongation [5d] [%]
Upper grid	3000	0	36	154	122	19
Irrad. channel 17	2000	0	32	147	118	18
	1000	$2*10^{21}$	33	-	-	-
	500	$5*10^{24}$	36	225	214	6
	100	$5*10^{26}$	81	-	-	-
Irrad. channel 2	2000	0	34	150	115	19
	1000	$2*10^{21}$	36	-	-	-
	500	$5*10^{24}$	44	-	-	-
	100	$5*10^{26}$	82	270	258	4
Degas pipe flange	2000	0	37	140	98	16
Inlet pipe flange	2000	0	35	146	87	13

Testing of R-AlMg2.5 alloy

The chemical composition of the R-AlMg2.5 alloy is given in Table 5.

Table 5 - *Chemical composition of R-AlMg2.5*

Cu%	Mg%	Mn%	Si%	Fe%	Ti%	Zn%	Cr%
0.001	2.55	0.054	0.04	0.05	0.037	0.006	0.001

The tensile properties of the R-AlMg2.5 alloy have been studied on smooth and notched tensile bars in as received and irradiated state. The tensile properties of the R-

AlMg2.5 alloy have been studied on smooth and notched tensile bars in as received and irradiated state. Fracture toughness measurements are not available on the low strength

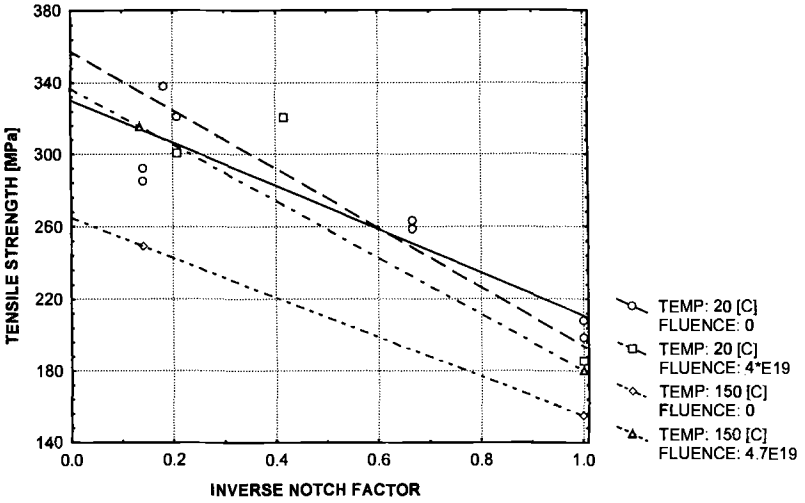


Figure 2a - *Tensile strength vs. inverse notch factor, R-AlMg2.5 alloy, at 20 and 100 °C before and after irradiation (4.7*10^{23} n/m^2 E>1.0 MeV)*

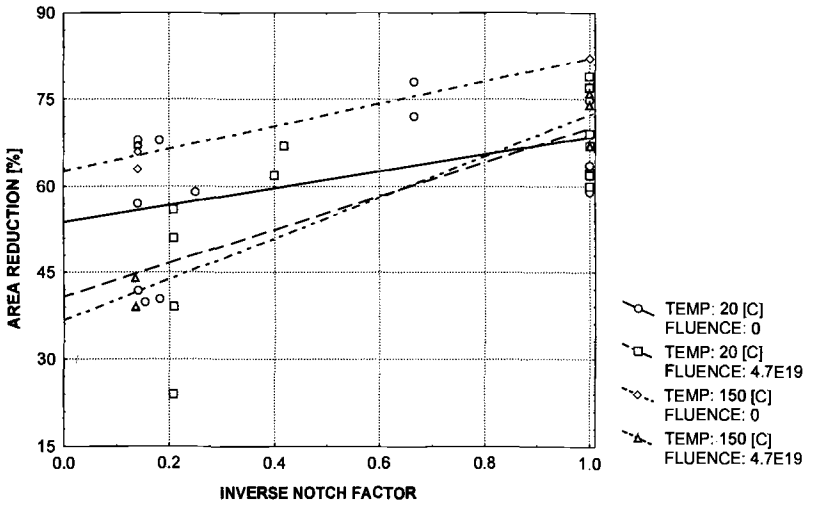


Figure 2b - *Reduction of area vs. inverse notch factor, R-AlMg2.5 alloy, at 20 and 100 °C before and after irradiation (4.7*10^{23} n/m^2 E>1.0 MeV)*

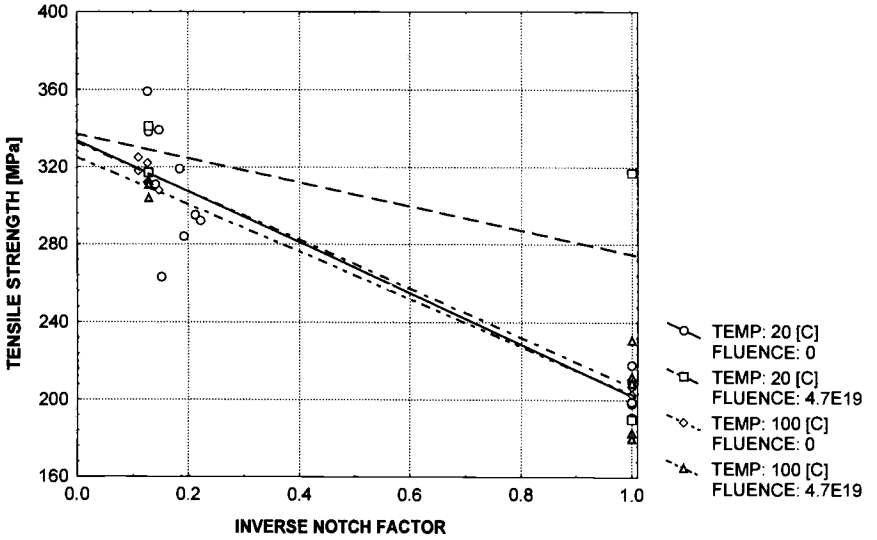


Figure 3a - *Tensile strength vs. inverse notch factor, R-AlMg2.5 alloy weld, at 20 and 100 ^{o}C before and after irradiation ($4.7*10^{23}$ n/m^2 E>1.0 MeV)*

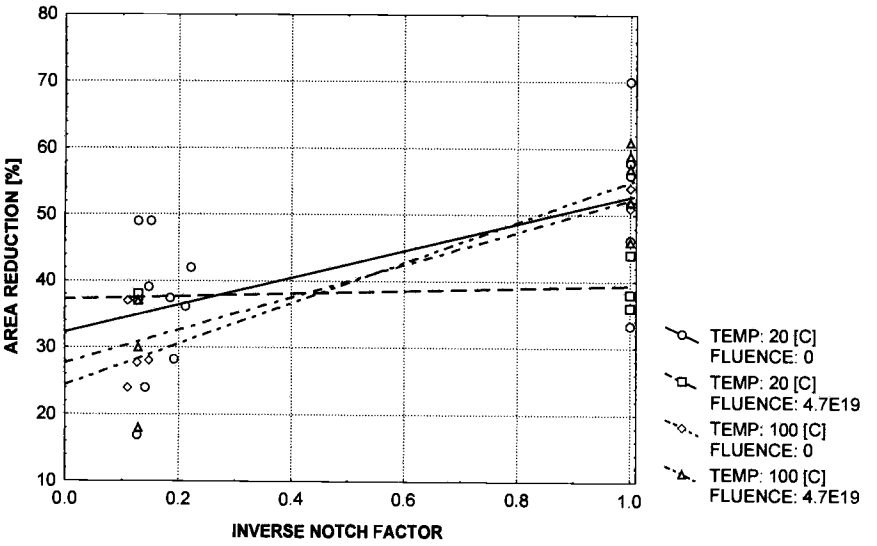


Figure 3b - *Reduction of area vs. inverse notch factor, R-AlMg2.5 alloy weld, at 20 and 100 ^{o}C before and after irradiation ($4.7*10^{23}$ n/m^2 E>1.0 MeV)*

highly ductile Al alloys, the results obtained on sharp notched tensile bars, however, can characterize the crack resistance. The mechanical properties of RAlMg2.5 base material, such as ultimate tensile strength (R_m) and area of reduction (Z) at 20 and 150 °C are displayed in function of the inverse notch factor. The extrapolation of the inverse notch factor to the zero value represents the absolutly sharp notches (cracks). Figure 2 shows the effect of the irradiation on the base material.

The tensile properties of weldments were similarly tested and are presented in Figure 3. The microstructure of the welds resembles the cast structures, rather than the structures of the plates. The welds have higher alloying element contents and therefore their properties are different from those of the base materials.

Standard smooth tensile bar testing results obtained on R-AlMg2.5 alloy are compared with SZAV-1 results in Table 6. As a further test to evaluate the toughness of the alloys Charpy impact energy measurement was performed [1,2]. Standard Charpy V notched specimens and a 300 J standard instrumented Charpy machine with ISO tup was used. The results are given in Table 7.

Table 6 - *Mechanical properties of non- and irradiated R-AlMg2.5 and SZAV-1 alloys and their weldments*

Material	Fluence [10^{23} n/m^2]	R_m [MPa]	$R_{p0.2}$ [MPa]	A_5 [%]	Z [%]
RAlMg	0.0	199	107	27	56
RAlMg	3.7	190	81	-	67
RAlMg	82.0*	210	-	-	-
RAlMg-W	0.0	184	80	22	74
RAlMg-W	3.7	185	-	-	74
RAlMg-W	82.0*	215	-	-	-
SZAV	0.0	119	101	27.6	74
SZAV	0.0	102	83	-	72
SZAV	3.7	116	74	-	70
SZAV-W	0.0	121	99	11	64
SZAV-W	3.7	196	124	-	33

*Irradiated and tested at Kurchatov Institute (Moscow)

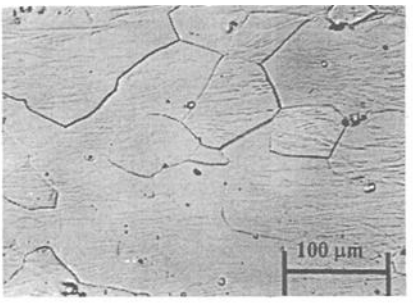
These results show that the applied irradiation has not changed the toughness of the plates and the R-AlMg2.5 weldment, while the toughness of the SZAV-1 weldment was significantly reduced. The different behavior of the two alloys and their weldments can be explained on the basis of their microstructure. The microstructure of R-AlMg2.5 base metal and weld are shown in Figures 4a and b, and of SZAV-1 in Figure 4c and d.

Having evaluated the metallography pictures of the alloys and welds we suppose that the quantity of the Mg_2Si segregation at the grain boundaries increased in the SZAV-1 weldments during irradiation and this caused the decrease in Charpy energy. This is in good agreement with literature data [3].

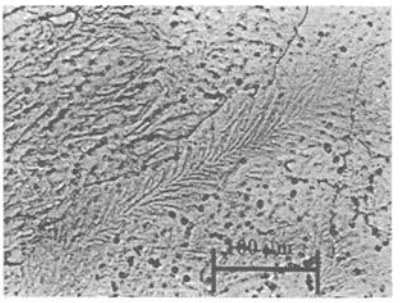
Table 7 - *Comparison of R-AlMg2.5 and SZAV-1 alloy toughness by Charpy test*

Material	Fluence [10^{23} n/m^2]	Testing temperature [°C]	Absorbed energy [J]
R-AlMg2.5	0	20	105
	3	-30	115
	3	-10	105
	3	20	101
	3	80	101
R-AlMg2.5-W	0	20	55
	3	20	67
SZAV-1	0	20	62
	3	20	77
SZAV-1W	0	20	52
	3	20	17

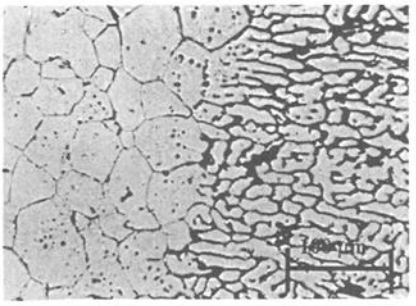
W= weld



a.) R-AlMg2.5 base metal



b.) R-AlMg2.5 weld



c.) SZAV-1 base metal and heat effected zone



d.) SZAV-1 weld

Figure 4 - *Microstructures of studied alloys*

Surveillance testing results of the VVRSZM-10 Reactor

A surveillance testing program for the VVRSZM-10 reactor was elaborated and carried out. The specimens were cut from different parts of the reactor (such as pressure vessel wall (E), axial weldment of pressure vessel wall (V), upper zone grid (Z) and horizontal radiation channel (X)). Sixty-four specimens were tested in as received condition and the same quantity was irradiated in one capsule at the core edge for 6216 hours resulting in a total fluence of $3.38*10^{24}$ n/m^2 E > 1 MeV ($4.95*10^{24}$ n/m^2 E > 0.5 MeV).

Table 8 –*Impact testing results obtained on VVRSZM-10 surveillance specimens*

Material	Cut location	Testing temperature [°C]	Fluence (E>1.0 MeV) [10^{24} n/m^2]	Absorbed energy [J]
R-AlMg2.5	wall	20	0	100.8
		20	4.95	100.8
		80	0	91.8
		80	4.95	91.8
R-AlMg2.5	grid	20	0	107.3
		20	4.95	148.5
		80	0	104.0
		80	4.95	155.5
R-AlMg2.5	horizontal channel	20	0	109.0
		20	4.95	139.0
		80	0	102.5
		80	4.95	142.5
R-AlMg2.5 weld	vessel vertical weld	20	0	60.3
		20	4.95	51.3
		80	0	56.3
		80	4.95	62.5

The specimens were tested at 20 and 80 °C. These temperatures represent the possible minimum and maximum operating temperatures of the reactor. The results are summarized in Table 8. The surveillance results also verify the application of the highly radiation resistant R-AlMg2.5 alloy.

Summary

The results of the tests can be summarized as follows:

- The reactor tank made from SZAV-1 alloy operated for 27 years in the VVRSZM-5 Research Reactor and no considerable degradation were observed.

- Laboratory results show that the SZAV-1 weldment (used in the dismantled VVRSZM-5 tank) is sensitive to irradiation ageing while the base materials and the AlMg type weldment (used for the new VVRSZM-10 tank) is resistant to irradiation embrittlement..
- Charpy impact energy measurements adequately characterise the irradiation induced toughness decrease of aluminum alloys.

References:

[1] Gillemot F., "**Comparison of Different Fracture Toughness Measuring Methods for Testing of Irradiated Aluminum Alloys**" in H.C. van Elsted. *ECF-6 Proceedings*. EMAS U.K. 1986 pp.477-489.

[2] Gillemot, L., Gillemot, F., Uri, G., Horváth, M., Geröly, E., "**Developing of Aluminum Standards for Impact Bending (Charpy) Tests**" *11th International Symposium of ICSOBA*, Balatonfüred, 21-24. May, 1996.

[3] Farrell, K., and King, R.T, "**Tensile properties of Neutron Irradiated 6061 Aluminum Alloy in Annealed and Precipitation Hardened Condition**." in *Effect of Radiation on Structural Materials,* ASTM STP 683. J.A. Sprague and D. Kramer, Eds., American Society for testing and Materials, 1979, pp. 440-449

Y. Matsukawa,[1] Y. Sumita,[1] S. Ohnuki,[1] S. Watanabe,[1] C. Namba,[2] and H. Takahashi[3]

Effect of Ion-Irradiation on Phase Transformation in TiNi Shape Memory Alloys

Reference: Matsukawa, Y., Sumita, Y., Ohnuki, S., Watanabe, S., Namba, C., and Takahashi, H., **"Effect of Ion-Irradiation on Phase Transformation in TiNi Shape Memory Alloys,"** *Effects of Radiation on Materials: 19th International Symposium, ASTM STP 1366,* M. L. Hamilton, A. S. Kumar, S. T. Rosinski, and M. L. Grossbeck, Eds., American Society for Testing and Materials, West Conshohocken, PA, 2000.

Abstract: Ion-irradiation induced amorphization and crystallization processes in TiNi shape memory alloys have been investigated. The primary concern is to clarify the relationship between the critical temperature for irradiation-induced amorphization and the thermal crystallization temperature. The critical temperature for irradiation-induced amorphization was 673K, however, the edge of the foil specimen crystallized during the irradiation at a lower temperature. The crystallization temperature of the specimen edge during irradiation decreased with increasing of incident ion energy. Thermal annealing experiments revealed that the thermal crystallization preferentially occurred at the specimen edge and the crystalline-amorphous (C-A) interface; The crystallization temperature of the preferential sites were 573K and 623K, respectively. These preferential nucleation indicate that the nucleation barrier dominates the thermal crystallization temperature; the critical temperature for amorphization is higher than the thermal crystallization temperature with no nucleation barrier.

Keywords: inter-metallic compounds, shape memory alloy, ion-irradiation, amorphization, crystallization

[1] Graduate Students, Associate Professor and Professor, respectively, Faculty of Engineering, Hokkaido University, N-13 W-8, Sapporo 060-8628, Japan.

[2] Associate Professor, National Institute for Fusion Science, Toki 509-52, Japan.

[3] Professor, Center for Advanced Research of Energy Technology, Hokkaido University, N-13 W-8, Sapporo 060-8628, Japan.

Copyright© 2000 by ASTM International www.astm.org

Introduction

Inter-metallic compounds have been examined for possible application in nuclear reactor environments. The applications are not limited to structural materials alone, but may be component making use of a functional property like shape memory alloys [1]. These alloys show different structural evolution from that of conventional metals during high-energy particle irradiation. The most characteristic phenomenon is irradiation-induced amorphization [2-3]. Since the crystalline-amorphous phase transformation is accompanied by the volume change in most cases, it brings detrimental effects such as swelling. Furthermore, the shape memory alloys lose their functional property during amorphization [4]. Therefore, amorphization is an important phenomenon not only from the fundamental viewpoint, but also from engineering viewpoint. Amorphization competes with crystallization during irradiation. The factors dominating this competition are the temperature and the damage rate [5]. Even in the case that the crystallization surpasses the amorphization, without keeping the original structure after the irradiation, the alloy's property would be change. Despite the importance of crystallization, the crystallization process has not been paid as much attention as the amorphization process.

In the present study the irradiation-induced amorphization and the thermal crystallization processes have been investigated. The primary concern is the critical temperatures for amorphization and crystallization. Based on the detailed in-situ observation, the relationship between them will be discussed.

Experimental Method

The TiNi alloy used for this experiment was supplied by the Furukawa Electric Co. Ltd. Electron Probe Micro Analyzer (EPMA) revealed the composition Ti-51.0at.%Ni, which was the calibrated value with TiNi having a well-established composition. Differential Scanning Calorimetry (DSC) measurement revealed the martensitic and its inverse transformation temperatures were 207K and 255K, respectively. The crystal structure at temperatures of the present study was B2. The alloy was delivered as sheets with the thickness of 0.2mm. They were cut into discs with diameter of 3mm. The discs were annealed in a quartz capsule in vacuo at 1273K for 1hr followed by quenching to water. They were thinned with a twinjet elector-polisher using 93% CH_3COOH and 7% $HClO_4$ by volume at 298K.

Ar^+ irradiation was performed to the foil specimens with the accelerating voltage 50 to 200kV at temperatures 298 to 673K. After the irradiation the microstructure was observed using 200kV Transmission Electron Microscope (TEM) at 298K. The foil thickness of specimen was evaluated by means of the contamination spot separation method improved by Sawai et al., which gave higher accuracy than conventional way [6-7]. The distribution of point defects and incident ions were evaluated by the calculation with

TRIM 95code [8]

In-situ observation of thermal crystallization process was performed in High Voltage Electron Microscope (HVEM) at temperatures 298 to 773K using the specimen irradiated with 50keV Ar^+ ion to the dose of $10^{19}n/m^2$ at 298K.

Results

Ar^+ Ion Irradiation-induced Amorphization and Crystallization

Fig.1 shows a typical TEM image of a wedge-shaped foil specimen amorphized by 50keV Ar^+ irradiation at 298K. The thin part near the edge showed no contrast related to Bragg diffraction; the Selected Area Diffraction (S.A.D.) pattern taken from there has only halo rings. These features indicate that the thin part transformed to amorphous phase with the irradiation. The thickness of amorphous area increased as the accelerating voltage of ion increased. Fig.2 shows the distribution of defects calculated by computer code TRIM 95 for both 50 and 200keV. Since the maximum thickness of complete contrast free region corresponds to the maximum depth of ion range, it can be stated that the region shallower than the maximum depth of ion range is completely amorphized. The S.A.D. pattern taken from thick part had both halo rings and diffraction spots. These features indicate that the Ar^+ irradiation produced an amorphous layer on top of a crystalline substrate as schematically shown in Fig.1. Fig.3 shows the dose dependence of the amorphous layer thickness. The thickness increased rapidly around the dose of $5\times10^{17}ions/m^2$, and then saturated about 1000Å with the dose of $10^{19}ions/m^2$.

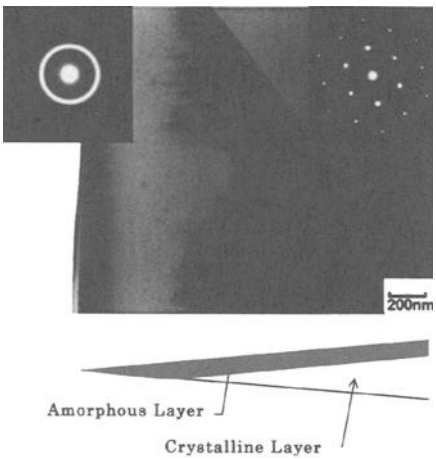


Fig.1 Bright fields image and cross sectional view of the TiNi induced amorphization by Ar^+ ion irradiation at 298K. The ion irradiation produces an amorphous layer on top of the crystalline substrate.

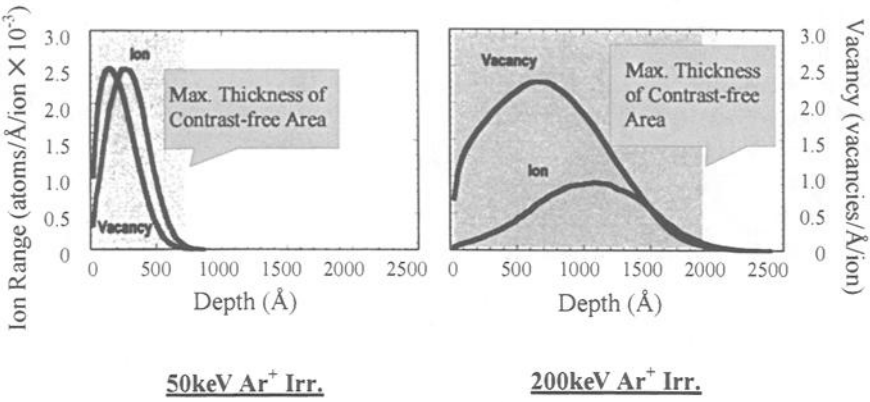


Fig.2 Calculated depth profile of the distribution of displaced atom and incident ion in TiNi irradiated with Ar^+ ion.

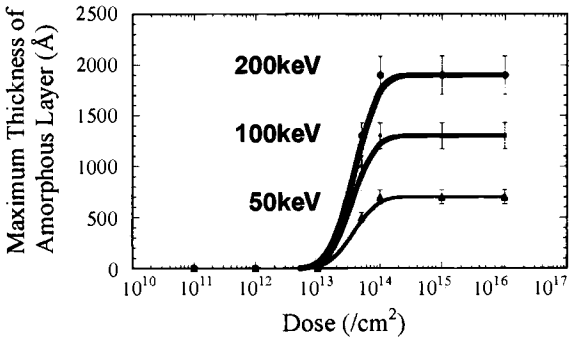


Fig.3 Dose dependence of the amorphous layer thickness. The thickness saturated with the dose of 10^{19}ions/m^2 irrespective of the accelerating voltage of ion.

Amorphization did not occur for irradiation above 673K, since no halo ring appeared in S.A.D. patterns taken from both thin and thick part of specimens. However, a crystalline phase was confirmed only at the specimen edge at the temperature lower than 673K (Fig.4). The crystalline phase of the specimen edge was poly-crystalline, which indicates that crystallization occurs at the specimen edge subsequently amorphization (Fig.5).

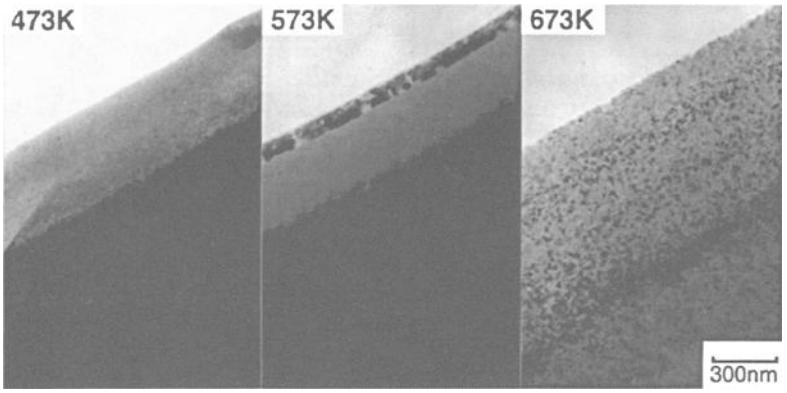


Fig.4 Microstructure of TiNi irradiated with Ar^+ ion at high temperature. Amorphization was not confirmed at the irradiation above 673K, however, a crystalline phase was confirmed at the specimen edge below 673K.

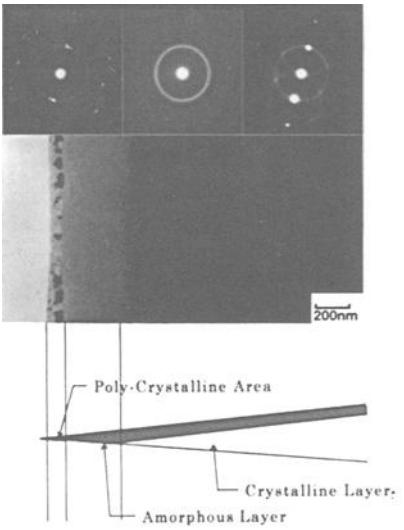


Fig.5 Bright fields images and cross sectional view of the TiNi induced amorphization by Ar^+ ion irradiation at middle temperature. The specimen edge was poly-crystal while the substrate was single crystal, which means that the crystallization of specimen edge occurred after amorphization.

Fig.6 shows the temperature dependence of the maximum thickness of the amorphous layer and poly-crystalline area after the irradiation to 10^{19}ions/m^2. The crystallization temperature of the specimen edge decreased with increasing of the accelerating voltage of ion. The temperature dependence of the critical dose, at which amorphous layer saturated to the thickness, indicates the critical temperature for amorphization is 673K (Fig.7).

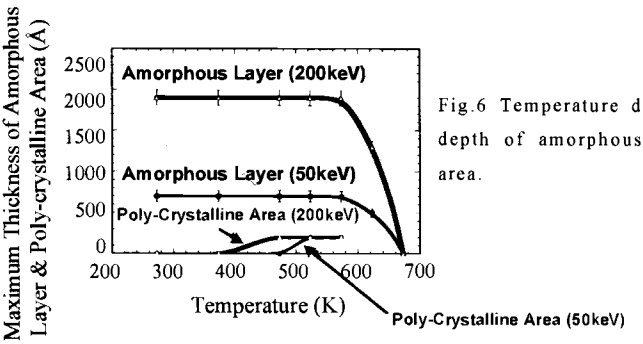


Fig.6 Temperature dependence of the maximum depth of amorphous layer and poly-crystalline area.

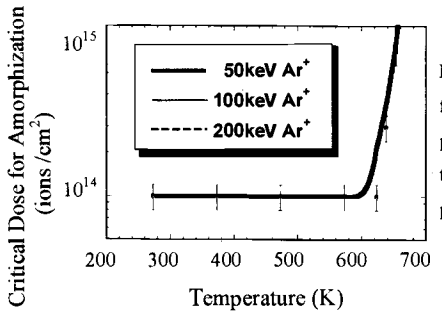


Fig.7 Temperature dependence of critical dose for amorphization. The critical dose did not depend on the accelerating voltage of ion. Critical temperature for Ar^+ irradiation-induced amorphization was 673K.

Thermal Crystallization

Thermal crystallization process of amorphous TiNi is as follows. The amorphous phase was produced by 50keV Ar^+ irradiation to the dose of 10^{19}ions/m^2 at 298K. The thermal crystallization occurred preferentially at the specimen edge and the C-A interface. It was the specimen edge that the crystallization was confirmed at the lowest temperature. The crystallization initially started along the specimen edge and the crack edge at 573K as shown in Fig.8.

With elevating temperature up to 623K the nucleation of crystals was also confirmed at the region except specimen edge as shown in Fig.9. The nucleation site was limited; crystals did not nucleate at thinner area than a certain thickness except specimen edge, which indicates that the crystals nucleated at the C-A interface shown in Fig. 1. However, the reason was not clear why crystals not to nucleate at extremely thick area in spite that the thick area also had the C-A interface.

Fig.10 shows the diffraction pattern taken from a crystal nucleated at 623K. The observation temperature was 298K. This pattern corresponds to the $[110]_{B2}$ zone axis pattern of a single variant of TiNi R phase [9], which means that TiNi nucleates without any preferential nucleation of metastable phase.

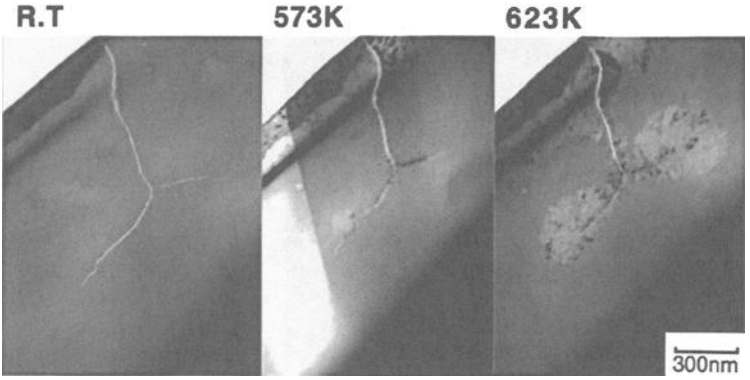


Fig.8 Crystallization process around the specimen edge. Initial crystallization occurred at the specimen edge (along the crack). Crystallization preferentially progressed at the crack tip front.

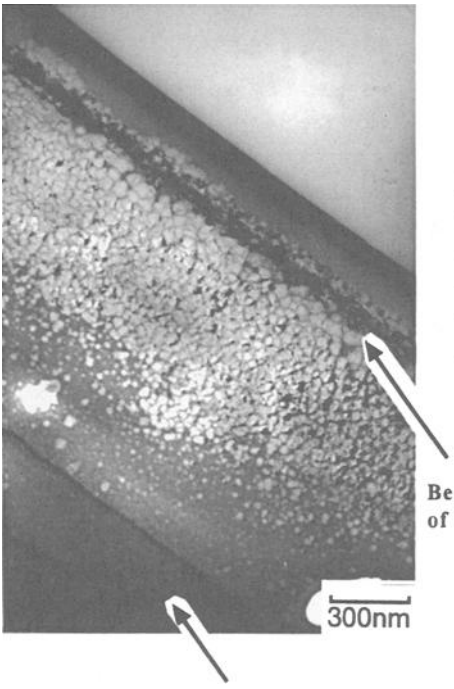


Fig.9 Microstructure of amorphous TiNi annealed at 623K for 4hrs. The nucleation site was conjectured to be the C-A interface schematically shown in Fig.1.

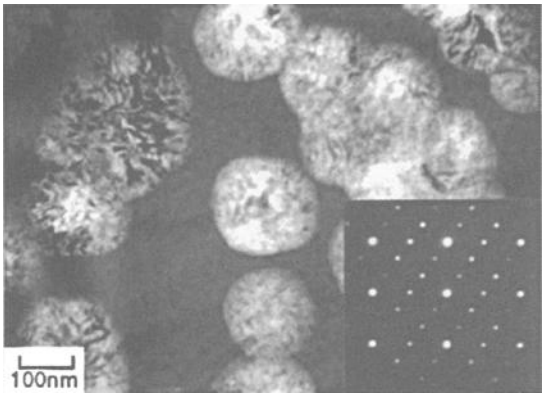


Fig.10 Diffraction pattern taken from a crystal nucleated at 623K, which corresponds to the pattern of $//[110]_{TiNi,B2(R\ phase)}$.

Discussion

Thermal Crystallization Temperature

Fig.11 shows the schematic diag ram of free energy change accomplished by the cry s-tallization of amorphous phase. Although below melting point T_m the free energy difference, which is the driving force for the phase transformation from amorphous to crystalline, increases with decreasing of temperature, the following discussion is under the assumption that the free energy difference does not depend on temperature; the crystallization temperature is discussed from the viewpoint of nucleation barrier.

According to the classical nucleation theory, the free energy change ΔG accomplished with the nucleation of crystalline phase from amorphous phase can be expressed by the following equation [11]:

$$\Delta G = (4/3)\pi r^3 (G_C - G_A) + 4\pi r^2 \gamma_{CA}$$

G_C and G_A represent the free energy of crystalline and amorphous phase, respe ctively. Critical radius of crystal nucleus is represented by r, and the interface energy is expressed by γ. The first term corresponds to the decrease in the volume free energy, and the second one means the increase in energy, which accompanies the formation of the C-A interface. The second term corresponds to the nucleation barrier.

Preferential nucleation was confirmed at the C-A interface and the specimen edge. Both of them are the sites, where the nucleation barrier is small, as schematically shown in Fig.12. Moreover, the nucleation barrier of the later is smaller than that of the former, as the specimen edge includes free surface. The preferential nucleation at these sites indicates that the crystallization temperature decreases as the nucleation barrier decreased.

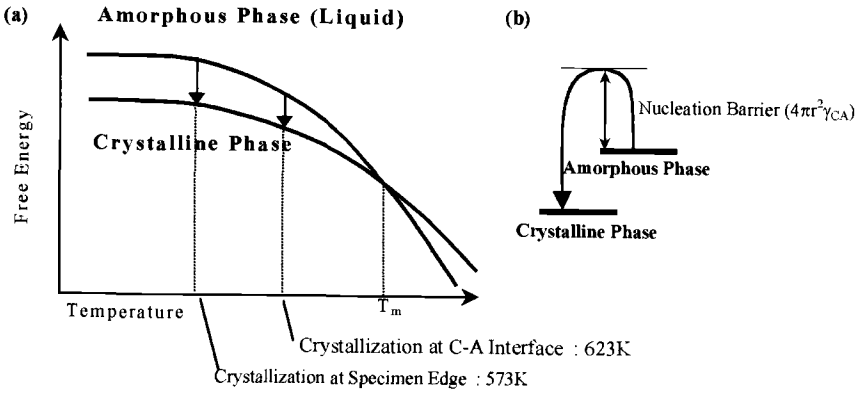


Fig.11 (a) Schematic diagram of free energy change accomplished by the crystallization of amorphous phase. (b) Schematic diagram of nucleation barrier of the crystallization.

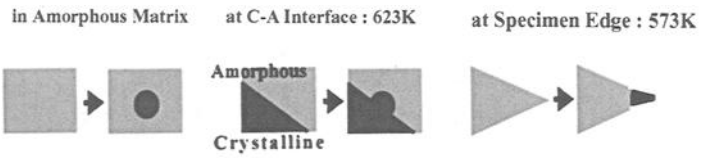


Fig.12 Schematic diagram of the relationship between the nucleation site and the surface resulted from nucleation.

Relationship between the Critical Temperature for amorphization and Thermal Crystallization Temperature

Koike et al. has reported that the critical temperature T_c for irradiation-induced amorphization increased with increasing of particles' mass and saturated a certain temperature T_u, which means materials have their own critical temperature, above which amorphization never be induced by any irradiation [12] (Fig.13). The results of the present study suggest that T_u of TiNi was 673K, since the critical temperature for amorphization was not dependent on the accelerating voltage of Ar^+. As described above, the specimen edge and the C-A interface thermally crystallized at 573K and 623K, respectively. These results suggest that the upper temperature for amorphization T_u is higher than the thermal crystallization temperature with no nucleation barrier. Therefore, it can be stated that T_u is predominated by the re-growth of crystals with some nucleation events.

Preferential crystallization during the irradiation was confirmed at the specimen edge;

the crystallization temperature decreased as the incident energy of ion increased. Since the preferential crystallization was not confirmed at any other incident surface except the specimen edge, it is conjectured to be independent of the damage level produced by the irradiation. Since specimen edge is the site where the free energy is higher level because of the contribution of free surface, it needs less energy to overcome the nucleation barrier of crystallization.

Moine et al. has reported that the critical temperature T_c for amorphization in TiNi was approx. 410K, which is quite lower than our result [13] (Fig.14). Regarding with both ion energy and ion mass their experimental condition is larger than ours, which leads to the expectation that their T_c will be same or higher than ours; however, the results are against it. Since Moine et al. determined the T_c from the irradiation to thin foil specimen, it is reasonable to understand that the difference results from how to interpret the crystallization behavior of the specimen edge. The T_c led by Moine et al. was lower than the temperature, at which preferential crystallization at the specimen edge during irradiation was confirmed in the present study. Since the incident ion energy of their experiment is larger than the one of the present study, it brings the further shifting of the preferential crystallization temperature.

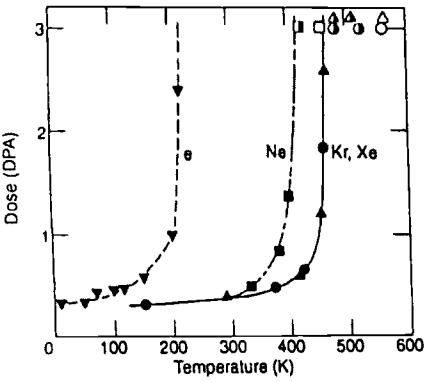


Fig.13 Temperature dependence of critical dose for amorphization in CuTi by 1MeV various particles irradiation reported by Koike et al. Critical temperature for amorphization depends on irradiated particles' mass, however, there is an upper temperature, above which amorphization was never induced by irradiation.

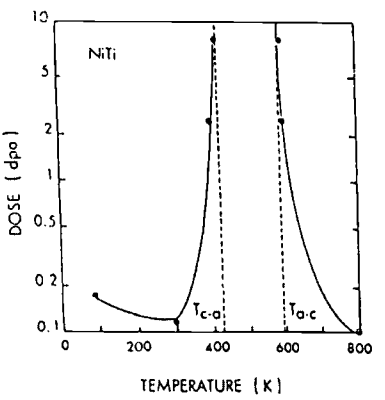


Fig.14 Temperature dependence of critical dose for amorphization and crystallization in TiNi by 250keV Ne^+ irradiation reported by Moine et al.

Conclusion

Ion irradiation-induced amorphization and crystallization in TiNi have been investigated. The findings are summarized as follows.

(1) Accelerating voltage of Ar^+ ion does not affect on the critical dose for amorphization and the temperature dependence in the range 50 to 200keV; the critical temperature for amorphization by Ar^+ irradiation is 673K. These results indicate that the temperature T_u above which amorphization is never induced by irradiation in TiNi is 673K.

(2) Thermal crystallization is preferentially confirmed at specimen edge and C-A interface in the amorphous specimen produced by Ar^+ irradiation. The lowest temperature is 573K at which crystallization confirmed at the specimen edge where the nucleation barrier is quite low. These results indicate that thermal crystallization temperature depends on the nucleation barrier.

(3) Critical temperature for irradiation-induced amorphization is higher than the thermal crystallization temperature with no nucleation barrier; T_u is predominated by the regrowth of crystals with some nucleation events.

(4) Preferential crystallization is confirmed at the specimen edge during ion irradiation. This results from the contribution of the free surface energy to overcome the nucleation barrier of crystallization.

References

[1] Nishikawa, M., Narikawa, T., Iwamoto, M., and Watanabe, K., "Quick Replacement of the Fusion Core Parts in a Cassette Compact Toroid Reactor," Fusion Technology, Vol.9, 1986, pp. 101-115.

[2] Mori, H., Fujita, H., and Fujita, M., "Electron Irradiation Induced Amorphization at Dislocations in NiTi," Japan J. Appl., Phys., Vol.22, No. 2, 1983, pp. L94-L96.

[3] Matsukawa, Y., and Ohnuki, S., "Electron Irradiation Effect on Phase Transformation in Ti-Ni Shape Memory Alloy," J. Nucl. Mat., **239**, 1996, pp. 261-266.

[4] Hoshiya, T., Shimakawa, S., Ichihashi, Y., and Nishikawa, M., "Restoration Phenomena of Ti-Ni Shape Memory Alloys in a Neutron Irradiation Environment," J. Nucl. Mat. 191-194, 1992, pp. 1070-1074.

[5] Jackson, K. A., "A Defect Model for Ion-induced Crystallization and Amorphization," J. Mater. Res. 3 (6), Nov/Dec, 1988, pp. 1218-1226.

[6] Sawai, T., and Suzuki, M., "Image Calculation of a Tilted Contamination Deposit for the Thickness Measurement of a TEM Foil," Scr. Met., Vol.24, 1990, pp.2047-2052.

[7] Sawai, T., Suzuki, M., Maziastz, P.J. and Hishinuma, A., "Comparison of Immersion Density and Improved Microstructural Characterization Methods for Measureing Swelling in Small Irradiated Disc Specimens," J. Nucl. Mat., **187,** 1992, 146-152.

[8] Ziegler, J. F., Biersack, J. P., and Littmark, U., *The Stopping and Range of Ions in Solids*, ch. 8, Pergamon Press, New York, 1985.

[9] Wu, S. K., and Wayman, C. M., "On the Reciprocal Lattice of the "Premartensitic" R-phase in TiNi Shape Memory Alloys ," Acta Metall, Vol.37, No.10, 1989, pp. 2805-2813.

[10] Lutton, R. T., Sabochick, M. J., and Lam, N. Q., "Calculation of Defect Properties of NiTi and FeTi," Mat. Res. Soc. Symp. Proc. Vol.209, 1991, PP. 207-211.

[11] Lorimer, G. W., "Sequences of Intergranular Nucleation and Precipitation," Proceedings of an international conference on *SOLID→SOLID PHASE TRANSFORMATIONS*, AIME, 1981, pp.613-635.

[12] Koike, J., Okamoto, P. R., Rehn, R. E., and Meshii, M., "The Dose, Temperature, ans Projectile-mass Dependence for Irradiation-induced Amorphization of CuTi," J.Mater. Res., **4**, 1989, pp. 1143-1150.

[13] Moine, P., and Jaouen, C., "Ion Beam Induced Amorphization in the Intermetallic Compounds NiTi and NiAl," J. Alloys and Comounds, 194, 1993, pp. 373-380.

Acknowledgements

The authors wish to express his sincere thanks to Mr. Susumu Mochizuki and Mr. Kenji Sugawara for their technical support to operate the HVEM. The authors thank to Furukawa Ltd. Co. for providing TiNi alloys.

Valentin K. Shamardin,[1] Gennady P. Kobylyansky,[2] and Vladimir M. Kosenkov[3]

Irradiation Growth of Zirconium Alloys at High Neutron Fluences

Reference: Shamardin, V. K., Kobylyansky, G. P., and Kosenkov, V. M., **"Irradiation Growth of Zirconium Alloys at High Neutron Fluences,"** *Effects of Radiation on Materials: 19th International Symposium, ASTM STP 1366,* M. L. Hamilton, A. S. Kumar, S. T. Rosinski, and M. L. Grossbeck, Eds., American Society for Testing and Materials, West Conshohocken, PA, 2000.

Abstract: The effect of high dose irradiation on irradiation growth in zirconium commercial Zr-1%Nb, Zr-2.5%Nb, Zr-1%Nb-1.3%Sn-0.4%Fe alloys at temperatures of ~80 and 320-360^{0}C has been investigated.

It is shown that the irradiation growth strain in Zirconium and Zr-Nb alloys as a function of neutron fluence sharply increases at fluences higher than (2-3)×10^{26} m^{-2} (E>0.1 MeV). Zr-1%Nb-1,3%Sn-0,4%Fe alloy was observed to exhibit radiation growth at high neutron fluences.

One of the methods to reduce anisotropy of properties and dimensional changes under irradiation is fast high-frequency treatment (FHF) consisting in quenching from beta-phase following quick heating with exposure.

Keywords: Zirconium alloy, irradiation, fuel cladding, texture, X-ray diffraction, irradiation growth.

Introduction

Irradiation-induced growth is one of the main causes of dimensional changes in PWR and BWR core components fabricated from zirconium alloys. Assessments show that up to 30% cladding shape changes of WWER fuel elements at burn-ups of ~ 45 MWd/kgU are due to the irradiation growth. At SSC RIAR the irradiation-induced growth of Russian zirconium alloys was studied during their irradiation up to high fluences at the BOR-60 reactor [*1-4*]. Russian zirconium alloys differ from Zircaloys in niobium (1% and 2.5%Nb) and iron contents, and contain no chromium in the multicomponent alloy Zr-Nb-Sn-Fe. Therefore, apart of application problems, an accumulation of experimental data on the irradiation growth of Russian alloys allows studying general features (in the scope of whole class of alloys including Zircaloys) of

[1]Head of laboratory, [2]leading scientific officer, [3]chief scientific officer, Materials Science Department, State Scientific Center of Russian Federation "Research Institute of Atomic Reactors", 433510, Dimitrovgrad, Ulyanovsk region, Russia.

Copyright© 2000 by ASTM International www.astm.org

radiation damage and evolution of the microstructure with increasing the neutron fluence taking into consideration texture, alloying, thermal treatment and other factors [5,6,7].

The report presents the experimental results on the dependence of irradiation-induced growth in Zr-1% Nb, Zr-1% Nb-1.3% Sn-0.4%Fe and Zr-2.5% Nb alloys on neutron fluence. Data are analyzed taking into consideration texture, alloying, thermomechanical treatment and irradiation conditions.

Experimental Procedures

In Table 1 the characteristics of Zirconium tubes, which were used for preparing samples to investigate the irradiation-induced growth are shown. Some data are given on production process and thermal treatment procedures.

Table 1 - *Characteristics of zirconium tubes for study of irradiation-induced growth*

Material[1)]	Transversal dimension mm	Rolling scheme[2)]	Treatment conditions	Texture factor		
				f_L[3)]	f_T[3)]	f_R[3)]
Zr	Ø36x4	A	40% c.w	0.08	-	-
			Annealing 623K, 2h	-	-	-
			Annealing 853K, 2h	-	-	-
Zr-1%Nb	Ø9.15x0.7	B	Annealing 853K, 2h	0.10	0.40	0.50
			Quenching 1173K-1193K+ annealing 773K,24h	0.32	0.30	0.28
Zr-2.5%Nb	Ø36x4	B	Annealing 723K, 5h	-	-	-
			Annealing 853K,5h	-	-	-
	Ø88x4	B	40% c.w.	0.04	-	-
			Annealing 823, 5h	0.03	0.48	0.49
	Ø98.2x6	B	Quenching 1173-1193+ annealing 773K, 24h FHF-treatment	0.31	0.36	0.33
	Ø88x4	C	Annealing 723K, 24h	0.06-0.25	0.39-0.47	0.32-0.44
Zr-1%Nb-1.3%Sn-0.4%Fe	Ø9.15x0.7	B	Annealing 853K, 2h	0.19	0.43	0.38
	Ø88x4	B	40%c.w.	-	-	-
			Annealing 823K, 5h	-	-	-

[1)] Oxygen content in the given materials is less than 0.1 wt%

[2)] A - single rolling to 40% deformation

B - multirolling with intermediate annealings

C - pressing with a large extension, 20% c.w.

[3)] f_L, f_T, f_R - grain fraction with resulting poles of basal planes in axial, tangential and radial directions.

Structural features of cladding and channel tubes prior to irradiation have been described elsewhere [*8-11*]. Channel tubes are characterized by structural nonuniformity expressed by the presence of recrystallized (large equiaxed) and partially recrystallized (very fragmented) grains. The volume fraction of these grains changes depending on alloy composition, production process and thermal treatment. For thermal treatment at 823K for 5 h the fraction of recrystallized grains is 75% in Zr - 2.5% Nb and 60% in Zr-1% Nb-1.3% Sn-0.4% Fe alloys respectively. Characteristically, in the initial state the multicomponent alloy has the highest density of <a+c> dislocations of 6.6×10^{14} m^{-2}, while <a> and <c> - type dislocations are slightly detected [*11*]. Unlike Zr-1%Nb alloy, the Zr 2.5% Nb alloy subjected to fast high-frequency (FHF) treatment in the starting state is characterized by the high-density of second phase precipitates ($\sim 10^{22}$ m^{-3}). The density of the β_{Nb} - phase is less almost by a factor of 10^3 at a smaller niobium content in the Zr-1% Nb alloy. The dose relationship of irradiation-induced growth deformation differences of which in neutron fluences are due to change of irradiation time was obtained during experiments in the BOR-60 reactor dismountable devices at the temperature of ~623K.

The device design allowed the removal of specimens during reactor shut-downs (2-3 times per year) and the measurement of dimensional changes in shielded cell with the subsequent their return to the reactor core again. The experiments were performed with samples like pieces of fuel element tubes 80 mm long or rods 4 x 4 x 80 mm long cut from channel tubes. The dimensional changes in longitudinal direction were determined using a device containing the clock-type indicator by subsequent comparison with the length of the standard sample. The error of measurements did not exceed 0.01%. The tube diameters were measured using a micrometer with the error of 0.1%.

The FHF treatment (Table 1) is accompanied by some increase in a grain size especially specific to the Zr-1%Nb alloy (from 7-8 to 30-35 μm). X-ray analysis of 1%Nb and Zr-1%Nb - 1.3%Sn - 0.4%Fe claddings was aimed to follow the shape change of diffraction lines from basal and prismatic planes that can be related to formation of dislocation loops accumulated in the crystal structure.

X-ray studies of specimens cut from tube sections of 40-80 mm in length were carried out with a diffractometer DÀRD. X-ray analysis was performed by using copper K_α -radiation. All lines were scanned at the step of 0.01°.

The microstructure of samples irradiated was studied in the electron microscope EMV-100L. The samples were prepared by the technique described in [*12*].]. V. N. Shishov's, [*13,14*], S. A. Averin's [*11*], V. I. Voevodin's [*9*] and Z. E. Ostrovsky's works made a large contribution to further investigations.

Examples of Irradiation Growth of Reactor Zirconium Alloy Core Components

For the first time a strong effect caused by irradiation growth was observed in specimens of Zr+1%Nb strips (20% c.w.) and Zr+2.5%Nb channel tubes in the annealed state (823K for 5 h) after long-term irradiation in the CM-2 reactor core at the temperature of ~ 373K [*1*].

The dependencies of irradiation growth strains and outer diameter on neutron fluence (E>0.1 MeV) in strips and channel tubes are shown in Figures 1 and 2.

With increasing the fluence, the relative elongation of strips increased and reached ~3.9% at the fluence of 5.3 x 10^{22} cm^{-2}.The initial outer diameter of channel area located in the core decreased significantly from 98.2 to 96 mm (Figure 2).

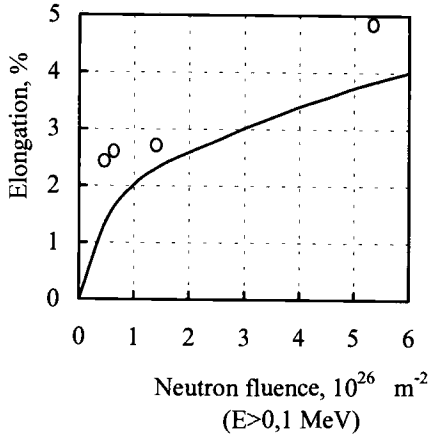


Figure 1 - *Irradiation growth of Zr-1%Nb alloy (20% c.w.) strip at 373K as a function of neutron fluence.*

Irradiation growth strain in the polycrystalline structures of nearly equiaxial grains is described by the formula

$$\varepsilon_d = S \cdot F_d (\phi t)^n, \qquad (1)$$

where ε_d is the growth strain in d-direction, S is the structural growth factor, ϕt the neutron fluence, n the exponent, F_d is the textural growth factor determined by the texture parameter f_d as follows: $F_d = 1-3f_d$.

Both the texture parameter f_d and growth factor F_d for the main directions of strips and channel tubes have been determined by X-ray analysis (Table 2).

Table 2 - *The texture parameters and growth factors of strips and channel tubes*

	f_A	f_R	f_T	F_A	F_R	F_T
CHANNEL	0.015	0.459	0.526	0.956	-0.377	-0.579
STRIP	0.023	0.067	0.910	0.931	0.799	-1.730

The irradiation growth deformation for unmeasured directions can be evaluated taking the parameters shown in Table 2 [*1*].

The calculated and measured changes of strip and tube dimensions as a result of irradiation growth are shown in Table 3.

The obtained results allowed the determination of structural growth factors to study alloy states (equation (1)). The structural factors for n=1 are as follows:

- Zr- 1%Nb alloy (20% c.w.) - 0.73 x 10^{-24}cm^2/neutron;
- Zr - 3.5%Nb alloy (823K, 5 h) - 0.42 x 10^{-24}cm^2/neutron.

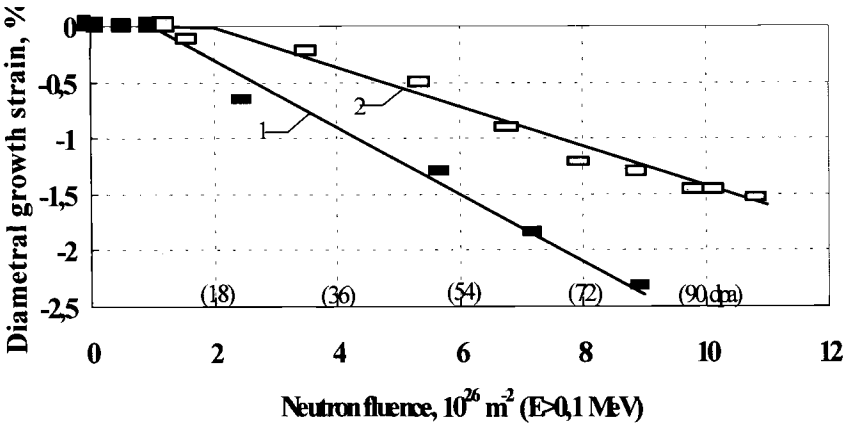


Figure 2 - *Transversal deformation of irradiation growth as a function of fluence in the CM-2 reactor Zr-2,5%Nb central channel:*

■ - *annealing at 823K (550^{0}C), for 5 h (f_L=0,015 f_T=0,526 f_R=0,459);*

□ - *FHF-treatment, quenching at 1173-1193K + annealing 823K (550^{0}C), for 24 h (f_L=0,334 f_T=0,310 f_R=0,313) regime 1.*

Table 3- *The calculated and measured irradiation growth of strip and channel*

Product	Dimensions	Initial, mm	After irradiation, mm	Δ, mm	Δ, %
Channel	Core length	350	362.6*	12.6*	3.6*
	Outer diameter	98.2	96	-2.2	-2.24
	Wall thickness	6	5.92*	-0.08*	-1.4*
Strip	Length	500	520	20	3.8
	Width	15	14.5*	0.5*	3.3*
	Thickness	0.5	0.46*	0.04*	-7.1*

*- calculated values

The irradiation-induced growth can be predicted for any direction by using the factor values obtained and also product texture.

The investigation results show that the structural coefficient S is a key parameter which determines the irradiation growth behavior i.e. technological factors (alloying, deformation production scheme, thermal treatment and so on) effect strains and relation character depending on dose and irradiation temperature.

The Effect of Thermal Treatment Conditions

A traditional technology of different zirconium alloy products fabrication involves the multiple deformation with intermediate and final annealing. Some conditions of the thermomechanical treatment are shown in Table 1.

The irradiation growth of Zr -2.5%Nb tube as a function of dose is shown in Figure 3. The tubes manufactured by the scheme of single and multiple rolling have various texture growth factors F_z (0.77 to 0.80 and 0.88, respectively).

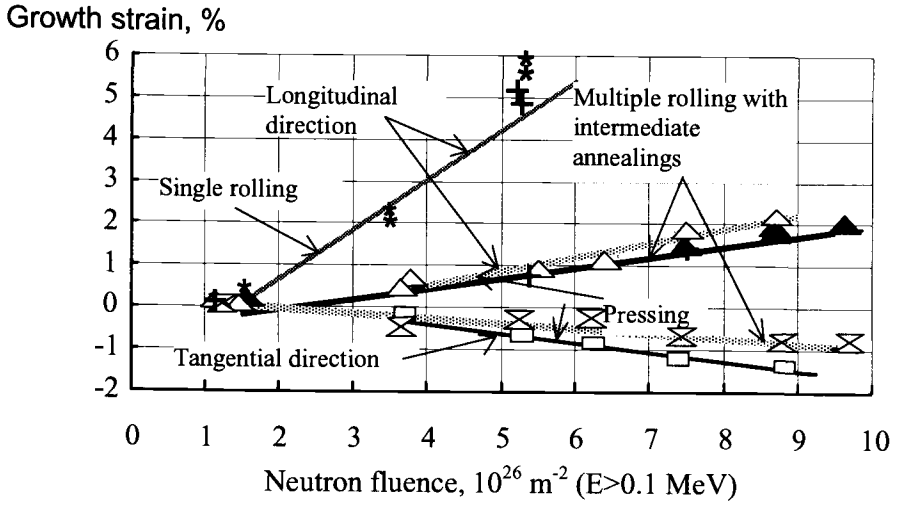


Figure 3 - *Transversal and longitudinal irradiation growth as a function of neutron fluence ($T_{irr.}$~623K) in Zr-2.5%Nb tubes with various thermomechanical treatment: + - 723K (450°C), 5h; △ - 748K (475°C), 24h; * - 853K (580°C), 2h; ⧖ - 823K (550°C), 5h; ▲ - 823K (550°C), 5h; □ - 748K (475°C), 24h.*

The growth index Gi=ΔLi/Li/ΔØi/Øi, where ΔLi is the increment of length at a fluence change from Øi to (Øi + ΔØi), low for tubes obtained by the scheme of multiple rolling. Since the tube texture slightly changes due to annealing, both the grain shape and size are important for irradiation growth [*15*].

Taking into consideration the data shown in Figure 2 and also previously published results in cooperation with Kharkov Physicotechnical Institute [*3.16*] one can conclude that the fast high frequency (FHF) treatment consisting in fast heating to 1173 - 1193K and following quenching + annealing at 823K for 24 h (regime 1) seems to be the most effective for decreasing the irradiation growth at the temperature of ~373K (Figure 4a).

The FHF treatment avoids a texture and results in anisotropic alloy structure. According to [*16*], the FHF treatment is more preferable if aging is carried out at 823 to 833K for 75-100 h (regime 2).

In comparison with the annealed state of Zr-1% Nb alloy (fuel element tubes) after the FHF treatment (regime1)(Figure 4b), the irradiation growth strain decreases by a factor of 5 at irradiation temperature from 600 to 623K and fluences of ~5 x 10^{26} m^{-2} (Figure 5).

The Effect of Alloying

The data obtained gave evidence that at high fluences both Russian alloys and Zircaloy alloys demonstrate a transition to the stage of accelerated irradiation growth (Figures 2-4). The alloying is one of the important factors which affect on the threshold value of neutron fluence, at which the stage of accelerated irradiation growth begins. The study of iodide zirconium (Figure 6) and Zr-2.5%Nb alloy (Figure 3) prepared by the single rolling scheme (Table 1) and specified by the similar texture factors of growth in the axial direction (F_Z = 0.75-0.80) demonstrated that the deformation of irradiation growth in the alloy was 3-4 times higher than in pure zirconium at fluences above 3 x 10^{26} m^{-2}.

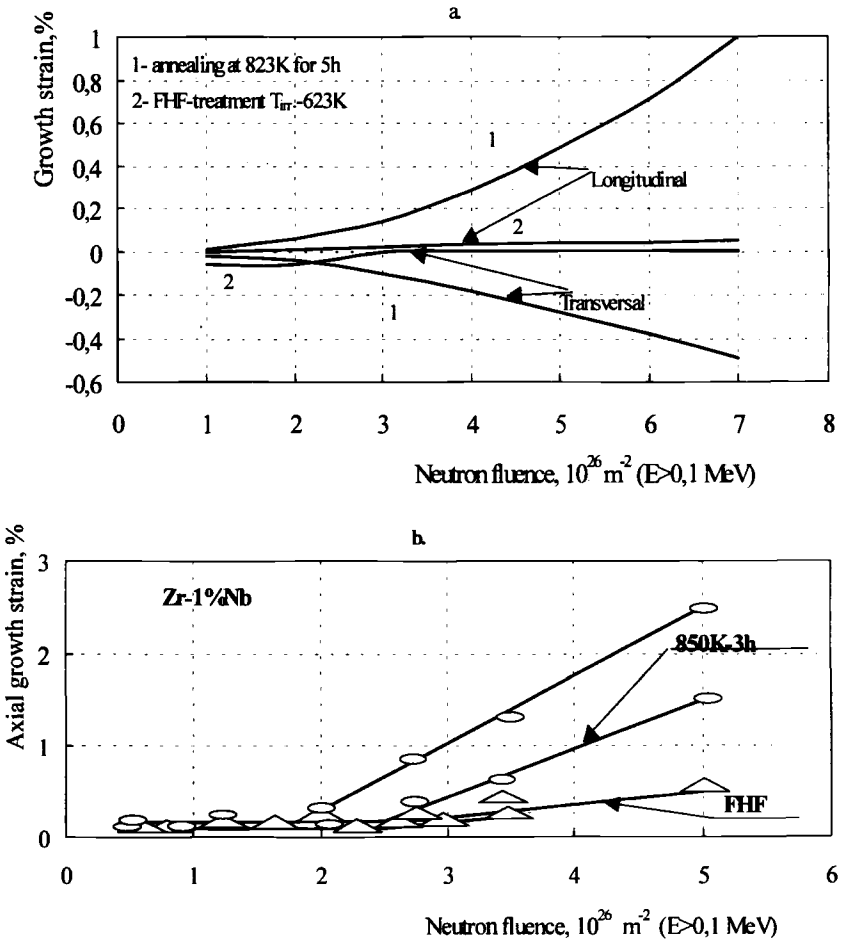


Figure 4 - *Irradiation induced growth of Zr-2.5%Nb: a) (under FHF-treatment, regime 2) and Zr-1%Nb. b) (under FHF-treatment, regime 1) quenching at 1173 to 1193K + annealing at 823K for 24 h.*

This fact is an indirect confirmation of that the interstitial and vacancy migration to different anisotropic sinks as well as dislocation loops formation and growth are affected by niobium atoms (having a larger size as compared with zirconium atoms). Zr - 1%Nb alloy fuel element tubes have the similar character of the dose dependence of irradiation growth (Figure 4). Attention is drawn to some decrease in the threshold value of fluence, after which the deformation of irradiation growth starts to change and a higher rate of irradiation growth (by 2.5 - 3 times) is observed in Zr -1%Nb as compared with Zr - 2.5%Nb alloy.

Alloying of zirconium with Fe, Sn and Nb results in a decrease the sensitivity to irradiation-induced growth at fluences of ~(6-7) x 10^{26} m^{-2}. Among all the studied alloys, the multicomponent alloy Zr-1%Nb-1.3%Sn-0.4%Fe was observed to have the weakest dependence of irradiation-induced deformation on fluence up to about (6-7) x 10^{26} m^{-2} (Figure 7). As for the multicomponent alloy, an initial state of tubes depending on the treatment condition has no significant effect on the dose dependence of irradiation growth deformation.

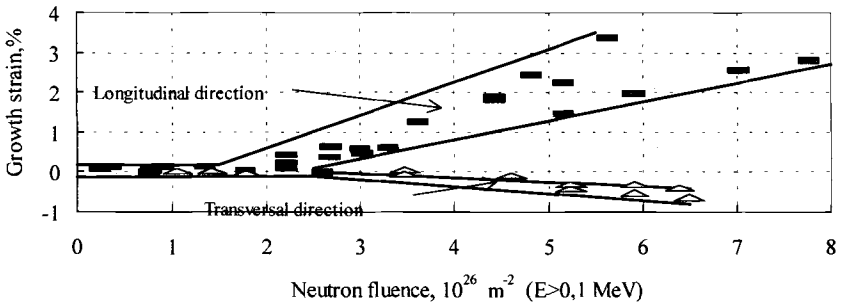


Figure 5 - *Longitudinal and transversal deformation of irradiation-induced growth as a function of fluence ($T_{irr.}$=623K) in Zr-1%Nb alloy fuel element tubes (annealed at 853K for 3 h).*

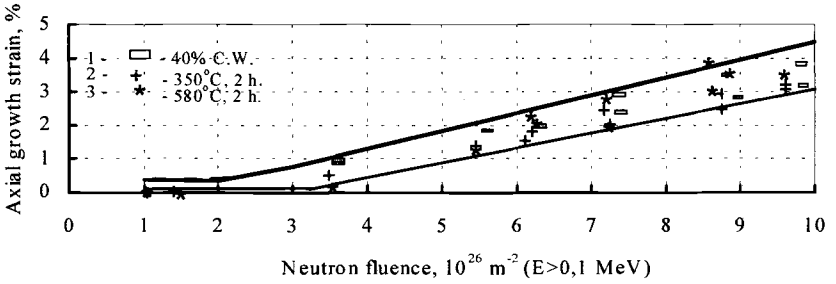


Figure 6 - *Irradiation-induced growth as a function of fluence in iodide zirconium (irradiation temperature of 623K): 1 - 40% c.w.; 2 - annealing at 623K for 2 h.; 3 - annealing at 853K for 2 h.*

Nevertheless, beginning from the threshold dose of ~7 x 10^{26} m^{-2}, it was experimentally checked that in this alloy the dependence of irradiation-growth deformation on neutron fluence changes. The change is manifested in increasing the strain rate by a factor of ~10 (Figure 8). However, the factor is 2 - 3 times less in comparison with Zr-1%Nb alloy.

The change of irradiation growth was also demonstrated with an identical specimen irradiated after short-term annealing with neutron fluence of ~5 x 10^{26} m^{-2}, at the temperature of 823K for 1 h (Figure 8). The transition to the accelerated growth stage was not detected in an annealed sample at fluence up to ~9 x 10^{26} m^{-2} and the change in behavior of irradiation-induced deformation in the annealed specimen is similar to that of the unirradiated specimen at the initial irradiation stage. A similar result was obtained for Zr-1%Nb and Zr-2.5% Nb alloys.

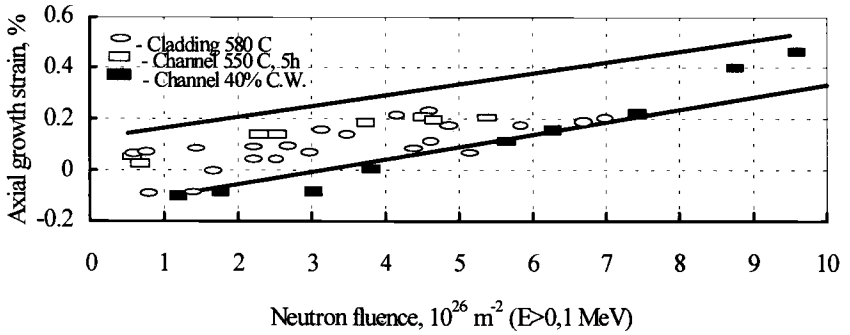


Figure 7 - *Irradiation-induced growth as a function of fluence in Zr-1%Nb-1.3%Sn-0.4%Fe alloy (irradiation temperature of 623K).*

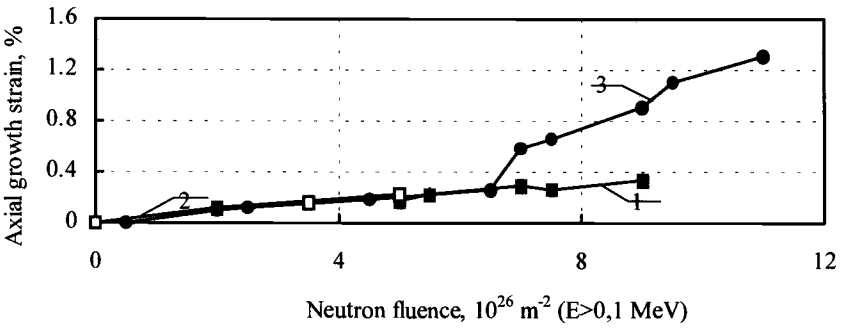


Figure 8 - *Longitudinal deformation of irradiation growth of Zr-1%Nb-1.3%Sn-0.4%Fe fuel element tubes (Ø9,15x0.7 mm) as a function of neutron fluence at 603-623K: 1 - annealing at 823K for 1h after irradiation to fluence 5x10^26 m^-2; 2,3 - without annealing.*

The diffraction line shapes in irradiated and unirradiated specimens fabricated from two alloys are shown in Figure 9. The measured half-widths and line asymmetry values are shown in Table 4. The irradiated materials are shown to have a slight broadening in the lines (0002), (2θ to ~35°) - by 11-33%, while the broadening of lines (1120), (2θ~57°) is extended by a factor of 2.

Table 4 - *The parameters of X-ray diffraction lines*

Alloy	State	0002		1120	
		$H_{1/2}$	δ	$H_{1/2}$	δ
Zr -1%Nb	Unirradiated	0.18	~1.0	0.29	1.20
	$2.8 \cdot 10^{26} m^{-2}$	0.22	~0.85	0.55	0.72
	$7.7\ 10^{26} m^{-2}$	0.24	~1.0	0.57	0.77
Zr-1%Nb-1.3%Sn - 0.4%Fe	Unirradiated	0.16	~1.1	0.18	1.6
	$7.0 \cdot 10^{26} m^{-2}$	0.20	~0.79	0.54	0.64
	$1.1 \cdot 10^{27} m^{-2}$	0.21	~1.0	0.63	0.94

Such a broadening is typical for all the diffraction lines: broadening of reflections from the basal planes and from planes close to them is higher than from the prismatic and close to them ones (Figures 9,10).

According to Krivoglaz's theory [*17*], the dislocation loops arranged in parallel to the crystalline lattice planes give rise to the formation of the diffusion scattering maxima.

The diffuse scattering maxima for vacancy loops are to be located at the small angle side of Bragg's maxima. It is this picture that was observed for irradiated specimens. It is seen from Table 4, that asymmetry of lines due to K_α doublet observed on line (1120) of unirradiated specimen is less than unity in irradiated specimens. In this case the change of line (1120) asymmetry is larger than for (0002) line. It means that the diffuse maximum is not far from the Bragg's maximum and has less value of angle. The more the asymmetry changes, the more the intensity of the diffuse maximum. At the largest lattice distortions (high density of dislocation loops) the diffuse maximum intensity can exceed the Bragg's intensity. Sometimes, whole (or almost whole) shape of lines is defined by the diffuse maximum. This will lead to a line symmetryzation. It is this case that is observed for the multicomponent alloy specimen at neutron fluence of $1.1 \times 10^{27} m^{-2}$.

Thus, the results obtained proved that dislocation loops of the vacancy type prevail. Their density in basal planes is lower than in the prismatic ones.

Discussion

TEM - study of the microstructure of the irradiated Zr-1%Nb alloy demonstrated that dislocation loops are the main irradiation defects which determine the property changes after irradiation (Figure 11). Both the mean loop diameter and loop number density do not change in the range of irradiation temperatures from 373 to 623 K, that seems to emphasize the kinetics of their nucleation and growth under irradiation. At 823 K loops disappeared completely that is accompanied the formation of dislocation network [*18*].

Two types of loops have been identified in the microstructure of irradiated Zr - Nb alloys [19]:

- <a> type with a/3<1120> Burgers vector
- <c> type with a/6<2023> Burgers vector.

The absence of dislocations with <c> component in the microstructure of irradiated Zr -1%Nb -1.3%Sn - 0.4%Fe alloy (Table 5) is one of the main factors determining its high resistance to irradiation growth (Figure 6) as compared with the Zr -1%Nb alloy [*10, 11, 13, 14*].

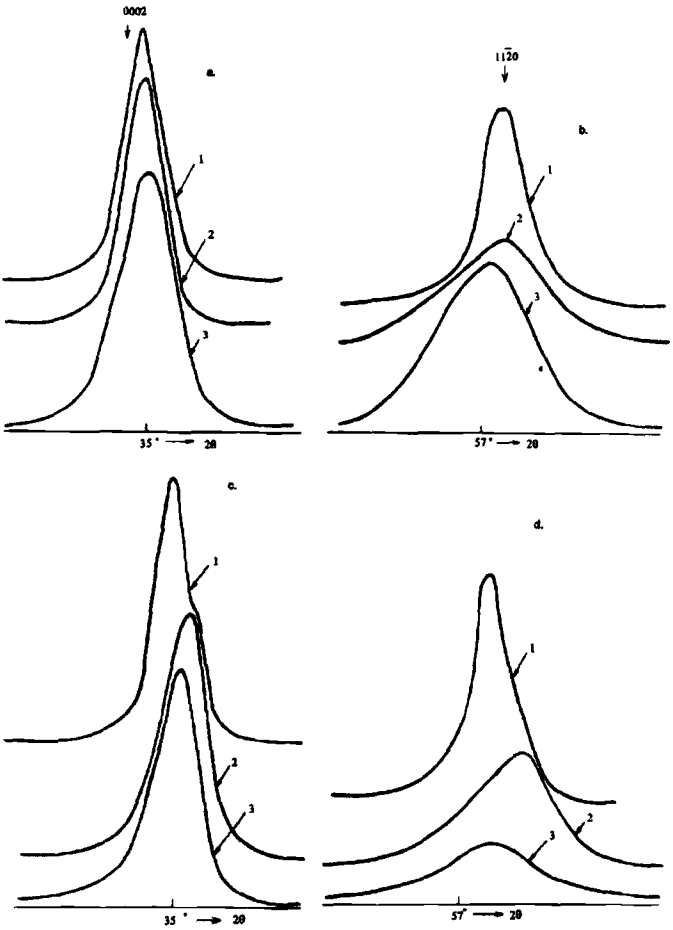


Figure 9 – *Diffraction line shapes (0002) and (1120) for Zr-1%Nb (a,b) and Zr-1%Nb-1.3%Sn-0.4%Fe (c,d). Without irradiation (1). F=2.8 x 10^{26} m^{-2} (2), Zr-1%Nb alloy; F=7 x 10^{26} m^{-2} (2), Zr-1%Nb-1.3%Sn-0,4%Fe alloy; F=7.7·10^{26} m^{-2} (3), Zr-1%Nb alloy; F=1.1 x 10^{27} m^{-2} (3), Zr-1%Nb-1.3%Sn-0.4%Fe alloy.*

Table 5 - *Microstructural parameters of irradiated zirconium alloys*

Material	Damage	SECOND-PHASE PRECIPITATES							<c> dislocation		< à > - loops
		Phase	Lattice,	Composition			Size,	Concentration,	density,	Size,	Concentration,
	dpa		nm	Zr at %	Nb at %	Fe at %	nm	m^{-3}, 10^{20}	m^{-2}, 10^{14}	nm	m^{-3}, 10^{20}
Zr 40 %	0	. . .	. . .	. . .	. . .	. . .	. .	. . .	2.0	. .	. . .
c.w.	40	. . .	. . .	. . .	. . .	. . .	. .	. . .	4.0	12	. . .
Zr-1%Nb recryst.	0	β- Nb	bcc à=0.333	15	85	. . .	50	2.5	0.2	. .	. . .
	2	β- Nb	bcc	25	75	. . .	70	1.0	0.4	9	3
	16	β- Nb	bcc à=0.340	40	60	. . .	50	0.8	3.8	12	. . .
Zr-1%Nb- - 1.3%Sn - 0.4%Fe recrystal.	0	$Zr(Nb,Fe)_2$	Hcp	35	35	30	120	0.5	0.1		. . .
	2	$Zr(Nb,Fe)_2$	hcp	35	40	25	200	0.4	0.1	10	5
	3	$Zr(Nb,Fe)_2$	hcp	35	40	25	100	0.3	. . .	10	4
	5	$Zr(Nb,Fe)_2$	hcp	30-40	30-40	15-30	120	0.5	0.1	10	5.0
	20	β- Nb	bcc a=0.341	42	50	8	100	0.1	0.3	10	4
40 % c.w.	0	$Zr(Nb,Fe)_2$	hcp	35	35	30	150	0.2	<1.0	. .	. . .
	39	β- Nb	bcc	48	49	3	<100	<0.1	3.0	10	5

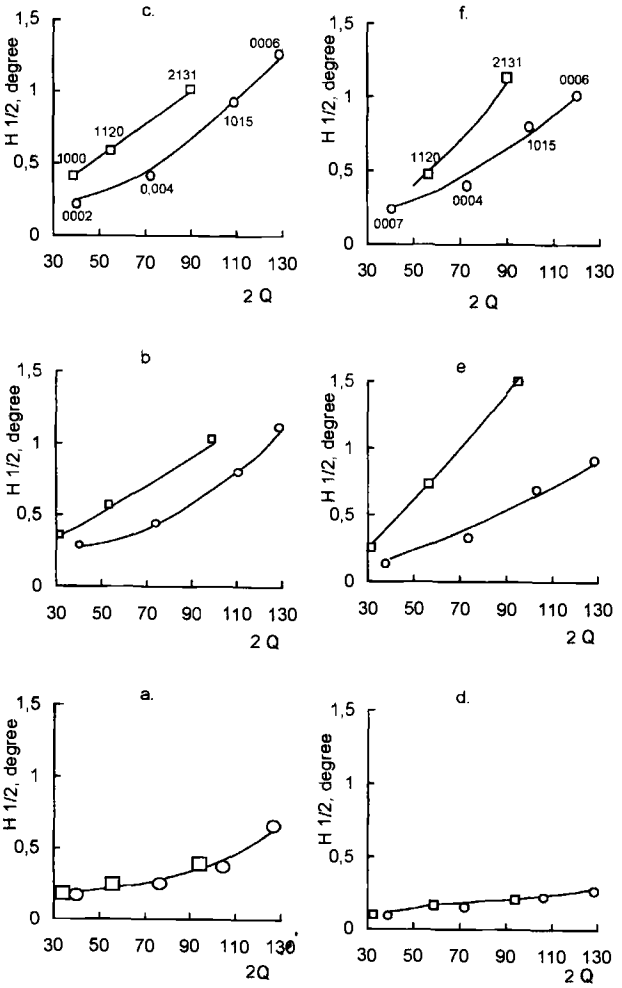


Figure 10 - *Half-widths of diffraction lines in Zr-1%Nb (a,b,c) and Zr-1%Nb-1.3%Sn-0.4%Fe (d,e,f) alloys. a,d-without irradiation; b- 2.8×10^{26} m^{-2}; c-7.7×10^{26} m^{-2}; e-7×10^{26} m^{-2}; f- 1.1×10^{26} m^{-2}.*

A high irradiation stability of precipitates like $(Zr, Nb)_3Fe$ and $Zr(Nb, Fe)_2$ provides a high resistance to irradiation-induced growth of the multicomponent alloy, at least at neutron fluences of $<5 \times 10^{25}$ m^{-2} and T_{irr}~623K [*14*]. As for Zircaloys, it is known that specific intermetallics of $Zr(Fe,Cr)_2$ and $Zr_2(Fe,Ni)$ type are subjected to an amorphization, dissolution and change of composition [*20,21*]. At present, a number of theoretical and experimental studies have been undertaken to explain various mechanisms of more intense recombination of point defects in decay of solid solution

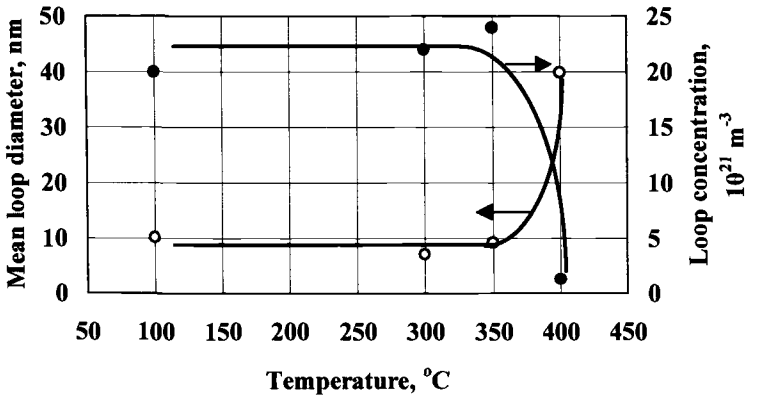


Figure11 - *Variation of the mean loop diameter and loop number density versus irradiation temperature in Zr-1%Nb alloy (at neutron fluences from 10^{25} to 10^{26} m^{-2}).*

under irradiation. The irradiation-induced growth may be affected by such a mechanism too [*22,23*]. This mechanism is especially effective at the stage when coherent precipitates exist and give rise to dilatation stresses around them. A finely dispersed irradiation-induced phase coherently bonded with the matrix (precipitate diameter of ~22 nm, density of 1.5 x 10^{15} cm^{-3}) was found to form in the multicomponent alloy under irradiation to high fluences [9]. The presence of such precipitates inhibits the formation and evolution of <c> type dislocation loops laying in basal planes. However, this delay of the accelerated irradiation growth stage is effective prior to coherency loss (Figure 8). In the multicomponent alloy the irradiation growth transition to the accelerated stage seems to be related to this factor.

The FHF treatment was found to be more effective for Zr-2.5%Nb alloy (the irradiation growth rate at the accelerated stage is significantly lower than in Zr-1%Nb alloy). This fact is well correlated with the density of coherent precipitates of the β Nb phase formed after quenching from the β-region [16]. This is a good confirmation of an idea of point defects recombination at the stage of coherent precipitates. The irradiation-induced precipitates can affect considerably the evolution of dislocation structure under irradiation. Irradiation growth as a function of fluence in both the recrystallized and cold-worked (40%) multicomponent alloy (Figure 12) was found to be almost similar up to fluences of (6-7) x 10^{26} m^{-2}. With increasing the fluence above 7 x 10^{26} m^{-2} a difference between the alloys increases (but no more than 2 times at a fluence of 9 x 10^{26} m^{-2}). In this case the alloy in cold-worked condition is more resistant against irradiation growth. The inhibition of <c> dislocation climb due to irradiation-induced precipitates resulted in lowest strains of irradiation growth in the multicomponent alloy (40% c.w.) as compared with zirconium (40% c.w.): -0.49 and 3.24%, respectively (Figure 12).

The effect of annealing at 823K for 1h, which results in a lower growth rate at high fluences (Figure 7), is needed in a detailed structure study. Such a study (Figure 8) will allow specifying the contribution of various factors to suppression of irradiation growth at different irradiation stages.

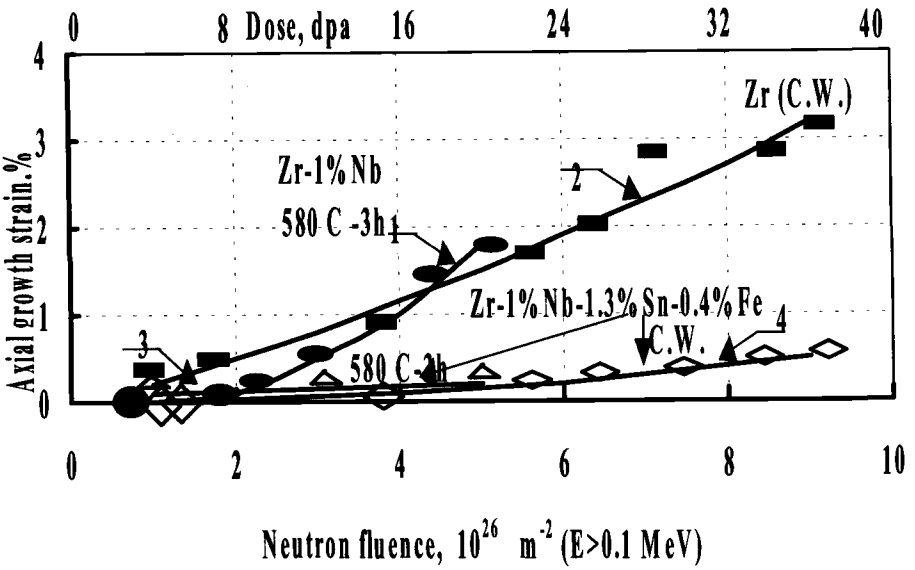


Figure 12 - *Irradiation growth as a function of fluence in alloys irradiated at T=600-620K: 1) Zr-1%Nb alloy (850K, 2h); 2) zirconium 40% c.w.; 3) Zr-1%Nb-1,3%Sn-0,4%Fe (850K, 3h); 4) Zr-1%Nb-1,3%Sn-0,4%Fe (40% c.w.).*

Conclusions

1. The investigations showed that a sharp increase of the irradiation growth strain in Zr-1Nb-1.3Sn-0.4Fe alloy as a result of irradiation at about 350°C took place at essentially higher neutron fluences (7 x $10^{22}cm^{-2}$) than in Zr-1Nb and Zr-2.5Nb alloys (2 x $10^{22}cm^{-2}$). In this case the growth rate increases by an order of magnitude but in the multicomponent alloy it is 2-3 times as low as in the Zr-Nb alloys system.
2. A summary of the new results and those obtained earlier gives the evidence that point defect recombination near secondary phase precipitates is the supposed mechanism that controls the "threshold" stage of the dose dependence of the irradiation growth strain and leads to a change in the dislocation structure under irradiation.
3. The irradiation growth of zirconium alloys can be reduced by conducting intermediate post-irradiation annealing that results into an increase of the incubation period duration prior to the threshold of the irradiation growth strain dose dependence.

References

[1] Tsykanov, V. A,..Davydov, E. F, Shamardin, V. K.et. al "Radiation Shape Change of Products Made of Zirconium Alloys Irradiated in SM-2 up to a High Neutron Fluence," *Atomnaya Energia*, vol.55, No.4, 1983, p.211.

[2] Kobylyansky, G. P., Shamardin, V. K., Ostrovsky, Z. E,.et.al "Radiation Deformation of Cladding and Channel Tubes Made of Zirconium Alloys at High Neutron Fluences", Proceedings of the International Conference on Radiation Materials Science, May 22-25, 1990, Alushta, vol.4, pp.64-72.

[3] Kobylyansky, G. P., Shamardin, V. K., Stukalov, A. I, "Irradiation Growth of Fuel Element Tubes Made of Zirconium Alloys at High Neutron Fluences" Voprosy Atomnoy Nauki i Techniki, Ser. Radiation Damage Physics and Radiation Materials Science, issue 2(53), pp.32-34.

[4] Kobylyansky, G. P., Shamardin, V. K., and Grigoryev, V. M., "Peculiar Features of Irradiation Growth of Zirconium and H-2.5 Alloy at High Neutron Fluences," Preprint, RIAR-9(772). M., TZNIIatominform.

[5] Adamson, R. B., "Irradiation Growth of Zircaloy, Zirconium in the Nuclear Industry", ASTM STP 633,

[6] Franklin, D. G., Adamson, R. B., J. Nuclear Mater. 159(1988), pp.12-21.

[7] Griffiths, M., Mecke, J. F., and Winegar, J. E., "Evolution of Microstructure in Zirconium Alloys during Irradiation of Zirconium in the Nuclear Industry", 11-th International Symposium, ASTM STP 1295 E. R. Bradley and G. P. Sabol, Eds, ASTM, 1996, pp.580-602.

[8] Kobylyansky, G. P., Shamardin, V. K., Ostrovsky, Z. E., Rayetzky, V. M., Nikulina, A. V., Peregud, M.M., and Grigoryev, V.M., "Radiation Shape Change of Zr Alloy Cladding and Channel Tubes at High Neutron Fleunces", Proceedings of the International Conference on Radiation Material Science, Alushta, May 22-25, 1990, V.4, Kharkov-1990, pp.64-72.

[9] Nikulina, A. V., Markelov, V. A., J. Nucl. Mater. 238(1996), pp.205-210.

[10] Shishov, V. N., Nikulina, A. V., Markelov, V. A., et al., "Evolution of Zirconium Based Alloys Irradiated in the Reactor," Proceedings of the 4-th Conference on Reactor Material Science, Dimitrovgrad, May 15-19, 1995, v.2, 1996, pp. 156-177.

[11] Averin, S. A., Panchenko, V. L., Kolbenkov,S.A., et al., "Investigations of the Influence of RBMK Reactor Neutron Irradiation on the Fine Structure of Zirconium Alloys", Proceedings of the 4-th Conference on Reactor Material Science, Dimitrovgrad, May 15-19, 1995, v. 12, 1996, pp.121-133.

[12] Pokrovsky, A. S., Kobylyansky, G. P., Demin,Yu. N., Malkov, V. M., "Production Method of Fine Foils from Refractory Materials and Definition of Geometry Characteristics of Irradiation Defects," Voprosy Atomnoy Nauki i Techniki, Ser. Radiation Material Science, Irradiation Methods and Technique, Dimitrovgrad, 1997, issue 2(9), p.7.

[13] Shishov, V. N., Nokulina, A. V., Markelov, V. A. et.al. "Influence of Neutron Irradiation on Dislocation Structure and Phase Composition in Zr-Based Alloys", Proceedings of the 11th International Symposium on Zirconium in the Nuclear Industry, ASTM STP 1295, E. R. Bradley and E.P.Sabol, Eds., ASTM, 1996, pp.603-622.

[14] Nikulina, A. V., Shishov, V. N., Peregud, M. M., Tselishev, A. N., Kobylyansky, G. P., Shamardin, V. K., "Irradiation Induced Growth and Microstructure Evolution Zr - 1.2Sn - 1Nb - 0.4Fe under Neutron Irradiation to High Doses",

Effects of Radiation on Materials 18-th International Symposium, ASTM STP 1325 Nanstad, R. N., Hamilton, M. L., Garner, F. A., and Kumar, A. S., Eds ASTM, 1997.

[15] Rogerson, A., Murgatroyd, R. A., J. Nucl. Mater., 1979, v.80, p.210.

[16] Zelensky, V. F., Stukalov, A. I., Nekhludov, I. M.,et al. "Irradiation Effect on the Strain and Mechanical Properties of Zr Alloys Treated by SVCH," VANT, Ser. FRP & RM, 1996, issue 1(64), p.39.

[17] Krivoglaz, M. A., "Diffraction of X-Rays and Neutrons in non-ideal crystals," "DKiev, Naukova Dumka, 1983, p.408.

[18] Kobylansky, G. P., Pokrovsky, A. S., Shamardin, V. K., "Irradiation Effects in Zr -%Nb Alloy," Voprosy atomnoy nauki i tekhniki, Ser.. Physics of Radiation Damage and Material Science, 1983, issue 2(25), pp.51-56.

[19] Gurovich, B. A., Astrakhantsev, M. S., .Platonov, P. A, Elesin, EL. A., "Physics of Metals and Metal Science," 61, 1986, p.922.

[20] Garzarolli, F., Goll, W, Seibold A. and Ray, I., "Effect of In-PWR Irradiation on Size, Structure and Composition of Intermetallic Precipitates of Zr-alloys, Zirconium in the Nuclear Industry," 11-th International Symposium, ASTM STP 1295, E. R. Bradley and G. P. Sabol, Eds, ASTM, 1996, pp.541-556.

[21] Griffiths, M., "A Review of Microstructure Evolution in Zirconium Alloy during Irradiation", J. Nucl. Mater., 159, 1988, p.190.

[22] Bakay, A. S., Zelensky, V. F., Matvienko, B. V. et al, "Enhancement of Structural Defects Recombination on Solid Solution Decay under Irradiation," VANT. Ser. FRP & RM, 1983 issue. 5(28) pp.3-11.

[23] Parshin, A. M, "Structure, Porosity, Radiation Damage of Steels and Alloys", Metallurgia, Chelabinsk, 1988, p.656.

Etsuo Ishitsuka,[1] Hisashi Sagawa,[1] Akira Nagashima,[2] Tatsuo Sugie,[2]
Takeo Nishitani,[2] Shin Yamamoto,[3] and Hiroshi Kawamura[1]

Neutron Irradiation Test of Optical Components for Fusion Reactor

Reference: Ishitsuka, E., Sagawa, H., Nagashima, A., Sugie, T., Nishitani, T., Yamamoto, S., and Kawamura, H., **"Neutron Irradiation Test of Optical Components for Fusion Reactor,"** *Effects of Radiation on Materials: 19th International Symposium, ASTM STP 1366,* M. L. Hamilton, A. S. Kumar, S. T. Rosinski, and M. L. Grossbeck, Eds., American Society for Testing and Materials, West Conshohocken, PA, 2000.

Abstract: The neutron irradiation effects on the window and mirror materials proposed as optical elements for plasma diagnostic components were studied. Specimens were sapphire and KU-quartz as the window material, molybdenum corner cubic reflector, gold-coated mirror and aluminum corner cubic reflector. These materials were irradiated by the Japan Materials Testing Reactor, and transmission and refraction spectrum, change of color and surface roughness were observed.

Keywords: fusion reactor material, neutron irradiation, optical element, window, transmission, mirror, reflectivity, sapphire, KU-quartz, molybdenum, gold-coated mirror, aluminum, PIE, in-situ measurement

Introduction

Optical components that are to be used for the measurement of plasma density and temperature in the ITER will be irradiated by neutrons. From this point of view, neutron irradiation tests of optical elements were carried out in the Japan Materials Testing Reactor (JMTR). Specimens were window materials (sapphire and KU-quartz) and mirror material {molybdenum corner cubic reflector (Mo-CCR), gold-coated mirror and aluminum corner cubic reflector (Al-CCR)}. Neutron irradiation tests for each specimen are summarized in Table 1.

[1] Japan Atomic Energy Research Institute, Oarai Research Establishment, Oarai-machi, Higashi Ibaraki-gun, Ibaraki-ken 311-1394, Japan.

[2] Japan Atomic Energy Research Institute, Naka Research Establishment, Naka-machi, Nka-gun, Ibaraki-ken 311-0193, Japan.

[3] ITER Garching JWS, Max-Planck-Institut fuer Plasmaphysik Boltzmannstr.2, D-85748 Garching bei Muenchen, Germany.

Copyright© 2000 by ASTM International www.astm.org

Irradiation Tests of Window Material

Preliminary Irradiation Tests

For the sapphire specimens Al_2O_3: 99.99wt%, the change of transmission spectrum by the effects of neutron irradiation was observed by post-irradiation examination (PIE) [*1*]. The transmission spectrum of sapphire was measured by light spectrometer (UV-3100 and FTIR-4100 of Shimadzu Co.) in the wavelength from ultraviolet to infrared range. The measured transmission spectrum is shown in Figure 1.

Table 1 - *Summary of Neutron Irradiation Tests*

Optical element	Material [Dimension] (mm)	Fluence (E>1MeV) $\times 10^{20}$(n/cm^2)	Irradiation temperature (°C)	Tested Item
Window	Sapphire*1 [$\phi 13 \times t1$]	0.5 3 4	250 400 500	Measurement of transmission spectrum by PIE
	Sapphire*1 KU-quartz*2 [$\phi 11 \times t1$]	~0.1 ~0.2	~300 ~400	Measurement of induced loss for transmission spectrum by in-situ measurement
Mirror	Mo-CCR*3 [$\phi 13 \times h15$]	1	200	Investigation of color and roughness by the appearance observation, interference measurement and SEM observations by PIE
	Gold-coated mirror*3 [$\phi 15 \times t1$]	1	200	Investigation of color and roughness by the appearance observation by PIE
	Al-CCR*3 [$\phi 52 \times h70$]	~1	~200	Measurement of induced loss for reflection spectrum by in-situ measurement

*1 Produced by Kyocera Co.
*2 Produced by Russian Company.
*3 Produced by Optic Mihara Co.

Transmission rate of neutron irradiated sapphire in the wavelength of 800-7000 nm did not change after irradiation. On the other hand, transmission rate in the wavelength of 200-800 nm decreased, and the decrease of transmission rate depended on neutron fluence. However, decrease of transmission rate for sapphire irradiated with total fast neutron fluence of 4×10^{20} n/cm^2 at 500 °C was smaller than that of specimen irradiated with total fast neutron fluence of 3×10^{20} n/cm^2 at 400 °C. This result showed that the annealing effect under high temperature irradiation was larger than that of irradiation effect in this case. However, the relation between annealing effect and irradiation effect

will be complicated. And these evaluations of dynamic radiation effects for the optical components must be indispensable for the design of plasma diagnostic component. Therefore, in-situ transmission spectrum measurement was carried out as follows by using special irradiation capsule.

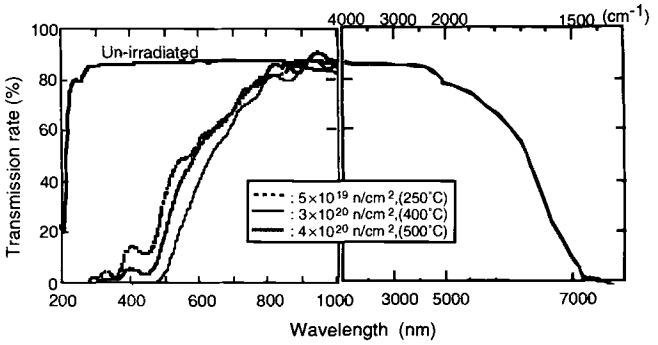


Figure 1 - *Transmission spectrum of neutron irradiated sapphire*

In-situ Measurement

Spectrum of induced loss for sapphire (Al_2O_3:99.99wt%) and KU-quartz (SiO_2:99.9wt%, OH:0.1wt%) was measured by using special irradiation capsule. Transmission rate of un-irradiated specimens measured by UV-3100 is shown in Figure 2. An absorption peak at a wavelength of 2700 nm caused by OH was observed in KU-quartz.

Special irradiation capsule was developed for this measurement, so called "in-situ transmission spectrum measurement capsule". Outline of capsule is shown in Figure 3. Capsule mainly consisted of 2 axis driving system, sample stage, Mo-CCR and heater. Light axis was adjusted by the two axes driving system to compensate the shift by thermal expansion of capsule, and a stepping motor for sample stage was provided as a sample changer.

Distinction of each specimen on the sample stage is possible by seeking for small hole without specimen, and this small hole was always used as a reference. This measurement procedure had been possible to remove the attenuation of transmission light for the fiber and lens by γ-ray effects. White light source (AQ-4303B, Ando Electric CO., LTD.) and optical spectrum analyzer (AQ-6315, Ando Electric CO., LTD.) were used as measurement equipment.

Induced loss of transmission spectrum at reactor power up is shown in Figure 4. Transmission spectrum of sapphire and KU-quartz were affected by neutron irradiation at low temperature even in low neutron fluence, and KU-quartz was more sensitive than that of sapphire. Induced loss of KU-quartz was evaluated as small [2]. However, we should pay attention to the case of low temperature irradiation.

The two peaks of about 650 and 900 nm were observed in the both specimens. The

peak of about 650 nm is likely due to the NBOHC (Nonbridgeing-Oxygen Hole Centers) band [*3,4*]. The peak of about 900 nm was not clear.

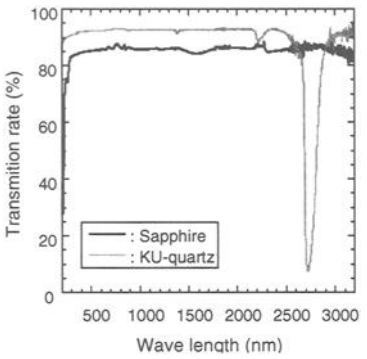


Figure 2 - *Transmission spectrum of un-irradiated specimen*

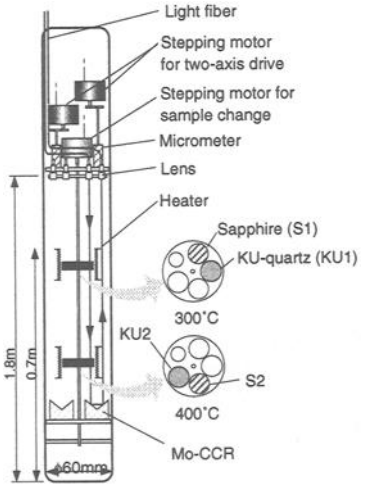


Figure 3 - *In-situ transmission spectrum measurement capsule*

Induced loss of transmission spectrum at 50MW (full power) is shown in Figure 5. Induced loss of each specimen increased with neutron fluence and decreased with higher irradiation temperature, and induced loss of KU-quartz was smaller than that of sapphire. Transmission spectrum of each specimen became constant up to ~10 days (Total irradiation was about 25 days). And, induced loss of each specimen increased at the reactor shut down.

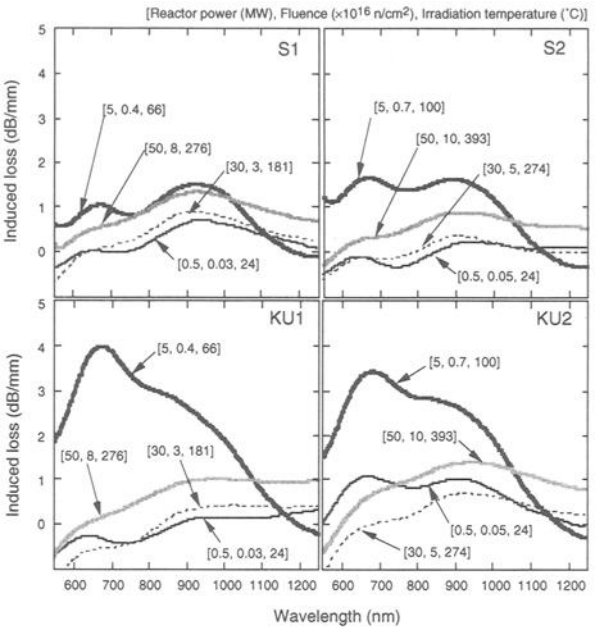


Figure 4 - *Induced loss of transmission spectrum at reactor power up*

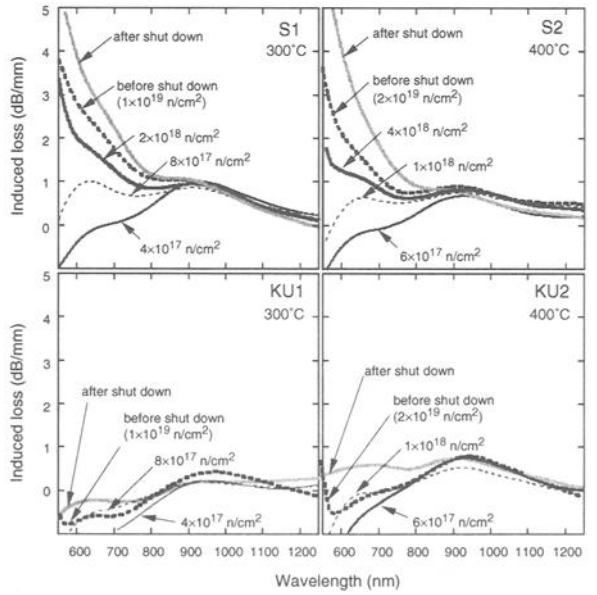


Figure 5 - *Induced loss of transmission spectrum at 50MW (full power)*

The amounts of induced loss in this study are three orders larger than that of the previous data for optical fiber [*3,4*]. However, induced loss shows the similar value with the PIE data [*2*]. The comparison previous data with this study were impossible because of the size effect and/or boundary conditions of specimens (cladding or coating, etc.). This suggestion means the diffusion effects of generated defects should be study.

In-situ heating test up to 700°C for each specimen was attempted to make clear the annealing effect under the neutron irradiation. Result of in-situ heating test is shown in Figure 6. Holding time of each temperature was about 30, 30 and 50 min for 500, 600 and 700°C, respectively. "After heating" in this figure means the measurement at 400°C after 700°C and 50 min heating. In the results of PIE, transmission spectrum was perfectly recovered by annealing of 700°C and 10 min [*2,5*]. However, in the result of in-situ heating test, the perfect recover could not be observed. These results mean that annealing effect should not be expected for sapphire and KU-quartz.

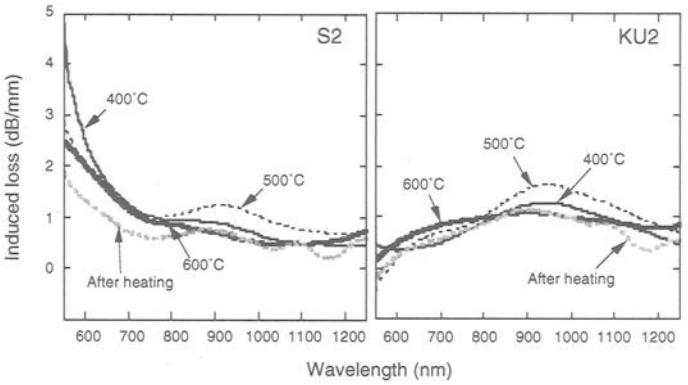


Figure 6 - *Result of in-situ heating test*

Irradiation Tests of Mirror Material

Preliminary Irradiation Test of Mo-CCR

Color change and roughness of mirror surface as to the Mo-CCR (Mo:99.9wt%) were observed by PIE (appearance observation, interference measurement and SEM observations). By the appearance observation, no significant change of color was observed [$^{98}Mo(n,\gamma)^{99}Mo \rightarrow ^{99}Tc, ^{99m}Tc \rightarrow ^{99}Ru$, this nuclear transmutation was very small, and the amount of generated ^{99}Ru was estimated as < 1 ppm in this neutron fluence]. Interference measurement by interferometer of He-Ne laser and SEM observation was carried out to investigate the change of mirror surface roughness. Interference measurement equipment is shown in Figure 7. This equipment was set in lead cell, and laser was introduced by single-mode fiber. Result of interference measurement is shown in Figure 8. The interference fringes of mirror surface were

parallel, and change of surface roughness was not observed. SEM observation also agreed with this result.

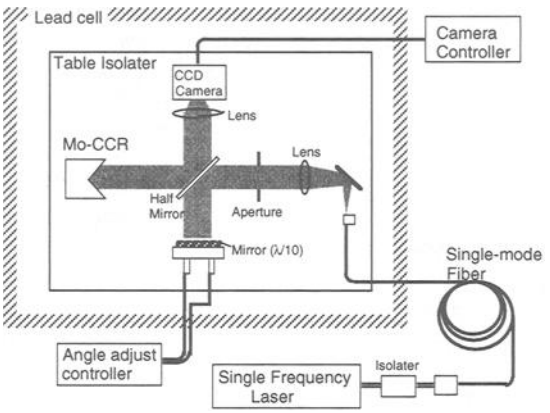
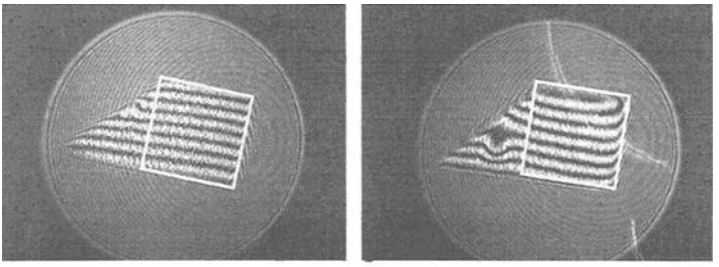


Figure 7 - *Interference measurement equipment*



(a) Unirradiated Mo-CCR (b) Irradiated Mo-CCR

Figure 8 - *Result of interference measurement*

Preliminary Irradiation Test of Gold-coated Mirror

Color change of gold-coated mirrors was investigated by PIE (appearance observation). Gold was coated at 300nm thickness on the base coating (Cr, 10~20nm). Substrate was low expansion coefficient glass. Color of mirror surface changed dark color. This reason was presumably caused by nuclear transmutation [^{197}Au (n,γ) ^{198}Au --> ^{198}Hg, 10 % of Au changed to Hg in this neutron fluence].

In-situ Measurement

Spectrum of induced loss for Al-CCR (Al:96.8wt%, Mg:2.5wt%) was measured by in-situ reflection spectrum measurement. Special irradiation capsule was developed for this measurement, so called "in-situ reflection spectrum measurement capsule". Outline of capsule is shown in Figure 9, and the mechanism was similar to former capsule (see Figure 3).

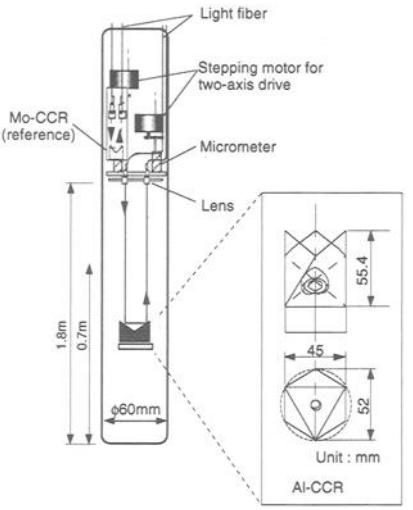


Figure 9 - *In-situ reflection spectrum measurement capsule*

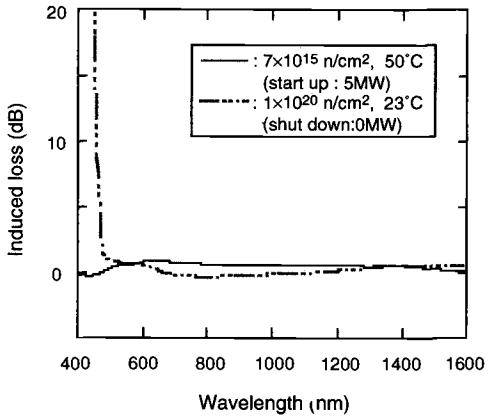


Figure 10 - *Induced loss of reflection spectrum*

Mo-CCR was set up to the upper part of capsule, and was used as a reference of reflection. Al-CCR as an irradiation specimen was set up to the middle part of capsule. White light source and optical spectrum analyzer were used as measurement equipment.

Induced loss of reflection spectrum is shown in Figure 10. The change of reflectivity for Al-CCR could not be observed (induced loss at short wavelength might be caused to induce loss of fiber). [^{27}Al (n, γ) ^{28}Al --> ^{28}Si, this nuclear transmutation was small, and the amount of generated ^{28}Si was estimated as < 0.1 wt% in this neutron fluence].

Conclusion

Induced loss of sapphire and KU-quartz, which are the candidate materials for instrumentation windows in the fusion reactors, was investigated in the JMTR. Induced loss of sapphire and KU-quartz increased with neutron fluence and decreased with higher irradiation temperature, and KU-quartz showed smaller decrease of induced loss than sapphire. Utilization of KU-quartz in the short wavelength and of sapphire in the infrared range is suitable. However, transmission spectrum in the short wavelength was significantly affected by the low temperature irradiation. Therefore, monitoring system of transmission spectrum for windows should be considered in the design of plasma diagnostic components. And, we should not expect the annealing effect under the neutron irradiation.

For mirror materials, change of surface roughness of Mo-CCR was not observed, color of mirror surface for the gold-coated mirror changed to dark, and the change of reflectivity for Al-CCR was not observed. From these results, utilization of Mo-CCR and Al-CCR will be possible. However, we should pay attention to nuclear reactions that affect the reflection spectrum.

Acknowledgments

This report has been prepared as an account of work assigned to the Japanese Home Team under Task Agreement number G 55 TD 02 95-11-24 FJ within the Agreement among the European Atomic Energy Community, the Government of Japan, the Government of the Russian Federation, and the Government of the United States of America on Cooperation in the Engineering Design Activities for the International Thermonuclear Experimental Reactor ("ITER EDA Agreement") under the auspices of the International Atomic Energy Agency (IAEA).The authors would like to acknowledge the support of the hot laboratory staff of the JMTR for the post-irradiation examinations.

References

[1] Nishitani,T., Ishitsuka E., et al., "Japanese Contribution to ITER Task of Irradiation Test on Diagnostic Components," Fourth International Symposium on Fusion

Nuclear Technology, Apr. 6-11, Tokyo, 1997.
[2] Yamamoto, S., "Design Description Document, Radiation effect (WBS 5.5.M)," ITER JCT, 1997.
[3] D.L.Griscom, "γ and fission –reactor radiation effects on the visible-range transparency of aluminum-jacketed, all-silica optical fibers," J. Appl. Phys. 80 (4) 15 August 1996, p.2142.
[4] D.W.Cooke, B.L.Bennett and E.H.Farnum, "Optical absorption of neutron –irradiated silica fibers," J. Nucle. Mater. .232, 1996, p.214.
[5] Umeda, Journal of the Atomic Energy Society of Japan ,Vol. 35, No. 6, 1993, p. 543.

Takeo Muroga,[1] Kazufumi Yasunaga,[2] Yutai Katoh, [3] Hideo Watanabe,[4] Naoaki Yoshida,[4] and Nobuaki Noda[1]

Correlation of Hardening and Microstructure of Tantalum Irradiated with Heavy Ions

Reference: Muroga, T., Yasunaga, K., Katoh, Y., Watanabe, H., Yoshida, N., and Noda, N., **"Correlation of Hardening and Microstructure of Tantalum Irradiated with Heavy Ions,"** *Effects of Radiation on Materials: 19th International Symposium, ASTM STP 1366,* M. L. Hamilton, A. S. Kumar, S. T. Rosinski, and M. L. Grossbeck, Eds., American Society for Testing and Materials, West Conshohocken, PA, 2000.

Abstract: The microhardness change of tantalum irradiated with heavy ions has been evaluated using a micro-indentation technique. The increase in hardness by irradiation was significant below ~900K and negligible above ~1100K. The hardness decreased steeply with temperature at ~1000K. Correlation of the results with microstructure data showed that the strength of voids and line dislocations as barriers against deformation should be very weak relative to that of loops and TEM-invisible defects. The temperature and fluence dependence of the hardening by TEM-invisible defects, derived by the correlation, implied an accumulation process of cascade vacancy clusters during irradiation.

Keywords: Tantalum, irradiation hardening, microstructure, micro-indentation

Introduction

Tantalum is one of the candidates for structural component materials of fusion reactors especially at the divertor position, because of tantalum's high corrosion resistance and easy fabricability[*1*]. Tantalum is also a candidate material for targets of spallation neutron sources[2]. Although, tantalum in both applications will be used in high flux neutron irradiation environments, its radiation response has been studied only limitedly.

Tantalum is also known as a low activation material from the waste-disposal viewpoints which is attractive for application to fusion reactors, although intense short-term (<30y) radioactivity with a short-half-life may be disadvantageous from the maintenance viewpoints[*3,4*]. Partly because of the high short-term radioactivity, experiments with tantalum after high fluence neutron irradiation have been limited. Thus, charged particle irradiation studies are considered to be necessary to study tantalum. It is particularly important to develop a methodology to obtain radiation-induced mechanical property changes applying small specimen test technology.

The objective of the present study is to evaluate the response of tantalum to heavy

[1] Professors, National Institute for Fusion Science, Oroshi, Toki, Gifu 509-5292, Japan.
[2] Graduate Student, Interdisciplinary Graduate School of Engineering Sciences, Kyushu University, Kasuga, Fukuoka 816-8580, Japan.
[3] Associate Professor, Institute of Advanced Energy, Kyoto University, Uji, Kyoto 611-0011, Japan.
[4] Associate Professor and Professor, respectively, Research Institute for Applied Mechanics, Kyushu University, Kasuga, Fukuoka 816-8580, Japan.

Copyright© 2000 by ASTM International www.astm.org

ion irradiation by means of micro-indentation technique. The technique was developed to extract the hardness within a very thin near-surface area subjected to ion irradiation damage (<500 nm). The results were compared to microstructural evolution for the purpose of hardness-microstructure mechanistic correlation.

Experimental

The material used is a 99.95% pure tantalum supplied by Plansee with major impurities of 100ppm W, 75ppm Fe, 50ppm Mo, 50ppm Ni, 30ppm O, 30ppm C and 20ppm N. The material, supplied as 0.25 mm sheets, was cold rolled and punched into 3mmϕ discs; the specimens were annealed at 2073 K for 300 sec. The specimen surface was electropolished prior to irradiation.

Heavy ion irradiations were performed with 2.4 or 3.0 MeV Cu^{2+} ions at 573 to 1546 K using the Tandem accelerator of Kyushu University. The fluence levels of the irradiation were 0.3, 3 and 20 dpa at the damage peak position. The damage rate was ~3.3×10^{-3} dpa/s. The depth distribution of the damage rate and the ion deposition rate, calculated with TRIM code [5] are shown in Fig. 1. In this calculation, a displacement threshold energy of 62 eV was used. The micro-indentation tests were carried out at room temperature using the Akashi MZT-3 apparatus of National Institute for Fusion Science with load of 0.1~5.0 gf. In these measurements, a triangular pyramidal diamond indentor with a semi-apex angle of 68 degrees was used. The microstructures of the specimens were observed at a depth of ~300 nm using JEM-2000EXII and JEM-2000FX electron microscopes of Kyushu University.

Procedure to Evaluate Microhardness

The microhardness of the irradiated area was derived using a contact pressure evaluation model proposed by Oliver and Pharr [6] and described in a recent paper[7]. In this model, the microhardness, H, is derived by

$$H = P/A(h_c) \qquad (1)$$

where P and A are the load of indentation and the projected area of the indentor-specimen surface contact. The contact depth, h_c, was determined based on the load-displacement properties[6]. The area, $A(h_c)$, as a function of h_c, was determined experimentally, taking into account the real shape of the indentor tip.

The depth distribution of the microhardness was derived by repeated measurements at different positions on a specimen with different indentation loads. By repeated measurements with different loads, the microhardness as a function of contact depth is derived. Fig. 2 shows a diagram of a microhardness of ion-irradiated specimens as a function of contact depth. Assuming a step function for the real depth distribution of ion irradiated specimens, a near-surface plateau of the microhardness, if it appears experimentally, would corresponds to the microhardness of the irradiated area. Beyond the plateau, the measured hardness would decrease due to the contribution from the unirradiated substrate.

Results

Microhardness Measurements

Fig. 3 shows the depth dependence of microhardness after irradiation at 773K. The microhardness near the surface increases with fluence, forming the plateau as

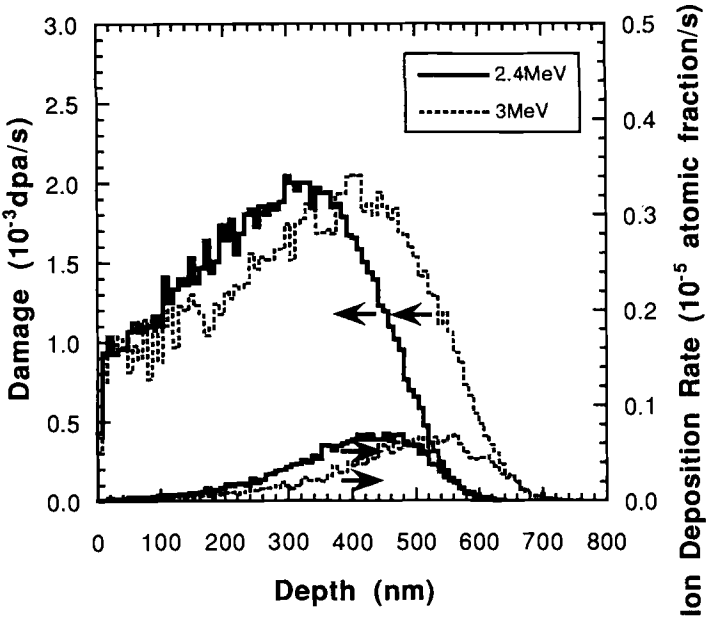


Fig. 1 *The depth distribution of the damage rate and the ion deposition rate in the present experiment, calculated by the TRIM code [5].*

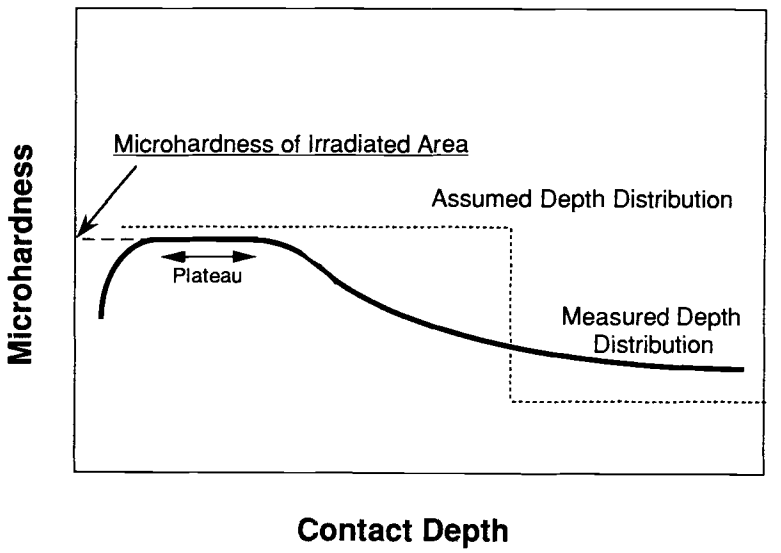


Fig. 2 *A diagram of microhardness of ion-irradiated specimens as a function of contact depth.*

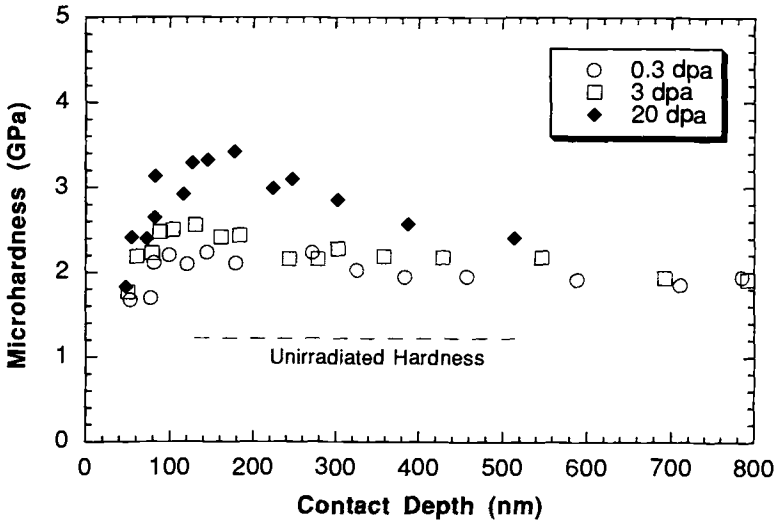


Fig. 3 *Depth dependence of microhardness after irradiation at 773K.*

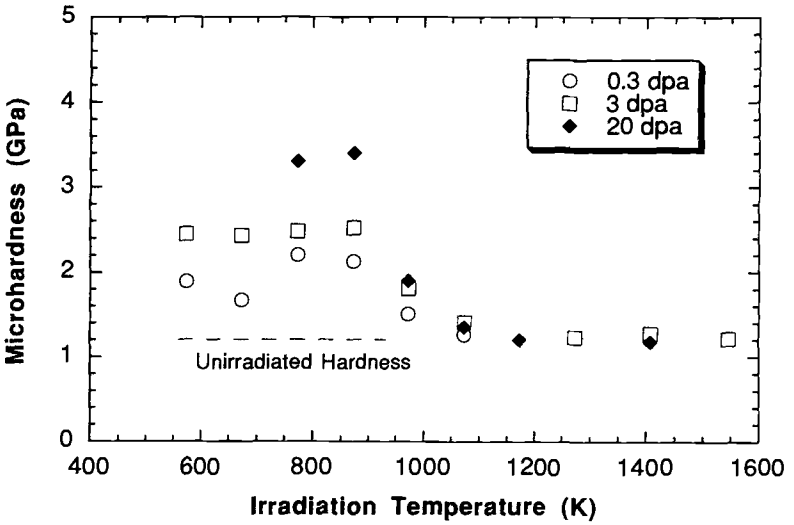


Fig. 4 *A summary of the microhardness measurements.*

schematically shown in Fig. 2.

Fig. 4 is a summary of the microhardness measurements. The hardness increases with fluence below ~900K, but the temperature dependence of the hardness is relatively small. The increase in hardness is negligibly small above ~1100K. The hardness rapidly decreases with temperature in the range 900K~1000K.

Microstructural Evolution

Fig. 5 shows temperature dependence of microstructure. At 1073 K and below a high density of loops is observed in the matrix. Voids are observed at 973 K and above. The void density decreases and its size increases with temperature. The density of line dislocations is low at all temperatures.

Microstructural observation at low fluence showed that the loops observed were of vacancy type[*8*]. They were shown to form by the following procedure.
(1) A low density of interstitial loops formed and grew in the matrix.
(2) A high density of smaller vacancy loops formed inside the growing interstitial loops.
(3) The interstitial loops continued to grow into a low density dislocation network.
(4) The vacancy loops in the matrix remained to high fluence.

Figs. 6 and 7 show the temperature dependence of loop density, void density, dislocation density and void swelling as functions of temperature. The loop density decreases gradually with temperature and disappears at ~1100K. The void density decreases steeply with temperature. The dislocation density is a moderate decreasing function of temperature. The peak of void swelling occurs at ~1400 K.

Discussion

Correlation of Hardness and Microstructure

As shown in Fig. 4, the microhardness drastically decreased at 900K~1000K. The features contributing to microhardness, however, did not change significantly in this temperature range as shown in Figs. 5~7. Thus, it is expected that defects which are not observable by TEM contributed to the hardening at lower temperature. In this section, correlation of the hardness and microstructure is examined for the purpose of investigating the nature and accumulation process of the TEM-invisible defects.

A number of quantitative correlations between hardness change and microstructure have been carried out using the following equation[*9*].

$$\begin{aligned} \Delta H &= C_1 \Delta\sigma \\ &= C_1 C_2 \Delta\tau \\ &= C_1 C_2\, \alpha G \mathbf{b}/\lambda \end{aligned} \qquad (2)$$

where $\Delta\sigma$, $\Delta\tau$, G, $\mathbf{b}$ and $1/\lambda$ are yield stress increase, shear stress increase, shear modulus, Burgers vector magnitude and reciprocal inter-barrier distance, respectively. $1/\lambda$ is expressed as

$$1/\lambda = (Nd)^{1/2} \qquad (3)$$

where N and d are the obstacles' number density and diameter, respectively. The constant α is a measure of the barrier strength. In the present analysis, a value of 9.0 was used for the product C_1C_2 assuming both C_1 and C_2 to be ~3.0[*10*]. The proportionality of ΔH and $\Delta\sigma$ is

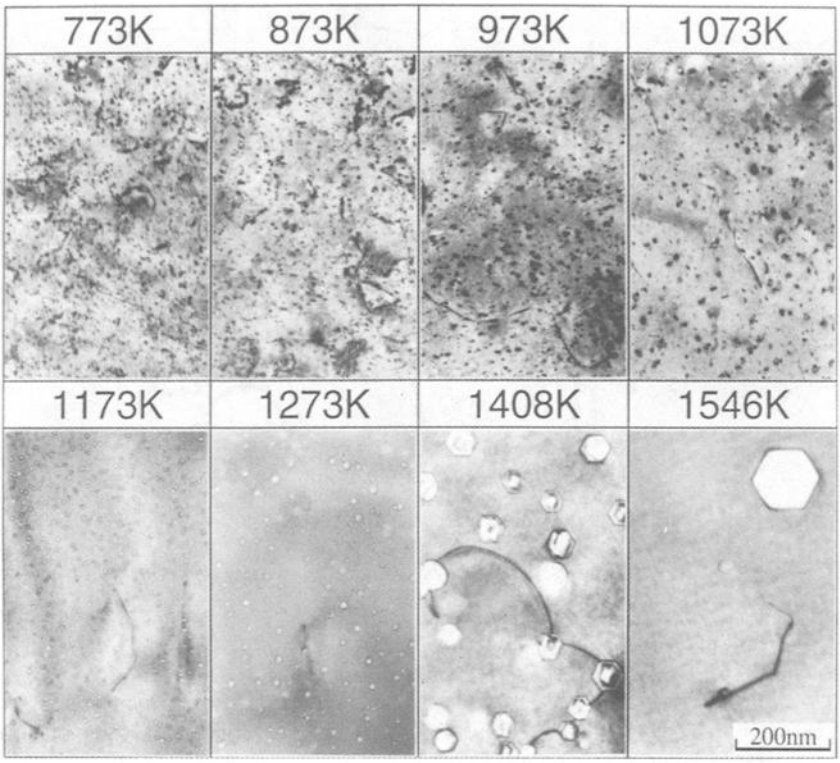


Fig. 5 *Temperature dependence of microstructures. (3 dpa)*

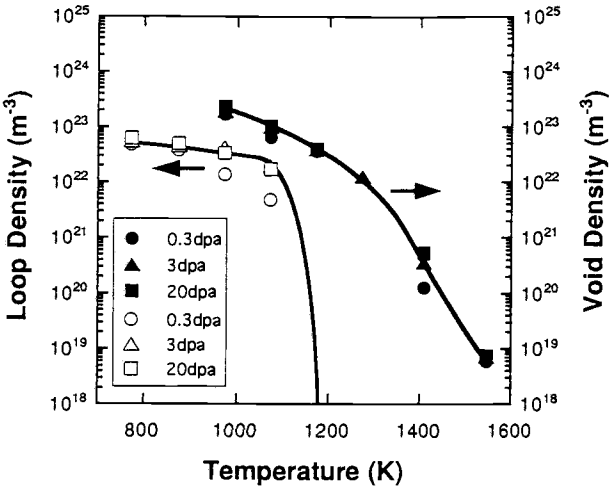


Fig. 6 *Temperature dependence of loop density and void density.*

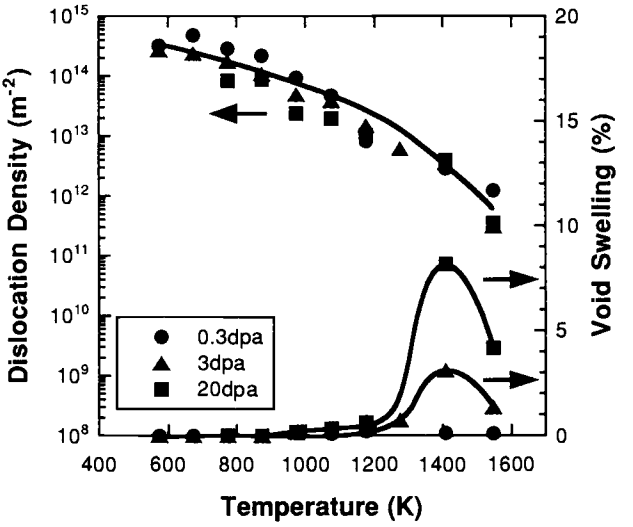


Fig. 7 *Temperature dependence of dislocation density and void swelling.*

Table 1 *Predicted hardness change (GPa) assuming α to be unity. (3 dpa except 20 dpa at 1173K)*

Temp (K)	ΔH (loops)	ΔH (dislocations)	ΔH (voids)	ΔH (measured)
573	2.20	2.87	0	1.21
673	2.25	2.71	0	1.19
773	2.05	2.33	0	1.24
873	2.16	1.83	0	1.28
973	2.51	1.23	6.6	0.57
1073	2.09	1.09	5.35	0.17
1173	0	0.56	3.43	-0.04
1273	0	0.436	1.83	-0.01

Table 2 *Predicted hardness change (GPa) at 1073 K assuming α to be unity.*

dpa	ΔH (loops)	ΔH (dislocations)	ΔH (voids)	ΔH (measured)	α (loops)
0.3	0.79	1.21	3.74	0.05	0.06
3	2.10	1.09	5.35	0.17	0.08
20	2.10	0.78	5.33	0.12	0.06

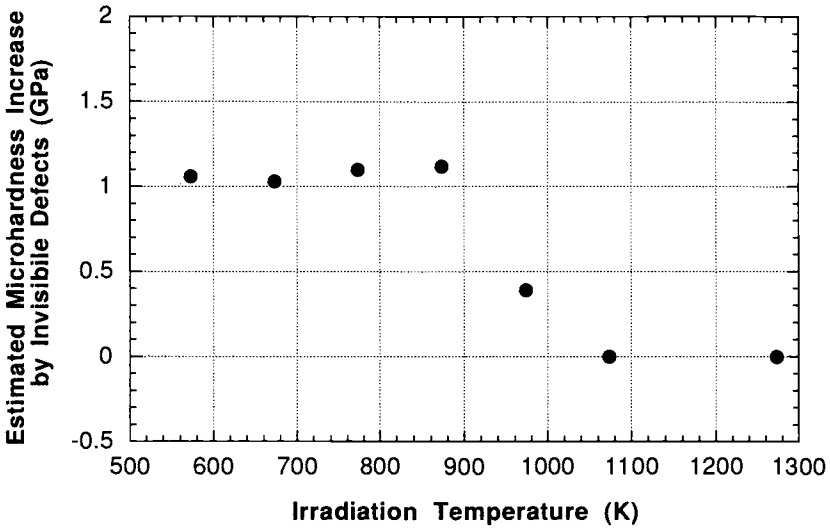


Fig. 8 *Temperature dependence of the estimated microhardness increase by TEM invisible defects (3 dpa).*

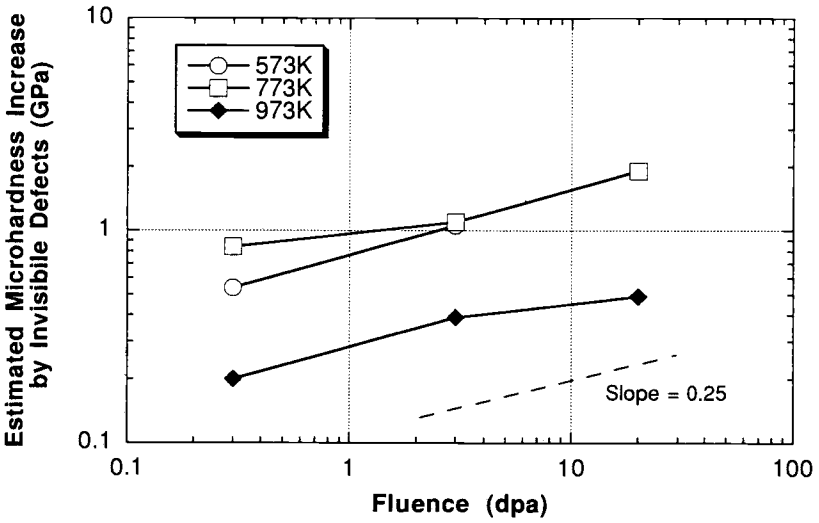


Fig. 9 *Fluence dependence of the estimated hardness increase by TEM-invisible defects.*

dependent on the work hardening [*10*] and expected to be applicable to tantalum because of its low degree of work hardening before and after irradiation [*11*]

Table 1 is a summary of the calculated hardness change by loops, dislocations and voids using eq. (2) and the microstructure data. In this calculation α for the all defects are tentatively assumed to be unity. Actual values of α will be estimated by comparison with the measured hardness changes, which are also listed in Table 1.

It should be noted that at temperatures of 1173 K and 1273 K, the measured hardness change is negligibly small although calculations assuming α to be unity predict significant hardening by dislocations and voids. This strongly suggests that the barriers of dislocations and voids are actually very weak, i.e. α(dislocations) ~ 0 and α(voids) ~ 0.

Table 1 implies that the TEM-invisible defects disappear at high temperature. Assuming that they disappear ~1000K, the hardening at 1073 K is considered to be due to TEM-visible defects.

Table 2 shows the calculation, in which the value of α for all defects are again tentatively assumed to be unity, and measurements of hardening at 1073 K for three fluence levels. Since the effects of dislocations and voids on hardening are thought to be very low, the hardening measured is considered to be due primarily to the loops. From the data in Table 2, α for loops is estimated by the ratio of ΔH(measured) to ΔH(loops). The results are also shown in the table and imply that α(loop) is ~0.07.

Evaluation of TEM-invisible Defects

Using α(dislocation) of ~0, α(void) of ~0, and α(loop) of ~0.07, the hardening by TEM-invisible defects can be quantitatively estimated. Fig. 8 shows the temperature dependence. The hardening is insensitive to temperature below ~900K and rapidly decreases with temperature. Fig. 9 shows the fluence dependence, showing that the hardness change is almost proportional to approximately the 1/4 power of fluence. This implies that the defect density is proportional to square root of the fluence if size of the defects does not change much with fluence.

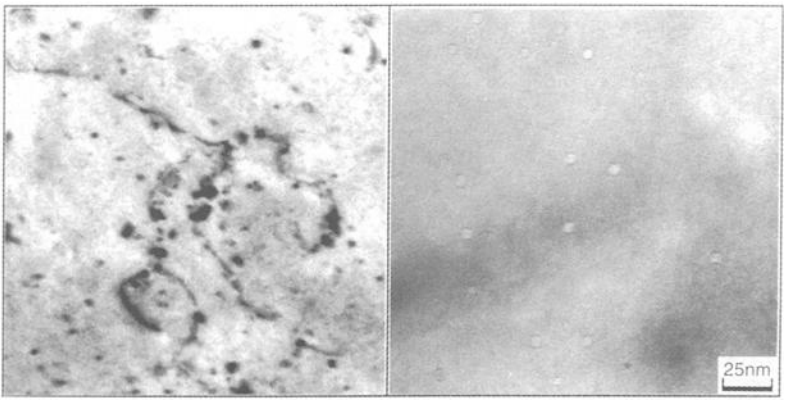


Fig. 10 *Microstructures of tantalum after irradiation at 873K to 0.3 dpa (left) and after subsequent annealing at 1273 K for 30 min (right).*

For the purpose of identifying the nature of the TEM-invisible defects, a post-irradiation annealing experiment was carried out. As shown in Fig. 10, cavities were formed after annealing to 1273 K in the matrix of a specimen irradiated at 873 K. Therefore, the TEM-invisible defects are most likely to be vacancy type defect clusters.

All these data strongly suggest that the TEM-invisible defects are small vacancy clusters induced by cascades. Past models suggested that the density of cascade vacancy clusters increases in proportion to the square root of fluence at relatively high fluence, where cascade overlapping affects the formation and annihilation of the clusters[*12*]. This interpretation is consistent with the present estimation.

Comparison with Neutron Irradiation Experiments

Limited number of void swelling data derived by neutron irradiations are available[*13,14*]. Remarkable differences of those data from the present ones are the swelling peak temperature and the swelling rate. In the neutron irradiation cases, the peak swelling temperature was ~900K, which is much lower than ~1400K derived in the present ion irradiation experiment. The difference in damage rate may be responsible for the difference. It should be noted that, according to Fig. 8, the TEM-invisible clusters are still stable at 900K. Thus, the existence of high density of clusters, probably of vacancy type, could be the reason of the lower swelling rate in the neutron irradiation cases.

Conclusion

The hardening of tantalum by heavy ion irradiation was quantitatively estimated by the micro-indentation technique. Significant hardening occurred below ~1000K. The correlation of hardening and microstructure made it possible to estimate the degree of hardening by TEM-invisible vacancy clusters induced by cascades. The results suggest an accumulation of cascade vacancy clusters proportional to the square root of the fluence.

References

[1] Gold, R.E. and Harrod, D.L., "Refractory Metal Alloys for Fusion Reactor Applications," *Journal of Nuclear Materials*, 85&86 (1979) 805-816.

[2] Kirk, M.A., Birtcher, R.C. and Blewitt, T.H., "Measurements of Neutron Spectra and Fluxes at Spallation-neutron Sources and Their Application to Radiation Effects Research," *Journal of Nuclear Materials*, 96 (1981) 37-50.

[3] Noda, T., Abe, F., Araki, H. and Okada, M., "Materials Selection for Reduced Activation of Fusion Reactors," *Journal of Nuclear Materials*, 155-157 (1988) 581-584.

[4] Sagara, A., Muroga, T., Motojima, O., Noda, T., Tanaka, S., Terai, T., Kohyama, A. and Matsui, H., "Materials Design and Related R&D Issues for the Force-free Helical Reactor (FFHR)," *Journal of Nuclear Materials*, 258-263 (1998) 2079-2082.

[5] Biersack, J.P. and Haggmark, L.G., "A Monte-Carlo Computer Program for the Transport of Energetic Ions in Amorphous Targets", *Nuclear Instruments and Methods*, 174 (1980) 257-269.

[6] Oliver, W.C. and Pharr, G.M., "An Improved Technique for Determining Hardness and Elastic Modulus Using Load and Displacement Sensing Indentation Experiments," *Journal of Materials research* 7 (1992) 1564.

[7] Katoh, Y., Muroga, T., Iwai, T. and Motojima, O., "Hardness Evaluation of MeV-ion Irradiated Materials by Means of Very Low-load Indentation Technique," *Journal of Japan Institute of Metals*, 61 (1997) 191-198.

[8] Yasunaga, K., Watanabe, H, Yoshida, N., Muroga, T., and Noda, N., "Microstructure of Tantalum Irradiated with Heavy Ions," *Journal of Nuclear Materials*, 258-263 (1998) 879-882.

[9] Bement, Jr., A.L., "Fundamental Materials Problems in Nuclear Reactors," *Proceedings of 2nd International Conference on The Strength of Metals and Alloys* (ASM, Metals Park, OH, 1970) 693-728.

[10] Lucas, G.E., Odette, G.R., Maiti, R. and Sheckherd, J.W., "Tensile Properties of Irradiated Pressure Vessel Steels," *Influence of Radiation on Materials Properties: 13th International Symposium, ASTM STP 956*, F.A. Garner, C.H. Henager, Jr., and N. Igata, Eds., American Society for Testing and Materials, 1987, pp.379-394.

[11] Brown, R.D. and Cost, J.R., "Mechanical Properties of 800-MeV Proton-irradiated Metals," *Effects of Radiation on Materials: 11th Conference, ASTM STP 782*, H.R. Brager and J.S. Perrin, Eds., American Society for Testing and Materials, 1982, pp.917-926.

[12] Kiritani, M., "Exposure Time and Recoil Energy Dependence of Defect Accumulation," *Journal of Nuclear Materials*, 206 (1993) 156-169.

[13] Wiffen, F.W., "The Effect of Temperature on the Microstructure of Neutron-irradiated Tantalum," *ANS Transactions*, 14 (1971) 603.

[14] Bates, J.F. and Pitner, A.L., "Volume Changes in Irradiated Tantalum," *ANS Transactions*, 14 (1971) 603-604.

Manabu Satou,[1] Toshinori Chuto,[1] Akira Hasegawa,[1] and Katsunori Abe[1]

Improvement of Post Irradiation Ductility of V-Ti-Cr-Si Type Alloys Neutron Irradiated Around 400°C

Reference: Satou, M., Chuto, T., Hasegawa, A., and Abe, K., **"Improvement of Post Irradiation Ductility of V-Ti-Cr-Si Type Alloys Neutron Irradiated Around 400°C,"** *Effects of Radiation on Materials: 19th International Symposium, ASTM STP 1366,* M. L. Hamilton, A. S. Kumar, S. T. Rosinski, and M. L. Grossbeck, Eds., American Society for Testing and Materials, West Conshohocken, PA, 2000.

Abstract: Mechanical properties after neutron irradiation at temperatures around 400°C of the V-Ti-Cr-Si type alloys were reported. Neutron irradiation was carried out at temperatures 374 °C and 406 °C with fluence of about 7 and 50 dpa, respectively. Tensile tests were conducted using miniaturized specimens at ambient temperature and irradiation temperature. Uniform elongation of the alloy V-5Ti-5Cr-1Si-1Al-1Y(nominal weight percentage) was maintained at about 4.2 and 5.9% after irradiation and testing at 374 and 406 °C, respectively. Increases in yield stress were 240 MPa and 160 MPa, respectively. Although the irradiation hardening was large, apparently smaller than that of V-Ti-Cr type alloys without Si, Al and Y additions, it was possible that the additional elements reduced the concentration of interstitial impurities in solution, which caused high irradiation hardening. It was found that a small addition of Si, Al and Y showed possible improvement in the ductility at lower temperature irradiation of vanadium alloys.

Keywords: vanadium alloy, radiation hardening, tensile properties, neutron irradiation

[1] Department of Quantum Science and Energy Engineering, Tohoku University, Aramaki-aza-Aoba 01, Sendai 980-8579 Japan.

Copyright© 2000 by ASTM International www.astm.org

Introduction

Vanadium alloys have preferable characteristics for fusion structural material, such as high melting temperature, high heat load capability, low induced radioactivity and good chemical compatibility with liquid lithium [1]. Therefore, alloy development studies has been carried out and the alloy of V-(4-5)Ti-(4-5)Cr type has been considered as a reference material [2]. Because of the large affinity of vanadium, interstitial impurities such as oxygen, nitrogen and carbon might be introduced into the material during thermo-mechanical treatments and during reactor operation. The impurities could affect the mechanical properties and post-irradiation behavior; therefore, improvement in oxidation resistance of vanadium alloys is one of the important issues for alloy development.

Alloys of V-Ti-Cr containing small amounts of Si, Al and Y for proof-oxidation have been developed, and these alloys showed good mechanical properties and low swelling behavior after neutron irradiation with or without helium charging at temperatures higher than 400 °C [3-15]. On the other hand, it was reported by S. J. Zinkle etal. [16-18] and E. van Osch [19] that neutron irradiation at temperatures below 300 °C caused loss of uniform elongation and work hardening capability for some vanadium alloys. Interstitial impurities were believed to strongly affect such a loss of elongation. In this paper, mechanical properties after neutron irradiation at temperatures around 400 °C of the V-Ti-Cr-Si type alloys are reported.

Experimental

The chemical analysis of the V-Ti-Cr-Si-type alloys is shown in Table 1. Detailed procedures for material preparation are described in ref. 4. The chemical analysis was done after hot rolling. The miniature tensile specimens with a gauge section of 5 mm long and 1.2 mm wide were punched out from 0.25 mm thick sheets. The specimens were annealed at 1100°C for 3.6 ks in vacuum-sealed-quartz-tubes wrapped with Ta and Zr foils, to obtain a fully recrystallized condition with a mean grain size of about 20 μm.

Neutron irradiation was performed in the Materials Open Test Assembly at the Fast Flux Test Facility (FFTF/MOTA) during cycles 11 and 12. The irradiation conditions are summarized in Table 2. The specimens were irradiated in Li-filled or He-filled capsules. After irradiation, the specimens irradiated in Li-filled capsules were processed to remove lithium and hydrogen isotopes at Argonne National Laboratory. The specimens retrieved from the capsules were immersed in ammonia and then in alcohol to remove lithium. They were immersed in a solution comprising 1 part HF, 1 part HNO_3 and 1 part

H_2O by volume for 10 seconds. In order to remove hydrogen isotopes, a vacuum bake-out was carried out at 400°C for 1 h or 20 h.

Table 1: *Chemical analysis of vanadium alloys (in wt.%).*

	V	Ti	Cr	Si	Al	Y	C	O	N
V-5Ti-5Cr-1Si-1Al-1Y	Bal.	4.79	4.01	0.85	0.95	0.77	0.0126	0.014	0.0054
V-25Ti-15Cr-1Si-0.5Al-1Y	Bal.	24.6	13.5	0.98	0.54	0.71	0.0187	0.025	0.0075
V-15Cr-5Ti	Bal.	5.0	15.3	-	-	-	0.017	0.052	0.023

Table 2: *Summary of irradiation conditions.*

Temperature [°C]	Fluence [$x10^{26}m^{-2}$(E>0.1MeV)]	dpa	MOTA position	Capsule environment
373	1.20	7.2	BC-B-5	Li
406	7.47	44.8	2D-4	He
406	8.36	50.2	2D-2	Li
407	8.96	53.8	2E-1	Li
430	4.49	25.0	4D-1	Li

Helium ions of 36 MeV were implanted into selected alloys by the Tohoku University cyclotron accelerator using energy degrader wheels [16], before neutron irradiation at the 2D-2 position in the FFTF/MOTA-2A. To obtain uniform helium distribution along the implanted direction, energy degrader wheels consisting of aluminum foils with 105 steps were used. The total amount of helium in the specimens was determined to be about 30 appm with displacement damage of about 0.012 dpa. The helium ion beam was scanned at 1 Hz horizontally and 10 Hz vertically. Specimens were fixed on a water-cooled holder by indium solder; therefore, the specimen temperature during implantation was kept below the melting point of the solder i.e. 156 °C. The results from the Dynamic Helium Charging Experiment (DHCE) done at FFTF/MOTA-2B, which was a helium charging method using tritium β-decay during neutron irradiation, is shown for comparison [10,24,25].

Tensile tests were carried out using an Instron-type machine with an external kanthal heater and the MATRON [21,22] in a vacuum of $1x10^{-3}$ Pa at a strain rate of $6.7x10^{-4}s^{-1}$ at ambient temperature and at temperatures around 400 °C. The MATRON is an automated A computerized data acquisition system was utilized for the tests. After tensile testing, specimens were examined by scanning electron microscopy (SEM, JEOL JEM-5300) in order to characterize the fracture surface. The gauge section of the

miniaturized tensile specimen was used for observation of the deformation microstructures. A schematic of the procedure is shown in Fig. 1. Coupons were punched out from the gauge section after deformation to a strain level of about 5%. The typical size of them was about 3x1.1x0.25 mm. The coupon was sandwiched with washers made of platinum, which had 0.6 mm inside and 3 mm outside diameters and 0.1 mm thick. The sandwich was placed in a twin-jet electro-polishing unit as an ordinary TEM disk. Thin foils were obtained after electro-polishing in a solution of 4 parts of methanol and 1 part of sulfuric acid by volume below –10 °C.

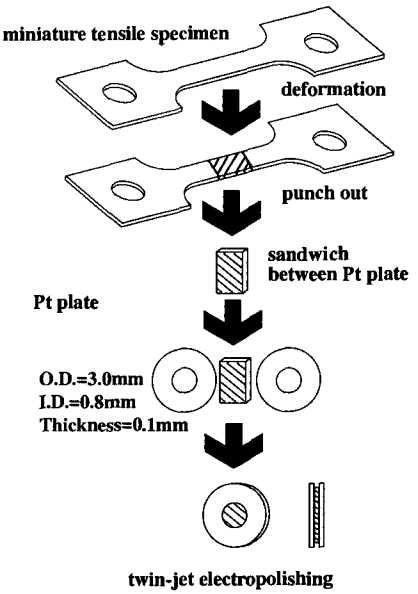


Fig. 1 *Thin film preparation from miniature tensile specimen.*

Results

Tensile properties

Typical stress-strain curves of the V-Ti-Cr-Si-type alloys after neutron irradiation are shown in Fig. 2. The 0.2% proof stress of the alloys after irradiation at 374 °C are higher than that at 406 °C, although radiation dose is low. The alloys containing Si, Al and Y have work-hardening capability and moderate elongation. The V-15Cr-5Ti alloy

shows high hardening and loss of elongation. Tensile properties of the V-Ti-Cr-Si-type alloy are summarized in Table 3. The yield stress of the V-5Ti-5Cr-Si-Al-Y alloy after irradiation is between 476 and 637 MPa. The specimen with He pre-implanted by the accelerator shows the lowest radiation hardening and the specimen He-charged by the DHCE shows the highest hardening. The yield stress for un-irradiated alloy was almost constant at temperatures ranging from 300 °C to 600 °C. The yield stress at the temperature range was between 340 and 375 MPa [4]. The radiation hardening increments, calculated by subtracting the yield stress, that is 350 MPa, from the yield stress after irradiation are 283 and 158 MPa for 406 °C irradiation in He and Li environment, respectively.

The yield stress of the V-25Ti-15Cr-Si-Al-Y alloys is twice as high as that of the V-5Ti-5Cr-Si-Al-Y alloy before irradiation. The radiation hardening, however, is not so higher compared to others. Although the yield stress of the V-15Cr-5Ti alloy in the un-irradiated condition is intermediate, radiation hardening is quite high. The radiation hardening of the V-Ti-Cr type alloy without Si, Al and Y addition, that is V-15Cr-5Ti, is more than 600 MPa. Total elongation of the V-Ti-Cr-Si-type alloys decrease by irradiation. The elongation of the V-Ti-Cr-Si-Al-Y alloys remained more than about 5%. The loss of elongation is large for V-15Cr-5Ti alloy. Uniform elongation and work hardening capability of the V-Ti-Cr-Si-Al-Y alloys are remarkably large compared to V-15Cr-5Ti. The fracture mode of the examined V-Ti-Cr-Si-Al-Y alloys was ductile as shown in Fig. 3. The V-15Cr-5Ti alloy irradiated at 374 °C shows partly cleavage fracture mode.

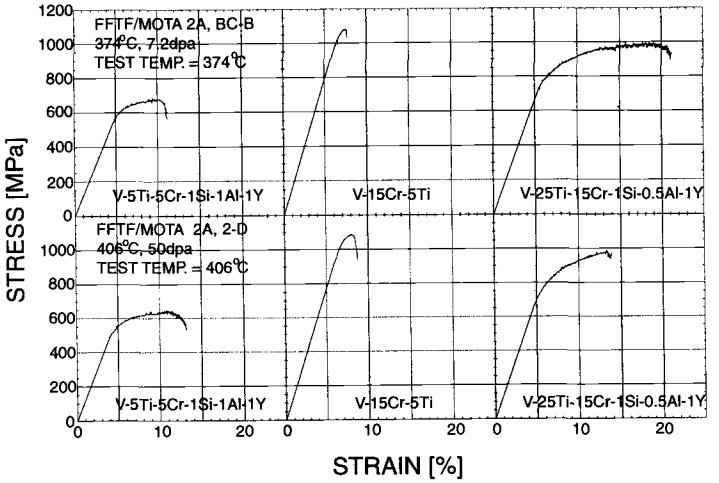


Fig. 2 *Typical stress-strain curves of the V-Ti-Cr-Si-type alloys after neutron irradiation.*

Table 3: *Summary of tensile properties of the V-Ti-Cr-Si-type alloys after neutron irradiation.*

Specimen I.D. code	Irrad. Temp. [°C]	Damage Level [dpa]	Test Temp. [°C]	Yield Stress [MPa]	UTS [MPa]	Total Elong. [%]	Uniform Elong. [%]	Work Hardening Rate*1	Capsule Env.	Bakeout Treatment
V-5Ti-5Cr-1Si-1Al-1Y										
F22D	374	7.2	374	591	686	5.9	4.2	27.0	Li	400 °C,20 h
F22R	406	44.8	370	634	765	8.4	3.8	40.5	He	
FZ05*2	406	50.0	450	476	663	5.0	3.3	70.0	Li	400 °C,20 h
F212	406	50.0	406	509	648	8.3	5.9	36.0	Li	400 °C,20 h
F231	407	53.8	400	535	613	5.8	2.0	28.8	Li	400 °C,20 h
F25D*3	430	25.0	400	637	714	8.1	3.2	45.5	Li	400 °C,1 h
F2--			400	351	481	8.8	5.5	32.7		un-irradiated
F2--			400	351	534	18.2	13.1			un-irradiated
V-25Ti-15Cr-1Si-0.5Al-1Y										
F12B	374	7.2	374	794	996	13.1	11.4	60.9	Li	400 °C,20 h
F12S	406	44.8	370	838	1006	9.5	7.5		He	
F12R	406	44.8	400	641	723	4.9	1.6		He	
F111	406	50.0	406	729	990	6.6	5.8	65.1	Li	400 °C,20 h
F131	407	53.8	400	763	944	8.8	6.3		Li	400 °C,20 h
F1--			400	752	991	18.1	13.4			un-irradiated
V-15Cr-5Ti										
F311	374	7.2	374	1082	1082	0.9	0.5	-	Li	400 °C,20 h
F31A	406	44.8	370	1079	1165	4.1	1.3		He	
F319	406	44.8	400	896	948	4.0	1.1		He	
F31L	406	50.0	406	1036	1089	2.5	0.8	-	Li	400 °C,20 h
F31X	407	53.8	400	999	1049	3.6	0.9		Li	400 °C,20 h
F3--			400	421	523	21.5	16.2			un-irradiated

*1 Work hardening rate = $(\sigma_{2\%}-\sigma_{0.5\%})/(2\%-0.5\%)$[MPa/%]

*2 Helium ion was implanted to about 30 appmHe with 0.012 dpa by an accelerator before neutron irradiation.

*3 Helium was charged to about 177 appmHe during neutron irradiation by the DHCE[24,25].

Microstructural Evolution

Figure 4 shows the dislocation microstructure in the neutron-irradiated V-5Ti-5Cr-Si-Al-Y alloy (374 °C, 7.2dpa) after tensile deformation to about 5% plastic strain at ambient temperature. Relatively straight dislocations observed in the neutron irradiated

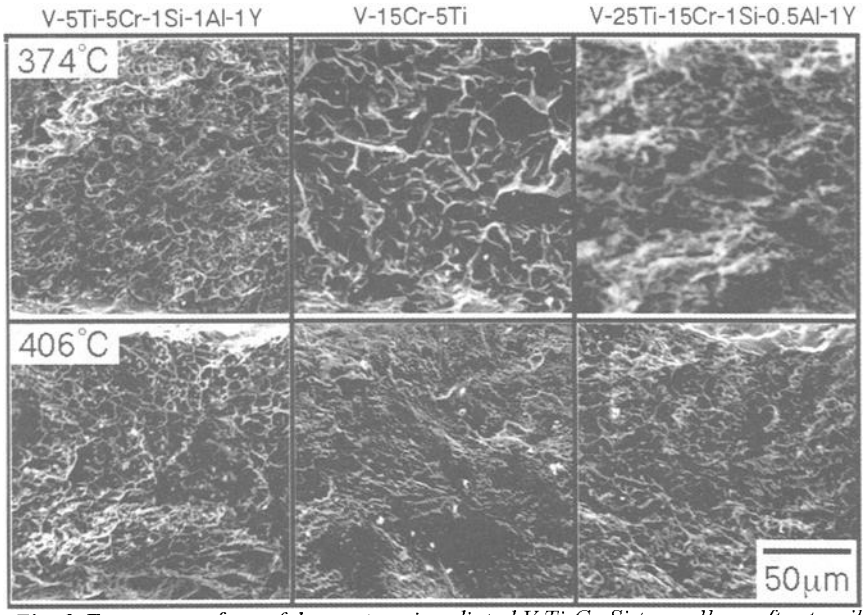


Fig. 3 *Fracture surface of the neutron irradiated V-Ti-Cr-Si-type alloys after tensile testing at the irradiation temperature. Neutron irradiation was carried out at 374 and 406 °C to the fluence of 7.2 and 50 dpa, respectively.*

alloy look like the dislocations observed in un-irradiated alloy. They were identified as screw dislocations, and the Burgers vector was **a**/2 <111>[5,9]. The dislocation bands those have a sub-micron interval might be corresponding to slip planes. The interval of the dislocations became larger than that of un-irradiated specimens. The dislocation structure would be more complex following 400 °C deformation, because serrated portions in the stress-strain curves were observed which correspond to dynamic strain aging.

The defect microstructure of the same specimen as Fig. 4 is shown in Fig. 5. Dislocation loops were observed. Dislocation channeling which result defects sweep away does not identified in the experimental conditions. Figure 6 shows the size distribution of the dislocation loops. The number density of the loops is $7.1 \times 10^{21} m^{-3}$ and the mean diameter is 20nm. The hardening of the alloy was evaluated by the following equation.

$$\Delta\sigma_y = \overline{M}\Delta\tau = \overline{M}\left(\alpha\mu b\sqrt{Nd}\right) \qquad (1)$$

Where M is an orientation factor, α is the interaction parameter of dislocations, N is number density of dislocation loops, and d is mean diameter of the loop. In this paper, the orientation factor 3 and the interaction parameter 0.3 are used. The shear modulus μ and Burgers vector for vanadium are 4.67×10^4 MPa and 0.26nm, respectively [26]. It was calculated that the total increase in yield stress was 130 MPa.

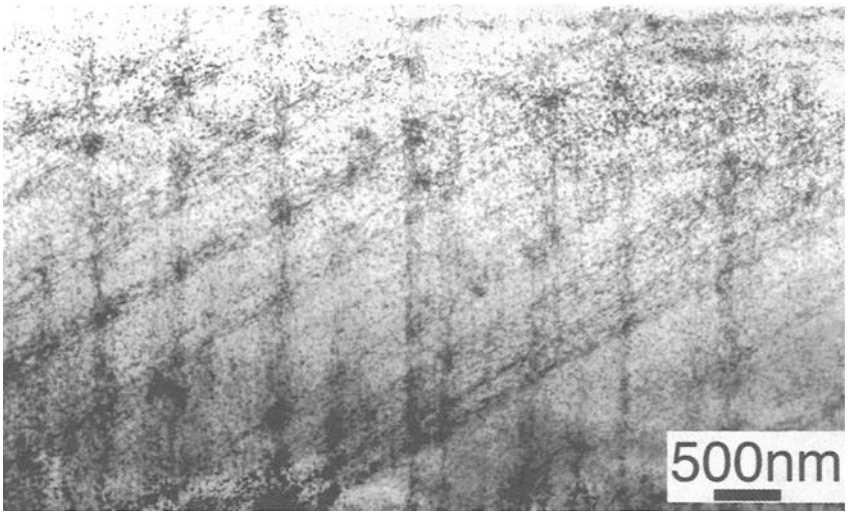


Fig. 4 *Dislocation microstructure in neutron irradiated V-5Ti-5Cr-Si-Al-Y alloy after tensile deformation to about 5% plastic strain at ambient temperature.(374 °C, 7.2 dpa.)*

Comparison with Reference V-4Cr-4Ti Alloys

Figure 7 shows irradiation and test temperature dependence of uniform elongation of several V-Ti-Cr alloys [17-20]. The uniform elongations at temperatures higher than 450 °C are several percent for the alloys. At temperatures lower than 350 °C, the V-4Cr-4Ti alloy shows complete loss of uniform elongation. The uniform elongation around 400 °C depends on alloy composition. The alloy containing Si, Al and Y shows greater elongation.

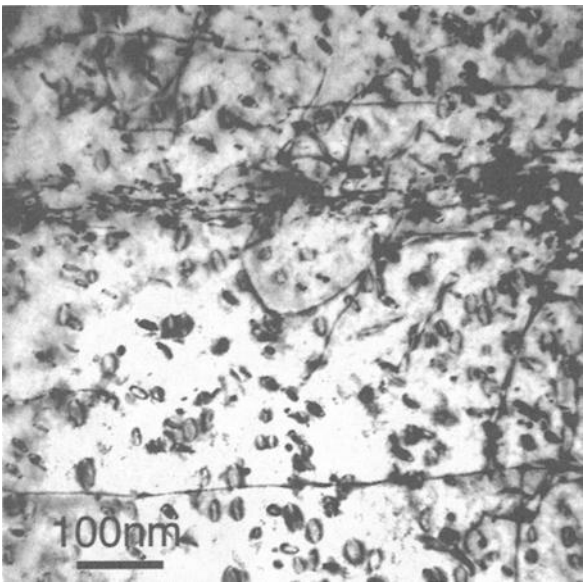


Fig. 5 *Defect microstructure of the V-5Ti-5Cr-Si-Al-Y alloy after neutron irradiation at 374 °C to 7.2 dpa. A thin film was prepared from the gauge section of a deformed tensile specimen.*

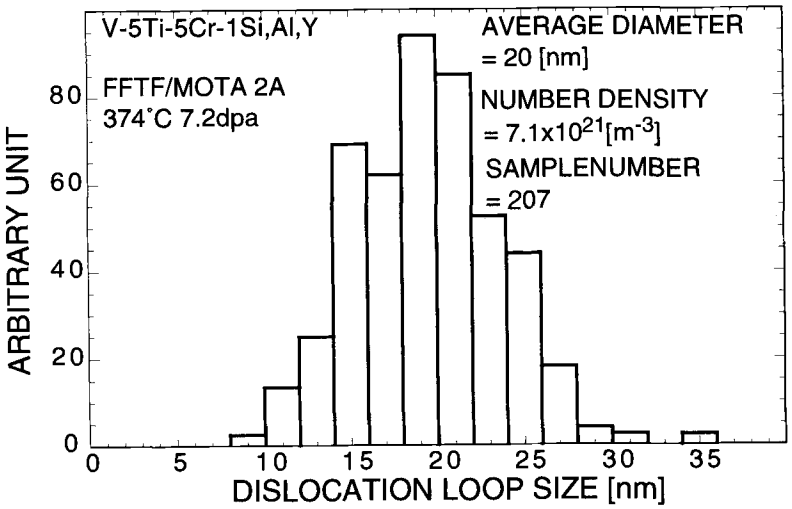


Fig. 6 *Size distribution of dislocation loops in the V-5Ti-5Cr-Si-Al-Y alloy after irradiation at 374 °C to 7.2 dpa.*

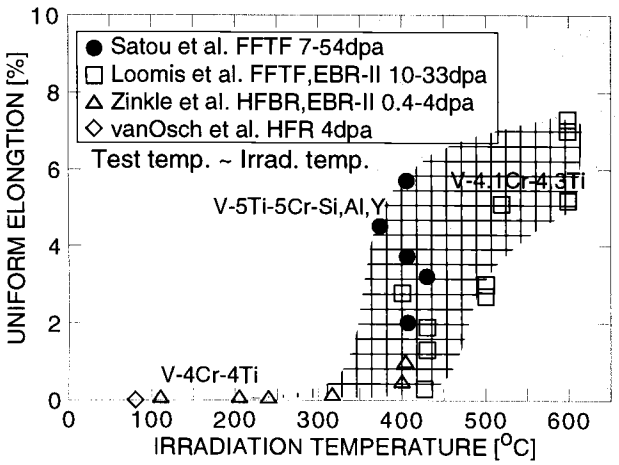


Fig. 7 *Irradiation and test temperature dependence on uniform elongation of the V-4Ti-4Cr type alloys after neutron irradiation.*

Discussion

Interstitial impurity atoms such as carbon, oxygen and nitrogen are considered to affect strongly the loss of ductility of the vanadium alloys. It was suggested that formation of small and dense complexes of irradiation defects cluster and interstitial impurity atom make such large hardening causing the loss of ductility [17]. The correlation between concentration of interstitial impurities and uniform elongation of the V-Ti-Cr type alloys after neutron irradiation around 400 °C is shown in Fig. 8. The uniform elongation of the alloys seems to have little dependence on carbon and nitrogen concentration, but perhaps a dependence on oxygen. The arrows in the Fig. 8 indicate a possible reduction of oxygen concentration in solution due to the formation of yttrium or aluminum oxides. Yttrium oxides were observed on the fracture surface after Charpy impact tests [27]. However most of the aluminum should be in solution [28]. The number density of the aluminum atoms is much larger than that of yttrium. Therefore aluminum and oxygen complexes might be formed and prevent the oxygen migration to the defect clusters, which caused a high degree of hardening.

Purification to reduce oxygen concentration was done during fabrication. The reduction of oxygen concentration occurred due to removal of yttrium oxide slagging due to the formation of insoluble yttrium oxide [3,13,29]. Therefore, it is possible that improvement in ductility of the V-Ti-Cr-type alloys by addition of such elements reduced the concentration of interstitial impurities in solution which caused high irradiation

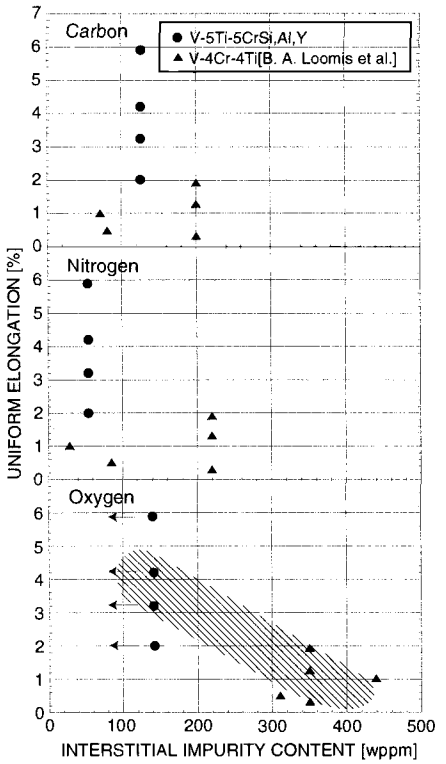


Fig. 8 *Dependence of uniform elongation on impurity concentration of V-Ti-Cr type alloy after neutron irradiation around 400 °C up to 53 dpa. Arrows indicate possible reduction of oxygen concentration in solution due to formation of yttrium or aluminum oxides.*

hardening. It was found that small addition of Si, Al and Y showed possible improvement in the ductility for lower temperature irradiation of vanadium alloys.

Remarkable effect of He pre-implantation on tensile behavior after irradiation was shown. As described in Table 3, the He pre-implanted V-5Ti-5Cr-Si-Al-Y alloys showed the lowest radiation hardening and the highest work hardening. Similar effects were reported by W. van Witzenburg et al.[30] as follows. Helium injection by a cyclotron accelerator was carried out at temperatures less than 100 °C. Neutron irradiation was carried out at 500 °C. The neutron irradiated V-5Ti alloy pre-injected with He exhibited the lowest strength and the highest ductility. Considering the accuracy of the data, He made no mention of these trends. The accuracy is almost the same for V-Ti-Cr-Si-Al-Y, but the effect of temperature variation [31,32] might be noted. At temperatures

below 150°C, the implantation temperature, vacancies are not mobile. At temperatures around 400 °C or higher, vacancies become mobile. The helium pre-implanted specimens experienced nucleation dominant temperature and then growth dominant temperature. It is possible that the varying temperature effect explains the behavior of the He pre-implanted specimens.

The irradiation position at 374 °C was the below core region of the FFTF/MOTA, therefore the neutron energy spectrum was rather soft. Transmutation of vanadium to chromium was estimated to about 0.2at.% after irradiation to 7 dpa[33,34]. However, the amount of transmutation to chromium was quite large compared to fusion conditions. It is not sufficient to affect mechanical properties of the V-Ti-Cr type alloys [20].

Summary

Tensile tests for the V-Ti-Cr-type alloys containing Si, Al and Y were carried out after neutron irradiation around 400 °C. Moderate radiation hardening was shown and the uniform elongation remained at several percent.

It was shown that the loss of elongation correlated with the concentration of interstitial impurities, especially oxygen. Therefore, it was suggested that purification was one of the ways to retain good uniform elongation in vanadium alloys after low temperature irradiation.

The addition of Si, Al and Y makes the concentration of oxygen low. Therefore modification by the addition of Si, Al and Y is one of the ways to improve the irradiation behavior of the V-Ti-Cr type alloys.

Acknowledgment

The authors express sincere appreciation to Dr. H. Kayano, Professor emeritus of Tohoku University for alloy development. The authors wish to thank Messrs. Y. Takahashi and M. Sato at RI Laboratory for post irradiation experiments, the CYRIC staff for implantation experiment and Messrs. T. Takahashi, K. Komatsu and T. Nagaya at the machine shop for making the experimental apparatus. This work was partly supported by a Grant-in-Aid from Ministry of Education, Science, Sports and Culture(Monbusho), and JUPITER program (Japan-USA Program of Irradiation Test for Fusion Research) based on Monbusho US-DOE Annex I.

References

[1] Matsui, H., Fukumoto, K., Smith, D.L., Chung, H. M., van Witzenburg, W., and Votinov, S. N., " Status of Vanadium Alloys for Fusion Reactors", Journal of Nuclear Materials, Vol. 233-237, 1996, pp. 92-99.

[2] Smith, D. L., Chung, H. M., Loomis, B. A., Tsai, H.-C., " Reference Vanadium Alloy V-4Cr-4Ti for Fusion Application", Journal of Nuclear Materials, Vol. 233-237, 1996, pp.356-363.

[3] Kayano, H., The Science Reports of The Research Institutes Tohoku University, "Material Development for Nuclear Fusion and Energy Development Using Actinoids", Vol. A40(1), 1994, pp.105-109.

[4] Satou, M., Abe, K., and Kayano, H., "High-Temperature Deformation of Modified V-Ti-Cr-Si Type Alloys", Journal of Nuclear Materials, Vol. 179-181, 1991, pp.757-761.

[5] Satou, M., Abe, K., and Kayano, H., The Science Reports of The Research Institutes Tohoku University, "Low Activation V-Ti-Cr-Si Type Alloys for Fusion Applications", A35, 1991, pp.219-228.

[6] Satou, M., Abe, K., and Matsui, H., "Neutron Irradiation Damage of Helium-Charged V-Ti-Cr-Si-type Alloys", Journal of Nuclear Materials, Vol. 191-194, 1992, pp.938-941.

[7] Satou, M., Abe, K., Kayano, H., and Takahashi, H., "Low Swelling Behavior of V-Ti-Cr-Si-type Alloys", Journal of Nuclear Materials, Vol. 191-194, 1992, pp.956-959.

[8] Satou, M., Abe, K., and Kayano, H., "Tensile Properties and Microstructures of Neutron Irradiated V-Ti-Cr-Si-type Alloys", Journal of Nuclear Materials, Vol. 212-215, 1994, pp.794-798.

[9] Satou, M., Abe, K., and Kayano, H., "Microstructures of Deformed V-Ti-Cr-Si Type Alloys after Neutron Irradiation", Journal of Nuclear Materials, Vol. 233-237, 1996, pp.426-430.

[10] Satou, M., Koide, H., Hasegawa, A., Abe, K., Kayano, H., and Matsui, H., "Tensile Behavior of Helium Charged V-Ti-Cr-Si Type Alloys", Journal of Nuclear Materials, Vol. 233-237, 1996, pp.447-451.

[11] Satou, M., Koide, H., Hasegawa, A., and Abe, K., The Science Reports of The Research Institutes Tohoku University, "Effect of Helium Implantation on Tensile Properties of V-Ti-Cr-Si Type Alloy", Vol. A45, 1997, pp.157-161.

[12] Matsushima, T., Satou, M., Hesegawa, A., Abe, K., and Kayano, H., "Tensile Properties of a Series of V-4Ti-4Cr Alloys Containing Small Amounts of Si, Al and Y, and the Influence of Helium Implantation", Journal of Nuclear Materials., Vol. 258-263, 1998, pp.1497-1501.

[13] Fujiwara, M., Satou, M., Hasegawa, A., and Abe, K., "Rapid Oxidation and its Effect

on Mechanical Properties of V-Ti-Cr-Si Type Alloys", Journal of Nuclear Materials, Vol. 258-263, 1998, pp.1507-1511.
[14] Shibayama, T., Yamagata, I., and Kayano, H., " Effect of Small Additional elements on DBTT of V-4Cr-4Ti irradiated at Low Temperatures", Journal of Nuclear Materials, Vol. 258-263, 1998, pp.1361-1368.
[15] Chuto, T., Satou, M., and Abe, K., "Radiation Hardening of V-C, V-O, V-N Alloys Neutron-Irradiated to High Fluences", Journal of Nuclear Materials, Vol. 258-263, 1998, pp.1502-1506.
[16] Rice, P. M., and Zinkle, S. J., " Temperature Dependence of the Radiation Damage Microstructure in V-4Cr-4Ti Neutron Irradiated to Low Dose", Journal of Nuclear Materials, Vol. 258-263, 1998, pp.1414-1419.
[17] Snead, L. L., Zinkle, S. J., Alexander, D. J., Rowcliffe, A. F., Robertson, J. P., and Eatherly, W. S., " Summary of the Investigation of Low Temperature, Low Dose Radiation Effects on the V-4Cr-4Ti Alloy", Fusion Materials, DOE/ER-0313/23, 1998, pp.81-98.
[18] Rice, P. M., Snead, L. L., Alexander, D. J., and Zinkle, S. J., " Microstructure of V-4Cr-4Ti Following Low Temperature Neutron Irradiation", *Materials Research Society Symposium Proceedings Volume 439*, I. M. Robertson, G. S. Was, L. W. Hobbs, and T.D. de la Rubia, Eds., Materials Research Society, Pittsburgh, PA, 1997, pp.343-348.
[19] van Osch, E. V., " Recent Results on Tensile Test of Irradiated V-Cr-Ti Alloys", Proceeding 2nd Workshop on Vanadium Alloy Development for Fusion, ECN-R-96-012, 1996, pp.417-434.
[20] Billone, M.C., " Revised ANL-Reported Tensile Data for Unirradiated and Irradiated (FFTF,HFIR) V-Ti and V-Cr-Ti Alloys", Fusion Materials, DOE/ER-0313/23, 1998, pp.3-61.
[21] Kohyama, A., Sato, S., and Hamada, K., " R & D an Automated Tensile Machine for Heavily Neutron Irradiated Materials", Journal of Nuclear Materials, Vol. 191-194, 1992, pp.1033-1037.
[22] Satou, M., Hamilton, M.L., Sato, S., and Kohyama, A., " Status of Automated Tensile Machine", Fusion Reactor Materials, DOE/ER-0313/12, 1992, pp.31-34.
[23] Masuyama, T., Morimoto, M., Konuma, O., and Abe, K., " Helium Ion Irradiation Experiments using Controlled Energy Degrader", Proceedings of the International Conference on Evolution in Beam Applications, Ed., Japan Atomic Energy Research Institute, Japan, 1991, pp.729-733.
[24] Smith, D. L., Matsui, H., Greenwood, L. R., and Loomis, B. A., "Experimental Method for Investigating Helium Effects in Irradiated Vanadium", Journal of Nuclear

Materials, Vol. 155-157, 1988, pp.1359-1363.
[25] Tsai, H., Chung, H. M., Loomis, B. A., and Smith, D. L., " Status of the Dynamic Helium Charging Experiment (DHCE)", Fusion Rector Materials, DOE/ER-0313/15, 1994, pp.247-252.
[26] Moteff, J., Michel, D. J., and Shikka, V. K., " The Influence of Irradiation Temperature on the Hardening Behavior of the Refractory BCC Metals and Alloys", *Defects and Defect Clusters in BCC Metals and Alloys*, Nuclear Metallurgy, Vol. 18, Ed. R.J.Arsenault, National Bureau of Standards, Gaithersburg, 1973, pp.198-215.
[27] M. Satou et al., to be published.
[28] Hayes, F. H., " Aluminum-Titanium-Vanadium System", Journal of Phase Equilibria, Vol. 16, 1995, pp.163-176.
[29] Lundin, Jr., C. E., and Klodt, D. T., " Improvement of the Ductility of Vanadium by Alloying", Transactions of the ASM, Vol. 53, 1961, pp.735-742.
[30] van Witzenburg, W., and de Vries, E., " Effect of Helium and dpa's on Tensile Properties of V-5Ti and V-3Ti-1Si", *Effects of Radiation on Materials, ASTM-STP 1125*, R. E. Stoller, A.S. Kumar, and D. S. Gelles, Eds., American Society for Testing and Materials, Philadelphia, 1992, pp. 915-927.
[31] Muroga, T., Nonaka, Y., Yoshida, N., " Dislocation Evolution in a Model and a Candidate Ferritic Alloy During Steady and Varying Temperature Electron Irradiations", Journal of Nuclear Materials, Vol. 233-237, 1996, pp. 1035-1039.
[32] Matsui, H., Kuji, K., Hasegawa, M., Kimura, A., " Effects of Temperature History During Neutron Irradiation on the Microstructure of Vanadium Alloys", Journal of Nuclear Materials, Vol. 212-215, 1994, pp. 784-789.
[34] Ohnuki, S., Takahashi, H., Garner, F. A., Pawel, J. E., Shiba, K., Hishinuma, A., " Transmutation-induced Embrittlement of Vanadium and Several Vanadium Alloys in HFIR", Journal of Nuclear Materials, Vol. 233-237, 1996, pp. 411-415.
[35] Garner, F. A., Greenwood, L. R., Loomis, B. A., Ohnuki, S., Sekimura, N., " Influence of Flux-spectra Differences on Transmutation, Dimensional Changes and Fracture of Vanadium Alloys", Journal of Nuclear Materials, Vol. 233-237, 1996, pp. 406-410.

S. Ohnuki,[1] H. Takahashi,[1] and F. A. Garner[2]

The Influence of Transmutation and Initial Composition on the Microstructural Evolution of Vanadium and V-Cr-Ti Alloys Irradiated in HFIR

Reference: Ohnuki, S., Takahashi, H., and Garner, F. A., **"The Influence of Transmutation and Initial Composition on the Microstructural Evolution of Vanadium and V-Cr-Ti Alloys Irradiated in HFIR,"** *Effects of Radiation on Materials: 19th International Symposium, ASTM STP 1366,* M. L. Hamilton, A. S. Kumar, S. T. Rosinski, and M. L. Grossbeck, Eds., American Society for Testing and Materials, West Conshohocken, PA, 2000.

Abstract: Pure vanadium and a series of V-Cr and V-5Ti-Cr alloys were irradiated at 300, 400, 500 and 600°C to doses of 8-10 dpa in the HFIR mixed spectra reactor. Transmutation of vanadium increased the chromium content by 6-7 additional percent. This compositional change had the largest impact on the microstructural and microchemical evolution of the alloys and also dominated the change observed in alloy density. Even more importantly, the results were quite different than would be expected from the results of similar irradiation in FFTF where transmutation is much lower.

Keywords: vanadium alloys, transmutation, swelling, phase stability, neutron irradiation

Introduction

In a series of earlier papers it was shown that vanadium and vanadium-base alloys were prone to a variety of degradation phenomena during neutron radiation in the Fast Flux Test Facility, FFTF, and the High Flux Isotope Reactor, HFIR, [*1-8*]. These phenomena involved the modification of starting alloy composition and microstructure with changes induced by transmutation, radiation-induced segregation and void swelling. When irradiated in HFIR where the transmutation rate was much larger than that in FFTF, as shown in Figure 1, vanadium alloys often became very brittle [*5,7,8*].

In the current study, vanadium and several V-Cr and V-5Ti-Cr alloys were irradiated in the HFIR JP-23 experiment in order to further examine the effect of displacement damage and transmutation on alloy properties.

[1] Professors, Hokkaido University, Sapporo, Japan.
[2] Senior Staff Scientist, Pacific Northwest National Laboratory, P.O. Box 999, MSIN P8-15, Richland, WA USA.

Copyright© 2000 by ASTM International www.astm.org

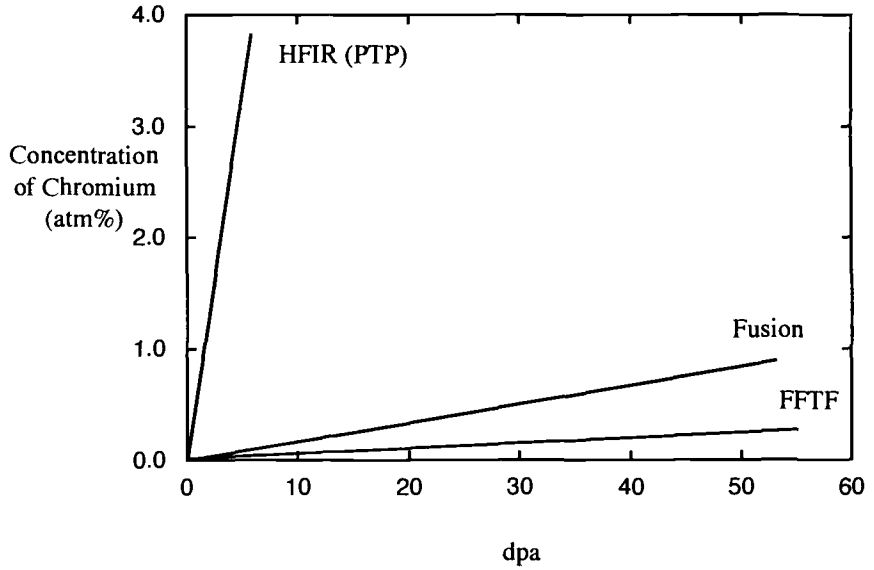


Figure 1 - *Calculation of transmutation of vanadium to chromium in three different neutron spectra.*

Experimental Details

The design and conduct of the JP-23 experiment is described in detail in reference 9. The irradiation assembly resided in HFIR for 110 effective full-power days. The specimens discussed in this report were placed in four stainless steel subcapsules, all located at various axial positions above the core mid-plane. There was no active temperature control and the temperatures were maintained using a gas gap design.

The nominal irradiation conditions of each capsule were (300°C, 8.3 dpa), (400°C, 9.3 dpa), (500°C, 9.9 dpa), and (600°C, 10.1 dpa) where the dpa are calculated for pure vanadium in this neutron spectra. Vanadium reaches a higher displacement rate in this spectrum than does stainless steel, however. The maximum mid-plane dose for the JP-23 experiment was 9.04 dpa for stainless steel and 10.4 dpa for pure vanadium [*10*].

The specimens were in the form of standard 3 mm diameter disks, marked with identification codes by a laser engraving technique.

After retrieval from the irradiation capsules, the specimens were submitted to immersion density measurements and then examined by electron microscopy. The immersion density procedure is known to be accurate to ±0.2% change in density.

The alloys examined were 99.9% pure vanadium, V-XCr where X = 1, 5 and 10 atomic percent, and V-5Ti-YCr where Y = 0, 1 and 5 atomic percent. All alloys were in

the annealed condition. The 1% Cr alloy had not previously been irradiated in any of the earlier series by the current authors.

Results

After irradiation it was calculated that significant transmutation of vanadium to chromium had occurred at an average rate of ~0.8%/dpa (V). At the core mid-plane at 10.4 dpa the pure vanadium and V-Cr alloys have become V-7.5Cr, V-8.4Cr, V-12.1Cr and V-16.7Cr, respectively. The final composition of the various alloys scales with the dpa level in each capsule, however, such that pure vanadium becomes V-6.0Cr at 300°C, V-6.7Cr at 400°C, V-7.1Cr at 500°C and V-7.3Cr at 600°C. A series of broad beam EDX scans of the 600°C pure vanadium specimen confirmed that the chromium level was 7-8%. Comparable transmutation-induced variations occur in the various V-Cr and V-5Ti-Cr alloys.

The measurements of starting and final densities of all alloys are shown in Figures 2 and 3. In both the unirradiated and irradiated conditions, the V-Cr alloys decrease in density a little for the first chromium addition of 1%, and then increase strongly at higher chromium levels. This initial decrease is not observed in the unirradiated V-5Ti-Cr alloys, however.

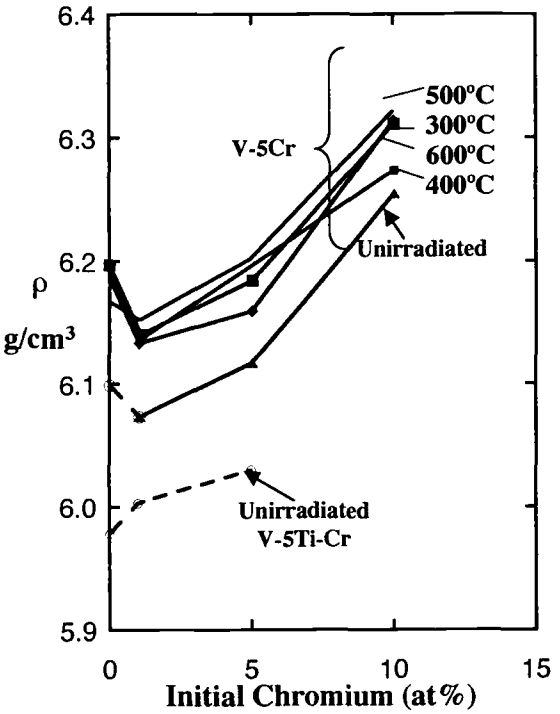


Figure 2 - *Influence of composition, transmutation and swelling on the density of V-Cr alloys.*

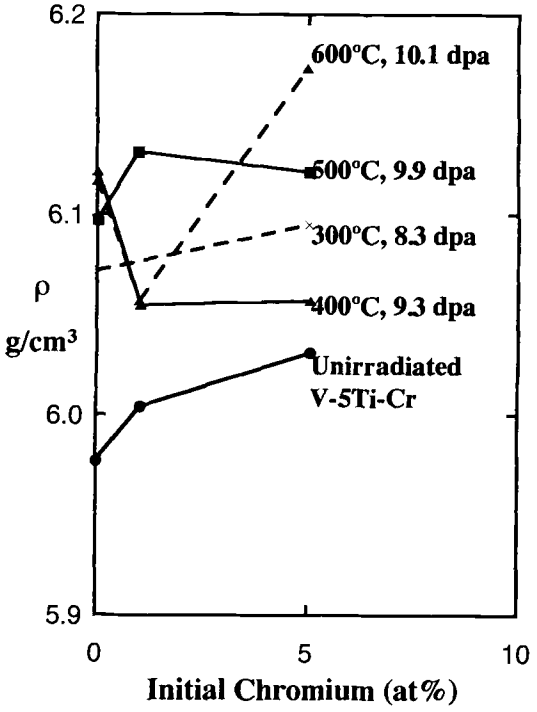


Figure 3 - *Influence of composition, transmutation and swelling on the density of V-5Ti-Cr alloys.*

After irradiation there is a pronounced increase in density of all alloys, reflecting the 6-7% increase in chromium content via transmutation. The trends with temperature and starting composition are not as consistent in the Ti-bearing alloys, when compared to the Ti-free alloys. The relative density changes at each temperature and associated dpa level reflect the competition of different levels of composition change, segregation, precipitation and void swelling. The microstructural origins of the observed changes are shown in Figures 4-7.

The complex dependence of void swelling on the competing variables is shown in Figures 8-11. In general, it appears that the transmutation-induced compositional changes in density are larger than the changes due to void swelling. Whereas transmutation causes an increase in density, swelling causes a decrease.

Transmutation-induced additions of chromium to alloys already containing chromium in general tend to decrease swelling. Addition of 5% titanium was observed to be very effective in the suppression of swelling.

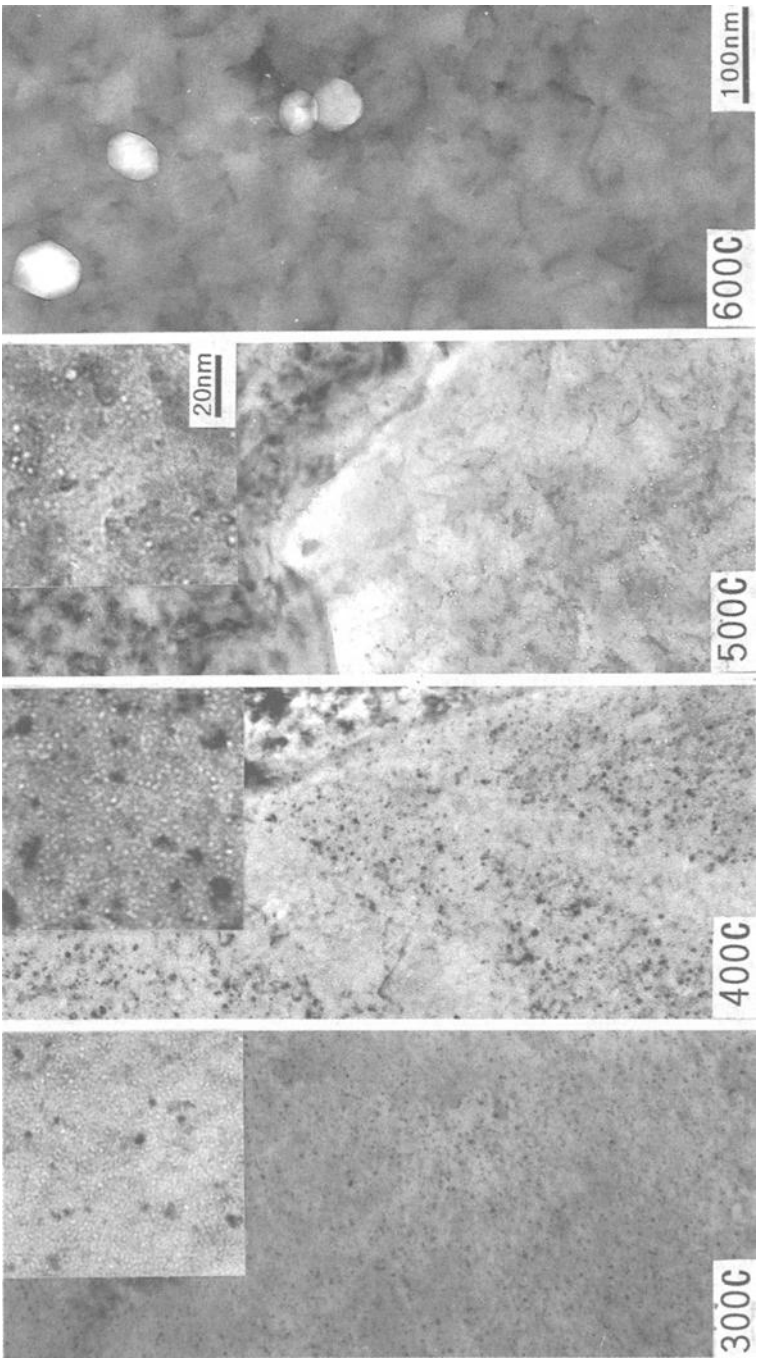


Figure 4 - *Microstructures observed in pure vanadium as a function of irradiation temperature.*

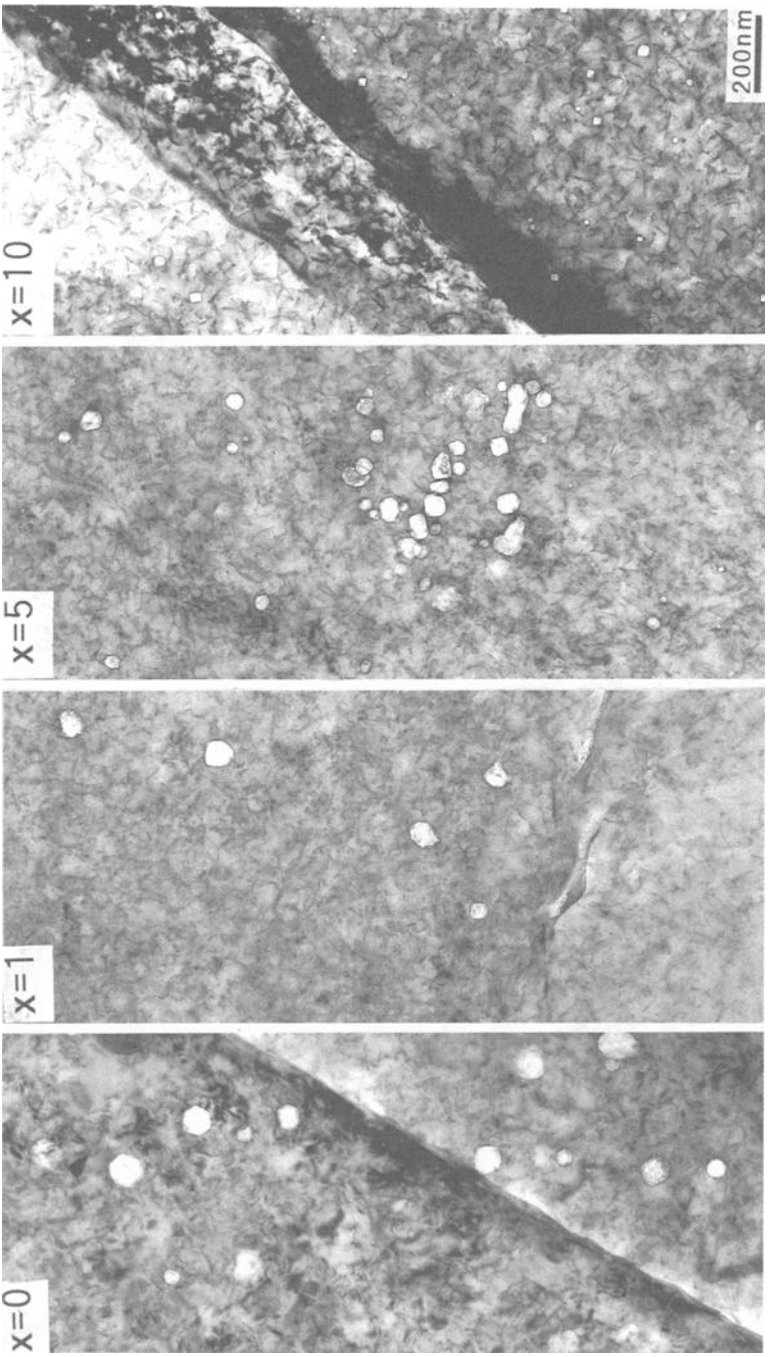


Figure 5 - *Microstructures observed in V-Cr alloys at 600 °C.*

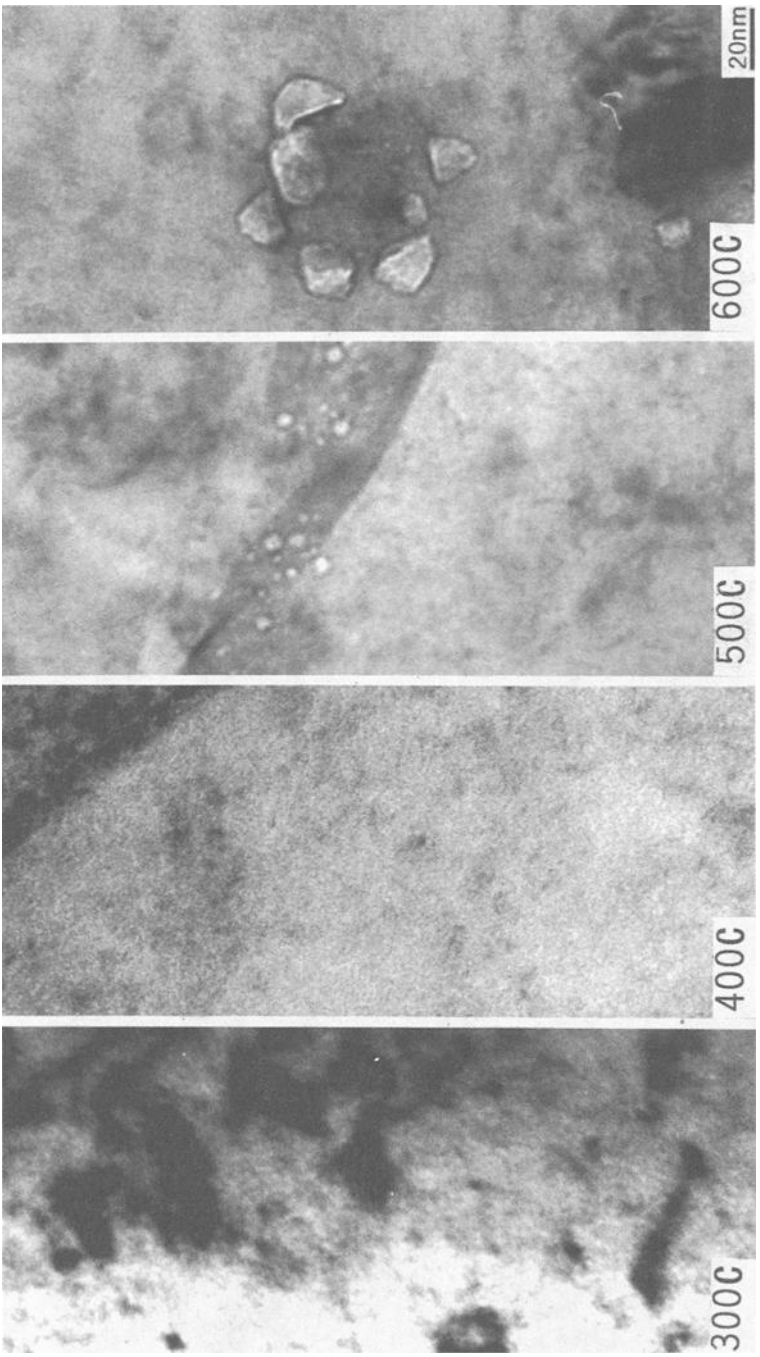


Figure 6 - *Temperature dependence of microstructure in V-5Ti.*

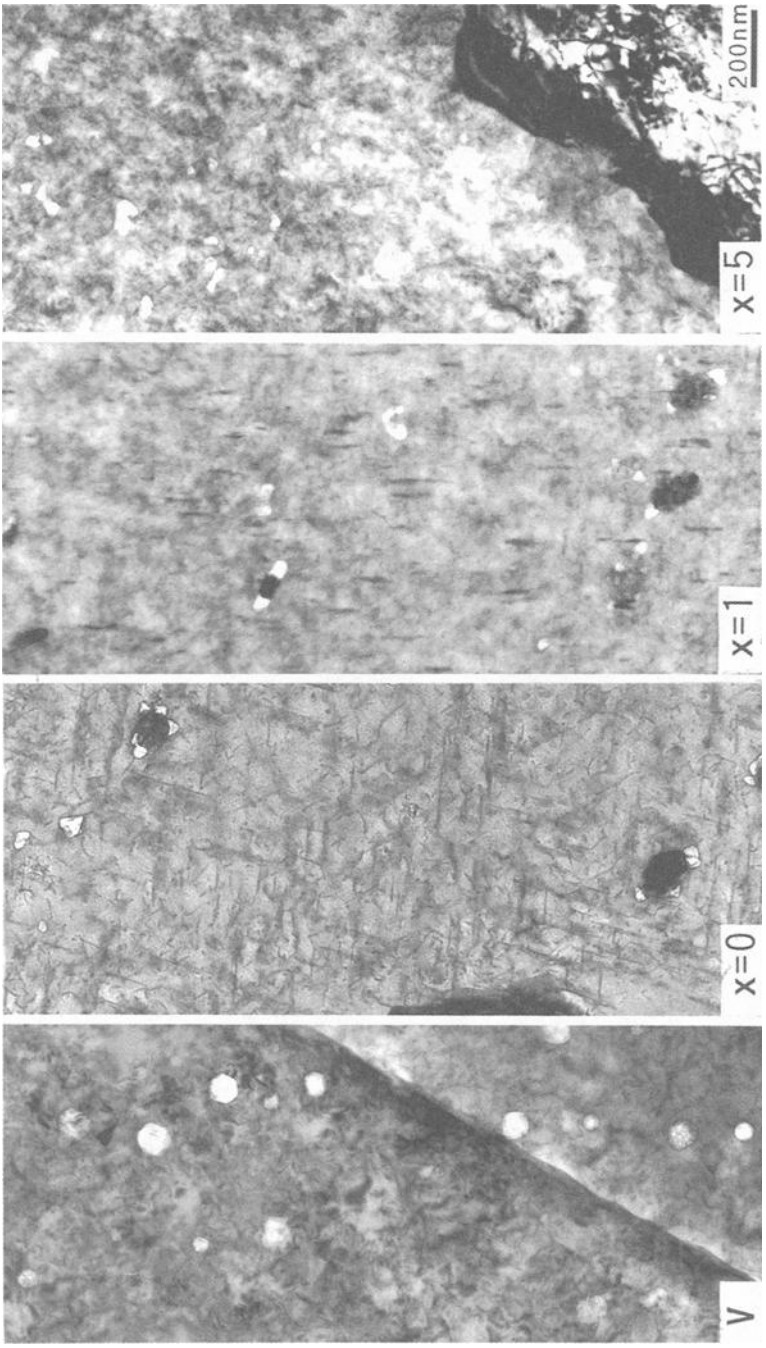


Figure 7 - *Microstructures observed in V-5Ti-Cr alloys at 600 °C.*

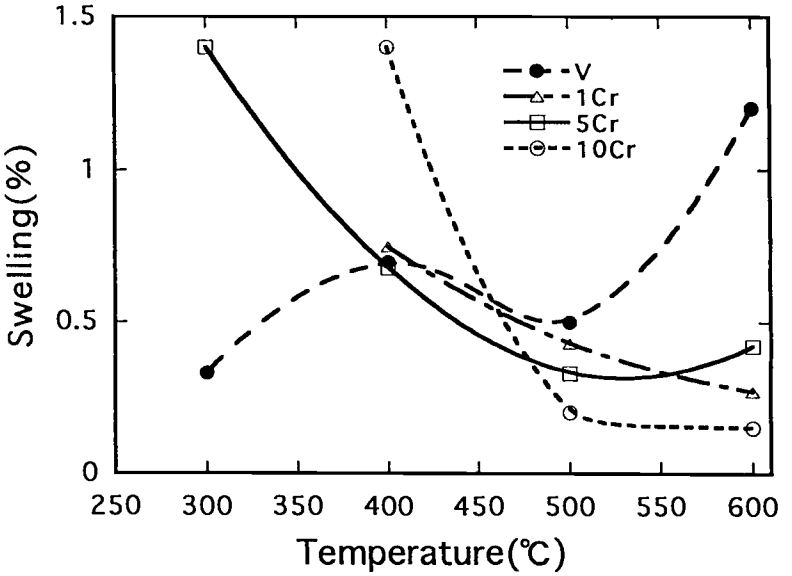


Figure 8 - *Temperature dependence of void swelling in V-Cr alloys, as measured by microscopy.*

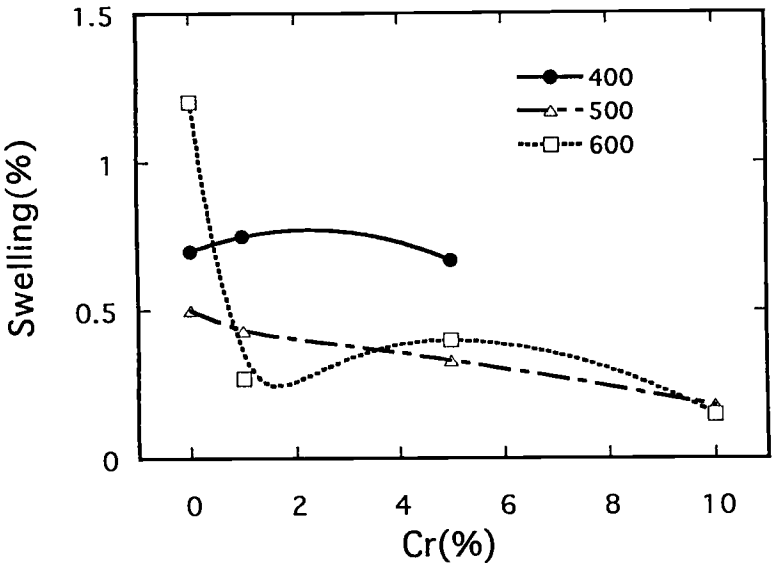


Figure 9 - *Chromium dependence of void swelling in V-Cr alloys, as measured by microscopy.*

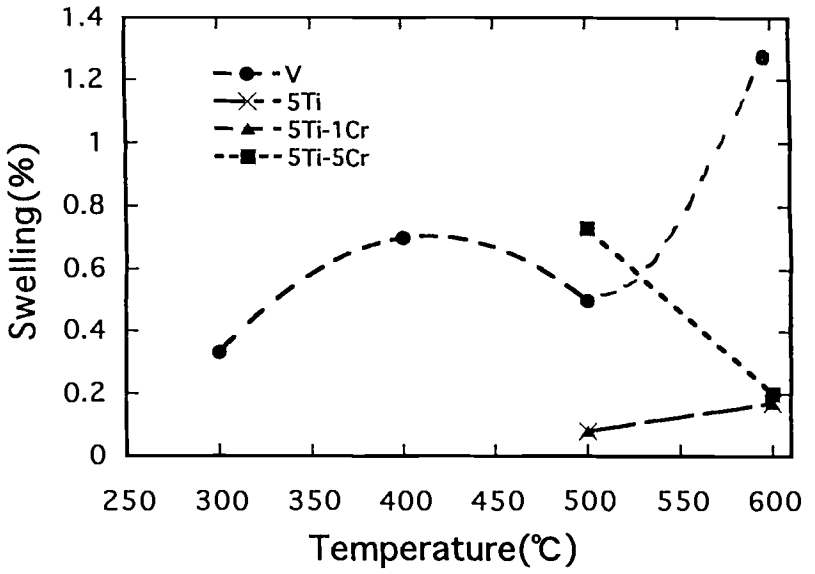


Figure 10 - *Swelling of pure vanadium and V-5Ti-Cr alloys, as measured by microscopy.*

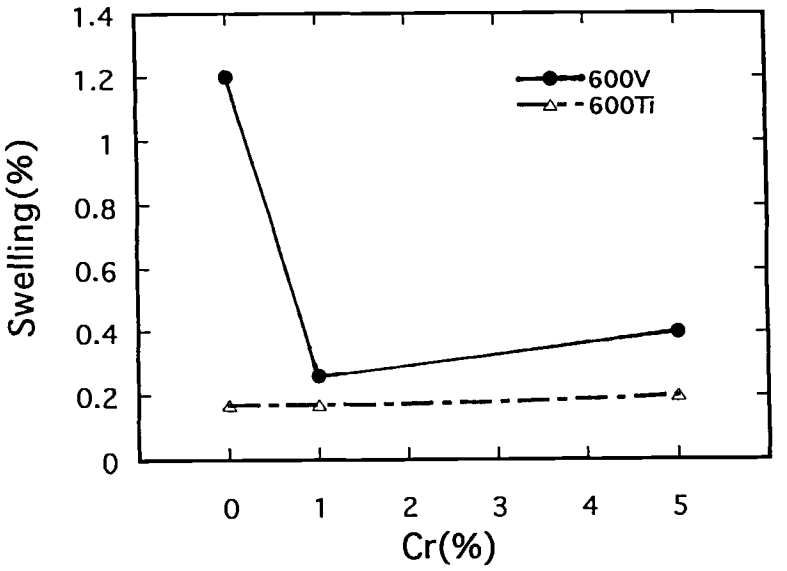


Figure 11 - *Chromium dependence of void swelling in V-Cr and V-5Ti-Cr alloys, as measured by microscopy.*

Discussion and Conclusions

The observed overall increase in density with increased chromium content is consistent with the behavior reported earlier by Garner and coworkers [8], but the slight decrease in density observed at ~1% Cr has not been previously reported, as no measurements were previously made at such low Cr levels.

The relative dependence of void swelling on temperature and starting composition attained in HFIR is quite different from that observed earlier in FFTF at higher exposure levels. Note in Figure 12 that swelling increased with temperature in FFTF-irradiated V-5Cr. Not also that increasing additions of Cr to V led to an increase in swelling at 600°C as shown in Figure 13. This is exactly contrary to the trends observed in HFIR.

This difference in behavior must be attributed to the major difference in the two test environments, i.e. the neutron spectra. Transmutation arises primarily from thermal neutrons, which are abundant in HFIR but not in FFTF. The higher rate of V→Cr transmutation in HFIR obviously exerts some as yet not understood influence on the microchemical and microstructural evolution, especially at the lower dpa levels explored in this current experiment. This suggests that care must be taken in the extrapolation of data from one reactor to that of another spectral environment.

A possible rationalization for the observed difference in swelling behavior in the two types of neutron spectra might be extracted from the comparison of data from different studies as shown in Figure 14, where the swelling data are plotted vs. final

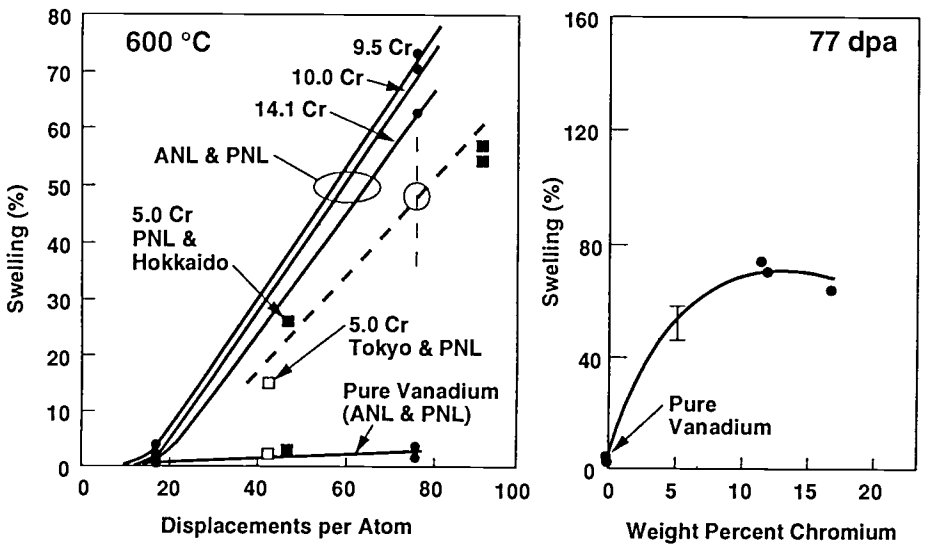


Figure 12 - *Swelling observed in V-5Cr irradiated in FFTF [11].*

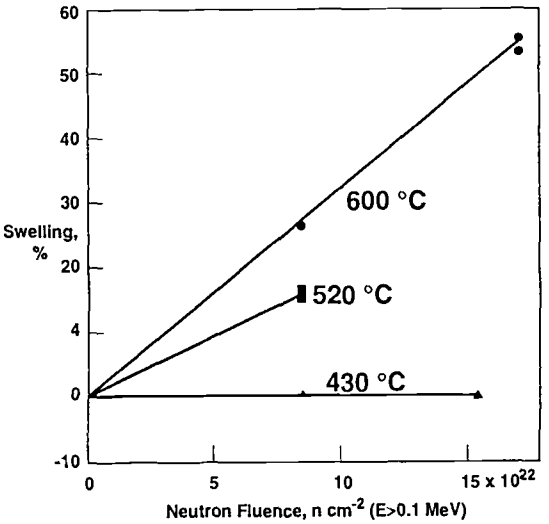


Figure 13 - *Swelling observed in V-Cr alloys irradiated in FFTF [8].*

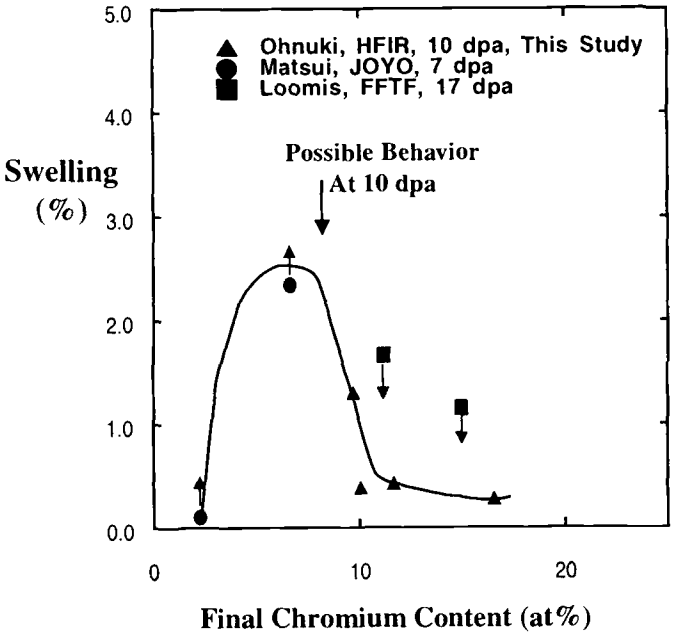


Figure 14 - *Comparison of reported swelling behavior of V-Cr alloys at relatively low dpa levels from various reactors [1,14]. JOYO and FFTF are fast reactors, while HFIR is a mixed spectrum reactor.*

chromium content. Pure vanadium is known to swell much less than V-5Cr at ~600°C in low-transmuting fast reactor spectra, as shown by various researchers [*8, 11-14*]. At higher chromium levels, however, there is a tendency for the swelling to saturate or even decline somewhat, as shown in Figure 13. At low dpa levels this nonmonotonic behavior may be more pronounced than at high dpa. It may be that chromium exerts one influence at low levels, but begins to exert some other influence, possibly on phase stability, at higher levels.

Acknowledgements

This research work is supported by Monbusho, the Japanese Ministry of Education, Science, and Culture and the US Department of Energy through the FFTF/MOTA collaboration and JUPITER programs.

References

1. Loomis, B. A., Smith, D. L., and Garner, F. A., "Swelling of Neutron-Irradiated Vanadium Alloys," *Journal of Nuclear Materials*, Vols. 179-181, 1991, pp. 771-774.

2. Ohnuki, S., Gelles, D. S., Loomis, B. A., Garner, F. A., and Takahashi, H., "Microstructural Examination of Simple Vanadium Alloys Irradiated in FFTF/MOTA," *Journal of Nuclear Materials*, Vols. 179-181, 1991, pp. 775-778.

3. Gelles, D. S., Ohnuki, S., Loomis, B. A., Takahashi, H., and Garner, F. A., "A Microstructural Explanation for Irradiation Embrittlement of V-15Cr-5Ti," *Journal of Nuclear Materials*, Vol. 186, 1991, pp. 77-82.

4. Garner, F. A., Gelles, D. S., Takahashi, H., Ohnuki, S., Kinoshita, H., and Loomis, B. A., "High Swelling Rates Observed in Neutron-Irradiated V-Cr and V-Si Binary Alloys," *Journal of Nuclear Materials*, Vols. 191-194, 1992, pp. 948-951.

5. Ohnuki, S., Takahashi, H., Shiba, K., Hishinuma, A., Pawel, J. E., and Garner, F. A., "Influence of Transmutation on Microstructure, Density Change, and Embrittlement of Vanadium and Vanadium Alloys Irradiated in HFIR," *Journal of Nuclear Materials*, Vol. 218, 1995, pp. 217-223.

6. Sekimura, N., Iwai, T., and Garner, F. A., "Influence of Boron-Generated Helium on the Swelling of Neutron Irradiated V, V-5Cr and V-5Fe," *Journal of Nuclear Materials*, Vols. 233-237, 1996, pp. 400-405.

7. Ohnuki, S., Takahashi, H., Garner, F. A., Pawel, J. E., Shiba, K., and Hishinuma, A., "Transmutation-Induced Embrittlement of Vanadium and Several Vanadium Alloys in HFIR," *Journal of Nuclear Materials*, Vols. 233-237, 1996, pp. 411-415.

8. Garner, F. A., Greenwood, L. R., Loomis, B. A., Ohnuki, S., and Sekimura, N., "Influence of Flux-Spectra Differences on Transmutation, Dimensional Changes and Fracture of Vanadium Alloys," *Journal of Nuclear Materials*, Vols. 233-237, 1996, pp. 406-410.

9. Ermi, A. M. and Gelles, D. S., "Preliminary Report on the Irradiation Conditions of the HFIR JP-23 Experiment," Fusion Materials Semiannual Progress Report for Period Ending September 30, 1994, DOE/ER-0313/17, 1995, pp. 35-49.

10. Greenwood, L. R. and Ratner, R. T., "Neutron Dosimetry and Damage Calculations for the HFIR JP-23 Irradiations," Fusion Materials Semiannual Progress Report for Period Ending June 30, 1998, DOE/ER-0313/24, pp. 231-235.

11. Previously unpublished data, Garner, F. A. and Ohnuki, S.

12. Sekimura, N., Iwai, T. and Garner, F. A., "Influence of Boron-Generated Helium on the Swelling of Neutron Irradiated V, V-5Cr and V-5Fe," *Journal of Nuclear Materials*, Vols. 233-237, 1996, pp. 400-405.

13. Nakajima, H., Yoshida, S., Kohno, Y., and Matsui, H., *Journal of Nuclear Materials*, Vols. 191-194, 1992, pp. 952-955.

14. Matsui, H., data from irradiations in the JOYO fast reactor, provided in advance of publication.

Sergey A. Fabritsiev,[1] Alexander S. Pokrovsky,[2] Steve J. Zinkle,[3] and Danny J. Edwards[4]

Neutron Irradiation Induced High Temperature Embrittlement of Pure Copper and High Strength Copper Alloys

Reference: Fabritsiev, S. A., Pokrovsky, A. S., Zinkle, S. J., and Edwards, D. J., **"Neutron Irradiation Induced High Temperature Embrittlement of Pure Copper and High Strength Copper Alloys,"** *Effects of Radiation on Materials: 19th International Symposium, ASTM STP 1366,* M. L. Hamilton, A. S. Kumar, S. T. Rosinski, and M. L. Grossbeck, Eds., American Society for Testing and Materials, West Conshohocken, PA, 2000.

Abstract: The effect of helium production during neutron irradiation on the high temperature tensile properties of copper and dispersion strengthened (DS) copper alloys was investigated in neutron-irradiated specimens containing different levels of boron. Sheet tensile specimens were irradiated at temperatures of 90°C, 150°C and 300°C to doses of 0.2-1 dpa. Considerable embrittlement (<3% total elongation at 400°C) was detectable in pure copper at He concentrations above 80 appm. The DS copper alloys tested under the same conditions showed higher resistance to helium embrittlement. Samples of DS copper alloy saturated to 60 appm helium on cyclotron also demonstrated high resistance to helium embrittlement. The present results indicate that under fusion energy conditions, where a high helium accumulation rate of ~10 appm/dpa is expected, helium embrittlement may limit the maximum temperature of copper alloys for structural applications to $\leq$ 400°C.

Keywords: helium embrittlement, copper alloys, tensile properties, radiation effects

Introduction

An accurate assessment of the anticipated behavior of materials in fusion reactors requires extrapolation of data obtained in fission reactors. However, the harder neutron spectrum of a fusion reactor can significantly affect radiation-induced processes in

[1] Head of Laboratory, D.V.Efremov Scientific Research Institute, 189631 St.Petersburg, Russia.
[2] Senior Scientist, Scientific Research Institute of Atomic Reactors, 433510 Dimitrovgrad, Russia.
[3] Senior Scientist, Oak Ridge National Laboratory, P.O. Box 2008, Oak Ridge, TN 37831-6376 USA.
[4] Senior Scientist, Pacific Northwest National Laboratory, P.O. Box 999, Richland, WA 99352 USA.

Copyright© 2000 by ASTM International www.astm.org

materials. For example, the helium generation rate is generally much higher in materials exposed to a fusion neutron spectrum compared to fission neutron spectrum. The higher He production rate in fusion reactors is due to threshold (n,α) reactions with high-energy neutrons (the flux of neutrons with energies above ~6 MeV will be considerably greater in fusion reactors than in the fission reactors currently used for radiation effects experiments). In particular, the He generation rate in copper irradiated in fission reactors is ~0.1 appm He/dpa, whereas in a first wall DT fusion reactor spectrum the corresponding value is ~10 appm He/dpa [*1*].

For copper alloys proposed to be used in fusion energy divertor and first wall structures [*1*], knowledge about the effect of helium on the operational properties is important for two reasons. First, only limited data exist on the effect of helium concentrations on copper properties at fusion-relevant conditions (~100 appm He/10 dpa), as for the most part the results were obtained during irradiation in fast fission reactors [*2,3,4*] at low concentrations of accumulated helium (~1-10 appm). Second, the assumed upper temperature of copper alloy operation in ITER and other fusion energy devices is T ~ 350°C (~ 0.45 T_{melt}) which is sufficiently high for both helium embrittlement [*5,6*] and helium effects on swelling [*7*] to manifest themselves.

One convenient method to produce fusion-relevant helium concentrations during fission reactor irradiation is to prepare dilute alloys containing boron. Due to the high thermal neutron cross-section for the $^{10}B(n,\alpha)^{7}Li$ reaction, significant amounts of helium can be generated in Cu-B alloys during irradiation in a mixed-spectrum fission reactor. This boron doping technique has been utilized in several previous studies of helium embrittlement [*8,9*] and cavity formation [*7,10-13*] in pure copper. A second convenient technique for investigating He embrittlement utilizes cyclotron implantation of He ions [*6*].

The present paper studies the effect of helium concentration on the tensile properties of copper-based alloys. Samples of pure copper and DS copper alloys were doped with 80-290 ppm of boron prior to irradiation in the SM-2 mixed-spectrum reactor in order to generate helium via the $^{10}B(n,\alpha)^{7}Li$ thermal neutron reaction. In addition, several copper and copper alloy specimens were irradiated with 40 MeV He ions in a cyclotron (20-60 appm He) in order to investigate He implantation effects at relatively low damage levels.

Experiment

Sheet tensile specimens from pure copper, Cu-B alloys, boron-doped dispersion-strengthened Cu-Al_2O_3 alloy GlidCop Al25, dispersion-strengthened MAGT 0.2 alloy were irradiated in the Channel 4 of the SM-2 reactor. Tables 1 and 2 summarize the alloy compositions and irradiation conditions used in this study. The average fast (E>0.1 MeV) and thermal neutron fluxes were $3x10^{18}$ and $2.5x10^{18}$ n/m^2s, respectively, in the Channel 4 position. The calculated helium concentrations in irradiated specimens are presented in Table 2. Further details on the irradiation technique and capsule design are presented elsewhere [*14*].

Two types of sheet tensile specimens were irradiated and tested. The large tensile sheet (LTS) specimens had an overall length of 56 mm and a thickness of 1 mm, with a gage length and width of 30 and 4 mm, respectively. The small tensile sheet (STS) specimens had an overall length of 34 mm and a thickness of 0.25 mm, with a gage length and width of 11 and 3.5 mm, respectively. The irradiated and control samples were tensile tested in vacuum at a cross head speed of ~ 1 mm/min in the temperature range of 20-400°C, which corresponds to an initial strain rate of 5.6×10^{-4} s^{-1} and 1.5×10^{-3} s^{-1} for the LTS and STS specimens, respectively. For the elevated temperature tests, the tensile specimens were held at temperature for 0.5 hour prior to testing. Part of neutron-irradiated samples was annealed at temperatures of 800°C and 900°C. Then annealed samples were tested for tension in the temperature range of 20-850°C.

The structure and morphology of the fracture surfaces was investigated by TEM and SEM.

In order to investigate further the role of helium on high temperature embrittlement of copper alloys, STS samples of copper, Cu - 0.2%Al, and MAGT 0.2 dispersion strengthened copper with a thickness of 0,2 mm were irradiated with 40-50 MeV helium ions at the cyclotron of the Institute of Nuclear Physics of Academy of Science of Kazakh SSR.

Table 1. Alloy composition, (wt %).

Material	Cu	Al (Al_2O_3)	Al	B	Fe	Pb	Ti	Hf
Pure Cu	bal	-	-	0.0001	0.014	-	-	-
Cu-B1	bal	-	-	0.008	0.01	-	-	-
Cu-B2	bal	-	-	0.0290	0.01	-	-	-
Cu-0.2Al	bal	-	0.19	0.0002	0.02	-	-	-
MAGT 0.2	bal	0.24	-	0.0001	0.017	-	0.14	0.03
MAGT 0.05	bal	0.10	-	0.0001	0.01	-	0.09	0.02
GlidCop Al25 IGO	bal	0.25	-	0.0100	0.0048	0.0008	-	-

Table 2 Irradiation conditions.

No	Material	T_{irr}, °C	Φt_{fast}, $x10^{25}$ n/m^2 E>0.1 MeV	Φt_{therm}, $x10^{25}$, n/m^2 E<0.68 eV	Damage, dpa	C_{He}, appm	C_{Boron} ppm
1	Pure Cu	90	2.35÷0.82	1.4÷1.0	~1	~1	1
2	Cu-B1	90	1.8÷1.0	1.3÷1.0	~1	~80	80
3	Cu-B2	90	1.9÷0.9	1.4÷1.0	~1	~300	290
4	GlidCop Al25 IGO	165	0.35÷0.28	0.29÷0.2	~0.2	~70	100
		150	0.65÷0.45	0.55÷0.45	~0.4	~95	100
		300	0.6÷0.4	0.6÷0.4	~0.4	~95	100

A uniform concentration of 20 to 60 appm He was implanted into the specimens at a temperature of 100°C by continuously rotating the specimens in the ion beam (damage

level 0.05 dpa). The helium implanted specimens were tensile tested in vacuum at a strain rate of 1.5×10^{-3} s^{-1}.

Results Of Experiment

Neutron Irradiation

Pure Copper and Cu-B Alloys - The calculated He concentration in the neutron irradiated pure copper and DS copper alloys was 0.5 to 1.5 appm He [*15*]. Between 80 and 300 appm He was accumulated in the boron-doped alloys, depending on the boron concentration and the thermal neutron flux (Table 2).

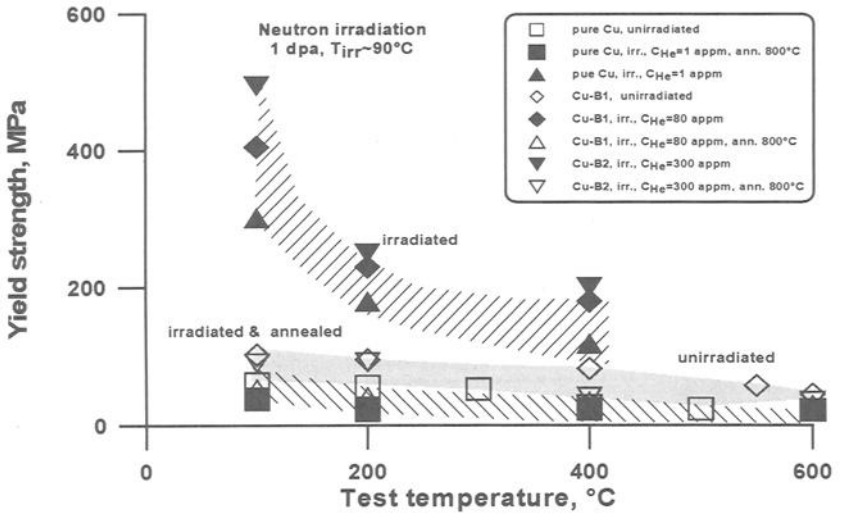


Fig. 1 The effect of neutron irradiation on the strength of pure Cu and Cu-B alloys.

Effect of Irradiation on the Strength of Copper Alloys - Irradiation of pure copper and copper alloys with boron to 1 dpa at T_{irr}=90°C results in a drastic strengthening of alloys at T_{test}=100°C. The yield strength of pure copper increases by 200 MPa, and for Cu-B2 by 300 MPa (Fig.1).

An increase in the testing temperature results in a drop in the yield strength of irradiated materials. At T_{test}=400°C the hardening level does not exceed 100 MPa. Annealing at 800°C of irradiated samples practically eliminates radiation hardening. Irradiated samples of pure copper and Cu-B alloys annealed at 800°C demonstrate a level of strength properties close to that of unirradiated materials throughout the testing temperature range.

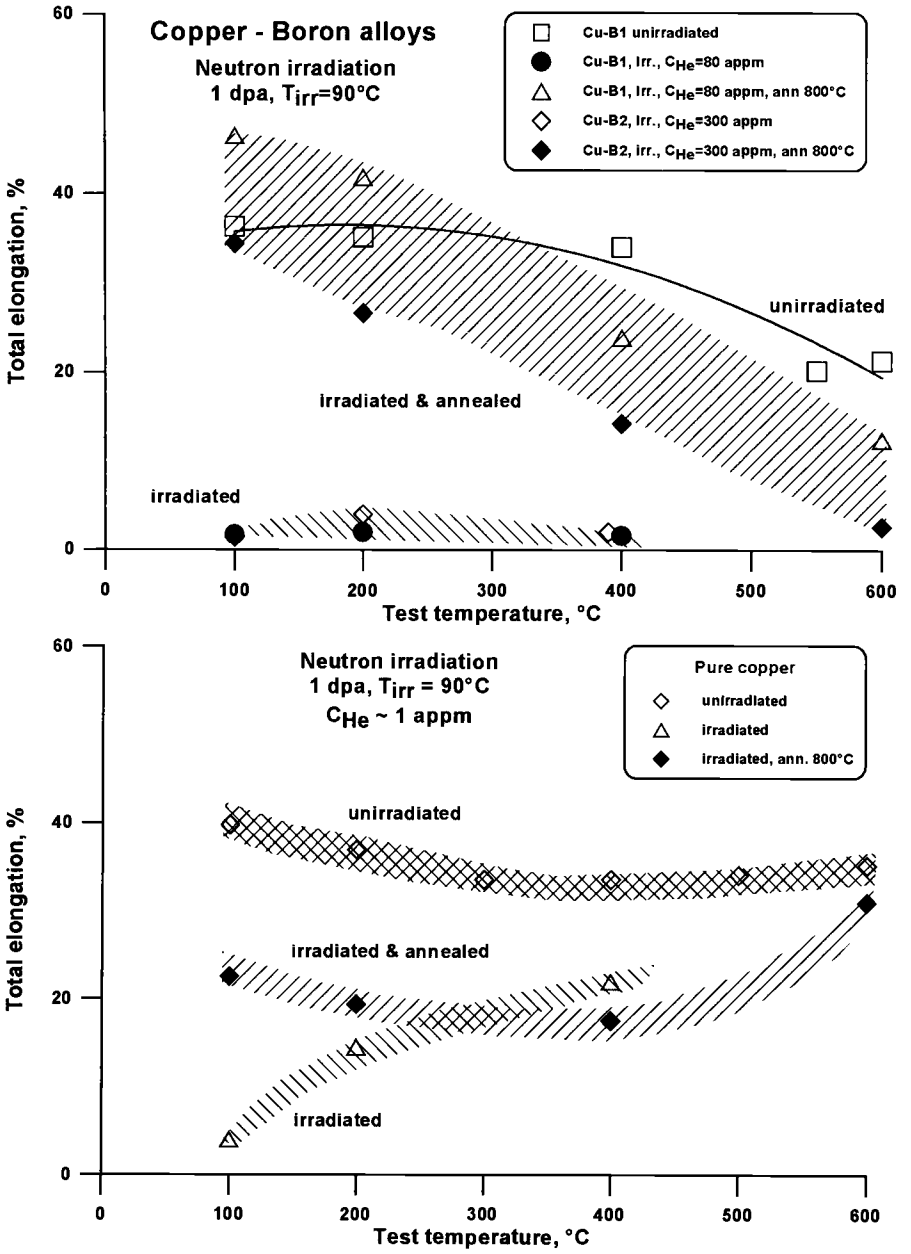


Fig.2,3 The effect of neutron irradiation on the total elongation of pure Cu and Cu-B alloy.

Effect of Irradiation on the Ductility of Copper Alloys – Fig 2 shows the total elongation as a function of testing temperature of pure copper, when unirradiated, after irradiation to 1 dpa and after irradiation to 1 dpa and annealing at 800°C. At T_{test}=100÷200°C irradiated pure copper demonstrates an appreciable low-temperature embrittlement.

Annealing at 800°C recovers partially the low-temperature ductility of pure copper. High-temperature (T_{test}~400÷600°C) ductility of irradiated, as well as irradiated and annealed pure copper is rather high, i.e. 20÷30%. Thus, at a low helium content in samples of ~ 1 appm the high-temperature ductility of pure copper remains at a high level close to the properties of unirradiated material.

Cu-B1 and Cu-B2 alloys after irradiation to 1 dpa at T_{irr}=90°C demonstrate an extremely low level of ductile properties of 0,5÷3% at T_{test}=100÷200°C (Fig.3). After annealing at 800°C the low-temperature ductility of irradiated samples recover. But, after annealing a marked manifestation of helium embrittlement is observed in Cu-B1 and Cu-B2 samples containing ~80 appm and 300 appm He, respectively. The ductility of irradiated Cu-B1 and Cu-B2 samples is similar to that of unirradiated samples at T_{test}=100÷200°C. At T_{test}=400÷600°C, however, the ductility of irradiated samples drops, while that of unirradiated samples it remains high, i.e. 15÷20%. In this case samples with maximum helium concentration demonstrate minimum ductility.

Thus, at high helium concentration in copper (≥80 appm) it is distinctly susceptible to helium embrittlement.

Dispersion-strengthened Copper Alloys – Fig 4 presents temperature dependencies of the total elongation of DS copper alloy GlidCopAl25 IGO in the initial state, after irradiation to 0,2 dpa at 165°C, to 0,4 dpa at 150°C and 300°C, as well as after irradiation to 0,4 dpa at 300°C and annealing at 900°C, 1 hour.

Evidently, after low-temperature irradiation to 0,2÷0,4 dpa GlidCopAl25 IGO demonstrates susceptibility to low-temperature radiation embrittlement. At T_{test}=150÷185°C samples irradiated to 0.2- 0.4 dpa at T_{irr}=150°C have the ductility by a factor of 2÷4 lower than unirradiated samples. With the testing temperature increasing to 200÷500°C, GlidCopAl25IGO, irrespective of the state (irradiated and unirradiated), has a high ductility of 15÷20%. After annealing at 900°C GlidCopAl25IGO alloy irradiated to 0,4 dpa also has a high ductility at the level of unirradiated material. Thus, when comparing Fig.3 and Fig.4, evident is the essential difference in the behavior of Cu-B and GlidCopAl25IGO alloys. Cu-B alloy, with a content of He≥80 appm, demonstrates, when annealed, a monotonous decrease in ductility with a rise in the testing temperature. This is a typical manifestation of helium embrittlement. DS copper alloy GlidCopAl25IGO containing ~80 appm He after irradiation, demonstrates both in the irradiated and irradiated and annealed state an increase in the material ductility with a rise in the testing temperature. This fact testifies that the alloy is highly resistant to helium embrittlement.

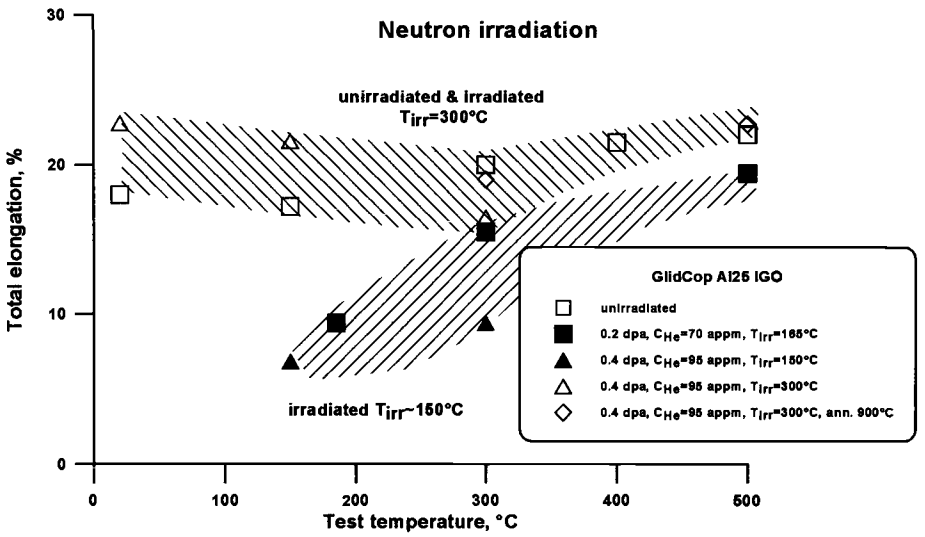


Fig. 4 The effect of neutron irradiation on the total elongation of GlidCop Al25 IGO.

Effect of Cyclotron Injection on Copper Alloys

As seen from the results of the previous chapter, embrittlement of copper alloys after neutron irradiation is quite a complicated combination of the effect of radiation defects, helium and possible lithium. To estimate the effect of "pure" helium on the ductility of copper alloys, i.e. at a very low level of radiation damage, some of the samples were saturated with helium on the cyclotron (at a radiation damage level of ~0,05 dpa).

As seen from Fig.5, pure copper, with a helium content of ~40 appm, demonstrates a strong embrittlement at T_{test}=350÷750°C.

The binary alloy Cu-0.2Al containing 20 appm of helium, also demonstrates a strong embrittlement at T_{test}=550÷850°C. Annealing at 850°C during 1 hour does not recover the high-temperature ductility of Cu-0.2Al alloy, it remains at an extremely low level.

Hence, pure copper and binary alloy Cu-0.2Al containing 20÷40 appm of helium demonstrate a strong susceptibility to helium embrittlement also in case when the radiation damage of materials is very small.

Thus, the cyclotron experiment confirms the decisive role helium plays in the observed high-temperature embrittlement of pure copper.

Fig.6 shows the temperature dependence of the total elongation of DS copper alloys MAGT0.2 and MAGT0.05 saturated with helium on the cyclotron to 60 appm and 40 appm of helium, respectively.

As follows from Fig.6, alloy MAGT0.2 with an Al_2O_3 volume content of ~0,5%, which is much of the same structure and properties as GlidCopAl25 alloy, has throughout the testing temperature range the same ductility, when irradiated, as in the initial state.

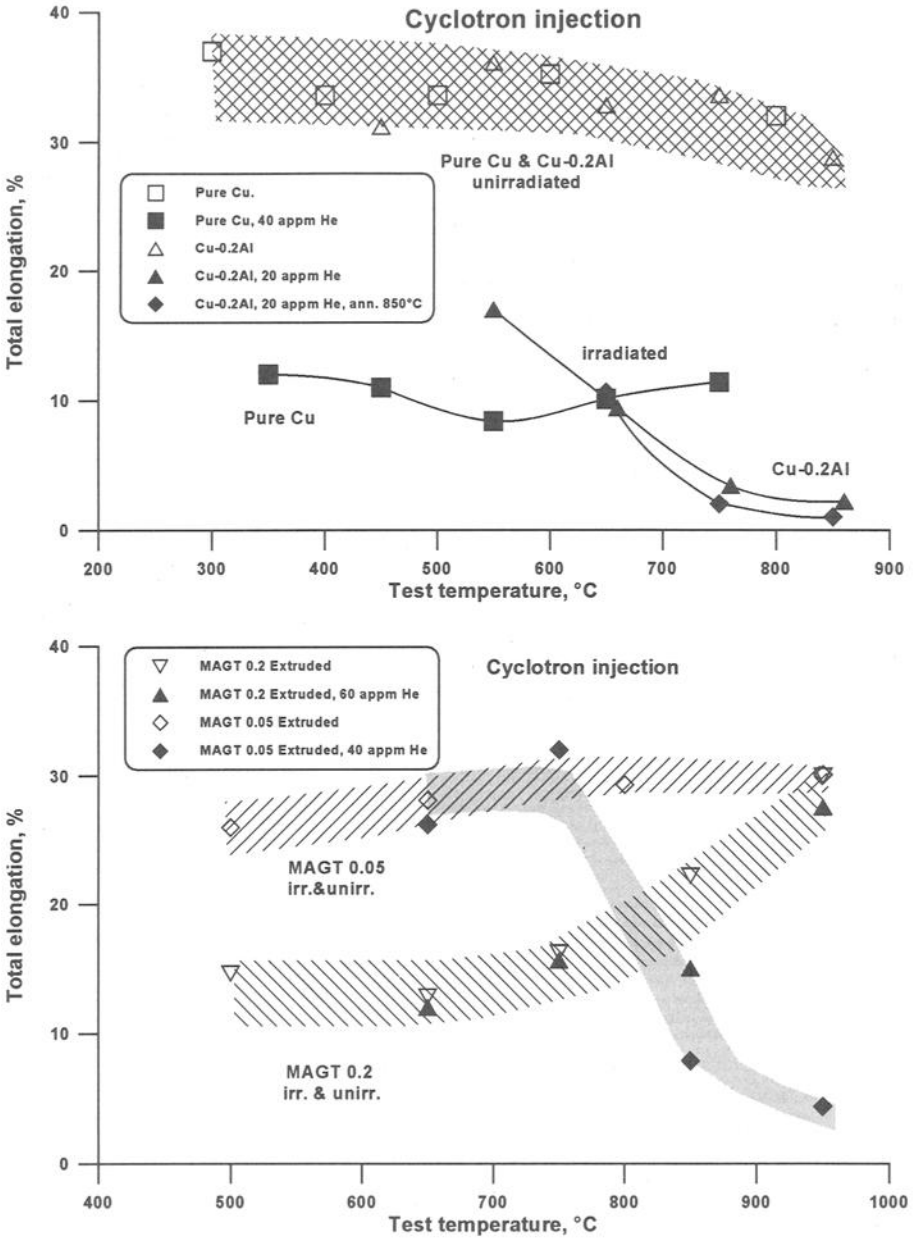


Fig. 5,6 The effect of cyclotron injected Helium on the total elongation of pure Cu and Cu alloys.

Another situation is realized for MAGT0.05 alloy manufactured by the same technology as MAGT0.2 but containing much less strengthening particles of ~0,1% Al_2O_3. MAGT0.05 alloy has the ductility nearly twice as high as MAGT0.2 in the unirradiated state. But after introduction of 40 appm of helium on the cyclotron the MAGT0.05 alloy at T_{test}=850÷950°C demonstrates a strong helium embrittlement.

Thus, the cyclotron experiments revealed that DS alloys have a high resistance to helium embrittlement. In this case it is evident that the factor controlling this resistance is high density of strengthening Al_2O_3 particles. That is the reason why alloys with a high Al_2O_3 content and GlidCopAl25IGO and MAGT0.2 with helium accumulated to 60÷80 appm are not prone to helium embrittlement. The density of Al_2O_3 particles in this alloy contains is very high. These particles effectively trap helium up to T_{test}=950°C.

TEM Investigation

TEM investigation revealed that pure copper samples and Cu-B and DS copper alloys irradiated to 1 dpa at T_{irr}=90°C contain small "black-dots" defect clusters produced during irradiation at this temperature. Such a structure for Cu-B2 alloy is exemplified in Fig.7a. It is seen that the density of defect clusters in the alloy is high. It is the high density of "black spots" that affects the hardening and embrittlement of copper alloys observed during low-temperature tensile tests. Annealing at 800°C recovers the structure. As seen from Fig.7b, small defect clusters, when annealed, decompose; dislocation networks are observed in the structure, and very large helium bubbles develop. After testing irradiated and annealed samples for tension at 600°C large bubbles up to 100 nm in diameter are observed on the grain boundaries (Fig.7c, d).

It should be noted that in DS alloy GlidCopAl25IGO samples irradiated to 0.4 dpa and annealed at 900°C no helium bubbles were observed, though He concentration in the alloy was higher, i.e. ~80 appm.

SEM Investigations

Neutron Irradiation - Pure copper samples irradiated to 1 dpa fractured, when subjected to tensile testing at 400°C, in ductile transcrystalline way (Fig. 8a). After annealing at 800°C irradiated samples from pure copper failed during tensile testing at 600°C in a combined, mostly transcrystalline, way.

Cu-B2 alloy samples irradiated to 1 dpa and annealed at 800°C failed solely over the grain boundaries during tensile testing at 600°C (Fig.8b).

GlidCopAl25IGO alloy samples irradiated to 0.2-0.4 dpa and annealed at 900°C fractured at T_{test}=300÷500°C in a ductile transcrystalline way.

Cyclotron Injection - Pure copper samples saturated with helium on the cyclotron to 40 appm and tested at 750°C demonstrated solely intergranular failure (Fig. 8c), with helium pores clearly observed on grain facets.

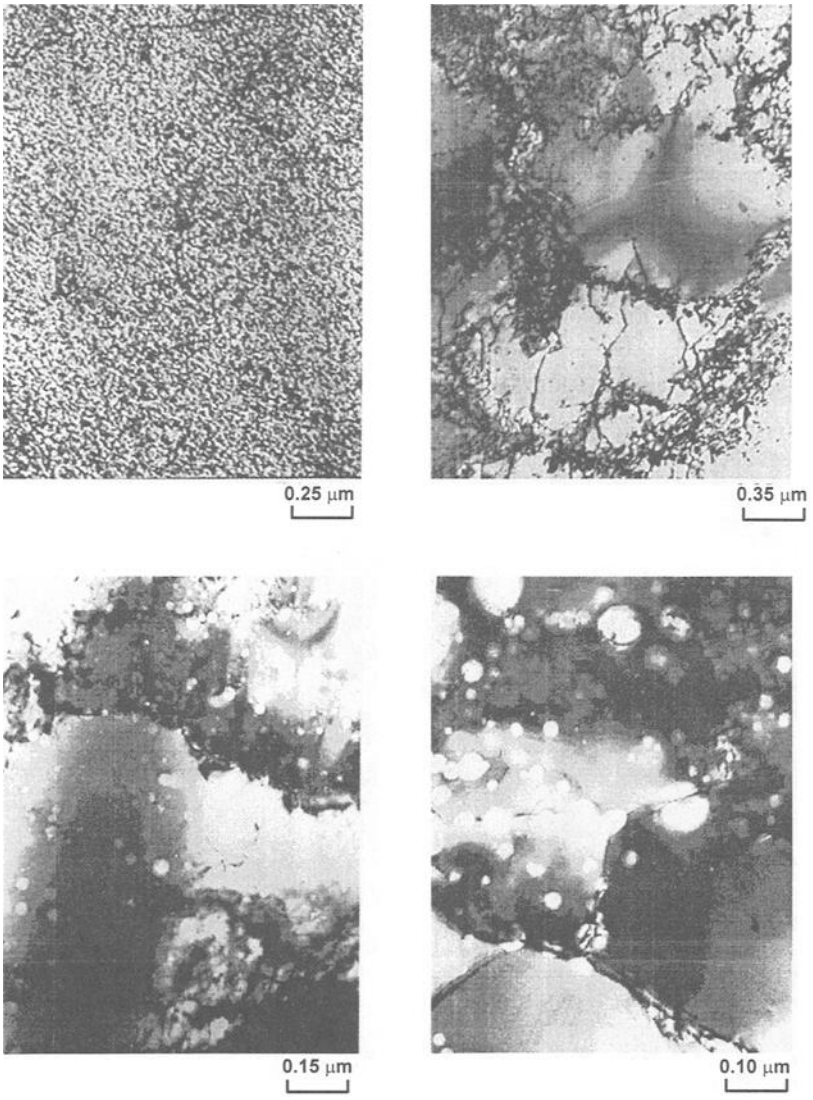


Fig. 7. Microstructure of Cu-B2 alloy irradiated up to 1 dpa at 90°C, (C_{He}=300 appm):

a) irradiated;

b) irradiated and annealed at 800°C, 10 min.;

c),d) irradiated and annealed at 800°C, 10 min., tensile tested at 600°C.

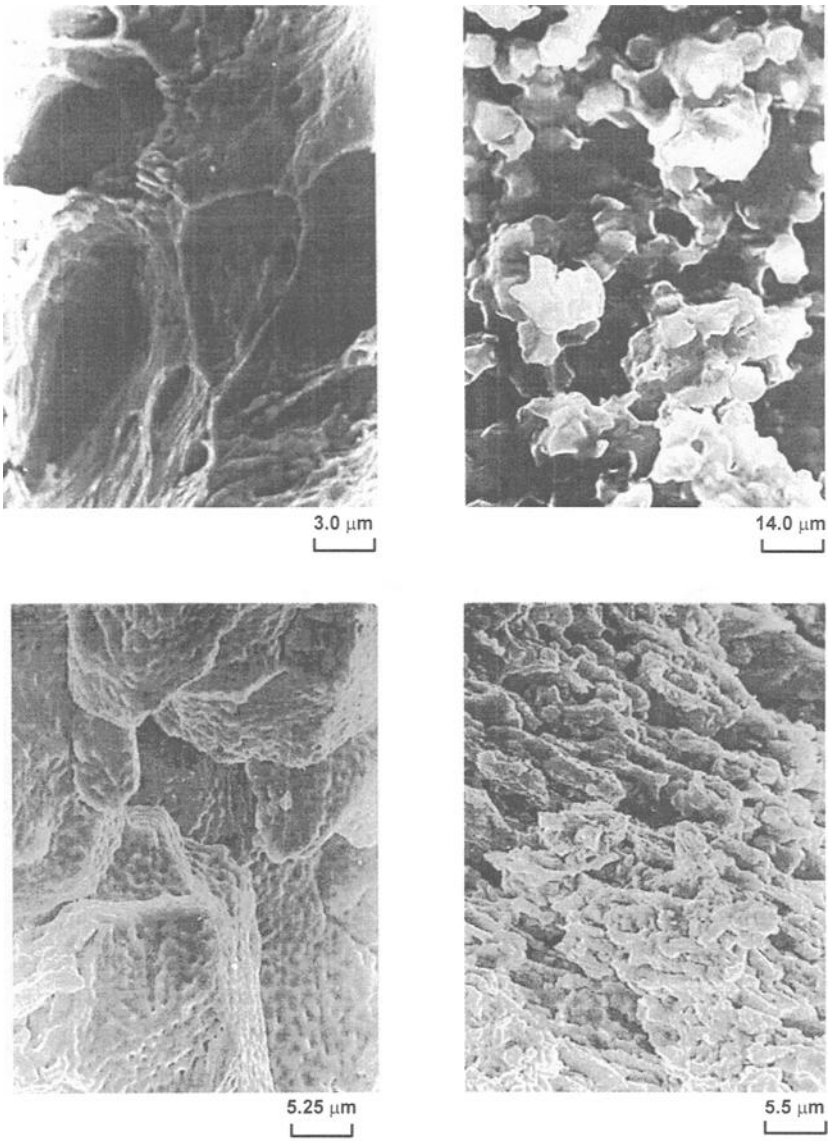


Fig. 8. SEM fracture surface photographs of pure Cu and Cu based alloys after tensile tests:

a) pure Cu, neutron irradiated at 90°C to 1 dpa (C_{He}=1 appm), (T_{test}=400°C);

b) Cu-B2 alloy, neutron irradiated at 90°C up to 1 dpa, (C_{He}=300 appm), annealed at 800°C, (T_{test}=600°C);

c) pure Cu, cyclotron saturated to 40 appm He, (T_{test}=750°C);

d) DS copper alloy MAGT 0.2 cyclotron saturated to 60 appm He, (T_{test}=750°C).

DS alloy MAGT0.2, containing 60 appm He at T_{test}=750°C, suffers ductile failure in a combined way partially over the grain body and partially over the boundaries of small ~5μm grains. Similar failure is observed also for an unirradiated alloy (Fig.8d).

Discussion

Previous microstructural studies on He-implanted copper and on Cu-B alloys irradiated with fission neutrons at low temperatures have found that helium bubbles become visible following annealing at temperatures between 300 and 400°C [*10,11,13,16,17*], which coincides with the temperature range where significant embrittlement was observed in the present study. Several studies have demonstrated that helium cavitation at grain boundaries is responsible for the dramatic decrease in tensile elongation in copper at temperatures above ~400°C [*8,9*]. Helium embrittlement of grain boundaries is generally acknowledged to cause low levels of ductility in numerous materials at elevated temperatures [*6,18,19*]. Due to the long times required for helium to diffuse to grain boundaries and form large cavities, it is well established that the amount of helium embrittlement is more severe for slow strain rate conditions (e.g., creep rupture tests) compared to typical tensile test conditions [*6*]. Several of the key issues regarding helium embrittlement in copper alloys are discussed in more detail in the following.

Role of Helium and Radiation Damage in High Temperature Embrittlement - The strength of the Cu-B alloys irradiated near 100°C increased with increasing boron content, in agreement with previous work [*20*]. The data from the present study demonstrate the prevailing role of helium in the embrittlement observed at elevated testing temperatures. The observed embrittlement of copper irradiated at T_{test}=100°C is attributable to two factors.

First, complexes of radiation defects, whose density at low irradiation temperature is very high, affect the ductility and strength of copper alloys. Such complexes of "black-dots" defects were observed in irradiated copper during TEM investigations in our work (Fig.7a) and in a number of other studies [*1,13,17*]. Defect complexes prevent the motion of dislocations, cause the yield strength to grow and the uniform elongation of copper alloys to reduce [*15*]. At increased testing temperatures (300÷400°C) the complexes become unstable and decompose, dislocation networks are observed in the structure. The decomposition of the strengthening structure at increased testing temperatures is accompanied with a reduction in the radiation hardening. But, during short-term tests at T_{test}=400°C the yield strength still does not regain values of ~70 MPa typical of unirradiated materials.

Helium produced by low-temperature neutron irradiation as a result of (n, α) reactions in Cu and Cu-B alloys does not diffuse in the matrix and partially goes into solid solution into complexes of He_mV type and partially is bound into complexes of radiation defects. Decomposition of these complexes at increased temperatures, i.e. T_{test}≥400°C, can result in helium passing to the near-boundary areas and intensify the process of grain-boundary failure.

On the other hand, helium, while trapped by radiation defect complexes, can stabilize the latter. In this case one can expect a slight hardening of samples irradiated to appreciable doses (≥0,5 dpa) and containing considerable amount of helium (≥50 appm) at increased testing temperatures. Such hardening is observed also in our experiment. It should be noted that helium embrittlement is determined by the interaction of two factors, i.e. the size of helium bubbles at grain-boundaries and the level of applied stresses [*18,21*]. Hence, copper hardening will also strengthen helium embrittlement.

Thus, the observed embrittlement of neutron-irradiated Cu-B samples at T_{test}=400°C is determined, first, by helium accumulation on the grain boundaries (that is why, it is observed only for Cu-B alloys and is lacking in pure copper). Besides, hardening of Cu-B alloys plays a role in strengthening of helium embrittlement due to dislocation networks stabilized by helium in the matrix.

As far as the estimation of the manifestation of purely helium embrittlement in copper is concerned, of prime interest are surely the results of testing of neutron-irradiated and annealed samples and samples saturated with helium on the cyclotron, for which the effect of radiation hardening is negligible.

The Effect of Testing Temperature and Helium Concentration - The strength of the irradiated specimens in the present study was significantly reduced at elevated test temperatures (400°C) compared to tensile testing at 100°C. Isochronal tensile test studies on irradiated Cu-B alloys have shown that the room temperature strength decreases rapidly for annealing temperatures above 250°C [*10,20*]. Half of the yield strength increase measured at room temperature was annealed out after a few minutes exposure at 300°C [*10,20*]. This decrease in radiation hardening can be attributed to annealing of the small vacancy-type defect clusters created by the neutron irradiation.

Samples of pure copper and Cu-B alloys irradiated to 1 dpa at T_{irr}=90°C and then annealed at 800°C have throughout the testing temperature range (20÷600°C) the same yield strength as or even somewhat less than unirradiated samples (Fig.1). Thus, embrittlement of irradiated and annealed samples is likely to be determined only by the size and density of helium bubbles produced therein (i.e. it depends on helium concentration). In fact, the annealed samples of Cu-B2 alloy (Cu=300 appm) regularly have at T_{test}=400°C÷600°C lower ductility than Cu-B1 alloy samples (Cu=80 appm) (Fig.3). These samples are also characterized by a monotonic drop in ductility with a rise in testing temperature, this being typical of helium embrittlement manifestation. Thus, annealing of irradiated Cu-B alloy samples containing appreciable amounts of helium (~80÷300 appm) results in the formation of helium bubbles at grain boundaries, which grow effectively in the process of high-temperature testing, as seen from TEM (Figs.7c,d). A growth of pores over the grain boundaries, when under stress, causes a sample to fail.

In Fig.9 we sum up our results and those obtained by G. Carpenter and R. Nicholson [*8*] during investigation of irradiated Cu-B alloys. The first to note is that at low testing temperatures T_{test}=20÷200°C samples with helium do not practically embrittle. At increased testing temperatures in samples containing appreciable amount of helium there is observed a distinct helium embrittlement. As also follows from Fig.9, at a small helium concentration of 0÷2,5 appm no essential drop in ductility of Cu-B alloys is observed up to T_{test}=700°C.

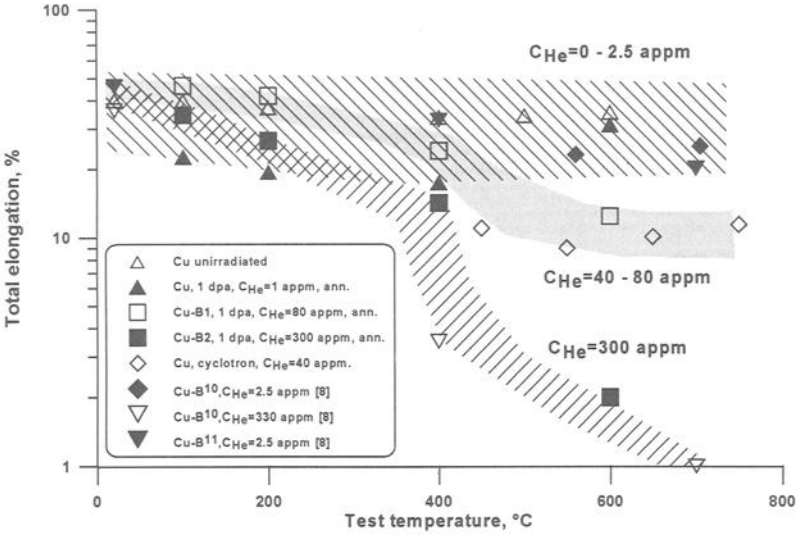


Fig. 9 The effect of test temperature and helium concentration on the embrittlement of copper.

At a helium content of ~40÷80 appm copper samples demonstrate nearly a twice decrease in ductility at T_{test}≥450°C, but note that the level of total elongation of materials up to T_{test}=750°C remains rather high, i.e. ~10%.

At higher helium concentrations of ~300 appm the Cu-B alloy demonstrates a strong embrittlement at T_{test}≥400°C. At T_{test}=700°C the total elongation of the Cu-B alloy amounts to only 1%. Fig.9 shows, in addition to the results of testing of neutron-irradiated and annealed samples, copper samples saturated with helium on the cyclotron (i.e. at ~0,05 dpa damage). Obviously, their ductility is practically the same as for samples irradiated with neutrons to 1 dpa and then annealed, with helium concentrations therein being close. Thus, in these samples it is the helium concentration that is crucial in embrittlement. A temperature of 400°C, at which an appreciable decrease in ductility of samples with 40÷300 appm He starts to be observed, can be considered as a transient temperature of the commencement of helium embrittlement manifestation in helium.

Reasons for DS Alloys' High Resistance to Embrittlement - The presented data on the effect of accumulation of ~60÷100 appm He on the properties of DS copper alloys

GlidCopAl25IG0 and MAGT0.2 allows for the conclusion that DS copper alloys possess extremely high resistance to helium embrittlement. Let's analyze possible mechanisms for suppression of helium embrittlement in DS copper alloys. As follows from the results of the study, doping of copper with aluminum does not suppress helium embrittlement. Binary alloy Cu-0.2Al demonstrated a strong tendency to helium embrittlement with only 20 appm He. Its ductility at increased testing temperatures $T_{test} \geq 750°C$ was low ($\delta_{tot} \sim 5 \div 2\%$) and did not recover after annealing.

High resistance of DS copper alloys to helium embrittlement might be attributable to the manufacturing technology (powder metallurgy) providing an extremely fine-grained (~5 μm) material structure. But, when comparing the structures of Cu-B2 alloy and MAGT0.2 (Fig.8b and 8d), it becomes apparent that Cu-B2 alloy also has a very fine-grained structure, but, still, is strongly susceptible to helium embrittlement.

On the other hand, it follows from Fig.8, that MAGT0.05 alloy produced by the same technology as MAGT 0,2 alloy is still distinctly prone to helium embrittlement. Since in MAGT 0,05 alloy the density of strengthening particles is essentially (by more than a factor of 10) less than in MAGT 0,2 alloy, the conclusion is reasonable that the main advantage of DS alloys is the high density of hardening particles providing their resistance to helium embrittlement.

Conclusion

The present study indicates that the maximum temperature for copper or copper alloys in fusion energy structural applications may be limited to ~400°C, due to helium embrittlement concerns associated with the high helium generation rate in a D-T fusion neutron spectrum.

The obtained data make it possible to assess the threshold temperature of helium embrittlement manifestation for pure copper as T_{thres}=400°C, and the threshold helium concentration C_{thres} as 40 appm. But it is well to bear in mind that these data were obtained under short-term testing conditions. During long-term loading under fusion reactor operation conditions a reduction both in T_{thres} and C_{thres} is to be expected. Thus, a high rate of helium accumulation in the ITER spectrum might limit the life time for pure copper to temperatures of $\leq 300 \div 400°C$. For a real estimation of T_{thres} helium-saturated samples should be tested for long-term strength and fatigue at increased temperatures.

The conclusion can be drawn that overheating and thermal conductivity degradation during operation, caused by neutron irradiation, would allow helium embrittlement to have a definite effect on copper alloys lifetime. In addition, the contribution of radiation defects into high-temperature radiation embrittlement needs to be estimated. For this purpose, alloys with high helium production (Cu-Be, Cu-Be-Ni) should be studied after irradiation in a mixed spectrum reactor. The main features of helium embrittlement in copper alloys are similar to results previously obtained in other FCC materials.

DS alloys are characterized by high resistance to helium embrittlement up to T_{test}=950°C and $C_{he}=60 \div 100$ appm due to high stability of the structure of these alloys at

high-temperature heating and high density of strengthening Al_2O_3 particles effectively confining helium in the matrix.

Acknowledgements

The authors thank B.N.Singh and V.R. Barabash for fruitful discussions, V.P. Chakin for assistance with the tensile testing of the neutron-irradiated specimens, and G.T. Zhdah and V.F. Reutov for their assistance with the cyclotron irradiations. This research was sponsored in part by the Office of Fusion Energy Sciences, U.S. Department of Energy under contracts DE-AC05-96OR22464 with Lockheed Martin Energy Research Corp. and DE-AC06-76RLO 1830 with Battelle Memorial Institute.

References

[1] Zinkle, S. J. and Fabritsiev, S. A., 1994, "Copper Alloys for High Heat Flux Structure Applications", *Atomic and Plasma Materials Interaction Data for Fusion* (supplement to the journal Nuclear Fusion) Vol. 5, pp. 163-192.

[2] Ames, M., Kohse, G., Lee, T. S., Grant, N. J. and Harling, O. K., 1986, *J. Nucl. Mater.* Vol.141-143, pp. 174-177.

[3] Brager, H. R., Heinisch, H. L. and Garner, F. A., 1985, *J. Nucl. Mater.* Vol.133-134, pp. 676-679

[4] Brager, H. R., 1986, *J. Nucl. Mater.* Vol. 141-143, pp. 79-83.

[5] Fabritsiev, S. A., Pokrovsky, A. S., Barabash, V. R. and Prokofiev, Yu. G., 1997, *Fusion Eng. and Design,* Vol. 36, pp. 505-513

[6] Ullmaier, H., 1984, *Nuclear Fusion*, Vol. 24, pp. 1039-1065.

[7] Zinkle, S. J., Farrell, K. and Kanazawa, H., 1992, *J. Nucl. Mat.* Vol. 179-181 pp. 994-998.

[8] Carpenter, G. J. C. and Nicholson, R. B., 1969, "An Investigation of the Nucleation and Growth of Gas Bubbles in Metals and Their Effects on Mechanical Properties Using Model System", *Radiation Damage in Reactor Materials*, Vol. II (IAEA, Vienna,1969) pp. 383-400; also G.J.C. Carpenter and R.B. Nicholson, *report AECL-3331* (Chalk River, Ontario, 1969)

[9] Muroga, T., Watanabe, H., Yoshida, N., Kurishita, H. and Hamilton, M. L., 1995, *J. Nucl. Mater.* Vol. 225, pp. 137-145.

[10] Vela, P. and Russell, B., 1966, *J. Nucl. Mater.* Vol.19, pp. 312-321.

[11] Vela, P., Hardy, J. and Russell, B., 1968, *J. Nucl. Mater.* Vol. 26, pp. 129-137.

[12] Barry, D.E., 1971, *Phil. Mag.* Vol. 23, pp. 495-499.

[13] Viswanathan, B., Amarendra, G. and Gopinathan, K. P., 1989, *Rad. Effects,* Vol. 107, pp. 121-123.

[14] Fabritsiev, S. A., Pokrovsky, A. S., Zinkle, S. J., Edwards, D. J., 1996, *J. Nucl. Mater.* Vol. 233-237, pp. 513-518.

[15] Fabritsiev, S. A., Karasiov, A. V., 1996, *J. Nucl. Mater.* Vol. 233-237, pp. 1481-1485.

[16] Barry, D. E. and Eyre, B. L., 1970, *Phil. Mag.* Vol. 22, pp. 717-720.

[17] Singh, B. N., Eldrup, M. and Möslang, A.,1993, " Effect of Hot Implantation of Helium in Copper on Bubble formation within Grains and on Grain Boundaries", *Effects of Radiation on Materials, ASTM STP 1175,* A. S. Kumar et al. Ed's., American Society for Testing and Materials, Philadelphia, 1993, pp. 1061-1073.

[18] Barnes, R. S., 1965, *Nature*, Vol. 206, pp. 1307-1308.

[19] Hyam, E. D. and Sumner, G., 1962, *Radiation Damage in Solids*, Vol. 1 (IAEA, Vienna, 1962) p. 323.

[20] Hasegawa, M., Koiwa, M. and Harabayashi, M., 1971, *Trans. Jap. Inst. Metals*, Vol. 12, pp. 39-43.

[21] Fabritsiev, S. A. and Yaroshevich, V. D., 1986, *Strength of Materials*, Vol. 18, pp 1194-2001.

Seppo J. Tähtinen,[1] Mika T. Pyykkönen,[1] Bachu N. Singh,[2] and Palle Toft[2]

Effect of Neutron Irradiation on Tensile and Fracture Toughness Properties of Copper Alloys and Their Joints with Stainless Steel

Reference: Tähtinen, S. J., Pyykkönen, M. T., Singh, B. N. and Toft, P., **"Effect of Neutron Irradiation on Tensile and Fracture Toughness Properties of Copper Alloys and Their Joints with Stainless Steel,"** *Effects of Radiation on Materials: 19th International Symposium, ASTM STP 1366,* M. L. Hamilton, A. S. Kumar, S. T. Rosinski, and M. L. Grossbeck, Eds., American Society for Testing and Materials, West Conshohocken, PA, 2000.

Abstract: Dispersion strengthened (CuAl25) and precipitation hardened (CuCrZr) copper alloys are being considered as candidate materials for the first wall and divertor components of ITER. In the present work, the tensile and fracture resistance properties of CuAl25 and CuCrZr alloys and their joints with 316LN stainless steel have been studied in the unirradiated and neutron irradiated conditions. The joints were produced by hot isostatic pressing (HIP) at 960°C for 3 hours at a pressure of 120 MPa. Test specimens of the base materials CuAl25 and CuCrZr alloys and of the joints (CuCrZr / 316LN and CuAl25 / 316LN) were irradiated with fission neutrons in the DR-3 reactor at Risø in the temperature range from 50°C to 350°C to a displacement dose level of about 0.3 dpa (NRT). Tensile specimens of these alloys were tested at temperatures in the range of 50°C to 350°C. Fracture resistance curves were determined using three point bend tests on specimens of the base materials and of the joints. Tensile and fracture toughness results, together with the metallography of the joints will be presented. Implications of these results and the deformation mechanisms will be briefly discussed.

Keywords: tensile strength, fracture toughness, copper alloys, austenitic stainless steel, hot isostatic pressing, joints, neutron irradiation

Introduction

The current design for ITER utilises copper alloys in the first wall and divertor components. The function of the copper alloy in the first wall is mainly to dissipate heat produced by plasma disruptions and therefore the copper alloy is not designed to provide structural support for the first wall. However, the copper alloy for the divertor is

[1]VTT Manufacturing Technology, P.O.Box 1704, FIN-02044 VTT, Finland.
[2]Risø National Laboratory, Materials Research Department, DK-4000 Roskilde, Denmark.

Copyright© 2000 by ASTM International www.astm.org

designed not only for heat dissipation but also for structural support of the divertor cassette. The anticipated range of operating temperature for copper alloys in the first wall and divertor cassette is from 100°C to 350°C.

On the basis of the currently available data, the dispersion strengthened CuAl25 alloy is being considered as the primary candidate alloy for the first wall. The precipitation hardened CuCrZr alloy has been chosen as the backup (alternate) alloy. Within the frame work of the ITER technology programme, screening experiments have been carried out to determine the effect of irradiation on the physical and mechanical properties of these alloys [1-4]. Some of the earlier experimental results on these alloys have been reviewed in [5]. Recently, results on the effect of irradiation on the low cycle fatigue behaviour have also become available [6-7]. However practically nothing on the effect of irradiation on the fracture toughness behaviour of these alloys has been reported in the open literature. Recently this problem has been investigated [8] and the effect of irradiation on tensile as well as fracture toughness behaviour of CuAl25 and CuCrZr alloys are presented in this report.

The candidate method for joining the copper alloy heat sink to the stainless steel primary wall module has been chosen to be Hot Isostatic Pressing (HIP). A limited number of experimental results on the mechanical performance of HIP joints between copper alloys and stainless steel have shown that the failure does not occur at the joint (i.e. interface between copper and stainless steel) but in the copper matrix [9-11].

Materials and Experimental Procedures

Two types of copper alloys, namely dispersion strengthened GlidCop® CuAl25 IG0 (ITER grade 0, produced by OMG Americas formerly SCM Metal Products Inc.) and precipitation hardened CuCrZr (produced by Outokumpu Oy), and their joints with austenitic stainless steel 316LN IG0 were studied. The chemical analysis of these materials is shown in (Table 1). The CuCrZr alloy plate (40 mm thick) was produced by conventional melting and hot rolling. The plate was solution annealed (F) at 960°C for 1 hour, water quenched and aged at 460°C for two hours and then air cooled. The CuAl25 IG0 alloy plate (20 mm thick) was produced by powder metallurgy followed by extrusion and cross rolling. The plate was heat treated (D) at 980°C for 2 hours.

Table 1 - *Chemical analysis (percent by weight)*

Alloy	Fe	Cr	Ni	Si	Mn	Mo	Zr	C	P	S	Al_2O_3	B_2O_3	Cu
CuCrZr	0.008	0.78					0.13		0.005	0.0005			bal
CuAl25 IG0											0.46	0.02	bal
316LN IG0	bal	17.3	12.2	0.35	1.70	2.35		0.032	0.025	0.002			

The joints between copper alloys and austenitic stainless steel type 316LN IG0 were produced by the HIP method at 960°C for 3 hours at a pressure of 120 MPa. The joints

between CuCrZr alloy and stainless steel were additionally heat treated at 460°C for 2 hours after the HIP treatment.

Test specimens were cut by electric wire discharge machining from the plates of the above described copper alloys and from the joints. The tensile and the fracture toughness specimens of the joints were cut from the joints such that the tensile axis was oriented perpendicularly across the joint in tensile tests and crack propagation occurred along the joint interface during fracture toughness tests. The dimensions of the thin foil tensile and single edge notched bend SEN(B) fracture toughness specimens are shown in (Figure 1). The tensile specimens of CuAl25 IG0 and CuCrZr alloys were tested in an INSTRON machine at a strain rate of 1.3×10^{-3} s^{-1}. Tensile testing at elevated temperatures was carried out in a vacuum of 10^{-5} torr. The fracture toughness specimens were 20% side grooved to enhance planar crack growth and constraint. The prefatigued crack length to specimen width ratio is about 0.5. Fracture resistance curves were determined using the displacement controlled three point bend testing with a constant displacement rate of 1.5×10^{-2} mm/min. Fracture resistance testing at elevated temperatures was carried out in a silicon oil bath. Load, displacement and crack length were measured during testing using the direct-current potential difference (DC-PD) method. Fracture resistance curves were determined following the ASTM Standard Test Method for J-Integral Characterization of Fracture Toughness, E 1737-96.

Both tensile and fracture toughness specimens of CuCrZr and CuAl25 IG0 were irradiated with fission neutrons in the DR-3 reactor at Risø National Laboratory at temperatures in the range of 50-350°C to a neutron fluence of $1.5\text{x}10^{24}$ n/m^2 (E > 1 MeV) corresponding to a displacement dose of 0.3 dpa (NRT). Irradiations were carried out with a neutron flux of $2.5\text{x}\ 10^{17}$ n/m^2s corresponding to a damage rate of $5\text{x}10^{-8}$dpa (NRT)/s. Irradiations were performed in a helium or a mixture of helium and argon atmosphere. Irradiations at 200°C and 350°C were carried out in a temperature controlled rig where the irradiation temperature was monitored, controlled and recorded continuously throughout the irradiation period.

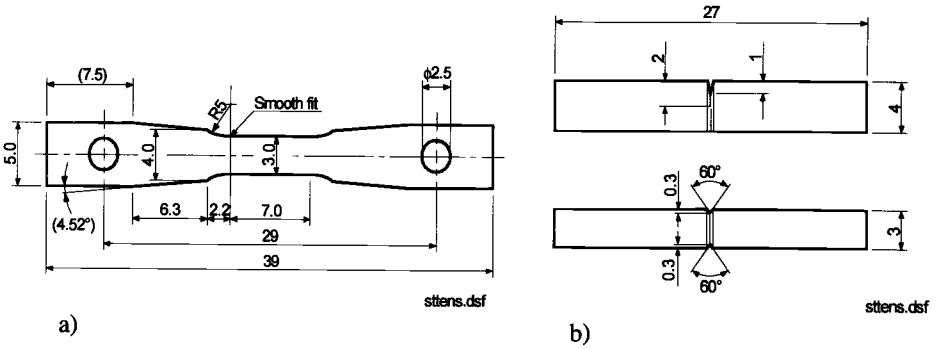


Figure 1 - *Dimensions of a) tensile and b) fracture toughness specimens.*

Results

Microstructure

The microstructure of the copper alloys is shown in (Figure 2). The two copper alloys with different processing histories also have clearly different microstructures. The powder metallurgy alloy CuAl25 IG0 had strongly elongated grain structure along the original extrusion direction with an average subgrain size of about 1 μm. The conventionally produced alloy CuCrZr had equiaxed grains with average grain size of about 150 μm.

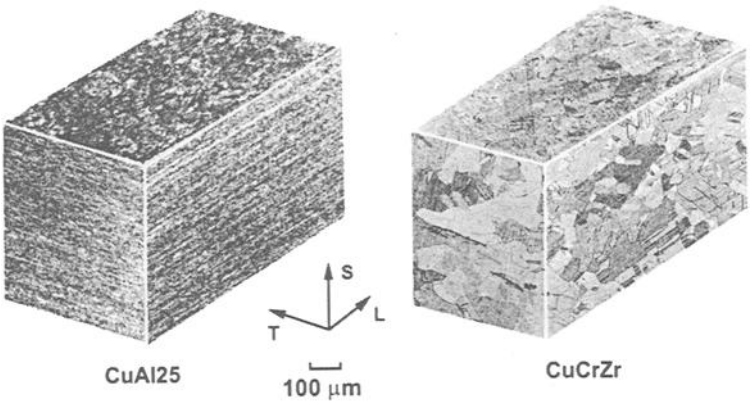


Figure 2 - *Optical micrographs of CuAl25 IG0 and CuCrZr alloys. The extrusion or hot rolling direction is indicated by direction L and direction T and S are transverse and short transverse directions, respectively.*

The microstructures of the HIP joints between copper alloys and austenitic stainless steel after HIP thermal cycle are shown in (Figure 3). During the HIP thermal cycle the diffusion of elements across the joint interface resulted in a different microstructure close to the joint interface depending on the alloying elements of the copper alloy. The HIP joint of the CuCrZr alloy was characterized by precipitation of zirconium rich carbonitrides at the joint interface, formation of a thin ferrite layer within the austenitic stainless steel side and a precipitate free zone within the copper alloy side of the joint interface. The redistribution of alloying elements and the thickness of the ferrite layer formed during the HIP thermal cycle can be clearly seen in the EDX analysis taken across the joint interface. The ferrite layer has enriched chromium and depleted nickel contents and the thickness of the ferrite layer was about 5 μm. The corresponding HIP joint of the CuAl25 IG0 alloy was characterized by the formation of iron and chromium rich precipitates in the copper alloy within a distance of about 30 μm from the joint interface as can be seen in (Figure 3). No ferrite phase was observed within the austenitic stainless steel.

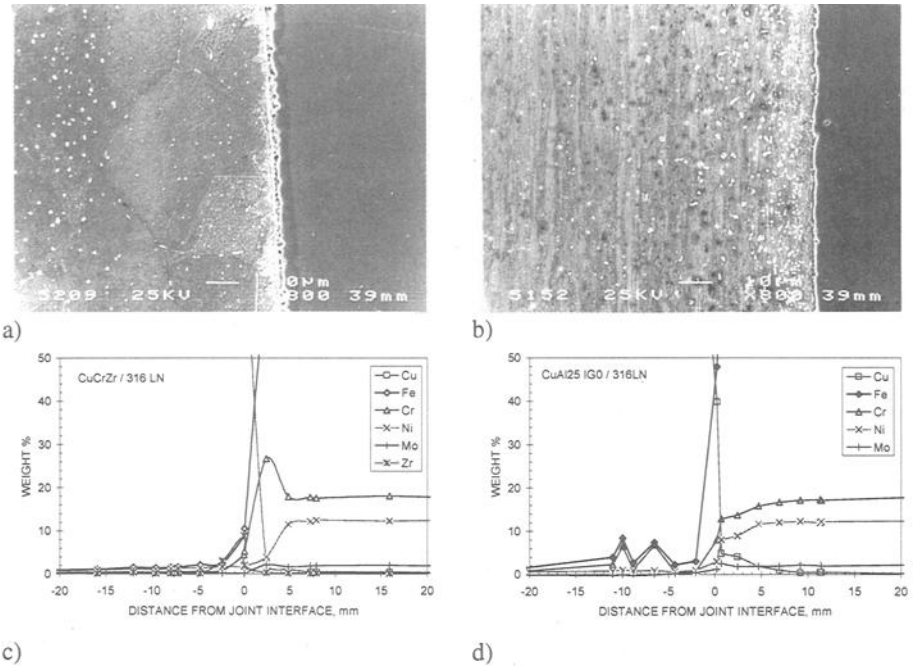


Figure 3 - *SEM micrographs and corresponding EDX analysis across the HIP joint interfaces between copper alloys a) CuCrZr, b) CuAl25 IG0 and austenitic stainless steel 316LN IG0. Thermal HIP cycle was performed at 960°C for 3 hours for both copper alloy joints followed by subsequent heat treatment at 460°C for 2 hours for CuCrZr alloy joint.*

Tensile Tests

Tensile results for the unirradiated CuCrZr and CuAl25 IG0 alloys tested at 22°C, 200°C and 350°C are quoted in (Table 2). Table 2 also contains the results for CuCrZr and CuAl25 IG0 alloys irradiated at 200°C and 350°C to a displacement dose level of 0.3 dpa and tensile tested (in vacuum) at the irradiation temperature. It should be pointed out that the $\sigma_{0.2}$ yield stress for CuCrZr increases significantly due to irradiation at 200°C whereas the irradiation at 350°C causes a noticeable softening of CuCrZr alloy. It should be also mentioned that the CuCrZr alloy irradiated and tested at 200°C does not exhibit any work hardening; on the contrary, it has a tendency to work soften. The specimen irradiated at 350°C on the other hand, shows significant amounts of work hardening when tested at 350°C. The corresponding stress-strain curves of CuAl25 IG0 and CuCrZr alloys in unirradiated and irradiated conditions are shown in (Figure 4). It should be noted that CuAl25 IG0 specimens irradiated and tested at 200°C also suffer from work softening.

Table 2 - *Tensile properties of unirradiated and irradiated CuCuZr and CuAl25 IG0 alloys in T-L orientation.*

Material	Irradiation Dose dpa	Irradiation Temperature °C	Testing Temperature °C	0.2 % Strength MPa	Tensile Strength MPa	Total Elongation %	Uniform Elongation plastic %
CuCrZr	-	-	22	265	370	22.0	19.8
	-	-	200	223	290	18.6	16.5
	-	-	350	213	263	17.5	14.9
	0.3	200	200	349	349	6.3	0.7
	0.3	350	350	187	233	19.0	14.5
CuA125 IG0	-	-	22	356	426	20.0	14.5
	-	-	200	272	290	17.0	6.8
	-	-	350	228	238	43.0	2.5
	0.3	200	200	343	375	14.4	1.3
	0.3	350	350	189	203	10.6	3.8

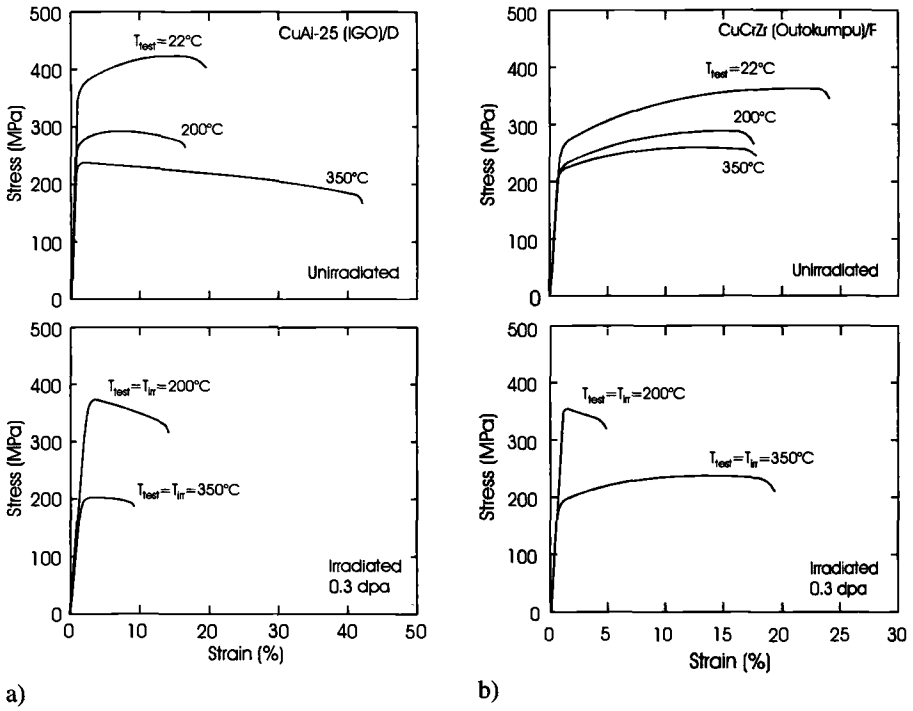


Figure 4 - *Tensile stress strain curves of a) CuAl25 IG0 (T-L) and b) CuCrZr (T-L) alloys in unirradiated and neutron irradiated condition at different temperatures. Note that the irradiation at 200°C causes work softening and induces plastic instability in both alloys.*

Fracture Toughness Tests

Typical experimental data showing the applied load and DC-PD potential difference versus load line displacement measured during fracture toughness experiment at 22°C are shown in (Figure 5). The data were used to identify the fracture initiation point and to calculate values of fracture toughness for the copper alloys and their joints with stainless steel. The crack initiation point is indicated by point (A) where the electrical potential deviated from the initial linear portion of the potential-load line displacement curve. For the CuCrZr alloy a "two-slope" behavior was observed and the crack initiation is associated with the second linear portion of the potential-load line displacement curve. It is noteworthy that fracture initiation in the CuAl25 IG0 alloy occurred at significantly lower displacement values compared to CuCrZr alloy.

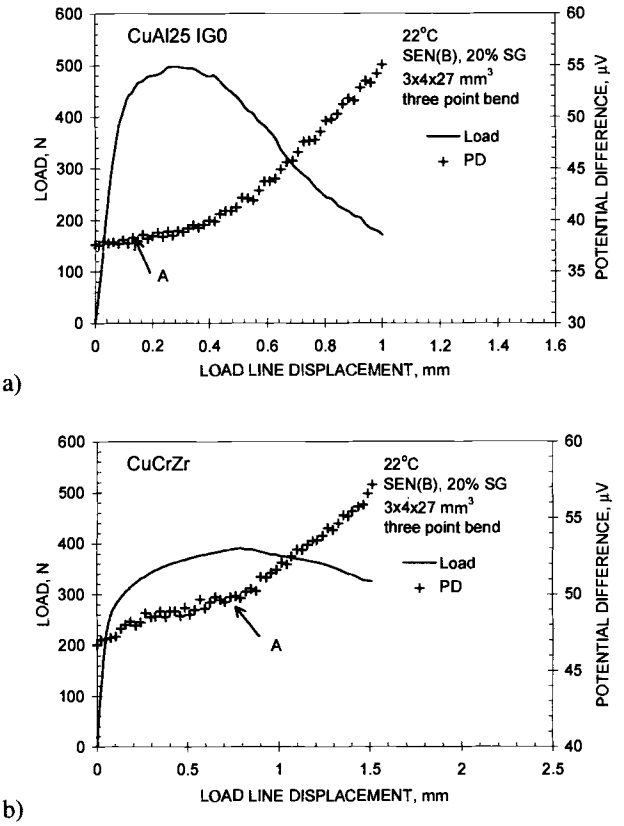


Figure 5 - *Typical experimental load and potential difference data used to calculate fracture toughness of CuAl25 IG0 and CuCrZr alloys at 22°C. Point A is associated with crack initiation.*

It was also evident that extensive plasticity e.g. crack tip blunting was needed in CuCrZr alloy to initiate ductile crack growth whereas practically no crack tip blunting occurred in CuAl25 IG0 alloy prior to crack propagation. The fracture surfaces of SEN(B) specimens of CuAl25 IG0 in the L-T, T-L and S-T orientation tested at room temperature are shown in (Figure 6). The fracture was a ductile dimple fracture. However, the appearance of the fracture surfaces in the L-T and T-L orientations were characterized by delaminations perpendicular to the fracture surface and along the direction of crack propagation whereas a layered structure was observed in the S-T orientation. The details in fracture surface morphology correspond with microstructure with strongly elongated grain structure along longitudinal or original extrusion direction. No such orientation dependency in fracture surface morphology was observed in the CuCrZr alloy.

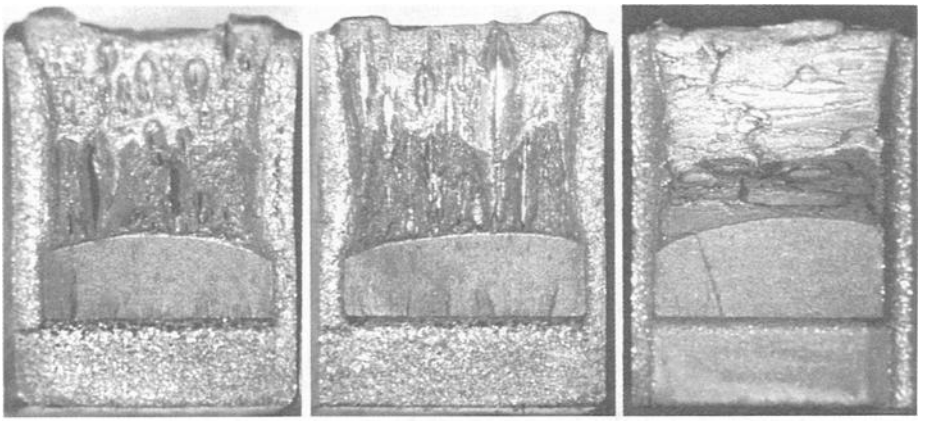
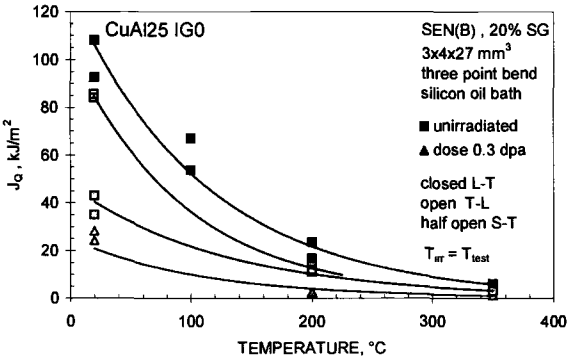


Figure 6 - *Optical micrographs showing the fracture surfaces of SEN(B) specimens of CuAl25 IG0 in different orientations a) L-T, b) T-L and c) S-T after fracture toughness testing at 22°C.*

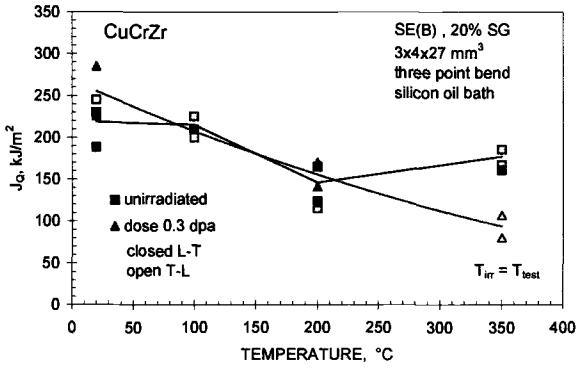
The effect of temperature, specimen orientation and neutron irradiation on the initiation fracture toughness, J_Q, for copper alloys is shown in (Figure 7). The CuAl25 IG0 alloy showed marked anisotropy in fracture toughness properties. In the L-T orientation the fracture toughness was somewhat higher than in the T-L orientation but in the S-T orientation the fracture toughness was markedly lower in the temperature range of 22°C to 350°C. The anisotropy in fracture toughness decreased with increasing temperature. The fracture toughness of CuAl25 IG0 alloy in the T-L and L-T orientations was relatively high at ambient temperature, on average 92 kJ/m^2, and decreased continuously with increasing temperature to about 6 kJ/m^2 at 350°C. In the S-T orientation the corresponding fracture toughness values were 40 kJ/m^2 and 2,5 kJ/m^2, respectively. A minimum in J_Q was not observed in the temperature range studied. On the other hand, CuCrZr alloy showed only a moderate orientation dependency of initiation fracture toughness. At ambient temperature the fracture toughness of CuCrZr

alloy was about 220 kJ/m^2 and decreased first to about 130 kJ/m^2 at 200°C and remained at about 170 kJ/m^2 at the test temperature of 350°C

A marked decrease in fracture toughness of CuAl25 IG0 alloy due to neutron irradiation to the dose level of 0.3 dpa was observed at temperatures in the range from 22°C to 350°C. Due to irradiation the fracture toughness of CuAl25 IG0 alloy decreased to about 26 kJ/m^2 at ambient temperature and to about 1.3 kJ/m^2 at 350°C. No significant effect of neutron irradiation was observed in the fracture toughness of CuCrZr alloy at or below 200°C. However, a clear decrease in fracture toughness was observed at the irradiation and test temperature of 350°C. Fracture toughness of CuCrZr alloy in the unirradiated condition was about 170 kJ/m^2 which decreased due to neutron irradiation to about 95 kJ/m^2 at 350°C. No changes in fracture mode were observed due to irradiation.



a)

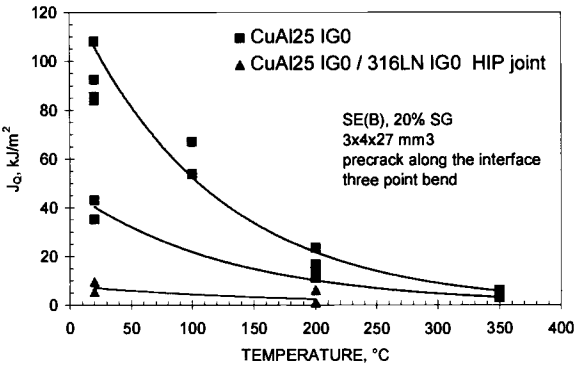


b)

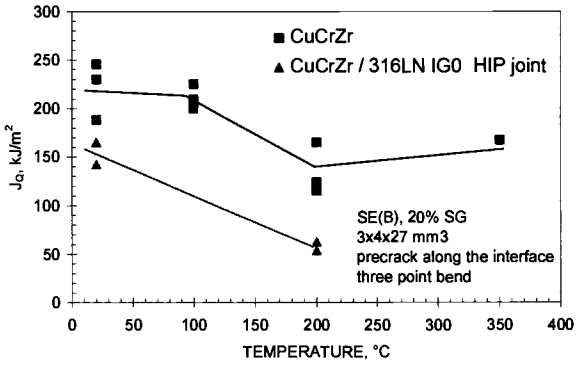
Figure 7 - *Effect of temperature, specimen orientation and neutron irradiation (dose 0.3 dpa) on initiation fracture toughness J_Q of a) CuAl25 IG0 and b) CuCrZr alloy.*

The effect of temperature on the initiation fracture toughness for copper alloys to stainless steel HIP joints is shown in (Figure 8). A significant reduction in the fracture toughness of both copper alloy HIP joints were observed at temperatures in the range 22°C to 350°C compared to the corresponding base copper alloys. The fracture toughness of CuCrZr alloy HIP joints was higher than that of CuAl25 IG0 alloy HIP joints. The HIP joints of CuAl25 IG0 showed very low fracture toughness of about 7 kJ/m^2 already at ambient temperature which further decreased to about 3 kJ/m^2 at 200°C. In the case of CuCrZr the fracture toughness at ambient temperature and at 200°C was 150 kJ/m^2 and 60 kJ/m^2, respectively.

Examination of fracture surfaces after fracture toughness tests showed that crack propagation did not occur at the joint interface but close to the interface on the copper alloy side of the joint interface. In CuAl25 IG0 alloy cracks propagated parallel to the joint interface and in CuCrZr alloy crack propagation seemed to deviate from the joint interface as can be seen in (Figure 9). It should be pointed out that the HIP joint



a)



b)

Figure 8 - *Effect of temperature on initiation fracture toughness, J_Q, of HIP joints of a) CuAl25 IG0 and b) CuCrZr alloy and 316LN IG0 austenitic stainless steel.*

geometry of the plate to plate type which leads to a S-T or S-L orientation of the fracture in reference to the copper alloy part of the joint. Therefore, the properties of the HIP joints should be compared with short transverse properties of corresponding copper alloys.

The effect of neutron irradiation on the fracture resistance behavior of the copper alloys to stainless steel HIP joint specimens can be seen in corresponding load versus load line displacement curves shown in (Figure 10). The CuAl25 IG0 HIP joint specimens showed a 'brittle-like' behavior with sudden drop in load at low displacement values compared to unirradiated HIP joint specimens. However, the fracture mode was ductile and the fracture surface morphology was similar to those of unirradiated HIP joints or base alloy in the S-T orientation. On the other hand the CuCrZr alloy HIP joint specimens showed extensive plasticity similar to unirradiated HIP joints or base alloy specimens. The preliminary examination of the irradiated fracture surfaces of HIP joint specimens indicated that ductile fracture occurred within the copper alloy side of the joint. Neutron irradiation reduced the fracture toughness of both copper alloys to stainless steel HIP joint when compared to fracture toughness of unirradiated HIP joints at 22°C shown in (Figure 11).

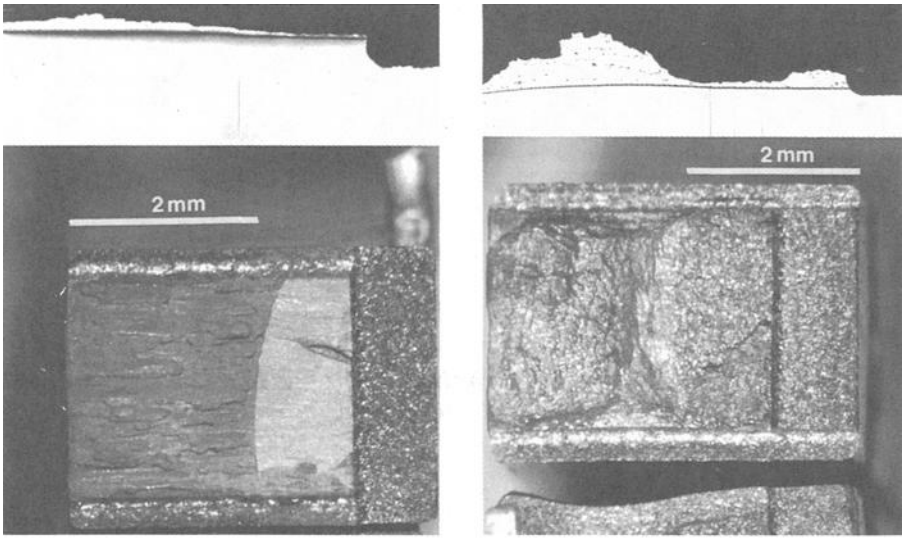
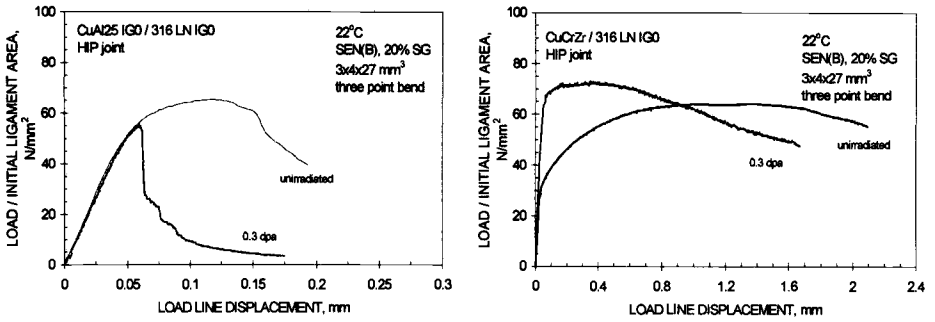
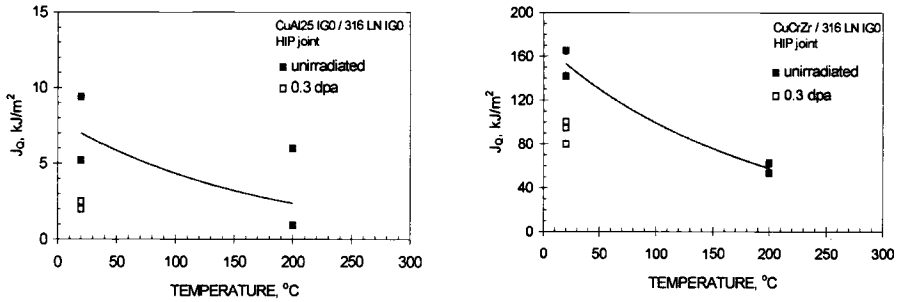


Figure 9 - *SEM and optical micrographs showing the fracture surfaces and cross sections of the HIP joints of a) CuAl25 IG0 and b) CuCrZr alloy and 316LN IG0 austenitic stainless steel after fracture toughness tests at 22°C.*



a) b)

Figure 10 - *Load versus load line displacement curves recorded during fracture resistance tests of HIP joint specimens of a) CuAl25 IG0 and b) CuCrZr with austenitic stainless steel 316LN IG0. HIP was performed at 960°C for 3 hours at pressure of 120 MPa and CuCrZr HIP joints were additionally heat treated at 460°C for 2 hours.*



a) b)

Figure 11 - *Effect of temperature and neutron irradiation (dose 0.3 dpa) on initiation fracture toughness J_Q of HIP joint of a) CuAl25 IG0 b) CuCrZr with 316LN IG0 austenitic stainless steel.*

Discussion

Microstructure

The microstructures of the conventionally produced CuCrZr and powder metallurgically produced CuAl25 IG0 alloys are markedly different from each other. The detailed microstructural studies of these copper alloys have been presented in [4]. The conventionally produced precipitation hardened CuCrZr alloy has a well defined

microstructure with uniformly distributed coherent precipitates and average equiaxed grain size of about 150 μm. The powder metallurgy produced dispersion strengthened CuAl25 IG0 alloy has a strongly elongated heterogeneous microstructure with an average subgrain size of about 1μm. There is also notable heterogeneity in the size, density and spatial distribution of incoherent aluminum oxide particles as well as in the grain size due to the manufacturing processes e.g. internal oxidation, extrusion and cross rolling processes used to produce the alloy. The heterogeneity due to manufacturing processes results in a layered microstructure along the short transversal direction of the plate which is clearly seen in microstructure (Figure 2) and in orientation dependency of fracture surface morphology in fracture toughness tests (Figure 6).

The applied HIP thermal cycle at 960°C is a commonly used solution annealing temperature for CuCrZr alloy where most of the coherent precipitates of zirconium and chromium dissolves in copper matrix. Zirconium atoms have high affinity for nitrogen and carbon atoms which became available from the stainless steel side of the joint and zirconium readily reacts to form carbonitrides which precipitates at the joint interface. Subsequently, the depletion of the austenite stabilizing elements like nitrogen, carbon and also nickel which diffuses into the copper promotes the austenite to ferrite transformation close to the joint interface. It is also noteworthy that the copper matrix is saturated by chromium which diffuses into stainless steel and enriches the ferrite layer close to the joint interface. On the other hand the applied HIP thermal cycle at 960°C does not dissolve the aluminum oxide particles and during the HIP cycle copper diffuses into stainless steel and iron, chromium, and nickel diffuses into copper and precipitates in copper as iron and chromium rich precipitates.

Mechanical Properties

Tensile strength and ductility of both copper alloys decrease continuously with increasing temperature in the unirradiated condition. The unirradiated CuAl25 IG0 alloy shows limited work hardening ability with increasing temperature whereas no changes in work hardening properties of unirradiated CuCrZr alloy can be observed. It is noteworthy that uniform elongation decreases more steeply with increasing temperature in CuAl25 IG0 than that in CuCrZr alloy.

Neutron irradiation is known to induce lattice defects in the form of clusters, loops and tetrahedrals which cause hardening and loss of tensile ductility in both copper alloys [2]. The hardening was most pronounced at low temperatures (below the recovery stage V ($\sim 0.3T_m$)) and almost no hardening or even softening in tensile test results were observed at 350°C in both copper alloys. At high temperatures where irradiation defects are able to recover, the level of hardening decreases and tensile ductility increases.

Fracture toughness of CuCrZr alloy is higher than that of CuAl25 IG0 alloy at temperatures in the range 22°C to 350°C both in unirradiated and irradiated (0.3 dpa) states. Fracture toughness of unirradiated CuAl25 IG0 alloy decreases continuously with increasing temperature from 22°C to 350°C whereas the fracture toughness of unirradiated CuCrZr alloy remained almost constant at temperatures up to 100°C and

then decreased significantly at 200°C and slightly increased at 350°C. These fracture toughness results are in good accord with earlier results [12-13].

In the CuAl25 IG0 alloy with ultra fine grain size, irradiation induced defects are expected to further retard work hardening ability leading to more extensive strain localization and lower fracture toughness values compared to that of the unirradiated copper alloy. In the CuCrZr alloy, on the other hand, the fracture toughness seems to be almost unaffected at low temperatures. However, at 350°C a significant decrease was observed in the fracture toughness of the irradiated CuCrZr alloy compared to that by the unirradiated condition. In view of the tensile results, the fracture toughness behavior is unexpected. In irradiated CuCrZr alloy, hardening together with a loss of uniform elongation and work hardening ability is expected to result in relatively low fracture toughness values at temperatures below 200°C and on the contrary in relatively high fracture toughness value at 350°C due to recovery of tensile properties. It is expected that due to relatively large grain size dislocation cells and tangles responsible for work hardening and relatively high fracture toughness may form to some extent in the vicinity of the crack tip of SEN(B) specimens of irradiated CuCrZr alloy. At higher temperatures irradiation induced coarsening of precipitates in CuCrZr alloy [1] may also be partly responsible for the observed reduction in tensile strength and also affect the fracture toughness behavior. The effect of irradiation on tensile and fracture toughness behavior of copper alloys is complicated and more experimental studies are needed to explain the observed temperature dependence of the fracture toughness.

The factors controlling the temperature dependency of the fracture toughness of ductile materials can be analyzed by applying stress modified critical strain criterion

$$K_{ICi} = \sqrt{J_{ICi} E'} \approx \sqrt{E' \sigma_{ys} \varepsilon_f l_0} \qquad (1)$$

where fracture is defined when a critical strain ε_f exists over a critical distance l_0 [14]. The initiation fracture toughness K_{ICi} or J_{ICi} can be roughly described by modulus E', yield strength σ_{ys}, and critical plastic strain over a characteristic distance. Parameters like modulus and yield strength have similar temperature dependence in both copper alloys as estimated from the tensile test results and therefore can not explain the different temperature dependencies of fracture toughness behavior in these alloys. It should be emphasized that the critical plastic strain and the characteristic distance play a significant role in determining the temperature dependent fracture toughness behavior. The crack initiation occurs when the local plastic strain exceeds a critical value specific to the relevant stress state. Although, the local critical plastic strain is not directly related to the tensile elongation values, it can be expected, however, from the observed decrease in the uniform elongation in tensile tests that the critical plastic strain is smaller and decreases more rapidly with temperature for CuAl25 IG0 than that for CuCrZr alloy. It is also noted that almost no plasticity e.g. crack tip blunting and stretch zone formation was observed prior to stable ductile crack growth in CuAl25 IG0 alloy compared to CuCrZr alloy where extensive crack tip blunting occurred before crack initiation (Figures 5, 9). The ultra fine grain size, dislocation interactions with dispersoids and grain boundaries, and apparent heterogeneity in particle distribution are expected to favour low work hardening ability which may lead to strain localization and an early increase in the local plastic strain in CuAl25 IG0 alloy compared to that in the CuCrZr alloy. At high stress

levels dislocations may shear through relatively small, weak and thin precipitates in the CuZrZr alloy. Consequently, dislocations may move, interact and form tangles in the CuCrZr alloy in a homogeneous fashion. This would tend to reduce the level and propensity of strain localization in the CuCrZr alloy. In the case of CuAl25 IG0, on the other hand, the presence of very strong and relatively large alumina particles as well as the large spatial variations in the concentration of the particles are likely to accentuate the strain localization.

Fracture toughness of HIP joint is lower than that of corresponding copper alloy. The fracture toughness of HIP joints between CuAl25 IG0 and 316LN is very low even at ambient temperature which indicates the strong anisotropy of CuAl25 IG0 alloy in short transverse direction of the original plate. The analysis of fracture resistance data of HIP joint specimens were based on ASTM E1737-96 procedure originally developed for homogeneous specimens. However, a detailed evaluation of fracture toughness behavior of dissimilar metal joint specimens needs analysis on crack tip stress and strain field and corresponding J-solutions as a function of mismatch of constituent metals. Based on the present preliminary results it seems that fracture toughness behavior of copper alloy to stainless steel HIP joints is determined by the behavior of constituent copper alloys both in unirradiated and irradiated conditions.

Conclusions

The tensile strength and ductility of unirradiated CuAl25 IG0 and CuCrZr alloys decreased with increasing temperature up to 350°C.

Fracture toughness of CuCrZr alloy was higher than that of CuAl25 IG0 alloy at temperatures in the range 22°C to 350°C both in the unirradiated and irradiated (0.3 dpa) states.

Fracture toughness of unirradiated CuAl25 IG0 alloy decreased with increasing temperature from 22°C to 350°C whereas the fracture toughness of unirradiated CuCrZr alloy remained almost constant at temperatures up to 100°C and decreased significantly at 200°C and increased slightly at 350°C.

Neutron irradiation to a dose level of 0.3 dpa resulted in hardening and reduction in uniform elongation to about 2-4% at 200°C in both copper alloys. At higher temperatures softening was observed and uniform elongation increased to about 5% and 16% for CuAl25 IG0 and CuCrZr alloys, respectively.

Fracture toughness of CuAl25 IG0 alloy decreased markedly due to neutron irradiation to dose level of 0.3 dpa at temperatures in the range from 22°C to 350°C. The fracture toughness of the irradiated CuCrZr alloy also decreased in the range from 22°C to 350°C, although it remained almost unaffected at temperatures below 200°C and decreased significantly at 350°C when compared with fracture toughness of unirradiated CuCrZr alloy.

Fracture toughness of HIP joints with stainless steel were lower than that of corresponding copper alloy. Fracture path in HIP joint specimen was always within copper alloy side of the joint. The very low fracture toughness of HIP joints between

CuAl25 IG0 and 316 LN stainless steel is due to the strong anisotropy of CuAl25 IG0 alloy in short transverse direction of the original plate. Neutron irradiation further decreased the fracture toughness of HIP joint specimens at 22°C.

References

[1] Singh, B. N., Edwards, D. I. and Toft, P., "Effects of neutron irradiation on mechanical properties and microstructures of dispersion and precipitation hardened copper alloys," *Journal of Nuclear Materials,* Vol. 238, 1996, pp. 244-259.

[2] Singh, B. N., Edwards, D. I, Eldrup, M. and Toft, P., "Pre- and post-irradiation properties of copper alloys at 250°C following bonding and bakeout thermal cycles," Risø Report, Risø-R-937 (EN), 1997.

[3] Singh, B. N., Edwards, D. I, Eldrup, M. and Toft, P., "Effect of bonding and bakeout thermal cycles on the properties of copper alloys irradiated at 350°C," Risø Report, Risø-R-971 (EN), 1997.

[4] Singh, B. N., Edwards, D. I, Eldrup, M. and Toft, P., "Effects of heat treatments and neutron irradiation on the physical and mechanical properties of copper alloys at 100°C," Risø Report, Risø-R-1008 (EN), 1998.

[5] Fabritsiev, S. A., Zinkle, S. J. and Singh, B. N., "Evaluation of copper alloys for fusion reactor divertor and first wall components," *Journal of Nuclear Materials*, Vol. 233-237, 1996, pp. 127-137.

[6] Singh, B. N., Stubbins, J. F. and Toft, P., "Fatigue performance of copper and copper alloys before and after irradiation with fission neutrons," Risø Report, Risø-R-991 (EN), 1997.

[7] Stubbins, J. F., Singh, B. N. and Toft, P., "Fatigue performance of copper and copper alloys before and after irradiation to 0.3 dpa at 50 and 100°C," *Journal of Nuclear Materials*, to be published.

[8] Tähtinen, S., Pyykkönen, M., Singh, B.N. and Toft, P., "Tensile and fracture toughness propertis of copper alloys and their HIP joints with austenitic stainless steel in unirradiated and neutron irradiated condition," Report VALB282, Technical Research Centre of Finland, Espoo, Finland, 1998.

[9] Sato, S., Kuroda, T., Kurasawa, T., Furuya, K., Togami I. and Takatsu, H., "Mechanical properties of HIP bonded joints of austenitic stainless steel and Cu-alloy for fusion experimental reactor blanket," *Journal of Nuclear Materials,* Vol. 233-237, 1996, pp. 940-944.

[10] Le Marois, G., Burlet, H., Gentzbittel, J.M. Briottet, L. and Saint-Antonin, F., "Advanced joining techniques for ITER modules manufacturing," Note Technique D.E.M. No32/97, CEA/CEREM, Grenoble, 1997.

[11] Lind, A., "Copper powder / stainless steel HIP joining techniques," Studsvik Report M-97-41, Studsvik, 1997.

[12] Solomon, R.R., Troxell, J. D. and Nadkarni, A. V., "GlidCop DSC properties in the tTemperature range of 20-350°C," *Journal of Nuclear Materials,* Vol. 233-237, 1996, pp. 542-546.

[13] Zinkle, S. J. and Alexander, D. J., ITER task related meeting on Development and Irradiation Test of Cu/SS and Be/Cu/SS joints, March 24-26, 1997, Garching.

[14] Ritchie, R.O. and Thompson, A.W., "On macroscopic and microscopic analyses for crack initiation and crack growth toughness in ductile alloys," *Metallurgical Transactions,* 16A, 1985, pp. 233-248.

Author Index

A

Abe, K., 626, 1197
Ahlstrand, R., 98
Aitkhozhin, E. S., 725
Alberman, A., 87
Allen, T. R., 739
Amaev, A. D., 98
Asano, K., 944
Auger, P., 435

B

Baldwin, D. L., 1062
Barbu, A., 816
Bartsch, R., 235
Bischler, P. J. E., 295
Black, C. A., 767
Böhmert, J., 323
Bolton, C. J., 295
Bond, G. M., 884
Brauer, G., 560
Brillaud, C., 87
Brumovsky, M., 56, 220
Budylkin, N. I., 679, 874
Burlet, H., 1093
Busby, J. T., 739

C

Chaouadi, R., 162, 279
Chernobaeva, A. A., 415
Chernov, V. M., 1084
Chin, B. A., 935
Chistiakov, D. A., 98
Chumakov, E. V., 725
Chuto, T., 1197
Čížek, J., 354
Corcoran, R. C., 473
Coste, J.-F., 1029
Cowan, J. R., 473

D

Dalle Donne, M., 1051, 1062
Davies, M., 3
Davies, R. W., 1018
Deydier, D., 87
Dubinin, S. F., 1122, 1131
Dvoriashin, A. M., 874

E

Edens, D. J., 366
Edwards, D. J., 1226
Ehrlich, K., 597, 778
Ellis, D., 383
English, C., 3
Erben, O., 220

F

Fabritsiev, S. A., 1226
Fabry, A., 162, 279
Falcnik, M., 56
Faulkner, R. G., 343, 383, 801, 1003, 1018
Ferguson, P. D., 1109
Flewitt, P. E. J., 343
Fukuzawa, Y., 713

G

Gan, J., 739
Garner, F. A., 655, 667, 679, 699, 767, 792, 850, 859, 874, 884, 1003, 1018, 1109, 1212
Gelles, D. S., 535, 579, 1051, 1062
Gillemot, F., 1137
Gillemot, L., 1137
Golovinov, A. V., 1084
Goodwin, C. C., 801
Goshchitskii, B. N., 1122
Greenwood, L. R., 548, 1062
Grossbeck, M. L., 935
Grosse, M., 323

H

Hamilton, M. L., 579, 1003, 1018, 1109
Hankin, G. L., 1003, 1018
Hardies, R., 143

Copyright© 2000 by ASTM International www.astm.org

Hardouin-Duparc, A., 816
Hasegawa, A., 626, 1197
Hasegawa, M., 560
Hashimoto, T., 973
Hawthorne, J. R., 16
Hempel, A., 560
Henry, J., 816
Hirose, T., 959
Horsten, M. G., 579, 612
Hübner, R., 778

I

Ino, H., 516
Iseki, M., 836
Ishitsuka, E., 1176
Iskander, S. K., 245
Itoh, K., 266

J

Jia, X., 69, 118
Johnson, K. I., 1018
Jones, R. B., 366, 473
Joyce, J. A., 177
Jumel, S., 1029

K

Kano, F., 560
Karpukhin, V. I., 525
Kasada, R., 448, 626
Kato, T., 756
Katoh, Y., 959, 1186
Katsura, R., 944
Kawai, A., 560
Kawamura, H., 988, 1051, 1062, 1075, 1176
Kawanishi, H., 492
Kawano, S., 944
Keilová, E., 354
Kenik, E. A., 739
Kevorkyan, Y. R., 399
Khaleel, M. A., 1018
Kimura, A., 266, 448, 535, 626
Kirk, M., 143
Kobylyansky, G. P., 1159
Kočík, J., 354
Kohyama, A., 959
Konobeev, Y. V., 679, 699, 850, 874
Korolev, Y. N., 415
Kosenkov, V. M., 1159
Koshiishi, M., 944
Krasikov, E., 98
Krasikov, Y. A., 525
Krigan, V. M., 874
Kruglov, A. S., 850
Kryukov, A., 3, 98
Kryukova, L. M., 1084
Kytka, M., 56

L

Langer, R., 235
Lind, A., 1093
Lopuga, A. D., 688
Lott, R., 143
Lucas, G. E., 612

M

Malek, J., 56
Maloy, S. A., 1109
Marmy, P., 343
Materna-Morris, E. I., 597
Matsui, H., 266, 448, 626
Matsukawa, Y., 1147
McCabe, D. E., 245, 306
Meade, D., 383
Miloudi, S., 435, 1029
Mironova, E. G., 679, 874
Mittendorfer, J., 1043
Mochizuki, M., 973
Morimura, T., 448, 626
Morosov, A. M., 98
Murase, Y., 713
Muroga, T., 1186

N

Nagakawa, J., 713
Nagashima, A., 1176
Nagel, G., 235
Nakamichi, M., 988, 1075
Namba, C., 1147
Nanstad, R. K., 245, 306, 415
Narui, M., 448, 959
Naruse, Y., 266
Neustroev, V. S., 645, 792
Nikolaenko, V. A., 525
Nikolaev, V. A., 98
Nikolaev, Y., 3, 399, 415, 460
Nikolaeva, A. V., 399, 460

Ning, G., 118
Nishitani, T., 1176
Noda, N., 1186
Novosad, P., 56, 220

O

Odette, G. R., 612
Ohnuki, S., 756, 919, 1051, 1147, 1212
Oliver, B. M., 1062, 1109
Onizawa, K., 204
Ostrovsky, Z. E., 792

P

Pareige, P., 435, 1029
Parkhomenko, V. D., 1122, 1131
Pavinich, W. A., 76
Pechenkin, V. A., 699
Pecherin, A. M., 792
Pevchikh, Y. M., 850
Pichon, C., 87
Platonov, P., 98
Plazaola, F., 560
Pokrovsky, A. S., 1226
Porollo, S. I., 679, 850, 874
Porter, D. L., 884
Procházka, I., 354
Puigh, R. J., 667
Pyatiletov, Y. S., 688, 725
Pyykkönen, M. T., 1243

R

Rieth, M., 597
Rintamaa, R., 98
Rosinski, S. T., 127, 143
Rybin, V. V., 98

S

Sagawa, H., 1176
Sakaguchi, N., 919
Saneyasu, M., 560
Satou, M., 1197
Scaffidi-Argentina, F., 1051, 1062
Schüle, W., 894
Scibetta, M., 279
Server, W. L., 3, 16, 127, 143
Shamardin, V. K., 645, 792, 1159
Shibayama, T., 535
Shtrombakh, Y., 98, 525
Singh, B. N., 1093, 1243
Sokolov, M. A., 16, 306, 415
Sommer, W. F., 1109
Song, S. H., 343
Soulat, P., 87
Spellward, P., 801
Stepanov, P. A., 1084
Stepanov, V. A., 1084
Stoller, R. E., 548
Sugie, T., 1176
Sumita, Y., 1147
Suzuki, M., 204, 492
Suzuki, T., 266, 959
Swain, R. L., 245

T

Tähtinen, S., 1093, 1243
Takahashi, H., 756, 919, 1147, 1212
Tang, Z., 560
Tavassoli, F., 1093
Teploukhov, S. G., 1122, 1131
Tobita, T., 204
Toft, P., 1243
Toloczko, M. D., 655, 667, 1003, 1018
Tregoning, R. L., 177
Tsuchiya, K., 988

U

Uri, G., 1137

V

Valo, M. J., 98
Van de Velde, J., 162, 279
Van Duysen, J.-C., 435, 1029
Van Osch, E., 579, 612, 1093
Van Walle, E., 162, 279
Victoria, M., 343
Vorobjev, A. N., 679, 874

W

Wallin, K., 98
Walmsley, J. C., 473, 801
Wang, C.-A., 935

Wang, J. A., 33
Was, G. S., 739
Watanabe, H., 859, 1186
Watanabe, S., 919, 1147
Welzel, S., 435
Wikle, H. C., III, 935
Wootton, M. R., 295, 366

X

Xu, Q., 516, 836
Xu, Y., 69, 118

Y

Yamaguchi, S., 560
Yamamoto, N., 713
Yamamoto, S., 1176
Yamashita, S., 756
Yanagita, S., 516
Yang, W., 69
Yasunaga, K., 1186
Yoon, K. K., 76
Yoshida, N., 1186
Yoshiie, T., 516, 836
Yu, Q., 118

Z

Zhang, C., 69, 118
Zhang, X. J., 177
Zinkle, S. J., 1226

Subject Index

A

Accelerator, linear, 1043
Accelerator Production of Tritium, 1109
Aging, 343, 354, 1137
Alloy 718
Alpha-ferrite, 894
Alpha-iron, 1029
Aluminum alloy, 1093, 1137
  vanadium-titanium-chromium-silicon-aluminum-yttrium, 1197
Aluminum corner cubic reflector, 1176
Aluminum oxide, 988
American Iron and Steel Institute
  AISI 304, 884, 944, 959
  AISI 316, 944, 1093
    alpha-ferrite formation, 894
    coated, 1075
    creep, 645, 655, 667
    creep-fatigue response, 713
    fracture toughness, 1243
    friction welded joints, 988
    grain boundary chromium depletion, 801
    mechanical properties, 988
    mechanical properties evolution, 1003
    microstructure modeling, 816
    neutron-induced evolution, 1003
    shear punch-tensile yield strength correlation, 1018
    stress modified welding, 935
    tensile tests, 1018
    void formation, 756
    void volume fraction, 699
Amorphization, 1147
Amorphization of solids, 1122
Annealing, 3, 98, 792, 1062
  gamma-irradiation, 525
  helium implanted stainless steel, 973
  low copper steel, 435
  martensitic steel, 448
  stepped measurements, 1109
  thermal, 1029, 1147
  VVER, 323, 415, 460
  WF-70, 306
ASME Boiler and Pressure Vessel Code, 127, 306
  K_{IC} curves, 143
  SA533B, 383
ASTM standards
  A 302B, 33, 162
  A 508, 69
  A 533B, 560
  E 208, 235
  E 900, 33, 76
  E 1921, 127, 143, 162, 177
Atomic disorder, 1131
Atomic displacement cascade, 1122
Atomic order, long and short range, 1122
Atom probe, 435
Auger spectroscopy, 473
Austenitic steels, 713, 739, 801
  fracture toughness, 1243
  irradiation creep, 645, 679
  microstructure modeling, 816
  segregation, composite model, 919
  swelling, 655
  void swelling, 767, 778

B

Bead on tube welding test, 973
Beryllium, 1051, 1062
  steel/copper/beryllium layers, 1093
Boiling water reactor, 548, 801
BOR-60 fast reactor, 645, 792
Boron, 612, 645, 679, 1226
  pyrolitic boron nitride, 1084
  transmutation, 366
BR3 reactor, 162

British Prototype Fast Reactor, 778
Burgers vector anisotropy, 535

C

Cadmium, 366
Carbon, 645, 778
  iron-phosphorus-carbon, 473
Cascade
  atomic displacement cascade, 1122
  displacement cascade simulations, 548
  vacancy clusters, 1186
Ceramics
  coatings, 1075
  pyrolitic boron nitride, 1084
Charpy impact, 162
  behavior, 579, 612
  energy, 76
Charpy notch toughness, 56
Charpy specimens, precracked, 279, 295
Charpy v-notch, 127, 266, 415, 626
  ductility, 16
  impact, 33, 118
  instrumented, 245
  transition curves, 306
Charpy v specimens, precracked, 204
Charpy v transition curves, 98
Chinese RPV steel, 118
Chinese simulated forged cylinder, 69
Chromium
  chromium-molybdenum steel, 343
  chromium-molybdenum-vanadium forgings, 16
  chromium-nickel, 874
  chromium-nickel-molybdenum, 399
  chromium-nickel-molybdenum-niobium, 645, 679
  chromium-tungsten, 448
  copper-chromium-zirconium, 1093, 1243
  depletion, 801
  iron-chromium-nickel, 739, 767, 859
  iron-chromium-nickel-titanium, 792
  steel, 579, 597, 612
  vanadium-chromium, 1212
  vanadium-titanium-chromium, 1197, 1212
  vanadium-titanium-chromium-silicon-aluminum-yttrium, 1197
Cladding, fuel, 1159
Cladding properties, 220
Coatings, ceramic, 1075
Composite model, 919
Composites, polymer matrix, 1043
Conductivity, radiation induced, 1075
Copper, 3, 33, 118, 235, 306, 836
  alloy, 1093, 1226, 1243
  copper-chromium-zirconium, 1093, 1243
  copper-manganese-molybdenum steel, 366
  copper-manganese plate steel, 366
  copper-nickel-manganese-silicon clusters, 435
  copper-stainless steel joints, 988
  creep regularities, 725
  iron-copper, 492, 516, 1029
  oxygen-free, 988
  precipitates, 366, 492, 560
  steel, 435
Correlation monitor materials, 33
Crack arrest, 245
Crack formation, 973
Cracking, intergranular, 944
Cracking, weld, 935
Crack notch, fatigue, 713
Cracks, 959
Crack tip constraint, 177
Creep, 688
  coefficients, 655
  fatigue, 713
  irradiation, 535, 645, 655, 667, 679
  regularities of copper, 725
Cross-linking, 1043

Crystallization temperature, thermal, 1147
Cyclotron, 1226

D

Damage, 1131
Damage analysis, 87
Damage dose, high, 645
Damage prediction, reactor vessel materials
E 900, 33, 76
Damage production, 548
Damage rate, 816, 836
Damage structures, 516
Dedicated electron beam facility, 1043
Defect clusters, 850
Defect free zones, 919
Defect production cross sections, 548
Deformation, 143, 1186
mechanisms, 1243
rate, 688
Degradation, neutron induced, 525
Degradation, radiation induced electrical, 1075
Density, alloy, 1212
DIN 1.4970, 778
Diffraction, neutron, 1122, 1131
Dislocations, 688, 725, 919
density, 679
line, 1186
loops, 354, 597, 816, 836
sliding, 725
stress-affected, 850
Displacement cascade simulations, 548
Displacement damage, 626
Displacement measuring system, 713
Displacement model 548
Displacement rate, 884
Doppler broadening, 354
Drop weight nil ductility transition, 306
Drop weight tests, 235
Ductile-to-brittle transition, 460
irradiation effect during, 204
temperature, 399, 597, 612
chromium steel, 579
heat-affected zone specimen, 266
small punch test evaluation, 626
toughness, 177
Ductility, 579, 612, 894, 1003, 1093
post-irradiation, 1197

E

Eastern steels, 3
EBR-II, 767, 1051, 1062
Electrical degradation, radiation-induced, 1075
Electrical insulator, 1075
Electrical resistivity, 1075
Electric Power Research Institute, 127
Electric power, thermoelectric, 1029
Electron beam facility, 1043
Electron microscopy, 492
high voltage, 699
Embrittlement, 3, 383, 399, 548
A 302B, 33
A 508, 69
A 533B-1, 33
AISI 304, 884
assessment model, 460
E1-847, 874
ferritic-martensitic steel, 579, 612
helium, 448, 1226
iron-phosphorus-carbon alloy, 473
low alloy steel, 87
neutron-induced, 235
prediction and measured, 76
recovery prediction, 435
reirradiation, 415
thermal neutron influence on, 366
void-induced, 874
VVER-440, 323, 460
WF-70, 306
Energy dispersive X-ray microanalysis, 343
European Fusion Technology Programme, 597

Experimental Breeder Reactor II, 767, 1051, 1062

F

Fast Flux Test Facility, 655, 1212
Fast Flux Test Facility/Materials Open Test Assembly, 535, 667, 1003
Fast high-frequency treatment, 1159
Fatigue crack starter notch, 713
Fatigue, in-beam creep-fatigue tester, 713
Fault formation, stacking, 1084
Ferrite, 884
Ferritic-martensitic steel, 535, 579, 597, 612, 1093a
Ferritic steel, 548, 1029, 1093
  ASTM E 208, 235
  ASTM E 1921, 127, 143, 162, 177
  ASME SA533B, 383
  JFMS, 535
Field emission gun scanning transmission electron microscopy, 343, 383, 801
Finite element model, 1018
Floating curve model, 460
Foil specimen, 1147
Foil surfaces, 699
Ford nuclear reactor, 16
Forging matrix, 118
Forging ring, 69, 98, 235
Fracture analysis, 597
Fracture mechanics, elastic plastic, 143
Fracture resistance curves, 1243
Fracture toughness, 127, 162, 245, 415, 579
  copper alloys, 1243
  irradiation effect in transition range, 204
  prediction, 76
  shifts, 279
  static, 56, 220, 612
  submerged arc weld samples, 295
  thermal annealing effects, 306
Frank loops, 850
French steel, 435
Friction welding method, 988
Fusion zone cracking, 935

G

Gamma ray intensity control, 525
Gas tungsten arc welding, 935
German austenitic steel, 778
Gibbon statistical scheme, 1131
Gold, 836
  gold-coated mirror, 1176
Grain boundary, 343, 801, 919, 973
  composition, 473
  energy release, 1084
  segregation, 383, 399
Graphite, 525

H

Hafnium, 756
Halden reactor, 366
Hardening, 366, 612, 1186
  ferritic-martensitic, 579
  iron-copper alloy, 492
  iron-phosphorus-carbon, 473
  martensitic, 597
  reduced-activation martensitic steel, 448
Hardness measurements
  Micro-Vickers, 266, 560
  Vickers, 626
Heat-affected zone, 266, 944, 959
Heat sink material, 988
Heavy Section Steel Technology Program, 415
Helium, 935, 959
Helium bubbles, 597, 944, 973
Helium embrittlement, 448, 1226
Helium generation, 1062
Helium implantation, 626
Helium release, 1062, 1109
High flux isotope reactor, 1212
High flux reactor, 579, 597, 612
High voltage electron microscope, 699
Hoop stress, 778
Hot isostatic pressing, 1243
HT-9, 935
Hungary VVRSZM-5 research reactor, 1137
Hydrogen release, 1109

Hyperbolic tangent fitting model, 33

I

Impact, 1093
Impact tests, 597
Impurity effects on radiation creep rate, 688
Intergranular fracture, 473
Interstitial atom, 688
Interstitial loops, 816
Iron alloys, 473, 548
  alpha-ferrite, 894
  ferrite, 884
  iron-chromium-nickel, 739, 767, 859
  iron-chromium-nickel-titanium, 792
  iron-copper, 492, 516, 560, 1029
  iron-phosphorus-carbon, 473
  iron-silicon, 492
  zirconium-niobium-tin-iron, 1159
Iron lattice, 323
Isostatic pressing, high temperature, 1093
Isostatic pressing, hot, 1243
ITER, 1093, 1243

J

Japanese curve, 204
Japanese steel, 204
  SA 508-3, 118
Japan Materials Testing Reactor, 204, 266, 492, 988, 1075, 1176
JFMS duplex ferritic steel, 535

K

KU quartz, 1176
Kyoto University Reactor, 836

L

LAHET code system, 1109
Life cycle management, 525
Light water reactor, 33
Linear accelerator, 1043
Loading, 713
  biaxial, 177
Los Alamos National Laboratory, 1109

M

Magnesium
  aluminum-magnesium, 1137
  magnesium oxide-aluminum oxide, 1075
Magnetic response, 894
Magnox reactor pressure vessel, 295
Manganese
  copper-manganese-molybdenum, 366
  copper-manganese plate, 366
  copper-nickel-manganese-silicon clusters, 435
  manganese-molybdenum
    A 302, 33, 162
    A 533B, 33, 177, 204, 560
  steel alloys, 894
Martensitic steel, 448, 597, 1093
Master curve, 127, 143, 177, 204, 279
  ASTM method, 306
  transition temperature, 245
Material test reactor database, 33
Matrix defects, 118
Medical devices, 1043
Micro-indentation, 1186
Microstructure, 323, 435, 597
  beryllium pebbles, 1051
  dislocation, 850
  evolution, 778, 816, 859, 919, 1212
  ferritic steel, 535
  modeling, 816
  radiation damaged, 959
  radiation-induced changes, 354, 894
  tantalum, 1186
  thermally aged iron-copper alloy, 492
Micro-Vickers hardness measurements, 266
Microvoid, 560, 836
Midland Unit I, 306
Mirror, gold-coated, 1176

Molybdenum
A 302, 33, 162
A 533B, 33, 177, 204, 560
chromium-molybdenum, 343
chromium-molybdenum-vanadium, 16
chromium-nickel-molybdenum-niobium, 645, 679
chromium-nickel-molybdenum, 399
copper-manganese-molybdenum, 366
corner cubic reflector, 1176
molybdenum-SIA, 801
Monte Carlo calculations, 1109

N

National Research Institute for Metals, 713
Naval Surface Warfare Center, master curve tests, 177
Neutron multiplier, 1051, 1062
Neutron spectra, 473
Neutron spectrum effect, 87, 548
Nickel, 3, 448, 836
A 302, 33, 162
chromium-nickel-molybdenum, 399
chromium-nickel-molybdenum-niobium, 645, 679
copper-nickel-manganese-silicon clusters, 435
iron-chromium-nickel, 739, 767, 859
iron-chromium-nickel-titanium, 792
nickel-containing steel, 894
nickel-modified A-302 grade B, 162
segregation, 884
titanium-nickel, 1147
titanium-nickelide, 1131
zirconium-niobium-tin-iron, 1159
Nil-ductility transition temperature, 245
Niobium
chromium-nickel-molybdenum-niobium, 645, 679
niobium stabilized chromium-nickel, 874
Nondestructive testing, ferritic alloys, 1029
Novovoronesh-1 reactor, 98

O

Oak Ridge National Laboratory, 177
73W weld material tests, 279, 415
Oak Ridge Research Reactor, 935
Optical components, 1176
Optical element, 1176
Optical microscopy, 1051
OSIRIS test reactor, 87
Oxygen free copper, 988

P

Pacific Northwest National Laboratory, 655, 1109
PAS, 354
Phase diagrams, stainless steel alloys, 894
Phase instability, void-induced, 884
Phase stability, 1212
Phase transformation, 1147
Phénix fast reactors, 655
Phosphorus, 3, 16, 343, 366, 473
grain boundary, 473
iron-phosphorus-carbon, 473
segregation, 383, 399
Plasma diagnostic components, 1176
Point defects, 323, 548, 688, 850, 1131
solute complexes, 801
Polymer matrix composites, 1043
Positron annihilation, 560, 836
lifetime spectrometry, 448
measurements, 354
Positron lifetime measurement, 516, 560
Power reactor database, 33
Precipitates, 323, 366, 492, 756
copper, 366, 492, 516, 560
Pressure temperature curves, 76
Pressure Vessel Research Council, 127
Pressurized tube experiment, 778

Pressurized water reactors, 3, 87, 118, 792
attenuation behavior, 548
end-of-life conditions, 874
first Russian, 98
microstructural evolution, 816
Novovoronesh-1 reactor, 98
Russian, 874
void swelling, 884
Prime Candidate Alloy, 935
Property-property correlation, 1018
Prototype Fast Reactor, British, 778
Punch test, small, 626

R

Radiation resistance, 16
Raman spectroscopy, 1084
Rate theory, 548, 816, 836
Reference materials, 33
IAEA, 220
Reference temperature, 279
Refraction spectrum, 1176
Ring forging, 69, 98, 235
Root bend test, 944
Russian alloys, 1159
Russian codes, 3
Russian steel, 415, 874

S

Sandvik HT-9, 935
Sapphire, 1176
Saturation, 767
Scanning electron microscopy, 597, 1051
Scattering, 33
small angle neutron (SANS), 323, 435
Segregation modeling, 383
Segregation, radiation-induced, 739, 801, 919
Shape memory alloy, 1147
Shear punch, 1003
shear punch-tensile yield strength, 1018
Side bend test, 944
Silicon, 778, 859
carbide, 525
copper-nickel-manganese-silicon clusters, 435
vanadium-titanium-chromium-silicon-aluminum-yttrium, 1197
SILOE CEA test reactor, 87
Single edge bend testing, 177
Site competition, 383
Small punch tests, 626
Soderberg theorem, 778
Solids amorphization, 1122
Solute addition, 756, 919
Specimen reconstitution, 56
SPECTRA, 548
Spectrometry, positron annihilation lifetime, 448
Spectroscopy, auger, 399, 473
Spinoidal-like decomposition, 859
Stacking fault formation, 1084
Steels (See also specific types), 56, 245, 279
15Kh2MFA, 220, 323
AMCR, 894
austenitic, 645, 713, 739, 778, 1243
Chinese domestic, 118
E1-847, 874
eastern, 3
EP-172, 679
Heavy Section Steel Technology Program, 415
Japanese SA 508-3, 118
low alloy, 87, 399
low copper, 435
plate, 366
Russian, 16, 874
stainless steel, 874, 973
dislocation development, 850
duplex, 1029
microstructural evolution, 859, 919
Type 316 (see AISI 316)
western, 3
X18H10T, 792
Sterilization, 1043
Strain rate, 667
Stress-affected dislocations, 850
Stress, applied, 679
Stress control, 713

Stress dependence, 725
Stress, effects on mechanical properties, 713
Stress-enhanced swelling, 655, 679, 778
Stress, internal, 699
Stress-modified welding, 935
Structural transformations, radiation-induced, 1084
Surface roughness, 1176
Surveillance capsules, 87, 143
Surveillance programs, 204, 235, 354, 1137
  reactor databases, 33
  specimens, 56, 220
Swelling, 645, 667, 699, 1212
  austenitic steels, 655, 679
  stress-induced, 778
  suppression, 756
  void, 739, 767, 778, 792, 874, 884

T

Tantalum, 1186
TEM disks, 1003
Temperature dependence, copper creep rates, 725
Tensile properties, 448, 612, 1003, 1018, 1197, 1226
Tensile specimens, 235, 1003, 1243
Tensile strength, 988, 1243
Tensile stresses, 973
Tensile tests, 162, 597, 944, 1093, 1197, 1243
Tensile yield strength, 1018
Tension tests, 988
Thermal aging, 473, 492, 560, 1029
Thermal annealing, 1147
  effects, 306
Thermal crystallization temperature, 1147
Thermal neutrons, 366
Thermoelectric power, 435, 1029
Three point bending, 162, 279, 1243
Through wall trepans, 98
TIG welded stainless steel, 959
Tin alloys
  zirconium-niobium-tin-iron, 1159
Titanium, 778, 859
  iron-chromium-nickel-titanium, 792
  nickelide, 1131
  titanium-nickel, 1147
  vanadium-titanium-chromium, 1212
  vanadium-titanium-chromium-silicon-aluminum-yttrium, 1197
Tomographic atom probe, 435
Toughness index, 127
Transition range, temperature determination, ferritic steel
  E 1921, 127, 143, 162, 177
Transition temperature, 33, 56, 306
  Charpy, 473
  drop-weight nil ductility, 127
  ductile-brittle, 399, 597, 612
    chromium steel, 579
    heat-affected zone specimen, 266
    small punch test evaluation, 626
    toughness, 177
  elevation, 16
  shift, 118, 245
  shifts, VVER steels, 56
  VVER-440 steels, 460
Transmission electron microscopy, 354, 516, 597
  beryllium pebbles, 1051
  disks, 1003
  TEM-invisible defects, 1186
  void structure analysis, 778
Transmission microscopy, 473
Transmission spectrum, 1176
Transmutation, vanadium, 1212
Trend curves, 366
Trepans, 162
  through wall, 98
Tube specimens, pressurized, 535
Tungsten
  chromium-tungsten steel, 448
  tungsten targets, 1109
Twinning, 492

U

Upper shelf energy, 16, 266, 279, 306, 597, 612
U.S. Naval Academy, master curve tests, 177
U.S. Nuclear Regulatory Commission, 177
  regulatory guide, 3, 33, 306
    transition temperature elevations, 16
U.S.-Russia Joint Coordinating Committee for Civilian Nuclear Reactor Safety, 415
Uniform elongation, 1197
Upper shelf energy, 16, 579, 612

V

Vacancy, 354, 560, 688
  binding, 756
  clusters, 836, 1186
  concentrations, 739
  diffusion, 739
  flux, 699
  migration distance, 516
Vanadium, 836
  chromium-molybdenum-vanadium forgings, 16
  vanadium-chromium, 1212
  vanadium-titanium-chromium, 1197
  vanadium-titanium-chromium-silicon-yttrium, 1197
Voids, 679, 688, 836
  denuded zone, 699
  formation, 756
  growth, 884
  microvoid, 560
  phase instability, 884
  shrinkage, 699
  strength, 1186
  structure analysis, 778
  swelling, 739, 767, 792, 859, 874, 884
Von Mises yield criterion, 1018
VVER, 98, 354, 399
  welds, 415
VVER-440 reactor, 16, 323, 415, 460
  VVER-440/V-213, 56, 220
VVER-1000, 56, 415
VVRSZM-5 research reactor, 1137

W

Weakest link theory, 204
Weibull distribution, 204
Weldability test, 944
Welds, 76, 87, 220, 973
  73W, 279
  core, 98
  cracking, 935, 959
  friction welding method, 988
  joints, 944
  multi-layer, 944
  stress-modified welding, 935
  submerged arc, 235, 295, 306
  SZAV-1, 1137
  upper shelf energy, 245
  VVER, 415
  WF-70, 245, 306
Western steels, 3
WWER, 3

X

X-ray diffraction, 1084, 1122, 1159
X-ray diffractometry, 894
X-ray microanalysis, energy dispersive, 343

Y

Yield strength, 850, 1003, 1018, 1197
Yield stress, 473, 579, 850
  copper, 725
  increase, 626, 1197
  shifts, 366
Yttrium
  vanadium-titanium-chromium-silicon-aluminum-yttrium, 1197

Z

Zircaloy, 1159
Zirconium, 756
  copper-chromium-zirconium, 1093, 1243
  zirconium-niobium, 1159
  zirconium-niobium-tin-iron, 1159